Université du Québec
Institut national de la Recherche scientifique
Centre – Eau Terre Environnement

MOBILITÉ DES ÉLÉMENTS ET FORMATION DE GÎTES POLYMÉTALLIQUES AU SEIN DES SYSTÈMES À OXYDES DE FER ET ALTÉRATION EN ÉLÉMENTS ALCALINS, ZONE MAGMATIQUE DU GRAND LAC DE L'OURS, TERRITOIRES DU NORD-OUEST, CANADA

Par

Jean-François MONTREUIL

Doctorat en sciences de la Terre, *Philosophiae doctor,* Ph.D.,
Programme interuniversitaire de doctorat en sciences de la Terre – INRS-ETE et Université Laval

Jury d'évaluation

Président du jury et examinateur interne	Georges Beaudoin Université Laval
Examinateur externe	James Franklin Franklin Geosciences
Examinateur externe	Roger Skirrow Geoscience Australia
Directrice de recherche	Louise Corriveau Commission Géologique du Canada
Codirecteur de recherche	Pierre-Simon Ross INRS Centre Eau Terre Environnement

REMERCIEMENTS

Je tiens à remercier chaleureusement ma directrice de thèse, Louise Corriveau, qui m'a donné cette opportunité unique de me familiariser avec les gisements à Oxydes de Fer–Cuivre–Or et de faire des travaux de terrain aux Territoires du Nord-Ouest. Sa disponibilité tout au long de ma thèse et sa contribution majeure dans mon cheminent en géologie et professionnel ont aussi été fort appréciés. Je remercie également Pierre-Simon Ross pour sa co-direction soutenue et la qualité de ses commentaires et suggestions lors de la rédaction de ma thèse.

Des remerciements particuliers sont adressés aux membres du jury de cette thèse, Georges Beaudoin, James Franklin et Roger Skirrow, aux réviseurs Christopher Lawley, Isabelle McMartin, Hamid Mumin, Patrick Williams et Gary Davidson pour certains chapitres soumis pour publication. Vos contributions ont fortement amélioré cette thèse et ont su y apporter une vision complémentaire à la mienne et celle de mes superviseurs qui fut fort appréciée.

Je tiens aussi à remercier tous les intervenants de la Commission géologique du Canada ainsi que les collaborateurs venant d'autres institutions académiques, gouvernementales et privées impliqués dans le projet Gisements à métaux multiples/IOCG **– Région du Grand lac de l'Ours** de la Commission géologique du Canada et du Bureau géoscientifique des Territoires du Nord-Ouest (NTGO) pour leurs contributions à cette thèse, plus particulièrement : Pedro Acosta, Georges Beaudoin, Pierre Brouillette, Carl Clouter, Bill Davis, Anthony De Toni, Randy Enkin, Étienne Girard, Eric Grunsky, Nathan Hayward, Simon Jackson, John Kerswill, Kathleen Lauzière, Isabelle McMartin, Philippe Normandeau, Ewan Pelleter, Eric Potter ainsi que Valerie Jackson et Luke Ootes du NTGO. Plusieurs organismes ont contribué à financer cette recherche et la diffusion de ses résultats ou à en permettre la réalisation en plus des organismes mentionnés ci-haut dont le Conseil de recherche en sciences naturelles et en génie du Canada, le Fonds québécois de la Recherche sur la Nature et les Technologies, le réseau de Diversification de l'Exploration minérale du Québec (DIVEX), l'INRS, Québec 2008, Fortune Minerals Limited, l'Institut de Recherche Aurora et le Wek'eezhii Land and Water Board.

Je tiens à remercier Marie-Hélène, mon épouse, qui m'a appuyé, mais aussi dans certaines situations, enduré, lors de la rédaction de cette thèse de doctorat.

RÉSUMÉ

Les gisements polymétalliques à Oxyde de Fer–Cuivre–Or (IOCG) ainsi que les gisements affiliés au sein de systèmes hydrothermaux régionaux à oxydes de fer et altération en éléments alcalins représentent des cibles d'exploration prometteuses dans plusieurs provinces géologiques canadiennes ainsi qu'à travers le monde. Toutefois, les territoires ciblés ont été jusqu'à présent faiblement explorés et dans plusieurs cas, les connaissances géologiques y sont fragmentaires et/ou acquises avant l'identification des gisements IOCG. Les districts IOCG se caractérisent aussi par de nombreux indices minéralisés d'associations métallifères diverses qui généralement ne sont pas intégrés au sein d'un modèle métallogénique unifié. Cette situation réduit les probabilités de reconnaître le potentiel IOCG de certaines provinces géologiques. Cette thèse de doctorat propose de nouvelles approches d'exploration pour les gîtes IOCG qui découlent de recherches dans une région d'étude canadienne. Les méthodes proposées aident à cibler, à l'échelle d'une région ou d'un gisement, les zones d'un système hydrothermal à oxydes de fer et altération en éléments alcalins (IOAA) ayant le plus haut potentiel de découverte de gîtes IOCG ou affiliés. Cette approche aide aussi à prédire les types de minéralisations qui peuvent s'y retrouver en fonction des altérations observées. Sont ainsi étudiés les gîtes à oxyde de fer apatite, les gîtes d'uranium encaissé dans des albitites, certains skarns et les gîtes IOCG à magnétite et à hématite.

Les contributions de cette thèse sont basées sur les systèmes IOAA de la zone magmatique du Grand lac de l'Ours (GBMZ), située aux Territoires du Nord-Ouest (Canada), et des études comparatives avec des systèmes IOAA retrouvés à travers le monde. La GBMZ comporte des édifices volcano-plutoniques et des batholites d'affinité calco-alcaline à shoshonitique et est interprétée comme un arc continental paléoprotérozoïque. Elle s'est formée entre 1,87 et 1,84 Ga sur les roches volcano-plutoniques et méta-sédimentaires du terrane d'Hottah accrétées au Craton de l'Esclave lors de l'orogenèse caldérienne à 1882 Ma. De nombreux systèmes IOAA, dont plusieurs contiennent des indices ou des gisements IOCG et affiliés, se sont formés le long de la GBMZ, principalement entre 1873 et 1866 Ma.

L'altération hydrothermale dans les systèmes IOAA évolue systématiquement d'altération sodique d'extension plurikilométrique vers des altérations de haute température (HT) calcique–fer, HT potassique–fer, de faible température (LT) potassique–fer et LT calcique–fer. Ces stades d'altérations sont typiquement suivis d'altérations épithermales et de veines de quartz communément minéralisées. Chaque altération IOAA documentée dans la GBMZ est caractérisée par une signature chimique et des enrichissements en métaux distincts. Les zones d'altérations sodiques sont principalement distribuées en marge des zones minéralisées, car elles sont formées plus près des centres thermiques du système et le long de plusieurs failles majeures de la région. L'altération sodique forme généralement des zones de lessivage pour plusieurs éléments. L'altération HT calcique–fer est caractérisée par d'importants enrichissements en Fe et dans certains secteurs en éléments du groupe des terres rares (ÉTR) et en vanadium, pouvant mener à la formation de gîtes de fer riches en ÉTR et/ou vanadium. Les métaux tel que le cobalt, le cuivre et le nickel peuvent aussi être faiblement à modérément enrichis à ce stade, mais en quantité insuffisante pour former des zones minéralisées d'importance. Les altérations calcique–fer–potassique, HT potassique–fer et LT potassique–fer, lorsqu'intenses et avec une étendue spatiale hectométrique à kilométrique, sont principalement associées à la formation de minéralisations IOCG et de gîtes d'uranium encaissés dans des albitites.

L'intensité de l'altération hydrothermale dans les systèmes IOAA de la GBMZ combinée à la formation de gîtes IOCG, d'uranium encaissé dans des albitites, d'oxyde de fer–apatite potentiellement riches en ÉTR et vanadium et de minéralisations polymétalliques épithermales

tardives calquent le portrait métallogénique des systèmes IOAA contenant des gîtes IOCG de classe mondiale. La GBMZ, avec ses nombreux systèmes IOAA potentiellement fertiles en divers styles de minéralisations polymétalliques, devient une cible attrayante pour l'exploration pour les gîtes IOCG, d'uranium encaissés dans des albitites et de fer±ÉTR–vanadium.

ABSTRACT

Iron oxide copper–gold (IOCG) and affiliated deposits are promising targets for geological exploration in many Canadian geological provinces, but also across the world. However, because metallogenic models for IOCG exploration were only recently developed, exploration and discoveries of IOCG and affiliated deposits have been hampered in under-explored territories and terrains where the geological knowledge is incomplete and/or where the main exploration and mapping campaigns took place before the recognition of the IOCG deposit clan. The formation of polymetallic showings with diversified metal associations characterizes many IOCG districts. However the relations between the showings are generally not integrated in a unified metallogenic model, minimizing the chances to recognize the IOCG potential of certain geological provinces. This thesis proposes new geological and geochemical methods for IOCG exploration in iron oxide alkali altered (IOAA) hydrothermal systems based on recent research in the Canadian IOAA province of the Great Bear magmatic zone (GBMZ; Northwest Territories). The methods developed in this thesis facilitates the recognition of the prospective sectors of an IOAA system at regional to deposit scales and the prediction of the metal assemblages likely to be found in potential ore zones. This thesis particularly focuses on iron oxide–apatite, albitite-hosted uranium deposit, some Zn–Pb–(Cu) skarns and magnetite to hematite group IOCG deposits.

The results and interpretations presented in this thesis are drawn from the IOAA systems of the GBMZ and comparative studies with other IOCG deposits around the world. The GBMZ is a volcano-plutonic belt of calc-alkaline to shoshonitic affinity interpreted as a paleoproterozoic continental volcanic arc. It was formed between 1.87 and 1.84 Ga on the volcano-plutonic and metasedimentary rocks of the Hottah terrane, accreted to the Slave Craton at 1882 Ma during the Calderian orogeny. Many IOAA systems comprising IOCG and affiliated mineralization and deposits were formed in the GBMZ mostly between 1873 and 1866 Ma.

Hydrothermal alteration in the GBMZ IOAA systems follows a systematic evolution sequence from regional-scale sodic alteration in the early stages to high temperature (HT) calcic–iron, HT potassic–iron and then to low temperature (LT) potassic–iron and LT calcic–iron alteration. Epithermal alteration and quartz veins typically followed the main IOAA alteration stages to form additional zones of mineralization in which the metal associations typically reflect the metal associations documented in their host IOAA alteration. Each hydrothermal alteration formed in an IOAA system has a specific chemical signature and distinct metal assemblages. Sodic alteration is formed close to the thermal centers and along regional structures of an IOAA district and is generally a leaching stage. It is characteristically external to the IOCG mineralization zones, either because of differential exhumation or its far larger spatial distribution. HT calcic–iron alteration is characterized by important iron enrichment and can be associated with substantial rare earth elements (REE) and vanadium enrichments that may lead to the formation of iron oxide–apatite (IOA) deposits enriched in vanadium and/or REE. Cobalt, copper and nickel can also be incipiently to moderately enriched at the HT calcic–iron alteration stage, but not to the extent of forming significant mineralized zones. Calcic–iron–potassic, HT potassic–iron and LT potassic–iron alteration stages are, where intense and hectometer to kilometer in scale, associated with IOCG and albitite-hosted uranium mineralization.

The intensity of hydrothermal alteration in the GBMZ IOAA systems combined with the formation of IOCG, albitite-hosted uranium, IOA potentially endowed in vanadium and REE, and polymetallic epithermal mineral deposits mimic the metallogenic portray of the IOAA districts elsewhere in the world that comprise world class IOCG or affiliated deposits. This makes the GBMZ an attractive target for mineral exploration.

Mots-clés français: Zone magmatique du Grand lac de l'Ours; Altérations hydrothermales; Oxydes de fer–cuivre–or; IOCG; Oxydes de fer et altération en éléments alcalins; IOAA; Oxydes de fer–apatite; IOA; Uranium encaissé dans des albitites; Géochimie; NICO; Sue-Dianne; Kiruna

Mots-clés anglais: Great Bear magmatic zone; Hydrothermal alteration; Iron oxide copper–gold; IOCG; Iron oxide alkali-altered; IOAA; Iron oxide–apatite; IOA; Albitite-hosted uranium; Geochemistry; NICO; Sue-Dianne; Kiruna

TABLE DES MATIÈRES

LISTE DES FIGURES

LISTE DES TABLEAUX

MOBILITÉ DES ÉLÉMENTS ET FORMATION DE GÎTES POLYMÉTALLIQUES AU SEIN DES SYSTÈMES À OXYDES DE FER ET ALTÉRATION EN EN ÉLÉMENTS ALCALINS, ZONE MAGMATIQUE DU GRAND LAC DE L'OURS, TERRITOIRES DU NORD-OUEST, CANADA

PREMIÈRE PARTIE : SYNTHÈSE

CHAPITRE 1 : Synthèse

«*a new interest was arising in the exploration and development of the northern parts of the Dominion of Canada. This was perhaps most evident among men of the mining industry, whose interest has always been aroused by the stories told by returning explorers and travellers of the evidences of mineral wealth that occur here and here throughout that vast northern region*.»

Charles Camsell (1916)

«*out of a total area of continental Canada of about 3,209,000 square miles, about 900,000 square miles must still be considered as unexplored*»

Charles Camsell (1918)

Et pourtant encore d'actualité un siècle plus tard

1.1 Introduction

Les gisements à oxyde de Fer–Cuivre–Or (IOCG) représentent des cibles d'exploration prometteuses dans plusieurs provinces géologiques canadiennes, dont certaines demeurent faiblement explorées ainsi que dans certains districts métallogéniques très bien définis tant au Canada qu'à travers le monde (Hitzman et al., 1992; Williams et al., 2005; Corriveau, 2007; Corriveau et al., 2010a; Porter, 2010). Les gisements IOCG sont polymétalliques (Cu, Au, U, éléments du groupe des terres rares légères, F, Ag, Bi, Co, W, Mo, etc.), géologiquement complexes et associés à l'échelle régionale à des indices aux associations métallifères communément inusitées et à des zones décamétriques d'altérations hydrothermales très diversifiées. L'absence de modèles métallogéniques régionaux unifiant les diverses minéralisations formées dans un district IOCG aux stades d'altérations hydrothermales caractéristiques au développement d'un district IOCG ont grandement contribué à la faible

représentation de ces gisements dans le portfolio métallogénique canadien (Corriveau et Mumin, 2010; chapitre 3).

Les gisements IOCG sont définis comme étant le pôle minéralisé en Cu et Au d'un groupe plus général de gîtes hydrothermaux, les gîtes à oxyde de fer et altération en éléments alcalins (iron oxide alkali-altered de Porter, 2010), une terminologie abréviée par IOAA et utilisée ici pour les systèmes hydrothermaux qui les encaissent et dont ils sont une conséquence. Cette classification a l'avantage de réconcilier les nombreuses différences entre les signatures métallifères retrouvées dans les gisements IOCG *sensu stricto* (Groves et al., 2010; Williams, 2010a) et les gisements couramment affiliés aux IOCG *sensu stricto* (Mumin et al., 2010; Williams, 2010a) en utilisant l'altération hydrothermale à éléments alcalins (sodique et potassique), couramment riche en oxyde de fer, comme dénominateur commun pour identifier et discriminer ces systèmes. Temporellement et spatialement, l'évolution de l'altération hydrothermale et de certaines associations métallifères sont généralement reproductibles et spécifiques entre différents systèmes IOAA. Ces relations spatio-temporelles sont bien démontrées dans les systèmes IOAA de la Zone magmatique du Grand lac de l'Ours (GBMZ), sujet de la présente thèse, et les analogues mondiaux (Hitzman et al., 1992; Barton et Johnson, 2000; Williams et al., 2005; Porter, 2010; Skirrow, 2010; Williams, 2010a, b),

Les altérations hydrothermales, communes entre les différents systèmes IOAA, reflètent les processus physico-chimiques qui régissent les interactions fluides aqueux–roches tels que:

1. l'influence de la composition du protolite,
2. la mobilité différentielle des éléments lors des différents stades d'altération,
3. les structures perméables préexistantes ou syngénétiques,
4. les sources des fluides,
5. les sources des métaux,
6. la température et gradients géothermiques,
7. la nature des ligands, etc.

L'étude des altérations et des minéralisations associées à chaque stade d'altération permet donc de quantifier ou qualifier l'influence des principales variables qui régulent la signature métallique des gisements formés au sein d'un système IOAA.

Pour tracer le portrait complet d'un système IOAA, le système étudié doit préserver et exposer les relations entre les divers types d'altérations hydrothermales et les divers types de

minéralisations. Comme ces systèmes sont de dimensions décakilométriques et que la distribution régionale des faciès d'altérations et des zones de minéralisations est généralement hétérogène à l'échelle du district, les affleurements de qualité doivent être abondants pour couvrir l'ensemble d'un système IOAA. La GBMZ (Figs. 1-1 et 1-2), située aux Territoires du Nord-Ouest (Canada), est la province géologique ayant le plus grand nombre de systèmes IOAA et de minéralisations IOCG connus au Canada (Hildebrand, 1986; Gandhi, 1989, 1992a, 1992b, 1994; Gandhi et Lentz, 1990; Readron 1992; Gandhi et Prasad, 1995, 1997; Goad et al., 2000a, b; Mumin et al., 2007, 2010; Corriveau et al., 2010a, 2010b).

Cette ceinture volcanoplutonique, interprétée comme un arc magmatique continental, et formée entre 1,87 et 1,84 Ga (Hildebrand et al., 1987, 2010a; Gandhi et al., 2001), s'étend selon un axe nord-sud sur plus de 1200 km et affleure sur une longueur de 450 km, principalement entre le Grand lac de l'Esclave et le Grand lac de l'Ours (Hildebrand et Bowring, 1984; Cook et al., 1999). Le faciès métamorphique inférieur à celui des schistes verts (Hildebrand et al., 2010a), un couvert végétal restreint et une épaisseur minime de météorisation de surface (quelques millimètres à quelques centimètres), offrent des affleurements d'une qualité exceptionnelle, faisant de la GBMZ un environnement idéal pour documenter les processus physico-chimiques reliés au développement régional d'un système IOAA (Fig. 1-3). La fenêtre temporelle au cours de laquelle se sont formés les principaux systèmes IOAA de la GBMZ s'échelonne entre 1873 Ma et 1866 Ma (Gandhi et al., 2001; Davis et al., 2011; Montreuil et al., 2016). Combinée à l'absence de remobilisation majeure des zones d'altérations et minéralisations formées dans les systèmes IOAA de la GBMZ après leur formation (outre certaines remobilisations locales) par une orogénie majeure ou une intense activité métasomatique, cette fenêtre temporelle restreinte de 7 Ma simplifie la compréhension des associations spatiales et temporelles entre les différentes phases d'altération et les épisodes de minéralisation.

En se basant sur l'étude des altérations propres aux systèmes IOAA de la GBMZ, ce projet de doctorat vise à définir la mobilité des éléments durant la formation d'un système IOAA et à contraindre les implications métallogéniques sous-jacentes. Les résultats de cette étude amélioreront le modèle de zonation de l'altération pour les systèmes IOAA présenté initialement par Corriveau et al. (2010b). Cette thèse démontrera les liens existants entre une grande variété d'associations métallifères et l'évolution d'un système IOAA, les liens entre la formation de gisements d'uranium encaissés dans des albitites et la formation de gisements IOCG et détaillera la mobilité des éléments à divers stades d'altération clés du développement d'un

système IOAA. Des indices d'altération identifiant les altérations IOAA à partir d'analyses chimiques de roches totales seront aussi développés.

Cette thèse est présentée par articles et est subdivisée en trois parties. La présente synthèse met en contexte les articles en présentant la problématique, la méthodologie et la contribution de l'auteur pour chaque article de même que les conclusions finales reliées à la problématique initiale de la thèse. Cette première partie comprend un seul chapitre. La deuxième partie comprend les articles scientifiques qui forment le corps principal de la thèse et est subdivisée en six chapitres distincts:

- *«Tectono-magmatic evolution of the southern Great Bear magmatic zone (Northwest Territories, Canada) – Implications on the formation of iron oxide alkali-altered hydrothermal systems* par Montreuil, J.-F. et Corriveau, L., Soumis à Economic Geology (chapitre 2);
- «*Linkages amongst IOCG, IOA and affiliated deposits: from the Great Bear magmatic zone records to an iron oxide alkali-alteration-facies ore deposit model*», par Corriveau, L. et Montreuil, J.-F., Soumis à Economic Geology (chapitre 3);
- «*On the relation between alteration signature and metal endowment of iron oxide alkali altered systems, southern Great Bear magmatic zone (Canada)*», par Montreuil, J.-F. et Corriveau, L., Soumis à Economic Geology (chapitre 4);
- «*Compositional data analysis of hydrothermal alteration in IOCG systems, Great Bear magmatic zone, Canada: to each alteration type its own geochemical signature*», par Montreuil, J.-F., Corriveau, L. et Grunsky, E.C., Publié dans la revue «*Geochemistry: Exploration, Environment, Analysis*» (chapitre 5);
- «*Formation of albitite-hosted uranium within IOCG systems: the Southern Breccia, Great Beat magmatic zone, Northwest Territories, Canada*», par Montreuil, J.-F., Corriveau, L. et Potter, E.G., Publié par «*Mineralium Deposita*» (chapitre 6);
- «*Element mobility and hydrothermal alteration distribution during the development of the magnetite-group Fab IOCG system, Northwest Territories, Canada*», par Montreuil, J.-F., Potter, E.G., Corriveau, L. et Davis, W.J., Publié par Ore Geology Reviews (chapitre 7);

La troisième partie comprend les annexes documentant les échantillons utilisés pour la réalisation de cette thèse.

Le reste du présent chapitre est organisé comme suit. D'abord, les caractéristiques générales des gisements IOCG et des systèmes IOAA sont décrites tout comme les principales altérations hydrothermales retrouvées dans ces systèmes. Cette description met en contexte les distinctions entre les gisements IOCG et les gîtes affiliés au sein des systèmes IOAA, pierre angulaire des études subséquentes sur la mobilité des éléments et la formation de minéralisations polymétalliques dans les systèmes IOAA de la GBMZ. Cette section est suivie par une brève présentation du contexte géologique et des principaux systèmes IOAA de la Zone magmatique du Grand lac de l'Ours suivi de la problématique, des objectifs, de la méthodologie et des avancées scientifiques réalisées par cette thèse.

1.2 Caractéristiques générales des gisements IOCG

1.2.1 Définition des gisements IOCG

Les gisements IOCG ont été initialement définis par Hitzman et al. (1992) comme des gisements à oxydes de fer protérozoïques à Cu–U–Au–éléments du groupe des terres rares (ÉTR) formés dans un environnement intracratonique. Cette définition est basée sur des observations faites aux gîtes d'Olympic Dam (Australie) et de Kiirunavaara (Suède), dans la zone magmatique du Grand lac de l'Ours (Canada) et parmi les minéralisations ferrifères au Missouri dans le terrane des *St. François Mountains* (Pea Ridge et Pilot Knob; États-Unis).

Actuellement selon Groves et al. (2010) et Williams (2010a), les gisements IOCG *sensu stricto* sont définis comme étant :

1. des minéralisations magmatiques-hydrothermales cuprifères épigénétiques (cuivre économique) avec ou sans or économique (Williams, 2010a) ou avec or économique (Groves et al., 2010);
2. des gisements dont la localisation est contrôlée par la structure;
3. pauvres en sulfures (pas de pyrite abondante);
4. caractérisés par une forte concentration d'oxydes de fer (>20 % magnétite et/ou hématite) pauvres en titane et riches en silicates de fer (p. ex. actinolite, biotite, grunérite);
5. localement enrichis en ÉTR légères;

6. associés à des zones d'altération régionales (jusqu'à 30 km d'extension) sodiques et Na–Ca±Fe antérieures à la minéralisation et dont la composition minéralogique reflète d'importants enrichissements en fer et/ou en éléments alcalins;
7. associés à des zones de bréchification tectonique, tectono-hydrothermale et hydrothermale d'échelle régionale; et
8. temporellement associés à un évènement magmatique majeur sans être nécessairement spatialement directement associés à une intrusion spécifique.

Suivant ces critères pour discriminer les IOCG *sensu stricto*, Williams (2010a) a défini deux grands groupes dans les gisements IOCG : les IOCG du groupe à magnétite (p. ex. Ernest Henry en Australie, Salobo au Brésil, Candelaria au Chili) et ceux du groupe à hématite (Olympic Dam en Australie, Mantoverde au Chili). Ces groupes correspondent aux subdivisions en gîtes de type Cloncurry et de type Olympic Dam de Corriveau (2007) basés sur Gandhi (2004). Certains gisements IOCG, avec des caractéristiques propres aux IOCG des groupes à magnétite et à hématite (groupe à magnétite–hématite; p. ex. Raul Condestable au Pérou), forment une catégorie transitionnelle de gisements IOCG du groupe à magnétite–hématite.

1.2.2 Description sommaire des gisements IOCG

Les IOCG du **groupe à magnétite** forment des gisements de forts tonnages à teneurs faibles à intermédiaires dans lesquels la magnétite prédomine comme oxyde de fer (voir tableau 1-1). Des gisements IOCG importants de ce groupe sont par exemple : Salobo dans la province métallogénique de Carajás au Brésil (Souza et Vieira, 2000), Ernest Henry dans le district de Cloncurry en Australie et La Candelaria au Chili. Ces gîtes se forment surtout à des profondeurs intermédiaires dans la croûte, les altérations à magnétite de haute température K–Fe prédominent et l'uranium n'est généralement pas un sous-produit (Williams, 2010b). Les IOCG du groupe à magnétite sont souvent spatialement associés à des gîtes du type oxydes de fer avec ou sans apatite (IO±A) et ces minéralisations (IO±A et IOCG) sont interprétées comme pouvant, dans certaines provinces géologiques, former un continuum (Corriveau et al., 2010b; Mumin et al., 2010; Williams, 2010b).

Dans les gisements du **groupe à hématite**, l'hématite est l'oxyde de fer prédominant, l'uranium peut être économique et ce sont les altérations à hématite de basse température K–Fe qui prédominent (voir tableau 1-1). L'exemple type des IOCG du groupe à hématite, quoiqu'exceptionnel en termes de tonnage, est le gisement d'Olympic Dam qui se trouve dans le Craton de Gawler en Australie. Le gisement d'Olympic Dam est le quatrième producteur de

cuivre, le cinquième d'or et le premier d'uranium dans le monde (BHP Billiton, 2009). D'autres gisements typiques du groupe à hématite sont les gisements de Mantoverde au Chili et Prominent Hill en Australie. Au Canada, le gisement se rapprochant le plus d'un IOCG±U du groupe à hématite est Sue-Dianne dans la GBMZ, avec un tonnage de 8,4 Mt @ 0,8 % Cu et 3 g/t Ag pour les ressources indiquées et 1,6 Mt @ 0,8 % Cu et 2 g/t Ag pour les ressources inférées (Hennessey et Puritch, 2008).

Tableau 1-1 Teneurs et tonnages de gisements IOCG à travers le monde

Gisement	Pays	District	Groupe	Mt	Teneur	Source
Ernest Henry	Australie	Cloncurry	Magnétite	226	1.10% Cu, 0.51 g/t Au	Porter, 2010
Mount Elliot	Australie	Cloncurry	Magnétite	570	0.44% Cu, 0.26 g/t Au	Porter, 2010
Candelaria	Chili	Ceinture férrifère	Magnétite	470	0.95% Cu, 0.22 g/t Au, 3.1 g/t Ag	Marschik et Fontboté, 2001a
Cristalino	Brésil	Carajás	Magnétite	±500	1.0% Cu, 0.3 g/t Au	Huhn et al., 1999
Igarapé Bahia/Alemão	Brésil	Carajás	Magnétite	219	1.4% Cu, 0.86 g/t Au	Tallarico et al., 2005
Salobo	Brésil	Carajás	Magnétite	986	0.82% Cu, 0.49 g/t Au	Porter, 2010
Sossego	Brésil	Carajás	Magnétite	245	1.1% Cu, 0.28 g/t Au	Porter, 2010
Guelb Moghrein	Mauritanie		Magnétite	33.4	1.12% Cu, 1.41 g/t Au	Porter, 2010
NICO	Canada	Great Bear	Magnétite	33	1.02 g/t Au, 0.11% Co, 0.14% Bi	Puritch et al., 2012
Sue-Dianne	Canada	Great Bear	Magnétite /Hématite	8.4	0.8% Cu, 3g/t Ag	Hennessy et Putrich, 2008
Carrapateena	Australia	Gawler	Hématite	800	0.8 % Cu, 0.3 g/t Au, 0.155 Kg/t U, 3.3 g/t Ag	Oz Minerals, 2014
Olympic Dam	Australia	Gawler	Hématite	9090	0.87% Cu, 0.32 g/t Au, 0.27 Kg/t U_3O_8	BHP 2009
Prominent Hill	Australia	Gawler	Hématite	283	0.89% Cu, 0.81 g/t Au, 2.48 g/t Ag	Porter, 2010
Hillside	Australia	Gawler	Hématite	337	0.6% Cu, 0.14 g/t Au	Rex Mineral, Juin 2013
Mantoverde (supergène)	Chili	Ceinture férrifère	Hématite	400	0.52% Cu, 0.1 g/t Au	Benavides et al., 2008a
Mantoverde (hypogène)	Chili	Ceinture férrifère	Hématite/ magnétite	440	0.56% Cu, 0.12 g/t Au	Reiger et al., 2010

L'âge des gisements IOCG est très variable et s'étend de l'Archéen avec le district de Carajás au Brésil (Requia et al., 2003) jusqu'au Phanérozoïque avec les gisements de la cordillère des Andes dans la ceinture ferrifère du Chili et au Pérou (Sillitoe, 2003 et les références qui y sont citées; Fig. 1-4). Pour les IOCG du groupe à magnétite, les terrains archéens du district de Carajás et les terrains protérozoïques semblent être présentement les plus fertiles. Pour les IOCG du groupe à hématite, ce sont les périodes Paléoprotérozoïque, Mésoprotérozoïque et

Mésozoïque qui sont les plus fertiles (p. ex. Craton de Gawler, district de Cloncurry, Tenant Creek Inlier, cordillère des Andes). Ces gîtes sont distribués sur tous les continents mais l'Australie et l'Amérique du Sud sont hôtes des principaux districts actuellement connus (Fig. 1-5). Les districts IOCG majeurs de l'Amérique du Sud sont le district de Carajás au Brésil qui comprend la plus importante concentration d'IOCG du groupe à magnétite à fort tonnages (Monteiro et al., 2008a, b) et la Ceinture ferrifère du Chili, qui comprend les gisements de Candelaria et Mantoverde (Sillitoe, 2003). Les districts majeurs australiens sont la province d'Olympic Dam (Skirrow et al., 2007) et le district de Cloncurry (Williams et al., 2005; Williams, 2010b). La Scandinavie et plus particulièrement la Suède, avec par exemple le gisement d'Aitik (Wanhainen, 2005), malgré qu'il soit un hybride porphyre Cu–Au/IOCG et le gisement IOA de Kirunavaara qui comprend également des régions fertiles pour les minéralisations IOCG à magnétite (Wanhainen et al., 2003; Gleeson et al., 2009; Billström, 2010; Smith et al., 2013).

1.2.3 Gîtes affiliés aux gisements IOCG et définition des systèmes IOAA

Plusieurs sous-groupes de gîtes qui ne sont pas des gisements IOCG au sens strict, soit par insuffisance d'oxydes de fer ou de minéralisation de cuivre, se retrouvent souvent spatialement et temporellement associés aux gisements IOCG, étant formés en continuum avec les minéralisations IOCG au sein du même système hydrothermal (Williams et al., 2005; Corriveau et al., 2010a; Mumin et al., 2010).

Les exemples types des gisements affiliés aux minéralisations IOCG selon Williams (2010a) et les chapitres 3, 4 et 6 sont :

1. les gisements à oxydes de fer–apatite±V±ÉTR légères (IOA; p. ex. Kirunavaara en Suède, Pea Ridge aux États-Unis) et ceux à oxyde de fer (p. ex. Lightning Creek en Australie; Marcona au Pérou)
2. les gisements à cuivre–or pauvres en oxydes de fer (p. ex *Khetri copper belt* en Inde)
3. les gisements à oxydes de fer–uranium pauvres en cuivre (p. ex. Southern Breccia dans la GBMZ au Canada, Valhalla en Australie)
4. les gisements à oxydes de fer–Co–As±Ni±W±Au±Ag±U±ÉTR±Bi et généralement pauvres en cuivre (*Idaho cobalt belt* aux États-Unis)

Les différents types de minéralisations énumérés ci-dessus, incluant les gisements IOCG, deviennent ainsi les composantes fertiles d'un système IOAA.

En considérant les nouveaux types de minéralisations retrouvées dans certains districts IOCG tel que le gisement Mo–Re de Merlin dans le district de Cloncurry (Australie; Inova Resources) et le continuum proposé par Mumin et al. (2010), Kreiner et Barton (2011) et Richard et Mumin (2013) entre les gisements IOCG et les gîtes du type porphyres ou épithermaux, l'importance métallogénique des systèmes IOAA ne cesse de croître.

1.3 Distribution spatio-temporelle des altérations hydrothermales dans les systèmes IOAA

La distribution spatio-temporelle des altérations hydrothermales, telle que caractérisée par Hitzman et al. (1992), Williams (2010b), Corriveau et al. (2010b) ainsi qu'au chapitre 3, suit une séquence relativement régulière des zones distales à proximales de la minéralisation et de précoce à contemporaine par rapport à la minéralisation. Cette évolution séquentielle des altérations hydrothermales est intimement liée à la décroissance de la température des fluides hydrothermaux et de la profondeur du système avec le temps. Pour les précurseurs silicatés la séquence va comme suit :

1. altération sodique typiquement de haute température (Na);
2. altération de haute température (HT) calcique–fer (HT Ca–Fe);
3. altération HT potassique–fer (HT K–Fe);
4. skarn potassique ou altération potassique; et
5. altération de basse température (LT) hydrolytique potassique–fer (LT K–Fe).

Les principaux minéraux formés à chacun des stades d'altérations sont présentés au tableau 1-2.

1.3.1 Altération sodique de haute température

L'altération sodique (±Ca–Fe) a une étendue régionale à l'échelle des districts IOCG (Figs. 1-6 à 1-10; Marschik et Fontboté, 2001a, b; Marschik et al., 2003; Oliver et al., 2004; Mark et al., 2006; Benavides et al., 2007; Monteiro et al., 2008a, b; Corriveau et al., 2010b, b; Porter, 2010) et se retrouve typiquement dans l'ensemble d'un district IOAA le long des structures majeures, près des intrusions et dans les unités perméables (Hildebrand, 1986; Oliver et al., 2004; Mark et al., 2006; Monteiro et al., 2008a, b; Corriveau et al., 2010b; Rubenach, 2013; Figs. 1-6 à 1-10).

L'altération sodique est généralement distale relativement aux gisements IOCG mais certains processus comme un soulèvement différentiel ou la bréchification préférentielle des albitites peuvent contribuer à spatialement superposer les zones d'altération sodique et les minéralisations IOCG.

Tableau 1-2 Liste des principaux minéraux retrouvés dans les altérations IOAA

Altération	Minéraux principaux	Principaux minéraux accéssoires et traces	Principaux minéraux formant les minéralisations
Sodique	Ab, Qz, Scp	Amp (Act), Mag, Ru, Ttn, Zrn	
HT Ca–Fe	Amp (Act, Cum, Hbl), Ap, Mag	Aln, Cb, Ccp, Cpx, Ep, Fl, Grt, Mzn, Py, Sch, Thr, Ttn, Urn	Ap, Mag
HT K–Fe	Amp (Act), Bt, Kfs, Mag	Ap, Grt, Ilm, Po, Py, Qz, Sp, Ttn, Tur, Xtm	Apy, Bis, Bn, Ccp, Cob, Mol, Mlr, Urn
Skarn potassique/ potassique	Kfs, Cpx (Di), Grt (Adr)	Ep, Ves, Tlc	Ccp, Gn, Sp
LT K–Fe	Cb, Chl, Hem, Kfs, Msc, Qz	Ab, Aln, Brt, Ep Fl, Ilt, Mnz, Py, Ru, Tur	Bn, Ccp, Cct, Hem, Pitch, Urn
LT Ca–Fe	Ep, Aln, Kfs, Qz		Bis, Bn, Ccp, Cct, Mol, Sp

Abréviations des minéraux selon Whitney et Evans (2010), Bis=Bismuthunite, Cob=Cobaltite

Temporellement, certains stades d'altération sodique peuvent précéder la formation du gisement de plusieurs millions d'années comme dans le cas du district de Cloncurry (Oliver et al., 2008) ou y être temporellement associée comme dans le cas du secteur de Contact Lake dans le district de Port Radium–Echo Bay dans la GBMZ (Fig. 1-10; Hildebrand, 1986; Corriveau et al., 2010a). Plusieurs sources peuvent générer les fluides associés à l'altération sodique : un fluide magmatique-hydrothermal (Pollard, 2001; Oliver et al., 2004; Somarin et Mumin, 2014) ou encore les eaux météoriques ou de bassin réchauffées par l'activité magmatique ou un gradient thermique élevé dans la région où ils circulent (Barton et Johnson, 1996; Kendrick et al., 2008; Seedorff et al., 2008). Dans ces fluides de bassins, une composante magmatique peut s'ajouter lors de leur évolution (Kendrick et al., 2008). La température de formation de l'altération sodique conduisant à des albitites peut atteindre plus de 450-500°C (Oliver et al., 2004; Davidson et al., 2007; Monteiro et al., 2008a; Perring et al., 2008; Somarin et Mumin, 2014) bien que communément les températures répertoriées (préservées par les inclusions fluides) sont de l'ordre de 350 à 500°C (Bardina et Popov, 1992; Kish et Cuney, 1981). Cette altération est généralement non minéralisée (à moins d'être subséquemment bréchifiée par des altérations fertiles; p. ex. Southern Breccia dans la GBMZ) et est principalement considérée comme une zone de lessivage où plusieurs éléments sont partitionnés dans le fluide aqueux (Oliver et al., 2004).

1.3.2 Altérations HT Ca–Fe

Les altérations à HT Ca–Fe sont généralement juxtaposées ou recoupent les zones d'altération sodique, ou encore dans certains systèmes y sont intimement liées. Elles sont précoces relativement aux gisements IOCG et forment le cœur des gisements du type IO±A tel que ceux du district de Kiruna en Suède ou ceux du Missouri dans le terrane des *St. François Mountains* (Pea Ridge et Pilot Knob; États-Unis; Figs 1-6 et 1-10; Corriveau et al., 2010b; Mumin et al., 2010; Williams, 2010a). Dans les zones d'altération sodique, l'augmentation de la proportion de veines d'amphibole±magnétite signale la proximité d'altération intense HT Ca–Fe (Figs 1-6 à 1-10). Cette zone d'altération transitionnelle entre les zones d'altération sodique et HT Ca–Fe est communément appelée altération Na–Ca (Figs 1-6 à 1-9) ou encore Na–Ca–Fe (Fig. 1-10). Lorsque très intense, l'altération HT Ca–Fe forme des roches qui ressemblent à des «ironstones» fortement magnétiques ou des roches mafiques métamorphisées au faciès des amphibolites (e.g., formation d'actinolitite à Sequeirinho, Fig. 1-6).

Des fluides magmatiques-hydrothermaux de haute température (400-800°C) sont généralement associées à la formation de ces zones d'altération (Hildebrand, 1986; Perring et al., 2000; Porter, 2010; Williams, 2010b; Chen et al., 2011; Smith et al., 2013; Somarin et Mumin, 2014). Baker et al. (2008) démontrent dans le district de Cloncurry (Australie) que les fluides impliqués dans les altérations régionales Na–Ca ont un contenu faible en K mais élevé en Ca avec une salinité variable. Le contenu en Cu dans les principaux fluides impliqués au stade HT Ca–Fe est généralement faible mais peut être élevé dans certains fluides similaires à ceux associés aux gisements IOCG qui se retrouvent dans certains gisements IOA (e.g., Lightning Creek, Cu > 10000 ppm; Perring et al., 2000; Baker et al., 2008). Ces études sur les inclusions de fluides associés au stade HT Ca–Fe indiquent que le Cu est présent dans certains fluides actifs à ce stade, mais qu'il n'a pas précipité dans des sulfures.

1.3.3 Altérations HT K–Fe

Les zones d'altérations sodiques et HT Ca–Fe sont généralement recoupées par les altérations HT K–Fe associées à la formation de gisements IOCG du groupe à magnétite (Figs 1-6 à 1-8, 1-10 et 1-11). La minéralisation cuprifère est principalement composée de chalcopyrite associée à de la pyrite, de la magnétite, du feldspath potassique et/ou de la biotite. Les zones minéralisées forment des zones de brèches polyphasées, des réseaux de veines ou encore des zones de remplacement concordantes de type mantos[1]. Dans certains gisements comme Salobo, la

bornite et la chalcocite peuvent aussi se former (Requia et al., 2003). À l'échelle régionale autour de certains gisements IOCG, une altération précoce HT K–Fe peut aussi se former (Mark et al., 2006; Benavides et al., 2008a; de Haller et Fontboté, 2009). Ces zones d'altérations sont généralement pré-minéralisation et peuvent être contemporaines ou précoces relativement à l'albitisation.

Les fluides impliqués au stade HT K–Fe associé à la minéralisation IOCG sont diversifiés et de haute température (400-600°C; Ulrich et Clark, 1997; Marschik et Fontboté, 2001a; Requia et al., 2003; Rieger et al., 2010; Rusk et al., 2010; Williams, 2010b). Ils ont une forte composante magmatique-hydrothermale, mais peuvent aussi avoir une composante météorique ou de bassin (Baker et al., 2008; Rusk et al., 2010; Williams, 2010b). Baker et al. (2008) démontrent que les fluides impliqués au stade HT K–Fe lors de la minéralisation dans le district de Cloncurry (Australie) ont un contenu élevé en Ca, Cu, Fe, K et Mn et sont très salins. Lors de la formation des gisements IOCG, plusieurs épisodes d'altération HT K–Fe peuvent être impliqués. Par exemple en profondeur dans les brèches tectono-hydrothermales minéralisées formant le gisement d'Ernest Henry se retrouvent des fragments composées de magnétite et de chalcopyrite plus grossièrement grenues qui sont corrodés/remplacés par l'altération HT K–Fe qui cimente les brèches minéralisées (Rusk et al., 2010). Rusk et al. (2010) interprètent ces fragments comme étant des indicateurs potentiels d'une zone de minéralisation précoce de plus haut grade se retrouvant sous le gisement d'Ernest Henry actuellement exploité et partiellement remontée vers la surface par un soulèvement différentiel.

1.3.4 Altération potassique et skarn potassique

À la transition entre les stade HT K–Fe et LT K–Fe, des skarns potassiques ou des altérations à feldspaths potassiques très intenses et communément bréchifiées peuvent se former (Marschik et Fontboté, 2001a; Corriveau et al., 2010b). Les skarns potassiques se forment lorsque les roches sont riches en carbonates (précurseur ou altération carbonatés) et cette altération est communément minéralisée en cuivre. L'altération potassique est transitionnelle aux stades HT K–Fe et LT–Fe et forme typiquement des zones de remplacement très intenses s'étendant sur une dizaine de mètres, qualifiées comme formant un «mur d'altération potassique» entre les zones d'altération HT K–Fe et LT K–Fe. Cette altération potassique ne doit pas être confondue à l'altération potassique régionale qui accompagne plusieurs gisement IOCG (Hitzman et al., 1992; Corriveau et al., 2010b). L'altération potassique régionale à feldspath potassique ou à biotite peut avoir une extension kilométrique et forme des zones aisément détectables en

surface des méthodes indirectes comme les levés radiométriques lorsque le couvert végétal ou aquatique est restreint (p. ex. NICO au Canada, Shives et al., 1997; Ernest Henry en Australie, Mark et al., 2000, 2006; Corriveau et al., 2010b; Rusk et al., 2010.

1.3.5 Altération LT K–Fe

L'altération LT K–Fe forme les zones minéralisées des gisements IOCG du groupe à hématite. Cette altération est soit surimposée sur les zones d'altération HT K–Fe à magnétite lors du refroidissement progressif du système hydrothermal, de l'exhumation différentielle des zones d'altération de haute température dans un environnement tectonique actif, ou encore se forme dans les sections de plus faibles profondeurs formant les parties sommitales des systèmes IOAA à des températures autour de 350-150°C (Figs 1-6, 1-9, 1-11 à 1-14; Fig. 1-14 montre les différents scénarios; Marschik et Fontboté, 2001a; Benavides et al., 2007; Monteiro et al., 2008a; Hayward et Skirrow, 2010; Mumin et al., 2010; Skirrow, 2010; Xavier et al., 2010; Williams, 2010b; Somarin et Mumin, 2014). Les fluides magmatiques-hydrothermaux impliqués aux stades d'altération antérieurs ayant progressivement refroidis et changés de composition, des fluides météoriques ou des saumures provenant de la surface et percolant dans les zones d'altération de plus haute température formées antérieurement sont tous potentiellement impliqués au stade LT K–Fe (Fig. 1-14) et la source des fluides est fortement influencée par l'environnement de formation du système IOAA. Dans les zones profondes de certains gisements IOCG à hématite ou juxtaposées à ceux-ci (p. ex Mantoverde au Chili), on retrouve donc des altérations similaires à celles observées dans les IOCG du groupe à magnétite (Figs 1-6, 1-11 et 1-14).

Dans plusieurs districts IOAA l'altération LT K–Fe est communément appelée altération hydrolytique. Cette altération hydrolytique est principalement composée d'hématite terreuse ou spéculaire et/ou de chlorite (Fig. 1-6; p. ex. Hitzman et al., 1992; Davidson et al., 2007; Monteiro et al., 2008a, b). Les sulfures de cuivre associés à l'altération LT K–Fe sont généralement plus diversifiés que dans les gisements IOCG du groupe à magnétite, comprenant régulièrement la bornite et la chalcocite en plus de la chalcopyrite. Les sulfures de cuivre sont également zonés, la chalcopyrite se retrouvant dans les sections profondes et la bornite/chalcocite dans les sections peu profondes des gisements (p. ex. gisements de Prominent Hill, Carrapateena et Olympic Dam en Australie; Fig. 1-13). Lorsque les gisements IOCG du groupe à hématite sont uranifères comme Olympic Dam ou Carrapateena, l'uraninite, la coffinite et la pitchblende constituent les principaux minéraux uranifères (Davidson et al., 2007; Freeman and Tomkinson,

2010; Skirrow, 2010). Dans les gisements IO±A, l'altération LT K–Fe est communément formée dans les sections les moins profondes du système hydrothermal, mais ces zones d'altération ne contiennent généralement pas de quantités significatives de sulfures de cuivre et sont généralement pauvres en métaux (e.g., Mag Hill et Port Radium, GBMZ, Mumin et al., 2010).

1.3.6 Autres altérations

Souvent tardive et représentant soit les fluides les plus évolués des systèmes IOCG ou des remobilisations subséquentes, une silicification intense et des veines à la minéralogie complexe où le quartz prédomine de même que des altérations épithermales acides peuvent se superposer et localement recouper les zones d'altérations IOCG. La formation d'altérations épithermales (e.g., argillique) indique une acidification marquée des fluides hydrothermaux passé le stade d'altération LT K–Fe (Fig. 1-10; Mumin et al., 2010; Kreiner et Barton, 2011; Somarin et Mumin, 2014). La formation dans certains cas extrêmes de systèmes de veines de quartz de plusieurs dizaines de kilomètres de longueur atteignant jusqu'à un kilomètre en largeur indique aussi une saturation du quartz dans les fluides tardifs, le quartz étant faiblement précipité dans les gîtes IOCG (Gandhi et al., 2000; Lobo-Guerrero, 2010; Williams et al., 2010). Dans la GBMZ, ces altérations tardives peuvent remobiliser les métaux déjà concentrés dans les altérations IOCG ou encore amener de nouveaux métaux pour former de nouvelles zones de minéralisation polymétallique contenues dans les veines (Mumin et al., 2007, 2010; Somarin et Mumin, 2012, 2014). Ces altérations épithermales sont généralement de faible température, évaluée autour de 224°C dans le district de Port Radium–Echo Bay (Somarin et Mumin, 2014) et autour de 200°C dans la Ceinture ferrifère du Chili (Kreiner, 2011).

1.4 Contexte géologique et systèmes IOAA de la zone magmatique du Grand lac de l'Ours

Pour définir la mobilité des éléments dans les systèmes IOAA de la zone magmatique du Grand lac de l'Ours (GBMZ), il faut aussi en cadrer le contexte géologique et tectonique. Cette section présente les principales caractéristiques géologiques et tectoniques de la GBMZ, développées plus en détails au chapitre 2.

1.4.1 Contexte tectonique de formation de la GBMZ

La GBMZ est interprétée comme un arc continental paléoprotérozoïque développé entre 1,87 et 1,84 Ga dans la zone de suture entre le craton archéen de l'Esclave et le terrane d'Hottah (pré 1,88 Ga; Hildebrand et al., 1987, 2010a; Gandhi et van Breemen, 2005). La formation de la GBMZ suit l'orogenèse caldérienne, qui résulte de la collision entre le craton de l'Esclave et l'arc d'Hottah à 1882,50 ± 0,91 Ma (Hoffmann et al., 2011). Précédant la collision, une séquence sédimentaire de marge passive s'est accumulée sur la marge ouest du craton de l'Esclave (*Coronation margin*) et une subduction à pendage vers l'ouest en milieu océanique est associée à la formation du terrane d'Hottah pour s'inverser par la suite et former la GBMZ (Hildebrand et al., 2010a). Alternativement selon Ootes et al. (2015), le terrane d'Hottah se serait accolé au craton de l'Esclave le long d'une grande faille transformante. Ce modèle tectonique n'implique pas une subduction à pendage vers l'ouest et son inversion subséquente suivant la collision mais simplement la formation d'une zone de subduction vers l'est sous le craton de l'Esclave pendant l'orogenèse caldérienne. À la marge du terrane d'Hottah se développe le Groupe de Treasure Lake d'âge maximal de 1886 ± 8 Ma (Gandhi et van Breemen, 2005) ou 1884 ± 6 Ma (Bennett et Rivers, 2006), également déformé lors de l'orogenèse caldérienne.

La GBMZ est limitée à l'est par la zone de faille Wopmay, qui a une extension verticale jusqu'à la croûte moyenne (Spratt et al., 2009) dans le sud de la GBMZ (pour le nord de la GBMZ se référer à la description de la zone médiale de Hildebrand et al., 2010a), et à l'ouest par le terrane d'Hottah. La limite ouest de la GBMZ est presqu'entièrement recouverte par des séquences sédimentaires phanérozoïques, étant seulement exposée autour du lac d'Hottah. À l'est de la GBMZ, la zone de faille Wopmay (et zone médiale) marque la limite en surface des séquences archéennes du craton de l'Esclave. Aucun affleurement de roche archéenne et aucun zircon hérité archéen n'ont été documentés dans les roches magmatiques de la GBMZ à l'ouest de cette faille. Ceci indique l'absence de roches archéennes au sein de la zone de fusion de la GBMZ (Housh et al., 1989; Gandhi et al., 2001; Gandhi et van 2005; Bennett et Rivers, 2006; Bennett et al., 2012). En revanche, des zircons, paléoprotérozoïques, dont l'âge correspond à certaines composantes du terrane d'Hottah, se retrouvent sporadiquement dans certaines intrusions de la GBMZ (exemple au chapitre 7; Bennett et al., 2012). Ces zircons hérités indiquent que certaines séquences du terrane d'Hottah sous la GBMZ ont fort probablement interagi et été assimilées par les magmas de la GBMZ. Plus en profondeur, une composante lithosphérique archéenne du craton de l'Esclave est interprétée comme s'étendant sous la GBMZ jusque sous l'expression en surface du terrane d'Hottah, qui lui aussi a une

racine cratonique profonde située à plus de 200 km sous la surface (Spratt et al., 2009). Cette architecture crustale dans laquelle s'est formée la GBMZ est fortement similaire à celle où s'est formé le gisement d'Olympic Dam dans le craton de Gawler en Australie, dans la zone de suture entre le noyau archéen du *Gawler craton* et le craton Nord-Australien (Heinson et al., 2006; Skirrow, 2010). Ces zones de sutures sont interprétées comme des structures clés pour la formation de gisements IOCG de fort tonnage, car elles forment un lien direct et perméable entre la croûte supérieure et le manteau (Drummond et al., 2006; Corriveau et Mumin, 2010; Skirrow, 2010). Quant aux prismes formés par les racines lithosphériques archéennes, ils focalisent la convection mantellique de même que l'activité magmatique et hydrothermale au-dessus de la zone de suture.

La GBMZ s'est ainsi formée sur les séquences accrétées et érodées du terrane d'Hottah, incluant le Groupe de Treasure Lake et deux phases d'activité magmatique la caractérisent. La première phase s'échelonne principalement entre 1873 et 1860 Ma et est constituée par du magmatisme shoshonitique intrusif à extrusif où se forment principalement des roches intermédiaires dans le nord et felsiques à intermédiaires dans le sud (chapitre 2). L'activité volcanique lors de la première phase est associée à de l'exhumation différentielle et à du basculement des séquences volcaniques (Mumin, 1997; Enkin et al., 2012). La deuxième phase d'activité magmatique de la GBMZ se déroule entre 1858 et 1843 Ma et se caractérise par du magmatisme intrusif principalement felsique (Hildebrand et al., 1987, 2010b; Gandhi et al., 2001; Bennett et Rivers, 2006; Bennett et al., 2012). Cependant, la présence de zircons magmatiques hérités dans les roches volcaniques et intrusives de la GBMZ, donc les âges vont de ~1879 à 1874 Ma (Bennett et al., 2012) et la mise en place de plutons dioritiques à 1877 Ma (Bennett et Rivers, 2006; Jackson et al., 2013) suivi de métamorphisme orogénique à ca. 1876 Ma, indiquent que l'activité magmatique associée à la formation de la GBMZ a fort probablement débutée dans les stades tardifs de l'orogenèse caldérienne (chapitre 2 et Jackson et al. 2013 pour une discussion de cette orogenèse et les complications observées dans le sud de la GBMZ).

Quatre grands groupes de roches volcaniques sont formés pendant la première phase magmatique de la GBMZ et sont regroupés dans le Supergroupe de McTavish. Chronologiquement les groupes mafiques à felsiques de LaBine et Dumas au nord et le Groupe felsique à intermédiaire de Faber au sud sont suivis par le Groupe intermédiaire à felsique de Sloan au nord et l'assemblage Bea du Groupe de Faber au sud. Ces séquences volcaniques représentent 35 % des roches exposées en surface dans la GBMZ (Gandhi et al., 2001). Les

descriptions plus détaillées des unités composant les groupes de Treasure Lake et de Faber se retrouvent aux chapitres 2-7.

1.4.2 Systèmes IOAA de la GBMZ

Plusieurs systèmes IOAA sont distribués sur l'ensemble de la longueur de la GBMZ et nombre d'entre eux sont actuellement reconnus comme étant potentiellement fertiles en minéralisations IOCG et affiliées (Fig. 1-2; Hildebrand, 1986; Gandhi, 1994; Mumin et al., 2007, 2010; Corriveau et al., 2010a, b; chapitres 2, 3). Parmi les plus importants il y a : les systèmes hôtes des gisements de NICO et Sue-Dianne (systèmes de Lou et Mazenod, respectivement; Fig. 1-15; chapitres 1, 4 et 5) au sud, au centre-sud les systèmes de Fab (chapitre 7) et de DeVries, au nord les systèmes du secteur de Camsell River (Terra Mine/Norrex, Grouard), de Port Radium–Echo Bay (Corriveau et al., 2010a; Mumin et al., 2007, 2010; chapitre 2) et d'East Hottah. Cependant, seulement les systèmes de Port Radium–Echo Bay et Lou/Mazenod ont été étudiés récemment en détail et représentent les systèmes IOAA les mieux documentés de la GBMZ (Goad et al., 2000a, b; Camier, 2002; Mumin et al., 2007, 2010; Corriveau et al., 2010a, b; Potter et al., 2013a, b).

Le système IOAA de Port Radium–Echo Bay s'est formé dans un complexe de stratovolcans appartenant au Groupe de LaBine (Hildebrand, 1981, 1983; Hildebrand et al., 1987, 2010b). Suivant sa formation, un épisode de plissement postdatant la formation de la GBMZ ou la déformation progressive et l'effondrement asymétrique de l'édifice volcanique ont mené au basculement et à l'exhumation différentielle des altérations IOAA, produisant une section en trois dimensions du système (Mumin et al., 2007, 2010, 2013). La séquence volcanique est composée principalement d'andésites porphyriques et est complétée par des unités volcanoclastiques, volcano-sédimentaires et plusieurs intrusions dioritiques sub-volcaniques. Les altérations de haute température du système IOAA sont centrées sur les intrusions dioritiques, interprétées par certains comme étant la principale source des fluides magmatiques-hydrothermaux associés à ces zones d'altérations (Hildebrand, 1986; Mumin et al., 2007, 2010; Somarin et Mumin, 2014). Ces intrusions sont également interprétées comme une source de chaleur qui énergise les cellules hydrothermales déjà en place et véhiculent les fluides magmatiques-hydrothermaux issus des chambres magmatiques sous–jacentes. Certains fluides de plus faible température documentés dans le système de Port Radium–Echo Bay peuvent également provenir de lacs salins intra-caldeira (Somarin et Mumin, 2014). Ces différentes hypothèses seront présentées plus en détails au chapitre 3.

L'altération sodique, Na–Ca–Fe et HT Ca–Fe prédomine près des intrusions dioritiques dans le système IOAA de Port Radium–Echo Bay et évolue vers des altérations potassiques HT K–Fe et LT K–Fe en s'éloignant des intrusions (voir figure 1 de Somarin et Mumin, 2014; Mumin et al., 2007, 2010; Corriveau et al., 2010a, b). Dans les zones externes du système se forment également des zones d'altérations épithermales ou de faibles températures (veines de quartz, altération phyllique et propylitique). Comme les séquences d'orientation NO-SE sont basculées inégalement vers le nord-est, la zonation de l'altération suit une coupe transversale par rapport aux intrusions dans la région de Contact Lake et une coupe plus longitudinale entre les secteurs de l'indice K2 et de Mag Hill, illustrant parfaitement l'évolution spatio-temporelle de l'altération. De plus, la zonation verticale des altérations à l'indice K2 est discordante avec la zonation de l'altération dans les séquences basculées, suggérant que le système IOAA de Port Radium–Echo Bay s'est développé avant et pendant le basculement des séquences volcaniques. Ce basculement des séquences volcaniques et l'altération qui y est contemporaine précède de plusieurs millions d'années l'épisode de plissement inféré par Hildebrand et al. (1987) entre 1860 et 1858 Ma (Corriveau et al., 2010a). Ces altérations se sont donc formées dans un contexte tectonique actif (Mumin et al. 2014) où plusieurs blocs s'effondraient en partie par la formation de caldeiras ou se soulevaient lors de l'altération, ce qui est typique d'un arc volcanique actif. Un tel contexte est aussi décrit pour le système de Lou, hôte du gîte de NICO, au chapitre 6.

Au sud de la GBMZ, les systèmes IOAA de Lou et de Mazenod associés aux gisements de NICO et Sue-Dianne comprennent plusieurs systèmes satellites hôtes de minéralisations IOCG et affiliées (Fig. 1-15). Cependant le contexte géologique et structural de formation des gisements de NICO et de Sue-Dianne diffère fortement. Dans le système de Lou, le gisement de NICO et les indices uranifères polymétalliques de la Southern Breccia sont principalement développés dans les roches sédimentaires du Groupe de Treasure Lake immédiatement sous sa discordance avec le Groupe de Faber (séquence volcanique sus-jacente). Au-dessus de NICO et de la Southern Breccia se trouve une séquence rhyolitique fortement altérée qui forme la plus forte anomalie radiométrique potassique au Canada (Charbonneau et al., 1988). Le gisement de NICO et les indices uranifères polymétalliques de la Southern Breccia sont recoupés par plusieurs générations d'essaims de dykes porphyriques sub-volcaniques (Gandhi et al., 2001; chapitres 2, 6).

Le gisement de Sue-Dianne, dans le système de Mazenod, s'est développé dans une zone de brèche tectono-hydrothermale hébergée dans les séquences volcaniques du Groupe de Faber

(Gandhi, 1989; Camier, 2002). Plusieurs zones de bréchification structurale, analogues à celles décrites par Oliver et al. (2006) dans le district de Cloncurry, ont été identifiées dans les systèmes IOAA du sud de la GBMZ. Les contacts lithologiques entre les séquences volcaniques du Groupe de Faber et les séquences métasédimentaires du Groupe de Treasure Lake ou encore entre le Groupe de Faber et les intrusions granitiques du batholite de Marian River semblent être particulièrement favorables à la formation de ces zones de brèches (e.g., corridors de déformation de Marian River, de Peanut et de Southern sur la figure 1-15).

1.5 Problématique

L'étude des systèmes IOAA est un sujet complexe qui requiert une approche multidisciplinaire. Cette thèse aborde ainsi plusieurs sujets complémentaires reliées à la géologie régionale du sud de la GBMZ (le point de départ), au contexte tectono-magmatique de formation des gîtes IOCG (les moteurs de mobilité des éléments), à la distribution des altérations dans les systèmes IOAA de la GBMZ (les résultantes stériles), aux relations entre gîtes IOCG et gîtes d'uranium encaissés dans des albitites (les résultantes fertiles), à la signature chimique de ces altérations (les vecteurs) et à la formation de zones minéralisées à différents stades d'altération.

1.5.1 Contexte tectono-magmatique de formation des gîtes IOCG du sud de la GBMZ

(chapitre 2)

Le contexte tectono-magmatique de formation de la GBMZ demeurait incertain au vu des nouvelles contraintes géochronologiques établies par Gandhi et al. (2001), Gandhi et van Breemen (2005), Bennett et Rivers (2006), Davis et al. (2011) et Bennett et al. (2012). Les liens entre les divers épisodes magmatiques et la formation des systèmes IOAA restaient à définir, plus particulièrement dans le sud de la GBMZ où la stratigraphie demeurait plus incertaine que dans le nord par manque de données géochronologiques publiées. Une question primordiale qui n'avait pas été étudiée en détail est celle touchant à l'évolution géochimique et au contexte tectonique des séquences volcaniques et intrusives du sud de la GBMZ. Les analyses géochimiques de roches totales par fusion et «*inductively coupled plasma-mass spectrometry*» (ICP-MS) et «*inductively coupled plasma-atomic emission spectrometry*» (ICP-AES) offrent une grande précision sur des éléments diagnostiques tels que ÉTR, Nb, Ta, Th, Y, Yb et Zr, et de telles données pourraient permettre de mieux cerner la signature magmatique et le contexte

tectonique le plus probable des roches volcano-plutoniques de la GBMZ. Une meilleure compréhension de l'évolution tectono-magmatique du sud de la GBMZ contraindrait aussi les fenêtres temporelles, magmatiques et tectoniques les plus favorables à la formation de minéralisations IOCG et affiliées polymétalliques dans les systèmes IOAA du sud de la GBMZ.

1.5.2 Nomenclature et définition de faciès d'altération dans les systèmes IOAA

(chapitres 3 et 4)

Il y a actuellement deux principaux systèmes de nomenclature utilisés dans la littérature pour nommer les altérations IOAA : ceux basés sur une notation chimique et ceux basés sur une notation minéralogique. Plus communément, diverses combinaisons plus ou moins systématiques de ces deux systèmes de nomenclature sont utilisées et dans certains cas seulement un minéral (généralement le principal ou un oxyde de fer) sert à nommer un stade complet d'altération (p. ex. Barton et Johnson, 2000; Davidson et al., 2007). Dans les systèmes de nomenclature basés sur une notation chimique, les altérations sont nommées en fonction des principaux cations qui caractérisent leur paragenèse minéralogique ou encore un élément qui définit le trait caractéristique du stade d'altération (Figs 1-6 à 1-13). Par-exemple, une zone d'albitisation est appelée altération sodique (p. ex. Marschik et Fontboté, 2001b; Mark et al., 2006; Monteiro et al., 2008a, b) selon cette nomenclature tandis qu'elle serait appelée altération à albite selon une nomenclature minéralogique (p. ex. Nirranen et al., 2007; Skirrow et al., 2007; de Haller et Fontboté, 2009). D'autres systèmes plus marginaux de nomenclature des altérations IOAA divergent considérablement de la nomenclature couramment utilisée en introduisant des termes comme désamphibolitisation pour nommer une albitisation/altération sodique (p. ex. Strauss, 2003) ou encore dénotent les stades principaux d'altération principaux en stades de bréchification (p. ex. Hunt et al., 2005; Bernard, 2006).

Les différents systèmes de nomenclature utilisés pour décrire les altérations IOAA dans la littérature compliquent la définition de faciès d'altération propres aux systèmes IOAA (tableau 3.1 au chapitre 3 et références présentées). Suivant Schmid et al. (2007) et Zharikov et al. (2007), un facies d'altération se définit comme une suite d'assemblages minéralogiques qui sont systématiquement associés dans le temps et l'espace et qui montrent une relation étroite entre leur assemblage minéralogique et leur composition chimique. Ainsi les paragenèses minéralogiques de deux faciès d'altération distincts reflètent des conditions physico-chimiques distinctes de formation. Bardina et Popov (1992) soulignent également que l'évolution du

métamorphisme orogénique est contraint par les cheminements P–T (pression–température) alors que ceux des faciès métasomatiques sont contraints par l'évolution des fluides en fonction de leur température et de leur pH.

Les faciès d'altération sont donc analogues pour contraindre l'évolution physico-chimique d'un système hydrothermal aux faciès métamorphiques utilisés pour contraindre l'évolution tectonique d'une orogenèse. L'utilisation de faciès d'altération facilite l'harmonisation et la production de cartes d'altération et la segmentation d'un système hydrothermal en différents domaines d'altération, ce qui devient très utile lorsque le système est polyphasé et comprend plusieurs types et générations d'altération hydrothermale qui se recoupent, se surimposent et se confondent. Cette approche facilite aussi la comparaison de l'altération hydrothermale entre différents systèmes IOCG et IOAA, ce qui peut être une tâche complexe avec les systèmes de nomenclature actuels (voir les différences dans la notation des altérations dans les figures 1-6 à 1-13).

1.5.3 Signature chimique des altérations

(chapitres 4 à 7)

L'évolution et la distribution reproductible des altérations dans les systèmes IOAA ont été démontrées par Hitzman et al. (1992), Barton et Johnson (2000), Williams et al. (2005), Corriveau et al. (2010b) et Mumin et al. (2010). Cependant, l'évolution géochimique des altérations et la mobilité des éléments entre chaque stade d'altération, qui appuieraient ces modèles d'évolution, ne sont pas systématiquement documentées dans les systèmes IOAA. Plusieurs questions restent aussi en suspens quant à la composition géochimique caractéristique de chaque altération, l'influence de la composition originale du protolite sur la composition finale de la roche altérée et le couplage/découplage entre des éléments généralement isovalents (ex : Sr–Ca, Nb–Ta). Les implications du lessivage intense et de la redistribution des éléments chimiques sur plusieurs dizaines de kilomètres résultant de la construction d'un système IOAA restaient ainsi encore à contraindre pour offrir des cas d'exemples représentatifs.

Des travaux non publiés d'Ewan Pelleter ont délimité certains traits géochimiques des altérations IOAA dans la région de Contact Lake du district de Port Radium–Echo Bay près du Grand Lac de l'Ours. Oliver et al. (2004) ont proposé une modélisation détaillée et exhaustive du rôle de l'altération sodique dans les systèmes IOAA du district de Cloncurry en Australie. En s'appuyant sur le comportement des éléments majeurs et des isotopes de l'oxygène dans les

systèmes IOCG de Mantoverde, Benavides et al. (2008a) ont commencé à élaborer des vecteurs géochimiques basés sur un indice d'altération corrélant les variations des rapports molaires entre les éléments majeurs dans les altérations et la fertilité du système hydrothermal hôte.

1.5.4 Relation entre altération et minéralisation dans les systèmes IOAA de la GBMZ

(chapitres 3 à 7)

Le potentiel en minéralisations IOCG et affiliées des systèmes IOAA de la GBMZ reste encore à définir pour plusieurs d'entre eux. En effet, excepté pour les systèmes IOAA de Port Radium–Echo Bay, Sue-Dianne et NICO qui ont été réexaminés en détail pendant les années 2000 (Goad et al., 2000a, b; Camier, 2002; Mumin et al., 2007, 2010; Corriveau et al., 2010a, b), les travaux les plus récents sur la majorité des systèmes IOAA de la GBMZ datent de la fin des années 1990 et même des années 1980 pour certains, au moment où le concept de gisements du type IOCG n'existait pratiquement pas ou encore que les connaissances sur les gîtes IOCG restaient très fragmentaires. En effet, c'est Gandhi (1994), dans sa synthèse sur les styles de minéralisations du centre et sud de la GBMZ, qui a associé certains des indices aux systèmes IOCG. Dans le nord de la GBMZ, Hildebrand (1986) reliait déjà les composantes sodiques et HT Ca–Fe aux systèmes du style Kiruna. Cette documentation n'allait toutefois pas jusqu'à l'identification des zones d'altérations HT et LT K–Fe à magnétite et hématite des districts de Port Radium–Echo Bay et de Camsell River ce qui implicitement restreignait largement le potentiel minéral au fer. Ces altérations n'ont pas été rapportées avant les travaux de Webb (2001) puis par Mumin et al. (2007, 2010) et Corriveau et al. (2010a, b) où un réexamen détaillé a permis d'élargir le potentiel minéral de la région comme le présent projet le fait avec la découverte de la Southern Breccia, 1 km au sud du gisement de NICO (chapitre 4). Cette zone d'albitites uranifères avait été initialement cartographiée comme des cornéennes associées à l'emplacement des batholithes (Goad et al., 2000a, b), appellation qui perdure d'ailleurs jusqu'à Mumin et al. (2010). La distribution des zones d'altération HT et LT K–Fe fertiles en minéralisations IOCG sont aussi à définir dans la majorité des systèmes IOAA de la GBMZ. Même dans le district de Port Radium–Echo Bay ces zones n'ont pas été clairement définies malgré tous les travaux effectués dans les années 2000, ce qui a mené au forage de plusieurs kilomètres de carottes dans des zones d'altérations Na–Ca–Fe et HT Ca–Fe qui se sont avérées peu fertiles en minéralisations polymétalliques cuprifères mais fortement minéralisées

en vanadium et ÉTR (chapitre 3). Cette connaissance fragmentaire de la distribution régionale des altérations et des associations minéralisation–altération est aussi valide pour le sud de la GBMZ dans le système de Nod (chapitre 4), où quelques centaines de mètres de forages ont ciblé les zones d'altération sodique et HT Ca–Fe±K, généralement peu fertiles en métaux autres que le Fe (voir MacKay et Eveleigh, 1997). Dans le système de Grouard, les zones d'altération intense HT Ca–Fe cartographiées lors de la campagne de terrain de 2010 avaient été étiquetées du terme «*rat shit*» sur les photos aériennes utilisées pour les campagnes de cartographie dans les années 1980. Cette anecdote résume bien la difficulté d'alors à décrire les altérations IOAA lors de campagnes de géocartographie régionale. Une meilleure connaissance de la distribution régionale des altérations et des relations altération/minéralisation améliorerait grandement les modèles métallogéniques et l'évaluation du potentiel minéral et énergétique (uranium) des systèmes IOAA de la GBMZ en gisements IOCG et affiliés. L'approche préconisée est basée sur la signature métallifère des différentes altérations associées aux indices minéralisés formés. Elle est applicable tant dans un contexte d'exploration préliminaire que dans la définition de zones minéralisées au Canada et ailleurs dans le monde. L'objectif est donc d'établir les relations entre altération et minéralisation dans les systèmes IOAA de la GBMZ.

1.5.5 Relation entre gîtes IOCG et gîtes d'uranium encaissés dans des albitites

(chapitres 3 et 6)

Les gîtes d'uranium encaissés dans les albitites sont caractérisés par une série de zones enrichies en uranium à faible teneur (< 1% U_3O_8) dispersées sur plusieurs kilomètres dans des roches préalablement fortement albitisées. Collectivement ces gîtes contiennent autant d'uranium que les gîtes d'uranium associés à une discordance, ce qui en fait une source significative d'uranium. Malgré leur fort potentiel, ces gîtes uranifères demeurent parmi les plus mal compris (Wilde, 2013). Individuellement, les zones minéralisées en uranium s'étendent sur plusieurs mètres en largeur et potentiellement plusieurs centaines de mètres en longueur formant des lentilles relativement étroites dans des corridors de déformation. Les altérations hydrothermales principales sont Na, Na+Ca+Mg et K polyphasées (Cuney et Kyser, 2008; Polito et al., 2009; Cuney et al., 2012; Wilde et al., 2013). Des exemples clés de ce type de minéralisation sont : Valhalla en Australie (Polito et al., 2009; 34.7 Mt @ 830 ppm U_3O_8, Paladin Energy LTD, 2013), Lagoa Real au Brésil (Porto da Silveira et al., 1991), le gisement de

Michelin au Labrador (Gandhi, 1977; Corriveau et al., 2010a) et les gisements uranifères du bouclier ukrainien (Cuney et al., 2012). Les gîtes d'uranium encaissés dans des albitites ont été reconnus comme étant potentiellement associés aux gîtes IOCG, mais aucune association directe n'a été documentée (Hitzman et Valenta, 2005; Williams, 2010a; Wilde, 2013). Les relations entre les oxydes fer et la minéralisation uranifère dans plusieurs de ces gîtes sont également mal comprises, et certains associent la formation d'oxydes de fer au métamorphisme régional (Wilde, 2013). Un des objectifs du chapitre 6 est de démontrer les relations temporelles et génétiques entre la formation de gîtes IOCG et de gîtes d'uranium encaissés dans des albitites en contextes non affectés par du métamorphisme orogénique régional.

1.6 Objectifs

L'objectif principal de cette thèse est de définir la mobilité des éléments dans les systèmes IOAA de la GBMZ pour établir les relations entre la mobilité et l'immobilité de ces éléments et les altérations hydrothermales et minéralisations qui en résultent. Plusieurs aspects, définis dans la section précédente, doivent être répondues pour bien cadrer la mobilité des éléments dans les systèmes IOAA.

Les objectifs de cette thèse sont donc :

1. Définir le contexte tectono-magmatique et les relations spatio-temporelles entre les nombreux indices, gîtes, gisements et zones minéralisées du sud de la GBMZ;

2. Définir un système de nomenclature systématique pour l'altération hydrothermale formées dans les systèmes IOAA de la GBMZ et cadrer l'évolution de l'altération au sein de ces systèmes;

3. Établir la signature chimique et métallifère des différents types d'altération hydrothermale identifiés dans les systèmes IOAA de la GBMZ;

4. Définir la mobilité des éléments entre chacun des stades d'évolution d'un système IOAA;

5. Établir des indices d'altération pour les systèmes IOAA afin de faciliter la reconnaissance de roches altérées par des données géochimiques; et

6. Contraindre les relations entre altération et minéralisation.

1.7 Méthodologie

1.7.1 Cadre logistique et scientifique

Les systèmes IOAA sont très complexes et nécessitent une approche multidisciplinaire pour bien les contraindre (Corriveau, 2007; Corriveau et Mumin, 2010). Ce projet de doctorat s'inscrit donc au sein du projet MGM010 intitulé «*Iron-oxide Copper–gold (IOCG) / Multiple Metals – Great Bear Region*» du programme de Géocartographie de l'énergie et des minéraux (GEM) de la Commission géologique du Canada (CGC; responsables Louise Corriveau et Kathleen Lauzière) et est réalisé en partenariat avec le *Northwest Territories Geoscience Office* (NTGO; responsable Valerie Jackson). Ce doctorat est aussi réalisé parallèlement avec celui de Pedro Acosta-Góngora de l'Université de l'Alberta sous la supervision de Sarah Gleeson et Iain Samson. Le projet de M. Acosta-Góngora porte sur la nature des minéralisations même en s'appuyant sur la composition des éléments en trace des magnétites, des isotopes stables (S, O, Cu) et des inclusions de fluides dans les principaux indices IOCG de la GBMZ, une approche qui complémente bien le portrait plus régional de ces systèmes défini dans cette thèse (Acosta, 2014; Acosta-Góngora et al., 2011, 2013, 2014, 2015a, b). En parallèle, l'étude a bénéficié des avancées sur la pétrographie des altérations d'Anthony Franco De Toni (étudiant à la maîtrise à l'INRS–ETE sous la supervision de Louise Corriveau et Pierre-Simon Ross) et de la chimie minérale par Philippe Normandeau (doctorant à l'université McGill sous la supervision de Jeanne Paquette et Isabelle McMartin) et Philippe Lypazewski (étudiant au baccalauréat à l'université McGill) (Lypaczewski et al., 2013; Normandeau et McMartin, 2013; De Toni, 2016).

Les travaux de terrain nécessaires à ce projet de doctorat ont été parrainés par le projet MGM010 de la CGC avec un soutien logistique du *South Wopmay Bedrock Mapping project* du NTGO, des compagnies Fortune Minerals Limited et Diamonds North ainsi que des Premières Nations Tłı̨chǫ, plus spécifiquement la communauté de Gamètì. Tous les arrangements administratifs (p. ex. permis de recherche pour les travaux de terrain, autorisation de voyage, ententes avec les Premières Nations, ententes avec les compagnies minières et d'exploration minérales), financiers (obtention et gestion des fonds) de même que les formations nécessaires (premiers soins, armes à feu, etc.) ont été pris en charge par l'équipe de la CGC ou par les partenaires du NTGO. Les études réalisées au cours de ce projet ont grandement bénéficiées de l'expertise de plusieurs chercheurs de la CGC, de l'INRS, du Bureau de recherche géologiques et minières de France et des universités Laval, Brandon, McGill et d'Alberta affiliées au projet. Entre autres Georges Beaudoin, Louise Corriveau, Bill Davis, Randy Enkin, Eric

Grunsky, Nathan Hayward, Simon Jackson, Bernard Long, Hamid Mumin, Ewan Pelleter, Eric Potter et Pierre-Simon Ross.

1.7.2 Levés de terrain et échantillonnage

Les levés de terrain pour ce doctorat ont ciblé plusieurs systèmes IOAA de la GBMZ en se basant sur l'ensemble des travaux de Sunil Gandhi, la prospection faite dans les années 1960 à 1990 ainsi que les travaux dirigés par Hamid Mumin et Robert Hildebrand. Dans le sud de la GBMZ, les systèmes IOAA étudiés sont ceux associés aux gisements de NICO et Sue-Dianne; dans le centre, la région autour des indices de Fab Lake (nom informel) de même que les indices de Ham/Hailstone et JLD près de la zone de faille de Wopmay; au nord les systèmes de Camsell River, East Hottah, Grouard et Port Radium–Echo Bay (Fig. 1-2). Lors des traverses, une attention particulière a été accordée aux altérations et aux brèches, aux relations entre celles-ci et leur relation avec les minéralisations lorsque présentes. Sur chaque affleurement, la séquence d'altération a été décrite en détail, le protolite décrit lorsque reconnaissable et le tout appuyé par une documentation photographique systémique. Les échantillons témoins représentent les altérations décrites et leurs relations avec les autres types d'altérations.

Les échantillons pour la géochimie ont été cassés en fragments de quelques centimètres sur le terrain pour garantir leur homogénéité, l'absence de veines et d'altération météorique et s'assurer d'avoir un volume suffisant pour obtenir des analyses représentatives de la phase d'altération sélectionnée et décrite. Ainsi, les échantillons de géochimie sont donc homogènes et ciblés sur l'unité décrite et identifiée par le numéro alors que les échantillons témoins avec les numéros de la même unité ont été sélectionnés avec le plus de relations possibles avec les autres unités et sont donc souvent très hétérogènes et variés. La quantité de matériel récolté pour la géochimie a été estimée en fonction de la granulométrie de la roche et de son homogénéité intrinsèque (Ignamells et Switzer, 1973). Typiquement pour les roches finement grenues un volume de 250 cm^3 a été échantillonné tandis que pour les roches moyennement à grossièrement grenues c'est plutôt des volumes de l'ordre de 1000 cm^3 qui ont été échantillonnés. Sur tous les affleurements décrits entre 2009 et 2011, des mesures ont été prises avec un spectromètre à rayons gammas portable (Radiation Solutions RS–230) équipé d'un détecteur au germanate de bismuth pour mesurer les concentrations en potassium et les concentrations équivalentes en thorium et uranium. La susceptibilité magnétique des altérations a aussi été systématiquement quantifiée avec un appareil de mesure de la susceptibilité

magnétique (Heritage Geophysics SM–20 et SM–30 ou Terraplus KT–10) (cf. Lee et Morris, 2013).

1.7.3 Pétrographie et colorations au cobaltnitrate des tranches de roche

La coloration des tranches de roche au cobaltnitrate est critique pour évaluer l'intensité de l'altération potassique et établir les relations entre l'altération potassique et les autres types d'altérations. Elle s'est aussi avérée très performante pour attaquer et colorer différemment plusieurs types d'altération IOAA notamment celles en séricite et en biotite. Cette méthode, établie par Gabriel et Cox (1929), débute par l'attaque de la tranche de roche à l'acide fluorhydrique concentré qui est suivie du rinçage à l'eau, du séchage à 100 ˚C puis du trempage de l'échantillon dans une solution de cobaltnitrate. Après ce traitement, tous les feldspaths potassiques sont colorés en jaune, la biotite en vert et les micas blancs en vert jaunâtre ou jaune blanchâtre. L'attaque à l'acide fluorhydrique donne à l'albite une couleur blanchâtre assez crayeuse lorsque la concentration modale de quartz avec l'albite est faible, les carbonates (calcite) deviennent eux aussi blanchâtres alors que les minéraux ferromagnésiens tout comme le quartz et les oxydes de fer autres que la biotite ne sont pas vraiment attaqués et gardent leur apparence originale. Les colorations ont été faites à l'INRS–ETE principalement par Philippe Girard sous la supervision de Stéphane Prémont. La description systématique des altérations présentes dans les tranches de roches a ensuite été utilisée pour guider l'interprétation des données géochimiques et la cartographie des altérations dans les systèmes IOAA de la GBMZ. L'histoire de l'évolution des systèmes hydrothermaux étudiés et leur séquence d'altération ont été définies par la caractérisation précise des relations de recoupement entre les altérations. La description et l'identification des altérations et de leurs paragenèses minéralogiques ont été complémentées pour les échantillons à grains fins par de la microscopie optique et le microscope électronique à balayage (MEB). La majeure partie de la microscopie optique a été faite par Anthony Franco De Toni pour son mémoire de maîtrise et par Eric Potter en complémentarité avec les descriptions macroscopiques faites pour cette thèse de doctorat. Les analyses au microscope à balayage électronique (MEB) ont été faites à l'INRS–ETE avec la collaboration d'Arnaud de Koninck et aux laboratoires de la CGC-Ottawa avec la collaboration de Patricia Hunt (information complémentaires sur les MEB aux chapitres 6 et 7).

1.7.4 Analyses des éléments majeurs et traces sur roche totale

Deux types de méthodes (destructives et non-destructives) ont été employés pour les analyses géochimiques des échantillons de roches utilisés dans cette thèse de doctorat (voir Corriveau et al., 2015 pour la compilation des analyses et les procédures de validation des données). Dans les méthodes destructives avec analyses par ICP-MS (Linge, 2007; Beauchemin, 2008) et ICP-AES, la poudre obtenue après concassage et broyage a été fusionnée puis mise en solution dans des acides ou directement mise en solution dans des acides sans fusion. Les analyses par activation neutronique non-destructives (poudre analysée directement sans mise en solution ou fusion) ont été utilisées afin d'investiguer si les mises en solutions des minéraux étaient totales ou laissaient des résidus non analysés. La minéralogie complexe des altérations des systèmes à oxydes de fer et altération en éléments alcalins ou les quantités extrêmes d'un seul minéral dans la roche peuvent compliquer la mise en solution ou la fusion complète de toutes les phases minéralogiques lors des analyses destructives. La diversité des éléments dans les altérations et minéralisations peuvent aussi être à la source de nombreuses interférences absentes lors de l'analyse d'échantillons plus «normaux». Excepté pour certains échantillons de la Southern Breccia et de Fab riches en Th et U, tous les échantillons ont été concassés, cartés et pulvérisés à l'INRS–ETE. La pulvérisation est principalement faite avec des creusets en agate mais certains échantillons de la série 09CQA ont également été pulvérisés avec des creusets en fer et pauvres en chrome. Les échantillons potentiellement riches en Th et U de Fab et de la Southern Breccia ont été concassés et pulvérisés aux laboratoires d'ALS par creusets de fer pauvre en chrome.

Les analyses géochimiques à l'ICP-MS et ICP-AES avec fusion préalable pour les éléments majeurs et traces ont été faites à l'INRS (échantillons de 2005-2011) sous la supervision de Stéphane Prémont tandis que les analyses par solution acide ont été faites par l'ICP-MS aux laboratoires certifiés d'AcmeLabs (méthode 1EX, 4 acides – ICP-MS; échantillons de 2005-2009) et d'ALS (méthodes ME-MS81U, fusion – ICP-MS; ME-MS61U, 4 acides – ICP-MS; échantillons de 2010-2011) à Vancouver. Plusieurs ré-analyses ont été faites par le laboratoire de l'INRS–ETE quand des résultats analytiques ou des dissolutions semblaient inhabituelles afin de confirmer les résultats reportés. Un suivi était fait selon le type de roches impliquées pour ajuster la procédure analytique et de mise en solution des échantillons selon leurs composantes atypiques (e.g., échantillons composés de barite à > 90% modal). Les analyses pour les halogènes (chlore et fluor) ont été réalisées, entre 2005 et 2008, par chromatographie liquide à la CGC-Ottawa. Entre 2009 et 2011, les analyses pour le fluor ont été faites avec une électrode

sélective d'ions précédée d'une fusion aux laboratoires d'AcmeLabs (méthode 2A F; échantillons 2005-2009) et d'ALS (méthode F-ELE81a; échantillons 2010-2011) et le chlore par activation neutronique au laboratoire certifié Becquerel (méthode CL-NAA06; Toronto). Toutes les analyses multi-éléments non-destructives par activation neutronique ont été faites au laboratoire Becquerel (protocole BQ-NAA-1).

1.7.5 Quelques considérations sur les méthodes analytiques

Une étude comparative de la qualité des résultats analytiques en fonction de la méthode d'analyses a été faite en utilisant les analyses faites par le protocole 1EX d'AcmeLabs (digestion par 4 acides+ICP-MS), le protocole analytique de l'INRS (fusion+ICP-AES, ICP-MS) et celui de Becquerel (activation neutronique). Cette comparaison visait à cerner les méthodes analytiques optimales en fonction des éléments ciblés dans les altérations IOAA et d'évaluer la qualité des analyses généralement faites par l'industrie. Cette étude comparative montre que certaines analyses faites après une digestion par 4 acides suivant le protocole 1EX d'AcmeLabs tendent à sous-estimer de façon variable le contenu en Al et K de certains échantillons, surtout lorsque les concentrations en Al et K sont supérieures à 6 et 3% respectivement (Fig. 1-16). Pour de faibles concentrations en Ca et P, la digestion par 4 acides donne de meilleurs résultats (Fig. 1-16). Pour les métaux et plus particulièrement pour le Bi, Cd et Pb, les analyses par 4 acides sont généralement plus précises lorsque les métaux sont en faibles concentrations mais à plus haute concentration les méthodes de dissolution par 4 acides et par fusion donnent des résultats comparables (1-17).

Pour les ÉTR, cette analyse démontre que les analyses par fusion sont celles qui donnent les meilleurs résultats, particulièrement pour les ÉTR lourdes et moyennes (Figs. 1-18 et 1-19).

Les relations précédemment décrites sont applicables uniquement à la comparaison des protocoles d'analyses 1EX d'AcmeLabs, BQ-NAA-1 de Becqurel et aux analyses de l'INRS faites entre 2005 et 2009, mais ne s'applique pas aux analyses de l'INRS faites de 2010 à 2012 de même qu'aux analyses faites par ALS en 2010 et 2011. L'INRS, avec le temps, a fortement amélioré son protocole d'analyse des métaux en abaissant les limites de détection. Le protocole ME-MS61u d'ALS donne des résultats comparables à ceux obtenus par fusion pour la majorité des élément excepté Rb et Ta qui donnent de meilleurs résultats par fusion à l'INRS–ETE et Zn qui donne de meilleurs résultats par la méthode ME-MS61u d'ALS (voir Tableau 1-3).

Tableau 1-3 Coefficients de corrélation pour les analyses faites à l'INRS–ETE (fusion) et celles faites ALS avec le protocole ME-MS61u

Élément	Corrélation	Élément	Corrélation
Al	0.952	P	0.995
Ba	0.977	Pb	0.735
Ca	0.999	Rb	0.624
Ce	0.992	Sn	0.888
Cr	0.917	Sr	0.984
Cu	1.000	Ta	0.651
Fe	0.996	Th	0.956
Hf	0.942	Ti	0.998
K	0.896	U	0.988
La	0.993	V	1.000
Mg	0.999	W	0.998
Mn	0.992	Y	0.966
Na	1.000	Zn	0.776
Nb	0.972	Zr	0.943

Cette étude comparative montre que chaque protocole et laboratoire a ses forces et faiblesses et que la qualité des résultats en est fortement influencée. Ces constats ont guidé le choix des différentes méthodes et laboratoires utilisés pour analyser les échantillons reliés au projet (voir la description des méthodes utilisées pour chaque cas d'études dans les chapitres suivants). Par contre les échantillons de la Southern Breccia et certains indices de la GBMZ (Cole U, Fab) ont été envoyé à un laboratoire spécialisé dans les analyses d'échantillons à concentrations élevées en U pour des raisons de santé et sécurité en laboratoire.

1.8 Articles composants la thèse et description de la contribution de chacun des auteurs

Cette section liste les articles qui forment la deuxième partie et le corps central de la thèse et défini la contribution de chacun des auteurs pour chaque article. La deuxième partie de la thèse comprenant les articles est suivie en troisième partie par la description de l'avancement des connaissances résultant de cette thèse et les conclusions sur les réponses apportées à la problématique centrale de cette thèse sur les relations entre la mobilité des éléments et la formation de différents gîtes dans les systèmes IOAA.

1.8.1 Chapitre 2

Ce chapitre représente l'article suivant:

> **Montreuil, J.-F., Corriveau, L**., Tectono-magmatic evolution of the southern Great Bear magmatic zone (Northwest Territories, Canada) – Implications on the formation of iron oxide alkali-altered hydrothermal systems, Soumis à «*Economic Geology*».

L'auteur de cette thèse en est le premier auteur. Il a défini les unités géologiques associées aux échantillons collectés dans le sud de la GBMZ en se basant sur la carte géologique de Gandhi et al. (2014) et l'observation des échantillons collectés dans chacune des unités, a défini l'affinité chimique des différentes roches plutoniques et volcaniques du sud de la GBMZ, a produit les cartes d'altération et créé la méthode de présentation des altérations IOAA en utilisant les concentrations molaires de Na, Ca, Fe, K et Mg et a proposé les principales interprétations reliées à ce chapitre. Louise Corriveau, qui est seconde auteure, a collecté et décrit plusieurs échantillons et zones d'altération présentés dans cette contribution, a validé et approfondi les descriptions et interprétations proposées dans l'article et amélioré la clarté générale du message qui y est véhiculé.

1.8.2 Chapitre 3

Ce chapitre contient l'article suivant:

> **Corriveau, Montreuil, J.-F., L., Potter, E.G.**, Linkages amongst IOCG, IOA and affiliated deposits: From the Great Bear magmatic zone records to an Iron Oxide Alkali-Alteration facies ore deposit model, Soumis à «*Economic Geology*».

Louise Corriveau est la première auteure du chapitre 3 et a élaboré le concept et défini la thématique principale de l'article, fait la majeure partie de la rédaction initiale, des travaux de terrain et de la collecte d'échantillons, a défini les principaux faciès d'altération et établi les lignes directrices de l'interprétation. L'auteur de cette thèse, second auteur sur cet article, à quantifier l'intensité des faciès d'altération avec un système novateur de code-barres utilisant la proportion molaire entre Na, Ca, K, Fe et Mg, a produit les cartes montrant la distribution de l'altération pour certains systèmes de la GBMZ, a défini par le profilage compositionnel des zones minéralisées le long de carottes de forage les relations entre enrichissement en métaux et altération, a interprété les faciès d'altération des gîtes IOCG utilisés comme références pour l'article, a contribué significativement à la rédaction des sections décrivant les zones d'altération de la GBMZ, a contribué à la description des faciès altérations sur le terrain et à la collecte

d'échantillons, a contribué à définir les principaux faciès d'altération de la GBMZ, a contribué à clarifier le message véhiculé par l'article et a activement contribué à la production des figures de ce chapitre. Eric Potter, qui est le troisième auteur, a contribué à clarifier le message véhiculé par la publication et mieux cadrer les descriptions des différentes zones minéralisées de la GBMZ.

1.8.3 Chapitre 4

Ce chapitre contient l'article suivant:

> **Montreuil, J.-F., Corriveau, L., Potter, E.G.,** On the relation between alteration signature and metal endowment of iron oxide alkali altered systems, southern Great Bear magmatic zone (Canada), Soumis à «*Economic Geology*».

Dans cette contribution, l'auteur de cette thèse est premier auteur. Il a réalisé conjointement avec Louise Corriveau et Eric Potter, la description des altérations et la collecte d'échantillons des principaux indices minéralisés du sud de la GBMZ. Il a aussi compilé les données géochimiques dans les rapports d'exploration et produit l'ensemble des sections chimiques associant altération et minéralisation pour chacun des indices. Par la suite, il a confirmé les altérations identifiées lors des travaux de terrain dans les principales zones minéralisées avec les tranches de roche colorées et les lames minces et a confirmé les stades d'altérations auxquels certains métaux ont été concentrés par la description de lames minces avec le microscope électronique à balayage (MEB). Louise Corriveau a contribué en validant et resserrant les descriptions des altérations pour chaque indice et les points abordés dans la discussion et en identifiant et décrivant les zones d'altérations principales sur le terrain. Eric Potter, qui est le troisième auteur, a contribué à clarifier le message véhiculé par l'article et mieux cadrer les descriptions des différentes zones minéralisées de la GBMZ. Il a aussi contribué à l'acquisition des images au MEB décrivant la minéralogie de l'indice uranifère de Cole et des indices de la Southern Breccia.

Cette contribution utilise également des descriptions de terrain de John Kerswill de la Commission géologique du Canada, quelques photos de lames minces prises par Anthony De Toni et des images acquises par MEB prises par Philippe Normandeau (Brooke) pour illustrer le propos discuté dans ce chapitre; leur contribution est soulignée dans les remerciements. L'auteur de cette thèse a cependant interprété l'information contenue dans les images utilisées relativement à la distribution des métaux à chacun des stades d'altération et intégré cette information dans l'article.

1.8.4 Chapitre 5

Ce chapitre contient l'article suivant:

> **Montreuil, J.-F., Corriveau, Grunsky, E.C.,** 2013, Compositional data analysis of hydrothermal alteration in IOCG systems, Great Bear magmatic zone, Canada: to each alteration type its own geochemical signature; Publié par «*Geochemistry: Exploration, Environment, Analysis*», v. 13, p. 229–247.

L'auteur de cette thèse est le premier auteur pour cette contribution. Il a identifié les roches altérées par hydrothermalisme utilisées pour faire la modélisation géochimique; a fait l'analyse statistique des compositions d'altération; a posé les lignes directrices des interprétations présentées dans l'article; et a mis sur pied et construit les diagrammes discriminant les altérations IOAA. Louise Corriveau a fait les travaux de terrain, échantillonné et décrit la plupart des altérations utilisées dans cette contribution; a contribué à l'interprétation des tendances observées dans les variations chimiques des altérations; et a revu et amélioré le contenu général de l'article. Eric Grunsky a fourni le script dans R pour faire l'analyse en composantes principales; a validé les résultats de l'analyse compositionnelle; et a validé l'utilisation de concentrations molaires pour les indices discriminant l'altération.

1.8.5 Chapitre 6

Ce chapitre contient l'article suivant:

> **Montreuil, J.-F., Corriveau, L., Potter, E.G.,** 2015, Formation of albitite-hosted uranium within IOCG systems: The Southern Breccia, Great Bear magmatic zone, Northwest Territories, Canada; Publié par «*Mineralium Deposita*», v. 50, p. 293–325.

L'auteur de cette thèse a fait la cartographie et l'échantillonnage initial des indices uranifères de la Southern Breccia sur le terrain après leur découverte et contraint les principaux types d'altération associés aux minéralisations uranifères. Louise Corriveau a par la suite poursuivi et affiné la cartographie et la description des types d'altération formés dans la Southern Breccia et collecté plusieurs échantillons de la minéralisation uranifère. Eric Potter, Anthony De Toni et l'auteur ont ensuite complété la cartographie et l'échantillonnage des zones uranifères de la Southern Breccia. L'auteur, en collaboration avec Louise Corriveau et Eric Potter, a fait les principales interprétations reliées à cette contribution ainsi que la description des principaux

faciès d'altération et des unités géologiques de la Southern Breccia. Eric Potter a contribué à établir la minéralogie de la minéralisation uranifère et à retracer l'association spatio-temporelle des gîtes d'uranium encaissés dans des albitites avec les gîtes IOCG. Louise Corriveau a également proposé l'hypothèse de l'exhumation différentielle syn-volcanique et syn-altération pour expliquer la zonation de l'altération dans le système de Lou.

1.8.6 Chapitre 7

Ce chapitre contient l'article suivant:

> **Montreuil, J.-F., Potter, E.G., Corriveau, L., Davis, W.J.,** 2016, Element mobility patterns in magnetite-group IOCG systems: The Fab IOCG system, Northwest Territories, Canada; Publié par «Ore Geology Reviews», v. 72, p. 562–584.

Dans cette publication sur le système de Fab, l'auteur de cette thèse a participé, avec Anthony De Toni, Eric Potter, Louise Corriveau et Pierre-Simon Ross, à la cartographie des altérations et la collecte des échantillons; a contribué à la compilation et l'interprétation des données de terrain, des analyses chimiques et des échantillons pour produire la carte des altérations et de la géologie publiée dans Potter et al. (2013b); a traité et interprété les données géochimiques et a posé les lignes directrices principales de la discussion et des conclusions proposées dans cette publication. Eric Potter et Louise Corriveau, qui sont respectivement deuxième et troisième auteur, ont approfondi et validé les interprétations proposées dans la discussion et recentré et resserré certaines sections de la publication sur la thématique de la mobilité des éléments dans ce système. William Davis a daté les échantillons pour géochronologie collectés par l'auteur et Eric Potter et contraint l'âge du système hydrothermal. Lors des travaux de terrain, Pierre-Simon Ross a contribué à clarifier la nature des roches affleurantes et démontré que la grande majorité de ces roches sont des intrusions subvolcaniques porphyriques. Enfin Christopher Lawley de la Commission géologique du Canada, avec ses commentaires détaillés et constructifs lors de sa révision de la publication, a grandement contribué à orienter la thématique de la discussion et à améliorer la qualité et la portée des interprétations.

Figure 1-1 Localisation de la GBMZ au Canada
(Tirée et modifiée de Google maps, 2014)

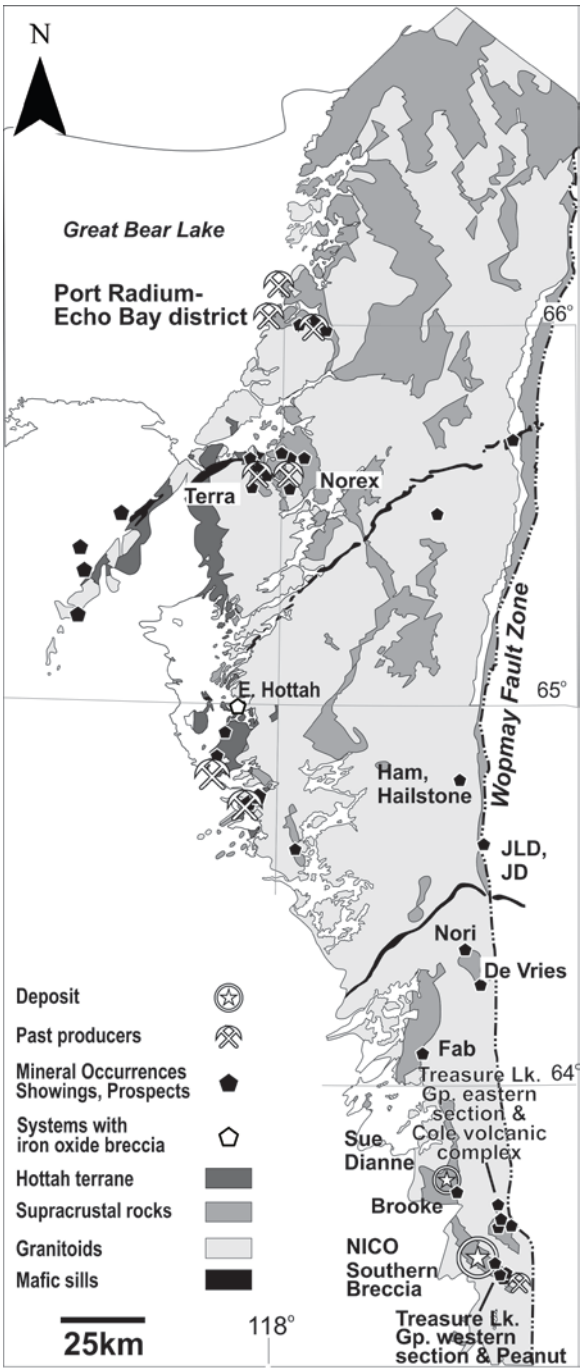

Figure 1-2 Carte géologique simplifiée de la GBMZ et localisation des principaux systèmes IOAA

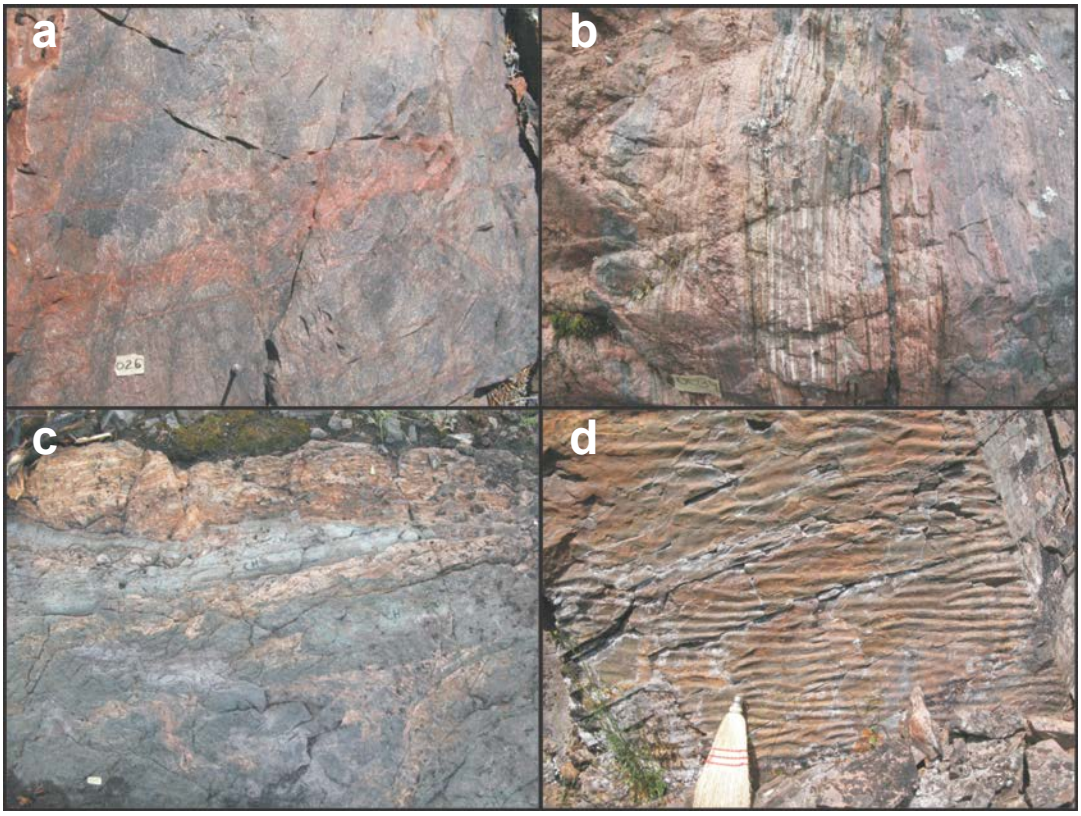

Figure 1-3 Photos de terrain témoignant de la qualité des affleurements dans la GBMZ

(a) Front d'altération potassique dans une roche volcanique felsique à l'indice de Brooke; (b) Remplacement lit-par-lit des roches sédimentaires du Groupe de Treasure Lake à l'indice de Hump; (c) Remplacement polyphasé de haute température Ca–Fe des roches sédimentaires du Groupe de Treasure Lake à l'indice LP's partiellement remplacé par l'altération de faible température K–Fe à chlorite; (d) Rides de plage préservées dans un lit de siltstone du Groupe de Treasure Lake près de l'indice LP's.

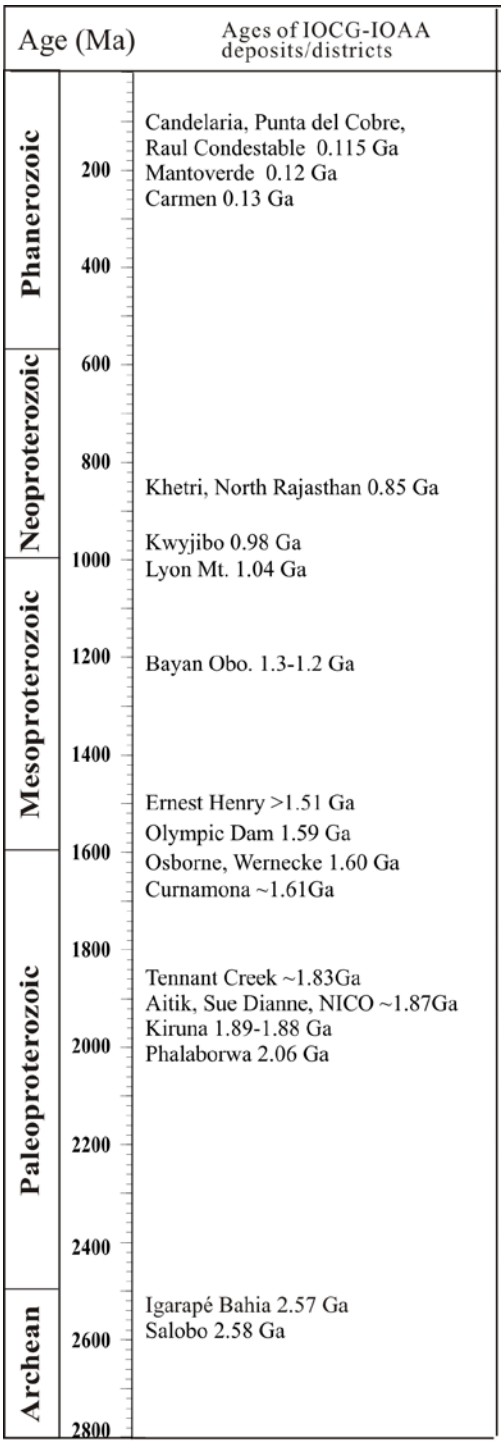

Figure 1-4 Age des principaux gisements IOCG à travers le monde.

L'âge de Kwijibo vient d'une veine minéralisée recoupant les altérations à magnétite métamorphisées

Modifié de Corriveau (2007)

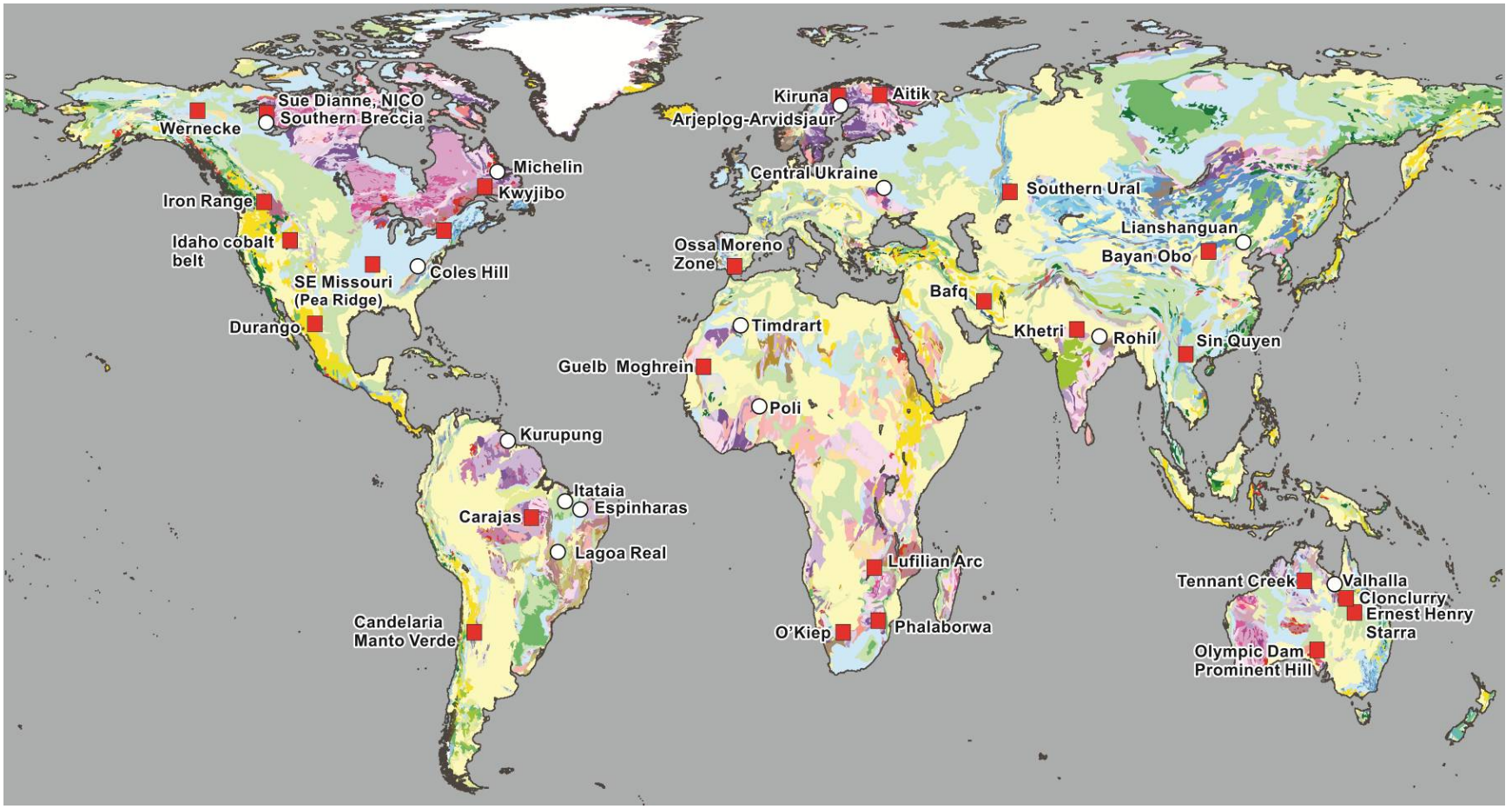

Figure 1-5 Localisation d'une sélection de systèmes IOAA (carrés rouges) et de gîtes d'uranium encaissés dans des albitites (cercles blancs)

Modifiée de Corriveau (2007).

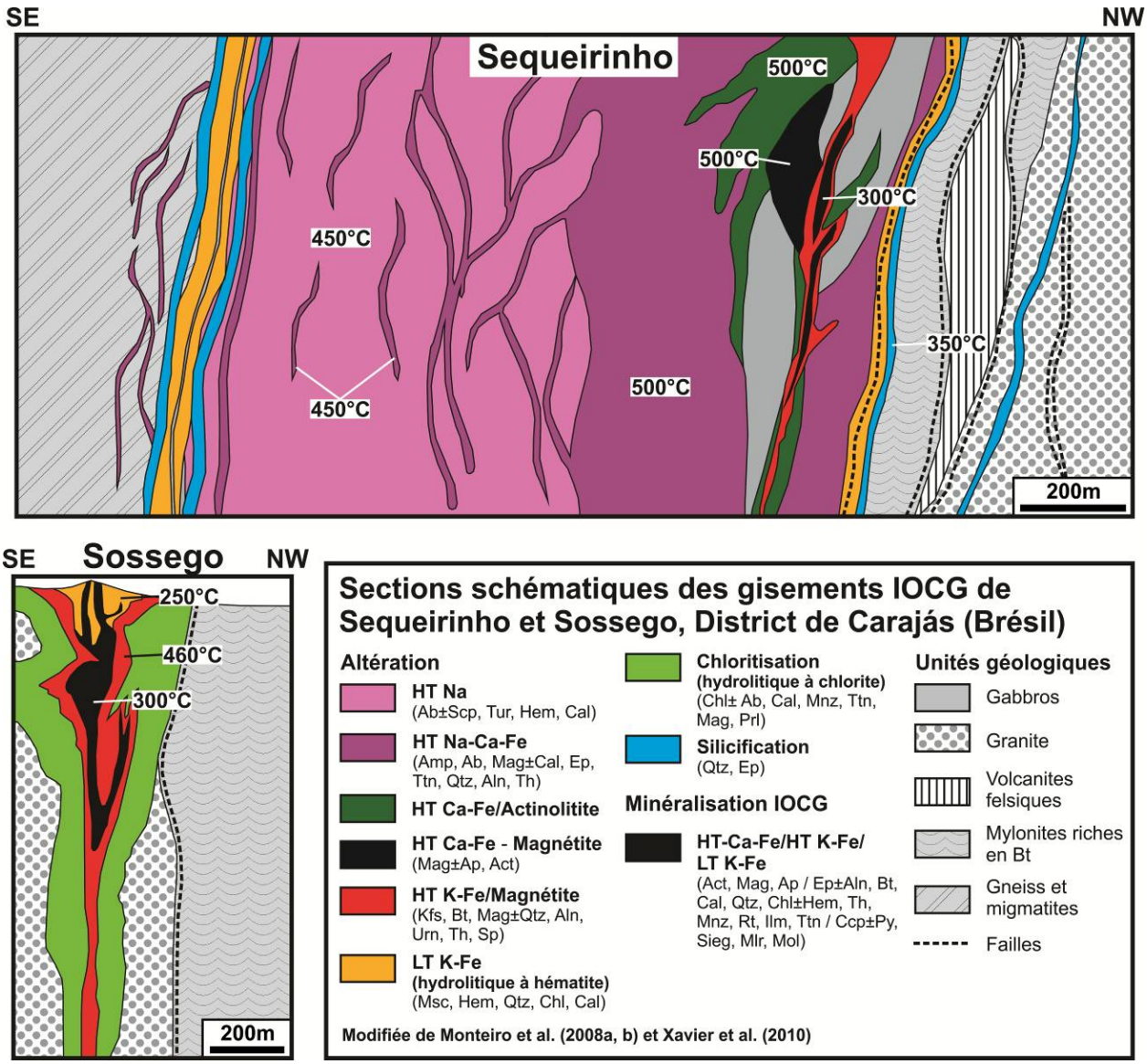

Figure 1-6 Zonation et températures de formation des altérations hydrothermales dans les gisements IOCG de Sequeirinho (groupe à magnétite) et de Sossego (groupe à hématite) dans le district de Carajás au Brésil

Les sections sont faites à partir de Monteiro et al. (2008a, b) et de Xavier et al. (2010).
Abréviations des minéraux selon Whitney et Evans (2010) sauf : Qtz = Quartz, Sieg = Siegenite, Th = Thorianite.

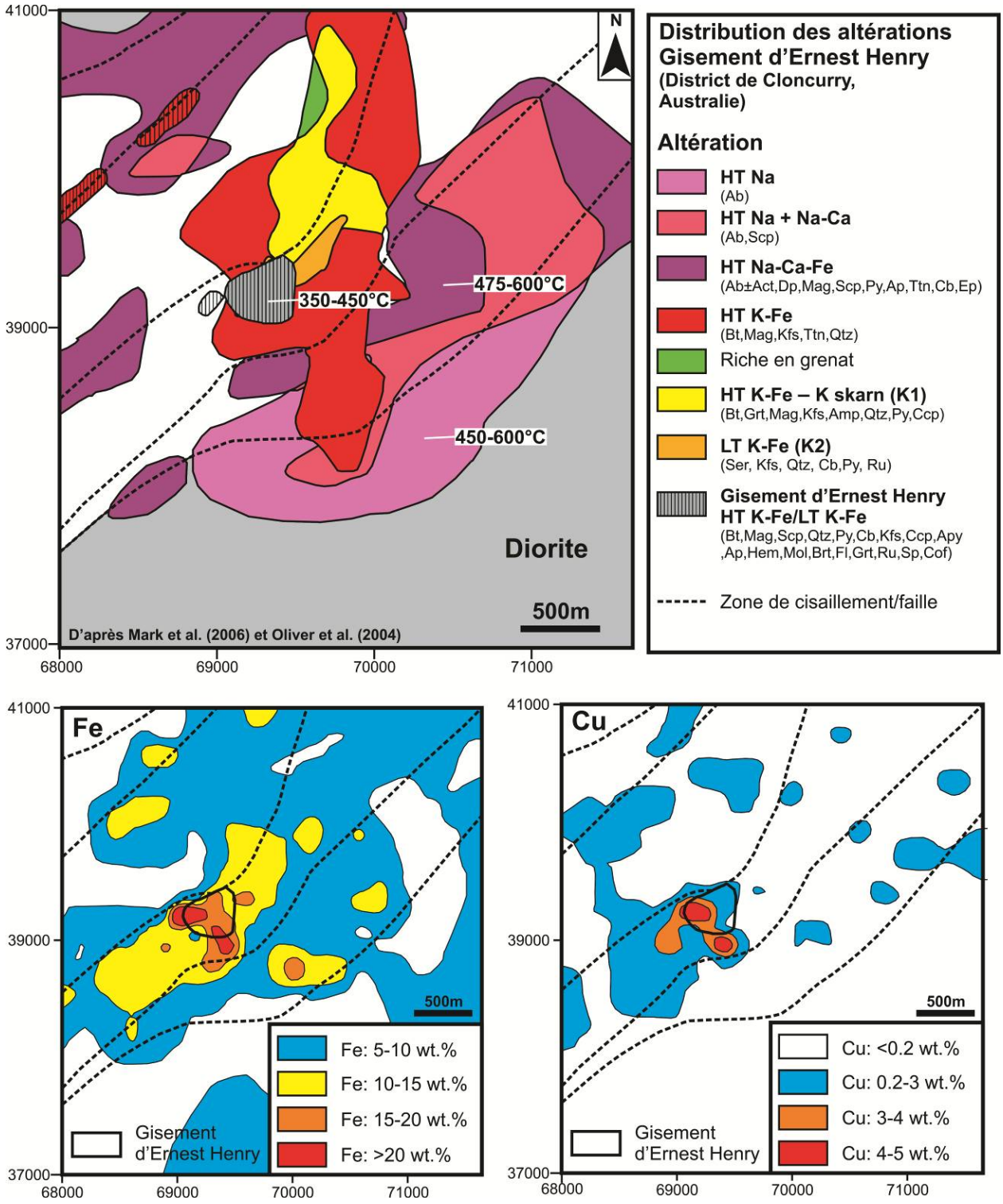

Figure 1-7 Zonation et températures de formation des altérations hydrothermales et distribution du cuivre et du fer dans le gisement IOCG du groupe à magnétite d'Ernest Henry dans le district de Cloncurry en Australie

Les cartes sont faites à partir de Mark et al. (2006); Les températures sont tirées de Oliver et al. (2004). Le système de coordonnée est en mètres et provient de la grille superposée sur la propriété.
Abréviations des minéraux selon Whitney et Evans (2010) excepté : Cof = Coffinite.

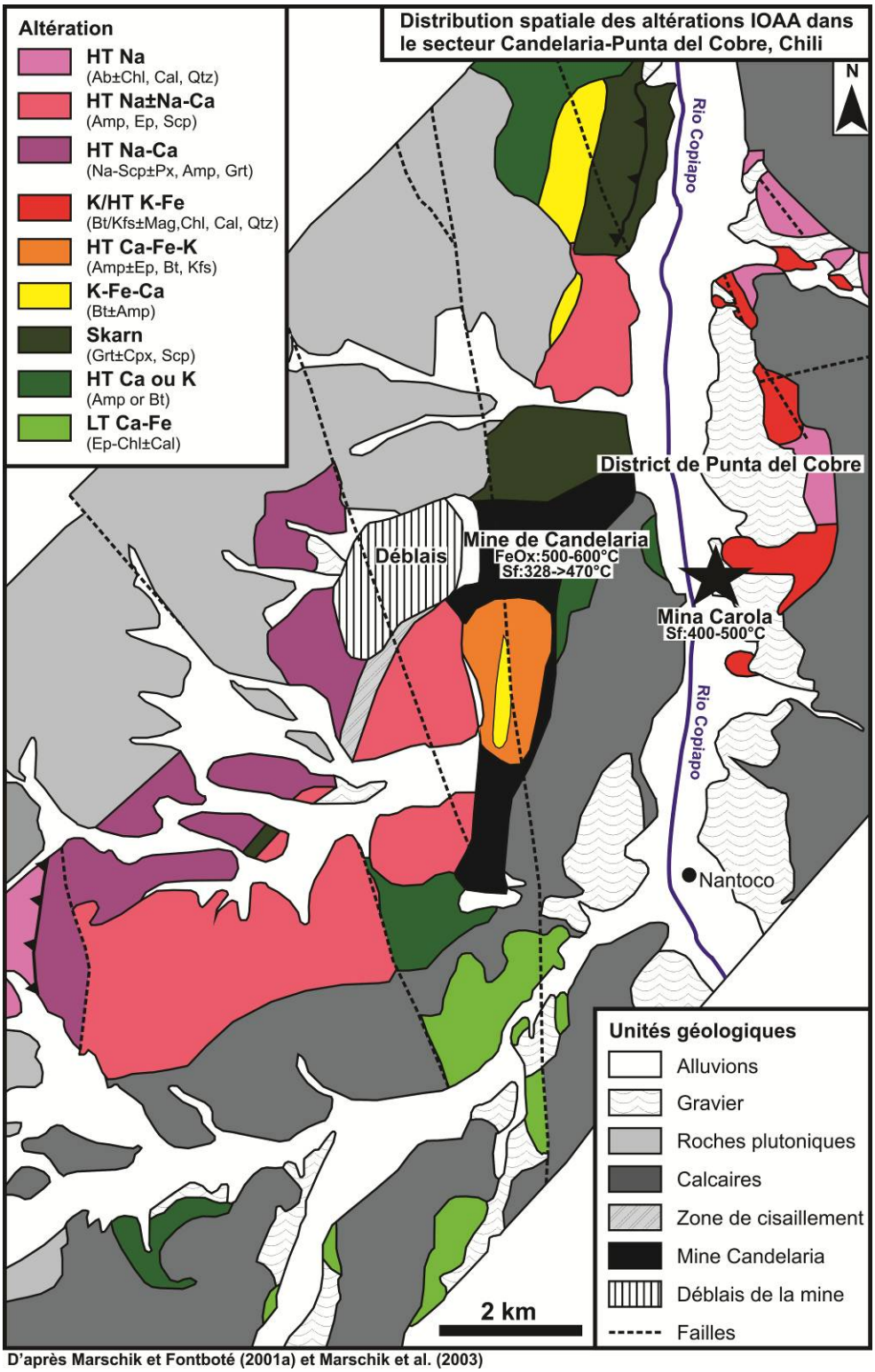

Figure 1-8 Distribution et températures de formation des altérations hydrothermales dans le district de *Punta del Cobre* au Chili, hôte du gisement IOCG du groupe à magnétite de Candelaria

La carte est tirée de Marschik et al. (2003). Les températures sont tirées de Marschik et Fontboté (2001a).
FeOx = Altération à magnétite, Sf = Formation des sulfures de cuivre (Ccp).
Abréviations des minéraux selon Whitney et Evans (2010) sauf: Qtz = Quartz.

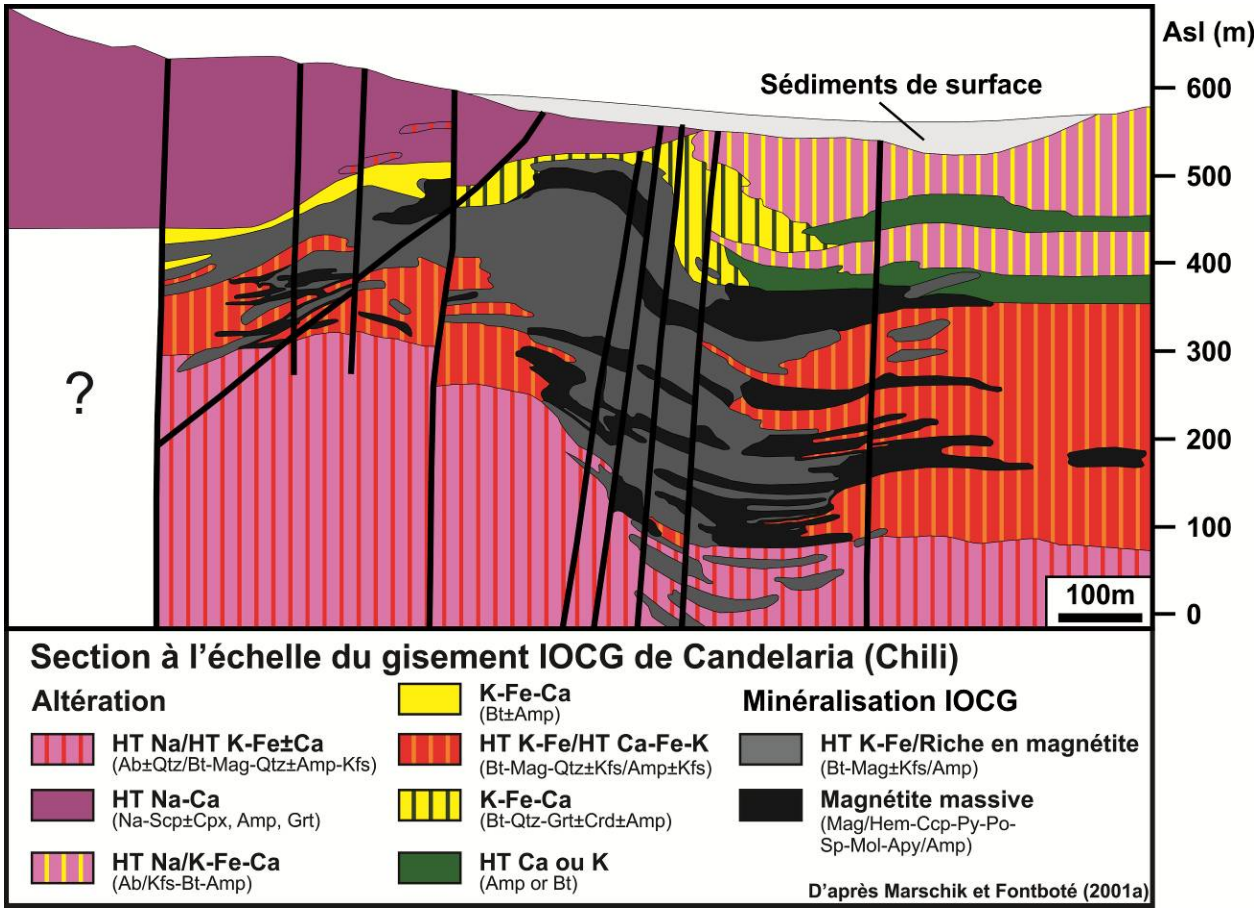

Figure 1-9 Distribution des altérations hydrothermales dans le gisement IOCG du groupe à magnétite de Candelaria, Ceinture ferrifère du Chili

La section et les altérations sont tirées et interprétées à partir de Marschik et Fontboté (2001a). Asl = Au-dessus du niveau de la mer.
Abréviations des minéraux selon Whitney et Evans (2010) sauf: Qtz = Quartz.

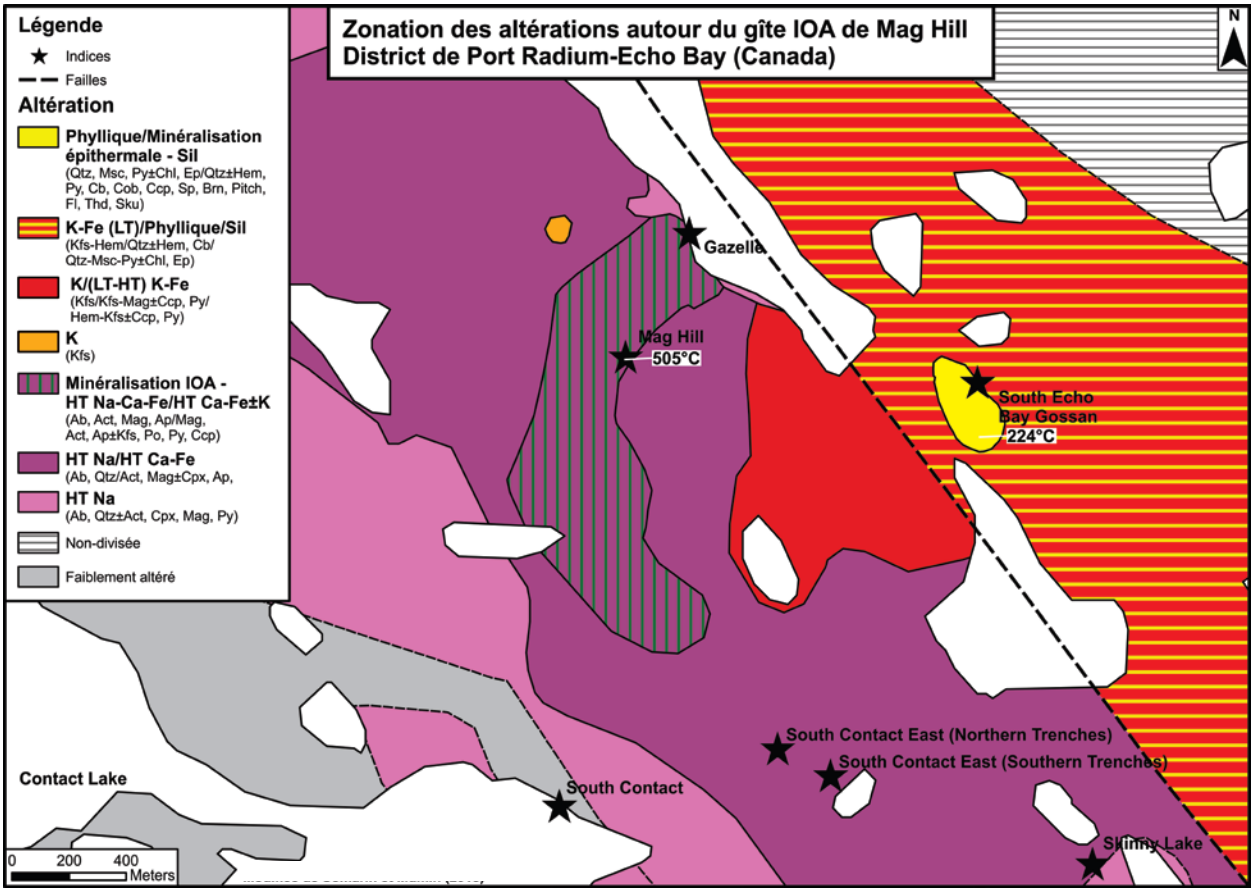

Figure 1-10 Zonation et températures de formation des altérations hydrothermales associées à l'indice IOA de Mag Hill dans le district de Port Radium –Echo Bay au nord de la GBMZ

La carte est modifiée et les températures sont tirées de Somarin et Mumin (2014).
Abréviations des minéraux selon Whitney et Evans (2010) excepté: Cob = cobaltite, Pitch = Pitchblende, Qtz = Quartz, Sku = Skuttérudite, Thd = Tetrahédrite.

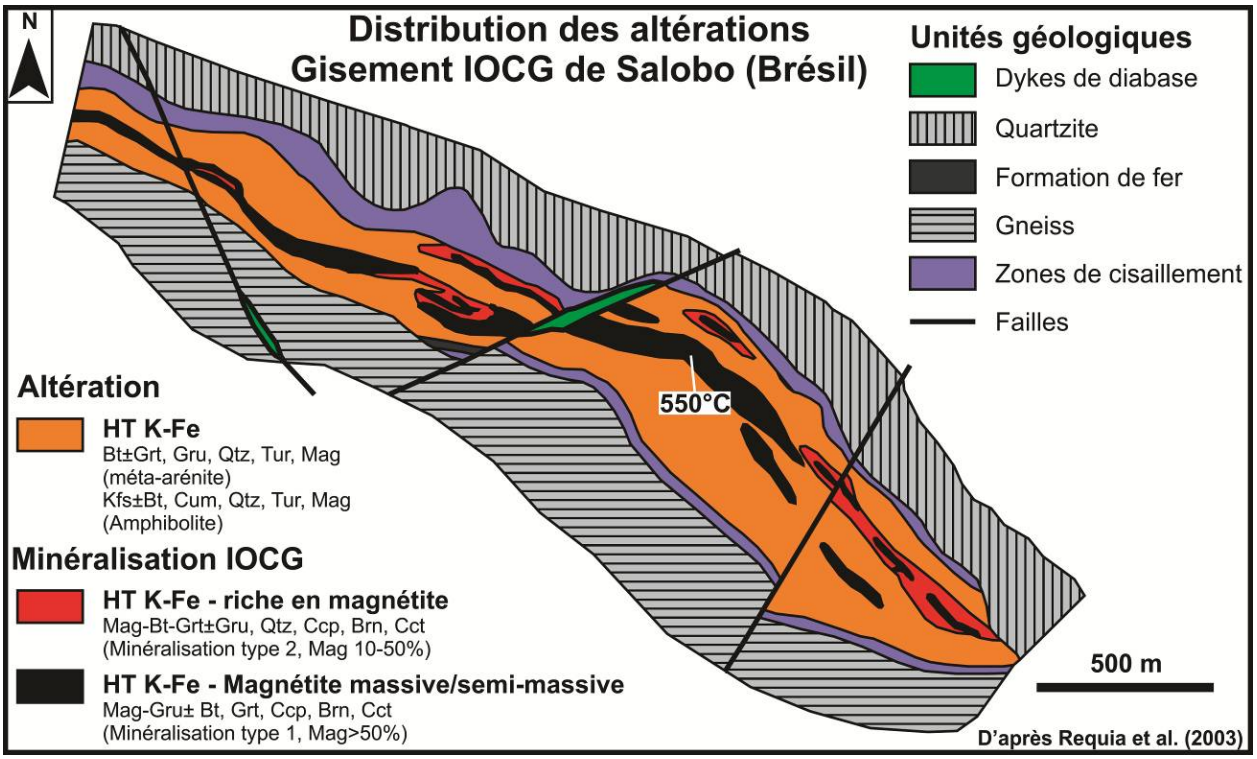

Figure 1-11 Zonation et températures de formation des altérations hydrothermales dans le gisement IOCG du groupe à magnétite de Salobo dans le district de Carajás au Brésil

La carte et les températures sont modifiées de Requia et al. (2003).
Abréviations des minéraux selon Whitney et Evans (2010) sauf: Qtz = Quartz.

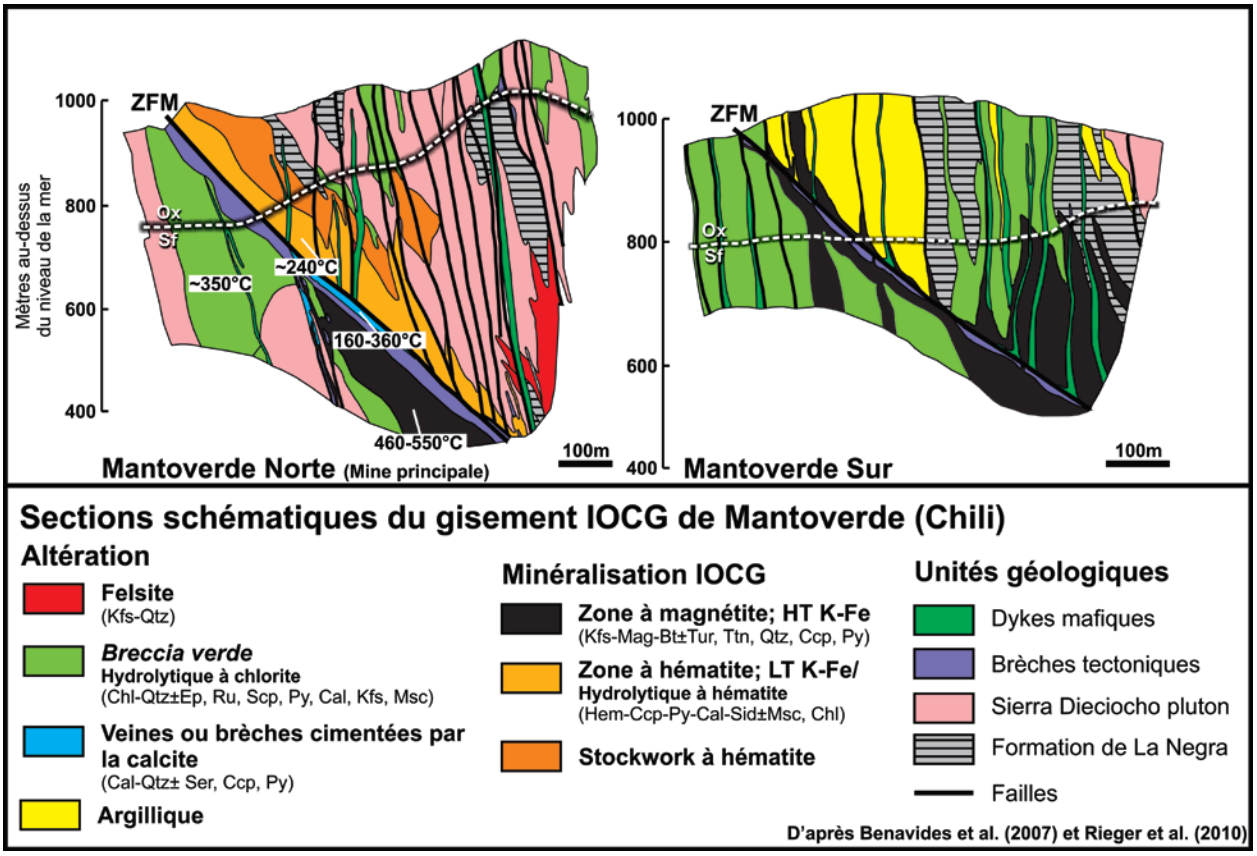

Figure 1-12 Sections montrant la zonation et températures de formation des altérations hydrothermales dans les deux zones principales du gisement IOCG du groupe à hématite de Mantoverde au Chili

La distance séparant les deux sections est de ±2,5 km et la carte montrant la localisation des sections est disponible dans Rieger et al. (2010).
Les sections et les températures sont tirées de Benavides et al. (2007) ainsi que de Rieger et al. (2010); ZFM = Zone de faille de Mantoverde; Ox = Zone supergène à oxydes, Sf = Zone hypogène à sulfures
Abréviations des minéraux selon Whitney et Evans (2010) sauf: Qtz = Quartz.

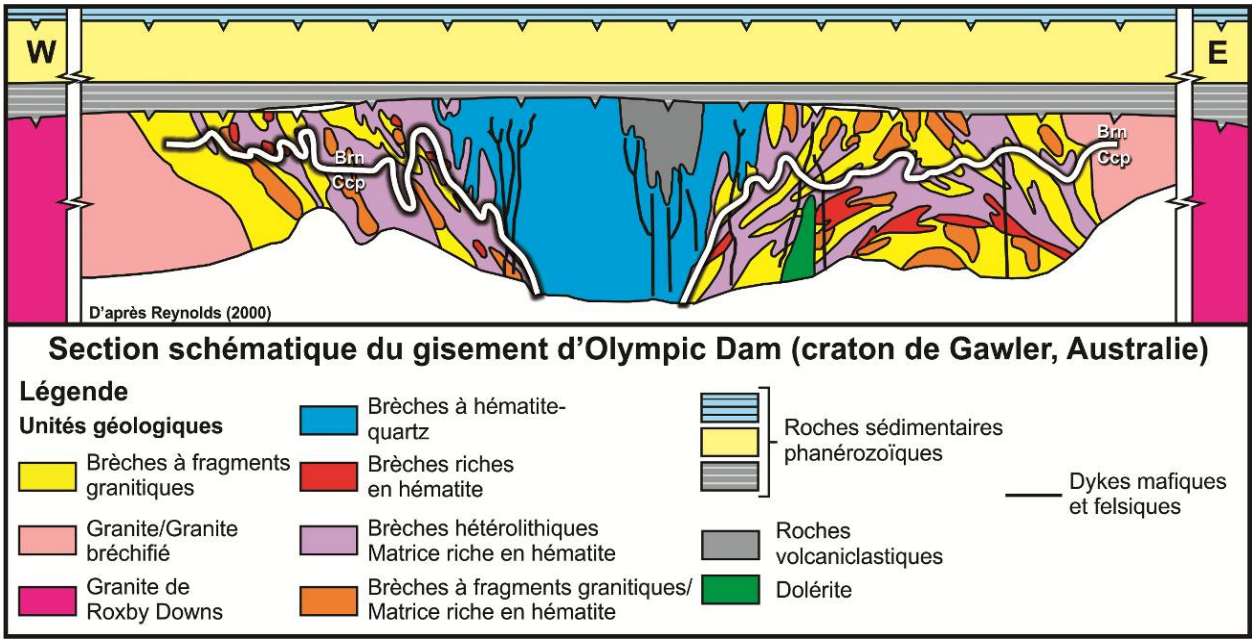

Figure 1-13 Section schématique du gisement IOCG du groupe à hématite d'Olympic Dam (craton de Gawler en Australie) montrant la zonation des sulfures, de la bréchification et de l'altération dans le gisement

La section est modifiée de Reynolds (2000).
Abréviations des minéraux selon Whitney et Evans (2010).

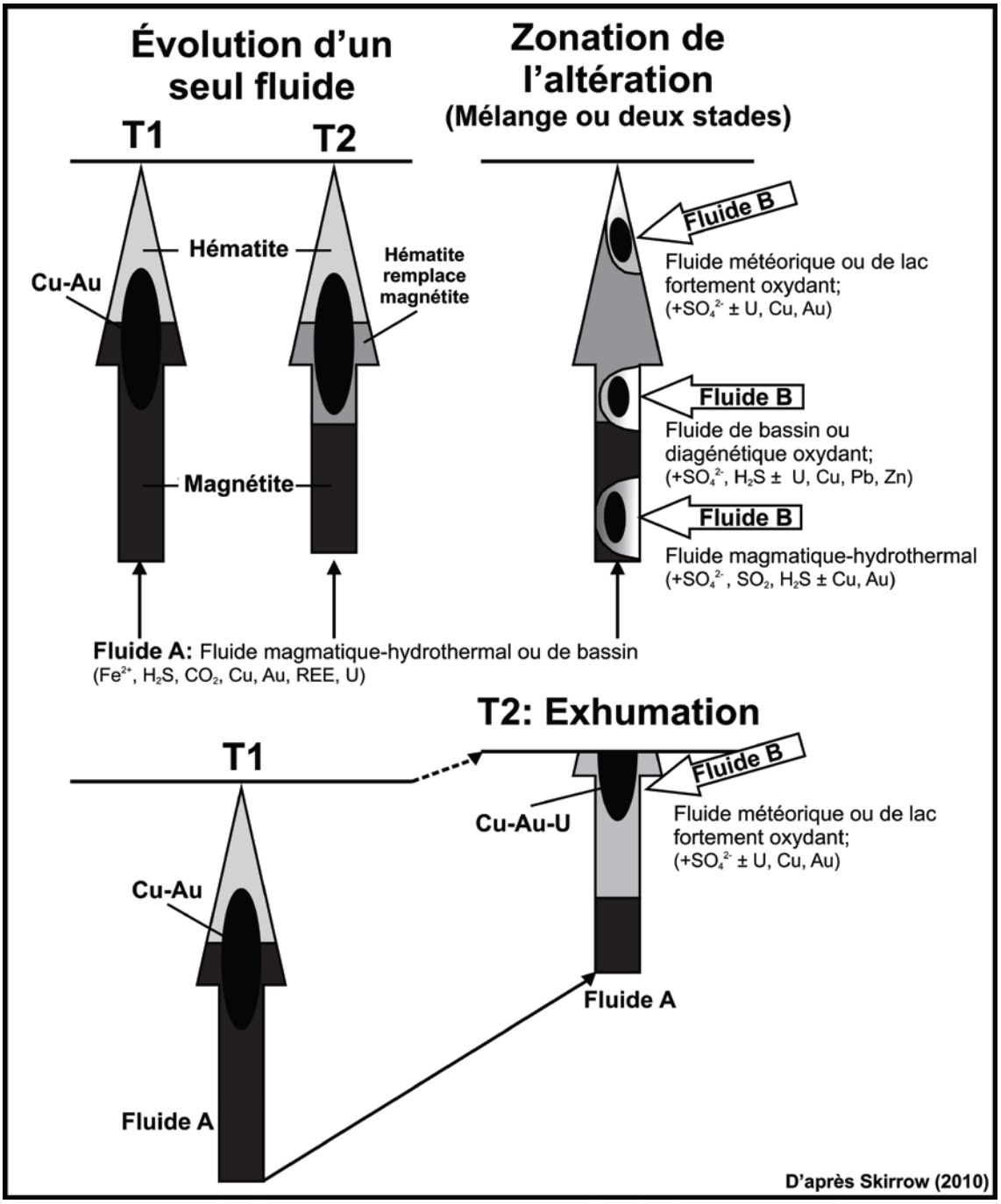

Figure 1-14 Modèle d'évolution de l'altération à magnétite vers les altérations à hématite dans les systèmes IOAA ainsi que sources et compositions probables des fluides hydrothermaux impliqués

Modifiée de Skirrow (2010).

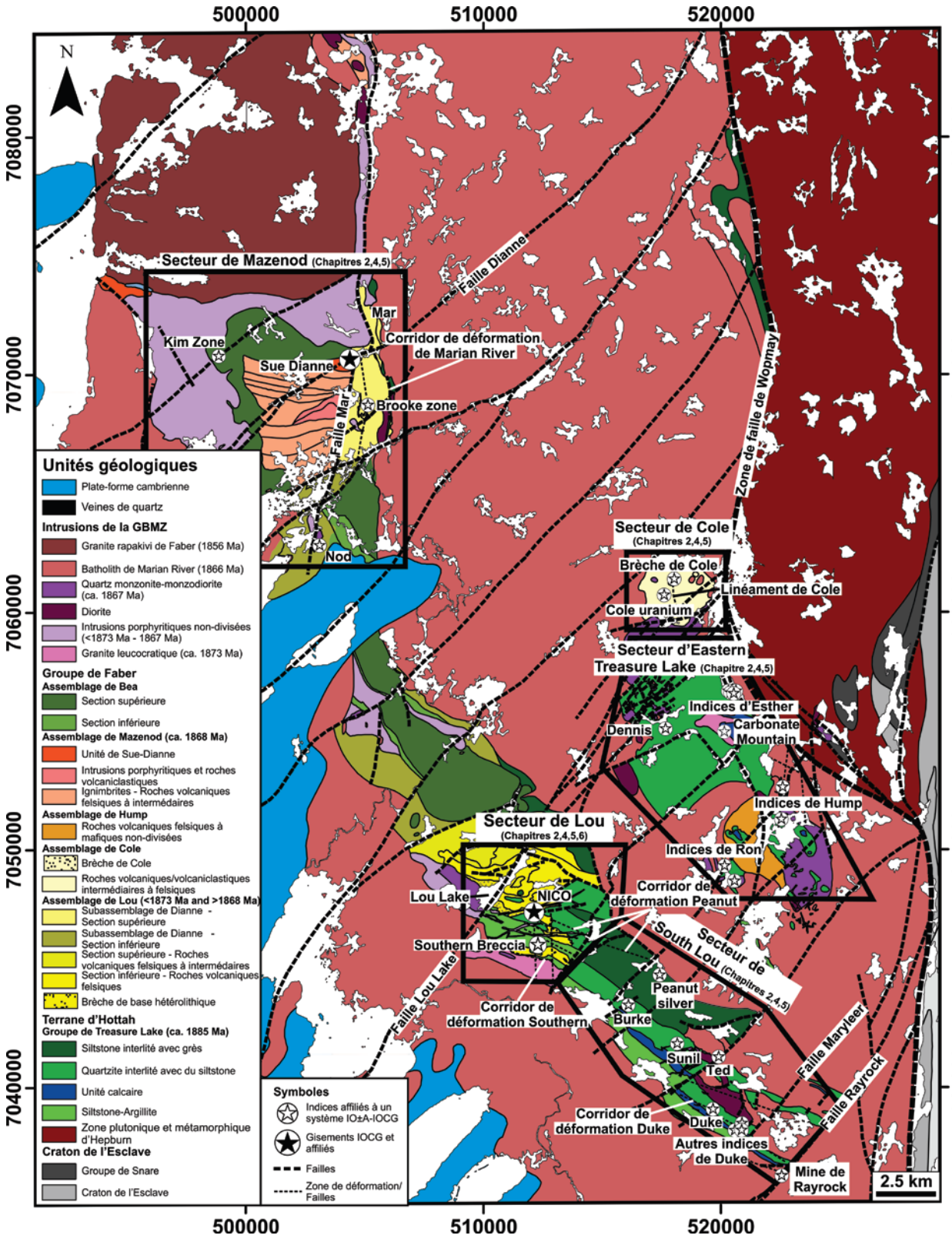

Figure 1-15 Carte géologique et distribution des systèmes IOAA et IOCG dans le sud de la GBMZ

Géologie d'après Gandhi et al. (2014); Coordonnées UTM en NAD83 pour la zone 11.

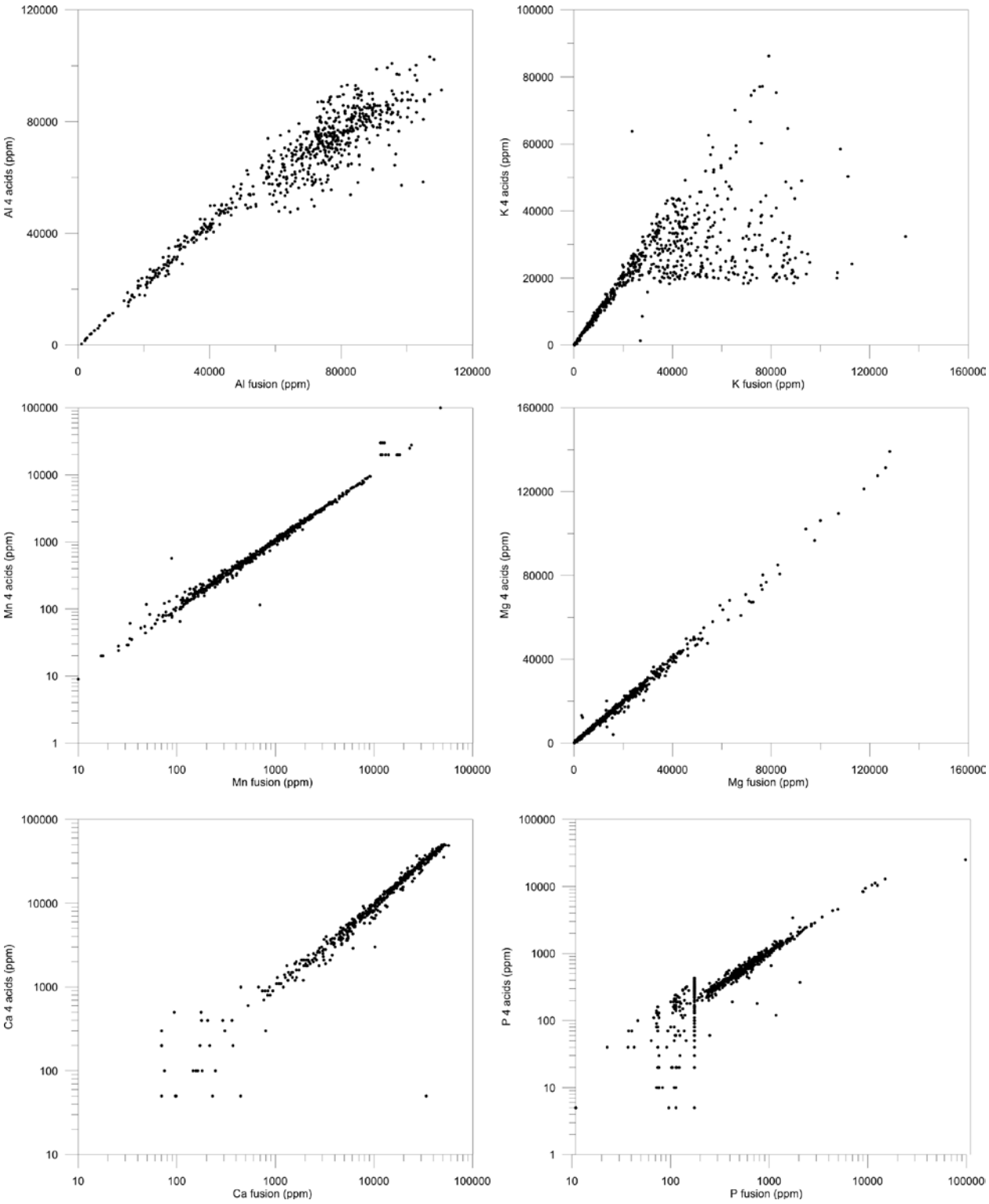

Figure 1-16 Comparaison entre les analyses d'éléments majeurs par ICP-MS suivant une digestion par fusion et 4 acides

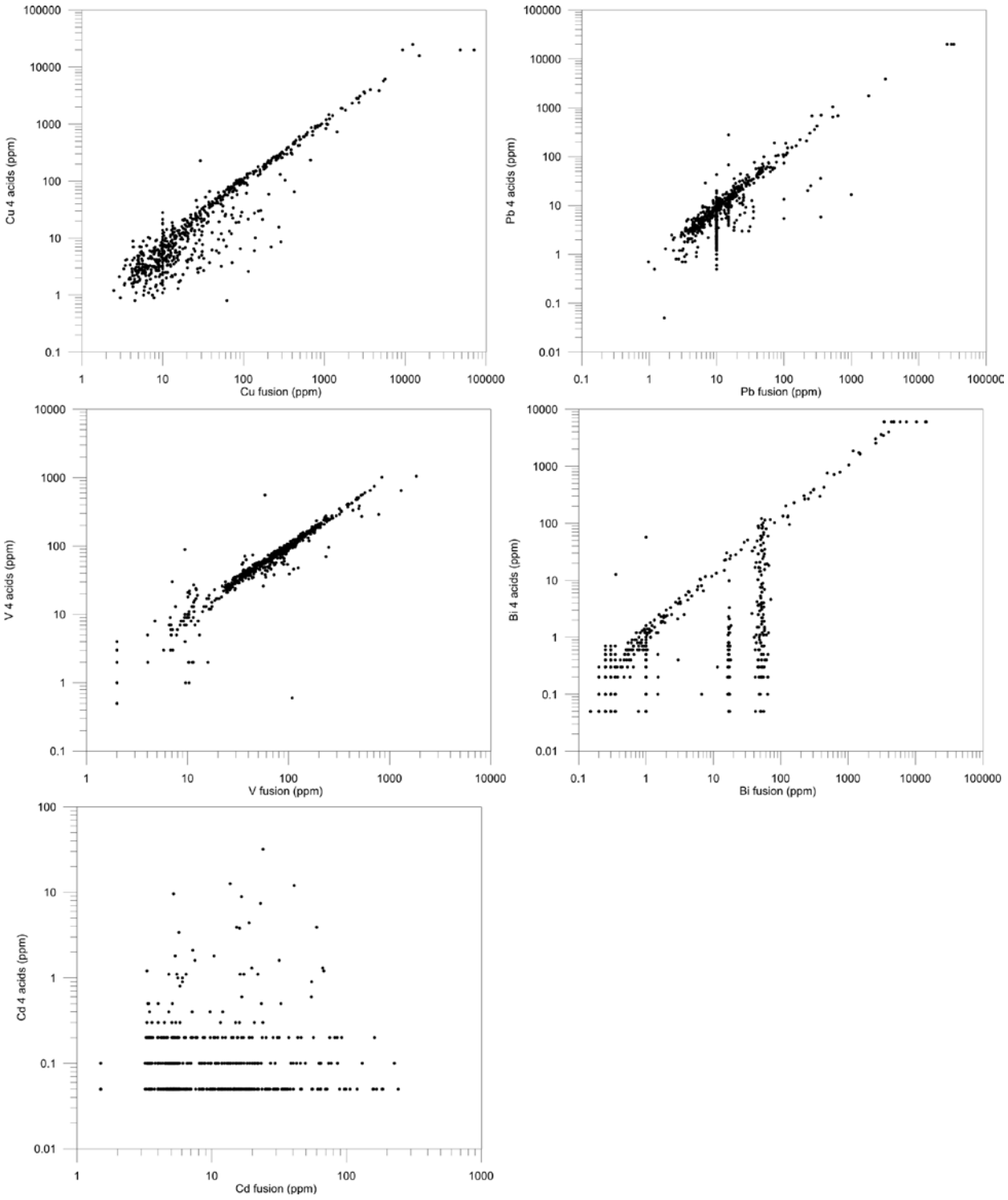

Figure 1-17 Comparaison entre les analyses de métaux par ICP-MS suivant une digestion par fusion et 4 acides

Les effets des limites de détection élevées pour les métaux (Bi, Cd, Cu et Pb) pour les analyses par ICP-AES de l'INRS faite entre 2005 et 2008 sont bien visibles

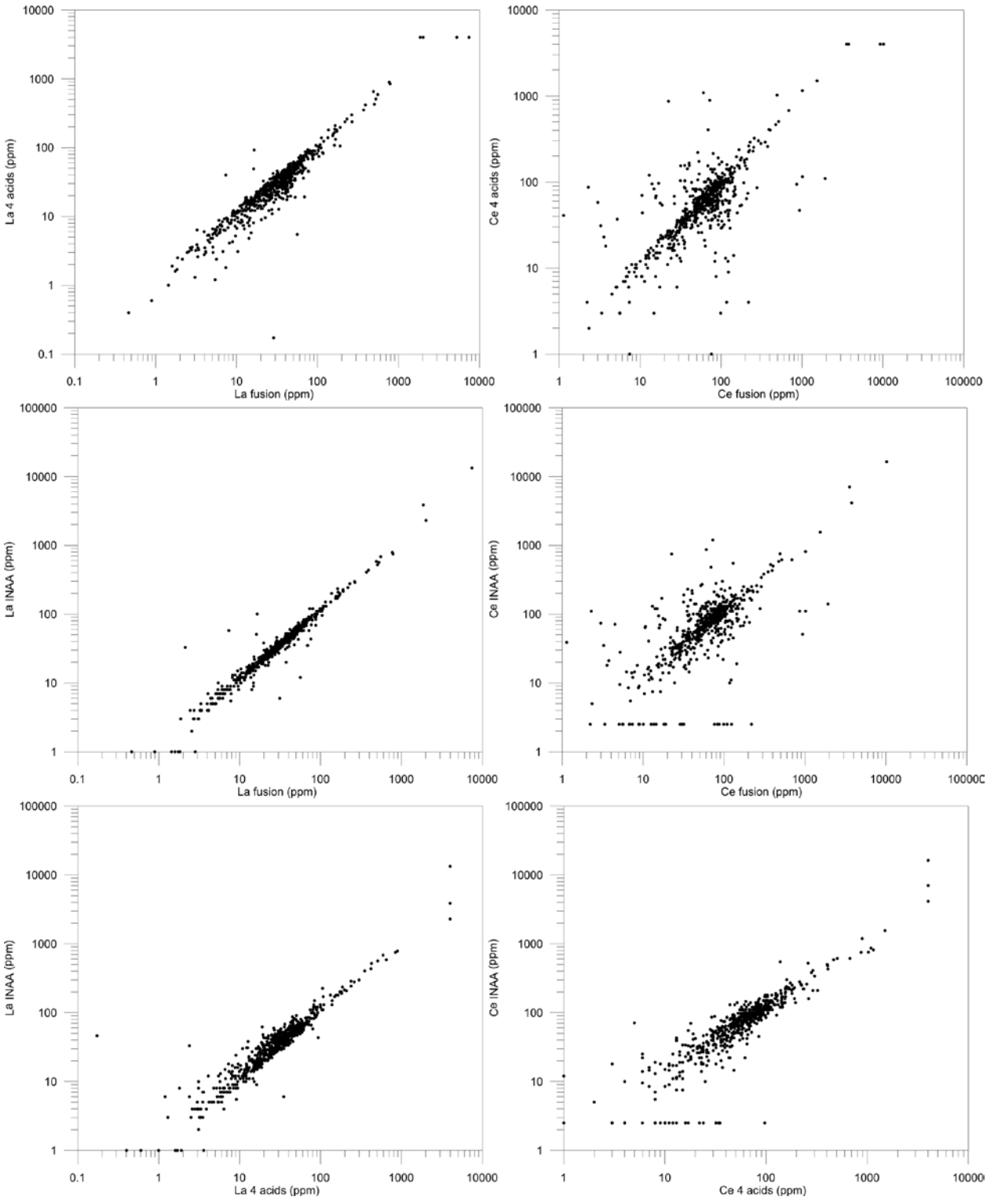

Figure 1-18 Comparaison entre les analyses de ÉTR légères par ICP-MS suivant une digestion par fusion et 4 acides ainsi que les analyses par activation neutronique

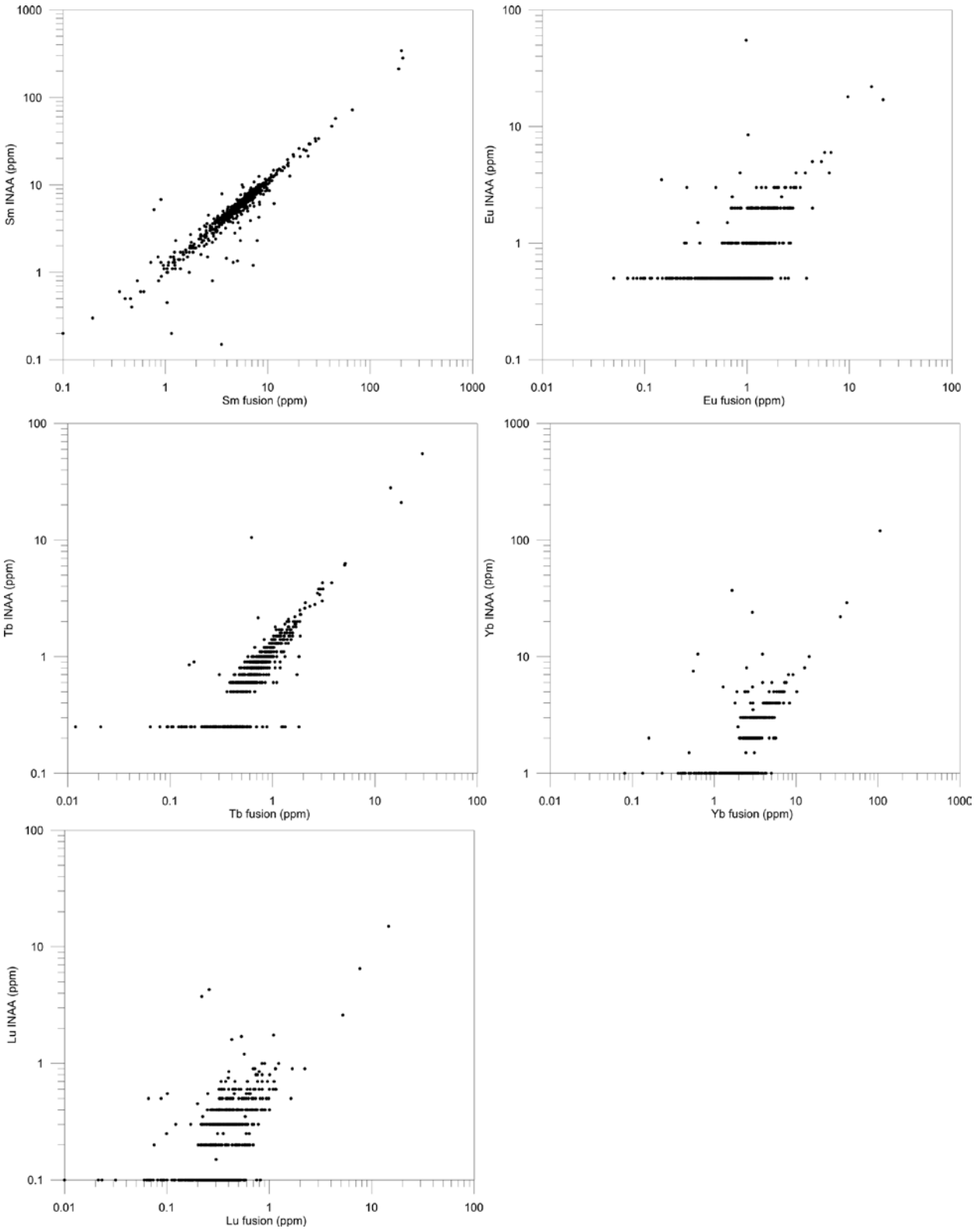

Figure 1-19 Comparaison entre les analyses de ÉTR moyennes et lourdes par ICP-MS suivant un digestion par fusion ainsi que les analyses par activation neutronique

MOBILITÉ DES ÉLÉMENTS ET FORMATION DE GÎTES POLYMÉTALLIQUES AU SEIN DES SYSTÈMES À OXYDES DE FER ET ALTÉRATION EN EN ÉLÉMENTS ALCALINS, ZONE MAGMATIQUE DU GRAND LAC DE L'OURS, TERRITOIRES DU NORD-OUEST, CANADA

DEUXIÈME PARTIE : ARTICLES

CHAPITRE 2 : TECTONO-MAGMATIC EVOLUTION OF THE SOUTHERN GREAT BEAR MAGMATIC ZONE (NORTHWEST TERRITORIES, CANADA) – IMPLICATIONS ON THE FORMATION OF IRON OXIDE ALKALI-ALTERED HYDROTHERMAL SYSTEMS

Évolution tectono-magmatique du sud de la Zone magmatique du Grand lac de l'Ours (Territoires du Nord-Ouest, Canada) – Implication sur la formation de systèmes hydrothermaux à oxydes de fer et altération en éléments alcalins

[1]Montreuil, J.-F., [2]Corriveau, L.

[1]Institut National de la Recherche Scientifique – Eau-Terre-Environnement

[2]Ressources naturelles Canada, Commission Géologique du Canada, division Québec

Soumis à «*Economic Geology*»

Abstract: This study demonstrates the intricate relationships between shoshonitic magmatism in the Paleoproterozoic Great Bear magmatic zone (GBMZ; Northwest Territories, Canada) and the development of regional scale Iron Oxide–Alkali–Altered (IOAA) systems fertile in Iron Oxide–Copper–Gold (IOCG) deposits (NICO and Sue-Dianne), Iron Oxide±Apatite (IO±A; e.g., Ron and Hump) showings and polymetallic albitite-hosted uranium mineralization (e.g., Southern Breccia). The GBMZ is interpreted as a continental volcanic arc formed above the collision zone between the Paleoproterozoic Hottah terrane and the Archean Slave craton during the Calderian orogeny. The resulting crustal geometry and high temperature magmatism is associated with IOAA activity within a short time frame of 7 m.y., from 1873 Ma to 1866 Ma, during shoshonitic to high-K calc-alkaline magmatism. Early magmatism in the southern GBMZ, between 1873–1870 Ma, resulted in predominantly rhyolitic volcanism and preferential emplacement of rhyolitic dikes in WNW- to W-oriented deformation corridors formed along pre-existing zones of weakness in the Treasure Lake Group metasedimentary rocks (e.g., bedding, intrusive contacts). During this early GBMZ magmatism, tectono-hydrothermal brecciation and intense IOAA hydrothermal alteration are also focused in the WNW- to W-oriented deformation corridors. Around 1870–1869 Ma, the emplacement of volcanic and intrusive rocks, predominantly andesitic to rhyolitic and locally mafic, is best explained by an increased magma production rate at the subduction zone with positive feedback between magmatism and the formation of crustal-scale conduits favoring faster ascension rates for the parent magmas. Some volcanic and many plutonic rocks generated at this stage have high F contents and A-type granite chemistry. The initial ascent of F-rich magma is associated with the formation of the NICO deposit and the Southern Breccia uranium showings, favored by a major input – in spatially constrained deformation zones – of a large volume of halogen- and CO_2-rich magmatic-hydrothermal fluids.

Résumé: Cette étude démontre les relations étroites entre magmatisme shoshonitique paléoprotérozoïque dans la Zone magmatique du Grand lac de l'Ours (GBMZ, Canada) et la formation de systèmes hydrothermaux à oxydes de fer et altération en éléments alcalins (IOAA) hôtes de gisements à oxydes de fer–cuivre–or (IOCG; NICO et Sue-Dianne) de même que des gîtes à oxydes de fer±apatite (IO±A; p. ex., Ron et Hump) et d'uranium encaissés dans des albitites (p. ex., Southern Breccia). La GBMZ est interprétée comme un arc volcanique continental formé au-dessus de la zone de collision entre le terrane paléoprotérozoïque d'Hottah et le craton archéen de l'Esclave résultant de l'orogenèse Caldérienne. La géométrie crustale

résultante de la GBMZ et l'activité magmatique shoshonitique à calco-alcaline riche en K de haute température sont associées à la formation de plusieurs systèmes IOAA dans une courte fenêtre temporelle de 7 m.a., entre 1873 et 1866 Ma. Le magmatisme précoce dans le sud de la GBMZ entre 1873 et 1870 Ma est principalement rhyolitique et résulte en la formation de rhyolites, de roches volcanoclastiques rhyoliques ainsi que de dykes rhyolitiques préférentiellement mis en place dans des corridors de déformation orientés ouest à ouest-nord-ouest formés dans des zones de faiblesses préférentielles dans les roches sédimentaires du Groupe de Treasure Lake. Pendant ce magmatisme précoce, plusieurs épisodes de bréchification tectono-hydrothermale accompagnés d'altération IOAA intense ont été canalisés eux aussi dans les corridors de déformation orientés ouest à ouest-nord-ouest. Autour de 1870–1869 Ma, la mise en place de roches volcaniques et intrusives, principalement de composition rhyolitique à andésitique et localement basaltique, peut s'expliquer par une augmentation du taux de production de magmas dans la zone de subduction et la rétroaction positive entre l'augmentation du taux de production de magmas et la vitesse d'ascension des magmas dans la croûte. Certaines roches volcaniques et plusieurs roches intrusives formées durant et après ce stade de transition ont une concentration élevée en F et une chimie de granites de type A. L'ascension initiale de ces magmas enrichis en F est associée à la formation du gisement de NICO et des indices polymétalliques uranifères de la Southern Breccia, favorisée par la circulation d'un large volume de fluides magmatiques-hydrothermaux enrichis en CO_2 et en halogènes dans des corridors de déformation d'une extension spatiale restreinte.

2.1 Introduction

The southern Great Bear magmatic zone (GBMZ) hosts the two Iron Oxide–Copper–Gold (IOCG) deposits currently known in Canada, the Au–Co–Bi–Cu NICO and the Cu–Ag–(Au) Sue-Dianne deposits. Both deposits were formed in regional (~10 km by 5 km) Iron Oxide Alkali–Altered (IOAA) hydrothermal systems (IOAA system as per definition of IOAA deposit type by Porter, 2010). Throughout the southern GBMZ, IOAA systems are predominantly developed in the supracrustal rocks (volcanic and sedimentary) and early intrusive suites of the GBMZ (Hildebrand, 1986; Gandhi, 1994; Goad et al., 2000a, b; Mumin et al., 2007, 2010; Corriveau et al., 2010a, b, 2011; Ootes et al., 2010; Acosta Góngora et al., 2011; Potter et al., 2013b; Fig. 1-15). This magmatism has a high-K calc-alkaline magmatism to shoshonitic composition and is interpreted as part of a continental magmatic arc formed between 1.87–1.84 Ga at the western edge of the Wopmay Orogen. The area is extremely well exposed across 450 by about 100 km (Fig. 1-2; Hildebrand et al., 1987; Gandhi et al., 2001). It was dissected by North-East-trending transcurrent faults at the end of its development. Nevertheless, once the belt is reconstructed, IOAA systems of the GBMZ are distributed along a pair of sub-parallel North-trending corridors: one located at the western margin of the GBMZ that straddles the easternmost components of the exhumed composite pre-1.90 Ga Hottah terrane (Hildebrand et al., 1987, 2010a; Gandhi et al., 2001) and the other along the eastern margin of the GBMZ that straddles the westernmost exposures of reworked components of the Archean Slave Craton (Fig. 1-2; Hayward et al., 2013). A compilation of existing U–Pb ages on zircon constrains the main IOAA hydrothermal event(s) across the GBMZ at ca. 1.87 Ga (Gandhi et al., 2001; Gandhi and van Breemen, 2005; Bennett and Rivers, 2006; Montreuil et al., 2009; Davis et al., 2011; Bennett et al., 2012; Potter et al., 2013b).

Previous work shows that the GBMZ IOAA systems encompass a wide variety of mono to polymetallic mineralization styles that form a continuum and evolve to an epithermal style of mineralization including (Corriveau et al., 2010b; Mumin et al., 2010):

1) magnetite- to hematite-group IOCG deposits, prospects and showings (e.g., NICO, Sue-Dianne; Gandhi, 1989; Goad et al., 2000a, b; Camier, 2002; Mumin et al., 2010);
2) albitite-hosted uranium mineralization (e.g., Southern Breccia; chapitre 6),
3) polymetallic vein-type deposits (e.g., Camsell River and Port Radium–Echo Bay district; Shegelski, 1973; Badham, 1978; Reardon, 1992; Ruzicka and Thorpe, 1996; Mumin et al., 2007, 2010);

4) Iron Oxide ±Apatite (IO±A) deposits potentially endowed in vanadium±rare earth elements (e.g., Camsell River and Port Radium–Echo Bay district; Badham and Morton, 1976; Hildebrand, 1986; Mumin et al., 2010); and

5) mineralized giant quartz veins and epithermal styles of mineralization (e.g., Rayrock mine; Gandhi et al., 2000; Byron, 2010; Mumin et al., 2010).

U–Pb ages on zircon constrain the main IOAA hydrothermal events across the GBMZ at ca. 1.87 Ga within a 7 m.y. period (Gandhi et al., 2001; Gandhi and van Breemen, 2005; Bennett and Rivers, 2006; Bennett et al., 2012; Potter et al., 2013b; chapitre 7). This short temporal window is ideal to define the relation between a large-scale continental magmatic flare and the formation of IOAA systems and associated mineralization.

This paper reports the results of renewed mapping and lithogeochemistry across the well-exposed supracrustal sequences of the southern GBMZ IOAA systems. This updated record of the magmatic, metasomatic and structural attributes of the area furthers the understanding of the tectonomagmatic environment and the space–time evolution of IOAA hydrothermal activity in the GBMZ. It also provides the required framework to re-examine GBMZ tectonic models and magmatic evolution (Davis et al., 2011; Ootes et al., 2015). Ultimately this contribution impacts a fundamental aspect of the genesis of IOAA deposits: their geodynamic setting of formation and association with shoshonitic to high-potassium calc-alkaline magmatism (Williams et al., 2005; Groves et al., 2010; Porter, 2010). Shoshonitic magmatism is used in this contribution for potassic magmatic rocks with K > Na, low TiO_2, and high contents of large ion lithophile elements (e.g., K, Rb, Ba) that plot in the fields for shoshonitic rocks as defined in the Peccerillo and Taylor (1976), Pearce (1982) and Hastie et al. (2007) discrimination diagrams. Such magmatic rocks form in tectonic settings related to the evolution of a continental volcanic arc (Joplin, 1968; Peccerillo and Taylor, 1976; Müeller et al., 1992; Müeller and Groves, 1993).

2.2 Geological framework

Magmatism in the GBMZ began at ca. 1.878 Ga following the short-lived ~ 1.90–1.88 Ga Calderian orogeny during which the Paleoproterozoic Hottah terrane was accreted to the Archean Slave craton. The geometry of the Slave–Hottah collision is currently debated and two distinct hypotheses are proposed: an oblique arc–continent collision model similar to the Luzon arc–Taiwan collision involving a pre-collisional ocean-verging subduction and a post-collisional

continent-verging subduction (cf. Hildebrand et al., 2010a) or an oblique collage of the Hottah terrane to the Slave craton along a major N-oriented transform fault without the involvement of a pre-collisional ocean-verging subduction zone attached to the Slave Craton (Ootes et al., 2015).

The Calderian orogeny affected a passive margin sequence deposited on the western edge of the Slave Craton (Coronation margin), Archean rocks of the Slave Craton and the composite Hottah terrane. Major members of the Hottah terrane deformed during the Calderian orogeny include the 1.90 Ga Bloom Basalt and Fishtrap gabbros, the Conjuror Bay Formation and its uppermost sedimentary basin, the 1.885 Ga Treasure Lake Group (TLG; Hildebrand, 2011). The TLG now forms a series of discontinuous supracrustal windows imbedded in the volcanic and plutonic rocks of the GBMZ (Hildebrand et al., 1987, 2010a, b; Gandhi et al., 2001; Bennett et al., 2012). During the Calderian deformation and lower greenschist to locally amphibolite facies metamorphism, onset of GBMZ formation led to syn-deformation emplacement of granitic dikes in a compressional deformation regime and to early hydrothermal alteration at 1878 Ma (Bennett and Rivers, 2006; Jackson et al., 2013). These early magmatic and IOAA alteration events are studied in more detail in the DeVries Lake area located 80 km north of the Sue-Dianne deposit (Fig. 1-2; Corriveau et al., 2007, 2010b; Ootes et al., 2010). Calderian orogenic metamorphism, dated using U-Pb on metamorphic zircons at 1876 ±3.5 Ma, accompanied the emplacement of early GBMZ intrusions (Jackson et al., 2013).

The main volcano-plutonic events in the GBMZ extend from 1873 to 1860 Ma and formed the McTavish Supergroup, subdivided into four distinct units: the early mafic to felsic LaBine and Dumas groups in the north, the Faber Group in the south, and in the north the younger and overlying Sloan Group (Hildebrand et al., 1987, 2010b; Gandhi et al., 2001; Bennett et al., 2012). The McTavish Supergroup formation was associated with repetitive emplacement of high-level intermediate-to-felsic intrusions within the volcanic pile as well as within the underlying metasedimentary rocks. Those dynamic magmatic environments were ideal to sustain regional IOAA hydrothermal cells across the GBMZ supracrustal sequences as they fostered the circulation and redistribution of important amounts of heat and fluids (Mumin et al., 2010; Richards and Mumin, 2013). Cover sequences such as the Sloan Group over the LaBine Group in the north and the Faber Group over the TLG in the south have also created stratigraphic traps for hydrothermal fluids. Detailed work in the Port Radium–Echo Bay IOCG district and the vicinity of the Sue-Dianne deposit (Fig. 1-2) also indicated that the shallow epithermal settings in the Faber and LaBine groups are generally preserved from erosion (Mumin et al., 2007, 2010; Corriveau et al., 2010b; Hildebrand et al., 2010b).

The northern GBMZ IOAA systems (e.g., Port Radium–Echo Bay, Camsell River and Grouard) are mostly hosted by the LaBine Group (Corriveau et al., 2010a, b; Mumin et al., 2010). In the central and southern GBMZ, they are mostly hosted by the Faber Group (e.g., southern GBMZ, Fab, DeVries) and the TLG (southern GBMZ, DeVries; Gandhi, 1994; Goad et al., 2000a, b; Mumin et al., 2010; Acosta Góngora et al., 2011; Potter et al., 2013b).

According to Hildebrand et al. (2010b), magmatism in the northern GBMZ began with small-scale local eruptions of basalt and volumetrically minor intermediate/felsic volcanism. Magma input gradually increased in volume and transitioned to predominantly intermediate composition until the formation of the Sloan Group and the final stage of the Great Bear batholith emplacement around 1862 Ma (Hildebrand et al., 2010b). Mafic magmatism is also apparent from localized intrusions and evidences of magma mixing in the voluminous Great Bear batholith (Hildebrand et al., 2010b), but remains scarce at the current surface exposure. Cogenetic plutons to the volcanic sequences of the McTavish Supergroup typically have high aspect ratios (10-20) and the volume of individual plutons increased with time (cf. Fig. 13 in Hildebrand et al., 2010b). Around 1860 Ma, volcanism and plutonic activity paused throughout the GBMZ and plutonic activity resumed at ca. 1858 Ma to form the intrusions of the biotite-granite suite (Gandhi et al., 2001; Hildebrand et al., 2010b). The intrusions of the biotite-granite suite show no evidence of IOAA-related hydrothermal alteration, but played an important role to bring new metals and to locally remobilize in late stage veins the metals and elements previously concentrated during the earlier IOAA event (Somarin and Mumin, 2012).

Tectonic deformation in the GBMZ intrusions decreases with time between 1877–1862 Ma. Tectonic foliations formed locally in plutons emplaced between 1877–1867, but tectonic fabrics in the ca. 1862 Ma intrusions were only developed near the Wopmay fault zone (Jackson et al., 2013). Plutons of the biotite-granite suite emplaced between 1858–1850 Ma are post-kinematic and generally undeformed (Jackson et al., 2013).

The eastern limit of the GBMZ and its known IOAA systems is the Wopmay fault zone (Jackson and Ootes, 2012), which marks the western limit of exposed Archean rocks of the Slave craton and was an important deformation corridor during the Calderian orogeny and during GBMZ magmatism (Hildebrand et al., 2010a; Jackson et al., 2013). The inversion of a magnetotelluric survey data shows that the fault zone has a mid-crustal vertical extension (± 20 km) and listrically merges westward with the highly resistive Slave craton lithosphere, and that the Slave craton lithosphere tapers out westward at depth below the GBMZ as far west as the outcropping exposures of Hottah terrane (Spratt et al., 2009). Cook (2011) interprets the wedged shape of

the Slave Craton lithospheric mantle as the product of the aborted subduction of the Slave continental margin during the Calderian orogeny.

The two-dimensional inversion of magnetotelluric data by Spratt et al. (2009) combined with the distribution of the known IOAA systems at surface (this work, Corriveau et al., 2010b) and of IOAA geophysical signatures (Hayward et al., 2013) shows that most of the largest IOAA systems and IOCG deposits (e.g., NICO, Sue-Dianne and the Port Radium–Echo Bay) of the GBMZ are aligned west of the Wopmay fault zone along the margin of the resistive Archean mantle and the Hottah terrane. The resulting crustal geometry of the GBMZ (cf. Figs. 9, 10 and 11 in Spratt et al., 2009) is similar to the crustal geometry of the Gawler Craton that hosts the Olympic Dam hematite-group IOCG deposit (cf. Fig. 2 in Heinson et al., 2006; Skirrow, 2010). The western and northwestern limits of the GBMZ are concealed under Proterozoic and Paleozoic sedimentary rocks but remain within reach of modern exploration drilling and geophysical modeling (Villeneuve et al., 1993; Aspler et al., 2003; Hayward et al. 2013).

2.3 Geological setting of the IOAA systems

The southern GBMZ comprises two northwesterly oriented supracrustal sections (herein referred to as the Western and Eastern section) composed of metasedimentary rocks of the TLG, volcanic rocks of the Faber Group as well as series of dikes swarms, sub-volcanic intrusions and batholiths (Fig. 1-15). The supracrustal sections are imbedded in the intrusions of the Great Bear batholith, entitled the Marian River batholith between the Eastern and Western sections (Gandhi et al., 2001). In this contribution, the name Marian River batholith is extended to encompass the undivided intrusive rocks located south of the Western section (Fig. 1-15).

The Western section is subdivided in three main sectors: Mazenod (Sue-Dianne deposit, and Brooke and Nod prospects, Mar showing), Lou (e.g., NICO deposit, Southern Breccia polymetallic uranium showings) and South Lou (e.g., Duke, Peanut and Sunil zone showings). The Eastern section is divided in two main sectors: Eastern Treasure Lake, hosting the Hump and Ron iron oxide showings (Gandhi, 1992a; Mumin et al., 2000), and Cole. The classification of deposits, prospects and showings follows those of the NORMIN database (Northwest Territories Geological Survey, 2015) and their main characteristics are summarized in Chapter 4.

2.4 Methods

2.4.1 Geochemical analysis

To constrain the magmatic evolution of the southern GBMZ volcano-plutonic rocks, 283 representative samples of the various volcanic units and intrusive suites were selected among a database of 1236 samples analyzed in the southern GBMZ for whole-rock geochemistry (see appendix 2 for representative analyses*;* Table 2-1).

Table 2-1 Number of samples per geological units of the southern GBMZ

Geological unit (volcanic rocks)	# Samples
Lou assemblage/Rhyolite dikes	56
Undivided rhyolite/Rhyolite dike – South Lou sector	7
Dianne subassemblage	23
Cole assemblage	13
Hump assemblage	9
Mazenod assemblage	22
Bea assemblage	15
Geological unit (intrusive rocks)	
Early granite	7
Sodic-altered granitic dikes	1
Bt–Fp/Fp–Bt-phyric dikes	19
Bt-phyric dikes	12
Fp-phyric dikes	22
Undivided porphyritic intrusions – Eastern Treasure Lk.	8
Diorite suite	2
Quartz monzonite–monzodiorite suite	26
Marian River batholith/Late-stage granitic dikes	28
U–Th-rich monzonitic dikes	13

Mineral abbreviations after Whitney and Evans (2010)

Rock chip preparation was done in the field and chips were carefully selected to avoid weathered and oxidized surface (normally less than a few mm thick), enclaves, crosscutting veins or superimposition of unwanted alteration. All the geochemical samples were crushed in a steel-plated jaw crusher and powdered using an agate ball mill. Major and trace elements where then analyzed by ICP-AES and ICP-MS following lithium borate fusion at INRS–ETE. F analyses were done at the Geological Survey of Canada in Ottawa by Dionex ion chromatography. Additional F analyses were done using fusion–Specific Ion Electrode at ALS (method F-ELE81a) and ACME (method 2A04–F) laboratories in Vancouver (Canada).

Petrographic observations using cobaltnitrate stained rocks slabs and thin sections were made to further support the field identification of alteration. For cobaltnitrate staining, polished slabs are immersed in hot and concentrated hydrofluoric acid (HF; 10 molar) for one minute, washed and dried, and then immersed in the saturated cobaltnitrate solution. A one minute dipping time in HF is used as this duration is long enough to etch hydrothermal K-feldspar but too short to allow the acid to sufficiently attack the igneous K-feldspars. All the plagioclase and albite are completely transformed into white to whitish yellow (after staining) clay minerals and biotite takes on a greenish hue.

The database of 1236 samples collected in the southern GBMZ also comprises analyses of IOAA alteration, including breccias and veins. Plotting of the molar ratios of Na, Ca, Fe, K and Mg of those samples in a selection of the southern GBMZ IOAA systems allows the chemical mapping of the spatial distribution of IOAA alteration (chapitre 5). Chemical alteration maps are also based on geochemical analyses compiled from Gandhi (1989), Gandhi and Lentz (1990), Gandhi (1992a), Gandhi and Prasad (1993), North (1995) and Camier (2002; Fig. 2-1).

2.4.2 Alteration nomenclature

To simplify the nomenclature of hydrothermal alteration described in the following sections, each alteration type is defined using the cations that best reflect the commonalities in the mineral assemblages formed during the alteration event. This nomenclature is used here as it takes into account that in IOAA systems, notable relative enrichments in some elements can also be induced through severe leaching of other elements across laterally extensive zones. It is also in line with the IOAA nomenclature systems used by Hitzman et al. (1992) and Williams (1999). Following this terminology and the Corriveau et al. (2010a, b) subdivision of IOAA alteration,

1) sodic alteration refers to mineral assemblages dominated by albite±quartz with accessory rutile, titanite and zircon;
2) sodic–calcic–iron alteration refers to mineral parageneses dominated by albite–amphibole/clinopyroxene±magnetite;
3) high temperature (HT) calcic–iron±magnesium alteration refers to mineral parageneses dominated by amphibole–magnetite, amphibole, clinopyroxene–amphibole±magnetite (see 8) and amphibole–magnetite–apatite;

4) potassic alteration refers to mineral assemblages dominated by K-feldspar and/or sericite;

5) high temperature (HT) potassium–iron alteration refers to mineral assemblages mostly composed of K-feldspar–magnetite, K-feldspar–biotite, biotite and biotite–magnetite;

6) low temperature (LT) potassic–iron±magnesium refers to mineral parageneses composed of hematite±K-feldspar, sericite–hematite, chlorite–hematite±K-feldspar±sericite, chlorite–K-feldspar and chlorite (see hydrolytic alteration of Hitzman et al., 1992);

7) low temperature (LT) calcic–iron±potassium alteration refers to mineral parageneses predominantly composed of epidote and can also comprise variable modal content of K-feldspar and allanite; and

8) skarn-type alteration refers to metasomatic rocks composed by calcium–magnesium–iron–manganese silicates which are free or poor in water, resulting in mineral parageneses with high modal contents of clinopyroxene, garnet and/or carbonates.

To identify the skarn-type alteration we have followed the nomenclature scheme of Einaudi et al. (1981), Einaudi and Burt (1982), Meinert (1992) and Zharikov et al. (2007) as we identified skarn-type alteration on the basis of the mineral paragenesis of the altered rock without assuming any genetic implications. In most cases, the main minerals of the paragenesis composing the described alteration types for each hydrothermal system will be specified.

2.5 Geological units

2.5.1 Treasure Lake Group

The TLG is a platform-type sedimentary sequence, which was metamorphosed, deformed and tilted to a generally steep dip before extrusion of the Faber Group volcanic sequence. The TLG is subdivided into four units (Gandhi et al., 2014; Fig. 2-2):

1) a basal siltstone unit evolving upward to

2) carbonaceous rocks;

3) quartz arenite interbedded with a few siltstone beds with primary sedimentary structures such as cross-bedding and ripple marks; and

4) an upper siltstone interbedded with sandstones.

Detrital zircons in a TLG metaquartzite constrain its maximum age at 1886 ± 8 Ma in the southern GBMZ (Gandhi and van Breemen, 2005) or at 1884 ± 6 Ma in the DeVries Lake sector (Bennett and Rivers, 2006). The age of 1.88 Ga Ma is thus taken as the absolute maximum age for the onset of IOAA hydrothermal activity in the southern GBMZ (Corriveau et al., 2010a). The minimum age of the TLG is given in the DeVries area at 1878±4 Ma by a syn-deformation granitic dike (Fig. 1-2; Bennett and Rivers, 2006).

Regional metamorphism is generally low grade (greenschist facies) in the TLG, but tectonic deformation increases towards the Wopmay fault zone. Gandhi et al. (2001) also reported increasing orogenic metamorphism near the Wopmay fault zone based on the presence of garnet-bearing amphibolite layers. Notwithstanding a general increase in both metamorphic grade and intensity of deformation prior to and at 1.87 Ga (cf. Jackson et al., 2013), care is required to relate the garnet-bearing amphibolites to amphibolite facies Calderian orogenic metamorphism. Away from the Wopmay fault zone in the greenschist facies metamorphosed TLG units of the South Lou sector, intense HT calcic–iron alteration, preferentially developed in deformation zones, is associated with the formation of garnet- and amphibole-rich hydrothermal mineral assemblages not related to Calderian orogenic metamorphism. The garnet amphibolites near the Wopmay fault zone can thus be of metasomatic origin and related to HT calcic–iron alteration that abounds near the Wopmay fault zone. Contact metamorphism in the Treasure Lake Group locally led to the formation of cordierite porphyroblasts proximal to certain intrusions of the Marian River batholith.

Northwestward from the South Lou to the Lou IOAA sectors, the carbonaceous unit of the TLG completely disappears along its expected extension where the NICO deposit is located (Fig. 1-15). In the Eastern section, the prevailing units of the TLG are the quartz arenite interlayered with siltstones beds and the upper siltstone interlayered with sandstone beds with localized occurrences of the carbonaceous unit (Gandhi et al., 2014; Fig. 1-15). In the Mazenod sector, elongate lenses of the basal siltstone unit occur along the eastern contact between of Faber Group volcanic rocks with the Marian River batholith and interpreted undivided metasedimentary rocks were noted in the vicinities of the Nod showings (North, 1995). In both the Western and Eastern sections in the TLG, there are localized occurrences of undivided volcanic rocks of the Faber Group, sub-volcanic porphyritic intrusions, intrusions of the dioritic and quartz

monzonite–monzodiorite suites, and intrusions of the Marian River batholith (Gandhi et al., 2014).

In the Western section, the typical dip and dip direction of the bedding in the TLG average 50–70° to the northeast and younging is typically oriented N–NE. In the Eastern section, bedding typically dips sub-vertically to vertically towards NNE to NE and is parallel to the regional foliation. Localized inversions of the younging directions in the Eastern Treasure Lake sector are indicative of localized folding.

2.5.2 Faber Group and sub-volcanic porphyritic intrusions

The Faber Group uncomfortably overlies the TLG, and is subdivided in five assemblages that are in stratigraphic order Lou, Cole, Hump, Mazenod and Bea (Gandhi et al., 2001, 2014; Fig. 2-2). Regional metamorphism is weak in the Faber Group, reaching only sub-greenschist facies.

IOAA metasomatism is pervasive and intense in most of the Faber Group volcanic rocks and significantly modifies the relative proportions of major elements including the SiO2 and/or alkali contents which are commonly used in discriminant diagrams to define volcanic rock types. The composition of the southern GBMZ volcanic rocks and porphyritic intrusions is herein based on the Pearce (1996a) chemical discrimination diagram for volcanic rocks that considers ratios of typically immobile elements (Nb, Ti, Y, Zr). Potential caveats to this protocol in IOAA settings are localized Zr and Ti enrichments combined with Nb and Y depletion in intensely sodic-altered rocks, and localized Ti and Nb enrichments in HT calcic–iron and some specific HT potassic–iron alteration zones (Oliver et al., 2004; chapitre 6, unpublished data). Samples representative of each of the characterized units were thus also constrained macroscopically and only least to weakly altered or potassic altered volcanic samples were chosen based on outcrop and stained rock slabs attributes. The immobility of Nb, Y, Ti and Zr is demonstrated in most of the selected samples by the clustering of samples from the same geological assemblage on bivariate diagrams of Zr/Nb vs Zr and Zr/Y vs Zr (Fig. 2-3a–b). This is illustrating weak variations of the Zr/Nb and Zr/Y ratios for increasing Zr content and preservation of the ratios in rocks of the same geological unit.

2.5.3 Lou assemblage in the Lou IOAA sector

In the Lou IOAA sector, the lowermost units of the Lou assemblage are predominantly composed of massive to flow-banded rhyolites intercalated with rhyolitic volcaniclastic rocks.

Volcaniclastic rocks increase in abundance towards the top of the Lou assemblage and rhyolitic ignimbrites were observed in its uppermost units (Gandhi et al., 2001, 2014). The Lou assemblage lowermost felsic volcanic rocks are locally cut by aphanitic to biotite-phyric andesite dikes. The Pearce (1996a) diagram illustrates that subalkaline dacite/rhyolite and alkali rhyolite predominate in the vicinity of the NICO deposit with andesite and trachyte remaining minor in abundance (Fig. 2-3c–d). In contrast, the northernmost sequences of the Lou assemblage at the northern margin of the Lou IOAA sector have an andesitic to predominantly dacitic/rhyolitic composition.

At the unconformity with the TLG, rhyolite fills small depressions in the tilted sedimentary beds that are not paleoweathered. At some localities, the originally vertical cracks are subsequently gently tilted towards the SW (Fig. 2-4a; this work; Enkin et al., 2012). Consequently tilting of the Treasure Lake Group and exhumation largely predates Faber Group extrusion, with local renewed tilting post extrusion. In the vicinity of the NICO deposit and Southern Breccia zone, the lower sequences of the Lou assemblage are shallowly dipping to the N–NE (sub-horizontal to 35°). Dip is then gradually increasing toward the top of the sequence (70°) with dip direction remaining the same.

The rhyolites/dacites in the Lou IOAA sector are aphanitic or feldspar, biotite–feldspar or locally quartz–feldspar±biotite phyric, typically with a low crystal content (<15% phenocrysts; this work; Mulligan, 1995; Gandhi et al., 2001). Ghosts of amphibole phenocrysts were identified in felsic volcanic rocks of the basal unit (Mulligan, 1995).

Potassic and locally sodic alteration is very intense in the lowermost units of the Lou assemblage in the vicinity of the NICO deposit and the Southern Breccia (Robinson, 2013; chapitre 6). Both alteration types typically destroyed most of the primary volcanic textures including the phenocrysts complicating the recognition of the different generations of felsic volcanic rocks based on the primary composition of their phenocrysts. This intense potassic alteration is centered on the NICO deposit, and generates a 3 by 4 km potassium anomaly in airborne radiometric surveys, in which potassium concentration reaches 7 wt. % K (Shives et al., 2000). It particularly affects tuff layers within the volcanic pile, TLG metasedimentary rocks along breccias underlying the interface between the volcanic and metasedimentary rocks and the immediate wall rocks of some porphyry dikes (Gandhi et al., 1996; Robinson, 2013).

2.5.4 Lou assemblage in the Mazenod sector (Dianne subassemblage)

In the Mazenod sector, the volcanic and volcaniclastic rocks pertaining to the Lou assemblage have been grouped into the Dianne subassemblage that stratigraphically overlies the Lou assemblage units in the Lou IOAA sector (Gandhi et al., 2014; Figs. 1-15 and 2-2).

The Dianne subassemblage is compositionally heterogeneous and varies from andesitic to dacitic/rhyolitic throughout its entire extent (Fig. 2-3c; Gandhi, 1989; Gandhi and Prasad, 1993; North, 1995). Rhyolites/dacites are feldspar and feldspar–quartz phyric, generally crystal-rich and are the main host of the Nod and Brooke prospects. The andesites are typically two feldspars- (plagioclase and K-feldspar) or feldspar–amphibole-phyric and crystal-rich to crystal poor (between 10% and 40% phenocrysts) although aphanitic andesites occur north of the Brooke prospect. In some cases, the absence of phenocrysts is related to their destruction by intensifying IOAA alteration.

The overall stratigraphic sequence of the Lou assemblage shows that it is spatially and temporally evolving from a predominantly rhyolitic composition in its basal sequences in the Lou IOAA sector close to the NICO deposit to an andesitic to dacitic/rhyolitic composition in its upper sequences in the Mazenod sector (Fig. 2-2).

2.5.5 Cole assemblage

The Cole assemblage, stratigraphically above the Dianne subassemblage (Gandhi et al., 2014; Fig. 2-2), predominantly consists of porphyritic andesitic to rhyolitic/dacitic volcanic rocks with localized occurrences of tuff and tuff breccia (Fig. 2-3c). The volcanic pile is intruded by many stocks and plutons of the quartz monzonite–monzodiorite suite and undivided uranium–thorium-rich monzonitic dikes. Plagioclase–amphibole-phyric andesites with few K-feldspar phenocrysts predominate. Their matrix is typically very fine-grained and proportion of crystals vary (<10% phenocrysts to >15% phenocrysts) as observed in andesites of the Dianne subassemblage. Rhyolites/dacites are subordinate and two feldspars-phyric (plagioclase and K-feldspar) with a K-feldspar-rich groundmass.

2.5.6 Hump assemblage

The Hump assemblage forms a large body of undivided mafic and intermediate to locally felsic volcanic and volcaniclastic rocks located west of Hump Lake (Figs 1-15, 2-3c). The volcanic rocks are aphanitic to plagioclase–biotite and biotite±plagioclase phyric and crystal-rich (up to

40% phenocrysts), have a fine-grained matrix and exhibit weak to strong, penetrative and southeasterly oriented tectonic foliations. Mafic to intermediate laminated tuffs were also observed in the sequence.

2.5.7 Mazenod assemblage

The 2–3 km thick Mazenod assemblage formed circa 1868 Ma, hosts the Sue-Dianne deposit, and consists of 12 distinct units dipping north to northeast, up to 70° and younging northward (Gandhi, 1989; Gandhi et al., 2001; Camier, 2002). Each individual unit of the Mazenod assemblage usually comprises tuffs rich in feldspar±quartz crystals (sodic plagioclase and minor K-feldspar; possibly indicative of variable sodic and potassic metasomatic imprint), welded tuffs, lapilli tuffs and volcaniclastic breccias in variable proportions (Camier, 2002). Aphanitic to feldspar- and two feldspar±quartz-phyric and crystal-rich volcanic rocks, and porphyritic intrusions are also composing some of the Mazenod assemblages units. Except for its lowermost unit that is predominantly andesitic, the volcanic and volcaniclastic rocks of the Mazenod assemblage are dacitic/rhyolitic to locally andesitic (Figs. 2-2, 2-3c). Some volcanic rocks and most of the sub-volcanic porphyritic intrusions emplaced in the Mazenod assemblage units have a trachy-andesitic, trachytic and andesitic composition and the uppermost unit that hosts the Sue-Dianne deposit is trachy-andesitic.

2.5.8 Bea assemblage

The Bea assemblage rests uncomformably on the Lou assemblage and is in transgressive contact with the Mazenod assemblage (Gandhi et al., 2001). A basal volcanosedimentary unit is overlaid by sub-volcanic intrusive to volcanic porphyritic rocks. In its lower section north of the Lou IOAA sector and in the southern part of the Mazenod sector south of Brooke, the Bea assemblage has a predominantly andesitic composition (Figs. 2-2, 2-3c). The Bea assemblage then becomes predominantly rhyolitic/dacitic in its uppermost section that circles the Mazenod assemblage in the Mazenod sector. The andesitic rocks are biotite–feldspar phyric, typically crystal-rich (up to 75% phenocrysts) and the groundmass is composed of biotite and K-feldspar whereas the rhyolite/dacite are feldspar±biotite phyric and crystal-rich (up to 60% phenocrysts), and their groundmass is typically composed of very fine-grained K-feldspar. Except for localized to widespread weak to moderate potassic alteration, no evidence of intense IOAA alteration has been so far observed in the Bea assemblage.

2.5.9 Undivided volcanic rocks

Many aphanitic to porphyritic and massive to foliated volcanic rocks are isolated into the metasedimentary rocks of the TLG. Near the Esther zone, volcanic rocks form scattered lenses, but the destruction of their primary textures and complete modification of their chemistry as a result of intense sodic alteration complicate their association to a specific assemblage of the Faber Group.

In the South Lou sector, localized occurrences of potassic-altered, aphanitic and massive rhyolite and alkali rhyolite dikes were observed in the Sunil zone whereas flow-banded and locally foliated rhyolites were observed southeast of Peanut Lake (informal name) in the Peanut zone.

2.5.10 Subvolcanic porphyritic dikes and sills

Many generations of subvolcanic porphyritic intrusions systematically cut the TLG metasedimentary rocks and depending of their timing of emplacement, may cut through certain assemblages of the Faber Group (Goad et al., 2000a; Camier, 2002; this work). Based on field-cross-cutting relationships and U–Pb age on zircon from the oldest to the youngest, the main types of subvolcanic porphyritic intrusions observed in the southern GBMZ consist of fine-grained feldspar-phyric to aphanitic rhyolite dikes, fine-grained biotite–feldspar±quartz-phyric dikes, biotite-phyric dikes, feldspar–biotite-phyric dikes and intrusions, feldspar-phyric intrusions and dikes, and quartz–feldspar±biotite-phyric dikes and sills (D'Oria, 1998; Gandhi et al., 2001; Camier, 2002; this work; Fig. 2-2). On the Pearce (1996a) diagram, most of the porphyritic dikes emplaced after the rhyolitic dikes and pertaining to the suites dated at 1869±1.3 Ma and 1868 ± 0.74 Ma (Davis et al., 2011) have an andesitic composition with some having a dacitic/rhyolitic composition (Fig. 2-3d).

Plagioclase-phyric to aphanitic rhyolite dikes were only observed in the Lou IOAA and South Lou sectors and their distribution appears restricted to west-northwest-oriented deformation corridors such as the Southern Breccia albitite breccia corridor where they were studied in most details. These dikes extend for several meters, are distinct from all younger generation of dikes in having non parallel and non linear dike margins, and have highly variable widths where sudden changes in widths occur at dike offset perpendicular to the main foliation orientation. Dikes taper off to form boudins and fragments within tectonohydrothermal breccia zones (Fig. 2-4b–c). Some

of the dikes were folded in a magmatic state forming elaborate irregular contacts. They are interpreted as emplaced between 1873 and 1871 Ma as they cross-cut an intrusion of the early granite suite dated at 1873±2 Ma, but occur as enclaves in albitized and porphyritic granitic dikes with a preliminary U–Pb age on zircon of 1871±0.8 Ma (Davis et al., 2011; Figs. 2-2, 2-4d). A sample from such dikes was processed for U–Pb dating of zircon but did not yield a date.

The biotite–feldspar±quartz-phyric dikes are massive to weakly WNW-foliated and andesitic. The dikes are linear, with fairly constant widths and abound in the Lou IOAA sector where they cut the calcic–iron and calcic–iron–potassic metasomatites hosting the ore zone of the NICO deposit. They are themselves locally cut by veins comprised of coarse-grained actinolite with K-feldspar selvages, which either record a weak stage of renewed high temperature calcic–iron alteration subsequent to their intense potassic alteration or late-stage veins. One biotite–feldspar-phyric dike located near the NICO deposit that cuts calcic–iron alteration typical of the NICO ore zone yielded an U–Pb age on zircon of 1869 ± 1.3 Ma (Davis et al., 2011).

The biotite-phyric dikes were mostly observed in the Southern Breccia, but also in the Peanut zone of the South Lou sector. In both sectors, they occur along the west-trending deformation corridors and in the Southern Breccia they host fragments of the rhyolite dikes and of the albitized porphyritic granitic dikes. Weak to moderate west-northwest trending tectonic foliations are developed in some of those dikes.

The feldspar–biotite-phyric dikes abound in the Lou IOAA sector where they cut the NICO ore zone and the Southern Breccia uranium showings. In the NICO deposit they are typically associated with intense potassic and more locally tourmaline alteration haloes, and are locally cross-cut by late-stage amphibole veins with K-feldspar selvages. They are generally massive without any west-northwest- to west-trending tectonic foliation and are emplaced at high to shallow angles to the west-northwest- and west-oriented deformation corridors and Treasure Lake Group metasedimentary rocks bedding that they cross-cut (Fig. 2-4e). A feldspar–biotite-phyric porphyritic dike cutting the Southern Breccia uranium mineralization was dated at 1868 ± 0.74 Ma (Davis et al., 2011), contemporaneous to the formation of the Mazenod assemblage and of the biotite–feldspar±quartz-phyric dikes within error.

In the Mazenod sector, feldspar±quartz-phyric rocks form a km wide intrusion that envelops the volcanic rocks of the Bea and Mazenod assemblages (Fig. 1-15). North of the Sue-Dianne deposit, this feldspar-phyric intrusion yielded an U–Pb age on zircon of 1867.9 +2.9/-2.4 Ma (Gandhi et al., 2001). Feldspar-phyric porphyritic rocks also form numerous dikes in the Cole sector and localized dikes in the Lou IOAA sector. They are generally massive and have a

dacitic/rhyolitic to andesitic composition (Fig. 2-3d). The feldspar phenocrysts are either oligoclase or andesine with minor potassic feldspar phenocrysts (Gandhi, 1989). In both the Cole and Mazenod sectors the feldspar±quartz-phyric rocks display evidences of IOAA alteration.

No U–Pb age on zircon has been obtained yet on the feldspar–quartz-phyric dikes but field relationships in the NICO assemblage indicate that they cut most of the IOAA alteration and the biotite±feldspar-phyric dikes dated at 1869 and 1868 Ma. This places their emplacement timing contemporaneous, slightly earlier or later than the 1867.9 Ma plagioclase-phyric dikes.

2.6 Intrusive rocks of the southern Great Bear magmatic zone

2.6.1 Early granite suite

Leucocratic granitic intrusions, dated at 1873 ± 2 Ma, are the oldest known intrusions of the southern GBMZ and are interpreted by Gandhi et al. (2001) to be the first manifestation of widespread magmatic activity in the southern GBMZ. In the southernmost part of the Lou IOAA sector, the early granite suite forms a km-scale, ovoid and compositionally heterogeneous intrusion. Its contact with the TLG coincides with a W-oriented deformation corridor with extensive IOAA alteration (Fig. 1-15; Southern deformation corridor). This intrusion also contains relicts of partially digested TLG metasedimentary rocks, suggesting assimilation of sedimentary rocks during magma emplacement (Fig. 2-4f). In the Eastern section, the early granite suite occurs as a crescent-shaped intrusion adjacent to the Carbonate Mountain showing.

In their least altered zones, intrusions of the early granite suite have a fine-grained, but phaneritic groundmass of mafic (hornblende and biotite; Gandhi, 1989, unpublished field descriptions) and felsic minerals with coarse- to medium-grained quartz and feldspar phenocrysts. Intense IOAA alteration is however ubiquitous in the intrusions of the early granite suite and preserved least altered zones are very rare. Sodic alteration predominates and is locally overprinted by potassic alteration fronts. Most of the primary magmatic textures are destroyed and the magmatic mafic minerals are typically entirely replaced by albite or K-feldspar, giving a leucocratic aspect to the altered granites. WNW-oriented and intensely potassic-altered shear zones and rhyolite dikes cross cut the early granite intrusion south of the Lou system (chapitre 6).

2.6.2 Sodic-altered granite dikes

A sodic-altered granite dike containing enclaves of a rhyolite dikes locally occurs in a deformation corridor located at the contact between the Treasure Lake Group and an intrusion of the early granite suite. The dike is thus postdating the swarm of rhyolite dikes. A preliminary U–Pb age on zircon places their emplacement timing to 1871 ±0.8 Ma (Davis et al., 2011; Figs. 2-2, 2-4d). The dikes are little deformed to locally foliated, and are partially fragmented and incorporated as fragments in the tectono-hydrothermal breccia. This is compatible with a syn- to late-deformation emplacement.

As all the observed dikes of this intrusive suite are overprinted by intense sodic and also potassic alteration, they have a leucocratic composition dominated by albite or K-feldspar and quartz that may not reflect their primary magmatic composition. This makes those granitic dikes compositionally and texturally similar to the albitized intrusions of the early granite suite.

2.6.3 Diorite suite

The diorite suite occurs as hectometer- to kilometer-scale biotite–feldspar-phyric intrusions and dikes of uncertain relative age in the Lou IOAA, South Lou, Sue-Dianne and Eastern Treasure Lake sectors (Gandhi et al., 2014; Fig. 1-15). Diorites typically contain feldspar and biotite/amphibole phenocrysts hosted in a fine to medium-grained groundmass that differentiates them from the biotite–feldspar and biotite-phyric dikes and intrusions that have a finer-grained groundmass. The larger intrusions of the dioritic suite are compositionally zoned from dioritic to granitic, interpreted internal differentiation (Gandhi et al., 2001). Intense IOAA alteration was locally observed in their immediate vicinity in the Eastern Treasure Lake sector. According to Gandhi et al. (2001), there are many generations of dioritic suites emplaced in the GBMZ, one which was dated at 1865.08±0.73 Ma by Bennett et al. (2012) in the DeVries area.

2.6.4 Quartz monzonite–monzodiorite suite

The quartz monzonite–monzodiorite suite forms massive ovoid to elongate plutons and stocks, one of which was dated at 1867 +1.6/-1.5 Ma (Gandhi et al., 2001; Figs. 1-15 and 2-2). Intrusions of the quartz monzonite–monzodiorite suite occur in all the sectors of the Southern GBMZ IOAA systems except for South Lou and form the prevalent intrusion type cutting the volcanic pile of the Cole assemblage (Fig. 1-15). Individual intrusions of the quartz monzonite–monzodiorite suite are porphyritic to equigranular and composed of euhedral to

subhedral plagioclase set in fine- to medium-grained matrix predominantly composed of amphibole with K-feldspar and minor quartz (Gandhi et al., 2001; this work). In the Cole sector, intrusions of the quartz monzonite–monzodiorite suite are typically associated with plagioclase-phyric porphyritic intrusions with a very fine-grained groundmass that likely represent their border facies.

In the Lou IOAA sector, the mineralized IOAA alteration zones are cut by the quartz monzonite–monzodiorite intrusive suite (Gandhi et al., 2001), providing a minimum age constraint of 1867 Ma for IOAA alteration in the Lou IOAA sector. In the Cole sector, IOAA alteration (sodic and HT calcic–iron) is extensive and intense in the intrusions of the quartz monzonite–monzodiorite suite.

On the Pearce (1996a) diagram, intrusions of the quartz monzonite–monzodiorite suite and their associated porphyritic intrusions form two clusters: one with an intermediate composition and the other with a transitional intermediate to felsic composition (Fig. 2-3d).

2.6.5 Marian River batholith

The Marian River batholith is formed by numerous monzonitic to granitic/granodioritic plutons. These plutons are assigned in the northern GBMZ to the biotite–hornblende monzogranite/granodiorite suite (Hildebrand et al., 2010b). Grain size varies between each intrusion from fine- to very coarse-grained and textures range from porphyritic to equigranular. One intrusion of the Marian River batholith, located between the two sections of the TLG, yielded an U–Pb age on zircon of 1866±2 Ma (Gandhi et al., 2001; Fig. 2-2). Older plutons are likely present in the Marian River batholith considering the large compositional variations observed within the various individual plutons and the studies of Hildebrand et al. (2010b), Bennett et al. (2012) and Jackson et al. (2013) that demonstrate intrusions of different ages and composition in the GBMZ batholith (1870 to 1862 Ma). The ca. 1866 Ma intrusions are generally devoid of any typical IOAA alteration (sodic, HT calcic–iron, HT potassic–iron; Fig. 2-4g), but localized potassic, chlorite and epidote alteration is common inside and around the 1866 Ma granitic intrusions of the Marian River batholith. Their emplacement is interpreted to postdate the main IOAA hydrothermal event in the southern GBMZ.

Many undivided and typically fine to medium-grained monzonitic dikes and stocks with elevated uranium and thorium content (thorium > 50 ppm) were also observed in the Cole sector, the Peanut zone of the South Lou sector, the Esther zone of the Eastern Treasure Lake sector and into the undivided intrusions of the Marian River batholith (Fig. 2-4h). Their respective uranium

and thorium content is up to 12.1 and 51.9 ppm in the Cole sector and up to 50 and ~100 ppm in the Peanut zone of the South Lou sector.

In the Cole sector and Peanut zone, these intrusions cut all the IOAA alteration, but locally exhibit evidences of potassic alteration and form potassic alteration halos in their host rocks. U–Pb ages on zircons of 1866.4 ± 1.3 and 1865.9 ± 0.9 Ma were obtained for uranium- and thorium-rich monzonitic dikes that cut IOAA alteration in the Cole sector. These ages are contemporaneous with the ages obtained from some of the Marian River batholith intrusions and further constrain 1866 Ma as the most likely minimum age of IOAA activity in the southern GBMZ (Davis et al., 2011).

2.6.6 Mafic dikes

Fine-grained, equigranular to porphyritic and variably altered mafic dikes were observed in both supracrustal sections of the southern GBMZ. In the Mazenod and Cole sectors, the mafic dikes cut IOAA alteration and the host volcanic units. In the Lou IOAA sector, some mafic dikes are emplaced in WNW- to E-oriented deformation corridors and also in the early granite. Although some mafic dikes exhibit evidences of chloritization and epidote alteration (e.g., near the Brooke prospect), their emplacement timing relative to IOAA alteration remains unconstrained.

2.7 Major structures

2.7.1 Western section

West to WNW striking deformation corridors are well developed in the Lou IOAA and South Lou sectors (Fig. 1-15). In the larger deformation zones predominantly located within the Treasure Lake Group metasedimentary rocks (e.g., Peanut, Southern, Duke), polyphase alteration and tectono-hydrothermal brecciation are intense and parasitic folds are locally formed (Fig. 2-5a–d). Tectonic foliations in the deformation zones, mostly defined by the preferred orientation of ferro-magnesian hydrothermal minerals like biotite and amphibole, typically strike W to WNW and are predominantly steeply dipping (80° to vertical) to the northeast, generally parallel to the TLG sedimentary rock bedding.

Strain is preferentially partitioned in the pervasively altered basal siltstone and carbonaceous units in the basal siltstone and carbonaceous units of the TLG and remains weaker in the more

competent and less altered sandstone unit of the TLG (Fig. 2-5c). The rhyolite dikes, the intrusions of the early granite suite and the albitized granitic dikes are spatially associated to most of the WNW- and W-oriented deformation corridors. These intrusions are deformed and included as fragments in the tectono-hydrothermal breccias zones (Fig. 2-4c). In the overlying, massive and competent volcanic units of the Lou assemblage, ductile deformation is not extensive. Some biotite and biotite–feldspar-phyric porphyritic dikes exhibit local weak WNW-striking tectonic foliations. Strain related to WNW deformation event is also very intense along a section of the unconformity between the Faber Group and the TLG north of the surface extension of the NICO deposit (Fig. 2-5e). At this locale, the unconformity is an extensive zone of tectono-hydrothermal brecciation in which the hydrothermal minerals (predominantly amphibole) of the breccia matrix are defining a WNW-striking tectonic foliation.

Individual tectono-hydrothermal breccia zones formed in the WNW-oriented deformation corridors characteristically range from 10 m to at least 100 m in width, hundreds of meters to kilometers in length (all remain open at their observed limits capped by the rhyolite) and most of the breccias are polymict. In most of the observed breccia zones, fragments from the Treasure Lake Group and rhyolite dikes predominate over fragments of the early granite suite, albitized granitic dikes and strongly altered rocks of uncertain origin. Fragment size varies from a few millimeters to meters, with the most common size ranging from centimeters to decimeters. Fragments have a high aspect ratio with their long axis parallel to the tectonic foliation and locally defining a stretching lineation (Fig. 2-5a). The systematic formation of intense and extensive alteration (sodic, HT calcic–iron and HT potassic–iron alteration; Fig. 2-5b–e) in all the documented WNW-oriented deformation corridors, the presence of dikes with syn-tectonic attributes and the abundance of intrusive rock fragments in the tectono-hydrothermal breccias indicate that they were major hydrothermal fluid and magma conduits during the main IOAA event in the Lou IOAA (NICO, Southern Breccia) and South Lou (Duke, Sunil, Peanut) sectors.

The N-oriented deformation corridors cut the WNW deformation corridors. The most important ones identified to date in the Western section are located in the Mazenod sector (N-trending Mar and Marian River deformation corridors; Figs. 1-15, 2-5b, 2-5f–h). The Mar deformation zone is interpreted as the main controlling structure for the formation of the Sue-Dianne deposit as well as the Nod prospect and Mar showing (Gandhi, 1989; Camier, 2002). The Brooke prospect is also located along a N-oriented lineament (Fig. 1-15). Hydrothermally altered and copper-mineralized mylonites in the Sue-Dianne deposit provide further indications of active deformation during IOAA activity in the Mazenod sector (Camier, 2002). The Marian River deformation

corridor is located east of the Sue-Dianne deposit at the contact between slivers of TLG metasiltstone, the Faber Group and the Marian River batholith. Strain is strongly partitioned into the TLG slivers; in contrast the volcanic rocks of the Dianne subassemblage are locally brecciated (Fig. 2-5f–g). Undeformed granitic dikes of the Marian River batholith cut the N-oriented tectonic foliation. Sodic and HT calcic–iron alteration, as well as zones of tectono-hydrothermal brecciation, similar in appearance to those hosted in the WNW-oriented deformation corridors, are well developed in the Marian River deformation corridor (Fig. 2-5f–g).

In the Lou IOAA and South Lou sectors, northerly oriented faults host HT calcic–iron and HT potassic–iron veins and some of the uranium-bearing veins of the Southern Breccia. At outcrop scale, intense hydrothermal alteration and tectonic brecciation is associated to N-oriented faulting (Fig. 2-5b, h). This indicates that N-oriented structures may have played a role in the formation of some of the Lou IOAA sector mineralized zones.

2.7.2 Eastern section

In the Eastern Treasure Lake sector, located closer to the Wopmay fault zone, tectonic deformation is penetrative in the TLG metasedimentary rocks and forms WNW-oriented and steeply NE-dipping tectonic foliation generally parallel to the sedimentary rock bedding. Weak to well developed and penetrative WNW-oriented tectonic foliations are also formed in the biotite–feldspar and biotite±feldspar-phyric volcanic rocks of the Hump assemblage (Gandhi, 1992a; this work).

Most of the intense IOAA alteration zones in the Eastern Treasure Lake sector (Ron, Hump, Carbonate Mountain and Dennis) are structurally controlled by WNW- and N-oriented faults or deformation corridors (Goad et al., 1996; Mumin et al., 2000; Figs. 1-15, 2-6a–b). Similar structural control is observed in the Cole sector where intensity of IOAA alteration and brecciation increases near N- to NW-oriented (0° to 330°) deformation corridors that led to the formation of an approximately 450 m-wide zone of tectono-hydrothermal brecciation (herein referred to as the Cole Breccia).

The Cole Breccia is formed by the coalescence of numerous small breccia zones in a NNW- to N-oriented deformation zone (Fig. 1-15). In the outer margins of the Cole Breccia, jigsaw-fit breccia cemented by HT calcic–iron (amphibole±magnetite–clinopyroxene) records the in situ fragmentation of a previously albitized plagioclase–amphibole-phyric andesite (Fig. 2-6c–f). The vicinities of the deformation zones are characterized by well-developed tectonic foliations, fragments with high aspect-ratios and increasing fragmentation and comminution of the host

rock with increasing strain (Fig. 2-6g). This indicates the role of tectonic activity in the fragmentation process. Numerous zoned fragments, in which the early sodic alteration is rimmed by HT calcic–iron alteration and/or incipient potassic alteration, indicate polyphase hydrothermal activity (Fig. 2-6h–i). Lobate and cuspate borders for many of those zoned fragments are interpreted as indicators of increasing chemical dissolution following the initial tectonic fragmentation. In the marginal zones of the Cole Breccia, the fragment fraction predominates and the cement/matrix content generally increases towards the center of the breccia zone where chemical dissolution of the fragments increases. This indicates that the maturity of the Cole Breccia, using the Jébrak (2010) breccia maturity criterion for IOAA systems, generally increases towards the center of the breccia complex. However zones of mature breccia, in which the fraction of hydrothermal cement strongly predominates over the fragment fraction, are rare in the Cole breccia. The cement-matrix/fragment ratio in the breccia rarely exceeds 1 and moderately mature to immature breccias, in which the fraction of hydrothermal cement/fragment range between 0 (immature) and 1 (moderately mature), predominate in the Cole Breccia.

2.7.3 NE-oriented faults

NE-oriented faults (±35° to 45°) are associated with a late dextral strike slip that bisected the IOAA alteration zones in the Western and Eastern sections, but host and are the controlling structure for most of the quartz veins-related mineralization (e.g., Rayrock mine; Gandhi et al., 2000; Byron, 2010). Important faults of this class include the Lou Lake, Dianne and Rayrock faults (Fig. 1-15).

In the Lou IOAA sector, the Lou assemblage significantly thickens northwest of the Lou Lake fault (e.g., 175 m below surface in Fortune Minerals Limited drill hole DDH NW-00-001; Robinson, 2013). The localized formation of IOAA alteration into NE-oriented veins (HT calcic–iron alteration) also indicates that some of these structures were active during the main IOAA event. U–Pb dating of pitchblende at Rayrock mine by Miller (1982) in the Rayrock fault yielded a late Ordovician age, indicating that periodic activity occurs along the NE-oriented from the Paleoproterozoic to at least the late Ordovician.

2.8 Distribution of IOAA alteration among supracrustal and intrusive units

As they represent diagnostic elements specific to the main IOAA alteration types observed in the southern GBMZ (chapitre 5), molar concentrations of Na, Ca, Fe, K and Mg are plotted on regional geological maps to illustrate the distribution of IOAA alteration in the main sectors of the southern GBMZ IOAA system (Figs. 2-7 to 2-11). Molar concentrations are used because they represent the best proxies for the rock mineralogy. The spatial distribution and relative proportions of these elements mimic and provide an efficient graphic representation of alteration distribution within the studied hydrothermal systems (Table 2-2; Fig. 2-1).

2.8.1 Sodic and sodic–calcic–iron alteration

At the current exposure level, sodic and sodic–calcic–iron alteration occurs in most units of the southern GBMZ (Figs. 2-7 to 2-11). The most notable exceptions are the 1866 Ma intrusions of the Marian River batholith, the quartz–feldspar porphyritic dikes and the uranium–thorium-rich monzonitic dikes that cut the iron oxide and alkali alteration in the Cole sector and the Peanut zone.

Weak to moderate sodic alteration preferentially replaces the feldspar phenocrysts in the Faber Group porphyritic rocks, the mafic groundmass in the early granite and some quartzofeldspathic beds in the Treasure Lake Group. Intense and pervasive albitization destroys the rock primary textures and replace all the original minerals by an assemblage primarily composed of fine-grained white to creamy albite with or without quartz and accessory titanium oxide, titanite and zircon as observed in the Southern Breccia, Nod, Dennis and Esther zones.

Many sodic and sodic–calcic–iron alteration zones are overprinted, cross-cut and/or brecciated by HT calcic–iron (e.g., NICO, Nod, Ron, Cole), HT potassic–iron (e.g., Brooke, Southern Breccia, Hump, Duke, NICO), LT potassic–iron (e.g., Esther, Southern Breccia, Sue-Dianne), potassic and skarn (Duke, Carbonate Mountain) alteration. The breccia are focused along west-northwest-oriented (Lou IOAA and South Lou sectors) and north-oriented deformation corridors (Sue-Dianne and Cole sectors) are superimposed over sodic alteration zones. The breccias are cemented by subsequent generations of HT calcic–iron alteration (e.g., Cole, Nod, NICO), HT potassic–iron (Southern Breccia) and LT potassic–iron alteration (e.g., Southern Breccia; further description in chapitre 6).

2.8.2 HT calcic–iron alteration

At the current level of exposure, HT calcic–iron alteration occurs in all sectors of the southern GBMZ IOAA system and occurs in all the rock units except the 1866 Ma intrusions of the Marian River batholith and the uranium–thorium-rich monzonitic dikes (Figs. 2-7 to 2-11). HT calcic–iron alteration characteristically follows sodic and sodic–calcic–iron alteration and is especially well-developed in the Duke, Sunil, NICO and Nod zones in the Western section and in the Hump, Ron, Cole and Carbonate Mountain zones in the Eastern Section.

Intense HT calcic–iron alteration is well developed in the reactive rocks units of the TLG (argillite, siltstone and carbonate) where it forms penetrative and selective to pervasive replacement zones extending discontinuously to continuously over hundreds of meters (e.g., NICO deposit, Duke and Sunil zones) as well as veins more locally. Within the least-altered section of the TLG, carbonate units are observed to initially form clinopyroxene- or garnet-rich skarns superimposed over sodic alteration. The skarn in the carbonate rocks are coeval with amphibole-rich HT calcic–iron in silicate rocks and can also be overprinted by amphibole-rich assemblages more typical of the calcic–iron stage. In the NICO deposit, early clinopyroxene-rich skarn is locally observed and almost entirely replaced by HT calcic–iron alteration zones (Sidor, 2000; Robinson, 2013).

In the less reactive and more competent quartz arenite beds of the TLG and into the volcanic rocks of the Faber Group, HT calcic–iron alteration typically occurs as veins although pervasive replacement of the quartz arenite and of the very fine-grained to aphanitic groundmass of the volcanic rocks is common. Pervasive and penetrative HT calcic–iron impregnation of the volcanic rock groundmass is particularly extensive in the Cole assemblage porphyritic andesite and in the vicinity of the Nod zone.

2.8.3 HT potassic–iron alteration

Zones of intense HT potassic–iron alteration zones are less extensive than the sodic and HT calcic–iron alteration zones (Figs. 2-7 to 2-11). They are spatially associated to polymetallic mineralization zones forming pervasive biotite±magnetite–K-feldspar replacement of earlier HT calcic–iron alteration in NICO and South Lou or magnetite-cemented and K-feldspar-rich hydrothermal breccias in the Southern Breccia zone and Mazenod sector (Brooke, Sue-Dianne). Pervasive HT potassic–iron replacement of the Lou assemblage felsic volcanic rocks aphanitic groundmass (K-feldspar–magnetite) is also observed between the NICO deposit and the

Southern Breccia, north of Lou Lake and south of Chalco Lake (cf. detailed descriptions at Chalco Lake in Robinson, 2013). In the Eastern section, HT potassic–iron alteration is only well developed in the Hump iron oxide showings, incipient within the Esther zone, and conspicuously absent from the Cole sector except for a weak calcic–iron–potassic alteration with the uranium mineralization.

Table 2-2 Major element composition of the samples used to make the typical bloc diagrams for each alteration type and least altered precursors

Sample	**0029C01**	**0043F03**	**0055G02**	**1009B04**	**1038A02**	**1041A02**	**1059H04**	**1074D02**
System	Brooke	Hump	Duke	Sue-Dianne	SDVC	SDVC	Esther	Cole
Precursor	Rhy	Sed	Silt	Ignim	Ignim	Ignim	Gr	Mf
Alteration	HT K–Fe	HT Ca–Fe	LT K–Fe	HT-LT K–Fe	weak	weak	Na	weak
CaO (wt. %)	0.11	19.81	10.32	0.75	5.73	2.08	0.55	7.31
Fe_2O_3	80.27	26.77	14.87	14.38	5.64	5.42	0.94	10.99
K_2O	2.82	0.07	0.09	10.52	3.62	4.23	0.93	2.65
MgO	0.41	5.56	19.64	0.46	1.56	2.28	0.49	4.54
Na_2O	0.02	0.3	0.09	0.21	3.18	2.56	10.03	2.09
Ca_{mol}	0.002	0.353	0.184	0.013	0.102	0.037	0.01	0.13
Fe_{mol}	1.005	0.335	0.186	0.18	0.071	0.068	0.012	0.138
K_{mol}	0.06	0.002	0.002	0.223	0.077	0.09	0.02	0.056
Mg_{mol}	0.01	0.138	0.488	0.011	0.039	0.057	0.012	0.113
Na_{mol}	0.001	0.01	0.003	0.007	0.10	0.083	0.32	0.068
Sample	**1086A02**	**1117B02**	**0163C03**	**0168A02**	**0514B02**	**0546E03**	**0049B03**	
System	Duke	ETLG	Cole	Cole	Cole	Cole	WTLG	
Precursor	Silt	Silt	Por	Gr	Por	Por	Silt	
Alteration	HT Ca–Fe	weak	weak	weak	Na–Ca–Fe	K	weak	
CaO (wt. %)	4.94	2.00	4.02	2.31	5.23	0.27	0.52	
Fe_2O_3	64.59	8.05	5.16	4.77	5.32	1.85	7.07	
K_2O	0.96	4.09	5.00	5.22	1.09	12.96	5.42	
MgO	4.48	2.73	2.3	1.59	3.37	0.41	2.45	
Na_2O	0.73	3.32	3.11	2.84	6.19	1.83	0.96	
Ca_{mol}	0.088	0.036	0.072	0.041	0.093	0.005	0.009	
Fe_{mol}	0.809	0.10	0.065	0.06	0.067	0.023	0.089	
K_{mol}	0.02	0.087	0.11	0.111	0.023	0.275	0.12	
Mg_{mol}	0.11	0.068	0.057	0.039	0.084	0.01	0.061	
Na_{mol}	0.024	0.11	0.10	0.092	0.2	0.059	0.031	

Rhy = Rhyolite, Sed= Sedimentary rock, Ignim = Ignimbrite, Gr = Granite, Mf = Mafic dike, Silt= Siltstone, Por Porphyry

2.8.4 LT potassic–iron alteration

LT potassic–iron alteration is incipient to strong in all the sectors and all rock units of southern GBMZ IOAA system, and forms systematically after the sodic, HT calcic–iron and HT potassic–iron alteration. In the Lou IOAA and South Lou sectors, LT potassic–iron alteration

typically occurs as partial but common chlorite±hematite±muscovite±K-feldspar replacement of the earlier HT calcic–iron and HT potassic–iron alteration and of the local to regional K-feldspar metasomatism of the volcanic rocks and the breccias underlying them (this work; Robinson, 2013). It also locally forms hematite-cemented hydrothermal breccias in the albitites of the Southern Breccia zone and in the Lou assemblage basal rhyolite near the Summit Peak showing and north of Lou Lake. Such alteration is associated with uranium mineralization in the Southern Breccia and with chalcopyrite at the Summit Peak prospect structurally above the NICO deposit. In the Mazenod sector, LT potassic–iron alteration primarily occurs as a pervasive hematite–K-feldspar±muscovite replacement of the HT potassic–iron alteration zones of the Sue-Dianne deposit and the Brooke prospect, but also forms new zones of hydrothermal brecciation with renewed copper mineralization, with either chalcopyrite or bornite–chalcocite as the main copper minerals.

In the Eastern section, LT potassic–iron alteration occurs as K-feldspar–hematite, K-feldspar–hematite–chlorite, sericite–hematite–chlorite and chlorite–hematite veins and impregnation and is particularly well developed in the surroundings of the Esther zone showings. In the Hump and Ron zones, specular hematite systematically rims the magnetite crystals formed during the calcic–iron and HT potassic–iron alteration stages.

2.8.5 LT calcic–iron alteration

A late-stage, and commonly allanite-bearing LT calcic–iron (epidote, epidote–K-feldspar, epidote–quartz) alteration, coeval or postdating the LT potassic–iron alteration, is present in all the sectors of the southern GBMZ IOAA system. In the Eastern Treasure Lake sector, LT calcic–iron alteration is particularly intense in the Dennis, Esther, Hump and Ron zones where it overprints all the previous IOAA alteration. Low temperature potassic–iron alteration zones can substantially change the mineralogy and chemistry of the altered rocks (Fig. 2-1). Low temperature Ca–Fe alteration overprint over HT Ca–Fe alteration can lead to the formation of epidote-rich ironstones (up to 40% modal epidote) in which epidote replaces actinolite and REE-rich allanite is formed at the expense of apatite (chapitre 4). In the South Lou and Mazenod sectors, such alteration is intense but systematically superimposed on the low temperature potassic–iron alteration zones. It is also abundant across the Sue-Dianne deposit and the Brooke prospect in the Mazenod sector. In the Cole and Lou IOAA sectors, LT calcic–iron alteration is not as intense and spatially extensive than in the other sectors of the GBMZ IOAA

2.9 Geochemistry of volcanic and intrusive rocks

Although designed for volcanogenic massive sulfide systems, the alteration box-plot of Large et al. (2001) is also used to better define the possible hydrothermal alteration imprints on the selected samples of the southern GBMZ. On these diagrams, the samples selected as representative of the volcanic and intrusive rocks plot largely within or close to the fields defined for least-altered samples except for the Lou assemblage felsic volcanic rocks (Fig. 2-12a, b). This confirms that the selected samples are devoid of any intense IOAA alteration that can substantially remobilize the high field strength elements (HFSE) and the rare earth elements (REE) such as observed in both HT calcic–iron and HT potassic–iron alteration (chapitre 5). Both diagrams however show a weak to strong potassic alteration imprint on the felsic volcanic rocks of the Lou assemblage, as well as on some rhyolite/dacite and andesite of the Dianne subassemblage, some porphyritic dikes and some uranium–thorium-rich monzonite dikes. In addition both diagrams show the moderate to mild sodic alteration imprint in samples from the Cole assemblage andesite, the Mazenod assemblage, some intrusions of the quartz monzonite–monzodiorite suite and some intrusions of the Marian River batholith. It also shows the intense sodic alteration imprint in the intrusions of the early granite suite and the sodic-altered granite dike.

In the following bivariate diagrams of major elements, Al is used as the dividing element in the molar ratios as it is not extensively mobile in IOAA alteration (Marschik and Fontboté, 2001b; chapitre 7) and enters in the chemical structure of most minerals formed in IOAA alteration zones except for the iron oxides. Plotting Zr/Ti versus $(K/Na+K)_{molar}$ illustrates that most of the biotite–feldspar-, biotite- and feldspar–biotite-phyric dikes emplaced in the Lou IOAA sector, including the least-altered ones, most of the biotite–feldspar-phyric felsic volcanic rocks of the Lou assemblage and many samples from the Dianne subassemblage have higher K contents than other rocks with similar Zr/Ti ratios (Fig. 2-13a). The felsic volcanic rocks of the Lou assemblage, irrespective of their Zr/Ti ratios, exhibit the highest $(K/Na+K)_{molar}$ ratios that highlight the predominance of K-feldspar in the mineral assemblage. This is primarily related to the pervasive potassic alteration overprint (K-feldspar) throughout the Lou assemblage. Conversely, most samples of the Cole assemblage, intrusions of the quartz monzonite–monzodiorite suite and feldspar-phyric porphyritic intrusions are less potassic and more sodic than their counterparts with similar Zr/Ti ratios. $(K/Na+K)_{molar}$ ratios below 0.2 reflect the sodic (albite) alteration overprints, visible in samples from the Cole and Mazenod assemblages, from the early granite and quartz monzonite–monzodiorite suites, some samples

from the Marian River batholith and some samples from undivided porphyritic intrusions in the Eastern Treasure Lake sector. No distinct pattern is observed in the granitic intrusions of the Marian River batholith and the uranium–thorium-rich monzonitic dikes and intrusions cutting IOAA alteration.

Plotting Zr/Ti versus $(Ca/Al)_{molar}$, $(Mg/Al)_{molar}$ and $(Fe/Al)_{molar}$ shows that the Ca, Mg and Fe content of the volcanic and intrusive rock decreases with increasing Zr/Ti (i.e., increasing differentiation; Fig. 2-13b–d). It also shows that the porphyritic dikes of the Lou IOAA sector and of the uppermost unit of the Mazenod assemblage have much lower Ca content than the other rocks with similar Zr/Ti ratios for higher K content. Conversely most of the rocks of the Dianne subassemblage have lower $(Mg/Al)_{molar}$ ratios than the other rocks with the same Zr/Ti ratios.

2.9.1 High field strength elements, Ti, Al and REE

To illustrate the behavior of less mobile elements in IOAA alteration and highlight the geochemical signature of the intrusive and volcanic rocks of the southern GBMZ, various ratios of high field strength elements, Ti, Al and REE are used.

Plotting Th/Yb versus Zr/Ti shows that the scattering of the Th/Yb ratios increases with increasing Zr/Ti ratios and is especially strong in the felsic volcanic rocks of the Lou assemblage in the Lou IOAA sector and for the intrusions of the Marian River batholith and the uranium–thorium-rich monzonitic dikes (Fig. 2-14a). In the other geological units of the southern GBMZ for similar Zr/Ti ratios, the Th/Yb ratios generally remain tightly clustered. For similar Zr/Ti ratios, samples of the Cole assemblage andesite, some porphyritic intrusions of the Eastern Treasure Lake sector and many intrusions of the Marian River batholith have low Th/Yb ratios. Conversely samples of the uppermost unit of the Mazenod assemblage hosting the Sue-Dianne deposit and most of the dacite/rhyolite of the Dianne assemblage have high Th/Yb ratios compared to other samples with similar Zr/Ti ratios. The Th/Yb ratios of the biotite-phyric dikes in the Lou IOAA sector, of least differentiated intrusions of the quartz monzonite–monzodiorite suite and of the feldspar–amphibole-phyric andesite of the Dianne subassemblage are similar to each other and close to those of the feldspar–amphibole-phyric andesite of the Cole assemblage.

Plotting Al/Ti versus Zr/Ti shows that the volcanic rocks of the Lou assemblage in the Lou IOAA sector, the rhyolite dikes, the undivided rhyolitic rocks in the South Lou sector and the intrusions of the early granite suite have higher Zr/Ti and Al/Ti ratios compared to all the other geological units of the southern GBMZ (Fig. 2-14b). Samples of these units also define a distinctive

differentiation trend that parallels the trend formed by the other volcanic and intrusive rocks of the southern GBMZ. Some of the uranium–thorium-rich monzonitic dikes plot in the trend formed by the Lou assemblage felsic volcanic rocks and rhyolite dikes whereas other samples of the Marian River batholith and uranium–thorium-rich monzonitic dikes form their own differentiation trend. This diagram shows that the samples from the Bea, Cole, Hump and Mazenod assemblage, the Dianne subassemblage, the porphyritic intrusions and the quartz monzonite–monzodiorite suite plot among the same fractionation trend. Plotting La/Yb versus Zr/Ti shows that, without considering the volcanic rocks of the Lou assemblage in the Lou IOAA sector, La/Yb typically increases with increasing Zr/Ti (differentiation; Fig. 2-14c). With La/Yb ratios above 30, some felsic volcanic rocks of the Lou assemblage, the porphyritic dikes and of the Marian River batholith exhibit considerable La/Yb fractionation. This diagram also shows that most of the andesites of the Cole assemblages and many feldspar–biotite/biotite–feldspar-, biotite- and feldspar-phyric dikes in the Lou sector have lower La/Yb ratios than the other rocks with similar Zr/Ti ratios, indicating their more primitive composition.

Plotting Zr/Hf versus Nb/Ta indicates that many felsic volcanic rocks of the Lou assemblage in the Lou IOAA sector and the undivided felsic volcanic rocks of the South Lou sector, some intrusions of the early granite suite and some biotite–feldspar/feldspar–biotite-phyric porphyritic dikes in the Lou IOAA sector have sub-chondritic Zr/Hf (below 30) and Nb/Ta ratios (between 8 and 2.4), well below the typical Zr/Hf (36.4) and Nb/Ta (13.3) ratios of the upper crust (Rudnick and Gao, 2007; Fig. 2-14d). Most of the volcanic and intrusive rocks of the southern GBMZ have higher, but still sub-chondritic Nb/Ta ratios between 8 and 13 that are more typical of the upper crust Nb/Ta ratio (13.3). It also shows that Nb/Ta generally increases with Zr/Hf and that the geological units of the southern GBMZ, except for the Lou assemblage felsic volcanic rocks, the Marian River Batholith and the uranium–thorium-rich monzonite, typically defines tight clusters with some outliers.

The observations made using HFSE and REE indicate only a weak mobility for elements that reflect the primary composition of the volcanic and intrusive precursor rocks. This conservative behavior of HFSE and HREE in regional IOAA alteration was also observed in the Punta del Cobre IOCG district in Chile (Marschik and Fontboté, 2001a).This justifies the use of HFSE and HREE for the Pearce (1996a) diagram to classify the southern GBMZ volcanic rocks and to assess the magmatic affinity and tectonic environment signature of the southern GBMZ igneous rocks.

2.9.2 Fluorine content of the volcanic and intrusive rocks

Most of the volcanic rocks of the Hump assemblage and some volcanic rocks of the Cole assemblage, some intrusions of the quartz monzonite–monzodiorite suite and of the Marian River batholith, most of the biotite-phyric andesite dikes, and some of the biotite–feldspar phyric dikes of the Lou IOAA sector and of the feldspar-phyric intrusion north of the Sue-Dianne deposit have high F content, above 750 ppm (Fig. 2-15a). This is in the lower range of typical A-type granites (Whalen et al., 1987; Eby, 1990) and volcanic and intrusive rocks of the shoshonitic clan (Corriveau and Gorton, 1993; Müller et al., 1994).

Plotting $(K/Al)_{molar}$, and $(Mg/Al)_{molar}$ versus F indicates that the F content of the GBMZ volcanic rocks and intrusions slightly increases with decreasing $(K/Al)_{molar}$ content in the rock (Spearman rank correlation of -0.30) whereas the content of F increases with $(Mg/Al)_{molar}$ (Spearman rank correlation of 0.58; Fig. 2-15b–c). Considering the mild to strong potassic alteration overprint in the felsic volcanic rocks of the Lou assemblage that may have destroyed most of their mafic minerals, their low F content may relate to the superimposed potassic alteration and not be a primary feature of these rocks. However, the maximal F content below 500 ppm in the least altered biotite–feldspar-phyric rhyolites of the Lou assemblage is indicative of generally low primary F content in most of the Lou assemblage felsic volcanic rocks and probably F-poor magmatism throughout the early stages of the GBMZ formation.

2.10 Tectono-magmatic evolution of the southern GBMZ

2.10.1 Tectonic setting and magmatic sources of volcanic and intrusive rocks

The Pearce (1982) Th/Yb versus Ta/Yb diagram and a revised version of the Peccerillo and Taylor (1976) diagram by Hastie et al. (2007) using Th and Co (less mobile) instead of K_2O and SiO_2 indicate that the volcanic and intrusive rocks of the southern GBMZ relate to potassic magmatism belonging to the shoshonitic series and to high-K calc–alkaline series (Fig. 2-16a–b). Although Co is potentially mobile and enriched in some zones of the southern GBMZ IOAA systems and was remobilized and enriched in some porphyritic dikes cutting the NICO deposit, the high Th content of all the volcanic and intrusive rocks of the southern GBMZ also indicates affiliation to the shoshonitic series. Similar observations are made on the Peccerillo

and Taylor (1976) diagram (not shown), but as it uses mobile elements the results are not as robust as those obtained with the thorium content. A-type and F-rich porphyritic intrusions of the shoshonitic series associated with extensive IOAA alteration and IOCG mineralization have also been identified in the Fab Lake area, located 45 km north of the Sue-Dianne deposit, in a porphyritic intrusive complex formed between 1870 and 1866 Ma (Azar, 2007, Potter et al., 2013b; chapitre 7).

The Müller et al. (1992) Zr/Al_2O_3 vs TiO_2/Al_2O_3 and Ce/P_2O_5 vs Zr/TiO_2 diagrams employed to identify the tectonic setting of potassic magmatic rocks containing between 41.4 and 62.1 wt. % SiO_2 (i.e., andesites and basalts) show that the potassic andesites and basalts of the southern GBMZ have a chemistry compatible with those a continental volcanic arc, in agreement with the previous interpretations of Hildebrand et al. (1987) and Gandhi et al. (2001; Fig. 2-16c–d).

The Pearce et al. (1984) Ta vs Yb discrimination diagram for granites is used to identify the potential tectonic environments of formation of the granites and with further caution of the felsic/intermediate volcanic rocks of the southern GBMZ (Fig. 2-12a–b). Hydrothermal alteration can modify the absolute concentrations of Ta and Yb in altered rocks. The clusters formed by the least altered rocks of each unit are most likely representative of their primary composition. That the sample distribution patterns match the observations made with ratios of immobile elements also supports Ta and Yb immobility.

Most of the Marian River batholith intrusions, which are generally devoid of iron oxide and alkali alteration, have a signature typical of volcanic arcs, but some of the 1866 Ma intrusions and the uranium–thorium-rich monzonitic dikes have a transitional to within plate affinity (Fig. 2-16e). As the tectonic settings highlighted on the Pearce et al. (1984) diagram reflect the tectonic environment of the magma sources (Pearce, 1996b), the diversified tectonic environments of formation of the intrusions forming the Marian River batholith indicate diverse magma sources and support polyphase intrusive events to form this batholith (Fig. 2-16e).

According to the Pearce et al. (1984) diagram (Fig. 2-16f), many felsic volcanic rocks of the Lou assemblage have a syn-collisional to volcanic arc affinity, corresponding to their low Nb/Ta ratios, whereas most of the remaining volcanic rocks of the Faber Group, the porphyritic dikes and intrusions of the quartz monzonite–monzodiorite suite have a volcanic arc affinity. Some samples of the feldspar-phyric porphyritic intrusions also plot into the within plate and transitional fields (Fig. 2-16f).

The compositional variations with time of each geological unit, beginning with the Lou assemblage and ending with the 1866 Ma intrusions of the Marian River batholith, highlights a

progression from syn-collisional and volcanic arc magma sources in the early stages of GBMZ magmatism to volcanic arc and then predominantly transitional to within-plate magma sources in the later stages (Fig. 2-2).

2.11 Ground preparation for the southern Great Bear magmatic zone IOAA systems

Tectono-hydrothermal events associated with the Calderian orogeny can have influenced the subsequent GBMZ formation. These include:

1) pre-collisional and extensive mafic magmatism in the Slave Craton western margin shown to be active at 1882.5 ± 0.9 Ma (Morel sills and mafic dikes of the Ghost swarm; see Buchan et al., 2010 for their spatial extension; Hoffman et al., 2011);

2) pre- to syn-collision and extensive felsic to mafic magmatism at ca. 1880 Ma to form the Hepburn plutonic suite in the northern GBMZ (Hildebrand et al., 2010a);

3) granitic magmatism at ca. 1877 Ma contemporaneous with Calderian orogenic metamorphism in the central GBMZ (Jackson et al., 2013);

4) formation of a generally low-standing and/or rapidly collapsing orogen (Hildebrand et al., 2010a);

5) post-collisional formation of an Andean-type active continental margin (Hildebrand et al., 2010a; Cook et al., 2011); and

6) a very short time interval between the beginning of the Calderian orogeny at 1882.5 ± 0.9 Ma (age of the foredeep sequence of the Calderian orogeny; Hoffman et al., 2011) and the beginning of extensive GBMZ continental magmatism coeval within error throughout the GBMZ, at ca. 1875 Ma in the north and at ca. 1873 Ma in the south (early granite suite; Gandhi et al., 2001).

The mafic magmatism that occurred on the Slave Craton margin before and during the early stages of the Calderian orogeny, demonstrated by the emplacement of the 1.882 Ga Morel Sill in the foredeep sequence, indicates a pre-GBMZ thermal anomaly in the mantle and a potential mantle to upper crust connection along most of the western margin of the Slave Craton. The emplacement of the Morel sills also signaled episodic extensional events in the Slave Craton prior to and during the early stages of the Hottah–Slave collision. In tectonic models proposed

for the Calderian orogeny and the pre-GBMZ Slave Craton continental margin evolution (Hildebrand et al., 2010a; Ootes et al., 2015), the mantle underlying the GBMZ was the site of a long-live subduction zone that favored the incorporation of crustal material. A further incorporation of crustal material may have occurred during the interpreted partial subduction of the Slave continental crust during the Hottah–Slave collision (Hildebrand et al., 2010a; Cook, 2011).

Incorporation of crustal material can have a substantial influence on the composition of the magmas subsequently formed above a collision zone (e.g., Australia and Sunda–Banda arc collision; Elburg et al., 2002, 2004; Tibetan shoshonitic rocks: Gao et al., 2010; shoshonitic volcanism in Sardinia; Beccaluva et al., 2013) as it can further enrich the overlying and already metasomatized mantle in alkali (K and Na), radioactive (U and Th) and large ion lithophile elements (Ba, Rb, Sr). This can be a key factor to explain the potassic magmatism in the southern GBMZ that extends at least to the Fab Lake area. Additionally, the GBMZ magmas may have incorporated crustal material of the Hottah terrane during their emplacement. This is also supported by the presence of inherited zircons of Hottah terrane age (chapitre 7; Bennett et al., 2012) in the GBMZ intrusions and the lead isotope work of Housh et al. (1989).

2.12 Tectono-magmatic evolution— late Calderian to 1866 Ma

The oldest magmatic rocks interpreted as related to GBMZ magmatism are syn-deformational granitic dikes emplaced in TLG metasedimentary rocks at 1878±4 Ma in the DeVries area (Bennett and Rivers, 2006). Inherited magmatic zircons yielding U–Pb ages between 1879 to 1875 Ma were also found in intrusive rocks of the GBMZ south of the DeVries area (Bennett and Rivers, 2006; Bennett et al., 2012) and syn-deformational intrusions in the central GBMZ yielded U–Pb ages on zircon of 1877±2 Ma (Jackson et al., 2013).

Early GBMZ magmatism, which was predominantly intrusive, exhibits many features of syn-deformation emplacement accompanied by orogenic metamorphism (Corriveau et al., 2007; Jackson et al., 2013), likely occurred in a compressive setting related to the on-going Calderian orogeny. The persistence of compressive deformation at 1877 Ma, Calderian orogenic metamorphism at ca. 1876 Ma in the central GBMZ, 5 m.y. after the initial collision between the Hottah arc and the Slave, and the widespread formation of ductile tectonic foliations in the GBMZ intrusions dated at ca. 1867 Ma near the Wopmay fault are good evidences that a compressive deformation persisted until the formation of the Lou assemblage.

Ongoing compression in the early stage of the Lou assemblage formation also accounts for:

1) thrusting of the Southern Breccia brecciated albitites against the calcic–iron alteration envelope of the NICO deposit (itself developed on mildly to moderately albitized Treasure Lake Group);

2) localized tilting of the Lou assemblage basal rhyolite during and after its deposition (Enkin et al., 2012) and would account for the felsic);

3) development of scattered breccias, least-altered or with local magnetite infill, within the Treasure Lake Group at the unconformity with volcanic rocks with ;

4) tilting of erosional troughs infilled with volcanic material within Treasure Lake Group; and

5) the syn-collisional compositional affinities of the Lou assemblage.

A compressive setting during the early stages of the GBMZ formation may have been favored by shallow dipping and east-verging subduction at the western margin of the Hottah arc. Evidences for a shallowly dipping subduction plane during the GBMZ formation have been documented by near-vertical and wide-angle seismic reflection data ~150 km south of the southern GBMZ (Oueity and Clowes, 2010).

The highly variable trace element signatures (e.g., Th/Yb, Nb/Ta, Al/Ti ratios) for most felsic volcanic rocks of the Lou assemblage in the Lou IOAA sector, which is relatively typical of rhyolites, and the fact that they plot in the volcanic arc and syn-collisional fields of the Pearce et al. (1984) diagram indicate a magma source strongly influenced by magma-crust interactions and/or assimilation/melting of crustal rocks (Pearce et al., 1982; Hastie et al., 2007; Pearce, 2008). Their highly evolved nature also likely indicates extended differentiation of the parent magmas in the crust. In addition, partial digestion of TLG enclaves is observed in the intrusions of the early granite suite. Combined with potential heterogeneities in the magma sources, partial assimilation and melting of a biotite-rich source (e.g., metasedimentary rocks of the TLG) can explain the low and variable Nb/Ta ratios observed in some intrusions of the early granite suite and many of the Lou assemblage felsic volcanic rocks as partition coefficients favor the retention of Nb in the biotite over Ta (Stepanov and Hermann, 2012).

Many factors indicate less extensive differentiation/assimilation and a weaker crustal component in the parent magmas following the Lou assemblage formation:

1) increasing chemical homogeneity of rocks with similar Zr/Ti ratios in the Bea, Dianne, Cole and Mazenod assemblage, the porphyritic dikes and intrusions and the quartz monzonite–monzodiorite intrusions, and their more primitive composition than the Lou assemblage rhyolites;

2) lower Th/Yb ratios in the rocks of the Cole assemblage, the biotite-phyric dikes as well as some intrusions of the Marian River batholith and quartz monzonite–monzodiorite suite; and

3) mafic volcanism in the Hump assemblage.

A gradual increase in the magma emplacement rate is also evidenced by the roughly coeval extrusion of the Dianne subassemblage and the Cole/Hump assemblage of the Faber Group as well as the regional emplacement of porphyritic intrusions around 1869–1868 Ma culminating with emplacement of the extensive Marian River batholith at 1866 Ma.

The increasing proportions of intrusive and volcanic rocks with a transitional to within-plate chemical signature, the more primitive andesite of the Cole and Dianne assemblages, the formation of F-rich volcanic and intrusive rocks, and mafic volcanism of the Hump assemblage signal a stronger input of mantle-derived magmas (Pearce et al., 1984; Pearce, 1996b; Mark, 1999; Frost and Frost, 2013; Pankhurst et al., 2013). This is indicative of a relaxation of the predominantly compressive stress regime active during the formation of the Lou assemblage. Higher magma input from the subduction zone, possibly related to asthenospheric upwelling, has a positive feedback relationship with strike-slip faulting that facilitates magma ascension and may have favored this transition to an extensional stress regime (Saint Blanquat et al., 1998; Cembrano and Lara, 2009). Higher rates of magma production are also demonstrated in the northern GBMZ during the progressive formation of the LaBine and then Sloan Groups and the accompanying intrusions that formed the Great Bear batholith (Hildebrand et al., 2010b). Transition to a less compressive tectonic regime as GBMZ magmatism evolved is also indicated by decreasing intensity of compressive deformation in the GBMZ intrusions in the vicinity of the Wopmay fault, from 1867 Ma to 1862 Ma (Jackson et al., 2013), and the absence of orogenic metamorphism in the GBMZ volcanic rocks and intrusions. An extensional regime during the main magmatic stage of the GBMZ formation associated with the IOAA systems of the Port Radium–Echo Bay and Camsell River districts has also been proposed by Mumin et al. (2014).

Enhanced crustal weakening because of increasing heat advection that facilitates transcurrent faulting may have also established a regional deformation-dominated strain regime (Saint Blanquat et al., 1998). This can explain the transition from predominantly WNW- to W-oriented

deformation in the early stage of GBMZ magmatism (magma-dominated strain regime) to N-oriented faulting during the subsequent stages of the Faber Group formation (regional deformation-dominated strain regime). Such changes in the main orientation of the deformations zones were observed during the formation of Sierra Nevada Cretaceous batholith in which early transcurrent faults formed in a magma emplacement-dominated strain are formed at high angle to the orientation of the subduction zone and the later fault zones formed in a regional deformation-dominated strain regime parallel the subduction zone (Tikoff and Saint Blanquat, 1997; Saint Blanquat et al., 1998).

2.13 Timing of the main IOAA alteration events

In the Lou IOAA sector, most of the intense sodic, HT calcic–iron and HT potassic–iron alteration types observed in the NICO deposit and the Southern Breccia are cut by the 1868 Ma feldspar–biotite-phyric dikes but have altered the 1873 Ma granitic intrusions of the early granite suite and the 1871 Ma sodic-altered granite dikes (Fig. 2-2). The late-stage LT potassic–iron alteration zones of the Southern Breccia are also cut by the feldspar–biotite-phyric dikes and were not observed in the 1867 Ma intrusion of the quartz monzonite–monzodiorite suite. This is indicating that most of the IOAA hydrothermal activity in the Lou IOAA sector occurred between 1871 and 1868 Ma to form the NICO deposit and the Southern Breccia. For South Lou, the predominance of HT calcic–iron alteration variably overprinted by biotite–rich HT potassic–iron alteration, the structural control of WNW-oriented deformation on IOAA alteration and formation of Co, Bi, Ni and W-rich mineralization zones mimics the observations in the Lou IOAA sector. The South Lou IOAA systems are thus interpreted as contemporaneous with the Lou IOAA system.

In the Sue-Dianne and Cole sectors sodic, HT calcic–iron and HT to LT potassic–iron alteration types are all developed after the 1868 Ma (and potentially younger) volcanic rocks of the Mazenod assemblage (Sue-Dianne) and intrusions of the 1867 Ma quartz monzonite/monzodiorite suite (Cole; Fig. 2-2). In the Cole sector all the IOAA alteration zones are cut by uranium–thorium enriched monzonitic dikes younger than the 1867 Ma intrusion of the quartz monzonite–monzodiorite suite. This is indicating that IOAA alteration in the Sue-Dianne and Cole sectors predominantly occurred between 1868 and 1866 Ma. These conclusions cannot be extended to the Brooke and Nod prospects with current knowledge as they are formed in undated rocks of the Lou assemblage. However, given the stratigraphic

location of the Dianne subassemblage in the Faber Group and the similarities between the Brooke prospect and the Sue-Dianne deposit in terms of alteration and metallic signature, we interpret that the Brooke prospect was also formed between 1868 and 1866 Ma.

In Eastern Treasure Lake, the maximum age of IOAA alteration is presumably 1873 Ma as intrusions of the early granite suite, as observed in the Lou IOAA sector, are extensively albitized and then overprinted by HT calcic–iron alteration. The minimum age of IOAA alteration is estimated at 1866 Ma as all the observed IOAA alteration zones are cut by granitic dikes similar to the 1866 Ma intrusions of the Marian River batholith. IOAA alteration in the Eastern Treasure Lake sector is thus contemporaneous with the IOAA events in the other sectors of the southern GBMZ IOAA system.

2.14 Implications on the development of a regional IOAA system

The southern GBMZ IOAA system demonstrates a direct temporal and spatial relationship between potassic magmatism (high-K calc-alkaline to shoshonitic) and the formation of IOCG-endowed IOAA systems in a magmatic belt with a continental arc signature. This association between potassic magmatism and IOAA hydrothermal activity has already been proposed for the Australian IOCG districts (Pollard, 2006), for the Candelaria area in Chile (Marschik and Söller, 2006), for the Marcona Fe deposit in Peru (Chen et al., 2010a, b), and for the Carajás Province in Brazil (Chiaradia et al., 2005; Dreher et al., 2008). The results obtained in this study further support a genetic association between potassic magmatism and the formation of IOCG deposits as IOCG hydrothermal activity and potassic magmatism are demonstrably contemporaneous in a 7 m.y. time interval. This is also supported by the observation of F-rich, A-type and shoshonitic porphyritic intrusions in the Fab Lake area located 45 km north of the Sue-Dianne deposit, formed between 1870 and 1866 Ma and associated with IOAA alteration and IOCG mineralization (Azar, 2007; Potter et al., 2013b; chapitre 7). A clear association is also established between the development of a Paleoproterozoic magmatic belt with a continental arc signature and the formation of IOCG deposits in an environment where many magma sources, including an important mantle component and a transition from a compressive to extensional stress regime, were involved.

In the early stages of IOAA activity in the southern GBMZ, the limited availability of permeable crustal-scale structures in a predominantly compressional stress regime likely focused early IOAA alteration and brecciation in WNW- and W- oriented deformation corridors interpreted as genetically related to early dike emplacement. Extensive and polyphase IOAA was sustained by the positive feedback relation between focused diking in the deformation zones, alteration and deformation. The transition to a more extensional stress environment is associated with increasing magma production, and a stronger mantle signature in the resulting magmatic rocks. This change favored the formation of within-plate to transitional magmas enriched in F and possibly Cl- and CO_2 (Eby, 1990 and Pankhurst et al., 2013; chapitre 7). The temporal and spatial association of F-rich magmatism with within-plate magmatic affinities and the formation of IOAA systems was also documented in the Gawler Craton (Agangi et al., 2010, 2011). In the early stage of their crustal ascent, these F-rich magmas of the GBMZ are interpreted to have exsolved large volume of magmatic-hydrothermal fluids focused in the limited permeable pathways associated with the main WNW-oriented deformation zones. Channeling of hydrothermal fluids into discrete fluid pathways is likely a critical factor for the formation of the NICO deposit and the Southern Breccia uranium showings, both formed around 1871–1868 Ma at the inferred transition from the compressive to the more extensional stress regime. The highly differentiated felsic volcanism of the Faber Group basal volcanic sequence (pre- to syn-IOAA activity), volumetrically significant in the NICO area, may also have contributed to the Bi content of the NICO deposit.

Subsequently during the formation of the Mazenod assemblage, IOAA activity became focused along the N-oriented deformation corridors during a progressive relaxation of the compressive stress in the arc. Localized zones of higher crustal permeability have favored focused discharge of hydrothermal fluids and are interpreted to have resulted in the formation of the Sue-Dianne deposit as well as the Brooke and Nod prospects and the Mar showing along the N-oriented Mar fault.

The distribution of the fertile and mature IOAA hydrothermal systems within the southern GBMZ, from the past-producing Ray Rock uranium mine (Byron, 2010) to the Sue-Dianne IOCG deposit, is focused into the Western section. The Eastern section sectors (Cole and Eastern Treasure Lake), more distal to this boundary, are characterized by a less mature alteration signature. The higher metamorphic grade in the Treasure Lake Group eastern section and the prevalence of sodic and HT calcic–iron alteration in both the Cole IOAA system and Treasure Lake Group eastern section IOAA systems is also indicative of differential uplift between the

eastern and western IOAA systems during the main IOAA event. The shallower systems in the west were more likely to reach the fertile HT and LT potassic–iron alteration window and accompanying mineralizing fluids whereas the more deeply buried systems of the east remained in the base metal-poor sodic and HT calcic–iron alteration window for most of the IOAA event.

2.15 Conclusions

The tectono-magmatic evolution of the southern GBMZ and emplacement of shoshonitic to high-K calc-alkaline magmas favored the formation of multiple IOAA hydrothermal systems within a short time frame of 7 m.y., extending from 1873 Ma to 1866 Ma. The initial rhyolitic magmatism that formed the basal sequence of the Lou assemblage occurred in a predominantly compressive tectonic regime and the resulting rhyolites are now one of the most intensely potassic altered volcanic units of the GBMZ. Around 1870–1869 Ma, a substantial increase in the magma emplacement rate is associated with a marked change of composition for the volcanic and plutonic rocks, from rhyolite to intermediate/felsic and locally mafic. This increase of magma emplacement rate and the compositional homogeneity of the intrusive and volcanic rocks of the Mazenod and Bea assemblages are interpreted to reflect a change in the regional stress regime, from compressional to extensional/transtensional.

The emplacement of F-rich volcanic and plutonic rocks during this shift in the regional stress regime and magma sources resulted in the development of many IOAA systems coeval with this predominantly shoshonitic magmatic event formed in an interpreted continental arc. Discharge of large volume of halogen- and CO_2-rich magmatic-hydrothermal fluids in spatially constrained deformation zones led to the formation of IOCG deposits (NICO and Sue-Dianne) as well as IO±A (Ron and Hump) and polymetallic albitite-hosted uranium mineralization (e.g., Southern Breccia). The resulting distribution of IOAA alteration zones in the southern GBMZ combined with the formation of large-scale metal-deficient iron oxide replacement and multiple IOCG-related mineralized occurrences mimic what has been observed in other major IOCG districts around the world.

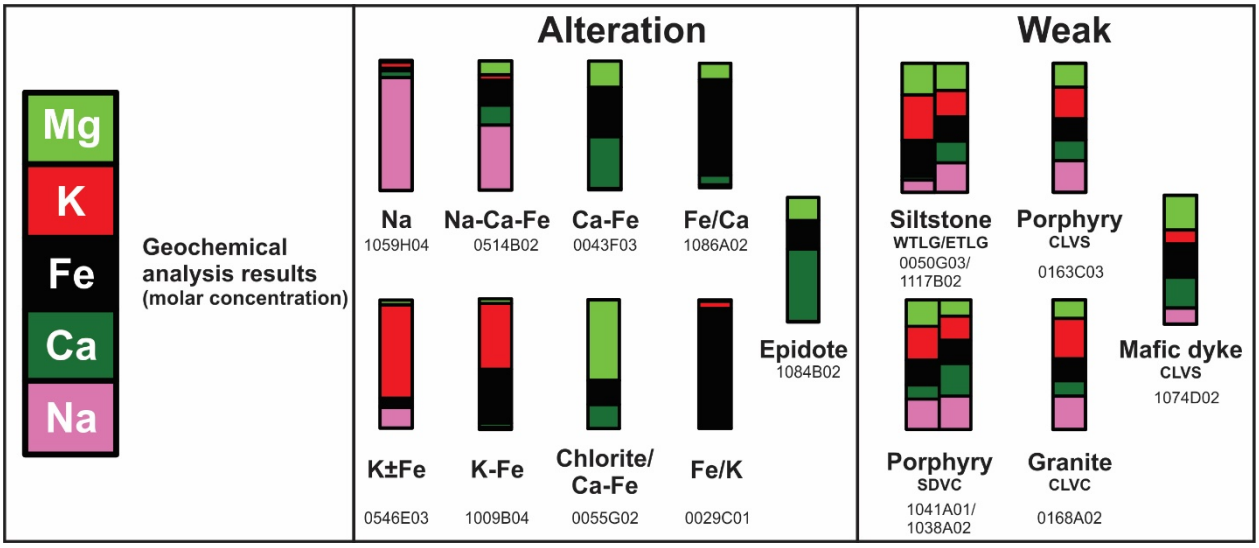

Figure 2-1 Geochemical symbology based on molar proportion of major elements used to portray IOAA alteration distribution in the studied areas of the southern GBMZ

Disproportions in Ca, Fe, K, Na and Mg molar concentration as exemplified in the figure highlight the alteration type. The amplitude of the disproportions provides a semi-quantitative measure of the alteration intensity.

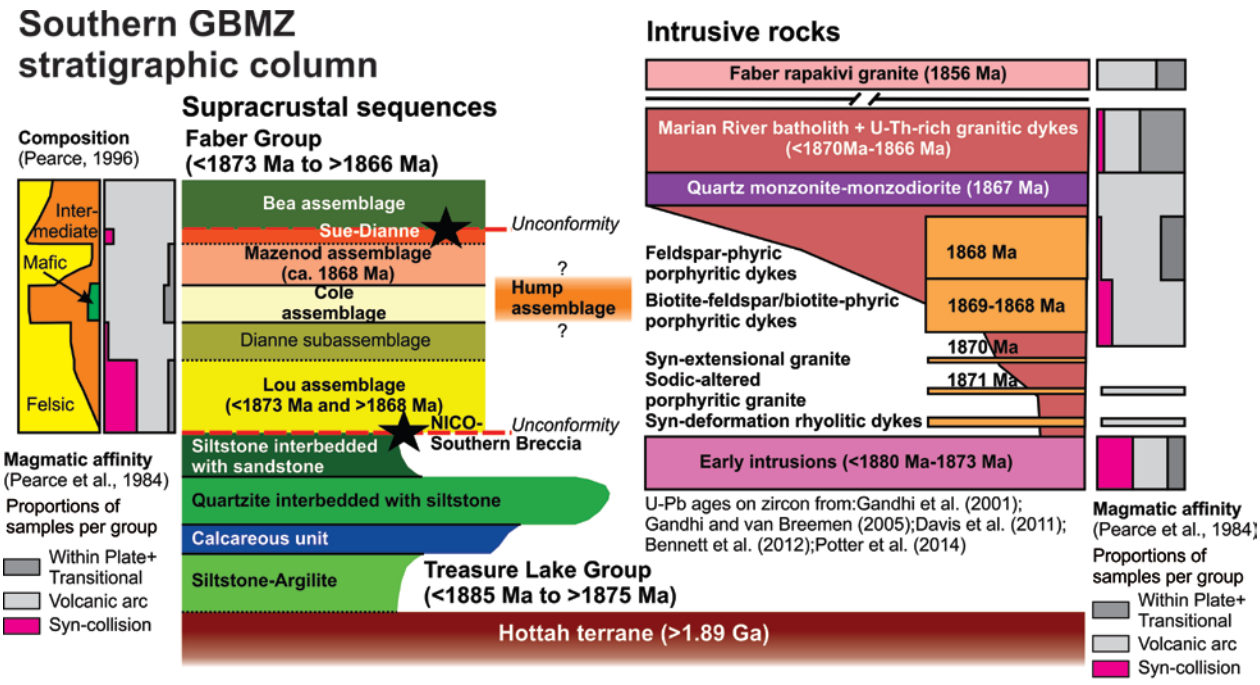

Figure 2-2 Stratigraphic column of the supracrustal sequences and intrusive events in the southern GBMZ

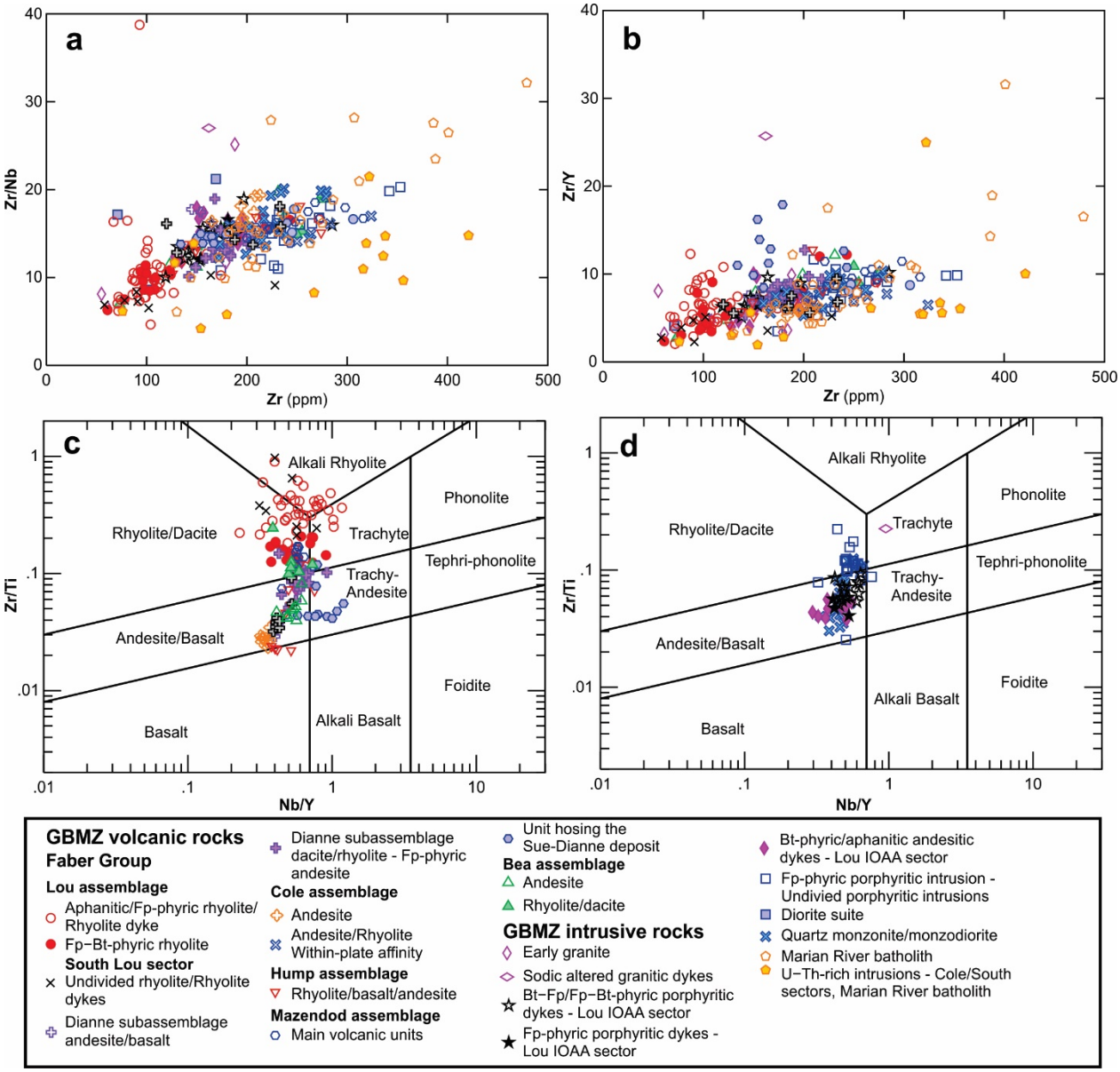

Figure 2-3 Bivariate diagrams of immobile elements and Pearce (1996a) discrimination diagram for volcanic and intrusive rocks

(a) Zr/Nb vs Zr; (b) Zr/Y vs Zr; (c) Pearce (1996a) Zr/Ti vs Nb/Y discrimination diagram for the southern GBMZ volcanic rocks; (d) Pearce (1996a) Zr/Ti vs Nb/Y discrimination diagram for the southern GBMZ intrusive rocks.

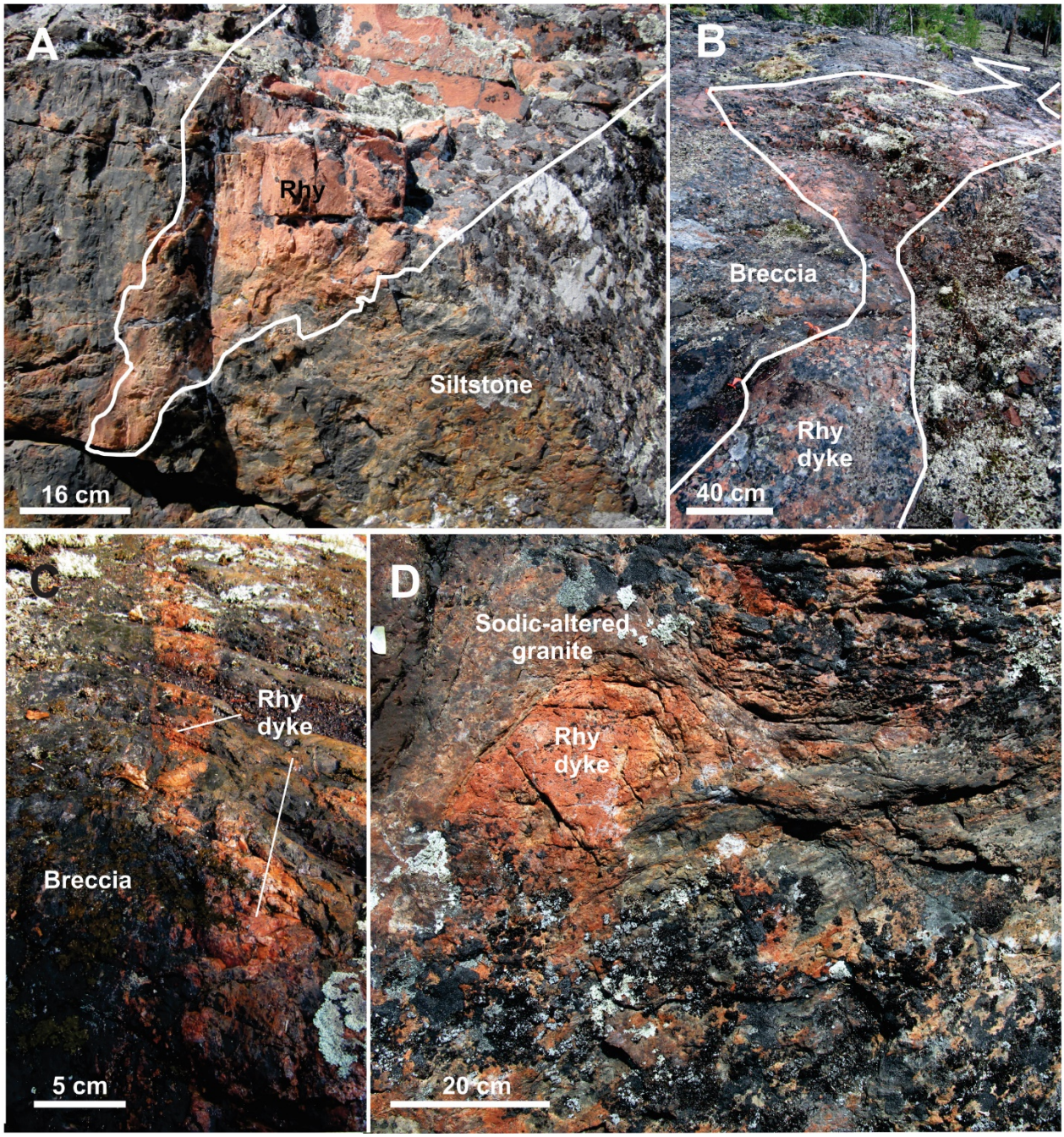

Figure 2-4 Photographs of typical rock types and relative timing relationships between intrusive rocks and tectono-hydrothermal events in the southern GBMZ

(a) Photograph of the sharp and unconformable contact between the Faber and Treasure Lake groups. The rhyolite filling the crack in the unconformity is slightly tilted to the SW (10CQA-1241); (b) Syn-deformation rhyolite dike emplaced in the Southern deformation corridor delimited by the white line on the photograph (10CQA-1242); (c) Partially fragmented rhyolite dike in the tectono-hydrothermal breccia of the Southern deformation corridor (10CQA-1242); (d) Rhyolite dike enclave in the sodic-altered porphyritic granite dike emplaced in the Southern deformation corridor (10CQA-1242);

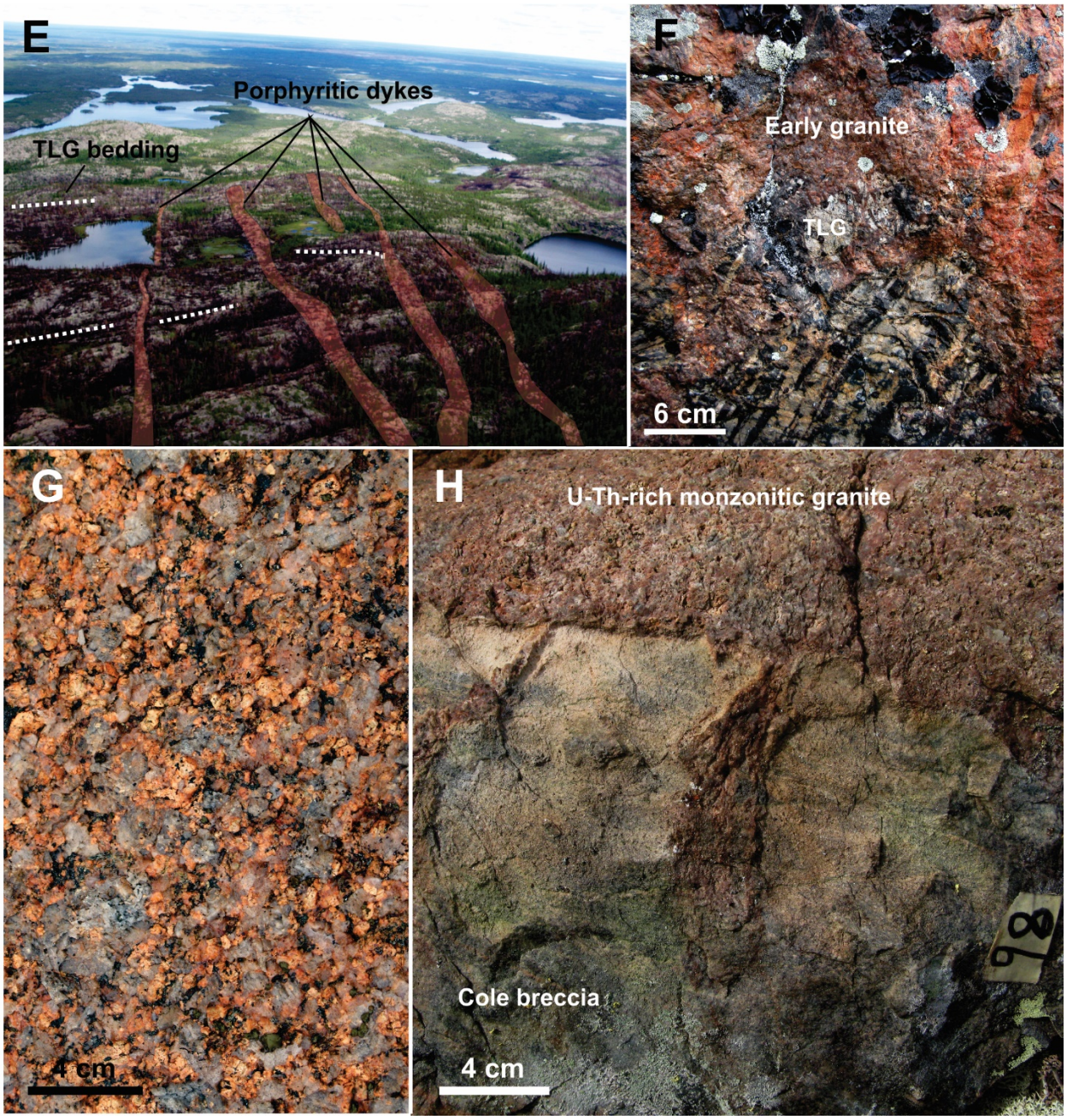

Fig. 2-4 suite – (e) Color-enhanced porphyritic dike swarm (feldspar–biotite-phyric and biotite–feldspar-phyric porphyritic dikes) cutting at high angle the TLG sedimentary rock bedding (southeastern Lou IOAA sector); (f) Partially assimilated TLG siltstone in an intrusion of the early granite suite south of the Lou IOAA sector (10CQA-1620); (g) granite of the Marian River batholith dated at 1866 Ma without any evidence of IOAA alteration (09CQA-1011); (h) Uranium–thorium-rich monzonitic dike cutting IOAA alteration in the Cole Breccia

Rhy = rhyolite

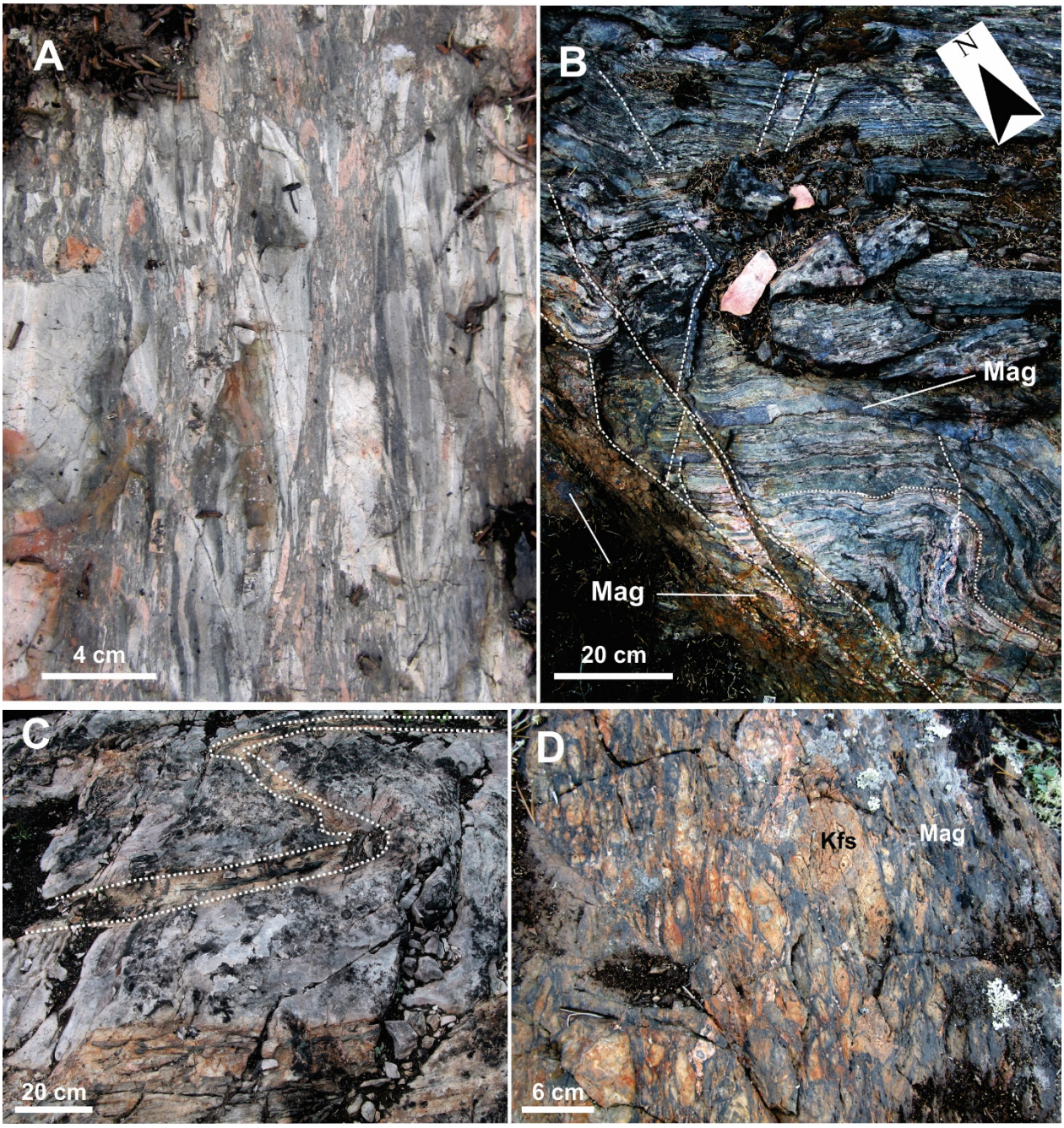

Figure 2-5 Photographs of the main deformation zones in the Western section

(a) Foliated tectono-hydrothermal breccia with many albitized TLG siltstone and potassic-altered rhyolite dike fragments formed in a WNW-oriented deformation zone (10CQA-1644); (b) Peanut deformation corridor where WNW-oriented deformation, associated parasitic folding, and accompanying concordant magnetite and amphibole-magnetite alteration are cut but a N-oriented fault zone filled by magnetite veins (11PUA-028); (c) Parasitic folding in the Treasure Lake Group quartz arenite unit with siltstone beds. Strain is partitioned in the siltstone (tectonic foliations); (d) Syn-deformation magnetite alteration in the Southern deformation corridor. This magnetite alteration overprints the rhyolite dike and the sodic-altered granite dike (10CQA-1615);

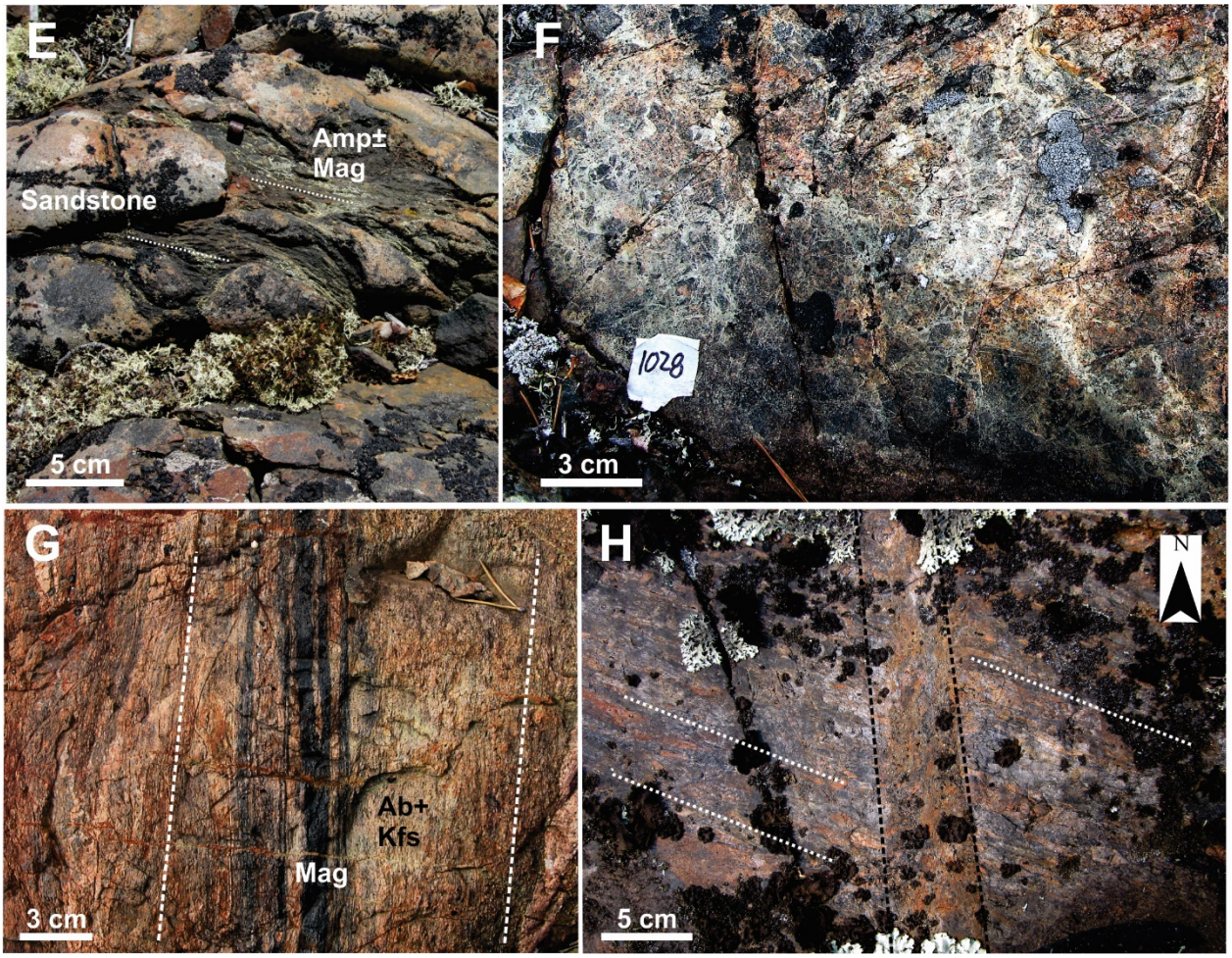

Fig. 2-5 suite – (e) Tectono-hydrothermal brecciation at the unconformity between the Faber Group and the TLG north of the NICO deposit (10CQA-1236). The hydrothermal cement predominantly composed of amphibole is foliated; (f) Tectono-hydrothermal brecciation in the Marian River deformation corridor formed in an andesite of the Dianne subassemblage; (g) Intense deformation and tectono-hydrothermal brecciation in the Marian River deformation zone east of Sue-Dianne formed after the metasedimentary rocks of the TLG (10CQA-1012); (h) N-oriented fault zone cutting the WNW-oriented fabric in the Southern deformation zone (10CQA-1619).

Mineral abbreviations after Whitney and Evan (2010).

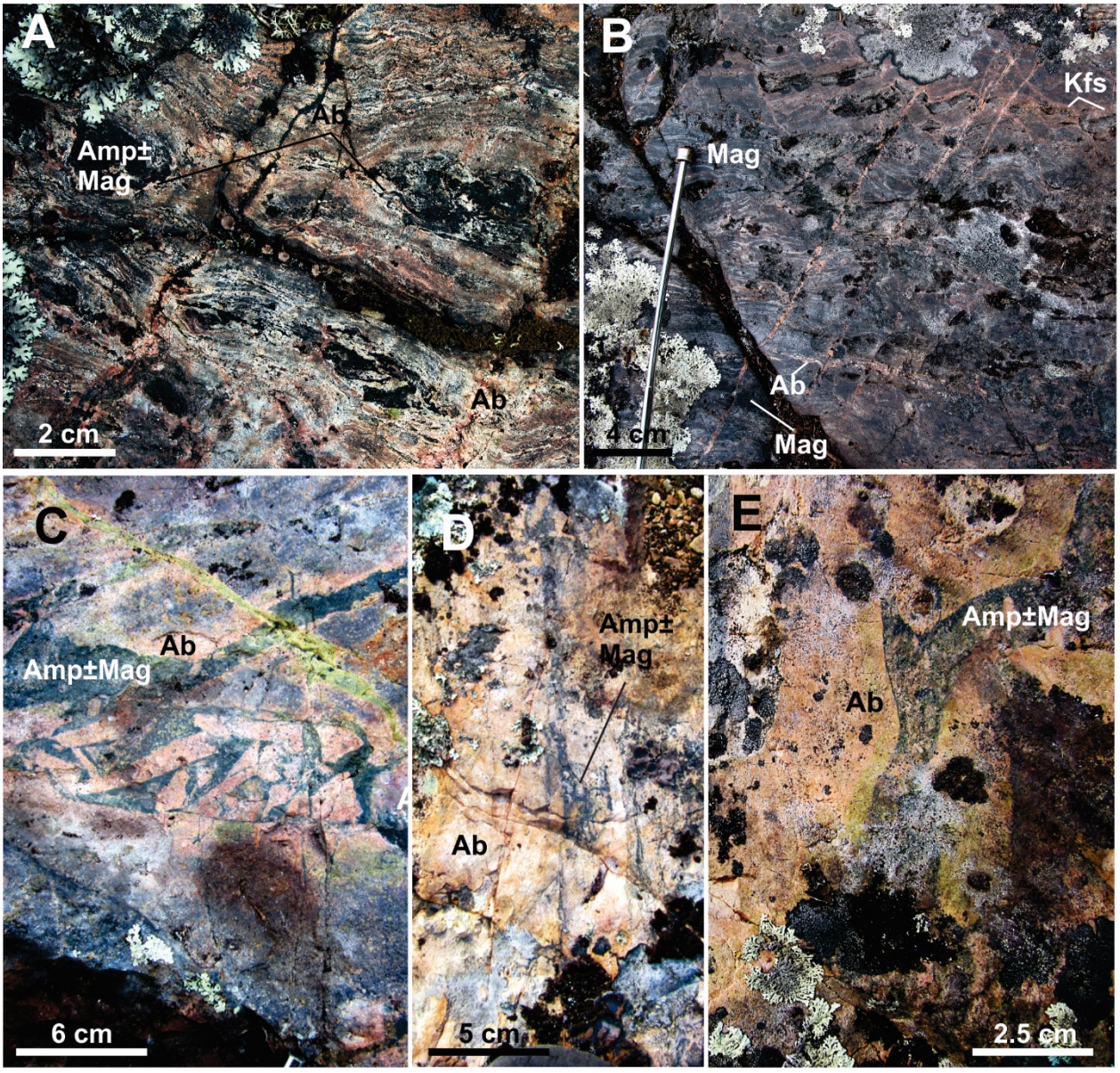

Figure 2-6 Photographs and microphotographs of the main deformation and breccia zones of the Eastern section

(a) Concordant deformation zone in the Hump showing where extensional jogs in the deformation zones are filled by coarse-grained amphibole±magnetite and albite. The initial fabric is slightly crenulated and cut by amphibole veins (09CQA-1020); (b) Concordant and early magnetite alteration of the TLG in the Hump showing cut by high-angle fault with a right-lateral movement and associated with a potassic alteration overprint (09CQA-0041); (c) Cole assemblage porphyritic andesite overprinted by sodic alteration that is incipiently brecciated and filled by a calcic-iron alteration cement (09CQA-1070); (d) Intense sodic alteration incipiently brecciated by calcic-iron alteration in the external margin of the Cole Breccia (10CQA-0550); (e) Intensification of the sodic alteration brecciation by calcic-iron alteration in the external margin of the Cole Breccia (10CQA-550);.

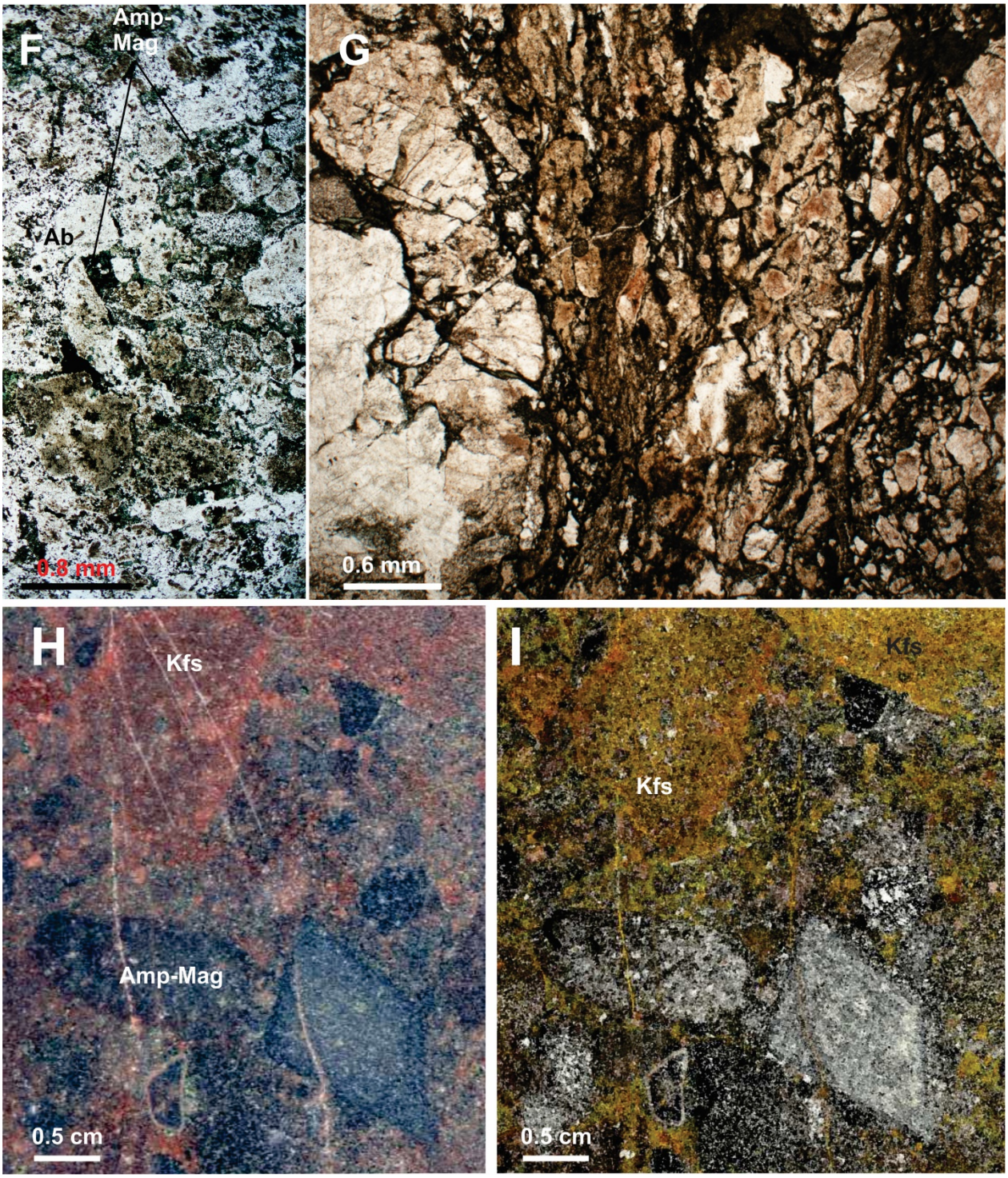

Fig. 2-6 suite – (f) Microphotograph taken in the marginal zone of the Cole Breccia showing the progressive hydrothermal fragmentation of the albitite (09CQA-1075, Microphotograph courtesy of Anthony De Toni); (g) Microphotograph illustrating the syn-deformation fragmentation in the Cole Breccia marginal zone showing the intricate relationships between deformation and brecciation in the Cole hydrothermal system (10CQA-0546); (h) Potassic alteration overprint in the Cole Breccia (09CQA-0102); (i) Stained slab to better illustrate the extent of the pervasive potassic alteration.

Mineral abbreviations after Whitney and Evans (2010).

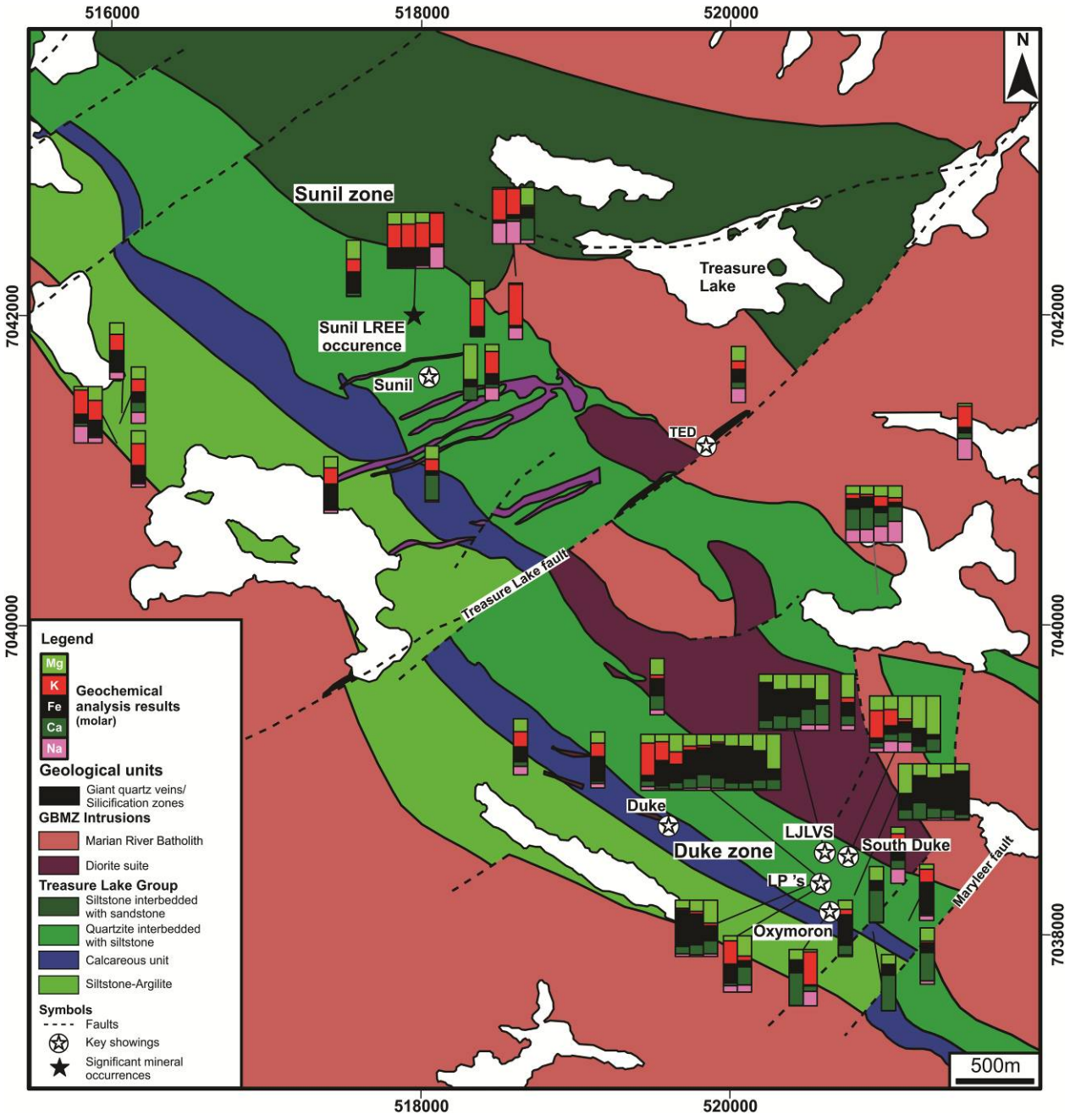

Figure 2-7 Geological map of the South Lou sector and distribution of hydrothermal alteration, mineral occurrences and showings in the Duke and Sunil zones

The geology is after Gandhi et al. (2014) and the UTM coordinates are in NAD83 for zone 11.

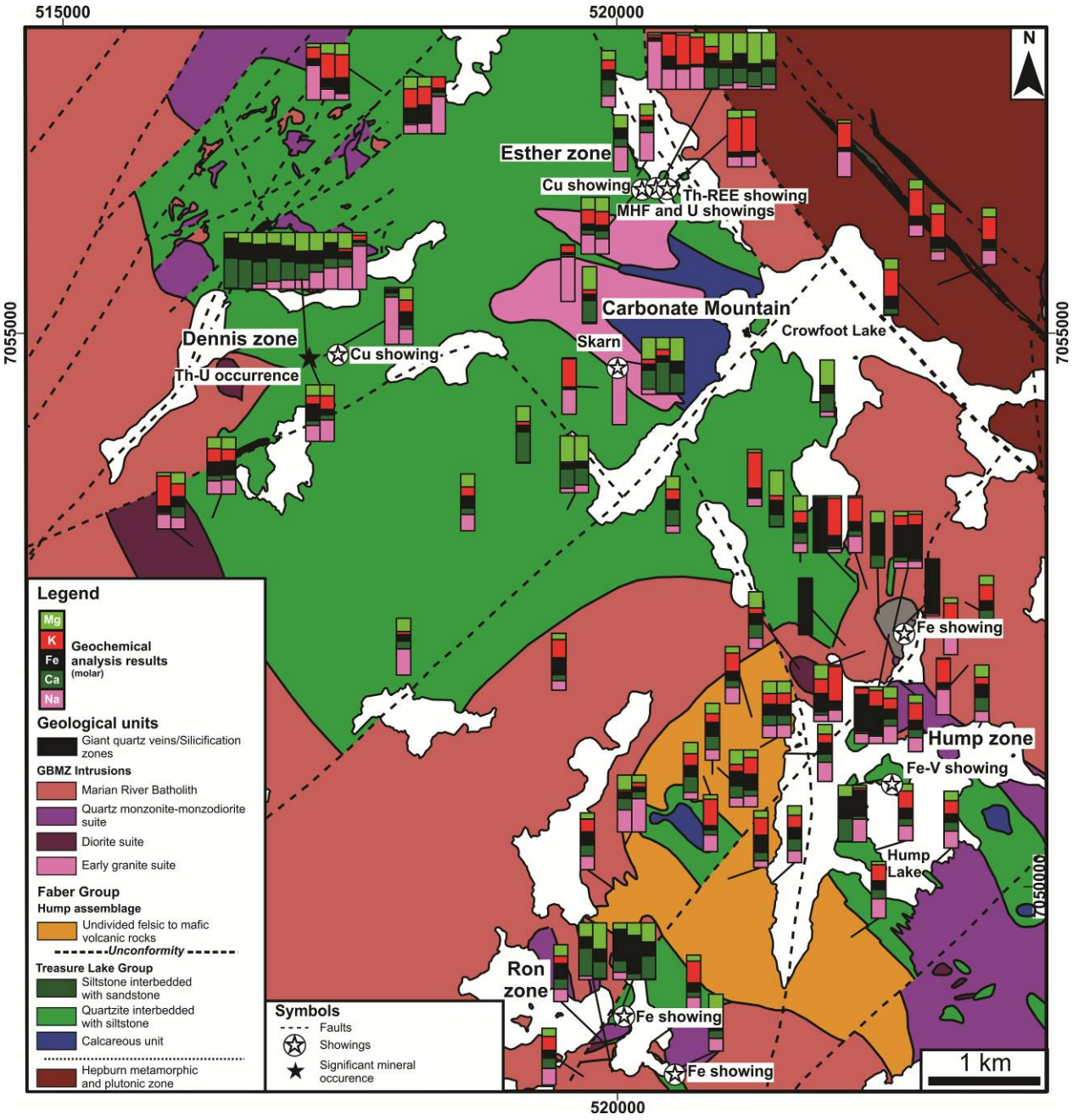

Figure 2-8 Geological map of the Eastern Treasure Lake sector and distribution of hydrothermal alteration, mineral occurrences and showings in the Carbonate Mountain, Dennis, Esther, Hump and Ron zones

The geology is after Gandhi et al. (2014) and the UTM coordinates are in NAD83 for zone 11.

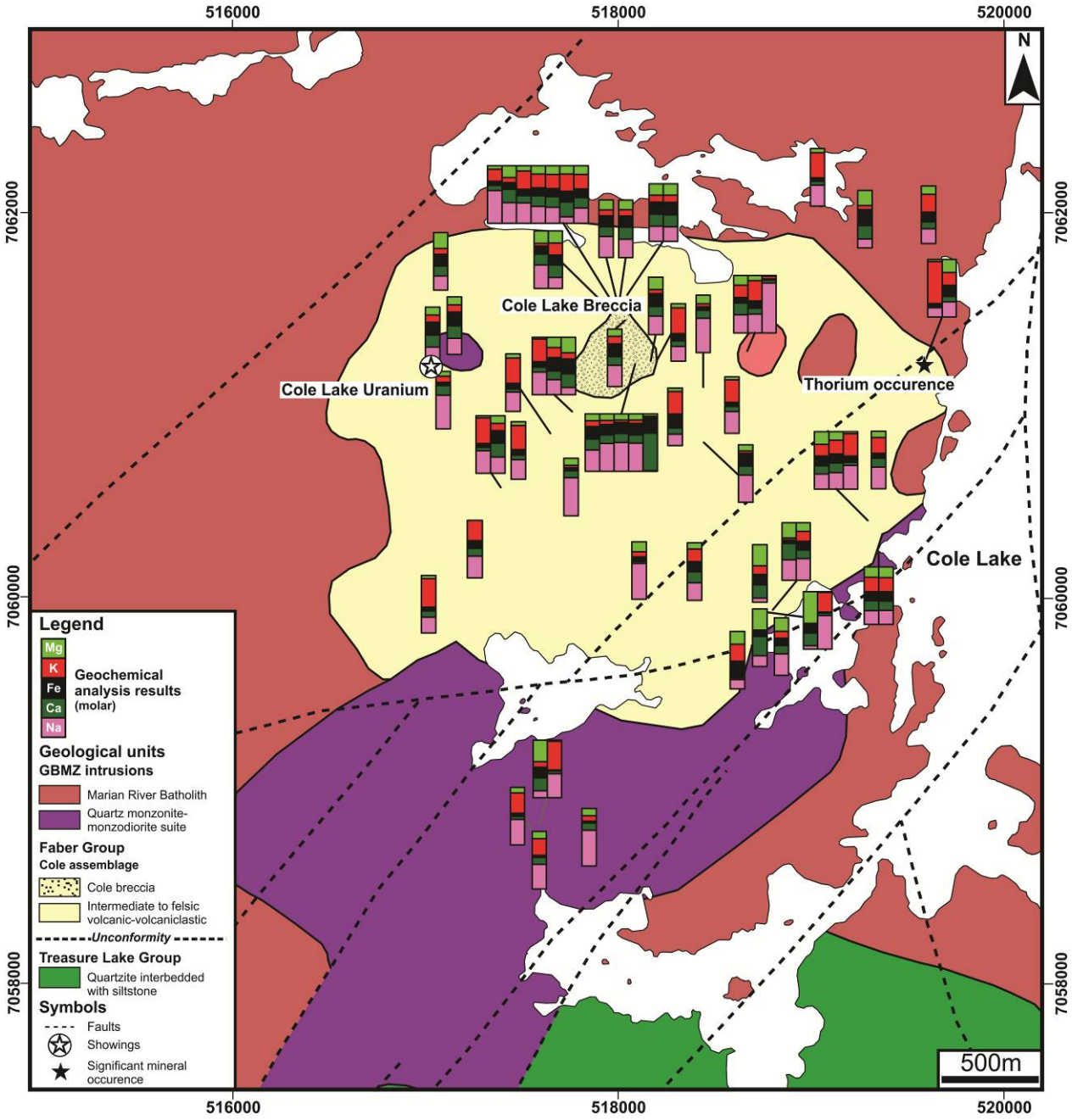

Figure 2-9 Geological map of the Cole sector and distribution of hydrothermal alteration, mineral occurrences and showings

The geology is after Gandhi et al. (2014) and the UTM coordinates are in NAD83 for zone 11.

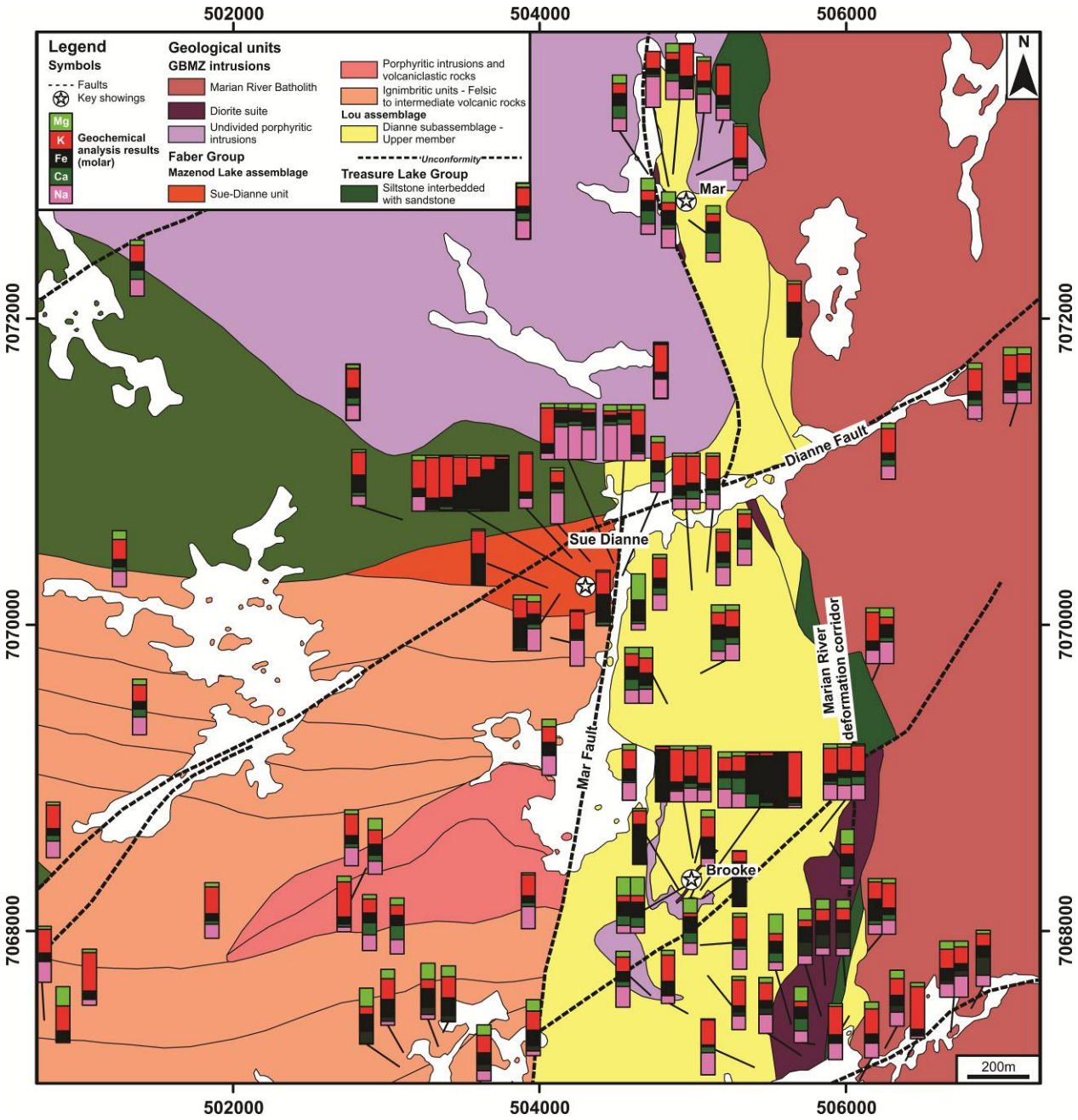

Figure 2-10 Geological map of the Mazenod sector and distribution of hydrothermal alteration, mineral occurrences and showings in the Brooke/Sue-Dianne zones

The geology is after Gandhi et al. (2014) and the UTM coordinates are in NAD83 for zone 11.

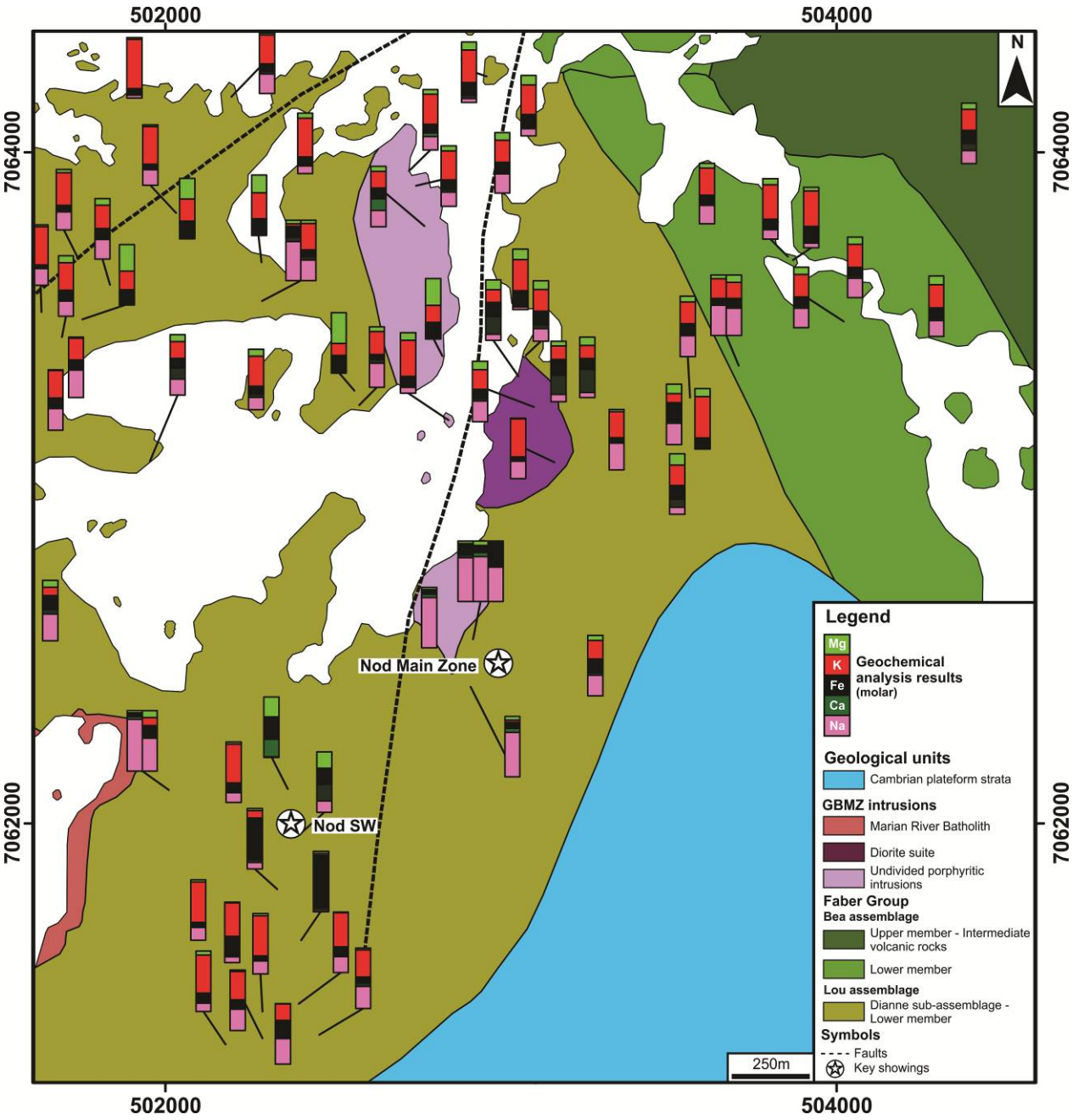

Figure 2-11 Geological map of the Mazenod sector and distribution of hydrothermal alteration, mineral occurrences and showings in the Nod zone

The geology is after Gandhi et al. (2014) and the UTM coordinates are in NAD83 for zone 11.

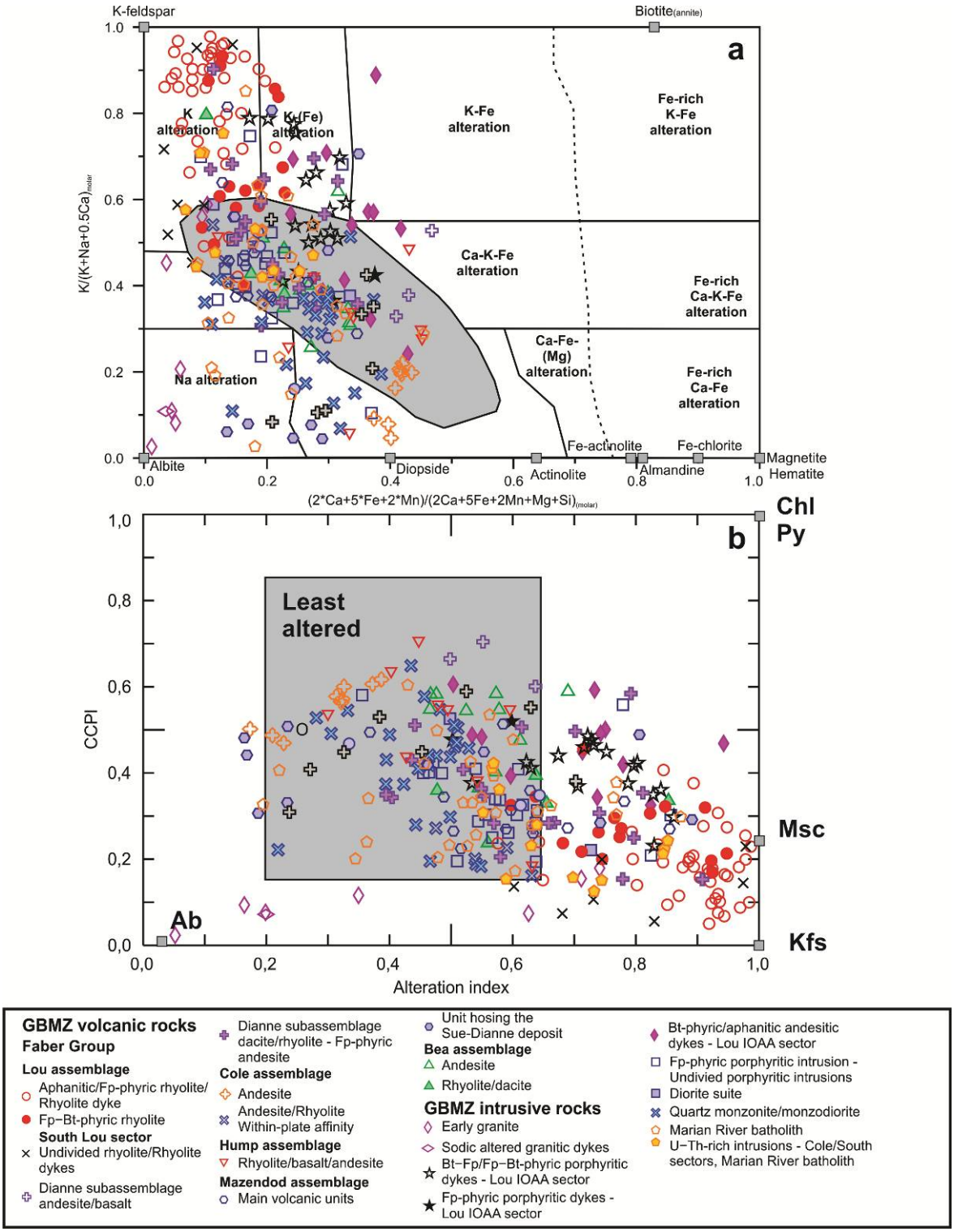

Figure 2-12 Southern GBMZ intrusive and volcanic rocks plotted on alteration discrimination diagrams

(a) Volcanic and intrusive rocks of the southern GBMZ plotted on the IOCG alteration discrimination diagram of chapitre 5; (b) Volcanic and intrusive rocks of the southern GBMZ plotted on the alteration box-plot diagram of Large et al. (2001).
AI = Ishikawa alteration index $(K_2O+MgO)/(K_2O+MgO+Na_2O+CaO)$ (Ishikawa et al., 1976).
CCPI = Chlorite–carbonate–pyrite alteration index $(FeO+MgO)/(FeO+MgO+K_2O+Na_2O)$.

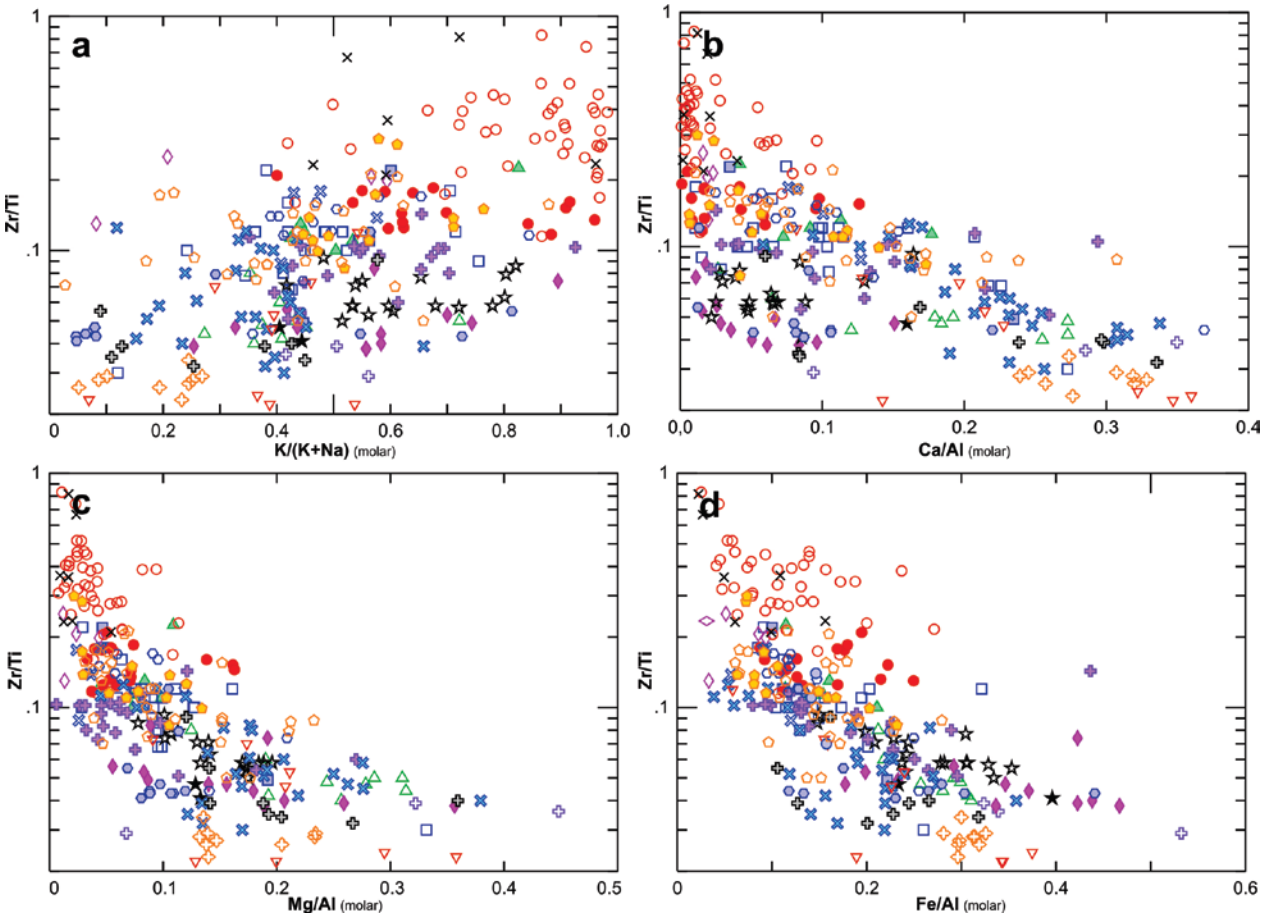

Figure 2-13 Bivariate diagrams to illustrate major elements variations in the southern GBMZ intrusive and volcanic rocks

(a) Zr/Ti vs K/(K+Na)(molar); (b) Zr/Ti vs (Ca/Al)(molar) diagram; (c) Zr/Ti vs (Mg/Al)(molar); (d) Zr/Ti vs (Fe/Al)(molar).

Symbols are the same than in Fig. 2-12.

Three samples of the early granite suite with Zr/Ti > 1 have not been included to improve the clarity of the diagrams.

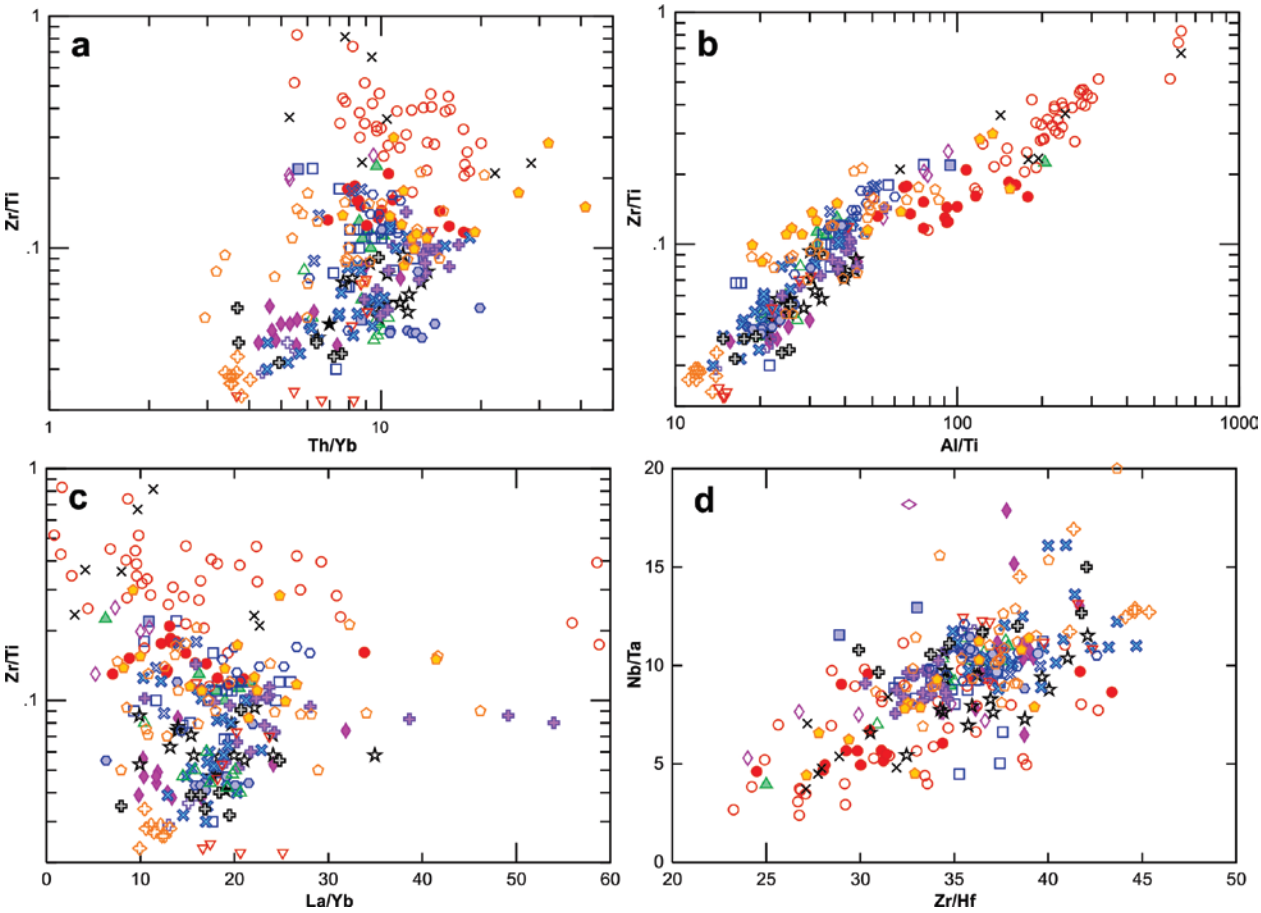

Figure 2-14 Bivariate diagrams to illustrate HFSE, Al and Ti variations in the southern GBMZ intrusive and volcanic rocks

(a) Zr/Ti vs Th/Yb; (b) Zr/Ti vs Al/Ti; (c) Zr/Ti vs La/Yb; (d) Nb/Ta vs Zr/Hf. Symbols are the same than in Fig. 2-12.

Three samples of the early granite suite with Zr/Ti > 1 have not been included to improve the clarity of the diagrams.

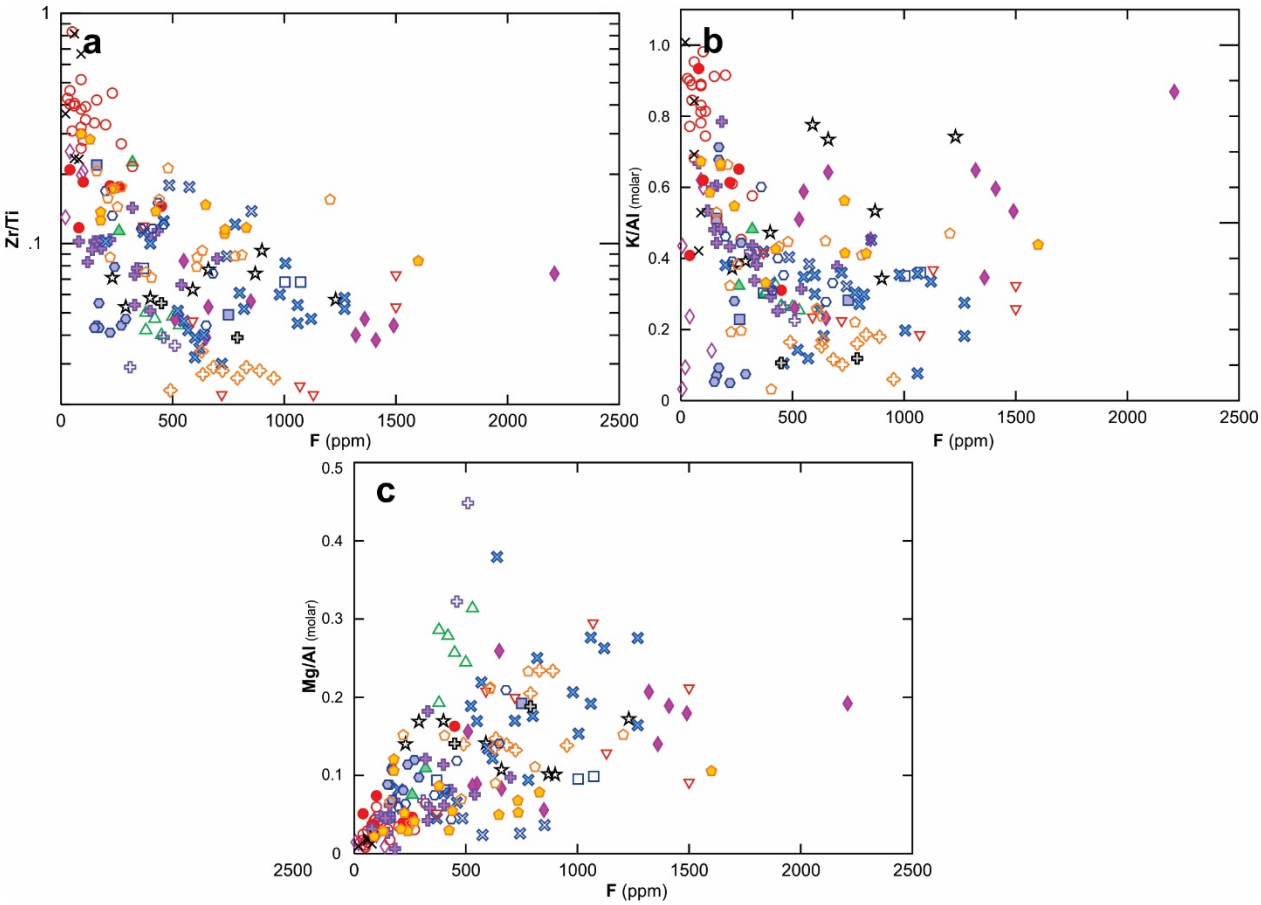

Figure 2-15 Fluorine variations in the southern GBMZ intrusive and volcanic rocks

(a) Zr/Ti vs F; (b) (K/Al)(molar) vs F; (c) (Mg/Al)(molar) vs F. Legend of symbols in Fig. 2-12.

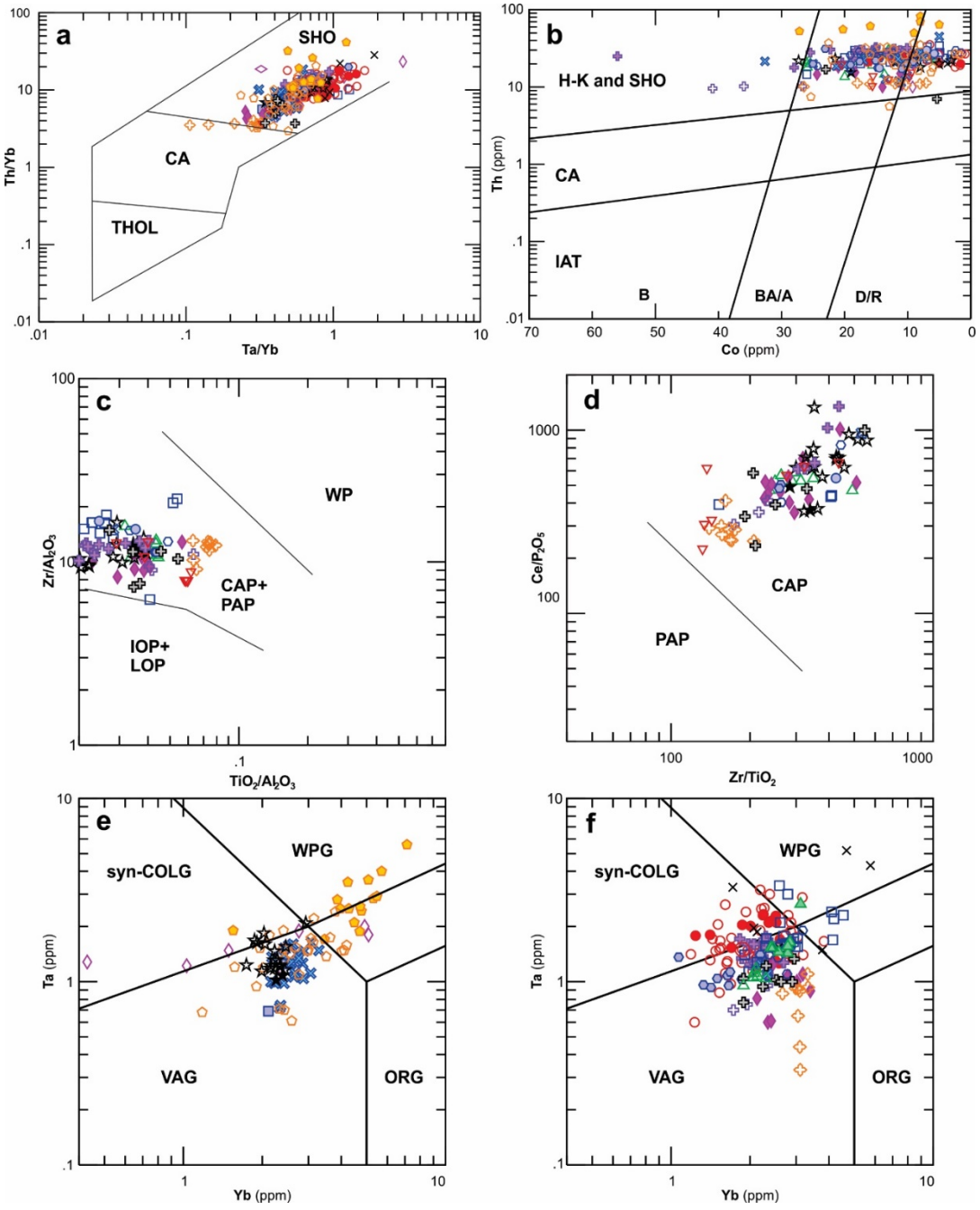

Figure 2-16 Samples of the southern GBMZ intrusive and volcanic rocks plotted on tectonic environments discrimination diagrams

(a) Volcanic and intrusive rocks of the southern GBMZ plotted on Pearce (1982) Th/Yb vs Ta/Yb diagram for the identification of the magmatic series; (b) Volcanic and intrusive rocks of the southern GBMZ plotted on the Hastie et al. (2007) modified version of the Peccerillo and Taylor (1976) diagram for the identification of the magmatic series using Th vs Co; (c) Andesitic and basaltic volcanic rocks of the southern GBMZ plotted on the Mueller et al. (1992) Zr/Al2O3 vs TiO2/Al2O3 tectonic setting discrimination diagram for rocks of the shoshonitic magmatic series; (d) Andesitic and basaltic volcanic rocks of the southern GBMZ plotted on the Mueller et al. (1992) Ce/P2O5 vs Zr/TiO2 tectonic setting discrimination diagram; (e) Intrusive rocks of the southern GBMZ plotted on the Pearce et al. (1984) Yb vs Ta magma source discrimination diagram; (f) Volcanic rocks of the southern GBMZ plotted on the Pearce et al. (1984) Yb vs Ta magma source discrimination diagram.

Symbols are the same than in Fig. 2-12.

CHAPITRE 3 : LINKAGES AMONGST IOCG, IOA AND AFFILIATED DEPOSITS: FROM THE GREAT BEAR MAGMATIC ZONE RECORDS TO AN IRON OXIDE ALKALI-ALTERATION-FACIES ORE DEPOSIT MODEL

Sur les relations entre les gîtes IOCG, IOA et affilié – De la Zone magmatique du Grand lac de l'Ours à un modèle faciès d'altération établissant les liens entre les gîtes formés dans un système IOAA

[1]Corriveau, L., [2]Montreuil, J.-F., [3]Potter, E.G.

[1]Ressources naturelles Canada, Commission Géologique du Canada, division Québec

[2]Institut National de la Recherche Scientifique – Eau-Terre-Environnement

[3]Ressources naturelles Canada, Commission Géologique du Canada, division Ottawa

Soumis à «*Economic Geology*»

Abstract: The Great Bear magmatic zone (Canada) constitutes one of the case examples of polymetallic hydrothermal iron oxide and alkali-alteration (IOAA) systems used in 1992 by Hitzman and colleagues to elaborate the classic zoning model for what was to become the iron oxide copper–gold (IOCG) deposit type. In this paper, we synthesise the alteration and breccias attributes of the prograde development of iron oxide and alkali-alteration facies that link the IOCG, iron oxide–apatite, albitite-hosted uranium and polymetallic skarn mineralisation of the Great Bear magmatic zones from the deeper roots of their host mineral systems to their paleosurface epithermal caps. Albitite corridors several kilometres in length form early and record the products of reaction between highly saline fluids and precursors at depth and preferentially along fault zones. Pervasive and intense leaching of precursor rocks recharges fluids in metals as sodium is discharged and leaves behind porous albitites which are mechanically susceptible to brecciation unless they are pervasively recrystallized to medium-to-coarse grain. Outgoing fluids rise along more focussed zones and react with precursors. Calcium, iron and specialised metals (vanadium, heavy rare-earth) are preferentially discharged to form high-temperature calcic–iron parageneses and iron oxide–apatite deposits. In the process, the outgoing fluids are recharged in sodium, potassium, and base and precious metals. As temperatures decline, fluid-rock reaction leads to high-temperature potassic–iron alteration parageneses with concomitant brecciation and precipitation of sulfides to form magnetite-group IOCG deposits. Fluids interaction with precursors towards surface leads to the development of lower temperature hydrolytic potassic–iron alteration parageneses, their breccias and their hematite-group IOCG deposits. Fine-grained and porous albitites uplifted within the potassic–iron alteration stability fields of the evolving regional-scale systems become preferential host to albitite-hosted uranium mineralisation. As all alteration facies and associated mineralisation are either undersaturated or barely saturated in silica, fluids evolving from and rising above IOAA systems leads to silicified epithermal caps including acid alteration and associated mineralisation. Diverse permutations of these facies can arise from differential uplift and cyclical build-up of alteration. In all cases, inferences can be drawn on the evolution of IOAA systems by mapping their metasomatic facies. Such empirical interpretation provides efficient vectors to potential undiscovered mineral resources within the iron oxide–apatite, IOCG, skarns and albitite-hosted uranium deposit continuum. Framed through the IOAA-facies model, commonly disparate mineral showings as well as prospects and deposits are shown to play a pivotal role to prognosticate the mineral potential of each sector of an IOAA system both at district to deposit scale, as well as providing significant insights into the composition of the evolving fluids.

Résumé: Les systèmes hydrothermaux polymétalliques à oxydes de fer et altération en éléments alcalins de la zone magmatique du Grand lac de l'Ours (Canada) ont été parmi les trois exemples utilisés pour définir en 1992 ce qui allait devenir les gîtes à oxyde de fer cuivre–or (IOCG). Ces systèmes minéralisés sont demeurés à la verticale, ou ont été soit basculés, soit légèrement plissés, ou encore soulevés et exhumés différentiellement ou repris par des failles en décrochement. Ils ont échappé à du métamorphisme orogénique ultérieur et leurs affleurements glaciaires polis, presque continus et avec altération de surface minime exposent en 3D l'évolution des faciès d'altération hydrothermale des systèmes à oxydes de fer et altération en éléments alcalins et leurs continua extraordinaire en termes de types de gîtes formés. Cet article documente comment les altérations à oxyde de fer et éléments alcalins forment des ensembles paragénétiques distincts et systémiques qui transforment intensément minéralogiquement et chimiquement tous les types de roches précurseurs là où l'altération est intense et généralisée. Chaque ensemble de paragenèses minérales correspond à un faciès métasomatique distinct avec une signature géochimique et des associations métallifères diagnostiques. De la racine des systèmes à leurs toits épithermaux encore préservés, en s'éloignant des sources de chaleur, et à mesure que s'abaisse les températures (et le Ph), les faciès d'altération évoluent de 1) sodique, 2) calcique–fer à haute température, 3) potassique–fer à haute température, 4) transitionnelle potassique (felsites bréchifiées) ou à skarns potassiques, et 5) hydrolytique à potassique–fer de plus faible température. Cette séquence prograde et les diverses permutations d'altération liées à leur transitions, juxtapositions, superpositions, télescopages, cyclicités et régressions fournissent des vecteurs d'exploration vers des gîtes à oxyde de fer–apatite (IOA), gîtes à métaux spécialisés et oxydes de fer, gîtes IOCG des groupes à magnétite, magnétite–hématite et hématite, certains gîtes d'uranium encaissés dans des albitites et certains gîtes de skarns. Disparates et communément mineurs en apparence, les indices minéralisés de la zone magmatique du Grand lac de l'Ours procurent une assise solide pour un nouveau cycle d'exploration où les faciès d'altération jouent un rôle clé pour pronostiquer les types de gîtes potentiels et la nature des fluides pré et post altération pour chaque secteur exploré tant à l'échelle des districts que des gîtes.

3.1 Introduction

The extraordinary range of iron oxide copper–gold (IOCG) and affiliated deposits have recently been re-examined under the umbrella of the iron oxide alkali-altered (IOAA) deposit type as defined by Porter (2010), a term we adopt for the regional-scale metasomatic alteration, breccia and ore systems that include IOCG deposits and the penecontemporaneous multiple metal deposits that occur within their districts. IOCG deposits *sensu stricto* are the polymetallic, base- and precious-metal endowed deposits with economic copper (± gold), low-titanium iron oxide gangue and consanguineous alkali alteration (Williams et al., 2005). They are classified into magnetite-, magnetite–hematite- and hematite-group IOCG deposits to highlight distinctiveness in geological and geophysical attributes relevant to mineral exploration (Williams, 2010a). Mineral districts where precursors are anomalously high in uranium contents can host uranium-rich IOCG deposits (Hitzman and Valenta, 2005). Other deposit types documented within IOAA districts include iron oxide±apatite deposits, alkaline intrusion-associated hydrothermal iron oxide deposits, some skarns and some albitite-hosted uranium deposits (Williams et al., 2005; Corriveau, 2007; Groves et al., 2010; Porter, 2010; Williams, 2010a, b; Barton, 2014; chapitre 6).

Alteration footprints hosting these deposits have been characterised at kilometre scale through mapping and drilling around known deposits (Marschik and Fontboté, 2001a; Mark et al., 2006; Monteiro et al., 2008a). The evolution of their alteration types is depicted from depth to surface through a series of zoning models modified from the original model of Hitzman et al. (1992) (Barton and Johnson, 1996; Williams et al., 2005, 2010; Xavier et al., 2010; Richards and Mumin, 2013; Barton, 2014). In most IOCG and iron oxide–apatite (IOA) districts, the linkage between the family of deposits formed in IOAA systems remains difficult to constrain because of limited field exposures, regional-scale sedimentary covers or distributions of drill cores largely focussed on single deposits. In addition, orogenic reworking is common and may further complicate pattern recognition at the scale of an IOCG district. Collectively, these issues conceal possible relationships among the vast range of deposit types observed in IOCG districts and the diversified metal associations observed (Hitzman, 2000; Corriveau, 2007; Corriveau and Mumin, 2010; Porter, 2010; Barton, 2014). This can lead to the proposition that iron oxide±apatite and IOCG deposits are not genetically related and do not form penecontemporaneously due to secular variations and distinct tectonic settings (Groves et al., 2010).

The Great Bear magmatic zone (GBMZ; Fig. 3-1) from the North-west Canadian Shield escaped pervasive orogenic reworking and its former Proterozoic and Phanerozoic sedimentary covers

have been eroded likely since Mesozoic time except at its western and north-western margins where the GBMZ remains covered (Aspler et al., 2003). In addition, the broad folding of the GBMZ at amplitudes of about 10 km in the Proterozoic and the Quaternary glaciation have resulted in semi-continuous exposures of IOAA systems in three dimensions from their metamorphic basement roots to their non-metamorphosed and non-penetratively deformed sub-volcanic intrusions, volcanic rocks and paleosurface epithermal caps (Hildebrand, 1986; Gandhi, 1994; Mumin et al., 2007, 2010, 2014).

The Sue-Dianne magnetite–hematite group IOCG deposit discovered in the 1970s (Gandhi, 1989), and the iron oxide±apatite mineralisation and magnetite-hosted prospects of the Port Radium and Camsell River districts studied by Hildebrand (1986) have led Hitzman et al. (1992) to base their classical zoning model for iron oxide (Cu–U–Au) deposits on the GBMZ in addition to Olympic Dam (Australia) and Kiruna (Sweden) among others. Since 1992, several geoscience mapping and research programs have re-examined the IOAA systems of the GBMZ. This paper summarises the alteration and breccia footprints and the metal associations of their mineralization to further elucidate the linkages among deposit types within IOAA systems. The IOAA metasomatic rocks that host GBMZ IOA, IOCG and affiliated deposits and prospects were mapped using the facies approach and timing relationships were constrained through field relationships and U–Pb geochronology. Though discussing the regional geology and the deposit-scale metasomatic processes in detail is beyond the scope of this paper, we summarise the various types and styles of alteration and their magmatic and tectonic triggers to reconcile the prograde, retrograde, telescoped and cyclical development of alteration, brecciation, mineralisation and metal association observed in the case examples presented. Comparison of GBMZ data with worldwide IOAA systems are integrated within a holistic IOAA-alteration facies model that refines the zoning model of Hitzman et al. (1992) and the alteration vector to deposit model of Corriveau et al. (2010b). The implication of the alteration zoning model for the detection of deeply buried resources are discussed using the Mag Hill sector of the Port Radium–Echo Bay district (Mumin et al., 2010) and the NICO deposit and Southern Breccia prospect of the Lou IOAA system (Hayward, 2013; Craven et al., 2013; chapitre 6; Fig. 3-1)

3.2 Great Bear magmatic zone IOAA systems

3.2.1 Geological environments

The GBMZ is interpreted as an Andean-type continental magmatic arc formed at the end of a short-lived orogeny (1.89–1.88 Ga) during which the accretion of the composite Hottah terrane to the western margin of the Archaean Slave craton led to the development of the Wopmay Orogen (Hildebrand et al., 2010b and citations therein). The GBMZ is delimited by the surface exposure of the Hottah terrane to the west and the Wopmay fault zone to the east (Fig. 3-1a). Crustal-scale fault zones and discontinuities, and lithospheric wedge that may have acted as fluid and magma pathways have been imaged by Spratt et al. (2009) and Craven et al. (2013). These available lithospheric models and those for the Gawler craton suggests that the lithospheric architecture of the GBMZ resembles the architecture of the Gawler craton. Basement rocks are characterised by the series of volcano-sedimentary basins of the Hottah terrane (Hildebrand, 2014; Hildebrand et al., 2014) with windows of its upper sedimentary basin (ca. 1.88 Ga Treasure Lake Group) outcropping within the central and southern GBMZ (Fig. 3-1a).

Treasure Lake Group sedimentary units are variably tilted; thinly- and medium-bedded wacke, siltstone, arenite and turbidite prevail (Gandhi and van Breemen, 2005). Among them is the largest carbonate unit exposed in the GBMZ (100 m thick and 10 km long; Gandhi et al., 2014). Treasure Lake Group rocks are metamorphosed to greenschist to lower-amphibolite facies; carbonate rocks are locally transformed into marble and skarn. Prior to the onset of ca. 1.87 Ga volcanism, the basement hosted several major stratigraphic and structural discontinuities, unconformities and chemically reactive units. In addition, the largely coeval volcano-sedimentary basins in the East Arm of Great Slave Lake at the south-eastern end of the GBMZ hosted evaporites (Stanworth and Badham, 1984; Pope et al., 2000; Potter et al., 2013c). Differential subsidence and uplift of basement and volcanic units are inferred based on detailed structural studies both in the northern and southern GBMZ (Enkin et al., 2012; chapitre 6; Mumin et al., 2014). These include potential exhumation of the Treasure Lake Group during GBMZ volcanism and tilting of the volcanic piles during the development of the IOAA systems.

Across the GBMZ IOAA systems, deposit-scale hydrothermal alteration zones contain combinations of ore and gangue minerals typical of IOCG, IOA and albitite-hosted uranium deposits (Table 3-1; Figs. 3-1b, 3-2; Gandhi et al., 1996; Goad et al., 2000b; Corriveau et al.,

2010b; Mumin et al., 2010; Acosta-Góngora et al., 2014; chapitre 6). They are coeval with the first pan-GBMZ volcanic event at 1.87 Ga (Hildebrand, 1986; Gandhi et al., 2001; Corriveau et al., 2007; Davis et al., 2011; Acosta-Góngora et al., 2015b) and hosted within volcanic centres formed close to sea level (Hildebrand and Bowring, 1984) in extensional basins (Mumin et al., 2014) that locally exhumed and further tilted basement rocks (Enkin et al., 2012). The volcanic centres and associated IOAA systems were largely distributed along two major north-south trending volcanic belts respectively at the eastern and western margin of the GBMZ prior to dissection by NE-trending transcurrent faults (Hayward and Corriveau, 2014). The 1.87 Ga andesitic to rhyolitic volcanic rocks and local basalts have been mapped in detail and their stratigraphy are well established (cf. LaBine, Dumas and Faber groups, Ellington Lake Complex, and Nadin succession; Hildebrand et al., 1987, 2010b, 2014; Reichenbach, 1991; Gandhi et al., 2001, 2014; Jackson, 2008; Hildebrand, 2011, 2014, in press; Jackson and Ootes, 2012; Jackson et al., 2013; Ootes et al., 2013, Potter et al., 2013b). Their distribution is summarised in Figure 3-1.

Pre-1.87 Ga large-scale volcanism comprises pillow lavas that attest to marine settings (Hildebrand et al., 2014). In contrast, 1.87 Ga volcanism was largely sub aerial and formed porphyritic to amygdaloidal volcanic flows and volcaniclastic units, both intracaldera and outflow sheets, as well as subordinate debris flow breccia and lacustrine-fluvial sediments (Hildebrand et al., 1987, 2010b; Gandhi et al., 2001). Composition is predominantly calc-alkaline (Hildebrand et al., 1987; Gandhi et al., 2001) to shoshonitic (Azar, 2010). The abundance of fragmental volcaniclastic rocks and carbonate units at the base of the LaBine Group and within the Dumas Group attest to the presence of highly permeable units and possible access to saline waters during IOAA metasomatism, respectively (Hildebrand and Bowring, 1988; Hildebrand, 2011; this work). In addition, fluid interaction with carbonate-rich precursors may have periodically liberated CO_2 during the evolution of the IOAA systems (Acosta-Góngora et al., 2014). The volcanic units were fed and intruded by syngenetic, sub-volcanic sheet-like intrusions, sills and laccoliths of mafic to felsic composition with a variety of phenocryst assemblages and compositions similar to those of their volcanic ejecta. All these units have widespread and intense iron oxide and alkali alteration footprints.

Emplacement of 1.87–1.86 Ga granodiorite to monzogranite batholiths followed deposition of the LaBine, Dumas and the lower sequences of the Faber Group and their IOAA metasomatism. This large-scale plutonism was accompanied by a large volume of intermediate-to-felsic ignimbrite, forming in the North the Sloan Group and in the South the uppermost assemblage of

Faber Group (Bea assemblage). Both volcanic assemblages rest above an unconformity with precursor volcanic and intrusive rocks (Hildebrand et al., 2010b; Gandhi et al., 2014). Dioritic to gabbroic intrusions are associated with this plutonic event and some of the granodiorite plutons include zones of magma mingling that record coevality with mafic magmas (Hildebrand et al. 2010b). Some dioritic bodies are dated as early as 1.878 Ga (Bennett et al., 2012). Their collective distribution as grouped in Figure 3-1 may locate preferential pathways for trans-crustal heat transfer which may have played a role in the development of the IOAA systems. Between 1.86 and 1.84 Ga volcanic activity stopped and gave way to extensive and predominantly A-type granitic plutonism to form the biotite-granite suite (Gandhi et al., 2001; Hildebrand et al., 2010b). Late-stage NW-oriented broad open folding contributed to provision of cross-sections of the GBMZ supracrustal rocks and IOAA systems, subsequently dissected by right-lateral NE-trending transcurrent faults (Hildebrand and Bowring, 1988; Hildebrand et al., 2010b).

3.2.2 Mineralisation types and distribution

Nearly 600 mineral occurrences have been described across the GBMZ (Fig. 3-1b–c; NWT Geoscience Office 2014; Bretzlaff et al. being submitted). They are subdivided into 1) showings where commodities are above NORMIN cut-off grade, 2) prospects where advanced exploration has included drilling, 3) deposits where mineral resources have been calculated and 4) past-producing mines (cf. NWT Geoscience Office, 2014). Most of the mineralisation occurs among ca. 1.87 Ga volcanic rocks or hypabyssal intrusions of the LaBine Group (e.g., Port Radium–Echo Bay, Camsell River and Grouard systems) and Faber Group (e.g., Sue-Dianne deposit), and the underlying Treasure Lake Group metasedimentary rocks (e.g., NICO deposit); some mineral occurrences and showings are hosted within Dumas Group or Hottah terrane units (Fig. 3-1; Table 3-1). Among the mineralisation zones, more than half consist of uranium, copper or polymetallic quartz-bearing veins (Bretzlaff et al., being submitted). These include the vast array of multiple metals and epithermal-style U–Ra–Ag, Fe ±Bi ±Au, Cu–Ag ±U, Mn–Co and Ag–Cu–U–Ni–Pb–Zn–Co showings, prospects, and past-producing mines of the Port Radium–Echo Bay and Camsell River districts (Badham, 1975; Mumin et al., 2010). Most polymetallic vein systems are hosted within extensive IOAA envelopes (Mumin et al., 2007, 2010; Corriveau et al., 2010a, b) for which we provide an overview of alteration types and metal associations (Fig. 3-2; Table 3-2).

Table 3-1 Summary of IOAA occurrences and alteration types in the GBMZ.

Sector	Showing/*Prospect*/**Deposit**	Metals	Prevailing precursor rock types	Model deposit-types	Alteration types					
					1	2	3	4	5	6
					Na	HT Ca–Fe	HT K–Fe	K-Sk	LT K–Fe	Si/Ph
Port-Radium–Echo Bay	*Port Radium*	**Fe,V,REE**,Zn,Pb,Ag,Cu,Co,	1.87 Ga LaBine Gp volcaniclastic and sedimentary (siliciclastic)	IOCG – Mag (± Hem)	x	X	x		x	X
	Camelback	Cu,Zn,Pb,Ag,U,V,Co,Au	1.87 Ga LaBine Gp andesite	Epithermal						X
	K2	**Cu**,**Ag**,Au,Co,As,Zn;**V–Fe**		IOCG to IOA at depth		X	X		x	X
	Mag Hill	**Fe,V**,REE		IOCG – Mag to Hem	X	X	x		x	
	Skinny Lake	Ag,Zn,Pb,Cu,Co,Fe		IOCG – Hem	x	x	x		X	
	Contact Lake End			IOA		X				
	Hook Island	Au,Ag,U,Cu		IOCG – Mag to Hem		X	X		X	
	E. Boundary			IOCG – Mag to Hem		X	X		X	
	Hoy Bay		1.87 Ga LaBine Gp volcaniclastic (1m of carbonate rocks of uncertain origin at Mile)	IOCG – Mag to Hem	X	x	X	x	x	
	Mile	Cu,Zn,Pb,Ag, Mo, W		IOCG – Mag to Hem, skarn	x	x	X	X	X	
Camsell River	**Terra, Norrex, Silver Bear**	**Ag,Cu,Fe,Pb, REE,Zn**,Bi,Co,Ni,U,Au,F	1.87 Ga LaBine Gp volcano-sedimentary host, sedimentary rocks largely siliciclastic	IOCG – Mag to Hem	X	X	X		X	X
	Grouard W Clutt, Bar,	Au,Ag,Cu,Pb		IOCG – Mag			X		X	
	Grouard N to NE		1.87 Ga LaBine Gp	IOCG		X			X	
	Grouard S (Ness, Hillside)	**Zn,Pb,Ag**,Bi,W,Cd,Cu	1.87 Ga LaBine Gp volcano-sedimentary host, includes carbonates with stromatolites	IOCG – Mag, skarn	X	X	x	X		
Central GBMZ	*Damp*	**Cu,U**,Co,Ni,Fe,Ag,Au,V,Bi,Zn,Mo,Pb	1.87 Ga rhyodacitic ignimbrite	IOCG – Hem breccia/Albitite-hosted U	X				X	
	Devil	Au,Ag,Co,Cu,As,Fe,Pb								
	Hottah East	**REE**	Hottah terrane, Zebulon Fm volcano-sedimentary, breccias	IOCG – Hem breccia		X	X		X	X
Wopmay fault	*Jackpot, McPhoo*	**U,Cu,Fe,REE**,Th,Co,Bi,Au,Mo	1.87 Ga porphyritic intrusions and Dumas Gp volcano-sedimentary rocks	IOA, IOCG – Mag	x		X			
	Ham	**U,Fe,Cu,REE**		IOCG – Mag		X	X			
	JLD	**U,Cu,Fe,REE**		IOCG		X				
	De Vries, NORI	U,Mo,Fe,Cu,Co,Ag,REE	Treasure Lake Gp siliciclastic rocks	IOCG – Mag	X	X	X		X	
Fab	Fab	**U,Cu,Fe,V,**F	Faber Gp porphyry intrusions	IOCG – Mag	X	X	X		x	X
Cole	Cole	**U,Fe**,Cu	Faber Gp porphyry intrusions + GBMZ intrusions	Albitite-hosted U IOCG – Mag ?	X	X	x			X
Mazenod	**Sue-Dianne**	**Cu,Ag,U**,**Au**,REE	Faber Gp rhyodacite/andesite	IOCG – Mag to Hem	X		X		X	X
	Nod	**Cu**,Ag,Fe,Au,U		IOA, IOCG – Mag	X	X	x			
	Brooke	**Cu,Ag,Fe,Bi,Mo, REE**		IOCG – Mag to Hem	X	X	X		X	

Duke	Duke	**Co,Bi,Au,Cu,Fe**, REE	Treasure Lake Gp siliciclastic + carbonate(?) rocks	IOCG – Mag to Hem		X	X	X	X	
	LP's	**W**,**Fe**,Cu		IOCG – Mag						
	LJLVS	**Co,Ni,U,Cu,Fe**		IOCG – Mag						
Eastern TLG	Ron	**Fe,REE**	Treasure Lake Gp siliciclastic + GBMZ intrusions	IOA	X	X				X
	Hump	**Fe,V,REE**,U,F, Cu,Fe,Ag	Treasure Lake Gp siliciclastic rocks	IOA	X	X	x		x	
	Esther	**U,Ta,Ag,Cu**	Treasure Lake Gp siliciclastic + GBMZ intrusions	Other	X	X	x		x	
	Carbonate Mountain	**Zn,Pb**,Cu	Treasure Lake Gp siliciclastic + carbonate rocks	IOA, skarn	X	X	x		x	
Lou	Southern Breccia	**U,Cu,Mo,Th,Au, Bi**	Treasure Lake Gp siliciclastic rocks	Albitite-hosted U, IOCG – Mag	X		X		X	
	NICO	**Co, Au, Bi, Cu, W, Fe**, As, Ag	Treasure Lake Gp siliciclastic + carbonate(?) rocks	IOCG – Mag	x	X	X		x	X

Alteration paragenetic sets: (1) Na = albite, albitite; (2) HT Ca–Fe = amphibole–magnetite ± apatite; (3) HT K–Fe = magnetite–biotite/K-feldspar±sulfides; (4) K-Sk = Skarn (clinopyroxene–K-feldspar±garnet±sulfides); (5) LT K–Fe = hematite–K-feldspar/sericite–carbonate–chlorite±sulfides; (6) Si = silicification, quartz veins and epidote-bearing alteration, Ph = phyllic alteration. REE= rare earth elements. X = intense to very intense alteration. x = mild to moderate intensity of alteration.

A few showings comprise Pb–Zn–Ag ±Cu skarns or porphyry-type mineralisation (Table 3-1; Neale et al., 1997; Knox, 1998). Approximately 25 showings and prospects consist of IOA (commonly described as Kiruna-type) mineralisation with or without rare-earth elements (REE), Th, W and V (Fig. 3-2a–b; Badham and Morton, 1976; Hildebrand, 1986; Mumin et al., 2007, 2010; Bretzlaff et al., being submitted). For example, the iron oxide alkali-altered waste rocks at the historic vein-type Echo Bay mine have up to 0.2 wt.% Yb and 2 wt.% Y (Ruzicka and Thorpe, 1995). The two known IOCG deposits and most of the other prospects are part of IOAA mineral systems. The Sue-Dianne deposit is a typical magnetite-to-hematite group IOCG deposit with chalcopyrite as the main ore mineral (Goad et al., 2000a). It contains National Instrument 43-101 compliant indicated resources of 8.4 Mt @ 0.8 % Cu, 0.07 g/t Au, 3.2 g/t Ag (Hennessey and Puritch, 2008). The NICO deposit is an atypical magnetite-group IOCG deposit in that cobaltian arsenopyrite prevails over chalcopyrite as the main ore mineral with cobaltite, bismuthinite, pyrite and pyrrhotite forming a 5 vol. % sulfide fraction in addition to native gold and bismuth. The ore is hosted within stratabound lenses of brecciated ironstones up to 70 m in thickness and followed for up to 1.3 km in length. National Instrument 43-101 compliant reserves comprise 33.08 Mt at 1.03 g/t Au, 0.11% Co, 0.14% Bi and 0.04% Cu (Burgess et al., 2014). The other prospects/showings of the GBMZ have attributes of magnetite-, magnetite-to-hematite and hematite-group IOCG deposits (cf. Williams, 2010a, b for classification attributes), skarns or

albitite-hosted uranium deposits (Table 3-1). Currently, the Port Radium–Echo Bay district including the Contact Lake belt (e.g., K2 to Skinny area) and the Lou system (from NICO to Burke) are most thoroughly mapped at regional scale (Mumin, 1997; Mumin et al., 2007, 2010, 2014, unpublished data; chapitre 6).

3.2.3 Geological attributes of the GBMZ that conform to geological environments hosting world-class IOCG deposits

The tectono-magmatic evolution and the metasomatic attributes of the GBMZ iron oxide alkali-altered systems satisfy the geological criteria of terranes with potential for world-class uranium-rich polymetallic IOCG deposits proposed by Skirrow (2010). Magmatism was voluminous, and led to repeated ascent and emplacement of mafic-to-felsic magmas of continental calc-alkaline, shoshonitic and I- to A-type affinities in the upper crust (Williams et al., 2005; Mumin et al., 2010; Ootes et al., 2013). U-rich sub-aerial felsic volcanic rocks formed and were intruded by high-level felsic intrusions of A-type composition in the form of small porphyritic sub-volcanic intrusions or series of extensive dike swarms (e.g., Faber Group; Ootes et al., 2013; chapitre 6). This important magmatic flare with diversified magmatic activity suggests the presence of large, dynamic magma chambers in the mid to basal upper crust (Reardon, 1992; see Fig. 13 of Hildebrand et al. 2010b). This regionally important magmatic event could have sustained the extreme thermal gradient required to drive the regional-scale coalescing IOAA hydrothermal cells depicted by Mumin et al. (2007, 2010) and documented in fertile IOAA districts worldwide (Williams et al., 2005; Porter, 2010; Williams, 2010a; Agangi et al., 2011). Most of the mineralization and alteration zones throughout the GBMZ show a strong spatial association with major structures, stratigraphic discontinuities and permeable units. For example in some setting the ascending fluids were preferentially channeled and their metal precipitated along series of aquitards (unconformities between basement basins such as East Hottah; Table 2; Reichenbach, 1991), between basement and volcanic sequences (NICO deposit; Goad et al., 2000a, b) or along unconformity within the volcanic sequence (Sue Dianne; Gandhi et al., 2014).

The dynamic tectono-magmatic setting of the GBMZ led to variable disturbances of the physico-chemical IOAA environment including by caldera collapse, extensive brecciation, differential uplift, exhumation, tilting and broad folding, and regional to local faulting (Mumin et al., 2010, 2014; Enkin et al., 2012; Hayward et al., 2013 and reference therein). The resulting hydrological settings permitted highly saline fluids and oxidized brines to percolate through metal-endowed host rocks (Mumin et al., 2010; Ootes et al., 2013; Somarin and Mumin, 2014;

Acosta-Góngora et al., 2015a, b). This dynamic tectonic setting induced permutation, telescoping or cyclical build-up of alteration types as observed in other IOAA districts (Haynes et al., 1995; Skirrow, 2010). Nevertheless, it is worth stating again here that despite high-temperature metasomatism, weak to no regional tectonic metamorphism is superimposed on the metasomatites except for slivers of amphibole- or biotite-rich metasomatites, m to tens of m thick along the Wopmay fault zone and SW-trending splays within Treasure Lake Group sequences as described by Jackson et al. (2013), Acosta-Góngora et al. (2015b), De Toni (2016) and Corriveau and others (unpublished data, 2015).

These attributes of the GBMZ IOAA systems indicates that, as in other IOAA districts (e.g., Marshall and Oliver, 2008; Kreiner and Barton, 2011), both magmatic and tectonic triggers drove the fluid flow during an interpreted switch from compressive orogenic deformation to extension (Mumin et al., 2014; chapitre 2).

3.3 Alteration overview and summary of mineralization style

This section summarizes the key attributes of alteration types observed in the GBMZ. The description sequence flows from the early alteration assemblages in the root of the systems outward to the late, shallow and low-temperature assemblages. Observations were made on outcrops at regional scale across selected metasomatic systems hosting historic prospects, along trenches and along the NICO deposit decline. Georeferenced muck piles across the NICO ore zone, each with a volume of 9 x 9 x 3 m, were studied in detail and selected drill cores were re-examined for the Sue Dianne and NICO deposits. Detailed deposit-scale descriptions were tailored to provide ample illustrations of IOAA alteration from the GBMZ (e.g., Ootes et al., 2006, 2008, 2013; Corriveau et al., 2010a, b; Mumin et al., 2007, 2010; Acosta-Góngora et al., 2014, 2015a, b; chapitre 6). Complementary to our descriptions and illustrations, we use those of Corriveau et al. (2010b) and Mumin et al. (2010) by referring to their figures as Fig. number$_{C10}$ and number$_{M10}$ respectively.

Table 3-2 Prograde alteration and brecciation evolution and associated mineralisation of selected IOAA systems of the GBMZ

System/ alteration	Sodic± calcic–iron	Calcic–iron± potassium (and skarn)	Potassic–iron (HT)	Potassic or K-skarn	Potassium–iron (LT)
Fab	$R_{(1,\uparrow)\ m\rightarrow i}$ (Ab) $V_{(3,\uparrow)\ mo\rightarrow s}$(Ab-Amp)	R-$V_{(2\text{-}4,\circlearrowleft)\ m\rightarrow i}$ (Amp±Mag±Ap)$V_{(4,\uparrow)\ mo}$(Mag) B-$V_{(2\text{-}4,\circlearrowleft)\ m\rightarrow i}$(Amp-Mag-Kfs)	R-$B_{(5,\uparrow)\ m\rightarrow i}$ (Kfs-Mag) $V_{(5,\uparrow)\ mo\rightarrow s}$(Kfs-Mag)	$R_{(\uparrow)\ m\rightarrow i}$ (Kfs)	$V_{(6,\uparrow)\ m\rightarrow mo}$ (Hem-Kfs) $V_{(6,\uparrow)\ m\rightarrow mo}$ (Chl)
		HREE, U, Th	Cu, LREE		
Cole Lk	$R_{(1\text{-}3,\uparrow)\ m\rightarrow i}$ (Ab)	$R_{(2,\uparrow)\ m\rightarrow i}$ (Amp-Mag) $V_{(4,\circlearrowleft)\ m\rightarrow i}$(Amp) B-$V_{(4,\circlearrowleft)\ m\rightarrow i}$(Amp-Mag)	$V_{(4,\uparrow)\ m\rightarrow mo}$ (Mag)	$R_{(5,\uparrow)\ m\rightarrow s}$ (Kfs) $R_{(\uparrow)\ m\rightarrow mo}$ (Skarn)	$V_{(6,\uparrow)\ m\rightarrow mo}$ (Hem-Kfs) $V_{(6,\uparrow)\ m\rightarrow mo}$ (Chl)
		Th	U, Y, LREE		
Southern Breccia	$R_{(1,\uparrow)\ m\rightarrow s}$(Ab) $R_{(2,\uparrow)\ s\rightarrow i}$(Ab)	$V_{(3,\uparrow)\ m\rightarrow mo}$(Amp-Mag) $R_{(2,\uparrow)\ m\rightarrow mo}$(Mag)	$R_{(1,\uparrow)\ m\rightarrow s}$(Mag-Bt) $R_{(3,\uparrow)\ m\rightarrow mo}$(Kfs-Mag) R-$B_{(3,\uparrow)\ m\rightarrow i}$(Mag-Bt±Kfs) $V_{(4,\uparrow)\ su}$ (Kfs-FeOx)V-$B_{(5,\uparrow)\ m\rightarrow s}$(Kfs-Mag)	$R_{(\circlearrowleft)\ m\rightarrow s}$(Kfs)	R-$B_{(6,\uparrow)\ m\rightarrow s}$(Chl-Hem) R-$B_{(3,\uparrow)\ m\rightarrow s}$(Phy)
	Ta, Nb, Th	Co, Ni	U, Th, Cu, Mo, V, Y, LREE, Ag, Fe		U
NICO	$R_{(1,\uparrow)\ m\rightarrow mo}$(Ab)	$R_{(2,\circlearrowleft)\ m\rightarrow i}$(Amp-Mag) $V_{(2,\uparrow)\ m\rightarrow s}$(Amp) $R_{(2,\circlearrowleft)\ m\rightarrow i}$(Amp-Mag-Bt) $V_{(2,\uparrow)\ m\rightarrow i}$(Mag)	$R_{(2,\circlearrowleft)\ m\rightarrow i}$(Mag-Bt) $R_{(2,\circlearrowleft)\ m\rightarrow i}$(Bt) R-$B_{(2,\uparrow)\ m\rightarrow mo}$(Kfs-Mag±Apy)	$R_{(4,\circlearrowleft)\ m\rightarrow s}$(Kfs)	$R_{(3,\circlearrowleft)\ m\rightarrow s}$(Sr; Chl-Hem-Apy)
		Co, Ni, Cu, LREE, Fe, Au	Co, Ni, Cu, LREE, Fe, Au		
Terra	$R_{(1,\uparrow)\ m\rightarrow i}$(Ab)	$R_{(2,\uparrow)\ m\rightarrow i}$(Amp-Mag±Ap)	R-$B_{(3,\uparrow)\ m\rightarrow i}$(Kfs-Mag)	R-$B_{(4,\uparrow)\ m\rightarrow i}$(Kfs) $V_{(4,\uparrow)\ m\rightarrow mo}$(Kfs)	$R_{(5,\uparrow)\ m\rightarrow i}$(Chl-Hem)
		V, Cu, REE		Pb, Ag	Cu
Grouard	$R_{(1,\circlearrowleft)\ m\rightarrow i}$(Ab) $V_{(3,\uparrow)\ m\rightarrow s}$(Ab-Amp-Mag)	R-$V_{(1,\circlearrowleft)\ m\rightarrow i}$(Skarn) B-$V_{(2\text{-}4,\circlearrowleft)\ m\rightarrow i}$(Amp-Mag) $R_{(2,\circlearrowleft)\ m\rightarrow i}$(Amp-Mag) $V_{(3,\circlearrowleft)\ m\rightarrow i}$(Amp-Mag) R-$B_{(5,\circlearrowleft)\ m\rightarrow i}$(Skarn)	R-$V_{(\uparrow)\ i\rightarrow m}$(Kfs-Mag)	$R_{(\uparrow)\ m\rightarrow s}$(Kfs)	R-$B_{(6,\circlearrowleft)\ m\rightarrow mo}$(Kfs-Hem) $R_{(6,\uparrow)\ m\rightarrow s}$(Chl) R-$V_{(7,\uparrow)\ m\rightarrow s}$(Ser)
		Cu, Pb, Zn		Cu	Cu, Pb

Alteration type (V: Veins, R: Replacement, B: Breccia), **evolution** (↑: Unidirectional, ↺: Cyclical), **intensity** (Su: Subtle, m: Mild, mo: Moderate, s: Strong, i: Intense), **sequence** 1(earlier) to 7(later)

3.3.1 Paragenetic subdivisions and chemical footprints of alteration

In IOAA systems, the same alteration stage can be recorded in many different ways across diverse rock types: variations in mineral parageneses, variations in modal compositions and variations in textures. As mapping progressed across the GBMZ, it became clear that each alteration stage shared similar mineral parageneses and that, where alteration was intense to complete, each alteration started also sharing similar variability in modal compositions of minerals and similar hydrothermal textures irrespective of the precursor rock types. These commonalities can be expressed in terms of the principal major elements that govern the paragenetic sets formed and their respective alteration facies named after them except in cases where metasomatites have already a name entrenched in the (English) literature (i.e., albitites and skarns). Figure 3-3 summarises the variety of parageneses for each end-member of the paragenetic sets as well as their transitional sets based on Corriveau et al. (2010b) and modified from Hitzman et al. (1992), Hitzman (2000) and Skirrow (2010).

The systemic alteration types and associated paragenetic sets documented across the various systems (Fig. 3-3) and their distinct and diagnostic chemical signatures have enabled the definition of lithogeochemical IOCG alteration indices (chapitre 5). The combination of these alteration indices on an IOCG-alteration box plot allows discrimination of alteration types and their portrayal on maps where rock sequences are dominantly silicic at regional scale such as in the GBMZ (Fig. 3-2a). The proposed lithogeochemical alteration box plot cannot be used in sedimentary basins where carbonates prevail with the current indices. The IOAA alteration types can also be highlighted through major element cations and metals contouring (Fig. 3-2b; Mark et al., 2006; Benavides et al., 2008a). Such contours do not account for precursor alteration leaching and should be used with caution.

In addition, block diagrams derived from the molar proportion of sodium, calcium, potassium, iron and magnesium provide highly visual bar codes of alteration evolution, intensity and types on geological maps and along drill cores; a similar caveat apply as that for metal contouring (Figs. 3-4, 3-5). The order of elements and their colour chosen for the molar bar codes consist, from bottom to top or from left to right, of Na in a pink colour as albitites are early, deeper and commonly light pink, then Ca (dark green) for the diagnostic dark green amphibole followed by Fe (black) as representative of iron oxides followed by K in red as per the brick red K-feldspar and then Mg because it is commonly precipitated in chlorite, abundant in some LT potassic–iron alteration zones. However in many systems, iron oxide–alkali alteration and their metal

associations need to be discriminated from those associated with their epithermal caps (described in detail in Mumin et al., 2010). Another bar code system uses the cationic proportion of silica instead of magnesium to discriminate silica-rich epithermal alteration from the silica under saturated or barely saturated iron oxide–alkali alteration as illustrated in Figure 3-4a. From south (deep) to north (shallow), the map in Figure 3-4a depicts a tilted 3 km depth profile of an IOAA system from its albitite root to its epithermal cap. At surface, the profile transects a 1.87 Ga diorite to monzodiorite intrusion and its albitite halo that evolves to a transitional sodic–calcic–iron alteration. Moving away from the intrusion, this alteration is then mildly overprinted by HT potassic–iron alteration, and evolves to a zone of LT potassic–iron alteration (hematitite surrounded by a K-feldspar halo) and then to argillic alteration typical of epithermal caps as described by Mumin et al. (2010).

Drilling in the sodic–calcic–iron alteration and localized HT calcic–iron alteration zones intersected iron oxide–apatite mineralisation enriched in REE and vanadium over length up to 200 m (Fig. 3-5). In the Echo Bay mine area, zones of potassic felsite breccias at the magnetite to hematite transition are enriched in REE. In contrast no such zones was observed at Port Radium and the iron oxide–apatite mineralisation remain poor in REE (Fig. 3-5). Finally, the K2 prospect consists of LT potassic–iron (hematite-bearing) alteration at surface that overly a copper-mineralised HT potassic–iron (magnetite-bearing) alteration as well as an iron oxide–apatite prospect locally enriched in REE (Mumin et al., 2010). Figure 3-5 illustrates that at depth the system did not evolved to alteration typical of epithermal systems.

3.3.2 Sodic and sodic–calcic–iron alteration (Facies 1 Na, Facies 1–2 HT Na–Ca–Fe)

Sodic alteration. In the GBMZ, albite rather than scapolite prevails in the regional sodic alteration, and calcium contents are commonly fairly low in the range of 0.5 to 2 wt.% CaO largely irrespective of precursor rock types (Fig. 3-2; *Annexe 3*; Corriveau et al., 2015). In 1.87 Ga bedded volcaniclastic and sedimentary rocks as well as in 1.88 Ga Treasure Lake Group metasedimentary rocks, albitisation starts as selective and stratabound alteration and if coeval with fracturation of host rocks, albitisation can be intense along fracture haloes. As intensity of albitisation increases, haloes along fractures coalesce into isotropic albitites prior to brecciation (Fig. 3-6a–d). In contrast, in 1.87 Ga volcanic rocks (Faber and LaBine groups) and high-level intrusions, incipient to intense albitisation forms variegated replacement ‘veins’ or amoeboid and

burgeoning alteration fronts that broaden or coalesce into pervasive replacement zones (Fig. 3-6e). In all precursors, intensification of albitisation leads to fairly homogeneous and commonly isotropic white to pink albitites including in carbonate rocks such as those at Grouard (Figs. 3-4c, 3-6c,e).

Prior to albitite development, albitized rocks can be both fractured and folded (Fig. 3-6b,d) but once formed, albitites are commonly brecciated forming crackle to clast- and matrix-supported breccias with angular fragments of albitite (Fig. 3-6d). Albitisation is particularly intense and pervasive along regional faults within Treasure Lake Group rocks and along the Wopmay fault (e.g., DeVries, Southern Breccia, Mazenod; Figs. 3-1, 3-2, 3-6d). The albitites are also common along the margins of the 1.87 Ga intrusions within coeval volcanic, volcaniclastic and sub-volcanic intrusions as well as within metasedimentary host rocks (Fig. 3-4a; e.g., Port Radium–Echo Bay, Camsell River, Fab, Cole, Southern Breccia; Shegelski and Murphy, 1973; Hildebrand, 1984, 1986; Gandhi, 1992a, b, 1994; Reardon, 1992; chapitre 6). Lateral extent of albitites can reach several kilometres near the intrusions, in particular in the Port Radium–Echo Bay and Camsell River districts (Fig. 3-4a; Hildebrand, 1986; Reardon, 1992; Mumin et al., 2007, 2010). Precursor stratigraphy remains locally identifiable such as within layered albitites that replace a 1.87 Ga volcaniclastic unit or Treasure Lake Group units (Figs. 3-6a, 3-7a–b, 16_{C10}). Where intense, albitisation also creates significant microporosity that remains preserved in fine-grained albitites (Fig. 3-6a; Engvik et al., 2008, 2009; Putnis, 2009; Montreuil et al., 2012). Such porosity is obliterated by recrystallization into medium- to coarse-grained albitites (Figs. 3-4c, 3-6b–c; Pelleter et al., unpublished data).

Alteration of albitites. Albitisation is the earliest alteration formed. Pervasive and complete replacement of albitites by other alteration types is atypical where the albitites have recrystallized to medium-to-coarse grained such as in the Port Radium–Echo Bay district (Fig. 3-4c). In such cases, the superimposed alteration rarely extends beyond a few metres and consists of K-feldspar and phyllic alteration and locally of amphibole (e.g., Terra, Fab, Port Radium–Echo Bay district). Conversely, the fine-grained albitites which were systematically brecciated were also commonly replaced by amphibole and magnetite assemblages or magnetite with and without biotite or K-feldspar (e.g., Cole, DeVries, Mar, Southern Breccia in Fig. 3-1; Fig. 3-6d; Table 3-2). Locally albitites were intensely replaced by tourmaline including fragments and matrix within an albitite breccia (e.g., Southern Breccia). In addition, relicts of fine-grained albitites are observed under the microscope within zones of transitional and intense amphibole–magnetite, amphibole, magnetite, or K-feldspar replacement stemming from arrays

of veins or within breccia matrices (DeToni, 2016). Late-stage albitisation was rarely observed in outcrops except as a local overprint on mineralised HT potassic–iron alteration at Fab and very locally in the ore zone at NICO. A metre-long albitisation front also cuts a pervasive K-feldspar alteration below and laterally away from mineralised iron oxide breccias at Sue-Dianne.

Relations between albitisation and albitite-hosted uranium mineralisation. The albitisation process itself was not observed to form potentially economic mineralisation as albite does not crystallise with sulfides and other metals within breccia matrices or veins. In contrast, albitite-hosted uranium mineralisation is common in the GBMZ where albitites are replaced by HT and LT potassic–iron alteration (e.g., Cole, Damp, Southern Breccia). As albitites are spatially associated to fault zones and fine-grained albitites generally develop a pervasive microporosity, brittle fracturing is preferentially partitioned in albitites and leads to the development of fractures network and breccias (Fig. 3-6c–d). This process creates zones of enhanced permeability that become preferential locations for the entrapment of metals to form polymetallic, uranium and uranium–thorium mineralisation as observed along the Southern Breccia. In such zones, a brick-red HT potassic–iron overprint on albitites over tens of metres proved to be proximal to mineralisation (e.g., along microscopic mesh textures; chapitre 6). With increasing brecciation, the albitites become the preferential site for the crystallisation of uranium-bearing specular hematite and/or magnetite with K-feldspar or biotite alteration (e.g., samples 10CQA-1665B04 and 11PUA-012E01 in Corriveau et al., 2015; e.g., Damp, Breccia Island, Mar, Nod and Southern Breccia; Tables 3-1, 3-2). Conversely, corridors of hypidiomorphic-granular albitites are largely non-brecciated and massive (e.g., Port Radium–Echo Bay) except within a 10 m-wide zone west of Mag Hill and at Terra where local brecciation is observed.

Transition from sodic to calcic–iron alteration. Variations in mineral parageneses, in modal compositions and in textures are significant at the transition from sodic to calcic–iron alteration but both end-members remain fairly similar whether the precursors are sedimentary in origin as displayed in Figure 3-7 or volcanic and intrusive in origin as displayed in Figure 3-8. Sodic–calcic–iron parageneses develop locally as transitional zones between the sodic and HT calcic–iron alteration zones and are most extensive among volcanic and hypabyssal intrusions (Fig. 3-4a; Potter et al., 2013b). Albite contents decrease and amphibole and magnetite contents increase within the replacement-type alteration assemblages and this leads to variations in the sodium, calcium and iron molar proportions in whole-rock composition (Fig. 3-7a–b; *e.g., sample CQA-05-124C in appendix 3*; Corriveau et al., 2015). An alternative or coeval transition consists in a gradual increase in the density of amphibole–magnetite±apatite veins within albitites and the

development of spatially extensive replacement zones to form amphibole, amphibole–magnetite, amphibole–magnetite–apatite and magnetite alteration (Table 3-1; Figs. 3-7a–e, 3-8a–c). Individual veins vary in width from millimetres to metres and increase in density from widely spaced veins (tens of metres to metres) to stockworks (Fig. 3-8a–b). These zones of dense amphibole-rich veining can evolve, typically along fault zones or at fault intersection(s), into zones of extensive tectono-hydrothermal breccias hundreds of metres in width; the host is most commonly albitites (e.g., Cole, Grouard, DeVries). Amphibole-bearing matrices have a medium-to-dark green colour and a highly variable grain size, ranging from fine grained to locally medium grained. Veins or breccias with very coarse grained HT calcic–iron parageneses occur locally (Fig. 3-4c).

3.3.3 HT calcic–iron alteration and calcic–iron–potassium alteration (Facies 2 HT Ca–Fe and facies 2–3 Ca–Fe–K)

HT calcic–iron alteration. Where intense, the HT calcic–iron alteration is commonly texture-destructive and forms irregular to pervasive, homogeneous to highly heterogeneous alteration fronts. Precursor bedding structure is commonly preserved (Fig. 3-7e–f, h–j). Mineral assemblages consist of calcic amphiboles (actinolite and hornblende) with and without magnetite and apatite. Megascopic apatite is either uncommon or a minor component in larger amphibole–magnetite and magnetite alteration zones, but distinctive apatite-rich veins and apatite-dominant breccia matrices occur at Mile, Fab, Dennis, Duke and Cole. Through their association with magnetite, the key discriminating cations of this alteration facies are calcium and iron (*e.g., samples 09CQA-0055E03 and 86E73135 in appendix 3*; Corriveau et al., 2015). Grain size varies from fine grained to locally very coarse grained or pegmatitic where HT calcic–iron alteration reaches its peak intensity. Such replacement occurs within the LaBine, Faber and Treasure Lake groups and laterally extends for several tens to hundreds of metres as observed at Fab, Terra, the LJLVS showing and in drill cores below Mag Hill, K2 and Port Radium where it forms iron oxide–apatite prospects (Figs. 3-4a,c, 3-8k–l).

Ductile deformation is most common in the HT calcic–iron and transitional calcic–iron–potassium alteration zones and strain leads to asymmetrically folded stratabound alteration or veins, local foliation and shear zones that can be traced to up to a few tens of centimetres in width and metres in length (Figs. 3-7e–f). Deformation was either coeval with the development of the alteration itself or superimposed on it. As the HT calcic–iron alteration evolves towards HT potassic–iron alteration, extensive hydrothermal brecciation can occur over tens to hundreds of

metres with K-feldspar-altered fragments hosted into a magnetite–amphibole matrix or biotite–magnetite–amphibole-altered breccias (Figs. 3-8f, 12_{M10}; Table 3-2).

HT calcic–iron alteration in carbonate-rich precursors. In carbonate-rich precursors, skarns rich in clinopyroxene (diopside) and locally in garnet (andradite, grossular) are associated with variable modal contents of amphibole, epidote, calcite, apatite and magnetite. Such skarns are commonly intertwined with, or superimposed on, earlier white albitites forming veins or local replacement zones. In extreme cases, a complete conversion of the carbonate-rich sequences of the GBMZ supracrustal sequence is observed at the sodic and HT calcic–iron stages and leads to the disappearance of carbonates from the stratigraphic sequences (e.g., Grouard, Carbonate Mountain and South Duke; Figs. 3-7, 3-9e–g). Zones of skarns can extend over hundreds of metres to a kilometre. Adjacent siliciclastic or volcanic units bear amphibole- or magnetite-rich assemblages typical of the HT calcic–iron alteration.

3.3.4 Mineralisation at the HT calcic–iron alteration stage

Iron oxide±apatite (IOA) mineralisation associated with HT calcic–iron alteration. Zones of iron oxide and iron oxide–apatite (IOA) mineralisation form where the modal concentration of the main iron ore mineral, magnetite, exceeds 20 vol. % within HT calcic–iron alteration zones; such zones remain poor in base and precious metals unless they evolve to more potassic alteration types or are crosscut by late stage veins (Table 3-1; Figs. 3-5, 3-8k, 19_{C10}, 20_{C10}, 28_{C10}; Fig. 45 in Hildebrand, 1984; Gandhi, 1992a; Mumin et al., 2010). Magnetite is typically crystalline, fine to medium grained and has a metallic grey colour with a dull aspect. Texture-destructive pervasive replacement fronts or magnetite-cemented breccias form most of the IOA mineralisation (Figs. 3-8k–l, $18_{\mathbf{M10}}$). Megascopically, magnetite modal composition can reach 100 vol. % and its crystallisation leads to very homogeneous or well layered or laminated magnetite-rich ironstones. In some of the GBMZ IOAA systems, magnetite precipitated during the transitional sodic–calcic–iron alteration and HT calcic–iron alteration can be substantially enriched in vanadium to yield vanadium-rich IOA mineralisation (e.g., samples CQA-05-0152C and CQA-060435C in Corriveau et al., 2015; Fig. 3-5; Port Radium–Echo Bay, Camsell River, DVF, Fab). Chemical analyses of vanadium-rich magnetite are available in Gandhi (1992a) and Acosta-Góngora et al. (2014). Some of the apatite-rich HT calcic–iron zones can also form IOA mineralisation substantially enriched in REE with or without anomalous uranium (e.g., *samples 86E73135, 86E731335 09CQA-1170D02 and 09CQA-1173B in appendix 3*; e.g., Ham, Terra, Hailstone). In most of those alteration zones, apatite is the main REE-bearing mineral with

subsidiary REE minerals like monzonite, britholite, allanite and some REE-rich fluorocarbonate (e.g., parisite; Lypaczewski et al., 2013; chapitre 7). The formation of the subsidiary minerals mostly relate to the intensity of the superimposed alteration types over the apatite-rich HT calcic–iron zones. Traces of pyrite and chalcopyrite occur in many HT calcic–iron alteration zones but are not a regular attribute. Sulfide precipitation is common where HT calcic–iron alteration zones transition to HT potassic–iron (Jackpot), or to HT calcic–potassic–iron alteration and LT potassic–iron or calcic–iron alteration (Port-Radium and East Hottah; Fig. 3-2; Table 3-2; *échantillon 10CQA-0780B02 à l'annexe 3*).

Skarn hosted Zn–Pb±Cu or tungsten mineralization is observed within zones of HT calcic–iron alteration formed at the expense of carbonate-rich precursor sequences. In such showings, the main ore minerals are galena and sphalerite with variable amounts of chalcopyrite within a gangue of magnetite, amphibole, garnet, clinopyroxene and talc (e.g., *sample 10CQA-0204F02 in appendix 3*; sample KZ-09-CM-01 in Corriveau et al., 2015; e.g., Carbonate Mountain showing; Neale and Camier, 1997). Where observed south of the NICO deposit in the Duke system, tungsten mineralization relates to crystallization of scheelite coeval with amphibole, magnetite and minor chalcopyrite in veins.

Transitional calcic–iron–potassium alteration. The transition zones between sulfide-depleted HT calcic–iron alteration zones and copper sulfide-rich HT potassic–iron mineralisation zones starts with the presence of K-feldspar selvages along amphibole–magnetite (with or without apatite) veins (Fig. 3-8c). The initial selvages gradually widen from millimetres to tens of centimetres. As stockworks evolve to breccias, haloes coalesce to form a pervasive K-feldspar alteration of the host rocks and their fragments (Figs. 3-8d–h, 23_{C10}). This alteration stage needs to be characterised taking into account the selvages to the infills to represent correctly the paragenesis.

3.3.5 High- to low-temperature potassic–iron alteration and IOCG mineralisation (Facies 3 HT K–Fe and 5 LT K–Fe)

High- to low-temperature potassic–iron alteration parageneses in siliceous precursors. Paragenetic sets of HT potassic–iron alteration forms selective to pervasive replacement zones, veins, haloes and breccias in the LaBine, Faber and Treasure Lake groups (Figs. 3-7g, 3-8m–o and 3-9a–f). Potassium-feldspar–magnetite, biotite–magnetite and/or K-feldspar–biotite±magnetite comprise the most common parageneses (Fig. 3-3). Hydrothermal minerals are fine-to-medium grained and their modal composition can reach nearly 80 volume%. K-

feldspar-stable HT potassic–iron alteration predominates in felsic rocks and leucocratic alteration zones (Faber Group above NICO, Fab, Brooke, Sue-Dianne) whereas biotite-rich HT potassic–iron alteration commonly occurs in HT calcic–iron altered or least-altered meta-siltstone (NICO) and mafic volcanic rocks. In many of the GBMZ IOAA systems, the LT potassic–iron stage is superimposed over the magnetite-rich mineral assemblages of the HT potassic–iron stage. For example, the magnetite-bearing breccias at Sue-Dianne, Hoy and Brooke are crosscut by networks of hematite veinlets and evolve to hematite-bearing breccias (Fig. 3-9c–f, q–v, 33_{C10}). Other minerals composing the LT potassic–iron alteration are K-feldspar, white mica (sericite), chlorite, carbonate and/or quartz.

Mineralisation formed at the HT and LT potassic–iron stage in siliceous precursors. Copper-sulfide mineralisation formed at the HT potassic–iron stage in the GBMZ is typically comprised of chalcopyrite and pyrite hosted within magnetite-cemented breccias in which the fragments are pervasively potassically altered (e.g., *samples 09CQA-0026G03 and 09CQA-0109F07 in appendix 3*; samples KZ-09-SD-03 in Corriveau et al., 2015; e.g., Sue-Dianne, Brooke, Fab; Fig. 3-9). As breccias are mapped from their most incipient form to the mineralised breccias (Fig. 3-8m–o), K-feldspar alteration commonly intensifies and chalcopyrite crystallises within the breccia matrix or within veins that crosscut the breccias. Outside of the HT potassic–iron alteration zones, copper sulfide veins were not observed to crosscut earlier alteration types. For example at Fab, the transitional calcic–iron–potassic alteration forms a halo separating the copper-sulfide mineralised HT potassic–iron alteration zones from the larger and external HT calcic–iron alteration zones devoid of base and precious metal mineralisation (Fig. 3-8f; Potter et al., 2013b). At Sue-Dianne, the Cu–Au–Ag ore-bearing breccias stand upright (Fig. 11_{M10}) with the deeper magnetite–K-feldspar–pyrite assemblages evolving upward to copper-sulfide mineralised magnetite–hematite K-feldspar and then to hematite–K-feldspar breccias locally bearing uranium towards surface (Fig. 3-9a–f; Table 4 in Mumin et al., 2010). As demonstrated by Southern Breccia albitite-hosted uranium showings, the mineralisation formed at the HT potassic–iron stage can also be predominantly uraniferous and mainly comprised of uraninite and brannerite with accessory chalcopyrite, molybdenite and pyrite (e.g., samples 10CQA-1665D03 and 10CQA-1690-N249998 in Corriveau et al., 2015; chapitre 6).

At the LT potassic–iron alteration stage, chalcopyrite, bornite and chalcocite are the observed copper sulfides and typically precipitate in that order (e.g., Sue-Dianne, Brooke). They are typically associated with pyrite and occur in hematite-cemented breccia zones in which the fragments are strongly potassically altered. Uraninite, pitchblende, monazite and allanite are

other accessory minerals that were commonly observed in the mineralised zones formed at the LT potassic–iron stage (e.g., Southern Breccia, Sue-Dianne). Where HT and LT potassic–iron alteration zones are minor in extent, they are not systemically host to copper-sulfide mineralisation (*e.g., samples 09CQA-0039B03 and 09CQA-1020I02 in appendix 3*; e.g., Hump).

HT and LT potassic–iron alteration in calcium-rich precursors. Geological environments with abundant calcium- and/or magnesium-rich precursors such as carbonate or overprinted HT calcic–iron alteration does not totally see these elements leached out as fluids react with them to form HT potassic–iron alteration in contrast to neighbouring zones with more usual precursor rocks. A high modal content of amphibole and biotite accompanies the magnetite. As such, timing relationships of the dominant calcium-rich potassic–iron alteration that host the Au–Co–Bi mineralisation at NICO is interpreted as time equivalent to the HT potassic–iron alteration formed above it within the kilometre-scale potassic (K-feldspar stable) alteration halo in the overlying volcanic rocks. A detailed study of 80 cubic metres of ore zone at NICO highlights that the Au–Bi–Co–Cu mineralisation is hosted within veins, their stratabound haloes and breccias that are part of up to 30 generations of HT calcic–iron, calcic–iron–potassic and HT potassic–iron replacement-type alteration, veins, vein selvages and breccias documented to crosscut and overprint each other (Table 3-2; Figs. 3-7h–m, 1–2_{C10}, 26–28_{C10}).

Where the LT potassic–iron stage occurs in calcium- and/or magnesium-rich precursor rocks (e.g., Duke, NICO, Carbonate Mountain, Hillside), chlorite is the predominant mineral whereas K-feldspar, specular hematite and white micas are generally relegated to accessory phases. Stratabound to pervasive chloritic alteration fronts, veins and veinlets are typically observed within both the Treasure Lake, LaBine and Faber groups. Incipient chlorite replacements generally preserve the precursor rock textures; conversely, intense chloritization destroys them. Chlorite-rich alteration is locally accompanied by K-feldspar and is commonly spatially associated with copper-sulfide mineralised zones (LJLVS). Intense chlorite±K-feldspar±talc replacements of skarns is common (e.g., South Duke, Carbonate Mountain), and talc alteration replaces skarnified volcanic rocks in the SE Echo Bay area. At NICO, the latest stage of mineralisation consists of a retrograde assemblage of chalcopyrite–bismuthinite–hematite–chlorite with hastingsite with and without emplectite and whittichenite (Acosta-Góngora et al., 2013, 2014). The GBMZ magnesium-rich chlorite–K-feldspar assemblages were observed in spatial association with LT potassic–iron alteration and were mapped under the LT hydrolytic potassic–iron alteration umbrella. This allows their distinction from other hydrogen ion-related

hydrothermal alteration types observed across the GBMZ, some of which are not directly linked to the IOAA systems development as described in Mumin et al. (2010).

Mineralisation formed at the HT potassic–iron stage in calcium-rich precursors. The metal assemblages observed in the HT potassic–iron zones formed in calcium-rich precursor rock sequences slightly differ from those observed in siliceous precursors. At the NICO deposit, arsenopyrite predominates over pyrite and chalcopyrite in the ore zones. At NICO, the mineralisation stages start with sulfarsenides- and arsenides-rich mineralisation comprised of cobalt-rich arsenopyrite, cobaltite, cobalt-rich loellingite, pyrite and locally scheelite (e.g., *samples CQA-07-0465A02, CQA-07-0466C01 and CQA-07-0467A in appendix 3*; Fig. 3-7k–m). The gangue minerals (magnetite, amphibole, biotite, quartz and K-feldspar) define an assemblage typical of HT potassium–iron replacing and remaining in part stable with calcium-rich precursor alteration. In this assemblage, sulfarsenides and arsenides contain up to 81 ppm gold (Fig. 3-7h–m; Acosta-Góngora et al., 2015a). Cobalt-rich sulfarsenides and arsenides are replaced by arsenopyrite in association with marcasite–pyrite–magnetite–hastingsite intergrowths, gold and native bismuth with or without bismuthinite (Acosta-Góngora et al., 2013, 2014). The presence of solidified native bismuth droplets interpreted as having crystallised from bismuth melts, combined with other observation led Acosta-Góngora et al. (2015a) to suggest a temperature range between 270 and <400°C for the genesis of Bi–Au inclusions within arsenopyrite and high-grading of the gold concentrations at NICO from precursor predominantly cobaltian mineralisation. A gold-rich zone has been delimited with a total underground reserve of 0.577 Mt at 4.96 g/t Au, 0.10% Co, 0.17% Bi and 0.02% Cu (Burgess et al., 2014).

3.3.6 Alteration types typical of the magnetite-to-hematite transition (Facies 4 K–Felsite and K–Skarn)

In some of the GBMZ IOAA systems, diagnostic hydrothermal alteration assemblages are formed at the magnetite to hematite transition. In silica-rich precursor rocks, this transitional stage typically occurs as microbrecciated to crackle brecciated K-feldspar felsite composed megascopically of more than 75 vol.% K-feldspar with modal contents of magnetite and hematite under 1–2 vol.%. The felsite breccias form proximal to copper sulfide mineralisation associated with HT and LT potassic–iron alteration (Fig. 3-9r; e.g., Sue-Dianne, Mile, Echo Bay, Summit Peak, Birchtree, Terra; Figs. 3-9b,r, 23–25$_{C10}$, 29$_{C10}$). Relicts of precursor albitites are common in such zones (Fig. 3-9r). Potassium-feldspar felsite breccia occurs among magnetite–K-feldspar-altered breccias near areas where they are overprinted by strong specular hematite

alteration (Fig. 3-9m–v). These felsite breccias should not be confused with the non-brecciated brick-red and generally barren K-feldspar alteration haloes pluri-kilometre in extent that are common in IOAA systems of the GBMZ both at regional to local scale. Potassic alteration is also very common along wall rocks of intrusive bodies and within the intrusive body themselves. In the GBMZ, such haloes mildly overprint albitized andesites and sub-volcanic diorite intrusions of the Port Radium–Echo Bay district (Mumin et al., 2007, 2010) and form an intense K-feldspar envelope that overlies the NICO deposit (Shives et al., 2000).

In carbonate-rich or carbonate-altered precursor rocks, this transitional stage typically forms skarn assemblages with a high modal content of K-feldspar that discriminates them from the skarn assemblages formed at the HT calcic–iron stage (Fig. 3-9g–l). Garnets (e.g., andradite, almandine), diopside, epidote and vesuvianite, in variable modal proportions, typically complete the skarn-type mineral assemblages. For example, at the magnetite-to-hematite transition across the Mile breccia from Mile to Hoy (Fig. 3-1), albitized and amphibole-altered volcaniclastic units as well as albitite breccias are replaced or crosscut by skarns that become significantly mineralised in chalcopyrite (Figs. 3-9g–l; 30–31$_{C10}$; *e.g., échantillon CQA-05-0220A01 à l'annexe 3*; sample CQA-07-0289 in Corriveau et al., 2015; May, 2007; Mumin et al., 2010). The skarn assemblages are crosscut by hematite veins and occur in close spatial association with a K-feldspar felsite breccia. The mineralisation is principally comprised of chalcopyrite, bornite, chalcocite, sphalerite and galena with accessory molybdenite. Tungsten enrichments were also documented in the mineralised zones of the Mile Lake breccia (Mumin et al., 2010).

Similar alteration evolution from albitisation to amphibole–magnetite alteration, magnetite–K-feldspar breccias, felsite breccias, hematite–K-feldspar breccias and copper mineralisation is observed in the IOAA system that hosts the past-producing Terra mine in the Camsell River district. As such four distinct types of K-feldspar-stable alteration are recognised across the GBMZ IOAA systems. Both the high- and low-temperature potassic–iron alteration types are spatially associated with base and precious metal mineralisation (see complementary discussion in Barton, 2014). Hence it is the association of K-feldspar with magnetite or hematite that vectors to mineralisation. Whether iron oxide is part of a mineralisation or not, it has to be included within alteration parageneses to highlight which alteration zones may vector to IOCG mineralisation (Figs. 3-8n–o and 3-9a–f, m–v). Conversely, potassic alteration without iron oxide only vectors to mineralisation where it is intensely brecciated and formed at the prograde magnetite to hematite transition. Other zones of potassic alteration are interpreted as orthomagmatic and spatially related to emplacement of porphyritic dikes or as part of the large-scale K-feldspar envelope in

the model of Hitzman et al. (1992). In both cases, the presence of such potassic alteration even if extensive is not a field evidence of the presence of an IOAA system and does not vector to mineralisation.

3.3.7 Other types of alteration

Epithermal alteration and mineralisation, including vein-type deposits, developed peripheral to or structurally above the HT and LT potassic–iron alteration (Figs. 3-4a, 4–5$_{M10}$, 24 $_{M10}$; Mumin et al., 2010). This is exemplified by the tilted crustal section of the Port Radium–Echo Bay district that records the development of an IOAA system from its sub-volcanic intrusions and albitites roots to an epithermal cap within less than 3 km depth (cf. Fig. 3-4a). Tourmaline-rich alteration and breccias also occur locally in some cases at an early stage in alteration development but in most cases it forms at or after the magnetite to hematite transition (e.g., Southern Breccia, Nori and K2; Mumin et al., 2010; Ootes et al., 2010). Tourmaline is also common within the matrix of breccias with sharp, linear dike-like aspect that crosscut volcanic rocks, as well as infill in veins across porphyritic intrusions. Epidote alteration (Grouard) and barite veins (Hottah, NICO) occur at a late stage most commonly within veins but epidote alteration leading to epidosite is fairly common. At NICO, late-stage veins of quartz, amphibole, K-feldspar, calcite or dolomite with local sulfides crosscut the ore assemblages.

3.3.8 Breccia development as a function of alteration types

Mapping of the GBMZ IOAA systems documents regular spatial and temporal associations between breccia development and the appearance and increasing intensity of some alteration types and mineralisation (Table 3-2). Albitites are the most regularly brecciated alteration type. Conversely, no brecciation occurs with intensifying albitisation nor was albite observed as a breccia filling mineral in the GBMZ breccia zones (Fig. 3-6a,e). Consequently, sodic alteration is not a breccia-forming event in itself. Albitite breccias where mineralised in base and precious metals only where overprinted by intense HT or LT potassic–iron alteration, otherwise mineralisation remains minor such as in the drilling results of the Nod prospect in MacKay and Eveleigh (1997). With their common pink colour, albitite breccias may however look significantly potassic or iron altered even if they are not. Hydrothermal breccias are not systematically developed at the HT calcic–iron alteration stage and where developed, they remain relatively immature (as per maturity criteria in Jébrak, 2010) and poorly mineralised in base and precious metals (e.g., Cole; Table 3-2).

Within replacement-type HT potassic–iron alteration, hydrothermal breccias regularly develop as soon as the modal concentration of K-feldspar becomes high (Fig. 3-8m–o). Brecciation continues during the formation of the K-feldspar felsite or potassic skarns at the transition from magnetite to hematite and during the LT potassic–iron alteration stage (Table 3-3; e.g., Fab, Mile, Birchtree; Figs. 23–25$_{C10}$). In K-feldspar felsites, crackle breccias prevail, are rarely mineralised and are regularly developed among outcrops that expose magnetite-bearing alteration zones evolving to hematite-bearing alteration zones (Fig. 3-9r). In contrast to brecciated albitites, the brecciated K-felsites are not systematically formed along a fault zone or deformation corridor. Volume gain is interpreted to lead to brecciation whereas tectonic activity appears to be relegated to a secondary role. Permissive evidence for a volume gain if K-feldspar replace albitites is provided by Norberg et al. (2011) which document molar volume loss during albitisation of K-rich alkali feldspar. In parallel, Jamtveit et al. (2009) have illustrated that volume gain in rocks initiates fracturing, an observation compatible with the systematic brecciation in K-feldspar dominant felsite at the magnetite to hematite transition. As magnetite or hematite-bearing HT and LT potassic–iron alteration intensifies, the formation of hydrothermal breccias hosting polymetallic mineralisation is systemic across zones tens to hundreds of metres in diameter (Figs. 3-1, 3-2; Corriveau et al., 2010b; Potter et al., 2013b). Sulfides (commonly pyrite and chalcopyrite in siliceous precursors and arsenopyrite in carbonate-rich sequences) crystallise either in breccia cements, in replacement zones or within veins (Fig. 3-9o–p, v). For example, incremental intensity of breccia development is locally observed at the Sue-Dianne deposit where the margin of the breccia system is exposed along the eastern flank of a hill that reaches the main ore zone to the top. In the marginal zones of the deposit and going up-section, localised crackle breccias predominate with copper-sulfide mineralised magnetite matrices and K-feldspar-altered fragments (Fig. 3-9a). This zone grades to a hectometre zone of felsite crackle breccias (Fig. 3-9b) and then progressively evolves towards the summit to mosaic and chaotic breccias with dilation ratios increasing from low to high. The breccia cement is comprised of copper-sulfides with magnetite and/or hematite (Figs. 3-9c–f; 10$_{M10}$). Here, as in other IOCG mineralisation in the GBMZ, mineralised breccias associated with HT potassic–iron alteration prevails over those with LT potassic–iron alteration though significant hematite-bearing alteration occur at Esther, Brooke, Southern Breccia, Hoy, K2 and Sue-Dianne (Tables 3-1, 3-2). Clast shape in the breccia zones formed at the HT and LT potassic–iron alteration stages ranges from having small to very high aspect (length to width) ratios (Fig. 3-9d, f–g, m–o, r–v). Roundness of fragments varies greatly and so does the complexity of the fragment contours with

many breccias having reached the stages of significant dissolution/chemical corrosion, indicative of a mature breccia zone as observed at East Hottah (cf. Jébrak, 2010).

3.4 Timing of IOAA system development in the GBMZ

The onset of IOAA hydrothermal activity at the waning stages of the Calderian orogeny is recorded by stratabound albitisation as well as stratabound amphibole and magnetite alteration within the Treasure Lake Group at DeVries. Here, the meta-siltstone and -wacke layers and their stratabound alteration are locally folded and cut by axial plane-parallel syn-deformation granitic dikes dated at 1878 ± 4 Ma (Bennett and Rivers, 2006; Corriveau et al., 2007). Further to the southwest, a small non-altered diorite plug with no tectonic fabric is dated at 1865.1 ± 0.7 Ma whereas a dike of hornblende granite that crosscuts veins of amphibole and magnetite gives an age of 1866.4 ± 0.6 Ma. South of the NICO deposit, a granite intrusion ca. 1.873 Ga in age is pervasively albitized along the Southern Breccia albitite corridor (Fig. 3-4b; Gandhi et al., 2001; chapitre 6). Syn-tectonic 1.87 Ga aphyric-to-porphyritic felsic dikes locally intruded the Southern Breccia and were subsequently themselves brecciated and potassically altered (Davis et al., 2011; chapitre 6). Enclaves of layered albitites occur within sodic-altered 1.87 Ga intrusions (Corriveau et al., 2010b). Collectively, these observations and age determinations record that the regional-scale albitisation started prior to the final emplacement of the early sub-volcanic plutons and continued during and/or after their emplacement as volcanic rocks were deposited. In addition to these timing constraints, mapping of the Sloan Group did not record the presence of IOAA alteration beyond quartz–hematite veins which may be very late stage such as the ca. 1854 Ma quartz–carbonate–chalcopyrite–titanite veins at NICO (Davis et al., 2011) possibly coeval with the emplacement of 1856 Ma rapakivi granite (Gandhi et al., 2001). Their emplacement suggests minor remobilisation or renewed hydrothermal activity associated with the later magmatic events (see also Somarin and Mumin, 2012). Field relationships and available U–Pb zircon ages circumscribe the development of the GBMZ IOAA systems and their IOCG deposits to a lesser than ca. 7 m.y. time window at 1.87 Ga (Bowring, 1984; Hildebrand, 1986; Gandhi et al., 2001; Davis et al., 2011).

3.5 Deposit types as a function of alteration facies development: an IOAA-facies model

3.5.1 Controlling factors on the formation of the IOAA alteration facies

The regularity of the space–time relationships, types of mineral assemblages and overall chemical signature of the IOAA alteration across the GBMZ and other IOAA districts highlights commonalities in the metasomatic processes and physico-chemical conditions under which these systems form (Williams, 2010a; Skirrow, 2010). In contrast, the variable sources of fluids and precursors rock sequences in which they were formed (Hunt et al., 2007; Nirranen et al., 2007; Baker et al., 2008; Williams et al., 2010; Somarin and Mumin, 2014) provide good indications that fluid sources and precursor composition are not the main controlling factors on the prograde development of the IOAA alteration facies. The main criterion regarding fluid composition is that the initial fluids must be highly saline. Such salinity is most easily achieved through reactions between magmatic fluids and evaporites (Li et al., 2015a). Nevertheless, based on research worldwide and mappable attributes of IOAA systems (e.g., Oliver et al., 2004; Williams et al., 2010; Rusk et al., 2015), fluids in IOAA systems can be ultimately derived from multiple sources that include:

1) mantle and mafic magmas pooling at the base of the crust,
2) large intermediate to felsic magma chambers which are episodically replenished in mafic magmas and heat,
3) saline brines that form evaporite-bearing basins and fluids derived from their regional metamorphism or their metasomatism,
4) seawaters and meteoric waters,
5) carbonate fluids derived from metasomatism of carbonate rocks or carbonate alteration,
6) fluids derived from metasomatism of precursor hydrous minerals as per albitisation of precursor biotite-bearing metasedimentary rocks (Fig. 3-6a–b).

In addition, the entire redistribution of elements within IOAA systems to form IOCG deposits can take place within a few million year time frame from depths of about 3 to 12 km depth to surface as observed in the Andes and in the GBMZ which have not been overprinted by subsequent

high-temperature orogenic events (Fig. 3-4a–b; De Haller et al., 2006; Davis et al., 2011; Hayward, 2013). Current work in the GBMZ highlights that early fluids were largely magmatic-hydrothermal in origin (Acosta-Góngora et al., 2015b). A distinct attribute of the GBMZ IOAA systems is the scarcity of scapolite formed at the sodic and sodic–calcic–iron alteration stages. This attribute may provide a mean to prognosticate during field work which systems may have had multiple fluid sources with evaporite-derived fluids (albite–scapolite parageneses) and which ones are magmatic-hydrothermal end-members (largely albite). Nevertheless, scapolite has been observed locally among lesser-altered carbonate-rich precursors near the type section of the Treasure Lake Group and interpreted as potentially preserving evidence for evaporite-sourced fluids (Acosta-Góngora et al., 2015b).

Based on the fieldwork in the GBMZ and its regional geological contexts, the critical aspect for the development of an IOAA system is the ability of the upper crust 1) to become charged in hyper-saline fluids (from one or many sources) where albitites form, and 2) to sustain both a high volume of fluid flow and a very high geothermal gradient at regional scale. The physico-chemical properties of precursor saline fluids (major and trace element composition, metal budget, pressure, temperature, pH, etc.) tremendously evolve in space and time through continuous chemical exchanges with host rocks as the fluids progress away from its source(s).This evolution is schematically portrayed in Figure 3-10 by the sequence of alteration and the chemical changes undergone at each alteration facies. Fluid-rock metasomatic reactions and mineral stability of products control ultimately the chemistry of the fluids. Mixing fluids of variable origins and contrasting physico-chemical properties and percolation of the fluids in a wide variety of precursor rocks can influence the final metal and elemental budget/signature of each alteration facies. Figure 3-10 portrays a prograde evolution as the fluid column rises from depth to surface and reacts with precursor rocks. At each stages though new fluids may reach the fluid column and recharge fluids in cations and metals.

Table 3-3 Overview of alteration types for selected IOCG deposits worldwide and IOAA systems of the GBMZ.

Deposit	Deposit type (Williams 2010)	Sodic±calcic-iron	Calcic-iron (HT)± potassium	Potassic-iron (HT)	Potassic/ Skarn	Potassium-iron (LT)
IOCG (Barton and Johnson 1996)		Ab±Scp-Amp-Cpx (1, D/R)	Mag±Ap (1, D/R)		Skarn with hydrous assemblage (?, P; Amp-Chl-Cb)	Hem-Sf-REE-hydrolitic minerals (2, O)
Cloncurry-type magnetite-group IOCG (Williams 2010a)		Na±Ca silicate (1, 3, D/R, 400-500°C)	Magnetite (2, R→P)	±K±Fe silicate (4-6, P→O, >400°C) Magnetite (4-6, P→O) Py-Ccp (5-6, O, 450- >250°C,)		Hematite (6, O)
Olympic Dam-type hematite group IOCG (Williams 2010a)			Magnetite (1, O) Sulfides (1, O, 450°C; Py)			Ser-Chl-Qz→Cb→Hem (2-4, O) Sulfides (2-4, O, Cc - 200°C; Ccp→Bn→Cc) Uranium oxide/silicate (2-4, O)
Hematite-group IOCG (Skirrow 2010)		Na-Ca-Fe (1, D/R; Ap-Cpx-Mag-Ttn-Scp)		Fe^{2+}-K (1) (potassic) (2, D/R; Bt-Mag±Py-Ccp-Po-Ttn-Ap) Fe^{2+}-K (2) (potassic) (3, D/R; Mag-Kfs-Act±Ccp-Py)		Fe^{3+}-K-H_2O-CO_2 (2) (hydrolitic) (4, O; Hem-Ser-Chl-Cb)
Laurinoja (Niiranen et al. 2007)	Iron oxide	Ab±Scp (1, D/R)	Cpx-Mag-Amp±Cal-Ab-Bt-Kfs-Scp (3, P) Mag-Cpx-Amp (4, O)	Kfs-Bt±Mag-Cpx-Ab (2, D/R)		
Kiruna (Hitzman et al. 1992)	Iron oxide-apatite	Sodic (1, D; Ab-Act-Mag-Ttn)	Mag-Ap (2, O)	Bt-Qz-Py (4, O)		Potassic (3, O; Kfs-Ser±Hem) Silicic (5, O;Ser-Qz) Hem±Qz-Ba-Fl (6, Oz)
Oak Dam (Davidson et al. 2007)	Iron oxide (Mag-Hem group IOCG)	Skarn-like assemblage (1, D→P, 450°C; Ab-CS±Mag)	Magnetite stage (3, O; Mag-Qz-Ap±Act-Chl)			Hematite stage 1 (2, O; Hem-Gth) Chlorite (6, P; Chl-Gth-Cov-Si) Hematite stage 2 (4, O, 170-190°C; Hem-Gth-Ccd-Py-Chl-Tur) Cu-U-(Au) mineralization (5, P; Ccp-Pch-Mnz-Urn-Ilt-Ms-Flo-Car)
Ernest Henry (Mark et al. 2006)	Mag-group IOCG	Early Na (albitization) (1, D/R; Ab-Ttn-Qz) Na-Ca (1) (3, D→P; Ab-Mag-Amp-Qz-Py) Na-Ca (2) (4, D→P; Ab-Scp-Cpx-Mag-Ep-Qz-Py-Ttn-Cb-Ap)	Albite-poor calcic (6, D→P; Mag-Act-Ap-Qz-Py)	Pre-ore K (2, D→P; Bt-Mag±Kfs) Pre-ore K(-Mn-Ba)-rich (7, D→P; Grt-Kfs-Bt-Mag-Amp-Scp-Qz-Py-Ttn-Cl-Fl) Cu-Au mineralization/breccia (9, O; Bt-Mag-Py-Cb-Kfs-Ccp-Fl-Ap-Hem-Mo-Brt±Sp-Apy-Grt-Amp)	Syn-ore K-feldspar (9, O→D; Kfs-Qz-Ru-Cb)	Sericitization (8, P; Ser)
Candelaria (Marschik and Fontboté 2001)	Mag-group IOCG	Iron oxide stage (1; Ab) Iron oxide stage (8; Ab)	Sulfide stage (9; Amp) Sulfide stage (11→12; Amp-Po→Py-Po-Amp-Ep)	Iron oxide stage (3→7, 500-600°C; 3-Bt-Qz→4-Cum-Kfs-Bt-Qz→5-Hem-Mag-Crd-Grt-Tur?-Bt-Qz→6-Mag-Bt-Qtz→7-Kfs-Bt) Sulfide stage (13→17, 370-440°C; 13-Ccp-Au-Po-Amp-Bt-Qz→14-Ccp-Au-Amp-Mo-Bt-Qz-Ep→15-Ccp-Qz-Ep-Anh→16-Ccp-Sp-Kfs-Chl-Tur→17-Mag-Kfs-Chl)	Sulfide stage (10; Kfs-Qz)	Late stage (18, 175-235°C; Ccp-Hem-Py-Qz-Cal)

Alteration/ System	System type (Williams 2010)	Sodic±calcic-iron	Calcic-iron (HT)± potassium	Potassic-iron (HT)	Potassic/ Skarn	Potassium-iron (LT)
Sequeirinho (Monteiro et al. 2008)	**Mag-Hem group IOCG**	**Sodic** (1, D/R; Ab±Tur-Scp) **Sodic-calcic** (2, D/R; Act-Ab±Mag-Cal-Ep-Qz-Ttn-Aln-Tho)	**Actinolitite** (3, D→P; Act) **Massive magnetite** (3, D→P; Mag-Ap) **Pre-ore** (7, O; Act-Ap-Mag-Py) **Calcic** (10, O; Act-Mag-Ep-Ap-Cal-Po)	**Potassic** (5; Kfs-Bt-Qz-Mag±Aln-Tho-Ccp) **Bt-Hast-Tur-Scp** (5)		**Ep-Cal-Hem-Qz** (4, D/R) **Chloritization grading to Cal-Ep haloes** (6, O; Chl±Ttn-Ru-Ap-Ab-Ccp) **Syn-ore** (8, O; Chl-Ep-Hem-Ru-Ilm-Mzn-REE Ep) **Syn-ore** (9, O; Ccp-Sieg-Mil) **Hydrolitic** (11; Msc-Chl-Cal-Qz-Hem-Ccp)
Alvo-118 (Torresi et al. 2012)	**Mag-Hem group IOCG**	**Sodic** (1, D/R; Ab-Scp)		**Potassic with silicification and FeOx** (2, P; Kfs-Bt-Mag-Qz) **Kfs-Bt-Qz-Mag-Ep-Act** (6, P)		**Chlorite** (3, P→O; Chl) **Cu-Au mineralization/breccia** (4, O; Ccp-Hem-Brn-Mag-Py-Cal-Chl-Ap) **Carbonate-Quartz** (5, P; Qz-Cal-Ap-Bt-Ccp-Hem) **Hydrolitic** (7, P; Qz-Ser-Cal-Fl)
Raul-Condestable (De Haller et al. 2006)	**Mag-Hem group IOCG**			**Bt-Mag** (1, P) **Act-Mag-Qz-Ttn-Ilm-Aln-Kfs-Ap-Msc-Mo-Sp** (3, P→O)		**Act-Hem-Scp-Qtz-Ttn-Ilm-Aln-Kfs** (2, P→O) **Ser-Chl** (2, P→O) **Hem-Chl-Ab±Ep-Cal** (4, D→P) **Ore zone** (5, D→P; Py-Sp-Gn-Chl→Chl-Ccp-Py-Au)
Mantoverde (Benavides et al. 2008)	**Hem group IOCG**	**Albitization** (1, D/R) **Scapolitization** (4, D/R; Scp)		**K and Fe** (3, D→P; Mag-Ap-Bt-Ttn-Tur-Kfs-Act) **Ore stage (1)** (7, O; Mag-Cal-Sid-Ccp-Py)		**Hydrolysis (1)** (2, D/R; Ilt-Ms-Chl) **Hydrolysis (2)** (5, P; Ms-Hem-Py) **Hydrolysis (3)** (6, P; Chl-Hem-Sid-Ccp-Py) **Ore stage (2-3)** (8-9, O; 8:Hem-Py→9:Ccp)
Wernecke Breccia (Hunt et al. 2007)	**Hem group IOCG**	**Sodic** (1, D/R; Ab±Scp)		**Early stage brecciation** (2, O; Mag±Hem)	**Potassic** (1, D/R; Kfs±Ser)	**Main brecciation** (3, O; Hem-Py±Mag→Ccp) **Carbonate alteration/breccia** (4;Cal or Ank/Dol ± Py-Ccp-Hem-Mag-Brt)

Alteration distribution and relation to ore R =Regional D = Distal P = Proximal O = Ore zone **Alteration sequence** 1 (earlier) to 18 (later)

3.5.2 System evolution leading to specialised-metal iron oxide±apatite deposits

Throughout this section, incoming fluids are numbered according to the IOAA alteration facies they form as per Figure 3-10. The discharge and recharge of cations with respect to the evolution of the fluid are empirically constrained based on the extreme metasomatism undergone by precursors as mapped in GBMZ. Plan maps and schematic sections of known magnetite-group (Ernest Henry, Australia; Candelaria, Chile; Sequeirinho and Sossego, Brazil) and hematite-group (Mantoverde, Chile) IOCG deposits of different age and districts are also presented. For each of the deposits, the alteration nomenclature used in the source reference was modified to the alteration facies nomenclature presented in this contribution to better highlight the similarities in the alteration type and their zonation.

Sodic alteration is the earliest, deepest and most regionally intense alteration across the GBMZ, but also in most of the IOAA districts worldwide (Figs. 3-10 – 3-13). In the GBMZ, albitisation and transitional sodic–calcic alteration preferentially takes place along fault zones within basement prior to and during 1.87 Ga volcanism. Pluri-kilometre long corridors of sodic alteration form at the expense of any type of volcanic rocks including basalt, intrusions including diorite, and sedimentary rocks including marble (e.g., Southern Breccia, Ham, JLD, DeVries; Fig. 3-2). That albitisation started prior to final emplacement of magmas within such intrusions and the presence of syntectonic to post-tectonic intermediate to felsic dikes within albitite corridors suggest that magmas and fluids were both channelled along the same structural discontinuities in a positive feedback relationship.

The resulting fluid-rock interactions must have been extremely efficient under high fluid/rock ratios. The high salinity of the fluids at the sodic alteration stage provides abundant ligands to efficiently carry leached metals, but also a wide variety of other elements. Where carbonates or evaporites (if present) occurred along such pathways, the metasomatic fluid-rock reactions typically devolatilised most of the carbonates and dissolved most of the halides and sulfates to incorporate large amount of CO_2 and/or $Cl+SO_4$ in locations such as Grouard, NICO and South Duke system. The starting depth of IOAA systems to form albitites can be as little as 3 km based on the Mag Hill cross section (Fig. 3-4a) and the exhumation of Treasure Lake Group units during the formation of the Southern Breccia near the NICO deposit. This is not without similarities to the depth documented by Reed et al. (2013) for porphyry systems.

Dissolution-reprecipitation processes during albitisation created porosity that can preferentially partition subsequent brecciation and fracturation in the albitite corridors during recurrent deformation and faulting under high or lower temperature regimes. For example, brecciated albitites are cemented by HT calcic–iron alteration at DeVries, LT potassic–iron alteration at Damp and uranium-rich HT potassic–iron alteration in the Southern Breccia (Table 3-1; Corriveau et al., 2007; Acosta-Góngora et al., 2014; chapitre 6). Brecciation and alteration of albitites have not been recorded where they have been pervasively recrystallized to or where they have crystallised with a medium-to-coarse grain size within the contact aureole of intrusive bodies (e.g., Mag Hill; Fig. 3-4a).

As the fluids percolate through the crust, continuous fluid-rock reactions, fluid mixing and changes in P–T progressively modify the physico-chemical properties of the initial fluid(s) involved at the sodic alteration stage. These interactions trigger a sequential precipitation of elements and metals in the following alteration stages (Fig. 3-10). As the incoming highly saline *Fluid(1)* reacts with *Precursors(1)* to form the *Facies 1* albitites, the outgoing *Fluid(2)* carries with it *Fluid(1)* metal budget as well as the precursor metal budget leached from *Precursors(a)* during albitisation. The highly charged *Fluid(2)* then reacts with *Precursors(2)* or *Facies 1* fine-grained albitites to form the highly diagnostic *Facies 2* HT calcic–iron alteration mineral parageneses. Such alteration crystallises across zones of tens to a few hundred metres in diameter (Fig. 3-12). Though minerals suitable for fluid inclusions are rare within *Facies 2* HT calcic–iron alteration and veins (cf. Acosta-Góngora et al., 2015a), the amphibole–magnetite paragenesis and the modal composition of this alteration facies provide conclusive evidence that the fluids had high contents of calcium and iron, with and without phosphorus. Vanadium (in magnetite), rare earth elements (primarily in apatite) and locally thorium precipitate leading to specialised-metal iron oxide±apatite (IOA) prospects among *Facies 2* HT calcic–iron alteration zones (Fig. 3-4c). The physico-chemical properties of the fluids that lead to such alteration and associated mineralisation have been studied in most details in the Mag Hill area (Somarin and Mumin, 2014).

Hitzman et al. (1992) modelled sodic (calcic) alteration as 1) deep, 2) regional in scale, 3) adjacent to intrusions or along major fault zones, and 4) lateral to zones of upward fluid flow that lead to IOCG deposits at higher levels. They include within their sodic (calcic) alteration sporadic zones of magnetite mineralisation (±Cu, ±Au, ± U) typical of Kiruna-type deposits (see also Barton and Johnson, 1996; Williams, 2010b; Williams et al., 2010; Barton, 2014). Their sodic (calcic) alteration paragenesis consists of albite with and without magnetite, amphibole and

clinopyroxene. However, GBMZ mapping highlights that *Facies 1* albitisation destroy magnetite instead of producing it and should be distinguished from *Facies 2* HT calcic–iron alteration to better guide exploration towards iron oxide±apatite and subsequent deposit types (Fig. 3-3; Annexe 3; see also Chen et al., 2010a).

For the purposes of vectoring to mineralisation, Corriveau et al. (2010b) distinguished alteration stages that are associated with polymetallic copper-sulfide mineralisation from those that served as ground preparation (albitisation) or were considered as only fertile in iron (IOA). Current research worldwide highlights that *Facies 2* HT calcic–iron and associated IOA mineralisation play a major role in the genesis of specialised metal associations and that albitite within IOAA systems can become preferential hosts for uranium mineralisation (Fig. 3-10; Corriveau et al., 2011; Fadda et al., 2012; Nold et al., 2013, 2014; Wilde, 2013; chapitre 6). Facies 1 is associated with all GBMZ IOAA systems irrespective of whether they include all subsequent alteration facies or not. This also applies to most of the IOAA systems observed worldwide (cf. compilation work of Williams et al., 2005 and Porter, 2010; Figs. 3-11 – 3-13). Facies 1 without laterally extensive transitional *Facies 1–2* HT sodic–calcic–iron alteration does not evolve to polymetallic mineralisation that includes base and precious metals (Fig. 3-2). In IOAA systems fertile in IOA or IOCG mineralisation, the *Facies 1–2* HT sodic–calcic–iron typically forms a transitional zone between zones of strong albitisation and zones of strong HT calcic–iron alteration (Figs. 3-2, 3-4 and 3-11; Port Radium–Echo Bay and Camsell River districts) or HT potassic–iron alteration (Figs. 3-11, 3-13).

Where well developed and rich in magnetite, the HT sodic–calcic–iron and HT calcic–iron alteration zones can yield vanadium-rich IOA mineralisation (Fig. 3-5); the HT calcic–iron alteration zones that transition to *Facies 2–3* HT calcic–iron–potassic or *Facies 3* HT potassic–iron alteration can have IOA mineralisation rich in vanadium and/or REE with or without uranium (Fig. 3-5). Among the GBMZ alteration types, such mineralisation has the highest heavy to light REE ratios (*e.g., samples 09CQA-1173B and 09CQA1170D02 in appendix 3*; Corriveau et al., 2015). This is also observed in other IOA deposits such as the Kwyjibo deposit in the eastern Grenville Province (Clark et al., 2010). Base and precious metals can also locally precipitate in HT calcic–iron zone where there is a *Facies 3* HT potassic–iron and *Facies 5* LT potassic–iron alteration overprint. Based on the work in the GBMZ and global analogues, progressive intensification of HT calcic–iron alteration vectors to iron deposits potentially endowed in specialised metals, in particular vanadium and/or heavy REE elements. The diagnostic mineral assemblages of this alteration are relatively simple to map and to discriminate

lithogeochemically, and typically predates IOCG mineralisation where present (see also Kiruna, Cloncurry, Missouri, Bafq, Kwyjibo; Hitzman et al., 1992; Clark et al., 2010; Daliran et al., 2010; Xavier et al., 2010; Nold et al., 2013, 2014; Barton, 2014). The apatite content of the HT calcic–iron alteration zones provides a first order indication of the REE potential of the associated IOA deposits.

3.5.3 From IOA to polymetallic IOCG deposits

The *Fluid(3)* released after *Facies 2* alteration reacts with a *Precursors(3)* or *Facies 1 or Facies 2* alteration zones if they were brought tectonically within the stability field of the ascending *Fluid(3)* to form *Facies 3* HT potassic–iron alteration and concomitant brecciation (Fig. 3-10). Copper-sulfides precipitate within such breccias either as disseminations within Facies 3 veins and breccia infills or form distinct quartz–sulfides veins that crosscut Facies 3 alteration. The appearance of copper-sulfide is regular where Facies 3 alteration becomes intense, penetrative and associated with brecciation. The commonalities in timing and spatial distribution with respect to other alteration types again is interpreted as a consanguineous development between *Facies 3* and the precipitation of copper-sulfides and highlights the importance of framing alteration linkages to mineralisation over the scale of alteration development (commonly hundreds of metres for the HT potassic–iron alteration) and not simply at the microscopic scale (Figs. 3-9o–p, v, 28_{C10}; Sue-Dianne, Southern Breccia, Brooke, Fab, Hoy, Mile, K2). Where Facies 1 and Facies 2 form at the expense of carbonate units, large amount of CO_2, calcium and magnesium are released into Fluid(2) and Fluid(3). This may significantly increase the stability field of amphibole which can then remain stable during Facies 3 development (Fig. 3-11a). In such cases, biotite commonly prevails over K-feldspar and arsenopyrite prevails over chalcopyrite within the resulting iron oxide-rich mineralised zones. In the GBMZ, this has resulted in Au–Co–Bi–Cu mineralisation at the NICO deposit and South Duke system.

At the magnetite-to-hematite transition, where carbonates occur as precursors or where carbonates are precipitated as alteration products prior to progression of isotherms through fluid influx, polymetallic skarns form and are systematically potassic altered (cf. paths in Fig. 3-3; Fig. 3-10). In silicic precursors, local zones of brecciated K-feldspar-rich (modal content of K-feldspar in the alteration > 75 %) felsite are formed (Fig. 3-10). Collectively, these alteration types form striking megascopic markers for the magnetite-to-hematite transition zones and potential base and precious metal IOCG mineralisation (Fig. 3-11b). These develop within veins, breccias and as disseminations as described in detail in Mumin et al. (2010) for the Sue-Dianne and NICO

deposits and IOCG prospects across the belt (Table 3-2). Such relationships are also observed at Ernest Henry, Candelaria and Mantoverde (Figs. 3-11, 3-13, 4_{C10}; Marschik and Fontboté, 2001a; Mark et al., 2006; Reiger et al., 2012).

Sericitic/hydrolithic (H^+) alteration as per Hitzman et al. (1992) comprises hematite with white mica (sericite), carbonate and/or chlorite with or without quartz, barite and fluorite. This alteration typically forms a few hundred metres below the paleosurface along zones of upward flow (Figs. 3-11b, 3-12). Such zones that can be shown to evolve from higher-temperature IOAA alteration form the immediate host to polymetallic hematite-group IOCG mineralisation with and without uranium and light REE as observed at the Olympic Dam, Prominent Hill, Sossego and Mantoverde deposits (Figs. 3-10, 3-11b, 3-12; Fig. 6 in Hitzman et al., 1992; Fig. 23 in Mumin et al., 2010; Fig. 18 in Williams et al., 2005; Fig. 1 in Williams et al., 2010; Skirrow, 2010). The occurrence of alteration assemblages constituted only of white mica and/or K-feldspar and/or chlorite does not vector to mineralisation nor does it constitute a diagnostic evidence of an IOAA system. The addition of specular hematite with these minerals marks the paragenesis that delimits the components of IOAA systems prospective for polymetallic hematite-group IOCG mineralisation (Figs. 43–44_{C10}; Corriveau et al., 2010b). Light REE-bearing minerals can be abundant in such mineralisation but largely occur as aphanitic minerals that cannot be mapped in the field without analytical equipment. Recent and properly configured portable XRF expands REE exploration effectiveness. In addition, uranium and thorium, where associated with this alteration, are easily detectable with a gamma-ray spectrometer, a rugged instrument that can be carried in any fieldwork conditions. Substantial changes in the eU/eTh ratios in IOAA alteration zones are typically diagnostic of underlying REE enrichments or depletions and may lead to the discovery of REE mineralisation.

During retrogression, alteration minerals of the high-temperature alteration (K-feldspar, amphibole or biotite for example) are predominantly replaced by hydrous minerals or carbonates (sericite, chlorite, calcite, siderite). As more oxidised conditions prevail, hematite instead of magnetite typically forms with these minerals such as observed at NICO (Acosta-Góngora et al., 2014). Where retrogression relates to the ingress of external lower temperature fluids, the precursor alteration zones are typically retrogressed at greater intensity then simple cooling of in situ fluids and new metals can be brought in by the incoming fluids. In cases where fluids associated with retrogression expand beyond the footprint of the earlier prograde alteration through recurrent faulting or highly permeable units for example, or that retrograde fluids are reheated by renewed higher temperature fluid influx, distinguishing the prograde from the

retrograde sequence can be difficult as discussed in Mumin et al. (2010). A practical empirical tool is to assess the degree of obliteration of precursor textures by specular hematite and the spatial extent of hematite breccias. For example, the complete replacement of precursors by specular hematite in the Port Radium–Echo Bay and East Hottah systems is prograde (Fig. 3-4a; Mumin et al. 2010). Where amphibole–magnetite alteration is overprinted by K-feldspar–chlorite–hematite such as at NICO and in the South Duke system then the K-feldspar–chlorite–hematite assemblage is interpreted as retrograde (Acosta-Góngora et al., 2015b).

3.5.4 Epithermal and polymetallic vein-type deposits

Many alteration types in IOCG systems are under saturated in silica and commonly dissolve quartz even though microcrystalline quartz may remain in quartz-rich precursors in many alteration facies (DeToni, 2016; Jeanne Percival et al., unpublished data). In contrast, the very last gasp of IOAA system development can lead to significant quartz precipitation associated with basic to acidic fluids and derived alteration types (phyllic, argillic, advanced argillic alteration; Fig. 3-10). The formation of veins of barite is interpreted to mark the transition to epithermal systems (Mumin et al., 2010; Pelleter et al., 2010; Kreiner and Barton, 2011). Silica flooding leads to decametre- and hectometre-wide quartz stockworks (e.g., Sue-Dianne deposit), to kilometre-long quartz veins with or without Ag and U vein-type mineralisation (GBMZ; Badham, 1975; Gandhi et al., 2000; Byron, 2010; Mumin et al., 2010) and to fairly massive silicification zones that can reach hundreds of metres in diameter (e.g., Greater Lufilian Arc; Lobo-Guerrero, 2010).

In many cases, metal associations of the lower temperature and/or peripheral mineralised veins reflect a local source of metals derived from their host IOAA systems and their higher temperature iron oxide and alkali-rich alteration envelope. For example, the metal association in the vein-type mineralisation of the historical Eldorado mine in the Port Radium district consists of Ag, As, Au, Bi, Co, Cu, Mn, Mo, Ni, Pb, Ra, Sb, U, V, Zn (Mumin et al., 2010; Bretzlaff et al., being submitted). In the sulfide- and magnetite-rich IOAA alteration zones hosting the polymetallic veins of the Eldorado deposit, the metal association consists of Ag, As, Co, Cu, Fe, Mn, Ni, Pb and Zn whereas that of the magnetite–apatite-rich IOAA alteration zones without sulfides consists of iron and vanadium. At NICO, the metal assemblage in the main ore zone consists of As, Au, Bi, Co, Cu and Fe whereas the metal association in the peripheral vein-type mineralisation of the NICO deposit (NICO zones 1 to 3 and Summit Peak) consists of Ag, As, Au, Bi, Co, Cu, Fe and W. Accordingly metal associations from known prospects including vein-

type mineralisation can be used to portray potential metal associations of their IOAA systems across the belt in Figure 3-1b. Their association with IOAA geological and geophysical signatures is highlighted by their spatial associations with the geophysical footprints of the IOAA systems as modelled by Hayward et al. (2013; Fig. 3-1c) and with the IOAA alteration types (Fig. 2) across the GBMZ. This has wide implications as a vector to potential IOCG and IOA mineralisation in historic uranium districts as gold and uranium rich veins have been discovered worldwide during decades of uranium exploration (Kish and Cuney, 1981).

3.6 A predictive exploration tool with case examples

The systematic space–time relationships between the various alteration and mineralisation types formed in IOAA districts with or without IOCG mineralisation can be framed within an IOAA deposit model (Fig. 3-10). The IOAA deposit model predicts that deposit types prograde from IOA at the HT calcic–iron alteration facies, to magnetite-group and hematite-group IOCG respectively at the HT potassic–iron and LT hydrolytic potassic–iron alteration facies. Albitites in IOAA systems is a common ground preparation stage for polymetallic albitite-hosted uranium mineralisation (Fig. 3-10) as observed worldwide including in the Romanet Horst of the Labrador Trough, Québec (Corriveau et al., 2014). In calcium-rich systems, a LT calcic–iron hydrolytic alteration can form at the end of the IOAA system development prior to, or coevally with, quartz flooding. Epithermal alteration develops subsequently and at a higher structural level than the IOAA systems per se or can be superimposed on it. The LT potassic–iron alteration facies is retrograde where the system has collapsed on itself through cooling of fluids or where the alteration is formed through ingress of low-temperature fluids where higher temperature alteration facies are telescoped to higher levels as in the two stage model of Skirrow (2010).

3.6.1 Immature sodic and HT calcic–iron alteration systems

The alteration facies model illustrates that sodic and HT calcic–iron alteration zones, even where mildly overprinted by fertile alteration types, do not correspond to facies that form significant base and precious metal-endowed polymetallic IOCG deposits. In contrast HT calcic–iron alteration facies can lead to magnetite–apatite and magnetite–apatite–specialised-metal deposits. In the GBMZ, drilling of conductors in positive magnetic anomalies in areas of ubiquitous sodic to HT calcic–iron alteration (Mag Hill, Port Radium) or where these alteration types are common in the area (K2) led to the discovery of vanadiferous magnetite–apatite

mineralisation at depth (Mumin et al., 2010) and of rare earth elements within the magnetite-rich HT calcic–iron–potassic alteration host to the historic Echo Bay mine (Fig. 5). At Nod, geochemical analyses along historic drilling (MacKay and Eveleigh, 1997) indicate systematic sodium enrichment (≤8 wt. % Na_2O) and low K contents in weakly mineralised HT calcic–iron–potassic alteration overprinting pink to red albitites. Nevertheless, these rocks were described as K-feldspar–iron oxide breccias, likely due to the colour of the albitites. In both the Mag Hill/Port Radium and Nod systems, the absence of intense HT and LT potassium–iron alteration is compatible with the low Cu–Au–Ag–Co–Bi contents of the intersected mineralised zones and highlights the need of distinguishing pink albitites from the potassic–iron alteration and the K-feldspar felsite breccias that are proximal to copper-sulfide mineralisation. Conversely, the lack of significant retrograde alteration suggests that remaining fluids and their metals (if present) have escaped the sector drilled and may have continued their evolution to form fertile alteration. Discrimination of sodic and potassic alteration from the fertile HT and LT potassic–iron alteration types also discriminates zones of intense alkali alteration that remove metals from those where iron oxide and metals are being precipitated. Near-offset geophysical high density but lower magnetic susceptibility anomalies can point out to magnetite-to-hematite transition and to base- and precious-metal mineralisation as observed in deposits worldwide (Smith, 2002; Belperio, 2007; Clark, 2014).

3.6.2 Property-scale implications of the cyclical development of fertile HT Ca–Fe–K and HT K–Fe alteration in an IOAA system

Many IOAA systems evolve through repetitive cycles of differential burial and exhumation, transtensional to transpressional faulting, and telescoping and translation of alteration types. Several pulses of stratabound to discordant alteration fronts, veins and breccias host the Au–Bi–Co–Cu ore zones at NICO and record cyclical development of HT calcic–iron and HT potassic–iron alteration in Treasure Lake Group metasedimentary rocks. Prior to renewed mapping of the NICO alteration envelope during the current project, laterally extensive zones of sodic alteration were conspicuously absent in maps and drill core description (Mumin, 1997; Goad et al., 2000a, b; Sidor, 2000) although sodium-rich and leucocratic granitic intrusions had been reported to the South (Gandhi et al., 2001). The only found record of potential albitisation was observed in the metasiltstone unit forming the footwall of the deposit (K. Neale description of drill hole 96-19; Mumin, 1997).

Considering the documented evolution and interpreted interdependence of alteration facies across the GBMZ illustrated in the alteration facies model of Figure 3-10, a re-examination of the NICO deposit area was undertaken to find the inferred missing intense and large-scale albitisation zones. In addition, the lack of very intense hematization in the deposit prompted a broadened search for HT potassic–iron (K-feldspar–magnetite), K-feldspar felsites and LT potassic–iron (K-feldspar/sericite–hematite±chlorite±carbonate) alteration zones that may have formed from the fluids potentially expelled from the NICO deposit HT calcic–iron alteration zone. Renewed alteration mapping led to the discovery of a NW-SE-trending, 3 km-long albitisation corridor that hosts a series of albitite-hosted U–Th±Cu–Mo showings related to ilmenite-, rutile- and titanite-rich HT to LT potassic–iron alteration (chapitre 6). Intense chloritization or K-feldspar alteration occurs locally over tens of metres.

In contrast to NICO, the Southern Breccia zone has nearly no HT calcic–iron alteration (except in its north-eastern sector where it developed locally). Albitites formed as the Treasure Lake Group was deformed, brecciated and locally folded along a deformation corridor regionally parallel to Treasure Lake Group bedding. At NICO, the prograde mineralisation is coeval with magnetite–biotite alteration superimposed over earlier HT calcic–iron alteration (Acosta-Góngora et al., 2014, 2015a) whereas in the Southern Breccia the mineralised HT potassic–iron alteration is directly superimposed over the albitites. Both the Southern Breccia and NICO are subsequently affected by hematite alteration but their mineralisation types are distinct with prevailing arsenopyrite at NICO and uraninite in the Southern Breccia (Goad et al., 2000a, b; chapitre 6). Differential exhumation, collapse and tilting of the Faber volcanic and underlying Treasure Lake Group sedimentary sequences as well as the alteration signatures of both sectors indicate differential exhumation of the NICO and Southern Breccia components during the formation of their host IOAA system (Mumin, 1997; Enkin et al., 2012; chapitre 6). The overall architecture of the host IOAA system (Fig. 4b) is interpreted as related to progressive thrusting of the Southern Breccia albitites to the crustal level of the NICO deposit ore zone. Precursor fluids formed albitites at depth and outflowing fluids reacted with the carbonate unit of the Treasure Lake Group and thoroughly replaced it and the underlying metasiltstone unit to form the pervasive, extensive and intense HT calcic–iron alteration which then evolved to HT calcic–iron–potassic alteration and precipitated metals in NICO. In contrast, the uplift of the early and previously deeper sodic alteration brought the Southern Breccia albitites to the crustal level where fluids had reached the stability field for HT potassic–iron alteration (see also Potter et al., 2013b; chapitre 6). Both NICO and Southern Breccia then evolved to LT potassic–iron alteration.

This case study illustrates that development of high temperature (e.g., HT calcic–iron and potassic–iron) or low temperature (e.g., LT potassic–iron) alteration in a section of a system can be indicative of complementary lower and higher temperature fluids in the shallower and deeper sections of the system. If preserved, these zones are prospective for polymetallic mineralisation. The observation of low temperature IOAA alteration at interpreted shallower crustal levels may indicate that higher temperature IOAA alteration types with IOCG mineralised zones can be present in the deeper part of the system. For example, Mina Carola shares alteration attributes and deposit size with NICO transitional calcic–iron–potassic alteration. This deposit is a satellite to the Candelaria magnetite-group IOCG deposit (Marschik and Fontboté, 2001a). The spatial relationship between these two deposits is compatible with their overall development within a single IOAA system and in line with the IOAA deposit model described in Fig. 10. This case example is of great significance for exploring the Great Bear magmatic zone and other prospective but under explored districts.

The NICO case example also illustrates the importance to revisit the genesis of Co–Cu–Au deposits hosted within metasedimentary rocks as done by Slack (2013) in the Blackbird–Idaho Cobalt Belt in the USA. To this effect, government surveys are currently re-examining the Missouri iron oxide–apatite district and the albite-hosted polymetallic mineralisation of the Romanet Horst in the Labrador Trough both well studied in the 1990s (e.g., Kish and Cuney, 1981; Day and Lane, 1992). Potter et al. (2013a) illustrate how historic mineral districts with IOAA attributes can be strategically re-examined and explored using current knowledge and exploration models. Application of this alteration facies model to under-explored or poorly exposed prospective terrains, districts and deposits provides a mean to target their fertile areas and enlarge the realm of deposit types to explore for. It also provides a structured framework to map the otherwise complex alteration zones of IOAA systems, comprehend their holistic interconnections and explore the extraordinary range of deposits efficiently at all scales. The distinctive geochemical footprints of the IOAA alteration facies and their vectoring potential to IOCG mineralisation that is independent of the intricacies of the complex interplay among sources for fluids and metals can also be applied to optimise alteration mapping while exploring for metamorphosed ore deposits (Corriveau and Spry, 2014).

3.7 Conclusions

In the GBMZ, the lateral and vertical bulk chemical transformation of precursor rocks and orderly spatial and temporal mass transfer of elements from sodic to HT calcic–iron, HT potassic–iron, K-feldspar-stable felsite breccias and skarns, and LT potassic–iron alteration facies led to a large spectrum of IOCG and affiliated mineralisation and deposits. As alteration facies prograded from the roots of the IOAA systems to their epithermal caps, precursor mineral assemblages of supracrustal and hypabyssal intrusive rocks were thoroughly destabilised at centimetre, metre and kilometre scales coevally with volcanism, emplacement of sub-volcanic intrusions and dikes swarms, build-up of magma chambers, and highly partitioned brittle and brittle-ductile deformation (e.g., Mile, Terra, NICO, Southern Breccia, South Duke).

Fluid-rock interactions resulted in a regular sequence of initial recharge of metals/elements during the sodic and sodic–calcic alteration stages and then progressive and selective metal/element discharge in the following alteration stages. Diagnostic mineral assemblages define each stage of the evolution of the IOAA system. Iron starts precipitating at the HT calcic–iron alteration facies followed by specialised metals to form specialised-metal IOA deposits as this alteration facies evolves towards the HT potassic–iron alteration facies. Base and precious-metals sulfide mineralisation is an intrinsic consequence of the development of the latter alteration facies and associated brecciation. Subsequently, K-feldspar-dominant felsite breccias and skarns form where magnetite crystallisation, within the HT potassic–iron alteration facies, wanes and gives way to precipitation of hematite within the LT potassic–iron alteration. The presence of carbonate alteration subsequently skarnified at the magnetite-to-hematite transition at the Mile breccia provides evidence that IOAA system fluids can generate their own skarn facies without being directly in contact with an intrusion. Sustained and iterative fluid ingress and induced heat advection are viewed as key elements in the development of the giant alteration systems of the GBMZ. Processes that favoured telescoping of alteration and fluid mixing appear to have enhanced the potential of IOAA systems to host significant polymetallic mineralisation, a condition also described for the most fertile districts worldwide. The alteration facies defined in this contribution, when systematically mapped across under explored and virgin territories of the GBMZ as well as in its most explored district, become key exploration vectors to IOCG mineralisation regardless of how the IOAA system evolved through time and space. This approach also provides a powerful tool to re-examine historic data and reassess the mineral prospectivity of their host IOAA system or to identify previously unrecognised IOAA systems.

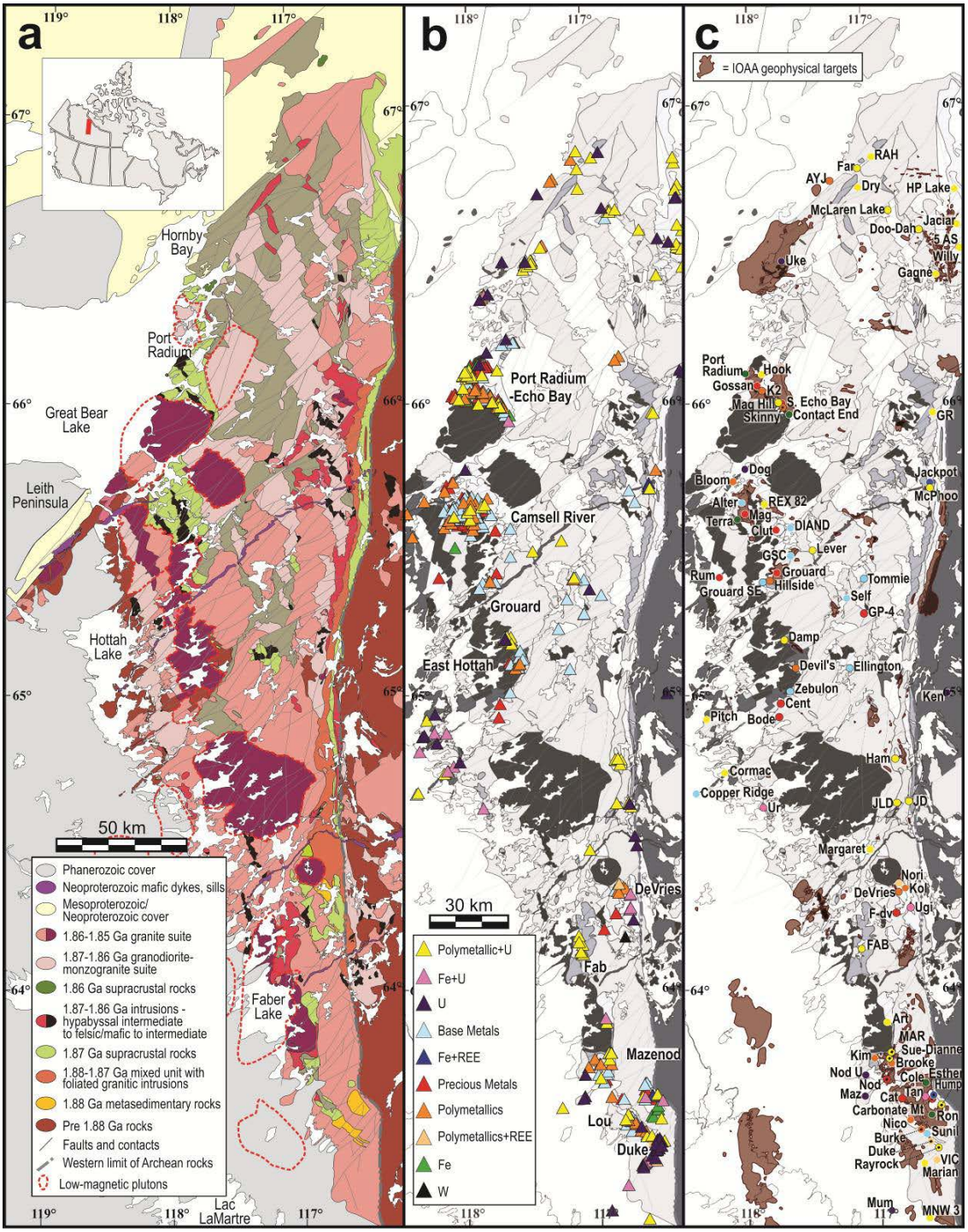

Figure 3-1 Geology and mineral occurrences of the Great Bear magmatic zone

(a) Synthesis geological map; inset locates the Great Bear magmatic zone in Canada. (b) Metal associations of deposits, mineral prospects and showings from NORMIN database (www.nwtgeoscience.ca/normin) and Bretzlaff et al. (being submitted). (c) Location of representative showings, prospects and deposits, and geophysical footprints of IOAA systems and potential systems after Hayward et al. (2013). Lithological units in grey shade refer to units in (a).

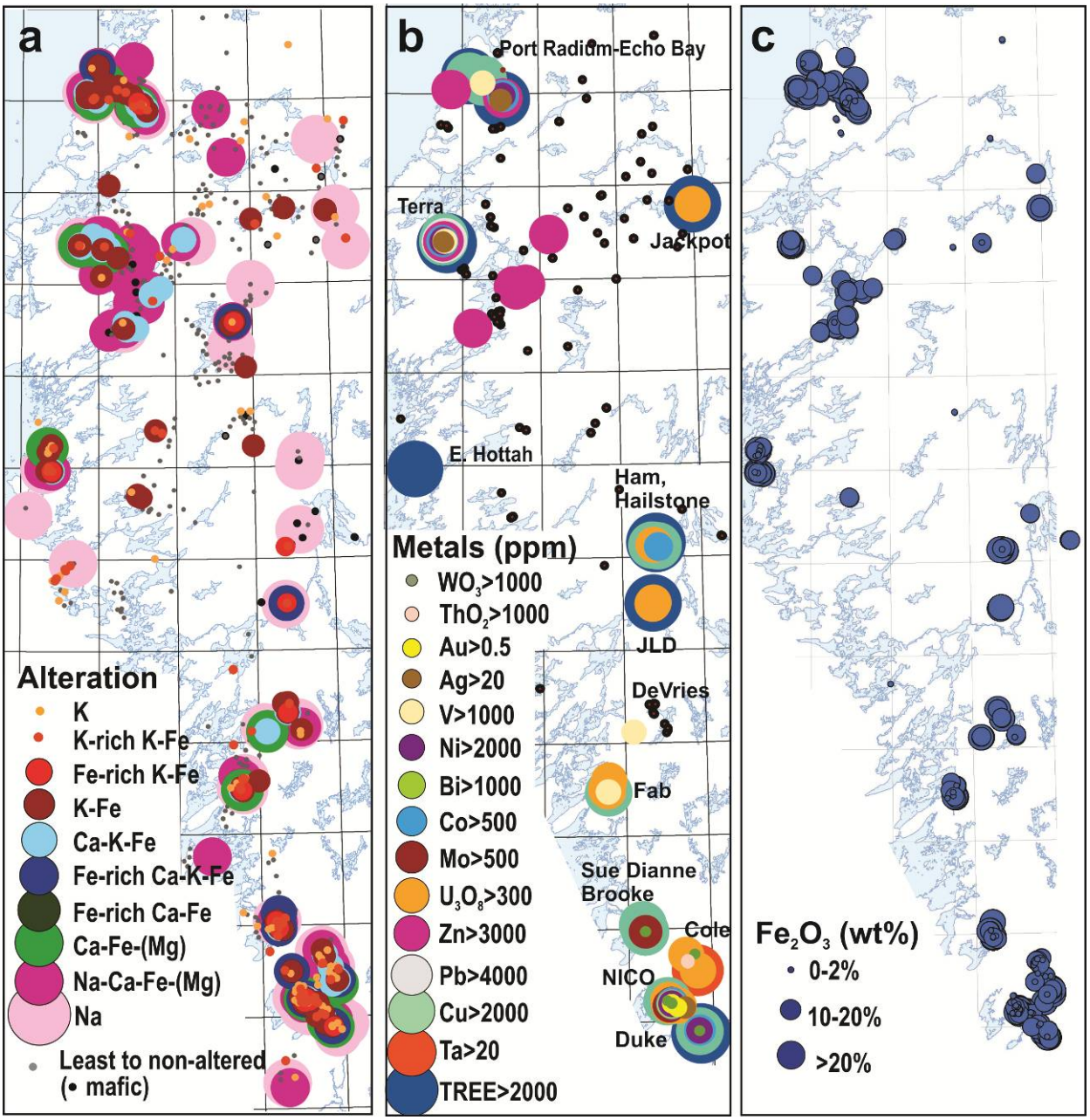

Figure 3-2 Alteration, metal and iron distribution in the IOAA systems of the Great Bear magmatic zone

(a) Alteration types based on the lithogeochemical signatures of the studied IOAA systems (geochemical data from Corriveau et al., 2015); alteration indexes used to estimate alteration after chapitre 5. (b) Distribution of anomalous metal concentrations (above the NORMIN threshold) based on geochemical data from Corriveau et al. (2015). (c) Fe_2O_3 concentrations measured throughout the GBMZ based on geochemical data from Corriveau et al. (2015). Such enrichments and depletion highlights location of IOAA systems and contrast potential discharges zones from leaching zones.

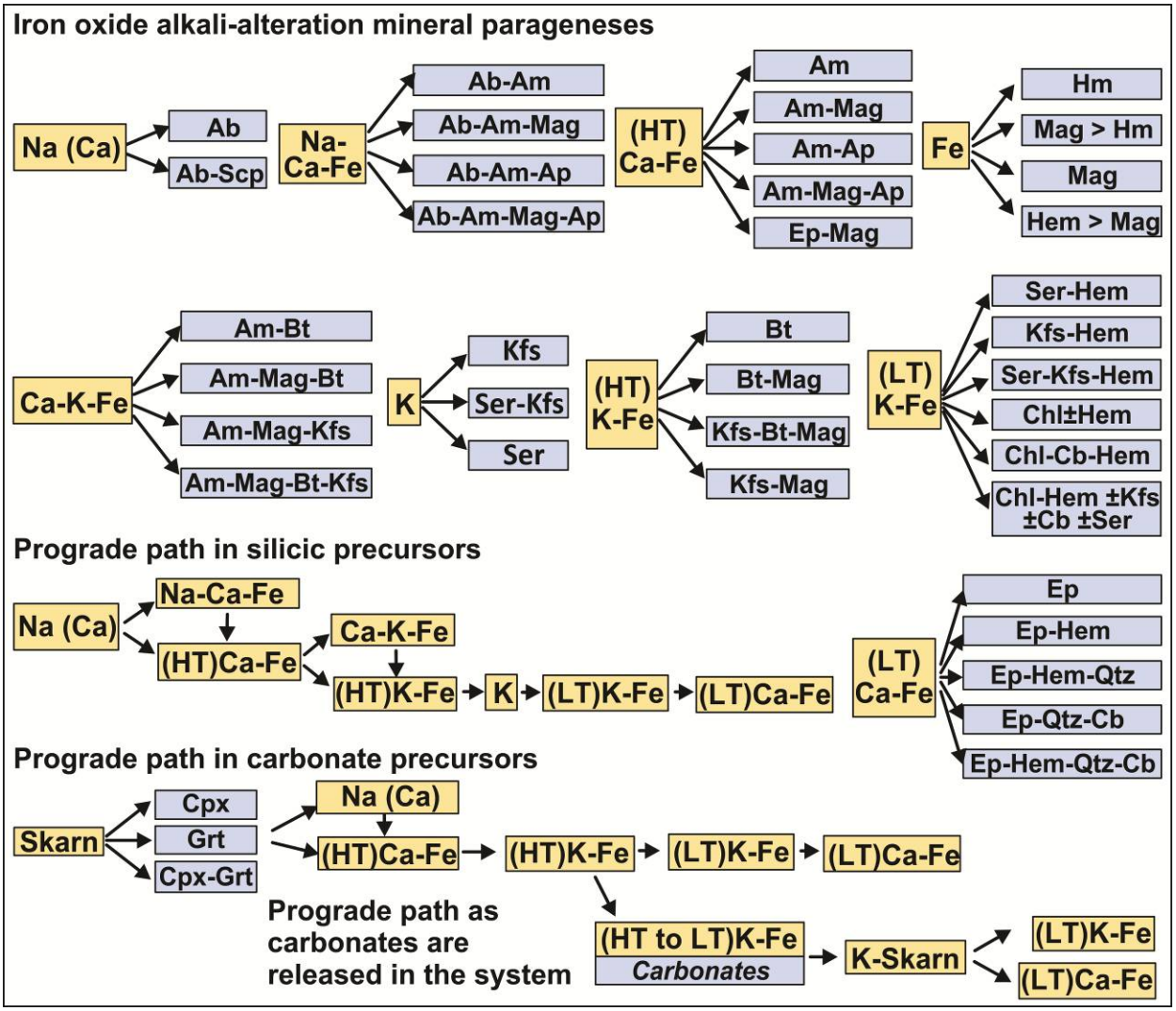

Figure 3-3 IOAA alteration mineral parageneses and prograde succession of alteration facies at the expense of silicic and carbonate units labelled by their discriminating major-element cations

This sequence is derived and expanded from the initial work of Corriveau et al. (2010b).

HT = high temperature; LT = lower temperature; mineral abbreviations in this and subsequent figures after Whitney and Evans (2010).

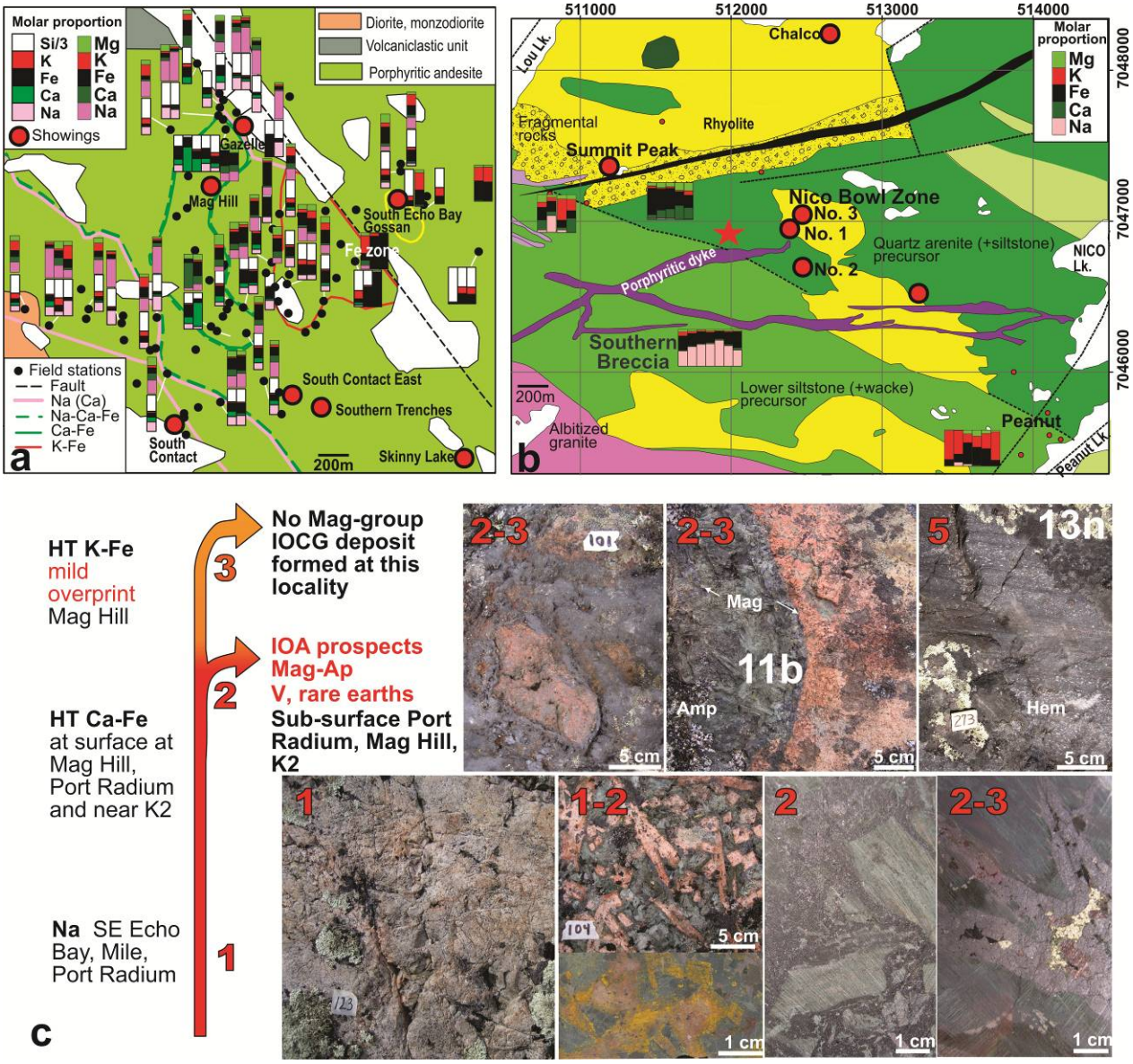

Figure 3-4 Alteration distribution and evolution across the eastern margin of the Port Radium–Echo Bay IOAA system and geological map of the NICO and Southern Breccia host sequences

(a) Structural depth profile across the eastern margin of the Port Radium–Echo Bay IOAA system. The system is tilted exposing the complete set of metasomatic facies as described in Fig. 3-4c. Alteration development is illustrated by the molar proportion of discriminating cations; geochemical data from Corriveau et al. (2015). (b) Geology of the precursor units of the NICO deposit and Southern Breccia corridor within the Lou IOAA system and location of prospects after Gandhi and Lentz (1990), Goad et al. (2000a, b) and chapitre 6. (c) Evolution of alteration leading to the development of the Mag Hill iron oxide–apatite prospect at depth (Mumin et al. 2010), (1) albitites, (1-2) Facies 1–2 HT sodic–calcic–iron alteration where the stained slab highlights the mild K-feldspar–magnetite-stable HT potassic–iron overprint (CQA-05-105), (2) Facies 2 HT Ca–Fe Mag Hill drill core with composition shown in Fig. 3-5, (2–3) transitional HT calcic–potassic–iron alteration observed at surface, and (5) Facies 5 LT potassic–iron hematitite (CQA-05-273). All metasomatites shown have replaced a porphyritic andesite of the LaBine Group mapped by Hildebrand (1981, 1983).

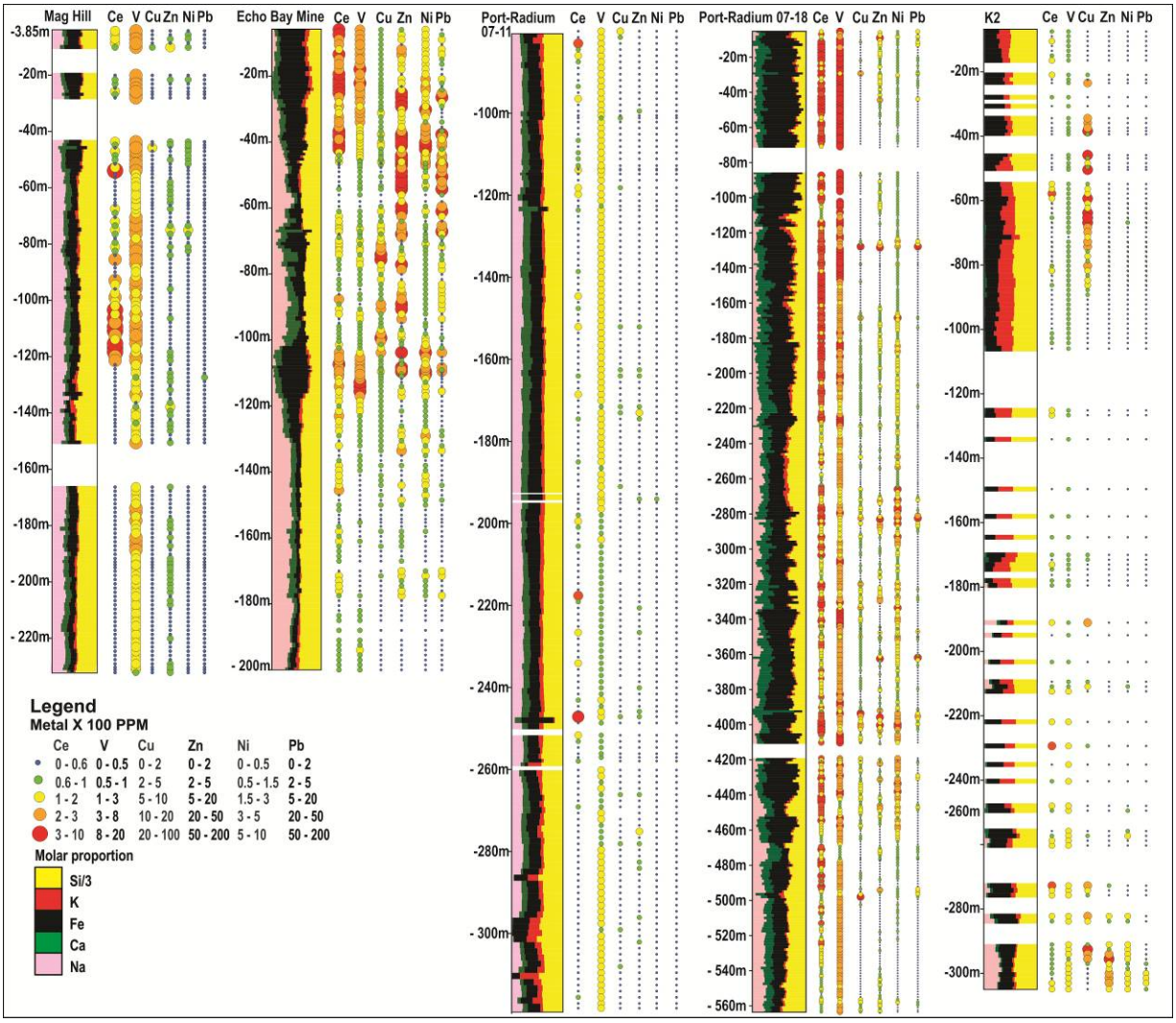

Figure 3-5 Alteration of porphyritic andesite portrayed by molar proportion of Na, Ca, Fe, K and Si along drill holes across IOA mineralisation at the Mag Hill, Echo Bay and Port Radium prospects and IOCG mineralisation at the K2 prospect of the Port Radium–Echo Bay district

Metal associations typical of IOA include vanadium and rare earths such as Ce. At Echo Bay, the imprint of potassic–iron alteration is significant and at K2, IOA mineralisation at depth transitions to IOCG mineralisation towards surface. Copper mineralisation is associated with coeval enrichment in iron and potassium (see also geochemical study of chapitre 5).

The mineralized zones are described in Mumin et al. 2010. The geochemical analyses are a courtesy of Alberta Star from their proprietary geochemical dataset of the Port Radium–Echo Bay district.

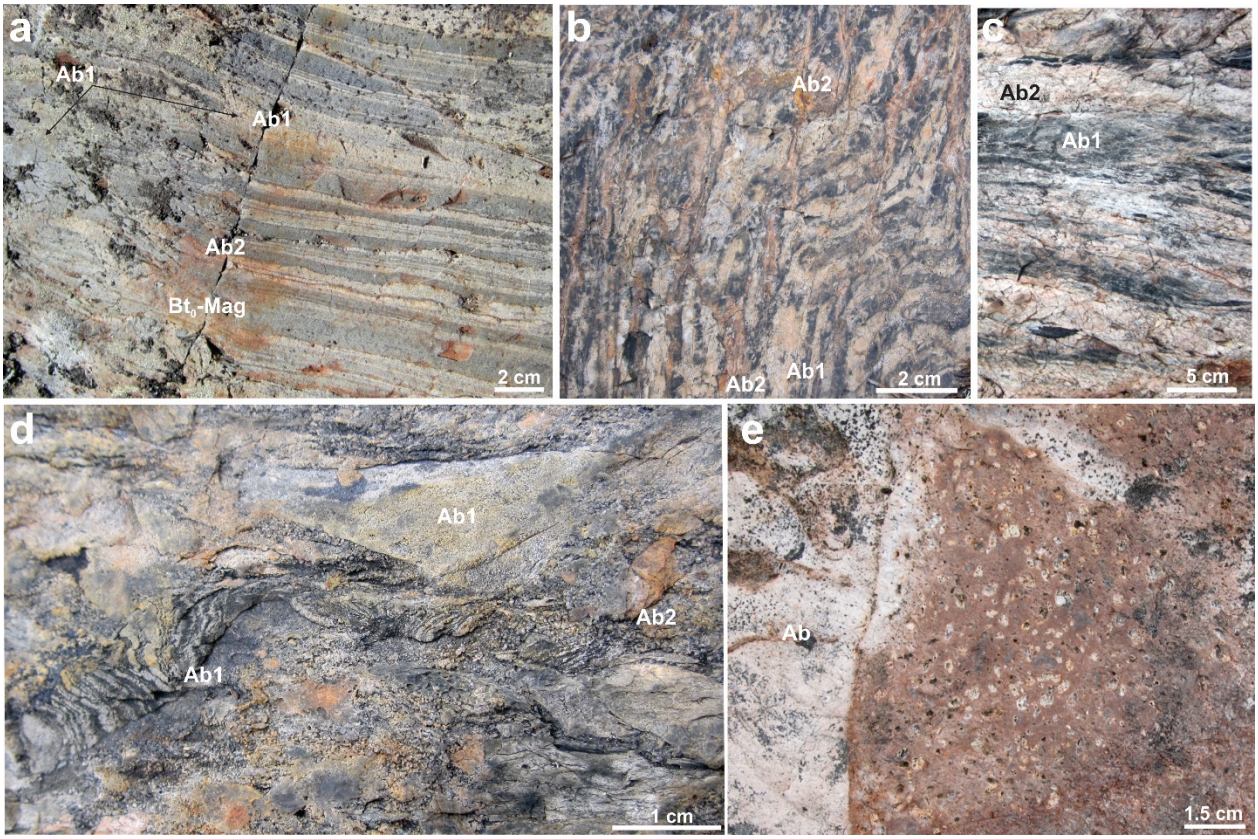

Figure 3-6 Sodic alteration textures in the Great Bear magmatic IOAA systems

(a) Selective stratabound magnetite–biotite (Bt_0–Mag) and sodic (Ab1) alteration of Treasure Lake Group metasedimentary rocks locally overprinted by a pervasive sodic alteration (Ab2) at Southern Breccia (11PUA-0517); (b) Concordant sodic alteration (Ab1) partially overprinted by a stronger sodic alteration (Ab2) front in the Treasure Lake Group at the Southern Breccia (10CQA-1636); (c) Intensification of the Ab2 sodic alteration front that destroys the primary sedimentary textures of the siltstone (10CQA-1637); (d) Complete brecciation and selective magnetite replacement of the intensely sodic-altered (Ab2) metasiltstone of the Treasure Lake Group at Southern Breccia (10CQA-1644); (e) Texture-destructive sodic alteration front of feldspar porphyry at Cole (09CQA-1122).

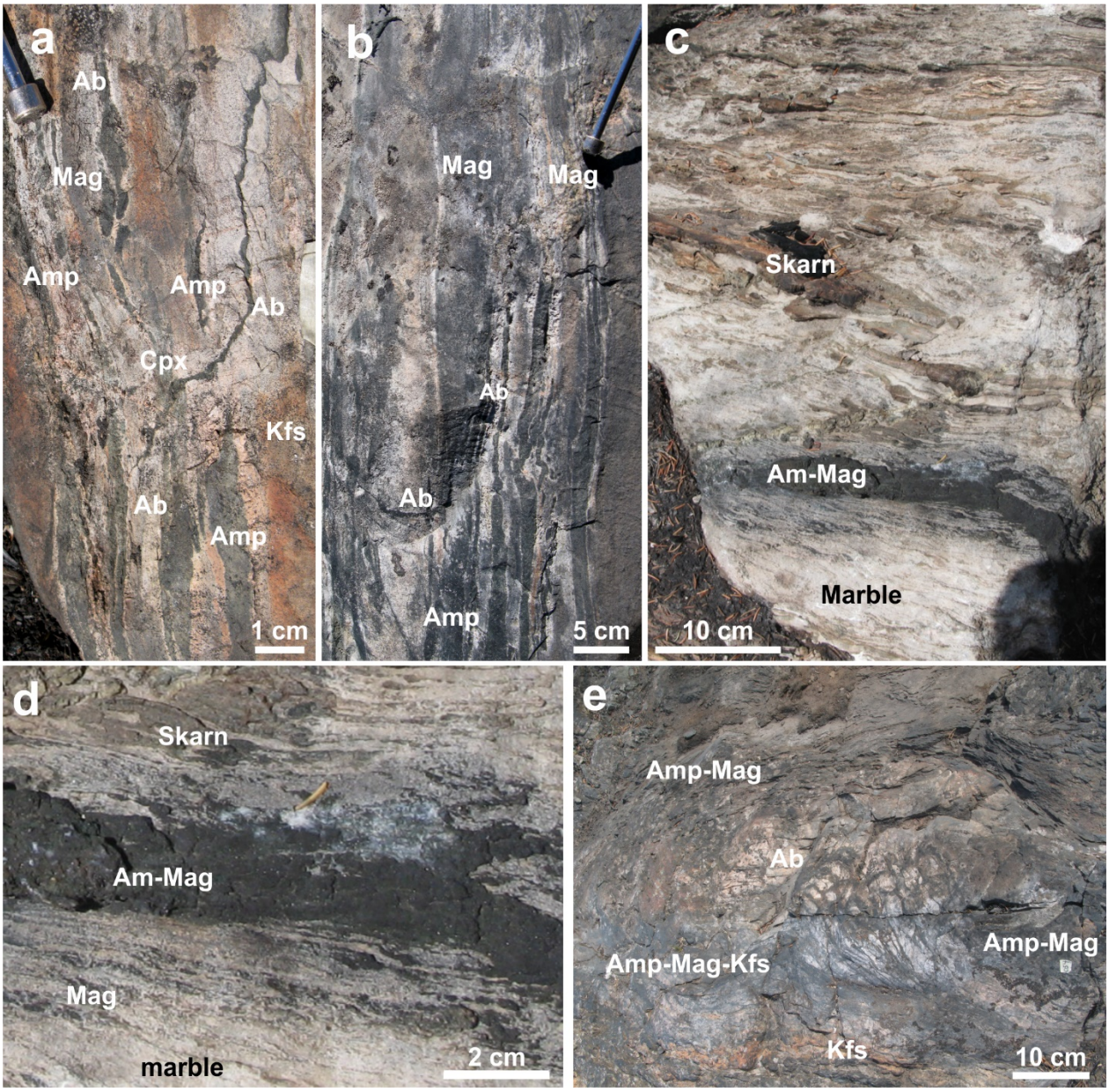

Figure 3-7 Development of IOAA alteration at the expense of precursor siltstone, carbonate (with calc-silicates, siltstones and wackes) and quartz-arenite members of the Treasure Lake Group

Alteration sequence starts from lesser-altered precursors adjacent to the type section as described in Gandhi and van Breemen (2005) and Acosta-Góngora et al. (2014) (area west of the Sunil showing in Fig. 1c) to culmination of alteration intensity and pervasiveness northwards at the NICO deposit and southwards to the South Duke system and its various showings (Fig. 1c; Gandhi et al. 2014).

(a–b) Very thin bedded metasandstone unit replaced by selective, incipient to locally intense, stratabound amphibole and/or magnetite alteration (HT calcic–iron) and albite (sodic) alteration. Such coeval replacement and presence of crosscutting amphibole veins with extensive albite haloes highlight diagnostic attributes of transitional HT sodic–calcic–iron alteration. Local overprints of albitized areas by K-feldspar (potassic) alteration take on a darker brown orangey colour. Precursor remains in a grey tone and consist largely of quartz, feldspar and biotite; (c–d) Stratabound skarn and host marbles are crosscut by amphibole–magnetite (HT calcic–iron) veins with magnetite haloes (09CQA-0053); (e–g) Pervasive, stratabound to discordant, HT calcic–iron alteration within metasedimentary rocks (09CQA-0054) where in (*e)* the upper section with pervasive stratabound alteration of laminated precursor resemble an iron formation;

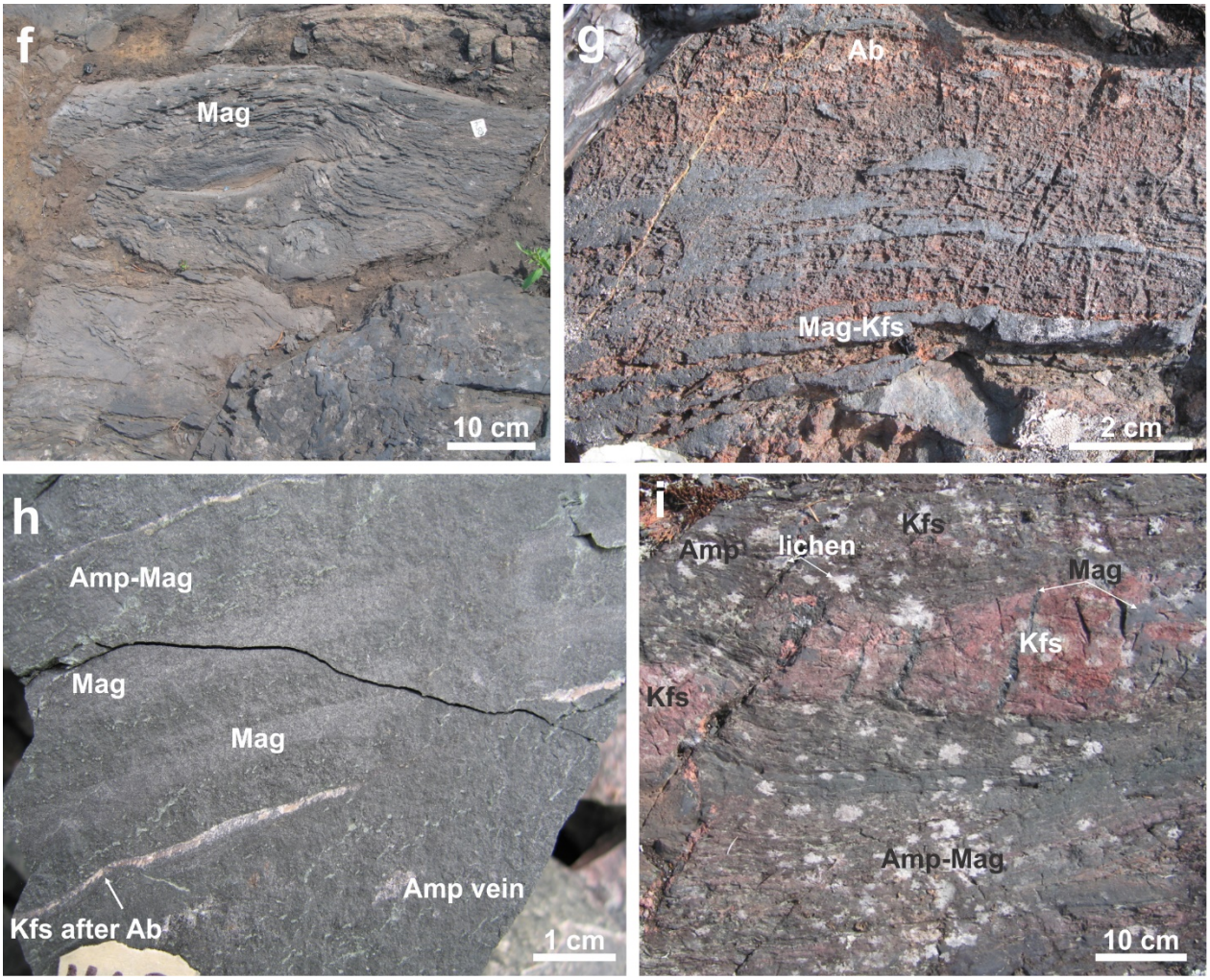

Fig. 3.7 suite – (f) Close-up of the upper section with pervasive stratabound alteration of laminated precursor that resembles an iron formation shown in (e). In (*g)* the magnetite replacement fronts are sharp and are associated with potassic selvages that replace albitized precursor; (h) Complete HT calcic–iron (amphibole–magnetite) replacement of the Treasure Lake Group quartz arenite cut by a subsequent generation of amphibole veins in the NICO deposit. The sample also contains relicts of potassic-altered albitized siltstone layers; (i) HT calcic–iron (amphibole±magnetite) replacement of a quartz arenite in the vicinity of the NICO deposit. Some of the arenite bed relicts are strongly K-feldspar altered (CQA-07-447);

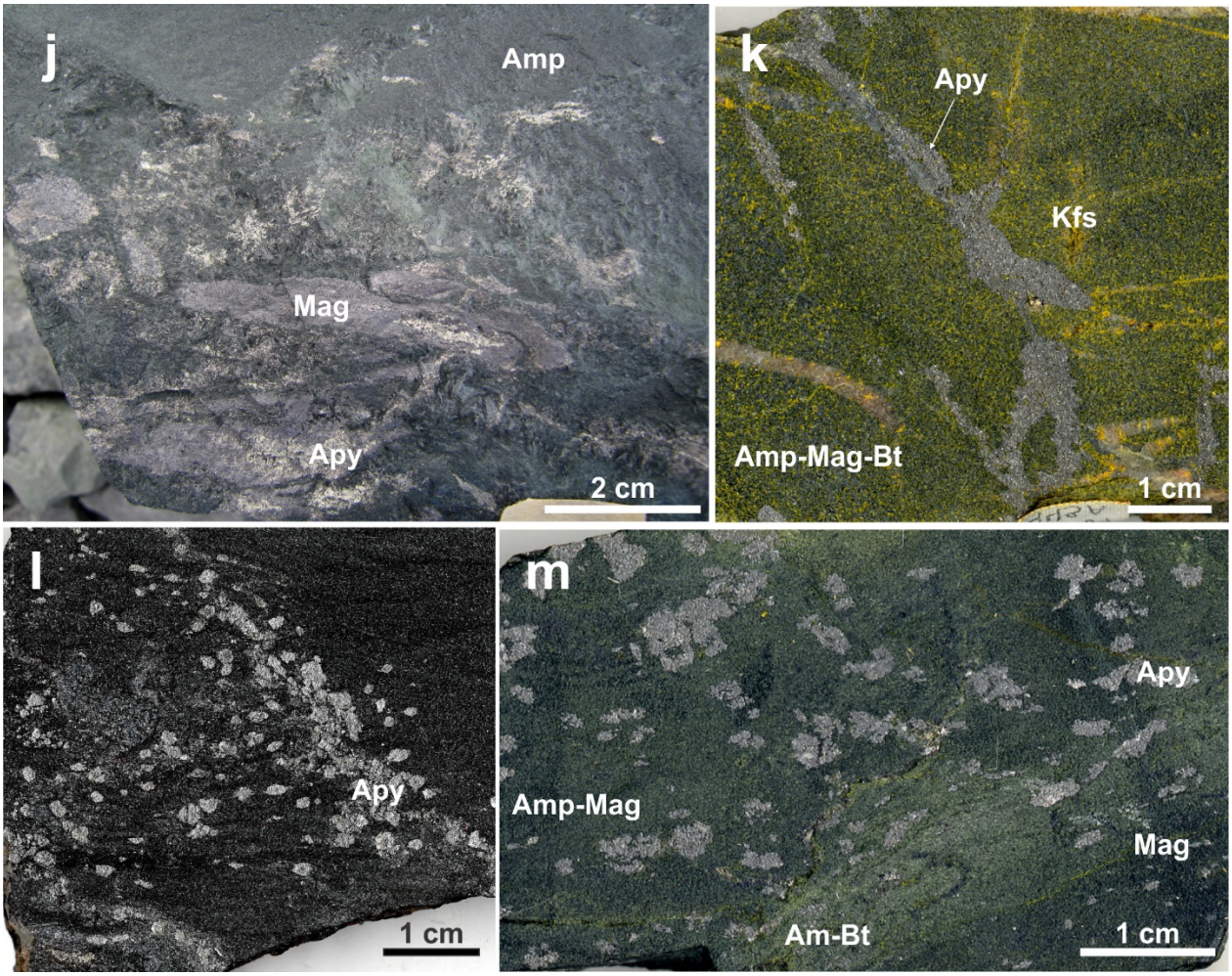

Fig. 3.7 suite – (j–m) Intense and pervasive magnetite–biotite–K-feldspar alteration at NICO cross-cut by arsenopyrite veins or disseminations along layering; k and m are stained slabs, magnetite stain black, amphibole dark green, amphibole–biotite light green and with K-feldspar the alteration take a yellowish green colour, K-feldspar stains yellow even if not abundant (j: CQA-07-480z, k: CQA-07-443, l: NICO Zone 1, m: CQA-07-465C).

Mineral abbreviations after Whitney and Evan (2010.

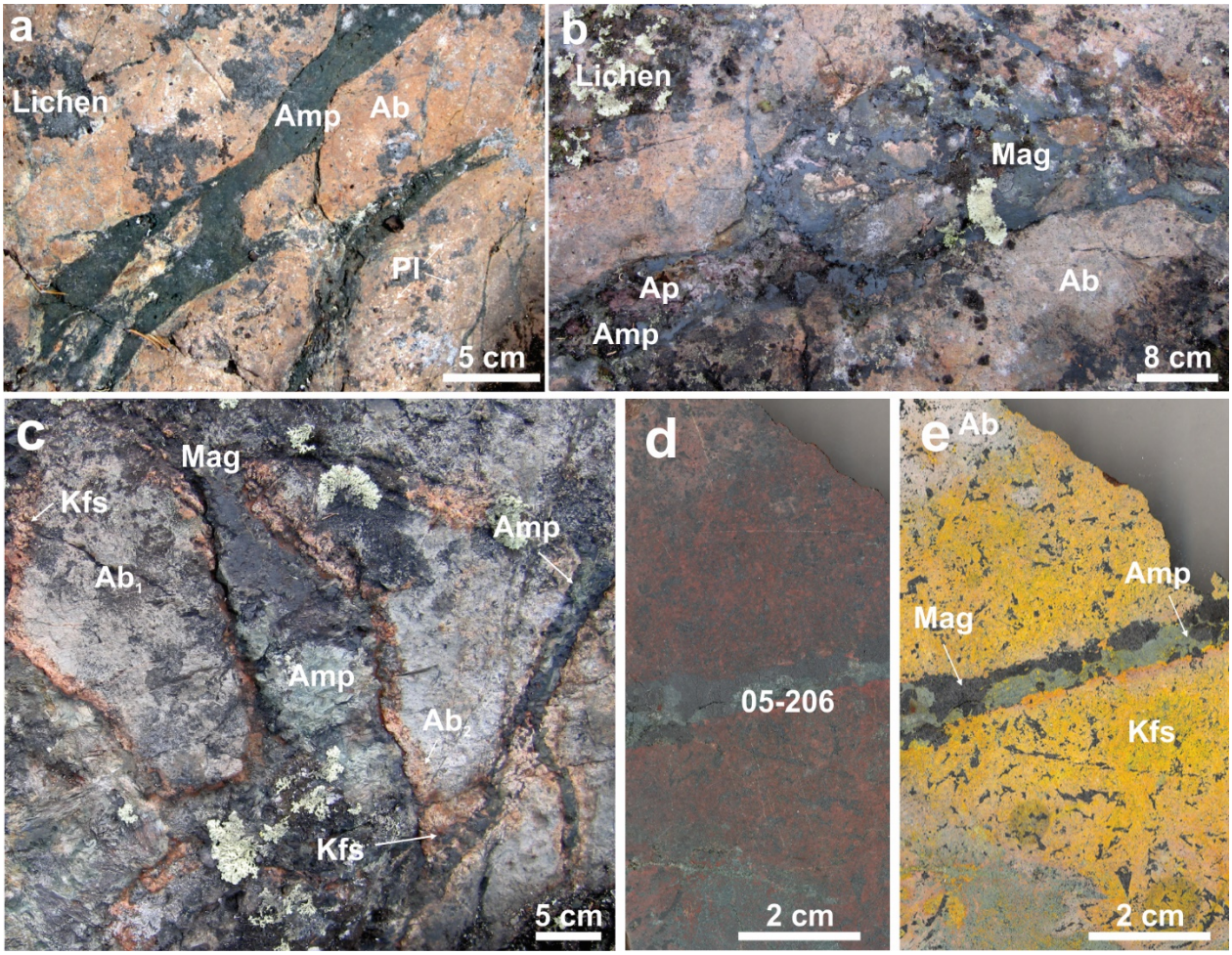

Figure 3-8 Typical examples of HT calcic–iron alteration and veins

(a) Amphibole veins in sharp contact with slightly albitized dacitic porphyritic intrusions at Fab (10CQA-0554); (b) Magnetite–amphibole–apatite stockwork cross-cutting strongly albitized porphyritic andesite (CQA-05-100); this zone is laterally proximal to drilled iron–vanadium mineralisation below the Mag Hill prospect; (c) Sodic-altered porphyritic andesite cut by amphibole veins with K-feldspar selvages at the transition between the calcic–iron and magnetite-bearing HT potassic–iron alteration stage in the Port Radium–Echo Bay district (CQA-05-201); (d-e) Transitional calcic–iron–potassic alteration comprised of an amphibole–magnetite vein with a K-feldspar selvage superimposed on a previously albitized porphyritic andesite (CQA-05-206). The cobaltnitrate staining of rock slabs in this and other figures follows the method of Gabriel and Cox (1929);

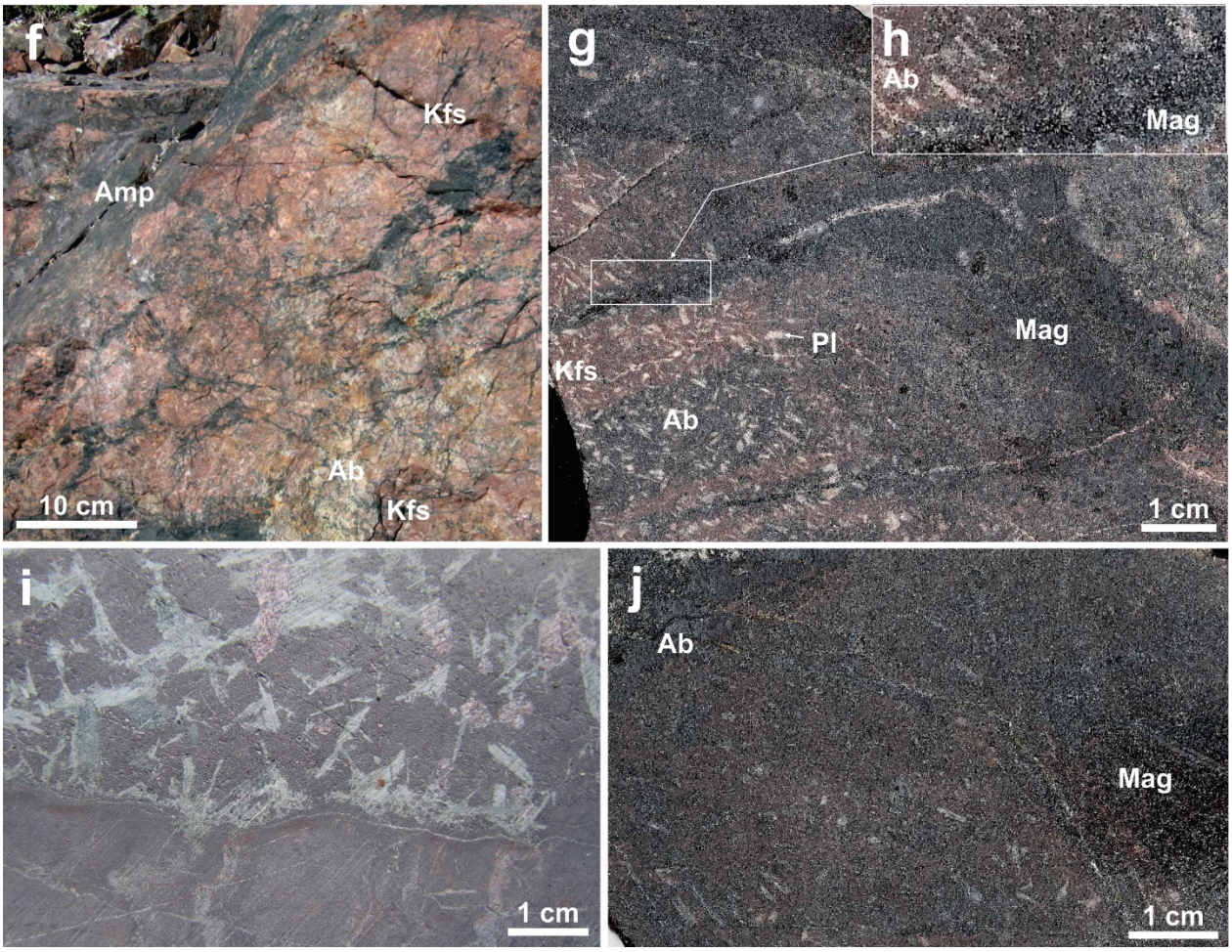

Fig. 3.8 suite – (f) Hydrothermal breccia formed at the calcic–iron–potassic alteration stage showing the partitioning between the ferromagnesian and felsic minerals as amphibole cements the breccia and K-feldspar alters the fragments, Fab system (CQA-06-392); (g-h) Selective in situ magnetite and K-feldspar replacement of the matrix of a sub-volcanic intrusion and prior albitisation of its plagioclase phenocrysts along haloes of a magnetite veins at the CAT showing (copper ± gold). Where the HT potassic–iron alteration is incipient (*g*), magnetite replaces preferentially the matrix but where most intense (*h*), magnetite replaces also the phenocrysts; (i-j) Drill core section of the Mag Hill vanadium-rich iron oxide prospect and associated HT calcic–iron alteration;

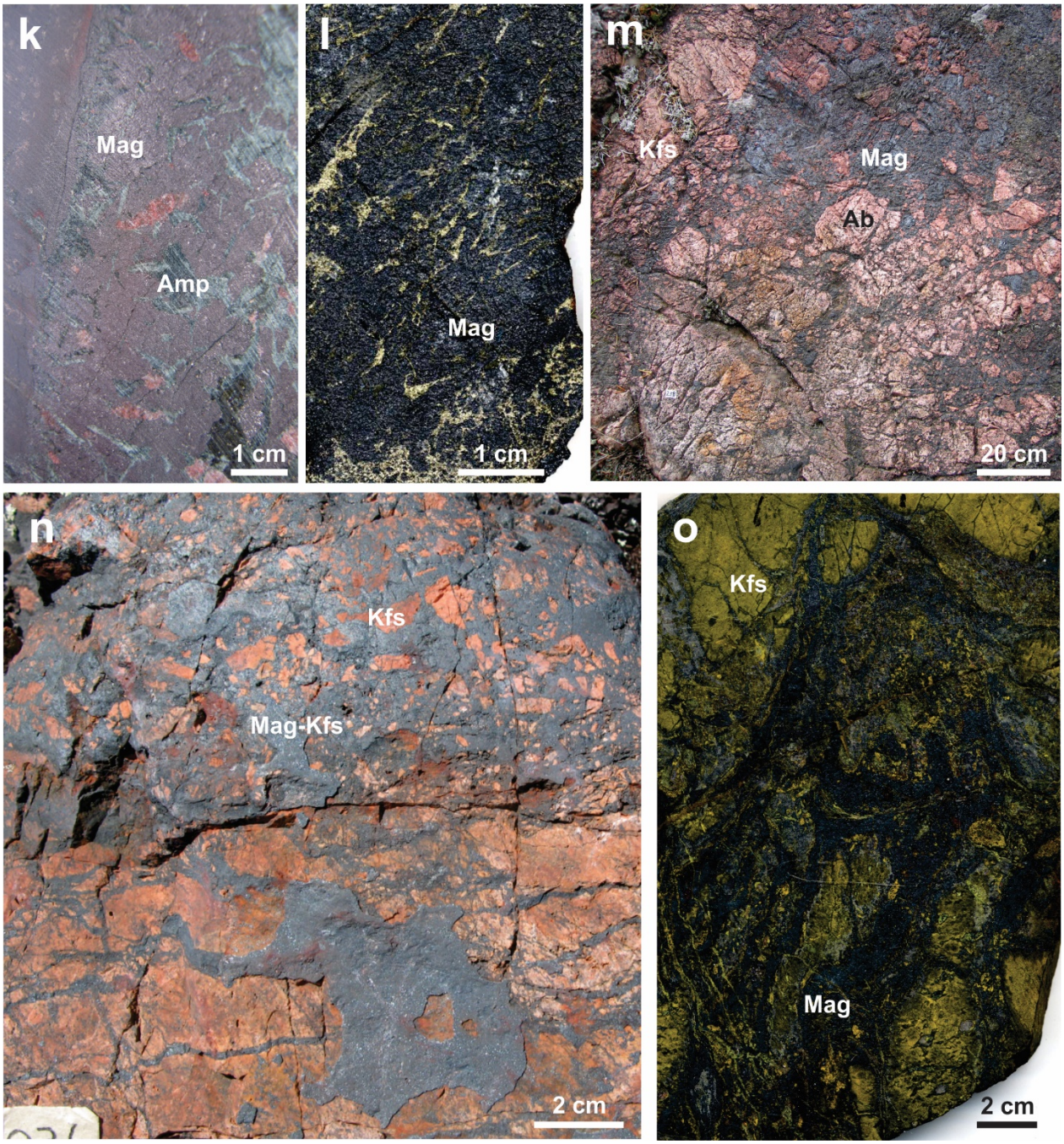

Fig. 3.8 suite – (k) Drill core section of the Mag Hill vanadium-rich iron oxide prospect and associated HT calcic–iron alteration; (l Chalcopyrite among magnetite and pyrite gangue within HT potassic–iron alteration at Ham (09CQA-1193; (m Magnetite breccia with K-feldspar alteration of fragments forming a HT potassic–iron alteration that replaces a previously albitized Faber Group volcanic unit at Mar in the Mazenod system (CQA-05-238; (n Magnetite-cemented breccia with strong K-feldspar alteration of the fragments at Brooke in the Mazenod system (09CQA-0026; (o Stained slab showing a REE-enriched magnetite-cemented breccia formed at the HT potassic–iron alteration stage in the East Hottah system (10CQA-0601.

Mineral abbreviations after Whitney and Evans (2010.

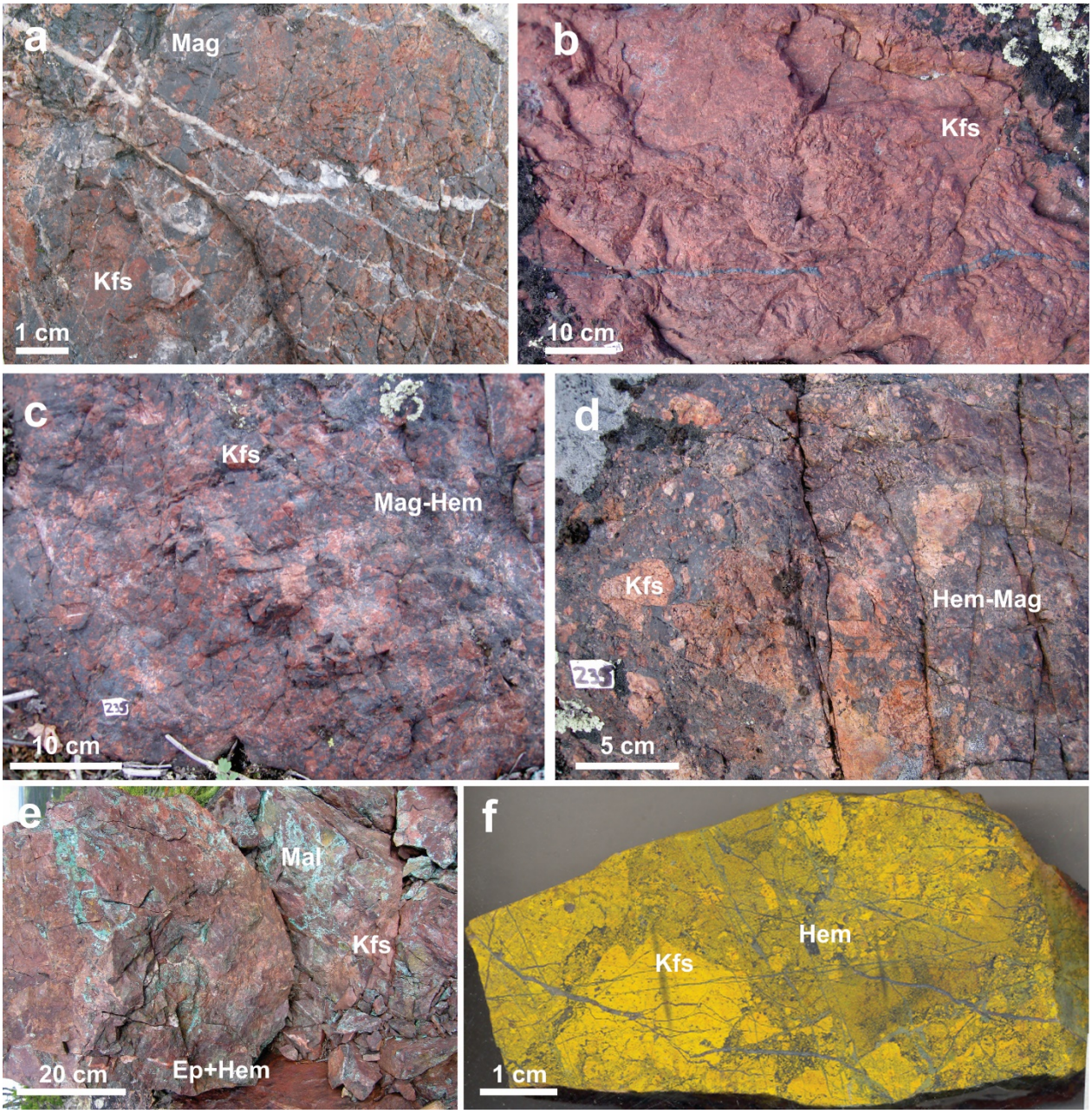

Figure 3-9 Typical alteration and mineralised zones of the HT potassic–iron, transitional K-felsite and K-skarn, and LT potassic–iron stages

(a–f) Transect across the margin of the Sue-Dianne ore zone as described in text; in *e* malachite forms on trench material of copper-sulfide mineralisation, otherwise malachite staining is extremely rare in natural outcrop of mineralisation in the GBMZ; in (*f*) the rock slab is stained and hematite veins remains a brilliant grey whereas magnetite and magnetite replaced by hematite are a dull dark grey-to-black colour (a: 09CQA-1024, b: CQA-05-234, c–f: CQA-05-235);

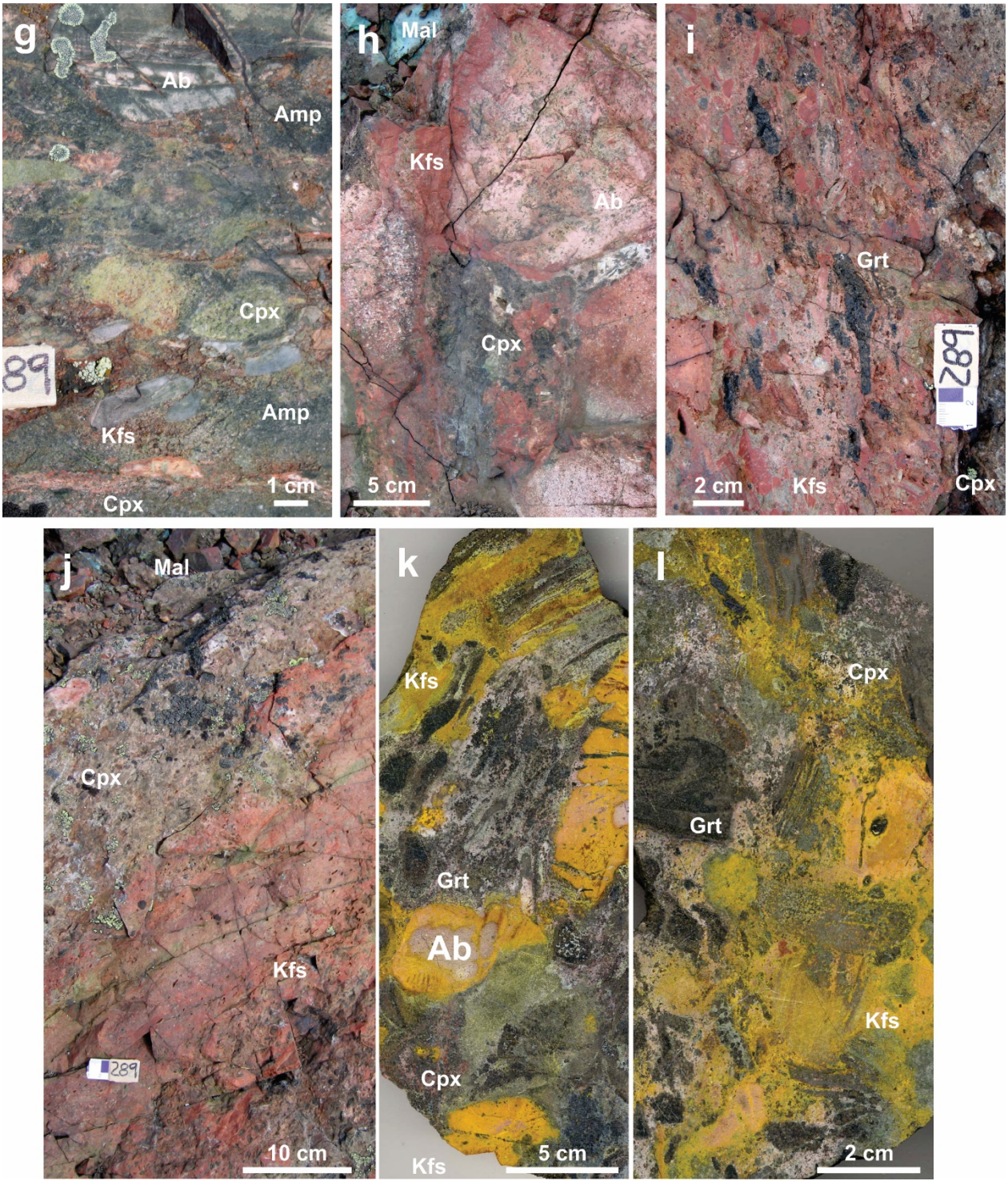

Fig. 3.9 suite – (g–l) K-feldspar-rich alteration and associated brecciation formed at the transition between the HT potassic–iron and LT potassic–iron alteration stages within albitized precursor fragmental or relatively equigranular volcaniclastic rocks at Mile in the Port Radium–Echo Bay district. Clinopyroxene-rich alteration is developed in a zone where intense K-feldspar and more localised amphibole, epidote or hematite alteration zones are also prominent, in (*g–j)* the K-feldspar alteration is observed to replace clasts along margins, internal fractures or pervasively whereas the extent of K-feldspar overprinting within matrix is best observed in (*k)* and (*l)* where feldspar is stained yellow by cobaltnitrate; clinopyroxene stains green, andradite garnet remains dark brown (CQA-06-289);

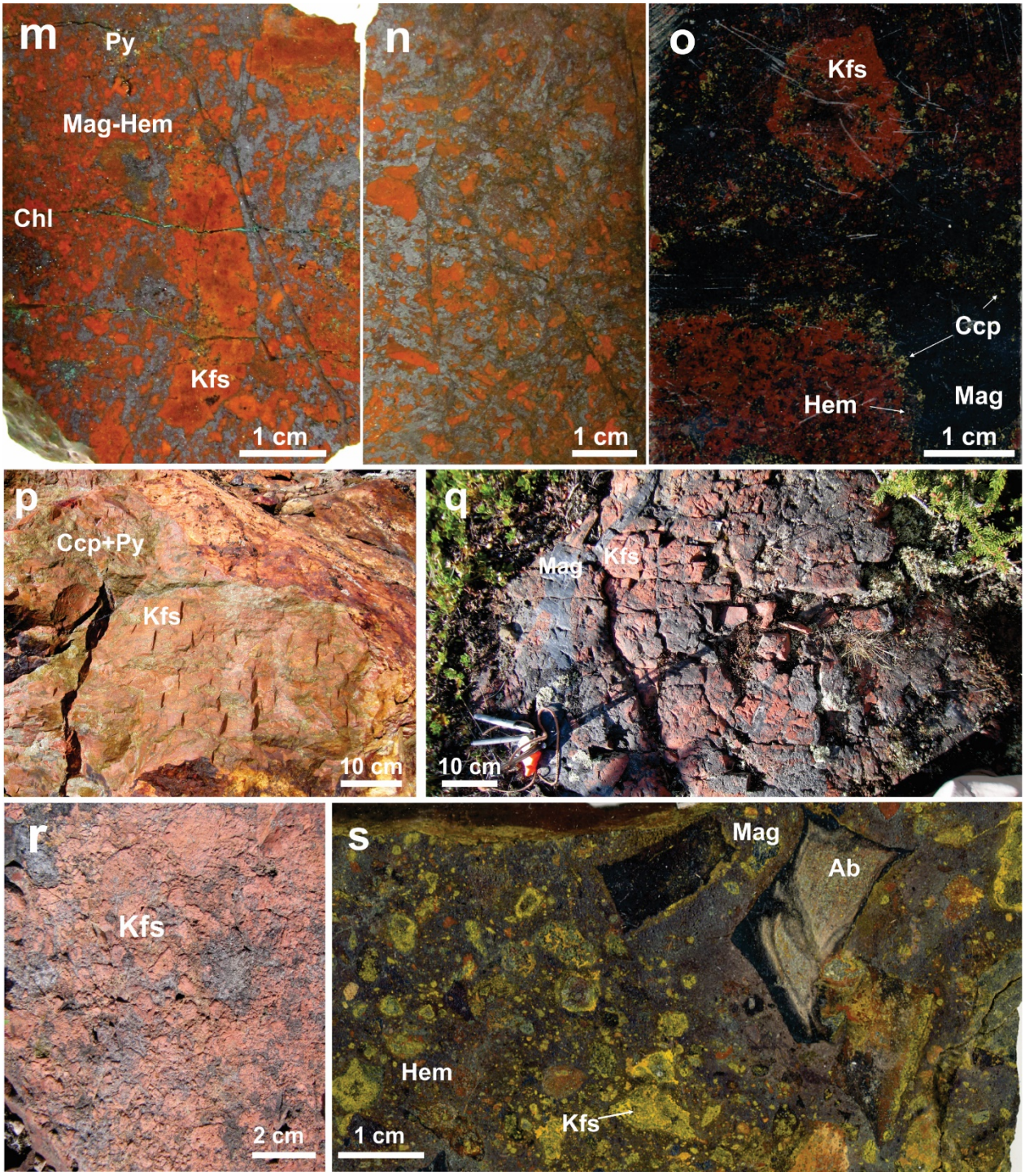

Fig. 3.9 suite – (m–o) Breccias with K-feldspar altered fragments and chalcopyrite-bearing magnetite and hematite fills at Sue-Dianne (KZ-09-SD-9, SD-10, drill hole SD-92-06 at 198.4 feet depth); (p) Chalcopyrite and gold mineralisation in intensely and pervasively K-feldspar-altered and mildly magnetite-altered Faber Group rhyolite at Summit Peak adjacent to the NICO deposit (10CQA-1647); (q–u) Hydrothermal iron oxide breccias with K-feldspar alteration of fragments associated with HT potassic–iron alteration of a previously albitized volcanic unit at Hoy Bay in the Port Radium–Echo Bay district. The HT potassic–iron alteration becomes overprinted by LT potassic–iron alteration and local potassic felsite developed at this magnetite to hematite transition (q–r: CQA-07-527, s: CQA-07-528h);

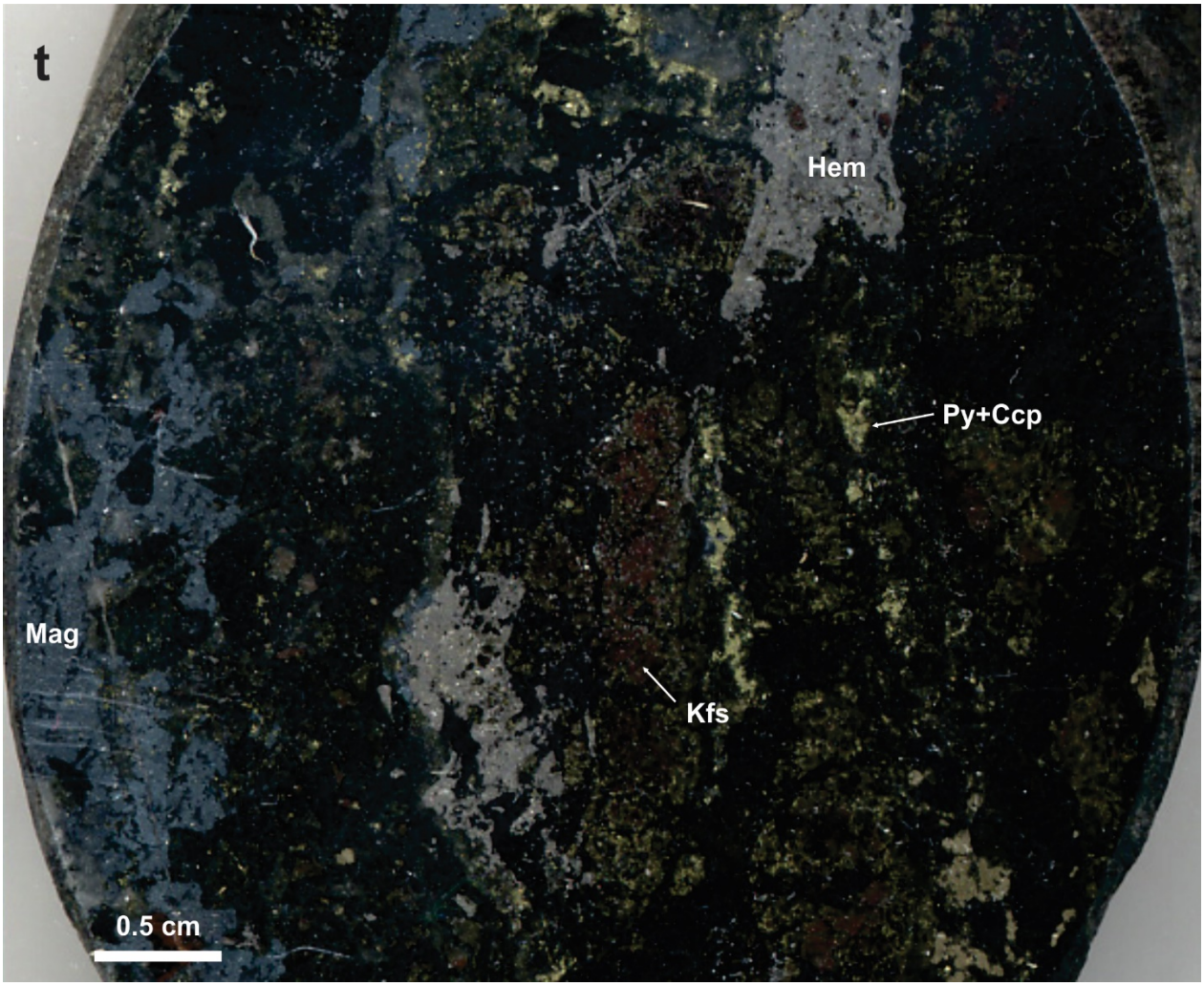

Fig 3.9 suite – (t) Cu-sulfide mineralisation at K2 prospect (drill hole CLK2, 255.75–255.95 feet depth)

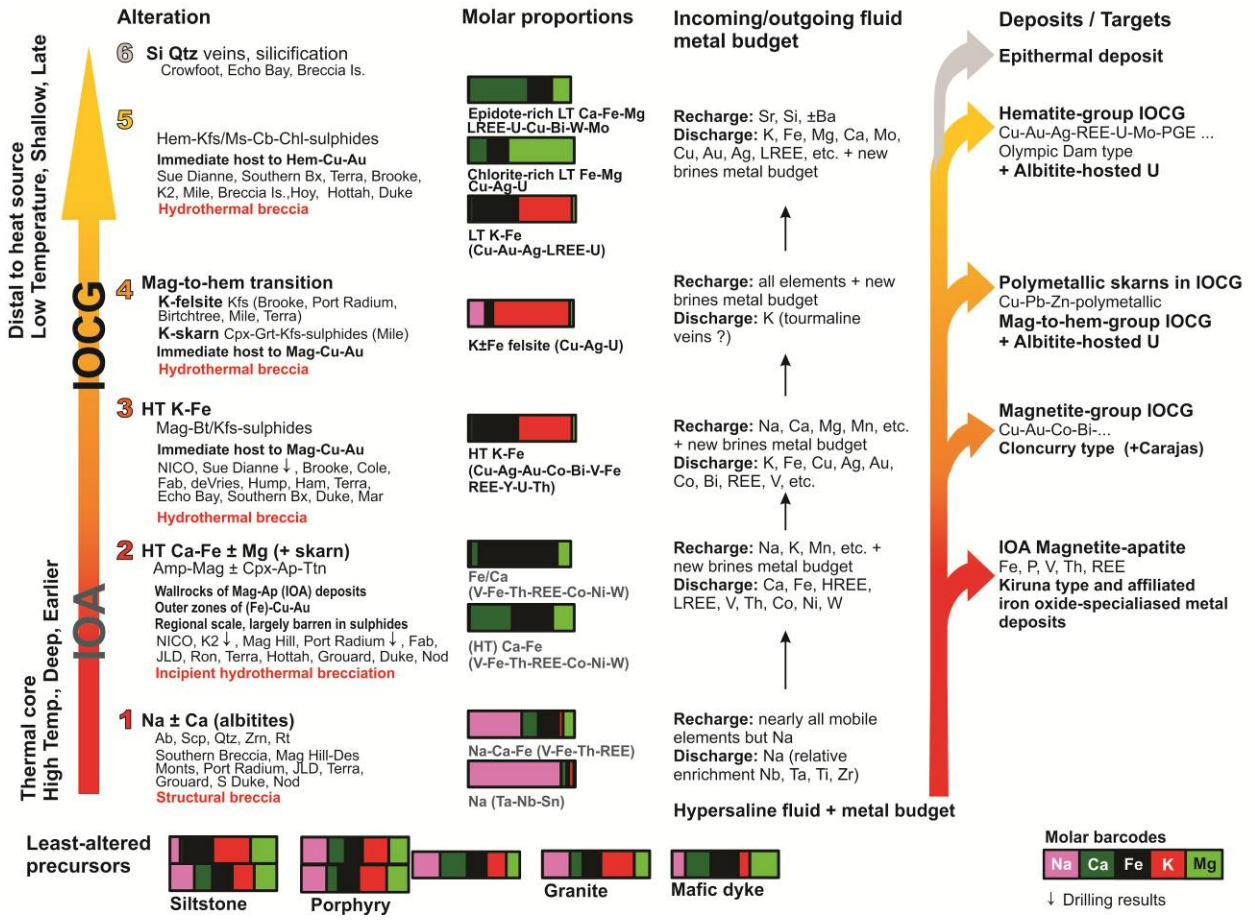

Figure 3-10 IOAA alteration facies model and observed metal associations as a framework for the development of the range of deposit types within IOAA systems

Modified from Corriveau et al. (2010b).

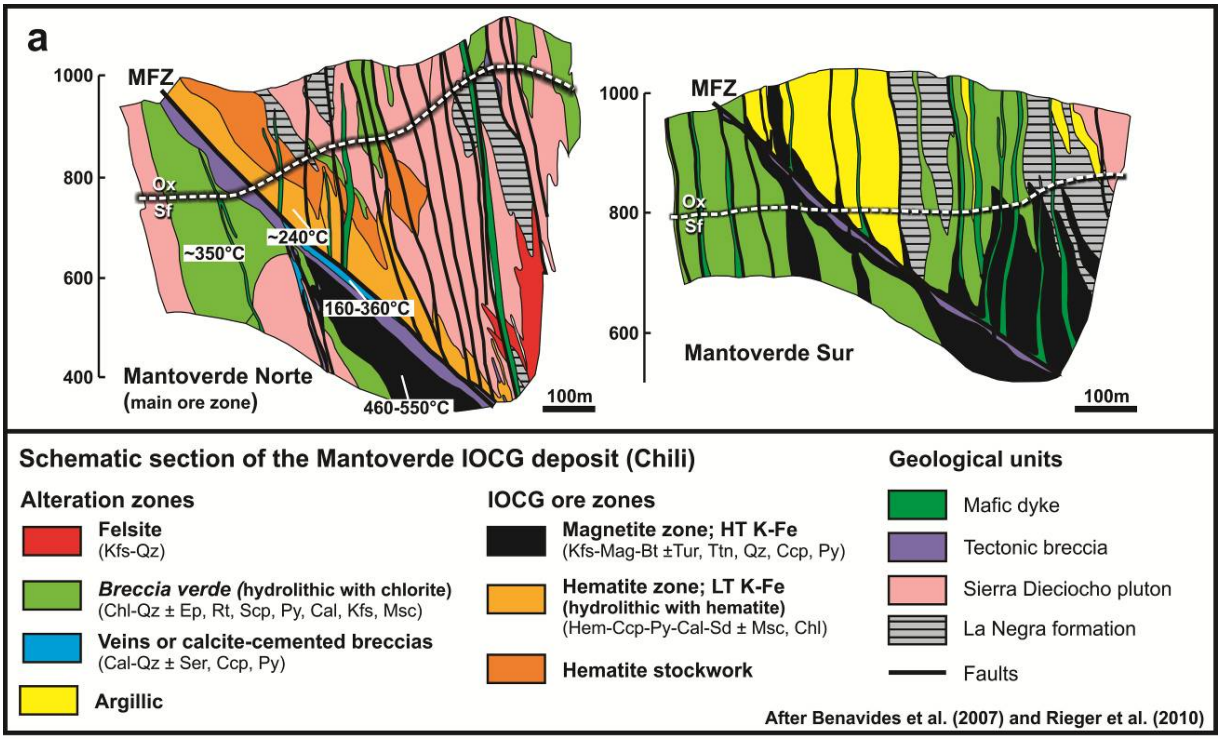

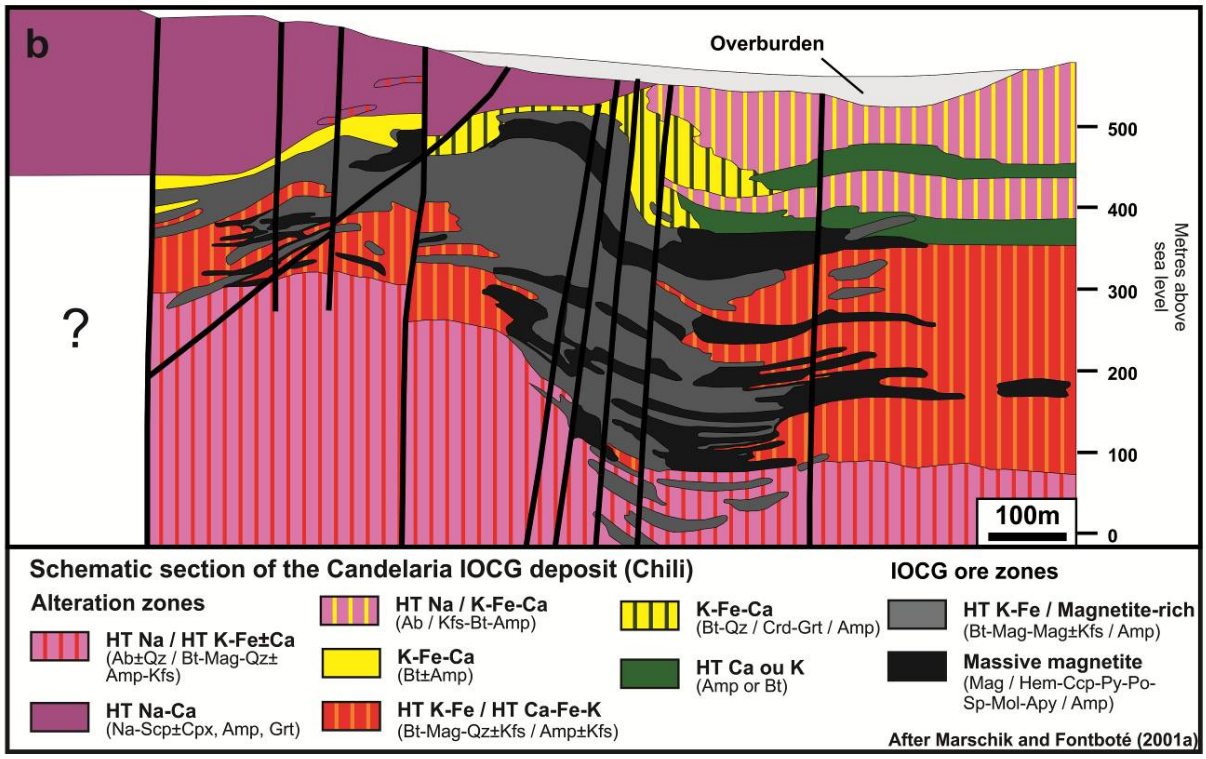

Figure 3-11 Schematic sections of the alteration facies of the Candelaria (Chile) magnetite-group and of the Mantoverde (Chile) hematite-group IOCG deposits

The sections are modified from Marschik and Fontboté (2001a), Benavides et al. (2007) and Reiger et al. (2010). Mineral abbreviations after Whitney and Evans (2010).

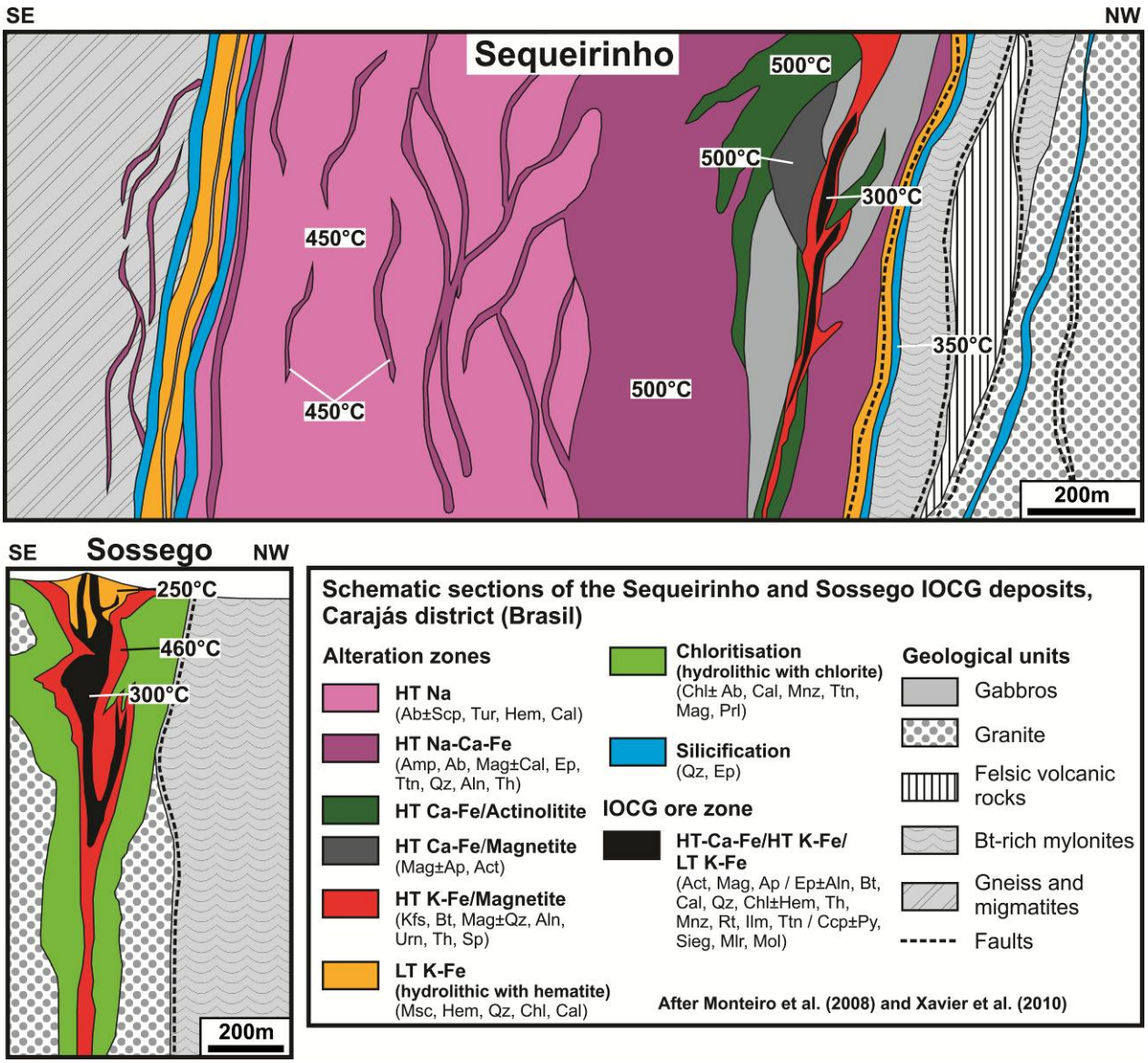

Figure 3-12 Schematic sections of alteration facies for the Sequeirinho and Sossego magnetite-group IOCG deposits of the Carajás district (Brazil)

The sections are modified from Monteiro et al. (2008a) and Xavier et al. (2010).

Mineral abbreviations after Whitney and Evans (2010) except Sieg for siegenite and Th for thorianite

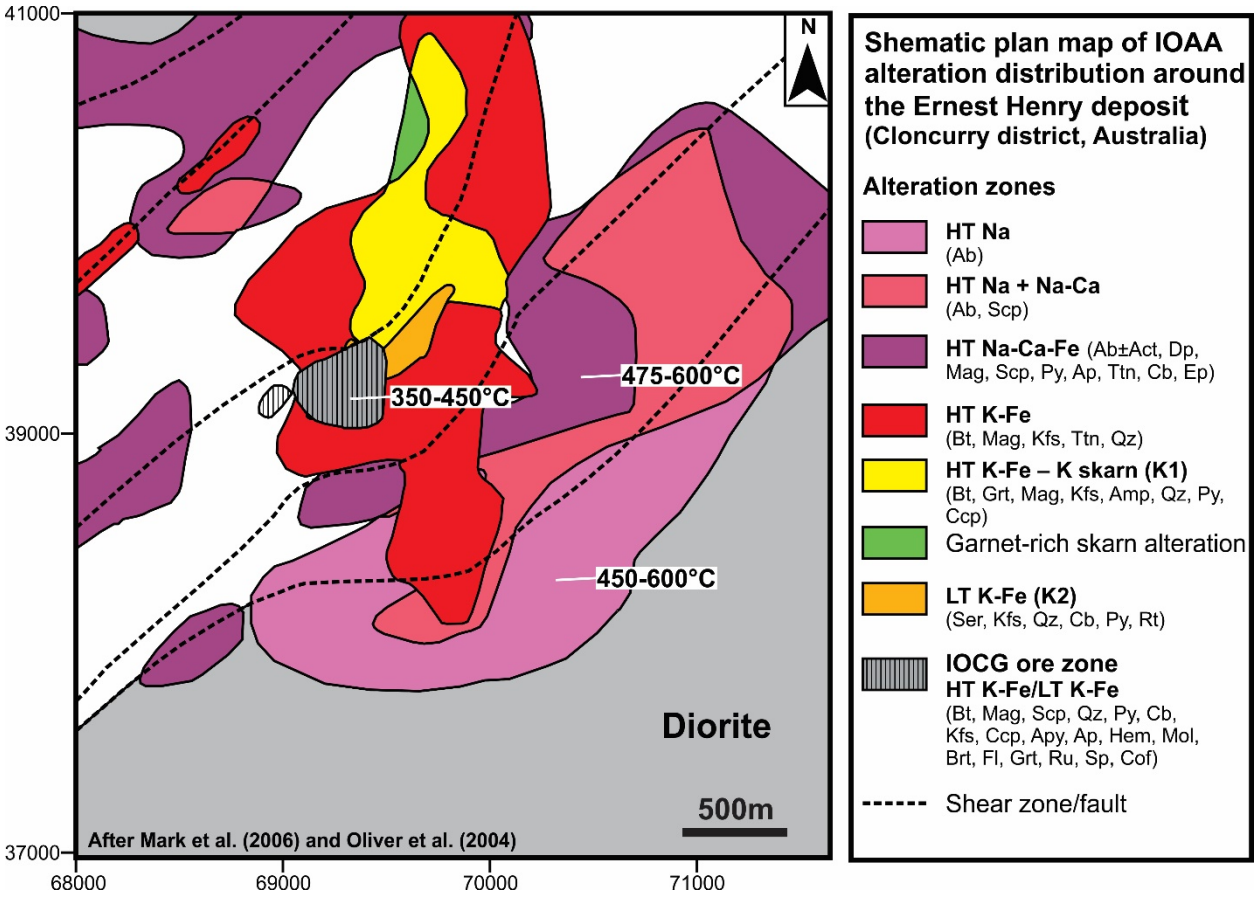

Figure 3-13 Schematic plan map of alteration facies for the Ernest Henry magnetite-group IOCG deposit of the Cloncurry district (Australia)

Plan map modified from Oliver et al. (2004) and Mark et al. (2006).

Mineral abbreviations after Whitney and Evans (2010) except Cof for coffinite.

CHAPITRE 4 : ON THE RELATION BETWEEN ALTERATION SIGNATURE AND METAL ENDOWMENT OF IRON OXIDE ALKALI ALTERED SYSTEMS, SOUTHERN GREAT BEAR MAGMATIC ZONE (CANADA)

Sur les relations entre l'altération hydrothermale et la signature métallifère des zones minéralisées formées dans des systèmes hydrothermaux à oxydes de fer et altération en éléments alcalins, sud de la Zone magmatique du Grand lac de l'Ours (Canada)

[1]Montreuil, J.-F., [2]Corriveau, L., [3]Potter, E.G.

[1]Institut National de la Recherche Scientifique – Eau-Terre-Environnement

[2]Ressources naturelles Canada, Commission Géologique du Canada, division Québec

[3]Ressources naturelles Canada, Commission Géologique du Canada, division Ottawa

Soumis à «*Economic Geology*»

Abstract: This paper documents the relationships between alteration types and metal associations in the Iron Oxide–Alkali–Alteration (IOAA) systems of the southern Great Bear magmatic zone (GBMZ), Canada. The southern GBMZ IOAA systems host the Au–Co–Bi–Cu NICO and the Cu–Ag–(U–Au) Sue-Dianne Iron Oxide Copper–Gold deposits. All the southern GBMZ IOAA systems were formed within a 7 m.y. time window (from 1873 Ma to 1866 Ma) and IOAA alteration spans with variable intensity the entire extent of the southern GBMZ supracrustal sequences distributed along two distinct sections (Western and Eastern section). The younger intrusions of the Marian River batholith, formed at 1866 Ma, are devoid of IOAA alteration. High temperature (HT) magnetite-bearing and low temperature (LT) hematite/chlorite-bearing potassic–iron alteration zones are extensively developed in the western sectors of the southern GBMZ IOAA system where most of the polymetallic mineralization zones comprise a wide variety of base, precious and high technology metals (Ag, Au, Bi, Co, Cu, Mo, Ni, REE, U, W, Zn). In contrast, the alteration zones of the eastern sectors, characterized by widespread sodic and HT calcic–iron alteration with a generally weak and spatially restricted HT potassic–iron alteration overprint, exhibit peculiar metallic signatures with varied associations of Ag, Cu, Nb, REE, Ta, Th, U and V. This is combined with marginal endowments in base metals although local enrichments in Bi, Co, Cu, Pb and Zn were observed. The distinct relationship between base metal-enriched and specialized metal-enriched mineralization and hydrothermal alteration types in IOAA systems provides a new exploration tool to reinterpret apparently unrelated mineralization types in IOAA districts and to predict the potential metallic signature of prospective deposits formed among this IOAA system.

Résumé: Cet article documente les relations entre les types d'altérations hydrothermale et les associations métallifères dans les zones minéralisées des systèmes à oxydes de fer et altération en éléments alcalins (IOAA) de la Zone magmatique du Grand lac de l'Ours (GBMZ), Canada. Les systèmes IOAA du sud de la GBMZ sont hôtes des gisements à oxydes de fer–cuivre–or (IOCG) à Au–Co–Bi–Cu de NICO (système de Lou) et à Cu–Ag–(U–Au) de Sue-Dianne (système de Mazenod). Tous les systèmes IOAA du sud de la GBMZ se sont formés dans une fenêtre temporelle de 7 m.a. (entre 1873 et 1866 Ma) et l'altération IOAA se surimpose avec intensité variable sur l'ensemble des roches supracrustales du sud de la GBMZ distribuées dans deux sections distinctes (*Western* et *Eastern sections*). Les intrusions du batholite de Marian River, datées à 1866 Ma, ne montrent pas d'évidences d'altérations IOAA. Les systèmes IOAA de la *Western section*, où les altérations du stade de haute température (HT) potassique–fer à magnétite et de faible température (LT) potassique–fer à hématite/chlorite

sont fortement développées, sont les principaux hôtes de minéralisations polymétalliques enrichies d'une grande diversité de métaux de base, précieux et spécialisés (Ag, Au, Bi, Co, Cu, Mo, Ni, REE, U, W, Zn). Cette signature métallique des zones minéralisées des systèmes IOAA du sud de la GBMZ contraste avec les assemblages métallifères dans les zones minéralisées de la *Eastern section* où les altérations sodiques et HT calcique–fer prédominent, principalement enrichies en Ag, Cu, Nb, REE, Ta, Th, U et V. Des enrichissements faibles à modérés en Bi, Co, Cu, Pb et Zn se retrouvent aussi dans certains systèmes IOAA du sud de la *Eastern section*. Les relations distinctes entre types d'altérations hydrothermales et enrichissements en métaux dans les systèmes IOAA fournissent un nouvel outil d'exploration pour réinterpréter les zones minéralisées des systèmes IOAA, ce qui permet de prédire la signature métallifère potentielle des gisements potentiellement formés au sein de ces systèmes.

4.1. Introduction

Temporal and spatial evolution of Iron Oxide Copper–Gold (IOCG) and affiliated mineralization in hydrothermal Iron Oxide–Alkali–Alteration (IOAA) systems (cf. Porter, 2010) result in the formation of diagnostic alteration facies (Corriveau et al., 2010b). Depending mainly upon the exposed crustal level and the size of the system, the surface footprints of an IOAA system can exceed tens of kilometers in lateral and longitudinal extent and kilometers in vertical extent (Oliver et al., 2008; Mumin et al., 2010; Porter, 2010). The regional development of an IOAA system is associated with influx of external metals and local to regional redistribution of available metals and major/trace elements as a consequence of protracted compositional reorganization in the crust itself (Oliver et al., 2008; Porter, 2010). This results in the superimposition of multiple alteration to brecciation and mineralization zones typically associated with pulsating and large-scale magmatic events causing periodic resetting of the hydrothermal system (Hitzman et al., 1992; Williams et al., 2005; Corriveau et al., 2010a, b; Williams, 2010a; Porter, 2010). Ultimately an extraordinary range of deposits form in a mature IOAA district (Mumin et al., 2010).

Fault zones, permeable units and major discontinuities (e.g., unconformities) serve as the main fluid conduits at regional to local scales during the development of IOAA systems and control the spatial location of metal discharge where the IOCG deposits can be formed (Oliver et al., 2006). Such preferential fluid pathways have been observed in association with zones of preferential sites for magma emplacement, extensive and polyphase tectono–hydrothermal brecciation, intense hydrothermal alteration or with deposits themselves (Oliver et al., 2006; Marshall and Oliver, 2008; Bertelli and Baker, 2010; Groves et al., 2010). Lithospheric discontinuities also play a critical role in ore distribution by providing a direct connection between shallow crustal levels and the mantle, enhancing the variety of magma and fluid sources tapped during the evolution of an IOAA system (e.g., Gawler Craton, Skirrow, 2010; Ossa-Morena zone in Spain, Tornos et al., 2005; Chilean Iron belt in Chile, Sillitoe, 2003; Cloncurry district in Australia, Oliver et al., 2006 and Austin and Blenkinsop, 2008).

Studies of the Sue-Dianne magnetite to hematite-group deposit (8.4 Mt @ 0.8 % copper, 0.07 g/t gold, 3.2 g/t silver; Hennessey and Puritch, 2008) and the numerous mineralized prospects, showings and occurrences of the southern and central Great Bear magmatic zone (GBMZ) in the Northwest Territories, Canada (Fig. 1-2; Gandhi, 1989, 1992a, 1992b; Gandhi and Lentz, 1990; Gandhi and Halliday, 1993; Gandhi and Prasad, 1995, 1997) contributed to an early recognition of the IOCG potential of the GBMZ and to the development of the first genetic model

for this deposit class by Hitzman et al. (1992). Subsequently the documentation of uranium and potassium anomalies several kilometers in widths (Hétu et al., 1994; Shives et al., 2000) in the Lou Lake area led to the discovery of the NICO Au–Co–Bi–Cu deposit (Fig. 1-2; Goad et al., 2000a, b; Mumin et al., 2010) currently with NI 43-101 compliant proven and probable reserves of 33 Mt @ 1.02 g/t gold, 0.112% cobalt, 0.14% bismuth, 0.04 % copper (Fortune Minerals Ltd. press release, July 5th, 2012). The NICO deposit is a magnetite-group IOCG deposit variant based on Williams (2010a) classification, as the copper content is currently lesser than gold, cobalt and bismuth and in that sulfarsenides are the main sulfides instead of chalcopyrite (Corriveau et al., 2010a, b, 2011). Recent studies by Acosta-Góngora et al. (2014, 2015a, b) provide additional details on the ore and genesis of the NICO deposit.

Recent work on both deposits and previous work on the iron oxide±apatite (IO±A; Williams, 2010a classification scheme) mineralization in the northern GBMZ (Shegelski, 1973; Badham and Morton, 1976; Hildebrand, 1986; Reardon, 1992) have shown that the GBMZ IOAA systems encompass magnetite-to-hematite IOCG deposits and showings (Goad et al., 2000a, b; Mumin et al., 2007, 2010; Corriveau et al., 2010a, b, 2011; Ootes et al., 2010; Acosta Góngora et al., 2011; Hayward et al., 2013; Potter et al., 2013b). In this paper, we examine the relationship between the alteration footprints and metallic signatures of IOCG deposits and their associated mineral showings and occurrences in the southern GBMZ IOAA systems. Many of the studied prospects and showings were formerly attributed to a variety of deposit types such as sedimentary/diagenetic iron formation, felsic volcanic-hosted stratiform magnetite–pyrite–chalcopyrite concentrations and volcanic-associated uranium occurrences (Gandhi et al., 1996; Mumin and Camier, 2000; Skanderberg, 2001; Gandhi, 2004). This study relies on extensive alteration mapping based on the IOAA facies subdivision of Corriveau et al. (2010b), complemented by lithogeochemical studies described in detail in chapters 5, 6 and 7. The paper also builds upon recent knowledge acquired in the Port Radium–Echo Bay and Camsell River districts (Mumin et al., 2010; Acosta-Góngora et al., 2011, 2014), the Fab magnetite-group IOAA system hosting numerous copper–uranium showings, some within magnetite-cemented breccias (Gandhi, 1988; Acosta Góngora et al., 2011; Potter et al., 2013a, b), and the DeVries system to the east (Corriveau et al., 2007; Jackson, 2008; Ootes et al., 2010; Figs. 1-2, 1-15). The nomenclature of hydrothermal alteration described in this paper is based on the diagnostic elements in the mineral parageneses and is listed in Table 4-1. The new constraints placed on the spatial and temporal evolution of mineralization in regional IOAA systems frame the wide variety of deposits that can be formed in IOAA systems worldwide.

Table 4-1 Paragenetic sets in the main alteration facies of the southern GBMZ IOAA systems (modified from Corriveau et al., 2010b); mineral abbreviations from Whitney and Evans (2010)

Alteration type	Mineral parageneses
Sodic	Ab±Qtz
Sodic–calcic–iron	Ab–Amp±Mag
HT calcic-iron	Amp–Mag, Amp–Mag–Ap, Amp
Skarn-type HT calcic–iron	Cpx±Grt±Mag
Calcic–iron–potassic	Amp–Mag–Kfs, Amp–Kfs, Amp–Bt–Mag±Kfs±Ap, Amp–Bt
HT potassic–iron	Kfs–Mag, Kfs–Bt–Mag, Bt–Mag
LT potassic–iron	Hem–Chl, Hem–Ms–Chl, Hem–Kfs±Chl, Tlc–Chl, Hem
LT calcic–iron	Ep±Kfs±Aln

4.2 Regional Geology

The Great Bear magmatic zone (GBMZ) is a post-collisional 1.87-1.85 Ga continental magmatic belt formed at the western edge of the Wopmay Orogen following the accretion of the Hottah terrane to the Archean Slave craton during the short-lived Calderian orogeny for which a Andean-type continental arc model prevails among the different tectonic scenarios proposed (Fig. 1-2; cf. Hildebrand et al., 2010a; Cook, 2011; Mumin et al., 2014; Ootes et al., 2015). Local intrusive activity at ca. 1.878 Ga records the onset of GBMZ magmatism and incipient IOAA hydrothermal activity. Such metasomatism reached its peak intensity in association with 1.87 Ga deposition and intrusion of shoshonitic to high-K calc-alkaline magmas across the Hottah terrane basement and overlying 1.88 Ga Treasure Lake Group sedimentary basin (Gandhi and van Breemen, 2005; Azar, 2007; Hildebrand et al., 2010b; Montreuil and Corriveau, chapitre 2). The 1.87 Ga volcanic centers are formed of stratovolcanoes, calderas and coeval sub- and intra-volcanic porphyritic intrusions that were rapidly capped by a second episode of volcanism at ca. 1.868 Ga and intruded by coeval to younger resurgent plutons, sub-volcanic porphyritic intrusions and voluminous granodiorite–monzogranite batholiths (Hildebrand et al., 1987, 2010b). At 1.86 Ga the GBMZ volcanic-plutonic sequences were broadly folded along a NW-oriented axis and then intruded between 1.86 Ga and 1.85 Ga by the biotite-granite suite (Hildebrand et al., 1987, 2010b; Gandhi et al., 2001). Subsequently, the geometry of the Great Bear magmatic zone was disrupted by dextral strike slip along NE-oriented (±35° to 45°) faults (see tectonic reconstruction by Hayward and Corriveau, 2014). Most of the GBMZ IOAA systems and their mineralized zones were segmented during this brittle faulting event genetically associated with many mineralized quartz veins such as the Lou Lake, Dianne and Rayrock faults

in the southern GBMZ (Gandhi et al., 2000, 2014; Byron, 2010). Uraninite U–Pb analysis of some grains from the Rayrock mine yielded late Ordovician ages (Miller, 1982), indicating that some of the northeast-trending faults have remained periodically active from the Paleoproterozoic to at least the late Ordovician.

The Treasure Lake Group is a ca. 1.885 Ga platform-type sedimentary sequence (Gandhi and van Breemen, 2005; Bennett and Rivers, 2006). This group is subdivided into: 1) a basal siltstone unit evolving upward to 2) carbonaceous rocks, 3) massive quartz arenite interbedded with few siltstone beds with primary sedimentary structures such as cross-bedding and ripple marks, and 4) an upper siltstone interbedded with sandstones (Gandhi et al., 2014). The Treasure Lake Group sedimentary rocks were predominantly metamorphosed to the greenschist facies, deformed and tilted to a generally steep dip during the Calderian orogeny.

In the southern GBMZ, the shoshonitic to high–K calc–alkaline andesitic to rhyolitic volcanic and volcaniclastic rocks of the Faber Group unconformably overlie the Treasure Lake Group (Gandhi et al., 2014; chapitre 2). Their angular unconformity is well exposed in the vicinity of the NICO deposit and the Southern Breccia showings, where rhyolite is the basal unit of the Faber Group. Gandhi et al. (2014) divided, in stratigraphic order, the Faber Group into five assemblages:

1) the predominantly rhyolitic to andesitic Lou;

2) the predominantly andesitic Cole;

3) the mafic to felsic Hump;

4) the rhyolitic to andesitic Mazenod; and

5) the predominantly andesitic to rhyolitic Bea assemblages.

Many generations of andesitic to rhyolitic porphyritic dikes related to the build-up of the Faber Group occur in the Treasure Lake Group, some of them also cut the Faber Group. The presence and absence of IOAA assemblages support field observations indicating intrusion of dikes before, contemporaneous with and after the main stages of IOAA, deformation and mineralization events. Zircon U–Pb crystallization ages of these porphyritic dikes between 1870–1867 provide minimum age constraints on the Lou IOAA and Mazenod sectors of the southern GBMZ (Gandhi et al., 2001; Davis et al., 2011). In terms of regional metamorphism and without considering extensive metasomatism, the dominant metamorphic facies in the Faber Group is sub-greenschist.

The southern GBMZ also comprises many generations of felsic to intermediate intrusive suites. The oldest one consists of 1873 Ma leucocratic granitic bodies, referred to as the early granite suite (Gandhi et al., 2001, 2014). Their leucocratic nature typically results from extensive and intense sodic and a more localized and later potassic alteration (chapitre 6; this work). A suite of dioritic to felsic intrusions (diorite suite) and of 1867 Ma quartz monzonite to monzodiorite intrusions (quartz monzonite–monzodiorite suite) follow the formation of the early granite suite (Gandhi et al., 2001). The supracrustal rocks of the southern GBMZ occur as rafts in the Marian River batholith, a composite intrusive body composed of many undivided plutons with an arc, syn-collisional, transitional and within-plate character (chapitre 2). Some plutons of the Marian River batholith yield zircon U–Pb ages of 1866 Ma and are devoid of any IOAA-related assemblages; they postdate the main IOAA hydrothermal event in the southern GBMZ. As the 1873 Ma intrusions of the early granite suite are extensively IOAA-altered and predate most of the intense IOAA event in the Lou IOAA sector (chapitre 6), they provide the maximum age constraints to the main IOAA hydrothermal event in the southern GBMZ. Through these age constraints, the IOAA systems are bracketed to a 7 m.y. time window from 1873 to 1866 Ma.

The eastern limit of the southern GBMZ and its known IOAA and the western limit of reworked Archean rocks of the Slave craton are defined by the Wopmay fault zone, an important deformation corridor related to the Calderian orogeny that was reactivated at 1.87 Ga (Jackson et al., 2013). The fault zone has a mid-crustal vertical extension (~20 km) and listrically merges with the highly resistive Slave craton lithosphere and is interpreted to taper out at depth further west below the GBMZ as far west as the outcropping exposures of the Hottah terrane (Spratt et al., 2009). The western and northwestern limits of the GBMZ are concealed under Proterozoic and Paleozoic sedimentary rocks, but remain within reach of modern exploration drilling and geophysical modeling (Villeneuve et al., 1993; Aspler et al., 2003; Hayward et al., 2013).

4.3 Geological setting of the IOAA system

Supracrustal rocks in the southern GBMZ are distributed into two northwesterly oriented sections referred to as the Western and Eastern sections. Both sections consist predominantly of metasedimentary rocks of the Treasure Lake Group and volcanic rocks of the Faber Group, but also include intrusions associated with all intrusive suites of the southern GBMZ. Most of the recognized IOAA hydrothermal activity is focused within the supracrustal sections.

The Western section encompasses the Lou IOAA, South Lou and the Mazenod sectors (Fig. 1-15). The Lou IOAA sector includes the NICO deposit and the Southern Breccia albitite-hosted uranium showings whereas the Mazenod sector hosts the Sue-Dianne deposit. The Eastern section is subdivided into the Eastern Treasure Lake and the Cole sectors (Fig. 1-15). No major base metal-endowed mineralized zones are known in the Eastern section, but the Eastern Treasure Lake sector hosts significant iron oxide showings in the Ron and Hump zones. A two-dimensional inversion of a magnetotelluric survey by Spratt et al. (2009) indicates that the Western section is located along the margin of the resistive Archean mantle and the Hottah terrane, providing a lithospheric connection between the upper crust and the mantle and resulting in an overall crustal geometry similar to that of the Gawler Craton, which hosts the Olympic Dam IOCG deposit (cf. Heinson et al., 2006; Skirrow, 2010). A potential discontinuity from surface to the upper mantle has also been imaged through a new regional magnetotelluric survey centered on the NICO deposit (Craven et al., 2013).

4.3.1 Western section

IOAA assemblages in the Lou IOAA and South Lou sectors are largely developed in the Treasure Lake Group metasedimentary rocks yet extend into the volcanic rocks of the Lou assemblage in the Lou IOAA sector and undivided rhyolitic rocks of the Faber Group in the South Lou sector. In the South Lou sector, IOAA facies are sporadic to continuous over hundreds of meters whereas the major IOAA zones in the Lou IOAA sector are associated with the NICO deposit and the Southern Breccia and extend over many kilometers at surface. Tectonic deformation in the Treasure Lake and Faber groups in the Lou IOAA and South Lou sectors is focused in meter to hundred meters wide and W- to WNW-oriented deformation corridors (e.g., Duke, Peanut, Southern; Fig. 1-15). Tectonic foliations in the deformation corridors typically strike W to WNW, are dominantly steeply dipping (80° to vertical) to the northeast and are concordant to slightly discordant with the bedding of the Treasure Lake Group metasedimentary rocks. The extent and intensity of IOAA in those deformation corridors indicate that they acted as important permeable pathways and focused hydrothermal fluid flow during IOAA activity in the Lou IOAA and South Lou sectors. Internal folding, several generations of porphyritic dike emplacement and extensive tectono-hydrothermal brecciation are also characteristic of these deformation corridors (chapitre 2).

The Mazenod sector hosts the Brooke, Mar and Nod polymetallic IOCG prospects and showings as well as the Sue-Dianne IOCG deposit. IOAA in this sector is developed in the Sue-Dianne

volcanic complex that encompasses volcanic and volcaniclastic rocks of the Lou, Mazenod and Bea assemblages of the Faber Group, feldspar-phyric intrusions, and scattered lenses and fault-bounded blocks of Treasure Lake Group metasedimentary rocks (Camier, 2002). Volcanic units of the Faber Group in the Sue-Dianne volcanic complex are faulted and gently folded as a result of asymmetric collapse of the volcanic edifice (Camier, 2002). Major faults include the N-trending Mar fault zone that has been dissected and displaced by the younger NE-trending Dianne fault and the Marian River deformation corridor (Fig. 1-15). The Mar fault zone is interpreted as the controlling structure for the formation of the Sue-Dianne deposit as well as the Brooke, Nod and the Mar prospects and showings (Gandhi, 1989; Camier, 2002). Localized faulting provides additional control over the distribution of the mineralization zones in the Sue-Dianne deposit where chalcopyrite-bearing mylonites with IOAA have been observed along some of these local faults, indicating that they were active before and likely during the formation of the Sue-Dianne deposit (Camier, 2002). Another important deformation zone in the Mazenod sector is the N-oriented Marian River deformation corridor that is located at the contact between the volcanic sequences and the Marian River batholith. Deformation is strongly partitioned into a thin sliver of the Treasure Lake Group metasedimentary rocks and extensive IOAA throughout the deformation zone indicates that it focused hydrothermal fluid flow and resulted in numerous zones of tectono-hydrothermal brecciation (Fig. 1-15).

4.3.2 Eastern section

IOAA in the Cole sector is developed in the Cole volcanic complex which includes volcanic and volcaniclastic rocks of the Cole assemblage of the Faber Group, feldspar-phyric intrusions and dikes, and intrusions of the quartz monzonite–monzodiorite suite. The Cole assemblage consists primarily of feldspar–amphibole-phyric andesite and locally rhyolite and volcaniclastic units. Late-stage granitic dikes with elevated uranium and thorium contents (up to 12.1 and 51.9 ppm, respectively) are devoid of any IOAA and cut IOAA in the Cole sector. The 1866 Ma plutons of the Marian River batholith nearly surround entirely the Cole volcanic complex and are devoid of IOAA facies in the Cole sector. They provide a minimum age of 1866 Ma for the IOAA event that matches the timing of the main IOAA events in the other sectors of the southern GBMZ. Major deformation zones in the Cole sector where intensity of IOAA and brecciation significantly increases include an important and N- to NW-oriented (0° to 330°) deformation corridor that led to the formation of an approximately 450 m-wide tectono-hydrothermal breccia zone referred to as the Cole Breccia (Fig. 1-15).

IOAA in the Eastern Treasure Lake sector mainly developed in a unit of metasiltstone interlayered with metaquartzite beds of the Treasure Lake Group, but also locally after the metacarbonaceous unit of the Treasure Lake Group, undivided volcanic rocks of the Faber Group and the Hump assemblage of the Faber Group. Intrusions of the early granite, some intrusions of the dioritic suites and some intrusions of the quartz monzonite–monzodiorite suites exhibit IOAA-assemblages. IOAA facies (sodic, sodic–calcic–iron and HT calcic–iron) in the quartz monzonite–monzodiorite suites are especially well-developed in the southern part of the Cole sector (Fig. 2-9 au chapitre 2). IOAA in the Eastern Treasure Lake sector is focused along WNW- and N-oriented faults or deformation corridors (Goad et al., 1996; Mumin et al., 2000). Weak to well developed, NE-dipping and penetrative WNW-oriented tectonic foliations are ubiquitous in the Eastern Treasure Lake sector and are roughly parallel to the Treasure Lake Group bedding. No direct timing constraints are available for the IOAA activity in the Eastern Treasure Lake sector. Considering that the 1873 Ma early granite intrusions exhibit extensive IOAA and that granitic dikes mineralogically similar to the 1866 Ma intrusions of the Marian River batholith that cut IOAA facies are not altered, most of the IOAA activity in the Eastern Treasure Lake sector likely occurred between 1873 and 1866 Ma.

4.4 Methods

4.4.1 Rock description and mineral identification

The mineralogy of IOAA facies and mineralization zones in the studied prospects and showings of the southern GBMZ were established using polished slabs, cobaltnitrate stained slabs, optical microscopy and scanning electron microscopy (SEM). A Zeiss EVO® 50 SEM equipped with INCAx-sight (Oxford instrument) energy dispersive spectrometry (EDS) located at INRS–ETE in Quebec City and the Geological Survey of Canada facilities in Ottawa were used. SEM operating conditions were set using a working distance of 8.5 mm, the high voltage (EHT) was set at 20 kV and the probe current was set at 1.5 nA.

4.4.2. Geochemical analysis

In situ measurements of %K, eTh (ppm) and eU (ppm) in IOAA facies were made during fieldwork using a portable gamma-ray spectrometer (Radiation Solution RS–230 unit). Each measurement lasted 120 seconds and was obtained on flat surfaces with sufficient volumes for

the analysis. The prefix “e” (eTh or eU) denotes that U and Th concentrations were determined indirectly from their daughter products (^{214}Bi and ^{208}Tl respectively) assumed to be in equilibrium with their parent isotopes.

Samples for whole rock geochemistry were carefully selected and chipped in the field to avoid unwanted veins or overprinting alteration and to collect a sufficient volume of megascopically uniform and non-weathered rock material. This sampling protocol optimized the compositional characterization of each alteration type as all other alteration types detectable at megascopic scale were avoided during sampling. Geochemical interpretation of element mobility patterns discussed in this paper thus rest on ample examples of each alteration types (cf. Corriveau et al., 2015 for the geochemical dataset and the QA/QC protocols; representative analyses are presented in Appendix 4). The samples were crushed in a steel-plated jaw crusher and powdered using an agate ball mill. Major and trace elements for most of the samples were analyzed by ICP-AES and ICP-MS following lithium borate fusion at INRS–ETE. Some metals (Bi, Co, Li, Mo, Ni, Pb and Sn) were analyzed by ICP-MS following 4-acid digestion at Acme Laboratories in Vancouver (Canada; method 1EX). Some highly volatile elements (As, Cs, Rb, Sb) were analyzed by instrumental neutron activation at Becquerel Laboratories in Toronto (Canada; Appendix 4). Sample with elevated uranium contents determined by gamma-ray spectrometry (e.g., Southern Breccia and Cole Uranium showings) were analyzed by ICP-AES and ICP-MS following an aggressive 4-acid digestion to dissolve all the potentially resistate/refractory minerals (e.g., zircon, rutile, Nb-bearing minerals, titanite; method ME-MS61U of ALS in Vancouver). A selection of samples from the Southern Breccia and Cole Uranium showings were also analyzed for rare earth elements (REE) contents by ICP-MS following alkaline fusion at ALS with a method suitable for uranium-rich samples (method ME-MS81u). Additional geochemical data were compiled from the literature (Sue-Dianne deposit, Camier, 2002; Nod prospect, North, 1995 and Mackay and Eveleigh, 1997; Duke showing, Goad et al., 1996; Hump, Ron, Esther and Carbonate Mountain showings, Mumin et al., 1996 and Neale and Camier, 1997; NICO deposit, Mumin, 1997).

As they represent diagnostic elements specific to the principal types of IOAA facies (chapitre 5), molar concentrations of Ca, Fe, K, Mg and Na are used to create pseudo-sections for the southern GBMZ prospects and showings to graphically illustrate the relationships between metal endowment and IOAA (Table 2-2; Fig. 2-1). The molar concentrations represent good proxies for the dominant mineral phases and are complemented on each section by the concentration of strontium and barium. Elevated strontium and barium concentrations signal intensifying LT

calcic–iron and potassium-rich alteration respectively as intense HT calcic–iron, HT potassic–iron, sodic and LT potassic–iron alteration types typically have very low strontium contents in the GBMZ IOAA systems (chapters 6, 7). Strontium is incorporated in epidote whereas barium is incorporated in K-feldspar.

4.5 IOAA distribution and relationships to mineralization styles and breccias

The relationship between IOAA and enrichments in metals during the regional evolution of the systems was examined using the main prospects, showings and mineral occurrences of the southern GBMZ in both the Western and Eastern sections.

In the Western section, prospects, showings and mineral occurrences were selected in the South Lou and Mazenod sectors to complement the detailed information available for the Lou IOAA sector in Goad et al. (2000a, b), Mumin et al. (2010), Acosta-Góngora (2014, 2015a) and chapitre 6. In South Lou, the selected prospects, showings and mineral occurrences are located in the area extending between the Duke showing and the Maryleer fault (here referred as the Duke zone; Fig. 1-15). In the Mazenod sector, the Sue-Dianne deposit, and the Brooke and Nod prospects are covered, forming the Sue-Dianne–Brooke and the Nod zones.

In the Eastern Section, prospects, showings and mineral occurrences were selected in both the Cole and Eastern Treasure Lake sectors. In Eastern Treasure Lake, detailed coverage was focused around the Ron and Hump showings (here referred as the Ron and Hump zones, respectively), the Esther prospects and showings (here referred as the Esther zone), the Carbonate Mountain prospect and the sector east of the Dennis showing (here referred as the Carbonate Mountain and Dennis zones; Fig. 1-15). In the Cole sector, detailed coverage was focused on the Cole Uranium showing.

4.6 Eastern section – Eastern Treasure Lake sector

In the Eastern Treasure Lake sector, the prevailing IOAA facies are sodic (albite), sodic–calcic–iron (albite–amphibole±clinopyroxene±magnetite±titanite±apatite), skarn-type HT calcic–iron (clinopyroxene-rich and/or garnet-rich) and HT calcic–iron (amphibole±magnetite±apatite).

Localized potassic (K-feldspar), HT potassic–iron (K-feldspar–magnetite and biotite), LT potassic–iron alteration (chlorite±K-feldspar and K-feldspar–hematite, hematite) and LT calcic–iron (epidote±allanite±K-feldspar) are also present.

4.6.1 Esther zone

The Esther zone is characterized by an early, pervasive and intense sodic alteration within the Treasure Lake Group metasedimentary rocks, undivided volcanic rocks of the Faber Group and a granitic intrusion that has become syenite-looking because of the intense albite replacement of its initial minerals (Fig. 4-1a–c). This sodic alteration is sequentially overprinted by HT calcic–iron, HT potassic–iron, LT potassic–iron and LT calcic–iron alteration that resulted in different types of base metal-poor polymetallic mineralization zones represented by the MHF tantalum–uranium, the Esther uranium and the Esther thorium–REE showings and one base and precious metal-bearing prospect, the Esther copper–silver prospect (Figs. 4-1a, 4-2c; Table 4-2).

The MHF tantalum–uranium showing is a meter-wide zone in the sodic-altered intrusion where sodic alteration is overprinted by a pervasive LT potassic–iron alteration front in which albite crystals are selectively replaced by K-feldspar while chlorite–specular hematite precipitated in veins (Fig. 4-1d). The MHF showing contains elevated uranium and thorium as high as 240 ppm *e*Th and 283 ppm *e*U. The alteration halo of the MHF showing also includes intense LT calcic–iron and HT calcic–iron alteration zones within the albitized intrusions and the metasedimentary rocks of the Treasure Lake Group.

The tantalum–uranium mineralization of the MHF showing is composed of three main minerals occurring in the following paragenetic order and precipitated during two distinct alteration stages: very porous, likely HFSE-enriched and subhedral to euhedral rutile; a Nb–Ti–Ce–Nd–Ta–(Y)±U±Th-rich mineral exsolved from rutile crystals; a Ta–U–Nb–Fe–Ti-rich mineral rimming the Nb–Ti–Ce–Nd–Ta–(Y)-rich mineral (Fig. 4-1e). This sequence of crystallization indicates progressive tantalum, niobium and uranium enrichment combined with LREE depletion where the Ta–U–Nb–Fe–Ti-rich mineral was formed. Cassiterite is also precipitated in the LT potassic–iron veins.

Whole-rock analyses of the MHF showing indicate significant changes in metal content related to the dominant IOAA facies. Sodic alteration (10.0 wt. % Na_2O, Na_2O/K_2O 6.2; Corriveau et al., 2015 and Appendix 4 for the geochemical analyses) contains elevated Nb, Th and U with lesser amount of Ta (215 ppm Nb, 36.6 ppm Ta; Ta/Nb of 0.17; 150 ppm total REE; 87.3 ppm Th and 82.8 ppm. U; U/Th=0.95). Where LT potassic–iron alteration is superimposed over the earlier

sodic alteration (8.6 wt. % K_2O content; Na_2O/K_2O of 0.55; Corriveau et al., 2015 and Appendix 4 for the geochemical analyses), both Nb and Ta contents increase, REE decrease and U is enriched relative to Th thorium (589 ppm Nb, 162 ppm Ta; Ta/Nb=0.28, 63 ppm total REE, 93.1 ppm Th and 234 ppm).

Table 4-2 Alteration types and metal assemblages in selected prospects of the southern GBMZ IOAA system

Host alteration / Metals	Na/Na-Ca-Fe	HT Ca-Fe	Ca-K-Fe	HT K-Fe	K	LT K-Fe	LT Ca-Fe
Ta-U-Nb-Ag-Th	X Esther					X Esther	
U-Th-Y-REE	X Cole		X Cole				
Th-U	X Dennis						
Fe-LREE		X Ron					X Ron
Fe-V		X Hump		X Hump			
Zn-Pb-Cu		X Cb Mt.				X Cb Mt.	
Fe-W-Cu-REE-Zn		X LP 's	X LP 's				
Fe-Co-Ni-U-Cu-Pb-Zn		X LJLVS	X LJLVS	X LJLVS			
Fe-Cu-Co-Ni-Au--LREE-Zn-Pb		X Duke	X Duke	X Duke			X Duke
Fe-Cu-Co-Bi-Au-Mo-LREE				X Brooke		X Brooke	X Brooke
Fe-Cu-Ag-U-Au-LREE				X Sue Dianne		X Sue Dianne	X Sue Dianne
Cu				X Esther		X Esther	
LREE-U-Th							X Oxy moron
Ag					X Peanut		
Cu-Zn						X South Duke	
Th-REE							X Esther
U						X Esther	

Elements in bold are in sufficient amount to exceed the minimum requirement of the NORMIN standard to be considered as commodities in a showing

Rutile in the MHF showing is associated with quartz and K-feldspar that pseudomorphs albite crystals, indicated by relicts of albite in some K-feldspar crystals (Fig. 4-1d). The sodic alteration

zones without intense LT potassic–iron alteration overprints exhibit higher niobium concentrations than the LT potassic–iron alteration zone of the showing. The initial niobium and tantalum enrichment in the showing is thus likely related to the crystallization of rutile and exsolution of the Nb–Ti–Ce–Nd–Ta–(Y)±U±Th mineral during the sodic alteration stage. Subsequently, during the LT potassic–iron alteration stage, local remobilization of Ta and Nb, LREE removal and addition of uranium resulted in the formation of Ta–U–Nb–Fe–Ti-rich mineral(s) after the Nb–Ti–Ce–Nd–Ta–(Y)-rich mineral and rutile. This LT potassic–iron stage is also associated with tin enrichment that locally precipitated cassiterite. The Esther uranium showing is located 50 m east of the MHF showing. The uranium mineralization is related to low temperature potassic–iron alteration (chlorite–earthy hematite) veins during the low temperature potassic–iron alteration stage. Uranium and thorium are fractionated in the showing, with values up to 1576 ppm eU, 82 ppm eTh (eU/eTh=18) that support uranium enrichment by lower temperature, oxidized fluids.

The chemical signature of the MHF showing, characterized by low REE and lithium contents, contrasts with published geochemical signatures of tantalum mineralization in peraluminous pegmatite and granite (Linnen, 1998; Fetherston, 2004; Küster, 2009). Although it shares some chemical similarities with tantalum mineralization hosted in peralkaline granite and quartz syenite (Küster, 2009), the mineralogical and chemical evolution of the MHF showing is demonstrably related to polyphase IOAA in the Esther zone. It also indicates that sodic alteration may, under certain conditions, concentrate HFSE that can be subsequently enriched in the following alteration stages.

The Esther copper–silver prospect is hosted in the metasiltstone unit of the Treasure Lake Group in a zone characterized by tectono-hydrothermal brecciation and potassic, HT potassic–iron, LT potassic–iron and LT calcic–iron alteration superimposed over the early sodic and HT calcic–iron alteration (amphibole±magnetite). The main copper mineralization event occurred during the LT potassic–iron and LT calcic–iron stages and consists of chalcopyrite with hematite, K-feldspar and pyrite that is cut by LT calcic–iron veins (Goad et al., 1996; Neale and Camier, 1997; Neale et al., 1997). Drill logs of the Esther copper–silver prospect (down to 51 m depth) note that the copper-bearing LT potassic–iron alteration (hematization–K-feldspar) is superimposed over the HT calcic–iron–potassic alteration (amphibole–K-feldspar±magnetite; Neale and Camier, 1997).

The Esther REE–thorium showing is related to a LT potassic–iron alteration (specular hematite±K-feldspar) superimposed over the same albitized granitic intrusion that hosts the

tantalum–uranium showing. Thorium and REE occur as micro-inclusions of thorite and REE oxides in specular hematite veins that brecciate the albitized intrusion (Fig. 4-1f; Goad et al., 1996; Mumin et al., 2000). An intense and allanite-bearing LT calcic–iron alteration is also present in the immediate vicinity of the showing and may have contributed to the LREE enrichment.

4.6.2 Dennis zone

The Dennis zone is characterized by base metal-poor thorium-rich occurrences with moderate uranium concentrations and very low REE contents. Thorium enrichment is primarily associated with intense sodic and sodic–calcic–iron alteration expressed in various proportions of clinopyroxene and/or amphibole and albite with minor magnetite and accessory titanite that pervasively replaced and locally recrystallized the metasiltstone unit of the Treasure Lake Group (Figs. 4-1g–k, 4-2d). The thorium-bearing sodic–calcic–iron alteration evolved from an intense albitization of the siltstone and was overprinted by pervasive HT calcic–iron alteration (amphibole), and locally very strong and late-stage LT calcic–iron alteration. LT potassic–iron (specular hematite) and HT calcic–iron (apatite) veins were also observed. With eTh concentrations up 906 ppm, mean eTh concentrations around 280 ppm and eU concentration up to 169 ppm, the metal content of these occurrences is not high enough to classify them as showings according to minimum commodity grades for the NORMIN database (NWT Geoscience Office, 2014).

Whole rock geochemistry reveals a sharp increase of the Th/Zr ratio between the least altered metasiltstone and Th-rich sodic alteration zone, from 0.1 to 1.1. This is indicative of Th ingress during sodic alteration assuming that zirconium has remained somewhat immobile in the process as shown in similar systems in the Great Bear magmatic zone (chapitre 7). This alteration is also associated with a sharp increase of the Zr/La and Zr/Yb ratios in the thorium-rich sample, respectively from Zr/La=4 and Zr/Yb=63 in the less altered metasiltstone to Zr/La=19 and Zr/Yb=225 respectively. This is combined with a sharp decrease of the total REE content in the thorium-rich zones (160 ppm versus 24 ppm total REE; Corriveau et al., 2015 and Appendix 4 for the geochemical analyses). The weak variation of the La/Yb ratio between the thorium occurrences and the least altered metasiltstone, of 12 and 16 respectively, indicates weak REE fractionation during the formation of the thorium-rich alteration whereas the sharp increases of the Zr/La and Zr/Yb is indicative of coeval leaching of the LREE and HREE (Corriveau et al., 2015 and Appendix 4 for the geochemical analyses).

4.6.3 Hump and Ron zones

The iron oxide mineralization in the iron showings of the Hump zone is principally related to intense and magnetite-rich HT calcic–iron (amphibole–magnetite±apatite) and HT potassic–iron alteration (K-feldspar–magnetite±biotite) superimposed over an earlier sodic (albite) alteration (Fig. 4-3a–e). The iron oxide-rich zones are locally intensely overprinted by LT potassic–iron and LT calcic–iron (epidote±allanite) alteration (Fig. 4-3f, g). The LT potassic–iron alteration overprint at Hump is typically associated with pervasive sericitization of the felsic minerals, chloritization of the mafic minerals and/or martitization of the iron oxide and forms the typical hydrolytic hematite–muscovite±chlorite assemblage observed in other IOA and IOCG systems (Hitzman et al., 1992). The iron oxide mineralization at Hump predominantly occurs as concordant replacements of the metasedimentary rocks, but also forms discordant zones and crosscutting veins that brecciate the metasedimentary rocks near discordant deformation zones (Fig. 4-3b; Goad et al., 1996, Mumin et al., 1996; this work). Along the same strata in zones of concordant iron oxide replacement, there are locally preserved relicts of the weakly altered metasedimentary rocks (Fig. 4-3b, h). The deformation zones and iron oxide veins predominantly have a W to WNW and N orientation. The intersection of N-oriented fault and W-oriented faults controls the spatial distribution of the tectono-hydrothermal breccia zones in the showings of the Hump zone (Goad et al., 1996; Mumin et al., 2000).

In the Hump island iron oxide showing, characterized by a stronger HT potassic–iron alteration overprint than in the other Hump zone iron showings, geochemical analyses reveal high vanadium concentrations, up to 780 ppm (Fig. 4-2a; Corriveau et al., 2015 and Appendix 4 for the geochemical analyses). Microprobe analyses from Gandhi (1992a) and De Toni (2016) confirm that vanadium is hosted in hydrothermal magnetite, ilmenite and hematite (likely formed after magnetite grains). An apatite- and magnetite-rich HT calcic–iron-altered sample of the Hump iron showing also contains elevated REE concentrations (Fig. 4-4; 1973 ppm for La+Ce+Nd+Sm, P concentration of 1.4%; neutron activation analysis from Goad et al., 1996). LREE and HREE are slightly decoupled with La/Yb ratio of 58 (Fig. 4-4).

These enrichments in vanadium and REE in the Hump iron showings are similar to the Port Radium vanadium mineralization in the northern GBMZ that is also strongly enriched in REE (0.28% V_2O_5 over 224 m; Mumin et al., 2010). Anomalous copper and zinc concentrations occur in the HT potassic–iron alteration zones of the Hump island iron showing, in support of the observations of S.S. Gandhi (unpublished field notes) who noted traces of copper sulfide

(chalcopyrite). Localized zinc (sphalerite) and potential LREE (allanite) anomalies are also associated with the LT calcic–iron alteration stage (Fig. 4-2a).

The Ron zone is characterized by an early sodic (albite) alteration overprinted by an intense and magnetite-rich HT calcic–iron (clinopyroxene/amphibole–magnetite±apatite) alteration (Fig. 4-3i–k). IOAA in the Ron zone occurs within intrusions of the quartz monzonite–monzodiorite suite and metasedimentary rocks of the Treasure Lake Group. The HT calcic–iron alteration is sequentially overprinted by weak potassic, and then strong and allanite-rich LT calcic–iron alteration (Fig. 4-3k–m). Magnetite predominates over hematite in the Ron iron showings and is only locally replaced by hematite along cracks and fractures during the LT calcic–iron alteration stage. Geochemical analyses indicate that the allanite-rich LT calcic–iron can result in significant LREE enrichments (1723 ppm for La+Ce+Pr+Nd; Corriveau et al., 2015 and Appendix 4 for the geochemical analyses; Table 4-2; Fig. 4-2b). Allanite is the principal REE-bearing phase in the Ron showings and some of the LREE-rich allanite is an alteration product of apatite containing inclusions of REE-bearing minerals (Fig. 4-3m). As allanite does not incorporate HREE (Exley, 1980; Gieré and Sorensen, 2004), LREE and HREE are strongly decoupled in the LREE-rich zones with La/Yb ratios up to 830 (Fig. 4-4). Geochemical analyses of the Ron iron showings, devoid of an intense HT potassic–iron alteration stage, also indicate no significant vanadium enrichment and microprobe analyses of magnetite crystals of the Ron iron showings indicate that they are not vanadium-bearing (Fig. 4-2b; Gandhi, 1992a). The LT calcic–iron alteration stage in the Ron zone is also associated with mild zinc and copper enrichments.

Although there are localized enrichments in copper and zinc in the Hump and Ron iron showings, the overall base metal content of the iron oxide mineralization in both zones remains low, localized and discontinuous. This is in line with the observations of Goad et al. (1996) and Mumin et al. (2000). The alteration signature of the Ron zone iron showings is characterized by extensive HT calcic–iron superimposed over an earlier sodic alteration, is typical of iron oxide apatite (IOA) systems (Williams, 2010a; Corriveau et al., 2010b; Mumin et al., 2010) whereas the Hump iron showings are characterized by extensive HT calcic–iron, potassic, HT and LT potassic–iron, and sodic alteration zones, and moderate base metal enrichments that are transitional between IOA and magnetite-group IOCG deposits (Williams, 2010a).

4.6.4 Carbonate Mountain zone

IOAA in the Carbonate Mountain zone replaces an intrusion of the early granite suite, and the metasiltstone and metacarbonaceous units of the Treasure Lake Group. All those rocks exhibit

an intense and pervasive sodic alteration followed by an intense, but more spatially constrained HT calcic–iron alteration (Fig. 4-5a–b). Drilling of the Carbonate Mountain prospect shows that sodic alteration remains well developed at depth (Na contents up to 6.1 wt. % in diamond drill holes; Neale and Camier, 1997). Skarn and HT calcic–iron alteration parageneses occur together in the Carbonate Mountain zone, but in distinct precursors. Carbonate-rich metasedimentary precursors are replaced by skarn parageneses of clinopyroxene (diopside), garnet (andradite) and variable modal contents of calcite, apatite and magnetite. Magnetite is also introduced by HT calcic-iron alteration that cuts the initial skarn parageneses.

In the metasiltstone beds, HT calcic–iron alteration is predominantly composed of amphibole with variable modal contents of magnetite and apatite, and can exhibit very high iron contents (Fe>25% wt. %; Fig. 4-2d; Neale and Camier, 1997). Clinopyroxene–rich veins also cut the albitized early granite intrusions (Fig. 4-5b). A locally pervasive calcic–iron–potassic (amphibole±biotite±magnetite or amphibole–K-feldspar) alteration cuts, overprints and brecciates the skarn-type alteration assemblages yet is overprinted by a pervasive and intense LT potassic–iron alteration, predominantly comprised of chlorite and talc. A late stage LT calcic–iron alteration overprint on the skarns was also noted by Mumin et al. (2010).

The Carbonate Mountain Zn–Pb±Cu mineralization occurs in two main stages (Fig. 4-2f). Lead precipitation post-dates the main stage of skarn alteration as galena is crystallized around the garnet crystals, but predates the HT calcic-iron alteration principally characterized by magnetite crystallization. The main zinc precipitation event post-dates the magnetite-rich HT calcic-iron alteration stage as sphalerite encapsulates galena is related to the later talc-rich LT potassic–iron alteration (Fig. 4-5c–e). Galena formation is partly coeval with the magnetite veins whereas sphalerite, rimming the galena crystals and cutting garnet and clinopyroxene, mostly precipitated during the LT potassic–iron alteration stage (Fig. 4-5c–e). Cassiterite also locally formed during the LT potassic–iron alteration stage (Fig. 4-5e). According to Neale and Camier (1997) the formation of pyrite and chalcopyrite predates or accompanies the formation of galena.

Although it shares some attributes with silver-poor zinc–lead skarns in terms of alteration and mineralization following the Einaudi et al. (1981), Meinert (1992) and Meinert et al. (2005) skarn classification, the Carbonate Mountain Zn–Pb±Cu prospect is also similar to the iron “skarns” of the Misi IOCG province in the Northern Fennoscandian Shield in northern Finland (Eilu and Niiranen, 2002). The Misi iron skarns are characterized by an alteration sequence similar to the alteration sequence in the Carbonate Mountain prospect. Alteration in the Misi iron skarns started with an extensive episode of sodic alteration followed by skarnification of the

carbonaceous rocks and then amphibolitization of the skarn assemblages (Eilu and Niiranen, 2002; Niiranen et al., 2005). The Hillside Zn–Pb±Ag prospect located in the Grouard area southeast of the Camsell River IOAA system (GBMZ, Fig. 1-2) shares similar attributes to the Carbonate Mountain prospect in its association with skarn alteration formed at the expense of extensively albitized carbonaceous rocks of the Labine Group (Knox, 1998; Hamel, 2013).

4.7 Eastern section – Cole sector

The prevailing IOAA facies in the Cole sector is a pervasive and generally texture-preserving HT calcic–iron (amphibole–magnetite) impregnation of the porphyritic andesite groundmass that is systematically overprinted by an intense and texture-destructive sodic (albite) alteration. This sodic alteration episode is followed by renewed HT calcic–iron alteration, potassic alteration and locally calcic–iron–potassic alteration. A widespread and incipient to moderate LT potassic–iron (chlorite±hematite) alteration overprint is present throughout the Cole volcanic complex. This LT potassic–iron alteration is subsequently overprinted by LT calcic–iron (epidote) alteration and localized silicification. HT potassic–iron alteration is very rare in the Cole sector and systematically weak.

The Cole Uranium showing occurs in a zone of strong sodic alteration superimposed over the early HT calcic–iron impregnation of the Cole assemblage andesite (Fig. 4-5f; Table 4-2). The uranium mineralization is related to localized calcic–iron–potassic alteration veins preferentially emplaced in the intense sodic alteration zone (Fig. 4-5g). The alteration halo of the showing also comprises localized potassic (K-feldspar), LT potassic–iron and LT calcic–iron alteration with low modal contents of pyrite and traces of chalcopyrite. All those alteration types postdate the uranium-bearing calcic–iron–potassic alteration.

The uraniferous calcic–iron–potassic veins of the Cole Uranium showing are composed of disseminated uraninite associated with amphibole, K-feldspar, magnetite, apatite, zircon, monazite and titanite in various proportions (Fig. 4-5h–j). In the mineralized zones, uranium and thorium are moderately fractionated, with a U/Th ratio of 11, and yttrium and REE contents are elevated (Fig. 4-4). With a La/Yb ratio of 9.3, LREE and HREE are not strongly fractionated (Corriveau et al., 2015 and Appendix 4 for the geochemical analyses). The overall mineralogy and chemical signature of the calcic–iron–potassic veins of the Cole Uranium showing, with enrichments in Ca, Fe, K, P, Ti, Th, U and Y, are very similar to the albitite-hosted uranium showings of the Southern Breccia zone, but without the base metal enrichment and the well-

developed HT potassic–iron alteration (chapitre 6; Fig. 4-2e; Corriveau et al., 2015 and Appendix 4 for the geochemical analyses). The Cole Uranium showing may thus represent another example of albitite hosted-uranium mineralization in the southern GBMZ and expands the prospective setting for this mineralization type outside the Southern Breccia.

4.8 Western section – Lou IOAA sector

The Lou IOAA sector hosts the NICO deposit and the polymetallic uranium showings of the Southern Breccia. IOAA in the Lou IOAA sector is mainly developed after the basal metasiltstone and the overlying quartz meta-arenite units of the Treasure Lake Group, but also significantly extends into the overlying Faber Group volcanic rocks.

The NICO deposit is formed through pulsating HT calcic–iron and HT potassic–iron alteration driven by high-level intrusive activity in the region. Early pyroxene-rich (hedenbergite + augite) skarn relicts are locally preserved and are extensively overprinted by amphibole-rich (actinolite and hornblende) HT calcic–iron, calcic–potassic–iron alteration and HT potassic–iron alteration (Table 4-2). Biotite (annite) and K-feldspar are the main potassic phases in the calcic–iron–potassic and HT potassic–iron alteration zones and magnetite is present in modal proportions varying between 1 and 90% in the HT calcic–iron, calcic–iron–potassic and HT potassic–iron alteration zones. IOAA assemblages predominantly occurs as semi-concordant to concordant replacements of the Treasure Lake Group metasedimentary units although clearly discordant breccia zones are also formed along fault zones (Goad et al., 2000a; Corriveau et al., 2010b). The main ore zone of the NICO deposit is named the “Bowl zone” and the mineralized lenses of NICO can be traced along strike in the Treasure Lake Group over 1.9 km (Goad et al., 2000b). Native Bi, Au and minor chalcopyrite mineralization are associated with magnetite-bearing alteration and are cross cut by a cobaltian arsenopyrite, cobaltite, bismuthinite, native Au, Au–Bi–Te alloys and pyrite with or without chalcopyrite mineralization (Goad et al. 2000a, b). Carbonate, tourmaline and earthy hematite alteration as well as biotite–hematite or chlorite–hematite assemblages typical of low-temperature (LT) potassic–iron alteration are associated with the later stages of mineralization within the NICO ore zone. In addition, late-stage veinlets comprised of chalcopyrite, hematite, quartz, chloropotassic hastingsite, chlorite, emplectite ($CuBiS_2$) and wittichenite (Cu_3BiS_3) cut the Co–As–Fe-rich sulfides and the magnetite-bearing alteration assemblages (Acosta-Góngora et al., 2014). This assemblage is slightly atypical of LT potassic–iron alteration in that amphibole remains stable with chlorite (cf. paragenetic

descriptions in Corriveau et al. 2010b). Tungsten, Ni and Zn concentrations are also elevated throughout the NICO ore zone and alteration envelope (Goad et al. 2000b; Acosta-Góngora et al., 2014).

An early sodic alteration is documented in the footwall of NICO and localized relicts of this early sodic alteration are preserved in the Bowl zone. In the Faber Group rhyolite capping the NICO deposit, IOAA is predominantly potassic (K-feldspar) with localized occurrences of HT calcic–iron, HT potassic–iron and LT potassic–iron alteration (Gandhi and Lentz, 1990; Goad et al., 2000a). Some of the iron oxide breccia zones, texturally similar to the iron oxide breccias of the Sue-Dianne deposit, and chloritized biotite±magnetite veins formed during the HT potassic–iron and LT potassic–iron alteration stage are chalcopyrite-rich. In the iron oxide-rich breccia zones of the Summit Peak showing, like in the Sue-Dianne deposit and the Brooke prospect, hematite systematically replaces magnetite (Fig. 4-6b–e). The rhyolite is also locally brecciated by sulfarsenide veins typical of the NICO mineralization in the immediate vicinity of the “Bowl zone”.

The Southern Breccia polymetallic uranium occurrences are exposed in a fault-bound 3 km-long by 500 m wide albitization corridor in the lowermost siltstone unit of the Treasure Lake Group previously mapped as hornfelsed sedimentary rocks (cf. Goad et al., 2000a, b; Mumin et al., 2010). Uranium mineralization in the Southern Breccia zone follows several episodes of sodic alteration and an early and regional HT potassic–iron alteration composed of biotite and magnetite. Uraninite is precipitated in HT potassic–iron veins composed in variable modal proportions of magnetite–ilmenite–K-feldspar–biotite–apatite–zircon locally enriched in pyrite, chalcopyrite and molybdenite and with traces of bornite, chalcocite, wolframite, bismuthinite and barite (Fig. 4-7a–e; Table 4-2; chapitre 6). In some of the magnetite–ilmenite-rich veins that predate the main uranium mineralization event, niobium is locally enriched and hosted in a Fe–Ti–Nb mineral (poss. titanian columbite) formed after the magnetite and ilmenite crystals of the veins. This Fe–Ti–Nb mineral is then retrograded to a wide variety of minerals containing in variable proportions Ca, Fe, Nb, REE (Nd, Dy Ce), Ti, U and Y precipitated with increasing intensity of a LT potassic–iron (chlorite, K-feldspar) alteration overprint (Fig. 4-7c; poss. various types of aeschynite). The LT potassic–iron overprint is also locally associated with retrograde replacement and/or rimming of some apatite crystal by xenotime. Northward toward the NICO deposit, the HT potassic–iron veins transition to calcic–iron–potassic veins richer in amphibole and with an overall mineralogy more typical of the NICO deposit calcic–iron–potassic alteration zones, but richer in titanium minerals (titanite, ilmenite, rutile; chapitre 6). Along the northern faulted margin, sodic (albite) alteration is also cross-cut by pyrite and arsenopyrite-bearing

calcic–iron alteration (amphibole+magnetite veinlets) (Potter, unpublished field notes). Progressive increases in oxygen fugacity during transient uplift of the Southern Breccia uranium zone late in the HT potassic–iron alteration stage marked the transition to LT potassic–iron alteration that locally redistributed uranium and transformed chalcopyrite and bornite into chalcocite. REE-bearing allanite and monazite were also formed during this alteration stage and concentrated LREE in some of the LT potassic–iron alteration zones of the Southern Breccia. Early REE enrichments relate to apatite and xenotime crystallization during the HT potassic–iron alteration stage and the precipitation of uraninite during the main uranium mineralization event (Fig. 4-7a). The chondrite-normalized REE profile of the REE-rich sample of the Southern Breccia, in which REE are weakly fractionated (La/Yb of 4.6; Corriveau et al., 2015 and Appendix 4 for the geochemical analyses), differs from those of the Ron LREE-rich sample, but is similar to some REE-rich samples of the Hump iron showing and Cole Uranium showing in which apatite is the main REE-bearing mineral (Fig. 4-4). Late stage and NE-oriented iron–magnesium (chlorite–hematite–uraninite) veins are associated with or trend parallel to the NE-oriented Lou Lake fault, but are minor in scale compared to the HT potassic–iron uranium mineralization event.

4.9 Western section – South Lou sector – Duke zone

The Duke zone is entirely hosted in the Treasure Lake Group metasedimentary rocks. An early and generally incipient to moderate sodic alteration and HT potassic–iron alteration assemblage (biotite±magnetite) are overprinted by skarns and multiple generations of intense and pervasive HT calcic–iron alteration that extend discontinuously over hundreds of meters. The skarns replace partially albitized carbonaceous metasedimentary precursor rocks while conversely the HT calcic–iron alteration preferentially replaces siliceous units. Interfingering of both parageneses is common along contacts between siliceous and carbonaceous units although the HT calcic–iron alteration also replaces the skarn-type HT calcic–iron paragenesis. In addition to hornblende/cummingtonite±anthophyllite, actinolite and magnetite (between 1% and 90%), the HT calcic–iron mineral assemblages also locally include apatite, garnet and titanite. Diopside generally prevails in the skarn but locally the modal content of garnet can exceed 70 modal %.

Into the main showings of the Duke zone, an intense HT potassic–iron alteration, principally composed of biotite and magnetite with accessory K-feldspar and locally garnet, typically overprints the HT calcic–iron alteration and is followed by extensive LT potassic–iron and then

LT calcic–iron alteration. Chlorite, accompanied by variable modal proportions of hematite, sericite, and minor carbonate minerals, is the main mineral formed in the LT potassic–iron alteration zones where it is superimposed on amphibole/clinopyroxene-rich HT calcic–iron or biotite-rich HT potassic–iron assemblages. Epidote±allanite±K-feldspar characterizes most of the LT calcic–iron alteration zones.

The different stages of IOAA in the Duke zone resulted in a wide variety of base metal-rich and polymetallic showings in a 350 m wide area. Among those are the Duke Co–Cu–Ni–Bi–Fe–REE showing with anomalous Au–Zn–Pb–Sn contents, the LJLVS Fe–Co–Ni–U showing with anomalous Cu–Pb–Zn contents, the LP's Fe–W showing with anomalous Cu–REE contents, the South Duke copper showing with anomalous zinc contents and the Oxymoron LREE showing with anomalous uranium and thorium contents (Corriveau et al., 2015 and Appendix 4 for the geochemical analyses; Table 4-2; Fig. 4-8a–d).

The Duke showing is located in a deformation zone at the contact between the metacarbonaceous and the basal metasiltstone units of the Treasure Lake Group (see Goad et al., 1996 for geological maps of the showing). Tectonic foliations strike between 285° and 320°, dip northeast and are slightly discordant to concordant with the Treasure Lake Group bedding (Goad et al., 1996; Mumin et al., 1996). Hydrothermal and tectonic breccias primarily cemented by magnetite are well developed in the deformation zone. HT calcic–iron (clinopyroxene, amphibole, magnetite) and calcic–iron–potassic alteration (amphibole, magnetite, biotite) types predominate and are superimposed over the partially to extensively albitized metacarbonate and metasiltstone beds (Figs. 4-8a, 4-9a–c). An epidote-bearing HT potassic–iron (K-feldspar–epidote±magnetite) evolving to a LT calcic–iron alteration is superimposed on the earlier HT calcic–iron and calcic–iron–potassic alteration zones (Fig. 4-8d). Magnetite was systematically retrograded to hematite in the showing during the late-stage LT calcic–iron alteration. The main mineralization event in the Duke showing is related to the calcic–iron–potassic alteration assemblage but is also hosted in epidote-bearing HT potassic–iron and late LT calcic–iron alteration facies. Pyrite, shown to be locally nickeliferous by EDS analyses, followed by chalcopyrite and cobaltite are the first sulfides to precipitate. Subsequently LREE-bearing allanite, sphalerite and cassiterite with minor galena and traces of scheelite precipitated with increasing intensity of LT calcic–iron alteration (Fig. 4-9e, f).

The LJLVS showing is hosted by carbonate-bearing metasandstone and metasiltstone of the Treasure Lake Group in a zone of polyphase and discordant to concordant HT calcic–iron alteration fronts and veins that overprint/cut an early sodic alteration. HT calcic–iron alteration is

subsequently overprinted by moderate to strong HT potassic–iron alteration, and then LT potassic–iron alteration (Figs. 4-8b, 4-9g–h, j). Clinopyroxene-rich skarns are locally present, but amphibole-rich HT calcic–iron alteration prevails. LT potassic–iron alteration is predominately composed of chlorite, but also includes a talc-rich zone that potentially reflects retrograded assemblages, similar to the talc-rich LT potassic–iron alteration in the Carbonate Mountain zone. Minor specular hematite also precipitated during the LT potassic–iron stage. Cobalt, nickel and uranium are concentrated into magnetite- and sulfarsenide-rich calcic–iron–potassic veins composed of Mn-rich amphibole and magnetite with minor biotite. This alteration cuts earlier amphibole-rich HT calcic–iron alteration. Nickeliferous skutterudite, locally rimmed by an unidentified Bi–Mo–Pb arsenide, precipitated first and was followed by the formation, in larger modal proportions, of cobaltian arsenopyrite and cobaltite, both with variable nickel contents and also of minor uraninite (Fig. 4-9i). Gamma ray spectrometer measurements recorded eU concentrations up to 329 ppm in the LJLVS showing. The Co–Ni–U-rich alteration is then cut by chalcopyrite-bearing HT calcic–iron veins and alteration fronts composed of hornblende and magnetite (Fig. 4-9k–m). Only a weak LT potassic–iron assemblage is superimposed over the main mineralized alteration zone of the LJLVS showing, as indicated by hematite rimming of the magnetite crystals and faint retrograde alteration of amphibole to chlorite. Tectonic deformation in the LJLVS showing is weak to moderate and the resulting tectonic foliations, striking 148-154° and steeply dipping to the SW, are concordant with the bedding at this locale, but discordant with the regional bedding in the Treasure Lake Group western section oriented around 270°-300° and dipping NE.

IOAA facies in the LP's showing are mostly constrained in a deformation zone within metasiltstone-rich interval of the quartz meta-arenite unit of the Treasure Lake Group (Fig. 4-10a). Tectonic foliation, striking at 300° and steeply dipping to the NE, is slightly discordant to the bedding striking between 260° and 280° and steeply dipping to the N and NNE. Small parasitic folds are also locally formed in the deformation zone (Fig. 4-10b, d). A few meters SW away from the deformation corridor, the metasiltstone is undeformed, weakly altered and exhibits well preserved ripple marks (Fig. 4-10c). This indicates the strong relation between tectonic deformation and IOAA alteration in the South Lou sector. Multiple generations of amphibole-bearing HT calcic–iron alteration (hornblende, cummingtonite, actinolite) overprinted by HT potassic–iron (biotite–magnetite±garnet) and then different generations of LT potassic–iron alteration (chlorite, hematite–chlorite±sericite, hematite) characterize the LP's showing alteration signature (Fig. 4-10a, d–g). The tungsten–iron mineralization is related to a magnetite-rich HT calcic–iron alteration that contains disseminated scheelite and minor chalcopyrite (Figs.

4-8c, 4-10g, h). The chemistry of this tungsten-rich HT calcic–iron alteration is similar to the tungsten-rich HT calcic–iron alteration of the NICO deposit in which tungsten contents average 200 ppm throughout the ore zone and up to 2 wt. % over a few meters and scheelite is the main tungsten-bearing phase (Fig. 4-6a; Goad et al., 2000a, b; Corriveau et al., 2015 and Appendix 4 for the geochemical analyses; Table 4-2). Subsequent stages of copper mineralization in the LP's zone occur as small veinlets composed of chalcopyrite and magnetite that crosscut the magnetite-rich and tungsten-bearing HT calcic–iron alteration and as LREE-rich K-feldspar veins with minor chalcopyrite that also cut HT calcic–iron alteration (Fig. 4-10i). REE in the K-feldspar veins are strongly fractionated, with La/Yb = 123.

The South Duke showing is located along strike of LP's showing and occurs in a zone of intense LT potassic–iron alteration superimposed over the earlier HT calcic–iron alteration in which hydrothermal magnetite and amphibole are completely replaced by hematite and chlorite (Fig. 4-10j–k). The copper mineralization consists of chalcopyrite–carbonate–hematite veinlets formed late in the LT potassic–iron alteration stage as they cut the main LT potassic–iron alteration zone (Fig. 4-10k; Corriveau et al., 2015 and Appendix 4 for the geochemical analyses; Table 4-2).

The Oxymoron showing, located in the transition zone between the carbonaceous and the quartz arenite units of the Treasure lake Group, is related to an intense and extensive LT calcic–iron alteration superimposed on HT calcic–iron alteration completely replaced by LT potassic–iron alteration (earthy hematite–chlorite; Fig. 4-10l–n). The REE mineralization is composed of uraniferous allanite precipitated during the LT calcic–iron alteration stage (Figs. 4-8d, 4-8n, o). REE are strongly fractionated in the Oxymoron showing (La/Yb ratio is up to 261) and on a chondrite-normalized diagram, the LREE profile of the Oxymoron showing is similar to the Ron LREE-rich iron showing, but with a higher MREE and HREE content that may reflect the REE content of the precursor rock (Fig. 4-4).

The overall metallic and alteration signature of the LJLVS, Duke and LP's showings mimic the alteration and metallic signature of the NICO ore zone, characterized by extensive amphibole-clinopyroxene-bearing HT calcic–iron and biotite-bearing calcic–iron–potassic and HT potassic–iron alteration, enrichment in Bi, Co and Cu with anomalous Ni, W and Zn and of sulfarsenide minerals as the main ore phases (Figs. 4-6a, 4-8a–c). The main discrepancies between the Duke zone showings and the NICO deposit metallic signature are that high gold and bismuth concentrations were not reported in every showings of the Duke zone and that allanite- and LREE-rich LT calcic–iron alteration was not reported in the NICO deposit (Figs. 4-6a, 4-8d), but

occurs in some Southern Breccia uranium showings where LT potassic–iron alteration is well developed (Fig. 4-7a; chapitre 6).

The NICO deposit HT calcic–iron and HT potassic–iron alteration zones are also devoid of uranium and thus differ from the same alteration zones in the South Lou sector that can be uraniferous (e.g., LJLVS). Most of the uranium in the Lou IOAA sector may have been concentrated in the Southern Breccia uranium showings (Fig. 4-7a–e). The intense LT potassic–iron alteration (chlorite±hematite), ubiquitous in the Duke zone, is also less extensive in the NICO deposit although highly potassic and copper endowed LT potassic–iron alteration is well developed in the rhyolite of the Faber Group capping the NICO deposit (Fig. 4-6b–e).

4.10 Western section – Mazenod sector

Potassic (K-feldspar) alteration with or without incipient magnetite enrichment predominates at the current level of exposure in the Mazenod sector and more particularly in the Sue-Dianne–Brooke zone where it forms the regional alteration envelope of the HT potassic–iron (K-feldspar–magnetite) and LT potassic–iron (K-feldspar–hematite) alteration zones of the Sue-Dianne deposit and Brooke prospect (Fig. 4-11a). Other alteration types include sodic (albite) and HT calcic–iron (amphibole–magnetite±apatite) assemblages across surface exposures in the Marian River deformation corridor, and in both surface exposures and drill holes at the Nod prospect (Fig. 4-11b, c; Mackay and Eveleigh, 1997; this work). Previous exploration work described the pervasive sodic and HT calcic–iron alteration zones in the Marian River deformation as hornfelsed dacite (North, 1995). LT calcic–iron alteration and zones of extensive silicification related to quartz vein systems formed in NE-oriented faults are also present in the Mazenod sector.

4.10.1 Mazenod–Sue-Dianne–Brooke zones

The Sue-Dianne deposit is primarily hosted in the uppermost unit of the Mazenod assemblage (Faber Group). The IOCG mineralization occurs in a tectono-hydrothermal breccia zone that extends vertically over 300 m and plunges steeply to the east (Gandhi, 1989a). The deeper part of the deposit is characterized by an intense sodic alteration zone predominantly hosted within the apex of a porphyritic intrusion and the host volcanic unit of the Mazenod assemblage (Goad et al., 2000a; Camier, 2002; Mumin et al., 2010). This sodic alteration extends to the surface.

Above and superimposed on the sodic alteration, a pyrite-rich HT potassic–iron alteration zone grades upward to chalcopyrite-bearing HT potassic–iron (magnetite–K-feldspar) and LT potassic–iron (K-feldspar–hematite–chlorite–fluorite±barite) alteration that is commonly overprinted by a pervasive LT calcic–iron (epidote±allanite) alteration (Fig. 4-11a). Most of the copper–silver mineralization in the Sue-Dianne deposit is related to the HT potassic–iron and LT potassic–iron alteration stages (Figs. 4-8f, 4-11d). Diamond drilling indicates moderate uranium enrichment related to the iron oxide-rich HT potassic–iron stage with concentrations up to 150 ppm U continuous over several meters of drill cores (Gandhi, 1989a). The intensity of LT potassic–iron alteration increases towards the top of the Sue-Dianne deposit, but the preservation of magnetite relicts in hematite crystals up to the present day surface indicates that HT potassic–iron alteration extended to the upper parts of the Sue-Dianne deposit and predated the LT potassic–iron event (Camier, 2002; this work). Magnetite replacement by hematite throughout the deposit is indicated by systematic lobate, corroded, wavy and irregular boundaries of magnetite crystals rimmed by hematite (Fig. 4-11e). In zones of intense LT potassic–iron alteration, chalcopyrite is sequentially rimmed by bornite and then chalcocite, indicating a progressive increase in oxygen fugacity during the LT potassic–iron alteration stage (Fig. 4-11f, g). The locally intense and commonly allanite-bearing LT calcic–iron alteration superimposed over LT potassic–iron alteration is distributed both in the immediate vicinity and throughout the Sue-Dianne deposit. This LT calcic–iron alteration is itself crosscut and overprinted by quartz veins and silicification related to the quartz vein systems of the GBMZ (cf. Gandhi, 2000; Byron, 2010).

In the immediate surroundings of the Sue-Dianne deposit at surface, sodic alteration very locally overprints potassic alteration related to the main HT potassic–iron and LT potassic–iron alteration stages (Fig. 4-11h). HT calcic–iron (amphibole and amphibole–magnetite) alteration, overprinted by HT potassic–iron and LT potassic–iron alteration, is also present at surface at the summit of the Sue-Dianne deposit, but has not been conclusively recognized in drilling in the deeper parts of the deposit.

The Brooke prospect is hosted by the rhyolitic to andesitic upper unit of the Dianne subassemblage of the Lou assemblage at the contact between a bedded volcanic unit and a massive rhyolite (Eveleigh, 1997). Early sodic alteration is overprinted by localized magnetite-rich HT calcic–iron, extensive HT potassic–iron (magnetite–K-feldspar), potassic (K-feldspar), LT potassic–iron (K-feldspar–hematite), and finally by LT calcic–iron (epidote) alteration (Figs. 4-8e, 4-11a, i). Metal enrichments in the Brooke prospect occurred during the HT potassic–iron, LT

potassic–iron and LT calcic–iron alteration stages. Mineralization began during pyrite-bearing HT potassic–iron alteration (± trace chalcopyrite) subsequently followed by chalcopyrite-bearing HT potassic–iron and then LT potassic–iron alteration (Fig. 4-11j–m). Copper mineralization is associated with extensive hydrothermal and tectono-hydrothermal brecciation. The LT calcic–iron alteration (epidote±K-feldspar) stage occurred during late-stage fracturing and right-lateral transcurrent faulting. Chalcopyrite is the dominant copper-bearing mineral of the LT calcic–iron alteration stage and is sequentially replaced by bornite and then chalcocite (Fig. 4-11o). Scheelite, molybdenite, and minor bismuthinite and thorite also precipitated in the LT calcic–iron alteration (Fig. 4-11p–r; Lypaczewski et al., 2013; this work). Coupled with the systematic replacement of magnetite by hematite, this epidote–bornite–chalcocite mineralization stage indicates a progressive increase in oxygen fugacity during the formation of the Brooke prospect similar to the Sue-Dianne deposit. The sulfide precipitation sequence mineral paragenesis alteration facies are also identical to the Sue-Dianne deposit.

Both the Sue-Dianne deposit and the Brooke prospect also exhibit moderate to important LREE enrichments (Fig. 4-8e–f). In the Sue-Dianne deposit, REE enrichments are related to HT potassic–iron, LT potassic–iron and LT calcic–iron alteration zones to a maximum total REE metal content of 1384 ppm (data of Camier, 2002). Apatite and allanite are the main REE-bearing minerals with minor monazite locally formed by retrograde alteration of apatite crystals (Camier, 2002; Lypaczewski et al., 2013; this work). Paragenetically the apatite are associated with the HT potassic–iron stage, the monazite retrograded from apatite are related to LT potassic–iron stage and allanite was formed at the LT calcic–iron stage. In the Brooke prospect, LREE are principally hosted by allanite and apatite up to a maximum of 1744 ppm REE metal. Lypaczewski et al. (2013) have also documented localized retrograde alteration of apatite into britholite during the LT calcic–iron alteration stage. With La/Yb ratio up to 457 in the Sue-Dianne deposit and up to 173 in the Brooke prospect, REE fractionation in the Sue-Dianne deposit is similar to LREE showings of Duke and Ron zones, but is less intense in the Brooke prospect. As the REE-bearing minerals are more diversified in the Brooke prospect and Sue-Dianne deposit, the chondrite-normalized LREE profiles of some samples from the Mazenod sector differ from those of the Ron and Duke zones LREE-rich showings (Fig. 4-4).

4.10.2 Nod zone

IOAA in the Nod zone is predominately developed in the andesitic to rhyolitic lower unit of the Dianne subassemblage (Faber Group), but also extends into lenses of the Treasure Lake Group

metasiltstone unit exposed in the area. Past drilling and drill core re-examination of the Nod prospect reveals that copper mineralization is dominantly related to a slightly potassic calcic–iron–potassic alteration that incipiently brecciates an earlier sodic alteration and extends to depths of at least 203 m (Fig. 4-12a–d; Mackay and Eveleigh, 1997). Copper is also accompanied by minor enrichments in gold (up to 0.4 ppm) and silver (up to 17.4 ppm; North, 1995; Mackay and Eveleigh, 1997). In the country rocks, HT calcic–iron alteration occurs as pervasive magnetite±amphibole and amphibole±magnetite replacements of the aphanitic matrix of the volcanic rocks or as veins cutting earlier sodic alteration. Localized overprints of cobalt-enriched HT potassic–iron alteration (up to 178 ppm Co) occur on surface, but drilling did not intersect this alteration assemblage at depth (Fig. 4-12a).

4.11 Relation between alteration and metal enrichments

The sodic and sodic–calcic–iron alteration stages in the southern GBMZ IOAA systems are typically not associated with economic metal enrichments (Table 4-2; Figs. 4-2, 4-6, 4-7, 4-8). However source rocks containing elevated content of least mobile elements like niobium and tantalum in titanium minerals (e.g., rutile, titanite) and thorium can contribute to the formation of HFSE showings such as the Esther zone MHF tantalum–uranium showing or the Dennis zone thorium occurrences. With its regional extent, characteristic mineralogy and distinct chemical signature, sodic alteration indicates a large-scale IOAA system. Discovery of IOAA systems can be facilitated in regions with large and public geochemical databases or where albitites have been described in the available literature. The metal associations observed in the sodic and sodic–calcic–iron alteration zones of the GBMZ (chapitre 7) mimic the metal-poor composition of sodic alteration observed in other major IOAA districts around the world (Oliver et al., 2004; Williams et al., 2005; Monteiro et al., 2008a, b; Benavides et al., 2008a, b).

The HT calcic–iron alteration stage is primarily related to iron mineralization without any significant enrichment in base or precious metals (Table 4-2; Figs. 4-2, 4-6, 4-7, 4-8). This is exemplified by the Ron and Hump iron showings. However, apatite crystallization during the HT calcic–iron alteration stage, as observed in some IOA showings of the Ron and Hump zones, the Fab system (chapitre 7) and the Port Radium–Echo Bay district (chapitre 3) can generate REE mineralization. Superimposition of later alteration stages on apatite-rich HT calcic–iron alteration can also remobilized some of the REE, especially the LREE. This is shown in the Ron system where LREE-rich allanite formed at the expense of earlier apatite and in the Sue-Dianne deposit where monazite and other REE phosphates formed during the retrograde alteration of

apatite at the LT potassic–iron alteration stage. Globally, REE enrichments at the HT calcic–iron alteration stage (or at the equivalent skarn development stage) have been observed in IOA deposits such as the Kiruna district in Sweden (Jonsson et al., 2013), the Pea Ridge/Pilot Knob deposits in the United States (Missouri Iron belt; Whitten and Yancey, 1990; Nold et al., 2014) and the Hillside deposit in Australia (Ismail et al., 2014). The geological constraints on a contemporaneous formation of the Hump and Ron IO±A showings with the NICO and Sue-Dianne IOCG deposits also genetically and temporally relates IO±A mineralization with IOCG formation, but illustrate their common spatial decoupling.

The alteration zones at the Duke and Carbonate Mountain alteration showings highlight that while siliceous precursor rocks are replaced by amphibole–magnetite assemblages during high temperature calcic-iron alteration, carbonate-rich units preferentially form skarn at first. These skarns themselves replace sodic alteration zones. This demonstrates that skarn assemblages can form in IOAA systems and their presence in prospective districts should spur further exploration for IOAA-related deposits. Their presence also implies that carbonate-rich (or calcium–magnesium) units remobilized can be intensely and extensively metasomatized during the formation of the IOAA systems. At NICO, Sidor (2000) proposed that the precursor rocks for many of the high temperature calcic–iron and high temperature potassic–iron alteration zones in the NICO deposit were carbonate-rich metasedimentary rocks. This is supported by:

1) the presence of potential dolomite bed relicts in the calcic–iron/HT potassic–iron alteration zone (Sidor, 2000);

2) relicts of skarn and clinopyroxene-rich HT calcic–iron alteration overprinted by amphibole-rich calcic–iron alteration; and

3) the location of the deposit along the expected continuation of the carbonate unit of the Treasure Lake Group as mapped in Gandhi et al. (2014).

The overall calcium- and magnesium-rich chemical signature of the deposit thus partially reflects the chemical nature of the host rocks (Fig. 8a; Acosta-Góngora et al., 2015a, b).

The calcic–iron–potassic alteration stage is either transitional between HT calcic–iron and HT potassic–iron alteration (e.g., Nod prospect) or forms instead of HT potassic–iron alteration in geological sequences where calcium- and/or magnesium-rich rocks are abundant (e.g., NICO and most of the South Lou sector showings). Calcic–iron–potassic alteration zones that are transitional to the HT calcic–iron and HT potassic–iron alteration stages are characterized by mild potassium enrichment, weak or absent HT potassic–iron alteration, and weak to moderate

metal enrichments. Typical examples from the southern GBMZ IOAA systems are the Cole Uranium showing in the Cole sector, enriched in uranium, REE and yttrium, and the Nod prospect in the Mazenod sector that is enriched in copper, silver and gold.

When developed in calcium- or magnesium-rich sources (i.e., earlier alteration zones or Ca- and/or Mg-rich precursor rocks), high temperature potassic–iron alteration is replaced by calcic–iron–potassic assemblages. These alteration zones are spatially extensive, and characterized by important potassium and metal enrichments. Known examples from the southern GBMZ IOAA systems occur in the South Lou and the Lou IOAA sectors, where calcic–iron–potassic alteration zones formed at the HT potassic–iron alteration stage are well developed and associated with significant enrichments in Au, Bi, Co, Fe, Ni, and W and weaker enrichments in Cu, Th and U (Table 4-2; Figs. 4-6a–b, 4-7a, 4-8a–d). The formation of calcic–iron–potassic alteration at the HT potassic–iron alteration assemblages is not unique to the GBMZ. Fertile calcic–iron–potassic alteration is well developed in the IOCG and affiliated deposits of the Punta del Cobre district in Chile that hosts the Candelaria magnetite-group IOCG deposit and the Ernest Henry magnetite-group IOCG deposit in Australia where carbonate-rich metasedimentary rocks are abundant (Marschik and Fontboté, 2001a; Mark et al., 2006). At Candelaria, the IOCG ore zones are hosted and/or related to K-feldspar–amphibole–magnetite±biotite alteration (Marschik and Fontboté, 2001a) whereas at Ernest Henry some of the IOCG mineralization is related to a garnet-rich K-feldspar–magnetite alteration (Mark et al., 2006). Both the Candelaria and Ernest Henry deposits are also enriched in Co, Ni and As, as observed at the NICO deposit, but with higher contents of Cu that may reflect the greater abundance of intermediate volcanic or intrusive rocks in the geological environment and/or differences in physico-chemical properties of the ore-forming fluids.

In the southern GBMZ, HT potassic–iron alteration is associated with important enrichments in Ag, Au, Cu, Th, U and Y+REE and weaker enrichments in Bi, Co and Ni. This alteration assemblage is spatially extensive in the Lou IOAA and Mazenod sectors (Table 4-2; Figs. 4-6, 4-8) and is associated with strong hydrothermal brecciation where magnetite forms the breccia cement and biotite and/or K-feldspar alters the fragments. Much like the southern Great Bear magmatic zone IOAA systems, Cu and Au mineralization at the Salobo magnetite-group IOCG deposit in the Carajás district (Brazil) is associated with biotite–magnetite–K-feldspar-grunerite±cummingtonite–garnet (Requia et al., 2003). These observations imply that extensive HT potassic–iron alteration may be an indicator of base metal-rich mineralization in IOAA systems. Conversely, at the transition toward HT potassic–iron alteration base metal

mineralization remains marginal but the transition can be a source of moderate vanadium and REE enrichments as illustrated in the southern GBMZ by the Hump zone iron–vanadium±REE showings (Fig. 4-2a). Such transitional zones to HT potassic–iron alteration can be easily identified in an IOAA district as they form relicts overprinted by sodic and HT calcic–iron alteration. Their poor base metal endowment is also observed in many other IOCG districts such as the Punta del Cobre (Chile; Marschik and Fontboté, 2001a) and Cloncurry (Australia; Mark et al., 2006).

In each sector of the southern GBMZ IOAA system, the metal endowment related to the LT potassic–iron alteration stage appears to be controlled by the previous alteration stages. In the Lou IOAA, South Lou and Mazenod sectors, where extensive and mineralized calcic–iron–potassic and HT potassic–iron alteration types occur, the LT potassic–iron alteration stage is generally associated with ingress and/or remobilization and concentration of copper, LREE and uranium. The Sue-Dianne deposit, in which an early and strong HT potassic–iron alteration is overprinted by LT potassic–iron alteration, represents potential ore forming processes that happen in hematite-group IOCG deposits in which some of the pre-concentrated Cu and REE enriched during the HT potassic–iron alteration are remobilized and concentrated during the LT potassic–iron alteration stage.

In the Eastern section sectors where HT potassic–iron alteration is neither spatially extensive nor intense, the LT potassic–iron alteration stage superimposed over HT calcic–iron and sodic alteration is typically associated with uranium and/or LREE enrichment, but without significant base metal enrichments. Exceptions include the spatially limited zinc mineralization in the Carbonate Mountain prospect and copper mineralization in the Esther copper prospect. LT potassic–iron alteration can also remobilize and concentrate certain elements enriched in earlier alteration stages such as Nb and Ta as noted in the MHF showing of the Esther zone and the Southern Breccia uranium showings. The composition of the precursor rocks or mineralogy of precursor alteration exert an important control on the mineral assemblages formed in the LT potassic–iron alteration zones. This is illustrated by the systematic formation of chlorite in LT potassic–iron alteration zones superimposed over HT calcic–iron alteration (Duke, NICO deposit and Carbonates Mountain zones), talc formation where LT potassic–iron alteration overprints skarn-type HT calcic–iron alteration and formation of hematite, K-feldspar and muscovite where LT potassic–iron alteration overprints HT potassic–iron or amphibole-poor HT calcic–iron alteration.

Metals in the LT calcic–iron alteration stage also appear to be scavenged from previous alteration types. In the Sue-Dianne and South Lou sectors, characterized by fertile HT potassic–iron and LT potassic iron alteration, the LT calcic–iron alteration stage is associated with important base metals enrichments as documented in the mineralized zones of the Sue-Dianne/Brooke (Bi, Cu, Mo, LREE) and of the Duke (Cu, LREE, Zn, U) zones. In the Eastern Treasure Lake and Cole sectors, characterized by the absence of fertile HT potassic–iron and LT potassic–iron alteration, the LT calcic–iron alteration stage is either barren or locally associated with LREE enrichment when superimposed on apatite-bearing iron oxide rich alteration zones (e.g., Ron zone). It is also locally associated with moderate zinc (Ron) and moderate to important copper enrichment (Esther).

4.12 Implications for REE mobility in IOAA systems

Throughout the southern GBMZ IOAA systems, REE±Y mineralization formed during the HT calcic–iron (Hump) and calcic–iron–potassic (Cole uranium, Southern Breccia) alteration stages whereas LREE mineralization formed during LT potassic–iron and LT calcic–iron alteration stages (e.g., Eastern Treasure Lake, South Lou, Sue-Dianne). Significant REE enrichment is a characteristic feature of many other IO±A and IOCG deposits in IOAA systems worldwide (e.g., Pea Ridge, Olympic Dam, Kiirunavaara, Cortez Mountains, Yinachan), and typically the REE-rich zones are spatially associated to zones rich in iron oxide (Oreskes and Einaudi, 1990; Whitten and Yancey, 1990; Jonsson et al., 2013; Gleason et al., 2000; Li et al., 2015b). REE are initially concentrated during the HT calcic–iron alteration, calcic–iron–potassic and HT potassic–iron alteration stages and precipitate in a wide variety of minerals (e.g., aeschynite, apatite, REE-carbonates, magnetite, monazite, thorite, titanite, uraninite, xenotime). REE remobilization and re-precipitation during subsequent LT potassic–iron alteration can further enhance metal grades. For example in the Pea Ridge deposit (United States), LREE mineralization relates to late-stage brecciation of the titanium-poor iron oxide mineralization, formed at the HT calcic–iron stage, during a sericite–chlorite–quartz–hematite alteration event (LT potassic–iron stage) with the REE are principally hosted in monazite and xenotime (Whitten and Yancey, 1990). In the Grängesberg IOA deposit from the Kiruna district in Sweden, REE are primarily hosted in fluoroapatite and in a variety of accessory minerals comprised of monazite, allanite, xenotime, LREE-bearing epidote and REE fluorocarbonates (Jonsson et al., 2013). In the Humboldt Buena Vista mine (United States), most of the REE are hosted in apatite formed as part of the main iron

oxide mineralization (HT calcic–iron alteration) whereas at Modarelli mine iron oxide deposit (Cortez Mountains, United States), REE-phosphates are principally hosted in jasperoidal siliceous breccia crosscutting the main iron oxide mineralization (Gleason et al., 2000; HT Ca–Fe stage overprinted by LT potassic–iron). In addition, hematite itself can be enriched in REE and U as documented by Ciobanu et al. (2013) from the Olympic Dam deposit.

Experimental work (Harlov et al., 2005; Budzyń et al., 2011) and petrographic studies of REE mineral solubility and REE mobility in the Kiruna area (Harlov et al., 2002), the Se-Chachun IOA deposit (Bafq district, Iran; Bonyadi et al., 2011), and the Western Carpathian (Ondrejka et al., 2012) demonstrate that changing the activity of the main alkali elements in a fluid overprinting apatite-bearing alteration zones results in the sequential breakdown of apatite in different suites of REE-bearing minerals (e.g., allanite, britholite, hydroxylbastnäsite, huttonite, secondary monazite and apatite, REE-carbonate, thorite, uraninite). For example, Bonyadi et al. (2011) related the initial breakdown of apatite formed during the HT calcic–iron alteration stage to the transition from a NaCl-dominant (sodic and HT calcic–iron alteration stages) to a KCl–CO_2-dominant (potassic, HT potassic–iron and LT potassic–iron alteration stages) system. Harlov et al. (2002) also demonstrated that in the Kiruna area LREE initially hosted in apatite were leached from magnetite ore (HT calcic–iron alteration stage) during low temperature alteration stages (they referred to it as greenschist facies metamorphism from fluids). In addition, host rock composition fosters a wide diversity of REE minerals according to the experimental work of Budzyń et al. (2011) on monazite, allanite and fluoroapatite stability in hydrothermal solutions.

These processes are exemplified in the southern GBMZ IOAA systems where apatite and other REE minerals went through many cycles of dissolution-precipitation reactions with each ingress of a fluid of different composition. This superimposition of alteration types and reequilibration of REE minerals resulted in the wide diversity of REE-bearing phases observed in the southern GBMZ. The widespread allanite-hosted LREE mineralization in the southern GBMZ IOAA systems may also reflects the prevalence of calcium-bearing rocks that resulted in extensive calcic alteration zones, as a Ca-rich environment strongly promotes allanite precipitation over monazite after the initial dissolution of apatite (Budzyń et al., 2011).

4.13 Implications for the evolution of IOAA systems

The ability of hydrothermal fluids to mobilize and precipitate regular suites of elements and metals at each alteration stage of the development of an IOAA system is interpreted as providing the following record of the evolution of their physico-chemical properties:

1) a progressive decrease in fluid temperatures (sodic and sodic–calcic–iron alteration 450°C to > 600°C; de Jong and Williams, 1995; Mark and Foster, 2000; Pollard, 2001; Oliver et al., 2006; Davidson et al., 2007; Williams et al., 2010; Somarin and Mumin, 2014; high temperature potassic–iron 400–500°C; Beane, 1974; Bastrakov and Skirrow, 2007; Baker et al., 2008; Skirrow, 2010; Williams, 2010; LT potassic–iron 170–250°C; Marschik and Fontboté, 2001a; Davidson et al., 2007; Skirrow, 2010; Williams, 2010b);
2) decreasing input of magmatic-hydrothermal fluids after the HT potassic–iron alteration stage (indicated by weaker element mobility and precursor-controlled metal enrichments at the LT potassic–iron and calcic–iron alteration stages and fluid inclusion studies; chapitre 7; fluid inclusion Baker et al., 2008; Williams et al., 2010; Somarin and Mumin, 2014);
3) progressive decrease of F activity in the hydrothermal fluids at the transition between the HT calcic–iron and potassic–iron alteration stages (indicated by weaker heavy REE, Nb, Ta, Th, Ti, and Zr mobility after the HT potassic–iron alteration stage; chapitre 7);
4) progressive decrease of PO_4^{3-} activity at the transition between the HT calcic–iron and potassic–iron alteration stages (indicated by the lower modal content of apatite in the HT and LT potassic–iron alteration zones);
5) transition from Na-dominated to Ca±Mg-dominated to K-dominated fluids (Baker et al., 2008);
6) gradual increase of fO_2 in the fluids as illustrated by martitization of magnetite, zoning of copper sulfides (chapitre 6, 7; this study);
7) pH decrease at the LT potassic–iron stage where white micas crystallization prevails over K-feldspar formation (Benavides et al., 2007; Kreiner, 2011; Girardi, 2014; and
8) gradual increase of fS in the fluids past the HT calcic–iron alteration stage which favors sulfide formation (indicated by higher modal content of sulfides in the HT and LT potassic–iron alteration zones).

These processes can significantly enhance the formation of polymetallic mineralized zones in an IOAA district (Baker et al., 2008; Rusk et al., 2010; Williams et al., 2010). In the southern Great

Bear magmatic zone IOAA systems, this is exemplified in the Duke zone by the weakly to strongly elevated concentrations of Au–Bi–Cu–Co–Fe–Ni–Pb–REE–Sn–W–U within a 350 m wide area related to the HT calcic–iron, HT potassic–iron, and LT potassic–iron alteration stages. In the Esther zone, this is exemplified by the weakly to highly elevated concentrations of Ag–Cu–Nb–REE–Ta–Th–U within a 200 m wide area predominantly related to the Na, LT potassic–iron and LT calcic–iron alteration stages, and in the Lou IOAA sector where Au–Bi–Co–Cu–Mo–Nb–Ni–REE–Th–U–W–Y–Zn are concentrated in either the Southern Breccia uranium showings and/or the NICO deposit during the HT calcic–iron, HT and LT potassic–iron alteration stages (Figs. 4-2, 4-6a–b, 4-7a, 4-8a–d).

The structures of the precursor rocks and regional host stratigraphy also have some influence on the final morphology of the alteration zones in an IOAA system. Most of the mineralized zones that developed within the Treasure Lake Group (Lou IOAA and South Lou sectors, Hump iron showings) occur as semi-concordant to concordant and tabular bodies by selective replacement and brecciation of sedimentary beds. A similar relationship is observed at Candelaria where the mineralized lenses originate from fault zones and create stratiform mineralized lenses and alteration zones in sedimentary and volcaniclastic rocks (Fig. 8 in Marschik and Fontboté, 2001a). In the Sue-Dianne and Cole sectors, most of the larger alteration zones (Cole Breccia, Brooke, Nod, Sue-Dianne) occur as discordant breccia zones in the volcanic rocks of the Faber Group but also in the rhyolites of the Faber Group that cap the NICO deposit.

4.14 Conclusions

The IOAA systems of the southern Great Bear magmatic zone comprise many sectors with different IOAA signatures that directly influence the metal contents and metal associations in their mineralized zones. The IOAA systems, like Lou and Mazenod, which exhibit large-scale zones of polyphase HT calcic–iron alteration overprinted by polyphase and extensive HT potassic–iron alteration, are very likely to form base metal-rich mineralization. Conversely, the IOAA systems where sodic and HT calcic–iron alteration predominates and HT potassic–iron alteration is weak and spatially restricted are more likely to host base metal-poor mineralization such as observed at Cole and Eastern Treasure Lake. Most of the polymetallic and base metal-rich mineralized zones of the southern Great Bear magmatic zone are concentrated in the Western section, in the Treasure Lake Group metasedimentary rocks and volcanic rocks of the Faber Group. The distribution of sodic and HT calcic–iron alteration in the Great Bear magmatic

zone, the formation of large scale sulfide-deficient, iron oxide-rich zones and the numerous IOCG-related mineralized occurrences mimic in extent and intensity what has been observed in other major IOCG districts around the world, demonstrating that the IOAA systems of the southern Great Bear magmatic zone reached the maturity of those hosting world-class IOCG±uranium deposits.

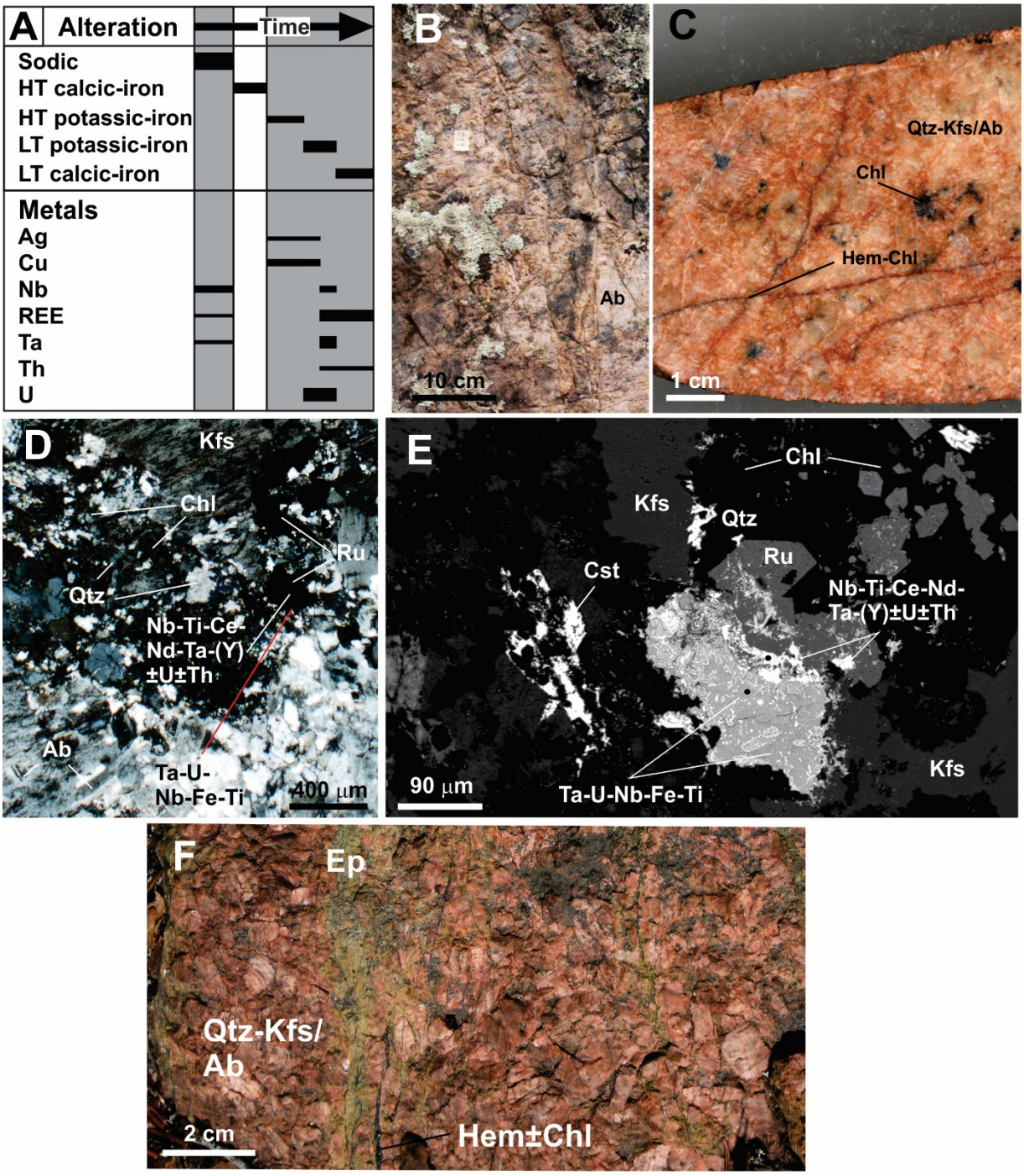

Figure 4-1 IOAA alteration and metal enrichments in the prospects and showings of the Esther and Dennis zones

(a) Sequence of alteration and associated metal enrichments in the Esther zone prospects and showings; (b) Intense and pervasive sodic alteration of a rhyolitic precursor in the Esther system (09CQA-0044); (c) Esther tantalum–uranium showing albitite overprinted by potassic alteration and crosscut by chlorite–quartz–hematite veins hosting the Ta–U–Nb–Th–Ag mineralization (09CQA-1059); (d) Cross-polarized microphotograph of the sodic altered granite with localized relicts of albite in the large K-feldspar crystals (09CQA-1059); (e) Back-scattered electron (BSE) image of the MHF tantalum–uranium mineralization illustrating the Nb–Ti–Ce–Nd–Ta– (Y)-rich mineral exsolved from the rutile crystals and rimmed by the Ta–U–Nb–Fe–Ti-rich mineral (09CQA-1059); (f) LT potassic–iron and subsequent LT calcic–iron veins and front in the albitized granite in the Esther REE–thorium showing (09CQA-0046);

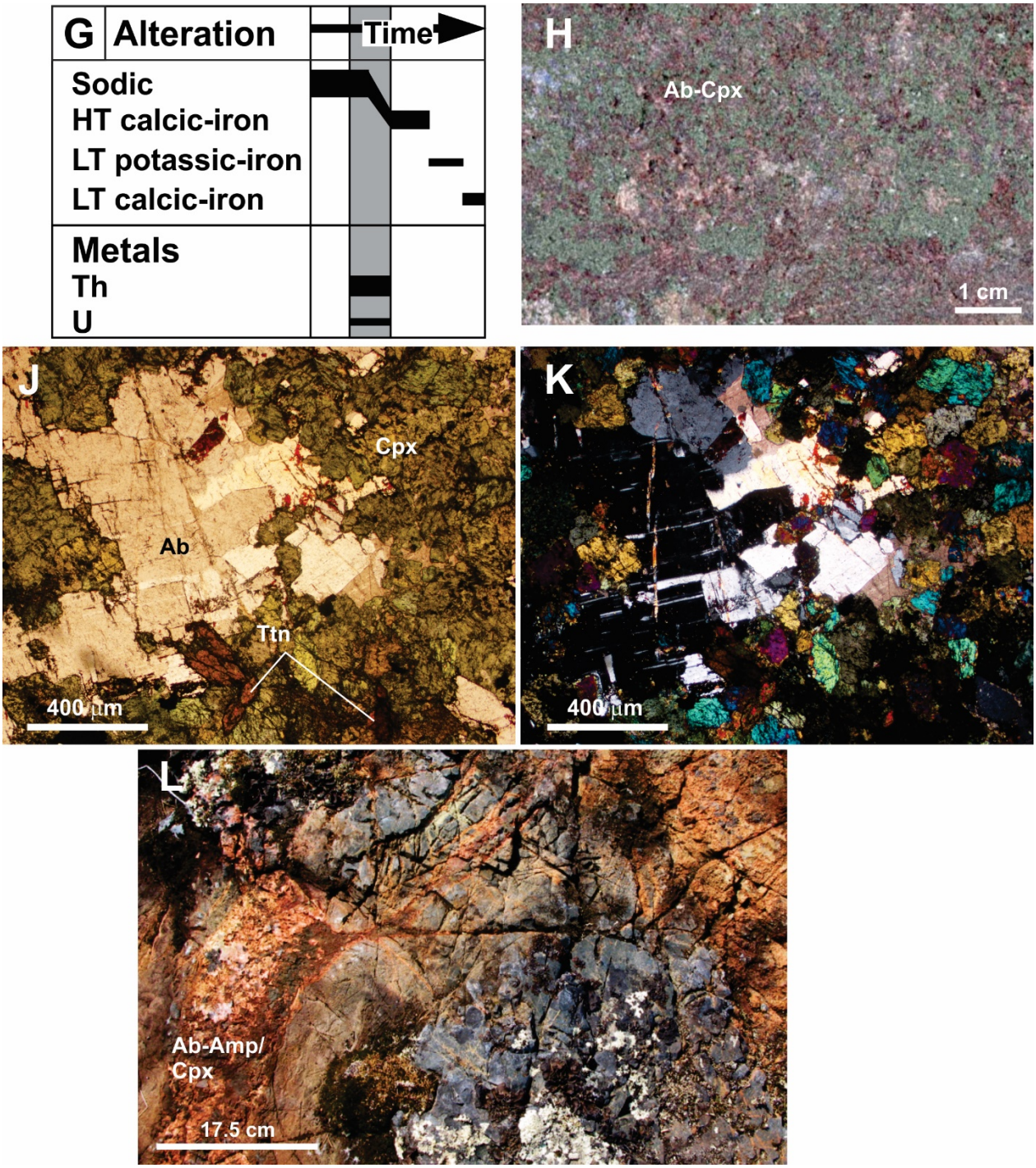

Fig. 4.1 suite – (g) Sequence of alteration and associated metal enrichments in the Dennis zone; (h) Cut slab of the intense and typically thorium-rich sodic–calcic–iron alteration in the Dennis zone (09CQA-1045); (i) Field picture of the pseudo-pegmatitic to coarse-grained and commonly Th-rich sodic–calcic–iron alteration in the Dennis system (09CQA-1045); (j) and (k) Polarized and cross-polarized microphotographs of the thorium-enriched sodic–calcic–iron alteration of the Dennis zone (09CQA-1059).

Mineral abbreviations after Whitney and Evans (2010).

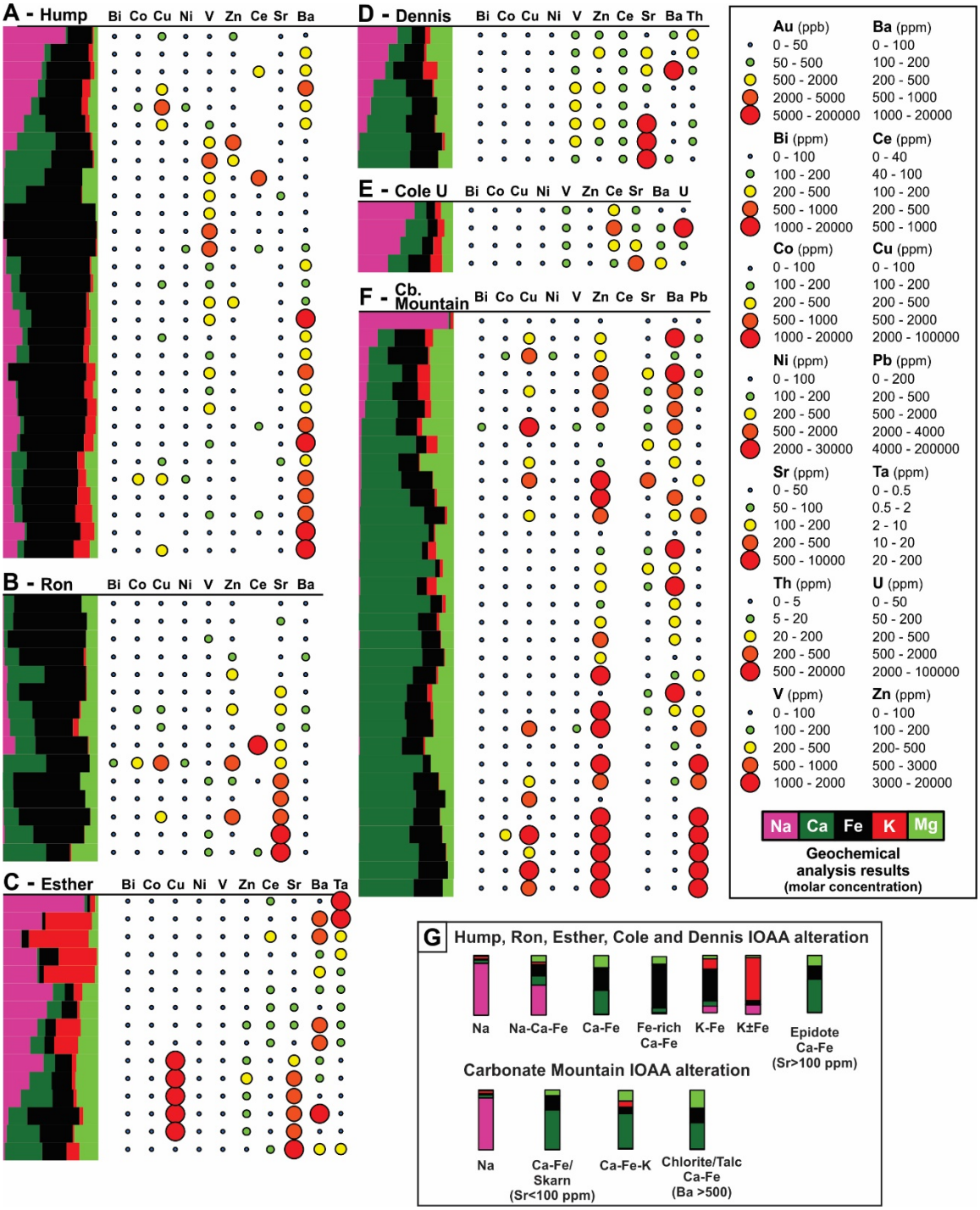

Figure 4-2 Chemical sections of the Eastern section prospects and showings to illustrate the relation between alteration and metal endowment

a) Hump iron showings; (b) Ron iron showings; (c) Esther zone MHF and Esther Cu prospects; (d) Dennis zone thorium occurrence; (e) Cole Uranium showing; (f) Carbonate Mountain prospect.

Sr and Ba are plotted as intensity indicators of LT calcic–iron and potassium-rich alteration respectively.

Geochemical analyses for the Hump, Ron, Esther and Carbonate Mountain prospects and showings were complemented with analyses from Mumin et al. (1996) and Neale and Camier (1997).

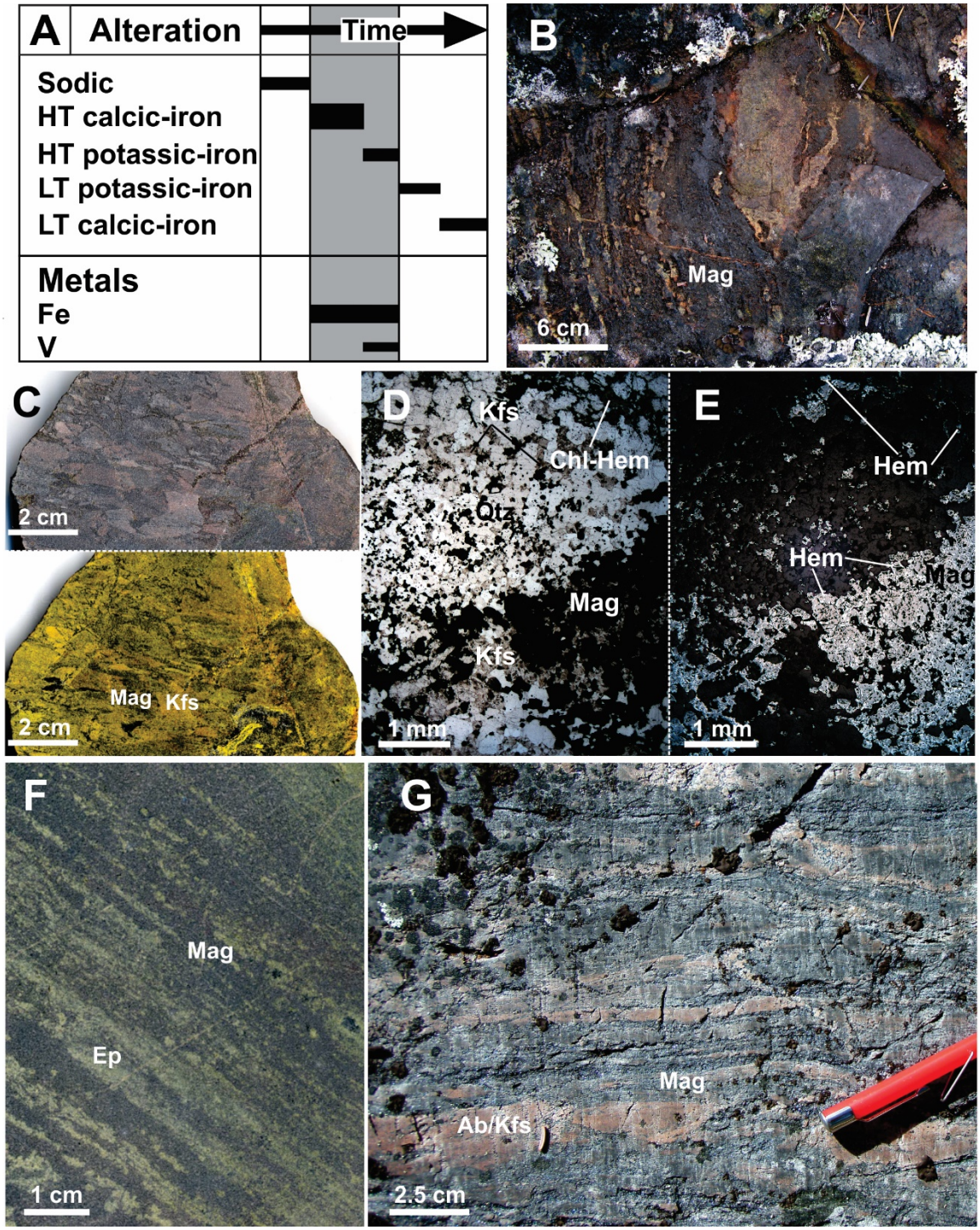

Figure 4-3 IOAA alteration and metal enrichments in the showings of the Ron and Hump zones

(a) Sequence of alteration and associated metal enrichments in the Hump zone showings; (b) Concordant iron oxide mineralization typical of the Hump showings (09CQA-1020); (c) Rock slab picture of the HT potassic–iron alteration in the Hump zone where magnetite cements the breccia and K-feldspar preferentially alters the fragments (09CQA-0040). Right part of the picture is the cobaltnitrate stained slab; (d) and (e) Polarized and reflected light microphotographs illustrating the K-feldspar–magnetite alteration in the Hump showing cut by chlorite veins associated with the partial hematization of the magnetite crystals (09CQA-0043; Microphotographs courtesy of Anthony De Toni); (f) Magnetite–hematite alteration with traces of epidote that is typical of the Hump iron showings

(09CQA-1028); (g) Concordant and intense iron oxide alteration overprinted by LT calcic–iron alteration in a Hump zone iron showing (09CQA-1020);

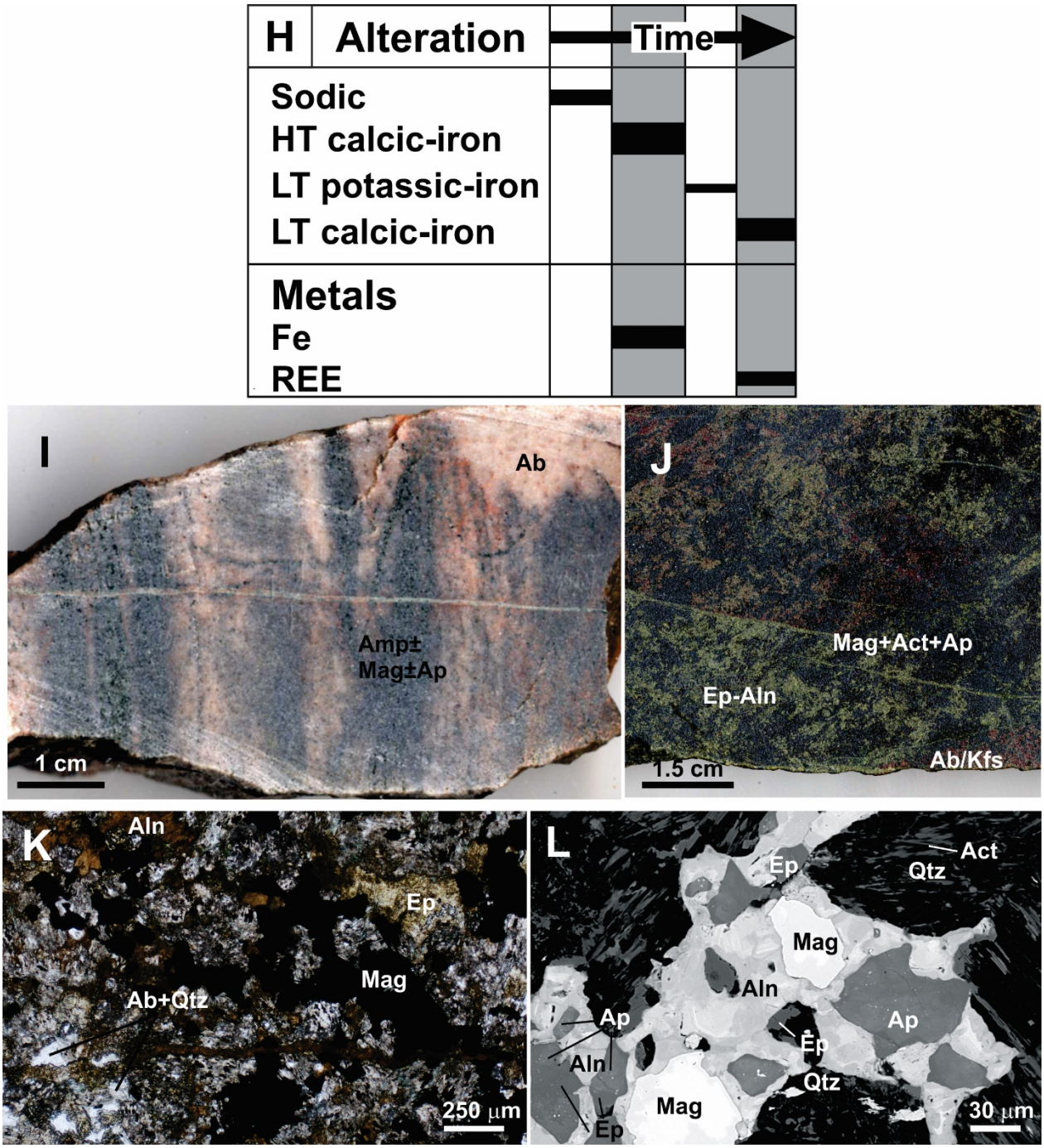

Fig. 4.3 suite – (h) Relicts of the Treasure Lake Group metasiltstone into an iron oxide mineralization zone of the Hump zone (09CQA-0042; Photograph courtesy of Madeline Lee); (i) Sequence of alteration and associated metal enrichments in the Ron zone showings; (j) Early sodic alteration overprinted by HT calcic–iron alteration in the vicinity of the Ron zone iron showings (GFA-90-0078); (k) Rock slab illustrating the pervasive allanite-rich LT calcic–iron overprint over the HT calcic–iron alteration typical of the Ron iron showings; (l) Polarized light microphotograph of the polyphase and allanite-rich LT calcic–iron alteration superimposed over the magnetite-rich HT calcic–iron alteration of the Ron iron showing (09CQA-0021); (m) BSE image of the LREE-rich allanite of the Ron iron showing replacing earlier apatite and magnetite crystals (09CQA-0021; BSE image courtesy of Anthony De Toni).

Mineral abbreviations after Whitney and Evans (2010).

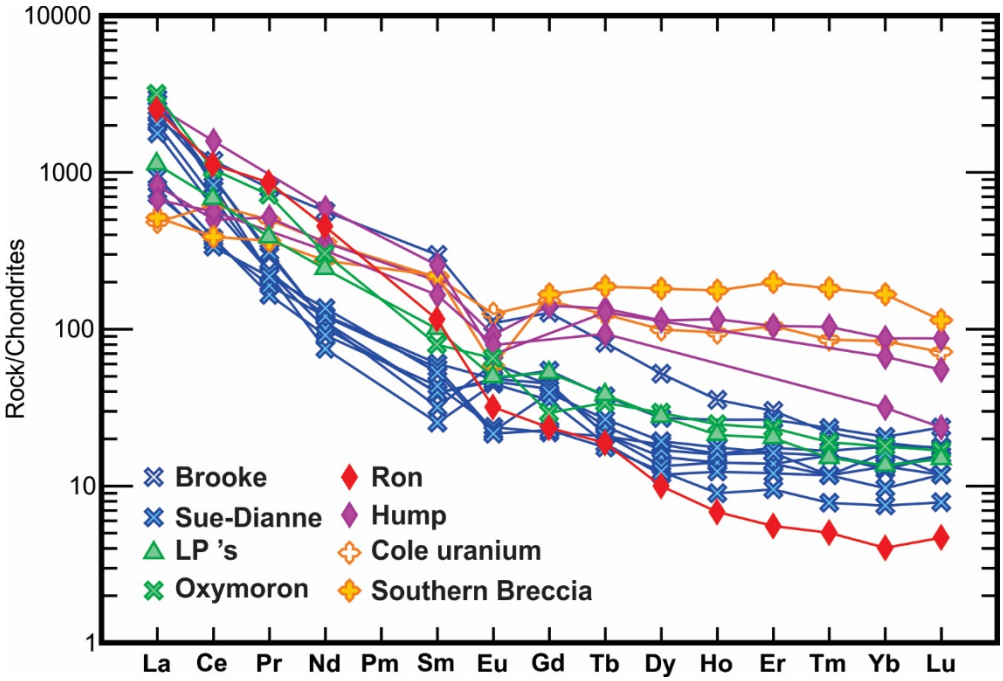

Figure 4-4 Chondrite-normalized REE profiles of samples of the southern GBMZ IOAA system with Ce content over 200 ppm

Chondrite normalization after Palme and Jones (2003).

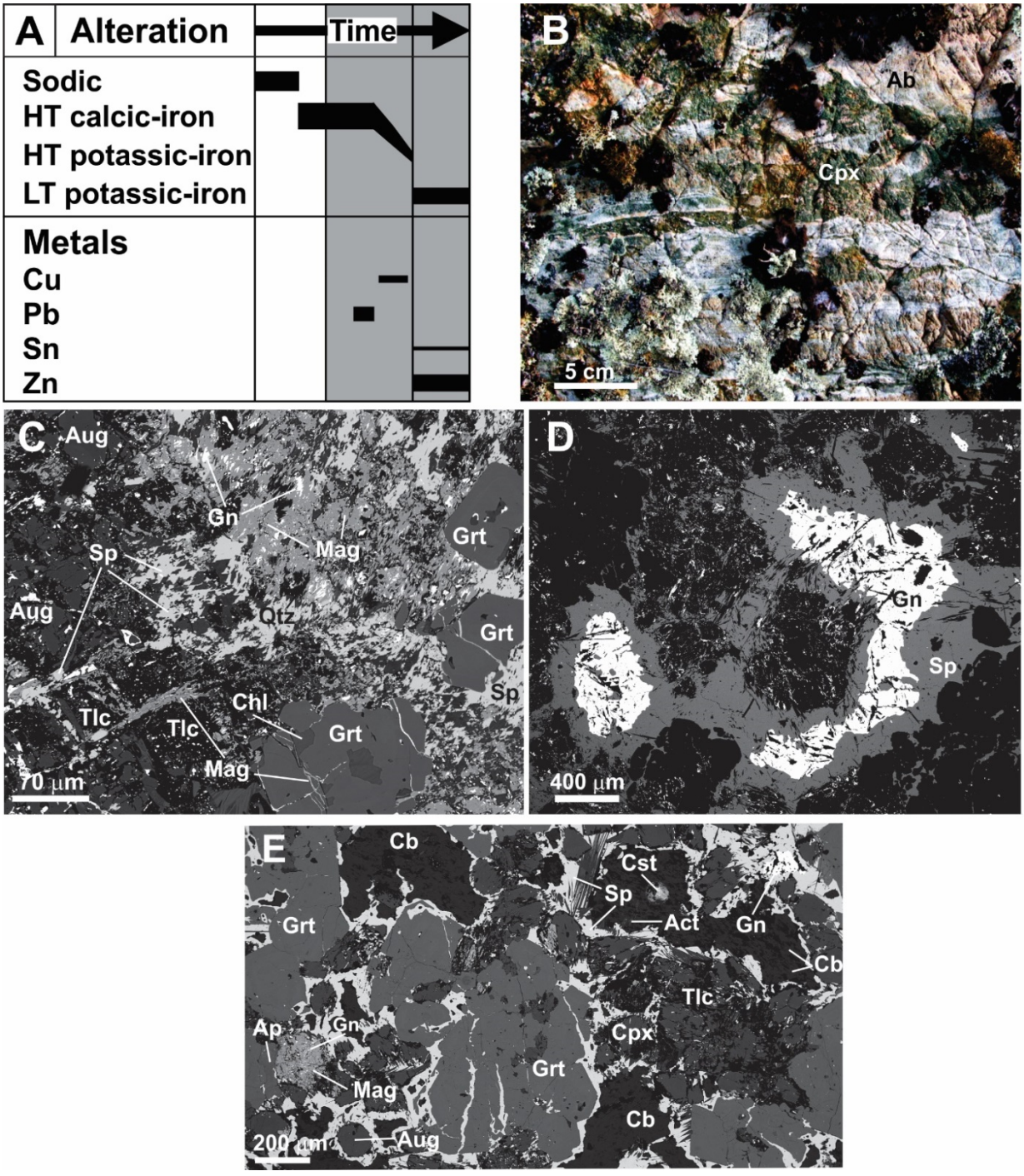

Figure 4-5 IOAA alteration and metal enrichments in the prospects and showings of the Carbonate Mountain zone and the Cole sector

(a) Sequence of alteration and associated metal enrichments in the Carbonate Mountain prospect; (b) Skarn-type HT calcic–iron alteration veins crosscutting the albitized metasedimentary precursor in the Carbonate Mountain system (09CQA-0036); (c) BSE image of the zinc–lead mineralization of the Carbonate Mountain prospect showing the galena-rich magnetite veins cutting the garnet crystals and cut by sphalerite associated with the LT potassic–iron alteration stage (KZ-09-CM-1); (d) BSE image of galena rimmed by sphalerite (KZ-09-CM-1); (e) BSE image of a carbonate-rich zone of the showing with localized cassiterite formation associated to the LT potassic–iron alteration stage also related to the extensive sphalerite precipitation at the border of the garnet and clinopyroxene crystals (KZ-09-CM-1);

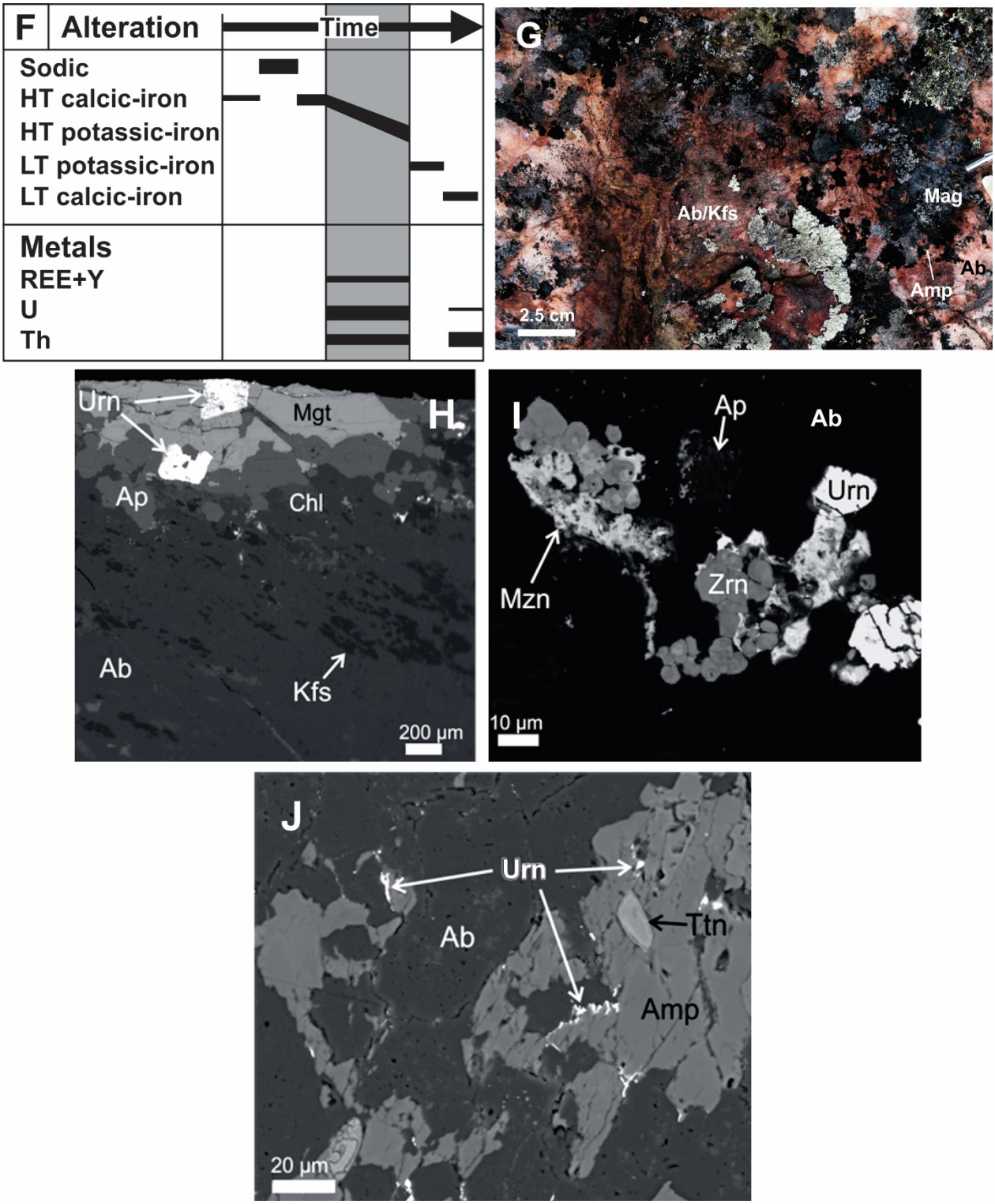

Fig. 4.5 suite – (f) Sequence of alteration and associated metal enrichments in the Cole Uranium showing; (g) Field picture of the sodic alteration zones in which the uranium-bearing calcic–iron–potassic veins are emplaced (09CQA-4011); (h), (i) and (j) BSE image of the Cole Uranium showing detailing the mineralogy of the calcic–iron–potassic veins (10CQA-0511; BSE images courtesy of Eric Potter).

Mineral abbreviations after Whitney and Evans (2010).

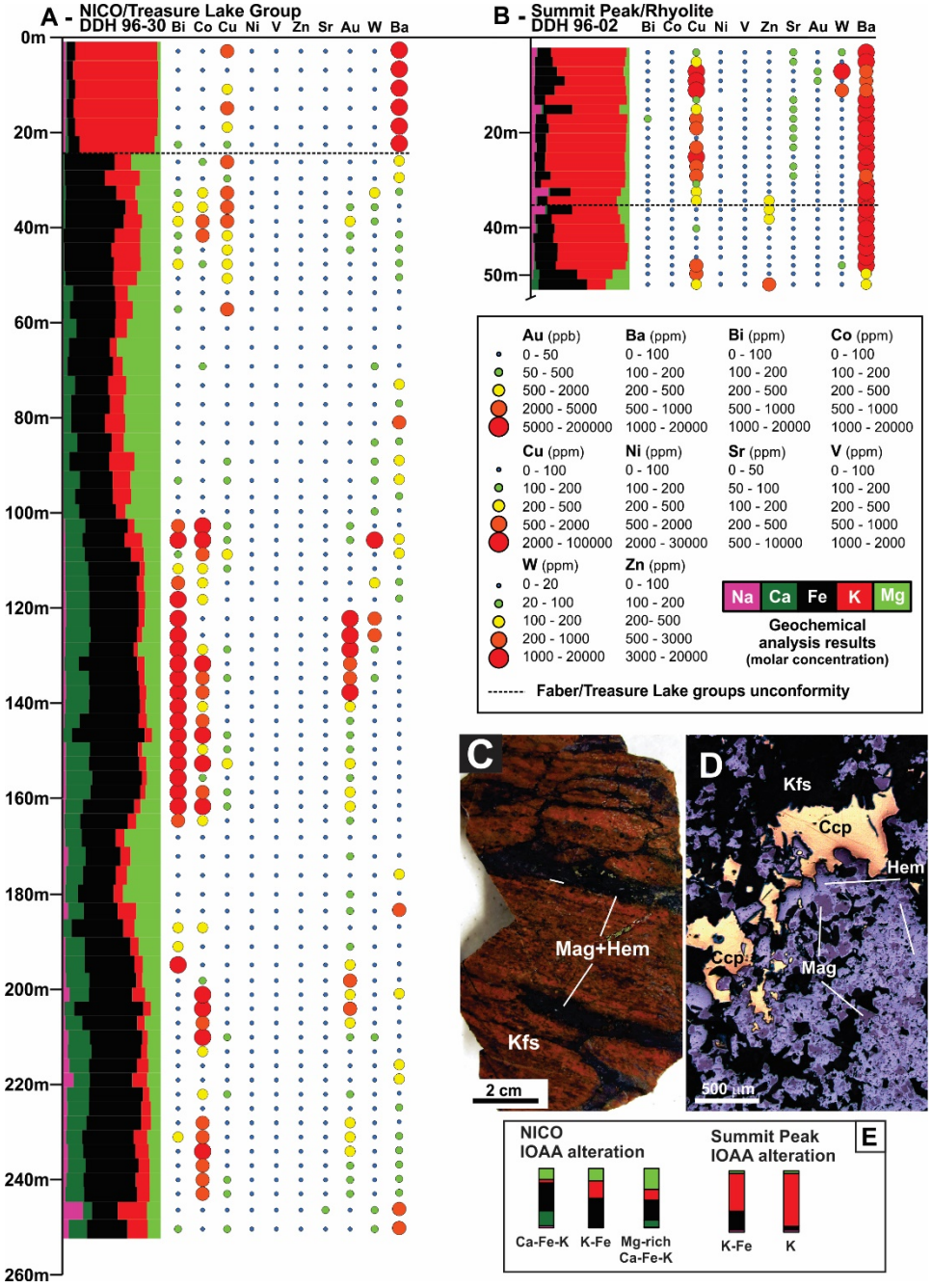

Figure 4-6 Chemical sections and mineralization of the NICO deposit and the overlying Faber Group rhyolite

(a) Chemical section of the main ore zone of the NICO deposit after the diamond drill hole 96-30. This section illustrates the chemical similarities of the NICO deposit ore zone with the South Lou Duke, LVLVS and LP's showings; (b) Chemical section in the Faber Group rhyolite overlying the NICO deposit after the diamond drill hole 96-02 drilled in the in Summit Peak prospect. This section illustrates the chemical similarities of the mineralization zones in the overlying rhyolites of the Faber Group with the Sue-Dianne deposit; (c) Field picture of a magnetite–hematite-cemented hydrothermal breccia formed in the Faber Group rhyolite in the Summit Peak area (11PUA-508); (d) Cut slab of a chalcopyrite- and pyrite-bearing magnetite–hematite-cemented breccia of the Summit Peak prospect (KZ09-SP-1); (e) Reflected light microphotograph of the chalcopyrite-rich iron oxide breccia of the Summit Peak prospect where hematite is replacing magnetite in the veins (KZ09-SP-1).

Geochemical analyses for the NICO deposit are from Mumin (1997) and mineral abbreviations are after Whitney and Evans (2010).

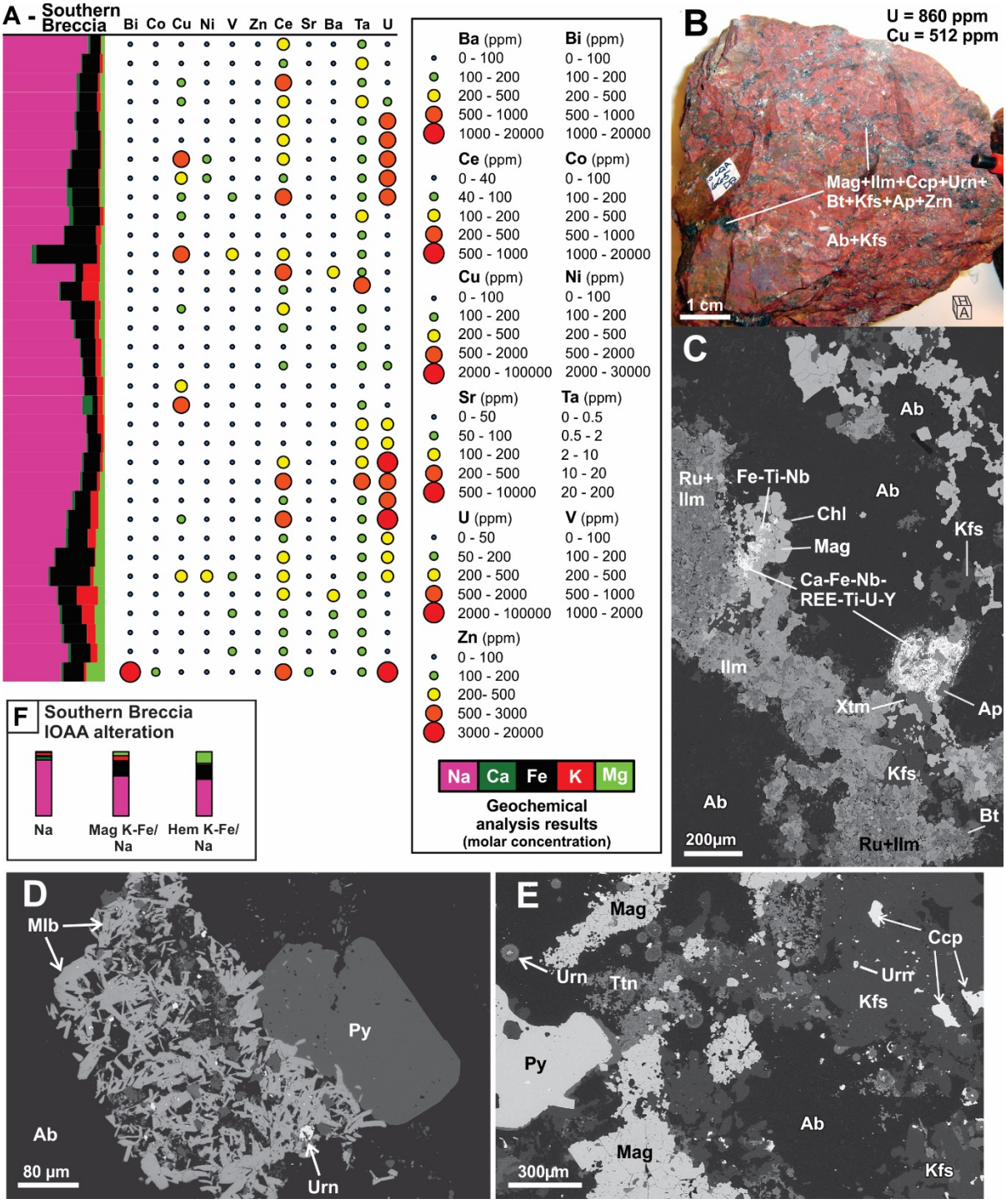

Figure 4-7 Chemical section and mineralization of the Southern Breccia uranium showings

(a) Chemical section of the Southern Breccia; (b) Hand sample showing the uranium-rich iron oxide-cemented breccias forming the main uranium mineralization event in the Southern Breccia (10CQA-1665); (c) BSE image of a Nb–Ta-bearing magnetite–ilmenite–rutile–K-feldspar–biotite vein of the Southern Breccia (10CQA-1643); (d) BSE image of molybdenite–uraninite mineralization associated with the main uranium mineralization event in the Southern Breccia (11PUA-019); (e) BSE image showing the typical mineralogy of the uraninite-rich veins of the Southern Breccia (11PUA-019).

Mineral abbreviations after Whitney and Evans (2010).

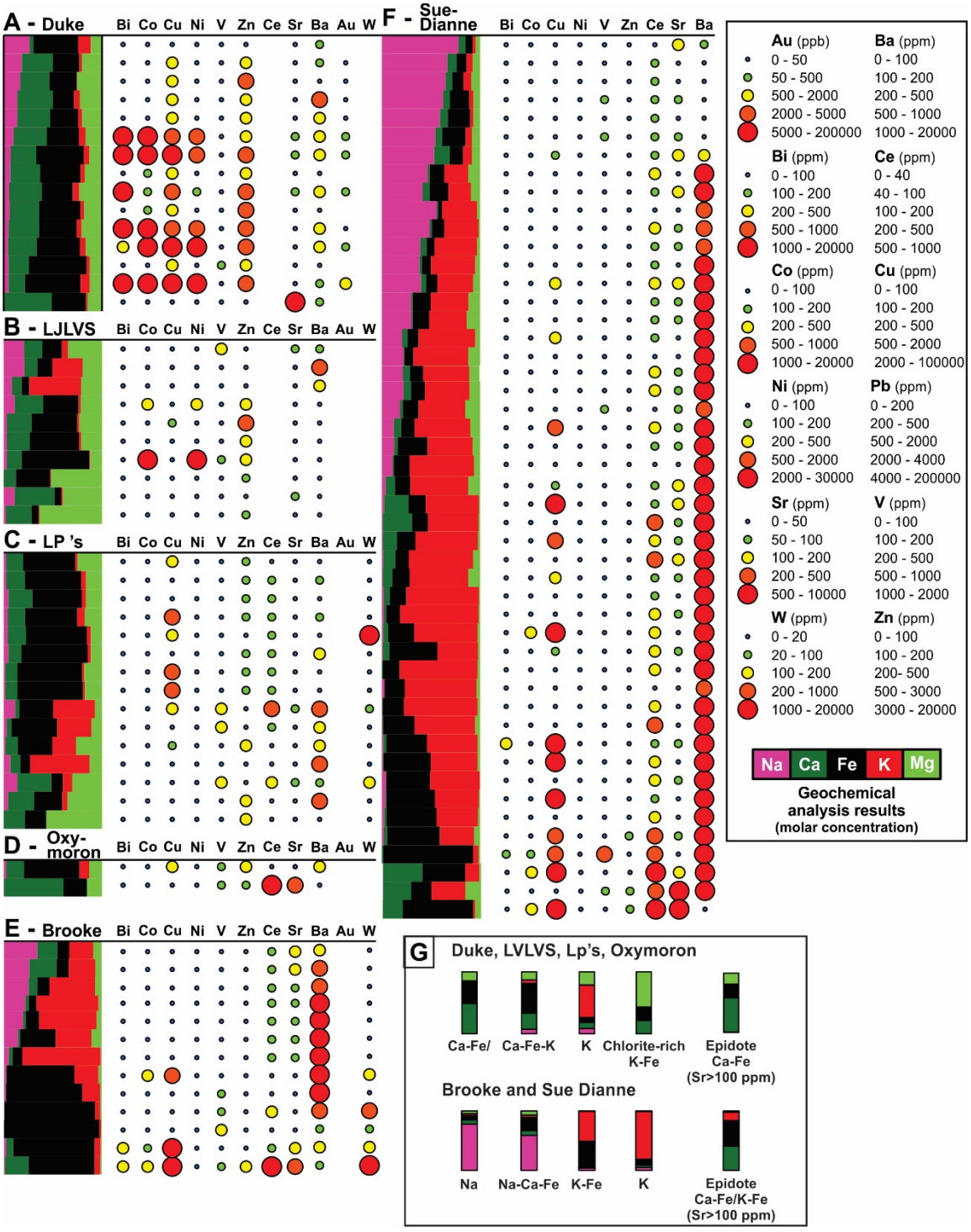

Figure 4-8 Chemical sections of the Western section showings to illustrate the relation between alteration and metal endowment

(a) Duke showing; (b) LJLVS showing; (c) LP's showing; (d) Oxymoron showing; (e) Brooke prospect; (f) Sue-Dianne deposit.

Sr and Ba are plotted as intensity indicators of LT calcic–iron and potassium-rich alteration respectively.

Geochemical analyses for the Duke prospect and Sue-Dianne deposit were complemented with analyses from Goad et al. (1996) and Camier (2002) respectively.

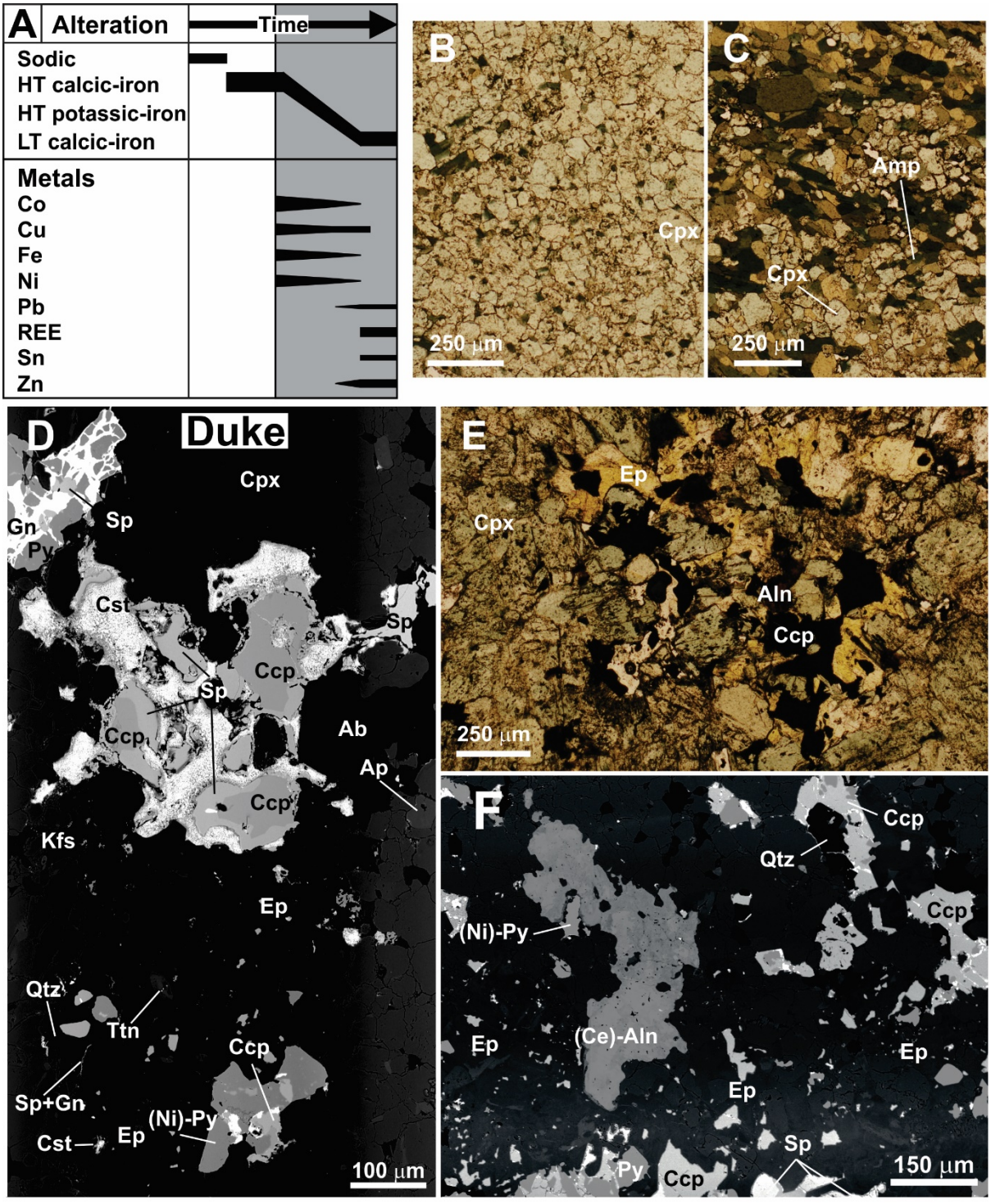

Figure 4-9 IOAA alteration and metal enrichments in the Duke and LJLVS showings of the Duke zone

(a) Sequence of alteration and associated metal enrichments in the Duke showing; (b) Polarized light microphotograph of the typical pyroxene-rich skarn-type HT calcic–iron alteration in the Duke showing (KZ09-DK-3-11); (c) Polarized light microphotograph of the transitional zone between the amphibole-rich and pyroxene-rich HT calcic–iron alteration in the Duke showing (KZ09-3-11); (d) Polarized light microphotograph of the epidote–K-feldspar replacement of the clinopyroxene-rich HT calcic–iron alteration associated with chalcopyrite formation (KZ09-3-4); (e) and (f) BSE images of the sulfide precipitation sequence related to the epidote-rich HT potassic–iron and LT calcic–iron alteration stages of the Duke showing (KZ09-3-4);

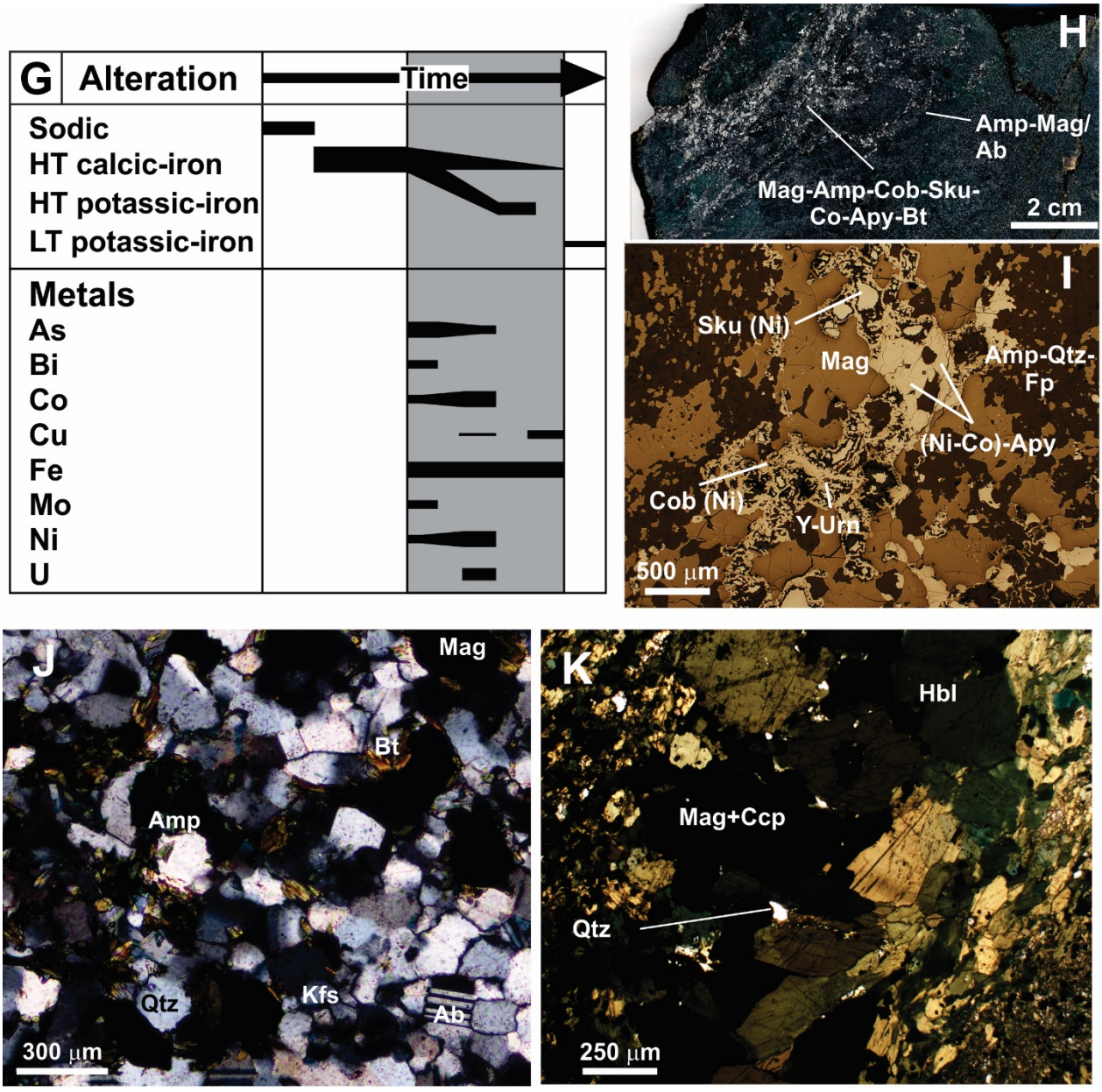

Fig. 4.9 suite – (g) Sequence of alteration and associated metal enrichments in the LCLVS showing; (h) Typical calcic–iron–potassic alteration hosting the cobaltian arsenopyrite mineralization of the LJLVS showing and cross cutting an earlier HT calcic–iron alteration (09CQA-1082); (i) Reflect light microphotograph of the sulfide and arsenide precipitation sequence in the calcic–iron–potassic alteration veins (09CQA-1082); (j) Cross-polarized microphotograph of the early sodic alteration of the sandstone cut by biotite–magnetite–amphibole veins of the calcic–iron–potassic alteration stage (09CQA-1082); (k) Cross-polarized of the chalcopyrite-bearing hornblende–magnetite veins (09CQA-1082);

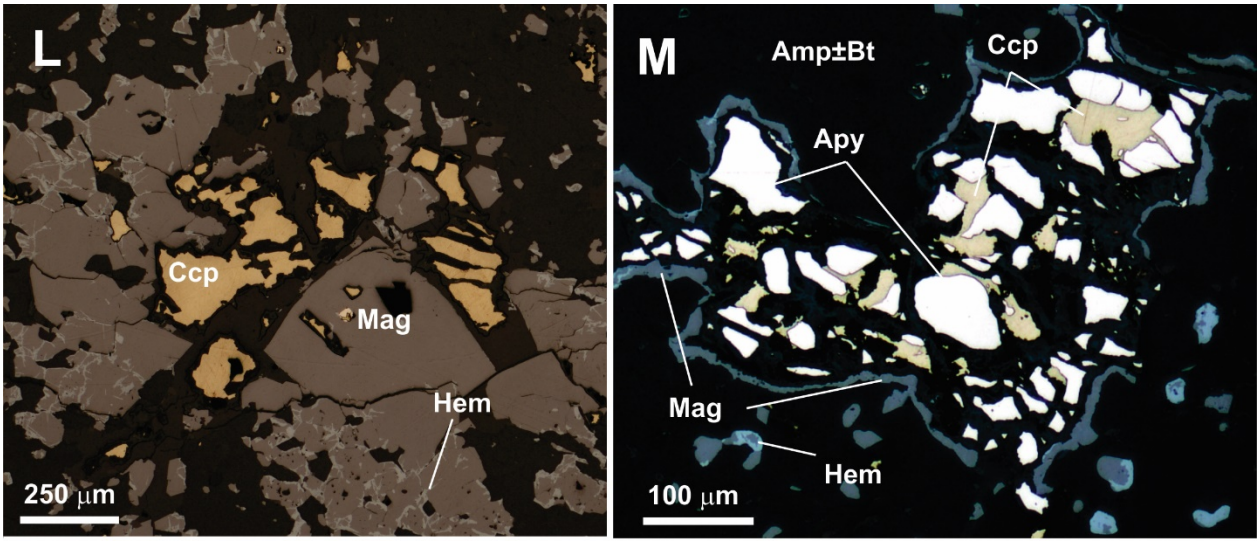

Fig. 4.9 suite – (l) Reflected light microphotographs of the chalcopyrite-bearing hornblende–magnetite veins (09CQA-1082); (m) Reflected light microphotograph of chalcopyrite cutting arsenopyrite crystals (09CQA-1082).

Mineral abbreviations after Whitney and Evans (2010); Cob = Cobaltite, Sku = Skutterudite.

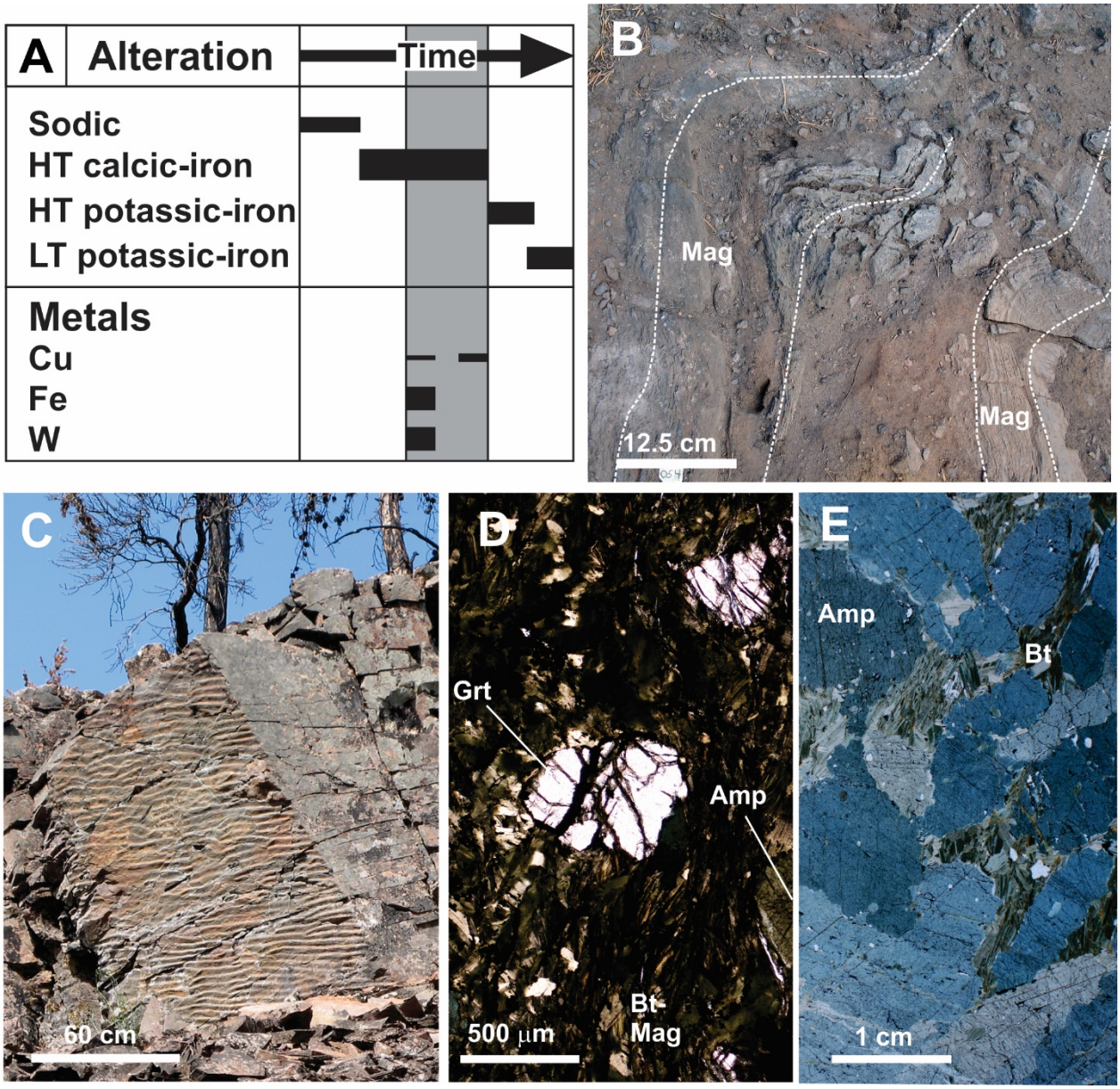

Figure 4-10 IOAA alteration and metal enrichments in the LP's, South Duke and Oxymoron showings of the Duke zone

(a) Sequence of alteration and associated metal enrichments in the LP's showing; (b) Parasitic fold formed after stratabound magnetite alteration in the LP's zone showing of the Duke system (09CQA-0054); (c) Weakly altered siltstone with beautifully preserved ripple marks just few meters away of the deformation corridor hosting the LP's showing of (09CQA-0055); (d) Well developed tectonic foliation along a small shear zone formed in the deformation corridor hosting the LP's showing (09CQA-0055, photo courtesy of Anthony De Toni); (e) HT potassic–iron (biotite) alteration forming a pervasive and interstitial replacement of the earlier HT calcic–iron (09CQA-0055, Microphotograph courtesy of Anthony De Toni);

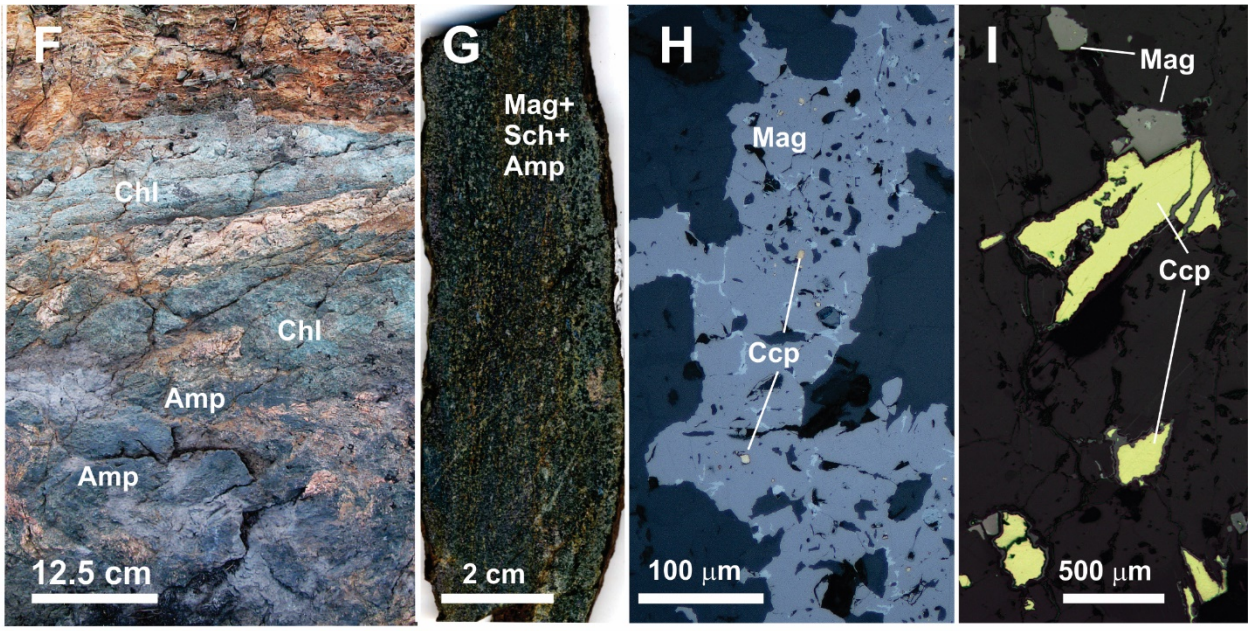

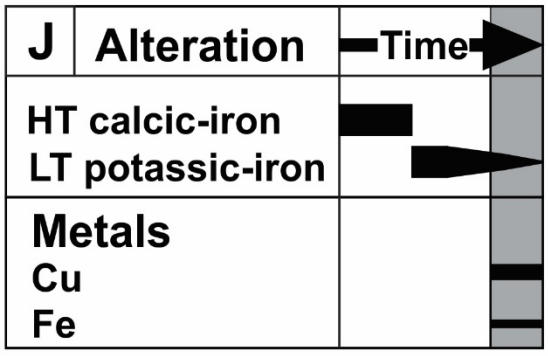

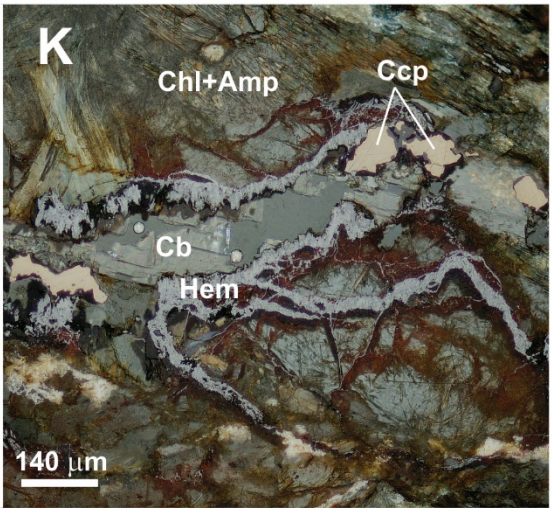

Fig. 4-10 suite – (f) Chlorite alteration front overprinting the earlier HT calcic–iron alteration of the LP's zone showing (09CQA-0054); (g) Intense magnetite-rich HT calcic–iron alteration hosting the tungsten (scheelite) mineralization of the LP's showing (09CQA-0055); (h) Microphotograph of the magnetite-rich HT calcic–iron alteration that exhibits disseminated chalcopyrite inclusions in the magnetite crystals; (i) Reflected light microphotograph of the magnetite–chalcopyrite veinlets cutting the iron- and tungsten-rich HT calcic–iron alteration of the LP's showing (09CQA-0055); (j) Sequence of alteration and associated metal enrichments in the South Duke showing; (k) Reflected light microphotograph of the chalcopyrite-bearing carbonate–hematite veins hosting the copper mineralization of the South Duke showing (09CQA-1085). These veins are closely associated with the slightly earlier LT potassic–iron (hematite–chlorite) replacement of the HT calcic–iron alteration;

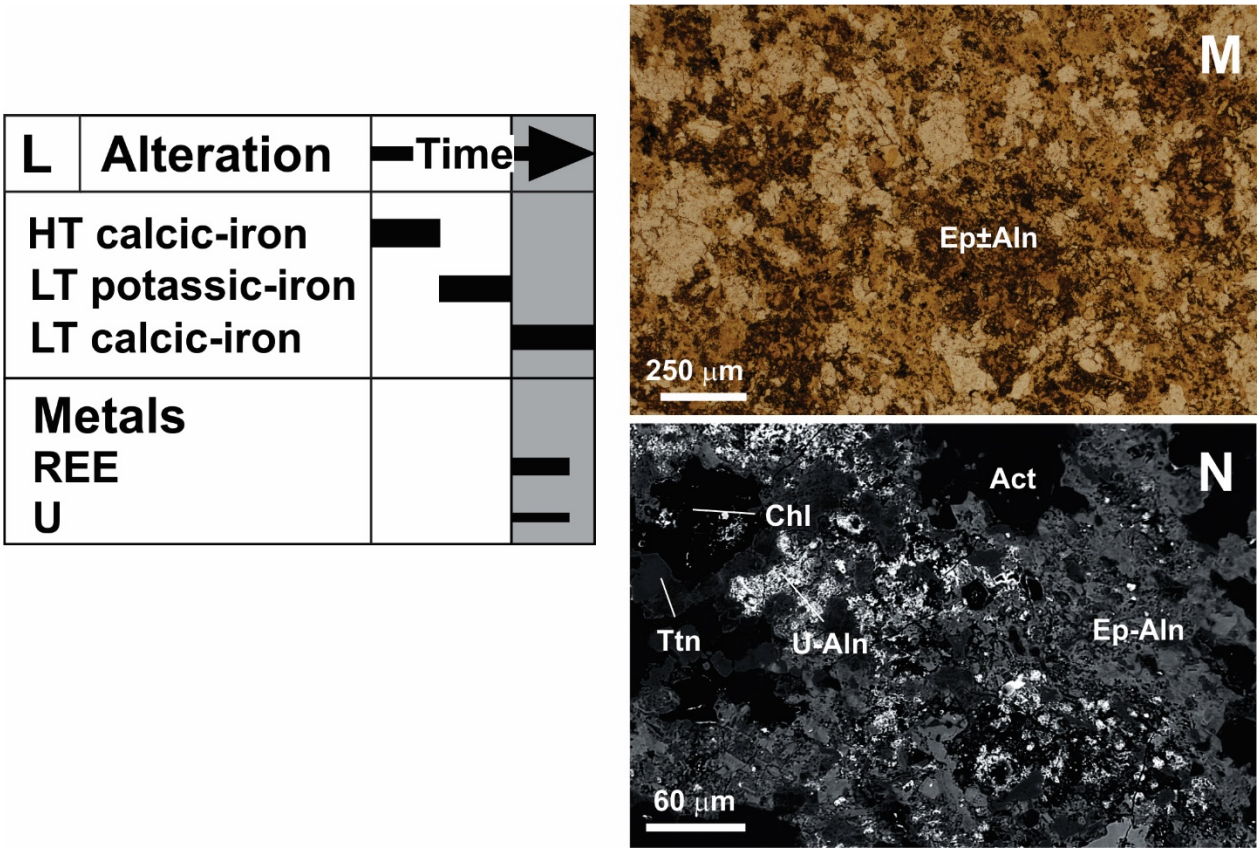

Fig. 4-10 suite – (l) Sequence of alteration and associated metal enrichments in the Oxymoron showing; (m) and (n) Polarized light microphotograph and BSE image of the Allanite-rich LT calcic–iron alteration hosting the LREE and uranium mineralization of the Oxymoron showing (09CQA-1084).

Mineral abbreviations after Whitney and Evans (2010).

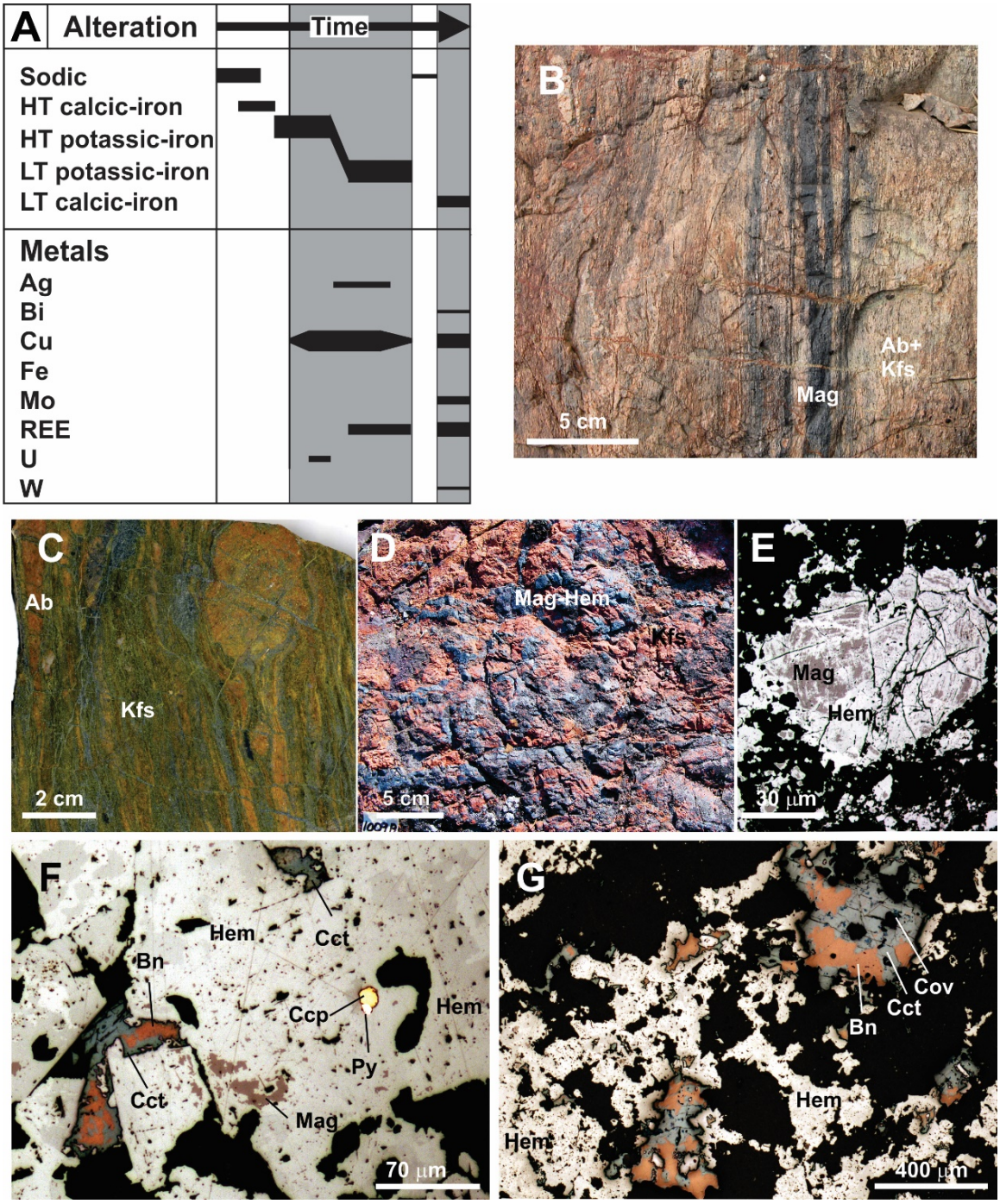

Figure 4-11 IOAA alteration and metal enrichments in the prospects and deposit of the Mazenod sector

(a) Sequence of alteration and associated metal enrichments in the Sue-Dianne deposit and Brooke showing; (b) Deformation corridor close to the contact between the Marian River batholith and the Sue-Dianne volcanic complex (09CQA-1012); (c) Foliated and brecciated sodic alteration overprinted by potassic alteration in the deformation corridor (09CQA-1012); (d) Iron oxide-cemented breccia formed by HT and LT potassic–iron alteration of the Sue-Dianne deposit (09CQA-1009); (e) Reflected light microphotograph of magnetite relicts in a specular hematite crystal in the uppermost section of the Sue-Dianne deposit (09CQA-1026); (f) Reflected light microphotograph of chalcopyrite inclusions and magnetite relicts in a hematite-cemented LT potassic–iron alteration superimposed over the earlier HT potassic–iron alteration. The LT potassic–iron alteration overprint is associated with bornite and then chalcocite formation (KZ09-SD-8); (g) Reflected light microphotograph of bornite- and chalcocite-mineralized LT potassic–iron alteration zone in the Sue-Dianne deposit (KZ09-SD-8);

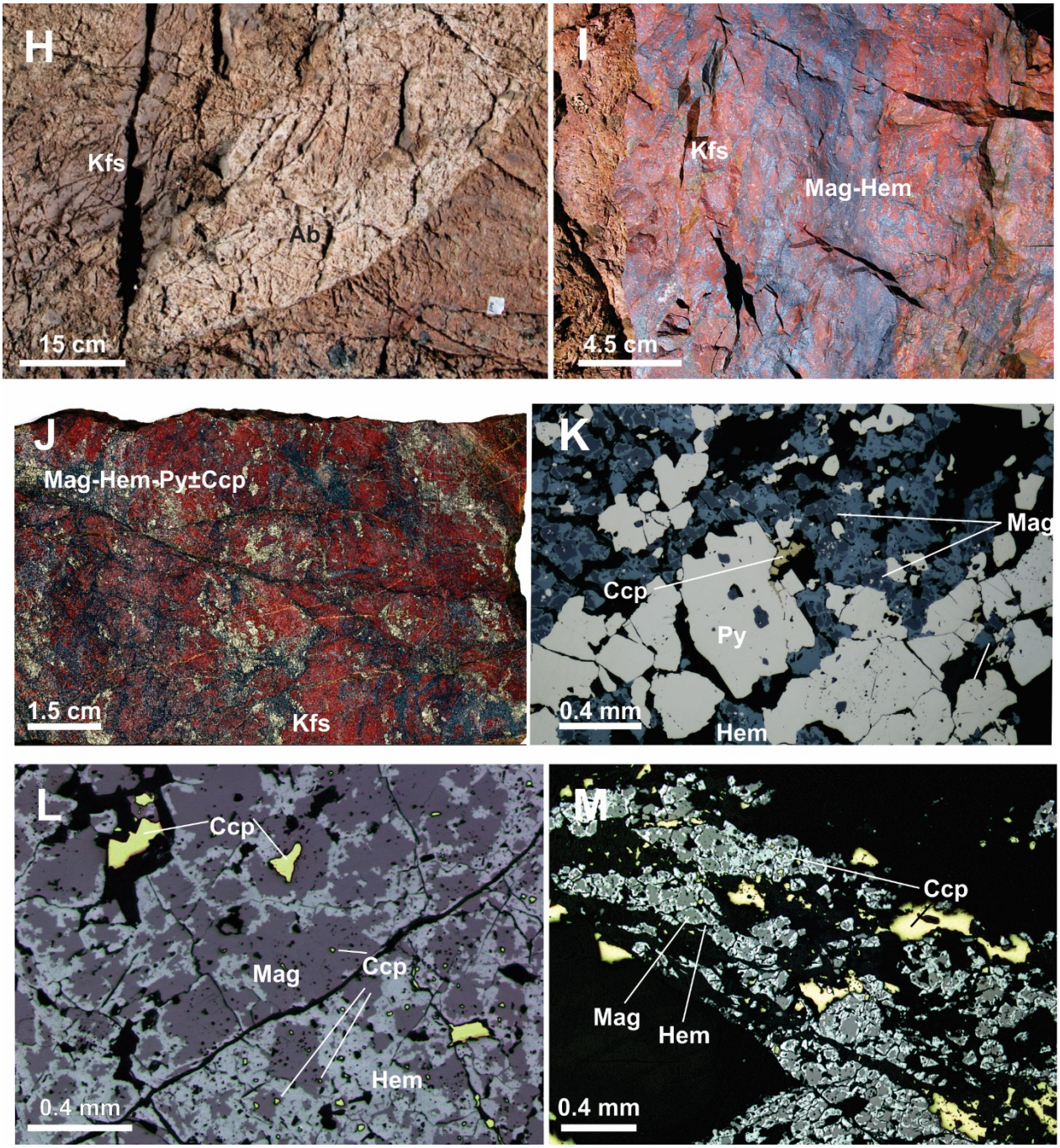

Fig. 4.11 suite – (h) Sodic alteration front overprinting earlier potassic alteration 75 meters below the summit breccia zone of the Sue-Dianne deposit (09CQA-1008); (i) Iron oxide-cemented breccia formed by HT and LT potassic–iron alteration in the Brooke prospect (09CQA-0026); (j) and (k) Slab and microphotograph of the pyrite-bearing HT potassic–iron alteration stage with minor chalcopyrite predating the chalcopyrite-bearing HT potassic–iron alteration stage. The pyrite-bearing HT potassic–iron alteration is overprinted by LT potassic–iron alteration (09CQA-0026); (l) and (m) Reflected light microphotograph of chalcopyrite-bearing HT potassic–iron alteration in which all the magnetite grains are rimmed and replaced by specular hematite, Brooke prospect (09CQA-0109);

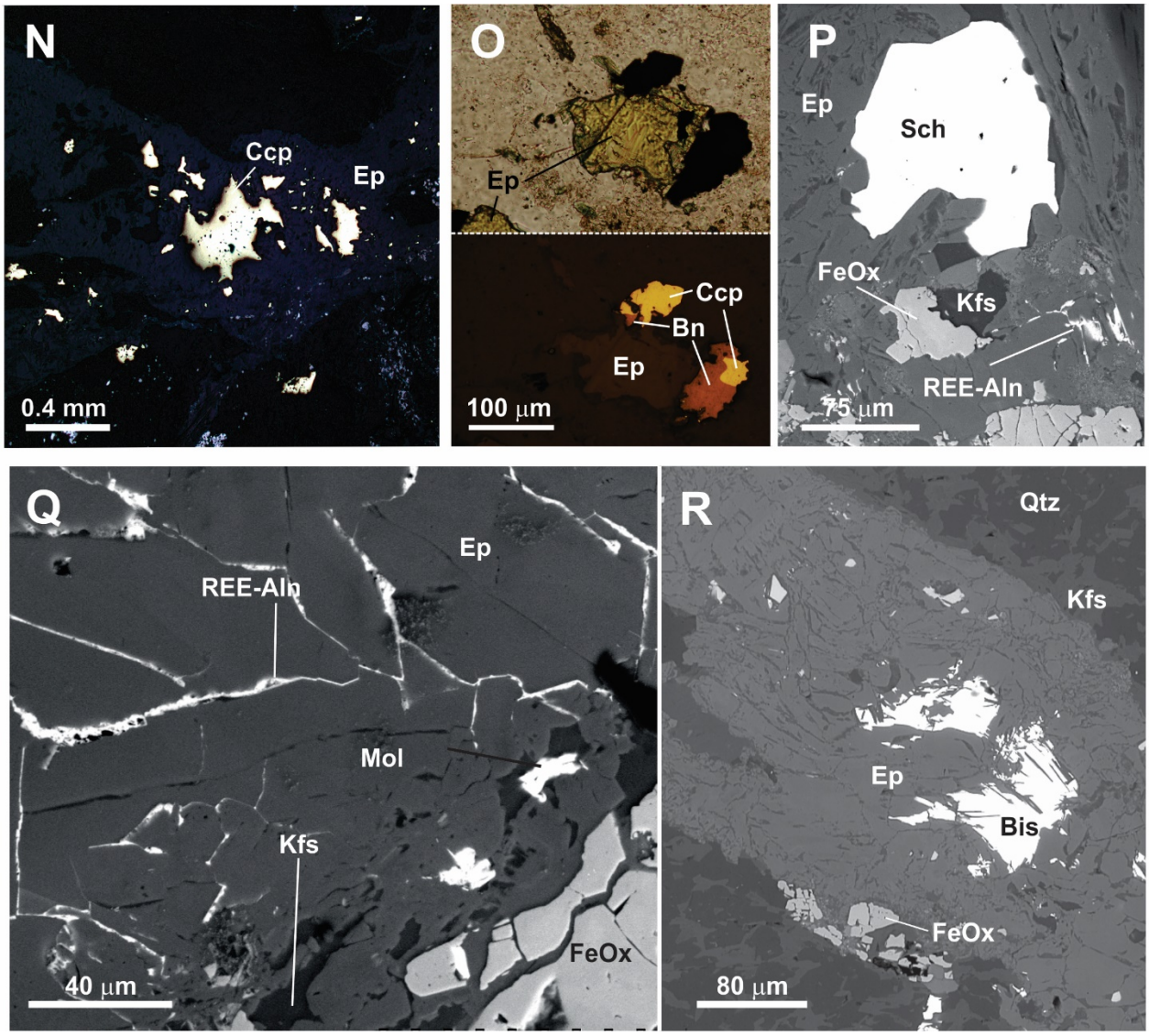

Fig. 4.11 suite – (n) Reflected light microphotograph of chalcopyrite emplaced in fractures filled by late-stage LT calcic–iron alteration fractures in the Brooke prospect (09CQA-0109); (o) Natural (upper) and reflected (lower) microphotographs of chalcopyrite transformation into bornite during the LT calcic–iron alteration stage in the Brooke prospect (KZ09-BK-1-A); (p) BSE image of LT calcic–iron alteration with scheelite and LREE-bearing allanite in the Brooke prospect (09CQA-0109; BSE image courtesy of Philippe Normandeau); (q) BSE image of LT calcic–iron alteration with molybdenite and LREE-bearing allanite filling fractures in the LT calcic–iron alteration vein in the Brooke prospect (09CQA-0109; BSE image courtesy of Philippe Normandeau); (r) BSE image of a bismuthinite-bearing LT calcic–iron alteration veins (09CQA-0109).

Mineral abbreviations after Whitney and Evans (2010); Bis = Bismuthinite, FeOx = Iron oxide.

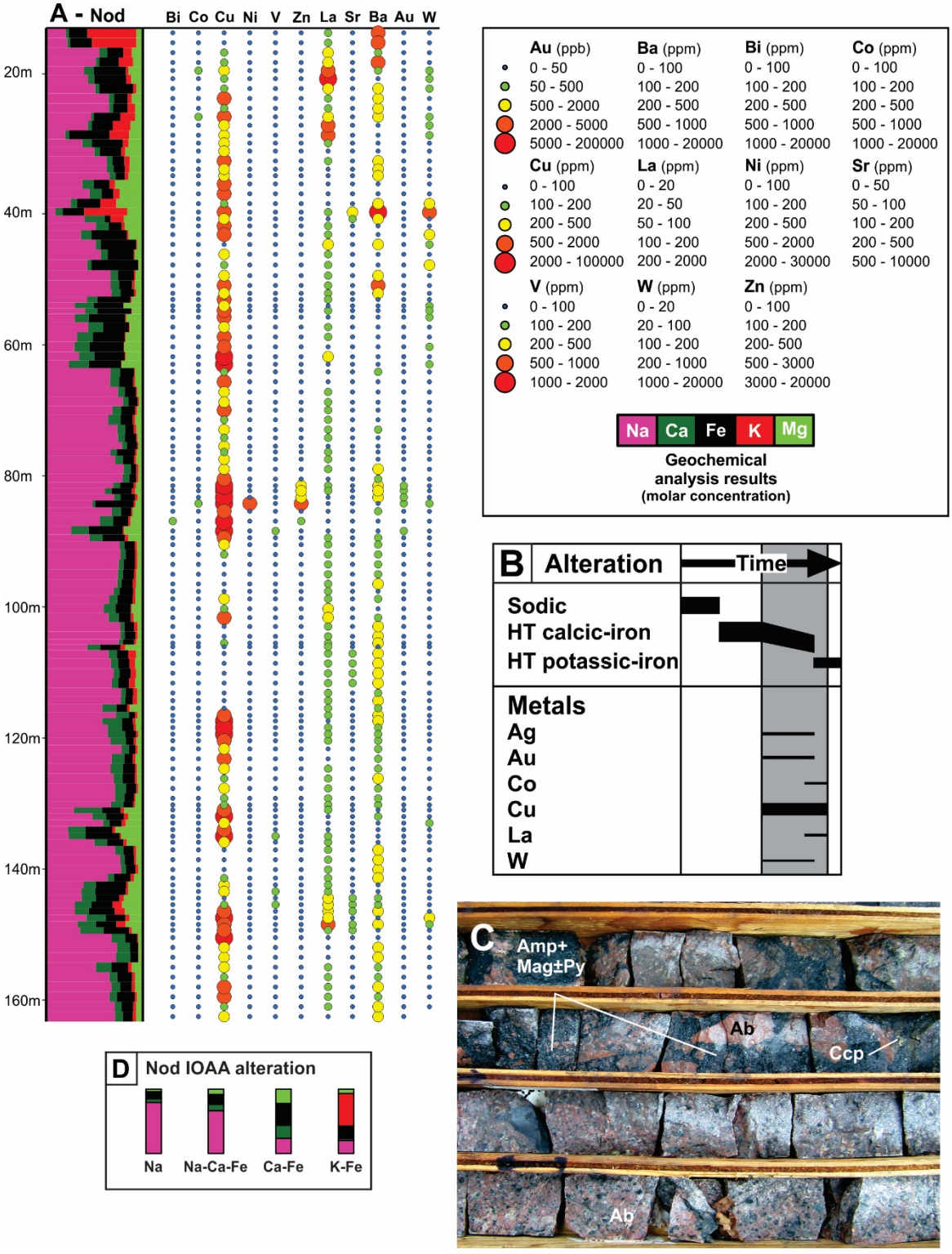

Figure 4-12 Chemical section, alteration and mineralization sequence of the Nod prospect

(a) Chemical section of the Nod prospect; (b) Alteration and mineralization sequence of the Nod prospect; (c) Drill core photograph of the mineralization zone of the Nod prospect.

Chemical analyses from Mackay and Eveleigh (1997) and mineral abbreviations after Whitney and Evans (2010).

CHAPITRE 5 : COMPOSITIONAL DATA ANALYSIS OF HYDROTHERMAL ALTERATION IN IOCG SYSTEMS, GREAT BEAR MAGMATIC ZONE, CANADA: TO EACH ALTERATION TYPE ITS OWN GEOCHEMICAL SIGNATURE

Analyse compositionnelle de l'altération hydrothermale dans les systèmes IOCG, Zone magmatique du Grand lac de l'Ours : À chaque altération sa signature géochimique

[1]Montreuil, J.-F., [2]Corriveau, L., [3]Grunsky, E.C.

[1]Institut National de la Recherche Scientifique – Eau-Terre-Environnement

[2]Ressources naturelles Canada, Commission Géologique du Canada, division Québec

[3]Ressources naturelles Canada, Commission Géologique du Canada, division Ottawa

Publié par «*Geochemistry: Exploration, Environment, Analysis*», v. 13, p. 229–247.

Abstract: Iron oxide copper–gold (IOCG) systems are characterized by a wide range of hydrothermal alteration types that can indiscriminately and intensively replace their host rocks over areas of > 100 km^2. Element mobility and chemical changes associated with alteration can be of a magnitude beyond that of many other types of hydrothermal systems, and may also affect normally immobile elements. Principal component analysis (PCA) of whole-rock geochemical data on hydrothermally altered samples coming from the Great Bear magmatic zone IOCG systems has enabled the characterisation of sodic, calcic–iron, to high to low temperature potassic–iron and potassic alteration types of IOCG systems. Results show that potassic and potassic–iron alteration are enriched in K, Al, Ba, Si, Rb, Zr, Ta, Nb, Th and U, with K–Fe alteration being richer in Fe. In contrast, calcic–iron alteration is enriched in Ca, Fe, Mn, Mg, Zn, Ni and Co. These compositional variations can be portrayed by IOCG alteration index and discriminant diagrams. Combined with an IOCG alteration sequencing model, the lithogeochemical footprint of IOCG systems provides a useful tool to assess the potential fertility and maturity of IOCG systems and ultimately a vector towards ore zones during exploration.

Résumé: Les systèmes à oxyde de fer–cuivre–or sont caractérisés par une grande diversité d'altérations hydrothermales qui peuvent remplacer sans discrimination et intensément leur roches hôtes, et ce sur des étendues exposées en surface > 100 km². La mobilité des éléments et les variations chimiques associées à l'altération IOCG surpasse l'intensité de l'altération observée dans les autres systèmes hydrothermaux connus, et peut même affecter les éléments considérés normalement considérés comme immobiles. L'analyse en composantes principales de données géochimiques d'altérations IOCG de la Zone magmatique du Grand lac de l'Ours a permis la caractérisation des altérations sodiques, calcique–fer, potassique–fer de haute à basse température et potassiques. Les altérations potassiques et potassique–fer sont enrichies en K, Al, Ba, Si, Rb, Zr, Ta, Nb, Th et U, les altérations potassique–fer étant plus riches en Fe. Les altérations calcique–fer sont enrichies en Ca, Fe, Mn, Mg, Zn, Ni et Co. Ces variations compositionnelles de l'altération peuvent être représentées par des indices d'altération IOCG et des diagrammes discriminants. Combinée à un modèle de zonation des altérations dans les systèmes IOCG, la signature chimique des altérations présentée dans cet article fournit un outil utile pour évaluer la fertilité potentielle et la maturité d'un système IOCG et ultimement pour servir de guide vers les zones minéralisées du système hydrothermal.

5.1 Introduction

Whole-rock geochemistry is a useful tool to detect prospective hydrothermal alteration at the regional scale and to vector towards base metal and/or precious metal mineralization for a wide variety of deposits (Madeisky and Stanley, 1993; Franklin, 1997; Large et al., 2001; Warren et al., 2007). These vectors are based on the systematic zonation of hydrothermal alteration types around ore zones and the compositional changes associated with fluid-rock interaction. Exploration for iron oxide copper–gold (IOCG) hydrothermal systems can benefit from the development of lithogeochemical discriminant diagrams (Benavides et al., 2008a, b). These systems are characterized by a wide range of hydrothermal alteration types that intensively replace their host rocks over areas that may exceed 100 km^2 and for which alteration sequencing, paragenesis and relationships to ore zone are well constrained by alteration zoning and evolutionary models (Hitzman et al., 1992; Williams et al., 2005; Corriveau et al., 2010b; Mumin et al., 2010). However the scarcity of large, publicly available geochemical databases across IOCG systems that encompass the entire spectrum of IOCG alteration types impedes the development of discriminant diagrams and alteration indexes that characterize individual alteration type signatures. The development of such lithogeochemical vectors to ores can increase the effectiveness of lithogeochemical exploration programs for IOCG deposits.

Corriveau et al. (2010b) made a thorough re-examination of the existing alteration zoning models for IOCG systems (Hitzman et al., 1992; Williams, 1999; Williams et al., 2005; Mumin et al., 2007, 2010) and proposed a revised version of those alteration zoning models to encompass the wide variations observed in the hydrothermal mineral assemblages formed during the different stages of IOCG systems development. They have demonstrated that five main alteration stages, reflecting declining temperatures and increasing oxygen fugacity, can be used to frame the evolution of IOCG hydrothermal systems and their iron oxide–apatite (IOA) and magnetite- and hematite-group IOCG deposits as well as to encompass the wide variety of mineral parageneses formed during these various alteration stages described below.

Corriveau et al. (2010b) also proposed an alteration notation that goes against the usual convention in metallogeny in that they labelled alteration using key discriminating chemical components without considering if their predominance in the altered rock results from significant influx or severe leaching of elements. This notation will be followed in this contribution as it considerably simplifies the nomenclature for IOCG alteration and accounts for most of the different mineral parageneses encountered in IOCG hydrothermal alteration described below.

The main alteration types in IOCG systems according to the Corriveau et al. (2010b) revised alteration zoning model are: sodic, calcic–iron, high temperature potassic–iron, low temperature and hydrolytic potassic–iron as well as transitional potassic/skarn alteration.

Early sodic (Na) (±calcic) and calcic–iron (Ca–Fe) (±sodic) alteration zones are commonly laterally extensive, regional in scale, and may host iron-oxide apatite (i.e., Kiruna-type) deposits but are largely barren in terms of polymetallic mineralization unless superimposed by fertile alteration types. Sodic alteration principally results in albitites which generally contain variable amounts of cryptocrystalline quartz. Accessory amphibole, magnetite and amphibole are locally formed whereas accessory titanite, apatite, allanite, monazite and xenotime are more common. Oliver et al. (2004) have demonstrated that sodic alteration results from extensive leaching of the precursor rock and that only Al, Zr, Ga±Ti remain somewhat immobile.

Mineral parageneses formed during the Ca–Fe alteration stage are predominantly composed by variable proportions of amphibole (predominantly actinolite or hornblende) and magnetite as well as locally accessory apatite, garnet and clinopyroxene. Epidote is also a locally important constituent of Ca–Fe alteration zones. Oliver et al. (2004) have demonstrated that Ca–Fe alteration is likely formed by Ca- and Fe-rich hydrothermal fluids originating from the sodic alteration stage. Perring et al. (2000), Pollard (2001) and Baker et al. (2008) fluid inclusion work in sodic and sodic–calcic alteration also demonstrate that the fluids involved in this alteration stage have a high Ca content.

Development of high temperature potassic–iron alteration (HT K–Fe) and lower-temperature potassic–iron/hematite (LT K–Fe) alteration types and associated breccias follows the sodic and calcic–iron alteration stages and lead to more localized alteration zones proximal to polymetallic mineralization. The HT K–Fe and LT K–Fe alteration types are commonly the immediate hosts for magnetite-group (i.e., Cloncurry-type) and hematite-group (i.e., Olympic Dam-type) IOCG deposits (Williams et al., 2005; Corriveau et al., 2010b; Mumin et al., 2010; Williams, 2010a, b; Skirrow, 2010). Mineral parageneses formed during the HT K–Fe alteration stage are composed of variable proportions of K-feldspar, magnetite and biotite whereas mineral parageneses formed during the LT K–Fe alteration stage are composed of variable proportions of hematite (both earthy and specular), chlorite, K-feldspar, white mica (sericite), carbonates and quartz. Where LT and HT K–Fe alteration and associated metals are superimposed on albitite, albitite-hosted uranium mineralization may be formed (Corriveau et al., 2011).

The fifth alteration type is a distinctive potassic alteration that was observed to form deposit-scale halos with or without iron oxide (see Hitzman et al., 1992; Goad et al., 2000a; Mumin et al.,

2007), localized felsites (metasomatic felsic rocks where hydrothermal K-feldspar composed most of the rock) at the transition between HT K–Fe and LT K–Fe alteration and K-feldspar haloes along porphyry dikes. Corriveau et al. (2010b) have considered these potassic alteration types distinct from the HT and LT K–Fe alteration types that serve as immediate ground preparation for and as host to polymetallic mineralization. Skarns and associated mineralization may also be observed close to the magnetite-to-hematite transition where carbonate-bearing rocks or earlier carbonate alteration were available to provide the required extra Ca for their development (e.g., Wang and Williams, 2001; Franchini et al., 2007; Mumin et al., 2010). Such skarn alteration can overprint and be overprinted by potassic alteration and may occur with abundant iron oxides (Corriveau et al., 2010b).

IOCG alteration systems commonly overprint a wide variety of precursor rock types, with their nature and original composition often camouflaged due to the intensity of alteration as hydrothermal alteration in IOCG systems commonly lead to complete transformation of precursor rock mineralogy, texture and geochemical composition (Fig. 5-1) and can be reproduced irrespective of the nature of the original host. This lack of constraints on the unaltered protolith original compositions make mass-balance systems analysis (e.g., Gresen's (1967) equations and the derivative Grant (1986, 2005) isocon method) or any other methods based on the knowledge of unaltered protolith composition difficult to use for systematic lithogeochemical characterization of zonation, element partitioning and geochemical signatures of hydrothermal alteration in IOCG systems.

Geochemical characterization of IOCG alteration requires alternative methods for whole-rock geochemistry data treatment. The compositional data analysis protocol, based on the logratio transformation, overcomes the closure constraint inherent with geochemical data and allows the use of multivariate statistical tools for geochemical process identification. Knowledge of unaltered protolith composition is not a prerequisite to apply these methods (Grunsky and Kjarsgaard, 2008).

IOCG hydrothermal systems of the Great Bear magmatic zone (GBMZ) in the north-western Canadian Shield (see Corriveau et al., 2010a, b; Mumin et al., 2010 for detailed review of the GBMZ IOCG systems) are good candidates to undertake such multivariate statistical studies using the logratio approach (Fig. 1-2). Due to the presence of cross-sectional exposures and differential exhumation, GBMZ IOCG systems comprise the entire spectrum of IOA and IOCG alteration types and are formed at the expense of a large variety of volcanic, sedimentary, plutonic and metamorphic precursor rock types. In many cases, alteration has occurred with a

sufficient intensity to completely replace precursor rocks. The evolution history of each system is well constrained and summarized within the IOCG alteration zoning models of Corriveau et al. (2010b) and Mumin et al. (2010) and a database of fully documented geochemical analysis is available.

In this study, we define the geochemical signature of the main IOCG hydrothermal alteration types from the GBMZ IOCG systems using commonly determined major and trace elements following an innovative approach based on multivariate statistical methods and more specifically principal component analysis (PCA). The geochemical patterns revealed by this method will refine discrimination parameters for these alterations, complement the already existing vectors for IOCG deposits (Benavides et al., 2008a), and will promote the development and use of IOCG alteration discrimination diagrams and alteration indexes.

5.2 Selected case examples of Great Bear magmatic zone IOCG systems

This section is a brief review of GBMZ IOCG systems covered in this study. Detailed information can be found in Hildebrand (1986), Gandhi (1989, 1992a, b), Gandhi and Prasad (1995, 1997), Goad et al. (2000a, b), Corriveau et al. (2010a, b, 2011), Mumin et al. (2007, 2010), Ootes et al. (2010), Acosta et al. (2011, 2013, 2014) and references therein. There are currently two recognized and largely documented IOCG districts in the GBMZ: Port Radium–Echo Bay in the northern GBMZ and Lou – Sue-Dianne in the southern GBMZ. Other significant systems and districts covered in this study are the Camsell River district and the Fab and DeVries IOCG systems in the north-central and central GBMZ (Fig. 1-2).

5.2.1 Port Radium–Echo Bay and Camsell River IOCG districts

The Port Radium–Echo Bay IOCG district hosts polymetallic mineral showings with typical features of iron oxide–apatite deposits (e.g., K-2 at depth and Mag Hill prospects and the past-producing Eldorado mine area) and magnetite- to hematite-group IOCG deposits (e.g., K-2 and to a lesser extent Mile Lake, Breccia Island, Hoy Bay and Birchtree showings and prospects) in the deposit classification scheme of Williams (2010a). The prospects are part of coalescing hydrothermal cells that were developed during the construction of host stratovolcano complexes and their coeval sub-volcanic intrusions following the final collapsing and tilting of the volcano-plutonic edifices (Hildebrand, 1986; Mumin et al., 2007, 2010; Hildebrand et al., 2010b). The iron

oxide–apatite bodies discovered to date are part of the sodic and sodic–calcic–iron alteration zones that developed at the margin of the sub-volcanic intrusions. Variable degrees of overprinting by potassic and potassic–iron alteration are also observed in these areas and are often accompanied by polymetallic sulfide mineralization (Corriveau et al., 2010a; Mumin et al., 2007, 2010). Epithermal-type alteration and mineralization are developed peripheral to the Port Radium–Echo Bay IOCG systems during the collapsing of the hydrothermal centres and remobilized a significant amount of metals to form past-producing vein-type deposits (see Mumin et al., 2010). Detailed description of the vein-type ore deposits is available in Badham (1975).

The Camsell River IOCG district is centered on the past-producing Terra and Norrex vein-type deposits (Badham, 1972, 1975; Hildebrand, 1986) hosted among Kiruna-type and IOCG-type alteration and mineralization. Amphibole, amphibole–magnetite and albite alteration were recognized by Hildebrand (1986) and thought to prevail at surface but recent work highlights significant K-feldspar, K-feldspar–magnetite and locally mineralized (chalcopyrite) chlorite alteration zones (Corriveau et al., 2009; Acosta et al., 2011). This is a typical alteration assemblage of a mature polymetallic IOCG system that evolved beyond the Kiruna-type stages of alteration and monometallic iron mineralization. Much of the Camsell River IOCG system is hosted within the LaBine–Dumas volcanic sequence and is similar in many aspects to the Port Radium–Echo Bay IOCG district although detail alteration mapping of IOCG-types alteration remains to be done.

5.2.2 Lou–Sue-Dianne IOCG district and other affiliated IOCG systems

The Lou IOCG system is located within the mildly metamorphosed 1.88 Ga Treasure Lake Group sedimentary sequence and overlying sub-greenschist volcanic rocks of the Faber Group. It hosts the Au–Co–Bi–Cu NICO deposit, the Southern Breccia U–Th–Cu–Mo mineralization and several polymetallic showings (Fig. 1-15; Goad et al., 2000a, b; Corriveau et al., 2010a; chapitre 6). The Treasure Lake Group is a platform-type sedimentary sequence consisting of medium-bedded marine wacke, siltstone, arkose, turbidite and minor carbonate units that were deposited just before final accretion of the Hottah Terrane to the Slave Craton between ca. 1.90-1.88 (Gandhi et al., 2001; Gandhi and van Breemen, 2005). Unconformably overlying the Treasure Lake Group metasedimentary rocks are the predominantly felsic, calc-alkaline volcanic rocks of the Faber Group. Basal massive- to flow-banded rhyolitic-rhyodacitic flows are overlain by a succession of volcaniclastic units dominated by ash flow tuff with minor porphyritic tuff and lapilli tuff (Gandhi and Lentz, 1990; Gandhi, 1994). The NICO deposit (NI 43-101 compliant mineral reserves of 32.98 Mt @ 1.02 g/t Au, 0.11% Co, 0.14% Bi; Puritch et al., 2012) is an atypical

magnetite-group IOCG deposit formed by the cyclical build-up of amphibole, amphibole–magnetite, biotite/K-feldspar–magnetite and tourmaline alteration with sulpharsenides–Co–Au overprint at and below the unconformity between the Treasure Lake and Faber group rocks (Goad et al., 2000a, b; Corriveau et al., 2010a, 2011). Styles of alteration and mineralization consist of replacement, veins and breccias. Syn and late porphyry dikes are associated with or crosscut most of the NICO IOCG alteration and led to localized and intense K-feldspar haloes along the dikes. The Southern Breccia is located one kilometre south of the NICO deposit. It hosts a large albitization corridor overprinted by magnetite, K-feldspar, magnetite–K-feldspar, tourmaline and chlorite alteration with hematite and biotite alteration. This albitization corridor hosts numerous U–Th±Cu–Mo anomalies similar to those documented in albitite-hosted uranium deposits (Corriveau et al., 2011). Hydrothermal alteration similar to the Lou IOCG system occurs in the southern extension of the Treasure Lake Group as far south as the Rayrock fault where amphibole–magnetite, amphibole, K-feldspar±magnetite and biotite±magnetite alteration types prevail and are locally mineralized with arsenopyrite, chalcopyrite and millerite (e.g., Duke and Burke showings; Fig. 1-15).

The Sue-Dianne IOCG system is hosted in the Faber Group volcanic sequence and is located 24 km north of the Lou IOCG system (Fig. 1-15). It hosts the magnetite to hematite-group Cu–Ag–(Au) Sue-Dianne IOCG deposit (indicated resources of 8.4 Mt @ 0.8 % Cu and 3.2 g/t Ag and inferred resources of 1.6 Mt @ 0.8 % Cu and 2.4 g/t Ag, Hennessey and Puritch, 2008). It formed in well-preserved rhyodacite ignimbrite sheets during the development of a structural-hydrothermal breccia complex (diatreme) at the intersection between the NE trending Dianne fault and the north trending MAR fault. Alteration in the Sue-Dianne deposit is zoned and ranges from sodic alteration (albite) in the deepest parts of the porphyry stock underlying the complex to potassic–iron and potassic alteration (magnetite–K-feldspar, magnetite–hematite–K-feldspar and K-feldspar) in the shallowest part of the diatreme (Goad et al., 2000a; Camier, 2002; Mumin et al., 2010). The Sue-Dianne deposit is actually related to a magmatic-hydrothermal cell originating from the underlying porphyry intrusion (Camier, 2002; Mumin et al., 2010). At a regional scale, Sue-Dianne is part of a larger magnetite- to hematite-group IOCG system that extends to the Brooke Zone and Mar showings, respectively south and north of the Sue-Dianne deposit. IOCG-type hydrothermal alteration also intermittently occurs throughout the volcanic complex and increases in intensity in the immediate vicinity of the main mineralized zones and within major structural corridors such as along the Dianne fault ESE of the Sue-Dianne deposit.

The Cole IOCG-affiliated hydrothermal system is hosted within the Faber Group volcanic sequence and is located ca. 10 km northeast of the NICO deposit on the north side of the Lou Lake fault (Fig. 1-15). Albite, amphibole amphibole–magnetite alterations mildly overprinted by K-feldspar predominate and led to the development of a 450-m wide tectono-hydrothermal breccia zone. Local development of intense K-feldspar alteration (locally with anomalous U values), scarce specular hematite, localized high U in albitized rocks and late-stage vein-type copper mineralization are also present. A late epidote±K-feldspar–chlorite alteration overprint is widespread throughout the Cole hydrothermal system.

The Treasure Lake Group metasedimentary rocks northeast of the NICO deposit host several IOCG-affiliated hydrothermal systems with diverse alteration types, including albite, amphibole, amphibole–magnetite, magnetite, hematite, biotite ± magnetite and K-feldspar ± magnetite/hematite. Significant systems in this area include the Ron and Hump iron oxide showings where massive hydrothermal iron-oxide bodies reach 100 m by 75 m at surface (Gandhi, 1994) and are hosted within amphibole–magnetite alteration typical of iron oxide–apatite deposits. A strong K-feldspar±magnetite alteration imprint is ubiquitous and locally very well developed in the Hump system. The Esther hydrothermal system, hosted by the Treasure Lake Group and some granitic bodies, is characterized by significant albitization and intense amphibole, K-feldspar, K-feldspar–hematite and chlorite alteration with localized anomalously elevated concentration in Cu, Ta, Nb, Th and U.

5.2.3 Central GBMZ IOCG systems

The Fab IOCG system is hosted by porphyries that are part of a calc-alkaline volcano-plutonic complex stratigraphically equivalent to the volcanic sequence hosting the Sue-Dianne IOCG system in the Faber Group (Gandhi, 1988). Pervasive albitization, numerous generations of amphibole, amphibole–magnetite and amphibole–magnetite–apatite veins and strong biotite–magnetite and K-feldspar–magnetite alteration prevail with Cu and U mineralization (Gandhi, 1988, 1994; Corriveau et al., 2010a). Numerous breccias were formed in the porphyritic units as the result of this hydrothermal activity. Main commodities in the Fab IOCG system mineralized zones are Cu and U (Gandhi, 1988, 1994). Mineralization occurs where potassic–iron alteration strongly overprints calcic–iron alteration.

DeVries is an IOCG system of the central GBMZ that includes the NORI showing (Gandhi and Prasad, 1993; Corriveau et al., 2010a; Ootes et al., 2010). Alteration occurs within metasedimentary rocks of the Treasure Lake Group (Corriveau et al., 2007, 2010a).

Documented alteration and associated mineralization are similar to those of Fab (Gandhi et al., 2001; Corriveau et al., 2010a) but older with early albitization crosscut by syn-deformation granitic intrusions dated at 1878±4 Ma (Bennett and Rivers, 2006; Corriveau et al., 2007) while host rocks at Fab were emplaced between 1870 and 1860 Ma (Gandhi et al., 2001; Acosta et al., 2011; Davis et al., 2011), indicating that IOCG alteration occurred in the DeVries system prior to and at the onset of Great Bear magmatism.

The JLD U–Cu–Fe showing is characterized by intense magnetite±amphibole alteration. The Ham and Hailstone Cu–U–Fe showings are characterized by strong and intense K-feldspar, biotite–magnetite and magnetite–amphibole alterations. These three showings are located close to the Wopmay fault zone (central GBMZ) in felsic volcanic rocks and intermediate intrusions (Fig. 1-2).

5.3 Methods

5.3.1 Sample selection and description

Samples collected for whole-rock geochemistry were taken on representative host rocks, breccias, alteration fronts (replacement-type alteration) or veins. Sample preparation started in the field with rock chips carefully selected to avoid crosscutting veins or superimposition of multiple alteration events as sampling aimed at documenting alteration processes and geochemical signatures of the individual alteration types encountered in IOCG systems. All the samples were carefully described and given an alteration name corresponding to the IOCG alteration sequencing model sub-division. Alteration names were based on field observation, gamma ray spectrometer measurement (K, eU, eTh) and magnetic susceptibility meter measurement, rock slab and stained rock slab description and geochemical composition. Alteration intensity for each sample was also quantified using the preceding criteria and the degree of preservation of the precursor rock textures (Corriveau et al., 2015 and appendices 3, 4 and 5 for sample descriptions and geochemical analyses).

5.3.2 Analytical methods

Samples in this study were analysed by instrumental neutron activation (INAA) at Becquerel Laboratories in Toronto, a combination of ICP-MS (trace elements) and ICP-AES (major and some trace elements) after alkaline fusion performed at INRS–ETE in Quebec and ICP-MS analysis after multi-acid digestion performed at AcmeLabs in Vancouver (Method 1EX). To

choose the best data for the geochemical modelling, the quality of the geochemical analyses was evaluated according to the precision of the standard analysis, analytical limitations of certain methods for specific elements, the detection limits for each element and the reproducibility of the results when the analytical methods are compared together. This data assessment indicates that for most major and trace elements alkaline fusion combined with ICP-MS and ICP-AES are the best analytical methods. For some base metals (Pb, Zn, Co, Bi, Sn and Ni) multi-acid digestion gives better or equivalent results compared to fusion and for some trace elements (As, Rb, Cs) INAA gives better results compared to multi-acid digestion and fusion.

5.3.3 Preparation of the dataset

For this study all the major elements are expressed as cations, as it better reflects modal mineralogy of the studied samples (Grunsky and Kjarsgaard, 2008), and converted to ppm. Iron, initially measured as $Fe_2O_{3(T)}$, was left as Fe^{3+}, as this cation is a major constituent of much of the IOCG alteration and conversion to Fe^{2+} would be too arbitrary. For elements with concentration below detection limit, the concentration was set to half the reported concentration expressed as < x. For example, if the reported concentration was < 1, the concentration in the dataset was set at 0.5. However, the statistical treatment was applied only to elements where the number of analyses below detection was under 5% of the total dataset and for most elements below 1% to minimize sample censoring and bias in statistical treatment of the data.

Within the dataset, all the transitional alteration, less common alteration (e.g., silicification, skarn) and weakly to unaltered altered rocks were removed to keep only the main alteration types (Na, Ca–Fe, K and K–Fe (HT and LT) alterations), which gives a total of 386 samples (Table 5-1). (HT) K–Fe and (LT) K–Fe were modelled together because of their similar geochemical signature and the low number of (LT) K–Fe altered samples that were available. As most mineralization in IOCG systems occurs within the (HT) K–Fe and (LT) K–Fe alteration, modelling the (HT) K–Fe and (LT) K–Fe alteration type together still facilitates the targeting of the most likely fertile zones of the systems. The various styles of K-alteration were also modelled together to simplify the modelling interpretation. The transitional alteration types were defined by superimposition of more than one alteration phase (e.g., potassic alteration superimposed over amphibole–magnetite alteration as shown by cobaltnitrate staining of rock slabs) or mineral parageneses transitional between two main alteration types.

Table 5-1 Number of samples per alteration type used for the geochemical modelling

Alteration type	Zoning model	# Samples
K (Kfs, Msc)	3-4	125
Ca-Fe (Amp-Mag±Ap, Amp, Mag)	2	89
Na (Ab)	1	47
K-Fe (Kfs-Mag, Kfs-Hem, Bt-Mag, Bt, Kfs-Chl)	3-4	125

Mineral abbreviations after Whitney and Evans (2010).

Typical alteration types with transitional mineralogy are the Na–Ca–Fe (albite–amphibole±magnetite transitional between Na and Ca–Fe) and Ca–K–Fe (amphibole–biotite–magnetite alteration transitional between Ca–Fe and K–Fe) alterations types. This approach simplifies definition of key geochemical footprint of alteration and extraction of first order vectors to mineralization. It also minimizes the problem where a mild alteration is superimposed on a previously strong alteration of a different composition masking addition or subtraction of elements related to the overprint (e.g., mild potassic alteration overprinting an albitite where original potassium was nearly totally leached in the first place, the resultant would not appear potassically altered with respect to original protolith of the albitites). Mineralized samples associated with the main alteration types were kept in the dataset to assess the geochemical distribution and association of base metals (Cu, Co, Zn, Ni) and radiogenic elements (U, Th). Samples from the Port Radium–Echo Bay, Lou, DeVries and Sue-Dianne IOCG systems predominate in the dataset and are supplemented by samples from Hump, Ron, Esther, Fab, JLD, Camsell River, Cole, Hailstone and Ham IOCG and IOCG-affiliated systems. Some geochemical analyses for the Sue-Dianne IOCG systems were taken from Camier (2002) as their associated alteration types were easily constrained based on their sample descriptions.

5.3.4 Centered logratio transformation of the raw geochemical data

Pearson (1897), Chayes (1960) and Aitchison (1986) demonstrate that using the raw geochemical data expressed in weight percent or ppm can lead to spurious correlations when studying bivariate relationships within a dataset and inconsistent covariance and correlation matrix. This is referred as the ‘closure problem’, inherent to all compositional dataset (Aitchison, 1986). Simply put, any composition (geochemical) that is expressed in whole or part, in %, ppm, ppb, etc., is constrained by a constant sum (100%, 1 000 000 ppm, etc.). This constraint results in inconsistent and unreliable results when statistical calculations are carried out on such data. A simple illustration of this is the calculation of correlation coefficients for a composition. If a composition consists of 10 variables (e.g., weight percent oxides), only 9 oxides are necessary

to describe the variability of the composition, If correlation coefficients are computed for the 10 oxides and any variation of 6 oxides, the coefficients will be different. This sub-compositional incoherence illustrates the core of the closure problem. As noted by Pearce (1968), ratios are more effective at describing relationships of geochemical compositions. As the method of principal component analysis is based on the covariance or correlation matrix of compositional data within a dataset, restrictions imposed by the closure constraint must be removed before modelling. Failure to do so may result in doubtful or invalid results and interpretations from PCA. In this study, the centered logratio (clr) transformation developed by Aitchison (1986) is used to overcome the closure on a compositional dataset and to move the data from the compositional data space to the real number (Euclidian) space. This logratio transformation is ideal for PCA as it preserves all the variables of the studied composition (Aitchison, 1986; Egozcue et al., 2003, Pawlowsky-Glahn and Egozcue, 2006). The caveat of the clr transformation is that the inverse of the covariance matrix of the clr-transformed compositions is singular and therefore cannot be used for statistical methods requiring a non-singular inverse covariance matrix, which is not an issue in this study.

For a D-part (elements) compositional vector **x,** the centered logratio transformation is defined as:

$z_i = \log(x_i/g(\mathbf{X}_D)) \qquad (i = 1,\ldots,D)$

where $g(\mathbf{X}_D)$ is the geometric mean of the compositional vector (i.e., the composition of the rock). All the required computation and graphs to achieve the statistical analysis were produced using the R project for Statistical Computing and StatDa package (R development Core Team, 2011). The usefulness of the R software and its applications in geosciences were demonstrated by Grunsky (2002).

5.4 Results

5.4.1 Alteration geochemical signatures – Bivariate relations

The perfect covariation between Na and Al and Na and Si for sodic alteration and for the main Ca–Fe (Na) alteration and the slope of this trend confirm previous observations that albite is the prevalent mineral formed during sodic alteration of the GBMZ (Hildebrand, 1986; Mumin et al.,

2007; Corriveau et al., 2010b; Fig. 5-2a–b, e). It is also noteworthy to mention that the trends resulting from the centering of the data are almost the same as those produced using classical element ratio following the recommendations of Pearce (1968), thus validating the interpretation on alteration processes made using the clr-transformed data (Fig. 5-2a–b). It indicates that, although the binary diagrams appear to be presented in the 'classical way', the interpretation is not. The value and meaning of these binary diagrams are further demonstrated by their identifiable trends in the data according to known features of alteration in the individual observations.

Potassium, K–Fe and some Ca–Fe alteration record a decoupling between Al and Na, which not only highlights the absence of albite but also potential leaching of Na while Al remained immobile during these alteration stages. That most of the Ca–Fe alteration follows the trend of the K and K–Fe alteration types may indicate a weak overprint of K–Fe and K alteration types that have crystallized K-feldspar at the expense of albite, maintaining the Al content while severely depleting the samples in Na. A strong positive covariation between K and Al and K and Si for most of K, K–Fe and some Ca–Fe alteration and the slope of the trend indicate that K-feldspar is the predominant mineral precipitated during K and K–Fe alteration (Fig. 5-2c, f). Dispersion of the data within the trend indicates that other K-rich minerals incorporating a different proportion of K such as biotite, common in some K–Fe alteration, or muscovite (sericite) may have formed during potassic alteration. Alternatively, this may record an original leaching of K in precursor alteration on which K/K–Fe alterations were superimposed. Some Ca–Fe alteration zones with magnetite record a negative covariation between K and Al, indicating the complete destruction of either biotite, K-feldspar or sericite during Ca–Fe alteration and their replacement by alkali- and Al-poor minerals among which magnetite likely prevails.

The variation between Al and Ca clearly demonstrates that the Ca–Fe alteration has the overall highest Ca content compared to the other alteration types and that Ca steadily increases for slightly decreasing Al (Fig. 5-2d). This is indicative of Ca enrichment during the Ca–Fe alteration stage, which is also supported by the fluid inclusions work done by Perring et al. (2000), Pollard (2001), Baker et al. (2008) and Billen (2010) and the modelling of Oliver et al. (2004). The overall inverse variation between Ca and K highlights a strong decoupling between these two elements during the evolution of IOCG systems (Fig. 5-3a).

The variation between Ca and Fe records progressive Fe enrichments for constant Ca concentrations for both Ca–Fe and K–Fe alteration, highlighting that the increase in Fe concentration is mostly related to increasing iron oxide in the alteration paragenesis. Some Na

and K alteration zones record an Fe depletion trend, inferred to be associated with Fe leaching during these alterations (Fig. 5-3b), a process that Oliver et al. (2004) have already documented in the Cloncurry district albitites and can now be extended to intense K-feldspar alteration.

The strong variation in Sr within a restricted field of Ca concentration associated with Ca–Fe alteration records a decoupling between these normally covalent elements (Fig. 5-3c). Though such a decoupling has been reported within advanced argillic alteration (Hikov, 2004), this is to our knowledge the first example of such decoupling in Ca–Fe alteration associated with IOCG systems. Within K, K–Fe and Na alteration, Ca and Sr display a weak and positive covariation although a large dispersion is observed. No definite trend was observed for Na and Sr, except for some of the strongly sodic-altered samples where a positive covariation between Na and Sr was defined. It highlights a coupling between these two elements during sodic alteration. Sodium alteration also generally correlates with the highest relative concentrations of Sr (Fig. 5-3d).

Some of the usual element association observed in magmatic systems are preserved in IOCG hydrothermal systems, as shown by the strong and positive covariation between Co and Fe and Ni and Fe (not shown) that is broken down by mineralized samples showing significant Co enrichments (Fig. 5-3e). Two distinct trends emerge between Fe and Cu as alteration evolves from alteration decoupled from mineralization (Na, Ca–Fe and K) and those associated with it (K–Fe and Ca–Fe±K–Fe), while a third trend of mild Cu enrichment or depletion is observed within Fe-poor K and Na alteration types.

In the first trend, barren in terms of mineralization, Fe concentration increases (either with magnetite or hematite alteration) while Cu concentration remains constant, highlighting episodes of iron oxide alteration sterile in terms of polymetallic mineralization. In the second trend both Cu and Fe increase together, highlighting stages of fertile magnetite or hematite alteration, the most fertile being where associated with potassium as of K-feldspar, biotite or sericite. That some Ca–Fe altered samples follow the K–Fe trend, as shown in Figure 5-2c, reinforces field and stained slab observations that these samples have a mild to moderate overprint of K–Fe alteration, even though their main alteration signature is defined by the Ca–Fe imprint (Fig. 5-3f). It demonstrates that geochemical modelling based on the logratio transform can detect these K–Fe and K alteration overprints; this can be of great help in exploration since they are a key indicator for mineralization-potential in IOCG systems (Corriveau et al., 2010b).

Light rare earth elements (LREE) remain strongly coupled during hydrothermal alteration as La and Ce are positively correlated (Fig. 5-4a). LREE and heavy rare earth element (HREE) are not

correlated together but exhibit variable enrichment and depletion trends recording REE mobility. None of the alteration types sampled provided a mechanism for systematic HREE enrichment in the systems studied (Fig. 5-4b).

Uranium and Th remain generally positively correlated during the development of IOCG alteration. Some alterations are enriched in U compared to Th, a feature diagnostic of hydrothermal alteration and others are enriched in both U and Th compared to the center of the dataset, illustrating that two distinct processes may control radiogenic elements enrichment within IOCG systems following a magmatic-like hydrothermal trend largely recorded by the Na and K alteration types (Fig. 5-4c). Copper and U are not correlated within IOCG alteration but their covariation highlights two trends (Fig. 5-4d). In the first trend Cu increases while U remains fairly constant and in the second trend U increases while Cu remains constant. These observations indicate that Cu and U may come at different stages during the hydrothermal system evolution and when both events were superimposed it results in Cu–U-rich alteration.

Hafnium-Zr and Na record a positive covariation for most of the sodic alteration, highlighting relative Zr and Hf enrichment during sodic alteration. This is compatible with the crystallisation of hydrothermal zircon in albitites and highlights the importance of such units in dating alteration within IOCG systems (Fig. 5-4e–f; Davis et al., 2011).

5.4.2 Alteration geochemical signatures – Principal component analysis

Principal component analysis (PCA) is used to highlight the key differences between each alteration geochemical signature as it determines the main evolution trends within a dataset. Each principal component represents a certain percentage of the total variability of the dataset and their computation is based on the covariance matrix of the data. Principal components were computed following the method of Zhou et al. (1983) using the clr transformed data. The screeplot presents ordered eigenvalue and their corresponding significance for the total dataset variation (Fig. 5-5). Principal component 1(PC1), PC2 and PC3 contribute respectively for 29.4 %, 16.0 % and 8.5 % of the total variance for a total of 53.9 %. PC4 to PC9, accounting for 27 % of the total variation, and PC10 to PC29 (remaining 20 % of the total variation) represent internal variations within the dataset that are currently difficult to interpret regarding alteration processes and signatures. These lower degrees of variations may result from compositional differences due to: (1) fluid ability to mobilize and precipitate different elements while forming the same alteration type; (2) heterogeneity of fluid composition as fluids evolve and fluid sources vary; and (3) the wide variety of protolith compositions that were hydrothermally altered.

Sample and variables scores are projected onto the first (PC1) and second (PC2) principal axes using the biplot representation of Gabriel (1971). From this projection, explaining 45.4 % of the total variation, results a clear discrimination of Ca–Fe, K–Fe and K alteration, each group forming a distinct cluster on the biplot (Fig. 5-6a), with Ca–Fe and K alteration forming two distinct poles discriminated by PC1. This distribution of the data clearly demonstrates the weak influence of the precursor rock composition where IOCG alteration is intense and well-developed as the observed principal variability on the biplot is controlled by the geochemical signature of the resulting alteration and not the initial protolith composition. It also demonstrates that IOCG alteration geochemical signatures can be considered as statistically distinct. Calcium–Fe alteration geochemical signature is mainly characterized by enrichment in Ca, Fe, Mn, Mg, Zn, Ni and Co, a combination of elements very similar to the geochemical signature of mafic–ultramafic rocks. The K alteration geochemical signature is characterized by enrichment in K, Al, Ba, Si, Rb, Zr, Ta, Nb, Th and to a lesser extent U, and very similar to the geochemical signature of felsic–intermediate rocks. The REE remain grouped together except for Eu, which is more related to the Ca–Fe alteration pole, reinforcing the similarity of elemental behaviour with mafic rocks and magmatic plagioclase. Calcium–Fe and some K–Fe altered samples are also more enriched in REE. Copper and P are on the side of the Ca–Fe alteration pole, but more central towards the K–Fe alteration pole, indicating that Cu and P are not exclusively associated with Ca–Fe alteration but also with K–Fe alteration. Samples from sodic alteration are distributed between the two poles, illustrating the diversity of the geochemical signature for Na alteration although it is generally characterized by high concentrations in Na and Sr.

To refine the observations made with PC1 and PC2, sample and variable scores were projected onto PC1 and PC3. The resulting biplot of PC1 and PC3 better discriminates Na alteration and clarifies its geochemical signature as it shows the relative enrichment in Na and Sr or Si, Zr, Ta, Th, Nb and Zr enrichment for few Na-altered samples (Fig. 5-6b). It also demonstrates that base metal enrichments in IOCG alteration are mostly related to Fe-rich alteration and that Fe is strongly and positively correlated with Co, and more weakly and positively correlated with Cu. The PC1–PC3 biplot also highlights that Ca–Fe with K–Fe alteration are more likely to be Co-rich and Cu-rich. It further shows that Zn is not a major element in the studied ore zones and is more related to Mg- and Mn-enriched Ca–Fe alteration. This graph better constrains Ca–Fe alteration enrichment in Eu and the strong partitioning of Eu with respect to the other REE. It also indicates that K and K–Fe altered samples are generally richer in U.

5.5 IOCG alteration empirical discrimination diagram

PCA demonstrates that IOCG alteration geochemical signatures, where hydrothermal alteration is intense and penetrative, can be considered mostly independent of the original protolith composition and that alteration types have statistically distinct compositions in both major and trace elements that can be modelled using four major compositional poles (K, Ca, Fe and Na). As such, this PCA analysis can help with the development of alteration indexes and discriminant diagrams to assist remote predictive mapping of alteration zones and alteration vectors to ore. Alteration indexes and discriminant diagrams already exist for a wide variety of deposit types such as the Ishikawa, Chlorite–Carbonate–Pyrite, silicification and per-aluminous indexes used for volcanic-hosted massive sulfide deposits (Ishikawa et al., 1976; Large et al., 2001; Pirajno, 2009). An alteration index for IOCG systems elaborated by Benavides et al. (2008a, b) helps detect IOCG alterations and characterize their intensity but is not designed to discriminate the distinct alteration parageneses observed in IOCG systems. Here, we propose alteration indexes that complement existing ones and form the basis for geochemical diagrams that help discriminate Na, Na–Ca–Fe, Ca–Fe, Ca–K–Fe, K–Fe (HT and LT) and K alteration types from a wide variety of protoliths according to the alteration sequencing model of Corriveau et al., (2010b).

5.5.1 Construction of the IOCG alteration discrimination diagram

Alteration index formulation is based on molar concentration in order to have a direct representation of the geochemical signature and mineralogy of the rocks (Pearce, 1968; Stanley and Madeisky, 1994; Grunsky and Bacon-Shone, 2011). Major elements were chosen to elaborate the IOCG alteration index as they encompass all the observed geochemical variations observed in IOCG systems. Moreover, these elements were commonly and precisely determined over the last 50 years, allowing reinterpretation of large historical datasets and elaboration of better guides for mineral exploration across the large territories studied before IOCG deposit definition in the nineties by Hitzman et al. (1992).

The first empirical index (AIOCG 1) is inspired from PCA results demonstrating that K, Na and Ca are key elements to discriminate Na, K and Ca–Fe alteration and the Madeisky (1996) $K/(K+Na+2Ca)_{molar}$ index, used to quantify K metasomatism. In this study, the Madeisky index was slightly modified to optimize discrimination of Na from K alteration and Ca–Fe from K–Fe alteration. Potassium is used as a proxy for the K-rich phases (K-feldspar, biotite, sericite) of the

K and K–Fe alteration. Calcium is used as a proxy for the Ca-rich minerals usually formed in Ca–Fe alteration (amphibole, apatite, clinopyroxene, garnet) and Ca-bearing scapolite formed in Na–Ca alteration. Sodium is used as a proxy for the Na-rich mineral formed during sodic alteration (albite and scapolite). The only difference with the Madeisky (1996) index is that the weight of Ca has been diminished to accentuate the contrast between Na-rich and K-rich alteration and to level the molar proportion of Ca in the commonly observed amphiboles in IOCG alteration to 1, equating the molar proportion of K and Na in K-feldspar and albite respectively. The resulting index is $K/(K+Na+0.5Ca)_{molar}$.

The second empirical index (AIOCG 2) is designed to discriminate alkaline (Na–K) alteration from Ca–Fe, K–Fe and Fe alteration. The selection of elements to define this index is based on the observed covariations in the bivariate analysis, PCA results, alteration mineralogy and empirical testing of different weighting factors for each element. In this alteration index Si is used as a proxy to estimate the concentration of Na- and K-bearing minerals in the alteration because of its positive covariation with Na and K for most of the Na, K and K–Fe alteration and because magnetite-rich or hematite-rich K–Fe and Ca–Fe alteration types are usually depleted in Si (Figs. 5-6a, 5-7). Calcium and Mn are used as proxy for Ca–Fe alteration (Fig. 5-6a). The Fe/Mg ratio is used to discriminate Ca–Fe and Fe alteration from mafic rocks by emphasizing Fe enrichments over Mg, as Fe enrichments in Ca–Fe and K–Fe IOCG alteration considerably surpass the usual Fe/Mg ratio for unaltered or weakly altered mafic rocks with the massive precipitation of iron oxide (Fig. 5-7).

The resulting index is $(2Ca+5Fe+2Mn)/(2Ca+5Fe+2Mn+Mg+Si)_{molar.}$

5.5.2 Main alterations from the GBMZ IOCG systems

Most of the main IOCG alterations (Na, K, K–Fe and Ca–Fe) and weakly altered rocks of the GBMZ IOCG systems plot in distinct clusters except for less intense main alteration that falls close to weakly altered rocks (Fig. 5-8a). The clusters formed by the main alteration and weakly altered rocks allow the subdivision of the diagram in alteration fields as per the alteration stages Na, Ca–Fe, HT–LT K–Fe and K of the Corriveau et al. (2010b) IOCG alteration model. The field of weakly altered rocks was further constrained with examples of fresh volcanic and plutonic rocks from the literature (Best et al., 2003; Kelemen et al., 2003; Kemp and Hawkesworth, 2003; Li and Schoonmaker, 2003; Rudnick and Gao, 2007). Superimposition of the field of Ca–Fe alteration with that of weakly altered mafic rocks makes discrimination of some Ca–Fe alteration solely based on whole rock geochemistry more delicate. In such cases, primary knowledge of

the protolith nature and provenance is important to interpret the results. Some diagrams were tested incorporating Sr and Ba to unravel this overlapping between Ca–Fe alteration and weakly altered mafic rocks but the integration of these trace elements mostly hindered alteration discrimination in our IOCG dataset. The field for the weakly altered rocks was defined using a dataset of the weakly altered rocks of the GBMZ complemented by a database of 4600 geochemical analyses of various rock types from the Andes (Georoc database, 2012) as they represent the closest analog of the GBMZ for which a large database of samples was available (Hildebrand et al., 1987).

5.5.3 Transitional and chlorite alterations from the GBMZ

The ability of the alteration diagram to discriminate transitional and chlorite alteration was also tested (Fig. 5-8b). Transitional Na–Ca–Fe (albite–amphibole–magnetite) and Ca–K–Fe (amphibole–magnetite–biotite or K-feldspar) alteration are effectively discriminated by the IOCG alteration discrimination diagram. Intense Ca–K–Fe (amphibole–biotite±magnetite) alteration mostly plots just above the intense Ca–Fe alteration in transition with intense K–Fe alteration whereas intense Na–Ca–Fe alteration plots in continuity with sodic alteration in transition to intense Ca–Fe alteration, further illustrating their transitional character. Transitional alteration types resulting from the superimposition of K alteration (K-feldspar) over Ca–Fe (amphibole±magnetite), Na–Ca–Fe (albite–amphibole±magnetite) or chlorite alterations are not as effectively discriminated by the proposed IOCG alteration diagram, especially where the K-feldspar alteration overprint is mild (Fig. 5-8b). This situation indicates that interpretation of the nature of the rocks falling in the weakly altered rock field should ideally rely on basic knowledge of the protolith, field constraints on its geological setting and basic description of the sampled rock. This is especially true for systems where numerous rocks fall within the potassic and potassic–iron alteration field of the diagram as weak potassic alteration superimpositions are more likely due to the large potassic alteration halos that form at deep to shallow levels of IOCG systems (Hitzman et al., 1992; Mumin et al., 2007). Chlorite alteration could not be readily discriminated with this diagram as it falls mostly within Ca–Fe and Na–Ca–Fe alteration fields although intense chlorite alteration without K-feldspar generally plots around a value of 0 for the AIOCG1 index and value of 0.5 for the AIOCG2 index because of their Mg-rich composition devoid of Na and K.

5.5.4 Samples from IOCG districts outside the GBMZ

Applicability and validity of the IOCG alteration discrimination diagram for other IOCG systems was then tested using 307 whole-rock analysis data coming from different IOCG systems around the world. The incorporated systems were chosen based on published whole-rock geochemical data and to encompass a wide variety of IOCG systems, from IOA deposits to hematite-group IOCG deposits. Geochemical data from an epithermal system was also incorporated in the dataset as these deposits are commonly formed in the apical part of large IOCG systems (Mumin et al., 2010) and are an indicator that the higher level sequences were preserved from erosion.

The geochemical analysis dataset include regional sampling and ore zones from the Chilean Punta del Cobre IOCG district that hosts the Candelaria magnetite-group IOCG deposit (Marschik and Fontboté, 2001a, b), regional and ore zones from the Mantoverde IOCG district (Benavides et al., 2008a) hosting the Mantoverde hematite-group IOCG deposit, IOCG prospects from the Kolari region in Finland (Niiranen et al., 2007), the Mont de l'Aigle hematite-group IOCG system in the Appalachian Orogen of Canada (Bernard, 2006) and the Tamlalt-Menhouhou IOCG system in Morocco (Pelleter, 2007). Regional alteration associated with IOA deposits was also incorporated and includes samples from the Tjårrojåkka iron oxide body in the Kiruna area of Sweden (Edfelt et al., 2005) and regional IOCG alteration from magnetite-group IOCG systems in the Cloncurry district in Australia (Oliver et al., 2004), including the Lightning Creek iron oxide body (Perring et al., 2000). Epithermal alteration types were represented by samples from El Penon Au–Ag system in Chile (Warren et al., 2007).

Plotting the samples coming from IOCG districts outside the GBMZ reproduces patterns similar to that observed with the GBMZ samples (Fig. 5-9a–b). End-member alteration types are efficiently detected by the IOCG alteration discrimination diagram and weakly altered rocks mostly fall within the weakly altered rock field. It highlights the evolved nature and prospectivity of the Chilean IOCG districts (Mantoverde and Punta del Cobre) and the Mont de l'Aigle IOCG system (Canada) (Fig. 5-9a) as hydrothermal alteration from these hydrothermal systems plot in all the fields of the diagram. This indicates that they have gone through all the evolution stages characterizing fertile IOCG systems. Alteration related to iron oxide±apatite hydrothermal systems (e.g., Lightning Creek in Australia, Kolari IOCG alteration in Finland) and regional barren Na alteration from the Cloncurry district (Australia) have AIOCG1 index values under 0.2 and AIOCG2 index value from 0 to almost 1 (Fig. 5-9b).

Intensely altered samples from the El Penon epithermal system (Chile) form a distinct cluster (top-left section of the diagram, Fig. 5-9a) resulting from the intense K–Si enrichment and Ca, Fe, Na, Mg and Mn depletion within this hydrothermal system. This indicates that intense Si–K-rich epithermal alteration, common within the peripheral and upper parts of evolved hematite-group IOCG systems (Corriveau et al., 2010b; Mumin et al., 2010; Skirrow, 2010), can be detected with the proposed discriminant diagram (Fig. 5-9a). Thus it can aid in assessing the potential fertility of an IOCG district for a hematite-group IOCG deposit following the criteria of Skirrow (2010), stipulating that preservation of shallow epithermal systems is a good indication of the preservation of hematite-group IOCG deposits.

The IOCG alteration diagram is unsuitable to discriminate IOCG alteration from: (1) rocks with unusual compositions such as banded-iron formation that may bear geochemical similarities to iron oxide-rich Ca–Fe alteration (Fig. 5-10a); (2) sodic alteration from Archean rhyolites (tested with rhyolites of the Superior Province) that are generally more sodic and/or calcic than their Palaeozoic and Proterozoic counterparts (Andes and GBMZ) (Fig. 5-10a); (3) mafic, ultramafic, and Ca-rich rocks (e.g., limestones, skarn, calc-silicates, marbles) rocks that may bear geochemical similarities with Na–Ca–Fe, Ca–Fe alteration or chlorite alteration (Fig. 5-10a–b); and (4) K-rich high-grade metamorphic rocks, pegmatites and arkosic sedimentary rocks that may bear similarities with potassic alteration or sodic alteration for some Na-rich pegmatites (Fig. 5-10b). These constraints emphasize the importance of acquiring basic knowledge about the protoliths and geological setting before using the proposed diagram, which are usually available in most of the public databases (e.g., USGS National Geochemical Database, Georoc database). Although they were defined using a large number of samples, the subdivisions on the diagram should be considered as indicative and not absolute since this study demonstrates that the geochemical composition of IOCG alteration is a compositional continuum between distinct and extreme end-members of Ca–Fe, K–Fe, K and Na alteration types. The compositional continuum between hydrothermal alterations in IOCG systems is further exemplified by the transitional alteration types (Na–Ca–Fe, Ca–K–Fe) that are formed between the main alteration types.

5.6 Conclusions and implications to exploration

This study demonstrates that principal component analysis carried out with logratio-transformed whole-rock geochemical data facilitates pattern detection and quickly highlights what controls

the main variation direction within a large compositional dataset. PCA confirms the field observations based on mineral paragenesis and modal proportions that the main alteration types of IOCG systems form distinct major element geochemical clusters and that geochemical signature is roughly independent of the nature of the protolith where alteration is intense and pervasive. PCA also documents which minor and trace elements are coupled with and decoupled from the major elements. It demonstrates that K and K–Fe alteration geochemical signatures have an affinity to elemental enrichment of felsic igneous rocks, these alterations being enriched in K, Al, Ba, Si, Rb, Zr, Ta, Nb and Th, with K–Fe alteration being richer in Fe. Calcium–Fe alteration geochemical signatures have an affinity to elemental enrichment of mafic rocks, these alterations being enriched in Ca, Fe, Mn, Mg, Zn Ni and Co.

Knowledge of the main variation patterns within the dataset helps to develop hydrothermal alteration discrimination diagrams designed to detect IOCG hydrothermal alteration using common major elements obtained with any standard whole-rock geochemical analysis method. Combined with the IOCG alteration evolution model, the proposed IOCG alteration discrimination diagram can be used to identify fertile and prospective alteration types within regional datasets and assess the potential fertility of the IOCG systems studied.

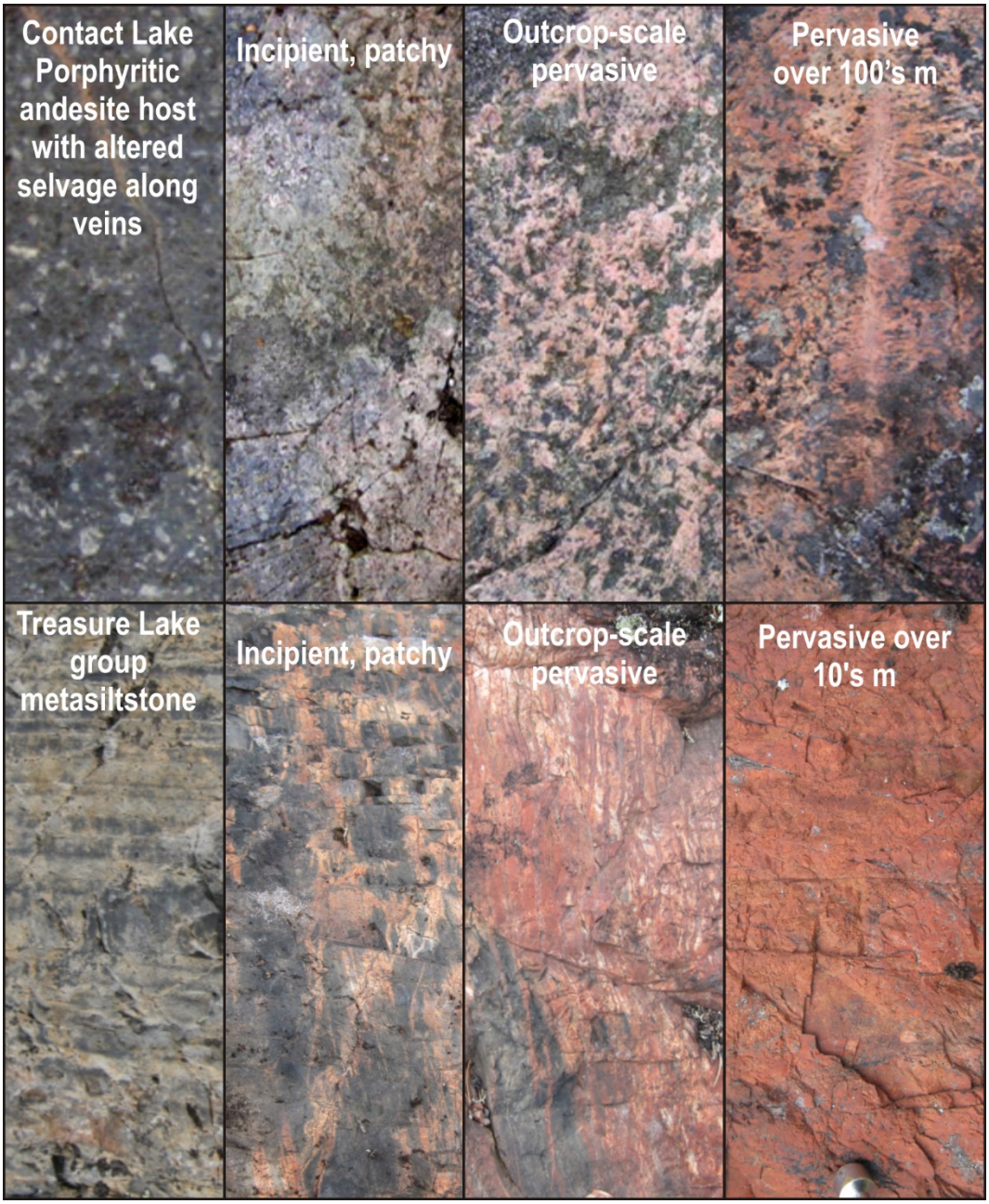

Figure 5-1 Field pictures illustrating the intensity of hydrothermal alteration in the Great Bear magmatic zone IOCG systems

Upper albite–amphibole–magnetite±apatite alteration transforming andesite in the Port Radium–Echo Bay district (northern GBMZ) into a pseudo-pegmatitic rock composed of albite, amphibole, magnetite and apatite with a weak K-feldspar alteration overprint; Lower Sodic alteration transforming the Treasure Lake Group metasiltstone into a rhyolite-looking albitite in the Southern Breccia zone (southern GBMZ).

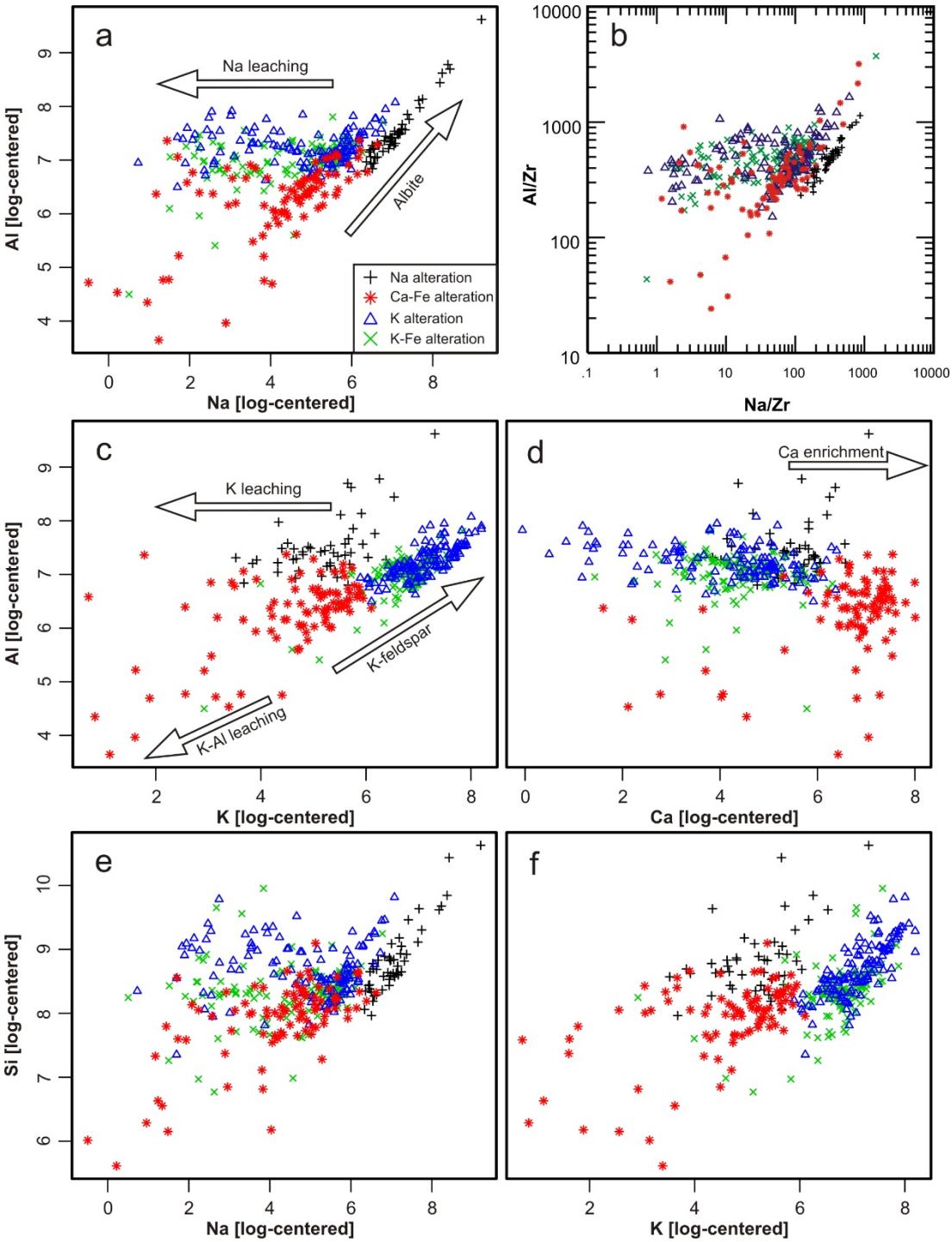

Figure 5-2 Major elements variations in the GBMZ IOCG alteration

(a) Na vs Al plot showing the positive covariation between Al and Na within sodic-altered samples; (b) Na/Zr vs Al/Zr plot showing the similarities with the Na (clr) vs Al (clr) plot a; (c) K vs Al plot showing the positive covariation between Al and K within the K- and some of the K–Fe altered samples; (d) Plot of Ca vs Al showing the Ca enrichment in the Ca–Fe-altered samples compared to the other alteration types; (e) Plot of Na vs Si; (f) Plot of K vs Si.

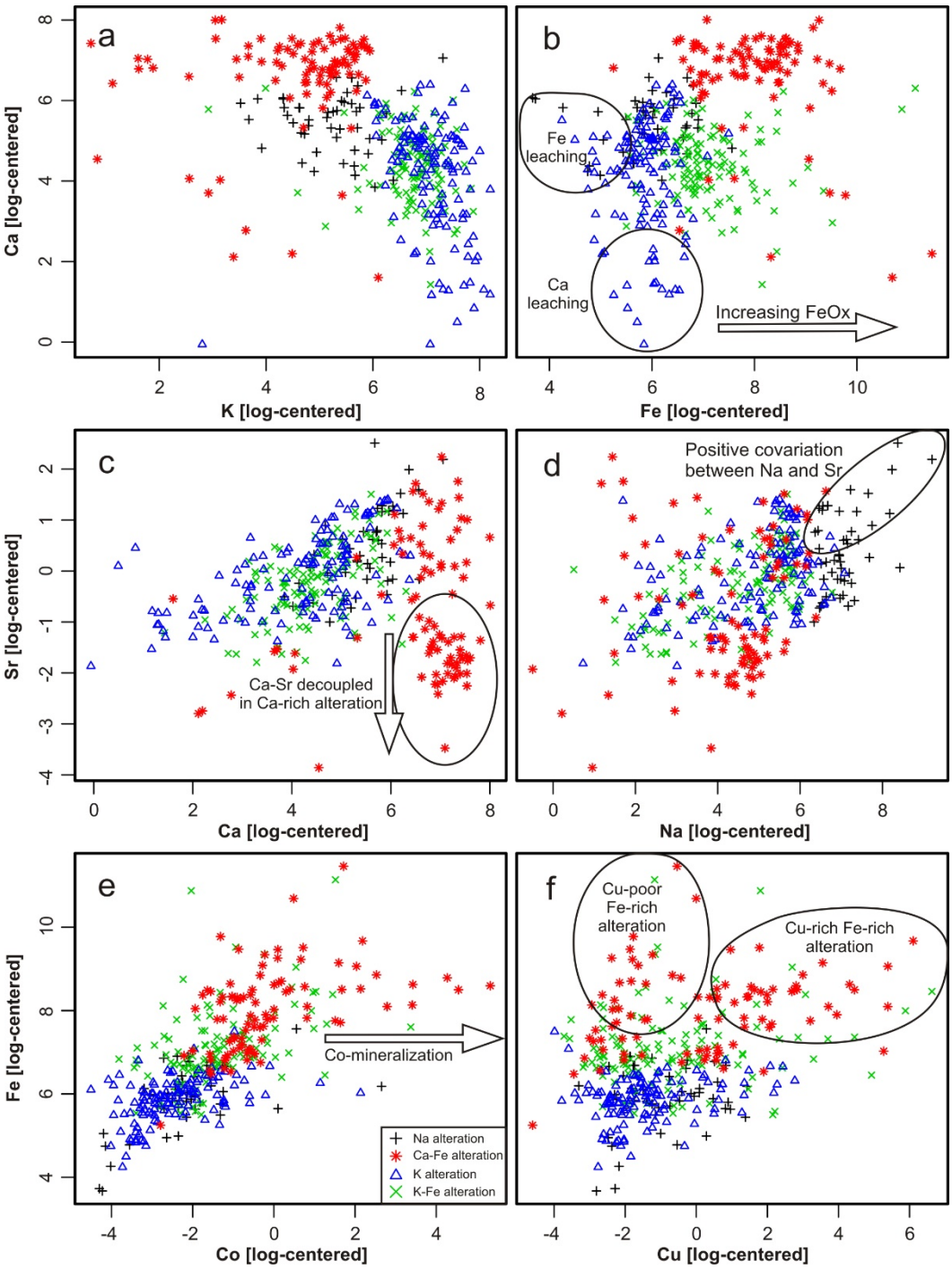

Figure 5-3 Major elements and metals variations in the GBMZ IOCG alteration

(a) Plot of K vs Ca; (b) Plot of Fe vs Ca; (c) Plot of Ca vs Sr showing the decoupling of Ca and Sr in Ca–Fe alteration; (d) Plot of Sr vs Na showing the weak positive covariation between these two elements for sample impacted by intense sodic alteration; (e) Plot of Co vs Fe showing the positive covariation between these two elements; (f) Plot of Cu vs Fe showing two trends indicating Cu-poor Fe-rich alteration (Ca–Fe stage of the IOCG alteration sequencing model) and Cu-rich Fe-rich alteration (HT K–Fe and LT K–Fe stages of the IOCG alteration evolution model).

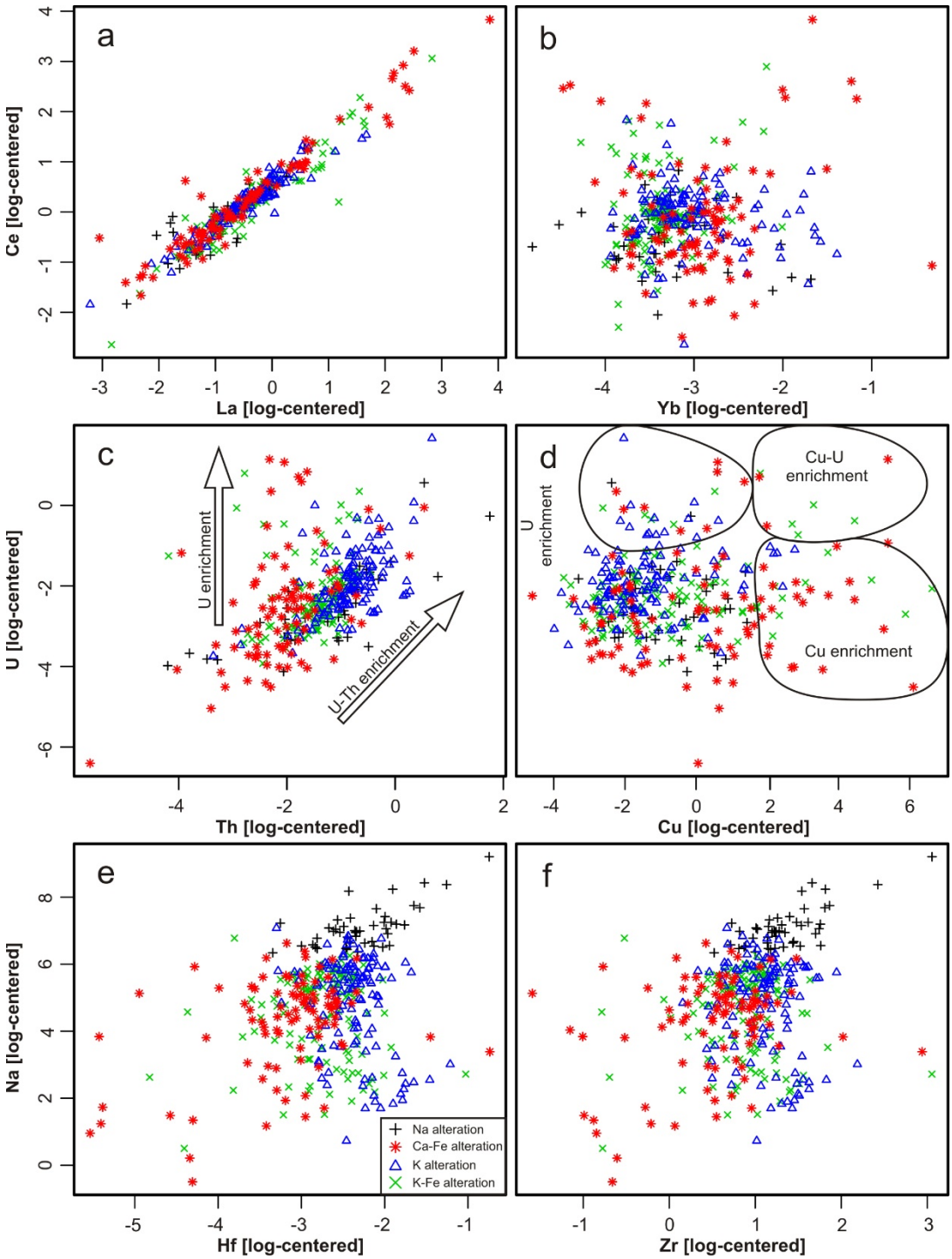

Figure 5-4 Trace elements variation in IOCG alteration of the GBMZ

(a) La vs Ce plot showing the positive covariation between these two elements; (b) Plot of Ce vs Yb showing the decoupling between LREE and HREE in IOCG alteration; (c) U vs Th plot showing that some IOCG alteration types get progressively enriched in U and other in U and Th; (d) U vs Cu plot illustrating the distinct trends of Cu enrichment and U enrichment within IOCG systems; (e) Plot of Hf vs Na showing the positive covariation between these two elements in sodic alteration; (f) Plot of Zr vs Na showing the positive covariation between these two elements in sodic alteration.

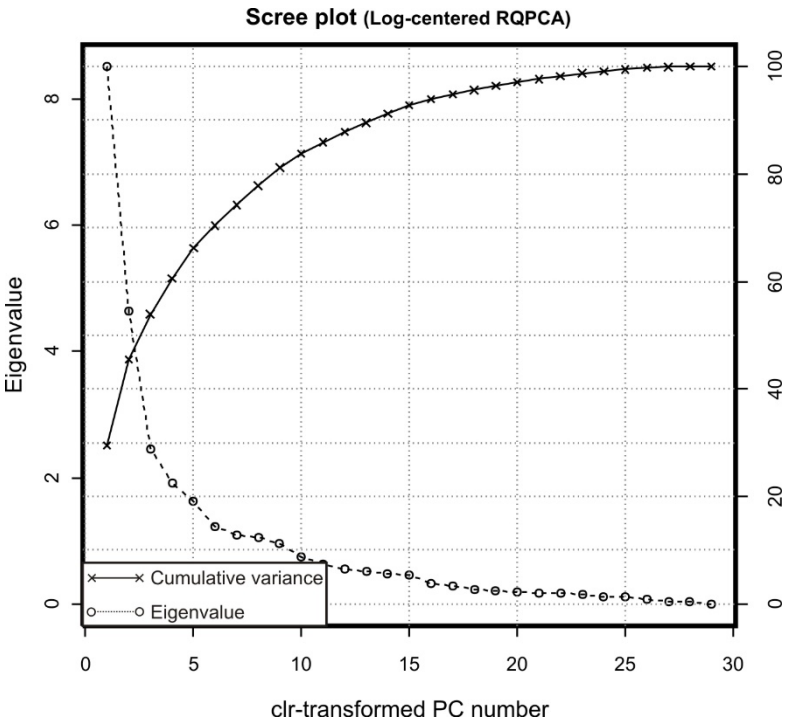

Figure 5-5 Screeplot of principal component analysis

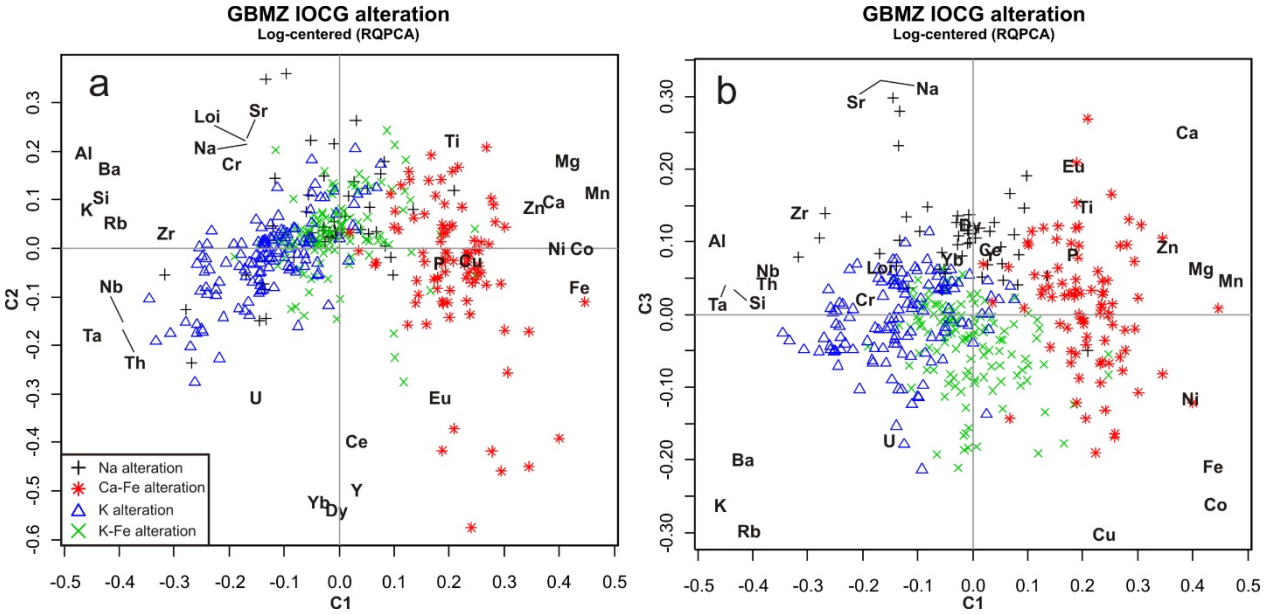

Figure 5-6 Biplots of the principal component analysis with IOCG alteration samples of the GBMZ

(a) Biplot of PC1 vs PC2; (b) Biplot of PC1 vs PC3.

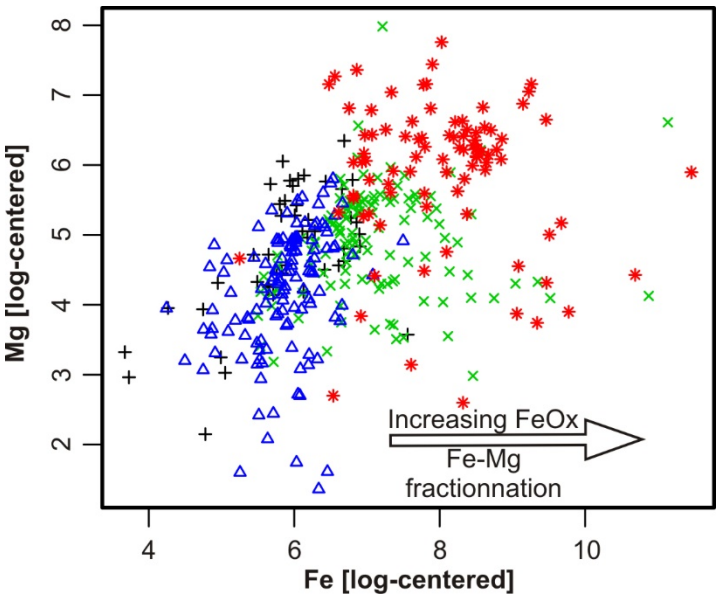

Figure 5-7 Plot of Fe vs Mg

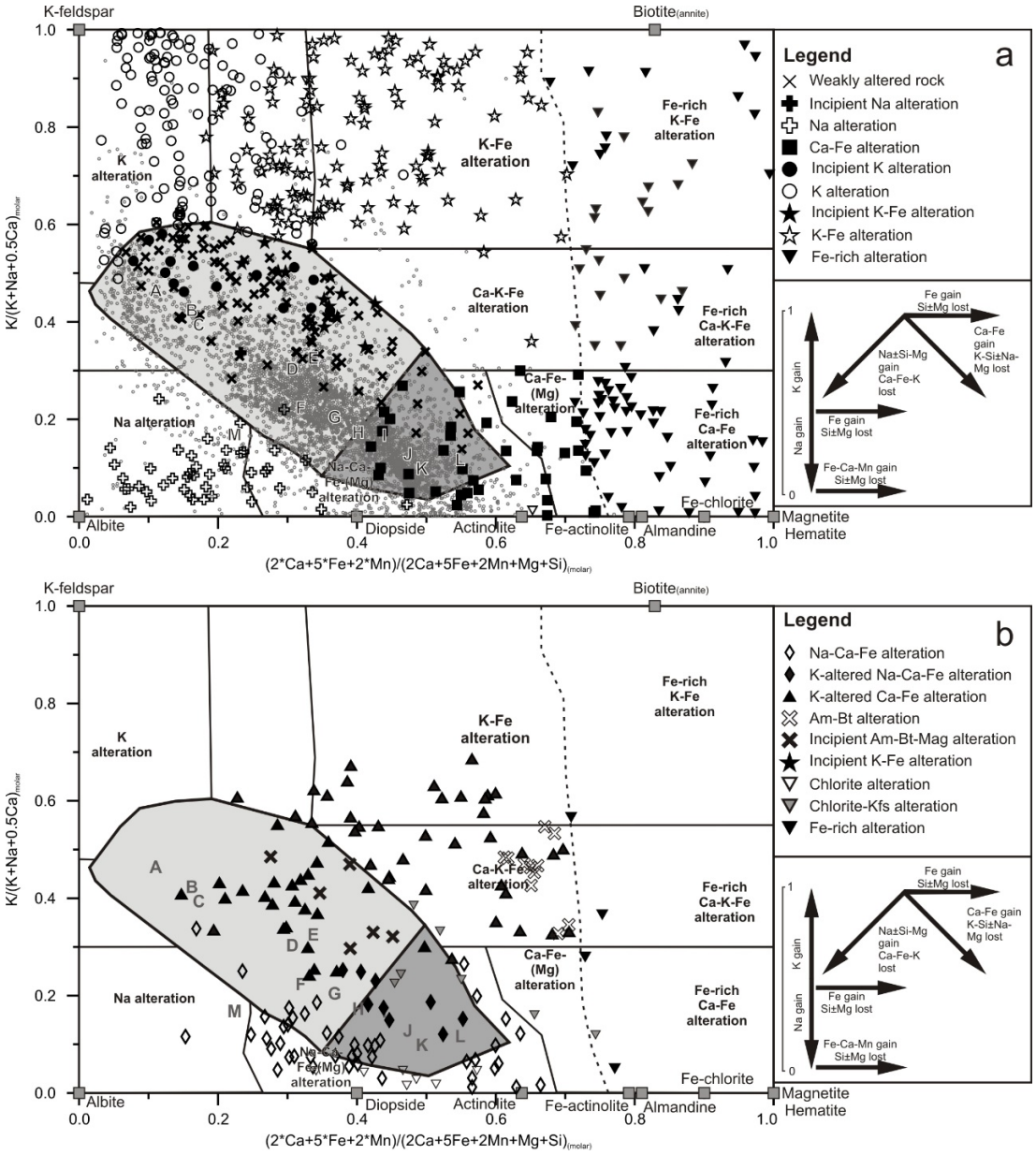

Figure 5-8 GBMZ IOCG alteration and weakly altered samples plotted in the IOCG alteration discrimination diagrams

(a) IOCG alteration discrimination diagram for main IOCG alteration types (Na, Ca–Fe, K–Fe and K) of the Great Bear magmatic zone; (b) IOCG alteration diagram for transitional IOCG alteration of the Great Bear magmatic zone. Transitional alterations include Na–Ca–Fe (albite–amphibole±magnetite), Ca–K–Fe (amphibole–biotite±magnetite) and the superimposition of K-feldspar alteration over Na, Na–Ca–Fe, Ca–Fe and chlorite alterations.

A – A-type granite from Padthaway from Kemp and Hawkesworth (2003); B – Rhyolite composition from Best et al. (2003); C – A-type granite from Kemp and Hawkesworth (2003); D – Upper crust from Rudnick and Gao (2007); E – Shale from Li and Schoonmaker (2003); F – Dacite from Best et al. (2003); G – Arc granite of the Peninsula Range batholith from Kemp and Hawkesworth (2003); H – Primitive Andean andesite from Kelemen et al. (2003); I – Andesite from Best et al. (2003); J – Primitive continental Andean basalt from Kelemen et al. (2003); K – Primitive arc basalt from Kelemen et al. (2003); L – Basalt from Best et al. (2003); M – TTG from Kemp and Hawkesworth (2003). Pale grey field for the superimposition of the weakly altered rock field and Ca–Fe alteration, grey field for the weakly altered rocks, dark grey circles for undiscriminated and mostly weakly altered rocks from the Andes from the Georoc database (2012).

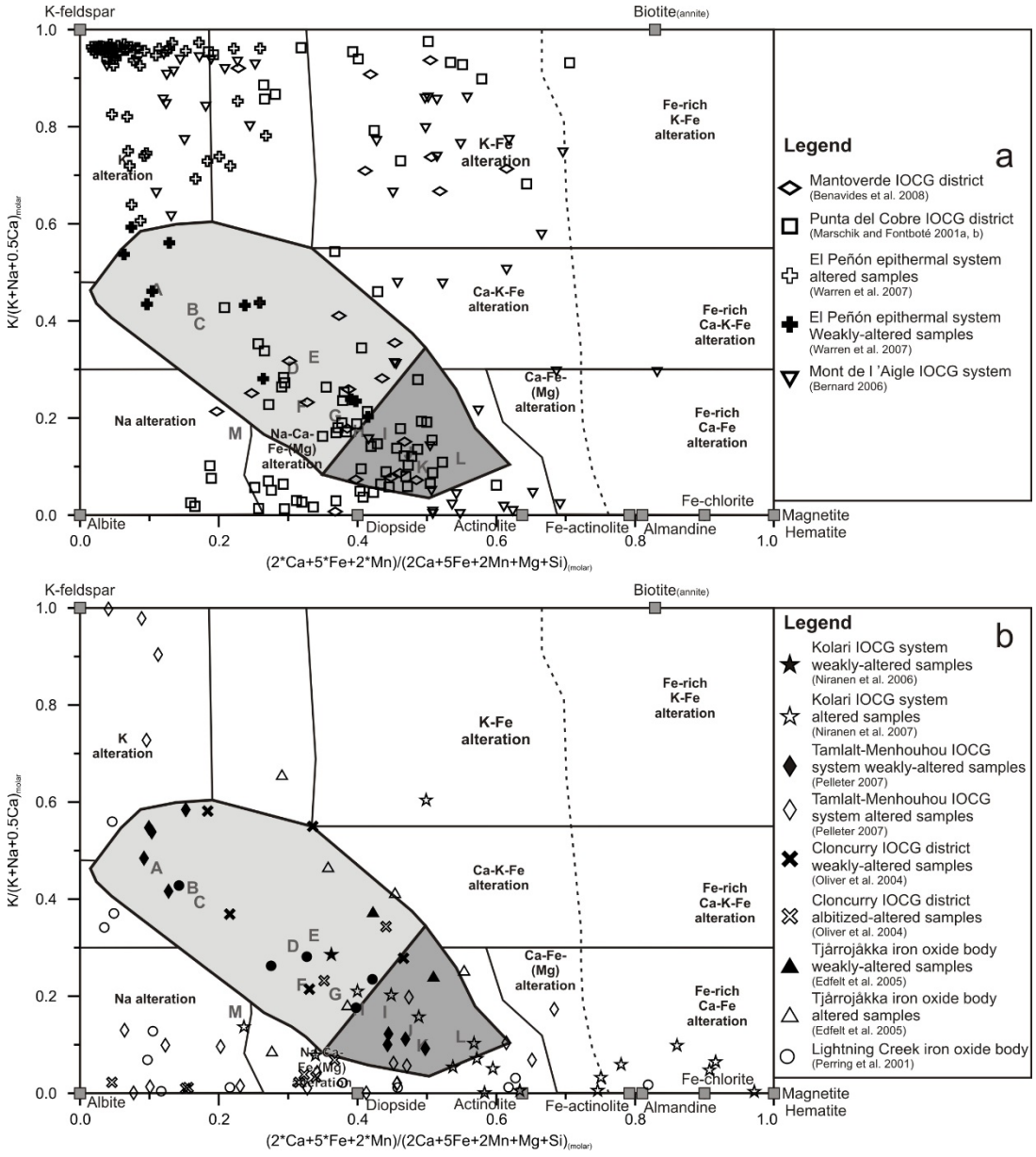

Figure 5-9 Samples from worldwide IOCG systems plotted on the IOCG alteration discrimination diagram

(a) Samples from the Mantoverde IOCG district (Chile), Punta del Cobre IOCG district (Chile), Mont de l'Aigle (Canada) IOCG system and El Penon (Chile) epithermal system plotted on the IOCG alteration discrimination diagram; (b) Samples from Kolari (Finland), Tamlalt-Menhouhou (Morocco), Cloncurry district (Australia), Tjårrojåkka (Sweden) and Lightning Creek (Australia) IOCG and IOA systems plotted on the alteration discrimination diagram.

Pale grey field for the superimposition of the weakly altered rock field and Ca–Fe alteration, grey field for the weakly altered rocks.

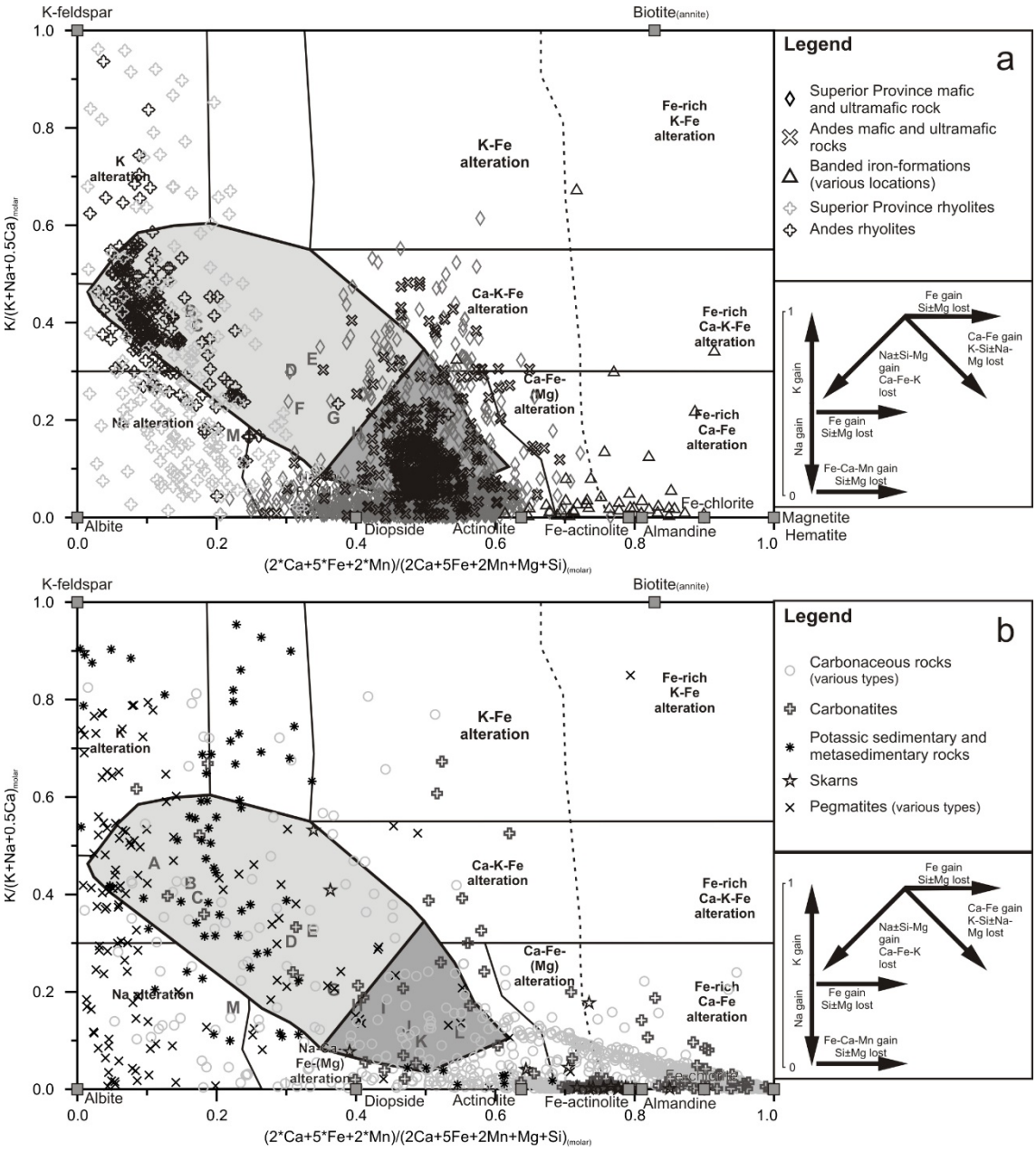

Figure 5-10 Various rocks types plotted on the IOCG alteration discrimination diagram

(a) Mafic and ultramafic rocks and rhyolites from the Andes (basalts, harzburgite, lamprophyre, lherzolite, websterite and wherlite) and the Superior Province (basalt, boninite, clinopyroxenite, dunite gabbro, komatiite, lamprophyre, peridotite, ferro-picrite, pyroxenite and wherlite) (Georoc database, 2012) as well as banded-iron formations samples (Beukes and Klein, 1990; Klein and Beukes, 1993; Klein and Ladeira, 2000, 2002) from various locales plotted on the IOCG alteration discrimination diagram. Its shows that vast majority of these samples are superimposed to the Ca–Fe alteration fields of the diagram. The alteration degree of these samples is unknown; (b) Carbonaceous and metacarbonaceous rocks (limestones, calc-silicates, carbonate, dolomite, marble), carbonatites, potassic sedimentary and metasedimentary rocks (arenite, meta-arkose), skarns and pegmatites samples plotted on the IOCG alteration diagram (National Geochemical Database of the U.S. Geological Survey, 2008). It shows that the carbonaceous rocks, the carbonatites and the skarns are mostly superimposed to the Ca–Fe alteration fields, and that the potassic sedimentary and metasedimentary rocks mostly overlap the K alteration field and the pegmatites overlap both the Na and K alteration fields. The alteration degree of these samples is unknown.

CHAPITRE 6 : FORMATION OF ALBITITE-HOSTED URANIUM WITHIN IOCG SYSTEMS: THE SOUTHERN BRECCIA, GREAT BEAR MAGMATIC ZONE, NORTHWEST TERRITORIES, CANADA

Formation de gîtes d'uranium encaissés dans des albitites dans les systèmes IOCG : Le système de la *Southern Breccia*, Zone magmatique du Grand lac de l'Ours, Territoires du Nord-Ouest, Canada

[1]Montreuil, J.-F., [2]Corriveau, L., [3]Potter, E.G.

[1]Institut National de la Recherche Scientifique – Eau-Terre-Environnement

[2]Ressources naturelles Canada, Commission Géologique du Canada, division Québec

[3]Ressources naturelles Canada, Commission Géologique du Canada, division Ottawa

Publié par «*Mineralium Deposita*», v. 50, p. 293–325.

Abstract: Uranium and polymetallic uranium mineralization hosted within albitite breccias occur one kilometer south of the magnetite-rich Au–Co–Bi–Cu NICO deposit in the southern Great Bear magmatic zone (GBMZ), Canada. Uranium concentrations up to 1 wt. % are distributed throughout a 3 by 0.5 km albitization corridor defined as the Southern Breccia zone. Two distinct mineralization events are observed. During the main uranium mineralization event, uraninite precipitates with or without pyrite–chalcopyrite±molybdenite within magnetite–ilmenite–biotite–K-feldspar-altered (high-temperature potassic–iron alteration) breccias. Subsequently pitchblende-bearing veins formed during an earthy hematite–specular hematite–chlorite (low-temperature iron–magnesium) alteration event. The main uranium mineralization postdates sodic (albite) and more localized high-temperature potassic–iron (biotite–magnetite±-K-feldspar) alteration and predates potassic (K-feldspar), boron (tourmaline) and potassic–iron–magnesium (hematite±K-feldspar±chlorite) alteration. The Southern Breccia zone shares attributes of the Valhalla (Australia) and Lagoa Real (Brazil) albitite-hosted uranium deposits but contains greater iron oxide contents and lower contents of riebeckite and carbonates. Potassium, nickel and thorium are also enriched whereas zirconium and strontium are depleted with respect to the aforementioned albitite-hosted uranium deposits. Field relationships, geochemical signatures and available U–Pb dates on pre-, syn- and post-mineralization intrusions place the development of the Southern Breccia and the NICO deposit as part of a single iron oxide alkali-altered (IOAA) system and illustrate that albitite-hosted uranium deposits can form in pre-ore albitization zones associated with the development of IOCG deposits.

Résumé: Des minéralisations uranifères et uranifères polymétalliques encaissées dans des albitites affleurent 1 km au sud du gisement à Au–Co–Bi–Cu et riche en magnétite de NICO dans la Zone magmatique du Grand lac de l'Ours, Canada. Les concentrations en uranium atteignent 1% dans certaines zones minéralisées distribuées dans un corridor d'albitisation large de 0.5 km et exposé longitudinalement sur 3 km. Le regroupement de ces zones minéralisées forme la Southern Breccia. La minéralisation uranifère principale se trouve dans des brèches hydrothermales et est formée d'uraninite± pyrite–chalcopyrite–molybdénite avec une gangue d'altération à magnétite–ilménite–biotite–feldspath potassique (altération de haute température potassique–fer). Des veines à pitchblende–hématite–chlorite se sont subséquemment mises en place lors d'un épisode tardif d'altération à fer–magnésium. La minéralisation uranifère principale postdate des stades d'altération sodique et de haute température potassique–fer,

mais précède des stades d'altération potassique (feldspath potassique), de bore (tourmaline) et potassique–fer–magnésium (hématite±chlorite±feldspath potassique). Les minéralisations uranifères de la Southern Breccia partagent des caractéristiques similaires avec les minéralisations uranifères encaissées dans des albitites de Valhalla (Australie) et Lagoa Real (Brésil). Cependant, les altérations uranifères de la Southern Breccia sont plus riches en oxydes de fer et plus pauvres en riebéckite et en carbonates. Les concentrations en potassium, en nickel et en thorium sont également plus élevées dans les minéralisations uranifères de la Southern Breccia alors que les concentrations en zirconium et en strontium sont généralement plus faibles relativement aux gîtes d'uranium encaissés dans des albitites mentionnés précédemment. Les relations de terrains, la signature géochimique de la Southern Breccia et les datations U–Pb sur des dykes pré-, syn- et post-minéralisation indique que la formation de ses indices uranifères est contemporaine à la formation du gisement de NICO et qu'ils font partie du même système à oxydes de fer et altération en éléments alcalins. Cette relation indique que des gîtes d'uranium encaissés dans des albitites peuvent se former dans les zones d'albitisation pré-minéralisation polymétallique riches en oxyde de fer lors de sa formation.

6.1 Introduction

The 1.87–1.84 Ga Great Bear magmatic zone (GBMZ) is interpreted as a continental magmatic arc built at the western margin of the Archean Slave craton on the composite Hottah arc terrane and the overlying 1.88 Ga Treasure Lake Group sedimentary basin in the Northwest Territories, Canada (Fig. 1-2; Gandhi et al., 2001; Gandhi and van Breemen, 2005; Hildebrand et al., 2010a). With its polymetallic vein-type U deposits (U, Ag, Cu ±Ra, Ni, Co, Bi; Badham, 1975), the GBMZ was a significant producer of U in Canada prior to the discovery of U deposits at Elliot Lake (Ontario) and in the Athabasca Basin (Saskatchewan). Today the GBMZ is the best documented mineral province in Canada for exploring the family of iron oxide alkali altered deposits (IOAA; cf. Porter, 2010) and has a high IOCG potential. This is illustrated by the discovery of two iron oxide-rich hydrothermal deposits with Cu, Au, Ag, Co and/or Bi (Sue-Dianne and NICO) as well as the presence of IOAA type mineralization in the Port Radium–Echo Bay and Camsell River districts and 30 other IOAA systems distributed across the belt (Badham and Morton, 1976; Gandhi, 1994; Hildebrand, 1986; Goad et al., 2000a; Corriveau, 2007; Corriveau et al., 2010b). In addition, the re-examination of the past-producing polymetallic vein-type U deposits highlight that they were formed within epithermal systems at the periphery of and structurally above larger IOAA systems (Fig. 1-2; Mumin et al., 2010). Other U showings of the GBMZ, hosted in part by a 1,740+5/-4 Ma Cleaver diabase dike, may represent exhumed, basement-hosted, unconformity-associated type mineralization (Gandhi et al., 2013).

High to anomalous U contents are typical of many of the GBMZ IOAA systems and their IOCG deposits and showings[1] (e.g., Sue-Dianne; Gandhi, 1989; Camier, 2002; Mumin et al., 2010; Fab magnetite-group IOCG system; Gandhi, 1988; Potter et al., 2013b). In contrast, the Au–Co–Bi–Cu NICO deposit, located southeast of Lou Lake (unofficial name; Fig. 1-15) has no U within its main ore zone (NI 43-101 compliant mineral reserves of 32.98 Mt @ 1.02 g/t Au, 0.11% Co, 0.14% Bi; Puritch et al., 2012). However, beyond the main ore zone of NICO (“Bowl Zone), the volcanic rocks that cap the deposit host airborne radiometric U anomalies several kilometers in diameter with eU concentrations up to 15 ppm and localized U mineralization in hematite-filled fractures (Gandhi and Lentz, 1990; Gandhi et al., 1996). At regional scale elevated U concentrations also characterize most of the GBMZ intrusive and subvolcanic porphyritic rocks (Ootes et al., 2013). In this paper, we characterize a newly discovered series of U and polymetallic U showings hosted in albitites located 1 km south of the NICO deposit that collectively form the Southern Breccia showing. The regional IOAA system hosting both the NICO deposit and the Southern Breccia is herein referred to as the Lou IOAA system (Fig. 1-15).

Albitite-hosted U deposits are characterized by discontinuous U-rich occurrences over several tens of kilometers hosted in extensive and strongly albitized deformation corridors (Cuney, 2009). This deposit type is currently recognized as having potential but uncertain IOCG affinities (Williams, 2010a). Individual ore zones can reach several meters in width, extend several thousand meters along strike and are associated with alteration haloes characterized by multiple stages of sodic, calcic–magnesian, and potassic-metasomatism (Cuney and Kyser, 2008; Polito et al., 2009; Cuney et al., 2012). Key examples include Valhalla in Australia (Polito et al., 2009; 34.7 Mt @ 830 ppm U_3O_8, Paladin Energy LTD, 2013), Lagoa Real in Brazil (Porto da Silveira et al., 1991), the Michelin deposit in Labrador (Gandhi, 1977; Corriveau et al., 2010b) and deposits in the central Ukraine shield (Cuney et al., 2012). However, as many of the albitite-hosted U system occurs in high-grade metamorphic or poorly exposed terrains, many questions remain on the processes leading to the U mineralization and the possible relations with IOCG systems (Wilde, 2013).

The albitite-hosted U showings of the Southern Breccia provide a detailed picture of the alteration, brecciation, deformation, volcanic and porphyritic intrusion processes associated with this type of U mineralization. Documentation of how non-metamorphosed albitite-hosted U mineralization can form within IOAA systems sheds light on the genesis of the other albitite-hosted U deposits, demonstrates that albitite-hosted U mineralization can develop in the regional-scale albitization corridors of IOAA systems as part of the genetic processes that lead to IOCG and other IOAA deposits and ultimately may provide impetus to search for IOCG-type mineralization in similar districts.

6.2 Regional geology of the Lou IOAA system

The Lou IOAA system is hosted in the greenschist-facies metasedimentary rocks of the Treasure Lake Group (TLG) at and below a regional unconformity defined by the overlying, non-metamorphosed (sub-greenschist facies) volcanic rocks of the Faber Group (Goad et al., 2000a, b; Gandhi et al., 2001; Fig. 1-15). The TLG is interpreted as a platform-type sedimentary sequence deformed and steeply tilted during the ca. 1.88 Ga Calderian orogeny related to the accretion of the Hottah terrane to the Slave craton (Gandhi and van Breemen, 2005). The maximum age of the TLG is constrained at 1,886±8 Ma in the southern GBMZ near NICO (Gandhi and van Breemen, 2005) and 1884±6 Ma in the central GBMZ in the DeVries sector (Fig. 1-2; Bennett and Rivers, 2006). These ages represent the absolute maximum age for the

onset of IOAA hydrothermal activity in the southern GBMZ (Corriveau et al., 2007, 2010a). Based on the type section exposed near Treasure Lake in the southern GBMZ, Gandhi et al. (2001) have subdivided the TLG into four distinct units: 1) a lower siltstone unit that evolves upward to, 2) carbonaceous rocks, 3) a massive quartz arenite unit with primary sedimentary structures such as cross-bedding and ripple marks intercalated with a minor proportion of siltstone beds, and 4) an upper siltstone unit. The main mineralization zones of the Lou IOAA system are hosted in the lower siltstone and quartz arenite units. While documented in the type section to the South, the carbonate unit in-between these units tapers out northward (i.e., towards the Lou IOAA system; Gandhi et al., 2014). Where present (i.e., preserved), the carbonate unit is significantly altered to skarn, or exhibits amphibole, magnetite, albite, biotite and/or K-feldspar alteration within paragenetic assemblages typical of sodic, high-temperature (HT) calcic–iron, potassic–iron and transitional calcic–iron–potassic alteration that characterizes the high temperature components of IOAA systems (Corriveau et al., 2010a).

The Faber Group felsic to intermediate volcanic and volcaniclastic rocks and associated porphyritic intrusions have a maximum age of 1,873±2 Ma, determined by U–Pb zircon data obtained from a sodic-altered granitic intrusion overlain by the basal Lou assemblage of the Faber Group (Gandhi et al., 2001). This sodic-altered granite represents the oldest known magmatic unit of the Lou IOAA system and is referred to as the early granite herein (sodic leucogranite in Gandhi et al., 2001). Subsequent assemblages of the Faber Group (Mazenod and Bea assemblages) are not exposed within the Lou IOAA system, but a U–Pb age on zircon of 1,868.6±1.2 Ma for a rhyodacitic ignimbrite of the Mazenod assemblage brackets the age of the Lou assemblage between 1,873 and 1,868.6 Ma (Gandhi et al., 2001). As such, the Lou assemblage was formed during a widespread volcanic and intrusive event documented throughout the GBMZ (Hildebrand et al., 1987, 2010b; Gandhi et al., 2001; Bennett et al., 2012). Faber Group volcanism faded at ca. 1,866 Ma and gave way to predominantly granitic plutonism (Gandhi et al., 2001). The plutonic rocks, formed at and after ca. 1,866 Ma, show no conspicuous evidence of IOAA-related hydrothermal alteration and are grouped within the Marian River batholith in the Southern GBMZ (Gandhi et al., 2001) and Great Bear batholith to the North (Hildebrand et al., 2010b).

Collectively, these observations constrain formation of the Faber Group and the main IOAA hydrothermal event in the southern GBMZ between 1,873 and 1,866 Ma. Hydrothermal fluids related to the post-volcanic intrusions are interpreted to have remobilized some of the metals and elements previously concentrated during the main IOAA event to form the polymetallic vein-

type U deposits, including those associated with giant quartz veins such as the past-producing Rayrock mine (Figs. 1-2 and 1-15; Gandhi et al., 2000; Byron, 2010; Somarin and Mumin, 2012). Intense deformation within the southern GBMZ is largely restricted to its eastern limit along the Wopmay fault zone (Jackson and Ootes, 2012). This orogen-scale vertical fault is interpreted to listrically merge westward with the highly resistive Slave craton lithosphere below ~20 km depth (Spratt et al., 2009). The GBMZ is largely concealed below a Paleozoic sedimentary cover to the west and the U deposit-bearing Hornby Bay Group and Dismal Lakes Group basins to the northwest (Gandhi, 1980; Aspler et al., 2003).

6.3 NICO deposit and associated alteration

The NICO deposit ore zone, as currently defined by exploration and definition diamond drilling, extends from the near surface to a depth of 300 m along the moderate to steeply north–northeast-dipping stratification of thick-bedded quartz arenite and interlayered laminar and thin-bedded metasiltstones of the TLG (Fig. 1-2; Goad et al., 2000b; Hennessey et al., 2007). These metasedimentary units are pervasively to selectively altered (each bed exhibits different alteration composition and alteration fronts are locally frozen in action as illustrated in Fig. 27 of Corriveau et al., 2010a) but ghost thick to laminar stratification is commonly preserved. Least-altered to moderately albitized quartz–biotite–feldspar metasiltstone with layers up to 3 cm thick are restricted to the footwall of the ore zone (Sidor, 2000; Montreuil and Corriveau, unpublished data). Prevailing phaneritic alteration assemblages across the deposit include amphibole (actinolite, ferrohornblende), amphibole–magnetite, amphibole–biotite, magnetite, amphibole–magnetite–biotite±K-feldspar, and K-feldspar (Goad et al., 2000a, b; Corriveau et al., 2010a). Detailed alteration mapping across the NICO ore zone (decline and derived muck piles) highlighted that the Au–Co–Bi–Cu mineralization occurred during many cycles of magnetite-rich HT calcic–iron, transitional HT calcic–potassic–iron and potassic alteration (cf. paragenetic descriptions in Corriveau et al., 2010a) that formed concordant to discordant alteration fronts, veins and breccias (Goad et al., 2000a, b; Sidor, 2000; Corriveau et al., 2010a, unpublished data; Acosta et al., 2013, 2014). Carbonate, tourmaline and earthy hematite alteration types as well as biotite–hematite or chlorite–hematite assemblages typical of low-temperature (LT) potassic–iron alteration are associated with the later stages of mineralization within the NICO ore zone. Native Bi, Au and minor chalcopyrite mineralization are associated with magnetite-bearing alteration and are cross cut by a cobaltian arsenopyrite, cobaltite, bismuthinite, native

Au, Au–Bi–Te alloys and pyrite with or without chalcopyrite mineralization (Goad et al., 2000a, b). In addition, late-stage veinlets comprised of chalcopyrite, hematite, quartz, chloropotassic hastingsite, chlorite, emplectite ($CuBiS_2$) and wittichenite (Cu_3BiS_3) cut the Co–As–Fe-rich sulfides and the magnetite-bearing alteration assemblages (Acosta et al., 2014). This assemblage is slightly atypical of LT potassic–iron alteration in that amphibole remains stable with chlorite (cf. paragenetic descriptions in Corriveau et al., 2010a). Tungsten, Ni and Zn concentrations are also anomalous throughout the NICO ore zone and alteration envelope (Goad et al., 2000b; Acosta et al., 2014).

The NICO deposit exhibits many of the alteration and breccia attributes of magnetite-group IOCG deposits such as a high modal content of Ti-poor magnetite, regional albitization halo and high K and Fe content of the ore-bearing alteration types also observed at the Salobo (Brazil), Ernest Henry (Australia) and Mina Carolla (Chile) deposits (Goad et al., 2000a, b; Corriveau et al., 2010a; Mumin et al., 2010; this work). However, the low Cu content of the NICO ore zone, where cobaltian arsenopyrite prevails over Cu sulfide minerals, precludes strict classification of the current ore zone as an IOCG deposit (cf. definitions of IOCG deposits by Williams et al., 2005 and Groves et al., 2010). The presence of Cu-rich IOCG-type showings in the footwall of the NICO ore zone and in the overlying volcanic rocks in its vicinity (e.g., Chalco, Summit Peak; Mumin et al., 2010; Montreuil and Corriveau, unpublished data) led Corriveau et al. (2010a) to classify NICO as a magnetite-group IOCG deposit.

6.4 Methods

6.4.1 Alteration mapping and sampling protocol

Style, mineral assemblages and textures of hydrothermally altered rocks and breccias as well as timing relationships of alteration and brecciation with respect to magmatic, mineralization and tectonic events were documented, sampled and photographed in a system-wide manner. Potassium (wt. %), eTh (ppm) and eU (ppm) and volumetric magnetic susceptibility were measured respectively by portable gamma-ray spectrometers (Radiation Solutions Inc. RS-230 spectrometers equipped with a bismuth germanate detector) and portable magnetic susceptibility meters (ZH instruments SM-30; Lee and Morris, 2013). The prefix “e” (i.e., eTh or eU) denotes that “equivalent” U and Th concentrations were determined indirectly from their daughter products (Bi_{214} and Tl_{208} respectively), assumed to be in equilibrium with their parent

isotopes (e.g., Adams and Fryer, 1964). The gamma-ray spectrometers were essential to detect and systemically sample cryptic to important potassic/sodic alteration zones and weak to highly anomalous U–Th enrichment and depletion in the field. Magnetic susceptibility measurements quantified the intensity of magnetite alteration and allowed detection of microcrystalline magnetite replacement of the rock groundmass or fine-grained minerals that did not destroy the precursor primary textures.

Samples for geochemistry were chipped in situ during fieldwork to avoid unwanted veins or overprinting alteration and to collect a sufficient volume of megascopically uniform rock material. This sampling protocol optimizes the robust compositional characterization of each alteration type as alteration targeted for sampling was in most cases very intense and pervasively developed across the material selected, and all the extraneous alteration types detected at megascopic scale were removed during sampling. Consequently, the sampling protocol optimizes geochemical interpretation of element mobility patterns related to the targeted alteration. The collection of U mineralization followed a series of guidelines for safe handling and transportation of radioactive material (e.g., Health Canada, 2000).

6.4.2 Rock description and mineral identification

The mineralogy of the U showings and alteration types was established using polished slabs, cobaltnitrate stained slabs, optical microscopy and scanning electron microscopy (SEM). Zeiss EVO® 50 SEM equipped with INCAx-sight (Oxford instrument) energy dispersive spectrometry (EDS) located at INRS–ETE in Quebec city and the Geological Survey of Canada facilities in Ottawa were used. SEM operating conditions were set using a working distance of 8.5 mm, the high voltage (EHT) was set at 20 kV and the probe current was set at 1.5nA.

The 3-D distribution of U minerals in the different styles of U mineralization was characterized through X-ray computed tomodensitometry (CT scan) based on the X-ray linear attenuation coefficient, which is a function of the density and atomic number of the material and the energy of the incoming X-ray beam (measured in KeV). The detection of U-bearing minerals and their discrimination from other mineral phases are particularly successful by this method due the high atomic number (92) of U and high density of uraninite (ideal calculated value of 10.97 g/cm^3, lower densities if uraninite is altered). The images were acquired at the INRS–ETE Scannography Laboratory in Quebec City (Canada) using a SOMATON Sensation 64 scanner equipped with the Extended Field of View capable of visualizing the dense minerals present in rocks. Images were acquired using an incoming X-ray beam energy of 140 KeV and a 500 mA

current to maximize X-ray penetration in the rock samples and to optimize the signal received by the scanner detectors. To reduce the beam hardening effects caused by the sharp edges and flat surface of the samples, they were scanned covered with sand to create a smooth and uniform surface to avoid unwanted reflection and refraction of the incoming X-ray beam (Duchesne et al., 2009).

6.4.3 Geochemistry

Eighty-five samples of the different alteration rock types, least-altered precursors and U showings from the Southern Breccia were submitted to ALS Laboratories (Vancouver, Canada) for major and trace element geochemical analysis. The samples were crushed using low chrome steel pulverizing bowls and then dissolved with four acids (HF, HNO_3, $HClO_4$, HCl) prior to element analysis by a combination of ICP-AES and ICP-MS (ALS method ME-MS61u). This method involves a very aggressive four acid digestion adapted to destroy all the resistive minerals that are potentially present in U-rich ore (Gandhi, 1977; Porto da Silveira et al., 1991; Polito et al., 2009; Alexandre, 2010), with detection limits comparable or better to fusion methods for many elements. In addition, thirty-two samples plus all the samples with non-elevated U concentrations that were analyzed at ALS were analyzed at INRS–ETE by ICP-MS (trace elements) and ICP-AES (major and some trace elements) after lithium metaborate fusion. The complete dataset and analytical methods are described in chapitre 5. The geochemical analyses of representative rock, alteration and mineralization types are presented in Corriveau et al. (2015; appendix 6 for representative analyses and sample descriptions).

Data reduction to identify element covariations within the dataset was done through principal component analysis (PCA) using the RQ-mode approach of Zhou (1983) which allows simultaneous plotting of the scores and the loadings (variable) for each principal component (PC). In this study, principal component loadings reflect the contribution of each chemical element on the computation of the PC value for each samples (PC scores). On the resulting biplot, the proximity of the PC score of a sample to an element or a group of elements indicates enrichment in those elements compared to samples plotting further away from the same element or group of elements. This is ideal to compare the chemical signature of hydrothermal systems as the location of the sample scores relative to the loading of each element for the first principal components highlights which elements define most of the variability between the two systems (Grunsky, 2010). Geochemical data were transformed before doing PCA to avoid biases in correlation/covariation matrices due to the closure constraint on geochemical compositional data

as defined by Chayes (1960). The centered logratio transformation (Aitchison, 1986) was used as it preserves the relationships between the variables without the need for a dividing element. For a D-part (elements) compositional vector x, the centered logratio transformation is defined as:

$$zi = \log(xi/g(xD)) \qquad (i = 1,\ldots,D) \qquad (1)$$

where g(xD) is the geometric mean of the compositional vector.

6.5 The Southern Breccia

6.5.1 Regional to local-scale attributes and precursor units

The Southern Breccia forms the southern component of the Lou IOAA system and hosts a series of U and polymetallic U showings distributed along the exposed section of a 3-km long albitization corridor developed into a regional west–northwest-oriented deformation zone (Fig. 6-1). Albitization is predominantly confined to the lower metasiltstone unit of the TLG, but also altered some porphyritic rhyolite dikes, granite dikes and intrusions. Bedding of the host metasiltstone is generally steeply dipping to the North–northeast. At regional scale, the orientation of the Southern Breccia albitization corridor parallels the TLG bedding. At outcrop scale, tectono-hydrothermal brecciation and ductile to brittle fabric development related to the west–northwest-oriented deformation event as well as syn-deformation IOAA alteration and porphyritic dikes both follow and cross cut the metasiltstone stratification. To the South, the Southern Breccia is bordered by the 1,873 Ma early granite intrusion. To the North and west of the Summit Peak fault (Fig. 6-1), the amphibole-poor potassic–iron alteration assemblages of the Southern Breccia superimposed on the sodic alteration transitions gradually to the amphibole-rich calcic–iron±potassic alteration assemblages of the NICO deposit within the lower metasiltstone unit. In contrast, the change in alteration types is sharper and fault bounded by the NICO fault east of the Summit Peak fault (Fig. 6-1). To the east–southeast and west–northwest, the sodic alteration corridor of the Southern Breccia remains open along strike under the Faber Group and buried west of the major northeast-striking, north-side down Lou Lake fault. The northeast-oriented Summit Peak fault dextrally offsets the Southern Breccia albitization corridor in its exposed center.

A review of mineral showings within the NORMIN database, geological maps and assessment reports (e.g., Thomas and Olsen, 1978; Gandhi and Lentz, 1990) indicates that we have identified 36 new individual U showings with eU contents exceeding the required NORMIN value of 0.03% U_3O_8 in the Southern Breccia sodic alteration zone (or 254 ppm eU; Fig. 6-1). According to their mineralization styles, metallic signatures and spatial distribution, the main U showings of the Southern Breccia are grouped into the Eastern, Lou Lake, Frank's, Frank's West and Red Hot zones. In the Red Hot and Frank's zones, anomalous U concentrations are present over 200 m along the west–northwest strike whereas they are perpendicular to this trend in the Lou Lake and Eastern zones (Figs. 6-1 and 6-2a–f). Exposed extents of U mineralization along strike in the Eastern, Lou Lake and Frank's West zones exceed 50 m (Fig. 6-2g–i). Within the U-rich zones, some showings are polymetallic with elevated concentrations in base, precious, rare earth elements (REE) and other specialized metals (Corriveau et al., 2015 and appendix 6 for sample descriptions and geochemical analyses). These include: one U–Th (+Pb) showing in the Red Hot zone (Fig. 6-2a–c); one U–Mo (+Cu–Ag), one U (+Cu–Ta–Nb–REE–Th–Mo) and one U–W (+Th) showing in the Frank's and Frank's West zones (Fig. 6-2d–f); and one U–Bi–Au (+Co–REE) showing in the Lou Lake zone (Fig. 6-2g–i; gold value from Gandhi and Lentz, 1990; anomalous metal concentrations below NORMIN cut offs are in parentheses).

6.5.2 Treasure Lake Group lower metasiltstone unit

Most of the IOAA alteration, brecciation and deformation related to the development of the Southern Breccia are confined to the lower metasiltstone of the TLG. Where only mildly altered, the metasiltstone is fairly texturally homogeneous and composed of alternating dark gray (magnetite- and biotite-rich) and whitish gray (quartzofeldspathic) beds (Fig. 6-3a). Those compositional variations are partly controlled by an early magnetite–biotite and albite alteration that selectively replaced certain beds in the metasiltstone. This early alteration is sporadic throughout the TLG south of the Lou IOAA system (Fig. 1-15; see Ab1 and K–Fe1 alteration). In the upper sections of the lower metasiltstone unit, scattered quartz arenite beds and carbonaceous layers were observed in the Southern Breccia; the latter is typically spatially associated with NICO-style amphibole-rich alteration.

6.5.3 Early granite

The 1,873 Ma early granite intrusion contains partially digested relicts of the TLG metasedimentary rocks and is pervasively overprinted by sodic alteration fronts (Fig. 6-3b; see

Ab2). In the least-altered zones, the early granite has a fine-grained groundmass comprised of biotite, hornblende and felsic minerals hosting coarse- to medium-grained quartz and feldspar phenocrysts (Gandhi, 1989, unpublished field descriptions). In the sodic-altered zones, albite±quartz initially selectively replaces most of the primary mafic minerals of the groundmass and with intensifying albitization the feldspars and quartz phenocrysts are also replaced and recrystallized to finer-grained albite and quartz. The albitized early granite has a leucocratic composition that considerably differs from its initial monzodioritic composition (Gandhi, 1989, unpublished field description). Albitized and least-altered early granite outcrops are also locally overprinted by potassic alteration fronts.

6.5.4 Faber Group volcanic rocks

The Lou assemblage rests uncomfortably on the TLG and consists of basal massive to flow-banded rhyolite overlain by a succession of predominantly felsic to locally intermediate volcanic and volcaniclastic units (Fig. 6-3c; Gandhi and Lentz, 1990; Gandhi, 1994). In the Southern Breccia, the basal rhyolite is the only volcanic unit observed and occurs as sub-horizontal to shallowly north-dipping and discontinuous lenses. It is aphanitic to finely porphyritic, with feldspar and locally biotite being the most commonly observed phenocrysts. Throughout the Lou IOAA system, the rhyolite is typically moderately to intensely K-feldspar (potassic) and magnetite–K-feldspar (potassic–iron) altered. The K-feldspar alteration prevails and generates a 3 x 4 km radiometric K anomaly that reaches 7 wt. % K in airborne surveys (Gandhi et al., 1996; Shives et al., 2000).

6.5.6 Porphyries and porphyritic dikes

Many generations of porphyritic dikes systematically cut the TLG sedimentary rocks and depending of their timing of emplacement, locally cut through the volcanic sequences of the Lou assemblage and the U showings of the Southern Breccia (Goad et al., 2000a; Camier, 2002; this work). From oldest to youngest, the main dike suites are: porphyritic rhyolite, sodic-altered porphyritic granite, biotite-phyric porphyritic dikes, post-deformation granite, and feldspar–biotite±quartz-phyric porphyritic dikes. Many of these dikes are mildly to intensely altered by K-feldspar (potassic).

Porphyritic rhyolite dikes. The oldest generation consists of feldspar-phyric to aphanitic and potassic to sodic-altered rhyolite dikes. They are compositionally similar to the basal volcanic flows of the Lou assemblage and are more abundant in the southern part of the Southern

Breccia, at the contact between the early granite and the metasiltstone (zone A on Fig. 6-1). They also cut the early granite and are characteristically emplaced parallel to the west–northwest-striking tectonic foliation prevalent in the deformation corridors of the Southern Breccia. The rhyolite dikes have a vertical to sub-vertical dip and widen in extensional zones oriented perpendicular to fabric. They are themselves non to weakly and even strongly west–northwest -foliated, locally boudinaged and massively incorporated as fragments into the tectono-hydrothermal breccia zones formed during the west–northwest-oriented deformation event (Fig. 6-3d). Severely potassic-altered and compositionally similar rhyolite dikes also occur in the NICO deposit and near Peanut Lake where they are overprinted by HT calcic–iron alteration typical of the NICO ore zone (this work; Fig. 3 of Goad et al., 2000a).

Sodic-altered porphyritic granite dikes. The sodic-altered, porphyritic granite dikes are compositionally and texturally similar to the intensely albitized early granite. However as they contain enclaves of the rhyolite dikes, they postdate emplacement of both the rhyolite dikes and the early granite. Because of the pervasive and intense sodic alteration overprint, they have a leucocratic composition dominated by albite. They were only observed in the zone A at the contact with the early granite. They were little deformed to locally foliated and deformed during the west–northwest-oriented deformation event, compatible with a syn- to late-deformation emplacement.

Biotite-phyric porphyritic dikes. Biotite-phyric porphyritic dikes have a fine-grained groundmass composed of biotite, magnetite and K-feldspar, include enclaves of the sodic-altered granite dikes, are massive to moderately west–northwest foliated, and typically cut at shallow angles the west–northwest-oriented fabrics related to the west–northwest-oriented deformation event. Such dikes were observed at many locations in the Southern Breccia zone. In zone A, the dikes are typically rich in pyrite and overprinted by potassic (K-feldspar) alteration.

Post-deformation granite dikes. Post-deformation granite dikes are fine-grained and emplaced into northerly-oriented and subvertical extension gashes that sharply cut the west–northwest-trending tectonic foliations. Dikes of this generation are sporadic and were only observed near the contact between the early granite and the metasiltstone (zone A, Fig. 6-1). The relative timing between those granitic dikes and the biotite-phyric porphyritic dikes has not been established but they postdate the sodic-altered porphyritic granites.

Feldspar–biotite ± quartz-phyric porphyritic dikes. Feldspar–biotite±quartz-phyric porphyritic dikes are massive, tens to hundreds of meters wide and longitudinally extend over few km. They cut at high angle the west–northwest-oriented tectonic foliations, the U showings of the Southern

Breccia and the main ore zone of the NICO deposit. They are typically associated with meter-wide potassic alteration haloes and locally tourmaline alteration haloes superimposed on previously formed IOAA alteration. One conspicuously non-altered, biotite–feldspar-phyric porphyritic dike that cuts the amphibole-rich alteration typical of NICO has been dated at ca. 1,869 Ma (Davis et al., 2011) whereas another dike that cuts the Southern Breccia uranium mineralization in the Red Hot zone has been dated at ca. 1,868 Ma (Potter et al., in press).

6.5.7 Quartz monzonite/monzodiorite stocks

On the western side of the Lou Lake fault, ovoid to elongate and massive quartz monzonite to monzodiorite stocks, dated at 1,867 ±1 Ma by Gandhi et al. (2001), intrude the Lou assemblage along strike and above the expected extension of the Southern Breccia. They are porphyritic, with euhedral to subhedral plagioclase phenocrysts set in an amphibole-rich and fine- to medium-grained groundmass that also contains K-feldspar and quartz (Gandhi et al., 2001; this work). In the Lou IOAA system, they exhibit no evidence of intense IOAA alteration.

6.6 Structures

6.6.1 Treasure Lake Group–Faber Group unconformity

In the Southern Breccia, at the unconformity between the Faber Group and TLG, the sub-horizontal basal rhyolite fills small troughs in the non-paleoweathered and tilted metasiltstone beds of the TLG, confirming that tilting to a subvertical dip predates Faber Group deposition and that erosion was not followed by significant weathering at these localities (Fig. 6-3c). Syn-alteration tilting also took place in the Southern Breccia as documented by a paleomagnetic study across the Southern Breccia (Enkin et al., 2012). At some localities, meter-long and originally vertical cracks now filled with rhyolite are themselves gently tilted towards the south. North of the NICO deposit along the unconformity, the west–northwest deformation event resulted in the formation of west–northwest-trending breccia zones up to 15 m wide by >300 m long with local development of west–northwest-trending tectonic foliation. Other breccia zones west of Lou Lake, subparallel to the unconformity, have been interpreted as decollement-type fault zones (Shepley, 1999). Finally, hematitic paleoweathering in the TLG occur locally in drill cores just below the unconformity within the NICO deposit. Collectively, these apparently conflicting observations can be explained through faulting, differential uplift, exhumation, tilting

and erosion of the TLG that occurred within a very short time gap before and at the onset of Faber Group volcanism. Along the unconformity, the potassic alteration fronts typically extend from the rhyolite into the metasiltstone for a few meters; localized remobilization of magnetite in the metasiltstone is also observed in the form of infilling of breccias along the unconformity.

6.6.2 Deformation zones and faults

Prominent structures in the Southern Breccia corridor are related to a west to west–northwest-oriented brittle-ductile deformation event and to later 330°- to 010–15°-oriented and northeast-oriented faulting (Figs. 6-1 and 6-3d–e). The west to west–northwest-oriented deformation event formed many tectono-hydrothermal breccia zones that are centimeter to decameter wide, extend discontinuously over at least 3 km, and are pervasively IOAA-altered. A dextral sense of movement can be documented in some west to west–northwest-oriented faults and shear zones associated with the localized development of penetrative tectonic foliations in TLG metasiltstone, rhyolite dikes and early granite.

The NICO deposit, which forms the northern component of the Lou IOAA system, also occurs along the westernmost extension of a west–northwest-oriented and decameter-wide deformation zone, exposed at the Zone C on Figure 6-1. In this deformation zone, porphyritic rhyolite dikes are boudinaged as are multiple generations of veins and alteration fronts replacing the TLG with sets of magnetite–amphibole (calcic–iron) and K-feldspar–magnetite±biotite (potassic–iron) assemblages (Fig. 6-3d). The boudinaged magnetite-bearing veins are cut by massive and crystalline magnetite-bearing veins that postdate west–northwest-oriented deformation. East of the Summit Peak fault, the southern limit of NICO-style amphibole–magnetite-rich IOAA alteration is also marked by the west–northwest-striking NICO fault.

West–northwest-oriented deformation was followed by 330°- to 010–15°-oriented, sub-vertical and largely left-lateral faulting. The 330°- to 010–15°-oriented faults were intruded by porphyritic granite dikes and are cut by the later northeast-oriented faults.

The late northeast-oriented faults include the Lou Lake fault to the northwest of NICO and the Summit Peak fault that dextrally offsets the Southern Breccia in its center. East of the Summit Peak fault, magnetite is the predominant iron oxide in IOAA alteration zones whereas northwest of the fault zone specular hematite becomes more abundant.

6.6.3 Tectono-hydrothermal breccias

Tectono-hydrothermal breccias typically formed along the high strain zones related to the west to west–northwest-oriented deformation event. Zones A and B on Figure 6-1 represent the largest individual tectono-hydrothermal breccias of the Southern Breccia. Hydrothermal minerals (typically biotite and magnetite) in the breccia matrix define strong to moderate tectonic foliations and the breccia fragments are aligned at shallow angles (e.g., ± 10°) to the general orientation of the west–northwest-striking foliation (Fig. 6-3d–e). Foliation is typically sub-vertical (80°–90°) with dips to the North. The widths of individual breccia zones range from 1 to 50 m yet their lengths can locally exceed 350 m (zone A). These breccias are typically polymict, although some zones of the breccias are monomict and contain fragments of the same protolith mildly to intensely and selectively to pervasively altered by distinct alteration types prior to, during or post-brecciation. Metasiltstone fragments generally prevail in abundance over fragments of porphyritic rhyolite dikes, sodic-altered porphyritic granite, boudinaged magnetite veins and strongly altered rocks of uncertain origin. Fragment size highly varies, from a few millimeters to meters, with the most common size ranging from centimeters to decimeters. The fragments have angular to rounded borders and are systematically elongated, with a high aspect ratio resulting from preferential fracturing of the metasiltstone along its bedding planes and/or from deformation. In the latter case, fragment elongation and tapering increases with increasing shearing and deformation, to the extent that some foliated breccias locally become proto-mylonites. Irregular boundaries (lobate and/or cuspate) or clouded margins observed in some fragments are indicative of significant chemical corrosion, fragment replacement and dissolution during brecciation. Where it can be determined from relict bedding, fragment rotation varies between 0° in the low strained breccias zones to ~90° in the highly strained breccia zones. In zone A, the breccia cement is dominantly of hydrothermal origin and is composed of magnetite±biotite, K-feldspar and sporadically quartz (Fig. 6-3f). Selective magnetite or K-feldspar alteration of fragments is common and the alteration is observed to extend into the matrix. Further away from the early granite in the northernmost and central breccia zones (B and Red Hot), argillic fault gouge and magnetite±biotite crystals are the main cement constituents. These breccia cements are fine-grained to microcrystalline, except for the crystalline magnetite and biotite (see K–Fe2 alteration below) in zone A that is locally medium-grained and associated with arsenopyrite forming a wispy lens emplaced parallel to foliation. The strong fabric of the breccias and fabric-controlled alteration distribution, the local transition to proto-mylonite, and the ductile elongation of some of the fragments highlight a brittle-ductile strain regime and syn-

deformation magnetite-bearing alteration. Some of the tectono-hydrothermal breccias in the Red Hot zone are U-bearing but the U concentrations are localized, rapidly decreasing to background values within meters of the showings.

6.7 Spatial distribution and paragenesis of hydrothermal alteration pre-uranium mineralization

Typical IOAA alteration types of the Southern Breccia include sodic, magnetite-bearing potassic–iron, hematite-bearing potassic–iron and potassic alteration. Localized magnetite-bearing calcic–iron alteration is also present along the northern limit of the Southern Breccia albitization corridor. The typical mineral assemblages related to each IOAA alteration are presented in Table 6-1 and the relative timing of each alteration stage in Figure 6-4.

6.7.1 Sodic alteration

Two main episodes of sodic alteration (Ab1 and Ab2) have been documented in the Southern Breccia. Ab1 occurs as a beige- to white-colored, fine-grained, selective and incipient to well-developed replacement-type albitization of the TLG metasiltstone (Fig. 6-3a). It is widespread in the southern portion of the Lou IOAA system and varies from well-stratified albitized metasedimentary rocks to folded, mottled, and brecciated units. This albitization variably overprints strata, ranging from selective to pervasive and texture-preserving to texture-destructive replacement of the metasiltstone.

Ab2 cuts Ab1 alteration and consists of pale pinkish to cream white fronts and replacement ‘veins’ that are very fine-grained, penetrative and variegated, and systematically destroy the primary texture of the altered rock (Fig. 6-3g). Ab2 is best preserved in the TLG metasiltstone but also overprints the early granite, the porphyritic rhyolite and the sodic-altered porphyritic granite. Ab2-altered rocks are predominantly composed of albite and quartz with minor zircon, ilmenite and Ti-oxides that replace precursor feldspar and mafic minerals. Ab2 forms large zones of continuous albitization that are preferential hosts for K–Fe3 alteration and for magnetite-bearing calcic–iron alteration typical of the NICO deposit (see Ca–Fe±K1; Fig. 6-3h).

Ab1- and Ab2-altered metasiltstone and porphyritic rhyolite dikes are systematically brecciated in the west–northwest-oriented deformation corridors and occur as fragments in all the tectono-hydrothermal breccias of the Southern Breccia. Albitization is restricted to fragments without any

evidence of albitization of the breccia matrix, indicating that Ab1 and Ab2 predate at least in part the west–northwest-oriented deformation event.

6.7.2 Magnetite-bearing calcic–iron±potassic alteration

This alteration (Ca–Fe±K1) is uncommon in the Southern Breccia and typically occurs in the northernmost parts of the albitization corridor where it overprints Ab2 and is overprinted by K–Fe–Mg1 alteration (Fig. 6-3h–i). It is composed of amphibole and magnetite with variable proportions of apatite, K-feldspar, allanite, ilmenite, titanite, pyrite, chalcopyrite and traces of thorite. This alteration occurs as straight to pinch-and-swell veins, incipient to complete replacement of the metasiltstone or crackle breccia fillings.

6.7.3 Magnetite-bearing potassic–iron alteration predating uranium mineralization

K–Fe1 alteration consists of fine-grained and incipient to intense alteration fronts that selectively replace distinct beds of the metasiltstone to which they impart a characteristic gray to dark-gray color (Fig. 6-3a). K–Fe1 is composed of biotite–magnetite±K-feldspar and locally evolves to biotite±magnetite veins. K–Fe1-altered fragments are common in the tectono-hydrothermal breccias within the west–northwest deformation corridors and this alteration is cut by all other alteration types except for Ab1. Based on field relationships, the iron oxides related to K–Fe1 alteration are interpreted to have been locally remobilized and concentrated at the unconformity when the rhyolite was emplaced, indicating that K–Fe1 predates the basal rhyolite of the Faber Group.

K–Fe2 alteration is mostly restricted to the tectono-hydrothermal breccia of zone A, but also locally occurs in other components of the Southern Breccia. It is massive to west – west–northwest foliated and selectively to pervasively replace breccia cement and fragments along tectonic foliations and bedding planes. At the peak intensity of K–Fe2 alteration, crystalline and fine- to medium-grained magnetite and biotite completely replaced the breccia over 5 meters to form biotite-bearing magnetitites (Fig. 6-3f). Accessory microcrystalline quartz and K-feldspar are typical. This alteration cuts/overprints K–Fe1, Ab1 and Ab2 alteration, and also overprints the porphyritic rhyolite and the sodic-altered porphyritic granite dikes.

Table 6-1 Mineral assemblages typical of each IOAA alteration type, and of uranium and polymetallic uranium showings of the Southern Breccia

Alteration stage	Mineral assemblage[1]	Accessory minerals	Rock type	Spatial relation to U mineralization
Ab1	Ab-Qtz-Zrn-TiOx		TLG lower metasiltstone	Regional throughout the Treasure Lake Group
Ab2	Ab-Qtz-Zrn-TiOx		TLG lower metasiltstone, Faber Group rhyolite, Albitized porphyritic granite, Tectono-hydrothermal breccias	Regional throughout the Southern Breccia
Ca-Fe±K1	Amp-Mag-Kfs-Ilm-Ttn	Ap-Ccp-Py	TLG lower metasiltstone; Faber Group rhyolite; WNW-foliated tectono-hydrothermal breccias	Northernmost boundaries of the Southern Breccia; Proximal to U
K-Fe1	Bt-Mag-Kfs		TLG lower metasiltstone	Regional throughout the Treasure Lake Group
K-Fe2	Bt-Mag-Kfs		TLG lower metasiltstone; Albitized porphyritic granite; WNW-foliated tectono-hydrothermal breccias	Confined to zone A breccia; Southern Breccia southern boundary
K-Fe3	Bt-Mag-Ilm-Rt-Ttn	Ap-Zrn-Ccp-Apy-Py-Mzn-Col-Thr-Wol	TLG lower metasiltstone; Faber Group rhyolite; Albitized porphyritic granite; WNW-foliated tectono-hydrothermal breccias	Ore zone; pre-uranium mineralization
K-Fe3/K-Fe4	**Red Hot zone:** Kfs-Mag-Rt-Ap-Chl- **Frank's zone:** Kfs-Mag-Rt-Ap-Chl	Ccp-Brn-Cct-Py-Cov-Urn-Thr-Zrn-Sch-BiTe-Gn Ccp-Py-Mlb-Brn-Cov-Urn-Thr-Zrn-Cof	TLG lower metasiltstone; Faber Group rhyolite; Albitized porphyritic granite; WNW-foliated tectono-hydrothermal breccias	Ore zone; syn-uranium mineralization
K-Fe5	Mag-Bt-Kfs		TLG lower metasiltstone; Faber Group rhyolite; Albitized porphyritic granite; WNW-foliated tectono-hydrothermal breccias	Regional throughout the Lou system but incipient at the current level of exposure
Hem1	Kfs-Chl-Hem-Rt	Mzn-Urn	TLG lower metasiltstone; Faber Group rhyolite; Albitized porphyritic granite; WNW-foliated tectono-hydrothermal breccias	Ore zone; syn- to post-uranium mineralization; Uranium remobilization
Hem2	Hem-Pit-Ccp-Qtz?		TLG lower metasiltstone; Faber Group rhyolite; WNW-foliated tectono-hydrothermal breccias	Ore zone; Second uranium mineralization event

1 Mineral abbreviations after Whitney and Evans (2010); Col: columbite, Wol: Wolframite, Pit: Pitchblende

6.8 Alteration types related to the first uranium mineralization event

6.8.1 Magnetite-bearing potassic–iron alteration

K–Fe3 alteration is typical of the Red Hot, Frank's West and Frank's zones where it occurs as millimeter to centimeter wide veins principally formed in Ab2-altered metasiltstone and porphyritic rhyolite dikes. It is composed in varying modal proportions of biotite, magnetite and ilmenite with accessory fluoroapatite, zircon, rutile, titanite, chalcopyrite, pyrite, arsenopyrite and

wolframite, and minor (Th)-monazite, ferrocolumbite and titanian ferrocolumbite. Many biotite crystals have ilmenite exsolutions and some ilmenite and magnetite crystals exhibit ferrocolumbite and titanian ferrocolumbite exsolutions (Fig. 6-3j–k). In its most intense stages, K–Fe3 alteration forms monomict crackle breccias in Ab2-altered metasiltstone and porphyritic rhyolite dikes (Fig. 6-3l). These crackle breccia zones can extend over 5 m in strike in the Red Hot, Frank's and Frank's West zones. Fragment size ranges from a few millimeters to centimeters and although fragments can locally be angular, most are rounded with cuspate boundaries. These textures imply fluid-driven corrosion of some of the fragments, following textural criteria of Jébrak (2010). K–Fe3-cemented crackle breccias laterally evolve to veins with variable orientations. Northerly oriented K–Fe3 veins cut the metasiltstone bedding at high angles whereas pinch-and-swell to straight veins are parallel to the metasiltstone bedding, indicating that this alteration occurred in the waning stages of west–northwest-oriented deformation event and the beginning of the 330° to 010–15° faulting event. Moreover, no west–northwest-oriented tectonic foliations are developed in any of the K–Fe3 metasomatic veins or crackle breccias. Vein widths do not exceed 30 cm and the largest veins frequently have a rusty weathered surface due to the presence of sulfides, including chalcopyrite. In the Frank's West zone, K–Fe3 alteration is related to the observed W mineralization (pos. wolframite) and occurs within albitized granitic dikes and the albitized metasiltstone.

K–Fe4 alteration, where incipient, occurs as wispy, intergranular and net-veined K-feldspar–iron oxide veinlets less than 0.5 mm in width emplaced along the margins of the albite and quartz crystals formed at the Ab2 stage. With increasing intensity, this alteration evolves locally to more pervasive K-feldspar replacement with disseminated iron oxides. K–Fe4 alteration imparts characteristic bright red color to some of the Southern Breccia albitites (Fig. 6-3m–n). Although K–Fe4 alteration occurs throughout the Southern Breccia, it is particularly intense in the U showings where it is semi-continuous over hundreds of meters along strike with a maximum width of 50 m in outcrop. Bright red fronts interpreted as K–Fe4 alteration also sporadically overprint sodic alteration in the early granite south of zone A and more extensively in the Lou Lake zone.

Mineralogically, in K–Fe3-altered zones, the appearance of K–Fe4 alteration is marked by the more widespread formation of K-feldspar, the transformation of ilmenite into rutile, localized transformation of chalcopyrite into chalcocite and covellite, progressive chloritization of the biotite, and the apparition of U minerals (Fig. 6-3o). All observed U showings related to the primary uraninite-bearing mineralization are spatially associated with K–Fe3 and K–Fe4

alteration, indicating that both alteration assemblages were involved in precipitation of the U minerals. K–Fe3/K–Fe4 terminology is used in the following section to indicate samples with K–Fe3 veins in which Ab2 alteration is replaced by the bright red hue typical of the K–Fe4 alteration.

Within 50 m of the U and base metal–U showings and less commonly away (> 50 m) from them, the apparition of U minerals is linked to the apparition of K-feldspar in K–Fe3 veins. In the peripheral parts of the showings, the nature of the U minerals is partially controlled by the composition of the adjacent mineral. For example, in the periphery of the Red Hot zone showings, brannerite is associated with ilmenite whereas U–K oxides (pos. compreignacite) and Fe- and K-bearing U oxides typically precipitate in contact with K-feldspar, chlorite and Mg-bearing grunerite. Other minor minerals observed in K–Fe3/K–Fe4 alteration in the external zone of the showings are allanite, galena, barite, (Y)-xenotime, U–Y±Th±F phosphates, various fine-grained U±Th minerals, Bi telluride and scheelite. K–Fe4 alteration is also related to the progressive transformation of ferrocolumbite and titanian ferrocolumbite crystals into unidentified Fe and/or Ti–Nb±Y±REE±U±Th-bearing (pos. pisekite) minerals.

In the U showings of the Red Hot and Frank's zones, uraninite precipitation at the K–Fe3/ K–Fe4 alteration stage is systematically associated with the presence of K-feldspar in K–Fe3 veins and the bright red fronts related to K–Fe4 alteration. In the Red Hot zone showings, uraninite is predominantly associated with magnetite, K-feldspar, chlorite, biotite, rutile, ilmenite, thorite, zircon, chalcopyrite and pyrite, and is weakly altered to coffinite. Zircon crystals occur as inclusions within biotite, chlorite, uraninite and thorite. Thorite is concentrated in chlorite and occurs as inclusions in both uraninite and zircon, but may also rim the uraninite crystals (Figs. 6-2b–c and 6-5a–c).

In the Frank's zone, the mineral paragenesis of the mineralization zones is more complex and variable. Uraninite is formed in K–Fe3/K–Fe4 veins in association with variable proportions of K-feldspar, magnetite, rutile, ilmenite, chlorite and biotite, and accessory apatite, pyrite, chalcopyrite, coffinite, molybdenite and bornite (Figs. 6-2e–f and 6-5d–f). The modal content of sulfides and their diversity is higher in Frank's zone whereas thorite and zircon are more abundant in the Red Hot zone.

6.9 Hydrothermal alteration postdating the main uranium mineralization event

6.9.1 Hematite-bearing iron–magnesium ± potassic alteration

K–Fe–Mg1 alteration is most intense in the western and eastern extremities of the Southern Breccia zone, reaching peak intensity in the Lou Lake and Eastern zones and is weakly to moderately developed in Frank's and Red Hot zones. Well-developed K–Fe–Mg1 alteration results in chlorite and specular hematite-cemented crackle breccias, some of which contain localized U mineralization (Fig. 6-6a–d). K-feldspar replaces albite in the fragments of the breccias and in selvages of the specular hematite–chlorite veins. Associated accessory minerals are chalcopyrite, pyrite, rutile and F-bearing monazite (Fig. 6-6b). K–Fe–Mg1 alteration appears to evolve from K–Fe4 alteration and is associated with intensifying chloritization of precursor mafic minerals (biotite, grunerite) and more typically a progressive hematization of the magnetite crystals in the Red Hot and Frank's zones (Fig. 6-6d). K–Fe–Mg1 alteration is generally weaker in the Red Zone than in the Frank's zone where it locally completely replaces magnetite into earthy and specular hematite. K–Fe–Mg1 alteration also contributed to the local redistribution of U precipitated during the K–Fe3/K–Fe4 alteration event (Fig. 6-6c). Outside the bright red alteration fronts related to K–Fe4 alteration and primary uraninite precipitation, K–Fe–Mg1 alteration is not systematically associated with U enrichment and accordingly is not directly related to the primary U mineralization event.

6.9.2 Late-stage magnetite-bearing potassic–iron alteration

K–Fe5 alteration forms very sporadic north to north–northwest -oriented crystalline magnetite veins with millimeter-wide biotite selvages. The veins are straight, have sharp contacts with their hosts, do not exceed 10 cm in width, are emplaced in small-scale dextral faults at high angle to the west–northwest-trending tectonic foliation (Fig. 6-6e), and cut much of the alteration observed in the Southern Breccia zone. This alteration is cross cut by the feldspar–biotite±quartz-phyric porphyritic dikes and postdates the formation of the west–northwest-oriented deformation corridors and the main U mineralization event.

6.10 Hydrothermal alteration related to the porphyritic dikes

6.10.1 K-feldspar alteration

K-feldspar alteration episodes are widespread and numerous in the Southern Breccia and are typically spatially related to intrusion of the porphyry dikes around which they formed well-defined to irregular haloes, suggesting a magmatic-hydrothermal origin. Only the most systematic episodes are described here. Kfs1 is largely confined to the tectono-hydrothermal breccia of zone A, where it forms pink to orange-pink, very fine-grained, pervasive and penetrative alteration fronts extending over tens of meters in diameter and overprints K–Fe1, Ab1 and Ab2 alteration, and the porphyritic rhyolite dikes.

Kfs2 alteration is very fine-grained, penetrative and reddish to brick red. It overprints and replaces the precursor sodic alteration and foliated breccias (matrix and fragments) in the B and Red Hot zones. Where most intense, the alteration commonly transforms the tectono-hydrothermal breccias into rhyolitic-looking rocks to the extent that this alteration can be easily misidentified as rhyolite or as the bright red albitization without carefully documenting the subtle alteration textures and taking systematic gamma-ray spectrometer measurements. Some of the foliated breccias overprinted by Kfs2 in the Red Hot zone are slightly enriched in U and Th. Kfs1 and Kfs2 assemblages were not observed in the Southern Breccia west of the Summit Peak fault.

6.10.2 Tourmaline alteration

Tourmaline alteration (Tur1) is widespread to the east of the Summit Peak fault but rare west of the fault. It cross cuts all the previously developed alteration in the Southern Breccia and varies in intensity from incipient to well developed. Tourmaline alteration overprints tectono-hydrothermal breccia infillings and forms decimeter to meter-wide crackle breccia in the Faber Group basal rhyolite, the porphyritic rhyolite dikes, feldspar–biotite±quartz-phyric dikes and the metasiltstones (Fig. 6-6f–g). Host rock fragments are angular in the crackle breccias. Tourmaline alteration also forms meter-wide chaotic breccias in which the fragments are angular to rounded and chemically corroded. Within these chaotic breccias, the particle size distribution is large, with fragment sizes ranging from a few millimeters to decimeters. Fragment aspect ratios are variable and the tourmaline infill is not foliated, but in the basal rhyolite and the metasiltstone,

the tourmaline infill is preferentially formed along preexisting planar structures such as flow banding in the rhyolite and bedding planes in the metasiltstone.

Where it overprints the tectono-hydrothermal breccias, this alteration is generally well-developed, penetrative, pervasive, and corrodes or replaces breccia fragments leading locally to selective tourmaline alteration of specific beds of the albitized metasiltstone fragments. The alteration is very fine-grained and associated with silicification.

6.11 Alteration related to the second uranium mineralization event

Fe–Mg1 alteration postdates K–Fe–Mg1 alteration and is emplaced as veins up to 30-cm wide in northeast-trending fractures oriented parallel to the Lou Lake and Summit Peak faults (Figs. 6-2h–i and 6-6h). These veins are principally composed of earthy hematite and chlorite with minor specular hematite and trace chalcopyrite, and locally exhibit millimeter-wide K-feldspar selvages. Localized enrichment in U is manifested by the presence of pitchblende, coffinite, becquerelite and fine-grained U–K-silicates (pos. compreignacite, boltwoodite or weeksite). These veins comprise the main U mineralization observed in the Lou Lake and Eastern zones (this work; Gandhi and Lentz, 1990) and cut all the observed alteration types of the Southern Breccia.

6.12 Element mobility during the main IOAA alteration stages in the Southern Breccia

The build-up of replacement zones, veins and breccias that overprint and cross cut earlier alteration types combined with the high intensity of alteration and systemic changes in their mineral paragenesis through time records intense element mobility. In the zones of intense alteration, the hydrothermal minerals are characteristically unrelated to the primary composition of their precursors. These features are typical of fluid-buffered systems with high water-rock ratios in which the composition of the alteration is primarily a function of the fluid composition and not of the host rock (cf. Smith et al., 2013). The chemical and mineralogical compositions of the different alteration types thus record which elements precipitated from the fluid and which

elements were leached from the rock and fingerprint the fluid physico-chemical conditions (Fig. 6-7; Online Resource 1; Bardina and Popov, 1992; Corriveau et al., 2010b).

Plotting $K/Al_{(molar)}$ against $Na/Al_{(molar)}$ indicates that albite is the predominant feldspar in most of the Southern Breccia albitites and that intensifying albitization replaces precursor K-feldspar and biotite by albite (Fig. 6-8a). Conversely, it illustrates that K-feldspar and/or biotite (both minerals have the same $K/Al_{(molar)}$ ratio) are the predominant potassic phases in intense potassic and magnetite-bearing potassic–iron alteration. Moreover, the transitional position of some Faber Group rhyolite and porphyritic rhyolite dikes between the clusters of sodic-altered and potassic-altered samples illustrates their progressive albitization during Ab2.

Plotting Ti/Al against Zr/Al discriminates the unalbitized Faber Group rhyolite (low Ti/Al) from TLG metasiltstone and provides a discriminant ratio for the albitized metasedimentary rocks that look identical to rhyolite once superimposed by Ab2 and K–Fe4 alteration (Fig. 6-8b). This diagram also highlights the Zr enrichment in some K–Fe3-altered and K–Fe3/K–Fe4-altered samples and the Ti enrichment in most of the Ab2-altered samples. It also supports the field and petrographic observations that intense albitization (Ab2) and the following K–Fe3/K–Fe4 alteration predominantly impacted the metasiltstone and early granite and less extensively the Faber Group rhyolite and associated porphyritic rhyolite dikes. Finally, it shows that the feldspar–biotite±quartz-phyric porphyritic dikes are chemically similar in terms of typically immobile elements.

Plotting Mg/Sr versus Ca/Sr shows that the Ca–Fe±K1-altered samples located in the northern parts of the Southern Breccia albitization corridor have Ca/Sr (≥1200) and Mg/Sr (≥800) ratios similar or close to those of the magnetite-bearing calcic–iron alteration of the NICO deposit (gray field Fig. 6-8c). The positive covariation between Mg/Sr and Ca/Sr for the NICO deposit samples indicates coeval Mg and Ca enrichments relative to Sr (Fig. 6-8c). The K–Fe3/K–Fe4-altered sample with the highest P content (apatite) has a high Ca/Sr ratio without any significant increases of the Mg/Sr ratio, whereas Ca–Fe±K1-, K–Fe3- and K–Fe3/K–Fe4- altered samples with a strong K–Fe–Mg1 alteration overprint exhibit high Mg/Sr ratios. The relationships described above indicate that high Ca/Sr ratios highlight Ca and Sr decoupling related to high modal content of amphibole (Ca–Fe±K1) or increases in the modal content of apatite (K–Fe3 and K–Fe3/K–Fe4; Fig. 6-5f). Conversely this diagram shows that high Mg/Sr ratios can be related to Mg and Sr decoupling in chloritized Ca–Fe±K1 alteration in which the Ca of the amphiboles was removed during chloritization or less typically biotite-rich K–Fe2 or K–Fe3

alteration. Plotting Ca/Sr and Mg/Sr ratios on the Southern Breccia geological map also indicates a northerly increase of the ratios (Fig. 6-9).

Plotting U/Al and Cu/Al versus $Na/Al_{(molar)}$ illustrates that U and Cu concentrations exhibit no apparent relationships with Na, supporting the field and petrographic observations that the mineralizing event is not related to the Ab2 sodic alteration event (Fig. 6-8d–e). Plotting V against Fe indicates that the intense K–Fe2 alteration of the zone A is enriched in V. This is different from the magnetite-rich alteration of the NICO ore zone that does not exhibit elevated V concentrations (this work; Acosta et al., 2014) and also for most of the iron oxide-bearing alteration of the Southern Breccia formed away from zone A (Fig. 6-8f).

To highlight the system-scale chemical budget of the Lou IOAA system beyond observed compatibility between the mineral paragenesis and modal composition of their main alteration zones, a principal component analysis (PCA) was done using samples from the NICO deposit and IOAA-altered samples from the Southern Breccia (Corriveau et al., 2015 and appendix 6 for samples descriptions and geochemical analyses). Samples from the tourmaline-altered (Tur1) and K-feldspar-altered (Kfs1 and Kfs2) metasedimentary rocks were not included into the dataset as they formed in spatial association with porphyritic dikes, subsequent to IOAA alteration. K-feldspar-altered samples from the rhyolite were not included either as they represent the regional alteration halo of the Lou IOAA system and potassic altered rhyolites occur in both the NICO deposit and the Southern Breccia.

In the principal component analysis (PCA) of NICO versus Southern Breccia, PC1, PC2 and PC3 represents respectively 36.7%, 18.8% and 8.4% of the total variation for 21 elements and 139 samples. The biplot of PC1 vs PC2 demonstrates that PC1 best illustrates the main chemical differences between the NICO and Southern Breccia sectors. The chemical signature of the NICO deposit can be defined using Ca, Fe, Mg, Mn and Co whereas the chemical signature of the Southern Breccia can be defined using Na, Th, U, Sr, Nb, Ti, V, Ce and Zr (Fig. 6-10a). Lower PC1 scores for Cu, Ni, Mo, K, Rb and Ba indicate that they are more equally distributed between the two sectors. The more polymetallic signature of the Frank's zone U showings is also highlighted with the PCA analysis as they have much lower PC2 value than the Red Hot zone U showings. Conversely, the PC1 vs PC2 and PC1 vs PC3 biplots highlight that the samples localized at the northeastern margin of the Southern Breccia zone, in which Ca–Fe±K1 alteration begins to appear, have a compositional signature transitional to that of the NICO deposit alteration (Fig. 6-10a–b).

6.13 Chemical and metallic signature of the Southern Breccia uranium-bearing showings

There are noticeable differences between the base metal content of the Frank's and Red Hot zones U showings even though both are related to the K–Fe3/K–Fe4 alteration stages. The showings of Frank's zone, with higher modal content and diversity of sulfides, have a more diversified metallic signature generally richer in base metals. This is exemplified by plotting U/Th against S, Cu, Ni and Zn (Fig. 6-11a–d). Plotting $Mg/K_{(molar)}$ versus $Ca/K_{(molar)}$ shows that the Frank's zone U showings and their alteration envelope are more calcic and magnesian than the showings and alteration envelope of the Red Hot zone, which are more potassic (Fig. 6-11e). Plotting $Fe/K_{(molar)}$ versus U/Th also shows that most of the Frank's zones U-rich samples have greater Fe contents than the Red Hot zone U-rich samples, richer in K (Fig. 6-11f).

Plotting U/Th versus U indicates that the typical U/Th ratios in U-mineralized zones of the Red Hot and Frank's zone showings are between 7 and 10 and that the Red Hot zone U showings, at equivalent U concentrations, are slightly richer in Th than the U showings of Frank's zone (Fig. 6-12a). The U showings related to Fe–Mg1 alteration in the Lou Lake and Eastern zones have low Th concentrations and U/Th ratios between 18 and >746. The contrast in U/Th ratios highlights distinctive changes in the fluid properties that supports the field observations indicating that the Fe–Mg1 veins are not coeval with the U showings of the Frank's and Red Hot zones.

The almost perfect positive covariation between (U+Th)/Al and Pb/Al is compatible with Pb being largely radiogenic in the Southern Breccia U showings (Fig. 6-12b). The formation of allanite and monazite at the K–Fe–Mg1 alteration stage, the formation of apatite at the K–Fe3 alteration stage and the formation of REE-rich uraninite at the K–Fe3/K–Fe4 alteration stage are related to localized La and Ce enrichments in the U mineralization of the Southern Breccia, with La+Ce reaching a combined content over 500 ppm. The highest REE concentrations were observed in the Lou Lake and Frank's zones U showings. Elevated Y concentrations up to 200 ppm were also documented in certain showings of the Southern Breccia.

Plotting U/Th versus U indicates that the typical U/Th ratios in uranium-mineralized zones of the Red Hot and Frank's zone showings are between 7 and 10 and that the Red Hot zone uranium showings, at equivalent uranium concentrations, are slightly richer in thorium than the uranium showings of Frank's zone (Fig. 6-11a). The uranium showings related to Fe–Mg1 alteration in the Lou Lake and Eastern zones have low thorium concentrations and U/Th ratios between 18

and >746. The change in U/Th ratios highlights a distinct chemical signature that supports the field observations indicating that the Fe–Mg1 veins are not coeval with the uranium showings of the Frank's and Red Hot zones.

The almost perfect positive covariation between (U+Th)/Al and Pb/Al is compatible with lead being largely radiogenic in the Southern Breccia uranium showings (Fig. 6-11b).

6.14 Timing constraints on the Southern Breccia and NICO formation

6.14.1 Field relationships and U–Pb ages on zircons

In both the NICO deposit and the Southern Breccia corridor, the Lou assemblage basal rhyolite and the rhyolite dikes are overprinted by the ore-forming alteration types (Goad et al., 2000b), indicating that the main mineralization event in both systems postdates deposition of the Faber Group and the 1,873 Ma early granitic intrusion that is cut by the rhyolite dikes. At surface above the NICO deposit ore zone, the basal rhyolite is also locally brecciated by cobaltian arsenopyrite veins rich in Bi. Conversely, the K–Fe3/K–Fe4-related U mineralization and most of the magnetite-bearing calcic–iron alteration of the NICO deposit ore zone are cut by feldspar–biotite±quartz-phyric porphyritic dikes dated respectively at ca. 1868 and 1869 Ma (Davis et al., 2011; Potter et al., in press). This indicates that the NICO deposit was almost entirely formed, and that the K–Fe3/K–Fe4-related U mineralization event in the Southern Breccia occurred before the emplacement of the feldspar–biotite±quartz-phyric porphyritic dikes and that most of the Lou IOAA system development is coeval with the volcanic activity of the Lou assemblage of the Faber Group (i.e., 1,873–1,868 Ma) according to field relationships and the Gandhi et al. (2001) U–Pb zircon ages. Both the ca. 1869 and 1868 Ma dikes are cut by the non IOAA-altered 1,867 Ma monzonite/monzodiorite stocks and postdate the Lou assemblage rhyolites and associated rhyolite dikes. Hence within an approximately 5 m.y. time window, polyphase IOAA metasomatism led to the formation of both the Southern Breccia and the NICO deposit.

6.14.2 Approximate CHIME ages of the uranium mineralization events

The almost perfect positive covariation between (U+Th)/Al and Pb/Al indicates that most of the Pb in the Southern Breccia U showings is radiogenic. This is supported by the very low Pb

content of the host Ab2 albitized-metasiltstone in which Pb was most likely leached during the Ab2 albitization event. Hence, the timing of the U mineralization events can be approximated using CHIME (CHemical U–Th-total Pb Isochon MEthod) ages, calculated by solving the equation presented in Cocherie and Albarède (2001):

$$Pb = Pb_0 + Th\{M_{208}/M_{232}\cdot(e^{\lambda 232t} - 1)\} + U\{[M_{206}/M_{238} \times 0.9928x(e^{\lambda 238t} - 1)] + [M_{207}/M_{235} x0.0072 (e^{\lambda 235t} - 1)]\}$$

Where, Pb_0 is the initial Pb content of the U-bearing K–Fe3/K–Fe4 veins and their host rock (Ab2-altered metasiltstone); Pb, Th and U are concentrations in ppm; M_{208}, M_{232}, M_{206}, M_{238}, M_{207}, and M_{235} are the atomic masses of ^{208}Pb, ^{232}Th, ^{206}Pb, ^{238}U, ^{207}Pb, and ^{235}U; λ_{232}, λ_{238}, and λ_{235} are the decay constants $4.9475x10^{-11}$, $1.55125x10^{-10}$, and $9.8485x10^{-10}$; 0.9928 is the natural abundance of ^{238}U calculated using $^{238}U/(^{235}U+^{238}U)$; 0.0072 is the natural abundance of ^{235}U calculated using $^{235}U/(^{235}U+^{238}U)$.

The equation was solved using the uniroot function in the R software (R development Core Team, 2013). To minimize the error due to analytical error on U, Th and Pb, and to minimize the effects of potential remobilization after the formation of the showings, CHIME ages were only calculated on samples with U concentration above 260 ppm. The Pb_0 content of Ab2-altered metasiltstone was estimated at 3 ppm based on the mean Pb content in the strongly albitized (Ab2) metasiltstone that hosts the U showings and the traces of galena observed in K–Fe3/K–Fe4 alteration zones.

Uranium showings of the Red Hot and Frank's zones, formed in the K–Fe4/K–Fe–Mg1 alteration stages, have calculated CHIME ages between 1.87 and 1.69 Ga with one exception at 1.97 Ga (Table 6-2). The closest age (1.87 Ga) to the estimated age of the mineralization (between 1,873 and 1,868 Ma) is given by a sample of the Red Hot zone that has the highest U, Th and Pb concentrations and where uraninite is shielded by thorite crystals (Fig. 6-5c). The lower CHIME ages around 1.8 Ga for many samples of the Frank's and Red Hot zones are interpreted to primarily reflect secondary U gains or recrystallization of the primary U minerals after remobilization of U which is compatible with the formation of secondary coffinite, becquerelite and various other K–U minerals in the Red Hot zone. U–Pb ages on uraninite and pitchblende, obtained for many of the GBMZ U showings by Miller (1982), also demonstrate a complex remobilization history of U and Pb (cf. Port Radium–Echo Bay U deposits and showings; Mumin et al., 2010; Somarin and Mumin, 2012; Gandhi et al., 2013).

The 0.4 Ga CHIME ages of the Lou Lake and Eastern zones U showings formed in the Fe–Mg1 alteration are much younger than the CHIME age of the Frank's and Red Hot zones U showings

but close to the U–Pb ages on pitchblende obtained by Miller (1982) on the U mineralization of the Rayrock mine (511±86 Ma) and the secondary U mineralization of the Sue-Dianne deposit (457±26 Ma), both hosted in earthy hematite-rich veins (Gandhi, 1989; Byron, 2010). Those CHIME ages, supported by pitchblende dating of Miller (1982), are interpreted to reflect periodic U remobilization along the northeast-oriented faults in the southern GBMZ from the Paleoproterozoic to the Devonian. Such periodic U and/or Pb remobilizations may also have impacted, to a lesser extent, the U showings of the Frank's and Red Hot zones.

Table 6-2 CHIME ages of the uranium-rich samples of the Red Hot, Frank's, Lou Lake and Eastern zone

SAMPLE	Zone	U-bearing alteration	Pb (ppm)	Th (ppm)	U (ppm)	CHIME age
P011F02	Eastern	Hem2	176.5	27.3	3090	393
P526D03	Lou Lk.	Hem2	564	13.5	10000	389
P526D04	Lou Lk.	Hem2	17.4	16.3	262	447
C1666/M612910	Frank's	K-Fe3/K-Fe4	587	147.5	2000	1705
C1705/M612913	Frank's	K-Fe3/K-Fe4	476	162	1460	1841
C1705/M612914	Frank's	K-Fe3/K-Fe4	162	33.8	560	1690
C1665B2	Frank's	K-Fe3/K-Fe4	279	88.9	880	1804
C1665B4	Frank's	K-Fe3/K-Fe4	535	174	1690	1801
C1665D3	Frank's	K-Fe3/K-Fe4	303	71.4	860	1969
P012E01	Red Hot	K-Fe3/K-Fe4	2590	880	7770	1873
P012E03	Red Hot	K-Fe3/K-Fe4	1010	369	3170	1806
P012E04	Red Hot	K-Fe3/K-Fe4	547	224	1730	1789

6.15 Sequence of events

Hydrothermal alteration in the Southern Breccia zone can be summarized in four main stages (Fig. 6-4):

1) pre west–northwest-oriented deformation Ab1 and K–Fe1;
2) pre to syn west–northwest-oriented deformation Ab2 albitization and K–Fe2;
3) late to post west–northwest-oriented deformation K–Fe3, Ca–Fe±K1, K–Fe4 and K–Fe–Mg1;
4 post west–northwest-oriented deformation K–Fe5, Tur1 and Fe–Mg1.

6.15.1 Pre WNW-oriented deformation Ab1 and K–Fe1 alteration types

Prior to onset of magmatic-hydrothermal activity, the steeply dipping TLG metasedimentary rocks were tilted (this work; Gandhi and Lentz, 1990; Goad et al., 2000a). This is supported by the steep angle between the steeply dipping bedding of the metasedimentary units and the sub-horizontal rhyolite above the unconformity and the filling of troughs in the sub-vertical metasiltstone by rhyolite in differentially eroded beds along the unconformity. Field relationships also discriminated the intense and irregular rhyolite-looking potassic alteration superimposed on the TLG metasedimentary rocks that could be misinterpreted as the unconformity.

Ab1 and K–Fe1 alteration stages, documented throughout the TLG southwest of the Lou IOAA system, may have been triggered by gradual heating of formation waters present in the TLG during the initiation of GBMZ-related magmatic activity, but predate the emplacement of the Faber Group basal rhyolite. This hydrothermal event resulted in selective albitization or biotite–magnetite alteration of the metasiltstone controlled by the original composition of the beds.

6.15.2 Pre to syn WNW-oriented deformation Ab2 albitization and K–Fe2 alteration

Prior to onset of magmatic-hydrothermal activity, the steeply dipping TLG metasedimentary rocks were tilted (this work; Gandhi and Lentz, 1990; Goad et al., 2000a). This is supported by the steep angle between the steeply dipping bedding of the metasedimentary units and the sub-horizontal rhyolite above the unconformity and the filling of troughs in the sub-vertical metasiltstone by rhyolite in differentially eroded beds along the unconformity. Field relationships also discriminated the intense and irregular rhyolite-looking potassic alteration superimposed on the TLG metasedimentary rocks that could be misinterpreted as the unconformity.

Ab1 and K–Fe1 alteration stages, documented throughout the TLG southwest of the Lou IOAA system, may have been triggered by gradual heating of formation waters present in the TLG during the initiation of GBMZ-related magmatic activity, but predate the emplacement of the Faber Group basal rhyolite. This hydrothermal event resulted in selective albitization or biotite–magnetite alteration of the metasiltstone controlled by the original composition of the beds.

6.15.3 Late to post WNW-oriented deformation K–Fe3, Ca–Fe±K1, K–Fe4 and K–Fe–Mg1 and main mineralization stages

In the Southern Breccia U showings and their surroundings, K–Fe3 alteration begins during the waning stages of west–northwest-oriented deformation and was preferentially developed in Ab2-altered and non-brecciated metasiltstone. The coexistence of ilmenite and magnetite in K–Fe3 alteration indicates reducing conditions. In parallel, the absence of tectonic foliation in K–Fe3 or any subsequent alteration types in combination with the emplacement of K–Fe3 veins within N-oriented extension gashes that cross cut the west to west–northwest-oriented fabrics, record a change in the tectonic regime and mechanical behavior of the crust, from largely compressive to largely extensional at the transition from brittle-ductile to brittle conditions. This brittle extensional regime likely favored the ingress of oxidized and probably U-bearing fluids responsible for K–Fe4 alteration. The bright red hue typical of K–Fe4-altered zones and the sequential formation of bornite, chalcocite and then covellite demonstrate the increasingly oxidizing nature of the fluid. Consequently, we propose that ingress of U-bearing and oxidizing K–Fe4 fluids favored by an extensional setting and increased availability of U sources (Faber Group volcanic rocks and earlier granitic intrusions), and mixing with reducing K–Fe3 fluids that precipitated magnetite and ilmenite formed the U and polymetallic U showings of the Southern Breccia. This ore-forming process accounts for the systematic spatial association between the U showings, K–Fe3 alteration and the bright red K–Fe4 alteration fronts. Considering the close relationship between U and Th in the Southern Breccia showings, a significant portion of the U must have been transported by K–Fe3 fluids and precipitated as U minerals during mixing with K–Fe4 fluids because of the drastic changes in the fluid chemistry, $fO2$ and temperature. Uranium brought by K–Fe4 has further enriched the showings in U and caused the variations in the U/Th ratio observed in the showings with its progressive evolution to K–Fe–Mg1.

K–Fe4 progressively evolved to K–Fe–Mg1, with varying intensity dependent on the exhumation levels of the system: shallower west of the Summit Peak fault and deeper to the East. As most of the U had already precipitated during interaction between the K–Fe3 and K–Fe4 related fluids, K–Fe–Mg1 only remobilized primary U minerals at sample to outcrop-scales. Remobilization under the low temperature and oxidizing conditions expected of K–Fe–Mg1 would make it difficult to also mobilize Th and can account for the higher U/Th ratios in the U mineralized zones with a stronger K–Fe–Mg1 overprint. In parallel, linking the main U precipitation events to the magnetite–hematite transition stage of the IOAA hydrothermal system, with a greater intensity of

K–Fe–Mg1 alteration west of the Summit Peak fault, supports a shallower level for this area and differential exhumation across the Southern Breccia zone during metasomatism.

The Frank's and Frank's West U showings, located closer to the NICO system, exhibit stronger S, Zn, Ni, Cu, W and Bi enrichments and higher Ca/Sr, Mg/Sr, $Ca/K_{(molar)}$ and $Mg/K_{(molar)}$ and $Fe/K_{(molar)}$ ratios compared to the Red Hot showings. Hence the alteration envelope and the U showings of Frank's zone are more calcic, magnesian and ferriferous than the potassic U showings and alteration envelope of the Red Hot zone. Relative to the Southern Breccia, the NICO ore zone and its alteration envelope are enriched in W, Ni, Bi and Zn and have very high Ca/Sr and Mg/Sr ratios (this work; Goad et al., 2000a). The northernmost boundaries of the albitization corridor are also characterized by formation of Ca–Fe±K1 alteration that is considered as coeval with K–Fe3 according to the following criteria:

1) Ca–Fe±K1 overprints Ab2 yet is overprinted by K–Fe–Mg1;
2) Calcic amphibole precipitates instead of biotite as the main mafic mineral, but magnetite and Ti minerals (titanite, ilmenite) are abundant in both Ca–Fe±K1 and K–Fe3;
3) Ca–Fe±K1 and K–Fe3 both exhibit local enrichments in Th, niobium and tantalum, and contain apatite; and
4) Ca–Fe±K1 is slightly potassic as it contains K-feldspar, which may indicate incipient transition to K–Fe4 or a faint K–Fe4 overprint.

The decoupling between Ca–Mg and Sr in the Southern Breccia alteration zones may result from:

1) Hydrothermal fluids with initially low Ca/Sr and/or Mg/Sr ratios for which the fluid/mineral partitioning coefficients for Sr favored its solubility into fluid over its precipitation in hydrothermal minerals (amphibole, apatite, biotite, chlorite); or
2) Involvement of fluids with initially high Ca/Sr and Mg/Sr ratios related either to previous depletion of Sr in the fluid (e.g., during albitization) or to a low Sr content of the source compared to Ca and Mg.

Strontium fractionation from Ca and Mg because of fluid/mineral partitioning coefficients is not considered to be the controlling factor for the high Ca/Sr and Mg/Sr ratios in the Southern Breccia K–Fe3 and Ca–Fe±K1 alteration types. Strontium can be incorporated in hydrothermal amphibole and apatite and the Sr content of those minerals typically reflects the chemistry of the fluid (Najorka et al., 1999; Belousova et al., 2002). The high Ca/Sr and Mg/Sr ratio for

amphibole- and apatite-bearing alteration are interpreted to result from the ingress of a fluid with initially high Ca/Sr or Ca/Sr and Mg/Sr ratios, likely similar to those involve in the formation of the NICO deposit in which all the ore-related alteration types have very high Ca/Sr and/or Mg/Sr ratios (Fig. 6-8c). The high Mg/Sr but low Ca/Sr ratios in the chloritized Ca–Fe±K1 alteration can be explained by Ca leaching during chloritization associated to K–Fe–Mg1 alteration with concomitant preservation of the Mg in the hydrothermal chlorite. Accordingly, the spatial variations in chemical and metallic signatures of the Southern Breccia showings, combined with the northerly increases of the Ca/Sr and Mg/Sr ratios observed in the Southern Breccia likely reflects a northerly increase of the chemical imprint of the NICO system in the Southern Breccia alteration zones and U showings.

6.15.4 Post WNW-oriented deformation K–Fe5, Tur1 and Fe–Mg1

The formation of late-stage crystalline magnetite (K–Fe5) veins after K–Fe–Mg1 east of the Summit Peak fault is interpreted as an indication of a potential rejuvenation of the system, either occurring at deeper crustal level through differential exhumation or related to temperature increases due to increased magmatic activity. For example, the feldspar–biotite±quartz-phyric porphyritic dike swarm subsequent to K–Fe5 is at least of an order of magnitude more voluminous than all previous porphyritic dikes preserved and coeval with the onset of intrusions of the Great Bear and Marian River batholiths, and renewed volcanism (Mazenod assemblage closely followed by Bea assemblage of the Faber Group; Jackson, 2008; Hildebrand et al., 2010b; Jackson and Ootes, 2012). Feldspar–biotite±quartz-phyric porphyritic dikes are coeval with the development of tourmaline breccias (Tur1) in the Treasure Lake Group and the overlying rhyolite and widespread potassic alteration.

The timing of the pitchblende-bearing Fe–Mg1 mineralization is difficult to constrain and can substantially postdate the formation of the Lou IOAA system. As shown by the CHIME ages and the U–Pb ages of Miller (1982) for similar U mineralization at Sue-Dianne and Rayrock, the calculated dates for the genesis of Fe–Mg1-type mineralization extend from Paleoproterozoic to Devonian ages. A post 1.84 Ga GBMZ, syn-northeast-oriented faulting and pre 1.74 Ga Cleaver dike interval is proposed by Gandhi et al. (2000) for the Ted U showing, an interval that can apply also to the Fe–Mg1 event as it is also spatially associated and shares the trends of northeast-oriented faults. However, an older age for the Fe–Mg1 event is also plausible based on field constraints for active northeast-striking faults during LaBine volcanism (i.e., 1.87 Ga; Mumin et al., 2014). In any case, periodic episodes of remobilization and recrystallization are

required to account for the very low Pb content of the U mineralization formed at the Fe–Mg1 stage compared to the U showings related to the K–Fe3/K–Fe4 alteration stage.

6.16 Implications on the Lou IOAA system formation

Repeated influx of heat and magmatic-hydrothermal fluids associated with granite and porphyritic dike emplacement took place within a very short time window (<5 m.y.) across the Lou IOAA system and fostered the formation of a large and fertile IOAA system. In the confined environment created by the regional unconformity with the Faber Group, very dynamic and powerful hydrothermal cells developed along sub-vertical fault zones that focused fluid, heat and magmatic circulation and led to the formation of the albitization corridor of the Southern Breccia. These cells leached metals on a regional scale and contributed to the metal endowment of the mineralized zones of the Southern Breccia and NICO deposit. In turn, incremental emplacement of porphyritic dike swarms sustained heat transfer from the magma chambers at depth to surface and were likely instrumental in the periodic resurgence of HT magnetite alteration throughout the development of the Southern Breccia. Mineralization was building up incrementally in the Southern Breccia, and the periodical influx of heat and magmatic-hydrothermal fluids also accounts for the incremental mineralization events in the NICO deposit (Goad et al., 2000a, b; Acosta et al., 2014).

The transition from intense albitization (Ab2) to K–Fe3/K–Fe4 alteration in the Southern Breccia, close to the magnetite-to-hematite transition, and very strong magnetite-bearing calcic–iron alteration in the NICO deposit to the northeast suggest that the Southern Breccia zone records an incremental post-Ab2 exhumation of the albitites. Faster exhumation rates to the southeast in the Lou IOAA system is indicated by the decreasing abundance of the Lou assemblage volcanic rocks to the southeast and the exhumation of the apical part of the early granite.

Accordingly, some of the key ingredients in the development of the Southern Breccia are the same as those for developing U-rich IOCG systems as per Skirrow (2010) and include:

1) Regional but highly portioned deformation event(s) and active magmatism that fostered system-scale transfer of heat and fluids, permitting the high fluid/rock ratios necessary for the intense and widespread (Ab2) albitization;
2) A competency contrast between rock units to focus fluid circulation in spatially constrained deformation corridors which promote effective leaching and discharge;

3) Repeated dike emplacement to re-energize the hydrothermal system likely in terms of both heat and magmatic-hydrothermal fluids;

4) A transition from a compressive to an extensional tectonic regime as the system evolved from brittle-ductile to brittle conditions to favor the entrance of oxidizing fluids into the system;

5) Subsequent fluid mixing and exhumation of generally deeply seated alteration in IOAA systems (albitites; cf. Hitzman et al., 1992; Williams et al., 2005; Corriveau et al., 2010b); and

6) Host rock units with high U and Th contents from which U and Th can be leached and concentrated in the fluids (Ootes et al., 2013; see also Hitzman and Valenta, 2005; Somarin and Mumin, 2012).

Based on the Southern Breccia, field characteristics of albitite-hosted U mineralization include:

1) Strongly hydrothermally altered and foliated tectono-hydrothermal breccia zones;

2) Coexistence of magnetite and ilmenite formed at the same alteration stage transitional to magnetite and then hematite that record increasingly oxidizing conditions;

3) Formation of bright red alteration fronts which may represent frozen oxidation fronts;

4) Abundance of albitites with intrinsic porosity that mechanically weakens the rock (Engvik et al., 2008; Putnis, 2009) and favors fracturing in brittle or brittle–ductile regimes; and

5) Coexistence of numerous generations of dikes, sills or laccoliths and batholiths formed in a short time window (cf. Hildebrand et al., 2010b).

6.17 Comparison to other albitite-hosted uranium deposits

Similarities between the Southern Breccia and other major albitite-hosted U deposits like Valhalla (Australia), Aricheng (Guyana), Espinharas and Lagoa Real (Brazil) include: a large-scale albitization event that predates the U–Th mineralization stage and hosts the U-bearing alteration types, and metal precipitation and deposit formation during the transition from brittle–ductile to brittle conditions at regional scale during deformation (Porto da Silveira et al., 1991; Polito et al., 2009; Alexandre, 2010). The high Na concentrations in the U showings of the Southern Breccia are also similar to those observed in the Valhalla deposit, the Aricheng South

U occurrences and the Lagoa Real deposit. Bright red albitites were also described in other albitite-hosted U deposits (e.g., Yangmeiwan occurrence in China; Zhao, 2006). At Yangmeiwan, the author does not indicate if the bright color of the albitites is related to a subsequent and pervasive potassic–iron alteration as observed in the Southern Breccia zone. The evolutionary sequence of iron oxide from magnetite (K–Fe2 to K–Fe4) to hematite (K–Fe–Mg1 and Fe–Mg1) is also observed in other albitite-hosted U deposits (Porto da Silveira et al., 1991; Polito et al., 2009; Alexandre, 2010).

In contrast, the mineral assemblages of the Southern Breccia U showings, composed primarily of iron oxide, K-feldspar, biotite and Ti oxides (rutile, ilmenite) with variable proportions of pyrite, chalcopyrite, scheelite, wolframite and molybdenite and low modal contents of zircon, contrast with the mineralogy of the U ore zones (low modal content in iron oxide and K-feldspar, high modal content of zircon) observed in the other known albite-hosted U deposits (McKay and Miezitis, 2001; Polito et al., 2009; Alexandre, 2010). Although hydrothermal zircon crystals are associated with uraninite in the Red Hot zone showings, the Southern Breccia lacks high zircon modal contents and intense carbonate alteration. Calcium-enriched alteration is largely expressed in amphibole-bearing alteration that is almost entirely outside of the U-bearing albitites of the Lou IOAA system. Moreover as the Lou IOAA system is not affected by regional orogenic metamorphism, such type of metamorphism (in contrast to metasomatism) is not a prerequisite for the formation of albitite-hosted U deposits. In the Southern Breccia, magmatic heat sources likely drove and sustained development of the system.

Using published geochemical analyses, representative data from the Southern Breccia U showings were compared to Valhalla (Polito et al., 2009) and Lagoa Real (Lobato and Fyfe, 1990). The Southern Breccia U showings have higher K, Ni and Th concentrations, similar Y and Ti concentrations and lower Ca, Fe, Mg, Sr, V and Zr concentrations (Fig. 6-13). The Fe/Ca ratio, higher in the Southern Breccia U-rich samples than in Valhalla and Lagoa Real U-rich samples, indicates the higher modal content of iron oxide in the Southern Breccia U mineralization. Compared to both the Southern Breccia and Lagoa Real, the Valhalla U ore zone is strongly enriched in Sr, Zr, Ca, Co and V and has a Cu content generally similar to the Southern Breccia U showings (Fig. 6-13). Plotting Zr/Al versus U/Al for the samples of the Valhalla, Lagoa Real and Southern Breccia systems reveals the strong association between Zr and U in Valhalla and the absence of any relationships in the two other systems in which the non-mineralized and mineralized rocks have similar Zr/Al ratios (Fig. 6-14). Experimental work on Zr-bearing mineral dissolution demonstrates that Zr solubility decreases with temperature in a

F-bearing hydrothermal fluid (Aja et al., 1995; Migdisov et al., 2011). Moreover, the solubility of F in a hydrothermal fluid, necessary to large-scale mobilization of Zr (Migdisov et al., 2011), is strongly related to the activity of Ca (fluorite) and Mg (sellaite; MgF_2) as both are highly insoluble in hydrothermal fluids (Salvi et al., 2000). At Valhalla, most of the U ore precipitated at the contact between a metabasalt unit and a metasedimentary unit at temperatures between 340–380°C, temperatures capable of mobilizing Zr. It is thus likely that the mixing of a hydrothermal fluid originating from or having percolated through the basalt and a F-, U- and Zr-bearing fluid contributed to the ore-forming process in Valhalla, as enrichment in Mg and Ca in the mixed fluid lead to fluorite and sellaite saturation, causing the precipitation of the uranoan-zircon noted by Polito et al. (2009). Contribution of the basalt to the fluid chemistry is also compatible with precipitation of the deposit highest Cu concentrations at the contact between the metabasalt and the metasedimentary sequence (Fig. 3 in Polito et al., 2009).

Conversely, Lagoa Real U mineralization, with an estimated temperature of formation between 500°C–550°C (Lobato and Fyfe, 1990), exhibits no significant enrichment in Zr. As per the Southern Breccia, U precipitation occurred at the magnetite–hematite oxidation buffer and the oxidation of reduced Fe in a mafic mineral assemblage was considered to trigger massive U precipitation. The low modal content of zircon in the Southern Breccia U showings, combined with the REE- and Th-rich composition of uraninite precipitated at the K–Fe3/K–Fe4 alteration stage (Potter et al., in press), indicates that the U mineralization occurred at high temperatures that do not favor Zr mobility. High temperatures are also supported by the mineralogy of the K–Fe3/K–Fe4 alteration zones in which magnetite–ilmenite and biotite coexist. The main U precipitation in the Southern Breccia occurred when the strongly oxidizing K–Fe4 fluid interacted with the reducing K–Fe3 fluid, which is similar to the inferred process at Lagoa Real. Hence at least two different genetic processes can lead to formation of albitite-hosted U deposits, dependent upon the physico-chemical conditions of the involved fluids and the geological environment. The first U precipitation process, exemplified by Valhalla, involves a F-rich fluid at moderately high temperatures (350-400°C). The main U mineralization event is triggered by the interaction of a reactive unit or fluid rich in Ca or Mg and the U-bearing fluid. This interaction brings fluorite and sellaite to saturation into the U-bearing fluid and the removal of F combined with potential fluid mixing changes the pH and eH conditions of the fluid and triggers U precipitation. Oxidation-reduction reactions, although important during U precipitation, are not the main trigger of the mineralizing event as U precipitation in those systems does not necessarily occur at the magnetite–hematite transition. The second process primarily involves oxidation-reduction reactions as the main trigger of U precipitation during mixing of oxidizing and

reducing fluids at the magnetite–hematite transition. Oxidation-reduction reactions that can trigger U mineralization may be more typical in higher temperature systems like Lagoa Real and the Southern Breccia (>500°C) at which Zr mobility is limited and result in mild Zr enrichments with the U mineralization.

6.18 Predictive exploration based on observed alteration facies and system-scale partitioning of chemical elements

Renewed mapping of the NICO deposit through examination of the decline and the muck piles extracted from the ore zone as well as reexamination of drill cores highlighted that ore emplacement occurred during cyclical episodes of magnetite-bearing calcic–iron and potassic–iron alteration (Corriveau et al., 2010a; Acosta et al., 2014). Considering the large extent of magnetite-bearing HT calcic–iron alteration, it was conceptually puzzling that intense sodic alteration, K-feldspar-rich magnetite-bearing potassic–iron and hematite-bearing potassic–iron alteration were only mildly developed in the NICO deposit (cf. alteration model of Corriveau et al., 2010b; Fig. 6-15). Before this work, albitization had only been locally observed in the footwall of the deposit whereas the Southern Breccia albitites were mapped as hornfelsed metasedimentary rocks (Goad et al., 2000a). Remapping led to the discovery of extensive albitization, and less intense magnetite–biotite–K-feldspar–Ti oxides and specular hematite–chlorite–K-feldspar alteration types and provided the impetus to further search the area for mineralization. These alteration types plus the uraninite and sulfide mineralization of the Southern Breccia now better conceptually and empirically fulfill the expected alteration and mineralization spectrum of the large-scale and fertile Lou IOAA/IOCG system.

PCA indicates that the system-scale redistribution of chemical elements between the NICO deposit and the Southern Breccia zone matches the system-scale distribution of IOAA alteration as characterized in chapter 5, supporting the inclusion of these distinct mineralization styles within a single IOAA system. A holistic view on the ore-forming events is as follows. Albitites of the Southern Breccia form a source of metals for NICO base and precious metal ores and for the Southern Breccia Th and U mineralization zones. Fluids exiting from the NICO deposit after precipitation of calcic–iron–potassic alteration and associated mineralization may have participated in formation of the Southern Breccia K–Fe3/K–Fe4 mineralized alteration with a decreasing influence from the north to the south. The integrated development of the Southern Breccia and the NICO deposit is also supported by 1) the northerly increase of the Mg/Sr and

Ca/Sr ratios that indicate a gradual enrichment in Ca and Mg in the U showings and their alteration envelope, 2) the northerly increase in the metal contents, metal diversity and Fe content of the Southern Breccia U showings and alteration envelope, and 3) the northerly transition from K–Fe3-dominant to Ca–Fe±K1-dominant alteration in the Southern Breccia.

6.19 Albitite-hosted uranium deposits in the development of large-scale IOAA systems

The potential of IOAA systems with IOCG deposits/showings to form albitite-hosted U deposits is demonstrated by 1) the very close space–time association between the Southern Breccia and the NICO deposit (~1 km apart and formed within a ca. 5 m.y. window) and 2) the complementary alteration and geochemical signatures between these two distinct deposit-type environments according to the alteration zoning models for IOAA systems and IOCG and affiliated deposit continua (Corriveau et al., 2010b; Mumin et al., 2010; Richards and Mumin, 2013). The time–space distribution of the major albitite-hosted uranium and IOCG/IOAA systems also highlights a potential linkage between the evolution of a major IOAA district and the formation of albitite-hosted uranium systems (Figs. 6-16, 6-17). A summary of published geochronological results shows that the formation timing of the major IOCG/IOAA districts roughly corresponds to the formation timing of the major albitite-hosted uranium systems. A map of global IOAA and albite-hosted uranium districts shows that some Proterozoic albitite-hosted uranium systems and IOCG/IOAA deposits occur in the same area (Valhalla/Cloncurry district, Southern Breccia/NICO–Sue-Dianne) and have overlapping ages. This overlap in their timing and spatial location is also indicative that the tectonic framework that led to the formation of some albitite-hosted uranium systems is likely similar to the tectonic framework leading to the formation of IOCG/IOAA deposits including the transition from compressive to extensional tectonic regime (cf. Skirrow, 2010).

Accordingly, the regional albitization zones associated with the development of major IOAA systems can host significant U mineralization that can be associated with subordinate Th, Cu, Ta, Bi, Au, REE and Mo anomalies or mineralization. The base-metal contents of U-mineralized zones can be a function of the ore fluid sources, proximity of metal-rich rocks such as basalts (e.g., Valhalla) and development of albitite-hosted U mineralization within IOCG systems. Spatial variations in the metallic signature of the U showings within an albitite-hosted system have potential to be a proximity indicator of polymetallic IOCG deposits. In the Southern Breccia, the

metal assemblage of the Frank's showings, closer to NICO, is more diversified than in the Red Hot zone, which is farther from NICO. Metal variation may also provide insights on the U precipitation processes, as illustrated by the Valhalla deposit. As a result, the discovery of albitite-hosted U mineralization amongst alkali alteration assemblages with or without exposed iron oxide alteration may provide an exploration tool to identify an IOCG deposit potential for the district and open new areas for IOCG exploration. Collaterally, systems that host IOCG deposits may hide albitite-hosted U deposits.

6.20 Conclusions

The similarities between the Southern Breccia polymetallic U showings and other albitite-hosted U deposits allow their classification as albitite-hosted U mineralization. In addition, the association of the main U mineralizing event with iron oxides (magnetite and to a lesser extent hematite) and K-feldspar alteration indicates a close affiliation to IOCG-type mineralization. The Southern Breccia is also Th rich, and not significantly enriched in Zr and Sr compared to other albitite-hosted U deposits such as Valhalla. Developed in a structural corridor just 1 km south of the NICO deposit, the Southern Breccia zone is distinct in terms of alteration and ore composition yet complementary to the NICO deposit in the larger Lou IOAA system. Cross-cutting relationships constrain the development of both the NICO deposit and Southern Breccia zone between 1,873–1,868 Ma. The recognition of an association between albitite-hosted U systems and IOCG deposits adds an exciting new exploration target for IOCG-affiliated deposit types documented in the GBMZ and demonstrates that the large albitization zones associated with evolution of IOCG systems in other districts around the world may be potential hosts of albite-hosted U deposits. Conversely, the discovery of non-metamorphosed albitite-hosted U mineralization in a hydrothermal system with many attributes of IOAA systems may serve as a vector for potential non to metamorphosed IOCG deposits. The discovery of the Southern Breccia, 1 km south of the most explored IOAA system to date in the GBMZ, further demonstrates that the GBMZ, previously recognized for its past-producing vein-type U deposits, remains significantly under-explored for other types of U deposits.

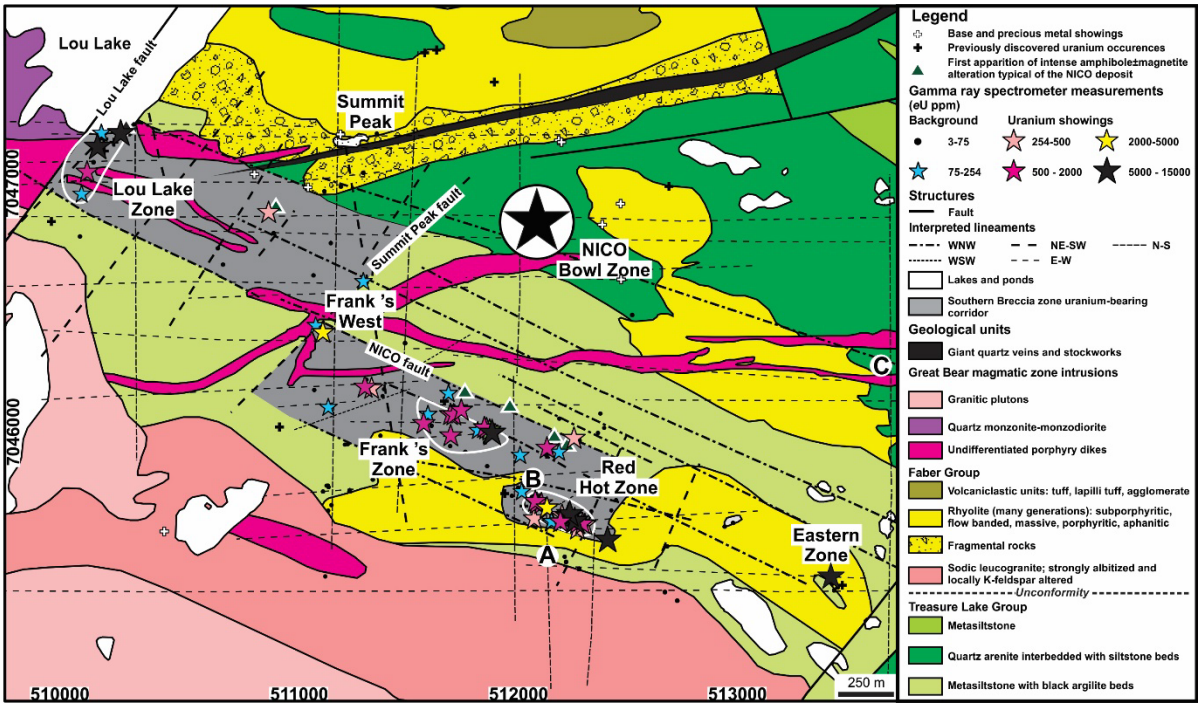

Figure 6-1 Detailed geology of the Lou IOCG system with focus on the uranium-bearing corridor of the Southern Breccia zone

Geology and mineral showings after Thomas and Olsen (1978), Gandhi and Lentz (1990), Goad et al. (2000a, b), Gandhi et al. (2014) and this work. The metasiltstone units, including layers within the quartz arenite unit are selectively to pervasively altered whereas hydrothermal alteration is milder in the quartz arenite unit though meter-scale zones of selective replacement of distinct beds and discordant alteration fronts occur

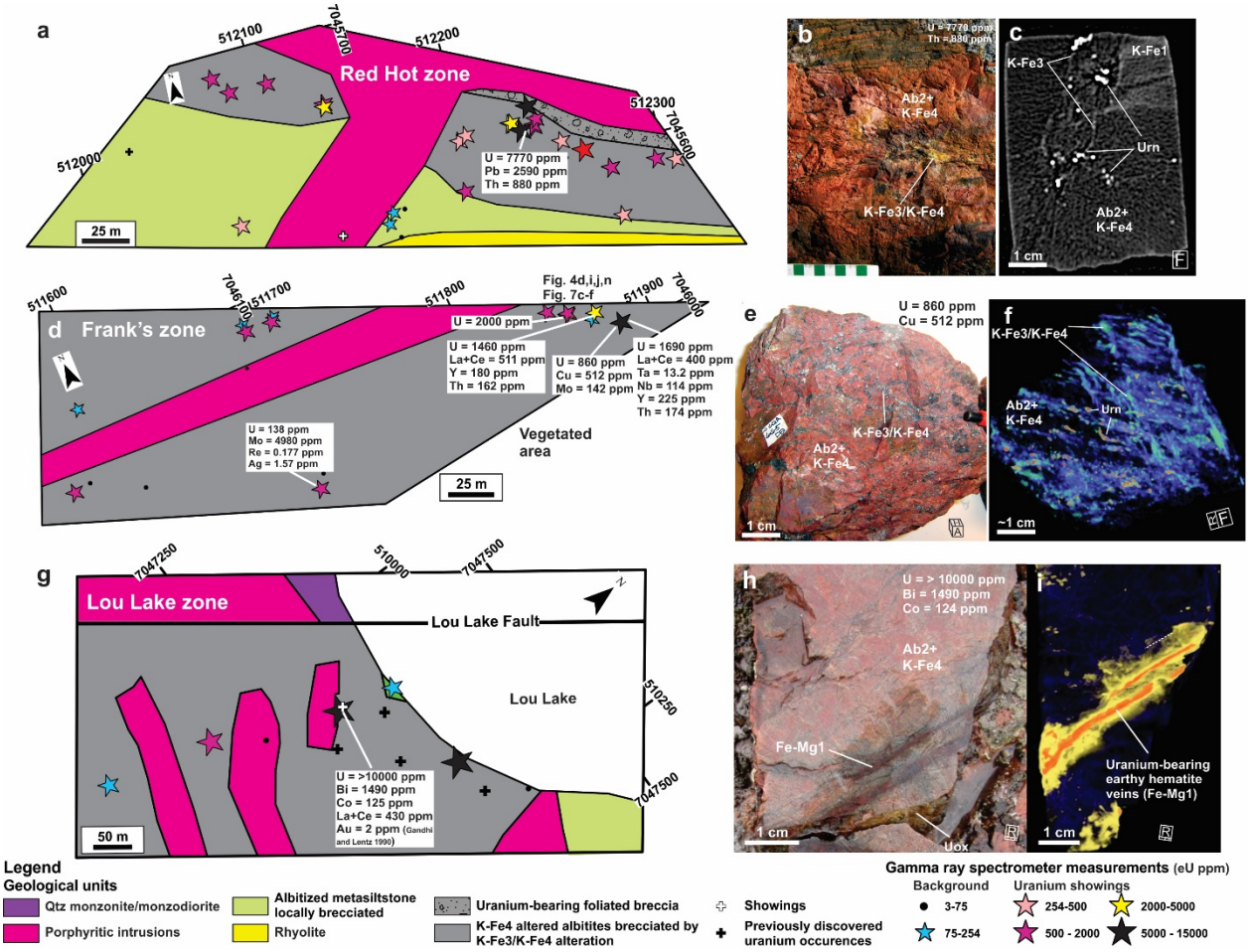

Figure 6-2 Detailed geology, selected gamma ray analyses and metal contents of the main uranium mineralization zones of the Southern Breccia

(a) Detailed geology and selected gamma-ray and whole rock metal contents of the Red Hot zone; (b) Yellow secondary uranium mineral within K–Fe3/K–Fe4-cemented crackle breccia developed in Ab2/K–Fe4-altered metasiltstone (white and green scale bar in cm); (c) CT Scan image section showing the distribution of individual uraninite grains in K–Fe3/K–Fe4 metasomatic veins. This sample is typical of the Red Hot zone uranium mineralization; (d) Detailed geology and selected gamma-ray and whole rock metal contents of the Frank's zone; (e) Polymetallic uranium mineralization associated with the K–Fe3/K–Fe4 crackle breccia developed into Ab2/K–Fe4-altered metasiltstone; (f) CT Scan image of the sample in e illustrating the 3D distribution of the individual uraninite grains (red dots) and the sulfides (green–yellow patches) in the K–Fe3/K–Fe4 veins (blue). This sample is typical of the first uranium mineralization event as seen in the Frank's zone; (g) Detailed geology and selected gamma-ray and whole rock assay numbers of the Lou Lake zone; (h) Uranium-bearing Fe–Mg1 earthy hematite vein developed into Ab2/K–Fe3-altered metasiltstone in the Lou Lake zone; and (i) CT Scan image of the sample illustrating the massive uranium mineralization (bright yellow and orange) in the Fe–Mg1 earthy hematite vein. This sample is typical of the second uranium mineralization event in the Lou Lake and Eastern zones.

The small cubes or squares on the CT Scan and samples images are at the same scale and indicate the 3D orientation of the rock when it was scanned. F stands for foot, H stands for head, A stands for anterior, R stands for right.

.

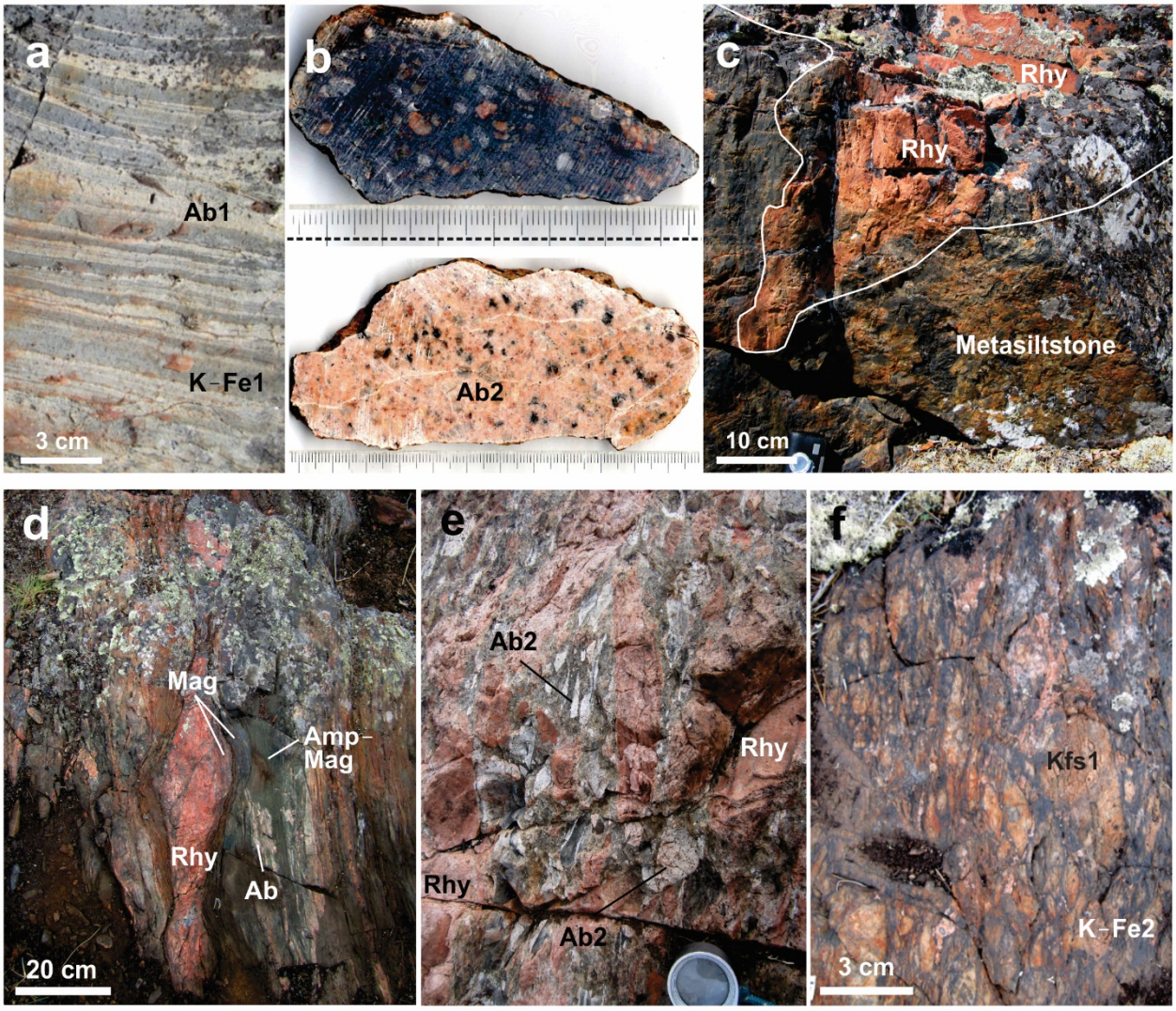

Figure 6-3 Photographs, microphotographs and BSE images of typical rock and alteration types in the Southern Breccia

(a) Selective Ab1 and K–Fe1 alteration of the TLG metasiltstone; (b) Least-altered (upper slab; GFA-89-241) and strongly albitized (lower slab; GFA-89-108) early granite samples (samples collected by Sunil Gandhi in 1989; scale bar in mm); (c) Unconformity between the Faber Group rhyolite (Rhy) and the TLG in the Southern Breccia – such differential erosion of and lack of weathering in the TLG is typical of the Southern Breccia zone; (d) Boudinaged porphyritic rhyolite dike in the WNW-oriented Peanut deformation corridor (Zone C on Fig. 6-1; extent of lichen coverage is fairly typical of the studied area). Magnetite-bearing calcic–iron alteration types typical of the NICO deposit (Mag and Amp–Mag) are also deformed but overprint the porphyritic rhyolite dike; (e) Typical tectono-hydrothermal breccia of the Zone B comprising porphyritic rhyolite and albitized (Ab2) metasiltstone fragments; (f) K–Fe2 alteration and replacement veining (i.e., replacement of damage zones and other porous channels taking the appearance of irregular veins) in the breccia of the Zone A;

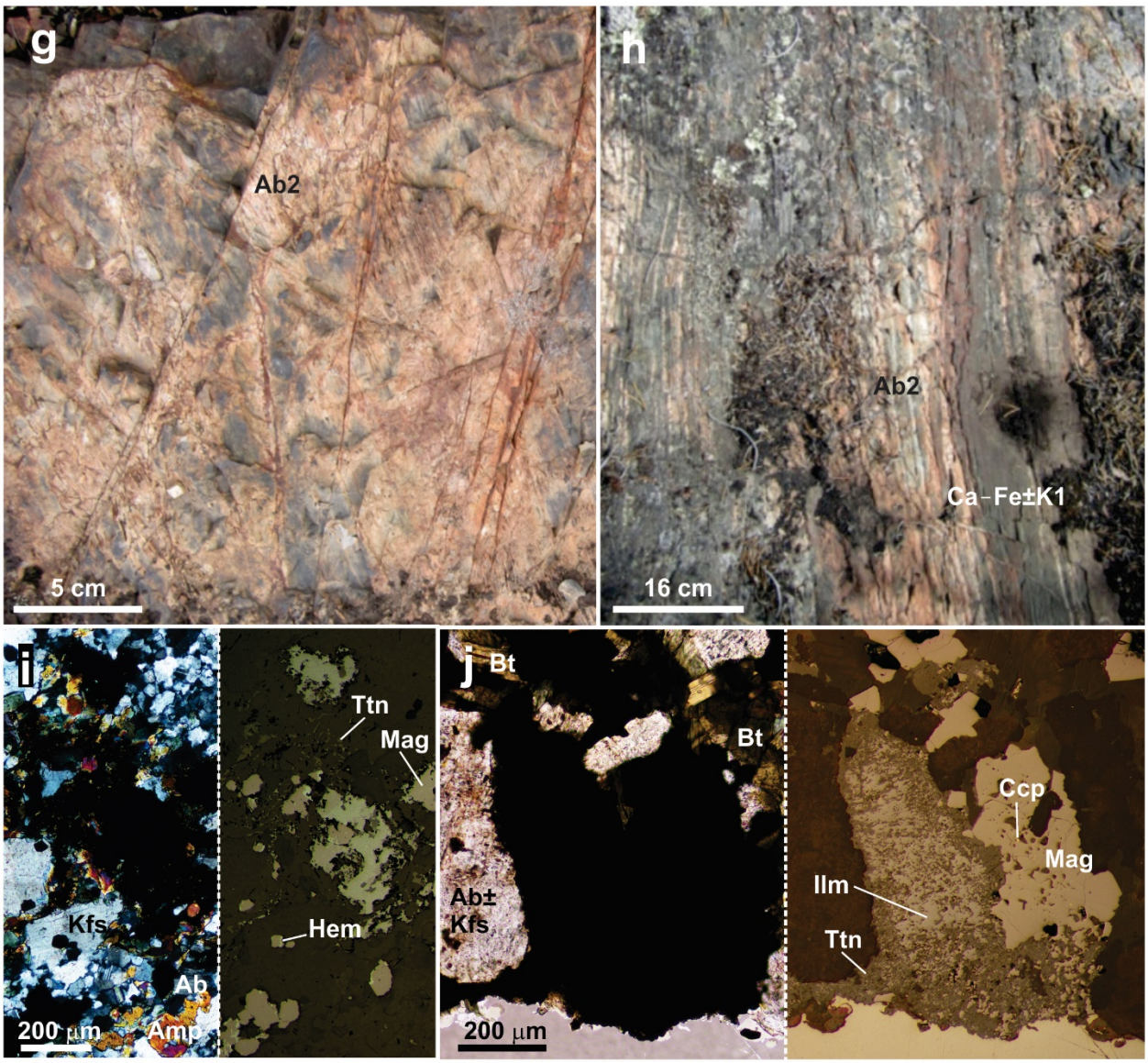

Fig. 6-3 suite – (g) Intense variegated Ab2 alteration fronts in the metasiltstone; (h) Ab2 alteration overprinted and cross cut by Ca–Fe±K1 alteration with amphibole and magnetite more typical of the NICO system; (i) Cross-polarized (left) and reflected light (right) microphotographs of Ca–Fe±K1 alteration overprint on Ab2 at the transition between the Southern Breccia and NICO system (same field of view and orientation); (j) Natural (left) and reflected light (right) microphotographs of K–Fe3 alteration illustrating coeval magnetite, ilmenite, biotite and traces of chalcopyrite as well as the retrogradation of ilmenite into titanite in association with incipient K–Fe4 overprint;

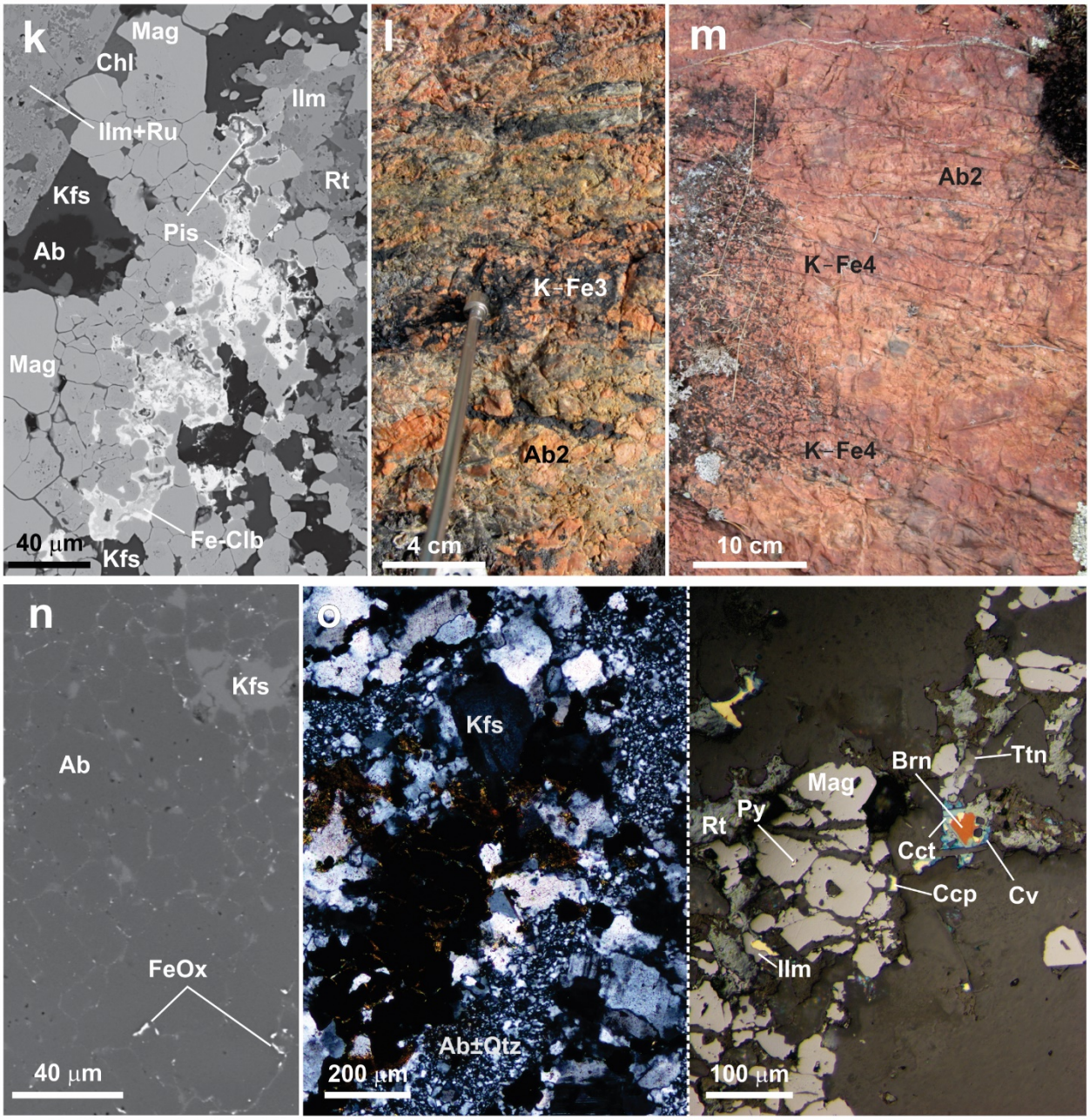

Fig. 6-3 suite – (k) Back-scattered electron image showing the typical paragenesis of a Nb-rich K–Fe3 vein overprinted by K–Fe4 that brings uranium and causes remobilization and recrystallization of the initial ferrocolumbite into uranium- and REE-bearing niobium–titanium–iron–calcium minerals; (l K–Fe3-cemented crackle breccia developed after Ab2-altered metasiltstone and overprinted by incipient variegated K–Fe4 alteration fronts; (m K–Fe4 alteration fronts and replacement veining in pervasive Ab2 alteration; (n Back-scattered electron image showing the incipient K-feldspar–iron oxide (K–Fe4 net-veining development along the albite grain boundaries (Ab2; (o Cross-polarized (left and reflected light (right microphotographs of a typical K–Fe3/K–Fe4 vein showing the following sequence of copper mineral formation: chalcopyrite → bornite → chalcocite → covellite, witnessing increasingly oxidizing conditions.

Mineral abbreviations after Whitney and Evans (2010; Col: columbite, Pis: Pisekite.

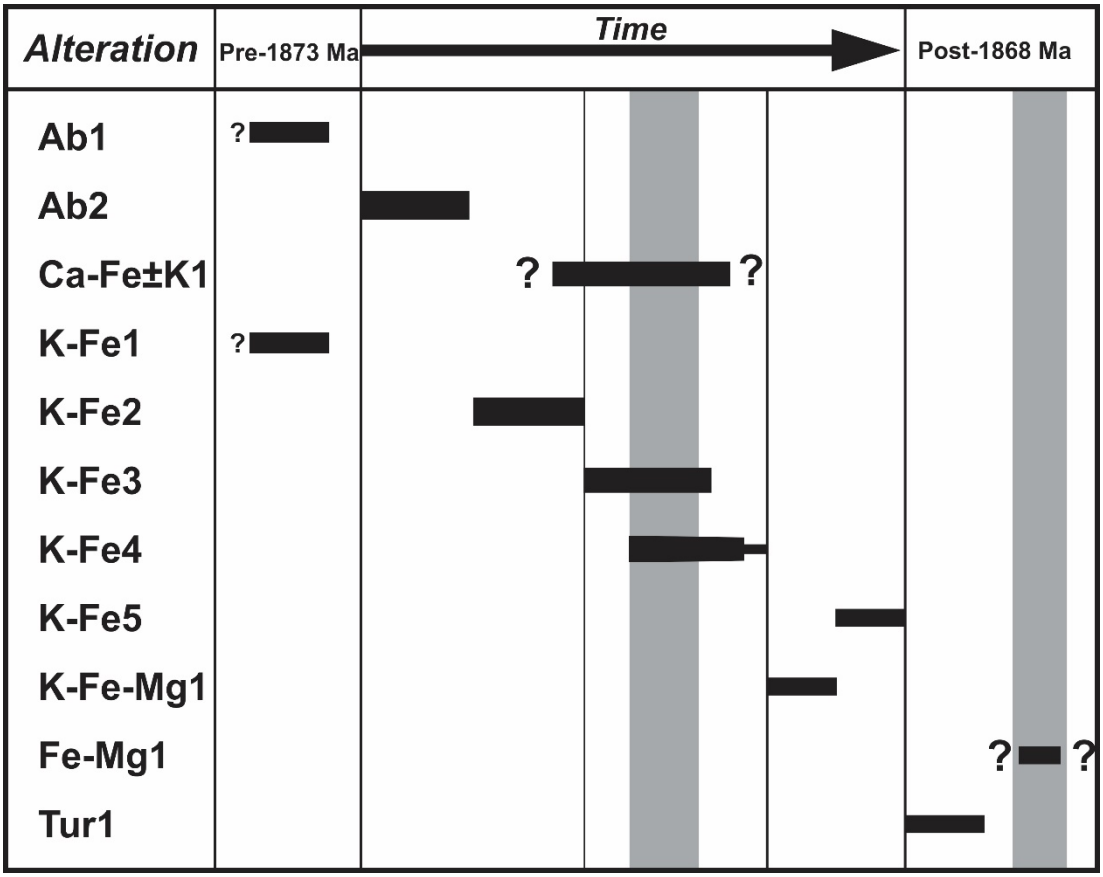

Figure 6-4 Sequence of IOAA alteration events in the Southern Breccia

Gray-shaded areas indicate the two uranium mineralization stages.

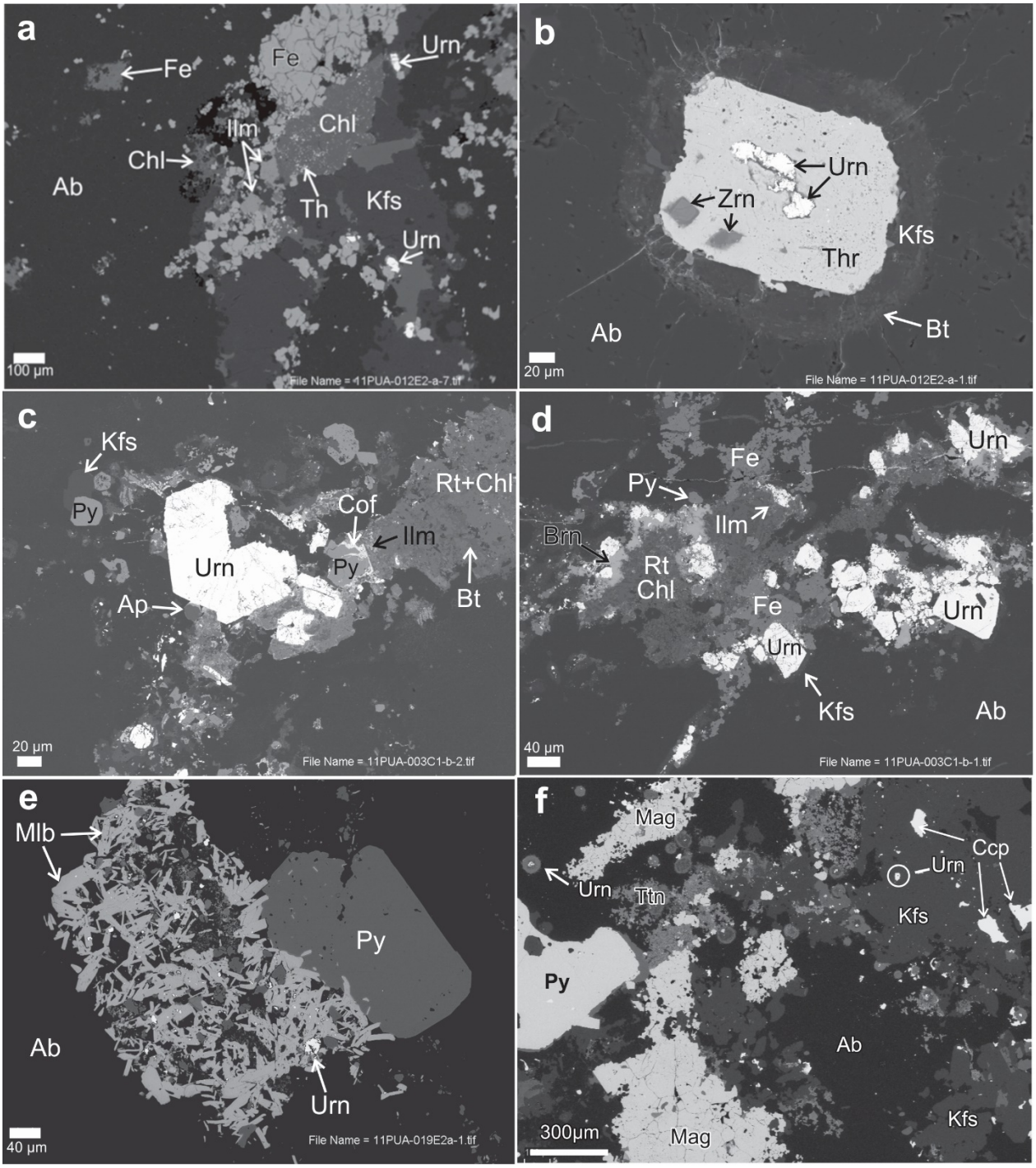

Figure 6-5 Back-scattered electron images of the Red Hot and Frank's zones uranium mineralization

(a) to (c) The Red Hot zone uranium showings related to K–Fe3/K–Fe4 alteration stages; (d) to (f) The Frank's zone main polymetallic uranium showings related to K–Fe3/K–Fe4 alteration stages.

Mineral abbreviations after Whitney and Evans (2010).

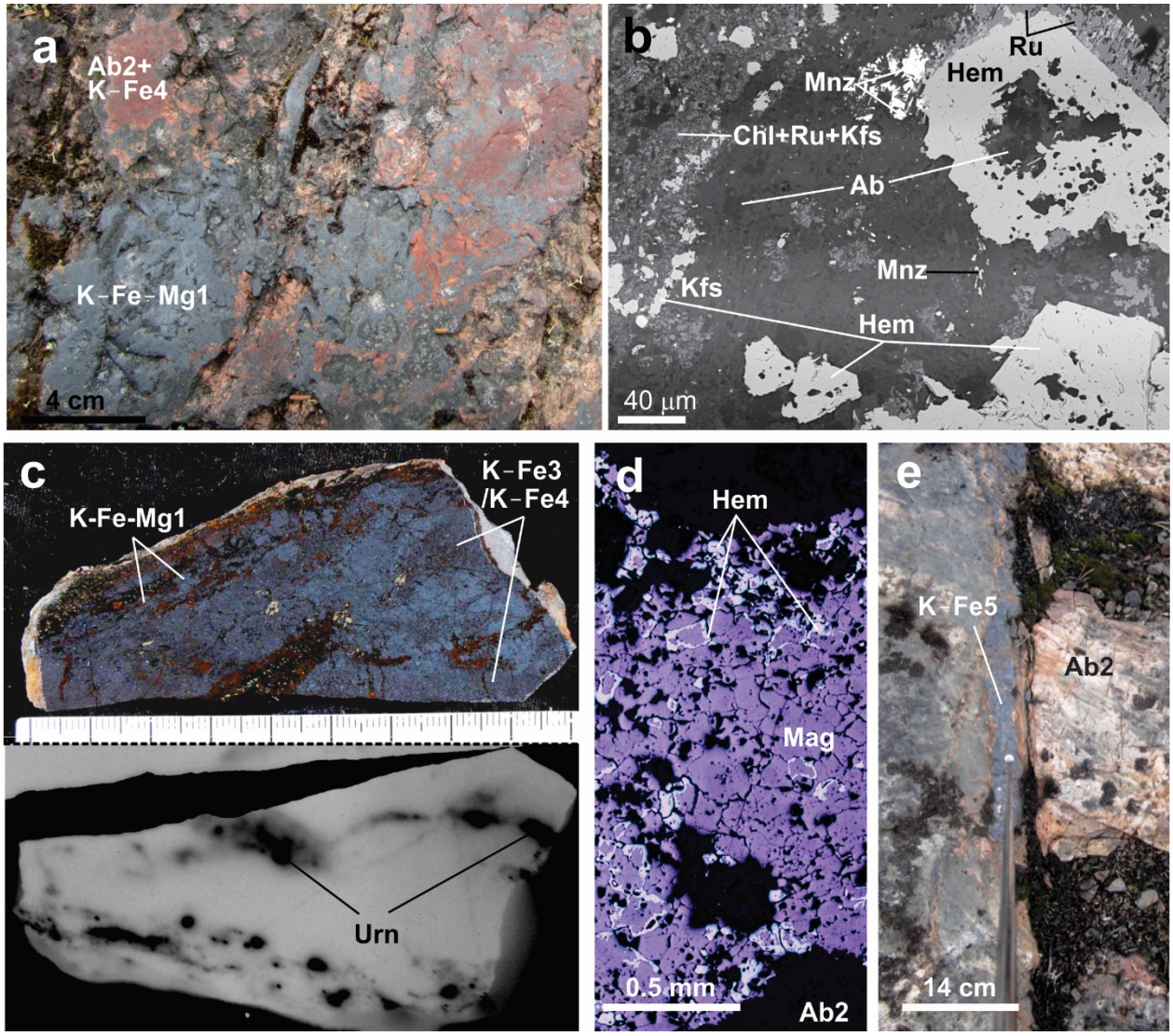

Figure 6-6 Photographs, microphotographs and back-scattered electrons images of the Southern Breccia late-stage alteration and uranium mineralization

(a) Ab2/K–Fe4-altered metasiltstone brecciated by specular hematite alteration in the Lou Lake zone (K–Fe–Mg1); (b) Back-scattered electron image showing the mineral paragenesis in the strong K–Fe–Mg1 alteration of the Lou Lake zone; (c) Rock slab natural (right) and autoradiograph (left) of a K–Fe3/K–Fe4 vein overprinted by K–Fe–Mg1 that shows the redistribution of uranium in the vein because of the Hem 1 overprint; (d) Incipient K–Fe–Mg1 overprint over the magnetite of K–Fe3 alteration in the Frank's zone; (e) –Fe5 veins cross cutting Ab2 at sharp angle;

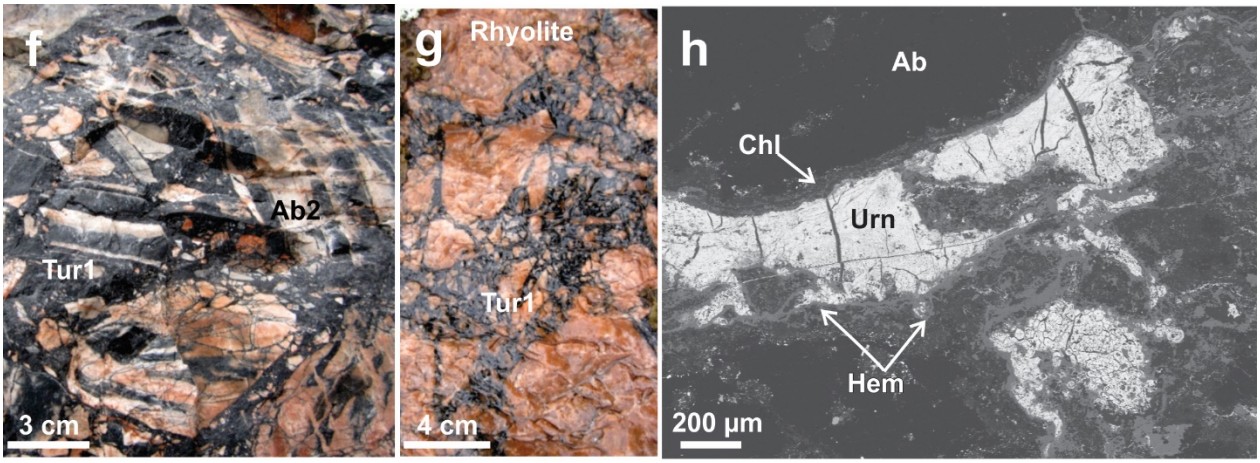

Fig. 6-6 suite – (f) Tur1-cemented breccia in the Zone B, with in situ selective replacement of TLG layering in fragments; (g) Tur1-cemented crackle breccia in the Faber Group rhyolite; (h) Back-scattered electron image of the Lou Lake zone uranium mineralization.

Mineral abbreviations after Whitney and Evans (2010.

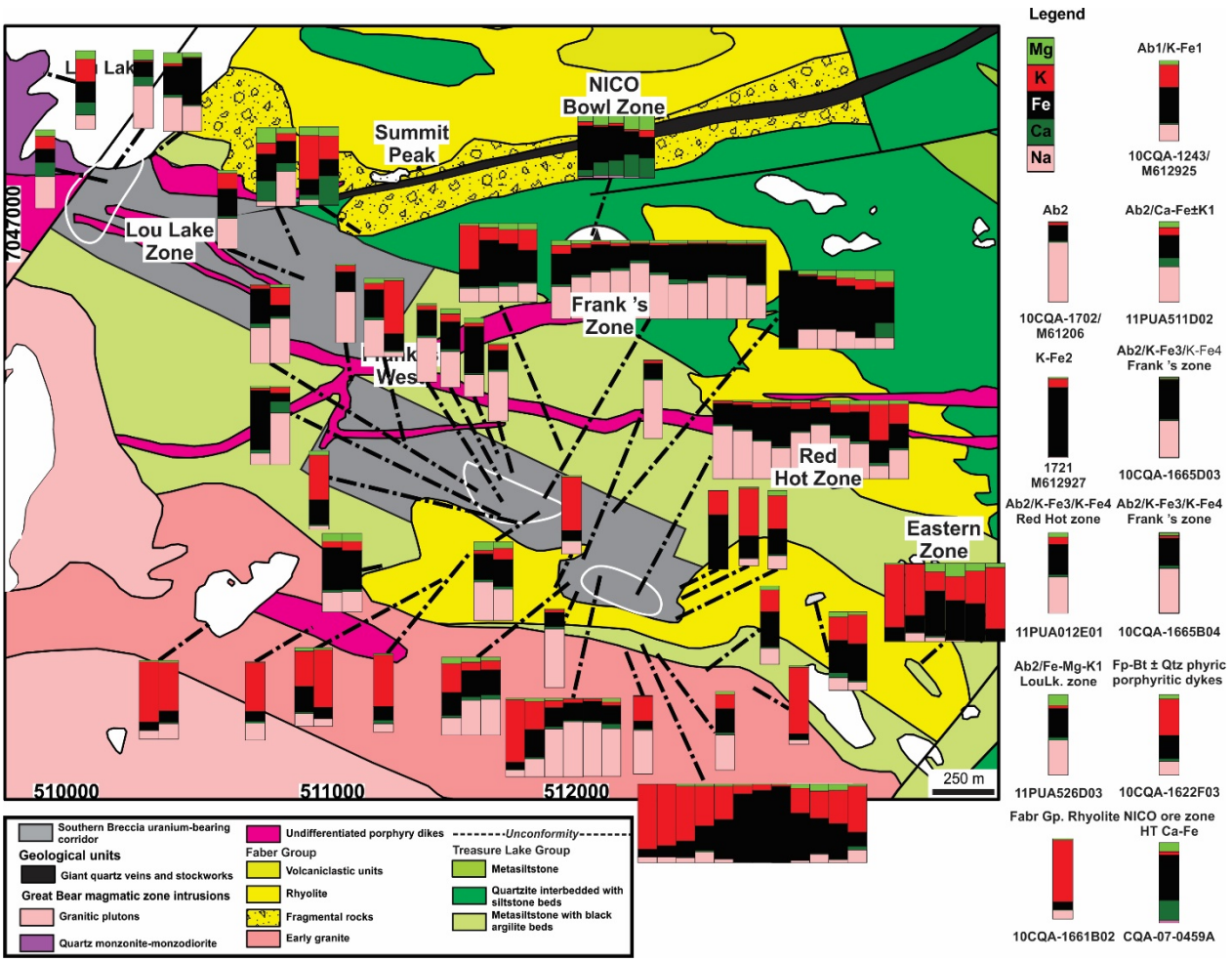

Figure 6-7 Schematized chemical map using normalized Ca, Fe, K, Na and Mg molar concentrations as a proxy for the distribution of hydrothermal alteration

Disproportions in the normalized concentrations of Ca, Fe, K, Na or Mg highlight the alteration type whereas the amplitude of the disproportions provides a semi-quantitative measurement of the alteration intensity. Typical signatures of precursor rocks and alteration types are shown at the right of the figure and examples of the NICO ore zone have been added for comparison with the Southern Breccia alteration.

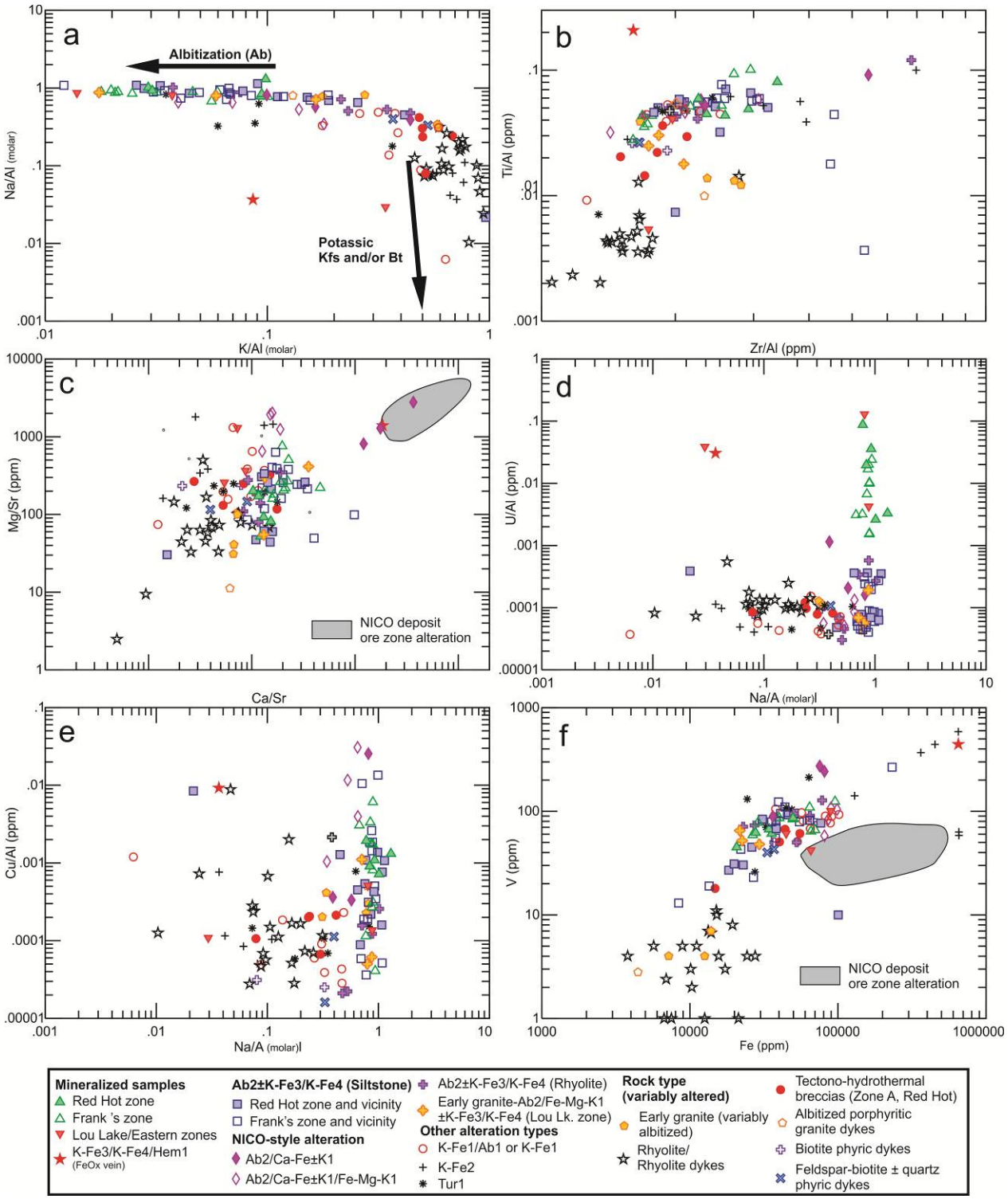

Figure 6-8 Bivariate diagrams to illustrate element variations

(a) $(Na/Al)_{(molar)}$ vs $(K/Al)_{(molar)}$; (b) Zr/Al vs Ti/Al (ppm); (c) Mg/Sr vs Ca/Sr (ppm); (d) U/Al (ppm) vs $(Na/Al)_{(molar)}$; (e) Cu/Al (ppm) vs $(Na/Al)_{(molar)}$; (f) V vs Fe (ppm)

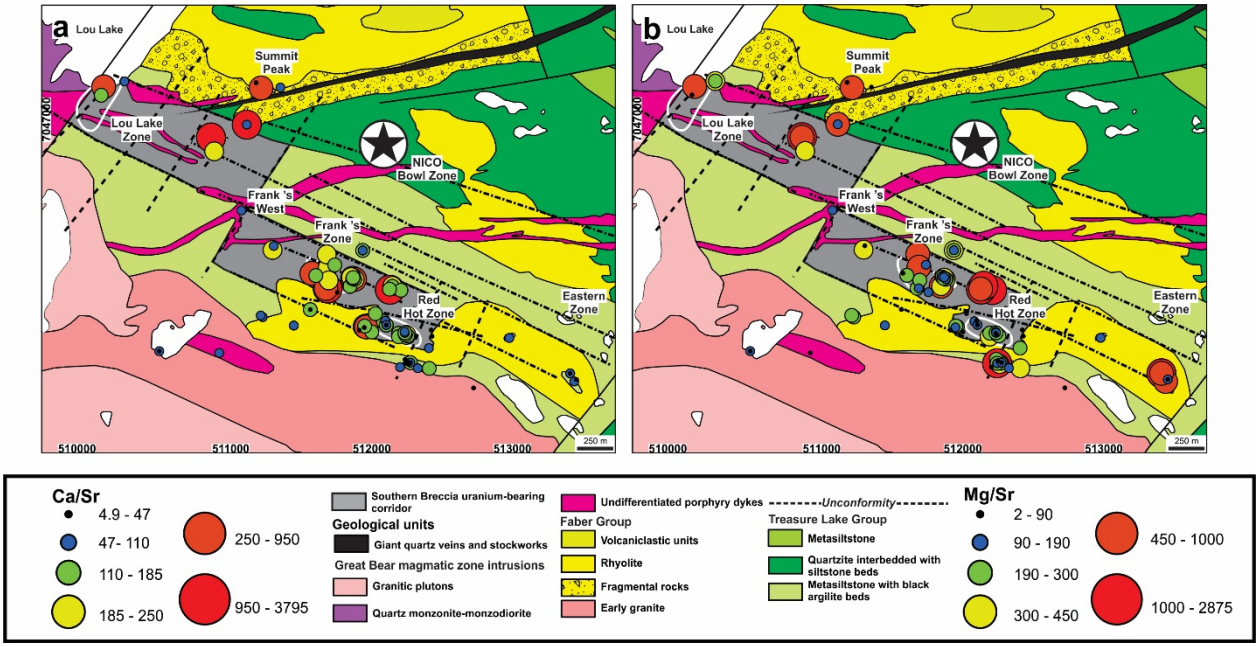

Figure 6-9 Spatial distribution in the Southern Breccia of the Ca/Sr ratios and the Mg/Sr ratios

(a) Ca/Sr ratios; (b) Mg/Sr ratios.

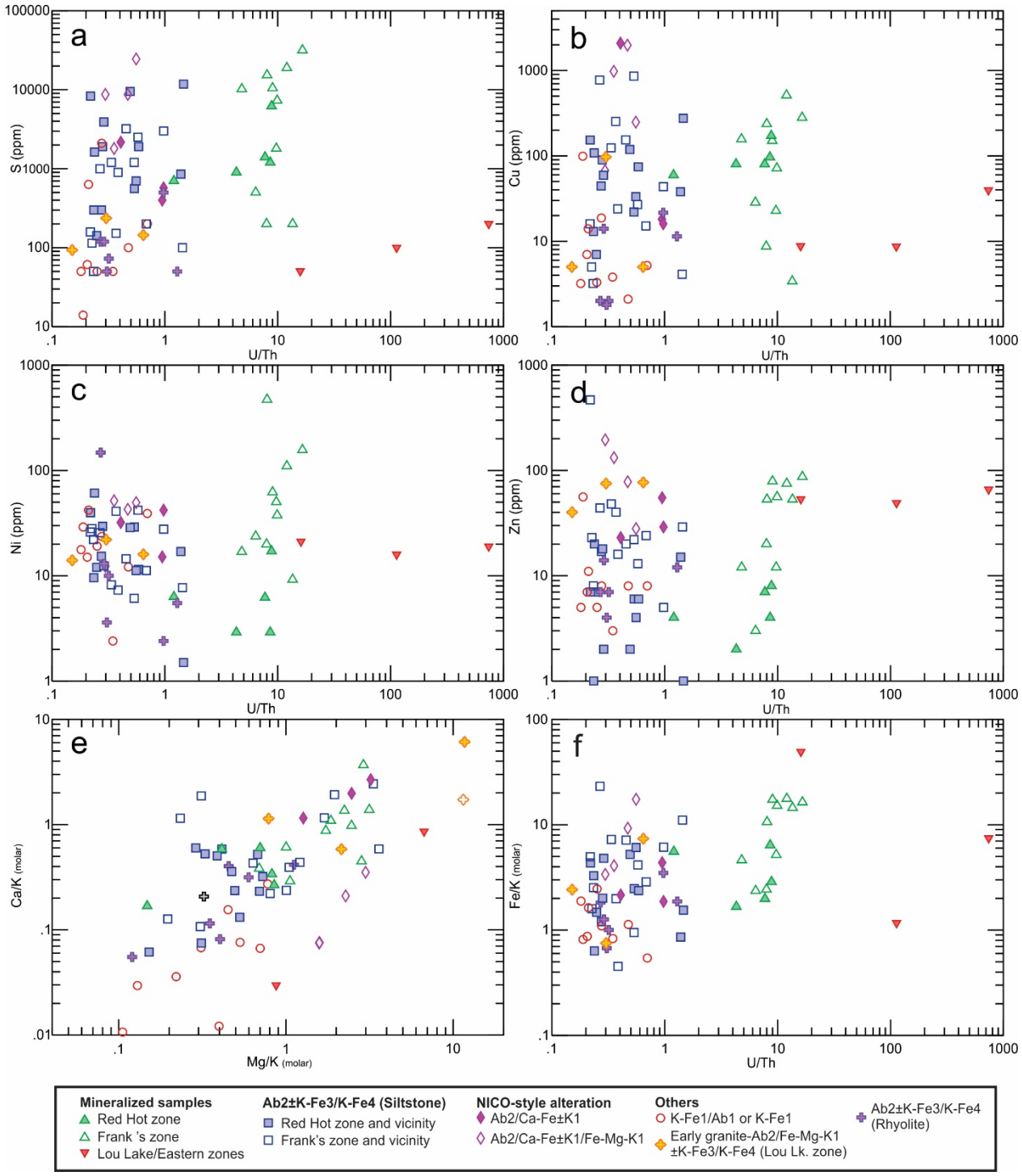

Figure 6-10 Bivariate diagrams of IOAA alteration types directly related to the Southern Breccia uranium mineralized zones

(a) S vs U/Th (ppm); (b) Cu vs U/Th (ppm); (c) Ni vs U/Th (ppm); (d) Zn vs U/Th (ppm); (e) $(Ca/K)_{(molar)}$ vs $(Mg/K)_{(molar)}$; (f) $(Fe/K)_{(molar)}$ vs U/Th (ppm).

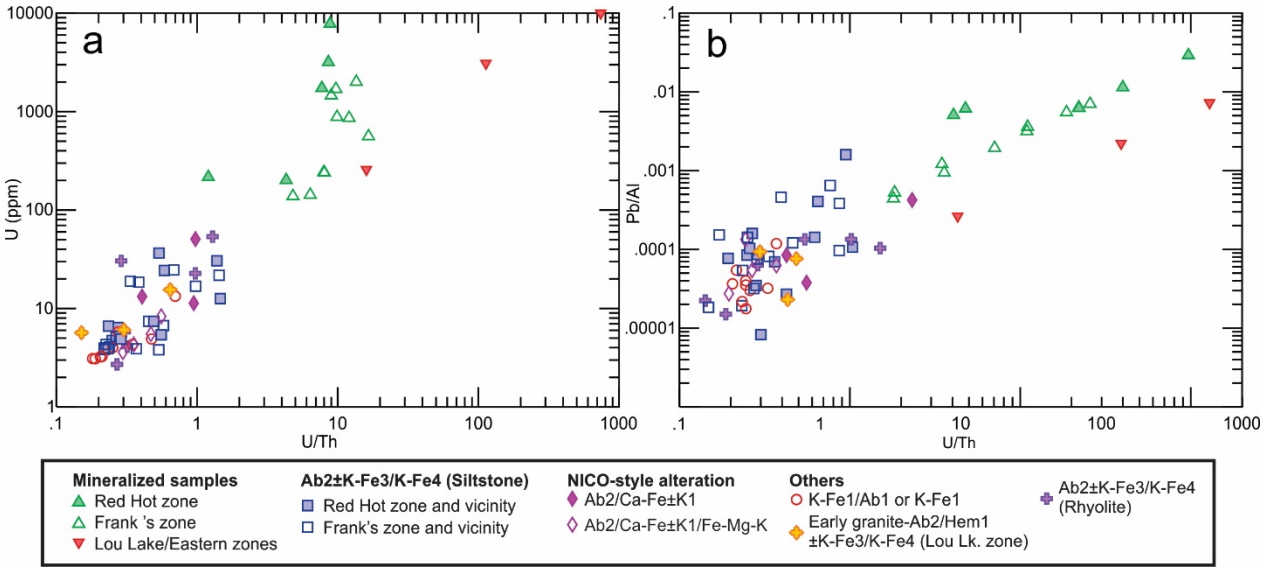

Figure 6-11 Bivariate diagrams of IOAA alteration types directly related to the Southern Breccia uranium mineralized zones

(a) Ce+La vs U/Th (ppm); (b) Y vs U/Th (ppm); (c) U vs U/Th (ppm); (d) Pb/Al vs (U+Th)/Al (ppm).

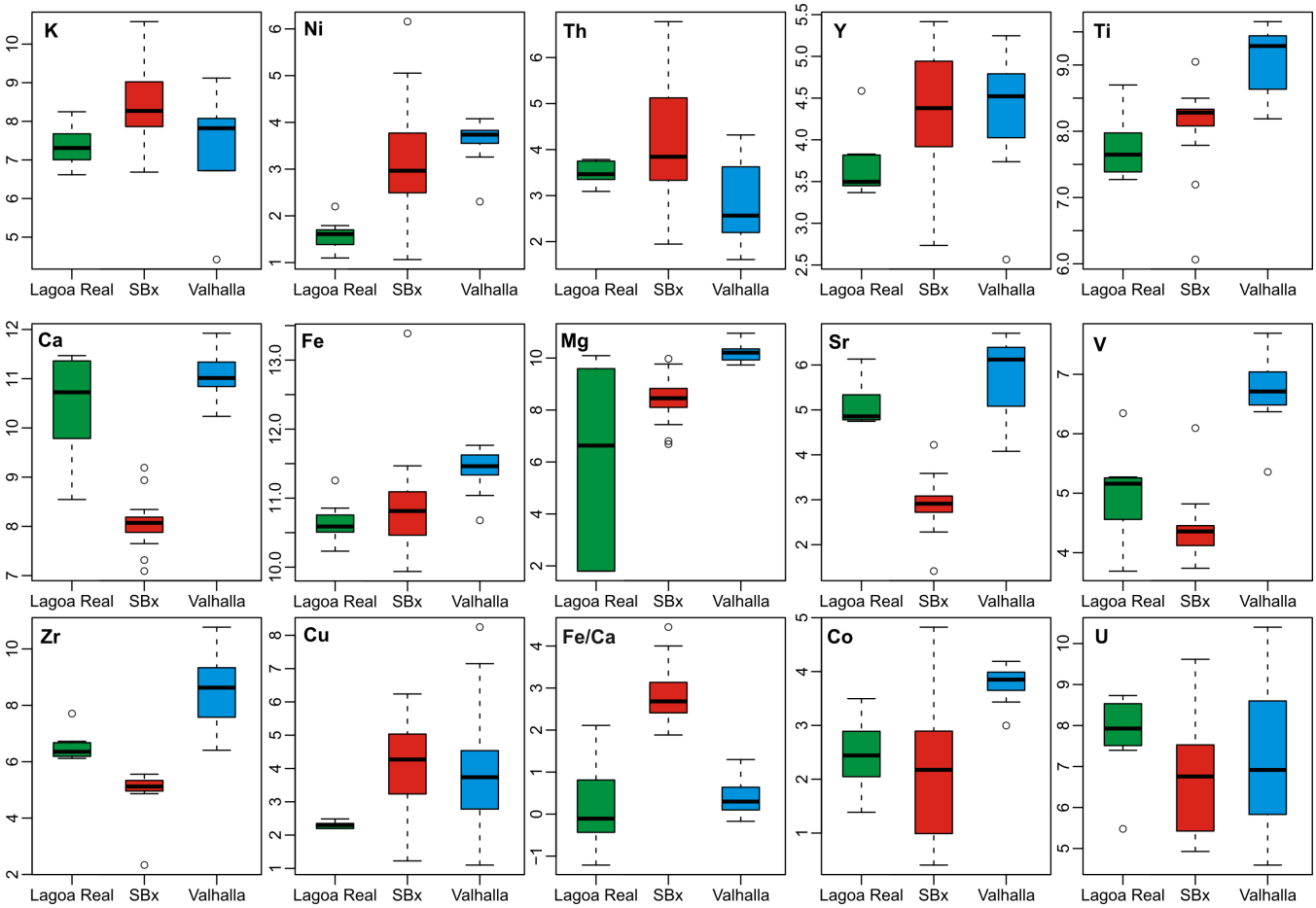

Figure 6-12 Boxplot diagrams to show the compositional differences and similarities between the Southern Breccia, Lagoa Real and Valhalla albitite-hosted uranium systems

Units are log(concentration) in ppm for each element. Each division of the box plot represent a quartile of the element analyses and dots are outliers to the general population.

SBx=Southern Breccia.

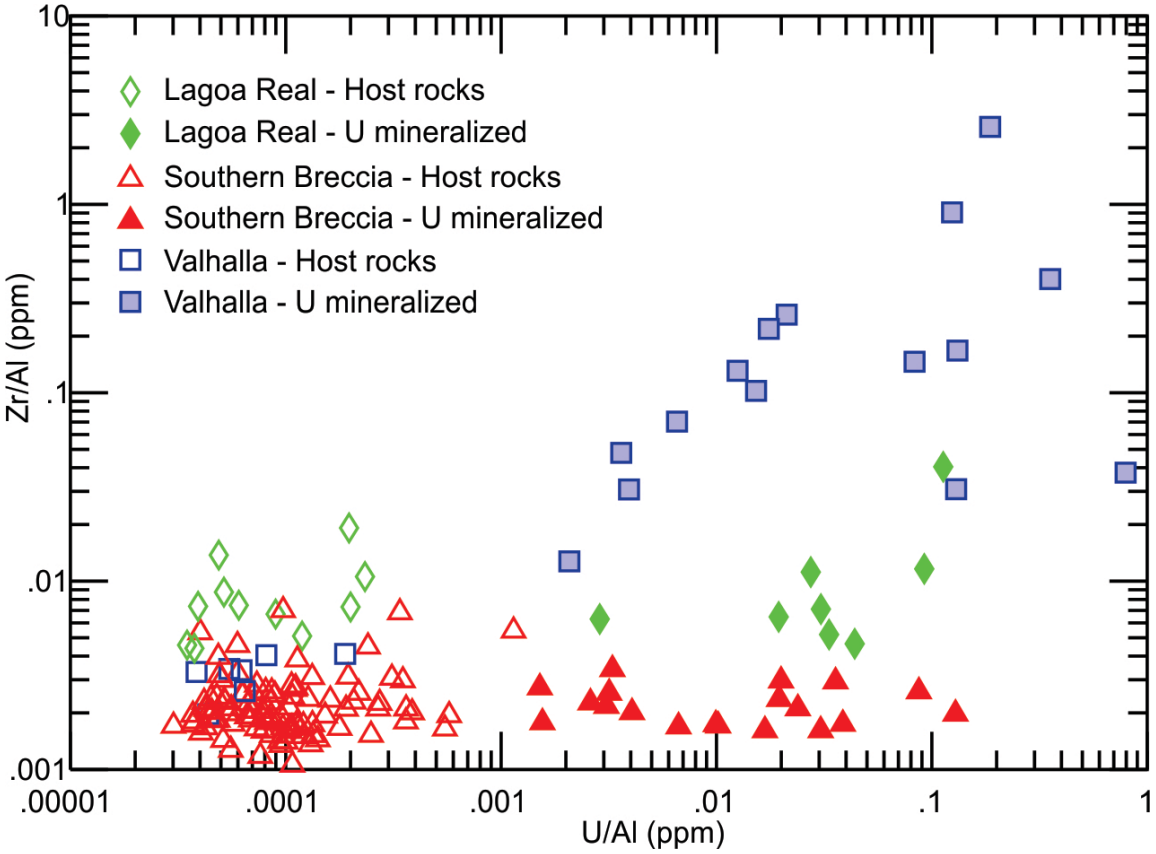

Figure 6-13 Bivariate diagram of U/Al vs Zr/Al for Lagoa Real, the Southern Breccia and Valhalla

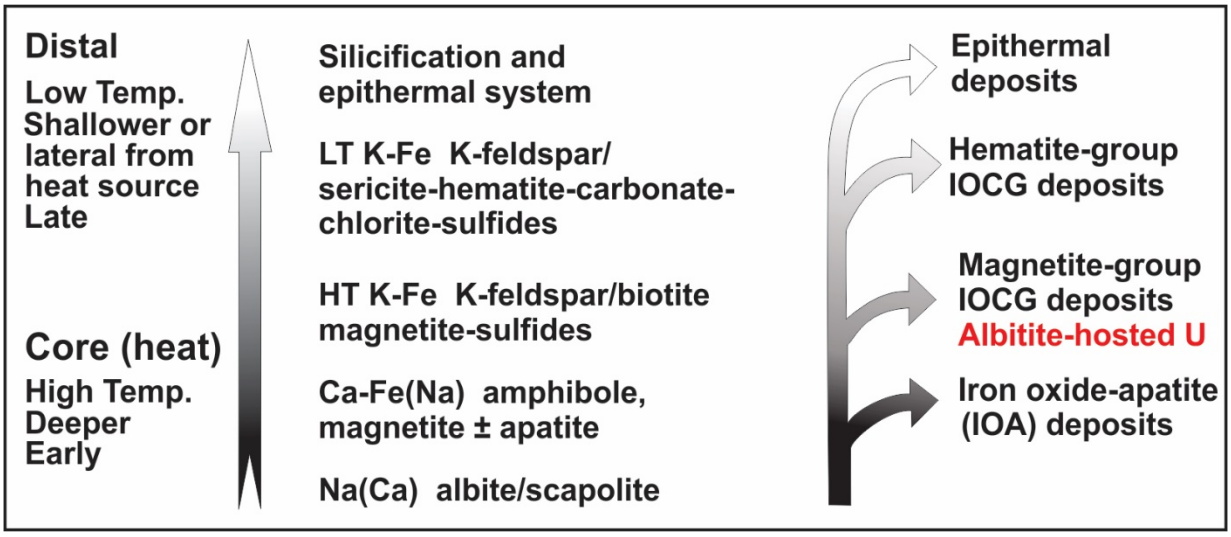

Figure 6-14 Albitite-hosted uranium mineralization within the alteration zoning model of Corriveau et al. (2010b)

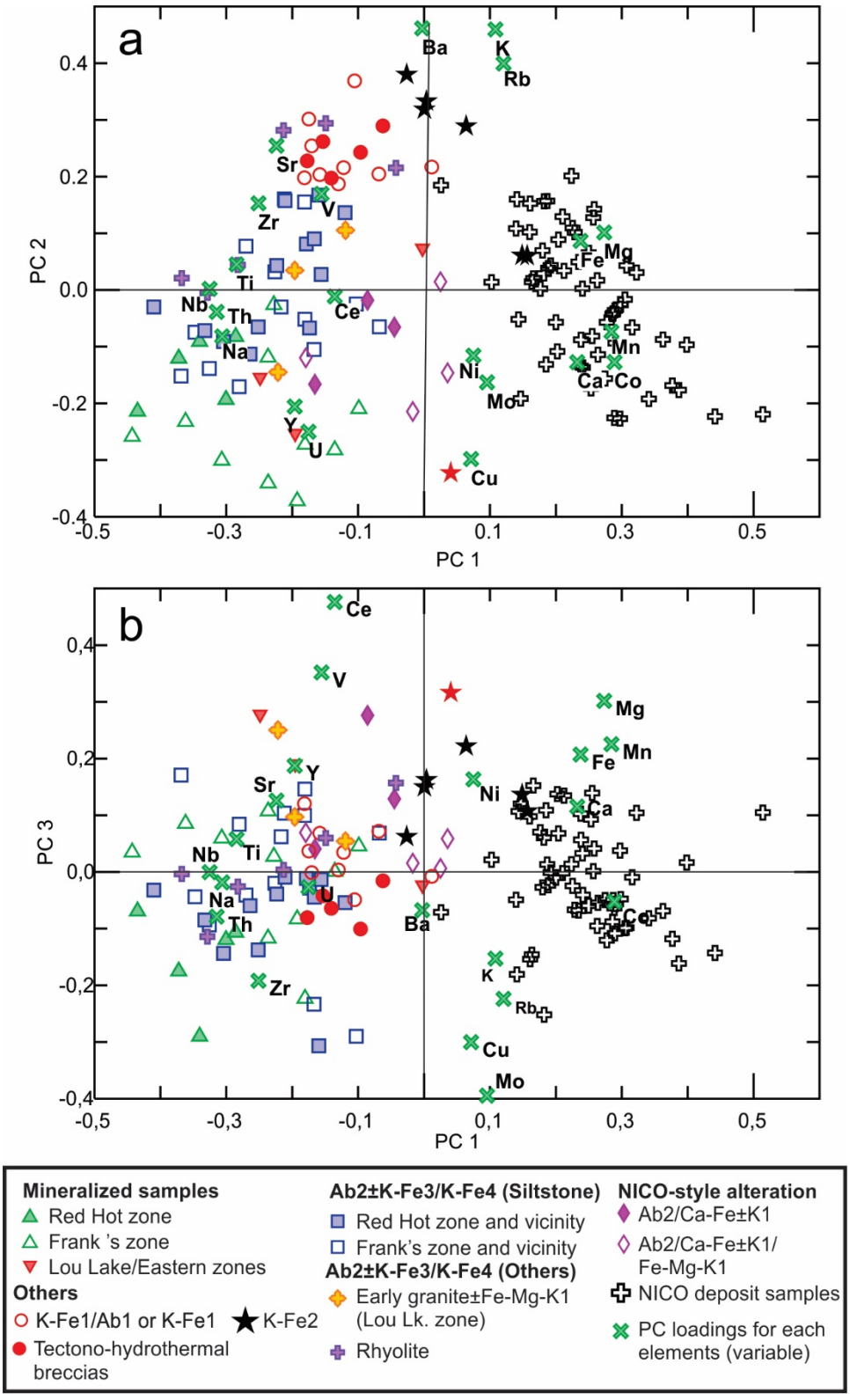

Figure 6-15 Principal component analysis contrasting the geochemical signature of the NICO deposit and the Southern Breccia

(a) PC1 vs PC2; (b) PC1 vs PC3

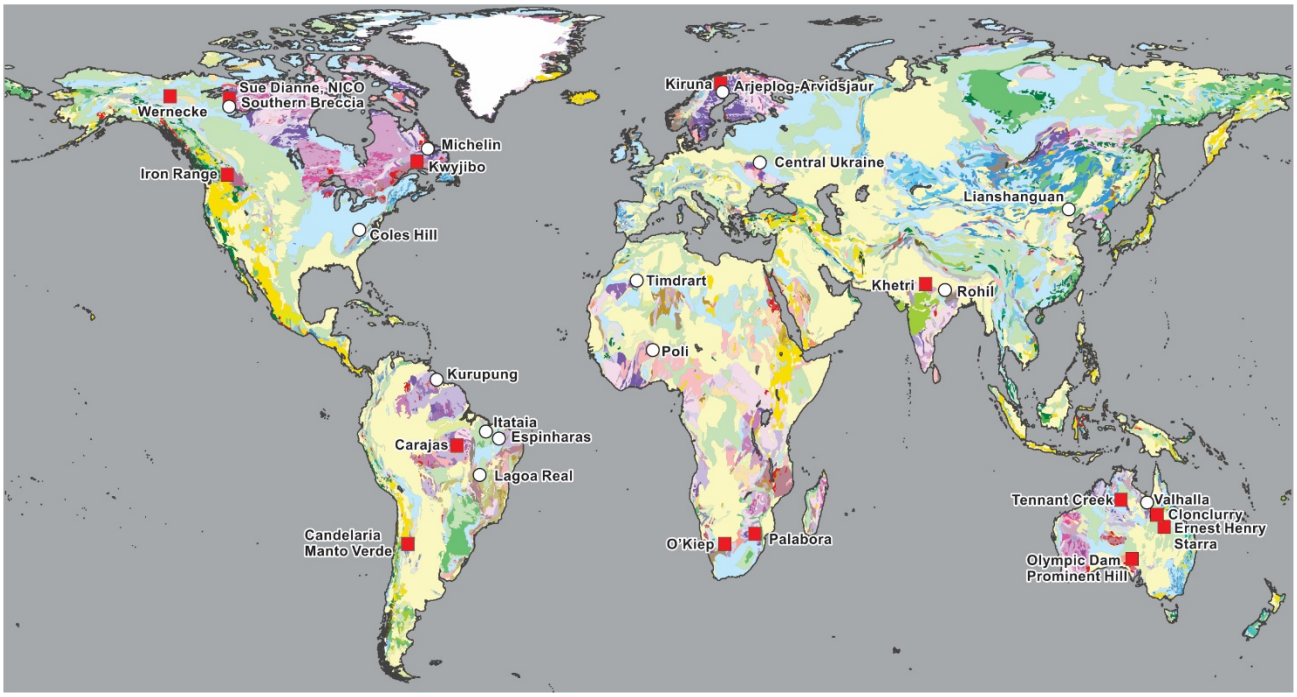

Figure 6-16 Location of selected IOCG/IOAA systems (red squares) and albitite-hosted uranium systems (white circles)

Geology from Chorlton (2007) and deposit/district locations from Cuney et al. (2012) and Corriveau (2007) .

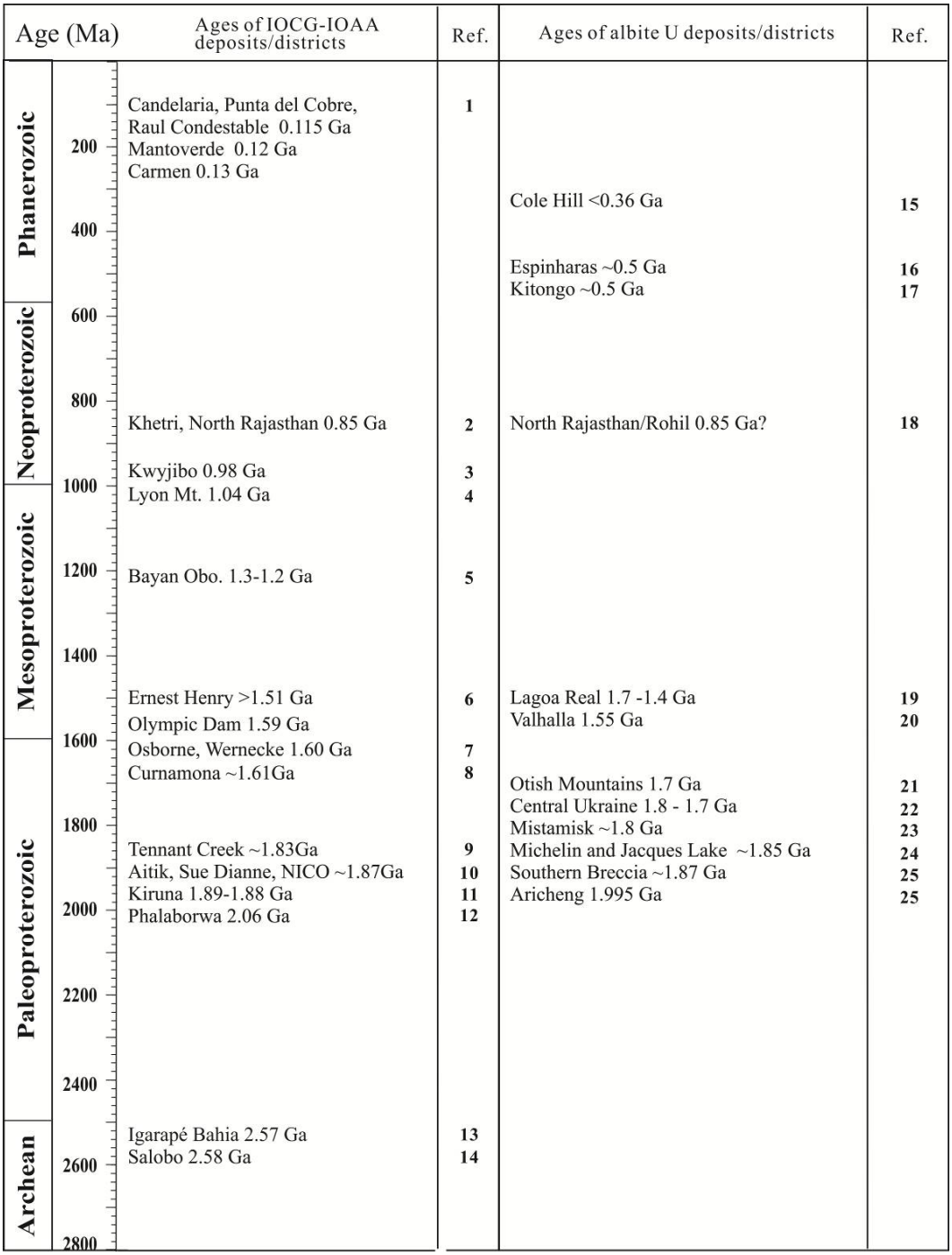

1 - Vila et al., 1996; ,Marschik et al., 1997, Mathur et al., 2002, Gelcich et al., 2005, de Haller et al., 2006; 2 - Knight et al., 2002; 3 - Gauthier et al., 2004; 4 - Selleck et al., 2004; 5 - Yang et al., 2003; 6 - Mark et al., 2000; 7 - Gauthier et al., 2001, Thorkelson et al., 2001; 8 - Williams and Skirrow, 2000; 9 - Skirrow, 2000; 10 - Gandhi et al., 2001, Wanhainen et al., 2003; 11 - Romer et al., 1994; 12 - Harmer, 2000; 13 - Tallarico et al., 2004; 14 - Requia et al., 2003; 15 - Jerden, 2001; 16 Ballhorn et al., 1981; Porto de Silveira et al., 1991; 17 - Vels and Fritsche, 1988; 18 - Yadav et al., 2010, Chaki et al., 2011 ; 19 -Chaves et al., 2010; Cordani et al., 1992; Turpin et al., 1988; 20 - Polito et al., 2009; 21 - Ruhlman et al., 1986; 22 - Cuney et al., 2012 and references therein; 23 - Kish and Cuney, 1981; 24 - Sparkes and Kerr, 2008; 25 - this study; 26 - Alexandre, 2010.

Figure 6-17 Temporal distribution of the major IOCG/IOAA systems and of the major albitite-hosted uranium systems

CHAPITRE 7 : ELEMENT MOBILITY AND HYDROTHERMAL ALTERATION DISTRIBUTION DURING THE DEVELOPMENT OF THE MAGNETITE-GROUP FAB IOCG SYSTEM, NORTHWEST TERRITORIES, CANADA

Mobilité des éléments et distribution de l'altération hydrothermale lors du développement du système IOCG du groupe à magnétite de Fab, Territoires du Nord-Ouest, Canada

[1]Montreuil, J.-F., [2]Potter, E.G., [3]Corriveau, L., [2]Davis, W.J.

[1]Institut National de la Recherche Scientifique – Eau-Terre-Environnement

[2]Commission Géologique du Canada, division Ottawa

[3]Commission Géologique du Canada, division Québec

Publié par «*Ore Geology Reviews*», v. 72, p. 562–584.

Abstract: This paper documents element mobility patterns from a magnetite-group Iron Oxide Copper–Gold (IOCG) showing in the Northwest Territories of Canada and explores implications for space–time chemical evolution of Iron Oxide Alkali-Altered (IOAA) systems. The Fab system, located in the Great Bear magmatic zone (GBMZ) of the Northwest Territories, Canada, contains numerous Fe–Cu–U showings associated with high temperature (HT) potassic–iron alteration overprinting extensive zones of sodic to HT calcic–iron alteration. Each hydrothermal alteration assemblage is associated with distinct element mobility patterns that record evolving physico-chemical properties of the hydrothermal fluids. New geochronological data constrain IOAA alteration and IOCG mineralization in the Fab system to a 3 m.y. window between 1870–1867 Ma, which is broadly contemporaneous with extensive high-level intrusive activity across the GBMZ. Regional- to local-scale element mobility patterns characteristic of the sodic and sodic–calcic–iron alteration type record leaching combined with weak to strong mass losses. Mass and volume losses were inferred to be compensated by porosity creation during pervasive host rock dissolution and precipitation of the alteration assemblages. Pure sodic alteration depleted the rocks in Ca, Co, Cu, Fe, Mg, Th, U and V. Conversely, sodic–calcic–iron alteration records significant depletions of Nb, REE, Ta, Ti, Th and U. These element mobility patterns differ from intense HT calcic–iron alteration that is enriched in Ca, Co, F, Fe, Mg, Mn, Ni and V with modest enrichments to locally significant mineralization in Th, U and REE. HT calcic–iron alteration is also characterized by substantial mass gains that translate into volume gains in stockwork zones and mass/volume gains in zones of intense host rock replacement. HT potassic–iron alteration is characterized by enrichments in Ba, K, Ni, U and V, along with locally Co and Cu. The temporal and spatial association of the Fab IOAA alteration and the emplacement of the porphyritic dacite are indicative of the predominant involvement of magmatic-hydrothermal fluids. The high F- and Cl- contents of the porphyritic dacite and of the HT calcic–iron alteration zones as well as Nb, REE, Ta, Th, and Ti mobility provide strong evidences of high halogen activities (F and Cl) in the hydrothermal fluids. High F- and Cl-activities in the hydrothermal fluid are interpreted to have facilitated the mobilization of normally immobile (Nb, Ta, Ti, Th) or weakly mobile elements as well as some metals (e.g., V, Ni, Co). The formation of REE fluorocarbonates and calcite in the early and incipient HT calcic–iron alteration zones indicates the presence of CO_2 in the hydrothermal fluids. Weaker HFSE, HREE and Ti mobility during later HT potassic–iron alteration is interpreted to reflect decreasing temperatures, pressures, F- and Cl-activities and increasing fO_2 as the fluids evolved and interacted with the host rocks.

Résumé: Cet article documente la mobilité des éléments dans un système à oxydes de fer–cuivre–or (IOCG) aux Territoires du Nord-Ouest et explore les implications sur l'évolution chimique dans l'espace et le temps d'un système hydrothermal à oxydes de fer et altération en éléments alcalins (IOAA). Le système de Fab, situé dans la Zone magmatique du Grand lac de l'Ours (GBMZ), contient plusieurs indices à Fe–Cu–U reliés à une altération haute température (HT) potassique–fer surimposée sur des zones d'altération sodique et HT calcique–fer. Chaque type altération est relié à des patrons de mobilité des éléments distincts reflétant des conditions physico-chimiques pour les fluides hydrothermaux impliqués en constante évolution. De nouveaux âges U–Pb mesurés dans des zircons magmatiques de différentes intrusions porphyriques du système de Fab contraignent l'altération IOAA et les minéralisations IOCG dans une fenêtre temporelle de 3 millions d'années, entre 1870–1867 Ma. L'altération sodique et sodique–calcique–fer est un stade de lessivage associé à une perte de masse faible à importante dans les roches altérées. Cette perte de masse, considérant un volume constant, est associée à la création de porosité dans les altérations résultantes. Des appauvrissements en Ca, Co, Cu, Fe, Mg, Th, U et V caractérisent l'altération sodique tandis que des appauvrissements en Nb, éléments du groupe des terres rares (ÉTR), Ta, Ti, Th et U caractérisent l'altération sodique–calcique–fer. L'altération HT calcique–fer est plutôt associée à des enrichissements importants en Ca, Co, F, Fe, Mg, Mn, Ni et V, des enrichissements modérés à localement important en Th, U et ÉTR et des appauvrissements marqués en Ba, K, Rb et Sr. Des veines avec paragenèse d'altération de HT calcique–fer se distinguent également par des gains de volume/masse importants dans les zones de stockworks entourant les zones de remplacements d'altération HT calcique–fer intenses caractérisées par des gains importants de masse et volume. Des enrichissements en Ba, K, Ni, U et V, combinés à des enrichissements locaux en Co et Cu, caractérisent l'altération HT potassique–fer. L'association spatiale et temporelle des zones d'altération IOAA du système de Fab avec une intrusion porphyrique dacitique sont compatibles avec une prépondérance de fluides magmatiques-hydrothermaux dans la formation du système de Fab. La concentration importante en F et Cl dans l'intrusion porphyrique dacitique et les zones d'altération HT calcique–fer ainsi que la mobilité de Nb, ÉTR, Ta, Th, et Ti dans les altérations sodique, sodique–calcique–fer et HT calcique–fer indiquent une activité importante de F et Cl dans les fluides hydrothermaux. La formation de calcite et de fluorocarbonates de ÉTR dans les zones d'altération HT calcique–fer précoces et de faible intensité suggèrent la présence de CO_2 dans les fluides hydrothermaux. La mobilité décroissante des ÉTR, de Nb, Ta, Ti et Th au stade d'altération HT potassique–fer est

indicative d'une activité décroissante de F associée à une diminution de la température, de la pression et de plusieurs autres ligands (p. ex. $PO4^{3-}$, CO_2), d'une augmentation de fO_2.

7.1 Introduction

Mineralogical and chemical alteration footprints of hydrothermal ore deposits reflect, in part, ore-forming processes and are used by the mineral exploration industry to vector towards ore zones (e.g., Ishikawa, 1976; Franklin, 1997). Iron Oxide Alkali-Altered (IOAA) hydrothermal systems (Porter, 2010), in which polymetallic Iron Oxide Copper–Gold (IOCG) deposits can form (Groves et al., 2010; Williams, 2010a), have the largest alteration footprints among all known types of hydrothermal systems, typically transforming precursor rocks over several hundred square kilometers (Hitzman et al., 1992; Porter, 2010; Corriveau and Mumin, 2010). Where intense, alteration leads to significant and diagnostic modification of rock composition regardless of the protolith (Oliver et al., 2004; Benavides et al., 2008a; chapitre 5). The systemic spatial and temporal distribution of alteration is constrained within numerous alteration zonation models for both magmatic and non-magmatic end-members (Hitzman et al., 1992; Barton and Johnson, 2000; Williams et al., 2005; Corriveau et al., 2010b; Mumin et al., 2010; Porter, 2010; Richards and Mumin, 2013).

The Paleoproterozoic Great Bear magmatic zone (GBMZ), located at the northwestern margin of the Canadian Shield (Fig. 1-2), hosts a wide variety of polymetallic occurrences and IOAA systems (Hildebrand, 1986; Goad et al., 2000a; Corriveau et al., 2010a; Mumin et al., 2010). The Fab system, located in the south central GBMZ (Fig. 1-2), was selected to investigate the effects of IOAA-related hydrothermal alteration on element mobility because of its relative simplicity, good exposure and restricted spatial extent. In addition, all of the characteristic alteration types of IOAA systems are represented and are hosted within the same porphyritic dacite intrusion, including least-altered zones that enable mass balance analysis using the Grant (1986, 2005) simplified approach of the Gresens' equations (Gresens, 1967). This approach is precluded in most of the GBMZ IOAA systems (chapitre 5) because of the wide variety of precursor rocks and the difficulties in finding least-altered units across regional metasomatic footprints (Mumin et al., 2010; Corriveau et al., 2010a, b).

At Fab, the regional IOAA alteration envelope comprises high temperature (HT) calcic–iron and sodic alteration types (Gandhi, 1988; Corriveau et al., 2010a, b; Acosta et al., 2011; Potter et al., 2013b). The Fe–Cu–U mineralization is coeval with hydrothermal breccia formation during HT potassic–iron alteration. The resulting alteration and metallic signatures for the showings are typical of magnetite-group IOCG mineralization based on the classification of Williams (2010a).

In this paper, we review the geological setting of the Fab system and constrain element mobility that is associated with the main alteration stages as a case example of the geochemical processes involved in the evolution of an IOAA system hosting magnetite-group IOCG mineralized zones. This study aims to increase the predictive lithogeochemical capabilities of alteration evolution models by explaining the multiple metallic assemblages developed in IOAA systems, complementing previous work by Perring et al. (2000), Pollard (2001), Oliver et al. (2004), Benavides et al. (2008a) and chapitre 5. This element mobility study is supported by new alteration and geological maps, an extensive geochemical and geological database and new geochronological data gathered under the Geo-mapping for Energy and Minerals (GEM) program of Natural Resources Canada (Jackson, 2008; Potter et al., 2013b; Gandhi et al., 2014; Corriveau et al., 2015).

7.2 Geological setting

The porphyritic dacite intrusion that hosts most of the Fab IOAA system is part of a series of undifferentiated shoshonitic to high-K calc-alkaline porphyritic intrusions (herein called the Fab porphyry complex; Azar, 2007) that form the northernmost extension of the Faber Group. The Faber Group is the southern component of the McTavish Supergroup that comprises all of the GBMZ volcanic sequences and porphyritic intrusions and is the principal host for many of the southern GBMZ IOCG deposits and showings (Fig.1-2; e.g., Sue-Dianne, Brooke, Mar, Nod; Hitzman et al., 1992; Gandhi, 1994; Goad et al., 2000a; Camier, 2002; Mumin et al., 2010). The Faber Group volcanism (1873–1866 Ma) occurred concurrently with the development of an Andean-type continental margin at the western extremity of the Wopmay orogen (1.87–1.84 Ga) and has been subdivided into five main assemblages termed the Lou, Cole, Hump, Mazenod and Bea (Hildebrand et al., 1987, 2010a; Gandhi et al., 2001, 2014; Ootes et al., 2010). Within the Faber Group, the Fab porphyry complex was interpreted as a transitional sequence that marks the evolution from the rhyolitic Lou Lake to the rhyodacitic Mazenod Lake assemblages (Gandhi et al., 2001). The Faber Group unconformably overlies the Treasure Lake Group sequences (ca. 1.88 Ga) that are preserved across the southern GBMZ and form the uppermost sequence of the composite ca. 2.4 to 1.9 Ga Hottah terrane, which is the basement to the GBMZ (Bowring, 1984; Gandhi et al., 2001; Gandhi and van Breemen, 2005; Davis et al., 2011).

The Faber Group is also linked to the formation of the 33 Mt Au–Co–Bi NICO deposit and the Southern Breccia albitite-hosted polymetallic U showings, both of which occur along an

unconformity between the Faber Group and an underlying metasedimentary sequence (Treasure Lake Group; Goad et al., 2000; Mumin et al., 2010; Corriveau et al., 2010a, 2011; chapters 4, 6). The Fab porphyry complex comprises a wide variety of porphyritic intrusions with aphanitic to phaneritic groundmass that includes: porphyritic dacitic intrusive rocks referred to as the dacite intrusion, porphyritic monzonite, amphibole–magnetite-bearing porphyritic monzodiorite and undivided porphyries (Figs. 7-1, 7-2). The porphyritic dacite intrusion occurs as an elongate intrusive body on the northwest and northeast shores of Fab Lake and is bisected by two fault sets that also cut the IOAA alteration envelope of the Fab system (Figs. 7-1, 7-2a). The first fault set is oriented north-south and defines the orientation of Fab Lake and the second fault set has a ~045° orientation and offsets geological contacts and IOAA alteration on both shorelines of Fab Lake. In its least-altered zones, the porphyritic dacite intrusion is characterized by fine- to medium-grained plagioclase phenocrysts set in an aphanitic mesocratic groundmass and is grey-pink in color on weathered surfaces (Gandhi 1988; this work). Trace amounts of amphibole phenocrysts are also typically present. The fine- to medium-grained plagioclase phenocrysts are generally destroyed with increasing hydrothermal alteration and the aphanitic matrix becomes bright pink with increasing potassic alteration, whitish to light pink with increasing sodic alteration or dark-green with increasing HT calcic–iron alteration. In thin section, the least-altered porphyritic dacite intrusion comprises 25 modal percent euhedral to subhedral plagioclase phenocrysts (oligoclase and andesine) with sporadic K-feldspar and quartz phenocrysts and aggregates of variably chloritized amphibole and clinopyroxene phenocrysts (Gandhi, 1988). The phenocrysts are set in a fine-grained to microcrystalline groundmass rich in felsic (saussuritized feldspar and quartz) minerals and disseminated iron oxides, zircon and apatite.

The porphyritic monzonite intrusion borders the porphyritic dacite intrusion and has coarse-grained plagioclase and K-feldspar phenocrysts in a proportion of 3:1 to 2:1 hosted within a bright pink and fine-grained groundmass. At regional scales, this unit is transitional to the amphibole–magnetite-bearing porphyritic monzodiorite, in which groundmass mineral phases and K-feldspar phenocrysts are replaced by amphibole + magnetite ± apatite ± biotite clots. To the north and east, the Fab porphyry complex is bordered by the composite ca. 1866 Ma Great Bear batholith and to the south and west it is bordered by the 1856 +2/-3 Ma Faber Lake rapakivi granite (Gandhi et al., 2001). Within the Fab porphyry complex, two feldspar phyric and meter-wide monzonite dikes and 1858.2 ± 6.1 Ma coarse-grained granitic bodies intrude the porphyritic dacite (Figs. 7-2, 7-3; Azar, 2007). As the dikes and granitic intrusions are devoid of

visible IOAA alteration, they are interpreted to mark the younger age limit of the IOAA systems (Potter et al., 2013b).

Exposed mineralization within the Fab Lake system occurs as nine mineral showings located primarily along the eastern shoreline of Fab Lake. The occurrences are characterized by magnetite-cemented hydrothermal crackle breccias developed in tension fractures or within extensive amphibole + magnetite-bearing replacement fronts and K-feldspar + magnetite alteration zones. Gandhi (1988) was the first to note similarities between these occurrences and the Sue Dianne IOCG deposit, laying the groundwork for recognition of an IOCG district in the GBMZ. In the Fab prospects, chalcopyrite is the main Cu-bearing mineral and U is mostly hosted in fine-grained uraninite that is variably altered to coffinite. Accessories minerals include titanite, ilmenite, fluorapatite, pyrite, scheelite, thorite and fluorite (Gandhi 1988; De Toni, 2016; this study). Historical (1969–1977) exploration trenching and sampling across widths of 0.75 to 1.50 m yielded grades of 0.010–0.065% U and 0.01–0.13% Cu with minor Zn and trace Au (Morris, 1977). Mineralized grab samples from bedrock collected during this study returned values of 227–3,010 ppm U, 36.8–95.7 ppm Th, 665 ppm Cu and 5.44–14.05 % Fe (Potter et al., 2013b).

7.3 Methods

7.3.1 Alteration mapping protocol and sampling

For each alteration type, the style, mineral paragenesis and timing relationships with the other alteration types and host rocks were documented, sampled and photographed. Measurements of %K, *e*Th (ppm) and *e*U (ppm) by portable gamma-ray spectrometers (Radiation Solutions Inc. RS-230 spectrometer) and volumetric magnetic susceptibility measurements by portable magnetic susceptibility meters (ZH instruments SM-30, Terraplus KT-10 and Terraplus KT-9) supported field recognition of mild and typically cryptic HT potassic–iron, HT calcic–iron and sodic alteration. The prefix "*e*" (i.e., *e*Th or *e*U) denotes that U and Th concentrations are determined indirectly from their daughter products (Bi^{214} and Tl^{208} respectively), assumed to be in equilibrium with their parent isotopes.

7.3.2 Analytical methods

All of the targeted rock types, alteration and breccia zones sampled for geochemistry were carefully selected during fieldwork to avoid heterogeneities such as veins or overprinting alteration. This protocol minimizes the superimposition of different alteration types, isolates the geochemistry of the targeted alteration assemblages and thus permits interpretation of element mobility and alteration processes. Each of the accompanying hand samples were then stained by cobaltnitrate (Bailey and Stevens, 1960) to highlight any cryptic potassic–iron, potassic and sodic alteration that may have been missed during fieldwork and petrography.

Table 7-1 Representative *e*U and *e*Th gamma-ray spectrometer measurements of the main alteration types of the Fab IOAA system compared to the ICP-MS measurements of U and Th

Sample	Lithology	eU	U (ICP)	eTh	Th (ICP)
09CQA-1158	HT potassic-iron alteration	32.2	49.9	38.4	12.8
10CQA-0187	U-rich HT potassic-iron alteration	331	439	49.9	23
10CQA-0192	K alteration	12.4	10.5	45.6	26
10CQA-0192	Th-rich HT calcic-iron alteration	23.3	23.7	144	26.7
10CQA-0562	U-rich HT potassic-iron alteration	3811	711	448	36.8
10CQA-0566	U-rich HT potassic-iron alteration	444	298	66.4	39.6
10CQA-0579	Incipient HT calcic-iron alteration	12.5	8.84	26.5	39.3
10CQA-1250	Weakly altered dacitic porphyry	11.8	11.5	42.2	42
10CQA-1258	Intense sodic alteration	3.8	2.6	11.8	46
11PUA031	Incipient HT calcic-iron alteration	9.5	6.8	30.8	172

The samples were pulverized using agate and low-chrome steel ball mill and were analyzed by inductively coupled plasma mass spectrometry (ICP-MS) for trace elements and atomic emission spectroscopy (ICP-AES) for major and some trace elements after lithium metaborate fusion at INRS–ETE in Quebec City for the Fab samples that were collected between 2006 and 2010. For samples collected during the 2010 and 2011 field seasons, geochemical analyses for major elements, base metals, U and Th were performed at ALS Minerals (Vancouver, Canada) using the procedure ME-MS61u, whereas trace elements and REE were analyzed using method ME-MS81u. The procedure ME-MS61u combines ICP-MS and ICP-AES analysis following a four acid digestion designed to digest any refractory minerals in U-rich ore, whereas the MS-MS81u procedure combines lithium metaborate fusion with ICP-MS analysis. Halogens (Cl and F) were analyzed for representative samples of each alteration type. Some of the Cl and F analyses were done at the Geological Survey of Canada in Ottawa by Dionex ion chromatography. Additional Cl analyses were completed using instrumental neutron activation at Becquerel Laboratories (method Cl-NAA06) in Toronto and supplementary F analyses were

acquired using fusion-S.I.E., techniques at ALS Minerals (method F-ELE81a) in Vancouver (Canada). International reference materials, blind standards and duplicates were used to confirm the reproducibility of the analyses provided by the various laboratories and techniques (see Corriveau et al. 2015 for the chemical analyses and the quality assurance/quality check protocols). The descriptions of the analyzed material are provided in Appendix 7. Representative chemical analyses used for this contribution are presented in Appendix 7 and in Corriveau et al. (2015).

7.3.3 U-Pb geochronological analyses

Heavy mineral concentrates were prepared by standard techniques (crushing, grinding, Wilfley™ table, and heavy liquids), and sorted by magnetic susceptibility using a Frantz™ isodynamic separator. Individual crystals were selected under a binocular microscope to avoid inclusions, spiked with a mixed ^{205}Pb-^{233}U-^{235}U tracer solution calibrated to ± 0.1% against a gravimetric solution, and dissolved in high-pressure bombs in HF-HNO_3. All zircon fractions were prepared using the annealing and chemical leaching technique (CA-TIMS) modified from that described by Mattinson (2005). Samples were annealed at 1000°C for 48 hours and then leached for 12–20 hours in HF-HNO_3 at 180°C in 3 ml Savillex PFA capsules within a Parr digestion vessel. Isotopic and U-Pb compositional data were determined by isotope dilution thermal ionization mass spectrometry (TIMS) at the Geological Survey of Canada geochronology laboratory. Additional details pertaining to sample dissolution and chemical methods are described in Parrish et al. (1987). Data reduction and error propagation follow methods outlined in Roddick (1987).

Uranium and Pb isotopic ratios were measured using a Triton mass spectrometer operated in either static multi-collection mode or using a secondary electron multiplier and ion counting system. The ^{205}Pb, ^{206}Pb, ^{207}Pb, and ^{208}Pb isotopes were measured simultaneously in Faraday collectors, with ^{204}Pb in an axial secondary electron multiplier. Faraday-multiplier gain was monitored and corrected by peak jumping ^{205}Pb into the axial cup. A Pb mass fractionation correction of 0.10 ± 0.04 %/amu was applied as determined by replicate analyses of the NBS981 standard (Appendix 7). Uranium fractionation was corrected using the ^{233}U-^{235}U double spike and is typically in the range of 0.12 %/amu. Deadtime for the ion counting system was determined by replicate analyses of the NBS982 solution. Accuracy and reproducibility of the ion counting measurements were monitored by analyses of the GSC standard 6266 with a $^{206}Pb/^{238}U$ ratio of 0.09063.

7.3.4 Alteration zonation models and nomenclature

Hydrothermal alteration in metasomatic systems that host IOCG deposits generally follows a typical evolutionary trend and depth to surface zoning profile (Hitzman et al., 1992; Williams, 1999; Williams et al., 2005) that was found to be applicable to the metasomatic systems of the Great Bear magmatic zone (Corriveau et al. 2010b). In addition, excellent field exposure, systematic development and crosscutting relationships among the various alteration types within all systems studied allowed to expand the zoning model in order to firm up genetic linkages in the development of IOCG and affiliated deposits within iron oxide and alkali alteration systems (Corriveau et al., 2010b). To simplify the nomenclature of the diagnostic alteration types and encompass the wide variations in their hydrothermal mineral assemblages, each alteration type is named according to the critical cations that define the major minerals that typically composed the set of similar mineral assemblages. The alteration types noted at the Fab system are characteristic of metasomatic systems hosting IOCG deposits. Based on detailed field observations and petrography (Potter et al., 2013b; DeToni, 2016), these include:

1) sodic, where an albite ± quartz assemblage predominates;
2) sodic–calcic±iron composed of albite with amphibole and with or without magnetite and apatite;
3) high-temperature (HT) calcic–iron alteration, comprising amphibole ± magnetite ± apatite ± clinopyroxene (as this alteration type develops skarns form early where precursors consist of carbonate units);
4) HT calcic–iron–potassic alteration composed of amphibole and K-feldspar/biotite with or without magnetite;
5) HT potassic–iron alteration, where the mineral assemblages consist primarily of K-rich minerals (K-feldspar, biotite) with variable proportions of magnetite; and
6) LT potassic–iron alteration, where the mineral paragenesis consists of hematite ± K-feldspar, sericite + hematite, chlorite + hematite ± K-feldspar ± carbonates.

In contrast to the other metasomatic systems of the GBMZ (Corriveau et al., 2010b, unpublished data), potassic K-feldspar-rich skarns and the potassic K-feldspar-rich felsite breccia that occur at the transition from magnetite to hematite were not observed at Fab. As documented in the other IOAA systems of the GBMZ (chapter 4) the composition of IOCG-related alteration of high intensity becomes to a great extent independent of the composition of its precursor host in terms

of major elements and some highly mobile trace elements. This is indicative of high fluid/rock ratio where the final composition of intense IOCG alteration is principally controlled by the chemistry of the fluids (cf. Putnis and Austrheim, 2010).

7.4 Main alteration types

All the main IOAA types are observed in the Fab Lake region except for skarn. This lack of skarn is attributed to the absence of carbonate host rocks or intense precursor carbonate alteration. The prograde alteration sequence mapped across the area consists of sodic, transitional sodic–calcic–iron, HT calcic–iron and transitional calcic–iron–potassic, HT potassic–iron and LT potassic–iron alteration. Their mineral assemblages are presented in Figure 7-3 and Table 7-2.

Table 7-2 Representative mineral parageneses of the main IOAA alteration types

Alteration type	Principal minerals parageneses	Important accesory minerals
Sodic	Ab±Qtz	Zrn, Ti-oxides
Sodic-calcic-iron	Ab-Amp±Mag	Zrn
HT calcic-iron	Amp-Mag, Amp-Mag-Ap, Amp-Mag-Ttn, Amp-Ttn, Amp	Par, Bas, F-REE, Thr, Qtz, Ab, Kfs, Ccp, Py, Ilm, Fl
Calcic-iron-potassic	Amp-Mag-Kfs, Amp-Kfs, Amp-Bt-Mag±Kfs±Ap, Amp-Bt	Thr, Ccp, Py, Ap, Ttn
HT potassic-iron	Kfs-Mag, Kfs-Bt-Mag, Bt-Mag	Ccp, Py, Pitch
LT potassic-iron	Hem-Chl, Hem-Ms-Chl, Ep-Chl-Ms	Aln, Cal, Py, Ccp

Bas = Bastnäsite, Par = Parisite, Pitch = pitchblende, Thr = Thorite

Mineral abbreviations after Whitney and Evans (2010).

7.4.1 Sodic and sodic–calcic–iron alteration

Sodic alteration is widespread and is overprinted by all alteration types. It typically occurs as mild to moderate albitization of feldspar phenocrysts and groundmass of the porphyritic dacite intrusion, resulting in milky and yellow colored phenocrysts (Fig. 7-4a). As it becomes more intense, sodic alteration locally evolves to patchy and/or vein-like replacement zones where the porphyritic dacite intrusion is completely albitized (Fig. 7-4b–d). Albitites are generally fine to very fine grained, have a grayish white to pinkish white color and possess a similar appearance and hardness to zones of intense silicification. The albitites contain low modal proportions of

zircon and titanite and are devoid of mafic minerals or iron oxides. Zones of intense and early albitization are restricted to a few tens of meters at the present surface exposure and were characteristically observed at the marginal zones of the system. The albitites are overprinted by K-feldspar alteration and cut by an early generation of calcic-iron-potassic alteration (amphibole + magnetite veins with K-feldspar selvages; Fig. 7-4b–c).

Sodic–calcic–iron follows sodic alteration and early HT calcic–iron alteration and is overprinted by later HT calcic–iron and HT potassic–iron alteration. It is generally positioned along the margins of the large HT calcic–iron and HT potassic–iron replacement zones. It forms amphibole ± magnetite veins with albite selvages and/or albite veins with amphibole ± magnetite selvages and pervasive albite–amphibole replacements that completely destroy the primary magmatic textures in the porphyritic dacite intrusion (Fig. 7-4e–f). The spatial extent of intense sodic–calcic–iron alteration is restricted to few tens of meters.

7.4.2 HT calcic–iron and calcic–iron–potassic alteration

High temperature calcic–iron (amphibole and amphibole + magnetite ± apatite ± titanite) and the transitional calcic–iron–potassic subtype (amphibole ± magnetite veins with K-feldspar selvages) are the predominant alteration assemblages at the current level of exposure (Fig. 7-4g–p). These assemblages were observed throughout the porphyritic dacite and amphibole–magnetite-altered monzodiorite intrusions.

In its early-stages and in the marginal zones of the Fab showings, HT calcic–iron alteration occurs as subtle, fine-grained and pervasive replacement of the porphyry aphanitic matrix and of igneous feldspar (Fig. 7-4g–i). In the most intensely altered zones, HT calcic–iron alteration forms decameter-size and discontinuous to continuous fine- to coarse-grained replacement zones of the porphyritic dacite intrusion where the primary igneous textures are completely obliterated (Fig. 7-4j–m). These zones are bordered by extensive stockworks formed by many tension veins varying from 0.01 to >10 cm wide (Fig. 7-4k). Typical minerals of the HT calcic-iron alteration stage are: amphibole ± magnetite ± titanite ± fluoroapatite ± ilmenite ± fluorite. Zones of incipient HT calcic–iron alteration also includes carbonate (pos. calcite) and also locally REE-rich fluorocarbonates (presumably a mixture of parisite and bastnäesite $(La,Ce,Nd)_2Ca(CO_3)_3F$ and $(La,Ce,Nd)CO_3F$ respectively). The plagioclase phenocrysts within weak HT calcic–iron alteration zones are variably albitized. Some of the grab samples of magnetite-rich HT calcic–iron and calcic–iron–potassic alteration zones have high V contents (up to 1112 ppm), which is enough to meet the definition of “showings”, as defined by the Northwest Territories Geoscience

Office NORMIN database (Fig. 7-4j; www.nwtgeoscience.ca/normin; V above 0.1% or 1000 ppm). Microprobe analyses in HT calcic–iron alteration indicate that magnetite is the main V repository (De Toni, 2016), similar to the observations of V enrichments in the magnetite formed at the HT calcic–iron alteration stage of the Hump showing in the southern GBMZ (Gandhi, 1992a) and the magnetite formed at the HT calcic–iron alteration stage of the Port Radium-Echo Bay district (Mumin et al., 2010; De Toni, 2016). Accessory chalcopyrite and pyrite are also locally precipitated in HT calcic–iron zones (modal content ≤ 1%; Fig. 7-4n).

A sub-type of intense HT calcic–iron alteration is titanite-rich (hornblende–actinolite–magnetite–quartz) that characteristically possesses high Th concentrations (*e*Th up to 626 ppm). Thorium is predominantly hosted in REE-, Y- and U-bearing thorite and locally associated with (Y)-tritomite, an F-bearing Th–REE–Y silicate. Titanite crystals also contain F-rich REE inclusions, with textures that are indicative of partial replacement and which are locally cut by Th–REE–F-rich veinlets, suggesting that Th, REE, and F have been locally redistributed after titanite crystallization (Fig. 7-4l–m). Anhedral and porous hydrothermal zircon crystals are associated with thorite in the veins, consistent with Zr remobilization or relative enrichment.

Transitional calcic–iron–potassic alteration occurs as amphibole ± magnetite ± biotite veins with K-feldspar selvages. Aside from the selvages, the veins are normally devoid or have very low modal contents of K-feldspar (Fig. 7-4c, o–p). This alteration assemblage formed early in the system and continuously throughout the main HT calcic–iron alteration event as evidenced by complex cutting/overprinting relationships between calcic–iron–potassic, HT calcic–iron and sodic–calcic–iron alteration. Meter-scale development of hydrothermal and Cu-mineralized breccia zones in the Fab system started during formation of calcic–iron–potassic alteration in the outer zones of the large HT potassic–iron alteration zones (Fig. 7-4p). This calcic–iron–potassic alteration is interpreted as being transitional to the HT potassic–iron alteration stage as it overprints HT calcic–iron alteration but is overprinted by HT potassic–iron alteration.

7.4.3 HT potassic–iron alteration

High temperature potassic–iron alteration occurs as pervasive and fine-grained metasomatic fronts and hydrothermal breccias that host most of the Fe–Cu–U mineralized zones. Cross-cutting relationships indicate that this alteration postdates the sodic and HT calcic–iron alteration stages. The main Fe–Cu–U mineralization occurs in hydrothermal breccias surrounded by decameter-size HT potassic–iron replacement zones. Hydrothermal breccia fragments typically comprise K-feldspar, whereas hydrothermal breccia cement comprises magnetite ± biotite ±

chalcopyrite ± pyrite ± uraninite (Fig. 7-5a–e). Some of the resulting iron oxide-cemented breccia zones bear textural and compositional similarities to those of the Sue-Dianne deposit (Gandhi, 1988).

High temperature potassic–iron alteration assemblages, in the replacement zones surrounding the hydrothermal breccias, consists of veins and alteration fronts of magnetite, biotite and K-feldspar in variable proportions with accessory pyrite and chalcopyrite. Identical to the hydrothermal breccias, it is either superimposed over earlier pervasive HT calcic–iron alteration or the weakly altered porphyritic dacite intrusion (Fig. 7-5d–h). However, the complete destruction of the precursor rock textures in intense HT potassic–iron alteration fronts and hydrothermal breccias make identification of the precursor rock equivocal without the careful description of the transitional textures between the least-altered zones and the intense HT potassic–iron alteration. The HT potassic–iron alteration superimposed on earlier HT calcic–iron alteration also typically has higher modal contents of biotite with or without magnetite and lower modal contents of K-feldspar.

In the immediate vicinity of the main Fab showings, HT potassic–iron alteration also forms centimeter-wide K-feldspar + magnetite veins with K-feldspar selvages (Fig. 7-5g). Those veins locally form meter-scale and uraniferous stockwork zones where potassic–iron alteration is well developed.

7.4.4 LT potassic–iron alteration

Low temperature potassic–iron alteration occurs as pervasive and selective replacement of the hydrothermal minerals formed in the HT calcic–iron and HT potassic–iron alteration stages and is typically more intense in the core of the system. Mafic minerals (biotite, amphibole) are typically chloritized, magnetite is hematized and the feldspars (albite and K-feldspar) are sericitized (Fig. 7-5h–l). Epidote-rich zones also occur amongst the LT potassic-iron alteration and locally show an association with minor sporadic pyrite and chalcopyrite. The retrograde replacement of titanite crystals by epidote and subsequently chlorite leads to the crystallization of thorite in Th-rich calcic–iron alteration. In the outer zones of the Fab system, LT potassic–iron also resulted in rare hematite veinlets with K-feldspar selvages and pervasive muscovite replacement of the porphyritic dacite groundmass (Fig. 7-5m).

7.5 Geochronology

U-Pb zircon geochronology was undertaken to constrain the age of the Fab IOAA system. The targeted units include the porphyritic monzonite dikes cutting IOAA alteration, the host porphyritic dacite intrusion and the amphibole + magnetite-altered porphyritic monzodiorite.

Sample 10CQA-0196A02 (Z010472) was collected from one of a series of porphyritic monzonite dikes that cut the HT calcic–iron and HT potassic–iron alteration and shows no evidence for IOAA alteration (Fig. 7-6a–b). It thus provides a minimum age for the Fab IOAA system. Zircon separates from the sample consists of a homogenous population of euhedral prismatic crystals. A weighted mean $^{207}Pb/^{206}Pb$ age of six analyses yields a date of 1866.8 ± 1.3 Ma interpreted as the minimum age of IOAA alteration in the Fab system (mean square weighted deviation (MSWD) = 1.81; probability of fit (POF) = 11%; Fig. 7-6c).

Sample 11PUA-085A01 (Z10690) is from the porphyritic dacite intrusion that hosts the mineralization and the majority of IOAA alteration. The sample was collected 1 km away from the main showings, but the continuity of the porphyritic dacite intrusion can be traced continuously into the zones of Fe–Cu–U mineralization (Fig. 7-6d–e). Zircon grains in this sample consist of clear, colourless euhedral prisms. Four of the five analyses yield a weighted mean $^{207}Pb/^{206}Pb$ age of 1868.8 ± 1.3 Ma (MSWD = 0.75; POF = 52%) interpreted as the age of the intrusion (Fig. 7-6f). The fifth analysis yielded a much older age of 1958 ± 4 Ma and is interpreted to be inherited. Material of this age is known from rocks of the Hottah terrane (Davis et al., 2011) and metasedimentary rocks of the Treasure Lake Group (Gandhi and van Breemen, 2005; Bennett and Rivers, 2006).

Sample 11PUA-061A1 is from the amphibole + magnetite-altered porphyritic monzodiorite intrusion (Fig. 7-1). In this sample, both groundmass and feldspar phenocrysts are pervasively altered by HT calcic–iron alteration (Fig. 7-6g–h). Zircon grains in this sample consist of clear colourless euhedral prisms. Five single grain analyses yield <0.4% discordant results with a weighted mean $^{207}Pb/^{206}Pb$ age of 1870.1 ± 1.7 Ma (MSWD = 2.1; POF = 7.9%), interpreted as the time of igneous crystallization (Fig. 7-6i).

7.6 Compositional signature of the main alteration types

Metasomatism of the host porphyry in the Fab system is both extensive and intense, producing systematic geochemical trends. Relative to the initial composition of the weakly altered porphyritic dacite, sodic and sodic–calcic–iron alteration, exhibits elevated concentrations in Al, Na and Ti in terms of major elements and Zr as trace elements (cf. chapitre 5), but very depleted Fe contents (Corriveau et al., 2015 and appendix 7 for samples descriptions and geochemical analyses). Sodic–calcic–iron alteration exhibits generally depleted Ti, HREE, MREE and Th contents. High temperature calcic–iron alteration and calcic–iron–potassic alteration are generally characterized by elevated concentrations in Ca, Fe, Mg, Mn and P for the major elements and REE and Th for trace elements (Appendix 7; Corriveau et al., 2015), coupled with either reduced Sr, Zr and/or enriched Ti contents. Zones of intense HT calcic–iron alteration may also possess elevated concentrations in transition metals such as Co, Ni and V. High temperature potassic–iron alteration is characterized by enriched concentrations of K, Fe, Cu and U while Zr contents are similar to the least-altered porphyritic dacite (Corriveau et al., 2015 and appendices 3 and 7 for samples descriptions and geochemical analyses). The high Cu and U content of HT potassic–iron alteration supports field and petrographic observations that the Fe–Cu–U mineralized zones at Fab are predominately associated with this alteration type. The HT potassic–iron and some calcic–iron–potassic alteration types also have elevated Ba and Rb contents (Appendix 7; Corriveau et al., 2015).

7.7 Modeling element mobility in the Fab system

7.7.1 Methods

The geochronological data indicates a maximum age of 1870.1 ± 1.7 Ma and a minimum age of 1866.8 ± 1.3 Ma for the IOCG-related metasomatic and mineralizing activity in the Fab system. This IOAA event is thus temporally related with the intrusion of monzodiorite and porphyritic dacite. Development of all the observed alteration types within a ca. 3 m.y. time window constrains these assemblages to a single, progressive IOAA event that culminated with the formation of magnetite-group IOCG showings. The element mobility should thus reflect the chemical evolution of the metasomatic system. Moreover, hydrothermal minerals within intense sodic, sodic–calcic–iron, HT calcic–iron alteration, calcic–iron–potassic and some HT potassic–

iron alteration zones, are characteristically unrelated to the primary composition of the least-altered porphyritic dacite intrusion. This is typical of high water-rock ratios in which composition of hydrothermal alteration is primarily a function of the fluid composition and not of the host rock (cf. Smith et al., 2013). In those intense alteration zones, the element mobility patterns indicate which elements precipitated from the fluid and which elements were leached from the rock, providing an estimation of the fluid physico-chemical properties.

Bivariate relationships between element pairs were determined using molar ratios for the major elements (Pearce element ratio; Pearce, 1968) and elemental ratios for the trace elements (Grunsky and Kjarsgaard, 2008). Molar ratios are used for major element ratios as they better represent the mineralogy of the altered rock and because ratios limit the effects of the closure constraint on the relationship between the observed elements (Chayes, 1960; Aitchison, 1986). The ratio of a mobile over a relatively immobile element also provides a first-order quantification of element mobility (Pearce, 1968).

As the precursor rocks of the Fab system consist of a single, well-constrained rock type, a mass balance analysis following the Grant (1986, 2005) simplification of the Gresens (1967) equations was conducted to quantify element mobility associated with the sodic, sodic–calcic–iron, HT calcic–iron and HT potassic–iron alteration types. The locations of samples selected for mass balance analysis are shown on Figure 2.

The simplified equation for composition-mass relations in hydrothermally altered rocks, according to Grant (2005), can be expressed as:

$C_i^A = M^O/M^A(C_i^O + \Delta C_i)$ (2)

Where, C_i^A is the concentration of element *i* in the altered rock, C_i^O is the concentration of the element *i* in the least-altered rock, M^O/M^A is the ratio of the equivalent mass before and after alteration.

In the case where an element is immobile, i.e., $\Delta C_i = 0$, equation 1 can be simplified to:

$C_i^A = (M^O/M^A)C_i^O$. (3)

The resulting estimation of the M^O/M^A ratio provides the slope of the constant mass isocon and allows the computation of the ΔC_i value for each element and provides an estimation of the mass gains (M^O/M^A <1) or losses (M^O/M^A >1) during hydrothermal alteration for each element based on the equation:

$\Delta C_i = C_i^A/(M^O/M^A) - C_i^O$ (4)

For mass balance calculations, major element concentrations were transformed into cationic concentrations and converted into ppm. Cationic form was chosen because of its closer association to the mineralogy of the rock (Stanley and Madeisky, 1994; Grunsky and Kjarsgaard, 2008). All of the apparent enrichment and depletion patterns are given relative to the least-altered porphyritic dacite. Except for the Th-rich HT calcic–iron alteration sample (10CQA-0557D02) that has a weak LT calcic–iron alteration overprint, the selected samples represent one alteration type superimposed on the previously weakly altered porphyritic dacite.

The composition of the precursor porphyritic dacite intrusion was approximated by averaging the analyses of the two best least-altered candidates. Both samples are overprinted by incipient K-feldspar alteration and are located near the main Fab showings in the northeastern part of the Fab system (samples 10CQA-1250A02 and 10CQA-0572B02; Fig. 7-7 a–b; location of the samples on Fig. 7-1). The samples were selected among a suite of weakly, sodic, incipient HT calcic–iron and HT potassic–iron altered samples of the porphyritic dacite intrusion in which the primitive mantle-normalized trace elements profiles are similar and not strongly modify by alteration (10 samples; Fig. 7-7 c–d). The similarity of the trace element profiles across the porphyritic dacite intrusion is consistent with a perception of relative homogeneity established during fieldwork; trace element chemistry of this rock type was also uniform (e.g., Gandhi, 1988; Potter et al., 2013b; this study).

To validate the covariation between immobile elements, the centered log-ratio (clr) transformations was used as it removed the effects of closure and eliminates the need of identifying immobile components (chapitre 5). The positive co-variation on the diagram is indicative of the coupling of the two elements.

For a D-part (elements) compositional vector $\mathbf{X}$, the clr transformation is defined as:

$$z_i = \log(x_i/g(\mathbf{X}_D)) \qquad (i = 1,\ldots,D) \quad (1)$$

where $g(\mathbf{X}_D)$ is the geometric mean of the compositional vector.

7.7.2 Bivariate relationships – Major elements

In the modeling of bivariate relations between major elements, Al was used as the main dividing element because it is a significant constituent in most of the major hydrothermal minerals formed in the Fab system (except iron oxides, apatite and titanite) and remains mainly immobile in most of the Fab alteration types.

Plotting Al-normalized Na_{molar} versus K_{molar} and Al-normalized Na_{molar} versus $K_{molar}/(Na_{molar}+K_{molar})$ indicates that incipient HT calcic–iron alteration is associated with progressive albitization. It also demonstrates that the progression to complete replacement of the porphyritic dacite intrusion by HT calcic–iron alteration (magnetite ± amphibole ± quartz) is accompanied by feldspar destruction and consequently liberation of K and Na. This process may explain, in part, the potassic and sodic alteration envelopes that are typically associated with HT calcic–iron alteration (Fig. 7-8a–c). Plotting Al-normalized Fe_{molar} versus Ca_{molar} confirms field observations and petrography in that HT calcic–iron alteration results in increased amphibole–magnetite modal contents whereas albitization is associated with complete destruction of mafic minerals (Fig. 7-8d–e).

The slight deviations of some HT calcic–iron alteration from the main trend reflect higher apatite (towards Ca) or magnetite contents (toward Fe). Plotting Al-normalized Fe_{molar} vs Mg_{molar} highlights the transitional signature and progressive overprint of some HT calcic–iron (amphibole predominant) by calcic–iron–potassic (amphibole + biotite ± K-feldspar) and HT potassic–iron (biotite + magnetite ± K-feldspar) alteration (Fig. 7-8f).

The break of the trend at Mg/Al ratio ≈ 0.2 illustrates higher K-feldspar and lower biotite modal contents in the HT potassic–iron alteration whereas offsets towards the Fe pole indicate higher magnetite contents in both the HT calcic–iron and HT potassic–iron alteration.

7.7.3 Bivariate relationships – Uranium, transition metals (Cu, Co, Ni, V, Cr) and major elements

Plotting Cu and U versus Fe indicates that the highest Cu concentrations are predominantly associated with the HT potassic–iron alteration whereas both the HT calcic-iron and HT potassic-iron can have elevated U content zones (Fig. 7-9a, b). On Al-normalized diagrams, V concentrations record a positive covariation with Fe, Ca and Mg for the HT calcic–iron, calcic–iron–potassic and HT potassic–iron alteration, with V contents up to 1112 ppm in calcic–iron–potassic alteration (Fig. 10c). Nickel and Co concentrations exhibit a strong positive covariation with Mg (Figs. 7-1, 7-9c). Nickel and Co concentrations exhibit a strong positive covariation with Mg (Fig. 7-9d–e) as well as with Fe and Ca on Al-normalized diagram for HT calcic–iron and some calcic–iron–potassic alteration. Chromium exhibits no obvious covariation with either Mg (Fig. 7-9f) or Ca and Fe (not shown), but the HT potassic–iron and HT calcic–iron alteration enveloping and hosting the main polymetallic mineralization have the highest Cr contents.

Table 7-3 Representative elemental enrichments and depletions in the main alteration types of the Fab system

Sample	10CQA-1258A3	CQA-05-0249C	CQA-06-0435F	09CQA-1158D03	10CQA-0557D02	CQA-06-0435A	09CQA-1158A03	CQA-06-0434C	10CQA-0192C01	10CQA-0566C03	10CQA-0187A2	10CQA-0562C05
Alteration	Na	Na-Ca-Fe	Ca-Fe	Ca-Fe	Ca-Fe	Ca-Fe-K	K-Fe	K-Fe	K-Fe	K-Fe	K-Fe	K-Fe
Mo/Ma	**1**	**1.4**	**0.21**	**0.18**	**0.41**	**0.65**	**0.92**	**0.80**	**0.98**	**0.79**	**1**	**0.55**
Alkali elements+P												
Na	**1.7**	**0.87**	0.64	-0.01	-0.33	-0.27	0.13	-0.56	-0.45	-0.4	-0.65	0.24
Ba	-0.61	-0.72	-0.8	**-0.99**	**-0.92**	0.14	0.3	0.6	0.21	0.40	0.9	0.16
Cs	**-0.96**	-0.64	0	-0.62	0.45	-0.34	-0.63	0.02	-0.39	-0.02	0.42	**4.6**
K	-0.57	-0.57	-0.36	**-0.79**	**-0.85**	0.47	0.32	0.66	0.47	0.32	0.22	0.62
Rb	-0.69	-0.56	-0.52	**-0.96**	**-0.8**	-0.12	0.05	0.07	0.02	-0.08	0.25	**1.3**
Ca	-0.63	0.1	**21**	**26**	**9.9**	**2.6**	-0.37	-0.71	-0.08	-0.56	-0.56	0.54
Mg	**-0.74**	-0.58	**75**	**102**	**24**	**11**	0.65	**1.2**	**1**	**1.1**	-0.38	**11**
Sr	-0.46	0.15	-0.52	**-0.86**	**1**	-0.37	-0.2	-0.39	-0.44	-0.37	-0.15	-0.33
P	**-0.94**	**-0.84**	**59**	**12**	**1**	-0.33	0.62	**1.4**	**1.7**	**3.5**	**2.1**	**5**
Transition metals + Pb-Sn-V-W												
Fe	**-0.9**	-0.33	**29**	**28**	**7.4**	**6.6**	0.86	**3**	**1.1**	**6.3**	**3.1**	**8.8**
Co	-0.58	-0.32	**33**	**39**	**13**	**6**	0.51	**2.9**	**6.9**	**26**	0.27	**8.5**
Cr	**0.46**	**0.51**	**35**	**5.9**	**4**	**2.8**	**2.5**	**2.8**	-0.44	-0.57	-0.31	**9.6**
Cu	**-0.67**	-0.18	**3.3**	-0.01	0.21	**1.4**	-0.05	**90**	**28**	**26**	-0.79	-0.42
Mn	**-0.77**	-0.44	**10**	**24**	**13**	**1.4**	-0.26	0.8	0.97	0.01	-0.37	0.78
Ni	-0.38	**-0.8**	**22**	**27**	**3.1**	**3.3**	0.96	**2.4**	0.19	**28**	-0.06	**7.1**
Zn	**-0.74**	-0.79	**3.5**	**14**	**5.4**	0.52	-0.1	0.66	0.9	-0.09	-0.04	**1**
Pb	**-0.88**	-0.69	-0.06	**1.5**	0.12	**6.5**	0.59	0.03	**1.2**	**2.1**	**2.9**	**12**
Sn	-0.41	-0.36	**9.2**	**11**	**15**	**3.2**	0.37	**1.9**	**1.7**	0.74	**1.3**	**1.5**
V	**-0.74**	0.3	**50**	**41**	**10**	**12**	**1.3**	**3.4**	**1.2**	**4.2**	**1.4**	**12**
W	**-0.81**	**-0.86**	-0.43	0.28	**1.3**	-0.31	-0.04	-0.02	-0.66	-0.49	**6.1**	-0.26
HFSE+U and Al												
Al	0.06	0.05	0.06	0.08	0.14	0.04	0.16	0.1	-0.06	0	0	0.49
Zr	-0.01	-0.07	0	-0.09	-0.2	-0.03	0	-0.05	-0.02	0	0.01	0.02
Hf	-0.08	-0.09	0	0.03	-0.06	-0.05	-0.02	-0.15	0.01	-0.01	-0.01	0.03
Nb	-0.07	**-0.98**	-0.26	**1.6**	**7.2**	-0.43	0.11	-0.02	-0.06	-0.31	-0.07	0.02
Ta	0.1	**-0.99**	-0.64	**1.3**	**2.3**	**-0.71**	0.32	0.04	0.02	0.08	0.15	-0.06
Th	**-0.7**	**-0.97**	**11**	**5.7**	**17**	**1**	0.03	-0.18	0.09	0.11	-0.05	0.16
Ti	0.47	**-0.97**	**1.9**	**4.8**	**6**	0.36	0.12	0.07	-0.07	0.11	-0.01	**1.5**
U	**-0.78**	-0.66	**21**	**4**	**8.7**	0.66	**3.8**	**6.6**	-0.08	**32**	**38**	**113**
REE+Y												
La	-0.42	**-0.95**	**2.4**	0.25	**4.2**	-0.27	-0.06	-0.41	0.09	-0.5	-0.6	-0.29
Ce	-0.21	**-0.93**	**2.2**	0.88	**5.4**	-0.14	-0.02	-0.26	0.18	-0.39	-0.61	0
Pr	-0.18	**-0.94**	**2.4**	**1.2**	**7.1**	-0.02	-0.04	-0.23	0.28	-0.33	-0.56	0.12
Nd	-0.16	**-0.92**	**2.5**	**1.6**	**6.8**	0.08	0.05	-0.15	0.27	-0.32	-0.54	0.17
Sm	-0.23	**-0.94**	**2.1**	**1.7**	**7.6**	0.03	0.01	-0.14	0.15	-0.26	-0.37	0.42
Eu	-0.26	**-0.88**	**2.2**	**1.3**	**6.8**	0.04	-0.08	-0.22	0.11	-0.03	-0.04	0.53
Gd	-0.22	**-0.95**	**2.9**	**1.7**	**7.9**	0.07	-0.1	-0.18	0.03	-0.25	-0.23	0.41
Tb	-0.32	**-0.95**	**2.4**	**1.4**	**8.4**	0	-0.13	-0.17	-0.04	-0.19	0.16	0.6
Dy	-0.25	**-0.93**	**3**	**2.1**	**8**	0.07	0.02	-0.14	-0.02	-0.18	0.57	0.64
Ho	-0.25	**-0.92**	**3**	**1.8**	**8.1**	0.13	-0.06	-0.09	0.03	-0.1	**0.9**	**0.85**
Er	-0.31	**-0.91**	**3**	**2**	**8.3**	0.09	-0.02	-0.11	-0.09	-0.01	**1.1**	**0.95**
Tm	-0.26	**-0.89**	**2.8**	**2.2**	**7.9**	0.1	0.01	-0.09	-0.03	-0.02	**0.99**	**0.9**
Yb	-0.27	**-0.86**	**2.9**	**2.5**	**7.9**	0.11	-0.01	-0.1	0.03	-0.02	**0.85**	**0.92**
Lu	-0.35	**-0.82**	**3.8**	**2.9**	**8.1**	0.32	-0.14	-0.1	0.04	0.03	0.52	**1**
Y	**-0.25**	**-0.9**	**3.3**	**2.7**	**7.4**	**0.08**	**0.09**	**-0.16**	**0.05**	**-0.22**	**0.55**	**0.54**

7.7.4 Bivariate relationships – U, Th and REE

Plotting of Al-normalized U versus Th concentrations highlights coeval Th and U enrichment in HT calcic–iron and calcic–iron–potassic alteration zones and U enrichment without Th in HT potassic–iron alteration zones (Fig. 7-10a–b). Plotting *e*Th and Th concentrations against

*e*U/*e*Th and U/Th obtained by gamma-ray spectrometer measurements and whole-rock geochemical analyses highlights only a minor decoupling between U and Th in HT calcic–iron and calcic–iron–potassic alteration (Fig. 7-10c–d). The slight decrease in *e*U/*e*Th ratios in HT calcic–iron alteration, from 0.3 in the background and least-altered precursors, to 0.1 within the Th ± U-rich alteration, indicates that the relative Th enrichment is greater than the U enrichment. In the U-rich HT potassic–iron alteration, the U/Th and *e*U/*e*Th ratios significantly increase with increasing U content, from 0.3 in the background to 10 in the zones with the highest U content, highlighting relative U enrichment over Th.

The positive covariation recorded by Th with Ti and the absence of covariation between P and Th (expected for monazite and/or apatite) for the Th-rich calcic–iron alteration on Al-normalized diagram matches the observation that Ti and Th are coevally enriched in HT calcic–iron alteration (Fig. 7-10d–f). This covariation is supported by the high modal content of titanite in Th-rich calcic–iron alteration.

The ubiquity of REE-bearing minerals within incipient to pervasive HT calcic–iron alteration indicates REE mobility and enrichment during this stage of the system. On Al-normalized diagrams, Ce, Gd and Yb exhibit a positive covariation with P, which is consistent with the phosphates being an important REE-bearing phase in most of the HT calcic–iron alteration (e.g., apatite; Fig. 7-11a–c). However, the positive covariation between Ti and Ce, Gd and Yb on Al-normalized diagrams also highlights the observed association between REE-fluorides and other REE-bearing minerals exsolved from titanite in the HT calcic–iron and calcic–iron–potassic alteration zones of the Fab system (Fig. 7-11d–f). In cases where both apatite and titanite are abundant in a HT calcic-iron alteration zone, whole-rock geochemistry alone is insufficient to discriminate which minerals are the main REE repositories.

7.7.5 Bivariate relationships – F, Cl, transition metals (Co, V, Ni, Cu) and Mg

On Zr-normalized diagrams, F exhibits strong positive covariations with Co, V, Ni and Mg that indicate their coeval enrichment during the HT calcic–iron, calcic–potassic–iron and to a lesser extent, HT potassic–iron alteration stages (Fig. 7-12a–d). No covariation between F and Cu was observed (Fig. 7-12e). A Zr-normalized plot of F versus Mg also shows that sodic and sodic–calcic–iron alteration zones are depleted in F (F=170 ppm, F/Zr = 0.54) and that HT calcic–iron (F≤ 15300 ppm, F/Zr ≤492), calcic–iron–potassic and HT potassic–iron superimposed on HT calcic–iron alteration (F ≤6910 ppm, F/Zr ≤40) are enriched in F. High temperature potassic–iron alteration not superimposed on previous HT calcic–iron alteration exhibits weak F enrichment

(F ≤1850 ppm, F/Zr ≤7.7), no enrichment, or even F depletion (F ≥430 ppm; F/Zr ≥1.4) relative to the least-altered porphyritic dacite intrusion (F/Zr = 4; Fig. 7-12d). Moreover, considering that the main minerals that can accommodate both Mg and F in the HT calcic–iron, calcic–iron–potassic and HT potassic–iron alteration zones are hydrothermal amphibole and biotite, the strong positive covariation between F/Zr and Mg/Zr (Pearson's correlation coefficient of 0.97 and 0.88 for the raw data) indicates that they are the main F repositories. Depending of the alteration type, fluorite, F-rich REE phases in titanite, apatite and fluorocarbonates can be marginal to important F repositories. Plotting Zr-normalized F versus Cl indicates that almost all the HT calcic–iron and calcic–iron–potassic alteration assemblages are enriched in Cl and that most of the HT potassic–iron alteration zones are depleted in Cl compared to the least-altered porphyritic dacite intrusion (Fig. 7-12f).

7.8 Mass balance analysis of element mobility

Selection of immobile elements

Immobile elements were selected based on the preservation, in the least-altered and altered samples, of the ratio of characteristically immobile elements with different geochemical behaviors (e.g., Al/Zr, Ta/Zr, Al/Nb). Element pairs that met this constraint, but for which the alteration mineralogy indicates enrichment or depletion relative to the least-altered porphyritic dacite intrusion, were not considered (for instance preservation of La/Yb ratio in an apatite-rich alteration).

Aluminum and Zr meet this constraint for most of the alteration types of the Fab systems and exhibit a strong positive correlation on a clr-transformed Zr versus Al diagram (Fig. 8e–f; Pearson's (R) correlation coefficient of 0.91 for clr-transformed data and 0.88 for raw data). The high Pearson's (R) correlation coefficient correlation between suspected immobile elements indicates that the initial Al/Zr ratio of the least-altered porphyritic dacite intrusion is preserved in most of the Fab system alteration zones. Moreover, depending of the alteration type, other elements were identified as immobile. Zirconium mobility was also tested by comparing the Zr/Hf ratios of the selected alteration to the Zr/Hf ratios of the least-altered porphyritic dacite. The preservation of the Zr/Hf ratio in zones of strong hydrothermal alteration is interpreted to reflect the preservation of the primary magmatic zircons of the porphyritic dacite that supports weak Zr and Hf mobility in the hydrothermal fluids. The preservation of the Zr/Hf ratios, in addition to the

preservation of the Al/Zr ratios also support that the precursor unit remains the porphyritic dacite in zones of intense alteration. Increase of the Zr/Hf ratios, for instance from 37 in the least-altered porphyritic dacite to 40 in zones of sodic alteration may indicate a possible crystallization of hydrothermal zircons with different Zr/Hf ratios, which is commonly observed in the sodic alteration zone of the GBMZ (Pelleter et al., 2010).

7.8.1 Sodic and sodic–calcic–iron alteration

Aluminum, Hf, Nb, Ta and Zr were selected as the immobile elements for the intense sodic alteration based on the preservation of the Zr/Al, Nb/Zr, Hf/Al and Ta/Zr ratios between the altered rocks and the precursor. Selection of these elements is also supported by the work of Oliver et al. (2004) and Clark et al. (2005) that also identified Zr and Al as being immobile in the sodic alteration stage. Sodic and sodic–calcic–iron alteration types are characterized by intense elemental depletions combined with systematic weak to important mass losses (Table 7-3). However, the slight increase of the Zr/Hf ratio from 37 in the least-altered porphyritic dacite to 40 in the sodic alteration versus may indicate weak Zr mobility and re-crystallization of hydrothermal zircons with different Zr/Hf ratios.

Overall, sodic alteration is characterized by Co, Cs, Cu, Fe, Mn, Mg, P, Pb, W, Th, U and V depletion and Cr, Na and Ti enrichment (Table 7-3; Fig. 7-13a). The REE, except for La and Lu, are slightly decoupled and moderately to weakly depleted (La/Yb = 14 versus 19 in least-altered samples). This element mobility pattern is consistent with the complete destruction and replacement of the primary ferro-magnesian minerals (amphibole, clinopyroxene), Fe-oxides, plagioclase and K-feldspar by albite and quartz with partitioning of the leached elements in the fluid phases. Immobile elements like Ti can be re-precipitated in minerals like titanite and Ti-oxides.

In the sodic–calcic–iron alteration (Fig. 7-13b), the Al/Ca, Al/Zr and Ca/Zr ratios are comparable to the least-altered porphyritic dacite intrusion. Aluminum, Ca, Hf and Zr were thus selected to calculate the constant mass isocon which indicates a 40% mass loss (M^O/M^A = 1.4). These mass losses can be compensated for by creation of significant porosity in the hydrothermal albite (cf. Putnis, 2009) and to a non-detectable contraction of the rock during alteration. Relative to the constant mass isocon, most of the analyzed elements are strongly depleted in this alteration type except for Na, Cr, V and Sr. Nb, REE Ta, Th and Ti exhibit the strongest depletion. The REE are also strongly fractionated from the primary igneous signature of the porphyritic dacite, with depletion of MREE and La. The extent of HFSE depletion in this alteration is further

demonstrated by the variations of the Zr/Ti, Zr/Ta and Zr/Nb ratios, from 0.1, 175 and 15 in the weakly altered precursor to 3.4, 12400 and 800, respectively, in the sodic–calcic–iron alteration. However, in contrast to pure sodic alteration, base-metals such as Co and Cu as well as Mg and Fe are less-depleted in this sodic–calcic–iron alteration (Fig. 7-13b).

7.8.2 HT calcic–iron and calcic–iron–potassic alteration types

The HT calcic–iron alteration samples used for the mass balance analysis were selected based on the preservation of Al/Zr and Zr/Hf ratios close to those of the least-altered porphyritic dacite intrusion. Initial Al is presumed to be trapped in feldspar (either albite ± K-feldspar for HT calcic–iron or K-feldspar for calcic–iron–potassic) and hydrothermal hornblende whereas Zr and Hf are preserved in zircon. The only exception is the titanite- and Th-rich HT calcic–iron alteration (Th = 317 ppm), in which the Al/Zr and Zr/Hf ratio differed from those of the least-altered porphyritic dacite intrusion. This is taken as an indicator of weak Zr and Al mobility during this alteration that is supported by the observation of hydrothermal zircons in this these HT calcic-iron alteration zones. However, as Al and Zr still exhibit the best preserved ratio of the least-altered precursors, they were selected to provide a semi-quantitative estimate of element mobility in this particular type of HT calcic–iron alteration.

Well-developed HT calcic–iron alteration exhibits significant mass gains associated with considerable enrichment in Ca, Co, Fe, Mg, Mn, Ni, Th, V and Zn and moderate to severe enrichment in Cr, P, Sn and Ti (Fig. 7-13c–e; Table 7-3). Notable elemental depletions include Ba, K, Rb and Sr, probably reflecting the instability of potassic minerals coupled with the destruction of plagioclase. The high modal content of amphibole and magnetite, and variable modal content of apatite and titanite crystallized in HT calcic–iron alteration reflect those chemical changes. The significant mass gains correspond to the observed quasi-complete dissolution of the precursor porphyritic dacite and its replacement by the HT calcic–iron mineral assemblage (constant volume component), and to a lesser extent to possible micro-scale to macro-scale brecciation (volume gain component). Copper either remains close to immobile or is moderately enriched. Another characteristic feature for most of the HT calcic–iron alteration is Sr depletion coupled with Ca and Mg enrichment (mean Ca/Sr = 9120 and Mg/Sr = 9580). The mean Ca/Sr and Mg/Sr ratios for the Fab system HT calcic–iron alteration are significantly higher than the least-altered porphyritic dacite intrusion (Ca/Sr = 91 and Mg/Sr = 30).

There are some differences in element mobility patterns based on Th contents of HT calcic–iron alteration, i.e., Th-rich (> 100 ppm) versus Th-normal (40–50 ppm) alteration described above.

Thorium-rich HT calcic–iron and calcic–iron–potassic alteration types are characterized by variable REE enrichment and fractionation patterns that depend on the amplitude of P and Ti enrichments (Fig. 7-13c, e; Table 7-3). Ratios of La/Yb in the Th- and P-rich alteration HT calcic–iron alteration are comparable to the least-altered porphyritic dacite intrusion (La/Yb = 16 and 19, respectively) and indicates coeval LREE and HREE enrichment (Fig. 14c). Conversely, La/Yb = 11 in the P-poor, Ti-rich and Th-rich HT calcic–iron alteration indicates stronger HREE enrichment that is also accompanied by Nb and Ta enrichments (Fig. 7-13e). High modal contents of titanite with exsolution of minerals rich-in REE, Y–U-bearing thorite and Y-tritomite attest to this element mobility pattern in this specific HT calcic–iron alteration, which is also slightly enriched in Sr (Ca/Sr = 491). The weak Sr enrichment observed in this alteration is attributed to the weak epidote alteration overprint in the analyzed sample.

Vanadium-rich calcic–iron–potassic alteration in the outer zone of the Fab V showing (Fig. 7-13f) is characterized by Sr depletion and Ca, Co, Fe, Mg, Mn, Ni, P, Th, V and Zn enrichments, typical of HT calcic–iron alteration. However milder HREE enrichment, MREE immobility and depletion in Ce, La, Na, Nb and Ta combined with Ba and K enrichments contrast with HT calcic–iron alteration. This alteration type also exhibits stronger Cu enrichments more typical of HT potassic–iron alteration stage.

The mineralogy of the V-rich calcic–potassic–iron alteration, primarily composed of amphibole, magnetite and K-feldspar with lower modal contents of apatite and an absence of albite, reflects the changes observed in the element mobility patterns of the alteration and stability of the Ca–Fe–P bearing minerals during this stage.

7.8.3 HT potassic–iron alteration

High temperature potassic–iron alteration can be divided into three subtypes when the absolute U and Cu contents are considered: those with normal Cu (< 50 ppm) and U (10–20 ppm) contents (Cu–U-normal potassic–iron alteration; Fig. 7-14a–b), those with high Cu (>500 ppm) contents (Cu-rich potassic–iron alteration; Fig. 7-14c–d) and those with high U (>254 ppm) contents (U-rich potassic–iron alteration Fig. 7-14e–f; Table 7-3). The main immobile elements in HT potassic–iron alteration are Hf, Nb, Ta, Ti and Zr, identified by preserved ratios between the least-altered porphyritic dacite intrusion and samples of the HT potassic–iron zones. Using these elements, this alteration assemblage records moderate to no mass gains (Fig. 7-14a–e). Mass gains are interpreted to represent increasing replacement of the rock associated with a volume gain component because of hydrothermal brecciation. In the absence of mass gains,

replacement is proposed to be isovolumetric, a process well documented in metasomatic dissolution-precipitation reactions that involves creation of porosity in the alteration products (cf. Putnis, 2009). Aluminum exhibits a variable behavior with weak depletion, immobility and weak enrichment all recorded. This can be related to the superimposition of the HT potassic–iron alteration over HT calcic–iron or sodic alteration or to superimposition of late stage LT potassic–iron alteration that forms muscovite at the expense of K-feldspar and chlorite at the expense of biotite.

High temperature potassic–iron alteration typically exhibits enrichments in Ba, Ca, Co, Fe, K, U and V and depletions in Ca, Na and Sr. Those chemical changes reflect the breakdown and progressive replacement of amphibole and plagioclase by biotite, magnetite and K-feldspar. Depending on the biotite content of the alteration, Mg and Mn can be either enriched or depleted. Magnesium enrichments are also typically associated with Zn enrichments and Mg depletions with Zn depletion. The REE are moderately to weakly fractionated, and along with Th, are typically immobile to slightly depleted or slightly enriched. Uranium is fractionated from Th and is generally enriched whereas Th remains immobile.

Element mobility patterns and mass gains for Cu-rich potassic–iron alteration (Fig. 7-15b–d) are comparable with those observed in the Cu–U-normal potassic–iron alteration (Fig. 7-15a), although the former is generally characterized by stronger K enrichment and generally exhibits stronger mass gains than the latter alteration (Fig. 7-15b–d). The higher mass gains in the mineralized HT potassic–iron alteration are related to the formation of hydrothermal breccias and the associated volume gains.

The element mobility patterns documented in HT potassic–iron alteration superimposed on HT calcic–iron alteration are closer to those documented in HT calcic–iron alteration (Fig. 7-15f) with stronger Ca and Sr decoupling and Ti enrichment. However, in both U-rich potassic–iron alteration zones, Th is barely mobilized. This is supporting strong fractionation between U and Th during the main U mineralizing event at the HT potassic–iron alteration stage. This behavior also contrasts HT calcic–iron alteration, in which U and Th are not as strongly fractionated.

7.9 Implications on the development and evolution of Fab system

7.9.1 Geochronology

The new geochronological data support the Gandhi et al. (2001) inference that the Fab porphyry complex is coeval with the 1873–1868 Ma Mazenod and Lou assemblages of the Faber Group. More precisely, the Fab porphyritic dacite intrusion is coeval with the ignimbrite sequence that hosts the Sue-Dianne deposit dated at 1868 ±1 Ma by Gandhi et al. (2001). The timing of alteration documented at Fab from 1872–1866 Ma is also similar to the other IOCG-hosting metasomatic systems of the GBMZ for which U–Pb ages on zircon constrain the minimum ages of the system. Examples are the DeVries system that formed between 1878–1866 Ma (Bennett and Rivers, 2006; Bennett et al., 2012) and the Lou system that formed between 1873–1868 Ma (Davis et al., 2011; Potter et al., in press).

7.9.2 Attributes of the hydrothermal fluids

The remobilization and precipitation of Nb, Ta, Ti, Th, U and REE-bearing minerals (including REE fluorocarbonates and fluoroapatite), and the overall F and Cl enrichments in several alteration assemblages suggest the involvement of F-, Cl-, PO_4^{3-} and/or CO_2-rich hydrothermal fluids in the Fab IOAA system. Precipitation of sulfide minerals during transitions from calcic–potassic–iron to HT potassic–iron alteration and LT potassic–iron alteration also indicate elevated *f*S in the fluids. All the physico-chemical conditions discussed in the following section are inferred from literature pertinent to the element mobility patterns, mineral assemblages and geochemical signature documented in the hydrothermal alteration types of the Fab system.

The porphyritic dacite intrusion hosting the Fab system has elevated F (1220 and 940 ppm F) and Cl (480 ppm Cl), high Zr content (258 ppm) and a Ga*10000/Al ratio of 2.63 that corresponds to A-type magmatic signature (Whalen et al., 1987; Eby, 1990), and shoshonitic to high-K magmatic suites (Azar, 2007). Higher F than Cl contents in the porphyritic dacite intrusion are also consistent with published works on A-type magmas, where F predominates over Cl in metaluminous to peraluminous compositions (Collins et al., 1982).

The geochronological evidence for a direct spatio–temporal association between the formation of the Fab mineralizing system and halogen-rich A-type magmatism is consistent with the involvement of hot, alkaline to acidic, halogen- and CO_2-rich magmatic-hydrothermal fluids. Sulfur isotopes in pyrite formed in the IOCG mineralization zones of the Fab system, with $\delta^{34}S$ ranging from -1‰ to 3‰, also support a magmatic-hydrothermal origin for the fluids (Acosta-Góngora, 2014). The involvement of a magmatic-hydrothermal fluid in the formation of the HT calcic–iron alteration zones of the Fab system is also supported by oxygen and hydrogen isotopes and fluids inclusion analyses in the mineralogically similar HT calcic–iron alteration zones of the Port Radium–Echo Bay district. The fluids in the Port Radium–Echo Bay HT calcic–iron alteration zones were described as moderately saline (10–14% NaCl equivalent) and high temperature (>500°C) with a magmatic source (Reardon, 1992; Somarin and Mumin, 2014). The strong hydrothermal mobilization and concentration of Nb, Ta, Th, U, W and REE are also typical of magmatic-hydrothermal systems (Ngwenya 1994; Salvi and Williams-Jones, 1996; Aksyuk, 2000). The involvement of magmatic-hydrothermal fluids during the sodic and HT calcic–iron stages has also been demonstrated in many other IOCG systems, in which halogens and other ligands like CO_2 play an important role in mobilizing elements to create distinct alteration facies (Hildebrand, 1986; Mark, 1998; Perring et al., 2000; Pollard, 2001; Oliver et al., 2004; Clark et al., 2005; Agangi et al., 2010; Smith et al., 2013). Repetitive ascent and emplacement of porphyritic dacitic dikes originating from the deep seated intrusions of the Great Bear batholith could have sustained hydrothermal cells and channelled magmatic-hydrothermal fluids in the Fab system.

7.9.3 Sodic and sodic–calcic–iron alteration

The sodic and sodic–calcic–iron alteration stages, which resulted in considerable elemental depletions, are interpreted to reflect an intense leaching event that enriched the hydrothermal fluids in many elements, as reported in Na-rich alteration zones of other IOCG districts (Mark, 1998; Oliver et al., 2004; Clark et al., 2005; Yang, 2008). The interconnected porosity developed in the resulting albitite is believed to be an integral feature of the interface-coupled dissolution–precipitation mechanism of re-equilibrating minerals in the presence of a fluid phase. The dissolution-precipitation process significantly enhances fluid and mass transfer to *(and away)* from the reactive front (Putnis, 2002, Putnis et al., 2005, 2007, Putnis and Putnis, 2007; Putnis, 2010, Putnis and Austrheim, 2012). Based on juxtapositions, transitional alteration zones and cross-cutting relationships, the mobilized elements were strongly partitioned into the leaching fluids and have possibly controlled the metal associations observed in subsequent alteration

stages. In the Cloncurry district, the hydrothermal fluids from the albitization stages have been shown to participate in the formation of the subsequent alteration types (Oliver et al., 2004; Williams et al., 2005; Corriveau et al., 2010b; Mumin et al., 2010; Skirrow, 2010).

The low F concentrations in these early alteration assemblages can be related to the partial to complete destruction and replacement of the primary (magmatic) and halogen-bearing minerals in the porphyritic dacite intrusion during albitization (e.g., amphibole and biotite) and instability of halogen-bearing minerals under the prevailing physico-chemical conditions. Moreover, because high temperatures favor F partitioning into the fluid (Zhu and Sverjensky, 1991), the high temperatures of sodic and sodic–calcic–iron alteration (450°C to > 600°C; de Jong and Williams, 1995; Mark and Foster, 2000; Pollard, 2001; Oliver et al., 2006; Davidson et al., 2007; Williams et al., 2010) favor F leaching from the rocks and inhibits crystallization of F-bearing minerals.

The differences between element mobility patterns in sodic and sodic–calcic–iron alteration assemblages imply different fluid properties and mineral stabilities for each stage, reflecting an evolving fluid chemistry. In the early sodic alteration, Nb and Ta immobility coupled with Ti enrichment (titanite/Ti-oxides crystallization) and severe depletion in transition metals (i.e., Mg, Ca and Fe) imply that the fluids were slightly acidic and had high Cl activity (Azimov and Bushmin, 2007; Smith et al., 2013). Precipitation of metasomatic titanite at temperatures between 400 to 600^{o}C has been reported during regional albitization processes in the Eastern Succession of the Mount Isa block of Australia (de Jong and Willams, 1995; Oliver et al., 2004). This may have favored Ca, Co, Cu, Fe, Mg and Ni leaching by the destruction of the mafic minerals in the porphyritic dacite intrusion, but may also reflect leaching of mafic rocks to source Co, Cu, Fe, Mg and Ni. No mafic rocks have been observed so far at surface in the Fab area, but the Hottah terrane that is the basement to the GBMZ contains mafic volcanic units (Bloom basalt) and intrusions (Fishtrap gabbro) that may have been leached during the vertical ascent of the hydrothermal fluids. The presence of the Hottah terrane rocks below the Fab system is supported by the inherited zircon dated at 1958 ± 4 Ma in the porphyritic dacite intrusion (this study).

Sodic–calcic–iron alteration and concurrent HFSE, REE and U–Th leaching likely reflect increased F activity in the fluid (Keppler and Wyllie, 1990; Salvi et al., 2000; Migdisov et al., 2009). Copper immobility during this stage indicates decreasing activities of other ligands such as Cl or SO_2, as F does not foster Cu mobility in hydrothermal fluids (Keppler and Wyllie, 1991). The weak mobility of Ca, Mg and Fe indicates the presence of an alkaline fluid (Azimov and Bushmin, 2007) which is ideal to preserve higher F activities in the fluid as it prevents fluorite

and sellaite saturation (Salvi et al., 2000). This change in the fluid chemistry may partially result from the breakdown of F-bearing minerals in the porphyritic dacite during the sodic alteration stage. It may also reflect a stronger input of F- and CO_2-rich, and alkaline magmatic-hydrothermal fluids exsolved from the underlying Great Bear batholith and channeled to shallower crustal levels by the successive emplacement of porphyritic dikes.

7.9.4 HT calcic–iron and calcic–potassic–iron alteration

Most of the elements partitioned to the hydrothermal fluid during the sodic and sodic–calcic–iron alteration stages are precipitated in the minerals that crystallized during the HT calcic–iron alteration stages. This stage is associated with significant mass changes in the HT calcic–iron and calcic–iron–potassic alteration zones interpreted to reflect the quasi-complete dissolution of the porphyritic dacite host where this alteration reaches its peak intensity associated with pervasive micro-brecciation of the porphyritic dacite.

Fluorine, Co, Ni and V are enriched in the HT calcic–iron and calcic–iron–potassic altered samples and incorporated in the stable mineral assemblages that are typical of those alteration stages. It indicates that Co, Ni and V solubility in hydrothermal fluids is possibly associated with high F activity. This inference also applies for REE (apatite, titanite) and U–Th (titanite, thorite, Y-tritomite), as high F and Cl activities are required in fluids to mobilize those elements (Keppler and Wyllie, 1990; Migdisov et al., 2009). The Co, Ni, REE, Th and V enrichments observed in HT calcic–iron and calcic–iron–potassic alteration indicates that large iron oxide ± apatite (IO ± A or Kiruna-type) deposits that form in F- and Cl-rich metasomatic systems hosting IOCG deposits may potentially be prospective for these elements (e.g., IOA deposits of Pilot Knob and Kiruna for REE; Sahlström, 2012; Nold et al., 2013; Port Radium IOA prospect for V and REE; Mumin et al., 2010), especially if they are locally remobilized and concentrated during subsequent alteration stages (HT potassic–iron or LT potassic–iron alteration). Uranium enrichment in the HT calcic–iron alteration stage can also result in remobilization during later stages of the hydrothermal system and the formation of spatially restricted U-mineralized zones.

The formation of extensive stockwork zones around the large HT calcic–iron and calcic–iron–potassic replacement zones indicates active fracturing during that alteration stage. Cyclical over-pressure and low-pressure conditions during fracturing may trigger the destabilization of F-complexes in the hydrothermal fluids as fluorite solubility in hydrothermal fluids increases as a function of $P^{1/2}$ (Tropper and Manning, 2007). Fracture-driven decompression can thus promote F partitioning to the crystallizing minerals and deplete the residual hydrothermal fluid in F. The

coeval removal of H_2O (OH^-), CO_2 and F from the hydrothermal fluid can significantly modify the chemical properties (Eh, pH, fO_2, salinity) of the residual fluid and destabilize many complexes. The fluid/mineral partitioning coefficients of the released elements (Co, Ni, REE, Th, U and V) then favor crystallization of new minerals (e.g., apatite, magnetite and amphibole in Fab) that were stable under the prevailing physico-chemical conditions during the HT calcic–iron alteration stage.

Two factors may have fostered active fracturing: the presence of CO_2 in the hydrothermal fluid (see explanation below) combined with an increasing volume of fluids channeled in the hydrothermal system, and a localized extensional stress regime to bring the porphyritic dacite intrusion closer to its tensile strength limit (e.g., jog in a transcurrent fault zone).

The localized crystallization of REE fluorocarbonates and carbonates in early and incipient HT calcic–iron alteration zones of the Fab system provide some indications of CO_2 in the hydrothermal fluids. Fluid inclusion work in the HT calcic–iron alteration zones of the Port Radium-Echo Bay (northern GBMZ) district also supports the presence of CO_2 the hydrothermal fluids active at the HT calcic–iron stage (Somarin and Mumin, 2014), but the presence of CO_2 in the Fab system remains to be further tested using fluid inclusion studies.

7.9.5 HT and LT potassic–iron alteration

High temperature potassic–iron alteration is characterized by small to moderate mass gains, weak HREE and HFSE mobility and small to moderate F, LREE and Th depletions or enrichments. Weak F enrichments or depletions combine with weaker Nb, Ta and Th mobility are taken as indicators of lower F activity in the fluid responsible for most of the HT potassic–iron alteration (Keppler and Wyllie, 1990). This also reflects the extensive F-trapping in the crystallizing minerals during the preceding HT calcic–iron alteration stage. Ubiquitous sulfide precipitation and significant Cu enrichment in the HT potassic–iron alteration also reflect changes in the dominant complexing elements (e.g., from F- to Cl- and H_2S) and physico-chemical properties of the involved fluids. Widespread formation of hydrothermal breccia zones, which require brittle conditions without cataclastic or elasto-frictional processes (Sibson, 1986; Jébrak, 1997), are also indicative of lower temperatures during the HT potassic–iron alteration stage. Work in other porphyry and IOCG districts indicates that the hydrothermal fluid temperatures typically drop during the HT potassic–iron alteration stage compared to the HT calcic–iron and sodic alteration events (typically 400–500°C; Beane, 1974; Bastrakov and Skirrow, 2007; Baker et al., 2008; Skirrow, 2010; Williams, 2010b). Continuous exsolution of

CO_2 in the alteration zones below the HT potassic–iron alteration zone may also have considerably promoted active fracturing. The subsequent evolution of the system to LT potassic–iron alteration and the formation of muscovite, chlorite and hematite record dropping temperatures, increasing fO_2 and lower pH conditions in the hydrothermal fluid. The weak LT potassic–iron imprint and limited spatial extent of these alteration zones point to lower volume of fluid at this alteration stage.

Because the element mobility patterns of the F-rich HT potassic–iron alteration are similar to those of HT calcic–iron alteration, this alteration is interpreted as transitional between HT calcic–iron and HT potassic–iron alteration in which the highest Cu contents are observed. Fluorine can be incorporated in biotite after release by replacement of amphibole and fluoroapatite, which are likely the main F repositories in the HT calcic–iron and calcic–potassic–iron alteration. This hypothesis can be further evaluated using mineral chemistry.

7.9.6 Sources of Cu in the Fab system

Minor chalcopyrite precipitation during HT calcic–iron alteration, Cu leaching during sodic alteration and more extensive chalcopyrite formation in calcic–iron–potassic alteration transitional to the HT potassic–iron alteration stage indicate that Cu was present in the fluids as the Fab system evolved. Fluid inclusion studies in other IOCG systems also reveal that the fluids involved in sodic and HT calcic–iron alteration stage contain Cu (Perring et al., 2000; Oliver et al., 2004; Baker et al., 2008; Smith et al., 2013). The overall weak Cu enrichment in HT calcic–iron and some calcic–iron–potassic alteration is not necessarily considered to be related to the absence of Cu in the fluids, but could also have been caused by low fS, high Cu solubility in the hydrothermal solutions, or lack of a mechanism to oxidize Cu^+-chloride species to Cu^{2+} in order to be accommodated in chalcopyrite (Ohmoto and Goldhaber, 1997). The presence of pyrite and chalcopyrite, especially in the large replacement zones, indicates that H_2S and Cu were present in the fluids during the HT calcic–iron and calcic–iron–potassic alteration stages.

Possible phase separation at the HT calcic–iron alteration stage may have also prevented Cu mineral precipitation. Possible effervescence and phase separation at the HT calcic–iron alteration is supported by the observation of vapor phases in fluid inclusions trapped at the HT calcic–iron alteration stage in the Port Radium-Echo Bay district (northern GBMZ; Somarin and Mumin, 2014) and those trapped at the sodic–calcic–iron stage in the Cloncurry district (Australia; Baker et al. 2008). Cycles of over-pressure and low-pressure conditions during fracturing at HT calcic–iron and initial stages of the HT calcic–iron–potassic alteration stages

may have also promoted effervescence and the exsolution of a vapor phase. The presence of CO_2 in the hydrothermal fluid at the HT calcic–iron alteration stage and repeated cycles high/low pressure may have further promoted phase separation (cf. Sibson, 1986; Jébrak, 1997) as CO_2 solubility in hydrothermal fluid increase with pressure (Bowers and Helgson, 1983).

Phase separation would preferentially partition Cu and S into the vapor phase, hindering the formation of Cu sulfides at the HT calcic–iron alteration stage, while intense fracturing and host rock dissolution could have facilitated the escape vapor phase to higher levels of the system. The liquid phase would have however preferentially retained Fe, K, Mn and Na (Heinrich et al., 1999), and most likely Mg and Ca as Cl-complexes. Subsequent condensation of this Cu- and S-rich vapor phase in cooler parts of the system above the HT calcic–iron alteration zones could have contributed Cu- and S to form the mineralization. Preferential enrichment of the lighter Cu isotopes in the Fab mineralization zones was interpreted as a possible indication of phase separation (effervescence) in the hydrothermal fluid prior to the formation of the Cu minerals (Acosta-Góngora, 2014). Further work on the mineralization zones of the Fab system will help evaluate the role of phase separation in the evolution of the Fab system and on Cu distribution in IOCG systems.

If no vapor phase was formed at the HT calcic–iron alteration stage in the Fab System, Cu and S may still have been enriched in the residual fluid active at the HT potassic–iron alteration stage by extensive precipitation of magnetite, amphibole and apatite. The lower temperature during formation of the HT potassic–iron stage may then have promoted chalcopyrite crystallization.

7.9.7 Inferred causes for Al and Zr immobility in most of the Fab system alteration types

Several factors may explain the weak mobility of Al and Zr in most of the HT sodic and sodic–calcic–iron, calcic–iron and calcic–iron–potassic alteration of the Fab system: high CO_2 activity, low F activity, high temperatures of the fluid and/or high pH levels. High CO_2 activity in a fluid lowers H_2O activity and hinders the formation of Zr and Al hydroxy-fluoride complexes necessary to effectively transport those elements (Salvi et al., 2000; Migdisov et al., 2011). Given the diversity of elements that were mobilized in the fluids in the sodic and sodic–calcic–iron alteration stages, the competition for H_2O between each complex-forming reaction may also have limited Al and Zr mobility, especially in fluids with low H_2O activity. Experimental work also shows that Zr solubility in hydrothermal solutions decreases with increasing temperature and with decreasing F activity (Aja et al., 1995; Migdisov et al., 2011). Therefore, the high fluid

temperatures characteristic of the sodic, sodic–calcic–iron, HT calcic–iron and calcic–iron–potassic alteration zones are not favorable for Zr mobility. The same applies to CO_2 activity in the fluid during early HT calcic–iron alteration. Thermodynamic modeling of the sodic and sodic–calcic–iron system has shown that Al remains immobile in Cl-rich systems (Dolejš and Wagner, 2008). This may reflect pH conditions of the fluids, as work in high-sulfidation epithermal systems has shown that pH levels <2 are required to extensively remobilize Al (Stoffregen, 1987). Finally, the dissolution-precipitation replacements of precursor Al-bearing minerals by albite in sodic and sodic–calcic–iron alteration and hornblende in HT calcic–iron alteration may also have prevented significant Al remobilization as it would have been immediately consumed in the formation of albite.

7.10 Conclusions

The geochemical signatures identified in this study illustrate the effects of progressive evolution of hydrothermal fluids in a magnetite-group IOCG system on mobility and partitioning of elements across metasomatic facies/alteration stages leading to mineralization. Magmatic-hydrothermal fluid(s) is the inferred fluid type for the Fab system and its progressive chemical through each alteration assemblage can be explained through coupled dissolution-reprecipitation mechanisms where reaction with existing mineral assemblages provided fluids with elements necessary to precipitate subsequent alteration assemblages.

More specifically this study has shown that:

1. Sodic-dominant alteration (albitization) records major leaching processes that enrich the fluids in elements required to precipitate the diagnostic alteration facies in the evolving metasomatic system that host IOCG deposits. Elements that were mobilized during sodic alteration were precipitated during subsequent HT calcic–iron alteration while destruction of feldspars during the widespread HT calcic–iron alteration enriched the fluids in K (±Na) for precipitation of later potassium-bearing alteration assemblages. These geochemical results validate field observations of transitional alteration assemblages (sodic–calcic–iron, calcic–iron–potassic, etc.) that imply an evolving fluid chemistry;
2. Copper (chalcopyrite) precipitation principally occurred during the HT potassic–iron alteration stages, after precipitation of magnetite, amphibole and apatite during the HT calcic–iron and calcic–iron–potassic alteration stages;

3. A Cu- and S-rich fluid(s) may have been generated by either effervescence and exsolution of a vapor phase rich in Cu and S at the HT calcic–iron alteration stage or gradual enrichment in Cu and S in the residual fluid from which large amounts of magnetite and amphibole crystallized during the HT calcic–iron alteration stage;
4. Uranium and REE were initially concentrated in the HT calcic–iron alteration zones, thereby facilitating their remobilization and precipitation during the following HT potassic–iron and hematite-bearing alteration stages;
5. High temperature potassic–iron alteration zones were formed in the later stages of the hydrothermal system, during which F-activity, temperature and element mobility significantly decreased;
6. The intricate relationships between halogen activity, mineral assemblage stability and element mobility during the development of metasomatic systems that form IOCG deposits played an important role in mobilizing Th, V, Co, Ni and REE; and
7. Geochronology illustrated that hydrothermal alteration in the Fab system, bracketed to the period 1870.1 ± 1.7 – 1866.8 ± 1.3 Ma, was closely related the production of halogen-rich magmas at ca. 1868 Ma that provided a source for the halogen-rich, magmatic-hydrothermal fluids in the Fab system.

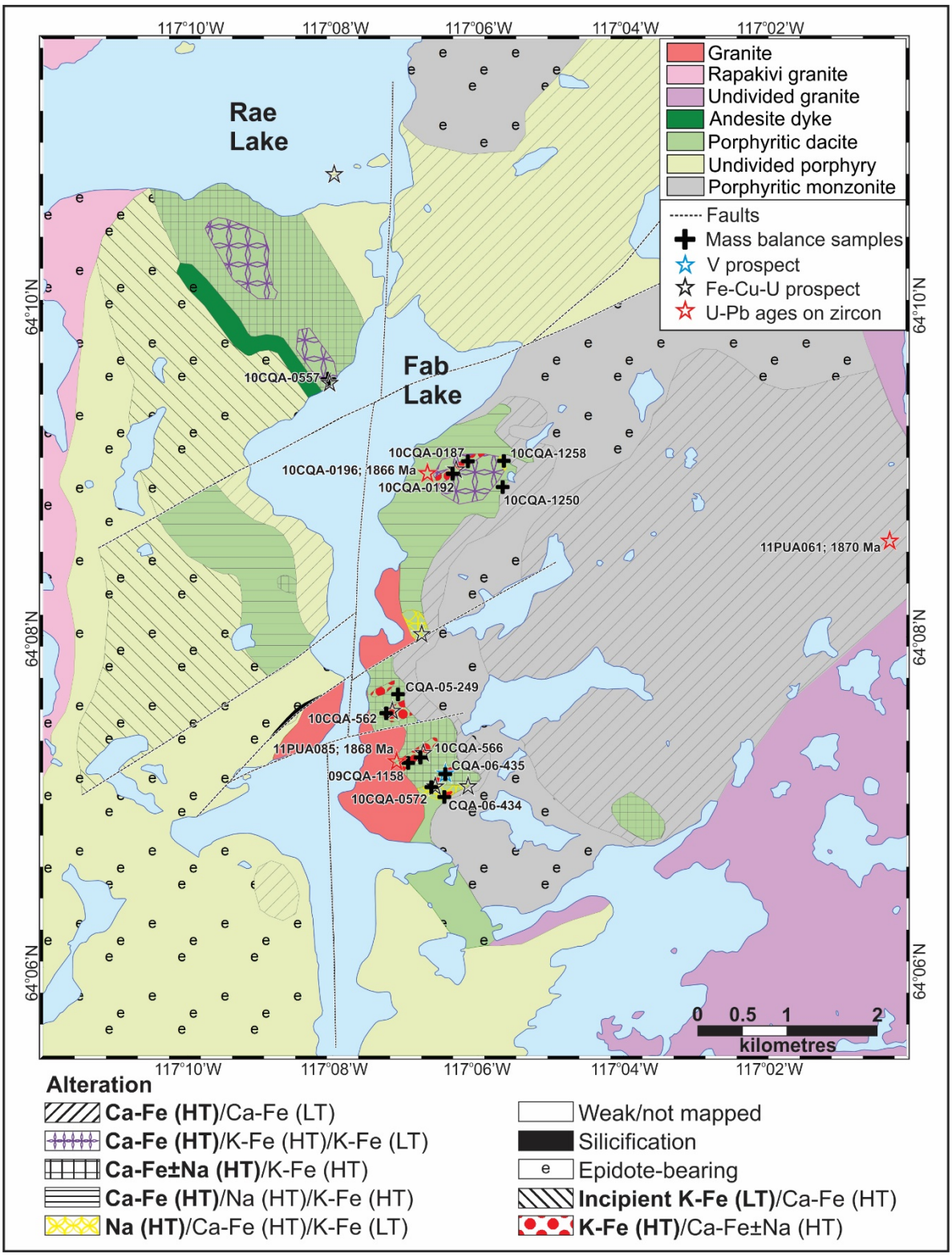

Figure 7-1 Geology and alteration map

The map illustrates the geology, the distribution of the Fe–Cu–U showings and the location of the samples used in the element mobility analysis and geochronology (geology after Gandhi, 1988, unpublished data; Azar, 2007; Jackson, 2008, alteration after Potter et al., 2013b).

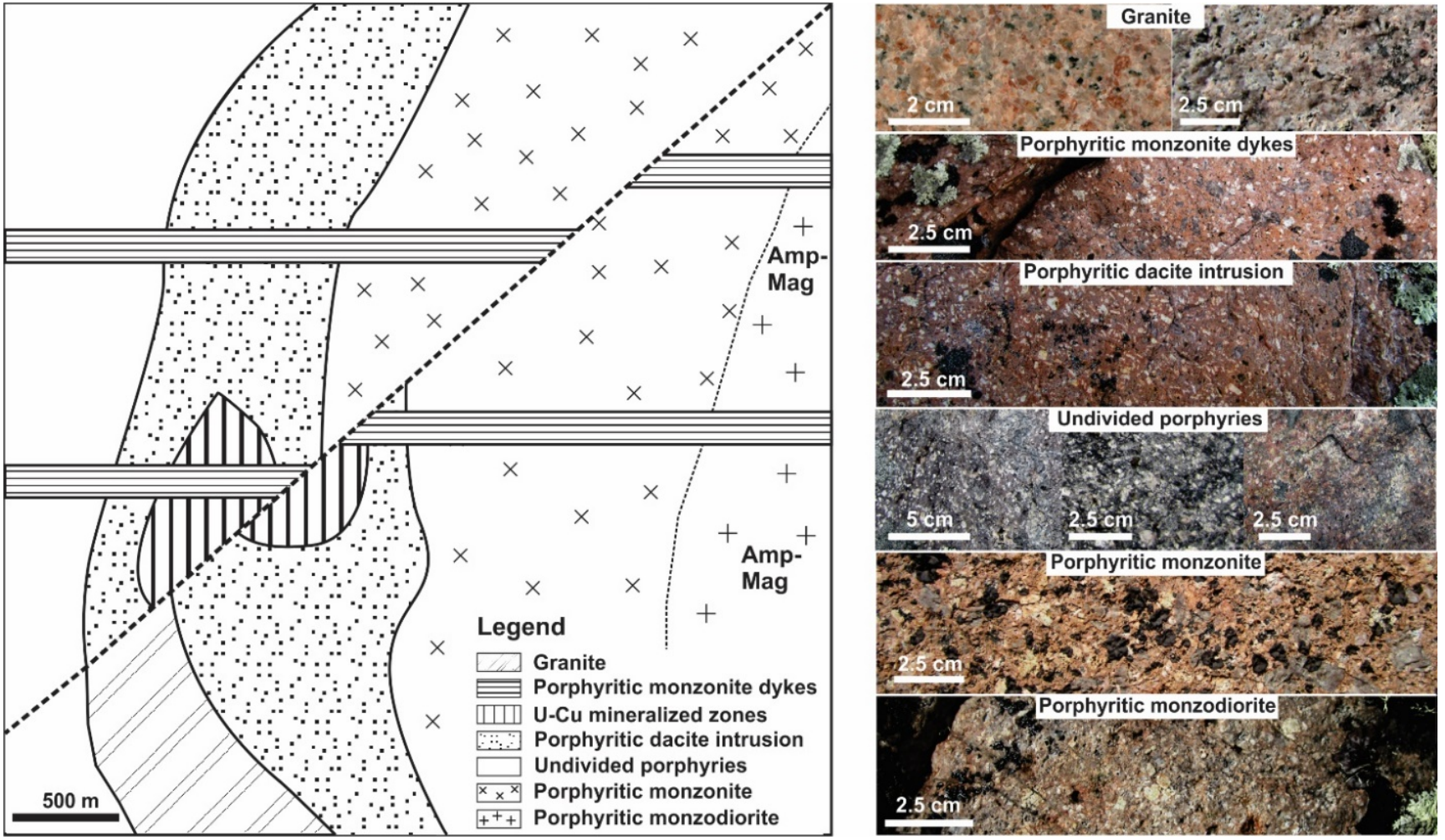

Figure 7-2 Schematic diagram and field pictures to illustrate the timing relationships of the various intrusions

The field and rock slab pictures of the intrusions are sequentially ordered (from top to bottom stations numbers: 11PUA-085; 10CQA-0185; 11PUA-535; 11PUA-565, 11PUA-589, 11PUA-562; 11PUA-056; 11PUA-062).

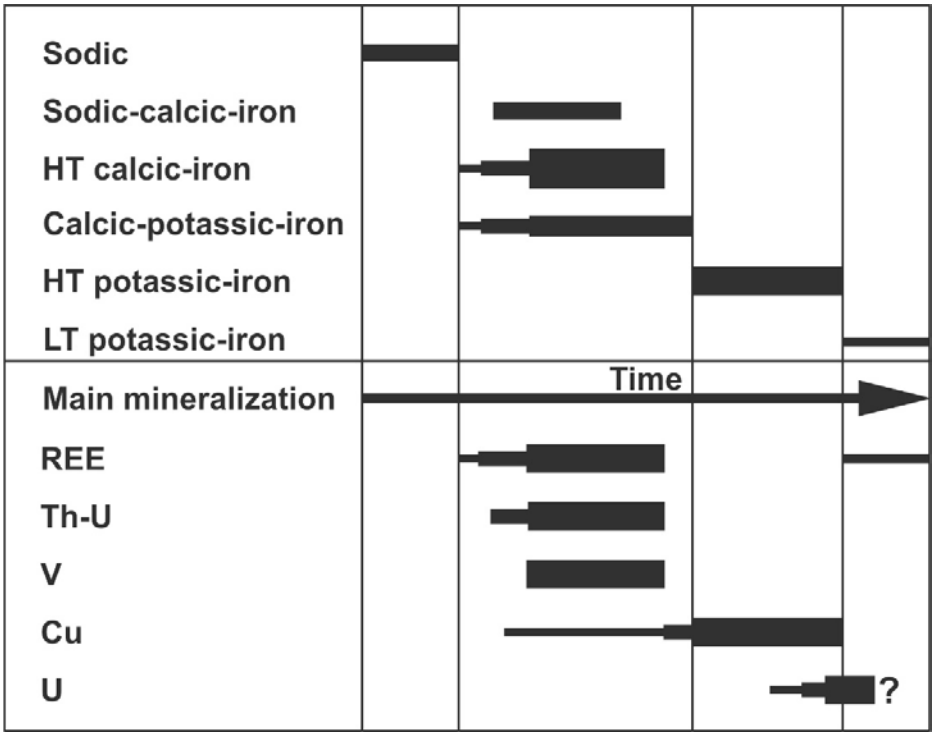

Figure 7-3 Schematic diagram to illustrate the timing of the main alteration and mineralization events at Fab.

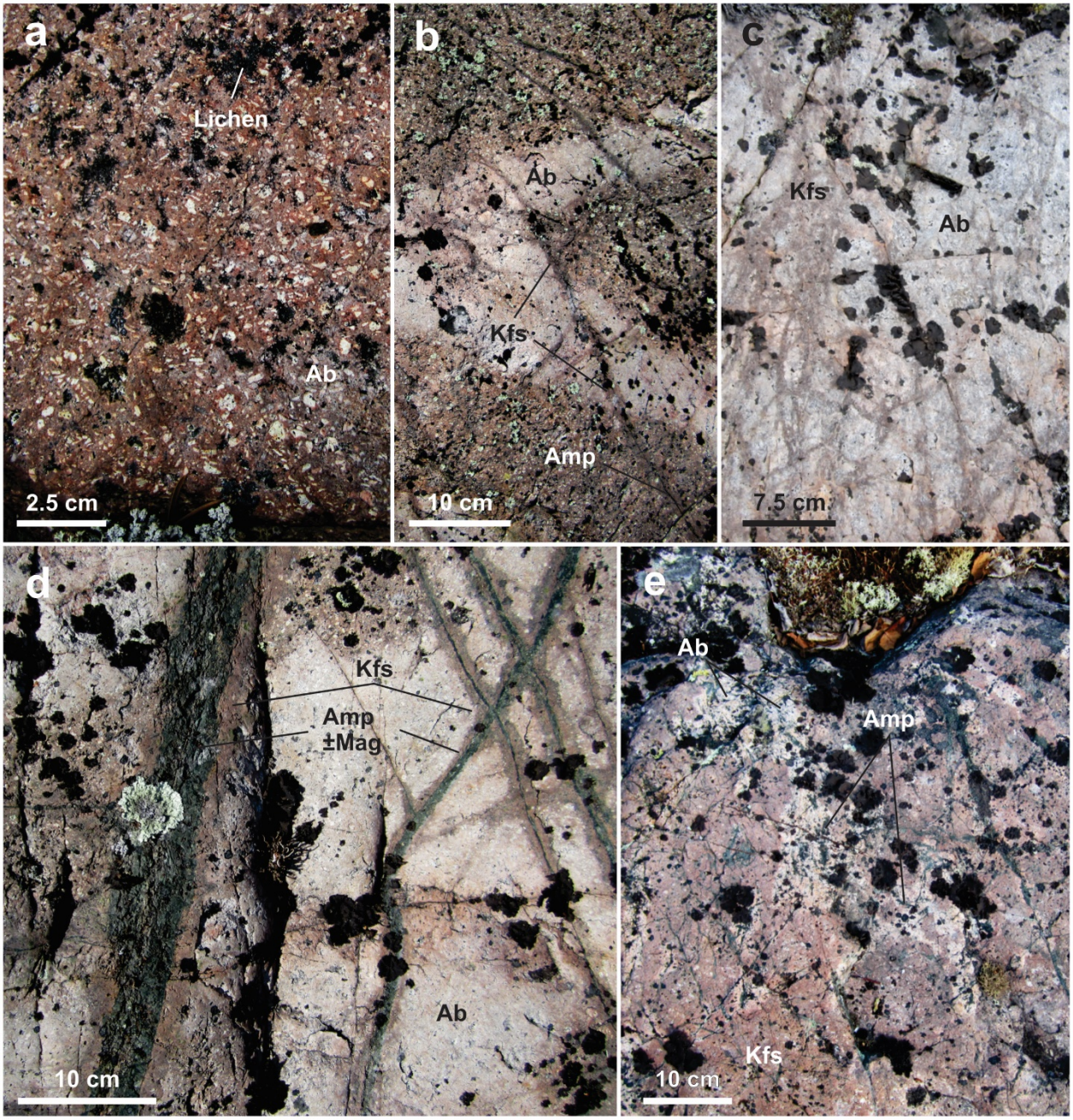

Figure 7-4 Field pictures, microphotographs and backscatter electron images of Na and HT Ca–Fe alteration

(a) Incipient and early albitization of feldspar phenocrysts and aphanitic matrix in the porphyritic dacite intrusion (11PUA-0536; note the black and creamy lichen); (b) Fairly sharp pervasive and texture-destructive albitization front cross cut by a set of parallel fractures with calcic-iron veinlets with cm-wide K-feldspar selvages marking a stage of incipient calcic-iron-potassic alteration (11PUA-1023); (c) Pervasive and texture-destructive albitization cut by incipient anastomosing to patchy potassic alteration (10CQA-1258); (d) Pervasive and texture-destructive albitization cut by calcic-iron-potassic alteration (amphibole + magnetite veins with K-feldspar selvages) (11PUA-1023); (e) Typical network of sodic-calcic-iron alteration veins composed of amphibole with variegated albite selvages (11PUA-0538);

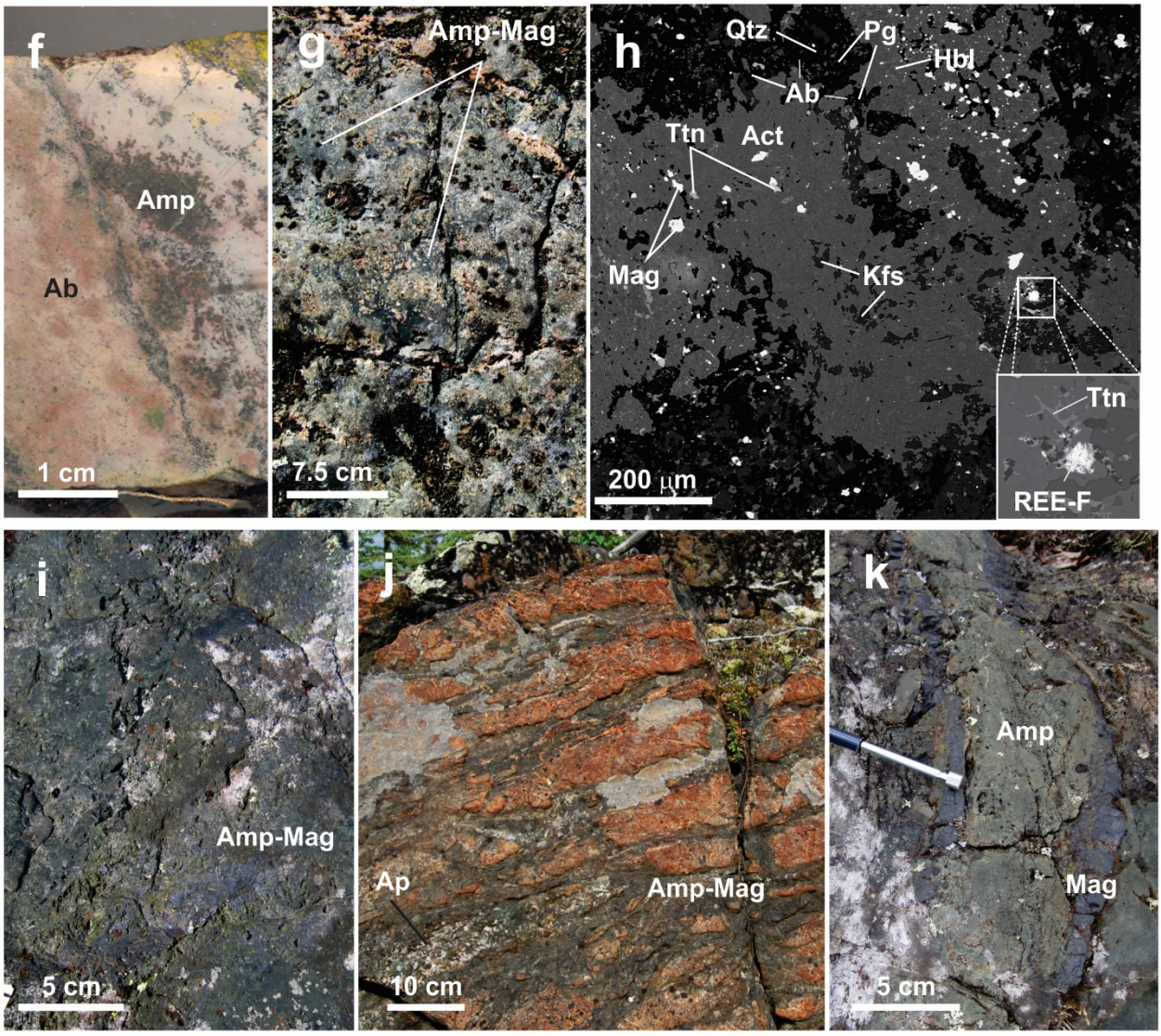

Fig. 7-4 suite – (f) Pervasive, texture-destructive and intense sodic-calcic-iron alteration with local zones of vein-like to variegated sodic-calcic-iron (albite + amphibole) replacement of the porphyritic dacite intrusion (CQA-05-0249); (g) Incipient, penetrative, variegated to anastomosing, HT calcic-iron alteration within the outer zones of the Fab system (11PUA-072); (h) BSE-image of the incipient HT calcic-iron alteration illustrating the mineralogy of that alteration in its early stage. Inset shows the presence of REE fluorocarbonate minerals associated with titanite (11PUA-072); (i) Incipient HT calcic-iron alteration illustrating the coeval crystallization of amphibole, magnetite, titanite, quartz and minor carbonate (pos. calcite; 11PUA-084); (j) V showing hosted in a decameter-size HT calcic-iron alteration zone consisting of coarse-grained amphibole and magnetite enveloping the Fe-Cu-U showings of the Fab system (CQA-06-0435); (k) Amphibole, amphibole-apatite and amphibole-magnetite veins typical of the HT calcic-iron alteration stockwork surrounding the large HT calcic-iron replacement zones (10CQA-0552);

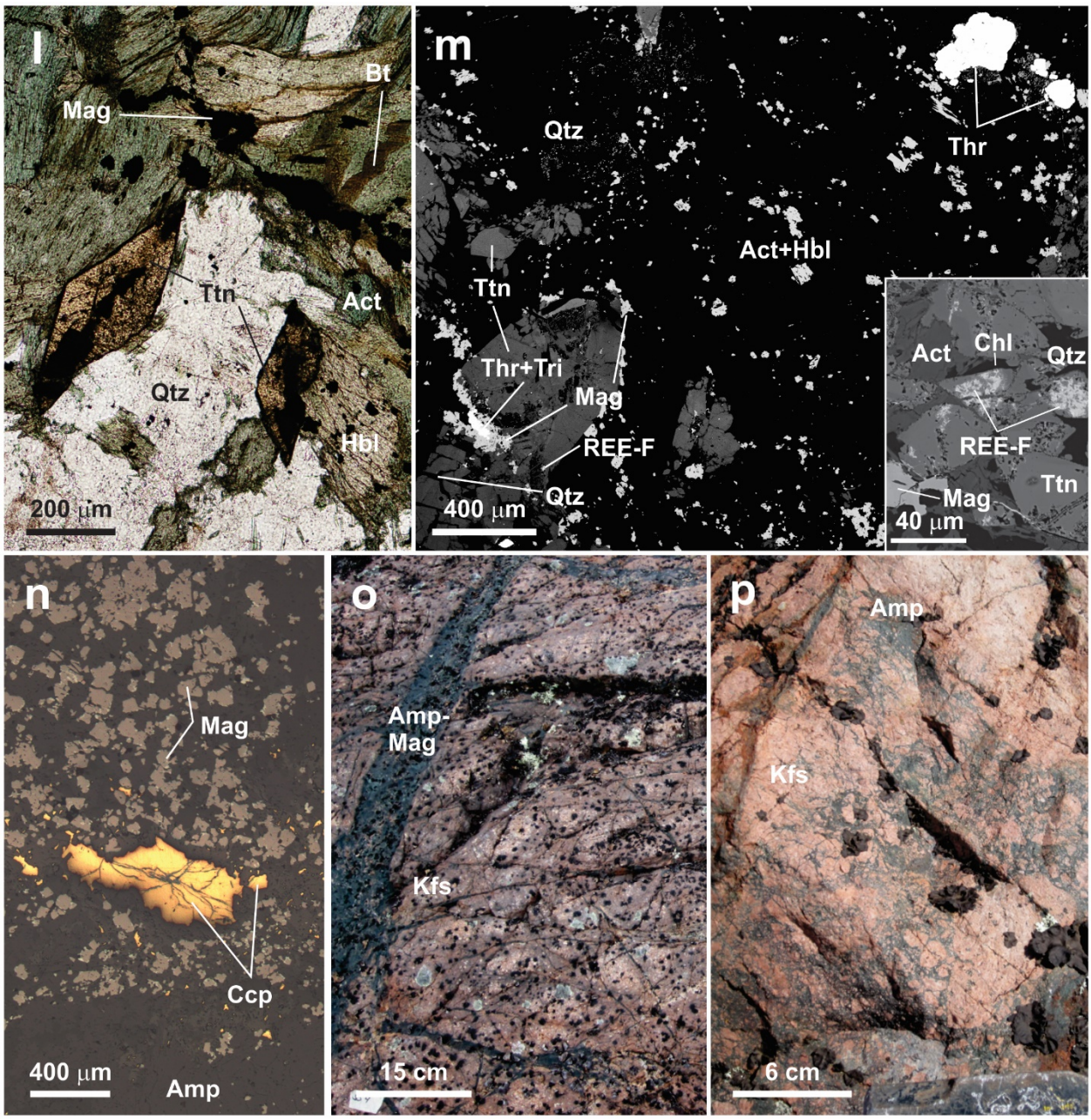

Fig. 7-4 suite – (l) Th- and titanite-rich HT calcic-iron alteration (10CQA-0557); (m) BSE-image of the HT titanite-rich calcic-iron alteration composed primarily of actinolite, hornblende, magnetite, titanite and quartz with accessory thorite, (Y)-tritomite and a REE- and F-bearing phase exsolved in the titanite crystals. Some of the titanite grains are metamict and other are locally replaced by late-stage chlorite. Inset shows the presence of the REE- and F-bearing minerals in the titanite; (n) Microphotograph showing chalcopyrite (yellow) disseminated within HT calcic-iron amphibole-magnetite (grey) veins (11PUA-053); (o) Typical calcic-iron-potassic alteration where the amphibole ± magnetite veins have centimeter-wide K-feldspar selvages (10CQA-558); (p) Hydrothermal breccia zone formed by intense calcic-iron-potassic alteration (10CQA-1249). Mineral abbreviations after Whitney and Evans (2010) except for Tri for the (Y)-tritomite.

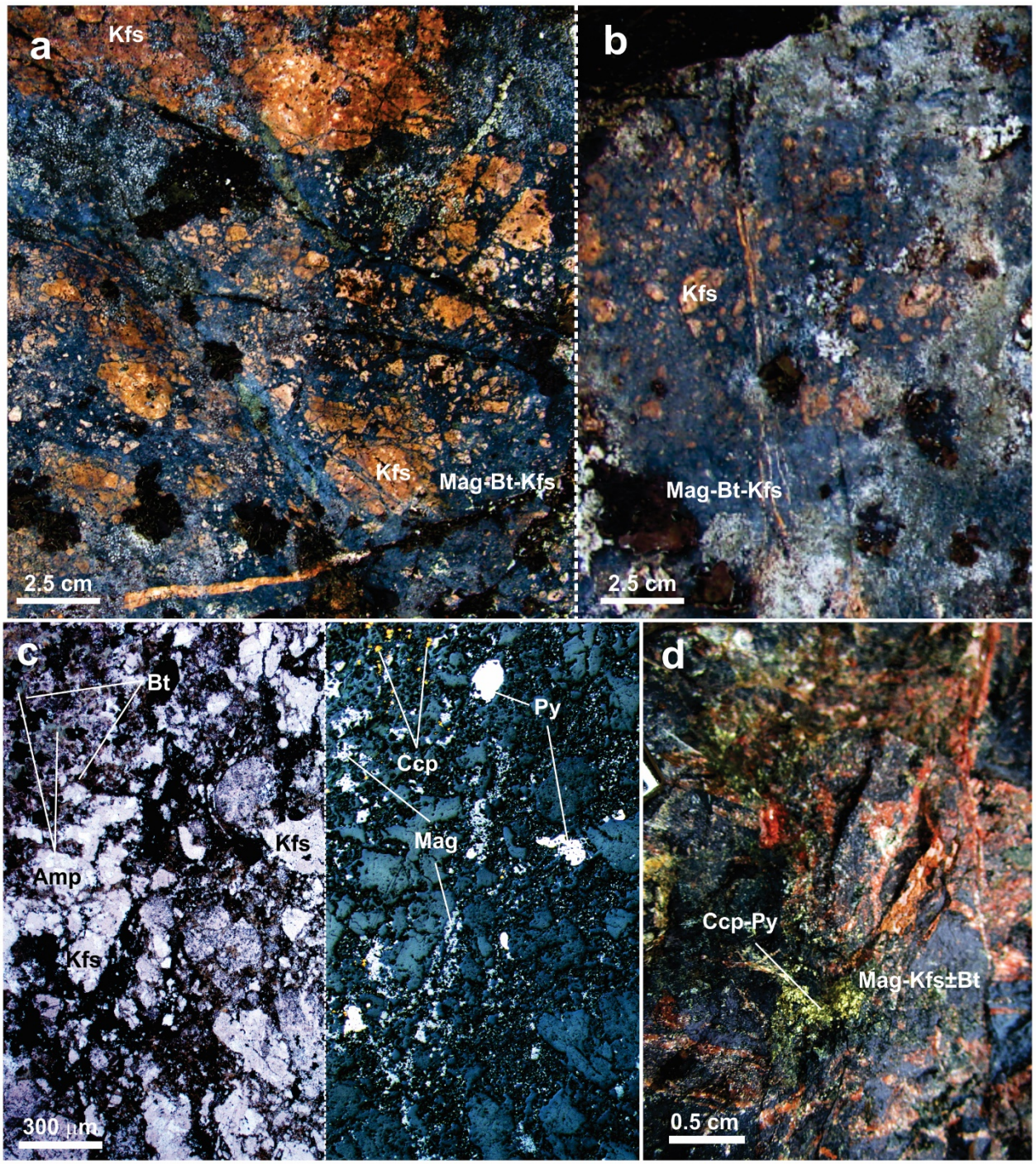

Figure 7-5 Field pictures and microphotographs of HT potassic-iron and LT potassic-iron alteration

(a) Typical magnetite- and local magnetite–amphibole–cemented hydrothermal breccias formed during the potassic–iron alteration stage in the outer parts of the intense and pervasive magnetite-bearing potassic–iron replacement of the Fab showings (09CQA-1157); (b) Transition from the magnetite-cemented hydrothermal breccias to the pervasive K-feldspar–magnetite replacement of the magnetite-bearing potassic–iron alteration (09CQA-1157); (c) Microphotograph of the transitional and biotite-rich HT potassic–iron alteration superimposed on HT calcic–iron alteration. The sample is incipiently brecciated and chalcopyrite with pyrite starts precipitating in the breccia cement with magnetite (09CQA-1159); (d) Main Fe–Cu–U mineralization zone of the Fab systems within hydrothermal breccias zones formed by HT potassic–iron alteration (11PUA-1000);

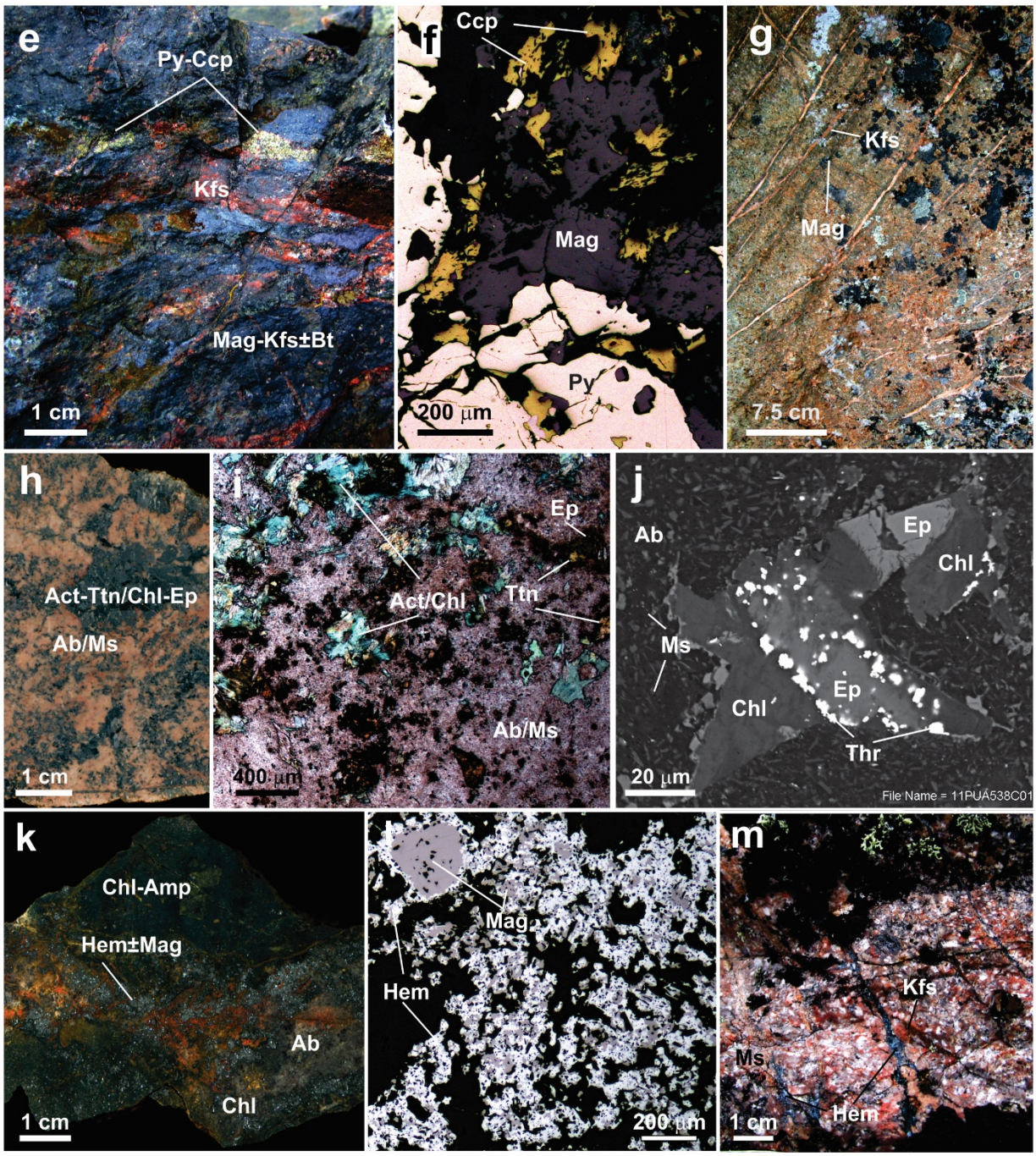

Fig. 7-5 suite – (e) Main Fe–Cu–U mineralization zone of the Fab systems within hydrothermal breccias zones formed by HT potassic–iron alteration (11PUA-1000); (f) Reflected light microphotograph of the copper-mineralized breccia zones of the Fab showings; (g) K-feldspar veins with magnetite selvages proximal to the main Fab showings (11PUA-031); (h and i) Sodic–calcic–iron (with amphibole dominant infill) pervasively overprinted by an incipient epidote–chlorite–muscovite alteration replacement of amphibole, titanite and albite (11PUA-538); (j) BSE-image of a titanite crystal completely replaced by epidote and then chlorite with precipitation of thorite indicating that titanite was initially Th-bearing; (k) Specular hematite and chlorite impregnation superimposed on HT calcic–iron with earthy hematite developed on least-altered precursor (11PUA-086); (l) Reflected light microphotograph showing the selective specular hematite replacement of magnetite. The silicates are predominantly chloritized amphiboles (11PUA-086); (m) Hematite veinlet with K-feldspar selvages observed in the undifferentiated porphyry in the outer alteration aureole of the Fab system (11PUA-062).

Mineral abbreviations after Whitney and Evans (2010).

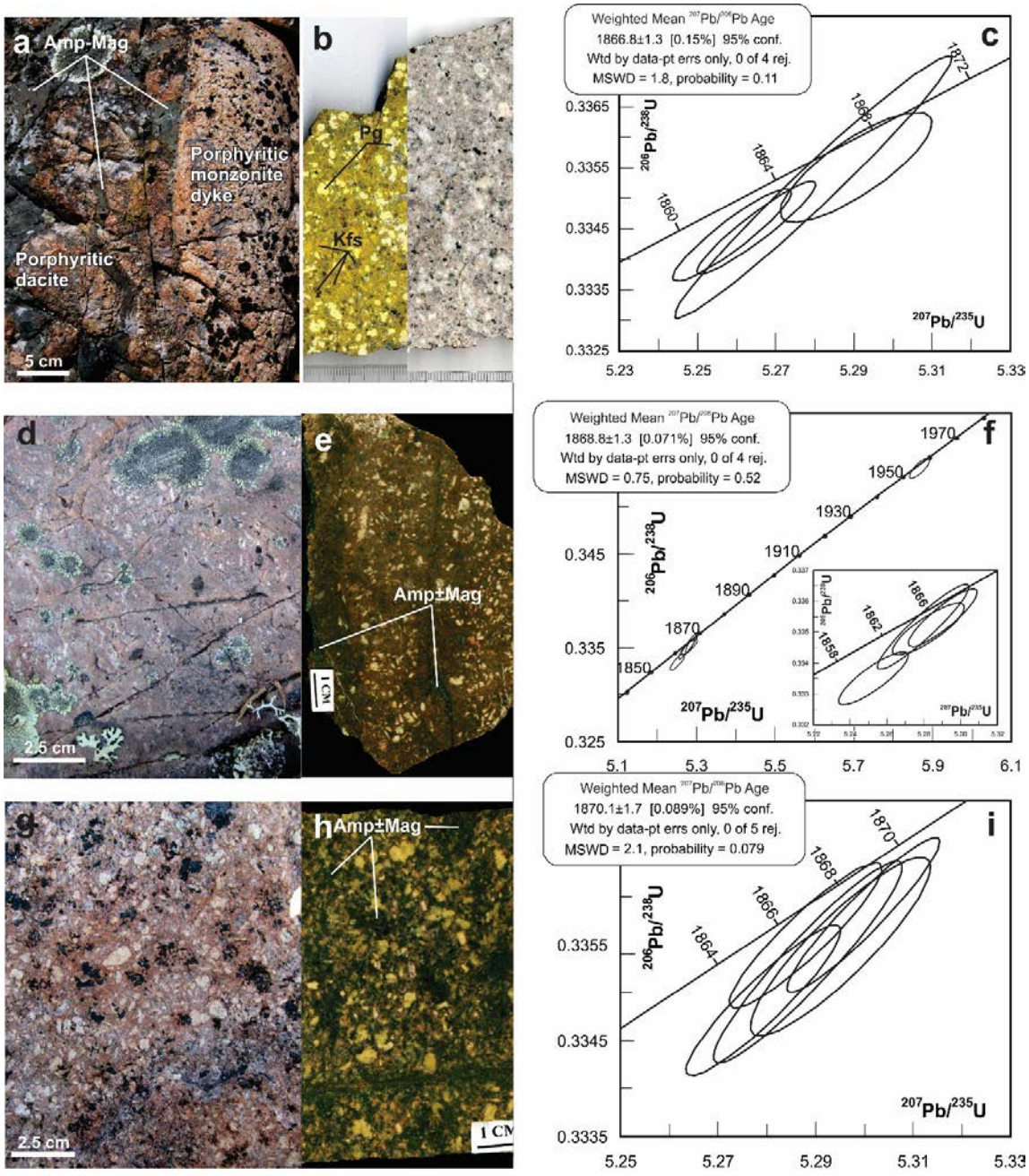

Figure 7-6 Geochronology samples

(a) Porphyritic monzonite dike cutting the main calcic–iron alteration of the porphyritic dacite intrusion in the Fab system; (b) Cut slab of the monzonitic porphyry dike. Left image is stained with cobaltnitrate to highlight pervasive potassic alteration; (c) U–Pb concordia plot for zircon grains from the monzonitic porphyry dike cross cutting the main IOAA alteration of the Fab system (10CQA-0196); (d) Field picture of the amphibole–magnetite-bearing porphyritic monzodiorite intrusion (11PUA-061); (e) Rock slab of amphibole–magnetite-bearing porphyritic monzodiorite showing the patchy and anastomosing calcic–iron replacement of the fine-grained groundmass and coeval amphibole veins impregnating the matrix; (f) U–Pb concordia plot for zircon grains from the amphibole–magnetite porphyritic monzodiorite east of the Fab system; (g) Field picture of the porphyritic dacite intrusion; (h) Rock slab of the porphyritic dacite intrusion cross cut by amphibole ± magnetite veins typical of the Fab system; (i) U–Pb concordia plot for zircon grains of the porphyritic dacite intrusion hosting most of IOAA alteration related to the Fab system (11CQA-085).

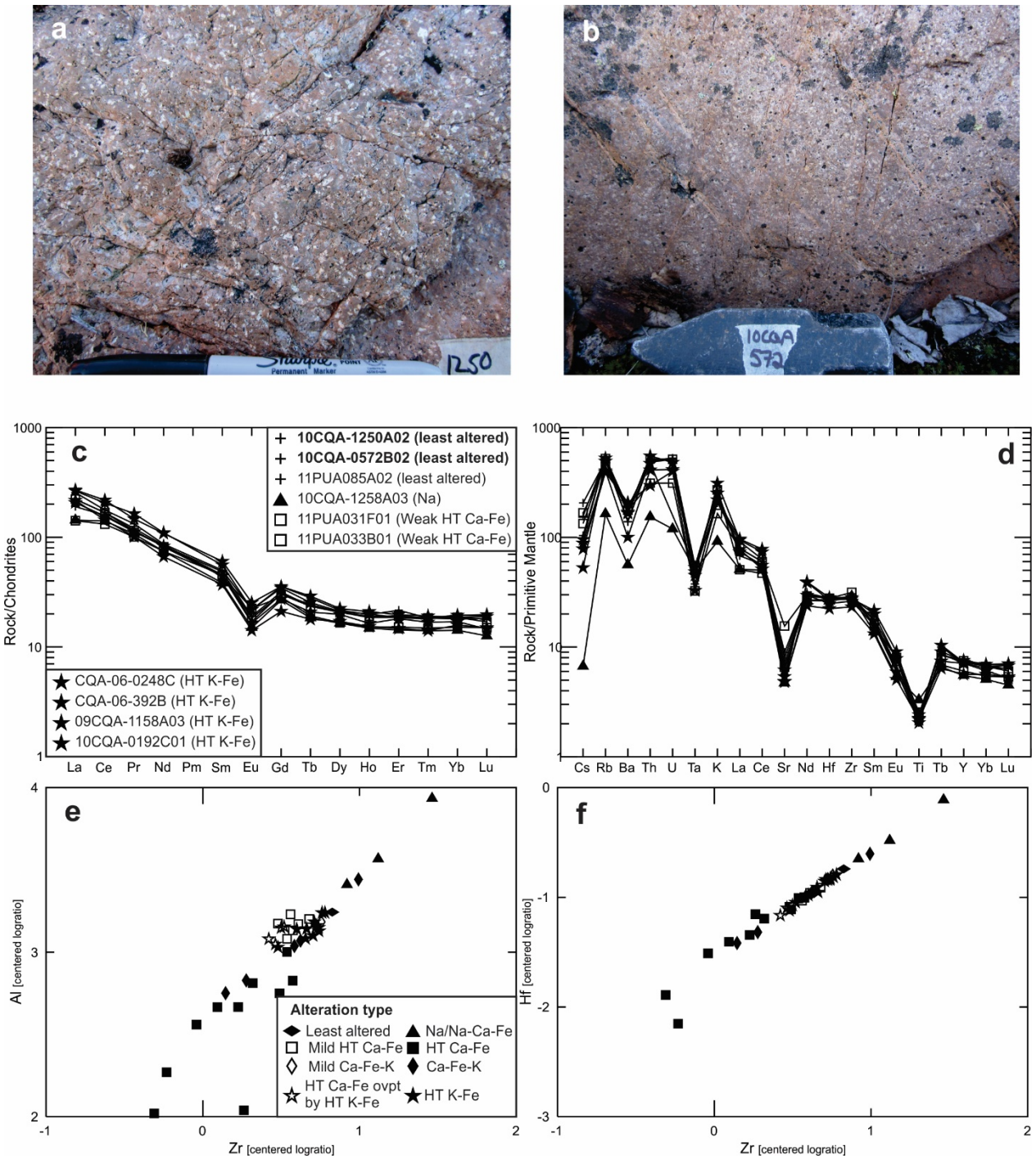

Figure 7-7 Field pictures and chemistry of the porphyritic dacite host

a) and (b) Field pictures of the sampling sites for the weakly altered porphyritic dacite intrusion samples used in the mass balance analysis (10CQA-1250A02 and 10CQA-0572B02); (c) Chondrite-normalized REE profile of the weakly altered porphyritic dacite samples used in the mass balance analysis; (d) Primitive mantle-normalized trace elements profiles of the weakly altered porphyritic dacite samples used in the mass balance analysis; Log-centered diagrams for all the chemical analyses used in this paper of (e) Hf vs Zr; (f) Al vs Zr. Chondrite normalization after Palme and Jones (2003) and primitive mantle normalization after Palme and O'Neill (2003)

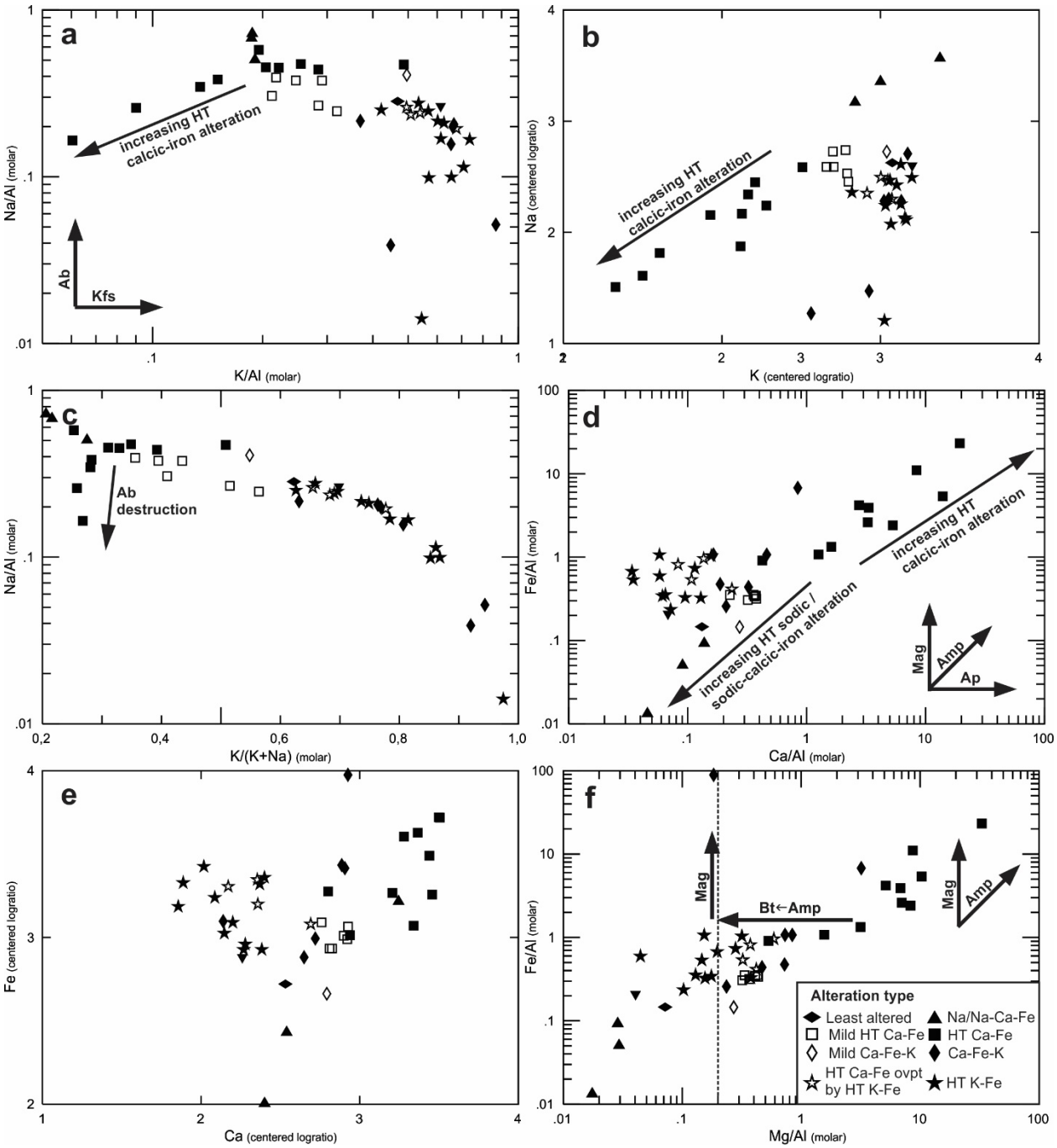

Figure 7-8 Bivariate diagrams for major element variations

(a) $(Na/Al)_{(molar)}$ vs $(K/Al)_{(molar)}$; (b) Clr-transformed plot of Na vs K with covariations very similar to those on the $(Na/Al)_{(molar)}$ vs $(K/Al)_{(molar)}$ diagram; (c) $(Na/Al)_{(molar)}$ vs $(K/(Na+K))_{(molar)}$; (d) $(Fe/Al)_{(molar)}$ vs $(Ca/Al)_{(molar)}$; (e) Clr-transformed plot of Fe vs Ca with covariations very similar to those on the $(Fe/Al)_{(molar)}$ vs $(Ca/Al)_{(molar)}$ diagram; (f) $(Fe/Al)_{(molar)}$ vs $(Mg/Al)_{(molar)}$.

.

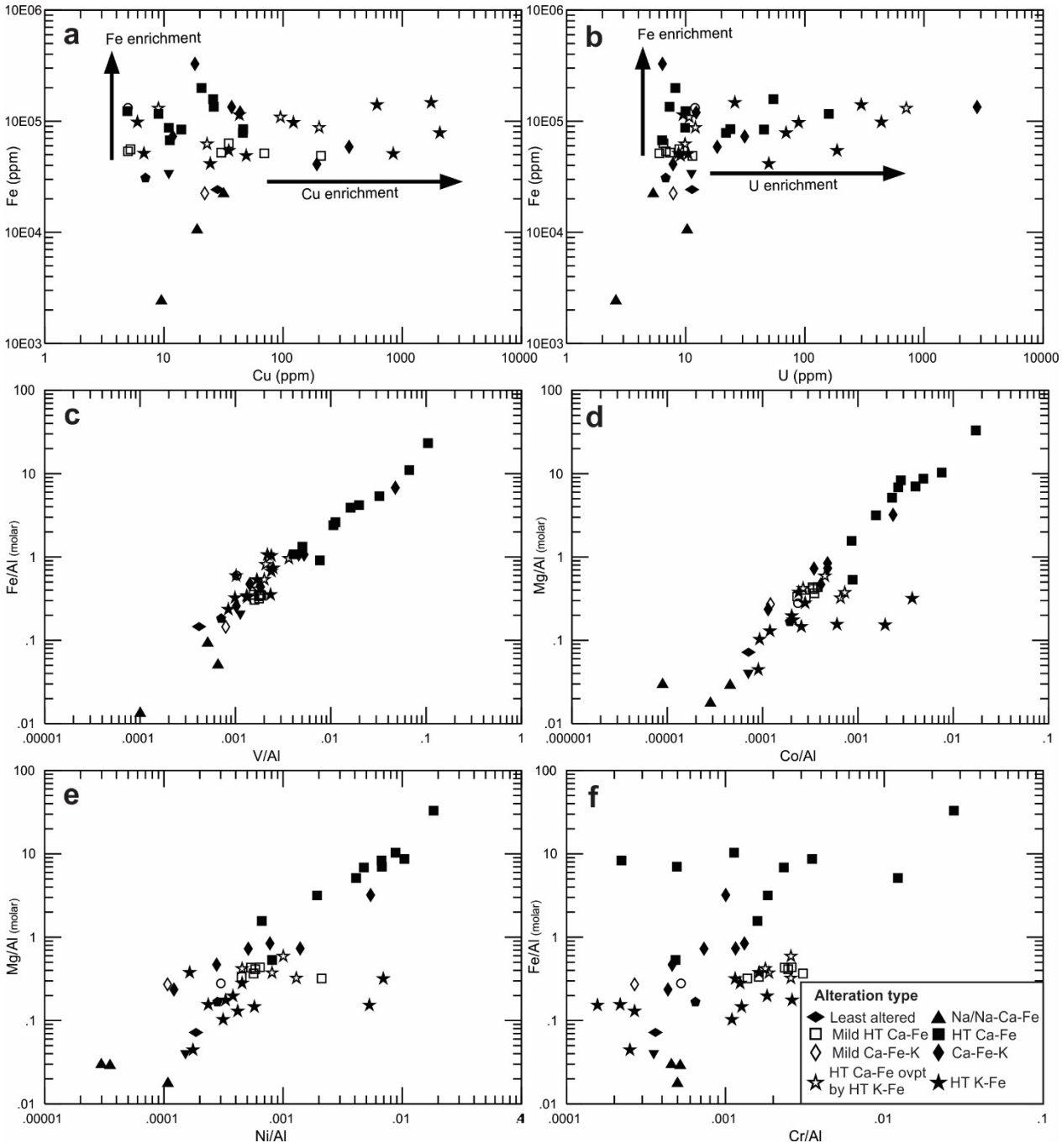

Figure 7-9 Bivariate diagrams of transition metal variations

(a) Fe vs Cu; (b) Fe vs U; (c) $(Fe/Al)_{(molar)}$ vs (V/Al); (d) $(Mg/Al)_{(molar)}$ vs (Co/Al); (e) $(Mg/Al)_{(molar)}$ vs (Ni/Al); (f) $(Mg/Al)_{(molar)}$ vs (Cr/Al).

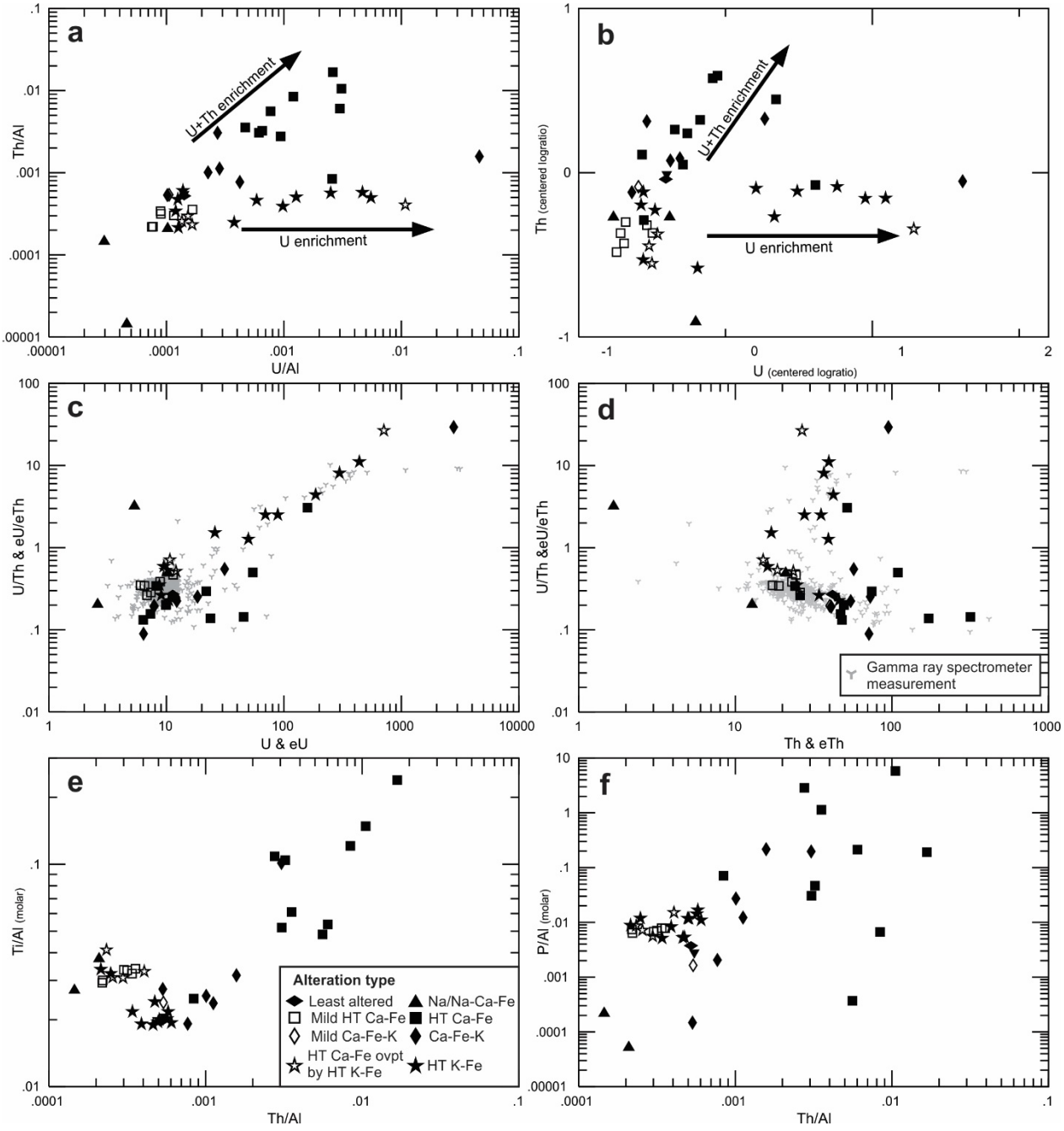

Figure 7-10 Bivariate diagrams for Th and U variations

(a) (Th/Al) vs (U/Al); (b) Clr-transformed plot of Th vs U with covariations very similar to those on the (Th/Al) vs (U/Al) diagram; (c) Plot of U/Th and eU/eTh vs U and eU; (d) Plot of U/Th and eU/eTh vs Th and eTh; Zr-normalized diagram of (e) $(Ti/Al)_{(molar)}$ vs (Th/Al); (f) $(P/Al)_{(molar)}$ vs (Th/Al).

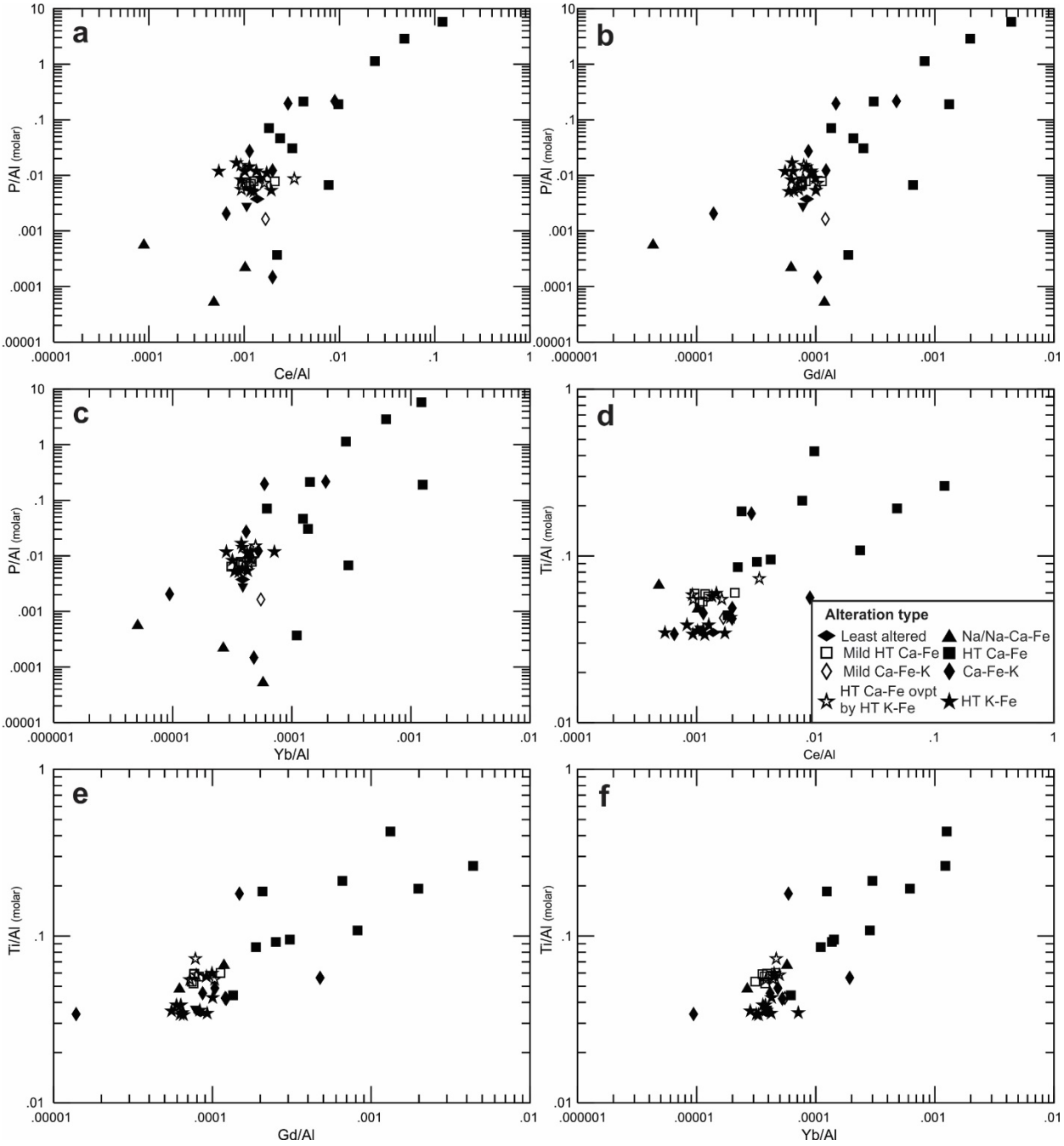

Figure 7-11 Bivariate diagrams for REE variations

(a) $(P/Al)_{(molar)}$ vs Ce/Al; (b) $(P/Al)_{(molar)}$ vs Gd/Al; (c) $(P/Al)_{(molar)}$ vs Yb/Al; (d) $(Ti/Al)_{(molar)}$ vs Ce/Al; (e) $(Ti/Al)_{(molar)}$ vs Gd/Al; (f) $(Ti/Al)_{(molar)}$ vs Yb/Al.

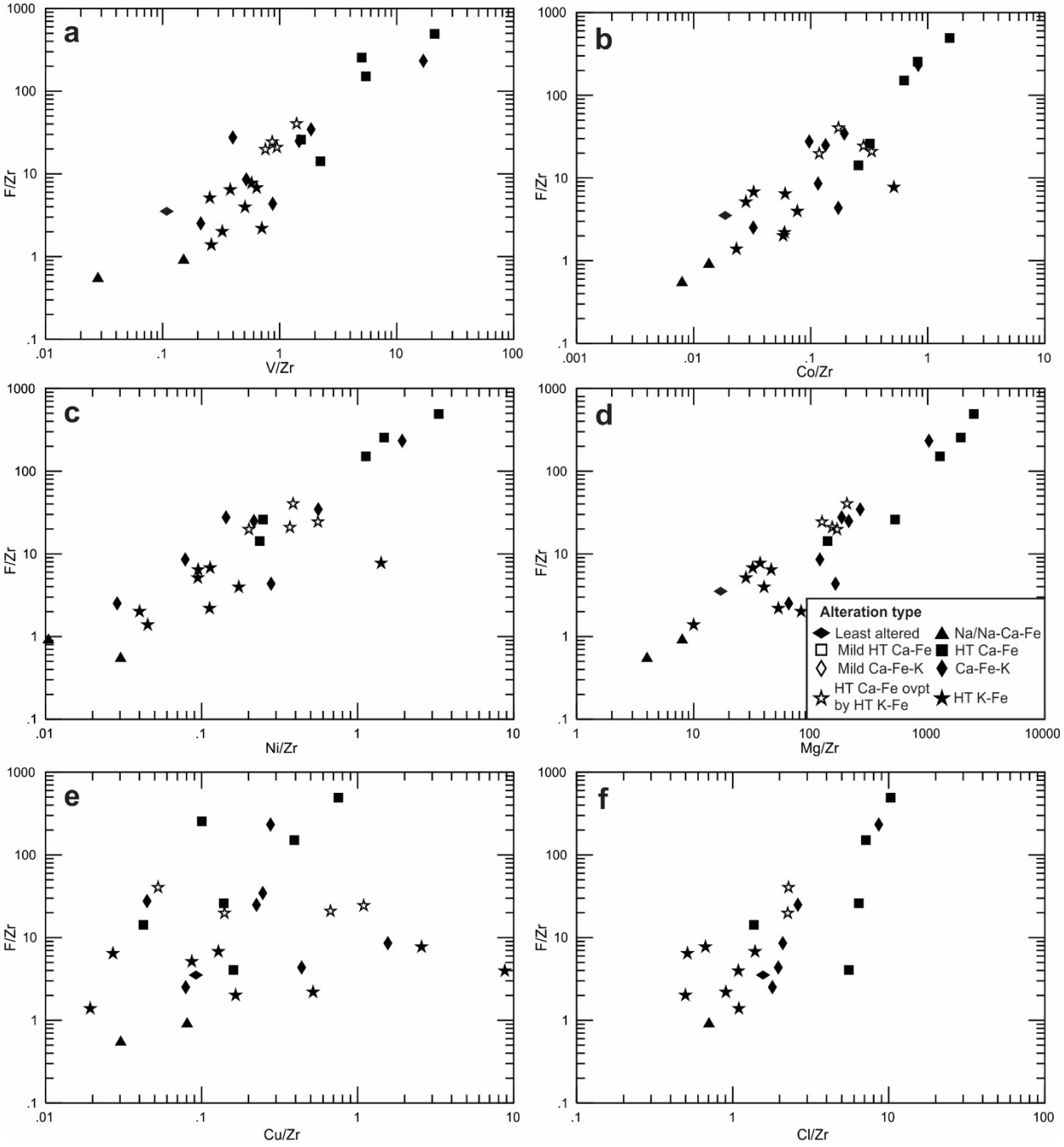

Figure 7-12 Zr-normalized bivariate diagrams showing F variations

(a) F vs V; (b) F vs Co; (c) F vs Ni; (d) F vs Mg; F vs Cu; F vs Cl.

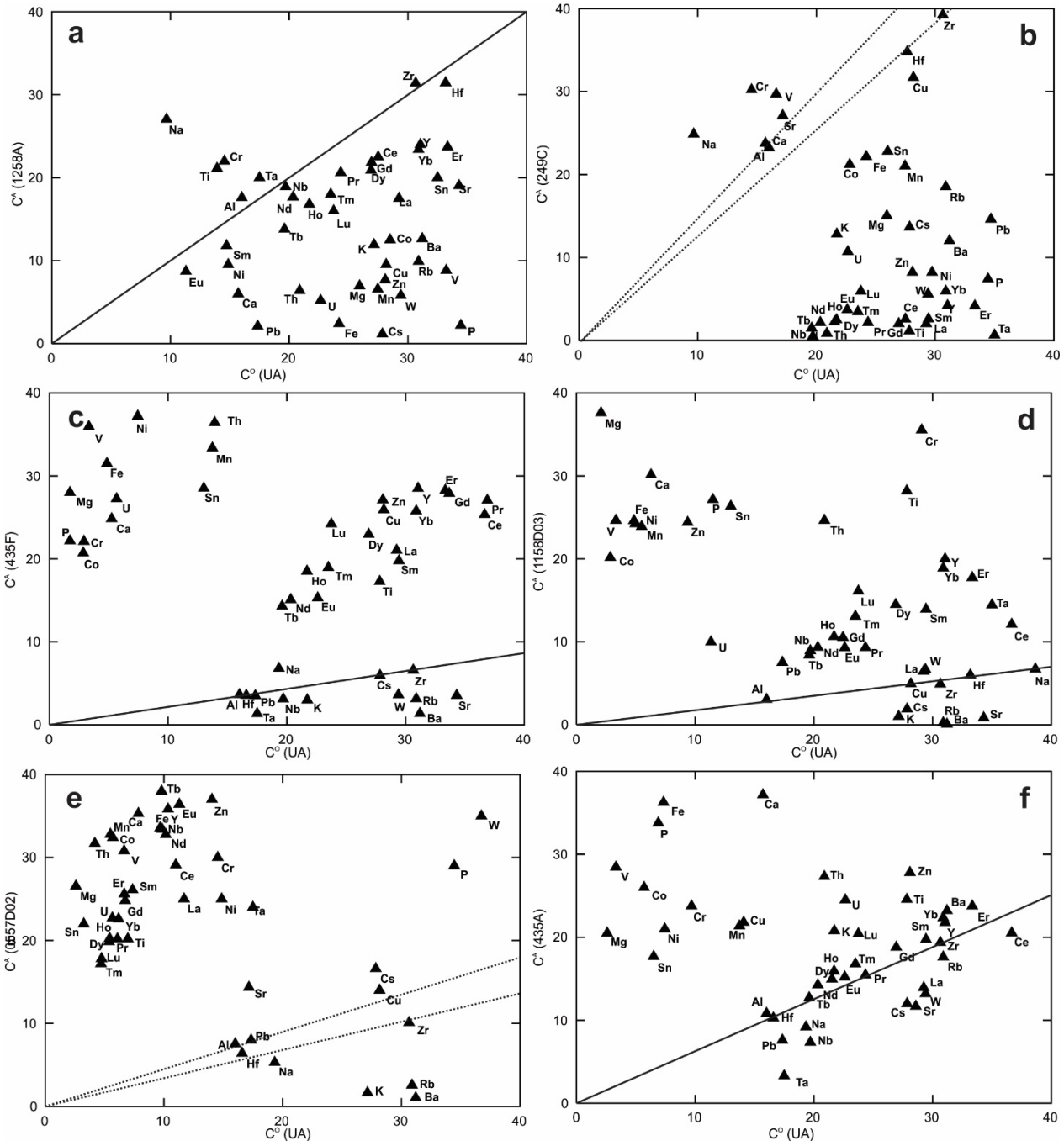

Figure 7-13 Isocon diagrams for sodic, sodic–calcic–iron and HT calcic–iron alteration

(a) Pervasive sodic alteration overprinted by weak potassic alteration (10CQA-1258A); (b) Intense sodic–calcic–iron alteration nearby the main Fab showings (CQA-05-249C); (c) Intense Th-rich and magnetite-rich HT calcic–iron alteration hosting the Fab V showing in the outer margins of the intense HT potassic–iron alteration zone (CQA-06-0435C); (d) Intense Th-normal HT calcic–iron alteration hosting the Fab V showing (09CQA-1158D03); (e) Extreme example of Th-rich HT calcic–iron alteration of the Fab system (10CQA-0557D02); (f) Th- and V-rich calcic–iron–potassic alteration located in the outer zones of the intense HT potassic–iron alteration hosting the main Fab showings (CQA-06-435A).

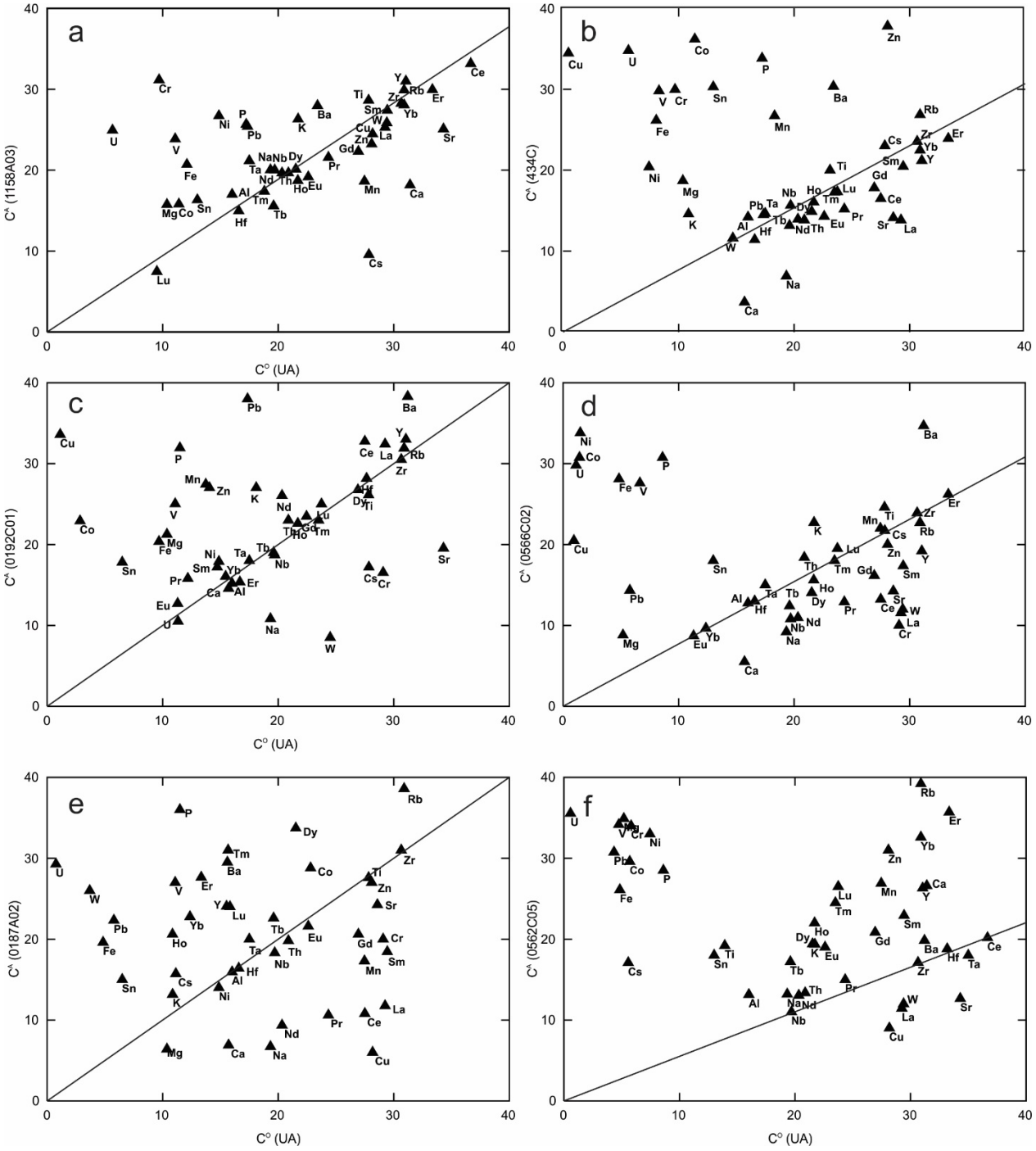

Figure 7-14 Isocon diagrams for calcic–iron–potassic and HT potassic–iron alteration

(a) Cu–U-normal potassic–iron alteration typical of the main Fab showings (09CQA-1158A03); (b), (c) and (d) Different types of Cu-rich potassic–iron alteration typical of the main Fab showings (CQA-06-0434C, 10CQA-0192C01 and 10CQA-0566C02); (e) U-mineralized HT potassic–iron alteration of the main Fab showings clearly superimposed on an earlier HT calcic–iron alteration (10CQA-0562C05); (f) U-mineralized HT potassic–iron alteration with an element mobility pattern more typical of the HT potassic–iron alteration.

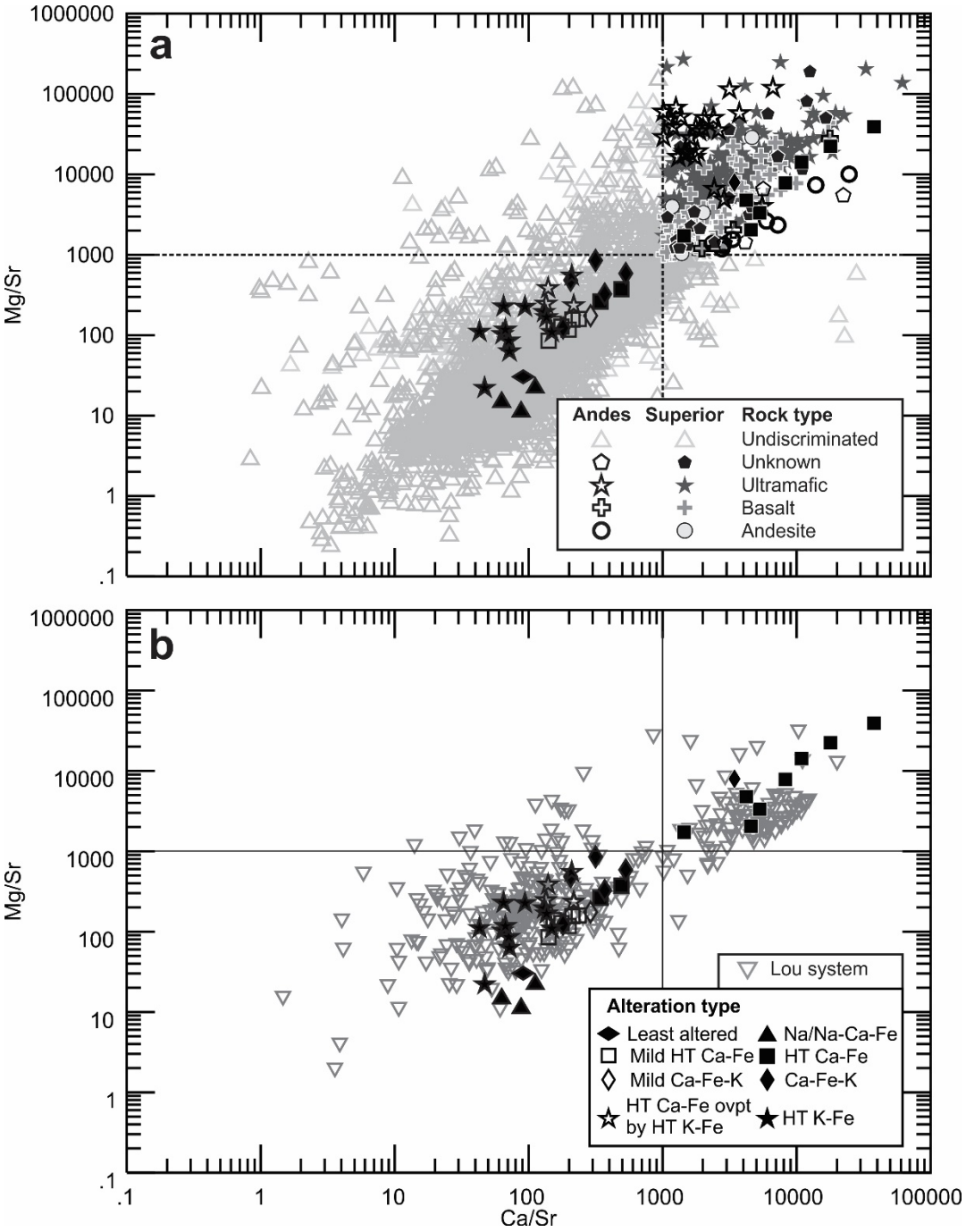

Figure 7-15 Bivariate diagrams showing the distribution of the Mg/Sr vs Ca/Sr ratios

(a) The Fab system, the Superior Province and the Andes; (b) The Fab and Lou systems. The Lou system encompasses the NICO deposit and the Southern Breccia albitite-hosted U showings.

MOBILITÉ DES ÉLÉMENTS ET FORMATION DE GÎTES POLYMÉTALLIQUES AU SEIN DES SYSTÈMES À OXYDES DE FER ET ALTÉRATION EN EN ÉLÉMENTS ALCALINS, ZONE MAGMATIQUE DU GRAND LAC DE L'OURS, TERRITOIRES DU NORD-OUEST, CANADA

TROISIÈME PARTIE : CONTRIBUTIONS À L'AVANCEMENT DE LA SCIENCE ET CONCLUSIONS

CHAPITRE 8 : AVANCEMENT DES CONNAISSANCES

Ce chapitre résume les principales contributions de cette thèse à l'avancement des géosciences.

8.1 Le contexte tectono-magmatique de formation du Groupe de Faber, sud de la GBMZ (chapitre 2)

Avant cette thèse de doctorat, les séquences volcaniques du Groupe de Faber dans le sud de la GBMZ étaient considérées comme étant d'affinité calco-alcaline (Hildebrand et al., 1987; Gandhi et al., 2001) et majoritairement felsiques (Gandhi et al., 2001). En réexaminant la composition en éléments majeurs et traces des roches volcaniques et intrusives du sud de la GBMZ avec de nouvelles données chimiques et une meilleure connaissance des effets de l'altération IOAA sur la mobilité des éléments, le contexte tectonique de formation du sud de la GBMZ a été attribué à un environnement d'arc où le magmatisme shoshonitique prédomine. Du magmatisme shoshonitique directement associé à la formation d'altérations hydrothermales IOAA et minéralisations IOCG a déjà été identifié dans le secteur de Fab Lake par Azar (2007). L'évolution de la composition des magmas au cours de la formation du Groupe de Faber varie de principalement felsique dans les stades initiaux de l'activité magmatique à intermédiaire et combiné à une plus grande abondance de magmas d'affinité intra-plaques à transitionnels. Cette évolution compositionnelle des magmas et une plus grande composante de magmas d'affinité intra-plaque à transitionnelle sous-tend que le régime de contraintes a évolué de principalement compressif à principalement extensif (chapitre 2). Un tel changement de régime a été interprété pour la région de DeVries par Corriveau et al. (2007). Dans le sud de la GBMZ, les effets directs de cette transition entre ces deux régimes tectoniques se sont principalement manifestés à partir de 1870–1869 Ma après la formation de l'Assemblage de Lou. Finalement il a été démontré que la séquence rhyolitique basale du Groupe de Faber, formée à la discordance avec les roches sédimentaires du Groupe de Treasure Lake et contemporaine au gisement de NICO et à la formation de la Southern Breccia, a une composition en ÉTR et en Al, Nb, Ta, Ti et Zr particulière et distincte des autres roches volcaniques et intrusives du Groupe de Faber.

8.2 La zonalité des altérations dans les systèmes IOAA et la distribution des métaux entre les différents faciès d'altération (chapitres 3 et 4)

Cette thèse définit les principaux faciès d'altération dans les systèmes IOAA de la GBMZ (chapitre 3) et démontre l'utilité des faciès d'altération pour contraindre l'évolution d'un système hydrothermal, car par définition (voir section 1.4.2), chaque faciès d'altération est formé sous des conditions physico-chimiques qui lui sont spécifiques (chapitre 3). Ensuite pour chaque faciès d'altération défini, les assemblages métallifères (chapitre 4) et les processus d'altération (veines, remplacement, bréchification; chapitre 3) qui leur sont caractéristiques sont décrits. Ces contributions confirment que le modèle de zonation des altérations développé par Corriveau et al. (2010b) s'applique dans l'ensemble des systèmes IOAA de la GBMZ et dans la majorité des systèmes IOCG à travers le monde. Les capacités prédictives du modèle de zonation des altérations, lorsque les assemblages métallifères caractéristiques de chaque stade d'altération y sont ajoutés, sont aussi démontrées en utilisant les exemples de Mag Hill dans le district de Port Radium–Echo Bay et de la Southern Breccia–NICO dans le système de Lou. Cette contribution illustre les applications du modèle de zonation qui permet de pronostiquer la signature métallifère des gisements potentiellement présents. Ces pronostics sont fonction des faciès d'altération observés dans chacun de ces systèmes IOAA et des assemblages métallifères observés dans les différents faciès d'altération. Cette étude des nombreux indices de la GBMZ élargit son potentiel pour les gîtes d'uranium encaissés dans des albitites ainsi que les gîtes IOA enrichis en V et/ou ÉTR. Le chapitre 4 contraint également la distribution et mobilité des ÉTR dans les altérations IOAA.

8.3 La signature chimique des altérations dans les systèmes IOAA (chapitres 3-5)

Cette thèse définie le portrait chimique général de l'altération des systèmes à oxydes de fer et éléments alcalins en utilisant les méthodes d'analyse compositionnelle par composantes principales (Aitchison, 1986). Cette contribution démontre que lorsque l'altération est intense, la

signature chimique des éléments majeurs et plusieurs éléments traces des altérations à oxydes de fer et éléments alcalins est faiblement influencée par la composition initiale du précurseur (protolite), qu'il soit intrusif, volcanique ou sédimentaire. En considérant que la signature chimique des altérations IOAA intenses est généralement indépendante du protolite, à l'exception des zones d'altération formées dans des séquences géologiques comprenant plusieurs unités carbonatées, un diagramme pour identifier les différents faciès d'altération dans les systèmes IOAA formés dans des roches volcano-plutonique a été établi. Ce diagramme distingue les roches altérées des roches fraîches (ou moins altérées) et discrimine les altérations IOAA entre elles. Cette publication a aussi mené au développement de la représentation schématique des altérations, telle qu'utilisée dans les cartes des chapitres 2, 4 et 6, en utilisant les concentrations molaires de Na, Ca, Fe, K et Mg, car l'analyse compositionnelle a indiqué que ce sont des éléments clés pour discriminer les altérations des altérations à oxydes de fer et éléments alcalins. Cette représentation schématique et très visuelle est d'une grande aide pour contraindre rapidement, avec des analyses d'éléments majeurs, la distribution spatiale des altérations IOAA dans une région donnée.

8.4 La relation entre les gisements d'uranium encaissés dans des albitites et les systèmes IOAA (chapitre 6)

La découverte des indices à U–Th±Cu±Mo encaissés dans des albitites de la Southern Breccia pendant la réalisation de cette thèse résulte d'un réexamen préalable des types d'altération reconnus autour du gîte de NICO, de la reconnaissance d'éléments manquants par comparaison avec ce qui serait pronostiqué d'un système IOAA complet et du test de cette hypothèse par de nouveaux levés de terrain. Ce faisant, la découverte des albitites et des zones uranifères associées aux faciès d'altération potassique à fer démontre l'applicabilité du modèle d'évolution des systèmes IOAA présenté dans au chapitre 3. De plus cette zone en élargie la portée en démontrant qu'il existe, dans certains systèmes IOAA, des liens génétiques et temporels étroits entre les gîtes d'uranium encaissés dans des albitites et les gîtes IOCG. Cette thèse démontre aussi que les roches métasédimentaires structuralement sous le gisement de NICO contiennent un corridor d'albitisation de 3 km de longueur. Collectivement les indices de la Southern Breccia et le gisement de NICO forment le système IOAA de Lou. Les relations de recoupement entre différentes générations d'intrusions dont l'âge U–Pb sur zircon est connu

montrent que le système de Lou s'est principalement formé dans un intervalle de moins de 5 millions d'années, entre 1873 Ma l'âge d'un granite précurseur et 1868 Ma l'âge d'un dyke recoupant le tout. La distribution des altérations entre NICO et la Southern Breccia, en fonction des faciès d'altérations établis au chapitre 3, est complémentaire et se reflète dans le partitionnement chimique des éléments entre ces deux composantes du système. La transition entre les zones d'altération calcique à fer de NICO et celles de la Southern Breccia se reflète par une augmentation progressive du contenu en Ca et Mg dans les zones d'altération de la Southern Breccia en se rapprochant du gisement de NICO. La minéralisation uranifère dans la Southern Breccia est principalement reliée à une altération HT potassium–fer composée de magnétite biotite feldspath potassique et comprenant une proportion importante d'ilménite ainsi que quelques zircons hydrothermaux. Ceci indique une mobilité importante du Ti et moindre du Zr dans les fluides hydrothermaux et une association paragénétique entre oxydes de fer et minéraux uranifères. Un second stade de minéralisation uranifère est relié à une altération tardive magnésium–fer riche en hématite et en chlorite. Cette thèse démontre ainsi que les oxydes de fer observés dans certains gîtes d'uranium encaissés dans des albitites sont contemporains à la précipitation de l'uraninite et que des réactions d'oxydoréduction à la transition magnétite hématite, probablement par mélange de fluides, forment les zones minéralisées. Bien que la majorité des gîtes d'uranium encaissés dans des albitites soient métamorphisés, le métamorphisme régional n'est pas un prérequis pour former ce type de gîte et des fluides magmatiques-hydrothermaux peuvent former la minéralisation uranifère. Enfin, ces travaux démontrent que l'uranium n'est pas associé au métasomatisme sodique, mais qu'il est une manifestation de l'évolution du même système hydrothermal. Une fois formées, les albitites peuvent servir d'hôtes préférentiels pour l'uranium.

8.5 La mobilité des éléments lors de l'évolution d'un système IOAA, du stade d'altération sodique au stade d'altération HT K–Fe (chapitre 7)

Ce chapitre, en utilisant le système de Fab situé dans le centre-sud de la GBMZ, illustre en détail la mobilité des éléments propres aux faciès d'altération sodique, HT Ca–Fe et HT K–Fe lors de la construction d'un système IOAA. Le système de Fab établit également un lien

temporel direct entre magmatisme potassique riche en F et la formation d'un système IOAA. Cette contribution montre que l'altération sodique, telle que décrite par Oliver et al. (2004) constitue les zones de lessivage d'un système IOAA tandis que les faciès d'altération HT Ca–Fe et HT K–Fe correspondent aux zones de précipitation. Cette contribution indique que les éléments majeurs enrichis lors du stade HT Ca–Fe sont principalement le Ca, le Fe, le Mg, le Mn et le P; les éléments mineurs enrichis sont les ÉTR, le Th, le V et l'U; les métaux enrichis sont le Co, le Ni et le V. Cette contribution démontre aussi que le Ca et le Mg sont fortement à extrêmement découplés du Sr lors de ce stade d'altération, ce qui représente un trait chimique caractéristique de l'altération HT Ca–Fe. Lors du stade HT K–Fe, le K, le Fe, le Mg et le Mn sont généralement enrichis pour les éléments majeurs, le Ba, Sr, Rb pour les traces. Les métaux tels que le Cu et le Co sont enrichis dans les zones minéralisées tout comme l'U.

Cette contribution appuie les tendances observées sur les enrichissements en métaux à chacun des stades d'altération décrits aux chapitres 3 et 4 et établit le rôle possible du F dans la mobilité de certains éléments tels que le Co, le Ni et le V de même que la mobilisation contemporaine de U et Th. De plus, il semble que l'activité du F décroît dans le fluide progressivement du stade d'altération sodique vers le stade d'altération HT K–Fe. Les patrons d'enrichissements ou d'appauvrissement propres à chaque stade d'altération présentés dans cette contribution aideront à interpréter les données de chimie minérale dans les altérations des systèmes IOAA, plus particulièrement les analyses sur les magnétites tel que le démontre les travaux de De Toni (2016).

8.6 Autres contributions réalisées en parallèle à cette thèse mais non incluses

L'auteur de cette thèse a également contribué à plusieurs résumés ainsi qu'aux publications suivantes :

Gandhi, S.S., Montreuil, J.-F., et Corriveau, L., 2014, Geology of the Mazenod area: Commission géologique du Canada, Séries des cartes géoscientiques du Canada, CGM 148P.

Hayward, N., Enkin, R.J., Corriveau, L., Montreuil, J.-F., et Kerswill, J., 2013, The application of rapid potential field methods for the targeting of IOCG mineralisation based on physical

property data, Great Bear magmatic zone, Canada: Journal of Applied Geophysics, v. 94, p. 42–58.

Potter, E.G., Corriveau, L., et Montreuil, J.-F., 2013, Iron oxide copper–gold±uranium in the Great Bear magmatic zone: Nature of uranium in IOCG systems: Commission géologique du Canada, Dossier Public 7254.

Potter, EG., Montreuil, J-F., Corriveau, L., et De Toni, A., 2013, Geology and hydrothermal alteration of the Fab lake region, Northwest Territories: Commission géologique du Canada, Dossier Public 7339, 26 p., 1 feuillet, doi:10.4095/292562.

Potter, E.G., Montreuil, J.-F., Corriveau, L., et Davis, W.J., sous presse, Linkages between Iron Oxide–Copper–Gold (IOCG) systems and albitite-hosted uranium: A case study of the Southern Breccia albitite uranium showings, Northwest Territories, Canada: Proceedings of IAEA conference.

CHAPITRE 9 : CONCLUSIONS

L'objectif principal de cette thèse était de définir la mobilité des éléments dans les systèmes IOAA de la zone magmatique du Grand lac de l'Ours (GBMZ) et d'établir les relations entre les types d'altération hydrothermale et les types de minéralisation qui en résultent. Pour y parvenir, cette thèse a couvert plusieurs sujets complémentaires reliés à la géologie régionale du sud de la GBMZ qui formait le point de départ en définissant le contexte tectono-magmatique de formation des gîtes IOCG (les moteurs de mobilité des éléments) dans la GBMZ. Les données géochimiques et pétrographiques ont ensuite contraint les relations entre la distribution de l'altération dans les systèmes d'altération à oxydes de fer et éléments alcalins (IOAA) de la GBMZ et les différents types de minéralisation formés à travers ces systèmes, soient les gîtes IOCG et leurs variantes à cobalt et bismuth, les gîtes d'uranium encaissés dans des albitites, les gîtes à oxydes de fer-apatite, les minéralisations en ÉTR et les skarns zincifères polymétalliques. La section qui suit résume les principales conclusions dérivées de cette thèse en s'appuyant sur les chapitres qui leur sont associés.

9.1 Contexte tectonique de formation des systèmes IOAA de la Zone magmatique du Grand lac de l'Ours

Il a été établi que dans le sud et centre-sud de la GBMZ, le développement des systèmes IOAA fertiles en minéralisations IOCG s'est principalement fait dans une fenêtre temporelle restreinte s'étalant de 1873 à 1866 Ma et au sein d'un environnement géodynamique compatible avec un contexte d'arc continental. La transition entre le régime de contraintes compressif au régime extensif s'étant produit entre 1870–1867 Ma, marqué par un changement graduel dans la composition des magmas, est considéré comme un événement clé pour la formation de gîtes polymétalliques dans le sud de la GBMZ et dans le système de Fab plus au nord. Cet intervalle de 3 Ma correspondant à la fenêtre temporelle approximative de formation de NICO, de Fab, de la Southern Breccia et de Sue-Dianne.

Dans cet intervalle temporel, les roches volcano-plutoniques formées font principalement partie de la série shoshonitique ou calco-alcaline riche en potassium et le régime de contraintes est interprété comme ayant évolué de compressif vers extensif. Plusieurs intrusions subvolcaniques et plutons de composition de type A, dont certains sont riches en F, sont formés dans cet

environnement d'arc continental, indiquant que la formation d'intrusions granitiques de type A n'est pas restreinte aux environnements tectoniques anorogéniques comme précédemment démontrés par Creaser et al. (1991) et Creaser (1996). L'association spatiale entre magmatisme shoshonitique, granitique de type A riche en F et minéralisations IOCG dans la GBMZ rejoint ce qui a été observé dans plusieurs districts IOCG majeurs à travers le monde (Andes, Carajás, Cloncurry, Gawler; Chiaradia et al., 2005; Marschik et Söller, 2006; Pollard, 2006; Dreher et al., 2008; Chen et al., 2010a, b; Groves et al., 2010). Les systèmes IOAA de la GBMZ démontrent aussi l'association génétique directe entre magmatisme shoshonitique et la formation de systèmes IOAA fertiles en minéralisations IOCG.

Les discontinuités (failles, discordances, contacts stratigraphiques) et l'activité tectonique ont exercé un contrôle important sur la morphologie et la distribution des gisements IOCG (NICO et Sue-Dianne), des zones d'altérations majeures et des indices minéralisés importants (p. ex. Southern Breccia, Hump, indices au sud de NICO dans South Lou) à travers la GBMZ.

9.2 Relations entre la mobilité des éléments et les minéralisations observées dans la Zone magmatique du Grand lac de l'Ours

L'altération hydrothermale dans chacun des systèmes IOAA de la GBMZ évolue selon une séquence relativement systématique comparable à celle des autres systèmes IOAA à travers le monde. Chacun des stades d'altération observés est caractérisé par une série de paragenèses minérales diagnostiques qui traduisent et sont le résultat de signatures chimiques en éléments majeurs distinctes. Les découplages des éléments majeurs en fonction des conditions physicochimiques des fluides et des paragenèses d'altération qui se forment conduisent à des enrichissements en éléments traces et en métaux distincts (Fig. 9-1).

9.2.1 Altération sodique

L'altération sodique est typiquement distribuée en marge des zones minéralisées en métaux usuels ou précieux. L'albitisation est typiquement une altération précoce formée dans les stades initiaux du développement du système IOAA. Les albitites formées à ce stade peuvent être

fortement poreuses et appauvries en plusieurs éléments par rapport à leur précurseur excepté pour le Na, le Zr et l'Al. Certaines albitites sont également enrichies en Ta, Nb et Ti, des éléments qui peuvent être reconcentrés pour former des indices lors de stades d'altération subséquents (p. ex. indice MHF dans la zone d'Esther). L'altération sodique représente donc les zones de lessivages pour plusieurs éléments dans les systèmes IOAA de la GBMZ. L'albitisation se fait par dissolution-reprécipitation et conduit communément à la formation de microporosité qui affaiblit mécaniquement les zones albitisées. Combinée à la localisation des zones d'albitisation généralement près des zones de déformation, la formation pénétrative de porosité dans les albitites en fait des zones préférentielles pour la formation de brèches tectonique-hydrothermales et de corridors de circulation de fluides (p. ex. corridors de déformation dans la Southern Breccia). Cependant, lorsque les albitites sont recristallisées à grains moyens à grossiers, leur bréchification n'a pas été observée mégascopiquement. L'altération Na–Ca–Fe, transitionnelle avec l'altération HT Ca–Fe, peut soit représenter une zone de lessivage (p. ex. Fab) ou de concentration de certains éléments (ÉTR, Ca, Fe, P, V; Mag Hill) dans des zones où il y a transition vers une altération potassique à fer (cristallisation de feldspath potassique ou de biotite stable avec la magnétite). Les éléments typiquement immobiles dans d'autres systèmes hydrothermaux ou d'autres stades d'altération (p. ex. Nb, Ta, Th et Ti) peuvent être fortement mobiles dans certaines altérations Na–Ca–Fe et peuvent se faire entièrement lessiver (p. ex. Fab). Dans le système de Fab, cette mobilité importante des HFSE a été associée à une activité élevée de F dans un fluide magmatique-hydrothermal.

Cette mobilité des éléments par association régulière implique une évolution progressive de la chimie des fluides impliqués ou encore une évolution structurée de fluides de différentes origines. La mobilité des éléments au stade Na–Ca–Fe indique un possible rôle important du F et une source magmatique pour le fluide. La mobilité des éléments dans les zones d'altération Na, lorsque les métaux usuels sont lessivés, indique une plus forte activité du Cl et des fluides pouvant provenir de diverses sources: magmatique, eau de mer ou météorique. Les fluides météoriques ou l'eau de mer peuvent s'infiltrer le long des discontinuités régionales, particulièrement lorsque le régime tectonique transitionne de compressif à extensif, et se faire progressivement réchauffés dans le gradient géothermique particulièrement élevé typique des régions ou se forment les systèmes IOAA. Le transfert majeur de chaleur du manteau vers la croûte relié au magmatisme actif lors de la formation des systèmes IOAA initie et maintient ces cellules hydrothermales régionales tandis que les discontinuités canalisent ensuite les fluides chargés de métaux dans des zones restreintes pour favoriser la formation de gisements.

9.2.2 Altération HT Ca–Fe

L'altération HT Ca–Fe, par-rapport aux minéralisations IOCG, est également distribuée à l'échelle régionale, mais généralement forme des zones d'une étendue spatiale plus restreinte. Certaines zones d'altération HT Ca–Fe sont également spatialement proximales aux minéralisations IOCG. Ce stade d'altération est caractérisé par d'importants enrichissements en Ca, Fe, et dans certains secteurs en Mg et Mn. Dans toutes les zones d'altération calcique, le Ca et le Mg sont fortement découplés du Sr, malgré l'isovalence de ces éléments. Ce découplage donne aux altérations intenses HT Ca–Fe de la zone magmatique du Grand lac de l'Ours des ratios Ca/Sr et Mg/Sr très distinctifs, particulièrement lorsqu'elles se forment dans des séquences comprenant des unités riches en Ca et Mg (p. ex. roches carbonatées, roches mafiques/ultramafiques). Les éléments du groupe des terres rares (ÉTR), lorsque l'altération HT calcique–fer est riche en apatite (ou en P), et le V peuvent être fortement enrichis à ce stade d'altération et mener à la formation de gîtes à oxydes de fer–apatite (IOA) enrichis en ÉTR et/ou en V.

Dans la GBMZ, les secteurs de Port Radium–Echo Bay, de Camsell River, de Fab, de Ron et de Hump contiennent des gîtes ou indices minéralisés d'importance reliés à ce stade d'altération (chapitres 3, 4; Mumin et al., 2007, 2010). Le Co, le Cu, le Ni et l'U sont également enrichis localement à ce stade d'altération, mais insuffisamment pour former des gîtes. Cependant, ces enrichissements précoces en Co, Cu, Ni et U dans les zones d'altération HT Ca–Fe, mais aussi en ÉTR, rendent ces éléments disponibles pour être remobilisés et potentiellement concentrés lors de stades d'altération subséquents pour former des gîtes. Les systèmes IOAA de Grouard, South Lou, Carbonate Mountain, et fort probablement Lou au niveau du gîte de NICO, démontrent que dans les environnements géologiques avec des unités riches en carbonates, des skarns peuvent se former au stade HT Ca–Fe. Ces skarns, lorsqu'associées à un système IOAA, sont surimposés sur ou recoupent l'altération sodique plus précoce, vont comprendre des zones riches en magnétite et vont être typiquement recoupés ou altérés par des altérations HT K–Fe ou LT K–Fe. Des gîtes de Pb et Zn de même que des enrichissements locaux en Sn sont associées à ces skarns. Les enrichissements en Pb et Zn sont particulièrement marqués lorsque l'altération HT K–Fe subséquente est relativement faible mais que l'altération LT K–Fe est forte (Carbonate Mountain et Grouard).

La mobilité des éléments observée au stade HT Ca–Fe, où presque l'ensemble du tableau périodique est mobilisé tel que démontré dans le système de Fab, implique des fluides de haute

température avec une grande diversité de ligands. Les enrichissements majeurs en F, P, les enrichissements locaux en S et les analyses d'inclusions de fluides dans les systèmes IOAA indiquant une concentration élevée en Cl montrent la diversité des ligands potentiellement actifs dans ces fluides. L'activité intense du F dans certaines zones HT Ca–Fe explique la mobilité contemporaine du Th et U de même que du Ta, Nb et des ÉTR lourdes. Cette forte activité du F peut aussi expliquer la faible concentration en métaux comme le cuivre dans les gisements IOA, faiblement transporté par le F. La précipitation importante du F dans les zones d'altération HT Ca–Fe au stade transitionnel à l'altération HT K–Fe provoque un changement important dans la composition des fluides. La précipitation du F décroît la mobilité du Th et des ÉTR lourdes, contraignant leurs enrichissements principalement dans les zones d'altération HT Ca–Fe transitionnelles à l'altération HT K–Fe. Une activité plus grande du Cl dans certaines générations de fluides actifs au stade HT Ca–Fe peut expliquer les concentrations élevées en Cu documentées dans certaines inclusions de fluides.

9.2.3 Altération HT K–Fe

Le stade d'altération HT K–Fe comprend les altérations du type Ca–Fe–K et HT K–Fe qui, lorsqu'intenses et avec une étendue spatiale considérable, sont systémiquement associées à la formation de minéralisations IOCG du groupe à magnétite (Fab, NICO, Sue-Dianne). Des indices d'uranium polymétalliques encaissés dans des albitites tels ceux de la Southern Breccia au sud de NICO et de Cole Uranium au nord-est de NICO indiquent que des gîtes d'uranium encaissés dans des albitites peuvent aussi se former à ce stade d'altération (chapitres 3, 4 et 6).

Les stades d'altération HT K–Fe et Ca–Fe–K sont caractérisés par d'importants enrichissements en Fe et K avec des enrichissements plus ou moins marqués en Ca, Mg et P. L'enrichissement en Ca et Mg au stade d'altération HT K–Fe et la formation d'altération Ca–Fe–K semblent être principalement fonction de la présence d'unités riches en Ca et Mg (carbonates, roches mafiques/ultramafiques) proximales aux zones d'altération (p. ex. NICO, Candelaria, Ernest Henry; chapitre 4; Marschik et Fontboté, 2001a; Mark et al., 2006). Les métaux concentrés lors du stade d'altération HT K–Fe sont donc multiples (Au, Bi, Co, Cu, ÉTR, Fe, Mo, U, V±Ni). Certains éléments dit immobiles, tel que le Nb, le Ta, le Th, le Ti, le Y et le Zr, sont localement (Zr, Nb, Ta) a largement (Th, Ti, Y) remobilisés au stade d'altération HT K–Fe dans certains systèmes IOAA, particulièrement lorsque ces zones d'altérations sont transitionnelles aux altérations HT Ca–Fe et n'évoluent pas en gîtes IOCG.

Tout comme dans les systèmes IOCG à travers le monde, la signature métallifère des zones minéralisées formées au stade d'altération HT K–Fe dans la GBMZ semble partiellement influencée par le type de roches hôtes dans la colonne stratigraphique des zones minéralisées (c.-à-d. à l'échelle régionale et non pas par rapport au type de précurseur altéré sur place). Ainsi, dans les indices et gisements formés à proximité des séquences sédimentaires du Groupe de Treasure Lake comprenant des unités riches en carbonates, le Co prédomine sur le Cu et les sulfarsénides de Co sur les sulfures de cuivre dans les zones minéralisées. Ce type de minéralisation représente un potentiel continuum entre les gîtes IOCG et certains gîtes de Co–Cu–Au dans les roches sédimentaires définies par Slack (2012, 2013; gîtes à Co–Cu–Au–Bi–Y–REE du district de Blackbird, États-Unis). Le Cu est aussi enrichi mais les zones riches en cuivre sont spatialement adjacentes aux zones riches en Co±Bi±Ni, le Cu étant principalement concentré dans les altérations HT et/ou LT K–Fe moins riches en Ca et formées dans des précurseurs volcaniques, intrusifs ou sédimentaires silicatés. Dans les séquences volcaniques et intrusives de la GBMZ de même que dans les zones d'albitisation intense, les altérations HT K–Fe prédominent sur les altérations Ca–Fe–K et forment des gîtes où le Cu et les sulfures de Cu prédominent. Cette influence des roches hôtes sur la signature chimique des minéralisations indiquent qu'elles contribuent fort probablement une partie des métaux contenus dans les gîtes associés aux systèmes IOAA.

La diversité des assemblages métallifères documentés au stade HT K–Fe indique des fluides d'une chimie variée dont le contenu en métaux est partiellement influencé par l'environnement dans lequel ils ont circulé, mais aussi par les principaux ligands actifs dans le fluide et possiblement les mécanismes qui déclenchent la précipitation des métaux. La mobilité contemporaine du Th, U, Ta, Nb et Zr de même que les faibles enrichissements en Cu dans les indices uranifères de la Southern Breccia indique des fluides de haute température avec une activité élevée du F. Un constat similaire s'applique aux minéralisations à Co et As pauvres en cuivre dans le gisement NICO, mais aussi celles documentées dans le district de Blackbird (États-Unis) où l'ensemble des ÉTR sont mobiles. L'activé élevée du F dans ces zones minéralisées est supportée par les enrichissements en F observés dans certaines de ces zones d'altération HT K–Fe tels que documenté au chapitre 2. Dans le gisement de NICO, l'unité carbonatée riche en Ca et Mg forme une trappe chimique idéale pour précipiter le F d'un fluide hydrothermal ainsi que les métaux qu'il contient et dont le transport est influencé par l'activité du F dans le fluide (Co, Ni; chapitre 7). Comme ce mécanisme de précipitation n'influence pas nécessairement le Cl dans le fluide, le Cu complexé au Cl ne précipite pas nécessairement avec le Co et peut ainsi rester en solution dans le fluide et être transporté dans d'autres zones du

système IOAA. Cette dispersion du cuivre est observée dans le système de Lou, où plusieurs indices de cuivre se retrouvent en périphérie du gisement de NICO et ne sont pas fortement enrichis en Co.

Les gîtes IOCG du groupe à magnétite, enrichis en cuivre, sont plutôt le résultat de fluides où le Cl est le principal ligand. Ceci est visible dans les indices IOCG du groupe à magnétite du système de Fab, où l'U est découplé du Th. La signature isotopique du cuivre observé dans les zones d'altération HT K–Fe indique plusieurs cycles de précipitation du cuivre et un fractionnement isotopique progressif (chapitre 7). Ce fractionnement est possiblement dû à plusieurs cycles d'effervescence des fluides tels qu'inférés au chapitre 7. Chaque cycle comprendrait un épisode d'effervescence et de fragmentation/bréchification avec précipitation des métaux suivi d'un épisode de remplacement de la matrice et des fragments nouvellement formés pendant la re-pressurisation des fluides. Ce mécanisme expliquerait l'association systématique des zones de bréchification avec les zones minéralisées au stade HT K–Fe. Ce mécanisme actif de fragmentation au stade HT K–Fe peux aussi favoriser le mélange de fluides de différentes sources et bonifier le contenu en métaux du gisement.

Ces mécanismes de précipitation des métaux pour les gîtes riches en Co et ceux riches en Cu sont donc complémentaire, les gîtes à Co étant plus dépendant d'un piège chimique tandis que les gîtes à Cu étant plus dépendant d'un processus physique et de séparation des fluides.

L'association spatio-temporelle des indices uranifères de la Southern Breccia avec le gîte de NICO montre une complémentarité des associations cationiques à l'échelle d'un système IOAA et appuie la relation génétique entre les gîtes d'uranium encaissés dans les albitites et les gîtes IOCG. L'identification de gisements ou d'indices minéralisés d'uranium encaissés dans des albitites dans un environnement géologique donné peut donc signaler un potentiel pour des gisements IOCG à proximité, surtout s'il y a abondance d'oxydes de fer associés à la minéralisation uranifère. La relation inverse est aussi applicable et indique que les corridors d'albitisation formés dans un système IOAA fertile en minéralisations IOCG peuvent contenir des gisements d'uranium encaissés dans des albitites.

9.2.4 Altération LT K–Fe

Les enrichissements en métaux, la minéralogie et la signature chimique générale des altérations formées au stade LT K–Fe dans les systèmes IOAA de la GBMZ sont variables et semblent couramment contrôlés par les types d'altération sur lesquels l'altération LT K–Fe est

surimposée. Ce facteur explique en partie les difficultés rencontrées au chapitre 5 lors de la tentative de séparer et discriminer les altérations HT K–Fe des altérations LT K–Fe. Lorsque l'altération LT K–Fe est formée dans un système IOAA où les altérations HT Ca–Fe ou Ca–Fe–K sont intenses et riches en Ca et en Mg, l'altération LT K–Fe est principalement composée de chlorite±hématite avec peu de minéraux felsiques et se caractérise par un enrichissement marqué en Mg par rapport au Ca et/ou le K, lessivés lors de la transformation des amphiboles et/ou biotite en chlorite. Lorsqu'elle est surimposée sur des altérations HT Ca–Fe de type *skarn*, l'altération LT K–Fe peut mener à une importante formation de talc et semble associée à des enrichissements importants en Zn et plutôt marginaux en Sn. Lorsque qu'elle est surimposée sur des altérations riches en feldspath potassique et en magnétite, l'altération LT K–Fe résulte en la formation importante d'hématite et de feldspath potassique et peut alors être enrichie en cuivre. Lorsqu'elle est surimposée sur des altérations riches en albite±magnétite±amphibole, les micas blancs±hématite±chlorite sont abondamment formés et résultent en une altération hydrolytique communément décrite au stade LT K–Fe dans d'autres systèmes IOAA (p. ex. Kiirunavaara en Suède; Oak Dam en Australie).

Cette transition vers la formation de micas blancs comme minéraux potassique dénote également une diminution graduelle du pH des fluides hydrothermaux qui, dans certains cas, mènent ultimement à la formation d'altération argillique. La formation de chlorite et micas blancs marque aussi la baisse de la température des fluides actifs à ce stade.

Le contrôle exercé par la composition des précurseurs sur la composition de l'altération LT K–Fe indique que la mobilité des éléments est plus faible à ce stade d'altération et explique pourquoi les enrichissements en métaux dans les zones d'altération LT K–Fe reflètent couramment les métaux concentrés aux stades d'altération antérieurs. Ainsi lorsque l'altération HT K–Fe est intense, les zones d'altération LT K–Fe sont typiquement enrichies en Ag et en Cu (p. ex. Brooke, Chalco, Sue-Dianne, Summit Peak) tandis que lorsque l'altération HT K–Fe est faible, les métaux tels que le Cu sont faiblement enrichis à ce stade (p. ex. Hump, Ron, Mag Hill).

L'uranium constitue une exception notable et est régulièrement enrichi au stade LT K–Fe même dans des zones où les altérations antérieures sont faiblement enrichies en U. Le découplage avec le thorium indique cependant des fluides de plus faible température avec une activité plus faible du F. La destruction des fluoro-apatites et des feldspaths potassiques riches en Ba au stade LT K–Fe peut aussi favoriser la cristallisation de barite et de fluorite dans certaines altérations LT K–Fe et augmenter la capacité du fluide à mobiliser plusieurs éléments. Les ÉTR légères, enrichies lors des stades d'altération HT Ca–Fe ou HT K–Fe, peuvent également être

remobilisées et concentrées dans de nouveaux minéraux au stade d'altération LT K–Fe (p. ex. Sue-Dianne, Southern Breccia) et ce processus d'enrichissement peut mener à la formation de gîtes potentiellement économiques en ÉTR légères (p. ex. Pea Ridge aux États-Unis; Whitten et Yancey, 1990). Dépendamment de l'environnement et des principaux cations dans les fluides (Ca, K ou Na), différent minéraux enrichis en ÉTR peuvent précipiter. La faible température des fluides prévient cependant la mobilisation massive des ÉTR lourdes, de même que du Nb, Ta et Th.

9.2.5 Altération LT Ca–Fe

L'altération LT Ca–Fe a un comportement similaire à l'altération LT K–Fe, car sa signature métallique reflète celles des altérations préalablement formées (p. ex. fort enrichissement en Cu, Bi, Mo et W à Brooke). Une des caractéristiques distinctives de l'altération LT Ca–Fe comparativement aux autres stades d'altération IOAA est que le Ca et le Sr ne sont pas découplés, donnant à cette altération, lorsqu'elle est intense, des rapports Ca/Sr plus faibles et nettement distincts de ceux des altérations HT Ca–Fe. Tout comme l'altération LT K–Fe, l'altération LT Ca–Fe est aussi associée à une remobilisation importante des ÉTR légères enrichies dans les stades d'altération antérieurs et peut mener à la formation de zones significativement enrichies en ÉTR légères (p. ex. Oxymoron, Ron).

9.3 Conclusions finales et perspectives

Cette thèse démontre les liens entre la mobilité des éléments à chacun des stades d'altération IOAA et le type de minéralisations qui peuvent s'y former. La signature métallifère des altérations régionales dans un district IOAA devient donc un indicateur important du type de gîtes pouvant s'y retrouver et sur les métaux qui peuvent y être concentrés. Les méthodes développées dans cette thèse s'appliquent autant à l'échelle régionale qu'à celle d'un gisement ou d'un indice et les modèles métallogéniques définis peuvent subséquemment guider la cartographie et significativement optimiser l'exploration dans les systèmes IOAA.

Cette thèse illustre aussi comment se forment les multiples assemblages métallifères retrouvés dans les zones minéralisées des systèmes IOAA de la GBMZ. Une campagne d'exploration faite dans un système IOAA doit donc porter attention non seulement aux gisements IOCG qui sont généralement la cible principale, mais aussi aux gisements affiliés qui peuvent potentiellement s'y former.

Plusieurs questions importantes soulevées par cette thèse sur les systèmes IOAA de la GBMZ restent en suspens. Dans les éléments critiques il y a :

1. les sources des magmas dans la GBMZ qui pourraient être mieux cernées en documentant les âges modèles Nd–Sm complémentés par des données des isotopes du Hf;
2. la distribution du magmatisme juvénile dans le sud de la GBMZ et les processus pétrogénétiques à la source du magmatisme shoshonitique;
3. le contexte structural détaillé et la cinématique des corridors de déformation identifiés dans la GBMZ afin de tracer précisément l'évolution des contraintes et leurs relations avec l'altération hydrothermale et les événements minéralisateurs;
4. la source du Mg des zones minéralisées très riches en Mg afin de comprendre le rôle des séquences carbonatées et de leur potentielle dévolatilisation dans l'apport du Ca, du CO_2 et de divers métaux; des analyses des isotopes stables du Mg dans la séquence carbonatée du Groupe de Treasure Lake, les altérations riches en Mg du gisement de NICO, dans l'indice de Duke, dans l'indice de Grouard et dans l'indice de Carbonate Mountain permettrait de mieux contraindre ce rôle des séquences carbonatées;
5. les sources potentielles des métaux et les processus de précipitation des sulfures dans les altérations IOAA minéralisées de la GBMZ (p. ex. analyses des isotopes stables du Cu, Fe et du Zn); et
6. une description détaillée de tous les minéraux des terres rares retrouvés dans les altérations IOAA de la GBMZ et les liens entre ces derniers, les métaux usuels et précieux et l'uranium.

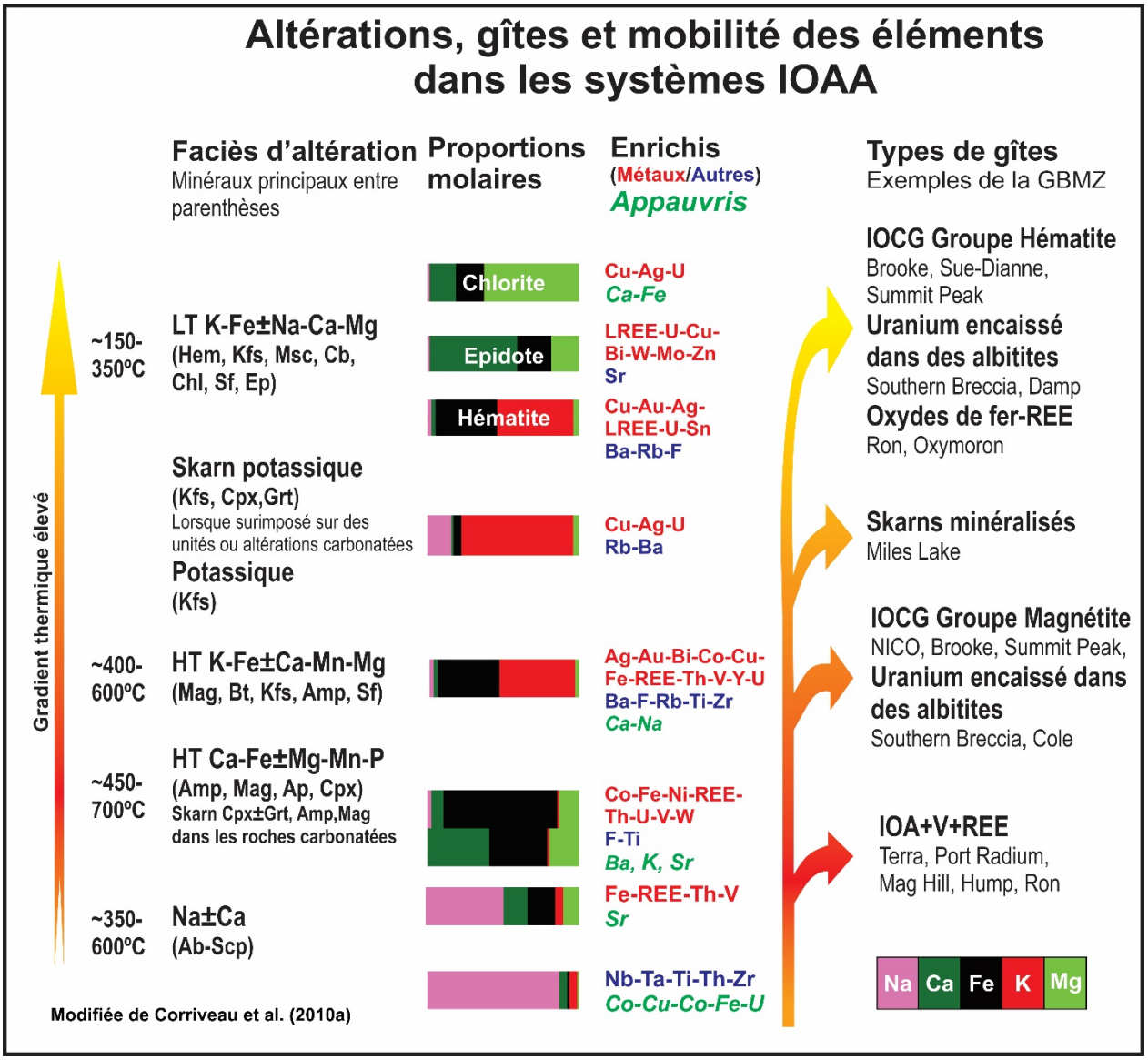

Figure 9-1 Relations entre altérations, gîtes et mobilité des éléments avec exemples de la GBMZ

Corriveau et Montreuil (chapitre 3) modifié de Corriveau et al. (2010ba). Échelle de températures selon Marschik et Fontboté (2001a), Requia et al. (2003); Davidson et al. (2007); Monteiro et al. (2008b); Skirrow (2010), Williams (2010b), Somarin et Mumin (2014).
Abréviations des minéraux selon Whitney et Evans (2010).

10 Références pour l'ensemble de la thèse

Acosta, P., 2014, Origins and geochemical characterization of the Iron-Oxide–Copper–Gold deposits in the Great Bear Magmatic Zone, NWT, Canada: Unpublished Ph.D. thesis, University of Alberta, Edmonton, 283 p.

Acosta Góngora, P., Gleeson, S.A., Ootes, L., Jackson, V.A., Lee, M., and Samson, I., 2011, Preliminary observations on the IOCG mineralogy at the Damp, Fab, and Nori showings and Terra–Norex mines, Great Bear magmatic zone: NWT Geoscience Office, NWT Open Report 2011–001.

Acosta-Góngora, P., Gleeson, S.A., Taylor, B., Samson, I., Ootes, L., and Corriveau, L., 2013, Sulfur isotope geochemistry and ^{187}Re–^{187}Os temporal constraints on the formation of polymetallic iron-oxide–alkali–altered deposits in the Great Bear magmatic zone, NWT, Canada: SGA2013–The 12th Biennial SGA Meeting of The Society for Geology Applied to Ore Deposits, Upsala, Sweden, Transaction volume.

Acosta-Góngora, P., Gleeson, S.A., Samson, I., Ootes, L., and Corriveau, L., 2014, Trace element geochemistry of magnetite and its relationship to mineralization in the Great Bear magmatic zone, NWT, Canada: Economic Geology, v. 109, p. 1901–1928.

Acosta-Góngora, P., Gleeson, S.A., Samson, I., Ootes, L., and Corriveau, L., 2015a, Gold refining by bismuth melts in the iron-oxide-dominated NICO Au–Co–Bi (±Cu±W) deposit, NWT, Canada: Economic Geology, v. 110, p. 291–314.

Acosta-Góngora, P., Gleeson, S., Samson, I., Corriveau, L., Ootes, L., Taylor, B.E., Creaser, R.A., and Muehlenbachs, K., 2015b, Genesis of the Paleoproterozoic NICO Iron-Oxide-Cobalt-Gold-Bismuth deposit, Northwest Territories, Canada: evidence from isotope geochemistry and fluid inclusions: Precambrian Research, v. 268, p. 168–193.

Adams, J.A.S, and Fryer, G.E., 1964, Portable γ–ray spectrometer for field determination of thorium, uranium and potassium, *in* Adams, J.A.S., and Lowder, W.M., eds., The natural radiation environment: University of Chicago Press, p 577–596.

Agangi, A., Kamenetsky, V.S., and McPhie, J., 2010, The role of fluorine in the concentration and transport of lithophile trace elements in felsic magmas: Insights from the Gawler Range Volcanics, South Australia: Chemical Geology, v. 273, p. 314–325.

Agangi, A., McPhie, J., and Kamenetsky, V.S., 2011, Magma chamber dynamics in a silicic LIP revealed by quartz: the Mesoproterozoic Gawler Range Volcanics: Lithos, v. 126, p. 68–83.

Aitchison, J., 1986, The statistical analysis of compositional data: Chapman and Hall, London, 416 p.

Aja, S.U., Wood, S.A., and Williams-Jones, A.E., 1995, The aqueous geochemistry of Zr and the solubility of some Zr-bearing minerals: Applied Geochemistry, v. 10, p. 603–620.

Aksyuk, A.M., 2000, Estimation of fluorine concentrations in fluids of mineralized skarn systems: Economic Geology, v. 95, p. 1339–1347.

Alexandre, P., 2010, Mineralogy and geochemistry of the sodium metasomatism-related uranium occurrence of Aricheng South, Guyana: Mineralium Deposita, v. 45, p. 351–367.

Aspler, L.B., Pilkington, M., and Miles, W.F., 2003, Interpretations of Precambrian basement based on recent aeromagnetic data, Mackenzie Valley, Northwest Territories: Geological Survey of Canada, Paper 2003-C2, 11 p., doi:10.4095/214184.

Austin, J.R., and Blenkinsop, T.G., 2008, The Cloncurry Lineament: Geophysical and geological evidence for a deep crustal structure in the Eastern Succession of the Mount Isa Inlier: Precambrian Research, v. 163, p. 50–68.

Azar, B., 2007, The lithogeochemistry of volcanic and subvolcanic rocks of the Fab Lake area, Great Bear magmatic zone, Northwest Territories, Canada: Unpublished B.Sc. thesis, Toronto, Canada, University of Toronto, 96 p.

Azimov, P.Y., and Bushmin, S.A., 2007, Solubility of minerals of metamorphic and metasomatic rocks in hydrothermal solutions of varying acidity: Thermodynamic modeling at 400–800°C and 1–5 kbar: Geochemistry International, v. 45, p. 1210–1234.

Badham, J.P.N., 1972, The Camsell River – Conjuror Bay area, Great Bear Lake, N.W.T: Canadian Journal of Earth Science, v. 9, p. 1460–1468.

Badham, J.P.N., 1975, Mineralogy, paragenesis and origin of the Ag–Ni, Co arsenide mineralization, Camsell River, N.W.T., Canada: Mineralium Deposita, v. 10, p. 153–175.

Badham, J.P.N., and Morton, R.D., 1976, Magnetite–apatite intrusions and calc-alkaline magmatism, Camsell River, N.W.T.: Canadian Journal of Earth Science, v. 13, p. 348–354.

Badham, J.P.N., 1978, Magnetite–apatite–amphibole–uranium and silver-arsenide mineralization in lower Proterozoic igneous rocks, East Arm, Great Slave Lake, Canada: Economic Geology, v. 73, p. 1474–1491.

Bailey, E.H., and Stevens, R.E., 1960, Selective staining of K-feldspar and plagioclase on rock slabs and thin sections: American Mineralogist, v. 45, p. 1020–1025.

Ballhorn, R.K., Thakur, V.K., da Fonte, J.E.C., and Suckau, V., 1981, Geology of the Espinhara uranium deposit, Brazil (AG. 162/27), in Uranium deposits in Latin America–Geology and exploration: Proceeding of Regional Advance Group Meeting, Lima, Peru, IAEA, Vienna.

Baker, T., Mustard, R., Fu, B., Williams, P.J., Dong, G., Fisher, L., Mark, G., and Ryan, C.G., 2008, Mixed message in iron oxide–copper–gold systems of the Cloncurry district, Australia, insights from PIXE analysis of halogens and copper in fluid inclusions: Mineralium Deposita, v. 43, p. 599–608.

Bardina, N.Yu., and Popov, V.S., 1992, Classification of metasomatic rocks and facies of shallow metasomatism: International Geology Review, v. 34, p. 187–196.

Barton, M.D., 2014, Iron oxide(–Cu–Au–REE–P–Ag–U–Co) systems, *in* Holland, H.D., and Turekian, K.K., eds., Treatise on Geochemistry, Second Edition: Elsevier, Amsterdam, p. 515–541.

Barton, M.D., and Johnson, D.A., 1996, Evaporitic source model for igneous related Fe oxide–(REE–Cu–Au–U) mineralization: Geology, v. 24, p. 259–262.

Barton, M.D., and Johnson, D.A., 2000, Alternative brine sources for Fe–oxide (–Cu–Au) systems: Implications for hydrothermal alteration and metals, *in* Porter T.M., ed., Hydrothermal iron oxide–copper–gold and related deposits: A global perspective, volume 1: Porter Geoscience Consultancy Publishing, Adelaide, Australia, p. 43–60.

Bastrakov, E.N., and Skirrow, R.G., 2007, Fluid evolution and origins of iron oxide–Cu–Au prospects in the Olympic Dam district, Gawler Craton, South Australia: Economic Geology, v. 102, p.1415–1440.

Beane, R.E., 1974, Biotite stability in the porphyry copper environment: Economic Geology, v. 69, p. 241–256.

Beauchemin, D., 2008, Inductively coupled plasma mass spectrometry: Analytical Chemistry, v. 80, p. 4455–4486.

Beccaluva, L., Bianchini, G., Mameli, P., and Natali, C., 2013, Miocene shoshonite volcanism in Sardinia: Implications for magma sources and geodynamic evolution of the central-western Mediterranean: Lithos, doi: 10.1016/j.lithos.2013.08.006.

Belousova, E.A., Griffin, W.L., O'Reilly, S.Y., and Fisher, N.I., 2002, Apatite as an indicator mineral for mineral exploration: Trace-element compositions and their relationship to host rock type: Journal of Geochemical Exploration, v. 76, p. 45–69.

Belperio, A., 2007, Prominent Hill. A hematite-dominated, iron oxide copper–gold system: Economic Geology, v. 102, p. 1499–1510.

Benavides, J., Kyser, T.K., and Clark, A.H., 2007, The Mantoverde iron oxide–copper–gold district, III región, Chile: The role of regionally derived, nonmagmatic fluids in chalcopyrite mineralization: Economic Geology, v. 102, p. 415–440.

Benavides, J., Kyser, T.K., Clark, A.H., Stanley, C., and Oates, C., 2008a, Exploration guidelines for copper-rich iron oxide–copper–gold deposits in the Mantoverde area, northern Chile: The integration of host-rock molar element ratios and oxygen isotope compositions: Geochemistry: Exploration, Environment, Analysis, v. 8, p. 343–367.

Benavides, J., Kyser, T.K., Clark, A.H., Stanley, C., and Oates, C., 2008b, Application of molar element ratio analysis of lag-talus composite samples to the exploration for iron oxide–copper–gold

mineralization, Mantoverde area, northern Chile: Geochemistry: Exploration, Environment, Analysis, v. 8, p. 369–380.

Bennett, V., and Rivers, T., 2006, U–Pb ages of detrital zircons from the southern Wopmay Orogen, Northwest Territories: NWT Geoscience Office, NWT Open Report 2006–007, 29 p.

Bennett, V., Rivers, T., and Jackson, V.A., 2012, A compilation of U–Pb zircon preliminary crystallization and depositional ages from the Paleoproterozoic southern Wopmay Orogen, Northwest Territories: NWT Geoscience Office, NWT Open Report 2012–003, 172 p.

Bernard, J., 2006, Origine des brèches à hématite du gîte de Mont-de-l'Aigle, Gaspésie: Unpublished M.Sc thesis, Université Laval, Canada.

Bertelli, M., and Baker, T., 2010, A fluid inclusion study of the Suicide Ridge Breccia pipe, Cloncurry district, Australia: Implication for breccia genesis and IOCG mineralization: Precambrian Research, v. 179, p. 69–87.

Best, M.G., 2003, Igneous and metamorphic petrology, 2nd edition: Oxford Blackwell Science, London.

Beukes, N.J., and Klein, C., 1990, Geochemistry and sedimentology of a facies transition – from microbanded to granular iron-formation – in the early Proterozoic Transvaal Supergroup, South Africa: Precambrian Research, v. 47, p. 99–139.

BHP Billiton, 2009, Annual Report 2009: 276 p.

Billström, K., Eilu, P., Martinsson, O., Niiranen, T., Broman, C., Weihed, P., Wanhainen, C., and Ojala, J., 2010, IOCG and Related Mineral Deposits of the Northern Fennoscandian Shield, *in* Porter, T.M., ed., Hydrothermal iron oxide copper–gold and related deposits: A global perspective, volume 4 - advances in the understanding of IOCG deposits: Porter Geoscience Consultancy Publishing, Adelaide, Australia, p. 381–414.

Bonyadi, Z., Davidson, G.J., Mehrabi, B., Meffre, S., and Ghazban, F., 2011, Significance of apatite REE depletion and monazite inclusions in the brecciated Se-Chachun iron oxide–apatite deposit, Bafq district, Iran: Insights from paragenesis and geochemistry: Chemical Geology, v. 281, p. 253–269.

Bowers, T.S., and Helgeson, H.C., 1983, Calculation of the thermodynamic and geochemical consequences of nonideal mixing in the system H_2O–CO_2–NaCl on phase relations in geologic systems: Equation of state for H_2O–CO_2–NaCl fluids at high pressure and temperatures: Geochimica et Cosmochimica Acta, v. 47, p. 1247–1275.

Bowring, S.A., 1984, Uranium–lead zircon geochronology of early Proterozoic Wopmay Orogen, Northwest Territories, Canada: An example of rapid crustal evolution: Unpublished Ph.D. thesis, University of Kansas, Lawrence, Kansas, 148 p.

Bretzlaff, R., Kerswill, J.A., and Chorlton, L.B., being submitted, Mineral occurrences of the Great Bear magmatic zone: Geological Survey of Canada, Open File Report.

Buchan, K.L., Ernst, R.E., Davis, W.J., Villeneuve, M., van Breemen, O., Bleeker, W., Hamilton, M.A., and Söderlund, U., 2010, Proterozoic magmatic events of the Slave craton, Wopmay Orogen and environs: Geological Survey of Canada, Open File Report 5985, 23 p.

Budzyń, B., Harlov, D.A., Williams, M.L., and Jercinovic, M.J., 2011, Experimental determination of stability relation between monazite, fluoroapatite, allanite, and REE-epidote as a function of pressure, temperature, and fluid composition: American Mineralogist, v. 96, p. 1547–1567.

Burgess, H., Gowans, R.M., Hennessey, B.T., Lattanzi, C.R., and Puritch, E., 2014, Technical report on the feasibility study for the NICO gold–cobalt–bismuth–copper deposit, Northwest Territories, Canada: NI 43-101 Technical Report No. 1335 prepared for Fortune Minerals Ltd., 385 p.

Byron, S.J., 2010, Giant quartz veins of the Great Bear magmatic zone, Northwest Territories, Canada: Unpublished M.Sc. thesis, Edmonton, Canada, University of Alberta, 147 p.

Camier, W.J., 2002, The Sue-Dianne Fe–oxide Cu–Ag–Au breccia complex, southern Great Bear Magmatic Zone, Northwest Territories, Canada: Unpublished M.Sc. thesis, London, Canada, University of Western Ontario, 210 p.

Camsell, C., 1916, The unexplored areas of continental Canada: The Geographical Journal, v. 48, p. 249–257.

Camsell, C., 1918, Some interesting geographical problems in the exploration of northern Canada: Geographical Review, v. 5, p. 208–215.

Charbonneau, B.W., 1988, Gamma spectrometric and magnetic anomalies associated with Cu–U mineralization, Faber Lake volcanic belt, district of Mackenzie, N.W.T.: Geological Survey of Canada, Paper 88-1C, p. 255–258.

Chaves, A.O., Rios, F.R., Alves, J.V., Chaves, A.M.D.V., Fuzikawa, K., and Neves, J.M.C., 2010, Physical and chemical properties of fluid and melt inclusions of the Lagoa Real uraniferous albitites (Brazil): Revista de Geologia, v. 23, p. 90–100.

Chayes, F., 1960, On correlation between variables of constant sum: Journal of Geophysical Research, v. 65, p. 4185–4193.

Cembrano, J., and Lara, L., 2009, The link between volcanism and tectonics in the southern volcanic zone of the Chilean Andes: A review: Tectonophysics, v. 471, p. 96–113.

Chen, H., Clark, A.H., and Kyser, K., 2010b, The Marcona magnetite deposit, south-central Peru: A product of hydrous, iron oxide-rich melts?: Economic Geology, v. 105, p. 1441–1456.

Chen, H., Clark, A.H, Kyser, T.K., Ullrich, T.D., Baxter, R., Chen, Y., and Moody, T.C., 2010a, Evolution of the giant Marcona-Mina Justa iron oxide-copper-gold district, south-central Peru: Economic Geology, v. 105, p. 155–185.

Chen, H., Kyser, T.K., and Clark, A.H., 2011, Contrasting fluids and reservoirs in the contiguous Marcona and Mina Justa iron oxide–Cu (–Ag–Au) deposits, south-central Perú: Mineralium Deposita, v. 46, p. 677–706.

Chiaradia, M., Banks, D., Cliff, R., Marschik, R., and de Haller, A., 2005, A non-magmatic component in fluids of South American Fe oxide–Cu–Au deposits inferred from ^{37}Cl, $^{87}Sr/^{86}Sr_i$ and Cl/Br: Mineral Deposit Research: Meeting the Global Challenge, p. 735–738.

Chorlton, L.B., 2007, Generalized geology of the world: Bedrock domains and major faults in GIS format; a small-scale world geology map with an extended geological attribute database: Geological Survey of Canada, Open File 5529, 48 p.

Ciobanu, C.L., Wade, B., Cook N.J, Schmidt Mumm, A., and Giles, D., 2013, Uranium-bearing hematite from the Olympic Dam Cu–U–Au deposit, South Australia: A geochemical tracer and reconnaissance Pb–Pb geochronometer: Precambrian Research, v. 238, p. 129–147.

Clark, C., Schmidt Mumm, A., and Faure, K., 2005, Timing and nature of fluid flow and alteration during Mesoproterozoic shear zone formation, Olary Domain, South Australia: Journal of Metamorphic Geology, v. 23, p. 147–164.

Clark, D.A., 2014, Magnetic effects of hydrothermal alteration in porphyry copper and iron-oxide copper–gold systems: A review: Tectonophysics, v. 624–625, p. 46–65.

Clark, T., Gobeil, A., and Chevé, S., 2010, Alterations in IOCG-type and related deposits in the Manitou Lake area, Eastern Grenville Province, Québec, *in* Corriveau, L., and Mumin, A.H., eds., Exploring for iron oxide copper–gold deposits: Canada and global analogues: Geological Association of Canada, Short Course Notes 20, p. 127–146.

Cocherie, A., and Albarède, F., 2001, An improved U–Th–Pb age calculation for electron microprobe dating of monazite: Geochimica et Cosmochimica Acta, v. 65, p. 4509–4522.

Collins, W.J., Beams, S.D., White, A.J. R., and Chappell, B.W., 1982, Nature and origin of A-type granites with particular reference to southeastern Australia: Contributions to Mineralogy and Petrology, v. 80, p. 189–200.

Cook, F.A., 2011, Multiple arc development in the Paleoproterozoic Wopmay orogen, Northwest Canada, *in* Brown, D., and Ryan, P.D., eds., Arc-continent collision, Frontiers in Earth Sciences: Springer-Verlag, Berlin, p. 403–427.

Cook, F.A., van der Veldon, A.J., Hall, K.W., and Roberts, B.J., 1999, Frozen subduction in Canada's Northwest Territories: Lithoprobe deep lithospheric reflection profiling of the western Canadian Shield: Tectonics, v. 18, p. 1–24.

Cordani, U.G., Lyer, S.S., Taylor, K., Kawashita, K, Sato, K., and McReath, I., 1992, Pb–Pb, Rb–Sr, and K–Ar systematic of the Lagoa Real uranium province (south-central Bahia, Brazil) and the Espinhaço Cycle (ca. 1.5–1.0 Ga): Journal of South American Earth Sciences, v. 5, p. 34–46.

Corriveau, L., 2007, Iron oxide copper–gold deposits: A Canadian perspective, *in* Goodfellow, W.D., ed., Mineral deposits of Canada: A synthesis of major deposit-types, district metallogeny, the evolution of geological provinces and exploration methods: Geological Association of Canada, Mineral Deposit Division, Special Publication 5, p. 307–328.

Corriveau, L., and Gorton, M.P., 1993, Coexisting K-rich alkaline and shoshonitic magmatism of arc affinities in the Proterozoic: A reassessment of syenitic stocks in the southwestern Grenville Province: Contributions to Mineralogy and Petrology, v. 113, p. 262–279.

Corriveau, L., and Mumin, A.H., 2010, Exploring for iron oxide–copper–gold (Ag–Bi–Co–U) deposits: Case examples, classification and exploration vectors, *in* Corriveau, L., and Mumin, A.H., eds., Exploring for iron oxide copper–gold deposits: Canada and global analogues: Geological Association of Canada, Short Course Notes 20, p. 1–13.

Corriveau, L., and Spry, P., 2014, Metamorphosed hydrothermal ore deposits, *in* Holland, H.D., and Turekian, K.K., eds., Treatise on Geochemistry, Second Edition: Elsevier, Amsterdam, v. 13, p. 175–194.

Corriveau, L., Ootes, L., Mumin, H., Jackson, V., Bennett, V., Cremer, J.-F., Rivard, B., McMartin, I., and Beaudoin, G., 2007, Alteration vectoring to IOCG(U) deposits in frontier volcano-plutonic terrains, Canada, *in* Milkereit, B., ed., Proceedings of Exploration 07: Fifth Decennial International Conference on Mineral Exploration, p. 1171–1177.

Corriveau, L., McMartin, I., Brouillette, P., Bleeker, W., Jackson, V.A., Montreuil, J.-F., Mumin, A.H., Harvey, B., Kiss, F., and Carson, J., 2009, The IOCG/multiple metals – Great Bear region (NWT) project, Geomapping for energy and minerals program: Field results, status and progress, *in* Jackson, V., and Palmer, E., eds., 37th Annual Yellowknife Geoscience Forum Abstracts: Northwest Territories Geoscience Office, Yellowknife, NWT, YKGSF Abstracts Volume 2009, p. 9.

Corriveau, L., Mumin, A.H., and Setterfield, T., 2010a, IOCG environments in Canada: Characteristics, geological vectors to ore and challenges, *in* Porter, T.M., ed., Hydrothermal iron oxide copper–gold and related deposits: A global perspective, volume 4 - advances in the understanding of IOCG deposits: Porter Geoscience Consultancy Publishing, Adelaide, Australia, p. 311–344.

Corriveau, L., Williams, P.J., and Mumin, A.H., 2010b, Alteration vectors to IOCG mineralization from uncharted terranes to deposits, *in* Corriveau, L., and Mumin, A.H., eds., Exploring for iron oxide copper–gold deposits: Canada and global analogues: Geological Association of Canada, Short Course Notes 20, p. 89–110.

Corriveau, L., Mumin, A.H., and Montreuil, J.-F., 2011, The Great Bear magmatic zone: The IOCG spectrum and related deposit types: Proceeding of the Eleventh Biennial SGA Meeting, Antofagasta, Chile.

Corriveau, L., Nadeau, O., Montreuil, J.-F., and Desrochers, J.-P., 2014, Report of activities for the Core Zone: Strategic geomapping and geoscience to assess the mineral potential of the Labrador Trough for multiple metals IOCG and affiliated deposits, Canada: Geological Survey of Canada, Open File 7714.

Corriveau, L., Lauzière, K., Montreuil, J.-F., Potter, and E.G., 2015. Dataset of geochemical data from iron oxide alkali-altered mineralizing systems of the Great Bear magmatic zone (NWT); Geological Survey of Canada, Open File 7643, 21 p.

Craven, J., Roberts, B., Hayward, N., Stefanescu, M., and Corriveau, L., 2013, A magnetotelluric survey and preliminary geophysical inversion and visualization of the NICO IOCG deposit, NWT: Geological Survey of Canada, Open File 7465, 26 p., doi:10.4095/292869.

Creaser, R.A., 1996, Petrogenesis of a Mesoproterozoic quartz latite-granitoid suite from the Roxby Down area, South Australia: Precambrian Research, v. 79, p. 371–394.

Creaser, R.A., Price, R.C., and Wormald, R.J., 1991, A-type granite revisited: Assessment of a residual-source model: Geology, v. 19, p. 163–166.

Cuney, M., 2009, The extreme diversity of uranium deposits: Mineralium Deposita, v. 44, p. 3–9.

Cuney, M., and Kyser, K., 2008, Deposits related to Na-metasomatism and high-grade metamorphism, *in* Cuney, M., and Kyser, K., eds., Recent and not-so-recent developments in uranium deposits and implications for exploration: Mineral Association of Canada, Short Course Series 39, p. 97–116.

Cuney, M., Emtz, A., Mercadier, J., Mykchaylov, V., Shunko, V., and Yuslenko, A., 2012, Uranium deposits associated with Na-metasomatism from central Ukraine: A review of some of the major deposits and genetic constraints: Ore Geology Reviews, v. 44, p. 82–106.

Daliran, F., Stosch, H.-G., Williams, P.J., Jamali, H., and Dorri, M.-B., 2010, Early Cambrian iron oxide–apatite–REE (U) deposits of the Bafq district, east-central Iran, *in* Corriveau, L., and Mumin, A.H., eds., Exploring for iron oxide copper–gold deposits: Canada and global analogues: Geological Association of Canada, Short Course Notes, v. 20, p 147–159.

Davidson, G., Paterson, H., Meffre, S., and Berry, R.F., 2007, Characteristics and origin of the Oak Dam East breccia-hosted, iron oxide Cu–U–(Au) deposit: Olympic Dam region, Gawler Craton, South Australia: Economic Geology, v. 102, p. 1471–1498.

Davis, W., Corriveau, L., van Breemen, O., Bleeker, W., Montreuil, J.-F., Potter, E.G., and Pelleter, E., 2011, Timing of IOCG mineralizing and alteration events within the Great Bear magmatic zone, *in* Fischer, B.J., and Watson, D.M., eds., 39th Annual Yellowknife Geoscience Forum Abstract Volume: NWT Geoscience Office, p. 97.

Day, W.C., and Lane, D.E., 1992, Strategic and critical minerals in the midcontinent region, United States: United States Geological Survey, Bulletin 1989.

De Haller, A., and Fontboté, L., 2009, The Raúl-Condestable iron oxide copper–gold deposit, central coast of Peru: Ore and related hydrothermal alteration, sulphur isotopes, and thermodynamic constraints: Economic Geology, v. 104, p. 365–384.

De Haller, A., Corfu, F., Fontboté, L., Schaltegger, U., Barra, F., Chiaradia, M., Frank, M., and Alvarado, J.Z., 2006, Geology, geochronology, and Hf and Pb isotope data of the Raúl-Condestable iron oxide–copper–gold deposit, central coast of Perú: Economic Geology, v. 101, p. 281–310.

De Jong, G., and Williams, P.J., 1995, Giant metasomatic system formed during exhumation of mid-crustal Proterozoic rocks in the vicinity of the Cloncurry Fault, northwest Queensland: Australian Journal of Earth Sciences, v. 42, p. 281–290.

De Toni, A., 2016, Les paragénèses à magnétite des altérations associées aux systèms à oxydes de fer et altérations en éléments alcalins, zone magmatic du grand lac de l'ours. Unpublished MSc thesis, Institut National de la Recherche Scientifique et l'Université Laval, 761 p.

Dolejš, D., and Wagner, T., 2008, Thermodynamic modeling of non-ideal mineral–fluid equilibria in the system Si–Al–Fe–Mg–Ca–Na–K–H–O–Cl at elevated temperatures and pressures: Implications for hydrothermal mass transfer in granitic rocks: Geochimica et Cosmochimica Acta, v. 72, p. 526–553.

D'Oria, R.-M., 1998, An investigation of the comagmatic signature of the intrusive / extrusive phases of the Faber Lake rapakivi suite, Great Bear Magmatic Zone, NWT: Unpublished B.Sc. thesis, London, Canada, University of Western Ontario, 105 p.

Dreher, A.M., Xavier, R.P., Taylor, B.E., and Martini, S.L., 2008, New geologic, fluid inclusion and stable isotope studies on the controversial Igarapé Bahia Cu–Au deposit, Carajás Province, Brazil: Mineralium Deposita, v. 43, p. 161–184.

Drummond, B., Lyons, P., Goleby, B., and Jones, L., 2006, Constraining models of the tectonic setting of the giant Olympic Dam iron oxide–copper–gold deposit, South Australia, using deep seismic reflection data: Tectonophysics, v. 420, p. 91–103.

Duchesne, M.J., Moore, F., Long, B.F., and Labrie, J., 2009, A rapid method for converting medical Computed Tomography scanner topogram attenuation scale to Hounsfield Unit scale and to obtain relative density values: Engineering Geology, v. 103, p.100–105.

Eby, G.N., 1990, The A-type granitoids: A review of their occurrence and chemical characteristics and speculations on their petrogenesis, *in* Wolley, A.R., and Ross, M., eds., Alkaline igneous rocks and carbonatites. Lithos, v. 26, p. 115–134.

Edfelt, Å., Amstrong, R.N., Smith, M., and Martinsson, O., 2005, Alteration paragenesis and mineral chemistry of the Tjårrojåkka apatite–iron and Cu (–Au) occurrences, Kiruna area, Sweden: Mineralium Deposita, v. 40, p. 409–434.

Egozcue, J.J., Pawlowsky-Glahn, V., Mateu-Figueras, G., and Barceló-Vidal, C., 2003, Isometric logratio transformations for compositional data analysis: Mathematical Geology, v. 35, p. 279–300.

Eilu, P., and Niiranen, 2002, Iron oxide-copper-gold deposits in Finland, Geological Survey of Finland, report M 10.1/2002/4, 7 p.

Einaudi, M.T., and Burt, D.M., 1982, Introduction; terminology, classification, and composition of skarn deposits: Economic Geology, v. 77, p. 745–754.

Einaudi, M.T., Meinert, L.D., and Newberry, R.J., 1981, Skarn Deposits, *in* Skinner, B.J., ed., Economic Geology Seventy-Fifth Anniversary Volume 1906-1980: Economic Geology Publishing Company, p. 317–391.

Elburg, M.A., van Bergen, M.J., Hoogewerff, J., Foden, J., Vroon, P.Z., Zulkarnain, I., and Nasution, A., 2002, Geochemical trends across an arc-continent collision zone: Magma sources and slab-wedge transfer processes below the Pantar Strait volcanoes (Indonesia): Geochimica et Cosmochimica Acta, v. 66, p. 2771–2789.

Elburg, M.A., van Bergen, M.J., and Foden, J.D., 2004, Subducted upper and lower continental crust contributes to magmatism in the collision sector of the Sunda-Banda arc, Indonesia: Geology, v. 32, p. 41–44.

Engvik, A., Putnis, A., Fitz Gerald, J.D., and Austrheim, H., 2008, Albitization of granitic rocks: The mechanism of replacement of oligoclase by albite: Canadian Mineralogist, v. 46, p. 1401–1415.

Engvik, L., Stöckhert, B., and Engvik, A.K., 2009, Fluid infiltration, heat transport, and healing of microcracks in the damage zone of magmatic veins: Numerical modeling: Journal of Geophysical Research, v. 114, doi:10.1029/2008JB005880.

Enkin, R., Montreuil, J.-F., and Corriveau, L., 2012, Differential exhumation and concurrent fluid flow at the NICO Au–Co–Bi–Cu deposit and Southern Breccia U–Th–REE–Mo anomaly, Great Bear magmatic zone, NWT – A paleomagnetic and structural record: Geological Association of Canada – Mineralogical Association of Canada, Program with Abstracts, v. 35, p. 41.

Eveleigh, A.J., 1997, Report of the prospecting ground geophysics, airborne geophysics, gravity survey on the Dianne Lake property, Mazenod Lake area, Mackenzie district, Northwest Territories, Canada: NWT Geoscience Office, NORMIN Assessment Report 083827, 54 p.

Exley, R.A., 1980, Microprobe studies of REE-rich accessory minerals: Implications for Skye granite petrogenesis and REE mobility in hydrothermal systems: Earth and Planetary Science Letters, v. 48, p. 97–110.

Fadda, S., Fiori, M., Grillo, S.M., and Prochaska, W., 2012, REE mobilization in complex hydrothermal–metasomatic systems: Fluid chemistry evidence of albitite and chlorite–talc mineralizations in central Sardinia, Italy, *in* Maarten, A.T., and Broekmans, M., eds., Proceeding of the 10th International Congress for Applied Mineralogy (ICAM): Springer-Verlag Berlin Heidelberg, doi: 10.1007/978-3-642-27682-8_22.

Fetherson, J.M., 2004, Tantalum in Western Australia: Western Australia Geological Survey, Mineral Resources Bulletin, v. 22, 162 p.

Franchini, M.B., de Barrio, R.E., Pons, M.J., Schalamuk, I.B., Rios, F.J., and Meinert, L., 2007, Fe skarn, iron oxide Cu–Au, and manto Cu–(Ag) deposits in the Andes Cordillera of southwest Mendoza Province (34°–36°S), Argentina: Exploration and Mining Geology, v. 16, p. 233–265.

Franklin, J.M., 1997, Lithogeochemical and mineralogical methods for base metal and gold exploration, *in* Gubins, A.G., ed., Proceeding of Exploration 97: Fourth Decennial International Conference on Mineral Exploration, p. 191–208.

Freeman, H., and Tomkinson, M., 2010, Geological setting of iron oxide related mineralisation in the southern Mount Wood domain, southern Australia, *in* Porter, T.M., ed., Hydrothermal iron oxide copper–gold and related deposits: A global perspective, volume 3 - advances in the understanding of IOCG deposits: Porter Geoscience Consultancy Publishing, Adelaide, Australia, p. 171–190.

Frost, C.D., and Frost, B.R., 2013, Proterozoic ferroan feldspathic magmatism: Precambrian Research, v. 228, p. 151–163.

Gabriel, A., and Cox, E.P., 1929, A staining method for the quantitative determination of certain rock minerals: American Mineralogist, v. 14, p. 290–292.

Gabriel, K.R., 1971, The biplot graphical display of matrices with application to principal component analysis: Biometrika, v. 58, p. 453–467.

Gandhi, S.S., 1977, Geological setting and genetic aspects of uranium occurences in the Kaipokok Bay–Big River area, Labrador: Economic Geology, v. 73, p. 1492–1522.

Gandhi, S.S., 1988, Volcano-plutonic setting of U–Cu bearing magnetite veins of FAB claims, southern Great Bear magmatic zone, Northwest Territories: Geological Survey of Canada, Paper 88-1C, p. 177–187.

Gandhi, S.S., 1989, Rhyodacite ignimbrites and breccias of the Sue-Dianne and Mar Cu–Fe–U deposits, southern Great Bear magmatic zone, Northwest Territories: Geological Survey of Canada, Paper 89-1C, p. 263–273.

Gandhi, S.S., 1992a, Magnetite deposits in metasiltstones of the Snare Group at Hump Lake, Northwest Territories: Geological Survey of Canada, Paper 92-1C, p. 225–235.

Gandhi, S.S., 1992b, Magnetite-rich breccia of the Mar deposit and veins of the Nod prospect, southern Great Bear magmatic zone, Northwest Territories: Geological Survey of Canada, Paper 92-1C, p. 237–249.

Gandhi, S.S., 1994, Geological setting and genetic aspects of mineral occurrences in the southern Great Bear magmatic zone, Northwest Territories, *in* Sinclair, W.D., and Richardson, D.G., eds., Studies of rare-metal deposits in the Northwest Territories: Geological Survey of Canada, Bulletin 475, p. 63–96.

Gandhi, S.S., 2004, World distribution of iron oxide +/– Cu +/– Au +/– U deposits: Geological Survey of Canada, Global Database System.

Gandhi, S.S., and Halliday, D., 1993, Gravity survey of the Sue-Dianne deposit, Northwest Territories: Geological Survey of Canada, Paper 93-1E, p. 231–238.

Gandhi, S.S., and Lentz, D.R., 1990, Bi–Co–Cu–Au–As and U occurrences in the Snare Group metasediments and felsic volcanics of the southern Great Bear magmatic zone, Lou Lake, Northwest Territories: Geological Survey of Canada, Paper 90-1C, p. 239–253.

Gandhi, S.S., and Prasad, N., 1993, Regional metallogenic significance of Cu, Mo and U occurrences at DeVries Lake, southern Great Bear magmatic zone, Northwest Territories: Geological Survey of Canada, Paper 93-1C, p. 29–39.

Gandhi, S.S., and Prasad, N., 1995, Geological setting of Bode copper and Damp polymetallic prospects, central Great Bear magmatic zone, Northwest Territories: Geological Survey of Canada, Paper 1995-C, p. 201–212.

Gandhi, S.S., and Prasad, N., 1997, Stratiform and vein-type magnetite–pyrite–chalcopyrite in a rhyolite-dacite assemblage at Tommie Lake, central Great Bear magmatic zone, Northwest Territories: Geological Survey of Canada, Paper 1997-C, p. 1–14.

Gandhi, S.S., and van Breemen, O., 2005, SHRIMP U–Pb geochronology of detrital zircons from the Treasure Lake Group - new evidence for Paleoproterozoic collisional tectonics in the southern Hottah terrane, northwestern Canadian Shield: Canadian Journal of Earth Sciences, v. 42, p. 833–845.

Gandhi, S.S., Prasad, N., and Charbonneau, B.W., 1996, Geological and geophysical signatures of a large polymetallic exploration target at Lou Lake, southern Great Bear magmatic zone, Northwest Territories: Geological Survey of Canada, Paper 1996-E, p. 147–158.

Gandhi, S.S., Carrière, J.J., and Prasad, N., 2000, Implications of a preliminary fluid-inclusion study of giant quartz veins of the southern Great Bear magmatic zone, Northwest Territories: Geological Survey of Canada, Paper 2000-1C, 13 p.

Gandhi, S.S., Mortensen, J.K., Prasad, N., and van Breemen, O., 2001, Magmatic evolution of the southern Great Bear continental arc, northwestern Canadian Shield: Geochronological constraints: Canadian Journal of Earth Sciences, v. 38, p. 767–785.

Gandhi, S.S., Potter, E., and Fayek, M., 2013, Polymetallic U–Ag veins at Port Radium, Great Bear magmatic zone, Canada: Main botryoidal pitchblende stage cuts 1.74 Ga diabase dykes and has REE signatures diagnostic of unconformity-type deposits: Geological Survey of Canada, Open File 7493, 1 sheet.

Gandhi, S.S., Montreuil, J.-F., and Corriveau, L., 2014, Geology of the Mazenod area: Geological Survey of Canada, Canadian Geoscience Map Series, CGM 148P.

Gao, Y., Yang, Z., Hou, Z., Wei, R., Meng, X., and Tian, S., 2010, Eocene potassic and ultrapotassic volcanism in south Tibet: New constraints on mantle source characteristics and geodynamic processes: Lithos, v. 117, p. 20–32.

Gauthier, M., Hall, G., Stein, H., and Schaltegger, U., 2001, The Osborne deposit, Cloncurry district: A 1595 Ma Cu–Au skarn deposit, *in* Williams, P.J., ed., A hydrothermal odyssey: Extended Conference Abstracts, Economic Geology Research Unit, Contribution 59.

Gauthier, M., Chartrand, F., Cayer, A., and David, J., 2004, The Kwyjibo Cu–REE–U–Au–Mo–F property, Quebec: A Mesoproterozoic polymetallic iron oxide deposit in the northeastern Grenville Province: Economic Geology, v. 99, p. 1177–1196.

Gelcich, S., Davis, D.W., and Spooner, E.T.C., 2005, Testing the apatite–magnetite geochronometer: U–Pb and $^{40}Ar/^{39}Ar$ geochronology of plutonic rocks, massive magnetite–apatite tabular bodies, and IOCG mineralization in northern Chile: Geochimica et Cosmochimica Acta, v. 69, p. 3367–3384.

Gieré, R., and Sorensen, S.S., 2004, Allanite and other REE-rich epidote-group minerals: Review of Mineral Geochemistry, v. 56, p. 431–493.

Girardi, J.D., 2014, Comparison of Mesozoic magmatic evolution and iron oxide (-copper-gold) ('IOCG') mineralization, central Andes and western North America: Unpublished Ph.D. thesis, Univeristy of Arizona, 363 p.

Gleason, J.D., Marikos, M.A., Barton, M.D., and Johnson, D.A., 2000, Neodymium isotopic study of rare earth element sources and mobility in hydrothermal Fe oxide (Fe–P–REE) systems: Geochimica et Cosmochimica Acta, v. 64, p. 1059–1068.

Gleeson, S.A., and Smith, M.P., 2009, The sources and evolution of mineralising fluids in iron oxide–copper–gold systems, Norrbotten, Sweden: Constraints from Br/Cl ratios and stable Cl isotopes of fluid inclusion leachates: Geochimica et Cosmochimica Acta, v. 73, p. 5658–5672.

Goad, R.E., Mumin, A.H., and Mulligan, D.L., 1996, A report on the geology of the JBG1-7 claims, Marian River area, Mackenzie (south) district, Northwest Territories, Canada: NWT Geoscience Office, NORMIN Assessment Report 083776, 89 p.

Goad, R.E., Mumin, A.H., Duke, N.A., Neale, K.L., and Mulligan, D.L., 2000a, Geology of the Proterozoic iron oxide-hosted NICO cobalt–gold–bismuth, and Sue-Dianne copper–silver deposits, southern Great Bear magmatic zone, Northwest Territories, Canada, *in* Porter, T.M., ed., Hydrothermal iron oxide copper–gold and related deposits: A global perspective, volume 1: Porter Geoscience Consultancy Publishing, Adelaide, Australia, p. 249–267.

Goad, R.E., Mumin, A.H., Duke, N.A., Neale, K.L., Mulligan, D.L., and Camier, W.J., 2000b, The NICO and Sue-Dianne Proterozoic, iron oxide-hosted, polymetallic deposits, Northwest Territories: Application of the Olympic Dam model in exploration: Exploration and Mining Geology, v. 9, p. 123–140.

Georoc database, http://georoc.mpch-mainz.gwdg.de, (accessed May 2012, June 2013)

Grant, J.A., 1986, The isocon diagram – A simple solution to Gresens' equation for metasomatic alteration: Economic Geology, v. 81, p. 1976–1982.

Grant, J.A., 2005, Isocon analysis: A brief review of the method and applications: Physics and Chemistry of the Earth, v. 30, p. 997–1004.

Gresens, R.L., 1967, Composition-volume relationships of metasomatism: Chemical Geology, v. 2, p. 47–55.

Groves, D.L., Bierlein, F.P., Meinert, L.D., and Hitzman, M.W., 2010, Iron oxide copper–gold (IOCG) deposits through Earth history: Implications for origin, lithospheric setting, and distinction from other epigenetic iron oxide deposits: Economic Geology, v. 105, p. 641–654.

Grunsky, E.C., 2002, R: A data analysis and statistical programming environment – an emerging tool for the geosciences: Computer and Geosciences, v. 28, p. 1219–1222.

Grunsky, E.C., 2010, The interpretation of geochemical survey data: Geochemistry: Exploration, Environment, Analysis, v. 10, p. 27–74.

Grunsky, E.C., and Bacon-Shone, J., 2011, The stoichiometry of mineral compositions: Conference Proceedings, CodaWork11, May 9-13, 2011, Saint Feliu de Guixols, Spain.

Grunsky, E.C., and Kjarsgaard, B.A., 2008, Classification of distinct eruptive phases of the diamondiferous Star kimberlite, Saskatchewan, Canada based on statistical treatment of whole rock geochemical analyses: Applied Geochemistry, v. 23, p. 3321–3336.

Hamel, F., 2013, Caractérisation de l'altération hydrothermale dans les roches du système de Grouard, zone magmatique du Grand lac de l'Ours, Territoires du Nord-Ouest: Unpublished B.Sc. thesis, Quebec City, Canada, Université Laval, 74 p.

Harlov, D.E., Andersson, U.B., Förster, H.J., Nyström, J.O., Dulski, P., and Broman, C., 2002, Apatite–monazite relations in the Kiirunavaara magnetite–apatite ore, northern Sweden: Chemical Geology, v. 191, p. 47–72.

Harlov, D.E., Wirth, R., and Förster, H.J., 2005, An experimental study of dissolution-reprecipitation in fluoroapatite: Fluid infiltration and the formation of monazite: Contributions to Mineralogy and Petrology, v. 150, p. 268–286.

Hastie, A.R., Kerr, A.C., Pearce, J.A., and Mitchell, S.F., 2007, Classification of altered volcanic island arc rocks using immobile trace elements: Development of the Th–Co discrimination diagram: Journal of Petrology, v. 48, p. 2341–2357.

Haynes, D.W., Cross, K.C., Bills, R.T., and Reed, M.H., 1995, Olympic Dam ore genesis: A fluid mixing model: Economic Geology, v. 90, p. 281–307.

Hayward, N., 2013, 3D magnetic inversion of mineral prospects in the Great Bear magmatic zone, NT, Canada: Geological Survey of Canada, Open File 7421.

Hayward, N., and Corriveau, L., 2014, Fault reconstructions using aeromagnetic data in the Great Bear magmatic zone, Northwest Territories, Canada: Canadian Journal of Earth Sciences, v. 51 p. 1–16.

Hayward, N., Enkin, R.J., Corriveau, L., Montreuil, J.-F., and Kerswill, J., 2013, The application of rapid potential field methods for the targeting of IOCG mineralisation based on physical property data, Great Bear magmatic zone, Canada: Journal of Applied Geophysics, v. 94, p. 42–58.

Health Canada, 2000, Canadian guidelines for the management of Naturally Occurring Radioactive Materials (NORM): Minister of Public Works and Government Services Canada, 47 p.

Heinrich, C.A., Günther, D., Audédat, A., Ulrich, T., and Frischknecht, R., 1999, Metal fractionation between magmatic brine and vapor, determined by microanalysis of fluid inclusions: Geology, v. 27, p. 755–758.

Heinson, G.S., Direen, N.G., and Gill, R.M., 2006, Magnetotelluric evidence for a deep-crustal mineralizing system beneath the Olympic Dam iron oxide copper–gold deposit, southern Australia: Geology, v. 34, p. 573–576.

Hennessey, B.T., and Puritch, E., 2008, A technical report on a mineral resource estimate for the Sue-Dianne deposit, Mazenod Lake area, Northwest Territories, Canada: Fortune Minerals Limited, Technical Report, 125 p.

Hikov, A., 2004, Geochemistry of strontium in advanced argillic alteration systems – possible guide to exploration: Bulgarian Geological Society, Annual Scientific Conference 'Geology 2004', p. 29–31.

Hildebrand, R.S., 1981, Early Proterozoic LaBine group of Wopmay Orogen: Remnant of a continental volcanic arc developed during oblique convergence, *in* Campbell, F.H.A., ed., Proterozoic basins of Canada: Geological Survey of Canada, Paper 81-10, p. 133–156.

Hildebrand, R.S., 1983, Geology - Echo Bay-MacAlpine Channel area, district of Mackenzie, Northwest Territories: Geological Survey of Canada, Map 1546A, scale 1:50 000.

Hildebrand, R.S., 1984, Geology of the Rainy Lake–White Eagle Falls area, District of Mackenzie: Early Proterozoic cauldrons, stratovolcanoes and subvolcanic plutons: Geological Survey of Canada, Paper 83-20, 42 p.

Hildebrand, R.S., 1986, Kiruna-type deposits: Their origin and relationship to intermediate subvolcanic plutons in the Great Bear magmatic zone, northwest Canada: Economic Geology, v. 81, p. 640–659.

Hildebrand, R.S., 2011, Geological synthesis of Northern Wopmay Orogen / Coppermine Homocline, Northwest Territories – Nunavut: Geological Survey of Canada, Open File 6390, NTGO Open Report 2010-011, 1 map, scale 1:500 000.

Hildebrand, R.S., 2014, Geology, Leith Peninsula: Geological Survey of Canada, Canadian Geoscience Map P153, scale 1:125 000.

Hildebrand, R.S., and Bowring, S.A., 1984, Continental intra-arc depressions: A non-extensional model for their origin, with a Proterozoic example from Wopmay Orogen: Geology, v. 12, p. 73–77.

Hildebrand, R.S., and Bowring, S.A., 1988, Geology of parts of the Calder River map area, central Wopmay Orogen, District of Mackenzie: Geological Survey of Canada, Paper 88-1C, p. 199–205.

Hildebrand, R.S., Hoffman, P.F., and Bowring, S.A., 1987, Tectono-magmatic evolution of the 1.9-Ga Great Bear magmatic zone, Wopmay Orogen, northwestern Canada: Journal of Volcanology and Geothermal Research, v. 32, p. 99–118.

Hildebrand, R.S., Hoffman, P.F., and Bowring, S.A., 2010a, The Calderian orogeny in Wopmay Orogen (1.9 Ga), northwest Canadian Shield: Geological Society of America Bulletin, v. 122, p. 794–814.

Hildebrand, R.S., Hoffman, P.F., Housh, T., and Bowring, S.A., 2010b, The nature of volcano-plutonic relations and shapes of epizonal plutons of continental arcs as revealed in the Great Bear magmatic zone, northwestern Canada: Geosphere, v. 6, p. 812–839.

Hildebrand, R.S., Bowring, S.A., and Pelletier, 2014, Geology, Calder River: Geological Survey of Canada, Canadian Geoscience Map P154, NWT Geoscience Office, NWT Open Report 2013-003, scale 1:125 000.

Hitzman, M.C., 2000, Iron oxide–Cu–Au deposits: What, where, when, and why?, *in* Porter, T.M., ed.,

Hydrothermal iron oxide copper–gold and related deposits: A global perspective, volume 1: Porter Geoscience Consultancy Publication, Adelaide, Australia, p. 9–25.

Hitzman, M.W., and Valenta, R.K., 2005, Uranium in iron oxide-copper-gold (IOCG) systems: Economic Geology, v. 100, p. 1657–1661.

Hitzman, M.W., Oreskes, N., and Einaudi, M.T., 1992, Geological characteristics and tectonic setting of Proterozoic iron oxide (Cu–U–Au–LREE) deposits: Precambrian Research, v. 58, p. 241–287.

Hoffman, P.F., Bowring, S.A., Buchwaldt, R., and Hildebrand, R.S., 2011, Birthdate for the Coronation paleocean: Age of the initial rifting in Wopmay Orogen, Canada: Canadian Journal of Earth Sciences, v. 48, p. 281–293.

Housh, T., Bowring, S.A., and Villeneuve, M., 1989, Lead isotopic study of early continental Proterozoic Wopmay Orogen, new Canada: Role of continental crust in arc magmatism: The Journal of Geology, v. 97, p. 735–747.

Hunt, J., Baker, T., and Thorkelson, D., 2005, Regional-scale Proterozoic IOCG-mineralized breccia systems: Examples from the Wernecke Mountains, Yukon, Canada: Mineralium Deposita, v. 40, p. 492–514.

Hunt, J., Baker, T., and Thorkelson, D., 2007, A review of iron oxide copper–gold deposits, with focus on the Wernecke Breccias, Yukon, Canada, as an example of a non-magmatic end member and implications for IOCG genesis and classification: Exploration and Mining Geology, v. 16, p. 209–232.

Ishikawa, Y., Sawaguchi, T., Iwaya, S., and Horiuchi, M., 1976, Delineation of prospecting targets for Kuroko deposits based on modes of volcanism of underlying dacite and alteration haloes: Mining Geology, v. 26, p. 105–117.

Ismail, R., Ciobanu, C.L., Cook, N.J, Giles, D., Schmidt-Mumm, A., and Wade, B., 2014, Rare Earths and other trace elements in minerals from skarn assemblages, Hillside iron oxide–copper–gold deposit, Yorke Peninsula, South Australia: Lithos, v. 184-187, p. 456–477.

Jackson, V.A., 2008, Preliminary geologic map of part of the southern Wopmay Orogen (parts of NTS 86B and 86C; 2007 updates); descriptive notes to accompany 1:100 000 scale map: NWT Geoscience Office, NWT Open Report 2008-007, 51 p.

Jackson, V.A., and Ootes, L., 2012, Preliminary geologic map of the south-central Wopmay Orogen (parts of NTS 86B, 86C, and 86D); results from 2009 to 2011: NWT Geoscience Office, NWT Open Report 2012-004, 1 map, 1:100,000 scale.

Jackson, V.A., van Breemen, O., Ootes, L., Bleeker, W., Bennett, V., Davis, W.J., Ketchum, J.W.F., and Smar, L., 2013, U–Pb zircon ages and field relationships of Archean basement and Proterozoic intrusions, south-central Wopmay Orogen, NWT: Implications for tectonic assignments: Canadian Journal of Earth Sciences, v. 50, p. 979–1006.

Jamtveit, B., Putnis, C.V., and Malthe-Sörensen, A., 2009, Reaction induced fracturing during replacement processes: Contributions to Mineralogy and Petrology, v. 157, p.127–133.

Jébrak, M., 1997, Hydrothermal breccias in vein-type ore deposits: A review of mechanisms, morphology and size distribution: Ore Geology Reviews, v. 12, p. 111–134.

Jébrak, M., 2010, Use of breccias in IOCG (U) exploration, *in* Corriveau, L., and Mumin, A.H., eds., Exploring for iron oxide copper–gold deposits: Canada and global analogues: Geological Association of Canada, Short Course Notes 20, p. 79–88.

Jerden, J.L., 2001, Origin of uranium mineralization at Coles Hill, Virginia (USA) and its natural attenuation within an oxidizing rock–soil–ground water system: Unpublished Ph.D. thesis, Virginia Polytechnic Institute and State University, Virginia, USA, 145 p.

Jonsson, E., Troll, V.R., Högdahl, K., Harris, C., Weis, F., Nilsson, K.P., and Skelton, A., 2013, Magmatic origin of giant 'Kiruna-type' apatite–iron-oxide ores in Central Sweden: Scientific Reports, v. 3, 8 p.

Joplin, G.A., 1968, The shoshonite association: A review: Journal of the Geological Society of Australia, v. 15, p. 275–294.

Kelemen, P.B., Hanghøj, K., and Greene, A.R., 2003, One view of the geochemistry of subduction-related magmatic arcs with an emphasis on primitive andesite and lower crust, *in* Rudnick, R.L., Holland, H.D., and Turekian, K.K., eds., Treatise on Geochemistry, volume 3, The Crust: Elsevier, Amsterdam, 70 p.

Kemp, A.I.S., and Hawkesworth, C.J., 2003, Granitic perspectives on the generation and secular evolution of the continental crust, *in* Rudnick, R.L., Holland, H.D., and Turekian, K.K., eds., Treatise on Geochemistry, volume 3, The Crust: Elsevier, Amsterdam, p. 349–410.

Kendrick, M.A., Baker, T., Fu, B., Phillips, D., and Williams, P.J., 2008, Noble gas and halogen constraint on regionally extensive mid-crustal Na–Ca metasomatism, the Proterozoic eastern Mount Isa Block, Australia: Precambrian Research, v. 163, p. 131–150.

Keppler H., and Wyllie, P.J., 1990, Role of fluids in transport and fractionation of uranium and thorium in magmatic processes: Nature, v. 348, p. 531–533.

Keppler H., and Wyllie, P.J., 1991, Partitioning of Cu, Sn, Mo, W, U, and Th between melt and aqueous fluid in the systems haplogranite–H_2O−HCl and haplogranite–H_2O−HF: Contributions to Mineralogy and Petrology, v. 109, p. 139–150.

Kish, L., and Cuney, M., 1981, Uraninite–albite veins from the Mistamisk Valley of the Labrador Trough, Québec: Mineralogical Magazine, v. 44, p. 471–483.

Klein, C., and Beukes, N.J., 1993, Sedimentology and geochemistry of the glaciogenic Late Proterozoic Rapitan iron-formation in Canada: Economic Geology, v. 88, p. 542–565.

Klein, C., and Ladeira, E.A., 2000, Geochemistry and petrology of some Proterozoic banded iron-formations of the Quadrilátero Ferrífero, Minas Gerais, Brazil: Economic Geology, v. 95, p. 405–428.

Klein, C., and Ladeira, E.A., 2002, Petrography and geochemistry of the least altered banded iron-formation of the Archean Carajás formation, northern Brazil: Economic Geology, v. 97, p. 643–651.

Knight, J., Lowe, J., Sojen, J., Cameron, J., Merrillees, J., Nag, S., Shah, N., Dua, G., and Jhala, K., 2002, The Khetri copper belt, Rajasthan: Iron oxide copper–gold terrane in the Proterozoic of NW India, *in* Porter, T.M., ed., Hydrothermal iron oxide copper–gold and related deposits: A global perspective, volume 2: Porter Geoscience Consultancy Publishing, Adelaide, Australia, p. 321–341.

Knox, A.W., 1998, Geological report of the Hillside zinc–lead–silver showing, Grouard Lake property, Grouard Lake, NWT: NWT Geoscience Office, NORMIN Assessment Report 084043, 47 p.

Kreiner, D.C., 2011, Epithermal style iron oxide(–Cu–Au) (=IOCG) vein systems and related alteration: Unpublished Ph.D. thesis, Tucson, United States, University of Arizona, 659 p.

Kreiner, D.C., and Barton, M.D., 2011, High-level alteration in iron-oxide(–Cu–Au) (IOCG) vein systems, example near Copiapó, Chile: Proceeding of the Eleventh Biennial SGA Meeting, p. 497–499.

Küster, D., 2009, Granitoid-hosted Ta mineralization in the Arabian-Nubian Shield: Ore deposit types, tectono-metallogenetic setting and petrogenetic framework: Ore Geology Reviews, v. 35, p. 68–86.

Large, R.R., Gemmel, J.B., Paulick, H., and Huston, D., 2001, The alteration box plot: A simple approach to understanding the relationship between alteration mineralogy and lithogeochemistry associated with volcanic-hosted massive sulfide deposits: Economic Geology, v. 96, p. 957–971.

Lee, M.D., and Morris, W.A., 2013, Comparison of magnetic-susceptibility meters using rock samples from the Wopmay Orogen, Northwest Territories: Geological Survey of Canada, Technical note 5, 10 p., doi:10.4095/292739

Li, X., Zhao, X., Zhou, M.-F., Chen, W.T., and Chu, Z., 2015, Fluid inclusion and isotopic constraints on the origin of the Paleoproterozoic Yinachang Fe–Cu–(REE) deposit, Southwest China: Economic Geology, v. 110, p. 1339–1369.

Li, W., Audétat, A., and Zhang, J., 2015a, The role of evaporites in the formation of magnetite–apatite deposits along the Middle and Lower Yangtze River, China: Evidence from LA-ICP-MS analysis of fluid inclusions: Ore Geology Reviews, v. 67, p. 264–278.

Li, Y.H., and Schoonmaker, J.E., 2003, Chemical composition and mineralogy of marine sediments, *in* Mackenzie, F.T., ed., Treatise on Geochemistry, volume 7, Sediments, Diagenesis, and Sedimentary Rocks: Elsevier, Amsterdam, p. 1–35.

Linge, K.L., 2007, Recent developments in trace element analysis by ICP-AES and ICP-MS with particular reference to geological and environmental samples: Geostandards and Geoanalytical Research, v. 29, p. 7–22.

Linnen, R.L., 1998, The solubility of Nb–Ta–Zr–Hf–W in granitic melts with Li and Li + F: Constraints for mineralization in rare metal granites and pegmatites: Economic Geology, v. 93, p. 1013–1025.

Lobato, L.M., and Fyfe, W.S., 1990, Metamorphism, metasomatism and mineralization at Lagoa Real, Bahia, Brazil: Economic Geology, v. 85, p. 968–989.

Lobo-Guerrero, A.S., 2010, Iron oxide copper–gold mineralization in the Greater Lufilian arc, Africa, *in* Corriveau, L., and Mumin, A.H., eds., Exploring for iron oxide copper–gold deposits: Canada and global analogues: Geological Association of Canada, Short Course Notes 20, p. 161–176.

Lypaczewski, P., Normandeau, P.X., Paquette, J., and McMartin, I., 2013, Petrographic and cathodoluminescence characterization of apatite from the Sue-Dianne and Brooke IOCG mineralization systems, Great Bear magmatic zone, Northwest Territories, Canada: Geological Survey of Canada, Open File 7319.

Mackay, M., and Eveleigh, A., 1997, Report on diamond drilling, Nod occurrence, Mazenod Lake property, Mazenod Lake area, Mackenzie district, Northwest Territories, Canada: NWT Geoscience Office, NORMIN Assessment Report 083901, 27 p.

Madeisky, H.E., 1996, A lithogeochemical and radiometric study of hydrothermal alteration and metal zoning at the Cinola epithermal gold deposit, Queen Charlotte Islands, British Columbia, *in* Coyner, A.R., and Fahey, P.L., eds., Geology and ore deposits of the American Cordillera: Geological Society of Nevada, Symposium Proceedings, v. 3, p. 1153–1185.

Madeisky, H.E., and Stanley, C.R., 1993, Lithogeochemical exploration of metasomatic zones associated with volcanic-hosted massive sulfide deposits using Pearce element ratio analysis: International Geology Review, v. 35, p. 1121–1148.

Marikos, M.A., Nuelle, L.M., and Seeger, C.M., 1990, Geologic mapping and evaluation of the Pea Ridge iron ore mine (Washington County, Missouri) for rare-earth element and precious metal potential–A progress report, *in* Pratt, W.P., and Sims, P.K., eds., The midcontinent of the United States–Permissive terrane for an Olympic Dam-type deposit?: U.S. Geological Survey, Bulletin 1932, p. 77–81.

Mark, G., 1998, Albitite formation by selective pervasive sodic alteration of tonalite plutons in the Cloncurry district, Queensland: Australian Journal of Earth Sciences, v. 45, p. 765–774.

Mark, G., 1999, Petrogenesis of Mesoproterozoic K-rich granitoids, southern Mt Angelay igneous complex, Cloncurry district, northwest Queensland: Australian Journal of Earth Sciences, v. 46, p. 933–949.

Mark, G., and Foster, D.R.W., 2000, Magmatic–hydrothermal albite–actinolite–apatite-rich rocks from the Cloncurry district, NW Queensland, Australia: Lithos, v. 51, p. 223–245.

Mark, G., Oliver, N.H.S., Williams, P.J., Valenta, R.K., and Crookes, R.A., 2000, The evolution of the Ernest Henry Fe–oxide–(Cu–Au) hydrothermal system, *in* Porter, T.M., ed., Hydrothermal iron oxide copper–gold and related deposits: A global perspective, volume 1: Porter Geoscience Consultancy Publishing, Adelaide, Australia, p. 123–136.

Mark, G., Oliver, N.H.S., and Williams, P.J., 2006, Mineralogical and chemical evolution of the Ernest Henry Fe oxide–Cu–Au ore system, Cloncurry district, northwest Queensland, Australia: Mineralium Deposita, v. 40, p. 769–801.

Marschik, R., and Fontboté, L., 2001a, The Candelaria-Punta del Cobre iron oxide Cu–Au(–Zn–Ag) deposits, Chile: Economic Geology, v. 96, p. 1799–1826.

Marschik, R., and Fontboté, L., 2001b, The Punta del Cobre Formation, Punta del Cobre–Candelaria area, northern Chile: Journal of South American Earth Sciences, v. 14, p. 401–433.

Marschik, R., and Söllner, F., 2006, Early Cretaceous U–Pb zircon ages for the Copiapó plutonic complex and implications for the IOCG mineralization at Candelaria, Atacama Region, Chile: Mineralium Deposita, v. 41, p. 785–801.

Marschik, R., Chiaradia, M., and Fontboté, L., 2003, Implications of Pb isotope signatures of rocks and iron oxide Cu–Au ores in the Candelaria-Punta del Cobre district, Chile: Mineralium Deposita, v. 38, p. 900–912.

Marshall, L.J., and Oliver, N.H.S., 2008, Constraints on hydrothermal fluids pathways within Mary Kathleen Group stratigraphy of the Cloncurry iron-oxide–copper–gold district, Australia: Precambrian Research, v. 163, p. 151–188.

Mathur, R., Marschik, R., Ruiz, J., Munizaga, F., Leveille, R.A., and Martin, W., 2002, Age of mineralization of the Candelaria Fe oxide Cu–Au deposit and the origin of the Chilean Iron Belt, based on Re–Os isotopes: Economic Geology, v. 97, p. 59–71.

Mattinson, J.M., 2005, Zircon U–Pb chemical abrasion ("CA-TIMS") method: Combined annealing and multi-step partial dissolution analysis for improved precision and accuracy of zircon ages: Chemical Geology, v. 220, p. 47–66.

May, L.H., 2007, Petrography of the Mile Lake breccia, Great Bear magmatic zone, N.W.T: Unpublished B.Sc. thesis, Brandon University, 77 p.

McKay, A.D., and Miezitis, Y., 2001, Australia's uranium resources, geology and development of deposits: ASGO – Geoscience Australia, Mineral Report 1, 184 p.

Meinert, L.D., 1992, Skarns and skarn deposits: Geoscience Canada, v. 19, p. 145–162.

Meinert, L.D., Dipple, G.M., and Nicolescu, S., 2005, World skarn deposits: Economic Geology 100th Anniversary Volume, p. 299–336.

Migdisov, A.A., Williams-Jones, A.E., and Wagner, T., 2009, An experimental study of the solubility and speciation of the rare earth elements (III) in fluoride- and chloride-bearing aqueous solutions at temperatures up to 300°C: Geochimica et Cosmochimica Acta, v. 73, p. 7087–7109.

Migdisov, A.A., Williams-Jones, A.E., van Hinsberg, V., and Salvi, S., 2011, An experimental study of the solubility of baddeleyite (ZrO_2) in fluoride-bearing solutions at elevated temperature: Geochimica et Cosmochimica Acta, v. 75, p. 7426–7434.

Miller, R.G., 1982, The geochronology of uranium in the Great Bear Batholith complex, Northwest Territories: Canadian Journal of Earth Sciences, v. 19, p. 1428–1448.

Monteiro, L.V.S., Xavier, R.P., Carvalho, E.R., Hitzman, M.W., Johnson, C.A., Souza Filho, C.R., and Torresi, I., 2008a, Space and temporal zoning of hydrothermal alteration and mineralization in the Sossego iron oxide–copper–gold deposit, Carajás Mineral Province, Brazil: Paragenesis and stable isotope constraints: Mineralium Deposita, v. 43, p. 129–159.

Monteiro, L.V.S., Xavier, R.P., Hitzman, M.W., Juliani, C., Souza Filho, C.R., and Carvalho, E.R., 2008b, Mineral chemistry of ore and hydrothermal alteration at the Sossego iron oxide–copper–gold deposit, Carajás Mineral Province, Brazil: Ore Geology Reviews, v. 34, p. 317–336.

Montreuil, J.F., Pelleter, E., van Breemen, O., Davis, W., Kerswill, J., Behnia, P., and Corriveau, L., 2009, IOCG environments in the Great Bear magmatic zone, *in* Jackson, V.A., and Palmer, E., eds., 37th Annual Yellowknife Geoscience Forum Abstracts: NWT Geoscience Office, Yellowknife, YKGSF Abstracts Volume, p. 83.

Montreuil, J.-F., Corriveau, L., and Long, B., 2012, Porosity in albitites and the development of albitite-hosted U deposits: insights from x-ray computed tomography: CT Scan workshop, Development on non-medical environment, Québec, INRS.

Morris, A., 1977, Geology of parts of the FAB option (FAB, MAC, RON, TED claims), Rae Lakeare, N.W.T., Claim Sheet 86-C-3; Ryowa-Rayrock Joint Venture. Department of Indian and Northern Affairs, Document 080803.

Müller, D., Rock, N.M.S., and Groves, D.I., 1992, Geochemical discrimination between shoshonitic and potassic rocks in different tectonic settings: A pilot study: Mineralogy and Petrology, v. 46, p. 259–289.

Müller, D., Heithersay, P.S., and Groves, 1994, The shoshonite porphyry Cu–Au association in the Goonumbla district, N.S.W., Australia: Mineralogy and Petrology, v. 51, p. 299–321.

Mulligan, D.L., 1995, Proterozoic iron oxide and As–Co–Bi–Cu vein mineralization at the NICO property, N.W.T.: Unpublished B.Sc. thesis, London, Canada, University of Western Ontario, 86 p.

Mumin, A.H., 1997. A qualifying report on the geology, diamond drilling and mineralization of the NICO 1-12 claims, Marian River area, Mackenzie (south) district, Northwest Territories, Canada: NWT Geoscience Office, NORMIN Assessment Report 084202, 57 p.

Mumin, A.H., and Camier, W.J., 2000, Proterozoic Fe-oxide hosted polymetallic mineralization associated with the Marian River Batholith, southern Great Bear magmatic zone, Northwest Territories: Geological Association of Canada–Mineralogical Association of Canada, Abstracts with Program.

Mumin, A.H., Goad, R.E., and Mulligan, D.L., 1996, A report on the geology of the Treasure (F49508), Island 1 (F51395), Island 2 (F51396), Island 3 (F51397), and Island 4 (F49511) claims, Marian River area, Mackenzie (south) district, Northwest Territories, Canada: NWT Geoscience Office, NORMIN Assessment Report 083776, 69 p.

Mumin, A.H., Goad, R.E., Neale, K., and Mulligan, D.L., 2000, A summary report on the geology and exploration potential of the JBG of claims, Mazenod Lake area, Mackenzie (south) district, Northwest Territories, Canada: NWT Geoscience Office, NORMIN Assessment Report 084276, 106 p.

Mumin, A.H., Corriveau, L., Somarin, A.K., and Ootes, L., 2007, Iron oxide copper–gold-type polymetallic mineralization in the Contact Lake Belt, Great Bear magmatic zone, Northwest Territories, Canada: Exploration and Mining Geology, v. 16, p. 187–208.

Mumin, A.H., Phillips, A., Katsuragi, C.J,. Mumin, A., and Ivanov, G., 2014, Geotectonic Interpretation of the Echo Bay Stratovolcano Complex, Northern Great Bear magmatic zone, Northwest Territories: NWT Geoscience Office, NWT Open File NWT Open File 2014-4.

Mumin, A.H., Somarin, A.K., Jones, B., Corriveau, L., Ootes, L., and Camier, J., 2010, The IOCG-porphyry-epithermal continuum of deposits types in the Great Bear Magmatic Zone, Northwest Territories, Canada, *in* Corriveau, L., and Mumin, A.H., eds., Exploring for iron oxide copper–gold deposits: Canada and global analogues: Geological Association of Canada, Short Course Notes 20, p. 59–78.

Najorka, J., Gottschalk, M., Franz, G., and Heinrich, W., 1999, Ca-Sr distribution among amphibole, clinopyroxene, and chloride–bearing solutions: American Mineralogist, v. 84, p. 596–606.

Neale, K., and Camier, J.W., 1997, Summary of diamond drill logs and results of the core sampling on the JBG 2 claim, Addendum to: A report on the geology of the JBG 1 (F51391) and JBG 2 (F51392) grid, Marian River area, Mackenzie (south) district, Northwest Territories, Canada: NWT Geoscience Office, NORMIN Assessment Report 084276, 55 p.

Neale, K., Parker, D.S., and Mumin, A.H., 1997, A report on the geology of the JBG 1 (F51391) and JBG 2 (F51392) grid, Marian River area, Mackenzie (south) district, Northwest Territories, Canada: NWT Geoscience Office, NORMIN Assessment Report 084276, 67 p.

Ngwenya, B.T., 1994, Hydrothermal rare earth mineralization in carbonatites in the Tundulu complex, Malawi: Process at the fluid/rock interface: Geochimica et Cosmochimica Acta, v. 58, p. 2061–2072.

Niiranen, T., Mänttäri, I., Poutianen, M., Oliver, N.H.S., and Miller, J.A., 2005, Genesis of Paleoproterozoic iron skarns in the Misi region, northern Finland: Mineralium Deposita, v. 40, p. 192–217.

Niiranen, T., Poutiainen, M., and Mänttäri, I., 2007, Geology, geochemistry, fluid inclusion characteristics, and U–Pb age studies on iron-oxide–Cu–Au deposits in the Kolari region, northern Finland: Ore Geology Reviews, v. 30, p. 75–105.

Nold, J.L., Davidson, P., and Dudley, M.A., 2013, The Pilot Knob magnetite deposit in the Proterozoic St. Francois Mountains Terrane, southeast Missouri, USA: A magmatic and hydrothermal replacement iron deposit: Ore Geology Reviews, v. 53, p. 446–469.

Nold, J.L., Dudleym, M.A., and Davidson, P., 2014, The Southeast Missouri (USA) Proterozoic iron metallogenic province—Types of deposits and genetic relationships to magnetite–apatite and iron oxide–copper–gold deposits: Ore Geology Reviews, v. 57, p. 154–171.

Norberg, N., Neusser, G., Wirth, R., and Harlov, D., 2011, Microstructural evolution during experimental albitization of K-rich alkali feldspar: Contributions to Mineralogy and Petrology, v. 162, p. 531–546.

Normandeau, P.X., and McMartin, I., 2013, Composition of till and bedrock across the Great Bear magmatic zone: field database and analytical results from the GEM IOCG-Great Bear project: Geological Survey of Canada, Open File 7307.

NWT Geoscience Office, 2014, NORMIN – The Northern Minerals Database: NWT Geoscience Office, http://www.nwtgeoscience.ca/normin/.

North, J., 1995, Report on geological reconnaissance, prospecting, lithogeochemical sampling, steam sediment sampling, and interpretation of the Squirrel Lake property, Great Bear magmatic zone, district of Mackenzie, Northwest Territories: NWT Geoscience Office, NORMIN Assessment Report 083647, 198 p.

Ohmoto, H., and Goldhaber, M.B., 1997, Sulfur and carbon isotopes, *in* Barnes, H.L., ed., Geochemistry of Hydrothermal Ore Deposits: Wiley, New York, p. 517–611.

Oliver, N.H.S., Cleverley, J.S., Mark, G., Pollard, P., Fu, B., Marshall, L.J., Rubenach, M.J., Williams, P.J., and Baker, T., 2004, Modeling the role of sodic alteration in the genesis of iron oxide–copper–gold deposits, eastern Mount Isa Block, Australia: Economic Geology, v. 99, p. 1145–1176.

Oliver, N.H.S., Rubenach, M.J., Baker, B.F., Blenkinsop, T.G., Cleverley, J.S., Marshall, L.J., and Ridd, P.J., 2006, Granite-related overpressure and volatile release in the mid crust: Fluidized breccias from the Cloncurry district, Australia: Geofluids, v. 6, p. 346–358.

Oliver, N.H.S., Butera, K.M., Rubenbach, M.J., Marshall, L.J., Cleverley, J.S., Mark, G., Tullemans, F., and Esser, D., 2008, The protracted hydrothermal evolution of the Mount Isa Eastern Succession: A review and tectonic implications: Precambrian Research, v. 163, p. 108–130.

Ondrejka, M., Uher, P., Putiš, M., Broska, I., Bačik, P., Konečny, P., and Schmidt, I., 2012, Two-stage breakdown of monazite by post-magmatic and metamorphic fluids: An example from the Veporic orthogneiss, western Carpathians, Slovakia: Lithos, v. 142–143, p. 245–255.

Ootes L., Davis, W.J., Jackson, V.A., and van Breemen, O., 2015, Chronostratigraphy of the Hottah terrane and Great Bear magmatic zone of Wopmay orogen, Canada, and exploration of a terrane translation model: Canadian Journal of Earth Sciences, doi: 10.1139/cjes-2015-0026.

Ootes, L., Goff, S., Jackson, V.A., Gleeson, S.A., Creaser, R.A., Samson, IMS, Evensen, N., Corriveau, L., and Mumin, A.H., 2010, Timing and thermo-chemical constraints on multi-element mineralization at the Nori/RA Cu–Mo–U prospect, Great Bear magmatic zone, Northwest Territories, Canada: Mineralium Deposita, v. 45, p. 549–566.

Ootes, L., Harris, J., Jackson, V.A., Azar, B., and Corriveau, L., 2013, Uranium-enriched bedrock in the central Wopmay Orogen: Implications for uranium mineralization: Exploration and Mining Geology, v. 21, p. 85–103.

Ootes, L., Jackson, V.A., Landry, J.-Y., Brzozowski, T., and Corriveau, L., 2006, Assay results from the South Wopmay Bedrock Mapping project (2004 – 2005 field seasons): NWT Geoscience Office, NWT Open Report, 2006-002, 28 p.

Ootes, L., Jackson, V.A., and Corriveau, L., 2008, Assay results from the South Wopmay Bedrock Mapping Project (2006 – 2007 field seasons): NWT Geoscience Office, NWT Open Report 2008-008, 13 p.

Oreskes, N., and Einaudi, M.T., 1990, Origin of rare earth element-enriched hematite breccias at the Olympic Dam Cu-U-Au-Ag deposits, Roxby Downs, South Australia: Economic Geology, v. 85, p. 1–28.

Oueity, J., and Clowes, R.M., 2010, Paleoproterozoic subduction in northwestern Canada from near-vertical and wide-angle seismic reflection data: Canadian Journal of Earth Sciences, v. 47, p. 35–52.

Paladin Energy LTD, 2013, Updated Valhalla mineral resource as at September 2010:

http://www.paladinenergy.com.au, accessed June 2013.

Palme, H., and Jones, A., 2003, Solar system abundances of the elements, *in* Holland, H.D., and Turekian, K.K., eds., Treatise on Geochemistry, volume 1: Meteorites, Comets, Planets: Elsevier, Amsterdam, p. 41–61.

Palme, H., and O'Neill, H.St.C., 2003, Cosmochemical estimates of mantle composition, *in* Holland, H.D., and Turekian, K.K., eds., Treatise on Geochemistry, volume 2: The Mantle and Core: Elsevier, Amsterdam, p. 1–38.

Pankhurst, M.J., Schaefer, B.F., Turner, S.P., Argles, T., and Wade, C.E., 2013, The source of A-type magmas in two contrasting settings: U–Pb, Lu–Hf and Re–Os isotopic constraints: Chemical Geology, v. 351, p. 175–194.

Parrish, R.R., Roddick, J.C., Loveridge, W.D., and Sullivan, R.W., 1987, Uranium-lead analytical techniques at the geochronology laboratory, Geological Survey of Canada, *in* Radiogenic Age and Isotopic Studies: Report 1: Geological Survey of Canada, Paper 87-2, p. 3–7.

Pawlowsky-Glahn, V., and Egozcue, J.J., 2006, Compositional data and their analysis: An introduction, *in* Buccianti, A., ed., Compositional data analysis in geosciences: From theory to practice: Geological Society of London Special Publications, v. 264, p. 1–10.

Pearce, J.A., 1982, Trace element characteristics of lavas from destructive plate boundaries, *in* Thorpe, R.S., ed., Andesite: John Wiley and Sons, p. 525–547.

Pearce, J.A., 1996a, A user guide to basalt discrimination diagrams, *in* Wyman, D.A., ed., Trace element geochemistry of volcanic rocks: Application for massive sulfide exploration: Geological Association of Canada, Short Course Note 12, p. 79–113.

Pearce, J.A., 1996b, Sources and settings of granitic rocks: Episodes, v. 19, p. 120–125.

Pearce, J.A., 2008, Geochemical fingerprinting of oceanic basalts with applications to ophiolite classification and the search for Archean oceanic crust: Lithos, v. 100, p. 14–48.

Pearce, J.A., Harris, N.B.W., and Tindle, A.G., 1984, Trace element discrimination diagrams for the tectonic interpretation of granitic rocks: Journal of Petrology, v. 25, p. 956–983.

Pearce, T.H., 1968, A contribution to the theory of variation diagrams: Contributions to Mineralogy and Petrology, v. 19, p. 142–157.

Pearson, K., 1897, Mathematical contributions to the theory of evolution. On a form of spurious correlation which may arise when indices are used in the measurement of organs: Proceedings of the Royal Society, v. 60, p. 489–498.

Peccerillo, R., and Taylor, S.R., 1976, Geochemistry of Eocene calc-alkaline volcanic rocks from the Kastamonu area, northern Turkey: Contributions to Mineralogy and Petrology, v. 58, p. 63–81.

Pelleter, E., 2007, Géologie, géochimie et géochronologie du gisement aurifère de Tamlalt-Menhouhou (Haut-Atlas oriental): Unpublished Ph.D. thesis, Centre de Recherches Pétrographiques et Géochimiques, France.

Pelleter, E., Gasquet, D., Cheilletz, A., and Mouttaqi, A., 2010, Alteration processes and impacts on regional-scale element mobility and geochronology, Tamlalt-Menhouhou deposit, Morocco, *in* Corriveau, L., and Mumin, A.H., eds., Exploring for iron oxide copper–gold deposits: Canada and global analogues: Geological Association of Canada, Short Course Notes, v. 20, p. 177–185.

Perring, C.S., Pollard, P.J., Dong, G., Nunn, A.J., and Blake, K.L., 2000, The Lightning Creek sill complex, Cloncurry district, northwest Queensland: A source of fluids for Fe oxide Cu–Au mineralization and sodic–calcic alteration: Economic Geology, v. 95, p. 1067–1089.

Pirajno, F., 2009, Hydrothermal Processes and Mineral Systems: Springer, Berlin, Germany, 1250 p.

Polito, P.A., Kyser, T.K., and Stanley, C., 2009, The Proterozoic, albitite-hosted, Valhalla uranium deposit, Queensland, Australia: A description of the alteration assemblage associated with uranium mineralization in diamond drill hole V39: Mineralium Deposita, v. 44, p. 11–40.

Pollard, P.J., 2001, Sodic(–calcic) alteration in Fe–oxide–Cu–Au districts: An origin via unmixing of magmatic H_2O–CO_2–NaCl±$CaCl_2$–KCl fluids: Mineralium Deposita, v. 36, p. 93–100.

Pollard, P.J., 2006, An intrusion-related origin for Cu–Au mineralization in iron oxide–copper–gold (IOCG) provinces: Mineralium Deposita, v. 41, p. 179–187.

Pope, M.C., Grotzinger, J.P., and Schreiber, B.C., 2000, Evaporitic subtidal stromatolites produced by in situ precipitation: textures, facies associations, and temporal significance: Journal of Sedimentary Research, v. 70, p. 1139–1151.

Porter, T.M., 2010, Current understanding of iron oxide associated-alkali altered mineralised systems: Part 1- An overview; Part 2 –A review, *in* Porter, T.M., ed., Hydrothermal iron oxide copper–gold and related deposits: A global perspective, volume 3 - Advances in the understanding of IOCG deposits: Porter Geoscience Consultancy Publishing, Adelaide, Australia, p. 5–106.

Porto da Silveira, C.L., Schorscher, H.D., and Miekeley, N., 1991, The geochemistry of albitization and related uranium mineralization, Espinharas, Paraiba (PB), Brazil: Journal of Geochemical Exploration, v. 40, p. 329–347.

Potter, E.G., Corriveau, L., and Montreuil, J.-F., 2013a, Iron oxide copper–gold ±uranium in the Great Bear magmatic zone: Nature of uranium in IOCG systems: Geological Survey of Canada, Open File 7254.

Potter, E.G., Montreuil, J.-F., Corriveau, L., and De Toni, A., 2013b, Geology and hydrothermal alteration of the Fab Lake region, Northwest Territories: Geological Survey of Canada, Open File 7339, 27 p.

Potter, E.G., Corriveau, L., and Kerswill, J.K., 2013c, Potential for iron oxide–copper–gold and affiliated deposits in the proposed national park area of the East Arm, Northwest Territories: Insights from the Great Bear magmatic zone and global analogs, *in* Wright, D.F., Kjarsgaard, B.A., Ambrose, E.J., and Bonham-Carter, G.F., eds, Mineral and energy resource assessment for the proposed Thaidene Nene

National Park reserve, East Arm of Great Slave Lake, Northwest Territories: Geological Survey of Canada, Open File 7196, Chapter 19.

Potter, E.G., Montreuil, J.-F., Corriveau, L., and Davis, W.J., in press, Linkages between Iron Oxide–Copper–Gold (IOCG) systems and albitite-hosted uranium: A case study of the Southern Breccia albitite uranium showings, Northwest Territories, Canada: Proceedings of IAEA conference.

Putnis, A., 2002, Mineral replacement reactions: From macroscopic observations to microscopic mechanisms: Mineralogical Magazine, v. 66, p. 689–708.

Putnis, A., 2009, Mineral replacement reactions: MSA Reviews in Mineralogy and Geochemistry, v. 70, p. 87–124.

Putnis, A., and Austrheim, H., 2010, Fluid-induced processes: Metasomatism and metamorphism: Geofluids, v. 10, p. 254–269.

Putnis, A., and Austrheim, H., 2012, Mechanisms of metasomatism and metamorphism on the local mineral scale: The role of dissolution-reprecipitation during mineral reequilibration, *in* Harlov, D.E., and Austrheim, H., eds., Metasomatism and the chemical transformation of rock: Lecture Notes in Earth System Sciences, p. 139–167.

Putnis, A., and Putnis, C.V., 2007, The mechanism of reequilibration of solids in the presence of a fluid phase: Journal of Solid State Chemistry, v. 180, p. 1783–1786.

Putnis, C.V., Tsukamoto, K., and Nishimura, Y., 2005, Direct observations of pseudomorphism: Compositional and textural evolution at a fluid-solid interface: American Mineralogist, v. 90, p. 1909–1912.

Putnis, C.V., Geisler, T., Schmid-Beurmann, P., Stephan, T., and Giampaolo, C., 2007, An experimental study of the replacement of leucite by analcime: American Mineralogist, v. 92, p. 19–26.

Puritch, E., Ewert, W., Armstrong, T., Brown, F., Orava, D., Pearson, J.L., Hayes, T., Duggan, T., Holmes, G., Uceda, D., Sumners, W., Mackie, D., Rougier, M., Bocking, K., Mezei, A., and Horne, B., 2012, Technical report and updated mineral reserve estimate and front-end engineering and design (FEED) study on the NICO gold–cobalt–bismuth–copper deposit, Mazenod Lake area, Northwest Territories, Canada: NI 43-101 Technical Report No. 247 prepared for Fortune Minerals Ltd., 307 p.

R Development Core Team, 2011, R: A language and environment for statistical computing: R Foundation for Statistical Computing, Vienna, Austria, ISBN 3-900051-07-0.

Reardon, N.C., 1992, Magmatic-hydrothermal systems and associated magnetite–apatite–actinolite deposits, Echo Bay, Northwest Territories: Unpublished M.Sc. thesis, Ottawa, Canada, University of Ottawa, 154 p.

Reed, M., Rusk, B., and Palandri, J., 2013, The Butte magmatic-hydrothermal system: one fluid yields all alteration and veins: Economic Geology, v. 108, p. 1379–1396.

Reichenbach, I.G., 1991, The Bell Island Bay Group, remnant of an Early Proterozoic ensialic marginal basin in Wopmay orogen, District of Mackenzie: Geological Survey of Canada, Paper 88-28, 43 p.

Reiger, A.A., Marschik, R., and Díaz, M., 2010, The Mantoverde district, northern Chile: An example of distal portions of zoned IOCG systems, *in* Porter, T.M., ed., Hydrothermal iron oxide copper–gold and related deposits: A global perspective, volume 3 - Advances in the understanding of IOCG deposits: Porter Geoscience Consultancy Publishing, Adelaide, Australia, p. 273–284.

Reiger, A.A., Marschik, R., and Díaz, M., 2012, The evolution of the hydrothermal IOCG system in the Mantoverde district, northern Chile: new evidence from microthermometry and stable isotope geochemistry: Mineralium Deposita, v. 47, p. 359–369.

Requia, K., Stein, H., Fontboté, L., and Chiaradia, M., 2003, Re–Os and Pb–Pb geochronology of the Archean Salobo iron oxide copper–gold deposit, Carajás mineral province, northern Brazil: Mineralium Deposita, v. 38 p. 727–738.

Reynolds, L., 2000, Geology of the Olympic Dam Cu–U–Au–Ag–REE deposit, *in* Porter, T.M., ed., Hydrothermal iron oxide copper–gold and related deposits: A global perspective, volume 1: Porter Geoscience Consultancy Publishing, Adelaide, Australia, p. 93–104.

Richards, J.P., and Mumin, A.H., 2013, Magmatic-hydrothermal processes within an evolving Earth: Iron oxide–copper–gold and porphyry Cu ± Mo ± Au deposits: Geology, v. 41, p. 767–770.

Robinson, G., 2013, Potassium metasomatism at the polymetallic NICO deposit, Northwest Territories, Canada Unpublished M.Sc. thesis, London, Canada, University of Western Ontario, 268 p.

Roddick, J.C., 1987, Generalized numerical error analysis with applications to geochronology and thermodynamics: Geochimica et Cosmochimica Acta, v. 51, p. 2129–2135.

Romer, R.L., Martinsson, O., and Perdahl, J.A., 1994, Geochronology of the Kiruna iron ores and hydrothermal alterations: Economic Geology, v. 89, p. 1249–1261.

Rubenach, M., 2013, Structural controls of metasomatism on a regional scale, *in* Blondel, P., Reitner, J., Stüwe, K., Trauth, M.H., and Yuen, D., eds., Lecture notes in Earth system sciences: Springer, p. 93–140.

Rudnick, R.L., and Gao, S., 2007, Composition of the continental crust, *in* Rudnick, R.L., Holland, H.D., and Turekian, K.K., eds., Treatise on Geochemistry, volume 3, The Crust: Elsevier, Amsterdam, p. 1–64.

Ruhlmann, F., Raynal, M., and Lavoie, S., 1986, Un exemple de metasomatisme alcalin albite uranium dans le bassin des Monts Otish Québec: Canadian Journal of Earth Sciences, v. 23, p. 1742–1752.

Rusk, B., Emsbo, P., Xavier, R.P., Corriveau, L., Oliver, N., and Zhang, D., 2015, A comparison of fluid origins and compositions in iron oxide-copper-gold and porphyry-Cu (Mo-Au) deposits: Australasian Institute of Mining and Metallurgy, PACRIM 2015 Congress, Proceedings, p. 271–280.

Rusk, B., Oliver, N., Blenkinsop, T., Zhang, D., Williams, P.J., Cleverley, J., and Habermann, P., 2010, Physical and Chemical Characteristics of the Ernest Henry Iron Oxide Copper Gold Deposit, Australia; Implications for IOCG Genesis, *in* Porter, T.M., ed., Hydrothermal Iron Oxide Copper-Gold and Related Deposits: A Global Perspective: PGC Publishing, Adelaide, v. 3, p. 201–218.

Ruzicka, V., and Thorpe, R.I., 1995, Arsenide vein silver, uranium, *in* Eckstrand, O.R., Sinclair, W.D., and Thorpe, R.I., eds., Geology of Canadian mineral deposits types: Geological Survey of Canada, Geology of Canada, No. 8, p. 287–305.

Ruzicka, V., and Thorpe, R.I., 1996, Gîtes filoniens d'argent et d'uranium à arséniures, *in* Eckstrand, O.R., Sinclair, W.D., and Thorpe, R.I., eds., Géologie des types de gîtes minéraux du Canada: Geological Survey of Canada, Geology of Canada, No. 8, p. 319–338.

Sahlström, F., 2012, Ore petrography and geochemistry of some REE-bearing Fe-oxide assemblages from the Idkerberget deposit, Bergslagen, Sweden: Unpublished B.Sc. thesis, Uppsala, Sweden, Uppsala Universitet, 38 p.

Saint Blanquat, M., Tikoff, B., Teyssier, C., and Vigneresse, J.L., 1998, Transpressional kinematics and magmatic arcs, *in* Holdsworth, R.E., Strachan, R.A., and Dewzy, J.E., eds., Continental transpressional and transtensional tectonics: Geological Society, London, Special Publications 135, p. 327–340.

Salvi, S., Fontan, F., Monchoux, P., Williams-Jones, A.E., and Moine, B., 2000, Hydrothermal mobilization of high field strength elements in alkaline igneous systems: Evidence from the Tamazeght Complex (Morocco): Economic Geology, v. 95, p. 559–576.

Schmid, R., Fettes, D., Harte, B., Davis, E., and Desmons, J., 2007, How to name a metamorphic rock: Recommendations by the IUGS subcommission on the systematics of metamorphic rocks, Web version 01/02/07, www.bgs.ac.uk/scmr/home.html.

Seedorff, E., Barton, M.D., Stavast, W.J.A., and Maher, D.J., 2008, Root zones of porphyry systems: Extending the porphyry model to depth: Economic Geology, v. 103, p. 939–956.

Shegelski, R.J., 1973, Geology and mineralogy of the Terra silver mine, Camsell River, N.W.T: Unpublished M.Sc. thesis, Toronto, Canada, University of Toronto, 169 p.

Shepley, M., 1999, The evidence for detachment fault breccias in the southern Great Bear magmatic zone, NWT: Unpublished H.B.Sc. thesis, London, Canada, University of Western Ontario, 42 p.

Shives, R.B.K., Charbonneau, B.W., and Ford, K.L., 2000, The detection of potassic alteration by gamma-ray spectrometry – Recognition of alteration related to mineralization: Geophysics, v. 65, p. 2001–2011.

Sibson, R.H., 1986, Brecciation processes in fault zones: Inferences from earthquake rupturing: Pure Applied Geophysics, v. 124, p. 159–174.

Sidor, M., 2000, The origin of the black rock alteration overprinting iron-rich sediments and its genetic relationship to disseminated polymetallic sulfide ores, Lou Lake, Northwest Territories, Canada: Unpublished M.Sc. thesis, London, Canada, University Western Ontario, 190 p.

Sillitoe, R.H., 2003, Iron oxide–copper–gold deposits: An Andean view: Mineralium Deposita, v. 38, p. 787–812.

Skanderberg, B.N., 2001, A synopsis of iron oxide ± Cu ± Au ± P ± REE deposits with emphasis on the geology, metallogenesis, and exploration potential of the Great Bear magmatic zone, Northwest Territories, Canada: Unpublished M.Sc. thesis, Grahamstown, South Africa, Rhodes University, 87 p.

Skirrow, R.G., 2000, Gold–copper–bismuth deposits of the Tennant Creek district, Australia: A reappraisal of diverse high-grade systems, *in* Porter, T.M., ed., Hydrothermal iron oxide copper–gold and related deposits: A global perspective, volume 1: Porter Geoscience Consultancy Publishing, Adelaide, Australia, p. 149–160.

Skirrow, R.G., 2010, "Hematite-group" IOCG±U ore systems: tectonic settings, hydrothermal characteristics and Cu–Au and U mineralizing processes, *in* Corriveau, L., and Mumin, A.H., eds., Exploring for iron oxide copper–gold deposits: Canada and global analogues: Geological Association of Canada, Short Course Notes 20, p. 37–56.

Skirrow, R.G., Bastrakov, E., Barovich, K., Fraser, G., Creaser, R., Fanning, C.M., Raymond, O.L., and Davidson, G., 2007, Timing of iron oxide Cu–Au–(U) hydrothermal activity and Nd isotope constraints on metal sources in the Gawler craton: Economic Geology, v. 102, p. 1397–1426.

Slack, J., 2012, Strata-bound Fe–Co–Cu–Au–Bi–Y–REE deposits of the Idaho Cobalt Belt: multistage hydrothermal mineralization in a magmatic-related iron oxide copper–gold system: Economic Geology, v. 107, p. 1089–1113.

Slack, J., 2013, Descriptive and geoenvironmental model for cobalt–copper–gold deposits in metasedimentary rocks: US Geological Survey Scientific Investigations, Report 2010–5070–G, 218 p., http://dx.doi.org/10.3133/sir20105070g.

Smith, M.P., Gleeson, S.A., and Yardley, B.W.D., 2013, Hydrothermal fluid evolution and metal transport in the Kiruna district, Sweden: Contrasting metal behaviour in aqueous and aqueous–carbonic brines: Geochimica et Cosmochimica Acta, v. 102, p. 89–112.

Smith, R.J., 2002, Geophysics of iron-oxide copper–gold systems, *in* Porter, T.M., ed., Hydrothermal iron oxide copper–gold and related deposits: A global perspective, volume 2: Porter Consultancy Publishing, Adelaide, p. 357–367.

Somarin, A.K., and Mumin, A.H., 2012, The Paleo-Proterozoic high heat production Richardson granite, Great Bear magmatic zone, Northwest Territories, Canada: Source of U for Port Radium?: Resource Geology, v. 62, p. 227–242.

Somarin, A.K., and Mumin, A.H., 2014, P–T composition and evolution of paleofluids in the Paleoproterozoic Mag Hill IOCG system, Contact Lake belt, Northwest Territories, Canada: Mineralium Deposita, v.49, p. 199–215.

Sparkes, G.W., and Kerr, A., 2008, Diverse style of uranium mineralisation in the Central Mineral Belt of Labrador: An overview and preliminary discussion: Newfoundland and Labrador Department of Natural Resources, Geological Survey Report, Paper 08-1, p. 193–227.

Spratt, J.E., Jones, A.G., Jackson, V.A., Collins, L., and Avdeeva, A., 2009, Lithospheric geometry of the Wopmay Orogen from a Slave craton to Bear Province magnetotelluric transect: Journal of Geophysical Research, v. 114, 18 p.

Stanley, C.R., and Madeisky, H.E., 1994, Lithogeochemical exploration for hydrothermal ore deposits using Pearce element ratio analysis, *in* Lentz, D.R., ed., Alteration and alteration processes associated with ore-forming systems: Geological Association of Canada, Short Course Notes, v. 11, p. 193–211.

Stanworth, C.W., and Badham, J.P.N., 1984, Lower Proterozoic red beds, evaporites and secondary sedimentary uranium deposits from the East Arm, Great Slave Lake, Canada: Journal of the Geological Society of London, v. 141, v. 235–242.

Stepanov, A.S., and Hermann, J., 2012, Fractionation of Nb and Ta by biotite and phengite: Implications for the “missing Nb paradox”: Geology, v. 41, p. 303–306.

Stoffregen, R.E., 1987, Genesis of acid-sulfate alteration and Au–Cu–Ag mineralization at Summitville, Colorado: Economic Geology, v. 82, p. 1575–1591.

Strauss, T.A.L., 2003, The geology of the Proterozoic Haveri Au–Cu deposit, southern Finland: Unpublished Ph.D. thesis, Grahamstown, South Africa, Rhodes University, 372 p.

Tallarico, F.H.B., Figueiredo, B.R., Groves, D.I., Kositcin, N., McNaughton, N.J., Fletcher, I.R., and Rego, J., 2005, Geology and SHRIMP U–Pb geochronology of the Igrapé Bahia deposit, Carajás copper–gold belt, Brazil: An Archean (2.57 Ga) example of iron oxide–Cu–Au–(U–REE) mineralization. Economic Geology, v. 100, p. 7–28.

Tallarico, F.H.B., McNaughton, N.J., Groves, D.I., Fletcher, I.R., Figueiredo, B.R., Carvolho, J.B., Rego, J., and Nunes, A.R., 2004, Geological and SHRIMP II U–Pb constraints on the age and origin of the Breves Cu–Au–(W–Bi–Sn) deposit, Carajás district, Brazil: Mineralium Deposita, v. 39, p. 68–86.

Thomas, M., and Olsen, R.A., 1978, Exploration 1977 and 1978 Loo, BW and C mineral claims, Mackenzie mining district, N.W.T: NWT Geoscience Office, NORMIN Assessment Report 080960, 44 p.

Thorkelson, D.J., Mortensen, J.K., Davidson, G.J., Creaser, R.A., Perez, W.A., and Abbott, J.G., 2001, Mesoproterozoic intrusive breccias in Yukon, Canada: The role of hydrothermal systems in reconstructions of North America and Australia: Precambrian Research, v. 111, p. 31–56.

Tikoff, B., and Saint Blanquat, M., 1997, Transpressional shearing and strike-slip partitioning in the Late Cretaceous Sierra Nevada magmatic arc, California: Tectonics, v. 16, p. 442–459.

Tornos, F., Casquet, C., and Relvas, J., 2005, Transpressional tectonics, lower crust decoupling and intrusion of deep mafic sills: A model for the unusual metallogenesis of SW Iberia: Ore Geology Reviews, v. 27, p. 133–163.

Tropper, P., and Manning, C.E., 2007, The solubility of fluorite in H_2O and H_2O–NaCl at pressure and temperature: Chemical Geology, v. 242, p. 299–306.

Turpin, L., Maruéjol, P., and Cuney, M., 1988, U–Pb, Rb–Sr and Sm–Nd chronology of granitic basement, hydrothermal albitites and uranium mineralisation (Lagoa Real, South-Bahia, Brazil): Contributions to Mineralogy and Petrology, v. 98, p. 139–147.

Ullrich, T.D., and Clark, A.H., 1997, Paragenetic sequence of mineralization in the main orebody, Candelaria copper–gold deposit, Chile: Phelps Dodge Exploration Corporation, unpublished internal report 3, 36 p.

U.S. Geological Survey, 2008, Geochemistry of rock samples from the National Geochemical Database: U.S. Geological Survey, Reston, VA.

Vels, B., and Fritsche, R., 1988, Sodium metasomatism in the Kitongo uranium occurrence near Poli, Cameroon: Uranium, v. 4, p. 365–383.

Villeneuve, M.E., Ross, G.M., Thériault, R.J., Miles, W., Parrish, R.R., and Broome, J., 1993, Tectonic subdivision and U–Pb geochronology of the crystalline basement of the Alberta Basin, western Canada: Geological Survey of Canada, Bulletin 447, 93 p., doi:10.4095/77642.

Wagner, R., Rosenberg, C.L., Handy, M.R., Möbus, C., and Albertz, M., 2006, Fracture-driven intrusion and upwelling of a mid-crustal pluton fed from a transpressive shear zone—The Rieserferner pluton (eastern Alps): Geological Society of America Bulletin, v. 118, p. 219–237.

Wang, S., and Williams, P.J., 2001, Geochemistry and origin of Proterozoic skarns at the Mount Elliott Cu–Au(–Co–Ni) deposit, Cloncurry district, NW Queensland, Australia: Mineralium Deposita, v. 36, p. 109–124.

Wanhainen, C., 2005, On the origin and evolution of the paleoproterozoic Aitik Cu–Au–Ag deposit, northern Sweden: Unpublished Ph.D. thesis, Luleå, Sweden, Luleå University of Technology, 151 p.

Wanhainen, C., Broman, C., and Martinsson, O., 2003, The Aitik Cu–Au–Ag deposit in northern Sweden: A product of high salinity fluids: Mineralium Deposita, v. 38, p. 715–726.

Warren, I., Simmons, S.F., and Mauk, J.L., 2007, Whole-rock geochemical techniques for evaluating hydrothermal alteration, mass change, and compositional gradients associated with epithermal Au–Ag mineralization: Economic Geology, v. 102, p. 923–948.

Webb, D.R., 2001, Report on the line cutting, prospecting, and geological mapping and sampling program on the Cobalt 1 to 5 claims, tag numbers F54375, F54513, F54514, F59519, and F59516 respectively, Cameron Bay area, district of Mackenzie, Northwest Territories: Department of Indian and Northern Affairs, Assessment Report, no. 08486, 26 p.

Whalen, J.B., Currie, K.L., and Chappell, B.W., 1987, A-type granites: geochemical characteristics, discrimination and petrogenesis: Contributions to Mineralogy and Petrology, v. 95, p. 407–419.

Whitney, D.L., and Evans, B.W., 2010, Abbreviations for names of rock-forming minerals: American Mineralogist, v. 95, p. 185–187.

Whitten, C.W., and Yancey, R.J., 1990, Characterization of the rare-earth mineralogy at the Pea Ridge deposit, Missouri: United States Department of the Interior, Bureau of Mines, RI-9331, 15 p.

Wilde, A., 2013, Towards a model for albitite-type uranium: Minerals, v. 3, p. 36–48.

Wilde, A., Otto, A., Jory, J., MacRae, C., Pownceby, M., Wilson, N., and Torpy, A., 2013, Geology and mineralogy of uranium deposits from Mount Isa, Australia: Implications for albitite uranium deposit models: Minerals, v. 3, p. 258–283.

Williams, P.J., 1999, Alteration associated with Fe-oxide–Cu–Au deposits, *in* Pollard, P.J., and Williams, P.J., eds., Short course on Fe oxide–copper–gold deposits (the Candelaria-Ernest Henry-Olympic Dam family): Economic Geology Research Unit, James Cook University, Townsville, Australia, Section F.

Williams, P.J., 2010a, Classifying IOCG deposits, *in* Corriveau, L., and Mumin, A.H., eds., Exploring for iron oxide copper–gold deposits: Canada and global analogues: Geological Association of Canada, Short Course Notes 20, p. 13–22.

Williams, P.J., 2010b, “Magnetite-group” IOCGs with special reference to Cloncurry (NW Queensland) and northern Sweden: Settings, alteration, deposit characteristics, fluid sources, and their relationship to apatite-rich iron ores, *in* Corriveau, L., and Mumin, A.H., eds., Exploring for iron-oxide copper–gold deposits: Canada and global analogues: Geological Association of Canada, Short Course Notes 20, p. 23–38.

Williams, P.J., and Skirrow, R.G., 2000, Overview of iron oxide copper–gold deposits in the Curnamona Province and Cloncurry district (eastern Mount Isa Block), Australia, *in* Porter, T.M., ed., Hydrothermal iron oxide copper–gold and related deposits: A global perspective, volume 1: Porter Geoscience Consultancy Publishing, Adelaide, Australia, p. 105–122.

Williams, P.J., Barton, M.D., Fontboté, L., De Haller, A., Johnson, D., Mark, G., Marschick, R., and Oliver, N.H.S., 2005, Iron oxide–copper–gold deposits: Geology, space-time distribution, and possible modes of origin: Economic Geology 100th Anniversary Volume, p. 371–405.

Williams, P.J., Kendrick, M.A., and Xavier, R.P., 2010, Sources of ore fluid components in IOCG deposits, *in* Porter, T.M., ed., Hydrothermal iron oxide copper–gold and related deposits: A global perspective, volume 3 - Advances in the understanding of IOCG deposits: Porter Geoscience Consultancy Publishing, Adelaide, Australia, p. 107–116.

Xavier, R.P., Monteiro, L.V.S., de Souza Filho, C.R., Torresi, I., de Resende Carvalho, E., Dreher, A.M., Wiedenbeck, M., Trumbull, R.B., Pestilho, A.L.S., and Moreto, C.P.N., 2010, The iron oxide copper–gold deposits of the Carajás mineral province, Brazil: An updated and critical review, *in* Porter, T.M., ed., Hydrothermal iron oxide copper–gold and related deposits: A global perspective, volume 3 - Advances in the understanding of IOCG deposits: Porter Geoscience Consultancy Publishing, Adelaide, Australia, p. 285–306.

Yang, C.L., 2008, Progressive albitisation in the "Migmatite Creek" region, Weekeroo Inlier, Curnamona: Unpublished M.Sc. Thesis, Adelaide Australia, University of Adelaide, School of Earth and Environmental Sciences, 142 p.

Yang, X.-F., Fan, H.-R., Santosh, M., Hu, F.-F., and Wang, K.-Y., 2011, Mesoproterozoic carbonatitic magmatism in the Bayan Obo deposit, Inner Mongolia, north China: Constraints for the mechanism of super accumulation of rare earth elements: Ore Geology Reviews, v. 40, p. 122–131.

Zhao, F., 2006, Alkali metasomatism and uranium mineralization, *in* Mao, J., and Bierlein, F.P., eds., Mineral deposit research: Meeting the global challenge: Proceedings of the Eighth Biennial SGA Meeting, p. 343–346.

Zharikov, V.A., Pertsev, F.N., Rusinov, V.L., Callegari, E., and Fettes, D.J., 2007, Metasomatism and metasomatic rocks: Recommendations by the IUGS subcommission on the systematics of metamorphic rocks, Web version 01.02.07, www.bgs.ac.uk/scmr/home.html.

Zhou, D., Chang, T., and Davis, J.C., 1983, Dual extraction of R –mode and Q –mode factor solutions: Mathematical Geology, v. 15, p. 581–606.

Zhu, C., and Sverjensky, A., 1991, Partitioning of F–Cl–OH between minerals and hydrothermal fluids: Geochimica et Cosmochimica Acta, v. 55, p. 1837–1858.

MOBILITÉ DES ÉLÉMENTS ET FORMATION DE GÎTES POLYMÉTALLIQUES AU SEIN DES SYSTÈMES À OXYDES DE FER ET ALTÉRATION EN ÉLÉMENTS ALCALINS, ZONE MAGMATIQUE DU GRAND LAC DE L'OURS, TERRITOIRES DU NORD-OUEST, CANADA

TROISIÈME PARTIE : ANNEXES

ANNEXE - 1 : COMPILATION DES ANALYSES DE STANDARDS FAITES À L'INRS–ETE, ACMELABS ET ALS

Standards analysés à l'INRS-ETE par ICP-AES

Élément		BHVO2							Moyenne	SD	2SD	Précision	Recommandée/ Mesurée	±	Min	Max	Certifiée (INRS)
Total	%	101	101	101	100	101	102	101.0	**101**	0.70	1.4	**1.01**					
Loi	%	0.00															
Al_2O_3	%	13.6	13.4	13.7	13.5	13.4	13.8	13.7	**13.6**	0.16	0.3	**1.02**	13.5	0.2	**13.3**	**13.7**	**13.5**
CaO	%	11.4	11.4	11.3	11.3	11.4	11.4	11.4	**11.4**	0.06	0.1	**1.01**	11.4	0.2	**11.2**	**11.6**	**11.4**
Fe_2O_3T	%	12.3	12.3	12.3	12.0	12.3	12.5	12.4	**12.3**	0.15	0.3	**1.02**	12.3	0.2	**12.1**	**12.5**	**12.3**
K_2O	%	0.51	0.51	0.53	0.51	0.51	0.53	0.52	**0.52**	0.01	0.0	**1.04**	0.52	0.01	**0.5**	**0.5**	**0.52**
MgO	%	7.19	7.30	7.50	7.08	7.30	7.54	7.28	**7.3**	0.16	0.3	**1.04**	7.23	0.12	**7.1**	**7.4**	**7.23**
MnO	%	0.16	0.16	0.16	0.16	0.16	0.17	0.17	**0.16**	0.00	0.0	**1.05**	0.167	0.005	**0.2**	**0.2**	**0.167**
Na_2O	%	2.29	2.30	2.26	2.20	2.30	2.22	2.25	**2.26**	0.04	0.1	**1.03**	2.22	0.08	**2.1**	**2.3**	**2.22**
P_2O_5	%	0.27	0.25	0.27	0.26	0.25	0.29	0.26	**0.27**	0.01	0.0	**1.10**	0.27	0.02	**0.3**	**0.3**	**0.27**
SiO_2	%	50.0	50.0	50.0	49.9	50.0	50.7	50.2	**50.1**	0.26	0.5	**1.01**	49.9	0.6	**49.3**	**50.5**	**49.9**
S	%	0.071	0.082	0.090	0.087	0.082	0.078	< 0.009	**0.08**	0.01	0.0	**1.17**					
TiO_2	%	2.66	2.72	2.72	2.67	2.72	2.80	2.7	**2.72**	0.04	0.1	**1.03**	2.73	0.04	**2.7**	**2.8**	**2.73**
As	ppm	< 30	< 30	< 30	< 40	< 30	< 20	< 108.4									
Ba	ppm	129	128	129	130	128	134	131	**130**	2.02	4.0	**1.03**	130	13	**117.0**	**143.0**	**130**
Cd	ppm	6.6	6.0	6.0	< 6	6.0	5.0	< 9	**6**	0.57	1.1	**1.20**					
Co	ppm	46					46	39	**44**	3.84	7.7	**1.18**	45	3	**42.0**	**48.0**	**45**
Cr	ppm	295	280	279	280	280	301	285	**286**	8.86	17.7	**1.06**	280	19	**261.0**	**299.0**	**280**
Cu	ppm	128	129	129	133	129	129	119	**128**	4.40	8.8	**1.07**	127	7	**120.0**	**134.0**	**127**
Ni	ppm	116	126	117	113	126	117	117	**119**	5.05	10.1	**1.08**	119	7	**112.0**	**126.0**	**119**
Sc	ppm	32	33	32	31	33	33	32	**32**	0.74	1.5	**1.04**	32	1	**31.0**	**33.0**	**32**
Sr	ppm	390	399	388	390	399	397	384	**392**	5.86	11.7	**1.03**	389	23	**366.0**	**412.0**	**389**
V	ppm	317	310	318	316	310	320	316	**315**	3.93	7.9	**1.02**	317	11	**306.0**	**328.0**	**317**
Y	ppm	26	27	27	26	27	29		**27**	0.82	1.6	**1.06**	26	2	**24.0**	**28.0**	**26**
Zn	ppm	104	101	98	96	101	101	105.7	**101**	3.15	6.3	**1.06**	103	6	**97.0**	**109.0**	**103**
Zr	ppm	174	162	171	171	162	181		**170**	7.30	14.6	**1.08**	172	11	**161.0**	**183.0**	**172**
Mo	ppm							< 27.1									
Dilution		686	1359	1359		1359	686	904									

Élément		BCR2									Moyenne	SD	2SD	Précision	Recommandée/ Mesurée	±	Min	Max	Certifiée (INRS)
Total	%	100	99	100	100	99	100	99.8	100.0	102.1	**100**	0.81	1.6	**1.01**					
Loi	%	0.00						0.0		0.0									
Al_2O_3	%	13.5	13.2	13.6	13.6	13.2	13.4	13.5	13.4	13.08	**13.4**	0.19	0.4	**1.02**	13.5	0.2	**13.3**	**13.7**	**13.5**
CaO	%	7.11	7.1	7.0	7.1	7.1	6.98	7.01	7.10	7.62	**7.12**	0.18	0.4	**1.04**	7.12	0.11	**7.0**	**7.2**	**7.12**
Fe_2O_3T	%	13.8	13.6	13.7	13.6	13.6	13.9	13.9	13.8	14.6	**13.8**	0.30	0.6	**1.03**	13.8	0.2	**13.6**	**14.0**	**13.8**
K_2O	%	1.77	1.79	1.85	1.81	1.79	1.80	1.75	1.80	1.79	**1.79**	0.03	0.1	**1.02**	1.79	0.05	**1.7**	**1.8**	**1.79**
MgO	%	3.62	3.61	3.73	3.56	3.61	3.73	3.40	3.55	3.83	**3.63**	0.12	0.2	**1.05**	3.59	0.05	**3.5**	**3.6**	**3.59**
MnO	%	0.19	0.19	0.19	0.19	0.19	0.19	0.19	0.20	0.21	**0.19**	0.01	0.0	**1.05**					**0.196**
Na_2O	%	3.19	3.23	3.20	3.16	3.23	3.12	3.10	3.16	3.14	**3.17**	0.04	0.1	**1.02**	3.16	0.11	**3.1**	**3.3**	**3.16**
P_2O_5	%	0.37	0.33	0.35	0.35	0.33	0.38	0.35	0.35	0.34	**0.35**	0.02	0.0	**1.07**	0.35	0.02	**0.3**	**0.4**	**0.35**

Élément		BCR2									Moyenne	SD	2SD	Précision	Recommandée/ Mesurée	±	Min	Max	Certifiée (INRS)
SiO_2	%	54.4	53.9	54.2	53.9	53.9	54.1	54.2	54.1	55.1	**54**	0.36	0.7	**1.01**	54.1	0.8	**53.3**	**54.9**	**54.1**
S	%	0.058	0.066	0.068	0.070	0.066	0.060	0.04	.015	0.04	**0.05**	0.02	0.0	**1.63**					
TiO_2	%	2.20	2.22	2.24	2.23	2.22	2.26	2.18	2.3	2.37	**2.24**	0.05	0.1	**1.04**	2.26	0.05	**2.2**	**2.3**	**2.26**
As	ppm	< 30	< 23	< 23	< 40	< 23	< 20	< 40	< 101.9	< 30									
Ba	ppm	673	658	670	682	658	680	679	683	670	**673**	8.87	17.7	**1.02**	683	28	**655.0**	**711.0**	**683**
Cd	ppm	7.5	7.8	6.0	< 6	7.8	5.7	32	< 8.5	35	**15**	11.97	23.9	**4.46**					
Co	ppm	41					42	42	31	35	**38**	4.55	9.1	**1.20**	37	3	**34.0**	**40.0**	**37**
Cr	ppm	16	15	16	17	15	14	48	< 17	16	**20**	10.81	21.6	**2.47**	18	2	**16.0**	**20.0**	**18**
Cu	ppm	13	17	17	18	17	8	21	17	< 20	**16**	3.69	7.4	**1.44**	19	2	**17.0**	**21.0**	**19**
Ni	ppm	13	20	< 7	< 12	20	11	37	< 42.5	< 7	**20**	9.09	18.2	**2.05**					
Sc	ppm	34	34	34	33	34	33	34	33	33	**33**	0.42	0.8	**1.02**	33	2	**31.0**	**35.0**	**33**
Sr	ppm	338	340	335	342	340	335	331	330	341	**337**	4.28	8.6	**1.02**	346	14	**332.0**	**360.0**	**346**
V	ppm	415	408	413	412	408	408	412	414	419	**412**	3.51	7.0	**1.01**	416	14	**402.0**	**430.0**	**416**
Y	ppm	36	38	38	37	38	39				**38**	0.79	1.6	**1.05**	37	2	**35.0**	**39.0**	**37**
Zn	ppm	134	128	129	129	128	138	127	144	116	**130**	7.41	14.8	**1.09**	127	9	**118.0**	**136.0**	**127**
Zr	ppm	192	168	190	194	168	195				**184**	11.70	23.4	**1.14**	188	16	**172.0**	**204.0**	**188**
Mo	ppm							228	251	220	**233**	12.97	25.9	**1.09**	248	17	**231.0**	**265.0**	
Dilution		806	1159	1159		1159	806	942	849	931									

Élément		W2									Moyenne	SD	2SD	Précision	Recommandée/ Mesurée	±	Min	Max	Certifiée (INRS)
Élément																			
Total	%	101	100	100	102	100	101	100.4	100.1	102.4	**101**	0.80	1.6	**1.01**					
Loi	%	0.00						0.0		0.0									
Al_2O_3	%	15.6	15.4	15.5	15.8	15.4	15.4	15.5	15.4	15.7	**15.5**	0.14	0.3	**1.01**	15.43	**0.2**	**15.3**	**15.6**	**15.5**
CaO	%	10.94	11.0	10.8	11.1	11.0	10.8	10.8	10.9	11.1	**10.9**	0.11	0.2	**1.02**	10.86	**0.078**	**10.8**	**10.9**	**10.86**
Fe_2O_3T	%	10.8	11.0	10.8	10.9	11.0	10.8	10.9	10.8	10.9	**10.9**	0.09	0.2	**1.01**	10.83	**0.21**	**10.6**	**11.0**	**10.83**
K_2O	%	0.63	0.62	0.63	0.63	0.62	0.63	0.61	0.62	0.67	**0.63**	0.01	0.0	**1.04**	0.626	**0.626**	**0.0**	**1.3**	**0.626**
MgO	%	6.37	6.55	6.61	6.44	6.55	6.58	6.13	6.37	6.45	**6.45**	0.14	0.3	**1.03**	6.37	**0.058**	**6.3**	**6.4**	**6.37**
MnO	%	0.16	0.16	0.16	0.16	0.16	0.16	0.16	0.17	0.17	**0.16**	0.00	0.0	**1.03**	0.167	**0.004**	**0.2**	**0.2**	**0.167**
Na_2O	%	2.32	2.33	2.24	2.25	2.33	2.19	2.20	2.22	2.31	**2.26**	0.05	0.1	**1.04**	2.2	**0.04**	**2.2**	**2.2**	**2.20**
P_2O_5	%	0.12	0.11	0.12	0.12	0.11	0.13	0.12	0.12	0.11	**0.12**	0.01	0.0	**1.09**	0.14	**0.12**	**0.0**	**0.3**	**0.14**
SiO_2	%	52.8	54.3	52.9	53.7	54.3	52.7	52.7	52.4	54.0	**53**	0.72	1.4	**1.02**	52.68	**0.29**	**52.4**	**53.0**	**52.68**
S	%	0.064	0.079	0.087	0.085	0.079	0.065	0.03	< 0.0077	0.03	**0.07**	0.02	0.0	**1.63**					
TiO_2	%	1.06	1.11	1.09	1.10	1.11	1.09	1.03	1.1	1.09	**1.08**	0.03	0.1	**1.04**	1.06	**0.01**	**1.05**	**1.07**	**1.06**
As	ppm	< 30	< 40	< 40	< 40	< 40	< 20	< 40	< 92.4	< 30									**1.2**
Ba	ppm	171	172	170	176	172	173	176	169	168	**172**	2.65	5.3	**1.02**	170	**11**	**159.0**	**181.0**	**170**
Cd	ppm	5.8	5.0	7.0	< 6	5.0	4.1	28.5	< 7.7	28.19	**12**	10.41	20.8	**5.05**					**#N/A**
Co	ppm	44					44	43	38	40	**42**	2.35	4.7	**1.09**	42	**2.1**	**39.9**	**44.1**	**43**
Cr	ppm	92	93	95	98	93	90	92	90	80	**92**	4.49	9.0	**1.08**	92	**4.4**	**87.6**	**96.4**	**92**
Cu	ppm	103	112	106	116	112	101	109	97	103	**106**	5.78	11.6	**1.09**	110	**4.9**	**105.1**	**114.9**	**110**
Ni	ppm	71	88	73	73	88	70	71	72	57	**74**	9.00	18.0	**1.21**	70	**2.5**	**67.5**	**72.5**	**70**

Élément		W2									Moyenne	SD	2SD	Précision	Recommandée/ Mesurée	±	Min	Max	Certifiée (INRS)
Sc	ppm	36	38	37	36	38	36	36	36	35	**36**	0.94	1.9	**1.04**	**36**	**1.1**	**34.9**	**37.1**	**36**
Sr	ppm	196	200	190	200	200	195	192	187	196	**195**	4.38	8.8	**1.04**	**190**	**3**	**187.0**	**193.0**	**190**
V	ppm	262	270	260	265	270	259	265	263	261	**264**	3.83	7.7	**1.02**	**260**	**12**	**248.0**	**272.0**	**260**
Y	ppm	22	22	22	22	22	23				**22**	0.44	0.9	**1.03**	**23**	**1.6**	**21.4**	**24.6**	**23**
Zn	ppm	79	80	72	73	80	80	57	79	65	**74**	7.78	15.6	**1.18**	**80**	**2**	**78.0**	**82.0**	**80**
Zr	ppm	97	102	104	116	102	100				**103**	5.91	11.8	**1.09**	**100**	**2**	**98.0**	**102.0**	**100**
Mo	ppm							< 9	< 23.1	10	**10**	0.00	0.0						
Dilution		737	1961	1961		1961	737	986	770	1031									

Élément		Sarm1							Moyenne	SD	2SD	Précision	Certifiée/Mesurée	95% confiance (min)	95% confiance (max)	Certifiée (INRS)
Total	%	96	99	99	98	99	97	98.5	**98**	1.25	2.5	**1.02**				
Loi	%	0.00														
Al_2O_3	%	11.8	11.7	12.1	11.9	11.7	11.8	12.0	**11.9**	0.16	0.3	**1.02**	**12.1**			**12.1**
CaO	%	0.77	0.77	0.77	0.77	0.77	0.76	0.79	**0.77**	0.01	0.0	**1.02**	**0.78**			**0.78**
Fe_2O_3T	%	1.93	1.92	1.95	1.89	1.92	1.94	1.95	**1.93**	0.02	0.0	**1.02**	**2.00**			**2.00**
K_2O	%	4.95	4.82	4.93	4.76	4.82	5.12	4.99	**4.91**	0.12	0.2	**1.05**	**4.99**			**4.99**
MgO	%	0.03	0.02	0.03	0.03	0.02	0.03	< 0.045	**0.03**	0.01	0.0	**1.45**	**0.06**			**0.06**
MnO	%	0.016	0.016	0.016	0.015	0.016	0.016	0.02	**0.02**	0.00	0.0	**1.05**	**0.020**			**0.020**
Na_2O	%	3.36	3.37	3.35	3.22	3.37	3.21	3.31	**3.31**	0.07	0.1	**1.04**	**3.36**			**3.36**
P_2O_5	%	< 0,01	< 0.0024	0.005	0.004	< 0.0024	0.003	< 0.056	**0.004**	0.00	0.0	**1.44**				**0.01**
SiO_2	%	73.2	76.2	76.2	74.9	76.2	73.8	75.2	**75.1**	1.23	2.5	**1.03**	**75.7**			**75.7**
S	%	0.014	0.020	0.023	0.023	0.020	0.011	< 0.011	**0.02**	0.00	0.0	**1.64**				
TiO_2	%	0.09	0.09	0.09	0.09	0.09	0.09	0.1	**0.09**	0.00	0.0	**1.03**				
As	ppm	< 30	< 40	< 40	< 40	< 40	< 20	< 135.4								**19.3**
Ba	ppm	112	113	114	114	113	114	114.5	**114**	0.88	1.8	**1.01**	**120**			**120**
Cd	ppm	< 4	< 2.2	< 7	< 6	< 2.2	< 1,1	< 11.3								
Co	ppm	< 4					< 3	< 22.6								**0.36**
Cr	ppm	11	14	22	20	14	10	< 22.6	**15**	4.85	9.7	**1.84**	**12**			**12**
Cu	ppm	47	14	12	13	14	46	12	**23**	16.18	32.4	**4.92**	**12**			**12**
Ni	ppm	72	< 11	< 13	< 12	< 11	71	85	**76**	7.88	15.8	**1.21**				**8**
Sc	ppm	< 1	< 1.6	< 2.2	< 1.5	< 1.6	0.4	1.3	**1**	0.60	1.2	**4.77**				**0.9**
Sr	ppm	10	10	10	10	10	10	11.1	**10**	0.39	0.8	**1.07**	**10**			**10**
V	ppm	< 3	< 7	< 4	< 2	< 7	< 3	< 22.6					**2**			**2**
Y	ppm	139	143	144	140	143	149		**143**	3.51	7.0	**1.05**	**143**	**120**	**159**	**143**
Zn	ppm	48	47	37	35	47	50	54.3	**45**	7.01	14.0	**1.33**	**50**			**50**
Zr	ppm	285	280	300	294	280	294		**289**	8.38	16.8	**1.06**	**300**			**300**
Mo	ppm							< 33.8								
Dilution		883	2224	2224		2224	883	1128								

Élément		Sarm5							Moyenne	SD	2SD	Précision	Certifiée/Mesurée	Certifiée (INRS)
Total	%	98	98	98	97	98	99	102.4	**99**	1.78	3.6	**1.03**		
Loi	%	0												
Al_2O_3	%	4.16	4.01	4.13	4.15	4.01	4.16	4.2	**4.12**	0.08	0.2	**1.04**	**4.18**	**4.18**
CaO	%	2.59	2.58	2.54	2.58	2.58	2.56	2.62	**2.58**	0.02	0.0	**1.02**	**2.66**	**2.66**
Fe_2O_3T	%	12.7	12.5	12.5	12.4	12.5	12.9	12.8	**12.6**	0.16	0.3	**1.02**	**12.7**	**12.7**
K_2O	%	0.09	0.09	0.09	0.10	0.09	0.09	0.11	**0.09**	0.01	0.0	**1.20**	**0.09**	**0.09**
MgO	%	24.0	24.4	25.2	24.1	24.4	24.8	26.6	**24.8**	0.90	1.8	**1.07**	**25.3**	**25.3**
MnO	%	0.21	0.21	0.21	0.20	0.21	0.22	0.22	**0.21**	0.01	0.0	**1.05**	**0.220**	**0.220**
Na_2O	%	0.33	0.36	0.37	0.35	0.36	0.35	0.36	**0.35**	0.01	0.0	**1.06**	**0.37**	**0.37**
P_2O_5	%	0.010	0.011	0.013	0.015	0.011	0.011	< 0.04	**0.01**	0.00	0.0	**1.34**	**0.02**	**0.02**
SiO_2	%	51.2	50.9	50.1	50.7	50.9	51.4	51.5	**51.0**	0.49	1.0	**1.02**	**51.1**	**51.1**
S	%	0.022	0.027	0.026	0.025	0.027	0.020	.041	**0.03**	0.01	0.0	**1.63**		
TiO_2	%	0.18	0.18	0.18	0.18	0.18	0.19	0.19	**0.18**	0.00	0.0	**1.03**	**0.20**	**0.20**
As	ppm	< 30	< 30	< 30	< 40	< 30	< 20	< 95.7					**0.3**	**0.3**
Ba	ppm	34	33	33	34	33	34	34	**34**	0.64	1.3	**1.04**	**46**	**46**
Cd	ppm	7.5	6.0	7.0	< 6	6.0	5.2	< 8	**6.3**	0.92	1.8	**1.31**		
Co	ppm	95					98	101	**98**	2.90	5.8	**1.06**	**110**	**110**
Cr	ppm	24954	23200	22700	22936	23200	25071	23953	**23716**	966	1932	**1.08**		**23950**
Cu	ppm	58	21	21	18	21	57	15	**30**	19	38	**3.72**	**18**	**18**
Ni	ppm	524	560	560	563	560	536	658	**566**	43	87	**1.15**	**555**	**555**
Sc	ppm	29	28	28	27	28	29	29	**28**	0.46	0.9	**1.03**		**27.3**
Sr	ppm	33	33	32	33	33	33	34	**33**	0.50	1.0	**1.03**	**32**	**32**
V	ppm	244	240	240	242	240	243	258	**244**	6.50	13.0	**1.05**	**230**	**230**
Y	ppm	< 5	< 3	2	2	< 3	4		**3**	0.90	1.8	**1.98**	**5**	**5**
Zn	ppm	120	117	114	115	117	105	130	**117**	7.18	14.4	**1.12**	**100**	**100**
Zr	ppm	10	9	7	7	9	12		**9**	2.17	4.3	**1.57**		**15**
Mo	ppm							< 23.9						
Dilution		782	1463	1463		1463	782	798						

Standards analysés à l'INRS-ETE par ICP-MS

Élément	BHVO2									Moyenne	SD	2SD	Précision	Recommandée/ Mesurée	±	Min	Max	Certifiée (INRS)
Co	48	44	45	45	44	45				**45**	1.40	2.8	**1.07**	**45**	**3**	**42**	**48**	
As	< 21					< 21												
Rb	9.2	8.4	9.4	9.4	8.4	9.3	9.2	9.3	9.1	**9.1**	0.40	0.8	**1.07**	**9.11**	**1**	**8.11**	**10.11**	**9.11**
Sr	400	397	401	401	397	388				**397**	4.93	9.9	**1.03**	**389**	**23**	**366**	**412**	
Y	27	26	27	27	26	27	26	27	28	**27**	0.59	1.2	**1.03**	**26**	**2**	**24**	**28**	**26**
Zr	176	174	179	179	174	174	170	167	174	**174**	3.89	7.8	**1.03**	**172**	**11**	**161**	**183**	**172**
Nb	18.0	17.5	18.1	18.1	17.5	18.0	18.1	17.2	18.2	**17.9**	0.36	0.7	**1.03**	**18**	**2**	**16**	**20**	**18.1**
Mo	4.8	4.0	4.0	4.0	4.0	5.0				**4.3**	0.47	0.9	**1.26**					
Ag	0.3	< 0.25	< 0.25	< 0.25	< 0.25	0.3				**0.3**	0.00	0.0	**1.00**					
In	< 0,21	< 0.4	< 0.4	< 0.4	< 0.4	< 0,21												
Sn	2.0	1.9	2.4	2.4	1.9	1.9				**2.1**	0.25	0.5	**1.29**	**1.90**				
Sb	< 4	< 8	< 8	< 8	< 8	< 4												
Te	< 0,8	< 1.7	< 1.7	< 1.7	< 1.7	< 0,8												
Cs	0.59	0.30	< 0.17	< 0.17	0.30	0.10	0.68	0.52	0.25	**0.39**	0.21	0.4	**2.38**	**0.10**		**0.1**	**0.1**	**0.1**
Ba	141	128	131	131	128	132				**132**	4.79	9.6	**1.08**	**130**	**13**	**117**	**143**	
La	15.10	14.70	15.20	15.20	14.70	15.00	14.89	15.12	15.30	**15.0**	0.22	0.4	**1.02**	**15**	**1**	**14**	**16**	**15.2**
Ce	38.10	36.80	35.80	35.80	36.80	38.10	35.86	37.71	38.67	**37.1**	1.11	2.2	**1.05**	**38**	**2**	**35.5**	**39.5**	**37.5**
Pr	5.19	5.20	5.20	5.20	5.20	5.25	5.57	5.13	5.42	**5.3**	0.14	0.3	**1.04**					**5.35**
Nd	25.10	24.20	24.40	24.40	24.20	24.40	24.04	25.12	24.88	**24.5**	0.40	0.8	**1.03**	**25**	**1.8**	**22.7**	**26.3**	**24.5**
Sm	6.44	5.94	6.34	6.34	5.94	6.22	5.92	6.17	6.21	**6.2**	0.20	0.4	**1.05**	**6.20**	**0.4**	**5.8**	**6.6**	**6.07**
Eu	2.02	2.00	2.10	2.10	2.00	2.03	2.04	2.08	2.10	**2.05**	0.04	0.1	**1.03**					**2.07**
Gd	6.40	6.32	6.33	6.33	6.32	6.20	6.15	6.35	6.24	**6.3**	0.08	0.2	**1.02**	**6.30**	**0.2**	**6.1**	**6.5**	**6.24**
Tb	0.99	0.91	0.94	0.94	0.91	0.92	0.99	0.92	0.98	**0.94**	0.03	0.1	**1.06**	**0.90**				**0.92**
Dy	5.27	5.12	5.14	5.14	5.12	5.25	5.35	5.36	5.41	**5.24**	0.12	0.2	**1.03**					**5.31**
Ho	1.04	0.94	0.99	0.99	0.94	0.99	1.03	0.96	1.00	**0.99**	0.04	0.1	**1.06**	**1.04**	**0.04**	**1**	**1.08**	**0.98**
Er	2.84	2.42	2.46	2.46	2.42	2.57	2.59	2.53	2.60	**2.54**	0.13	0.3	**1.08**					**2.54**
Tm	0.33	0.32	0.31	0.31	0.32	0.34	0.36	0.33	0.35	**0.33**	0.02	0.0	**1.09**					**0.33**
Yb	2.12	2.00	2.02	2.02	2.00	2.00	1.94	1.97	2.05	**2.01**	0.05	0.1	**1.04**	**2.00**	**0.2**	**1.8**	**2.2**	**2**
Lu	0.28	0.27	0.28	0.28	0.27	0.28	0.31	0.27	0.29	**0.28**	0.01	0.0	**1.06**	**0.28**	**0.01**	**0.27**	**0.29**	**0.274**
Hf	4.53	4.60	4.60	4.60	4.60	4.48	4.73	3.94	4.54	**4.51**	0.23	0.5	**1.08**	**4.10**	**0.3**	**3.8**	**4.4**	**4.36**
Ta	1.32	1.18	1.13	1.13	1.18	1.15	1.27	1.12	1.15	**1.18**	0.07	0.1	**1.10**	**1.40**				**1.14**
Pb	2.8	2.3	1.6	1.6	2.3	0.9	3.2	2.7	2.4	**2.2**	0.72	1.4	**1.67**					**1.6**
W	0.5	< 0.8	< 0.8	< 0.8	< 0.8	< 0,4												
Bi	< 0,4	< 0.8	< 0.8	< 0.8	< 0.8	< 0,4												
Th	1.28	1.2	1.2	1.2	1.2	1.3	1.19	1.50	1.2	**1.25**	0.10	0.2	**1.13**	**1.20**	**0.3**	**0.9**	**1.5**	**1.22**
U	0.45	0.42	0.39	0.39	0.42	0.4	0.43	0.49	0.4	**0.42**	0.03	0.1	**1.12**					**0.403**
Dilution							52062	52022	33050									

Élément	BCR2									Moyenne	SD	2SD	Précision	Recommandée/ Mesurée	±	Min	Max	Certifiée (INRS)
Co	38	36	37	37	36	36				**37**	0.82	1.6	**1.05**	**37**	**3**	**34**	**40**	
As	< 25					< 25												
Rb	45	47	52	52	47	48	47	48	46	**48**	2.27	4.5	**1.08**	**48**	**2**	**46**	**50**	**46.9**
Sr	322	345	340	340	345	331				**337**	9.02	18.0	**1.06**	**346**	**14**	**332**	**360**	
Y	35	36	37	37	36	37	34.5	37.1	36.5	**36**	0.98	2.0	**1.04**	**37**	**2**	**35**	**39**	**37**
Zr	175	182	180	180	182	179	171	179	184	**179**	3.96	7.9	**1.03**	**188**	**16**	**172**	**204**	**184**
Nb	11.2	12.1	12.5	12.5	12.1	12.1	11.6	12.4	11.9	**12**	0.43	0.9	**1.06**					**12.6**
Mo	248	247	252	252	247	276				**254**	11.18	22.4	**1.10**	**248**	**17**	**231**	**265**	
Ag	0.3	< 0.21	< 0.21	< 0.21	< 0.21	0.3				**0**	0.03	0.1	**1.24**					
In	< 0,25	< 0.4	< 0.4	< 0.4	< 0.4	< 0,25												
Sn	2.3	2.1	2.5	2.5	2.1	2.4				**2**	0.18	0.4	**1.18**					
Sb	< 5	< 7	< 7	< 7	< 7	< 5												
Te	< 1	< 1.4	< 1.4	< 1.4	< 1.4	< 1												
Cs	1.01	0.72	0.50	0.50	0.72	0.99	1.10	1.10	1.31	**0.88**	0.28	0.6	**1.66**					**1.1**
Ba	56900	680	687	687	680	693				**685**	5.50	11.0	**1.02**	**683**	**28**	**655**	**711**	
La	23.60	24.00	25.00	25.00	24.00	24.60	23.05	24.82	23.89	**24.22**	0.68	1.4	**1.04**	**25**	**1**	**24**	**26**	**24.9**
Ce	50.70	52.50	50.90	50.90	52.50	53.50	48.14	53.56	52.36	**51.67**	1.71	3.4	**1.05**	**53**	**2**	**51**	**55**	**52.9**
Pr	6.19	6.72	6.66	6.66	6.72	6.67	6.70	6.68	6.66	**6.63**	0.17	0.3	**1.04**	**6.8**	0.3	**6.5**	**7.1**	**6.7**
Nd	27.90	28.30	28.90	28.90	28.30	28.10	26.62	29.84	28.03	**28.32**	0.88	1.8	**1.05**					**28.7**
Sm	6.68	6.60	6.73	6.73	6.60	6.70	6.06	6.78	6.49	**6.60**	0.22	0.4	**1.05**	**6.7**	0.3	**6.4**	**7**	**6.58**
Eu	1.90	1.90	2.00	2.00	1.90	1.90	1.82	1.99	1.93	**1.93**	0.06	0.1	**1.05**	**2**	**0.1**	**1.9**	**2.1**	**1.96**
Gd	6.68	6.78	6.96	6.96	6.78	6.70	6.15	6.90	6.45	**6.71**	0.26	0.5	**1.06**	**6.8**	**0.3**	**6.5**	**7.1**	**6.75**
Tb	1.05	1.01	1.05	1.05	1.01	1.01	1.04	1.04	1.07	**1.04**	0.02	0.0	**1.03**	**1.07**	0.04	**1.03**	**1.11**	**1.07**
Dy	6.00	6.38	6.39	6.39	6.38	6.32	6.01	6.46	6.31	**6.29**	0.17	0.3	**1.04**					**6.41**
Ho	1.25	1.26	1.34	1.34	1.26	1.29	1.29	1.27	1.28	**1.29**	0.03	0.1	**1.04**	**1.33**	0.06	**1.27**	**1.39**	**1.28**
Er	3.75	3.63	3.64	3.64	3.63	3.66	3.45	3.63	3.64	**3.63**	0.08	0.2	**1.03**					**3.66**
Tm	0.50	0.51	0.51	0.51	0.51	0.53	0.53	0.52	0.54	**0.52**	0.01	0.0	**1.04**	**0.54**		**0.54**	**0.54**	**0.54**
Yb	3.38	3.34	3.39	3.39	3.34	3.38	3.08	3.33	3.31	**3.33**	0.10	0.2	**1.05**	**3.5**	**0.2**	**3.3**	**3.7**	**3.38**
Lu	0.48	0.50	0.51	0.51	0.50	0.51	0.52	0.50	0.51	**0.50**	0.01	0.0	**1.04**	**0.51**	0.02	**0.49**	**0.53**	**0.503**
Hf	4.81	4.91	4.90	4.90	4.91	4.82	4.74	4.37	4.77	**4.79**	0.17	0.3	**1.06**	**4.8**	0.2	**4.6**	**5**	**4.9**
Ta	0.85	0.79	0.74	0.74	0.79	0.77	0.80	0.79	0.74	**0.78**	0.04	0.1	**1.07**					**0.74**
Pb	12.7	9.2	9.4	9.4	9.2	11.8	10.2	10.0	10.9	**10.3**	1.25	2.5	**1.21**	**11**	2	**9**	**13**	**11**
W	1	< 0.7	< 0.7	< 0.7	< 0.7	0.9												
Bi	< 0,5	< 0.7	< 0.7	< 0.7	< 0.7	< 0,5												
Th	6.2	5.6	5.6	5.6	5.6	6.1	5.8	6.4	5.8	**5.9**	0.31	0.6	**1.08**	**6.2**	**0.7**	**5.5**	**6.9**	**5.7**
U	1.67	1.67	1.69	1.69	1.67	1.55	1.57	1.71	1.7	**1.66**	0.06	0.1	**1.05**	**1.69**	**0.19**	**1.5**	**1.88**	**1.69**
Dilution							47113	47471	30295									

Élément	W2	Moyenne	SD	2SD	Précision	Recommandée /Mesurée	±	Min	Max	Certifiée (INRS)
Co						**43**	**3**	**40**	**46**	

Élément	W2				Moyenne	SD	2SD	Précision	Recommandée /Mesurée	±	Min	Max	Certifiée (INRS)
As									1.2				
Rb	19	19	20	19	19	0.55	1.1	1.10	21	1.1	19.9	22.1	21
Sr													
Y	22	22	22	22	22	0.12	0.2	1.02	23	1.6	21.4	24.6	22
Zr	81	86	93	94	89	5.89	11.8	1.24	100	2	98	102	92
Nb	7.5	8.1	8.4	7.2	7.8	0.57	1.1	1.26	7.9				7.5
Mo													
Ag													
In													
Sn													
Sb													
Te													
Cs	0.92	0.93	0.9	0.92	0.93	0.01	0.0	1.02	0.99				0.92
Ba													
La	10.49	10.36	10.92	10.09	10.47	0.35	0.7	1.11	10	0.59	9.41	10.59	10.8
Ce	22.40	23.63	24.35	23.04	23.35	0.83	1.7	1.12	23	1.5	21.5	24.5	23.4
Pr	3.09	2.89	3.03	2.99	3.00	0.08	0.2	1.09					3
Nd	12.98	12.98	13.84	12.85	13.17	0.46	0.9	1.12	13	1	12	14	13
Sm	3.24	3.26	3.46	3.25	3.30	0.11	0.2	1.11	3.3	0.13	3.17	3.43	3.3
Eu	1.09	1.10	1.13	1.07	1.10	0.02	0.0	1.07	1	0.06	0.94	1.06	1.08
Gd	3.63	3.69	3.91	3.56	3.70	0.15	0.3	1.14					3.66
Tb	0.61	0.65	0.61	0.63	0.63	0.02	0.0	1.09	0.63				0.62
Dy	3.87	3.83	3.93	3.83	3.86	0.05	0.1	1.04	3.6	0.8	2.8	4.4	3.79
Ho	0.78	0.77	0.77	0.79	0.78	0.01	0.0	1.03	0.76				0.79
Er	2.28	2.28	2.25	2.20	2.25	0.04	0.1	1.05	2.5				2.22
Tm	0.34	0.34	0.32	0.33	0.33	0.01	0.0	1.09	0.38				0.33
Yb	2.01	2.02	2.01	2.05	2.02	0.02	0.0	1.03	2.1	0.2	1.9	2.3	2.05
Lu	0.32	0.31	0.31	0.30	0.31	0.01	0.0	1.08	0.33				0.31
Hf	2.50	2.44	2.13	2.5	2.38	0.17	0.3	1.26	2.6	0.18	2.42	2.78	2.45
Ta	0.49	0.44	0.48	0.44	0.47	0.03	0.1	1.20	0.5				0.47
Pb	9.0	9.2	9.0	7.8	8.7	0.65	1.3	1.27	9.3				7.7
W													
Bi													
Th	2.5	2.4	2.6	2.1	2.4	0.20	0.4	1.30	2.4	0.1	2.3	2.5	2.17
U	0.53	0.52	0.59	0.51	0.54	0.04	0.1	1.25	0.53				0.51
Dilution	49298	49298	55163	27783	45385	######	24112.7						

Élément	Sarm1		Moyenne	SD	2SD	Précision	Certifiée/Mesurée	95% confiance (min)	95% confiance (max)	Certifiée (INRS)
Co	2	1								

Élément	Sarm1						Moyenne	SD	2SD	Précision	Certifiée/Mesurée	95% confiance (min)	95% confiance (max)	Certifiée (INRS)
As	< 30	< 30												
Rb	338	340	317	325			330	10.80	21.6	1.11	325			325
Sr	12	10									10			
Y	143	143	143	143			143	0.11	0.2	1.00	143	120	159	143
Zr	310	314	283	297			301	13.82	27.6	1.16	300			300
Nb	51.6	53.8	47.5	52.9			51.4	2.81	5.6	1.19	53			53
Mo	5.9	6.1												
Ag	0.5	0.5												
In	< 0,3	< 0,3												
Sn	5.8	5.8												
Sb	< 5	< 5												
Te	< 1,1	< 1,1												
Cs	0.89	0.89	0.56	1.16			0.87	0.24	0.5	2.58				0.94
Ba	112	113									120			
La	107.0	111.0	108.1	109.0			108.8	1.69	3.4	1.05	109	100	116	109
Ce	203.0	208.0	202.1	208.7			205.4	3.39	6.8	1.05	195	190	203	195
Pr	20.30	21.30	20.41	21.48			20.87	0.60	1.2	1.10				19.5
Nd	73.0	73.1	73.0	72.3			72.85	0.36	0.7	1.02	72	67	84	72
Sm	15.30	15.20	14.69	14.69			14.97	0.33	0.7	1.07	15.8	14	18	13.8
Eu	0.30	0.33	0.4	0.3			0.33	0.02	0.0	1.24	0.35	0.34	0.47	0.326
Gd	15.40	15.80	14.33	14.05			14.90	0.84	1.7	1.20	14			14
Tb	2.80	2.70	2.62	2.82			2.74	0.09	0.2	1.11	3	2.4	3.5	3
Dy	17.90	18.60	18.28	18.77			18.39	0.38	0.8	1.07	17			17
Ho	4.23	4.22	4.02	4.15			4.16	0.10	0.2	1.08				
Er	14.3	13.6	13.0	13.6			13.62	0.54	1.1	1.14				
Tm	2.05	2.19	2.03	2.19			2.11	0.09	0.2	1.14	2			2
Yb	14.40	14.50	13.62	14.23			14.19	0.40	0.8	1.09	14.2	12.8	16	14.2
Lu	1.99	2.1	2.02	2.1			2.07	0.07	0.1	1.12	2			2
Hf	12.3	12.5	10.9	12.5			12.1	0.7	1.5	1.22				12.4
Ta	4.9	4.6	4.3	4.5			4.6	0.2	0.5	1.18				4.5
Pb	2.7	2.8	28.6	38.4			18.1	18.2	36.4	-4.35	40			40
W	40	40												
Bi	< 0,5	< 0,5												
Th	53.8	53.1	48.7	51.0			52	2.29	4.6	1.15	51	48	55	51
U	17.4	16.1	16.1	18.1			16.9	0.97	1.9	1.20	15			15
Dilution			62367	40454										

Élément	Sarm5						Moyenne	SD	2SD	Précision	Certifiée/Mesurée	Certifiée (INRS)
Co	108	110	108	108	110	110	109	1.10	2.2	1.02	110	

Élément	Sarm5						Moyenne	SD	2SD	Précision	Certifiée/Mesurée	Certifiée (INRS)
As	< 24					< 24						
Rb	2.8	3	3.1	3.1	3	3	**3**	0.12	0.2	**1.09**		**2.8**
Sr	32	37	34	34	37	33	**35**	1.83	3.7	**1.12**	32	
Y	3.3	3.6	3.2	3.2	3.6	3.5	**3.4**	0.19	0.4	**1.12**	5	**3.6**
Zr	17	21	28	28	21	17	**22**	5.08	10.2	**1.64**		**8.84**
Nb	1.0	0.7	0.8	0.8	0.7	1.0	**0.8**	0.13	0.3	**1.39**		
Mo	< 0,5	1.20	0.90	0.90	1.20	0.70	**1.0**	0.22	0.4	**1.60**		
Ag	< 0,14	< 0.27	< 0.27	< 0.27	< 0.27	< 0,14						
In	< 0,24	< 0.4	< 0.4	< 0.4	< 0.4	< 0,24						
Sn	< 0,5	< 0.9	1.10	1.10	< 0.9	< 0,5	**1.1**	0.00	0.0	**1.00**		
Sb	< 5	< 9	< 9	< 9	< 9	< 5						
Te	< 1	< 1.8	< 1.8	< 1.8	< 1.8	< 1						
Cs	0.14	0.40	< 0.18	< 0.18	0.40	0.14	**0.27**	0.15	0.3	**3.80**		**0.11**
Ba	32.7	40.9	34.0	34.0	40.9	32.2	**35.8**	4.03	8.1	**1.27**	46	
La	1.8	1.9	1.9	1.9	1.9	1.9	**1.9**	0.04	0.1	**1.05**	2	**1.88**
Ce	3.9	4.0	3.8	3.8	4.0	4.0	**3.9**	0.13	0.3	**1.07**		**4.2**
Pr	0.46	0.49	0.46	0.46	0.49	0.49	**0.48**	0.02	0.0	**1.08**		**0.471**
Nd	1.9	2.0	1.9	1.9	2.0	2.0	**2.0**	0.05	0.1	**1.06**		**1.86**
Sm	0.44	0.41	0.39	0.39	0.41	0.44	**0.41**	0.02	0.0	**1.12**		**0.424**
Eu	0.13	0.14	0.10	0.10	0.14	0.13	**0.12**	0.02	0.0	**1.37**	0.2	**0.127**
Gd	0.49	0.40	0.46	0.46	0.40	0.50	**0.45**	0.04	0.1	**1.22**		**0.461**
Tb	0.08	0.08	0.06	0.06	0.08	0.08	**0.07**	0.01	0.0	**1.35**		**0.076**
Dy	0.52	0.53	0.49	0.49	0.53	0.55	**0.52**	0.02	0.0	**1.10**		**0.478**
Ho	0.11	0.11	0.09	0.09	0.11	0.126	**0.11**	0.01	0.0	**1.32**		**0.11**
Er	0.39	0.35	0.34	0.34	0.35	0.38	**0.36**	0.02	0.0	**1.13**		**0.343**
Tm	0.06	0.05	0.05	0.05	0.05	0.06	**0.05**	0.01	0.0	**1.28**		**0.051**
Yb	0.42	0.41	0.37	0.37	0.41	0.42	**0.40**	0.02	0.0	**1.13**	0.6	**0.388**
Lu	0.065	0.066	0.05	0.05	0.066	0.068	**0.06**	0.01	0.0	**1.34**		**0.061**
Hf	0.46	0.53	0.71	0.71	0.53	0.483	**0.57**	0.11	0.2	**1.52**		**0.3**
Ta	0.06	< 0.04	< 0.04	< 0.04	< 0.04	0.05	**0.06**	0.01	0.0	**1.31**		
Pb	< 0,5	< 0.9	< 0.9	< 0.9	< 0.9	< 0,5						**1.45**
W	1.4	2.0	1.5	1.5	2.0	0.6	**1.5**	0.51	1.0	**2.12**		
Bi	< 0,5	< 0.9	< 0.9	< 0.9	< 0.9	< 0,5						
Th	0.3	0.5	0.5	0.5	0.5	0.5	**0.5**	0.08	0.2	**1.45**		**0.26**
U	0.24	0.2	0.174	0.174	0.2	0.22	**0.2**	0.03	0.1	**1.31**		**0.275**
Dilution												

Standards analysés à ALS par ME-MS61u

Élément	Unité	AMIS0076					Moyenne	SD	2SD	Précision	Certifiée/Recommandée	2SD	2SD min	2SD max
Ag	ppm	4.27	4.21	4.09	4.12	4.29	4.20	0.09	0.2	1.05	4.2	0.8	3.4	5
Al	%	1.63	1.67	1.61	1.64	1.66	1.64	0.02	0.0	1.04	1.70	0.07	1.63	1.78
As	ppm	571	525	518	510	590	543	35	71	1.18	556	58	498	614
Ba	ppm	100	100	100	100	100	100	0.00	0.0	1.00				
Be	ppm	0.96	0.75	0.74	0.77	0.84	0.81	0.09	0.2	1.33				
Bi	ppm	2.36	2.35	2.33	2.33	2.65	2.40	0.14	0.3	1.15				
Ca	%	0.22	0.23	0.22	0.22	0.25	0.23	0.01	0.0	1.15	0.22	0.014	0.21	0.24
Cd	ppm	0.8	0.83	0.83	0.89	0.84	0.84	0.03	0.1	1.10	0.82	0.16	0.66	0.98
Ce	ppm	84.0	81.0	83.9	78.6	89.0	83.3	3.9	7.8	1.12				
Co	ppm	115	117	119	114	117	116	1.9	3.8	1.04	119	12	107	131
Cr	ppm	881	806	874	852	916	866	41	81	1.12	1026	137	890	1163
Cs	ppm	1.97	1.98	2.05	2	2.21	2.04	0.10	0.2	1.13				
Cu	ppm	87.6	83.3	80.2	80.5	84.5	83.2	3.1	6.1	1.10	86	10	76	96
Fe	%	3.88	3.92	3.80	3.89	3.95	3.89	0.06	0.1	1.04	3.80	0.13	3.68	3.93
Ga	ppm	5.04	4.69	4.55	4.57	4.85	4.74	0.2	0.4	1.11				
Ge	ppm	0.29	0.17	0.14	0.17	0.21	0.20	0.06	0.1	2.17				
Hf	ppm	3.8	3.6	3.4	3.5	3.5	3.6	0.2	0.3	1.11				
In	ppm	0.025	0.027	0.024	0.027	0.029	0.026	0.002	0.0	1.20				
K	%	0.36	0.37	0.36	0.37	0.37	0.37	0.01	0.0	1.04	0.38	0.02	0.37	0.40
La	ppm	42.3	39.3	42.4	42.2	42.5	41.7	1.4	2.7	1.08				
Li	ppm	8.2	6.9	6.9	7.6	7.4	7.4	0.5	1.1	1.20				
Mg	%	0.30	0.30	0.29	0.30	0.30	0.30	0.004	0.0	1.04				
Mn	ppm	349	359	342	356	370	355	11	21	1.08				
Mo	ppm	8.0	8.0	8.4	8.8	7.8	8.2	0.4	0.7	1.12	8.6	1.6	7	10.2
Na	%	0.09	0.09	0.07	0.09	0.09	0.09	0.01	0.0	1.30				
Nb	ppm	8.8	9.6	10	9.6	10	9.6	0.5	1.0	1.14	9	2	7	11
Ni	ppm	187	191	179	189	192	187	5.1	10.1	1.07	191	22	169	213
P	ppm	160	160	160	170	180	166	9	17.9	1.14				
Pb	ppm	684	693	648	679	696	680	19	38.3	1.07	697	94	603	791
Rb	ppm	19.0	18.0	19.5	18.5	21.2	19.2	1.2	2.5	1.17				
Re	ppm	0.005	0.003	0.004	0.003	0.005	0.004	0.001	0.0	1.90				
S	ppm	2.3	2.4	2.3	2.3	2.4	2.3	0.05	0.1	1.06	2.3	0.26	2.04	2.56
Sb	ppm	53.7	53.9	53.5	54.3	50.3	53.1	1.6	3.2	1.08				
Se	ppm	6	5	5	5	5	5	0.4	0.9	1.24				
Sn	ppm	2	2.1	2	2	2.1	2	0.1	0.1	1.07				
Sr	ppm	31.5	33.6	33.3	31.6	33.3	32.7	1.0	2.0	1.08				
Ta	ppm	4.3	4.4	4.4	4.5	4.6	4.5	0.12	0.2	1.07				
Te	ppm	0.39	0.37	0.38	0.38	0.39	0.38	0.01	0.0	1.06				
Th	ppm	156	155	149	162	157	156	4.5	9.0	1.07				

Élément	Unité	AMIS0076					Moyenne	SD	2SD	Précision	Certifiée/Recommandée	2SD	2SD min	2SD max
Ti	%	0.082	0.088	0.083	0.088	0.082	**0.085**	0.003	0.0	**1.10**	**0.108**	**0.012**	**0.096**	**0.12**
Tl	ppm	0.23	0.22	0.2	0.23	0.24	**0.22**	0.02	0.0	**1.18**				
U	ppm	1430	1460	1440	1450	1450	**1446**	11	23	**1.02**	**1502**	**166**	**1336**	**1668**
V	ppm	24	25	24	24	26	**25**	0.9	1.8	**1.09**				
W	ppm	1.2	1.3	1.3	1.3	1.3	**1.3**	0.04	0.1	**1.09**				
Y	ppm	61.8	67.3	67.0	65.3	64.6	**65.2**	2.2	4.4	**1.09**				
Zn	ppm	447	457	434	453	474	**453**	15	29	**1.08**	**443**	**84**	**359**	**527**
Zr	ppm	116	114	115	114	121	**116**	3.1	6.2	**1.07**				

Élément	Unité	BL-2				Moyenne	SD	2SD	Précision	Certifiée/Mesurée
Ag	ppm	1.55	1.38	1.38	1.08	**1.35**	0.20	0.4	**1.60**	
Al	%	7.08	7.14	6.91	7.4	**7.13**	0.20	0.4	**1.09**	**7.3**
As	ppm	8.1	7.7	6.9	7.2	**7.5**	0.53	1.1	**1.26**	
Ba	ppm	300	300	290	320	**303**	12.58	25.2	**1.14**	**350**
Be	ppm	164.5	164	151.5	147.5	**156.9**	8.67	17.3	**1.19**	
Bi	ppm	0.92	0.88	0.91	1	**0.93**	0.05	0.1	**1.19**	**20**
Ca	%	2.96	2.96	2.79	3.08	**2.95**	0.12	0.2	**1.14**	**2.8**
Cd	ppm	0.11	0.11	0.13	0.12	**0.12**	0.01	0.0	**1.30**	
Ce	ppm	68.7	71.0	63.4	68.3	**67.9**	3.20	6.4	**1.16**	
Co	ppm	23.9	23.9	25.3	24.9	**24.5**	0.71	1.4	**1.10**	**25**
Cr	ppm	85	85	84	84	**85**	0.58	1.2	**1.02**	
Cs	ppm	0.52	0.57	0.52	0.5	**0.53**	0.03	0.1	**1.20**	
Cu	ppm	84.9	83.1	77.3	81.6	**81.7**	3.24	6.5	**1.13**	**78**
Fe	%	5.4	5.43	5.23	5.59	**5.41**	0.15	0.3	**1.09**	**5.4**
Ga	ppm	20.5	20.9	21.1	22	**21.13**	0.63	1.3	**1.10**	
Ge	ppm	0.29	0.30	0.28	0.27	**0.29**	0.01	0.0	**1.16**	
Hf	ppm	4.5	4.5	4.1	4.8	**4.5**	0.29	0.6	**1.23**	
In	ppm	0.077	0.075	0.084	0.085	**0.080**	0.00	0.0	**1.22**	
K	%	0.61	0.64	0.58	0.63	**0.62**	0.03	0.1	**1.15**	**0.66**
La	ppm	32.7	34.3	29.5	31.1	**31.9**	2.07	4.1	**1.23**	
Li	ppm	17.7	17.7	14.5	15.1	**16.3**	1.69	3.4	**1.40**	
Mg	%	1.36	1.37	1.32	1.41	**1.37**	0.04	0.1	**1.09**	**1.4**
Mn	ppm	578	582	585	619	**591**	18.89	37.8	**1.11**	
Mo	ppm	38.0	39.2	33.8	46.0	**39.3**	5.06	10.1	**1.52**	**36**
Na	%	4.1	4.12	3.87	4.26	**4.09**	0.16	0.3	**1.13**	**4.2**
Nb	ppm	9.3	9.7	10.3	10.4	**9.9**	0.52	1.0	**1.18**	
Ni	ppm	164	169	161	173	**166**	5.51	11.0	**1.11**	
P	ppm	740	730	720	790	**745**	31.09	62.2	**1.14**	
Pb	ppm	1215	1225	1175	1250	**1216**	31.19	62.4	**1.09**	**922**
Rb	ppm	25.3	26.6	23.2	29.9	**26.3**	2.81	5.6	**1.41**	
Re	ppm	0.097	0.101	0.104	0.116	**0.105**	0.01	0.0	**1.28**	

Élément	Unité	BL-2				Moyenne	SD	2SD	Précision	Certifiée/Mesurée
S	ppm	0.37	0.36	0.36	0.38	**0.37**	0.01	0.0	**1.09**	0.33
Sb	ppm	0.17	0.17	0.17	0.18	**0.17**	0.00	0.0	**1.10**	
Se	ppm	13	12	12	14	**13**	0.96	1.9	**1.27**	
Sn	ppm	4.3	4.4	4.1	4.6	**4.4**	0.21	0.4	**1.16**	
Sr	ppm	241	241	230	247	**240**	7.09	14.2	**1.10**	70
Ta	ppm	0.91	0.94	0.97	1	**0.96**	0.04	0.1	**1.14**	
Te	ppm	0.21	0.22	0.19	0.20	**0.21**	0.01	0.0	**1.22**	
Th	ppm	12.8	13.1	11.6	13.3	**13**	0.76	1.5	**1.21**	16
Ti	%	0.391	0.397	0.382	0.406	**0.394**	0.01	0.0	**1.09**	
Tl	ppm	0.18	0.18	0.18	0.2	**0.19**	0.01	0.0	**1.19**	
U	ppm	4190	4220	4120	4370	**4225**	105.36	210.7	**1.08**	4530
V	ppm	772	776	733	809	**773**	31.12	62.2	**1.14**	841
W	ppm	2.7	2.7	2.8	3	**2.8**	0.14	0.3	**1.17**	
Y	ppm	26.1	26.8	25.5	28.1	**26.6**	1.12	2.2	**1.14**	
Zn	ppm	68	69	70	73	**70**	2.16	4.3	**1.10**	
Zr	ppm	192	191	192	199	**193**	3.94	7.9	**1.07**	

Élément	Unité	SY-4		Moyenne	Certifiée/Recommandée/Mesurée		95% confiance (min)	95% confiance (max)
Ag	ppm	<0.01	0.03	**0.03**	0.6	0.16	0.44	0.76
Al	%	8.02	8.51	**8.27**	10.95	0.04	10.91	10.99
As	ppm	<0.2	<0.2		0.1 - 2			
Ba	ppm	320	340	**330**	340	5	335	345
Be	ppm	2.92	2.75	**2.84**	2.6	0.1	2.5	2.7
Bi	ppm	0.01	0.01	**0.01**	0.1 - 0.3			
Ca	%	5.23	5.84	**5.54**	5.75	0.029	5.72	5.78
Cd	ppm	0.08	0.08	**0.08**	0.1 - 2			
Ce	ppm	64	125	**95**	122	2	120.0	124.0
Co	ppm	2.4	2.5	**2**	2.8	0.2	2.6	3.0
Cr	ppm	8	8	**8**	12	1	11.0	13.0
Cs	ppm	1.56	1.63	**1.60**	1.5	0.1	1.4	1.6
Cu	ppm	3.3	5.2	**4**	7	1	6.0	8.0
Fe	%	**4.03**	**4.28**	**4.2**	4.34	0.02	4.32	4.36
Ga	ppm	**38.3**	**41.8**	**40.05**	35	1	34	36
Ge	ppm	0.25	0.33	**0**	1 - 4			
Hf	ppm	1.4	1.9	**2**	10.6	0.4		
In	ppm	0.039	0.044	**0.042**	0.04 - 0.1			
K	%	1.25	1.38	**1.32**	1.38	0.02	1.36	1.39
La	ppm	24.8	55.3	**40.1**				
Li	ppm	36.6	36.3	**36.5**				
Mg	%	0.19	0.21	**0.20**	0.33	0.01	0.32	0.33

Élément	Unité	SY-4		Moyenne	Certifiée/Recommandée/Mesurée		95% confiance (min)	95% confiance (max)
Mn	ppm	791	842	817	836	8	829	844
Mo	ppm	0.28	0.29	0.29	0.2 - 3			
Na	%	5.03	5.6	5.32	5.27	0.04	5.23	5.30
Nb	ppm	14.4	15	14.7	12	1	11	13
Ni	ppm	6.6	7	7	57	1	56	58
P	ppm	510	520	515	572	17	554	589
Pb	ppm	10.4	10	10	10	1	9	11
Rb	ppm	27.5	60.6	44.1	55	1.5	54	57
Re	ppm	0.002	0.002	0.002				
S	ppm	0.01	0.01	0.01				
Sb	ppm	0.07	0.07	0.1	0.01 - 0.3			
Se	ppm	3	4	4	0.01 - 4			
Sn	ppm	7.3	8	8	7.1	0.6	7	8
Sr	ppm	1195	1310	1253	1191	12	1179	1203
Ta	ppm	0.82	0.82	0.82	0.9	0.1	0.80	1.00
Te	ppm	<0.05	<0.05					
Th	ppm	0.7	1.3	1	1.4	0.2		
Ti	%	0.159	0.169	0.164	0.172	0.002	0.170	0.174
Tl	ppm	0.27	0.28	0.28	0.2 - 0.5			
U	ppm	0.4	0.6	1	0.8	0.1	0.7	0.9
V	ppm	5	6	6	8	1.6	6.4	9.6
W	ppm	0.2	0.2	0	0.2 - 15			
Y	ppm	72.9	125	99.0	119	2	117	121
Zn	ppm	99	108	104	93	2	91	95
Zr	ppm	74	91	82	517	16	501	533

Élément	Unité	UTS-1	Certifiée
Ag	ppm	0.19	
Al	%	6.52	6.24
As	ppm	5.3	
Ba	ppm	320	324
Be	ppm	11.5	
Bi	ppm	0.22	
Ca	%	5.24	5.24
Cd	ppm	0.09	
Ce	ppm	259	
Co	ppm	20.4	
Cr	ppm	79	
Cs	ppm	5.07	
Cu	ppm	17.7	
Fe	%	4.78	4.87

Élément	Unité	UTS-1	Certifiée
Ga	ppm	27.6	
Ge	ppm	0.31	
Hf	ppm	46.9	
In	ppm	0.049	
K	%	1.67	
La	ppm	159.5	
Li	ppm	66.9	
Mg	%	1.83	
Mn	ppm	1110	
Mo	ppm	5.2	
Na	%	3.58	
Nb	ppm	42.2	
Ni	ppm	43.8	
P	ppm	960	
Pb	ppm	61.9	
Rb	ppm	193.5	
Re	ppm	0.002	
S	ppm	1.13	1
Sb	ppm	0.89	
Se	ppm	4	
Sn	ppm	3.7	
Sr	ppm	675	
Ta	ppm	2.68	
Te	ppm	0.06	
Th	ppm	140.5	138
Ti	%	0.541	0.54
Tl	ppm	1.03	
U	ppm	44.8	49
V	ppm	118	
W	ppm	0.6	
Y	ppm	76	
Zn	ppm	104	
Zr	ppm	>500	

Élément	Unité	UTS-3				Moyenne	SD	2SD	Précision	Certifiée
Ag	ppm	0.7	0.67	0.68	0.75	**0.70**	0.04	0.1	**1.18**	
Al	%	5.82	5.95	6.02	6.16	**5.99**	0.14	0.3	**1.08**	5.8
As	ppm	3.4	3.4	3.4	3.6	**3.5**	0.10	0.2	**1.10**	
Ba	ppm	200	200	190	190	**195**	5.77	11.5	**1.10**	212
Be	ppm	196	198.5	204	198	**199**	3.42	6.8	**1.06**	
Bi	ppm	0.23	0.22	0.23	0.25	**0.23**	0.01	0.0	**1.19**	
Ca	%	3.84	4	3.7	3.99	**3.88**	0.14	0.3	**1.12**	4.03
Cd	ppm	0.05	0.07	0.06	0.08	**0.07**	0.01	0.0	**1.92**	

Élément	Unité	UTS-3				Moyenne	SD	2SD	Précision	Certifiée
Ce	ppm	44.5	47.9	43.9	47.3	**45.9**	1.99	4.0	**1.15**	
Co	ppm	12.1	11.3	12.2	13.3	**12.2**	0.82	1.6	**1.24**	
Cr	ppm	47	49	52	49	**49**	2.06	4.1	**1.14**	
Cs	ppm	0.28	0.31	0.29	0.3	**0.30**	0.01	0.0	**1.15**	
Cu	ppm	33.5	32.7	31.6	36.3	**33.5**	2.01	4.0	**1.21**	
Fe	%	3.08	3.2	3.14	3.21	**3.16**	0.06	0.1	**1.06**	3.25
Ga	ppm	16.75	17.1	16.45	16.7	**16.8**	0.27	0.5	**1.05**	
Ge	ppm	0.16	0.1	0.14	0.1	**0.1**	0.03	0.1	**2.24**	
Hf	ppm	4.3	4.7	4	4.4	**4.4**	0.29	0.6	**1.24**	
In	ppm	0.032	0.035	0.034	0.036	**0.034**	0.00	0.0	**1.17**	
K	%	0.26	0.26	0.25	0.26	**0.26**	0.01	0.0	**1.06**	
La	ppm	22.3	26.1	22.2	25.2	**24.0**	2.00	4.0	**1.31**	
Li	ppm	20.8	22.8	19.5	20.3	**20.9**	1.41	2.8	**1.24**	
Mg	%	1.47	1.52	1.47	1.53	**1.50**	0.03	0.1	**1.07**	
Mn	ppm	555	581	569	564	**567**	10.84	21.7	**1.06**	
Mo	ppm	2.88	2.68	3.6	2.85	**3.00**	0.41	0.8	**1.55**	
Na	%	3.71	3.74	3.66	3.74	**3.71**	0.04	0.1	**1.03**	
Nb	ppm	8.2	8.1	8	8.7	**8.3**	0.31	0.6	**1.13**	
Ni	ppm	28.7	26.2	28.4	29.4	**28.2**	1.38	2.8	**1.17**	
P	ppm	820	850	810	830	**828**	17.08	34.2	**1.07**	
Pb	ppm	253	251	250	255	**252**	2.22	4.4	**1.03**	
Rb	ppm	10.6	11.8	11.5	11.3	**11.3**	0.51	1.0	**1.15**	
Re	ppm	0.036	0.036	0.035	0.039	**0.037**	0.00	0.0	**1.16**	
S	ppm	0.25	0.25	0.24	0.25	**0.25**	0.01	0.0	**1.07**	0.23
Sb	ppm	0.1	0.12	0.11	0.1	**0.11**	0.01	0.0	**1.33**	
Se	ppm	3	2	2	2	**2**	0.50	1.0	**2.09**	
Sn	ppm	2.5	2.9	2.4	2.9	**2.7**	0.26	0.5	**1.37**	
Sr	ppm	296	302	294	302	**299**	4.12	8.2	**1.04**	
Ta	ppm	0.75	0.8	0.76	0.81	**0.78**	0.03	0.1	**1.13**	
Te	ppm	0.06	0.06	0.06	0.06	**0.06**	0.00	0.0	**1.00**	
Th	ppm	9	8.9	8.1	9.9	**9.0**	0.74	1.5	**1.30**	10
Ti	%	0.22	0.22	0.22	0.22	**0.22**	0.00	0.0	**1.03**	0.23
Tl	ppm	0.12	0.13	0.12	0.18	**0.14**	0.03	0.1	**2.00**	
U	ppm	510	520	490	520	**510**	14.14	28.3	**1.09**	513
V	ppm	343	349	339	353	**346**	6.22	12.4	**1.06**	
W	ppm	0.8	0.8	0.8	0.9	**0.8**	0.05	0.1	**1.21**	
Y	ppm	14	14.5	12.8	13.6	**13.7**	0.72	1.4	**1.18**	
Zn	ppm	43	47	44	50	**46**	3.16	6.3	**1.25**	
Zr	ppm	211	221	222	231	**221**	8.18	16.4	**1.13**	

Élément	Unité	AMIS0078	Certifiée/Mesurée			
Ag	ppm	0.92	**0.88**	**0.13**	**0.75**	**1.01**

Élément	Unité	AMIS0078	Certifiée/Mesurée			
Al	%	0.84	0.85	0.05	0.79	0.90
As	ppm	134.5	128	9	119.00	137.00
Ba	ppm	50	50	2	48.00	52.00
Be	ppm	0.36				
Bi	ppm	0.56				
Ca	%	2.46	2.43	0.07	2.36	2.50
Cd	ppm	0.35	0.35	0.08	0.27	0.43
Ce	ppm	30.3	29	7.2	21.80	36.20
Co	ppm	25.5	25	3	22.00	28.00
Cr	ppm	481	433	58	375.00	491.00
Cs	ppm	0.86				
Cu	ppm	28.7	28.5	3.3	25.20	31.80
Fe	%	1.93	1.89	0.07	1.82	1.96
Ga	ppm	2.52	2.31	0.42	1.89	2.73
Ge	ppm	0.13				
Hf	ppm	1.4	1.34	0.43	0.91	1.77
In	ppm	0.015				
K	%	0.26	0.25	0.01	0.24	0.26
La	ppm	14.1	14.8	1.8	13.0	16.6
Li	ppm	3.5	3.92	0.34	3.58	4.26
Mg	%	1.36	1.45	0.12	1.33	1.57
Mn	ppm	2280	2323	232	2091	2556
Mo	ppm	5.36	5.12	1	4.12	6.12
Na	%	0.05	0.07	0.01	0.06	0.09
Nb	ppm	3	2.53	0.7	1.83	3.23
Ni	ppm	59.8	62	5	57.0	67.0
P	ppm	80	87	44	43.6	130.9
Pb	ppm	157.5	163	11	152.0	174.0
Rb	ppm	11.2	10.9	1.3	9.6	12.2
Re	ppm	<0.002				
S	ppm	0.51	0.5	0.05	0.45	0.55
Sb	ppm	3.82	3.97	0.39	3.58	4.36
Se	ppm	2				
Sn	ppm	1.7	1.92	0.48	1.44	2.4
Sr	ppm	17.2	16	2.4	13.6	18.4
Ta	ppm	0.9	1.05	0.18	0.87	1.23
Te	ppm	0.1				
Th	ppm	33.6	36.1	3.5	32.6	39.6
Ti	%	0.094	0.12	0.01	0.11	0.13
Tl	ppm	0.09				
U	ppm	324	332	34	298	366

Élément	Unité	AMIS0078	Certifiée/Mesurée			
V	ppm	24	**24.4**	**2.9**	**21.5**	**27.3**
W	ppm	0.7				
Y	ppm	17	**17.2**	**2**	**15.2**	**19.2**
Zn	ppm	149	**146**	**9**	**137**	**155**
Zr	ppm	48	**42.1**	**11.7**	**30.4**	**53.8**

Standards analysés à ACME LAB par la méthode 1EX

STD OREAS24P

Élément	Unité	Analyses																					
Ag	ppm	<0.1	0.1	<0.1	<0.1	<0.1	<0.1	<0.1	<0.1	<0.1	<0.1	<0.1	<0.1	<0.1	<0.1	<0.1	<0.1	<0.1	<0.1	<0.1	<0.1	<0.1	<0.1
Al	%	8.02	7.88	7.94	7.94	7.93	8.35	8.10	8.30	7.88	7.74	8.05	8.33	8.29	7.85	7.94	7.85	7.79	8.36	8.17	7.82	7.98	7.11
As	ppm	1	<1	1	1	1	<1	<1	2	2	1	2	1	<1	2	1	<1	<1	1	<1	1	2	<1
Au	ppm	<0.1	<0.1	<0.1	<0.1	<0.1	<0.1	<0.1	<0.1	<0.1	<0.1	<0.1	<0.1	<0.1	<0.1	<0.1	<0.1	<0.1	<0.1	<0.1	<0.1	<0.1	<0.1
Ba	ppm	299	279	274	296	266	289	295	305	300	286	313	277	294	294	274	277	287	313	309	278	306	251
Be	ppm	<1	1	1	1	<1	<1	1	1	<1	1	1	1	<1	1	1	1	1	1	1	1	<1	<1
Bi	ppm	<0.1	<0.1	<0.1	<0.1	<0.1	<0.1	<0.1	<0.1	<0.1	<0.1	<0.1	<0.1	<0.1	0.5	<0.1	<0.1	<0.1	<0.1	0.3	<0.1	<0.1	<0.1
Ca	%	6.21	5.68	5.97	6.21	5.60	5.99	6.12	6.47	6.15	5.87	6.24	5.76	5.78	6.02	5.97	5.79	5.75	5.91	5.78	5.82	6.14	5.45
Cd	ppm	0.2	0.2	0.2	<0.1	0.1	0.2	0.1	0.2	<0.1	0.2	0.3	0.1	0.2	0.1	0.2	0.2	0.1	0.1	0.2	0.2	0.2	0.1
Ce	ppm	39	36	34	38	33	37	37	41	37	35	41	36	37	37	34	36	39	39	38	36	37	32
Co	ppm	48.4	45.7	44.7	49.0	43.3	47.8	50.8	51.1	46.1	46.3	45.9	47.4	47.4	48.4	44.7	47.9	47.4	48.1	47.1	47.1	49.3	42.2
Cr	ppm	218	204	207	210	178	221	203	222	202	191	200	199	195	189	207	198	201	196	214	191	214	180
Cu	ppm	51.5	51.9	46.3	50.5	46.9	56.1	48.3	56.8	51.5	46.4	50.9	52.1	54.8	52.5	46.3	54.1	57.5	58.3	55.9	53.5	49.8	50.5
Fe	%	7.73	7.48	7.94	7.79	7.33	7.80	8.07	8.19	7.71	7.70	8.12	7.39	7.42	7.96	7.94	7.53	7.55	7.52	7.53	7.52	8.13	7.01
Hf	ppm	3.9	3.6	3.7	3.8	3.7	3.5	3.8	4.0	3.8	3.4	3.8	3.6	3.6	3.9	3.7	3.5	3.5	3.7	3.6	3.6	3.6	3.0
K	%	0.67	0.69	0.69	0.67	0.67	0.68	0.71	0.73	0.66	0.67	0.67	0.66	0.67	0.71	0.69	0.64	0.65	0.66	0.68	0.63	0.67	0.64
La	ppm	20.3	18.5	17.4	21.8	16.7	19.1	17.0	19.4	21.4	17.7	20.2	18.1	20.1	20.1	17.4	19.0	19.4	20.3	19.4	18.4	17.3	15.8
Li	ppm	7.1	8.6	8.7	7.9	8.0	7.3	9.7	9.8	8.8	9.0	8.1	7.6	8.1	8.7	8.7	8.6	10.3	7.9	7.5	6.9	8.4	6.3
Mg	%	4.19	3.99	4.30	4.19	3.95	4.09	4.38	4.35	4.14	4.09	4.26	4.15	4.05	4.22	4.30	3.99	4.02	4.12	4.05	4.04	4.29	3.74
Mn	ppm	1156	1104	1113	1155	1122	1176	1161	1187	1142	1121	1120	1172	1175	1119	1113	1121	1123	1169	1148	1125	1148	1029
Mo	ppm	1.5	1.3	1.5	1.6	1.4	1.5	1.6	1.5	1.3	1.5	1.4	1.5	1.4	1.6	1.5	1.6	1.5	1.6	1.5	1.5	1.5	1.2
Na	%	2.39	2.26	2.34	2.40	2.25	2.38	2.42	2.50	2.39	2.40	2.40	2.39	2.39	2.43	2.34	2.30	2.32	2.40	2.33	2.06	2.41	2.23
Nb	ppm	21.3	18.5	22.5	22.2	21.6	21.0	22.6	23.4	21.8	20.8	21.6	21.4	21.3	20.4	22.5	21.4	20.4	21.7	21.9	20.0	22.1	19.2
Ni	ppm	150.6	144.4	153.6	154.8	148.1	149.2	162.8	161.7	150.7	145.5	149.2	150.9	141.1	145.0	153.6	152.1	150.3	146.4	142.5	154.6	155.6	131.0
P	%	0.148	0.141	0.134	0.144	0.127	0.150	0.148	0.146	0.144	0.145	0.135	0.138	0.145	0.147	0.134	0.140	0.131	0.134	0.138	0.137	0.149	0.130
Pb	ppm	3.1	3.8	3.1	3.2	2.8	3.1	2.8	1.9	2.9	2.7	3.8	2.8	2.8	3.2	3.1	2.9	3.1	3.0	3.0	3.1	2.6	2.6
Rb	ppm	24.6	20.8	20.0	22.7	18.6	24.2	21.4	28.5	21.6	20.4	22.7	22.6	23.3	23.2	20.0	23.2	21.9	25.0	21.9	22.1	19.2	21.2
S	%	<0.1	<0.1	<0.1	<0.1	<0.1	<0.1	<0.1	<0.1	<0.1	<0.1	<0.1	<0.1	<0.1	<0.1	<0.1	<0.1	<0.1	<0.1	<0.1	<0.1	<0.1	<0.1
Sb	ppm	0.1	0.2	0.1	<0.1	<0.1	0.1	<0.1	<0.1	<0.1	<0.1	0.2	<0.1	0.1	<0.1	0.1	<0.1	0.1	<0.1	<0.1	<0.1	<0.1	<0.1
Sc	ppm	21	20	18	21	20	22	21	22	21	21	21	21	21	22	18	20	20	21	21	20	21	18
Sn	ppm	2.0	1.7	1.7	1.5	1.5	1.9	1.8	1.6	1.8	1.5	1.9	1.5	1.6	1.7	1.7	1.7	1.8	1.9	1.9	1.5	1.7	1.5
Sr	ppm	407	353	406	415	390	403	411	417	409	399	422	381	378	382	406	390	386	407	386	364	447	357
Ta	ppm	1.1	1.0	1.1	1.1	1.1	1.0	1.0	1.1	1.1	1.0	1.2	1.0	1.1	1.1	1.1	1.1	1.1	1.1	1.0	1.0	1.1	0.9
Th	ppm	3.2	3.0	2.6	3.2	2.6	2.9	2.7	2.9	3.2	2.6	3.4	2.6	2.9	3.0	2.6	2.9	2.7	3.1	3.1	2.9	2.7	2.4
Ti	%	1.08	1.03	1.14	1.10	1.05	1.08	1.12	1.16	1.08	1.11	1.12	1.04	1.04	1.13	1.14	1.03	1.05	1.07	1.06	1.04	1.14	0.96
U	ppm	0.8	0.7	0.6	0.8	0.7	0.7	0.6	0.8	0.8	0.7	0.9	0.6	0.7	0.8	0.6	0.6	0.8	0.8	0.8	0.7	0.6	0.6
V	ppm	170	156	171	168	160	167	174	177	165	169	164	166	164	170	171	160	160	168	165	158	176	149

STD OREAS24P

Élément	Unité	Analyses																						
W	ppm	0.6	0.5	0.5	0.5	0.4	0.4	0.5	0.4	0.4	0.3	0.5	0.3	0.5	0.6	0.5	0.5	0.6	0.4	0.5	0.5	0.4	0.4	
Y	ppm	23.8	21.5	20.7	23.1	19.3	23.5	20.9	23.1	23.7	20.9	24.2	21.5	24.7	22.8	20.7	25.1	24.6	26.0	25.0	23.6	19.8	17.5	
Zn	ppm	120	116	116	118	108	122	121	126	116	109	122	116	119	116	116	115	118	125	119	116	125	99	
Zr	ppm	147	132	148	146	141	144	153	148	144	134	148	144	139	136	148	138	143	140	144	133	143	128	

STD OREAS45P

Élément	Unité	Analyses																						
Ag	ppm	0.3	0.3	0.3	0.3	0.3	0.3	0.3	0.3	0.3	0.4	0.3	0.3	0.3	0.4	0.3	0.3	0.3	0.3	0.3	0.3	0.3	0.3	0.3
Al	%	6.68	7.12	6.96	6.85	7.19	7.39	6.97	7.18	6.89	6.95	7.12	7.15	7.19	7.02	7.00	6.96	6.89	6.87	6.88	6.92	6.86	7.22	6.76
As	ppm	12	13	10	12	11	12	13	12	13	8	12	11	12	13	11	10	11	12	12	11	11	12	11
Au	ppm	<0.1	<0.1	<0.1	<0.1	<0.1	<0.1	<0.1	<0.1	<0.1	<0.1	<0.1	<0.1	<0.1	<0.1	<0.1	<0.1	<0.1	<0.1	<0.1	<0.1	<0.1	<0.1	<0.1
Ba	ppm	279	302	275	295	262	307	298	292	304	289	300	291	313	292	272	275	286	281	309	324	270	329	286
Be	ppm	<1	1	<1	<1	<1	<1	1	1	<1	<1	<1	<1	<1	<1	<1	<1	<1	1	<1	1	<1	<1	<1
Bi	ppm	0.2	0.4	0.2	0.2	0.2	0.3	0.2	0.2	0.3	0.5	0.3	0.2	0.3	0.6	0.3	0.2	0.3	0.3	0.2	0.6	0.3	0.2	0.2
Ca	%	0.27	0.30	0.29	0.26	0.28	0.31	0.28	0.30	0.27	0.28	0.27	0.29	0.29	0.29	0.29	0.29	0.29	0.28	0.28	0.28	0.29	0.28	0.28
Cd	ppm	0.2	0.2	0.2	<0.1	0.1	0.2	0.2	0.1	<0.1	0.1	0.2	0.1	0.2	0.2	0.1	0.2	0.2	0.2	0.2	0.2	0.1	0.2	0.1
Ce	ppm	50	50	44	52	45	51	49	48	49	49	51	51	50	50	45	44	48	50	51	50	47	49	47
Co	ppm	123	128	110	125	112	129	124	130	122	123	112	127	124	126	115	110	125	123	120	123	123	124	120
Cr	ppm	1057	1110	1058	1074	1092	1156	1094	1123	1037	1115	1061	1104	1074	1122	1136	1058	1018	1068	1077	1109	1081	1150	1071
Cu	ppm	707	734	712	726	732	768	734	740	730	742	714	746	726	749	747	712	728	730	728	737	722	776	712
Fe	%	18.94	18.97	17.85	19.74	19.27	20.26	18.56	19.54	19.63	18.21	18.83	18.63	18.93	18.29	18.52	17.85	18.54	18.33	18.20	18.86	18.48	19.05	17.54
Hf	ppm	4.1	4.3	4.1	4.0	3.9	4.1	4.1	4.0	4.1	3.8	4.0	3.7	4.1	4.4	4.2	4.1	3.9	4.0	3.9	4.4	3.8	4.3	3.8
K	%	0.33	0.37	0.34	0.34	0.35	0.36	0.35	0.35	0.33	0.35	0.34	0.36	0.35	0.36	0.34	0.34	0.33	0.34	0.33	0.34	0.32	0.38	0.34
La	ppm	27.7	26.5	22.3	29.0	22.0	25.9	22.3	23.8	27.7	24.4	26.2	25.6	27.4	26.7	22.0	22.3	25.9	25.2	26.6	26.8	25.4	24.5	23.6
Li	ppm	14.7	16.4	13.8	14.6	15.0	16.9	15.7	14.3	15.8	14.7	13.2	14.8	16.4	16.8	13.0	13.8	15.6	14.8	12.6	15.7	13.7	15.7	14.0
Mg	%	0.19	0.22	0.15	0.19	0.16	0.22	0.18	0.19	0.20	0.18	0.18	0.19	0.22	0.22	0.15	0.15	0.21	0.21	0.22	0.22	0.22	0.20	0.19
Mn	ppm	1302	1355	1273	1343	1359	1418	1321	1405	1331	1334	1301	1349	1356	1326	1334	1273	1343	1342	1314	1361	1315	1373	1299
Mo	ppm	2.1	2.1	2.0	2.3	2.2	2.1	2.0	2.0	2.0	2.1	2.2	1.9	2.1	2.1	2.2	2.0	2.1	2.1	2.1	1.9	2.1	2.1	1.8
Na	%	0.068	0.092	0.078	0.072	0.082	0.091	0.077	0.083	0.076	0.080	0.067	0.081	0.087	0.087	0.076	0.078	0.082	0.078	0.093	0.088	0.068	0.084	0.081
Nb	ppm	21.6	20.1	21.2	21.1	21.5	21.2	22.0	21.6	20.5	20.3	19.4	20.6	21.5	21.1	22.9	21.2	20.3	21.5	19.9	22.4	20.1	21.5	19.6
Ni	ppm	383	395	392	399	393	412	409	412	396	415	381	398	390	410	414	392	390	391	390	391	384	436	392
P	%	0.044	0.049	0.041	0.045	0.044	0.053	0.050	0.046	0.045	0.048	0.043	0.044	0.047	0.047	0.041	0.041	0.044	0.046	0.046	0.046	0.043	0.044	0.046
Pb	ppm	21.4	24.6	18.8	22.8	19.4	21.8	20.7	20.1	22.9	19.9	24.8	20.5	23.8	23.5	18.6	18.8	22.4	21.9	21.7	24.3	21.5	20.0	21.1
Rb	ppm	23.2	26.2	22.0	23.8	22.3	26.4	21.4	24.9	23.8	23.1	24.4	21.8	26.9	27.3	21.8	22.0	25.2	23.9	25.3	26.4	23.4	20.7	24.9
S	%	<0.1	<0.1	<0.1	<0.1	<0.1	<0.1	<0.1	<0.1	<0.1	<0.1	<0.1	<0.1	<0.1	<0.1	<0.1	<0.1	<0.1	<0.1	<0.1	<0.1	<0.1	<0.1	<0.1
Sb	ppm	1.0	0.9	0.8	0.9	0.7	0.9	0.8	0.8	0.8	0.8	0.8	0.7	0.8	0.8	0.9	0.8	0.8	0.8	0.8	1.0	0.8	0.7	0.8
Sc	ppm	71	70	58	73	71	73	69	79	73	71	71	71	69	73	73	58	67	67	68	66	68	72	65
Sn	ppm	2.6	2.6	2.1	2.7	2.1	2.4	2.6	2.9	2.5	2.5	2.3	2.5	2.6	2.5	2.3	2.1	2.8	2.5	2.8	3.0	2.4	2.9	2.4

STD OREAS45P

Élément	Unité	Analyses																							
Sr	ppm	34	36	31	35	32	36	30	34	34	34	37	33	37	38	32	31	36	36	36	37	35	35	34
Ta	ppm	1.1	1.2	1.1	1.1	1.1	1.3	1.2	1.2	1.1	1.1	1.1	1.1	1.2	1.3	1.1	1.1	1.1	1.1	1.1	1.3	1.1	1.1	1.1
Th	ppm	10.9	10.7	8.8	11.1	8.9	10.6	9.0	9.1	11.3	8.7	11.6	8.7	10.5	10.7	8.6	8.8	10.2	10.3	10.6	11.4	10.3	9.5	9.2
Ti	%	1.04	1.02	1.03	1.04	1.03	1.09	1.04	1.12	1.05	1.10	1.02	1.01	1.02	1.03	1.07	1.03	0.99	1.05	0.98	1.06	0.99	1.08	0.98
U	ppm	2.3	2.4	1.9	2.5	2.0	2.4	2.2	2.2	2.4	2.0	2.6	2.1	2.4	2.5	2.0	1.9	2.1	2.2	2.3	2.5	2.7	2.3	2.1
V	ppm	275	273	272	282	275	294	276	292	274	281	257	272	273	280	282	272	262	268	272	276	259	290	256
W	ppm	1.0	1.2	1.1	1.1	0.9	1.0	1.0	1.1	1.2	1.0	1.4	1.2	1.2	1.0	1.2	1.1	0.8	1.0	1.0	1.2	0.9	1.0	1.0
Y	ppm	13.3	14.0	12.1	14.0	12.8	14.4	12.1	13.4	13.7	13.0	14.2	13.6	15.5	14.1	12.8	12.1	15.2	14.9	15.0	14.8	14.1	12.7	12.8
Zn	ppm	140	150	134	142	138	154	143	144	146	139	139	137	150	149	143	134	148	143	150	147	143	147	141
Zr	ppm	157	155	160	160	177	157	160	154	151	151	151	154	158	161	168	160	149	155	145	161	149	156	151

STD OREAS24P

Élément	Moyenne	SD	2SD	Précision	Recommandée	95% confiance (min)	95% confiance (max)
Ag					± 0.1		
Al	7.98	0.28	0.6	1.03			
As	1	0.50	1.0	1.39	2.0	0.7	3.4
Au							
Ba	289	16.03	32.1	1.05			
Be							
Bi					< 0.05		
Ca	5.94	0.24	0.5	1.04			
Cd	0.2	0.06	0.1	1.35	< 0.3		
Ce	37	2.31	4.6	1.06			
Co	47.1	2.17	4.3	1.04	44.0	41.5	46.4
Cr	202	11.97	23.9	1.05	221	191	250
Cu	51.9	3.70	7.4	1.07	52.0	44.0	60.0
Fe	7.70	0.30	0.6	1.04			
Hf	3.7	0.21	0.4	1.05			
K	0.67	0.02	0.0	1.03			
La	18.9	1.57	3.1	1.08			
Li	8.3	0.97	1.9	1.11			
Mg	4.13	0.15	0.3	1.03			
Mn	1136	34.38	68.8	1.03			
Mo	1.5	0.11	0.2	1.07			
Na	2.35	0.09	0.2	1.04			
Nb	21.3	1.14	2.3	1.05			
Ni	149.7	6.89	13.8	1.04	141	138	145
P	0.140	0.01	0.0	1.04			
Pb	3.0	0.39	0.8	1.12	2.9	2.6	3.1
Rb	22.2	2.18	4.4	1.09			
S							
Sb	0.1	0.05	0.1	1.39	0.14	0.02	0.26
Sc	21	1.19	2.4	1.05			
Sn	1.7	0.16	0.3	1.09			
Sr	396	22.24	44.5	1.05			
Ta	1.1	0.07	0.1	1.06			
Th	2.9	0.26	0.5	1.08			
Ti	1.08	0.05	0.1	1.04			
U	0.7	0.09	0.2	1.12			
V	166	6.74	13.5	1.04			

STD OREAS24P

Élément	Moyenne	SD	2SD	Précision	Recommandée	95% confiance (min)	95% confiance (max)
W	0.5	0.08	0.2	1.18			
Y	22.5	2.18	4.4	1.09			
Zn	117	6.07	12.1	1.05	114	112	117
Zr	142	6.14	12.3	1.04			

STD OREAS45P

Élément	Moyenne	SD	2SD	Précision	Recommandée	95% confiance (min)	95% confiance (max)
Ag	0.3	0.03	0.1	1.08	0.32	0.27	0.36
Al	7.00	0.17	0.3	1.02			
As	12	1.16	2.3	1.09	13.4	11.9	14.86
Au							
Ba	293	17.09	34.2	1.05			
Be	1	0.00	0.0	1.00			
Bi	0.3	0.12	0.2	1.45			
Ca	0.28	0.01	0.0	1.03			
Cd	0.2	0.05	0.1	1.29	< 0.2		
Ce	49	2.34	4.7	1.04			
Co	122	6.06	12.1	1.04	120	113	127
Cr	1089	35.25	70.5	1.03	1103	1065	1141
Cu	733	17.22	34.4	1.02	749	740	759
Fe	18.74	0.66	1.3	1.03			
Hf	4.0	0.19	0.4	1.04			
K	0.35	0.01	0.0	1.04			
La	25.2	2.06	4.1	1.07			
Li	14.9	1.21	2.4	1.07			
Mg	0.19	0.02	0.0	1.11			
Mn	1336	35.70	71.4	1.02			
Mo	2.1	0.11	0.2	1.05			
Na	0.080	0.01	0.0	1.08			
Nb	21.0	0.88	1.8	1.04			
Ni	398	13.13	26.3	1.03	385	369	401
P	0.045	0.00	0.0	1.06			
Pb	21.5	1.89	3.8	1.08	22	22	23
Rb	24.0	1.91	3.8	1.07			
S							
Sb	0.8	0.08	0.2	1.09	0.92	0.83	1.01
Sc	69	4.69	9.4	1.06			
Sn	2.5	0.25	0.5	1.09			

STD OREAS45P

Élément	Moyenne	SD	2SD	Précision	Recommandée	95% confiance (min)	95% confiance (max)
Sr	**34**	2.17	4.3	**1.06**			
Ta	**1.1**	0.07	0.1	**1.06**			
Th	**10.0**	1.01	2.0	**1.09**			
Ti	**1.04**	0.04	0.1	**1.03**			
U	**2.3**	0.23	0.5	**1.09**			
V	**274**	10.08	20.2	**1.03**			
W	**1.1**	0.13	0.3	**1.11**			
Y	**13.7**	1.02	2.0	**1.07**			
Zn	**144**	5.37	10.7	**1.03**	**141**	**136**	**146**
Zr	**157**	6.77	13.5	**1.04**			

Standards analysés à ACME Lab par la méthode 2AF

	STD STSD-1																
F (ppm)	940	900	940	960	950	970	955	865	885	955	900	970	850	880	830	920	850
	870	1010	930	850	950	940	980	960	900	970	918	898	893	923			
Moyenne	920																
SD	45																
2SD	91																
Precision	1.04																

Standards analysés à ALS par la méthode F-ELE81a

	SARM-1								
F (ppm)	4130	4190	4150	4160	4180	4100	4140	4170	4050
Moyenne	4141								
SD	44								
2SD	87								
Precision	1.02								
Certifiée	4200								

	SARM-3										
F (ppm)	4230	4130	4140	4070	4130	4160	4080	3990	4230	4090	3990
Moyenne	4113										
SD	80										
2SD	161										
Precision	1.03										
Certifiée	4400										

	STSD-1	
F (ppm)	1000	1050
Moyenne	1025	
Mesurée	950	

ANNEXE - 2 : ÉCHANTILLONS UTILISÉS ET ANALYSES REPRÉSENTATIVES POUR LE CHAPITRE 2 : ROCHES INTRUSIVES ET VOLCANIQUES DU SUD DE LA ZONE MAGMATIQUE DU GRAND LAC DE L'OURS

Les minéraux sont abbrégés suivant Whitney et Evans (2010) sauf Qtz pour quartz.

Sample	Rock type	Pearce (1996)	Location	Alteration	Alteration intensity	Sample classification
09CQA-0003A03	Monzodioritic Fp-phyric porphyry	Andesite/Basalt	Mazenod - East of Sue-Dianne	HT Ca-Fe	Mild	Dianne subassemblage
09CQA-0003D03	Fp-phyric andesite	Andesite/Basalt	Mazenod - East of Sue-Dianne	K/LT Ca-Fe	Mild	Dianne subassemblage
09CQA-0004A03	Aphanitic rhyolite	Rhyolite/dacite	Mazenod - South of Sue-Dianne	K	Mild	Mazenod Assemblage-27
09CQA-0005A03	Fp-phyric rhyolite	Rhyolite/dacite	Mazenod - South of Sue-Dianne	Na	Moderate	Mazenod Assemblage-29
09CQA-0006A03	Fp–Qtz-phyric rhyolite	Rhyolite/dacite	Mazenod - South of Sue-Dianne	Weakly altered	N.A.	Mazenod Assemblage-31
09CQA-0007A03	Fp-phyric porphyry	Rhyolite/dacite	Mazenod - North of Sue-Dianne	Weakly altered	N.A.	Bea Assemblage-35
09CQA-0008A02	Fp-phyric rhyolite	Alkali Rhyolite	Lou - NICO deposit vicinity	K	Moderate	Lou Assemblage-13
09CQA-0009A03	Ampp–Fp-phyric porphyry	Andesite/Basalt	Mazenod - East of Sue-Dianne	HT Ca-Fe	Mild	Dianne subassemblage - Primitive andesite
09CQA-0011A03	Aphanitic andesite	Andesite/Basalt	Mazenod - East of Sue-Dianne	HT K-Fe	Moderate	Dianne subassemblage - Primitive andesite
09CQA-0011B02	Monzonite	Trachyte	Mazenod - East of Sue-Dianne	Weakly altered	N.A.	Marian River batholith
09CQA-0012A02	Fp-phyric porphyry	Andesite/Basalt	Mazenod - East of Sue-Dianne	K	Mild	Dianne subassemblage
09CQA-0012B02	Fp-phyric dacite	Rhyolite/dacite	Mazenod - East of Sue-Dianne	K	Mild	Dianne subassemblage
09CQA-0012C02	Fp-phyric dacite	Rhyolite/dacite	Mazenod - East of Sue-Dianne	K	Mild	Dianne subassemblage
09CQA-0013A03	Aphanitic andesite	Andesite/Basalt	Mazenod - East of Sue-Dianne	Weakly altered	N.A.	Dianne subassemblage - Primitive andesite
09CQA-0014A03	Monzonite	Andesite/Basalt	Eastern Treasure Lake - Ron	K	Mild	Marian River batholith
09CQA-0026B02	Aphanitic dacite	Rhyolite/dacite	Mazenod - Brooke	HT K-Fe	Moderate	Dianne subassemblage
09CQA-0026C03	Fp-phyric dacite	Rhyolite/dacite	Mazenod - Brooke	K	Moderate	Dianne subassemblage
09CQA-0026C05	Fp-phyric dacite	Rhyolite/dacite	Mazenod - Brooke	K	Strong	Dianne subassemblage
09CQA-0028A03	Fp–Qtz-phyric andesite	Andesite/Basalt	Mazenod - Brooke	Silicification	Moderate	Dianne subassemblage
09CQA-0034A03	Leucocratic granite	Alkali Rhyolite	Eastern Treasure Lake - Carbonate Mountain	Na	Intense	Granite-leucogranite
09CQA-0034B03	Leucocratic granite	Alkali Rhyolite	Eastern Treasure Lake - Carbonate Mountain	Na/K	Intense	Granite-leucogranite
09CQA-0039D03	Monzonite	Andesite/Basalt	Eastern Treasure Lake - Hump zone	LT K-Fe	Mild	Granitic intrusions, undivided
09CQA-0046C02	Qtz syenite	Rhyolite/dacite	Eastern Treasure Lake - Esther	LT Ca-Fe/K	Strong	U-Th rich monzonitic granite
09CQA-0046D03	Qtz syenite	Rhyolite/dacite	Eastern Treasure Lake - Esther	K	Strong	U-Th rich monzonitic granite
09CQA-0047B02	Porphyritic granite	Alkali Rhyolite	Eastern Treasure Lake - Carbonate Mountain	Na	Intense	Granite-leucogranite
09CQA-0049E03	Monzonite	Rhyolite/dacite	Eastern Treasure Lake - Hump zone	K	Mild	Granitic intrusions, undivided
09CQA-0081A02	Monzonite	Rhyolite/dacite	South Lou - North of Duke	K	Mild	Marian River batholith
09CQA-0082A02	Monzonite	Rhyolite/dacite	South Lou - North of Duke	K	Mild	Marian River batholith

Sample	Rock type	Pearce (1996)	Location	Alteration	Alteration intensity	Sample classification
09CQA-0091A03	Aphanitic rhyolite	Rhyolite/dacite	Cole	K/LT Ca-Fe	Moderate	Cole assemblage - Volcanic rock
09CQA-0092A03	Fp-phyric intermediate volcanic rock	Andesite/Basalt	Cole	K/Na	Mild	Cole assemblage - Volcanic rock
09CQA-0095A03	Breccia andesitic	Andesite/Basalt	Cole - Vicinity Cole Breccia	Na-HT Ca-Fe	Strong	Cole Assemblage - Andesite
09CQA-0095F02	Breccia andesitic	Andesite/Basalt	Cole - Cole breccia	Na-HT Ca-Fe	Strong	Cole Assemblage - Andesite
09CQA-0095F08	Breccia andesitic	Andesite/Basalt	Cole - Cole breccia	Na-HT Ca-Fe	Strong	Cole Assemblage - Andesite
09CQA-0098D03	Monzonite dyke	Trachyte	Cole - Cole breccia	K	Moderate	U-Th rich monzonitic granite
09CQA-0103C02	Monzodioritic Fp-phyric porphyry	Andesite/Basalt	Cole - Cole breccia	Na-HT Ca-Fe	Mild	Cole assemblage - Qtz monzonite-Monzodiorite
09CQA-0104A02	Monzonitic Fp-phyric porphyry	Andesite/Basalt	Mazenod - North of Sue-Dianne	Weakly altered	N.A.	Porphyritic intrusions, undivided
09CQA-0104B02	Monzonitic Fp-phyric porphyry	Andesite/Basalt	Mazenod - North of Sue-Dianne	Weakly altered	N.A.	Porphyritic intrusions, undivided
09CQA-0109A03	Fp-phyric dacite	Rhyolite/dacite	Mazenod - Brooke	K	Weak	Dianne subassemblage
09CQA-0109B02	Fp-phyric dacite	Rhyolite/dacite	Mazenod - Brooke	K	Mild	Dianne subassemblage
09CQA-0109C03	Fp-phyric rhyolite	Trachy-andesite	Mazenod - Brooke	K	Strong	Dianne subassemblage
09CQA-0127C03	Fp–Bt-phyric rhyolite	Rhyolite/dacite	Lou - North of Lou Lake	LT K-Fe	Strong	Lou Assemblage-14
09CQA-0127G02	Bt–Fp-phyric rhyolite	Rhyolite/dacite	Lou - North of Lou Lake	LT K-Fe	Mild	Lou Assemblage-14
09CQA-1006A03	Qtz–Fp-phyric porphyry	Trachy-andesite	Mazenod - Sue-Dianne deposit vicinity	Na/Si	Moderate	Mazenod Assemblage - Sue-Dianne deposit unit
09CQA-1006D03	Qtz–Fp-phyric porphyry	Andesite/Basalt	Mazenod - Sue-Dianne deposit vicinity	HT K-Fe	Moderate	Mazenod Assemblage - Sue-Dianne deposit unit
09CQA-1006E01	Qtz–Fp-phyric porphyry	Trachy-andesite	Mazenod - Sue-Dianne deposit vicinity	Na/LT K-Fe	Moderate	Mazenod Assemblage - Sue-Dianne deposit unit
09CQA-1007A03	Fp–Qtz porphyry	Andesite/Basalt	Mazenod - Sue-Dianne deposit vicinity	Silicification	Unknown	Mazenod Assemblage - Sue-Dianne deposit unit
09CQA-1008A03	Fp–Qtz porphyry	Trachy-andesite	Mazenod - Sue-Dianne deposit vicinity	HT K-Fe	Moderate	Mazenod Assemblage - Sue-Dianne deposit unit
09CQA-1008B03	Fp–Qtz porphyry	Trachy-andesite	Mazenod - Sue-Dianne deposit vicinity	Na/HT Ca-Fe	Moderate	Mazenod Assemblage - Sue-Dianne deposit unit
09CQA-1008C02	Fp–Qtz porphyry	Trachy-andesite	Mazenod - Sue-Dianne deposit vicinity	Na/HT Ca-Fe	Moderate	Mazenod Assemblage - Sue-Dianne deposit unit
09CQA-1008D03	Fp–Qtz porphyry	Trachy-andesite	Mazenod - Sue-Dianne deposit vicinity	Na/HT Ca-Fe	Moderate	Mazenod Assemblage - Sue-Dianne deposit unit
09CQA-1010A03	Coarse-grained Qtz monzonite	Andesite/Basalt	East Mazenod - East Sue Dianne	Weakly altered	N.A.	U-Th rich monzonitic granite
09CQA-1011A02	Coarse-grained monzonite (1866 Ma)	Andesite/Basalt	East Mazenod - East Sue Dianne	K	Mild	Marian River batholith
09CQA-1012D02	Monzonite	Trachyte	Mazenod - East of Sue-Dianne	LT K-Fe	Moderate	Marian River batholith

Sample	Rock type	Pearce (1996)	Location	Alteration	Alteration intensity	Sample classification
09CQA-1015A03	Fp-phyric porphyry	Andesite/Basalt	Mazenod - South of Brooke	Weakly altered	N.A.	Porphyritic intrusions, undivided
09CQA-1025A02	Intermediate volcanic rock	Trachy-andesite	Mazenod - Sue-Dianne deposit vicinity	HT Ca-Fe/K	Moderate	Mazenod Assemblage - Sue-Dianne deposit unit
09CQA-1028D03	Granitic foliated	Rhyolite/dacite	Eastern Treasure Lake - Hump zone	K	Moderate	Granitic intrusions, undivided
09CQA-1033A02	Fp-phyric andesite	Andesite/Basalt	Mazenod - East of Sue-Dianne	K	Mild	Dianne subassemblage
09CQA-1034A02	Fp-phyric andesite	Andesite/Basalt	Mazenod - East of Sue-Dianne	K	Mild	Dianne subassemblage
09CQA-1035B02	Fp-phyric andesite	Andesite/Basalt	Mazenod - East of Sue-Dianne	LT Ca-Fe	Moderate	Dianne subassemblage
09CQA-1035D02	Fp-phyric andesite	Andesite/Basalt	Mazenod - East of Sue-Dianne	K	Moderate	Dianne subassemblage
09CQA-1036B02	Fp-phyric andesite	Andesite/Basalt	Mazenod - East of Sue-Dianne	K	Mild	Dianne subassemblage
09CQA-1037B03	Fp-phyric andesite	Andesite/Basalt	Mazenod - East of Sue-Dianne	K	Mild	Dianne subassemblage
09CQA-1038A02	Fp-phyric andesite	Andesite/Basalt	Mazenod - South of Sue-Dianne	K	Weak	Mazenod Assemblage-24
09CQA-1041A02	Fp-phyric andesite	Andesite/Basalt	Mazenod - South of Sue-Dianne	K	Mild	Mazenod Assemblage-25
09CQA-1043A03	Lapilli tuff trachytic	Trachyte	Mazenod - South of Sue-Dianne	K	Moderate	Mazenod Assemblage-26
09CQA-1044A03	Fp-phyric dacite	Rhyolite/dacite	Mazenod - South of Sue-Dianne	K	Weak	Mazenod Assemblage-26
09CQA-1047A03	Bt–Fp-phyric porphyry	Andesite/Basalt	Lou - North of Lou Lake	K	Weak	Bea Assemblage-35
09CQA-1048A02	Bt–Fp-phyric porphyry	Andesite/Basalt	Lou - North of Lou Lake	K	Weak	Bea Assemblage-35
09CQA-1051A02	Bt–Fp-phyric porphyry	Andesite/Basalt	Lou - North of Lou Lake	K	Mild	Bea Assemblage-35
09CQA-1052A02	Fp–Bt-phyric porphyry	Andesite/Basalt	Lou - North of Lou Lake	K	Mild	Bea Assemblage-35
09CQA-1054A02	Fp-phyric Porphyry	Andesite/Basalt	Lou - North of Lou Lake	K	Weak	Bea Assemblage-35
09CQA-1055A02	Felsic tuff	Rhyolite/dacite	Lou - North of Lou Lake	Silicification	Moderate	Bea Assemblage-35a
09CQA-1055B02	Fp-phyric porphyry	Andesite/Basalt	Lou - North of Lou Lake	K	Mild	Bea Assemblage-35
09CQA-1057E02	Fp–Bt-phyric rhyolite	Rhyolite/dacite	Lou - North of Lou Lake	Silicification	Strong	Lou Assemblage-15
09CQA-1070A03	Fp–Hbl-phyric andesite	Andesite/Basalt	Cole	HT Ca-Fe	Mild	Cole Assemblage - Andesite
09CQA-1070B03	Monzonite dyke	Rhyolite/dacite	Cole	K	Mild	U-Th rich monzonitic granite
09CQA-1071A03	Fp–Hbl-phyric felsic volcanic rock	Rhyolite/dacite	Cole	K	Mild	Cole assemblage - Volcanic rock
09CQA-1073A03	Monzonite dyke	Rhyolite/dacite	Cole	K	Mild	U-Th rich monzonitic granite
09CQA-1074A02	Aphanitic andesite	Andesite/Basalt	Cole - Vicinity Cole Breccia	Weakly altered	N.A.	Cole assemblage - Volcanic rock
09CQA-1074B02	Fp–phyric felsic volcanic rock	Rhyolite/dacite	Cole - Vicinity Cole Breccia	K	Unknown	Cole assemblage - Volcanic rock
09CQA-1080C02	Monzonite	Rhyolite/dacite	Cole	K	Strong	Granitic intrusions, undivided
09CQA-1080D02	Monzonite	Rhyolite/dacite	Cole	Na/K	Moderate	Granitic intrusions, undivided

Sample	Rock type	Pearce (1996)	Location	Alteration	Alteration intensity	Sample classification
09CQA-1088A02	Fp–Bt-phyric andesite	Andesite/Basalt	South Lou - South of Duke	K	Mild	Porphyritic intrusions, Lou system
09CQA-1096B02	Granitic	Andesite/Basalt	South Lou - Peanut	Na/ K (HT)	Moderate	Granitic intrusions, undivided
09CQA-1097A02	Bt-rich granite	Andesite/Basalt	South Lou - Peanut	K/HT K-Fe	Strong	Porphyritic intrusions, Bt phyric porphyry
09CQA-1098A02	Aphanitic rhyolite	Rhyolite/dacite	South Lou - Peanut	K	Strong	Undivided volcanic/intrusive rocks Western section
09CQA-1098A04	Aphanitic rhyolite	Rhyolite/dacite	South Lou - Peanut	K	Strong	Undivided volcanic/intrusive rocks Western section
09CQA-1102-B2	Granitic	Rhyolite/dacite	South Lou - Peanut	K	Mild	U-Th rich monzonitic granite
09CQA-1103A02	Aphanitic andesite	Andesite/Basalt	South Lou - Peanut	HT K-Fe	Moderate	Porphyritic intrusions, Bt phyric porphyry
09CQA-1106A02	Fp–Bt-phyric andesite	Andesite/Basalt	South Lou - Peanut	Na-Ca-Fe	Mild	Porphyritic intrusions, Bt phyric porphyry
09CQA-1107A02	Bt–Fp-phyric porphyry	Andesite/Basalt	South Lou - Peanut	K	Weak	Porphyritic intrusions, Lou system
09CQA-1109A02	Granitic	Trachyte	South Lou - Sunil	K/Silicification	Weak	Undivided volcanic/intrusive rocks Western section
09CQA-1109C02	Aphanitic rhyolite	Alkali Rhyolite	South Lou - Sunil	K	Mild	Undivided volcanic/intrusive rocks Western section
09CQA-1110A02	Aphanitic rhyolite	Alkali Rhyolite	South Lou - Sunil	K	Strong	Undivided volcanic/intrusive rocks Western section
09CQA-1119A02	Fp–Bt-phyric porphyry	Andesite/Basalt	Eastern Treasure Lake - South Dennis	Weakly altered	N.A.	Diorite-38
09CQA-1119C02	Qtz monzonite	Rhyolite/dacite	Eastern Treasure Lake - South Dennis	K	Mild	Diorite-38
09CQA-1123A02	Monzodiorite	Andesite/Basalt	Cole - Vicinity Cole Breccia	Na-HT Ca-Fe	Mild	Cole assemblage - Qtz monzonite-Monzodiorite
09CQA-1123A04	Monzonitic Fp-phyric porphyry	Rhyolite/dacite	Cole - Vicinity Cole Breccia	K	Mild	Cole assemblage - Qtz monzonite-Monzodiorite
09CQA-1123B03	Monzodioritic Fp-phyric porphyry	Andesite/Basalt	Cole - Vicinity Cole Breccia	Na-HT Ca-Fe/K	Weak	Cole assemblage - Qtz monzonite-Monzodiorite
09CQA-1123-B2	Monzodioritic Fp-phyric porphyry	Andesite/Basalt	Cole - Vicinity Cole Breccia	Na-HT Ca-Fe/K	Moderate	Cole assemblage - Qtz monzonite-Monzodiorite
09CQA-1123-B5	Monzodioritic Fp-phyric porphyry	Andesite/Basalt	Cole - Vicinity Cole Breccia	HT Ca-Fe/K	Mild	Cole assemblage - Qtz monzonite-Monzodiorite
09CQA-1123-C3	Fp-phyric andesite	Andesite/Basalt	Cole - Vicinity Cole Breccia	HT Ca-Fe/K	Moderate	Cole assemblage - Qtz monzonite-Monzodiorite
09CQA-1123I02	Monzonite	Rhyolite/dacite	Cole - Vicinity Cole Breccia	Na/K	Mild	Granitic intrusions, undivided
09CQA-1124A02	Bt–Fp-phyric intermediate porphyritic rock	Andesite/Basalt	Eastern Treasure Lake - Hump assemblage	K	Weak	Hump assemblage - Undivided volcanic/intrusive rocks
09CQA-1125A03	Fp–Bt-phyric andesite	Andesite/Basalt	Eastern Treasure Lake - Hump assemblage	K	Weak	Hump assemblage - Undivided volcanic/intrusive rocks
09CQA-1125A05	Fp–Bt-phyric andesite	Andesite/Basalt	Eastern Treasure Lake - Hump assemblage	K	Weak	Hump assemblage - Undivided volcanic/intrusive rocks
09CQA-1126A02	Fp-phyric basalt	Basalt	Eastern Treasure Lake - Hump assemblage	K	Moderate	Hump assemblage - Undivided volcanic/intrusive rocks
09CQA-1126B02	Fp–Bt porphyritic rock	Andesite/Basalt	Eastern Treasure Lake - Hump assemblage	K	Mild	Hump assemblage - Undivided volcanic/intrusive rocks

Sample	Rock type	Pearce (1996)	Location	Alteration	Alteration intensity	Sample classification
09CQA-1127F02	Fp-phyric basalt	Basalt	Eastern Treasure Lake - Hump assemblage	K	Mild	Hump assemblage - Undivided volcanic/intrusive rocks
09CQA-1128A02	Felsic tuff	Rhyolite/dacite	Eastern Treasure Lake - Hump assemblage	K	Moderate	Hump assemblage - Undivided volcanic/intrusive rocks
09CQA-1132-A2	Monzonitic Fp-phyric porphyry	Andesite/Basalt	Eastern Treasure Lake - West of Hump Lake	Na	Strong	Undivided volcanic/intrusive rocks Eastern section
09CQA-1132-B2	Mafic volcanic rock	Basalt	Eastern Treasure Lake - West of Hump Lake	Na/HT Ca-Fe	Moderate	Hump assemblage - Undivided volcanic/intrusive rocks
09CQA-1138-A03	Qtz–Fp–Bt-phyric porphyry	Andesite/Basalt	Lou - Southern Breccia	K	Moderate	Porphyritic intrusions, Lou system
09CQA-1141C03	Bt-phyric andesite	Andesite/Basalt	Lou - Southern Breccia	K	Mild/Moderate	Porphyritic intrusions, Bt phyric porphyry
09CQA-1141C04	Bt-phyric andesite	Andesite/Basalt	Lou - Southern Breccia	K	Mild/Moderate	Porphyritic intrusions, Bt phyric porphyry
09CQA-1141C05	Bt-phyric andesite	Andesite/Basalt	Lou - Southern Breccia	K	Mild/Moderate	Porphyritic intrusions, Bt phyric porphyry
09CQA-1141F03	Aphanitic rhyolite	Alkali Rhyolite/Rhyolite	Lou - Southern Breccia	K	Strong	Lou assemblage - Southern Breccia
09CQA-1142B02	Leucocratic granite	Rhyolite/dacite	Lou - Southern Breccia	Na	Moderate	Granite-leucogranite
09CQA-1143A02	Bt–Fp-phyric porphyry (1869 Ma)	Andesite/Basalt	Lou - Southern Breccia	K	Mild	Porphyritic intrusions, Lou system
09CQA-4006A02	Monzonite	Andesite/Basalt	Eastern Treasure Lake - GS showing	Na	Strong	Marian River batholith
09CQA-4008A03	Fp-phyric dacite	Rhyolite/dacite	Mazenod - Scinter Lk showing	HT Ca-Fe/K	Mild	Mazenod Assemblage-27
09CQA-4009-A2	Fp-phyric porphyry	Andesite/Basalt	Cole - North Cole uraniun	Na-Ca-Fe/K	Moderate	Cole assemblage - Qtz monzonite-Monzodiorite
09CQA-4010A03	Fp-phyric andesite	Andesite/Basalt	Cole - North Cole uraniun	HT Ca-Fe/K	Mild	Cole Assemblage - Andesite
09CQA-4011A03	Fp-phyric andesite	Andesite/Basalt	Cole - Cole uranium	HT Ca-Fe/K	Mild	Cole Assemblage - Andesite
09CQA-4012B03	Fp–Porphyritic monzonite	Rhyolite/dacite	Cole	Na/K	Moderate	Cole assemblage - Qtz monzonite-Monzodiorite
10CQA-0147A2	Aphanitic rhyolite	Alkali Rhyolite	Lou - Summit Peak showing vicinity	K	Strong	Lou Assemblage 12
10CQA-0156A02	Monzonite	Rhyolite/dacite	Cole - Cole South	K	Mild	Qtz monzonite-Monzodiorite
10CQA-0156B02	Monzonite	Rhyolite/dacite	Cole - Cole South	K	Moderate	Qtz monzonite-Monzodiorite
10CQA-0163C03	Porphyritic monzonite	Andesite/Basalt	Cole - Cole South	Na-HT Ca-Fe/K	Moderate	Qtz monzonite-Monzodiorite
10CQA-0163D02	Porphyritic monzonite	Andesite/Basalt	Cole - Cole South	Na-HT Ca-Fe/K	Moderate	Qtz monzonite-Monzodiorite
10CQA-0165A02	Porphyritic monzonite	Andesite/Basalt	Cole - Cole South	Na-HT Ca-Fe/K	Moderate	Qtz monzonite-Monzodiorite
10CQA-0166A02	Porphyritic monzonite	Rhyolite/dacite	Cole - Cole South	Na/HT Ca-Fe	Mild	Qtz monzonite-Monzodiorite
10CQA-0166C04	Porphyritic monzonite	Andesite/Basalt	Cole - Cole South	Na-HT Ca-Fe/K	Weak	Qtz monzonite-Monzodiorite
10CQA-0168A02	Coarse-grained Qtz monzonite	Andesite/Basalt	Cole	K	Weak	U-Th rich monzonitic granite
10CQA-0171C02	Monzonite	Rhyolite/dacite	Cole	K	Mild	Marian River batholith

Sample	Rock type	Pearce (1996)	Location	Alteration	Alteration intensity	Sample classification
10CQA-0177A01	Monzonite	Andesite/Basalt	Cole	Na/K	Mild	Qtz monzonite-Monzodiorite
10CQA-0177D02	Monzonite	Rhyolite/dacite	Cole	K	Mild	U-Th rich monzonitic granite
10CQA-0182A02	Monzonitic Fp-phyric porphyry	Rhyolite/dacite	Cole	K	Mild	Cole assemblage - Qtz monzonite-Monzodiorite
10CQA-0509C2	Monzonite	Rhyolite/dacite	South Lou - Peanut	K	Mild	U-Th rich monzonitic granite
10CQA-0509C4	Monzonite	Rhyolite/dacite	South Lou - Peanut	K	Mild	U-Th rich monzonitic granite
10CQA-0514B02	Monzodioritic Fp-phyric porphyry	Andesite/Basalt	Cole	Na/HT Ca-Fe	Moderate	Cole assemblage - Qtz monzonite-Monzodiorite
10CQA-0514C02	Monzonitic Fp-phyric porphyry	Andesite/Basalt	Cole	Na/HT Ca-Fe/K	Moderate	Cole assemblage - Qtz monzonite-Monzodiorite
10CQA-0515B02	Fp-phyric andesite	Andesite/Basalt	Cole	Na/HT Ca-Fe	Weak	Cole Assemblage - Andesite
10CQA-0516A02	Aphanitic andesite	Andesite/Basalt	Cole	Na/HT Ca-Fe	Weak	Cole Assemblage - Andesite
10CQA-0516B02	Aphanitic andesite	Andesite/Basalt	Cole	HT Ca-Fe	Mild	Cole Assemblage - Andesite
10CQA-0520C02	Monzonite	Andesite/Basalt	Cole	Fe-Mg/LT Ca-Fe	Moderate	Marian River batholith
10CQA-0528A02	Monzonitic Fp-phyric porphyry	Andesite/Basalt	Cole - Cole South	K/LT Ca-Fe	Mild	Qtz monzonite-Monzodiorite
10CQA-0529C02	Monzonitic Fp–Hbl porphyry	Andesite/Basalt	Cole - Cole South	Na/HT Ca-Fe/K	Mild	Qtz monzonite-Monzodiorite
10CQA-0546C04	Monzodiorite	Andesite/Basalt	Cole	Fe-Mg	Weak	Marian River batholith
10CQA-1240B02	Aphanitic rhyolite	Trachyte	Lou - Southern Breccia	Na/K	Strong	Lou assemblage - Southern Breccia
10CQA-1240B04	Bt-phyric andesite	Andesite/Basalt	Lou - Southern Breccia	Na/K	Moderate	Porphyritic intrusions, Bt phyric porphyry
10CQA-1241B01	Bt-phyric andesite	Andesite/Basalt	Lou - Southern Breccia	Na/K	Moderate	Porphyritic intrusions, Bt phyric porphyry
10CQA-1241B03	Bt-phyric andesite	Andesite/Basalt	Lou - Southern Breccia	Na/K	Moderate	Porphyritic intrusions, Bt phyric porphyry
10CQA-1242C10	Fp–phyric rhyolitedyke	Trachyte	Lou - Southern Breccia	K	Moderate	rhyoliteolitic dykes, undivided
10CQA-1242G01	Leucocratic granite (1871 Ma)	Trachyte	Lou - Southern Breccia	Na	Strong	Granitic intrusions, undivided
10CQA-1615B03	Bt-phyric andesite	Andesite/Basalt	Lou - Southern Breccia	K	Strong	Porphyritic intrusions, Bt phyric porphyry
10CQA-1619A02	Aphanitic rhyolite	Rhyolite/dacite	Lou - Southern Breccia	K	Strong	Lou assemblage - Southern Breccia
10CQA-1619C02	Aphanitic rhyolite	Trachyte	Lou - Southern Breccia	K	Strong	Lou assemblage - Southern Breccia
10CQA-1619I02	Aphanitic rhyolite	Alkali Rhyolite	Lou - Southern Breccia	Na/K	Strong	Lou assemblage - Southern Breccia
10CQA-1620A02	Leucocratic granite	Rhyolite/dacite	Lou - Southern Breccia	Na/K	Strong	Granite-leucogranite
10CQA-1622F03	Fp–Bt porphyry (1868 Ma)	Andesite/Basalt	Lou - Southern Breccia	Weakly altered	N.A.	Porphyritic intrusions, Lou system
10CQA-1627A02	Aphanitic andesite	Andesite/Basalt	Lou - Southern Breccia	Na/HT K-Fe	Moderate	Porphyritic intrusions, Bt phyric porphyry
10CQA-1627C02	Aphanitic rhyolite	Alkali Rhyolite	Lou - Southern Breccia	Na/K	Strong	Lou assemblage - Southern Breccia
10CQA-1627G02	Aphanitic rhyolite	Alkali Rhyolite	Lou - Southern Breccia	Na/K	Moderate	Lou assemblage - Southern Breccia

Sample	Rock type	Pearce (1996)	Location	Alteration	Alteration intensity	Sample classification
10CQA-1629A	Felsic lapilli tuff	Rhyolite/dacite	Lou - NICO deposit vicinity	Si	Mild	Lou Assemblage 13
10CQA-1633A02	Volcanic breccia	Rhyolite/dacite	Lou - Chalco Lake showing vicinity	LT K-Fe	Moderate	Lou Assemblage 13
10CQA-1634A02	Aphanitic rhyolite	Rhyolite/dacite	Lou - Chalco Lake showing vicinity	K/LT K-Fe	Moderate	Lou Assemblage 13-12
10CQA-1634B02	Aphanitic rhyolite	Alkali Rhyolite/Rhyolite	Lou - Chalco Lake showing vicinity	HT K-Fe/K	Strong	Lou Assemblage 13-12
10CQA-1634B04	Aphanitic rhyolite	Alkali Rhyolite/Rhyolite	Lou - Chalco Lake showing vicinity	K	Strong	Lou Assemblage 13-12
10CQA-1641A02	Fp–Bt porphyry	Andesite/Basalt	Lou - Southern Breccia	Weakly altered	N.A.	Porphyritic intrusions, Lou system
10CQA-1642A02	Fp–phyric rhyolite	Alkali Rhyolite	Lou - Southern Breccia	K	Moderate	Lou assemblage - Southern Breccia
10CQA-1647A02	Aphanitic rhyolite	Alkali Rhyolite	Lou - Summit Peak showing vicinity	K	Strong	Lou Assemblage 12
10CQA-1649B02	Fp–Bt-phyric rhyolite	Trachyte	Lou - Southern Breccia	K	Moderate	Lou assemblage 19
10CQA-1654A02	Aphanitic rhyolite	Rhyolite/dacite	Lou - Southern Breccia	K	Moderate	Lou assemblage - Southern Breccia
10CQA-1654C02	Fp-phyric rhyolite	Alkali Rhyolite	Lou - Southern Breccia	Weakly altered	N.A.	Lou assemblage - Southern Breccia
10CQA-1661A02	Monzonitic Fp-phyric porphyry	Rhyolite/dacite	Lou - Southern Breccia	K	Moderate	Granite-leucogranite
10CQA-1661B02	Fp-phyric rhyolite	Rhyolite/dacite	Lou - Southern Breccia	K	Moderate	Lou assemblage - Southern Breccia
10CQA-1663A02	Monzonitic Fp-phyric porphyry	Rhyolite/dacite	Lou - Southern Breccia	K	Moderate	Granite-leucogranite
11PUA010F02	Fp-phyric porphyry	Andesite/Basalt	Lou - Southern Breccia	Weakly altered	N.A.	Porphyritic intrusions, Lou system
11PUA011D01	Aphanitic rhyolite	Rhyolite/dacite	Lou - Southern Breccia	Na/K	Strong	Lou assemblage - Southern Breccia
11PUA027B02	Volcaniclastic breccia	Rhyolite/dacite	Lou - Southern Breccia	K	Moderate	Lou Assemblage 13
11PUA516B01	Porphyritic rhyolite dyke	Alkali Rhyolite	Lou - Southern Breccia	K	Strong	rhyoliteolitic dykes, undivided
11PUA519B01	Fp-phyric rhyolite	Alkali Rhyolite	Lou - Southern Breccia	K	Moderate	Lou assemblage - Southern Breccia
11PUA519B02	Fp-phyric rhyolite	Trachyte	Lou - Southern Breccia	K	Moderate	Lou assemblage - Southern Breccia
11PUA524A01	Monzonite	Andesite/Basalt	Lou - Southwest of Lou Lake	K	Mild	Qtz monzonite-Monzodiorite
85N730001	Felsic intrusive rock	Rhyolite/dacite	South of Rarock fault - Rex Showing	Unknown	Unknown	Porphyritic intrusions, undivided
85N730004	Intermediate intrusive rock	Andesite/basalt	South of Rarock fault - Rex Showing	Unknown	Unknown	Porphyritic intrusions, undivided
85N730005	Intermediate intrusive rock	Andesite/basalt	South of Rarock fault - Rex Showing	Unknown	Unknown	Porphyritic intrusions, undivided
85N730016	Felsic intrusive rock	Rhyolite/dacite	South of Rarock fault - Rex Showing	Unknown	Unknown	Porphyritic intrusions, undivided
85N730018	Intermediate intrusive rock	Andesite/basalt	South of Rarock fault - Rex Showing	Unknown	Unknown	Porphyritic intrusions, undivided
85N730019	Felsic intrusive rock	Rhyolite/dacite	South of Rarock fault - Rex Showing	Unknown	Unknown	Porphyritic intrusions, undivided

Sample	Rock type	Pearce (1996)	Location	Alteration	Alteration intensity	Sample classification
85N730021	Felsic volcanic rock	Rhyolite/dacite	South Lou - North of Duke	Unknown	Unknown	Undivided volcanic/intrusive rocks Western section
85N730023	Intermediate intrusive rock	Andesite/basalt	South Lou - North of Duke	Unknown	Unknown	Marian River batholith
85N730029	Felsic volcanic rock	Rhyolite/dacite	Mazenod - North of Mar showing	Unknown	Unknown	Mazenod Assemblage - Undivided
85N730033	Feldspar porphyries	Rhyolite/dacite	Mazenod - Sarah Lake	Unknown	Unknown	Porphyritic intrusions, undivided
85N730035	Felsic intrusive rock	Rhyolite/dacite	Mazenod - Nod	Unknown	Unknown	Granitic intrusions, undivided
85N730036	Felsic intrusive rock	Rhyolite/dacite	Mazenod - Nod	Unknown	Unknown	Granitic intrusions, undivided
85N730037	Intermediate volcanic rock	Trachy-andesite	Mazenod - Sarah Lake	Unknown	Unknown	Mazenod Assemblage - Sue-Dianne deposit unit
85N730040	Feldspar porphyries	Rhyolite/dacite	Mazenod - Sarah Lake	Unknown	Unknown	Porphyritic intrusions, undivided
85N730043	Intermediate intrusive rock	Andesite/basalt	Mazenod - Sarah Lake	Unknown	Unknown	Porphyritic intrusions, undivided
85N730045	Felsic volcanic rock	Trachyte	Mazenod - Kim Zone	Unknown	Unknown	Bea Assemblage-35
85N730046	Felsic volcanic rock	Rhyolite/dacite	Mazenod - Kim Zone	Unknown	Unknown	Bea Assemblage-35
85N730052	Intermediate intrusive rock	Trachy-andesite	Mazenod - South of Brooke	Unknown	Unknown	Porphyritic intrusions, undivided
85N730054	Intermediate intrusive rock	Trachy-andesite	Maznod - Pic showing	Unknown	Unknown	Porphyritic intrusions, undivided
85N730058	Felsic volcanic rock	Rhyolite/dacite	Mazenod - North of Sue-Dianne	Unknown	Unknown	Bea Assemblage-35
85N730063	Intermediate volcanic rock	Andesite/basalt	Mazenod - South of Brooke	Unknown	Unknown	Dianne subassemblage
85N730066	Intermediate volcanic rock	Andesite/basalt	Mazenod - South of Brooke	Unknown	Unknown	Bea Assemblage-35
85N730067	Intermediate volcanic rock	Andesite/basalt	Mazenod - Nod	Unknown	Unknown	Dianne subassemblage
85N730079	Intermediate intrusive rock	Trachy-andesite	South Lou - North of Ted	Unknown	Unknown	Marian River batholith
85N730081	Intermediate intrusive rock	Trachy-andesite	South Lou - North of Ted	Unknown	Unknown	Marian River batholith
85N730083	Felsic intrusive rock	Rhyolite/dacite	South Lou - Peanut	Unknown	Unknown	Undivided volcanic/intrusive rocks Western section
85N730086	Felsic intrusive rock	Rhyolite/dacite	Mazenod - South of Brooke	Unknown	Unknown	Granitic intrusions, undivided
85N730087	Felsic intrusive rock	Rhyolite/dacite	Mazenod - South of Brooke	Unknown	Unknown	Granitic intrusions, undivided
85N730092	Felsic volcanic rock	Alkali Rhyolite	Mazenod - South of Brooke	Unknown	Unknown	Lou assemblage - Southern Breccia
85N730099	Felsic volcanic rock	Rhyolite/dacite	Lou - North of Lou Lake	Unknown	Unknown	Lou Assemblage-17
85N730100	Felsic volcanic rock	Rhyolite/dacite	Lou - North of Lou Lake	Unknown	Unknown	Lou Assemblage-17
85N730105	Felsic intrusive rock	Rhyolite/dacite	Cole	Unknown	Unknown	U-Th rich monzonitic granite
85N730107	Intermediate intrusive rock	Andesite/basalt	Cole	Unknown	Unknown	Qtz monzonite-Monzodiorite
85N730109	Intermediate volcanic rock	Andesite/basalt	Eastern Treasure Lake - Honk showing	Unknown	Unknown	Undivided volcanic/intrusive rocks Eastern section
85N730117	Intermediate rock	Trachy-andesite	Eastern Treasure Lake - West of Hump Lake	Unknown	Unknown	Hump assemblage - Undivided volcanic/intrusive rocks

Sample	Rock type	Pearce (1996)	Location	Alteration	Alteration intensity	Sample classification
85N730119	Intermediate intrusive rock	Andesite/basalt	Eastern Treasure Lake - West of Hump Lake	Unknown	Unknown	Marian River batholith
85N730121	Felsic intrusive rock	Trachyte	Marian River Batholith-40	Unknown	Unknown	U-Th rich monzonitic granite
85N730124	Felsic intrusive rock	Trachyte	Marian River Batholith-40	Unknown	Unknown	Marian River batholith
85N730128	Intermediate intrusive rock	Andesite/basalt	South Lou - North of Peanut	Unknown	Unknown	Marian River batholith
85N730134	Intermediate volcanic rock	Andesite/basalt	Lou - North of Lou Lake	Unknown	Unknown	Bea Assemblage-35
85N730135	Intermediate intrusive rock	Andesite/basalt	Lou - North of Lou Lake	Unknown	Unknown	Porphyritic intrusions, undivided
85N730136	Felsic intrusive rock	Rhyolite/dacite	Lou - North of Lou Lake	Unknown	Unknown	Porphyritic intrusions, undivided
85N730138	Intermediate volcanic rock	Andesite/basalt	Lou - North of Lou Lake	Unknown	Unknown	Bea Assemblage-35
85N730140	Felsic volcanic rock	Rhyolite/dacite	Lou - North of Lou Lake	Unknown	Unknown	Lou Assemblage-18
85N730146	Felsic volcanic rock	Rhyolite/dacite	Lou - North of Lou Lake	Unknown	Unknown	Bea Assemblage-35
85N730149	Felsic intrusive rock	Rhyolite/dacite	Lou - Southwest of Lou Lake	Unknown	Unknown	Porphyritic intrusions, undivided
85N730165	Intermediate intrusive rock	Andesite/basalt	Mazenod - North of Mar showing	Unknown	Unknown	Porphyritic intrusions, undivided
85N730167	Intermediate intrusive rock	Andesite/basalt	Mazenod - North of Mar showing	Unknown	Unknown	Marian River batholith
85N730172	Intermediate intrusive rock	Trachy-andesite	Mazenod - North of Mar showing	Unknown	Unknown	Porphyritic intrusions, undivided
85N730176	Felsic volcanic rock	Rhyolite/dacite	Mazenod - North of Mar showing	Unknown	Unknown	Mazenod Assemblage - Undivided
85N730177	Felsic volcanic rock	Rhyolite/dacite	Mazenod - North of Mar showing	Unknown	Unknown	Mazenod Assemblage - Undivided
85N730182	Felsic volcanic rock	Rhyolite/dacite	Mazenod - North of Mar showing	Unknown	Unknown	Mazenod Assemblage - Undivided
85N730190	Intermediate intrusive rock	Andesite/basalt	Mazenod - Faber Lake	Unknown	Unknown	Porphyritic intrusions, undivided
85N730191	Intermediate intrusive rock	Andesite/basalt	Mazenod - Faber Lake	Unknown	Unknown	Porphyritic intrusions, undivided
85N730196	Felsic intrusive rock	Rhyolite/dacite	Mazenod - Faber Lake	Unknown	Unknown	Porphyritic intrusions, undivided
CQA-05-0227A	Aphanitic rhyolite	Rhyolite/dacite	Lou - NICO deposit vicinity	K	Strong	Lou Assemblage 12
CQA-07-0436A	Aphanitic andesite	Andesite/Basalt	Eastern Treasure Lake - North Dennis	Na/HT Ca-Fe	Strong	Undivided volcanic/intrusive rocks Eastern section
CQA-07-0437A	Aphanitic andesite	Andesite/Basalt	Eastern Treasure Lake - North Dennis	Na-HT Ca-Fe/K	Moderate	Undivided volcanic/intrusive rocks Eastern section
CQA-07-0438C	Monzonitic Fp-phyric porphyry	Andesite/Basalt	Eastern Treasure Lake - North Dennis	K	Mild	Undivided volcanic/intrusive rocks Eastern section
CQA-07-0438D	Monzodiorite	Andesite/Basalt	Eastern Treasure Lake - North Dennis	Na/HT Ca-Fe	Mild	Undivided volcanic/intrusive rocks Eastern section
CQA-07-0438G	Monzodiorite	Andesite/Basalt	Eastern Treasure Lake - North Dennis	Na/HT Ca-Fe	Moderate	Undivided volcanic/intrusive rocks Eastern section

Sample	Rock type	Pearce (1996)	Location	Alteration	Alteration intensity	Sample classification
CQA-07-0439A	Monzonitic Fp-phyric porphyry	Andesite/Basalt	Lou - Southern Breccia	K	Weak	Undivided volcanic/intrusive rocks Eastern section
CQA-07-0441C	Bt–Fp-phyric rhyolite	Rhyolite/dacite	Lou - NICO deposit vicinity	K	Moderate	Lou Assemblage 12
CQA-07-0441D	Qz–Fp-phyric porphyry	Rhyolite/dacite	Lou - NICO deposit vicinity	HT K-Fe	Moderate	Lou Assemblage 12
CQA-07-0441E	Qz–Fp-phyric porphyry	Rhyolite/dacite	Lou - NICO deposit vicinity	K	Moderate	Lou Assemblage 12
CQA-07-0442A	Qz–Fp-phyric porphyry	Rhyolite/dacite	Lou - NICO deposit vicinity	K	Strong	Lou Assemblage 12
CQA-07-0445B1	Qz–Fp-phyric porphyry	Rhyolite/dacite	Lou - NICO deposit vicinity	K	Strong	Lou Assemblage 12
CQA-07-0448A	Fp–Bt-phyric rhyolite	Rhyolite/dacite	Lou - North of Lou Lake	K	Strong	Lou Assemblage 15
CQA-07-0449A	Fp-phyric porphyry	Andesite/Basalt	Lou - North of Lou Lake	K/LT Ca-Fe	Mild	Porphyritic intrusions, Lou system
CQA-07-0452A	Monzonite	Andesite/Basalt	Lou - Southwest of Lou Lake	Weakly altered	N.A.	Qtz monzonite-Monzodiorite
CQA-07-0455A	Aphanitic rhyolite	Rhyolite/dacite	Lou - NICO deposit vicinity	K	Strong	Lou Assemblage 12
CQA-07-0459F	Bt–Fp-phyric porphyry	Andesite/Basalt	Lou - NICO deposit vicinity	K	Strong	Porphyritic intrusions, Lou system
CQA-07-0459G	Bt–Fp-phyric rhyolite	Trachyte	Lou - NICO deposit vicinity	K	Moderate	Lou Assemblage 12
CQA-07-0463L	Fp–phyric rhyolite	Rhyolite/dacite	Lou - NICO deposit vicinity	K	Strong	Lou Assemblage 12
CQA-07-0464I1	Aphanitic rhyolite	Rhyolite/dacite	Lou - NICO deposit vicinity	K	Strong	Lou Assemblage 12
CQA-07-0464I2	Aphanitic rhyolite	Trachyte	Lou - NICO deposit vicinity	K	Strong	Lou Assemblage 12
CQA-07-0464I4	Fp–Bt-phyric rhyolite	Rhyolite/dacite	Lou - NICO deposit vicinity	K	Strong	Lou Assemblage 12
CQA-07-0466G1	Bt–Fp-phyric porphyry	Andesite/Basalt	Lou - NICO deposit vicinity	K	Mild	Porphyritic intrusions, Lou system
CQA-07-0466i3	Fp-phyric porphyry	Andesite/Basalt	Lou - NICO deposit vicinity	K	Mild	Porphyritic intrusions, Lou system
CQA-07-0469E	Fp–Bt-phyric andesite	Andesite/Basalt	Lou - NICO deposit vicinity	K	Strong	Porphyritic intrusions, Lou system
CQA-07-0469F	Fp–Bt-phyric rhyolite	Trachyte	Lou - NICO deposit vicinity	K	Moderate	Lou Assemblage 12
CQA-07-0478F	Aphanitic rhyolite	Rhyolite/dacite	Lou - NICO deposit vicinity	K	Strong	Lou Assemblage 12
CQA-07-0479D	Aphanitic rhyolite	Rhyolite/dacite	Lou - NICO deposit vicinity	K	Strong	Lou Assemblage 12
CQA-07-0480A	Bt–Fp-phyric porphyry	Andesite/Basalt	Lou - NICO deposit vicinity	K	Moderate	Porphyritic intrusions, Lou system
CQA-07-0480E	Bt–Fp-phyric porphyry	Andesite/Basalt	Lou - NICO deposit vicinity	K	Strong	Porphyritic intrusions, Lou system
CQA-07-0484A	Bt–Fp-phyric porphyry	Andesite/Basalt	Lou - NICO deposit vicinity	K	Moderate	Porphyritic intrusions, Lou system
CQA-07-0484B	Bt–Fp-phyric porphyry	Andesite/Basalt	Lou - NICO deposit vicinity	K	Moderate	Porphyritic intrusions, Lou system
CQA-07-0484F	Bt–Fp-phyric andesite	Andesite/Basalt	Lou - NICO deposit vicinity	K	Strong	Porphyritic intrusions, Lou system
CQA-07-0484G	Aphanitic rhyolite	Rhyolite/dacite	Lou - NICO deposit vicinity	K	Strong	Lou Assemblage 12
FM00-249-33,11	Bt–Fp-phyric porphyry	Andesite/Basalt	Lou - NICO deposit vicinity	K	Mild	Porphyritic intrusions, Lou system

Sample	Rock type	Pearce (1996)	Location	Alteration	Alteration intensity	Sample classification
GR-06-012W	Felsic volcanic rock	Rhyolite/dacite	Lou - NICO deposit vicinity	K	Strong	Lou Assemblage 12
GR-06-014W	Aphanitic rhyolite	Rhyolite/dacite	Lou - NICO deposit vicinity	K	Strong	Lou Assemblage 12
GR-06-077	Felsic volcanic rock	Trachyte	Lou - NICO deposit vicinity	K	Strong	Lou Assemblage 12
M612922/10 CQA-1658	Felsic volcanic rock	Rhyolite/dacite	Lou - Southern Breccia	K	Strong	Lou assemblage - Southern Breccia
M612924/10 CQA-1248	Aphanitic rhyolite	Rhyolite/dacite	Lou - Southern Breccia	K	Strong	Lou assemblage - Southern Breccia
N249995/10 CQA-1687	Aphanitic rhyolite	Rhyolite/dacite	Lou - Southern Breccia	K/Tur	Moderate	Lou assemblage - Southern Breccia
Porphyry_Mafic_E	Amp–Fp–Bo-phyric porphyry having mafic enclave #1	Andesite/Basalt	Lou - NICO deposit vicinity	Weakly altered	Mild	Porphyritic intrusions, Lou system
Vent area, Nico. Enclave mafique porphyre Fp-Am-Bo	Mafic enclave into Fp–Amp–Bo-phyric porphyry	Andesite/Basalt	Lou - NICO deposit vicinity	Weakly altered	Mild	Porphyritic intrusions, Bt phyric porphyry

Sample	10CQA-1663A02	09CQA-1142B02	10CQA-1242C10	09CQA-0008A02	10CQA-1629A	11PUA519B02	10CQA-1619C02	CQA-07-0455A
Sector	Lou	Lou	Lou	Lou	Lou	Lou	Lou	Lou
Geological unit	Early Gran.	Early Gran. (1873 Ma)	Rhy. Dyke	Lou Ass.	Lou Ass.	Lou Ass.	Lou Ass.	Lou Ass.
Rock type	Alt. Gran.	Alt. Gran.	Rhy. Dyke	Fp Fel. Vol.	Lap. Tuff	Fp Fel. Vol.	Aph. Fel. Vol.	Aph. Fel. Vol.
SiO2 (% wt.)	69.83	72.75	69.8	71.27	71.98	70	71.22	71.3
TiO2	0.15	0.26	0.05	0.07	0.1	0.05	0.05	0.052
Al2O3	12.97	16.1	13.36	14.6	13.97	12.9	12.64	11.23
Fe2O3	1.74	0.84	0.99	1.79	2.56	3.48	1.57	2.03
MgO	0.24	0.17	0.26	0.2	0.34	0.157	0.08	0.57
MnO	0.02	0.01	0.01	0	0.01	0.006	< 0.003	0.026
CaO	0.33	0.35	0.31	0.45	0.91	0.1	0.06	1.13
Na2O	2.68	7.58	1.42	3.34	2.53	1.71	0.68	0.186
K2O	7.18	1.39	9.64	6.81	5.85	9.06	10.37	10.56
P2O5	0.04	< 0.08	0.04	< 0.08	0.01	0.04	0.04	< 0.043
LOI	0.5	0.4	0.5	0.3	0.8	0.29	0.3	0.9
S	< 0.006	0.03	0	< 0.01	< 0.006	0.004	< 0.006	0.0183
%Total	96	100	96.5	99	99.1	98	97.1	98.2
Ag (ppm)	< 0.4	< 0.2	< 0.4	0.4	< 0.4	0.23	< 0.4	< 2
Ba	594	114	1047	841	653	1080	1417	990
Bi	< 1	2	< 1	< 0.6	< 1.3	< 0.5	< 1.3	< 87
Cl	840	N.A.	110	N.A.	110	N.A.	<100	N.A.
Co	5	< 8	< 5	18	< 5	< 0.5	< 5	< 17
Cr	29	147	34	144	15	7	7	374
Cs	0.3	0.3	0.3	1.4	1	0.7	0.3	< 30
Cu	31	51	< 3	10	< 1	< 7	7	31
F	100	20	90	160	270	N.A.	50	N.A.
Hf	5.2	5.8	3.3	5.4	3.8	3.7	2.8	2.9
Mo	< 4	< 9	< 20	12	< 4	3	8	< 43
Nb	15.3	14.4	12.8	17	12.6	22.4	10.7	4.1
Ni	< 9	< 20	< 8	< 20	16	< 4	< 9	< 43
Pb	26.1	6.4	1.7	6.8	7.6	2.2	6	< 20
Rb	242	18	235	258	197	217	245	263
Sc	10.7	4.6	3.4	8.9	3.2	4	3.2	2.4
Sn	5	< 5	4	< 6	4	1	8	< 0.2
Sr	31	31	22	61	33	21	43	24
Ta	2	1.9	1.4	1.9	1.6	2.3	1.3	1.5
Th	26	28.2	21	26.9	26	25	16.8	28.6
U	6.1	5.6	7.1	6.1	10.2	5.9	4.5	25.8
V	5	7	2	< 4	3	4	6	30
W	7	6	3	9.4	7	2	1	< 87
Y	53	30	15.1	28.6	20	23.7	10.5	13
Zn	18	< 10	17	10	3	6	2	8
Zr	179	201	99	174	160	104	86	67
La	54	14.4	22	76.2	37	26.9	19	23
Ce	108	35.6	42.2	146.6	69.7	58	42.9	45
Pr	11.7	4.5	4.7	17.7	6.8	6.2	4.4	5
Nd	42.1	17.9	16.8	57.3	22.7	22.2	16.1	17.5
Sm	8.3	4	2.9	9.6	3.8	4.1	2.7	3.1
Eu	1	0.5	0.4	1.4	0.5	0.5	0.3	0.3
Gd	8.3	4.3	2.4	6.6	3.7	3.8	2.1	2.3
Tb	1.3	0.7	0.4	1	0.5	0.6	0.3	0.4
Dy	8	5	2.3	5.1	3.2	3.9	1.9	2
Ho	1.7	1	0.5	1	0.7	0.9	0.4	0.4
Er	5	3.1	1.8	2.9	2	2.8	1.3	1.3
Tm	0.8	0.5	0.3	0.5	0.3	0.4	0.2	0.2
Yb	4.9	2.8	2.2	2.9	2.3	2.8	1.4	1.6
Lu	0.7	0.4	0.4	0.5	0.4	0.4	0.2	0.3

Key: Maf = Mafic, Int - Intermediate, Fel = Felsic, Vol = Volcanic, Gran = Granite, Dior = Diorite, Monz = Monzonite, Lap = Lapili, Aph = Aphanitic, Porph = Porphyritic, Und = Undivided, Ass = Assemblage

Mineral abbreviations after Whitney and Evans (2010)

Sample	11PUA027B02	10CQA-1661B02	09CQA-0127C03	85N730099	09CQA-0127G02	09CQA-1098A02	09CQA-1109A02	10CQA-1242G01
Sector	Lou	Lou	Lou	Lou	Lou	South Lou	South Lou	Lou
Geological unit	Lou Ass.	Lou Ass.	Lou Ass.	Lou Ass.	Lou Ass.	Undiv. Vol.	Undiv. Vol.	Alt. Gran. (1871 Ma)
Rock type	Fel. Vol.	Fp Fel. Vol.	Fp-Bt Fel. Vol.	Fel. Vol.	Fp-Bt Fel. Vol.	Fel. Vol.	Fel. Vol.	Granitic rock
SiO2 (% wt.)	72.8	73.69	62.24	75.2	72.99	75.96	76.1	76
TiO2	0.09	0.04	0.1	0.07	0.1	0.04	0.07	0.12
Al2O3	11.8	12.45	17.3	12.8	12.2	10.97	14.2	13.16
Fe2O3	2.74	1.19	4.87	1.75	3.72	1.87	1.36	0.64
MgO	0.524	0.24	1.01	0.55	0.49	0.08	0.14	0.04
MnO	0.019	0.02	0.09	0.03	0.08	0.01	0.01	< 0.003
CaO	0.46	0.15	0.02	0.59	0.07	0.03	0.63	0.17
Na2O	1.47	1.21	2.32	1.95	3.36	0.24	3.11	6.37
K2O	6.89	8.87	9.9	4.89	4.6	10.21	5.52	1.59
P2O5	0.05	0.01	< 0.08	0.03	< 0.08	0.01	< 0.08	< 0.006
LOI	0.76	0.3	0.9	1.16	0.5	0.3	0.3	0.2
S	0.014	< 0.006	< 0.01	0.01	< 0.01	< 0.006	< 0.01	0.01
%Total	98	98.3	98.9	99.07	98.2	99.7	101.5	98.3
Ag (ppm)	0.23	< 0.4	< 0.2	< 0.19	< 0.2	23.5	< 0.2	< 0.3
Ba	880	1096	1079	642	620	1077	166	89
Bi	< 0.6	< 1.2	< 0.5	< 0.6	< 0.6	< 0.6	< 0.7	< 1.1
Cl	N.A.	120	N.A.	N.A.	N.A.	N.A.	N.A.	390
Co	2	< 5	16	2	15	4	< 8	< 5
Cr	15	12	77	4	160	8	169	17
Cs	2.7	< 0.25	1	2.7	1	2.1	1.6	< 0.22
Cu	< 7	11	7	7	7	< 20	6	35
F	N.A.	40	100	N.A.	40	20	80	30
Hf	3.2	3	3.4	2.8	4	2.9	3.7	5
Mo	< 1	< 4	< 9	1	16	< 8	< 9	< 20
Nb	12.7	7.6	12.5	10.4	12	12.5	15.7	6
Ni	< 4	< 9	33	< 6	< 20	< 7	< 20	< 8
Pb	5	26.2	4.9	9.6	5.2	5	19	3.1
Rb	289	303	322	225	152	271	293	20
Sc	5	2.9	4.1	3	3.6	3	1.2	1.8
Sn	5	3	5	7	< 6	< 6	< 7	3
Sr	43	40	17	64	21	13	44	20
Ta	1.5	1.7	2.3	2.1	2.3	1.5	3.3	0.3
Th	19	24	20.9	20	23.7	20	48.7	19
U	3.5	14.3	9.7	21.3	17	3.6	21.6	3.6
V	9	4	30	4	17	4	< 4	3
W	7	< 1	6	7	3	10	6	4
Y	25.8	16.2	31	25.6	19.7	40	20	6.3
Zn	15	21	48	15	53	< 5	< 10	< 10
Zr	98	101	108	77.9	124	91	102	162
La	90	38	33.2	34.8	29.5	15.7	38.1	12.4
Ce	175	66.8	65.6	64.3	56.4	31	68.9	26
Pr	18.5	7.1	7.6	6.6	6.4	3.8	6.9	3
Nd	64.8	23.6	24.4	22.9	20.6	18.9	22.2	10.7
Sm	12.6	4.2	4.8	4.4	3.7	3.5	3.7	1.9
Eu	1.9	0.6	0.6	0.5	0.4	0.4	0.3	0.3
Gd	10.3	4	4.3	4	2.9	4.2	2.8	1.5
Tb	1.2	0.5	0.8	0.6	0.5	0.8	0.4	0.2
Dy	5.6	3	4.9	3.9	3.3	5.8	2.7	1.2
Ho	0.8	0.6	1	0.8	0.7	1.2	0.4	0.3
Er	1.9	1.6	2.8	2.3	2.1	3.8	1.6	0.8
Tm	0.3	0.3	0.4	0.4	0.4	0.6	0.3	0.1
Yb	1.5	1.7	2.5	2.5	2.3	3.8	1.7	1
Lu	0.2	0.3	0.4	0.4	0.4	0.6	0.2	0.2

Key: Maf = Mafic, Int - Intermediate, Fel = Felsic, Vol = Volcanic, Gran = Granite, Dior = Diorite, Monz = Monzonite, Lap = Lapili, Aph = Aphanitic, Porph = Porphyritic, Und = Undivided, Ass = Assemblage

Mineral abbreviations after Whitney and Evans (2010)

Sample	10CQA-1240B04	09CQA-1141C03	09CQA-1143A02	CQA-07-0466G1	CQA-07-0480A	CQA-07-0480E	FM00-249-33,11	Porphyry_Mafic_E
Sector	Lou	Lou	Lou	Lou	Lou	Lou	Lou	Lou
Geological unit	Bt-Porph.	Bt-Porph.	Lou Porph. (1869 Ma)	Lou Porph.	Lou Porph.	Lou Porph.	Lou Porph.	Lou Porph.
Rock type	Bt Int. Porph.	Bt Int. Porph.	Bt-Fp Int. Porph.	Bt-Fp Int. Porph.	Bt-Fp Int. Porph.	Bt-Fp Int. Porph.	Bt-Fp Int. Porph.	Amp-Bt-Fp Int. Porph.
SiO2 (% wt.)	64.42	60.11	63.79	64.2	61.6	68.2	62.8	63.1
TiO2	0.3	0.56	0.54	0.525	0.502	0.321	0.52	0.56
Al2O3	15.07	16	15.6	14.65	14.34	13.92	14.9	14.6
Fe2O3	5.31	9.3	7.46	6.38	7.38	4.32	7.8	7
MgO	1.06	2.27	2.09	2.13	1.95	1.24	2.06	2.26
MnO	0.02	0.02	0.02	0.035	0.037	0.023	0.019	0.031
CaO	0.3	0.63	0.43	1.42	1.04	0.64	0.36	1.1
Na2O	2.99	2.74	2.9	3	1.858	1.293	3.36	2.45
K2O	8.18	7.87	6.81	7.01	9.83	10.83	7.32	7.43
P2O5	0.1	0.16	0.11	0.123	0.114	0.079	0.124	0.138
LOI	0.5	0.8	0.9	1.2	0.9	1	0.42	0.94
S	0	0.19	< 0.01	< 0.01	< 0.0092	0.011	0.01	0.02
%Total	98.4	100.8	100.8	100.8	99.7	102	100	100
Ag (ppm)	< 0.4	0.2	0.2	< 2	< 2	< 2	0.24	0.4
Ba	889	1168	1128	756	1021	1160	795	950
Bi	< 1.4	< 0.7	0.6	< 104	< 92	< 109	1	6
Cl	740	N.A.	N.A.	N.A.	N.A.	N.A.	N.A.	N.A.
Co	< 5	11	< 8	27	< 19	< 22	3	9
Cr	31	66	114	169	26	221	37	46
Cs	5.3	2.7	1.7	< 30	< 30	< 30	8.6	8.3
Cu	< 3	7	9	59	13	< 11	54	14
F	550	1490	400	N.A.	1230	N.A.	N.A.	N.A.
Hf	4	4	4.6	5	4.8	4.3	4.5	5.5
Mo	< 20	< 9	< 9	< 52	< 46	< 55	1	3
Nb	10.1	10.7	12.7	11.7	11.5	12.8	10	10.4
Ni	8	22	29	< 52	< 46	< 55	27	22
Pb	2.6	6.2	5.8	< 20	< 20	< 20	1.6	11.4
Rb	220	308	173	392	484	379	301	355
Sc	9.4	17.6	11.7	10.9	11.4	6.8	12	13
Sn	8	10	< 7	< 0.2	0	< 0.2	4	4
Sr	27	62	36	123	53	39	28	101
Ta	1.6	1.1	1.2	1.2	1.2	1.8	1.3	1.3
Th	18	14.9	24.6	21.9	21.3	28	22	23
U	7.6	5.8	5	6.7	7.2	10.6	6.8	6.8
V	50	152	86	83	73	55	75	78
W	3	3	2	< 104	< 92	< 109	5	9
Y	15.8	36	24	23	25	21	22	22
Zn	58	14	40	19	16	13	11	24
Zr	153	146	190	181	172	153	156	197
La	28	37.3	75.5	41	43	40	40.5	45.5
Ce	51.7	73.5	146.4	76	79	75	77.4	87.2
Pr	5.5	8.5	15.7	8.4	8.7	8.6	7.8	8.8
Nd	19.8	33	56.2	30	31.2	31.6	28.2	31.9
Sm	3.4	6.7	9.5	5	5.3	5.4	4.9	5.6
Eu	0.5	1.2	1.2	1	1	0.8	0.8	0.9
Gd	3	6.2	6.4	4.1	4.4	4.1	4.5	5
Tb	0.4	0.9	0.8	0.6	0.7	0.6	0.6	0.7
Dy	2.4	6	4.4	3.7	4	3.4	3.6	3.6
Ho	0.5	1.1	0.7	0.7	0.8	0.7	0.7	0.8
Er	1.7	3.4	2.3	2.2	2.4	1.9	2.3	2.4
Tm	0.3	0.5	0.3	0.3	0.4	0.3	0.3	0.3
Yb	2	3.2	2.2	2.2	2.3	2	2.2	2.3
Lu	0.3	0.4	0.3	0.3	0.4	0.4	0.3	0.3

Key: Maf = Mafic, Int - Intermediate, Fel = Felsic, Vol = Volcanic, Gran = Granite, Dior = Diorite, Monz = Monzonite, Lap = Lapili, Aph = Aphanitic, Porph = Porphyritic, Und = Undivided, Ass = Assemblage

Mineral abbreviations after Whitney and Evans (2010)

Sample	10CQA-1622F03	11PUA010F02	09CQA-0104A02	85N730005	85N730018	85N730019	09CQA-0009A03	09CQA-0003A03
Sector	Lou	Lou	Mazenod	RexShowing	RexShowing	RexShowing	Mazenod	Mazenod
Geological unit	Lou Porph. (1868 Ma)	Lou Porph.	Porph./Und. (1867.9 Ma)	Porph./Und.	Porph./Und.	Porph./Und.	Dianne Sub.	Dianne Sub.
Rock type	Fp-Bt Int. Porph.	Fp Int. Porph.	Fp Int. Porph.	Porph./Und.	Porph./Und.	Porph./Und.	Amp-Fp Int. Vol.	Fp Int. Vol.
SiO2 (% wt.)	64.48	61.1	63.58	67.8	62.9	72.8	53.83	62.9
TiO2	0.33	0.63	0.86	0.37	0.32	0.16	0.67	0.57
Al2O3	14.96	15	16	14.3	15.2	13.8	16.1	14.6
Fe2O3	5.36	9.3	5.9	3.88	7.65	1.97	8.55	6.76
MgO	1.2	1.575	1.25	1.43	1.33	0.32	5.7	1.31
MnO	0.02	0.039	0.05	0.12	0.14	0.05	0.18	0.04
CaO	0.64	1.41	3.82	0.74	0.86	1.13	5.05	4.17
Na2O	2.93	3.48	3.56	4.47	1.06	3.81	2.29	2.85
K2O	7.36	5.7	5.32	2.92	5.44	4.82	3.34	4.23
P2O5	0.1	0.11	0.27	0.08	0.07	0.03	0.15	0.13
LOI	0.7	0.52	0.7	1.36	2.19	0.37	2.6	1
S	< 0.006	0.14	0.02	0.02	0.01	0.01	0.01	0.02
%Total	98.2	99	101.5	97.69	97.35	99.45	98.7	98.7
Ag (ppm)	< 0.3	0.3	< 0.2	< 0.4	0.3	0.3	0.2	0.3
Ba	837	889	1074	470	633	646	677	820
Bi	< 1	1	< 0.6	< 1.3	< 0.6	< 0.6	< 0.5	< 0.6
Cl	760	N.A.	N.A.	N.A.	N.A.	N.A.	N.A.	N.A.
Co	< 5	19	16	20	13	3	41	20
Cr	26	109	108	1140	553	150	151	199
Cs	3.1	5.1	3.1	2.7	3.6	1.5	1.3	1
Cu	< 1	170	9	14	10	7	11	9
F	870	N.A.	1073	N.A.	N.A.	N.A.	510	400
Hf	3.6	4.2	8.9	6.3	6.1	6.1	4.1	5.2
Mo	< 4	< 1	< 9	3	1	1	17	20
Nb	10.9	12.7	17.4	15.1	13.9	17.7	8.2	11.3
Ni	12	31	32	30	19	< 6	51	36
Pb	8.9	9.4	16.7	9.8	11.9	40.6	6.2	27.2
Rb	255	189	322	150	371	217	235	193
Sc	8.9	17	13.5	7.6	6.4	5.3	25.9	13
Sn	6	8	< 6	29	8	6	< 5	< 6
Sr	48	97	199	94	60	95	208	262
Ta	1.2	1.1	1.6	3	2.1	2.2	0.7	1.3
Th	20	15.4	23.9	24	21	26	9.6	20.8
U	7.6	2.9	6.7	7.1	8.1	7.1	2.5	6.7
V	45	97	63	65	42	10	149	198
W	3	7	8	5	20	5	3	7
Y	23	24	35.8	27	27.3	40.3	19.3	22.7
Zn	13	27	48	109	72	140	85	21
Zr	144	154	353	234	230	214	145	174
La	34	45.5	59.8	48	64.7	57.8	26.2	42.7
Ce	70.8	92	118.9	95	115	104	53.5	79.6
Pr	7	10.1	14.4	10.3	12.4	11.4	6.9	9.4
Nd	24.6	37	49.4	35.7	43.9	40.5	24.6	30.9
Sm	4.7	6.8	8.9	6.3	7.3	7.1	4.6	5.3
Eu	0.8	1	1.6	0.9	1.2	0.8	1	1.1
Gd	4.5	5.7	6.9	5.7	6.2	6.4	3.9	4.4
Tb	0.6	0.7	1.1	0.7	0.8	1	0.6	0.7
Dy	3.9	4.1	6.1	4.3	4.6	6.2	3.4	3.9
Ho	0.8	0.8	1.2	0.9	0.9	1.3	0.7	0.8
Er	2.3	2.4	3.4	2.7	2.6	3.9	1.9	2.3
Tm	0.4	0.4	0.5	0.4	0.4	0.6	0.3	0.4
Yb	2.4	2.4	3	2.8	2.6	4.2	1.7	2.1
Lu	0.4	0.4	0.5	0.4	0.4	0.7	0.3	0.4

Key: Maf = Mafic, Int - Intermediate, Fel = Felsic, Vol = Volcanic, Gran = Granite, Dior = Diorite, Monz = Monzonite, Lap = Lapili, Aph = Aphanitic, Porph = Porphyritic, Und = Undivided, Ass = Assemblage

Mineral abbreviations after Whitney and Evans (2010)

Sample	09CQA-1037B03	09CQA-1033A02	09CQA-0012B02	09CQA-0109A03	09CQA-1070A03	10CQA-0515B02	09CQA-1071A03	09CQA-0091A03
Sector	Mazenod	Mazenod	Mazenod	Mazenod	Cole	Cole	Cole	Cole
Geological unit	Dianne Sub.	Dianne Sub.	Dianne Sub.	Dianne Sub.	Cole Ass.	Cole Ass.	Cole Ass.	Cole Ass.
Rock type	Fp Int. Vol.	Fp Int. Vol.	Fp fel. Vol.	Fp fel. Vol.	Amp-Fp Int. Vol.	Int. Vol.	Fp-Amp fel. Vol.	Fel. Vol.
SiO2 (% wt.)	70.43	68.89	68.05	72.1	56.17	56.72	70.17	71.35
TiO2	0.35	0.46	0.3	0.32	1.14	1.24	0.25	0.39
Al2O3	14.3	14.4	13.4	14.5	18	16.7	14.6	15.7
Fe2O3	5.08	5.14	2.72	2.68	8.4	7.77	2.14	1.4
MgO	1.1	0.86	0.57	0.93	2.09	2.7	0.52	0.45
MnO	0.05	0.16	0.05	0.03	0.07	0.05	0.04	0.03
CaO	2.37	3.4	2.22	3.31	6.5	5.87	1.22	1.74
Na2O	3.25	3.11	2.26	3.03	4.24	5.02	2.91	2.35
K2O	4.98	4.18	5.36	3.37	2.82	2.47	5.44	6.55
P2O5	< 0.08	0.11	< 0.08	< 0.08	0.18	0.28	< 0.08	< 0.08
LOI	0.5	0.8	0.9	0.8	0.9	1.1	0.8	1.1
S	0.01	0.01	< 0.01	0.02	0.02	0.03	< 0.01	0.01
%Total	102.7	101.7	95.9	101.2	100.7	100	98.3	101.3
Ag (ppm)	< 0.2	< 0.2	0.2	< 0.2	0.2	< 0.3	0.4	0.3
Ba	1385	792	914	457	641	514	899	1222
Bi	< 0.5	< 0.6	0.5	< 0.6	< 0.6	< 1.1	1	< 0.5
Cl	N.A.	N.A.	N.A.	N.A.	N.A.	340	N.A.	N.A.
Co	18	13	18	15	< 8	12	< 8	16
Cr	166	165	135	165	69	< 6	132	107
Cs	3.3	1.8	1.6	2.2	1.6	0.5	1.2	1.9
Cu	20	11	7	11	16	7	25	14
F	700	540	220	433	635	790	485	853
Hf	5.4	5.2	5.7	6.3	4.8	4.9	7	8.8
Mo	19	13	10	< 9	< 9	< 20	< 9	32
Nb	13.6	13.7	13.3	14	12.9	10.7	17.7	19.1
Ni	57	31	< 20	27	26	< 8	32	< 20
Pb	10.8	16.6	14.9	10.3	7.9	43.9	8.6	18
Rb	251	198	306	216	110	82	239	324
Sc	7.9	9.3	5.6	5.6	21.2	21.1	5.1	6.9
Sn	< 5	< 6	5	< 6	< 6	5	< 6	5
Sr	172	179	132	131	253	222	59	104
Ta	1.4	1.3	1.6	1.7	0.9	0.4	1.9	2
Th	29.7	26.2	30.5	31.4	12.5	11	28.1	28
U	7.6	7.5	8.9	8.6	3.1	3.1	8.9	7.4
V	40	61	29	30	144	136	7	15
W	9	7	6	10	3	2	5	9
Y	24.4	30.6	23.7	23.1	34.8	33	35.3	50
Zn	14	24	51	24	22	117	20	18
Zr	178	182	191	218	184	194	264	324
La	107.6	54.6	52.4	53.7	35.5	39	51.4	50.2
Ce	206.7	113.2	99.3	101.6	74.2	75.4	92.5	101.8
Pr	20.2	11.3	11.5	11.4	8.4	8.5	9.9	13.2
Nd	68.9	39.9	35.9	35.8	33.3	32.9	36.1	46.1
Sm	10.7	6.9	5.8	5.6	6.9	6.7	6.5	9.3
Eu	1.6	1.1	0.8	0.8	1.7	1.8	0.7	1.3
Gd	6.9	5.3	4.1	3.9	6	6.4	4.8	8
Tb	1	0.9	0.7	0.7	0.9	1	0.8	1.4
Dy	4.6	4.9	3.7	3.8	5.7	5.6	5.1	8
Ho	0.8	1	0.8	0.8	1.2	1.2	1.1	1.7
Er	2.2	2.8	2.4	2.3	3.4	3.3	3.3	4.8
Tm	0.4	0.5	0.4	0.4	0.5	0.5	0.5	0.8
Yb	2.2	2.7	2.4	2.3	3.1	3.1	3.2	4.3
Lu	0.3	0.4	0.4	0.4	0.5	0.5	0.5	0.7

Key: Maf = Mafic, Int - Intermediate, Fel = Felsic, Vol = Volcanic, Gran = Granite, Dior = Diorite, Monz = Monzonite, Lap = Lapili, Aph = Aphanitic, Porph = Porphyritic, Und = Undivided, Ass = Assemblage

Mineral abbreviations after Whitney and Evans (2010)

Sample	09CQA-1126A02	09CQA-1127F02	09CQA-1124A02	09CQA-1038A02	09CQA-0004A03	09CQA-1044A03	09CQA-1025A02	85N730037
Sector	East. TL	East. TL	East. TL	Mazenod	Mazenod	Mazenod	Mazenod	Mazenod
Geological unit	Hump Ass.	Hump Ass.	Hump Ass.	Maz. Ass. (1868 Ma)	Maz. Ass.	Maz. Ass.	Maz. Ass. SD	Maz. Ass. SD
Rock type	Fp Maf. Vol.	Fp Maf. Vol.	Bt-Fp Int. Vol.	Fp Int. Vol.	Fel. Vol.	Fp Fel. Vol.	Int. Vol.	Int. Vol.
SiO2 (% wt.)	56.04	56.96	61.88	63.12	69.72	72.4	62.18	67.4
TiO2	1.13	1.03	0.58	0.71	0.26	0.28	0.52	0.34
Al2O3	18.9	17.5	19.9	14.5	14.2	14	17.8	15
Fe2O3	10.14	9.43	4.84	5.8	2.66	3.23	6.25	3.01
MgO	1.92	2.76	1.43	1.61	0.67	0.7	1.6	1.24
MnO	0.05	0.1	0.07	0.14	0.05	0.05	0.08	0.09
CaO	2.96	6.68	2.81	5.88	0.89	1.04	1.77	0.22
Na2O	2.7	2.8	3.4	3.26	2.14	2.85	5.44	2.72
K2O	6.42	3.63	5.94	3.72	6.05	5.06	4.6	7.23
P2O5	0.38	0.26	0.14	0.21	< 0.08	< 0.08	0.13	0.08
LOI	1.5	0.6	0.6	3.8	1.9	1.7	1.2	1.25
S	< 0.01	< 0.01	< 0.01	0.02	0.01	0.01	< 0.01	0
%Total	102.5	101.9	101.8	103	98.7	101.5	101.7	98.8
Ag (ppm)	< 0.2	< 0.3	< 0.2	< 0.2	0.3	< 0.2	< 0.2	0.4
Ba	1909	1111	787	1029	1134	883	1202	930
Bi	< 0.6	< 0.7	< 0.6	< 0.6	< 0.6	1	1	< 0.6
Cl	N.A.	N.A.	N.A.	N.A.	N.A.	N.A.	N.A.	N.A.
Co	16	13	16	24	12	19	23	15
Cr	190	182	102	121	122	132	90	597
Cs	11.9	11.6	8.3	4	2	2.7	1.4	1.2
Cu	4	8	11	11	13	15	15	5
F	1130	720	1500	650	200	230	240	N.A.
Hf	4.2	3.7	6.4	5.3	7.4	6.3	6.8	6.5
Mo	< 9	< 9	< 9	< 9	27	< 9	< 9	1
Nb	11.4	10	14	12.6	14.9	14.3	17.5	14.8
Ni	48	44	< 20	22	25	< 20	< 20	7
Pb	33.4	18.2	47.8	14.5	13.7	15.3	10.3	8.1
Rb	190	98	242	146	249	207	182	321
Sc	24.4	23.4	11.6	16.8	5.4	5.7	12	7.4
Sn	< 6	< 7	23	< 6	< 6	< 6	6	2
Sr	392	592	353	250	143	148	103	40
Ta	0.9	0.8	1.3	1.1	1.6	1.4	1.5	1.4
Th	13.8	12.5	21.5	18.6	28.1	25.7	31.2	22
U	2.7	2.2	7.3	5	7.8	7.3	7.2	6.3
V	156	178	71	81	8	9	45	48
W	18	4	5	7	9	7	6	2
Y	22	24	28	26.3	25.4	25.9	22.6	19
Zn	55	80	75	85	30	54	33	64
Zr	149	138	253	187	261	223	243	240
La	42	39	48.4	40	52.1	51.9	52.9	30.5
Ce	85.3	79.6	93.1	84.8	98.9	103	104.7	64.5
Pr	10	9.4	10.4	8.9	11.8	10.5	10.5	7.3
Nd	40	37.5	38.7	33.6	37	37.2	36.1	27
Sm	7.5	7.1	6.7	6.1	6.2	6.3	5.6	5.4
Eu	1.6	1.5	1.5	1	1	1	0.8	1.1
Gd	5.8	5.6	5.3	5	4.7	4.7	4	4.7
Tb	0.7	0.7	0.7	0.8	0.8	0.7	0.6	0.6
Dy	4.2	4.2	4.6	4.4	4.3	4.3	3.6	3.4
Ho	0.7	0.7	0.8	0.9	0.9	0.8	0.7	0.6
Er	2.1	2.2	2.6	2.5	2.6	2.6	2.3	2
Tm	0.3	0.3	0.4	0.4	0.4	0.4	0.4	0.3
Yb	1.7	1.9	2.4	2.3	2.6	2.6	2.4	2.2
Lu	0.2	0.2	0.3	0.4	0.5	0.4	0.4	0.3

Key: Maf = Mafic, Int - Intermediate, Fel = Felsic, Vol = Volcanic, Gran = Granite, Dior = Diorite, Monz = Monzonite, Lap = Lapili, Aph = Aphanitic, Porph = Porphyritic, Und = Undivided, Ass = Assemblage

Mineral abbreviations after Whitney and Evans (2010)

Sample	09CQA-1052A02	09CQA-1048A02	09CQA-0007A03	85N730046	11PUA524A01	09CQA-1123A02	09CQA-1123-C3	09CQA-4009-A2
Sector	Lou	Lou	Mazenod	Mazenod	Lou	Cole	Cole	Cole
Geological unit	Bea Ass.	Bea Ass.	Bea Ass.	Bea Ass.	Monz. Mdior. (1867 Ma)	Qtz Monz.-Mdior.	Qtz Monz.-Mdior.	Qtz Monz.-Mdior.
Rock type	Fp-Bt Int. Vol.	Fp-Bt Int. Vol.	Fp Fel. Vol.	Fel. Vol.	Monzodiorite	Monzodiorite	Monzonite	Monzonite
SiO2 (% wt.)	66.13	65.21	65.66	64.8	62.6	60.69	61.04	56.91
TiO2	0.6	0.64	0.41	0.41	0.54	0.82	0.92	0.83
Al2O3	13.8	14.4	14.8	16	15.7	17.4	14.18	13.91
Fe2O3	6.39	7	3.58	3.48	4.52	4.26	4.86	7.8
MgO	3.12	2.92	0.88	1.25	2.187	3.01	1.9	4.17
MnO	0.18	0.06	0.07	0.05	0.044	0.04	0.06	0.08
CaO	2.72	4.04	2.88	1.28	2.79	6.02	4	4.71
Na2O	2.47	3.07	2.91	2.67	3.05	5.18	3.27	3.73
K2O	3.85	3.54	4.41	6.26	4.37	1.91	4.71	2.33
P2O5	0.14	0.16	0.1	0.09	0.13	0.16	0.23	0.18
LOI	1.8	1.2	1.7	1.44	1.77	0.9	1.5	1.8
S	0.02	0.01	0.01	0.01	0.03	0.02	0.03	0.03
%Total	101.4	102.4	97.6	97.89	98	100.6	96.6	96.3
Ag (ppm)	< 0.2	< 0.2	0.3	0.5	0.4	< 0.2	0.3	0.3
Ba	963	831	952	970	836	467	682	557
Bi	< 0.6	< 0.6	< 0.6	< 0.6	< 0.5	< 0.6	< 0.5	< 0.5
Cl	N.A.	N.A.	N.A.	N.A.	N.A.	N.A.	N.A.	N.A.
Co	26	26	14	8	12	< 8	11	21
Cr	147	151	119	365	22	172	7	98
Cs	1	2.6	2.1	3.6	1.8	0.3	5.3	2.2
Cu	19	8	20	14	32	25	26	38
F	380	450	260	N.A.	N.A.	570	720	640
Hf	5	4.3	7.4	7	7.3	5.6	4	4.6
Mo	9	15	9	2	< 0.5	< 9	< 8	< 8
Nb	11.4	10.8	14.2	16.7	13.8	14.6	11.6	12.7
Ni	50	42	23	< 6	7	37	< 7	16
Pb	39.7	21.1	48.6	28.4	7.1	58.9	27.1	5.4
Rb	170	134	197	241	200	61	250	133
Sc	13.3	15.3	8.3	7.8	11	16.4	11.9	16.9
Sn	< 6	< 6	< 6	5	4	< 6	< 5	< 5
Sr	216	247	215	156	230	238	198	209
Ta	1.1	1	1.5	1.6	1.3	1.4	1.1	1
Th	21.8	18	26.3	25	23	22.5	12	18.6
U	6.5	5.6	7	8	6.1	7.1	4.1	5.2
V	92	99	38	40	55	112	69	126
W	4	6	8	4	3	3	4	1
Y	21	19.1	27.4	28.3	28.2	32	30	38
Zn	245	29	96	50	31	85	37	27
Zr	180	152	275	255	274	205	167	200
La	41.6	39	52.9	51.4	50.7	55.5	44.8	58.1
Ce	82.1	75.1	99.6	98	101	103.2	81	108
Pr	8.3	7.8	11.8	10.7	10.6	11.6	9.2	11.9
Nd	29.6	28	37.5	38.5	38	43.8	34.2	45.5
Sm	5.1	4.8	6.2	6.9	6.8	7.9	6.3	8.2
Eu	1	1.1	1.1	1.2	1.2	1.6	1.7	1.5
Gd	3.9	3.9	4.9	5.7	6	6.5	5.4	6.7
Tb	0.6	0.6	0.8	0.8	0.8	0.9	0.8	0.9
Dy	3.7	3.4	4.6	4.6	4.6	5.5	5	5.6
Ho	0.7	0.7	1	1	1	1	1	1.1
Er	2.1	2	2.7	2.8	2.7	3.1	2.8	3.4
Tm	0.3	0.3	0.4	0.4	0.4	0.4	0.4	0.5
Yb	2.1	1.9	2.6	2.8	2.7	2.7	2.6	2.9
Lu	0.3	0.3	0.4	0.5	0.4	0.4	0.4	0.5

Key: Maf = Mafic, Int - Intermediate, Fel = Felsic, Vol = Volcanic, Gran = Granite, Dior = Diorite, Monz = Monzonite, Lap = Lapili, Aph = Aphanitic, Porph = Porphyritic, Und = Undivided, Ass = Assemblage

Mineral abbreviations after Whitney and Evans (2010)

Sample	09CQA-4012B03	10CQA-0177A01	09CQA-1123-B5	09CQA-1011A02	09CQA-1012D02	10CQA-0520C02	09CQA-1096B02	09CQA-0014A03
Sector	Cole	Cole	Cole	East Maz.	Mazenod	N. Cole	South Lou	East. TL
Geological unit	Qtz Monz.-Mdior.	Qtz Monz.-Mdior.	Qtz Monz.-Mdior.	MRB (1866 Ma)	MRB	MRB	MRB	MRB
Rock type	Monzonite	Monzonite	Fp Porph.	Granite	Qtz Monz.	Granite	Granite	Monzonite
SiO2 (% wt.)	69.39	60.39	59.44	68.24	65.43	50.52	69.21	57.28
TiO2	0.35	0.69	0.79	0.49	0.33	0.91	0.32	0.6
Al2O3	16.9	17.66	15.53	14.5	16.1	19.26	16	17.3
Fe2O3	1.42	3.28	5.34	4.34	4.04	8.43	4.04	5.18
MgO	0.87	2.29	1.65	1.27	0.84	3.54	1.09	2.07
MnO	0.03	0.03	0.07	0.06	0.05	0.44	0.04	0.1
CaO	3	4.94	5.14	2.58	0.19	6.51	0.74	4.53
Na2O	5.91	4.3	1.28	2.52	2.43	3.39	4.17	4.07
K2O	1.63	4.49	5.06	5.47	7.87	3.92	4.89	5.16
P2O5	0.08	0.21	0.22	0.14	< 0.08	0.29	< 0.08	0.15
LOI	1	0.7	2.5	1	1.1	2.9	0.5	1.4
S	< 0.01	0.01	0.02	0.02	< 0.01	0.02	< 0.01	0.02
%Total	100.6	99.1	96.9	100.8	98.6	100.4	101.1	98.1
Ag (ppm)	< 0.2	< 0.3	0.3	0.2	0.2	< 0.4	0.3	0.2
Ba	148	883	606	915	812	1264	937	1239
Bi	< 0.7	< 1.1	< 0.6	< 0.6	< 0.6	< 1.2	< 0.6	< 0.6
Cl	N.A.	460	N.A.	N.A.	N.A.	220	N.A.	N.A.
Co	< 8	9	10	23	14	14	< 8	22
Cr	166	46	12	143	112	33	116	101
Cs	0.7	< 0.22	3.6	3	1.9	0.4	0.8	0.9
Cu	7	2	60	23	17	< 3	4	38
F	460	1270	600	810	160	780	380	220
Hf	6.4	5.2	4.3	7.1	10.7	11.1	4.4	8.1
Mo	16	< 4	< 8	< 9	< 9	< 20	< 9	< 9
Nb	18.1	15.1	12.1	19	15.2	14.9	14.5	14.9
Ni	23	25	< 7	29	< 20	23	22	39
Pb	11.4	11.4	23.4	12.1	11.6	85	8.5	18.3
Rb	37	135	424	236	321	131	129	148
Sc	6.1	12.6	11.6	8	11.9	16.2	11	11.1
Sn	8	6	< 6	< 6	< 6	6	8	< 6
Sr	155	365	274	323	110	688	43	474
Ta	1.6	1.1	1.1	1.7	1.2	0.6	1.5	1.3
Th	30.4	20	13.9	36.9	32.2	22	19.2	22.5
U	6.5	5.3	4.5	5.5	5	6.4	4.1	3.1
V	51	91	55	46	25	105	28	69
W	4	< 1	4	2	3	2	6	2
Y	32	28	31	37.3	12.7	29	41	29.4
Zn	14	20	42	35	52	534	12	84
Zr	262	215	185	263	401	479	144	312
La	29.4	47.6	39.5	74.6	25.1	88.2	42.7	65.8
Ce	85.7	103	77	149.5	58.7	171	90.7	121.1
Pr	11	10.9	8.9	15.7	6.4	18.2	10.5	14.5
Nd	42.7	39.9	34.2	56.4	23.2	64.1	39.5	47.5
Sm	8	7.1	6.5	9.7	4.2	9.9	7.8	8
Eu	1.2	1.5	1.6	1.5	0.9	2.1	0.9	1.5
Gd	6.2	6.7	5.9	7.4	3.3	8.1	6.4	5.9
Tb	0.9	0.9	0.9	1.1	0.5	1	1	1
Dy	5.2	5	5.5	6.3	2.5	5.2	6.5	5.2
Ho	0.9	1	1.1	1.2	0.5	1	1.3	1
Er	3	2.8	3.1	3.5	1.5	2.7	4	2.8
Tm	0.4	0.4	0.5	0.5	0.2	0.4	0.6	0.4
Yb	2.9	2.7	3.1	3.1	1.6	2.6	4	2.4
Lu	0.4	0.4	0.5	0.4	0.3	0.4	0.6	0.4

Key: Maf = Mafic, Int - Intermediate, Fel = Felsic, Vol = Volcanic, Gran = Granite, Dior = Diorite, Monz = Monzonite, Lap = Lapili, Aph = Aphanitic, Porph = Porphyritic, Und = Undivided, Ass = Assemblage

Mineral abbreviations after Whitney and Evans (2010)

Sample	09CQA-1010A03	09CQA-1102-B2	09CQA-0098D03
Sector	East Maz.	South Lou	Cole
Geological unit	MRB	U-Th Monz. dyke	U-Th Monz. dyke
Rock type	Qtz Monz.	Monz. dyke	Monz. dyke
SiO2 (% wt.)	66.52	68.1	71.08
TiO2	0.63	0.07	0.41
Al2O3	14.5	10.59	13.1
Fe2O3	5.27	1.22	3.26
MgO	1.21	0.18	0.7
MnO	0.08	0.01	0.05
CaO	2.76	0.14	1.65
Na2O	2.65	2.33	2.58
K2O	5.87	6.58	6.8
P2O5	0.18	0.02	0.1
LOI	0.7	0.5	0.3
S	0.02	0.01	0.01
%Total	100.5	89.6	100.2
Ag (ppm)	0.2	0.3	0.2
Ba	968	111	491
Bi	< 0.5	< 0.6	< 0.6
Cl	N.A.	N.A.	N.A.
Co	20	< 3	27
Cr	158	9	159
Cs	4	4.5	6
Cu	8	71	9
F	1600	90	733
Hf	8.7	3.9	7.8
Mo	< 9	< 8	11
Nb	28.9	11	32.4
Ni	< 20	< 7	< 20
Pb	21	13.3	27.5
Rb	320	308	426
Sc	12.5	2.2	6.5
Sn	8	< 6	8
Sr	278	24	110
Ta	2.6	2.4	3.5
Th	55.5	52.2	52.6
U	6.8	38.1	11.2
V	47	< 4	30
W	3	8	6
Y	57.8	42	43.7
Zn	52	< 5	11
Zr	316	128	267
La	101.8	44.1	70.2
Ce	214.8	85	143.5
Pr	22.5	8.7	17.1
Nd	81.4	29.2	54.8
Sm	14.2	5.7	9.4
Eu	1.7	0.2	1.1
Gd	10.9	5.1	6.9
Tb	1.7	0.9	1.2
Dy	9.3	5.9	6.8
Ho	1.8	1.3	1.4
Er	5.1	4.2	4.1
Tm	0.8	0.7	0.7
Yb	4.7	4.8	4.2
Lu	0.7	0.8	0.7

Key: Maf = Mafic, Int - Intermediate, Fel = Felsic, Vol = Volcanic, Gran = Granite, Dior = Diorite, Monz = Monzonite, Lap = Lapili, Aph = Aphanitic, Porph = Porphyritic, Und = Undivided, Ass = Assemblage
Mineral abbreviations after Whitney and Evans (2010)

ANNEXE - 3 : ANALYSES REPRÉSENTATIVES POUR LE CHAPITRE 3

Les minéraux sont abbrégés suivant Whitney et Evans (2010) sauf Qtz pour quartz.

Sample	10CQA 1375A2	CQA05 121A	CQA05 124C	CQA05 208B	CQA06 330A	09CQA 93A3	09CQA 1046F1	09CQA 1059H4	10CQA 1653C2	10CQA 1643A2	10CQA 1621A3	CQA05 110A	CQA05 132A	CQA05 113C	CQA05 195A1	CQA05 206F	09CQA 55E3	09CQA 128B2	86E 731350	86E 731335
Sector	Terra	Mag Hill	Mag Hill	Des Monts	Des Monts	Cole	Dennis	Esther	S. Breccia	S. Breccia	S. Breccia	Mag Hill	Mag Hill	Mag Hill	Des Monts	Des Monts	Duke	Terra	Terra	Terra
Protolith	And	And	And	And	And	Rhy	Sed	Gran	Sed	Rhy	Sed	And	And	And	And	And	Sed	Sed	LG	LG
Paragenesis	Ab-Amp	Ab-Amp	Ab-Amp	Ab-Hem	Ab-Amp	Ab-Hem	Ab	Ab	Ab ovpt by Kfs-FeOx-Chl-Py	Ab xcut by Mag	Ab xcut by Mag-Kfs	Ab-Amp Mag-Py	Ab-Amp Mag	Ab ovpt by Amp-Mag-Ap	Ab ovpt by Amp	Ab ovpt by Amp-Mag-Kfs	Mag-Amp	Mag-±Ap	Mag-Amp-Ap	Mag-Amp-Ap
Facies				Na (HT)		Kfs			Na/K-Fe (HT)	Na+Fe(HT)		Na-Ca-Fe (HT)		Na/Ca-Fe (HT)		Na/Ca-Fe-K (HT)		Ca-Fe (HT)		
SiO_2(wt%)	61.28	62.45	65.12	64.90	63.45	63.69	65.26	66.47	67.93	64.61	62.46	50.32	42.65	42.80	60.23	49.57	38.89	8.68	12.0	13.1
TiO_2	0.59	1.08	1.52	0.04	0.10	0.57	0.05	0.05	0.23	1.07	0.71	0.68	0.81	0.87	0.62	0.79	0.31	0.08	0.70	0.38
Al_2O_3	16.58	20.22	19.84	20.89	19.45	16.04	17.75	19.9	16.20	18.81	16.42	16.83	11.83	12.30	16.70	15.74	7.59	0.39	1.3	0.9
Fe_2O_3	4.76	2.46	2.03	0.48	2.39	2.91	1.18	0.94	2.01	2.94	7.51	16.41	21.51	20.59	4.42	19.35	30.27	87.17	57.30	71.80
MnO	0.06	0.15	0.05	0.02	0.08	0.02	0.03	0.02	0.01	0.02	0.02	0.12	0.14	0.22	0.19	0.19	1.69	0.08	0.15	0.12
MgO	0.30	0.83	0.51	0.08	1.01	2.54	0.66	0.48	0.70	0.13	0.67	2.31	3.96	4.41	3.55	2.04	4.92	0.37	2.04	0.65
CaO	5.68	2.21	0.66	1.19	1.51	0.96	1.46	0.55	0.34	0.38	0.41	2.08	7.00	8.27	5.36	2.76	10.22	4.62	13.90	6.66
Na_2O	8.75	9.15	9.42	9.82	9.44	8.98	9.71	10.01	7.17	10.04	8.22	6.19	4.57	3.67	6.94	4.21	1.23	< 0,05	0.07	0.04
K_2O	0.22	0.96	1.01	1.32	0.68	2.01	1.68	0.92	2.62	0.50	1.04	1.85	0.17	1.41	1.01	4.04	1.62	< 0,04	0.56	0.02
P_2O_5	0.30	*0.001*	*0.001*	*0.002*	< 0.03	0.11	0.01	< 0.08	0.03	0.04	0.11	1.01	0.10	2.72	< 0.03	< 0.03	0.05	2.87	9.600	4.580
LOI	0.7	1.18	0.8	1.33	1.17	1.2	0.8	0.5	0.6	0.2	0.9	2.27	6.66	1.54	1.45	0.87	0.6	-1.4	-0.85	-1.47
S	0.01	*0.1*	0.05	< 0.007	*0.1*	< 0.006	0.01	< 0.01	0.06	0.02	0.20	0.45	0.32	0.04	< 0.007	< 0.007	0.04	0.02	0.09	0.06
Total	99.2	100.8	101.2	100.1	99.4	98.9	98.5	99.9	98.0	98.8	98.7	100.8	99.9	99.0	100.7	99.9	97.4	102.8	97.5	97.6
F (ppm)			*70*	*10*		*2110*	*140*	*80*				*2390*	*1450*	*2878*	*150*		*1200*	*2430*		
Cl												*144*	*141*	*343*						
Sc	9	5	26	< 0.3	3	20	4	5	5	6	14	14	21	37	30	19	4	1	9	5
V	48	26	*13*	*3*	46	78	16	*4*	19	29	100	275	540	570	69	475	66	837	1050	1040
Cr	16	100	291	59	92	51	16	77	84	81	93	114	394	101	136	141	27	< 6	17	21
Co	< 5	*3.4*	*2*	*0.3*	*3.9*	4.5	3.4	*0.9*	< 5	1.5	13	87	53	24	*11*	16	7.7	30	23	20
Ni	9	*3.3*	*2.9*	*1.5*	*3*	10	*3.7*	*2.6*	< 9	34	49	224	143	68	61	112	76	56	87	101
Cu	40	115	35	10	14	*4.3*	32	7	23	15	165	508	181	19	163	*2.9*	*5.4*	*21.3*	14	56
Pb	3	*10.6*	*6.9*	*2.3*	*5.7*	2	7	6	8	2	15	*14.4*	*20*	*13.5*	23	*4.2*	7	9	7	7
Zn	33	197	44	9	122	*3*	10	*5*	16	3	14	129	68	209	150	140	149	139	129	168
As	< 10	*10*	< 91	*5*	*8*	*1*	*2*	*2*	22	64	8.3	*17*	*12*	*37*	*22*	*9*	*20*	*33*	< 40	< 40
Ag	< 0.3	*<.1*	*<.1*	*0.2*	*<.1*	0.3	0.2	1.0	0.03	0.08	0.12	*0.2*	*0.1*	*0.1*	*0.2*	*<.1*	0.3	0.4	< 0.3	< 0.4
Cd	6	*0.5*	*0.1*	*<.1*	*0.1*	5.7	< 3	< 8	2	4	9	13	19	18	*0.2*	22	64	186	21	30
In	< 0.6	NA	NA	NA	*NA*	< 0.2	0.4	< 0.3	0.022	0.016	0.016	NA	NA	NA	NA	NA	2.0	1.1	< 0.6	< 0.6
Sn	2.6	*1.4*	*12*	*0.2*	*0.7*	5	*1.5*	9.0	4	9.4	11.1	*3*	*1.9*	*3.6*	*2.1*	*2.8*	16	16	11.1	17.4
Mo	4.5	*0.6*	*0.5*	*0.4*	*0.2*	*0.1*	*<0.1*	*0.6*	0.44	< 4	10	*1.3*	*0.2*	*1.1*	*0.4*	*0.3*	*0.5*	*0.4*	1.8	4
W	8.1	*2.4*	*1.1*	*1*	*0.7*	10	5	8	5	22	25	*1.1*	*0.8*	*1.5*	*1.3*	*1.9*	1	2	2.3	1.9
Bi	< 1.1	*0.2*	*<.1*	*<.1*	*0.2*	*<0.1*	*0.3*	*0.1*	0.85	0.49	3	*0.7*	*0.2*	*0.6*	*0.5*	*0.2*	1	*0.3*	< 1.1	< 1.3
Rb	4.5	31.5	28.4	31.6	17.8	99.5	26.1	10.1	65.6	11.6	108	55.6	4.7	24.5	23.1	98.8	17.3	5.1	54	2
Cs	< 0.23	0.66	0.58	0.20	0.31	3.40	< 0.1	0.87	0.81	0.37	2.5	1.22	0.34	< 0.3	0.12	0.28	0.39	1.62	3.0	< 0.26
Sr	52.0	147	199	65.6	136	24.6	62.5	28.7	16.8	14.7	17.3	128	86.7	229	312	269	19.4	30.4	82	36
Ba	24	288	399	218	207	127	90	65	270	39	58	1080	96	177	625	1310	78	7	24	11
Zr	189	154	182	156	114	141	94	211	343	239	190	125	118	107	112	105	183	43	28	72
Hf	4.83	3.93	4.59	3.48	2.77	3.38	1.78	9.81	9.90	5.96	4.70	3.35	2.58	2.55	2.85	2.61	3.95	0.24	0.84	1.00
Nb	11.8	14.2	20.0	0.2	0.6	10.0	3.3	215	14.6	39.1	19.5	14.5	14.1	12.3	6.3	2.1	10.2	12.8	9.9	11.5
Ta	0.39	1.01	1.85	< 0.03	0.04	0.90	0.19	36.6	1.26	2.10	1.90	0.70	0.83	0.70	0.20	0.20	0.55	1.05	0.86	0.93
La	9.10	5.11	5.42	3.99	5.04	27.4	5.09	22.6	91.0	5.70	74.2	107	22.0	263	19.5	6.24	33.5	528	1180	765
Ce	24.2	11.4	7.46	5.66	7.27	54	10	36.5	190	14.3	166	196	56.7	516	30.1	15.6	77	1.015	2320	1520
Pr	3.30	1.50	0.49	0.37	0.78	6.08	1.15	7.45	20.4	1.41	17.1	20.3	7.98	57.1	3.61	2.18	8.95	93.2	236	159
Nd	14.4	7.01	2.14	1.77	3.00	22.0	4.09	29.6	76.4	5.75	65.5	73.8	33.5	202	14.6	10.3	35.7	309	800	559
Sm	3.10	1.58	0.19	< 0.2	0.63	3.77	0.72	11.5	13.8	1.65	12.9	10.6	8.44	29.0	3.40	2.51	7.25	42.1	109	79.8
Eu	0.79	0.59	0.55	0.35	0.32	0.57	0.10	0.38	1.31	0.43	1.16	1.38	1.11	3.71	1.04	0.79	1.96	2.65	7.44	4.90
Gd	3.06	1.37	0.20	< 0.2	0.57	2.95	0.58	11.8	11.4	2.94	10.8	6.77	7.94	21.1	3.24	2.22	8.06	26.5	86.8	62.2
Tb	0.52	0.20	0.02	0.01	0.10	0.45	0.09	1.32	1.31	0.70	1.64	0.84	1.17	2.74	0.48	0.35	1.39	3.78	9.20	6.70
Dv	3.40	1.34	0.14	0.08	0.61	2.81	0.60	11.4	7.62	5.63	10.3	4.77	7.78	15.5	3.19	2.23	9.10	20.5	48.6	35.1
Ho	0.75	0.26	0.03	0.01	0.14	0.57	0.10	2.11	1.50	1.20	2.00	0.94	1.51	2.82	0.66	0.44	1.84	3.87	9.3	6.76
Er	2.35	0.77	0.06	0.02	0.44	1.83	0.38	6.62	4.78	3.88	5.80	2.40	4.21	7.84	1.92	1.16	5.71	11.5	24.2	17.2
Tm	0.37	0.12	0.02	< 0.007	0.07	0.29	0.06	0.67	0.68	0.60	0.87	0.33	0.62	1.09	0.29	0.18	0.73	1.33	2.96	2.21
Yb	2.38	0.89	0.13	0.08	0.50	2.01	0.42	7.56	4.65	4.10	5.73	2.03	4.11	5.76	1.93	1.16	4.35	7.22	15.9	11.6
Lu	0.36	0.15	0.02	< 0.02	0.08	0.32	0.07	1.10	0.67	0.55	0.76	0.26	0.53	0.74	0.30	0.18	0.67	0.96	1.71	1.30
Y	24.0	6.8	1.2	0.9	4.0	18.0	3.4	67.6	41.0	32.0	51.5	25.0	44.4	83.7	18.8	12.4	61.4	131	255	189
Th	12.7	0.5	0.4	4.3	2.4	15.0	111	87.3	44.0	27.0	15.3	8.3	11.6	24.6	4.2	1.2	8.0	22.7	45.0	34.0
U	3.4	0.6	0.4	0.2	0.3	3.2	13.9	82.8	15.5	5.7	3.7	2.6	0.6	2.1	0.5	0.5	1.7	2.8	9.2	7.8
Tl										0.06	0.33									
Sb		*14.6*	*0.5*	*0.4*	*2*	*0.4*	*1.2*	*2.4*	0.46	2.47	2.83	*2.8*	*0.8*	*12*	*3.2*	*1.8*	*9.5*	*1.1*		
Be		*1*	*<1*	*1*	*2*	*2*	*2*	*13*	1.78	3.39	1.88	*2*	*2*	*2*	*2*	*2*	*3*	*8*		
Li		*13*	*8*	*8.9*	*15.6*	*25.8*	*7.5*	*8.9*	5.6	2	6.2	*28.9*	*18.3*	*54.2*	*6.7*	*22.3*	*15.8*	*3.2*		

Minerals: Whitney and Evans (2010); values in normal black font: INRS, normal blue: ALS, italic black: ACME, italic blue: GSC laboratories (metadata in Corriveau et al. in press); LOI: Loss on ignition

Blank: not analysed; EBG: Echo Bay Gossan, And: Andesite, Por : Porphyry, Rhy: Rhyolite, Gran: Granitic, Sed: Sedimentary, Vol: Volcanic, LG: LaBine Group, TLG: Treasure Lake Group; Sample location in Online Resource 2

Sample	86E 731344	09CQA 1173B3	09CQA 1193C2	09CQA 21B3	09CQA 1170D2	09CQA 43F3	CQA06 435D	09CQA 55F3	09CQA 1082E3	CQA06 435A	CQA07 466C1	CQA07 467A	CQA07 480V2B	CQA07 465A2	10CQA 1615G2	09CQA 109F7	09CQA 26G3	09CQA 56D3	09CQA 109D2
Sector	Terra	JLD	Hailstone	Ron	Ham	Hump	Fab	Duke	Duke	Fab	NICO	NICO	NICO	NICO	S. Breccia	Brooke	Brooke	Duke	Brooke
Protolith	LG	Por	Gneiss	Sed	Por	Rhy	Por	Sed	Sed	Por	Sed	Sed	Sed	Sed	Brx	Felsic vol.	And	Sed	Por
Paragenesis	Mag-Amp-Ap	Mag	Mag	Mag-Amp	Mag-Py-Amp-Ap-Grt-Fl	Amp-Mag-Ap	Amp-Mag-Ap	Mag-Amp-Sch	Mag-Amp-Apy	Amp-Mag-Kfs	Mag-Amp-Bt-Apy	Amp-Bt-Apy	Mag-Amp-Bt-Apy	Amp-Mag-Bt-Apy	Mag-Bt	Mag-Kfs-Cpy xcut by Ep	Kfs-Mag-Py±Cpy	Bt-Mag-Grt	Mag-Kfs
Facies					Ca-Fe (HT)							Ca-Fe-K (HT)					K-Fe (HT)		
SiO_2(wt%)	7.1	8.74	8.17	39.50	26.54	41.82	34.71	36.84	32.26	51.73	36.6	42.3	28.8	43.7	11.45	37.73	41.99	43.08	8.60
TiO_2	0.34	0.28	0.24	0.09	0.30	0.67	0.28	0.20	0.11	0.41	0.26	0.32	0.25	0.22	0.19	0.15	0.23	0.91	0.13
Al_2O_3	0.6	2.63	1.04	11.1	6.42	1.23	1.65	5.85	3.67	10.23	4.54	5.83	5.19	5.07	2.03	7.42	9.82	15.95	1.56
Fe_2O_3	79.70	87.71	87.58	32.0	52.86	26.7	28.35	37.77	47.51	17.11	47.76	28.06	55.15	29.10	80.70	42.76	31.44	20.80	88.32
MnO	0.05	0.22	0.08	0.14	0.36	0.37	0.06	2.27	0.88	0.06	0.12	0.21	0.11	0.21	0.04	0.03	0.03	2.20	0.02
MgO	2.02	0.33	0.57	2.70	4.16	5.55	11.29	3.45	4.23	6.80	2.76	6.70	2.73	5.75	1.17	0.21	0.70	2.41	0.20
CaO	5.99	0.17	0.94	8.69	2.39	19.76	15.20	8.14	7.44	5.20	2.55	8.93	4.38	9.75	0.02	2.66	0.18	1.62	< 0,02
Na_2O	0.04	< 0,05	< 0,05	2.96	< 0,05	0.30	0.47	0.96	0.85	1.24	0.21	0.52	0.58	0.59	0.04	0.40	0.34	0.54	< 0,05
K_2O	0.08	0.53	< 0,04	0.35	0.84	0.07	0.74	1.44	0.41	6.26	2.94	2.39	2.36	1.55	1.28	1.80	6.53	9.17	0.76
P_2O_5	4.160	0.18	0.74	0.19	0.82	2.16	6.53	0.05	< 0,005	0.39	0.056	0.063	< 0.052	< 0.051	< 0,01	0.27	0.05	0.21	0.01
LOI	-1.65	-1.7	0.6	0.8	2.2	1.1	0.37	0.3	-0.8	0.83	-1.02	0.03	-0.92	-0.07	-2.2	1.9	6.2	0.9	0.5
S	0.05	0.8	4.1	0.02	1.5	0.05	0.01	0.04	0.3	< 0.007	0.2	0.3	0.1	0.3	< 0.006	5.0	8.6	0.01	< 0.006
Total	99.0	99.3	99.9	98.7	96.9	99.9	99.8	97.2	96.6	100.4	98.5	98.2	99.0	98.4	99.7	95.4	97.4	97.7	100.0
F (ppm)		*225*	*695*	*230*	*3625*	*1840*	*13540*	*1138*	*555*	*4825*	*1080*	*1620*	*967*	*1230*		*263*	*260*	*1660*	*60*
Cl							*283*			*507*	*4170*	*4480*	*29340*	*5330*					
Sc	3	35	23	3	11	16	12	8	8	22	5	6	6	5	17	8	4	41	3
V	1170	388	367	59	734	333	580	59	116	285	36	36	48	29	611	86	56	238	250
Cr	11	8	12	71	7	67	31	17	23	71	70	49	61	60	68	15	12	476	*5*
Co	49	52	470	40	97	69	33	32	3060	24	936	7830	1010	6685	39	134	223	11	28
Ni	133	52	252	96	154	96	78	12	2150	45	*13.5*	87	88	132	23	20	8	35	*4.7*
Cu	< 6	307	11130	9	617	19	21	294	57	44	91	565	53	591	1.3	47950	1440	27	*18.1*
Pb	5	233	11	22	189	20	*1.4*	6	11	*7.6*	*2*	*5*	*1.4*	*9*	1	19	14	8	4
Zn	70	686	205	101	957	100	14	88	235	28	15	20	17	22	81	182	42	72	79
As	< 40	*2*	*9*	*2*	*24*	*<0.1*	*132*	*75*	10300	*12*	8760	10550	1170	9175	0.6	<1	58	*13*	*1*
Ag	< 0.4	0.8	0.6	*<0.1*	0.6	< 0.2	*<0.1*	*<0.1*	0.2	*<0.1*	*0.5*	*0.3*	*<0.1*	*0.4*	0.32	*7.2*	0.3	0.3	0.2
Cd	30	189	183	70	110	64	13	72	89	*0.1*	*<0.1*	*0.1*	*<0.1*	*<0.1*	128	96	64	43	183
In	< 0.6	2.4	2.4	0.6	1.5	1.0	NA	3.6	1.7	NA	NA	NA	NA	NA	0.017	1.9	1.5	0.8	1.2
Sn	15.8	85	15	7.1	35	30.1	10.49	10	20	17.69	12.44	16.76	19.41	16.29	4	7	8	*4*	8
Mo	2.1	11	240	*0.4*	*4.4*	*0.6*	*0.5*	23	*4.4*	*2.7*	*8.2*	*64.5*	*13.1*	57.0	0.55	72	32	*0.8*	*8.8*
W	< 1.3	57	6	2	5	6	*1*	11150	3	*3.3*	*2.9*	2950	*23.2*	1950	0.6	170	447	2	96
Bi	< 1.3	1	4	*0.3*	3	*0.2*	*0.1*	4	32	*0.2*	4410	3400	*93.8*	3420	0.12	158	6	*0.6*	*0.3*
Rb	7	34.5	4.1	7.6	82	1.6	45.7	27.9	6.2	176	417	291	305	108	105	82.9	303	448	27.7
Cs	< 0.25	2.59	0.96	0.66	7.84	0.74	1.16	2.75	< 0.2	1.20	43.43	17.57	30.81	6.02	1.9	0.68	22.9	12.4	< 0.1
Sr	37	9.1	*1*	198	44	14.1	20.5	13.9	4.5	70.0	4.9	7.7	6.7	7.2	3.8	116.0	49.3	31.2	8.1
Ba	14	17	5	79	84	27	11	66	13	696	57	45	95	26	87	200	1225	461	127
Zr	37	81	31	27	157	210	27	111	63	194	125	163	85	96	115	79	125	168	34
Hf	0.48	1.95	0.28	0.81	4.08	4.53	0.33	2.45	1.28	5.13	3.23	4.09	2.28	2.86	3.09	1.56	3.04	3.44	0.44
Nb	18.1	56.0	10.4	2.2	25.4	10.8	3.1	3.6	7.7	7.3	5.7	7.5	5.1	3.4	3.4	6.8	9.4	8.5	8.9
Ta	1.23	2.05	0.68	0.16	1.65	0.59	0.17	0.37	0.27	0.33	0.43	0.57	0.52	0.34	0.75	0.57	0.88	0.49	0.44
La	747	1835	15.9	554	555	191	227	37.4	13.5	27.8	13.7	10.4	40.7	2.83	15.1	31.9	16.2	57.0	17.7
Ce	1450	3.680	26	871	1.270	407	419	83	37	61.6	28.2	21.5	71.1	6.23	34.6	46	34	96	30
Pr	152	297	3.03	83.4	128.3	49.7	41.2	10.2	5.30	7.73	3.43	2.64	8.27	0.78	3.40	4.92	3.69	9.85	3.13
Nd	528	970	14.27	216	521	169	135	39.5	22.1	28.5	13.4	10.4	31.5	3.18	11.6	17.2	12.7	35.04	10.9
Sm	75.0	148	6.51	17.9	127	31.2	17.7	7.68	5.44	4.94	2.87	2.25	6.06	0.90	1.73	3.21	2.39	5.64	1.74
Eu	4.60	14.91	0.63	1.86	18.7	5.33	2.08	1.74	0.97	0.76	0.50	0.50	1.15	0.26	0.22	0.58	0.39	1.33	0.26
Gd	59.5	74.9	17.2	4.83	111	28.9	17.3	6.74	6.60	4.70	3.22	2.70	5.14	1.60	1.27	3.20	1.77	5.36	1.10
Tb	6.40	11.5	4.23	0.71	18.7	5.07	2.02	1.06	1.33	0.63	0.61	0.51	0.74	0.34	0.13	0.61	0.33	0.81	0.13
Dv	33.8	62.4	37.7	2.56	117	28.9	10.9	6.43	9.34	3.74	4.05	3.50	3.95	2.56	0.65	4.40	1.83	4.89	0.57
Ho	6.35	12.5	10.4	0.39	23.7	6.57	2.10	1.26	1.92	0.80	0.87	0.79	0.75	0.61	0.14	0.92	0.36	0.96	0.07
Er	16.6	38.7	40.3	0.93	70.0	17.4	6.31	3.62	5.65	2.37	2.61	2.53	2.18	2.09	0.47	3.06	1.18	2.96	0.24
Tm	2.08	6.09	6.84	0.13	10.1	2.65	0.85	0.52	0.78	0.34	0.37	0.40	0.32	0.35	0.08	0.35	0.19	0.43	0.03
Yb	11.0	43.6	51.6	0.67	67.3	14.4	5.39	3.49	4.75	2.24	2.44	2.99	2.30	2.95	0.70	2.04	1.21	2.78	0.23
Lu	1.20	7.25	9.78	0.12	10.5	2.22	1.01	0.54	0.72	0.41	0.43	0.59	0.46	0.64	0.12	0.30	0.22	0.46	0.03
Y	181	328	381	11.4	655	184	74.2	38.6	61.2	21.8	25.3	25.0	23.8	19.9	4.9	34.9	14.2	29.6	4.8
Th	30.0	30.6	19.6	18.1	38.3	37.1	24.1	4.6	10.9	54.6	6.3	8.3	5.5	5.1	2.3	9.7	20.2	7.0	4.5
U	5.1	370	25.9	6.3	930	20.7	8.2	2.6	22.6	12.2	19.7	11.0	10.4	5.1	1.4	6.7	5.6	1.5	2.5
															0.27				
Sb		*0.9*	*0.8*	*0.8*	*2.5*	*5.9*	*0.4*	*13.5*	*6.1*	*0.8*	*68.4*	*35.1*	*16.2*	*60.7*	1.07	*4*	*1.2*	*1.8*	*2.4*
Be		*4*	*3*	*4*	*8*	*2*	*7*	*2*	*2*	*5*	*7*	*3*	*5*	*2*	2.1	*<1*	*1*	*2*	*<1*
Li		*12.3*	*3.8*	*8.1*	*54.4*	*25.8*	*30.9*	*16.4*	*14.5*	*15.4*	*6.5*	*9.4*	*5.9*	*9.6*	6.7	*11.2*	*6.7*	*44.1*	*1.6*

Sample	09CQA 1114D3	09CQA 1159A3	09CQA 26B2	09CQA 39B3	09CQA 1020I2	10CQA 601C2	10CQA 602C2	10CQA 779B3	10CQA 780A2	10CQA 780B2	10CQA 780D3	10CQA 780E3	09CQA 109C3	09CQA 1170A3	09CQA 142B2	CQA07 451A	10CQA 1647A02
Sector	Sunil	Fab	Brooke	Hump	Hump	East Hottah		Jackpot	Jackpot	Jackpot	Jackpot	Jackpot	Brooke	Ham	Terra	NICO	Summit
Protolith	Sed	Por	Rhy	Sed	Sed	Basalt	Basalt	Por	Por	Por	Por	Por	Por	Por	Sed	Rhy	Rhy
Paragenesis	Bt-Kfs	Kfs-Mag-Bt	Mag-Kfs-Hem	Kfs-Mag	Mag-Kfs	Mag-Kfs	Mag-Kfs-Aln-Ep	Bt-Mag	Bt-Mag	Bt-Mag-Cp	Bt-Mag	Bt-Mag	Kfs	Kfs	Kfs+Amp relicts	Kfs	Kfs-Py-Cpy
Facies						K-Fe (HT)							K felsite		K felsite		K/K-Fe
SiO_2 (wt%)	46.41	54.63	67.11	50.49	1.57	40.04	58.04	45.58	66.10	63.67	61.72	63.96	71.54	67.58	68.51	61.6	67.62
TiO_2	1.02	0.79	0.19	0.60	0.32	0.68	0.86	0.64	0.27	0.26	0.31	0.26	0.33	0.52	0.16	0.08	0.04
Al_2O_3	15.52	12.21	12.0	12.8	0.70	9.34	9.60	16.42	12.21	11.73	12.19	12.70	14.1	14.9	12.3	17.88	14.38
Fe_2O_3	14.25	15.53	8.20	22.9	105.8	40.76	25.54	24.46	10.35	13.00	18.13	15.86	2.05	4.27	2.89	1.73	1.31
MnO	0.12	0.03	0.02	0.11	0.07	0.10	0.02	0.48	0.18	0.21	0.25	0.55	0.01	0.03	0.09	.010	0.02
MgO	3.88	3.61	1.15	1.18	0.47	1.07	0.22	3.15	0.40	0.40	1.09	1.39	0.07	0.80	1.37	.48	0.32
CaO	0.87	1.12	0.33	1.00	< 0.02	1.39	0.15	0.56	0.25	0.47	0.20	0.62	0.64	1.69	2.70	.23	0.39
Na_2O	0.55	1.44	1.24	2.34	< 0.04	0.15	0.10	0.55	0.39	0.32	0.07	0.06	0.40	2.33	0.17	.601	0.53
K_2O	11.43	7.64	4.83	7.42	0.08	5.85	6.14	4.64	8.08	7.35	3.24	2.08	10.22	5.86	9.82	16.21	11.76
P_2O_5	0.19	0.15	< 0.08	0.12	< 0.08	0.28	0.11	0.26	0.05	0.26	0.08	0.11	< 0.08	0.09	< 0.08	< 0.061	0.02
LOI	1.4	1.6	0.7	0.1	-1.9	0.9	0.7	2.2	0.4	0.8	1.8	1.1	0.5	0.8	1.9	0.5	0.6
S	0.05	0.2	< 0.01	0.01	< 0.01	0.01	< 0.004	0.00	0.01	0.01	0.02	0.02	0.01	< 0.01	0.01	< 0.01	< 0.006
Total	95.6	98.8	95.9	99.5	107.3	100.8	101.6	99.3	99.1	99.1	99.3	99.2	100.2	99.1	100.2	99.6	97.2
F (ppm)	*2070*	*2970*	*320*	*278*	*70*								*183*	*795*	*80*	*109*	
Cl																*244*	
Sc	39	21	7	17	2	17	12	20	6	11	8	18	5	10	3	1	3
V	234	134	35	110	501	64.0	71.3	136.3	20.4	26.0	41.5	27.9	24	39	15	*23*	1
Cr	197	121	206	133	253	10	< 6	92	10	8	< 6	25	167	154	148	211	41
Co	60	37	25	20	99	12	< 5	27	61	137	21	78	12	9	14	*1.2*	0.9
Ni	11	52	39	49	238	25	8	69	85	141	36	37	*5.5*	23	21	*4.1*	0.5
Cu	58	95	20	5	6	< 3	4	< 3	56	1633	272	157	82	10	7	*2.4*	13
Pb	5	12	13	4	2	13	12	38	488	513	40	122	22	18	7	*4.7*	8
Zn	23	18	33	19	73	87	< 10	1030	336	1540	441	463	11	43	59	10	7
As	1315	*9*	*1*	14	*1*	< 30	< 30	< 30	< 30	1.7	< 30	< 30	*3*	*4*	*4*	*6*	2.1
Ag	0.2	0.3	*<0.1*	0.2	*<0.1*	< 0.4	< 0.4	< 0.3	< 0.3	1.39	< 0.4	< 0.3	*<0.1*	*<0.1*	0.3	*<0.1*	0.03
Cd	31	30	15	49	242	69	40	38	16	19	27	24	10	< 8	14	*<0.1*	1
In	0.5	0.5	0.4	0.5	0.3	1.1	< 0.7	1	< 0.6	0.493	0.9	1.5	< 0.3	< 0.4	0.3	2.0	0.013
Sn	*5.3*	18	*4.5*	*4.9*	6.7	3	4	50	8.3	10.4	20	21	*3*	6.4	*3.6*	*0.6*	1.3
Mo	*0.7*	*1.5*	20	9	< 9	< 20	< 20	< 20	< 20	1.34	< 20	< 20	*1.3*	*10.2*	*0.6*	*12.8*	0.05
W	7	4	11	3	3	127	35	34	9.8	16.7	12.3	63	10	3.4	3	0.6	19
Bi	3	*0.3*	*0.6*	*<0.1*	*0.1*	3	< 1.3	1.9	< 1.1	1.29	< 1.3	5	1.1	*0.4*	*<0.1*	*0.4*	4
Rb	604	210	270	209	*6.5*	226	275	408	340	337	210	249	498	213	396	545	224
Cs	20.9	2.02	1.31	0.89	0.38	4.9	3.1	11.1	2.1	2.5	1.5	7	1.98	1.66	2.98	< 40	0.7
Sr	40.7	56.7	98.1	24.5	< 1	42	24	41	82	74	21	26	95.6	113	48.8	51.0	57.2
Ba	1280	1030	1355	3740	24	778	755	711	1540	1440	451	160	2290	1070	2220	2000	1810
Zr	160	142	168	121	12	146	194	111	244	233	239	213	201	444	131	144	134
Hf	3.53	3.68	5.21	3.65	0.26	3.54	4.57	3.13	6.60	6.27	6.55	6.02	5.95	11.5	4.38	4.65	3.45
Nb	11.1	12.5	8.9	11.0	4.9	7.2	9.0	33.9	14.7	16.8	24.7	39.0	14.6	28.8	15.0	12.1	11.4
Ta	0.79	0.93	1.10	1.01	0.28	0.47	0.56	1.25	0.95	1.36	1.38	2.1	1.71	2.46	1.47	2.10	2.30
La	371	165	37.2	18.4	3.40	742	98	1820	1130	1200	652	3480	42.9	51.2	1.44	20.3	22.0
Ce	687	217	68.8	35.7	3.58	1790	138	2880	1800	1920	1080	5490	79.8	122	5.21	35	41.1
Pr	59.9	17.9	8.02	4.79	0.53	205	14.6	252	157	167	98.0	482	8.81	15.0	0.84	3.36	4.20
Nd	166	52.5	25.8	18.2	1.93	812	49.6	777	475	515	294	1450	28.41	59.3	4.20	10.7	15.1
Sm	15.6	7.37	4.59	3.62	0.46	194	9.1	104	56.9	64.9	35	173	4.42	12.2	1.06	1.87	2.50
Eu	2.52	1.22	0.84	0.72	0.07	19.5	2.40	10.3	3.60	4.30	2.30	9.60	0.54	2.06	0.16	0.39	0.33
Gd	7.86	5.05	3.62	3.31	0.68	176	8.7	71.4	40.0	48.1	25.6	117	2.78	11.4	1.34	1.77	2.48
Tb	1.18	0.84	0.62	0.51	0.14	24.6	1.28	6.28	3.50	4.70	2.60	10.50	0.43	1.78	0.25	0.31	0.41
Dv	5.80	4.85	3.61	3.23	1.04	134	7.00	25.2	15.2	23.4	12.9	48.3	2.50	11.8	1.70	2.08	2.90
Ho	1.01	0.95	0.74	0.62	0.18	25.6	1.40	4.02	2.75	4.54	2.7	9.5	0.50	2.43	0.37	0.45	0.64
Er	2.77	2.82	2.26	1.90	0.55	67.8	3.73	10.1	7.53	13.4	8.67	29.6	1.66	7.20	1.30	1.51	1.96
Tm	0.38	0.43	0.37	0.29	0.08	9.3	0.53	1.49	1.13	2.14	1.46	4.84	0.28	1.01	0.23	0.26	0.29
Yb	2.46	3.01	2.34	1.88	0.57	56.0	3.49	9.90	7.33	14.1	10.1	34.0	1.83	6.46	1.60	1.79	2.24
Lu	0.39	0.46	0.41	0.30	0.07	7.87	0.50	1.67	1.20	2.27	1.77	5.68	0.31	0.90	0.27	0.31	0.37
Y	30.5	28.9	20.7	18.3	2.2	1070	47	103	76	133	72	256	15.8	73	10.6	15.6	18.0
Th	6.2	15.1	27.9	10.2	0.2	4.1	5.1	18.0	23.0	23.0	30.0	29.0	31.4	31.8	22.6	35.7	20.0
U	2.9	10.7	46.9	1.9	2.2	12.2	3.6	30.6	28.6	88.5	122	333	8.1	5.3	4.8	9.1	7.2
										1.58							0.59
Sb	*0.7*	*0.8*	*0.9*	*11.6*	*0.4*					0.85			*1.9*	*0.9*	*5.5*	*0.8*	2.69
Be	*5*	*2*	*2*	*1*	*<1*					1.11			*<1*	*4*	*1*	*<1*	1.38
Li	*51.8*	*30.7*	*4.9*	*8.3*	*4*					12			*2.7*	*20.8*	*9.5*	*6.5*	2.2

Sample	10CQA 202B2	10CQA 202L2	10CQA 204F2	CQA05 220A1	09CQA 48A3	09CQA 37B3	CQA05 132B	09CQA 55G2	09CQA 1083C2	09CQA 1026A2	09CQA 1027A3	CQA05 144E	CQA05 166C	CQA05 138B	CQA06 376A
Sector	Grouard	Grouard	Grouard	Mile S.	TLG	Carbonate	Mag Hill	Duke	Duke	Sue Dianne	Sue Dianne	K2 zone	W. Echo Bay	K2 zone	EBG
Protolith	Sed	Sed	Sed	Volcaniclastic		Sed	And	Sed	Sed	And	Felsic vol.	And	And	Vein	And
Paragenesis	Skarn	Skarn	Skarn	Adr-Ves Kfs-Ep	Dp-Grt Kfs	Dp-Cb-Chl	Chl-Cb-Hem-Kfs	Chl-Cb-Hem-Amp	Chl-Mag-Cb	Kfs-Hem-Cpy±Mag	Kfs-Hem	Chl-Kfs-Hem	Kfs-Ac+ vn Ccp-Mo	Qtz-Jsp-Hem	Qtz-Ser
Facies		Skarn		Skarn K					K-Fe (LT)				HT-LT=Kfe	Silicification	
SiO_2 (wt%)	35.43	41.90	53.58	54.20	49.20	45.74	39.57	45.96	30.81	48.78	59.63	66.30	57.90	73.98	73.73
TiO_2	0.10	0.22	0.89	0.49	0.490	0.45	0.16	0.19	0.22	0.54	0.32	0.49	0.53	0.02	0.56
Al_2O_3	3.69	6.66	15.43	10.80	7.02	12.1	4.16	2.84	3.45	12.13	10.96	14.70	13.10	0.76	10.09
Fe_2O_3	2.07	2.66	5.73	8.71	7.18	6.03	9.16	14.76	26.94	22.82	17.52	8.59	10.90	24.02	5.63
MnO	0.18	0.16	0.28	0.524	0.130	0.17	2.97	1.08	0.16	0.14	0.05	0.082	0.207	0.03	0.00
MgO	1.50	1.61	3.44	4.58	10.46	4.49	8.73	19.50	20.42	1.29	0.38	1.09	2.40	0.18	0.16
CaO	32.63	24.52	8.81	12.90	17.35	21.36	11.30	10.24	7.04	1.09	0.65	0.27	0.77	0.09	0.20
Na_2O	1.73	3.84	6.14	2.38	0.54	0.47	0.04	0.09	< 0,05	0.33	0.30	1.82	0.58	0.03	0.09
K_2O	0.28	< 0,03	0.58	4.18	2.92	3.71	1.40	0.09	0.58	8.71	8.41	6.83	6.22	0.01	3.31
P_2O_5	0.02	0.05	0.30	0.12	0.10	0.09	0.06	0.03	0.03	0.16	0.09	0.10	0.37	0.12	0.40
LOI	24.0	18.8	3.9	1.20	4.10	5.1	21.8	4.5	6.8	1.5	0.7	2.00	4.00	0.8	4.3
S	0.2	0.06	0.4	0.023	0.04	0.06	0.07	0.03	0.02	0.05	< 0,006	*0.1*	0.327	0.01	0.7
Total	101.8	100.5	100.2	100.1	99.5	99.9	99.6	99.2	96.4	97.4	98.9	102.4	97.31	100.1	99.3
F (ppm)					*6010*	*388*		*978*	*2385*	*420*	*180*			*60*	*510*
Cl															*<100*
Sc	4	6	29	21.2	13.38	14	27	4	4	13	8	9.71	41.5	5	4
V	16	43	182	101	88	88	91	30	55	66	60	86.7	140	124	25
Cr	10	18	105	175	95.1	94	202	20	21	16	25	149	177	241	142
Co	2.4	< 5	33	30	25.4	23	*12.2*	12	17	64	30	15	44.8	*2.6*	*7.3*
Ni	3.4	< 8	18	*30*	33.3	53	111	*8.4*	15	14	*4*	42.6	*17.2*	*7.4*	*4.5*
Cu	423	< 3	268	411	17	5	494	*5.1*	*3.8*	1825	73	139	2520	133	189
Pb	10	1	3230	50.4	6.56	11	*9.7*	7	4	11	26	*14.4*	*16.7*	*8*	*5.1*
Zn	10	< 10	2980	644	80	26	68	187	128	114	43	75.1	41.4	5	*6*
As	<5	< 30	< 30	*27*	*5*	*3*	*3*	*6*	*10*	*10*	*5*	*41*	*161*	*44*	*45*
Ag	0.02	< 0,4	0.3	*0.7*	*<0.1*	0.2	*0.1*	0.2	0.2	0.5	0.8	*0.2*	*0.3*	*0.3*	*2.4*
Cd	3	3	15	7.5	23.2	17	9.8	27	56	46	37	7.6	10.6	22	*0.2*
In	0.048	< 0.6	< 0.6		0.4	0.4	NA	0.6	0.6	0.7	1.4			NA	
Sn	2.7	4	4	*13.9*	13.9	< 6	*1.2*	8	17	10	8	*1.1*	*4.8*	*14.5*	*2.9*
Mo	0.37	< 20	< 20	31.6	*0.3*	12	*1.1*	*0.4*	*<0.1*	*2.7*	*2.1*	*0.4*	198.2	29.6	*7.2*
W	44	3	8	*2.9*	1.9	3	*1.8*	1	3	10	12	*4.3*	*7*	232	*2.3*
Bi	0.38	< 1.3	< 1.1	*1.2*	*0.4*	*<0.1*	*0.5*	*0.6*	*0.1*	21	4	*1.1*	*1.5*	*1.5*	7.12
Rb	7.2	< 0,26	25.2	123	143.3	144	48.0	7.2	56.3	257	220	168.4	80	2.4	88.1
Cs	0.16	< 0,26	0.4	0.6	0.86	1.56	0.79	0.60	3.64	3.12	2.74	1.5	<2	0.45	0.42
Sr	61.9	76.1	121	55.1	60	104	28.4	4.1	5.6	84.0	44.5	70	60.9	7.7	10.7
Ba	57	9	166	1170	123.3	492	166	12	47	4150	3330	1680	980	46	461
Zr	29	68	110	128	187	127	28	90	76	232	188	290	160	11	171
Hf	0.91	1.90	2.59	3	4.41	3.78	0.85	1.74	1.46	5.63	4.29	7	*4.6*	0.15	4.15
Nb	2.5	4.8	5.3	8	10.8	9.3	2.0	4.6	5.1	15.1	11.4	18	9	1.3	11.2
Ta	0.33	0.89	0.57	0.6	0.92	0.87	0.23	0.24	0.31	1.36	0.97	1.6	*0.6*	< 0.05	0.79
La	15.3	16.6	14.6	35.2	34.4	16.0	34.6	2.75	4.52	219	154	28	5260	29.7	6.04
Ce	29	33.7	32.2	65.4	74	35.1	68.3	7	9	228	172	58.9	9250	57.6	10.05
Pr	3.40	4.10	4.40	7.5	10.76	4.89	8.57	1.03	1.10	15.94	12.65	7.4	955	6.62	1.23
Nd	11.4	14.7	16.4	26.3	39	18.2	33.7	5.11	4.90	43.4	39.2	28	2840	23.7	4.63
Sm	2.00	2.90	3.30	5	9.1	3.76	9.20	1.49	0.95	6.69	6.34	5	300	4.46	1.22
Eu	0.39	0.62	0.95	0.7	1.42	0.71	1.95	0.20	0.07	1.38	1.24	1.1	14	1.22	0.31
Gd	1.48	2.52	2.81	4	7.55	3.36	9.62	1.73	0.93	4.47	4.49	4	170	2.88	1.50
Tb	0.20	0.40	0.41	0.6	1.21	0.54	1.60	0.27	0.13	0.78	0.67	0.6	19	0.33	0.27
Dy	1.07	2.10	2.50	4	6.22	3.30	11.1	1.66	0.81	4.68	3.68	3	90	1.58	1.66
Ho	0.27	0.44	0.58	0.7	1.2	0.65	2.23	0.31	0.12	0.91	0.68	0.6	14	0.25	0.37
Er	0.60	1.16	1.61	2.1	3.14	1.98	6.22	1.00	0.42	2.90	2.06	1.7	40	0.56	1.00
Tm	0.09	0.16	0.25	0.3	0.47	0.32	0.95	0.13	0.06	0.43	0.30	0.28	6	0.09	0.14
Yb	0.58	1.14	1.67	2.3	2.56	1.95	6.87	0.80	0.41	2.94	1.96	1.8	30	0.64	0.80
Lu	0.08	0.17	0.26	0.3	0.4	0.33	0.94	0.13	0.07	0.45	0.31	0.25	5	0.09	0.12
Y	6.1	12.5	15.0	22	35.1	18.7	60.9	11.5	4.6	29.5	20.9	19	500	7.1	9.5
Th	4.3	6.8	4.3	10	9.09	8.5	5.9	2.6	4.4	24.0	18.9	28	50	0.6	9.2
U	1.2	1.7	1.5	4	7.44	2.3	4.9	1.4	1.8	43.3	21.5	4	12	1.5	1.9
	0.03														
Sb	0.82			*3.4*	*2.7*	*9*	*1.3*	*3.5*	*1.1*	*2.7*	*1.3*	*7.5*	*7.6*	*25.3*	*11.9*
Be	0.98			*1*	*7*	*3*	*2*	*3*	*<1*	*3*	*2*	*2*		*1*	*<1*
Li	1.2			*15*	*38.5*	*20.3*	*36.7*	*30.7*	*4.1*	*37.1*	*12.8*	*14*	*27.6*	*14.7*	*1.2*

ANNEXE - 4 : ÉCHANTILLONS UTILISÉS ET ANALYSES REPRÉSENTATIVES POUR LE CHAPITRE 4 : ÉCHANTILLONS DES DIFFÉRENTS INDICES MINÉRALISÉS ET DES ALTÉRATIONS IOAA DU SUD DE LA ZONE MAGMATIQUE DU GRAND LAC DE L'OURS

Les minéraux sont abbrégés suivant Whitney et Evans (2010) sauf Qtz pour quartz.

Region	Treasure Lk. Gp. western section									
Showing	LP's	LP's	LP's	LJLVS	LJLVS	LJLVS	LJLVS	South Duke	South Duke	Oxymoron prospect
Sample	0055F03	0055B02	0056B03	1082E03	1082H02	1082I02	1083E02	1085A02	1086A02	1084A02
Precursor	Sed. rock	Sed. rock	Sed. rock	Sed. rock	Sed. rock	Sed. rock	Sed. rock	Sed. rock	Sed. Rock	Sed. rock
Alteration	HT Ca-Fe	Ca-Fe-K	K-Fe	HT Ca-Fe	HT Ca-Fe	HT Ca-Fe	LT Ca-Fe/ LT K-Fe	LT K-Fe	HT Ca-Fe	K
ICP-AES/MS (INRS)										
Loi (wt. %)	0.3	1.5	1.1	-0.8	0.8	0.3	2.6	2.9	-0.8	1.1
Al_2O_3	5.85	9.38	18.33	3.67	5.59	7.29	3.22	4.31	5.18	18
CaO	**8.14**	**7.68**	1.14	**7.44**	**11.69**	**10.95**	**12.05**	8.16	**4.95**	2.01
Fe_2O_3T	**37.77**	**31.56**	**12.55**	**47.51**	**30.64**	**19.42**	4.92	**18.7**	**64.81**	0.58
K_2O	1.44	2.74	**9.07**	0.41	0.78	0.66	0.29	0.23	0.97	**10.28**
MgO	3.45	5.3	1.32	4.23	7.65	5.88	**20.96**	**13.71**	4.5	0.5
MnO	2.27	1.81	0.38	0.88	0.7	0.72	0.14	1.49	0.62	0.05
Na_2O	0.96	0.96	1.68	0.85	0.79	2.35	0.56	0.3	0.74	2.99
P_2O_5	0.05	0.1	0.27	< 0.005	0.08	< 0.005	< 0.08	0.06	0.05	< 0.08
S	<0.1	<0.1	0.02	0.3	<0.1	<0.1	0.01	0.1	<0.1	< 0.01
SiO_2	36.84	37.36	47.81	32.26	37.81	48.74	54.75	46.25	18.15	66.08
TiO_2	0.2	0.53	1.1	0.11	0.44	0.23	0.18	0.3	0.36	0.33
TOTAL	97.2	98.9	94.7	96.6	96.9	96.5	99.7	96.5	99.5	102
Y (ppm)	39	53	46	61	38	44	12.6	26	25	28.2
Zr	111	249	184	63	282	118	82	131	110	278
Nb	3.6	7.5	10.1	7.7	10.0	8.1	5.3	6.1	6.5	18.2
Hf	2.45	5.88	4.03	1.28	6.51	2.51	2.17	2.96	2.42	7.24
Ta	0.37	0.73	0.69	0.27	1	0.46	0.33	0.47	0.51	1.24
Th	4.56	4.49	8.83	10.88	9.98	5.96	2.57	5.96	1.61	22.27
U	2.6	3.25	3.37	22.6	3.47	**77.2**	0.61	15.1	0.86	5.08
Ag	< 0.2	0.3	0.3	0.2	0.7	0.2	0.2	0.2	0.2	0.2
In	3.6	3.8	0.5	1.7	1.5	1.4	< 0.3	1.1	1.3	< 0.3
W	**11,149**	2	21	3	4	4	1.2	2	2	4.3
Ba	66	145	764	13	44	23	25	23	52	297
Cd	72	62	22	89	60	39	< 8	40	131	< 8
Cr	17	50	576	23	32	19	33	25	19	56
Cu	294	**1096**	389	57	151	< 20	4	**2677**	82	4
Sc	8.26	9.82	35.33	8.25	6.18	2.53	2.64	4.49	4.66	7.84
Sr	14	16	52	5	22	15	2	< 3	5	29
V	59	77	238	116	62	87	32	40	89	9
Zn	88	162	48	235	725	258	159	158	320	95
La	37.40	21.20	266.66	13.50	134	16.74	5.51	9.06	7.04	47.24
Ce	83	45	403	37	226	42	17.66	19	18	104.47
Pr	10.18	5.8	37.35	5.3	21.21	5.54	2.46	2.43	2.69	11.05
Nd	39.5	23.69	115.48	22.15	65.68	22.42	11.32	10.21	12.15	42.09
Sm	7.68	6.27	15.57	5.44	8.51	4.89	2.85	2.41	3.23	7.49
Eu	1.74	1.63	2.89	0.97	1.63	1	0.41	0.29	0.76	1.21
Gd	6.74	7.11	10.81	6.6	6.26	5.38	2.66	2.67	3.71	5.61
Tb	1.06	1.32	1.44	1.33	1.03	1	0.4	0.51	0.61	0.85
Dy	6.43	8.55	7.09	9.34	5.96	6.81	2.34	3.66	3.88	4.97
Ho	1.26	1.71	1.21	1.92	1.13	1.41	0.45	0.77	0.76	0.97
Er	3.62	5.26	3.39	5.65	3.2	4.07	1.3	2.51	2.28	2.7
Tm	0.52	0.7	0.39	0.78	0.44	0.6	0.19	0.36	0.31	0.41
Yb	3.49	4.28	2.25	4.75	2.73	3.83	1.14	2.23	1.93	2.56
Lu	0.54	0.64	0.38	0.72	0.39	0.53	0.17	0.34	0.27	0.39
REE total	203	133	868	115	478	117	49	56	58	232
La/Yb	10.7	5.0	118.6	2.8	49.2	4.4	4.8	4.1	3.6	18.4
Zr/La	3.0	11.8	0.7	4.7	2.1	7.0	14.9	14.4	15.6	5.9
Zr/Yb	32	58	82	13	103	31	72	59	57	108
Ta/Nb	0.1	0.1	0.07	0.04	0.1	0.06	0.06	0.08	0.08	0.07

Region	Treasure Lk. Gp. western section					Treasure Lk. Gp. eastern section				
Showing	Oxymoron prospect	Peanut	Peanut silver	Sunil REE	Dennis	Dennis Th	GBmz batholith	MHF prospect	MHF prospect	Esther
Sample	1084B02	1097A02	1098A02	1114D04	1045A03	1046F01	1132A02	1059H04	1059C02	1059B05
Precursor	Sed. rock	Sed. Rock	Sed. Rock	Sed. Rock	Sed. Rock	Sed. Rock	Granitic	Granitic	Granitic	Sed. Rock
Alteration	LT Ca-Fe	HT K-Fe	K	HT K-Fe	Na-Ca-Fe	Na	Na	Na	K/Na	HT Ca-Fe
ICP-AES/MS (INRS)										
Loi (wt. %)	1.3	0.4	0.3	1.4	1.5	0.8	0.6	0.5	0.7	2.3
Al_2O_3	13.9	17.2	10.97	18.1	15.2	17.75	16.57	19.9	16.22	9.74
CaO	**23.86**	0.29	0.03	0.83	**2.09**	1.46	3.08	0.55	0.16	14.5
Fe_2O_3T	**13.36**	**5.35**	1.87	**13.9**	**10.95**	1.18	2.75	0.94	0.92	8.45
K_2O	< 0.05	**10.2**	**10.21**	**11.14**	3.16	1.68	1.62	0.92	**8.59**	0.78
MgO	4.27	1.13	0.08	3.8	2.8	0.66	1.84	0.48	1.02	16.19
MnO	0.42	0.02	0.01	0.11	0.07	0.03	0.03	0.02	0.01	0.17
Na_2O	0.1	2.13	0.24	0.48	**3.99**	**9.71**	**8.03**	**10.01**	**4.68**	1.37
P_2O_5	0.22	0.14	0.01	0.18	0.15	0.01	0.19	< 0.08	0.02	< 0.08
S	0.03	< 0.01	<0.1	0.04	0.02	<0.1	<0.1	< 0.01	<0.1	0.01
SiO_2	42.99	63.45	75.96	49.19	62.43	65.26	61.85	66.47	65.48	45.81
TiO_2	0.84	0.6	0.04	1.02	0.61	0.05	0.57	0.05	0.09	0.48
TOTAL	101.5	101.1	99.7	100.5	103.2	98.5	97.1	99.9	97.8	99.9
Y (ppm)	44.5	12.6	40	21.4	23.7	3	25	67.6	22	37.7
Zr	174	191	91	165	138	94	188	211	94	129
Nb	32.7	13.8	12.5	11.2	10.2	3.4	13.2	**215**	**589**	15.2
Hf	4.2	4.94	2.89	4.29	3.95	1.78	4.5	9.81	3.24	3.55
Ta	1.74	1.25	1.49	0.87	0.79	0.19	1.04	**36.6**	**162**	0.83
Th	**63.43**	13.19	20.02	7.38	14.17	111.05	6.98	**87.25**	**93.09**	7.22
U	**87.6**	2.38	3.64	3.41	1.85	13.9	2.02	**82.8**	**234**	2.51
Ag	0.3	0.2	**23.5**	< 0.2	< 0.2	0.2	0.3	1	4.9	0.3
In	0.7	1.5	0.6	< 0.3	< 0.3	0.4	0.2	< 0.3	0.3	0.4
W	4.1	7.7	10	5.9	5.8	5	2	8.2	9	1.2
Ba	64	1587	1077	1396	1277	90	340	65	582	52
Cd	24	< 8	< 3	20	26	< 3	5	< 8	< 3	< 8
Cr	391	78	8	223	179	16	25	77	10	68
Cu	14	5	< 20	21	23	32	< 20	7	< 20	5
Sc	43.08	13.36	3.02	41.62	21.66	3.55	11.25	4.58	18.93	10.96
Sr	288	50	13	48	148	62	184	29	35	17
V	193	51	4	234	105	16	59	< 4	4	101
Zn	170	13	< 5	25	76	10	10	< 10	5	105
La	**769**	50.72	15.66	**505**	34.25	5.09	46.90	22.55	5.65	53.05
Ce	**1017**	97.95	31	**935**	69.94	10	91	36.47	22	78.55
Pr	**69.65**	10.65	3.76	**77.34**	7.66	1.15	10.56	7.45	3.28	13.65
Nd	**145**	40.43	18.94	**220**	29.09	4.09	39.75	29.65	13.21	46.83
Sm	12.34	7.59	3.54	20.7	5.31	0.72	7.6	11.52	4.9	9.05
Eu	3.81	1.25	0.4	3.31	1.03	0.1	1.66	0.38	0.16	1.17
Gd	6	5.94	4.21	11.29	4.36	0.58	6.27	11.83	5.09	7.27
Tb	1.28	0.75	0.81	1.32	0.67	0.09	0.89	1.32	0.8	0.67
Dy	7.5	4.39	5.79	6.57	4.02	0.6	4.89	11.39	3.91	6.05
Ho	1.41	0.75	1.2	1.1	0.8	0.1	0.85	2.11	0.58	1.15
Er	3.91	2.33	3.79	2.96	2.4	0.38	2.24	6.62	1.53	3.47
Tm	0.49	0.34	0.57	0.39	0.35	0.06	0.31	0.67	0.23	0.31
Yb	2.97	2.1	3.78	2.37	2.17	0.42	1.89	7.56	1.51	3
Lu	0.43	0.29	0.61	0.33	0.32	0.07	0.27	1.1	0.22	0.44
REE total	**2040**	225	94	**1786**	162	24	215	150	63	224
La/Yb	**258.8**	24.2	4.1	**213.3**	15.8	12.1	24.8	3.0	3.8	17.7
Zr/La	0.2	3.8	5.8	0.3	**4.0**	**18.6**	4.0	9.4	16.7	2.4
Zr/Yb	58	91	24	70	**63**	**225**	100	28	63	43
Ta/Nb	0.05	0.09	0.12	0.08	0.08	0.06	0.08	0.17	0.28	0.05

Region		Treasure Lk. Gp. eastern section				Cole	Sue Dianne volcanic complex			
Showing	Ron Fe+REE	Carbonate Mountain	Carbonate Mountain	Hump V	Hump	Cole Breccia	Brooke	Brooke	Sue Dianne	Sue Dianne
Sample	0021B03	0030B03	0036A03	0042A03	1020I02	0095F02	0109F03	0109F07	1008B03	1009B04
Precursor		Sed. Rock	Sed. Rock	Sed. Rock	Unk.	Volcanic	Volcanic	Volcanic	Volcanic	Volcanic
Alteration	LT Ca-Fe/ HT Ca-Fe	Na	Skarn-type	HT K-Fe	Fe	Na-Ca-Fe	LT Ca-Fe/ HT K-Fe	LT Ca-Fe/ HT K-Fe	Na/HT K-Fe	LT K-Fe/HT K-Fe
ICP-AES/MS (INRS)										
Loi (wt. %)	0.8	0.5	3.3	-0.1	-1.9	0.7	2.9	1.9	1.8	0.8
Al_2O_3	11.1	12.5	13	3.1	0.7	16.16	9.71	7.42	13.9	14
CaO	**8.69**	1.07	**13.38**	0.15	< 0.02	**4.25**	**6.91**	**2.66**	1.62	0.74
Fe_2O_3T	**32**	0.98	**6.29**	**72**	**105.84**	**7.95**	**27.39**	**42.76**	**6.6**	**14.2**
K_2O	0.35	0.21	2.8	**0.78**	0.08	1.51	**1.33**	**1.8**	0.68	**10.4**
MgO	2.7	0.24	8.55	0.23	0.47	1.69	0.24	0.21	0.97	0.45
MnO	0.14	0.01	0.2	0.04	0.07	0.03	0.06	0.03	0.03	0.05
Na_2O	2.96	**6.63**	1.96	1.06	< 0.04	**7.8**	0.12	0.4	**6.77**	0.21
P_2O_5	0.19	< 0.08	0.11	< 0.08	< 0.08	0.26	0.47	0.27	0.15	0.14
S	0.02	0.01	0.06	< 0.01	< 0.01	<0.1	**7.4**	**5**	< 0.01	0.15
SiO_2	39.5	74.28	48.26	19.78	1.57	56.92	29.87	37.73	68.24	57.1
TiO_2	0.09	0.08	0.57	0.24	0.32	1.17	0.2	0.15	0.65	0.72
TOTAL	98.7	96.5	98.8	97.5	107.3	98.3	79.8	95.4	101.5	100.1
Y (ppm)	11.4	5.9	25.1	37.1	2.2	34	57	35	13	15.8
Zr	27	138	141	39	12	195	89	79	167	128
Nb	2.2	3.3	11.3	1.5	4.9	11.9	8.3	6.8	12.0	10.0
Hf	0.81	4.68	3.89	1.23	0.26	4.37	2.11	1.56	4.66	3.56
Ta	0.16	1.26	1.08	0.07	0.28	0.92	0.67	0.57	1.13	0.69
Th	18.07	50.48	14.93	5.85	< 0.3	10.95	13.95	9.73	21.38	9.78
U	6.34	3.54	2.48	1.77	2.19	2.86	8.01	6.7	5.09	18.4
Ag	< 0.2	0.2	0.3	< 0.2	< 0.2	0.3	2.3	2.3	< 0.2	< 0.2
In	0.6	< 0.3	< 0.3	0.5	0.3	0.3	1.5	1.9	< 0.3	0.3
W	1.6	6.3	2.1	7.6	3.2	10	5,610	170	4.5	6.3
Ba	79	23	2832	141	24	325	145	200	67	**7623**
Cd	70	< 8	15	167	242	15	55	96	15	25
Cr	71	198	112	135	253	64	30	15	183	182
Cu	9	14	13	7	6	< 20	**71089**	**47953**	10	**2506**
Sc	3.4	3.87	18.99	6.66	2.37	16.72	15.33	7.99	13.23	14.83
Sr	198	29	97	6	< 1	116	300	116	39	64
V	59	9	106	**780**	**501**	97	119	86	83	75
Zn	101	28	60	< 10	73	13	234	182	< 10	45
La	**554**	9.76	57.12	44.82	3.40	40.23	**491**	31.88	27.55	37.48
Ce	**871**	19.62	106.57	78.86	3.58	75	**837**	46	69.05	53.65
Pr	**83.39**	2.35	12.83	8.34	0.53	8.36	**76.3**	4.92	7.51	4.72
Nd	**216**	7.53	41.31	30.21	1.93	31.49	**268**	17.2	28.03	15.93
Sm	17.9	1.34	6.48	5.79	0.46	6.05	45.85	3.21	5.42	3.15
Eu	1.86	0.26	0.98	1.06	0.07	1.52	6.35	0.58	1.07	0.7
Gd	4.83	1.12	4.63	5.34	0.68	5.7	26.01	3.2	3.86	2.59
Tb	0.71	0.17	0.73	0.87	0.14	0.9	3.07	0.61	0.51	0.46
Dy	2.56	1.02	4.15	5.67	1.04	5.51	13.21	4.4	2.71	2.82
Ho	0.39	0.18	0.85	1.09	0.18	1.09	2.01	0.92	0.51	0.59
Er	0.93	0.67	2.42	3.3	0.55	3.24	5	3.06	1.6	1.92
Tm	0.13	0.12	0.38	0.46	0.08	0.47	0.56	0.35	0.26	0.34
Yb	0.67	0.76	2.27	2.77	0.57	3.06	3.1	2.04	1.68	2.21
Lu	0.12	0.15	0.39	0.38	0.07	0.48	0.44	0.3	0.27	0.35
REE total	**1753**	45	241	189	13	183	**1776**	118	150	127
La/Yb	**829.8**	12.9	25.1	16.2	5.9	13.2	**158.5**	15.6	16.4	17.0
Zr/La	0.1	14.2	2.5	0.9	3.6	4.9	0.2	2.5	6.1	3.4
Zr/Yb	41	183	62	14	21	64	29	39	99	58
Ta/Nb	0.07	0.39	0.1	0.04	0.06	0.08	0.08	0.08	0.09	0.07

Region	Lou		
Showing	Summit Peak	Summit Peak	Summit Peak
Sample	1646B03	1647A02	1647B02
Precursor	Rhy	Rhy	Rhy
Alteration	K-Fe (HT)/Cu-Fe-S	K	K/Cu-S-Fe
ICP-AES/MS (INRS)			
Loi (wt. %)	2.3	0.6	4.0
Al_2O_3	15.42	14.38	11.85
CaO	2.26	0.39	0.02
Fe_2O_3T	11.62	1.31	9.04
K_2O	11.39	11.76	9.71
MgO	2.28	0.32	0.38
MnO	0.06	0.02	0.01
Na_2O	0.47	0.53	0.12
P_2O_5	0.16	0.02	0.02
S	51.75	67.62	62.42
SiO_2	0.49	< 0,006	0.02
TiO_2	0.56	0.04	0.04
TOTAL	99.4	97.2	98.6
Y (ppm)	14.8	18	12.1
Zr	297	134	96
Nb	10.8	11.4	9.6
Hf	6.46	3.45	2.74
Ta	1.35	2.3	1.47
Th	10.5	20	16.6
U	3.41	7.21	6.79
Ag	< 0,4	< 0,4	< 0,3
In	< 0,6	< 0,6	< 0,5
W	84	18.5	4.5
Ba	1253	1813	1370
Cd	16	1	12
Cr	73	41	13
Cu	3490	13	7619
Sc	12.9	3.4	3.3
Sr	28.1	57.2	36.6
V	76.0	< 2	2.2
Zn	33	7	35
La	61.00	22.00	19.00
Ce	116.0	41.10	36.10
Pr	12.50	4.20	3.90
Nd	47.20	15.10	13.00
Sm	7.90	2.50	2.40
Eu	1.39	0.33	0.41
Gd	6.71	2.48	2.25
Tb	0.62	0.41	0.33
Dy	3.30	2.90	2.00
Ho	0.55	0.64	0.47
Er	1.44	1.96	1.42
Tm	0.21	0.29	0.22
Yb	1.45	2.24	1.58
Lu	0.25	0.37	0.25
REE total	261	97	83
La/Yb	42.1	9.8	12.0
Zr/La	4.9	6.1	5.1
Zr/Yb	205	60	61
Ta/Nb	0.13	0.20	0.15

Region	Treasure Lk. Gp. western section									
Showing	LP's	LP's	LP's	LJLVS	LJLVS	LJLVS	LJLVS	South Duke	South Duke	Duke REE showing
Sample	0055F03	0055B02	0056B03	1082E03	1082H02	1082I02	1083E02	1085A02	1086A02	1084A02
Precursor	Sed. rock	Sed. rock	Sed. rock	Sed. rock	Sed. rock	Sed. rock	Sed. rock	Sed. rock	Sed. Rock	Sed. rock
Alteration	Ca-Fe	Ca-Fe-K	K-Fe	Ca-Fe	Ca-Fe	Ca-Fe	LT K-Fe	LT K-Fe	Ca-Fe	K
1EX (Acme)										
Mo (ppm)	23.4	0.7	1.5	4.4	0.3	0.5	0.2	0.1	1.3	0.2
Pb	5.7	9.5	16.5	8.7	424	11.4	2.5	5.2	9.1	8.6
Ni	24	41.5	26.3	**2524**	13.1	254.6	27.1	28.1	13.5	4.2
Co	22.5	68.1	9.3	**3642**	25.3	313.1	12.6	39.8	38.9	1.4
Bi	6.3	3.0	46.2	50.6	11.7	7.8	0.1	22.8	4.8	0.3
Sn	12.0	15.0	2.4	25.0	40.5	20.2	6.3	1.7	35.8	2.4
Li	16.4	49.1	37.9	14.5	18.9	11.2	14.1	21.6	5.2	2.8
INAA (Becquerel)										
Sb (ppm)	11.5	6.7	8.3	< 3.8	3.1	2.7	0.6	2.4	3.4	1.3
As	56	192	22	**10500**	6.5	891	2.3	3.2	25	8
Cs	3.0	17.0	8.7	< 1.3	0.7	0.6	< 0.5	< 0.5	3.3	0.5
Rb	24	140	300	< 28	18	< 5	7	11	34	250

Region	Treasure Lk. Gp. western section					Treasure Lk. Gp. eastern section				
Showing	Duke REE showing	Peanut	Peanut silver	Sunil REE	Dennis	Dennis Th	GBmz batholith	Esther	Esther	Esther
Sample	1084B02	1097A02	1098A02	1114D04	1045A03	1046F01	1132A02	1059H04	1059C02	1059B05
Precursor	Sed. rock	Sed. Rock	Sed. Rock	Sed. Rock	Sed. Rock	Sed. Rock	Granitic	Granitic	Granitic	Sed. Rock
Alteration	Epidote	HT K-Fe	K	HT K-Fe	Na-Ca-Fe	Na	Na	Na	K/Na	Ca-Fe
1EX (Acme)										
Mo (ppm)	0.7	0.8	7.4	0.5	0.4	<0.1	0.2	0.6	<0.1	0.2
Pb	77.3	6.3	4.1	3	6.4	9.1	5.4	4.7	4.4	1.3
Ni	27.3	8.6	9	17.5	27.1	3.7	17.8	2.6	1.5	33
Co	21.6	4.1	3.6	59.9	17	2	6.6	0.9	1.6	18.8
Bi	6.8	<0.1	<0.1	5.5	0.5	0.3	0.1	0.1	0.6	0.1
Sn	40.4	7.3	3.0	4.8	3.9	1.5	4.6	9.7	14.7	14.4
Li	14.0	9.9	9.8	57.4	24.4	7.5	13.0	8.9	8.2	26.6
INAA (Becquerel)										
Sb (ppm)	17.2	2.8	1.4	< 0.4	1	1.3	0.4	2.9	2.6	0.7
As	13	1.4	3	1050	2.5	2.8	1.4	3.1	3.2	2.6
Cs	< 0.5	3.5	1.7	17.0	7.2	0.9	< 0.5	< 0.5	1.9	< 0.5
Rb	< 13	310	290	676	130	< 14	38	< 16	280	22

Region		Treasure Lk. Gp. eastern section				Cole	Sue Dianne volcanic complex			
Showing	Ron Fe+REE	Carbonate Mountain	Carbonate Mountain	Hump V	Hump	Cole Breccia	Brooke	Brooke	Sue Dianne	Sue Dianne
Sample	0021B03	0030B03	0036A03	0042A03	1020I02	0095F02	0109F03	0109F07	1008B03	1009B04
Precursor		Sed. Rock	Sed. Rock	Sed. Rock	Unk.	Volcanic	Volcanic	Volcanic	Volcanic	Volcanic
Alteration	Epidote/ Ca-Fe	Na	Skarn	HT K-Fe	Fe	Na-Ca-Fe	Epidote/ HT K-Fe	Epidote/HT K-Fe	Na/HT K-Fe	LT K-Fe/HT K-Fe
1EX (Acme)										
Mo (ppm)	0.4	1.5	0.4	1.1	7.8	1	**667**	101.6	0.8	6.6
Pb	22.4	7.7	12.3	0.7	<0.1	6.6	28.4	22.6	2.1	6
Ni	16.7	5.1	33	105.2	43.7	3	12.1	14.7	16.3	8.7
Co	23.4	1.3	22.6	7.7	43.4	9.4	**303.4**	178.3	4.3	36
Bi	0.3	0.3	0.2	<0.1	0.1	0.2	**303.6**	**228.3**	0.1	**265.3**
Sn	8.0	3.9	3.9	3.4	5.8	5.6	10.2	8.5	4.2	6.4
Li	8.1	2.5	45.0	3.4	4.0	14.3	11.1	11.2	11.1	27.3
INAA (Becquerel)										
Sb (ppm)	0.8	1.4	5.5	264	0.5	2.1	5.5	4.2	0.7	2.6
As	2	3.1	5.5	< 1.4	< 0.5	6.8	< 1.7	2	3.3	16
Cs	< 0.5	< 0.5	1.6	< 0.5	< 0.5	< 0.5	< 1	1.4	< 0.5	2.3
Rb	< 5	5	120	17	< 5	51	75	76	< 5	360

Region		Lou	
Showing	Summit Peak	Summit Peak	Summit Peak
Sample	1646B03	1647A02	1647B02
Precursor	Rhy	Rhy	Rhy
Alteration	K-Fe (HT)/Cu-Fe-S	K	K/Cu-S-Fe
ME-MS61u (ALS)			
Mo (ppm)	3.1	0.1	2.2
Pb	4	8	2.5
Ni	44.5	0.5	21.3
Co	13.2	0.9	126.0
Bi	2.4	4.2	7.5
Sn	8.1	1.3	4.5
Li	20.0	2.2	4.2
ICP-AES/MS (INRS)			
Sb	< 13	< 13	< 11
As (ppm)	< 10	< 10	292
Cs	3.8	0.7	0.4
Rb	306	224	190

ANNEXE - 5 : ÉCHANTILLONS UTILISÉS POUR LE CHAPITRE 5 : ALTÉRATIONS IOAA DE LA ZONE MAGMATIQUE DU GRAND LAC DE L'OURS

Les minéraux sont abbrégés suivant Whitney et Evans (2010) sauf Qtz pour quartz.

Sample	Location	Rock type	Alteration	Lab
05JY-2249B	DeVries	unknown	Na	ACME 1-EX/INRS-ETE/Becquerel
05JY-2253	DeVries	unknown	Na	ACME 1-EX/INRS-ETE/Becquerel
09CQA-0002A02	Lou	Sedimentary	HT K-Fe	ACME 1-EX/INRS-ETE/Becquerel
09CQA-0008A02	Lou	Volcanic	K	ACME 1-EX/INRS-ETE/Becquerel
09CQA-0011A03	Mazenod	Volcanic	HT K-Fe	ACME 1-EX/INRS-ETE/Becquerel
09CQA-0016B03	Eastern Treasure Lake	Sedimentary	HT Ca-Fe	ACME 1-EX/INRS-ETE/Becquerel
09CQA-0020D03	Eastern Treasure Lake	Granitic	HT Ca-Fe	ACME 1-EX/INRS-ETE/Becquerel
09CQA-0021B03	Eastern Treasure Lake	Subvolcanic intrusion	HT Ca-Fe	ACME 1-EX/INRS-ETE/Becquerel
09CQA-0026B02	Mazenod	Volcanic	HT K-Fe	ACME 1-EX/INRS-ETE/Becquerel
09CQA-0026C03	Mazenod	Volcanic	K	ACME 1-EX/INRS-ETE/Becquerel
09CQA-0026C05	Mazenod	Volcanic	K	ACME 1-EX/INRS-ETE/Becquerel
09CQA-0026G03	Mazenod	Volcanic	HT K-Fe	ACME 1-EX/INRS-ETE/Becquerel
09CQA-0028A03	Mazenod	Volcanic	K	ACME 1-EX/INRS-ETE/Becquerel
09CQA-0029C01	Mazenod	Breccia	HT K-Fe	ACME 1-EX/INRS-ETE/Becquerel
09CQA-0030B03	Eastern Treasure Lake	Granitic	Na	ACME 1-EX/INRS-ETE/Becquerel
09CQA-0034A03	Eastern Treasure Lake	Granitic	Na	ACME 1-EX/INRS-ETE/Becquerel
09CQA-0034B03	Eastern Treasure Lake	Granitic	K	ACME 1-EX/INRS-ETE/Becquerel
09CQA-0039B03	Eastern Treasure Lake	Sedimentary	HT K-Fe	ACME 1-EX/INRS-ETE/Becquerel
09CQA-0039E03	Eastern Treasure Lake	Sedimentary	HT K-Fe	ACME 1-EX/INRS-ETE/Becquerel
09CQA-0041C03	Eastern Treasure Lake	Sedimentary	HT K-Fe	ACME 1-EX/INRS-ETE/Becquerel
09CQA-0042A03	Eastern Treasure Lake	Sedimentaryimentary	HT Ca-Fe	ACME 1-EX/INRS-ETE/Becquerel
09CQA-0043F03	Eastern Treasure Lake	Sedimentary	HT Ca-Fe	ACME 1-EX/INRS-ETE/Becquerel
09CQA-0044A03	Eastern Treasure Lake	Volcanic	Na	ACME 1-EX/INRS-ETE/Becquerel
09CQA-0045A03	Eastern Treasure Lake	Volcanic	Na	ACME 1-EX/INRS-ETE/Becquerel
09CQA-0046C02	Eastern Treasure Lake	Granitic	K	ACME 1-EX/INRS-ETE/Becquerel
09CQA-0046D03	Eastern Treasure Lake	Granitic	K	ACME 1-EX/INRS-ETE/Becquerel
09CQA-0047B02	Eastern Treasure Lake	Granitic	Na	ACME 1-EX/INRS-ETE/Becquerel
09CQA-0051A03	South Lou	Sedimentary	HT K-Fe	ACME 1-EX/INRS-ETE/Becquerel
09CQA-0054C03	South Lou	Sedimentary	HT Ca-Fe	ACME 1-EX/INRS-ETE/Becquerel
09CQA-0054G03	South Lou	Sedimentary	HT Ca-Fe	ACME 1-EX/INRS-ETE/Becquerel

Sample	Location	Rock type	Alteration	Lab
09CQA-0055E03	South Lou	Sedimentary	HT Ca-Fe	ACME 1-EX/INRS-ETE/Becquerel
09CQA-0055F03	South Lou	Sedimentary	HT Ca-Fe	ACME 1-EX/INRS-ETE/Becquerel
09CQA-0055F05	South Lou	Sedimentary	HT Ca-Fe	ACME 1-EX/INRS-ETE/Becquerel
09CQA-0055F06	South Lou	Sedimentary	HT Ca-Fe	ACME 1-EX/INRS-ETE/Becquerel
09CQA-0055F08	South Lou	Sedimentary	HT Ca-Fe	ACME 1-EX/INRS-ETE/Becquerel
09CQA-0056A02	South Lou	Sedimentary	K	ACME 1-EX/INRS-ETE/Becquerel
09CQA-0056B03	South Lou	Sedimentary	HT K-Fe	ACME 1-EX/INRS-ETE/Becquerel
09CQA-0056D03	South Lou	Sedimentary	HT K-Fe	ACME 1-EX/INRS-ETE/Becquerel
09CQA-0070A02	South Lou	Sedimentary	HT K-Fe	ACME 1-EX/INRS-ETE/Becquerel
09CQA-0073B03	South Lou	Sedimentary	HT Ca-Fe	ACME 1-EX/INRS-ETE/Becquerel
09CQA-0079-K02	South Lou	Sedimentary	HT Ca-Fe	ACME 1-EX/INRS-ETE/Becquerel
09CQA-0079-K06	South Lou	Sedimentary	HT Ca-Fe	ACME 1-EX/INRS-ETE/Becquerel
09CQA-0091A03	Cole	Volcanic	K	ACME 1-EX/INRS-ETE/Becquerel
09CQA-0093A03	Cole	Volcanic	Na	ACME 1-EX/INRS-ETE/Becquerel
09CQA-0109C03	Mazenod	Volcanic	K	ACME 1-EX/INRS-ETE/Becquerel
09CQA-0109-F07	Mazenod	Volcanic	HT K-Fe	ACME 1-EX/INRS-ETE/Becquerel
09CQA-0123-C03	Eastern Treasure Lake	Sedimentary	Na	ACME 1-EX/INRS-ETE/Becquerel
09CQA-0125B02	Mazenod	Volcanic	HT K-Fe	ACME 1-EX/INRS-ETE/Becquerel
09CQA-0127C03	Lou	Volcanic	K	ACME 1-EX/INRS-ETE/Becquerel
09CQA-0128-B02	Terra	Sedimentary	HT Ca-Fe	ACME 1-EX/INRS-ETE/Becquerel
09CQA-0133A03	Terra	Subvolcanic intrusion	K	ACME 1-EX/INRS-ETE/Becquerel
09CQA-0135A04	Terra	Subvolcanic intrusion	Na	ACME 1-EX/INRS-ETE/Becquerel
09CQA-0139B02	Terra	unknown	HT Ca-Fe	ACME 1-EX/INRS-ETE/Becquerel
09CQA-0139E02	Terra	unknown	Na	ACME 1-EX/INRS-ETE/Becquerel
09CQA-0142B02	Terra	Sedimentary	K	ACME 1-EX/INRS-ETE/Becquerel
09CQA-0142E02	Terra	Breccia	HT Ca-Fe	ACME 1-EX/INRS-ETE/Becquerel
09CQA-0143A03	Terra	Sedimentary	HT K-Fe	ACME 1-EX/INRS-ETE/Becquerel
09CQA-0144A03	Terra	Sedimentary	HT Ca-Fe	ACME 1-EX/INRS-ETE/Becquerel
09CQA-1006A03	Mazenod	Volcanic	Na	ACME 1-EX/INRS-ETE/Becquerel
09CQA-1006D03	Mazenod	Volcanic	HT K-Fe	ACME 1-EX/INRS-ETE/Becquerel

Sample	Location	Rock type	Alteration	Lab
09CQA-1006E01	Mazenod	Volcanic	Na	ACME 1-EX/INRS-ETE/Becquerel
09CQA-1008A03	Mazenod	Volcanic	LT K-Fe	ACME 1-EX/INRS-ETE/Becquerel
09CQA-1008B03	Mazenod	Volcanic	Na	ACME 1-EX/INRS-ETE/Becquerel
09CQA-1008C02	Mazenod	Volcanic	Na	ACME 1-EX/INRS-ETE/Becquerel
09CQA-1008D03	Mazenod	Volcanic	Na	ACME 1-EX/INRS-ETE/Becquerel
09CQA-1009B02	Mazenod	Breccia	LT-HT K-Fe	ACME 1-EX/INRS-ETE/Becquerel
09CQA-1009B04	Mazenod	Breccia	LT-HT K-Fe	ACME 1-EX/INRS-ETE/Becquerel
09CQA-1009E02	Mazenod	Breccia	LT-HT K-Fe	ACME 1-EX/INRS-ETE/Becquerel
09CQA-1012D02	Mazenod	Granitic	K	ACME 1-EX/INRS-ETE/Becquerel
09CQA-1016A02	Eastern Treasure Lake	Subvolcanic intrusion	K	ACME 1-EX/INRS-ETE/Becquerel
09CQA-1020H06	Eastern Treasure Lake	Sedimentary	HT Ca-Fe	ACME 1-EX/INRS-ETE/Becquerel
09CQA-1020I02	Eastern Treasure Lake	Sedimentary	HT Ca-Fe	ACME 1-EX/INRS-ETE/Becquerel
09CQA-1026A02	Mazenod	Breccia	LT-HT K-Fe	ACME 1-EX/INRS-ETE/Becquerel
09CQA-1027A03	Mazenod	Breccia	LT-HT K-Fe	ACME 1-EX/INRS-ETE/Becquerel
09CQA-1028D03	Eastern Treasure Lake	Granitic	K	ACME 1-EX/INRS-ETE/Becquerel
09CQA-1028G04	Eastern Treasure Lake	Granitic	LT K-Fe	ACME 1-EX/INRS-ETE/Becquerel
09CQA-1032C02	Eastern Treasure Lake	Sedimentary	HT K-Fe	ACME 1-EX/INRS-ETE/Becquerel
09CQA-1035B02	Mazenod	Volcanic	K	ACME 1-EX/INRS-ETE/Becquerel
09CQA-1035D02	Mazenod	Volcanic	HT K-Fe	ACME 1-EX/INRS-ETE/Becquerel
09CQA-1043A03	Mazenod	Volcanic	K	ACME 1-EX/INRS-ETE/Becquerel
09CQA-1046F01	Eastern Treasure Lake	Sedimentary	Na	ACME 1-EX/INRS-ETE/Becquerel
09CQA-1059A02	Eastern Treasure Lake	Granitic	LT K-Fe	ACME 1-EX/INRS-ETE/Becquerel
09CQA-1059B02	Eastern Treasure Lake	Sedimentary	HT Ca-Fe	ACME 1-EX/INRS-ETE/Becquerel
09CQA-1059B04	Eastern Treasure Lake	Sedimentary	HT Ca-Fe	ACME 1-EX/INRS-ETE/Becquerel
09CQA-1059B05	Eastern Treasure Lake	Sedimentary	HT Ca-Fe	ACME 1-EX/INRS-ETE/Becquerel
09CQA-1059C02	Eastern Treasure Lake	Granitic	K	ACME 1-EX/INRS-ETE/Becquerel
09CQA-1059C04	Eastern Treasure Lake	Granitic	K	ACME 1-EX/INRS-ETE/Becquerel
09CQA-1059H04	Eastern Treasure Lake	Granitic	Na	ACME 1-EX/INRS-ETE/Becquerel
09CQA-1059I04	Eastern Treasure Lake	Sedimentary	HT Ca-Fe	ACME 1-EX/INRS-ETE/Becquerel
09CQA-1062A02	Crowfoot	Granitic	K	ACME 1-EX/INRS-ETE/Becquerel

Sample	Location	Rock type	Alteration	Lab
09CQA-1066A02	Crowfoot	Granitic	K	ACME 1-EX/INRS-ETE/Becquerel
09CQA-1079C02	Eastern Treasure Lake	Sedimentary	HT K-Fe	ACME 1-EX/INRS-ETE/Becquerel
09CQA-1079I02	Eastern Treasure Lake	Sedimentary	HT K-Fe	ACME 1-EX/INRS-ETE/Becquerel
09CQA-1080A02	Eastern Treasure Lake	Sedimentary	HT K-Fe	ACME 1-EX/INRS-ETE/Becquerel
09CQA-1080C02	Eastern Treasure Lake	Granitic	K	ACME 1-EX/INRS-ETE/Becquerel
09CQA-1080D02	Eastern Treasure Lake	Granitic	Na	ACME 1-EX/INRS-ETE/Becquerel
09CQA-1082E03	South Lou	Sedimentary	HT Ca-Fe	ACME 1-EX/INRS-ETE/Becquerel
09CQA-1082H02	South Lou	Sedimentary	HT Ca-Fe	ACME 1-EX/INRS-ETE/Becquerel
09CQA-1082I02	South Lou	Sedimentary	HT Ca-Fe	ACME 1-EX/INRS-ETE/Becquerel
09CQA-1082J02	South Lou	Sedimentary	HT Ca-Fe	ACME 1-EX/INRS-ETE/Becquerel
09CQA-1083D02	South Lou	Sedimentary	HT Ca-Fe	ACME 1-EX/INRS-ETE/Becquerel
09CQA-1084A02	South Lou	Sedimentary	K	ACME 1-EX/INRS-ETE/Becquerel
09CQA-1084B02	South Lou	Sedimentary	HT Ca-Fe	ACME 1-EX/INRS-ETE/Becquerel
09CQA-1085A02	South Lou	Sedimentary	HT Ca-Fe	ACME 1-EX/INRS-ETE/Becquerel
09CQA-1086A02	South Lou	Sedimentary	HT Ca-Fe	ACME 1-EX/INRS-ETE/Becquerel
09CQA-1086A03	South Lou	Sedimentary	HT Ca-Fe	ACME 1-EX/INRS-ETE/Becquerel
09CQA-1086B02	South Lou	Sedimentary	HT Ca-Fe	ACME 1-EX/INRS-ETE/Becquerel
09CQA-1087A02	South Lou	Sedimentary	HT Ca-Fe	ACME 1-EX/INRS-ETE/Becquerel
09CQA-1092A02	South Lou	Sedimentary	HT K-Fe	ACME 1-EX/INRS-ETE/Becquerel
09CQA-1097A02	South Lou	Subvolcanic intrusion	HT K-Fe	ACME 1-EX/INRS-ETE/Becquerel
09CQA-1097B03	South Lou	Subvolcanic intrusion	HT K-Fe	ACME 1-EX/INRS-ETE/Becquerel
09CQA-1098A02	South Lou	Volcanic	K	ACME 1-EX/INRS-ETE/Becquerel
09CQA-1098A04	South Lou	Volcanic	K	ACME 1-EX/INRS-ETE/Becquerel
09CQA-1098B02	South Lou	Volcanic	K	ACME 1-EX/INRS-ETE/Becquerel
09CQA-109-D02	Mazenod	Volcanic	HT Ca-Fe	ACME 1-EX/INRS-ETE/Becquerel
09CQA-1102B02	South Lou	Granitic	K	ACME 1-EX/INRS-ETE/Becquerel
09CQA-1103A02	South Lou	Volcanic	HT K-Fe	ACME 1-EX/INRS-ETE/Becquerel
09CQA-1109C02	South Lou	Volcanic	K	ACME 1-EX/INRS-ETE/Becquerel
09CQA-1110A02	South Lou	Volcanic	K	ACME 1-EX/INRS-ETE/Becquerel
09CQA-1111A02	South Lou	Sedimentary	HT K-Fe	ACME 1-EX/INRS-ETE/Becquerel

Sample	Location	Rock type	Alteration	Lab
09CQA-1114D02	South Lou	Sedimentary	HT K-Fe	ACME 1-EX/INRS-ETE/Becquerel
09CQA-1114D03	South Lou	Sedimentary	HT K-Fe	ACME 1-EX/INRS-ETE/Becquerel
09CQA-1114D04	South Lou	Sedimentary	HT K-Fe	ACME 1-EX/INRS-ETE/Becquerel
09CQA-1114H02	South Lou	Sedimentary	K	ACME 1-EX/INRS-ETE/Becquerel
09CQA-1116A02	South Lou	Sedimentary	HT Ca-Fe	ACME 1-EX/INRS-ETE/Becquerel
09CQA-1119C02	Eastern Treasure Lake	Granitic	K	ACME 1-EX/INRS-ETE/Becquerel
09CQA-1128A02	Eastern Treasure Lake	Subvolcanic intrusion	K	ACME 1-EX/INRS-ETE/Becquerel
09CQA-1132A02	Eastern Treasure Lake	Subvolcanic intrusion	Na	ACME 1-EX/INRS-ETE/Becquerel
09CQA-1138A03	Lou	Subvolcanic intrusion	HT K-Fe	ACME 1-EX/INRS-ETE/Becquerel
09CQA-1139B02	Lou	Subvolcanic intrusion	HT K-Fe	ACME 1-EX/INRS-ETE/Becquerel
09CQA-1139H02	Lou	Breccia	HT K-Fe	ACME 1-EX/INRS-ETE/Becquerel
09CQA-1141A07	Lou	Breccia	HT K-Fe	ACME 1-EX/INRS-ETE/Becquerel
09CQA-1141F03	Lou	Subvolcanic intrusion	K	ACME 1-EX/INRS-ETE/Becquerel
09CQA-1142B02	Lou	Granitic	Na	ACME 1-EX/INRS-ETE/Becquerel
09CQA-1158A03	Fab	Subvolcanic intrusion	HT K-Fe	ACME 1-EX/INRS-ETE/Becquerel
09CQA-1158D03	Fab	Subvolcanic intrusion	HT Ca-Fe	ACME 1-EX/INRS-ETE/Becquerel
09CQA-1159A03	Fab	Subvolcanic intrusion	HT K-Fe	ACME 1-EX/INRS-ETE/Becquerel
09CQA-1160B02	Fab	Subvolcanic intrusion	HT K-Fe	ACME 1-EX/INRS-ETE/Becquerel
09CQA-1163D03	Ham	Metamorphic rock	HT K-Fe	ACME 1-EX/INRS-ETE/Becquerel
09CQA-1163E03	Ham	Metamorphic rock	K	ACME 1-EX/INRS-ETE/Becquerel
09CQA-1164A02	Ham	Metamorphic rock	HT K-Fe	ACME 1-EX/INRS-ETE/Becquerel
09CQA-1170D02	JLD	Subvolcanic intrusion	HT Ca-Fe	ACME 1-EX/INRS-ETE/Becquerel
09CQA-1170E03	JLD	Subvolcanic intrusion	HT Ca-Fe	ACME 1-EX/INRS-ETE/Becquerel
09CQA-1173B03	JLD	Subvolcanic intrusion	HT Ca-Fe	ACME 1-EX/INRS-ETE/Becquerel
09CQA-1193C02	Hailstone	Metamorphic rock	HT Ca-Fe	ACME 1-EX/INRS-ETE/Becquerel
09CQA-1195A03	Hottah	Volcanic	K	ACME 1-EX/INRS-ETE/Becquerel
09CQA-1202A02	Hottah	Volcanic	K	ACME 1-EX/INRS-ETE/Becquerel
09CQA-1209B03	Hottah	Subvolcanic intrusion	K	ACME 1-EX/INRS-ETE/Becquerel
09CQA-1210A02	Hottah	Volcanic	K	ACME 1-EX/INRS-ETE/Becquerel
09CQA-1210B02	Hottah	Volcanic	K	ACME 1-EX/INRS-ETE/Becquerel

Sample	Location	Rock type	Alteration	Lab
09CQA-1211A02	Hottah	Volcaniclastic	K	ACME 1-EX/INRS-ETE/Becquerel
09CQA-1218A03	Hottah	Volcanic	K	ACME 1-EX/INRS-ETE/Becquerel
09CQA-1221A03	Hottah	Volcanic	K	ACME 1-EX/INRS-ETE/Becquerel
09CQA-4006A02	unknown	Granitic	Na	ACME 1-EX/INRS-ETE/Becquerel
09CQA-4012D03	Cole	Subvolcanic intrusion	Na	ACME 1-EX/INRS-ETE/Becquerel
Chemex 40503J (-31a)	Mazenod	Granitic	K	ACME 1-EX/INRS-ETE/Becquerel
Chemex 40508J (-66a)	Mazenod	Subvolcanic intrusion	K	ACME 1-EX/INRS-ETE/Becquerel
CQA-05-0060C	Contact Lake	Volcanic	LT K-Fe	ACME 1-EX/INRS-ETE/Becquerel
CQA-05-0076A	Contact Lake	Volcanic	LT K-Fe	ACME 1-EX/INRS-ETE/Becquerel
CQA-05-0083A	Contact Lake	Volcanic	K	ACME 1-EX/INRS-ETE/Becquerel
CQA-05-0095A	Contact Lake	Volcanic	HT Ca-Fe	ACME 1-EX/INRS-ETE/Becquerel
CQA-05-0097A	Contact Lake	Volcanic	K	ACME 1-EX/INRS-ETE/Becquerel
CQA-05-0102A	Contact Lake	Subvolcanic intrusion	HT Ca-Fe	ACME 1-EX/INRS-ETE/Becquerel
CQA-05-0113B	Contact Lake	Volcanic	HT Ca-Fe	ACME 1-EX/INRS-ETE/Becquerel
CQA-05-0113C	Contact Lake	Volcanic	HT Ca-Fe	ACME 1-EX/INRS-ETE/Becquerel
CQA-05-0118A	Contact Lake	Volcanic	Na	ACME 1-EX/INRS-ETE/Becquerel
CQA-05-0121A	Contact Lake	Volcanic	Na	ACME 1-EX/INRS-ETE/Becquerel
CQA-05-0124B	Contact Lake	Granitic	K	ACME 1-EX/INRS-ETE/Becquerel
CQA-05-0124C	Contact Lake	Volcanic	Na	ACME 1-EX/INRS-ETE/Becquerel
CQA-05-0127A	Contact Lake	Granitic	K	ACME 1-EX/INRS-ETE/Becquerel
CQA-05-0129A	Contact Lake	Volcanic	Na	ACME 1-EX/INRS-ETE/Becquerel
CQA-05-0131B	Contact Lake	Volcanic	Na	ACME 1-EX/INRS-ETE/Becquerel
CQA-05-0131C	Contact Lake	Volcanic	Na	ACME 1-EX/INRS-ETE/Becquerel
CQA-05-0136A	Contact Lake	Volcanic	LT K-Fe	ACME 1-EX/INRS-ETE/Becquerel
CQA-05-0138D	Contact Lake	Volcanic	LT K-Fe	ACME 1-EX/INRS-ETE/Becquerel
CQA-05-0139D	Contact Lake	Breccia	LT K-Fe	ACME 1-EX/INRS-ETE/Becquerel
CQA-05-0140A	Contact Lake	Volcanic	LT K-Fe	ACME 1-EX/INRS-ETE/Becquerel
CQA-05-0144E	Contact Lake	Volcanic	HT K-Fe	ACME 1-EX/INRS-ETE/Becquerel
CQA-05-0154B	Contact Lake	Volcanic	HT K-Fe	ACME 1-EX/INRS-ETE/Becquerel
CQA-05-0166C	Contact Lake	Volcanic	HT K-Fe	ACME 1-EX/INRS-ETE/Becquerel

Sample	Location	Rock type	Alteration	Lab
CQA-05-0167B	Contact Lake	Volcanic	HT K-Fe	ACME 1-EX/INRS-ETE/Becquerel
CQA-05-0208B	Contact Lake	Volcanic	Na	ACME 1-EX/INRS-ETE/Becquerel
CQA-05-0213A	Contact Lake	Volcanic	Na	ACME 1-EX/INRS-ETE/Becquerel
CQA-05-0215A	Contact Lake	Volcanic	Na	ACME 1-EX/INRS-ETE/Becquerel
CQA-05-0222A	Contact Lake	Volcanic	HT Ca-Fe	ACME 1-EX/INRS-ETE/Becquerel
CQA-05-0226A	Contact Lake	Volcanic	Na	ACME 1-EX/INRS-ETE/Becquerel
CQA-05-0227A	Lou	Volcanic	K	ACME 1-EX/INRS-ETE/Becquerel
CQA-05-0228A	Lou	Sedimentary	HT K-Fe	ACME 1-EX/INRS-ETE/Becquerel
CQA-05-0230D	Lou	unknown	HT K-Fe	ACME 1-EX/INRS-ETE/Becquerel
CQA-05-0238A	Lou	Breccia	HT Ca-Fe	ACME 1-EX/INRS-ETE/Becquerel
CQA-05-0243C-1|2204	DeVries	Sedimentary	HT K-Fe	ACME 1-EX/INRS-ETE/Becquerel
CQA-05-0243C-2|2204	DeVries	Sedimentary	HT K-Fe	ACME 1-EX/INRS-ETE/Becquerel
CQA-05-0248C	DeVries	Volcanic	HT K-Fe	ACME 1-EX/INRS-ETE/Becquerel
CQA-05-0260A|2226A	DeVries	Sedimentary	HT K-Fe	ACME 1-EX/INRS-ETE/Becquerel
CQA-05-0260D	DeVries	Sedimentary	HT K-Fe	ACME 1-EX/INRS-ETE/Becquerel
CQA-05-0266A|2232A	DeVries	Sedimentary	HT K-Fe	ACME 1-EX/INRS-ETE/Becquerel
CQA-05-0269A|2235A	DeVries	Subvolcanic intrusion	HT Ca-Fe	ACME 1-EX/INRS-ETE/Becquerel
CQA-05-0270B|2236B	DeVries	Subvolcanic intrusion	HT Ca-Fe	ACME 1-EX/INRS-ETE/Becquerel
CQA-05-0270C|2236C	DeVries	Granitic	HT Ca-Fe	ACME 1-EX/INRS-ETE/Becquerel
CQA-05-0271B|2237B	DeVries	Breccia	HT K-Fe	ACME 1-EX/INRS-ETE/Becquerel
CQA-06-0061	Contact Lake	Sedimentary	HT Ca-Fe	ACME 1-EX/INRS-ETE/Becquerel
CQA-06-0273D	Contact Lake	Volcanic	LT K-Fe	ACME 1-EX/INRS-ETE/Becquerel
CQA-06-0273F	Contact Lake	Volcanic	LT K-Fe	ACME 1-EX/INRS-ETE/Becquerel
CQA-06-0274D	Contact Lake	Volcanic	Na	ACME 1-EX/INRS-ETE/Becquerel
CQA-06-0275C	Contact Lake	Volcanic	HT K-Fe	ACME 1-EX/INRS-ETE/Becquerel
CQA-06-0281B	Contact Lake	Sedimentary	HT K-Fe	ACME 1-EX/INRS-ETE/Becquerel
CQA-06-0287C	Contact Lake	Breccia	HT Ca-Fe	ACME 1-EX/INRS-ETE/Becquerel
CQA-06-0287G	Contact Lake	Volcanic	HT Ca-Fe	ACME 1-EX/INRS-ETE/Becquerel
CQA-06-0289F	Contact Lake	Sedimentary	HT K-Fe	ACME 1-EX/INRS-ETE/Becquerel
CQA-06-0310A	Contact Lake	Granitic	HT K-Fe	ACME 1-EX/INRS-ETE/Becquerel

Sample	Location	Rock type	Alteration	Lab
CQA-06-0325C	Contact Lake	Volcanic	Na	ACME 1-EX/INRS-ETE/Becquerel
CQA-06-0330A	Contact Lake	Volcanic	Na	ACME 1-EX/INRS-ETE/Becquerel
CQA-06-0330F	Contact Lake	Volcanic	Na	ACME 1-EX/INRS-ETE/Becquerel
CQA-06-0340D	Contact Lake	Granitic	K	ACME 1-EX/INRS-ETE/Becquerel
CQA-06-0355C	Contact Lake	Breccia	LT K-Fe	ACME 1-EX/INRS-ETE/Becquerel
CQA-06-0363A	Contact Lake	Sedimentary	HT Ca-Fe	ACME 1-EX/INRS-ETE/Becquerel
CQA-06-0366A	Contact Lake	Breccia	HT K-Fe	ACME 1-EX/INRS-ETE/Becquerel
CQA-06-0370B	Contact Lake	unknown	HT K-Fe	ACME 1-EX/INRS-ETE/Becquerel
CQA-06-0379A	Contact Lake	Volcanic	HT Ca-Fe	ACME 1-EX/INRS-ETE/Becquerel
CQA-06-0380A	Contact Lake	Volcanic	LT K-Fe	ACME 1-EX/INRS-ETE/Becquerel
CQA-06-0390B	Fab	Subvolcanic intrusion	K	ACME 1-EX/INRS-ETE/Becquerel
CQA-06-0391D	Fab	Subvolcanic intrusion	K	ACME 1-EX/INRS-ETE/Becquerel
CQA-06-0393A	Fab	Sedimentary	HT K-Fe	ACME 1-EX/INRS-ETE/Becquerel
CQA-06-0404A	DeVries	Sedimentary	Na	ACME 1-EX/INRS-ETE/Becquerel
CQA-06-0411A	DeVries	Granitic	K	ACME 1-EX/INRS-ETE/Becquerel
CQA-06-0422A	DeVries	Granitic	HT K-Fe	ACME 1-EX/INRS-ETE/Becquerel
CQA-06-0427A	DeVries	Volcanic	K	ACME 1-EX/INRS-ETE/Becquerel
CQA-06-0434A	Fab	Subvolcanic intrusion	HT K-Fe	ACME 1-EX/INRS-ETE/Becquerel
CQA-06-0434C	Fab	Breccia	HT K-Fe	ACME 1-EX/INRS-ETE/Becquerel
CQA-06-0435D	Fab	Subvolcanic intrusion	HT Ca-Fe	ACME 1-EX/INRS-ETE/Becquerel
CQA-06-0435F	Fab	Subvolcanic intrusion	HT Ca-Fe	ACME 1-EX/INRS-ETE/Becquerel
CQA-07-0289	Contact Lake	Breccia	HT Ca-Fe	ACME 1-EX/INRS-ETE/Becquerel
CQA-07-0436A	Lou	Subvolcanic intrusion	Na	ACME 1-EX/INRS-ETE/Becquerel
CQA-07-0438C	Lou	Subvolcanic intrusion	HT K-Fe	ACME 1-EX/INRS-ETE/Becquerel
CQA-07-0439A	Eastern Treasure Lake	Volcanic	K	ACME 1-EX/INRS-ETE/Becquerel
CQA-07-0441A	Lou	Sedimentary	HT K-Fe	ACME 1-EX/INRS-ETE/Becquerel
CQA-07-0441B	Lou	Sedimentary	K	ACME 1-EX/INRS-ETE/Becquerel
CQA-07-0441C	Lou	Volcanic	HT K-Fe	ACME 1-EX/INRS-ETE/Becquerel
CQA-07-0441D	Lou	Volcaniclastic	K	ACME 1-EX/INRS-ETE/Becquerel
CQA-07-0441E	Lou	Volcaniclastic	K	ACME 1-EX/INRS-ETE/Becquerel

Sample	Location	Rock type	Alteration	Lab
CQA-07-0442A	Lou	Volcaniclastic	K	ACME 1-EX/INRS-ETE/Becquerel
CQA-07-0443A	Lou	Sedimentary	HT K-Fe	ACME 1-EX/INRS-ETE/Becquerel
CQA-07-0443B	Lou	Sedimentary	HT K-Fe	ACME 1-EX/INRS-ETE/Becquerel
CQA-07-0445B1	Lou	Volcaniclastic	K	ACME 1-EX/INRS-ETE/Becquerel
CQA-07-0448A	Lou	Volcanic	K	ACME 1-EX/INRS-ETE/Becquerel
CQA-07-0451A	Lou	Volcanic	K	ACME 1-EX/INRS-ETE/Becquerel
CQA-07-0455A	Lou	Volcanic	K	ACME 1-EX/INRS-ETE/Becquerel
CQA-07-0457B1	Lou	Sedimentary	HT Ca-Fe	ACME 1-EX/INRS-ETE/Becquerel
CQA-07-0459A	Lou	Sedimentary	HT Ca-Fe	ACME 1-EX/INRS-ETE/Becquerel
CQA-07-0459F	Lou	Subvolcanic intrusion	K	ACME 1-EX/INRS-ETE/Becquerel
CQA-07-0459G	Lou	Volcanic	K	ACME 1-EX/INRS-ETE/Becquerel
CQA-07-0460D	Lou	Volcanic	K	ACME 1-EX/INRS-ETE/Becquerel
CQA-07-0460E1	Lou	Volcanic	HT K-Fe	ACME 1-EX/INRS-ETE/Becquerel
CQA-07-0463L	Lou	Volcanic	K	ACME 1-EX/INRS-ETE/Becquerel
CQA-07-0465A	Lou	Sedimentary	HT Ca-Fe	ACME 1-EX/INRS-ETE/Becquerel
CQA-07-0466A1	Lou	Sedimentary	HT Ca-Fe	ACME 1-EX/INRS-ETE/Becquerel
CQA-07-0466A3	Lou	Sedimentary	HT Ca-Fe	ACME 1-EX/INRS-ETE/Becquerel
CQA-07-0466i1	Lou	Subvolcanic intrusion	HT K-Fe	ACME 1-EX/INRS-ETE/Becquerel
CQA-07-0466W1	Lou	Breccia	HT K-Fe	ACME 1-EX/INRS-ETE/Becquerel
CQA-07-0467D	Lou	Sedimentary	HT Ca-Fe	ACME 1-EX/INRS-ETE/Becquerel
CQA-07-0469E	Lou	Subvolcanic intrusion	HT K-Fe	ACME 1-EX/INRS-ETE/Becquerel
CQA-07-0469F	Lou	Volcanic	K	ACME 1-EX/INRS-ETE/Becquerel
CQA-07-0475B	Lou	Subvolcanic intrusion	K	ACME 1-EX/INRS-ETE/Becquerel
CQA-07-0475H	Lou	Sedimentary	K	ACME 1-EX/INRS-ETE/Becquerel
CQA-07-0478F	Lou	Volcanic	K	ACME 1-EX/INRS-ETE/Becquerel
CQA-07-0479D	Lou	Volcanic	K	ACME 1-EX/INRS-ETE/Becquerel
CQA-07-0480A	Lou	Subvolcanic intrusion	HT K-Fe	ACME 1-EX/INRS-ETE/Becquerel
CQA-07-0480E	Lou	Subvolcanic intrusion	HT K-Fe	ACME 1-EX/INRS-ETE/Becquerel
CQA-07-0480G1	Lou	Sedimentary	HT Ca-Fe	ACME 1-EX/INRS-ETE/Becquerel
CQA-07-0480O1	Lou	Sedimentary	HT Ca-Fe	ACME 1-EX/INRS-ETE/Becquerel

Sample	Location	Rock type	Alteration	Lab
CQA-07-0480O2	Lou	Sedimentary	HT Ca-Fe	ACME 1-EX/INRS-ETE/Becquerel
CQA-07-0480W3	Lou	Sedimentary	HT K-Fe	ACME 1-EX/INRS-ETE/Becquerel
CQA-07-0480Y1	Lou	Sedimentary	HT K-Fe	ACME 1-EX/INRS-ETE/Becquerel
CQA-07-0480Z	Lou	Sedimentary	HT Ca-Fe	ACME 1-EX/INRS-ETE/Becquerel
CQA-07-0483A	Lou	Subvolcanic intrusion	HT K-Fe	ACME 1-EX/INRS-ETE/Becquerel
CQA-07-0483B	Lou	Subvolcanic intrusion	K	ACME 1-EX/INRS-ETE/Becquerel
CQA-07-0484A	Lou	Subvolcanic intrusion	HT K-Fe	ACME 1-EX/INRS-ETE/Becquerel
CQA-07-0484B	Lou	Subvolcanic intrusion	HT K-Fe	ACME 1-EX/INRS-ETE/Becquerel
CQA-07-0484F	Lou	Subvolcanic intrusion	K	ACME 1-EX/INRS-ETE/Becquerel
CQA-07-0484G	Lou	Volcanic	K	ACME 1-EX/INRS-ETE/Becquerel
CQA-07-0509E	Contact Lake	Volcanic	Na	ACME 1-EX/INRS-ETE/Becquerel
CQA-07-0511B	Contact Lake	Breccia	Na	ACME 1-EX/INRS-ETE/Becquerel
CQA-07-0511G	Contact Lake	Breccia	Na	ACME 1-EX/INRS-ETE/Becquerel
CQA-07-0520A	Contact Lake	Breccia	Na	ACME 1-EX/INRS-ETE/Becquerel
CQA-07-0522D	Contact Lake	Volcanic	HT K-Fe	ACME 1-EX/INRS-ETE/Becquerel
CQA-07-0523E	Contact Lake	Volcanic	LT-HT K-Fe	ACME 1-EX/INRS-ETE/Becquerel
CQA-07-464F	Lou	Volcanic	K	ACME 1-EX/INRS-ETE/Becquerel
CQA-07-464i2	Lou	Volcanic	K	ACME 1-EX/INRS-ETE/Becquerel
CQA-07-464i4	Lou	Volcanic	K	ACME 1-EX/INRS-ETE/Becquerel
CQA-07-465A2	Lou	Sedimentary	HT Ca-Fe	ACME 1-EX/INRS-ETE/Becquerel
CQA-07-465E1	Lou	Sedimentary	HT K-Fe	ACME 1-EX/INRS-ETE/Becquerel
CQA-07-465F	Lou	Sedimentary	HT K-Fe	ACME 1-EX/INRS-ETE/Becquerel
CQA-07-465i	Lou	Sedimentary	HT Ca-Fe	ACME 1-EX/INRS-ETE/Becquerel
CQA-07-465L1	Lou	Sedimentary	HT Ca-Fe	ACME 1-EX/INRS-ETE/Becquerel
CQA-07-468C1	Lou	Sedimentary	HT Ca-Fe	ACME 1-EX/INRS-ETE/Becquerel
CQA-07-468G1	Lou	Sedimentary	HT Ca-Fe	ACME 1-EX/INRS-ETE/Becquerel
CQA-07-484J	Lou	Breccia	K	ACME 1-EX/INRS-ETE/Becquerel
CQA-07-484L	Lou	Breccia	K	ACME 1-EX/INRS-ETE/Becquerel
CQA-07-484V1	Lou	Sedimentary	HT Ca-Fe	ACME 1-EX/INRS-ETE/Becquerel
CQA-07-484V2	Lou	Sedimentary	HT Ca-Fe	ACME 1-EX/INRS-ETE/Becquerel

Sample	Location	Rock type	Alteration	Lab
CQA-07-484X	Lou	Sedimentary	HT Ca-Fe	ACME 1-EX/INRS-ETE/Becquerel
CQA-07-485U	Lou	Breccia	HT K-Fe	ACME 1-EX/INRS-ETE/Becquerel
CQA-07-485W	Lou	Breccia	HT K-Fe	ACME 1-EX/INRS-ETE/Becquerel
CQA-07-485Y	Lou	Breccia	K	ACME 1-EX/INRS-ETE/Becquerel
CQA-07-486A	Lou	Sedimentary	HT K-Fe	ACME 1-EX/INRS-ETE/Becquerel
CQA-07-487A1	Lou	Volcanic	K	ACME 1-EX/INRS-ETE/Becquerel
CQA-07-487A2	Lou	Volcanic	K	ACME 1-EX/INRS-ETE/Becquerel
CQA-07-514B	Contact Lake	Breccia	Na	ACME 1-EX/INRS-ETE/Becquerel
CQA-07-516J	Contact Lake	Breccia	HT Ca-Fe	ACME 1-EX/INRS-ETE/Becquerel
CQA-07-519A	Contact Lake	Volcanic	HT Ca-Fe	ACME 1-EX/INRS-ETE/Becquerel
CQA-07-527N	Contact Lake	Breccia	HT Ca-Fe	ACME 1-EX/INRS-ETE/Becquerel
CQA-07-534A	Contact Lake	Subvolcanic intrusion	HT Ca-Fe	ACME 1-EX/INRS-ETE/Becquerel
CQA-07-538A	Contact Lake	Volcanic	K	ACME 1-EX/INRS-ETE/Becquerel
CQA-07-542A	Contact Lake	Volcaniclastic	HT Ca-Fe	ACME 1-EX/INRS-ETE/Becquerel
CQA-07-542B2	Contact Lake	Breccia	HT K-Fe	ACME 1-EX/INRS-ETE/Becquerel
CQA-08-0608B	unknown	Granitic	HT Ca-Fe	ACME 1-EX/INRS-ETE/Becquerel
CQA-08-561C	unknown	unknown	HT Ca-Fe	ACME 1-EX/INRS-ETE/Becquerel
CQA-08-581B	unknown	Subvolcanic intrusion	HT K-Fe	ACME 1-EX/INRS-ETE/Becquerel
CQA-08-592C	Ham	Granitic	HT Ca-Fe	ACME 1-EX/INRS-ETE/Becquerel
CQA-08-598B	Ham	Subvolcanic intrusion	HT Ca-Fe	ACME 1-EX/INRS-ETE/Becquerel
CQA-08-599A	Hottah Lake	Volcanic	K	ACME 1-EX/INRS-ETE/Becquerel
CQA-08-599B	Hottah Lake	Volcanic	K	ACME 1-EX/INRS-ETE/Becquerel
CQA-08-600C	Hottah Lake	Volcanic	K	ACME 1-EX/INRS-ETE/Becquerel
CQA-08-600D	Hottah Lake	Volcanic	K	ACME 1-EX/INRS-ETE/Becquerel
CQA-08-602D	Hottah Lake	Volcanic	K	ACME 1-EX/INRS-ETE/Becquerel
CQA-08-602E	Hottah Lake	Volcanic	K	ACME 1-EX/INRS-ETE/Becquerel
CQA-08-602F	Hottah Lake	Volcanic	K	ACME 1-EX/INRS-ETE/Becquerel
CQA-08-603A	Hottah Lake	Volcanic	LT K-Fe	ACME 1-EX/INRS-ETE/Becquerel
J8G-1	Mazenod	Granitic	K	ACME 1-EX/INRS-ETE/Becquerel
JCSD-06	Mazenod	Volcaniclastic	K	ACME 1-EX/INRS-ETE/Becquerel

Sample	Location	Rock type	Alteration	Lab
JCSD-08	Mazenod	Volcaniclastic	Na	ACME 1-EX/INRS-ETE/Becquerel
JCSD-11	Mazenod	Breccia	LT K-Fe	ACME 1-EX/INRS-ETE/Becquerel
JCSD-18	Mazenod	Volcaniclastic	K	ACME 1-EX/INRS-ETE/Becquerel
JCSD-20	Mazenod	Breccia	HT Ca-Fe	ACME 1-EX/INRS-ETE/Becquerel
JCSD-26	Mazenod	Volcaniclastic	Na	ACME 1-EX/INRS-ETE/Becquerel
JCSD-31	Mazenod	Granitic	K	ACME 1-EX/INRS-ETE/Becquerel
JCSD-31/40503J Aver	Mazenod	Granitic	K	ACME 1-EX/INRS-ETE/Becquerel
JCSD-35	Mazenod	Volcanic	K	ACME 1-EX/INRS-ETE/Becquerel
JCSD-36	Mazenod	Breccia	K	ACME 1-EX/INRS-ETE/Becquerel
JCSD-42	Mazenod	Subvolcanic intrusion	K	ACME 1-EX/INRS-ETE/Becquerel
JCSD-43	Mazenod	Subvolcanic intrusion	K	ACME 1-EX/INRS-ETE/Becquerel
JCSD-46	Mazenod	Volcanic	K	ACME 1-EX/INRS-ETE/Becquerel
JCSD-49a	Mazenod	Subvolcanic intrusion	HT K-Fe	ACME 1-EX/INRS-ETE/Becquerel
JCSD-50	Mazenod	Subvolcanic intrusion	HT K-Fe	ACME 1-EX/INRS-ETE/Becquerel
JCSD-66	Mazenod	Subvolcanic intrusion	K	ACME 1-EX/INRS-ETE/Becquerel
JCSD-66/40508J Aver	Mazenod	Subvolcanic intrusion	K	ACME 1-EX/INRS-ETE/Becquerel
JCSD-68	Mazenod	Subvolcanic intrusion	K	ACME 1-EX/INRS-ETE/Becquerel
JCSD-70 (Chemex 40	Mazenod	Volcaniclastic	Na	ACME 1-EX/INRS-ETE/Becquerel
JCSD-72 (Chemex 40	Mazenod	Breccia	LT K-Fe	ACME 1-EX/INRS-ETE/Becquerel
JCSD-73 (Chemex 40	Mazenod	Volcanic	K	ACME 1-EX/INRS-ETE/Becquerel
JCSD-74 (Chemex 40	Mazenod	Volcanic	LT K-Fe	ACME 1-EX/INRS-ETE/Becquerel
JCSD-83	Mazenod	Breccia	LT K-Fe	ACME 1-EX/INRS-ETE/Becquerel

Samples used in the study for which the alteration type has been revised

Sample	Location	Rock type	Zoning model	Revised alteration	Lab
09CQA-0004A03	Mazenod	Subvolcanic intrusion	K	Mild	ACME 1-EX/INRS-ETE/Becquerel
09CQA-0007A03	Mazenod	Subvolcanic intrusion	HT K-Fe	Weakly altered	ACME 1-EX/INRS-ETE/Becquerel
09CQA-0011B02	Mazenod	Granitic	K	Weakly altered	ACME 1-EX/INRS-ETE/Becquerel
09CQA-0012A02	Mazenod	Subvolcanic intrusion	HT K-Fe	K - Mild	ACME 1-EX/INRS-ETE/Becquerel
09CQA-0012B02	Mazenod	Subvolcanic intrusion	HT K-Fe	K - Mild	ACME 1-EX/INRS-ETE/Becquerel

Sample	Location	Rock type	Zoning model	Revised alteration	Lab
09CQA-0012C02	Mazenod	Subvolcanic intrusion	HT K-Fe	K - Mild	ACME 1-EX/INRS-ETE/Becquerel
09CQA-0030A03	Eastern Treasure Lake	Sedimentary	HT K-Fe	K - Mild	ACME 1-EX/INRS-ETE/Becquerel
09CQA-0094A03	Cole	Volcanic	HT K-Fe	K - Mild	ACME 1-EX/INRS-ETE/Becquerel
09CQA-1044A03	Mazenod	Volcanic	K	K - Mild	ACME 1-EX/INRS-ETE/Becquerel
09CQA-1046H02	Eastern Treasure Lake	Sedimentary	K	K - Mild	ACME 1-EX/INRS-ETE/Becquerel
09CQA-1055A02	Lou	Volcanic	K	Silicification - Mild	ACME 1-EX/INRS-ETE/Becquerel
09CQA-1060A02	Crowfoot	Granitic	K	Weakly altered	ACME 1-EX/INRS-ETE/Becquerel
09CQA-1070B03	Cole	Granitic	K	K - Mild	ACME 1-EX/INRS-ETE/Becquerel
09CQA-1071A03	Cole	Volcanic	K	K - Mild	ACME 1-EX/INRS-ETE/Becquerel
09CQA-1073A03	Cole	Granitic	K	K - Mild	ACME 1-EX/INRS-ETE/Becquerel
09CQA-1074B02	Cole	Volcanic	K	K - Mild	ACME 1-EX/INRS-ETE/Becquerel
09CQA-1109A02	South Lou	Granitic	K	K/Silicification	ACME 1-EX/INRS-ETE/Becquerel
09CQA-1119A02	Eastern Treasure Lake	Subvolcanic intrusion	K	K - Mild	ACME 1-EX/INRS-ETE/Becquerel
09CQA-1123A04	Cole	Subvolcanic intrusion	K	K - Mild	ACME 1-EX/INRS-ETE/Becquerel
09CQA-1141C03	Lou	Subvolcanic intrusion	HT K-Fe	K - Mild/moderate	ACME 1-EX/INRS-ETE/Becquerel
09CQA-1141C04	Lou	Subvolcanic intrusion	HT K-Fe	K - Mild/moderate	ACME 1-EX/INRS-ETE/Becquerel
09CQA-1141C05	Lou	Subvolcanic intrusion	HT K-Fe	K - Mild/moderate	ACME 1-EX/INRS-ETE/Becquerel
CQA-05-0125A	Contact Lake	Granitic	K	K - Mild	ACME 1-EX/INRS-ETE/Becquerel
CQA-05-0145A	Contact Lake	Granitic	K	K - Mild	ACME 1-EX/INRS-ETE/Becquerel
CQA-06-0275D	Contact Lake	mafic dyke	HT Ca-Fe		ACME 1-EX/INRS-ETE/Becquerel
CQA-06-0349A	Contact Lake	Granitic	K	K - Mild	ACME 1-EX/INRS-ETE/Becquerel
CQA-06-0350A	Contact Lake	Granitic	K	K - Mild	ACME 1-EX/INRS-ETE/Becquerel
CQA-06-0375A	Contact Lake	Granitic	K	K - Mild	ACME 1-EX/INRS-ETE/Becquerel
CQA-06-0384A	Fab	Subvolcanic intrusion	HT K-Fe	K - Mild	ACME 1-EX/INRS-ETE/Becquerel
CQA-07-0437A	Eastern Treasure Lake	Volcanic	HT K-Fe	Na-Ca-Fe/K - Moderate	ACME 1-EX/INRS-ETE/Becquerel
CQA-07-0452A	Lou	Subvolcanic intrusion	HT K-Fe	Weakly altered	ACME 1-EX/INRS-ETE/Becquerel
CQA-07-0466G1	Lou	Subvolcanic intrusion	HT K-Fe	K - Mild	ACME 1-EX/INRS-ETE/Becquerel
CQA-07-0466i3	Lou	Subvolcanic intrusion	HT K-Fe	K - Mild	ACME 1-EX/INRS-ETE/Becquerel

ANNEXE - 6 : ÉCHANTILLONS UTILISÉS ET ANALYSES REPRÉSENTATIVES POUR LE CHAPITRE 6 : ALTÉRATIONS ET MINÉRALISATIONS URANIFÈRES DE LA SOUTHERN BRECCIA

Les minéraux sont abbrégés suivant Whitney et Evans (2010) sauf Qtz pour quartz.

Les échantillons en gras sont minéralisés en uranium.

Sample	Rock type	Location	Alteration
09CQA-1141C03	Bt-phyric andesite dike	Southern Breccia - Zone A	HT K–Fe
09CQA-1142B02	Early granite	Early granite	Ab2
09CQA-1143A02	Fp-Bt phyric dike (1869 Ma)	East of NICO	Weakly altered
10CQA-1240B02	FG - Aphanitic rhyolite	East of Red Hot Zone	Ab/K
10CQA-1240B04	FG - Altered Volcanic rock	East of Red Hot Zone	Ab/HT K–Fe
10CQA-1241A03	Tectono-hydrothermal breccia	East of Red Hot Zone	Ab1/K–Fe1/K/Ab2
10CQA-1241B01	FG - Altered Volcanic rock	East of Red Hot Zone	Ab/HT K–Fe
10CQA-1241B03	FG - Altered Volcanic rock	East of Red Hot Zone	Ab/HT K–Fe
10CQA-1241I02	TLG - Siltstone	East of Red Hot Zone	K–Fe1/Ab2
10CQA-1241J01	Magnetite vein	East of Red Hot Zone	HT K–Fe
10CQA-1241J02	Magnetite vein	East of Red Hot Zone	HT K–Fe
10CQA-1242 hydrothermal vein	Tectono-hydrothermal breccia	Southern Breccia - Zone A	Ab/HT K–Fe
10CQA-1242C10	Porphyritic rhyolite dike	Southern Breccia - Zone A	K
10CQA-1242E	Tectono-hydrothermal breccia	Southern Breccia - Zone A	Ab/HT K–Fe
10CQA-1242G01	Sodic altered granite dike	Southern Breccia - Zone A	Ab
10CQA-1243A03	TLG - Siltstone	East of Red Hot Zone	Ab2/K–Fe3
10CQA-1243D03	TLG - Siltstone	East of Red Hot Zone	Ab2/K–Fe2
10CQA-1612A02	Early granite/Siltstone	Southern Breccia - Zone A	K–Fe1/Ab2
10CQA-1615A02	Tectono-hydrothermal breccia	Southern Breccia - Zone A	K–Fe1/K–Fe2
10CQA-1615B03	Bt-phyric andesite dike	Southern Breccia - Zone A	HT K–Fe
10CQA-1615G02	Tectono-hydrothermal breccia	Southern Breccia - Zone A	K–Fe2
10CQA-1616A03	TLG - Siltstone	Southern Breccia - Zone A	K–Fe1/K
10CQA-1616B04	Bt-phyric andesite dike	Southern Breccia - Zone A	K
10CQA-1619A02	FG - Aphanitic rhyolite	Southern Breccia - Zone A	K
10CQA-1619C02	FG - Aphanitic rhyolite	Southern Breccia - Zone A	K
10CQA-1619I02	FG - Aphanitic rhyolite	Southern Breccia - Zone A	Ab2/K
10CQA-1620A02	Early granite	Early granite	Ab2/K
10CQA-1621A03	TLG - Siltstone	Red Hot Zone	Ab2/K–Fe4
10CQA-1622F03	Fp–Bt porphyry (1868 Ma)	Red Hot Zone	Weakly altered
10CQA-1627A02	FG - Altered Volcanic rock	Southern Breccia - Zone B	Ab2/K–Fe
10CQA-1627A03	FG - Altered Volcanic rock	Southern Breccia - Zone B	Ab2
10CQA-1627A04	FG - Altered Volcanic rock	Southern Breccia - Zone B	Ab2/K–Fe3
10CQA-1627C02	FG - Aphanitic rhyolite	Southern Breccia - Zone B	Ab2/K
10CQA-1627G02	FG - Aphanitic rhyolite	Southern Breccia - Zone B	Ab2/K
10CQA-1640B03	Tectono-hydrothermal breccia	Southern Breccia - Zone B	Ab2/Tur1
10CQA-1641A02	Fp–Bt porphyry	Southern Breccia - Zone B	Weakly altered
10CQA-1642A02	FG - Fp-phyric rhyolite	Southern Breccia - Zone B	K
10CQA-1643A02	FG - Altered Volcanic rock	Southern Breccia - Zone B	Ab2
10CQA-1649B02	FG - Fp–Bt-phyric rhyolite	NICO - Southern Breccia transition zone	K
10CQA-1649C02	TLG - Siltstone	NICO - Southern Breccia transition zone	K–Fe1/Ab1/HT K–Fe
10CQA-1649C04	TLG - Siltstone	NICO - Southern Breccia transition zone	K–Fe1/Ab1
10CQA-1649E02	TLG - Siltstone	NICO - Southern Breccia transition zone	K–Fe1/Ab1
10CQA-1651C3	**TLG - Siltstone**	**West of Frank's**	**Ab2/K–Fe3/K–Fe4**
10CQA-1653C02	TLG - Siltstone	West of Frank's	Ab2/K–Fe3/K–Fe4
10CQA-1654A02	FG - Aphanitic rhyolite	Southern Breccia SW	K
10CQA-1654C02	FG - Fp-phyric rhyolite	Southern Breccia SW	Weakly altered

Sample	Rock type	Location	Alteration
10CQA-1655A02	Tectono-hydrothermal breccia	Southern Breccia SW	Ab2/HT K–Fe
10CQA-1655B03	Tectono-hydrothermal breccia	Southern Breccia SW	K
10CQA-1661A02	Monzonitic Fp porphyry	Southern Breccia SW	K
10CQA-1661B02	FG - Fp-phyric rhyolite	Southern Breccia SW	K
10CQA-1663A02	Monzonitic Fp porphyry	Southern Breccia SW	K
10CQA-1665A02	TLG - Siltstone	Frank's zone	K–Fe1/Ab2
10CQA-1665B02	**TLG - Siltstone**	**Frank's zone**	**Ab2/K–Fe3/K–Fe4**
10CQA-1665B04	**TLG - Siltstone**	**Frank's zone**	**Ab2/K–Fe3/K–Fe4**
10CQA-1665C02	TLG - Siltstone	Frank's zone	Ab2/KFe4
10CQA-1665D03	**TLG - Siltstone**	**Frank's zone**	**Ab2/K–Fe3/K–Fe4**
11PUA006C01	TLG - Siltstone	Franks's west	Ab2/K–Fe4
11PUA010A01	TLG - Siltstone	Southern Breccia east	K–Fe1/Ab1
11PUA010F02	Fp-phyric porphyry	Southern Breccia east	K–Fe1/Ab1
11PUA011A01	TLG - Siltstone	Eastern showing	K–Fe1
11PUA011D01	FG - Aphanitic rhyolite	Eastern showing	K
11PUA011F02	**TLG - Siltstone**	**Eastern showing**	K–Fe1/K/Fe–Mg1
11PUA012E01	**TLG - Siltstone**	**Red Hot Zone**	**Ab2/K–Fe3/K–Fe4**
11PUA012E03	**TLG - Siltstone**	**Red Hot Zone**	**Ab2/K–Fe3/K–Fe4**
11PUA012E04	**TLG - Siltstone**	**Red Hot Zone**	**Ab2/K–Fe3/K–Fe4**
11PUA017C01	TLG - Siltstone	Franks's west	Ab2/K-Fe3
11PUA023A01	Unidivided porphyritic intrusion	Lou Lake zone	Ab2/Hem1
11PUA500B02	TLG - Siltstone	Red Hot zone	K–Fe1/Ab2/K–Fe4
11PUA504B01	TLG - Siltstone	Red Hot zone	K–Fe1/Ab2
11PUA504C01	TLG - Siltstone	Red Hot zone	K–Fe1/Ab2
11PUA511D01	TLG - Siltstone	NICO - Southern Breccia transition zone	Ab2/K-Fe3/Ca-Fe±K1/K-Fe4
11PUA511G01	TLG - Siltstone	NICO - Southern Breccia transition zone	Ab2/Ca-Fe±K1/K-Fe4
11PUA516B01	Porphyritic rhyolite dike	Eastern showing	K
11PUA517A01	TLG - Siltstone	Eastern showing	K–Fe1
11PUA519B01	FG - Fp-phyric rhyolite	Eastern showing	K
11PUA519B02	FG - Fp-phyric rhyolite	Eastern showing	K
11PUA524A01	Quartz monzodiorite (1867 Ma)	West Lou Lake zone	Weakly altered
11PUA525A01	Undivided porphyritic intrusion	Lou Lake Zone	Ab2/Hem1
11PUA526B01	Undivided porphyritic intrusion	Lou Lake Zone	Ab2/Hem1
11PUA526D04	**TLG - Siltstone**	**Lou Lake zone**	**Ab2/Fe-Mg1**
11PUA-526D3	**TLG - Siltstone**	**Lou Lake Zone**	**Ab2/Fe-Mg1**
11PUA528A01	FG - Altered Volcanic rock	NICO - Southern Breccia transition zone	K
M612904/10CQA-1693	**TLG - Siltstone**	**Frank's zone**	**Ab2/K–Fe3/K–Fe4**
M612905/10CQA-1694	**TLG - Siltstone**	**Frank's zone**	**Ab2/K–Fe3/K–Fe4**
M612906/10CQA-1702	TLG - Siltstone	Center of the Southern Breccia	Ab2
M612907/10CQA-1640	Tectono-hydrothermal breccia	Southern Breccia - Zone B	Ab2/Tur1
M612908/10CQA-1641	TLG - Siltstone	Southern Breccia - Zone B	Ab2/K–Fe3/K–Fe4
M612909/10CQA-1666	**TLG - Siltstone**	**Frank's zone**	**Ab2/K–Fe3/K–Fe4**
M612910/10CQA-1666	**TLG - Siltstone**	**Frank's zone**	**Ab2/K–Fe3/K–Fe4**
M612911/10CQA-1705	TLG - Siltstone	Frank's zone	Ab2/K–Fe4/Hem1

Sample	Rock type	Location	Alteration
M612912/10CQA-1705	TLG - Siltstone	Frank's zone	Ab2/K–Fe3/K–Fe4
M612913/10CQA-1705	**TLG - Siltstone**	**Frank's zone**	**Ab2/K–Fe3/K–Fe4**
M612914/10CQA-1705	**TLG - Siltstone**	**Frank's zone**	**Ab2/K–Fe3/K–Fe4**
M612915/10CQA-1707	TLG - Siltstone	NICO - Southern Breccia transition zone	Ab2/Mag/Hem1
M612916/10CQA-1707	TLG - Siltstone	NICO - Southern Breccia transition zone	Ab2/HT K–Fe/Hem1
M612917/10CQA-1709	TLG - Siltstone	NICO - Southern Breccia transition zone	Ab2/Mag/Hem1
M612918/10CQA-1709	TLG - Siltstone	NICO - Southern Breccia transition zone	K–Fe2–Hem1
M612919/10CQA-1709	TLG - Siltstone	NICO - Southern Breccia transition zone	Ab2/Ca–Fe±K1
M612920/10CQA-1712	Tectono-hydrothermal breccia	NICO - Southern Breccia transition zone	Tur1
M612921/10CQA-1712	Tectono-hydrothermal breccia	South_Sb	Tur1
M612922/10CQA-1658	FG - Altered Volcanic rock	West of Frank's	K
M612923/10CQA-1658	TLG - Siltstone	West of Frank's	Ab2/K–Fe3/K–Fe4
M612924/10CQA-1248	FG - Aphanitic rhyolite	Red Hot Zone	K
M612925/10CQA-1243	TLG - Siltstone	East of Red Hot Zone	K–Fe1/Ab1
M612926/10CQA-1721	Tectono-hydrothermal breccia	Southern Breccia - Zone A	K–Fe1/K–Fe2
M612927/10CQA-1721	Tectono-hydrothermal breccia	Southern Breccia - Zone A	K–Fe2
M612928/10CQA-1721	Tectono-hydrothermal breccia	Southern Breccia - Zone A	K–Fe2
M612929/10CQA-1722	Tectono-hydrothermal breccia	Southern Breccia - Zone A	Tur1
M612930/10CQA-1621	**TLG - Siltstone**	**Red Hot Zone**	**Ab2/K–Fe3/K–Fe4**
M612931/10CQA-1725	**TLG - Siltstone**	**Red Hot Zone**	**Ab2/K–Fe3/K–Fe4**
M612932/10CQA-1726	**TLG - Siltstone**	**Red Hot Zone**	**Ab2/K–Fe3/K–Fe4**
M612933/10CQA-1724	TLG - Siltstone	Frank's zone	Ab2/K–Fe3/K–Fe4
M612934/10CQA-1727	TLG - Siltstone	Frank's zone	K–Fe4/Cb
N249993/10CQA-1677	TLG - Siltstone	East of Red Hot Zone	Ab2
N249994/10CQA-1626	Tectono-hydrothermal breccia	East of Red Hot Zone	Ab2/Tur1
N249995/10CQA-1687	FG - Aphanitic rhyolite	Frank's zone	K/Tur1
N249996/10CQA-1688	TLG - Siltstone	Frank's zone	Ab2
N249997/10CQA-1689	TLG - Siltstone	Frank's zone	Ab2/HT Ca–Fe
N249998/10CQA-1690	TLG - Siltstone	Frank's zone	Ab2/K–Fe3/K–Fe4
N249999/10CQA-1691	TLG - Siltstone	West of Frank's	Ab2/K–Fe3/K–Fe4
N250000/10CQA-1698	TLG - Siltstone	NICO - Southern Breccia transition zone	Ab2/Ca-Fe±K1/Hem1

Samples in bold are U-mineralized; FG = Faber Group, TLG = Treasure Lake Group

Sample	C1665B02	C1665B04	C1665D03	C1666-M612910	C1705-M612913	C1705-M612914	C1690-N249998	P012E01	P012E03	P012E04
Rock type	Msilt	Msilt	Msilt	Msilt	Msilt	Msilt	Msilt	Msilt	Msilt	Msilt
Alteration	Ab2/K-Fe3/K-Fe4	Ab2/K-Fe3/K-Fe4	Ab2/K-Fe3/K-Fe4	Ab2/K-Fe3/K-Fe4	Ab2/K-Fe3/K-Fe4	Ab2/K-Fe3/K-Fe4	Ab2/K-Fe3/K-Fe4	Ab2/K-Fe3/K-Fe4	Ab2/K-Fe3/K-Fe4	Ab2/K-Fe3/K-Fe4
Lab	ALS	ALS	ALS	ALS	ALS	ALS	ALS	ALS	ALS	ALS
Zone	Frank's	Frank's	Frank's	Frank's	Frank's	Frank's	Frank's	Red Hot	Red Hot	Red Hot
SiO_2 (wt. %)	N.A.	N.A.	N.A.	N.A.	N.A.	N.A.	N.A.	N.A.	N.A.	N.A.
TiO_2	0.55	1.42	0.50	0.66	0.4	0.61	1.42	0.65	0.72	0.66
Al_2O_3	16.74	15.99	15.93	15.8	16.4	15.85	17.21	16.86	16.74	16.71
Fe_2O_3(t)	7.13	4.13	9.39	7.11	9.21	10.01	5.75	7.11	5.1	4.9
MgO	0.53	0.70	0.50	0.78	0.78	0.76	0.63	1.06	0.28	1.03
MnO	0.03	0.02	0.03	0.04	0.04	0.06	0.04	0.02	0.02	0.02
CaO	0.45	0.49	0.41	0.48	1.37	0.42	0.53	0.46	0.34	0.59
Na_2O	9.07	8.52	8.64	8.99	8.63	8.16	9.31	7.97	9.41	8.49
K_2O	0.28	0.47	0.31	0.29	0.31	0.36	0.73	1.46	0.47	1.46
P_2O_5	0.10	0.11	0.17	0.15	0.88	0.12	0.05	0.05	0.05	0.05
LOI	N.A.	N.A.	N.A.	N.A.	N.A.	N.A.	N.A.	N.A.	N.A.	N.A.
S	0.73	0.18	1.89	0.02	1.05	3.16	1.02	0.62	0.12	0.14
Total	N.A.	N.A.	N.A.	N.A.	N.A.	N.A.	N.A.	N.A.	N.A.	N.A.
Ba (ppm)	20	20	30	30	20	30	30	80	40	90
Be	5.09	2.12	2.75	2.63	4.83	2.01	2.79	3.4	3.71	4.27
Cr	65	101	42	65	76	59	99	60	41	81
Cs	0.18	1.32	0.26	0.09	0.31	0.47	2.7	7.9	1.3	7.35
Ga	31.8	33.9	29.6	32.6	36.9	29.9	30.7	33.3	31	31.5
Ge	0.33	0.41	0.32	0.29	0.39	0.24	0.3	0.65	0.45	0.39
Hf	4.9	8.7	4.3	4.9	3.7	3.9	7.2	6.2	7.7	6.4
In	0.016	0.026	0.032	0.011	0.022	0.019	0.038	0.033	0.018	0.024
Li	4.1	4.8	5.3	6.6	7	8.3	5.9	7.8	4.2	7.5
Nb	20.3	114	20.3	26.7	12.8	18.1	43.8	20.9	37.2	21.8
Rb	9.7	40.6	14.4	13	15.9	19.9	61.3	172	29.4	162.5
Re	0.003	0.007	0.013	0.004	0.004	0.002	0.166	0.009	<0.002	0.002
Sb	0.86	0.9	0.87	0.88	1.23	1.57	1.27	8.94	4.25	2.85
Sc	N.A.	N.A.	N.A.	N.A.	N.A.	N.A.	N.A.	N.A.	N.A.	N.A.
Se	6	9	6	4	5	5	8	8	6	4
Sn	11.2	52.6	10.6	15.7	11.2	14.6	18.2	10.3	8.6	9.7
Sr	20.1	15.7	13.7	17.9	21.3	22.4	18.6	32	18.4	36.1
Ta	1.37	13.15	1.29	1.92	0.89	1.07	3.32	1.76	3.83	1.92
Te	0.08	0.1	0.35	0.08	0.12	0.19	0.63	0.94	0.14	0.09
Th	88.9	174	71.4	148	162	33.8	28.7	880	369	224
Tl	0.05	0.11	0.09	0.05	0.07	0.09	0.25	0.46	0.08	0.4
U	880	1690	860	2000	1460	560	138	7770	3170	1730
V	85	78	64	84	109	66	86	86	61	67
Zr	153.5	250	143.5	176	139.5	141.5	247	231	259	208
Ag	0.19	0.1	0.77	0.15	0.2	0.2	1.57	0.11	0.04	0.04
As	13.1	8.6	89.5	10.1	21.3	34.7	14.1	51.6	17.9	14.8
Bi	1.9	0.6	3.3	0.8	3.6	3.9	2.5	2.4	0.9	0.7
Co	5.7	1.5	11.9	2.9	9.8	72.4	35	10.8	4.9	8.8
Cu	71.5	22.7	512	3.4	150	280	157	171	96.1	79.8
Mo	7.5	9.6	142	12.2	4.9	3.3	4980	18.8	2.4	3.8
Ni	37.6	50.2	110	9.2	62.2	156	16.9	17.1	2.9	6.2
Pb	279	535	303	587	476	162	47.9	2590	1010	547
W	8	23	10	21	6	8	15	8	9	7
Zn	56	12	75	53	79	87	12	8	4	7

Msilt= Metasiltstone Gran = Granite Po = Porphyritic Rhy = Rhyolite Msed=Metasedimentary rock
Mineral abbreviations after Whitney and Evans (2010)

SAMPLE	P526D03	P526D04	P011F02	C1142B02	C1242G01	C1242C10	C1661B02	P519B01	C0445B1	C0478F
Rock type	Msilt	Msilt	Msilt	Early gran (1873 Ma)	Po Gran	Po Rhy dyke	Rhy	Rhy	Rhy	Rhy
Alteration	Ab2/Fe-Mg1	Ab2/Fe-Mg1	Kfs/Fe-Mg1	Ab2	Ab2	Kfs	Kfs	Kfs	Kfs	Kfs
Lab	ALS	ALS	ALS	INRS	INRS	INRS	INRS	INRS	INRS	INRS
Zone	Lou Lk.	Lou Lk.	Eastern	S zone A	Zone A	Zone A	S Frank's	Eastern	NICO	NICO
SiO_2 (wt. %)	N.A.	N.A.	N.A.	72.75	76.00	69.80	73.69	70.30	72.70	72.80
TiO_2	0.53	0.59	0.07	0.26	0.12	0.05	0.04	0.04	0.14	0.05
Al_2O_3	14.67	12.21	15.08	16.10	13.16	13.36	12.45	12.70	12.22	11.64
Fe_2O_3(t)	6.39	12.77	9.38	0.84	0.64	0.99	1.19	2.77	2.14	1.80
MgO	2.90	1.54	3.55	0.17	0.04	0.26	0.24	0.31	0.36	0.55
MnO	0.08	0.05	0.03	0.01	< 0.003	0.01	0.02	0.01	0.02	0.02
CaO	0.52	0.32	0.17	0.35	0.17	0.31	0.15	0.06	0.21	0.79
Na_2O	7.18	6.52	0.27	7.58	6.37	1.42	1.21	0.19	0.68	0.19
K_2O	0.51	0.16	4.75	1.39	1.59	9.64	8.87	11.07	10.54	10.55
P_2O_5	0.06	0.05	0.05	< 0.08	< 0.01	0.04	0.01	0.05	< 0.05	< 0.07
LOI	N.A.	N.A.	N.A.	0.40	0.20	0.50	0.30	0.40	0.40	0.90
S	0.02	<0.01	0.01	0.03	0.01	0.00	< 0.01	0.00	< 0.01	< 0.013
N.A.	N.A.	N.A.	N.A.	100.00	98.30	96.50	98.30	98.00	99.60	99.50
Ba (ppm)	50	20	860	114	89	1047	1096	1240	1088	1045
Be	9.75	2.92	5.29	N.A.	N.A.	N.A.	N.A.	N.A.	N.A.	N.A.
Cr	66	54	12	147	17	34	12	5	311	
Cs	0.43	0.16	1.06	0.3	< 0.2	0.3	< 0.3	0.9	2.0	2.1
Ga	19.7	15.6	17.05	N.A.	N.A.	N.A.	N.A.	N.A.	N.A.	N.A.
Ge	0.91	0.39	0.29	N.A.	N.A.	N.A.	N.A.	N.A.	N.A.	N.A.
Hf	4.9	4	5.2	5.8	5.0	3.3	3.0	3.9	3.6	3.3
In	0.174	0.016	0.024	< 0.3	< 0.5	< 0.6	< 0.6	< 0.3	N.A.	N.A.
Li	40.6	12.1	33.2	N.A.	N.A.	N.A.	N.A.	N.A.	N.A.	N.A.
Nb	19.7	15.9	11.8	14.4	6.0	12.8	7.6	12.5	9.6	9.1
Rb	6.9	2.7	112	18	20	235	303	338	294	278
Re	0.004	0.003	0.002	N.A.	N.A.	N.A.	N.A.	N.A.	N.A.	N.A.
Sb	54.7	2.48	5.33	N.A.	N.A.	N.A.	N.A.	N.A.	N.A.	N.A.
Sc	N.A.	N.A.	N.A.	4.6	1.8	3.4	2.9	5.0	2.2	2.7
Se	6	3	2	N.A.	N.A.	N.A.	N.A.	N.A.	N.A.	N.A.
Sn	15.7	13.2	8	< 5	3.0	4.0	2.5	1.9	13.6	8.5
Sr	68	26.4	16.5	31	20	22	40	11	31	29
Ta	1.1	0.95	1.6	1.89	0.33	1.43	1.73	1.80	2.04	2.49
Te	1.06	<0.05	0.97	N.A.	N.A.	N.A.	N.A.	N.A.	N.A.	N.A.
Th	13.5	16.3	27.3	28.2	19.0	21.0	24.0	27.1	33.2	32.0
Tl	0.08	<0.02	0.64	N.A.	N.A.	N.A.	N.A.	N.A.	N.A.	N.A.
U	>10000	262	3090	5.6	3.6	7.1	14.3	4.9	13.0	19.7
V	61	100	42	7.0	2.8	2.4	3.6	8.0	33.2	
Zr	153	129.5	139	201	162	99	101	111	100	88
Ag	0.12	0.18	0.18	< 0.2	< 0.3	< 0.4	< 0.4	0.22	< 2	< 2
As	192	5.1	129	< 40	< 30	< 30	< 10	< 20	5	21
Bi	1490	30.3	3.7	2	< 1.1	< 1.3	< 1.2	< 0.5	0.2	1
Co	124.5	9.2	34.8	< 8	< 5	< 5	< 5	1	2	5
Cu	39.6	8.5	8.7	51	35	< 3	11	49	6	8
Mo	0.6	0.2	1.4	< 9	< 20	< 20	< 4	< 0.5	20	5
Ni	19	20.6	15.9	< 20	< 8	< 8	< 9	7	8	3
Pb	564	17.4	176	6.4	3.1	1.7	26.2	0.8	12	5
W	9	11	4	6	4	3	< 1.2	6	2	2
Zn	66	52	49	< 10	< 10	17	21	10	9	10

Msilt= Metasiltstone Gran = Granite Po = Porphyritic Rhy = Rhyolite Msed=Metasedimentary rock
Mineral abbreviations after Whitney and Evans (2010)

SAMPLE	C1141C03	C1143A02	C1622F03	P524A01	P010A01	C1243-M612925	C1615G02	M612927	C1643A02	C1702-M612906
Rock type	Bt Po Dyke	Fp-Bt Po Dyke	Fp-Bt Po Dyke	Monzo (1867 Ma)	Msilt	Msilt	Bx	Msilt	Msilt	Msilt
Alteration	K-Fe		Least altered	Least altered	K-Fe1/Ab1	K-Fe1/Ab1	K-Fe2	K-Fe2	Ab2	Ab2
Lab	INRS	INRS	INRS	INRS	INRS	INRS	INRS	INRS	INRS	INRS
Zone	Zone A	East NICO	Red Hot	W Lou Lk.	Eastern	Eastern	Zone A	Zone A	W Red Hot	W Red Hot
SiO_2 (wt. %)	60.11	63.79	64.48	62.60	60.22	61.74	11.45	20.31	64.61	65.70
TiO_2	0.56	0.54	0.33	0.54	0.60	0.76	0.19	0.20	1.07	0.40
Al_2O_3	16.00	15.60	14.96	15.70	14.60	17.56	2.03	5.30	18.81	19.00
Fe_2O_3(t)	9.30	7.46	5.36	4.52	11.76	5.55	80.70	69.70	2.94	2.42
MgO	2.27	2.09	1.20	2.19	0.88	1.26	1.17	0.90	0.13	0.11
MnO	0.02	0.02	0.02	0.02	0.02	0.02	0.04	0.03	0.02	0.01
CaO	0.63	0.43	0.64	2.79	0.28	0.26	0.02	0.07	0.38	0.22
Na_2O	2.74	2.90	2.93	3.05	2.74	2.90	0.04	0.39	10.04	10.70
K_2O	7.87	6.81	7.36	4.37	7.97	9.69	1.28	3.93	0.50	0.36
P_2O_5	0.16	0.11	0.10	0.13	0.10	0.11	< 0.01	0.03	0.04	0.04
LOI	0.80	0.90	0.70	1.77	0.00	0.51	-2.21	-1.53	0.18	0.61
S	0.19	< 0.01	< 0.01	0.03	0.01	0.02	< 0.01	0.02	0.02	0.13
Total	100.80	100.80	98.20	99.34	98.01	99.72	100.59	99.35	98.80	99.70
Ba (ppm)	1169	1128	837	836	1160	1360	87	474	39	14
Be	N.A.	N.A.	N.A.	N.A.	N.A.	N.A.	N.A.	N.A.	N.A.	N.A.
Cr	66	114	26	22	94	98	68	60	81	40
Cs	2.7	1.7	3.1	1.8	3.7	7.8	1.9	1.8	< 0.3	0.2
Ga	N.A.	N.A.	N.A.	N.A.	N.A.	N.A.	N.A.	N.A.	N.A.	N.A.
Ge	N.A.	N.A.	N.A.	N.A.	N.A.	N.A.	N.A.	N.A.	N.A.	N.A.
Hf	4.0	4.6	3.6	7.3	4.5	4.5	3.1	3.6	6.0	5.6
In	< 0.4	0.3	< 0.5	< 0.3	< 0.3	< 0.3	< 0.6	< 0.3	< 0.6	< 0.3
Li	N.A.	N.A.	N.A.	N.A.	N.A.	N.A.	N.A.	N.A.	N.A.	N.A.
Nb	10.7	12.7	10.9	13.8	13.4	14.8	3.4	4.2	39.1	13.9
Rb	308	173	255	200	233	390	105	138	12	9
Re	N.A.	N.A.	N.A.	N.A.	N.A.	N.A.	N.A.	N.A.	N.A.	N.A.
Sb	N.A.	N.A.	N.A.	N.A.	N.A.	N.A.	N.A.	N.A.	N.A.	N.A.
Sc	17.6	11.7	8.9	11.0	16.3	21.7	16.9	16.5	6.3	5.6
Se	N.A.	N.A.	N.A.	N.A.	N.A.	N.A.	N.A.	N.A.	N.A.	N.A.
Sn	10.1	< 7	5.5	3.5	16.5	14.3	4	15.9	9.4	3.4
Sr	62	36	48	230	34	31	4	12	15	11
Ta	1.10	1.22	1.16	1.30	1.11	1.44	0.75	0.40	2.10	1.02
Te	N.A.	N.A.	N.A.	N.A.	N.A.	N.A.	N.A.	N.A.	N.A.	N.A.
Th	14.9	24.6	20.0	23.0	15.7	19.0	2.3	7.6	27.0	15.4
Tl	N.A.	N.A.	N.A.	N.A.	N.A.	N.A.	N.A.	N.A.	N.A.	N.A.
U	5.8	5.0	7.6	6.1	3.2	14.8	1.4	1.6	5.7	4.5
V	152.0	86.0	45.0	55.0	89.8	108.6	610.8	455.6	29.3	26.4
Zr	146	190	144	274	176	160	115	124	239	192
Ag	0.2	0.2	< 0.3	0.4	0.3	0.24	< 0.4	< 0.17	< 0.4	0
As	< 40	< 40	< 10	< 20	< 20	30	< 10	< 30	64	< 30
Bi	< 0.7	0.6	< 1	< 0.5	< 0.6	< 0.6	< 1.3	< 0.6	< 1.3	0.7
Co	11	< 8	< 5	12	2	4	39	14	< 5	2
Cu	7	9	< 1	32	7	11	< 1	< 9	15	78
Mo	< 9	< 9	< 4	< 0.5	< 0.6	1	< 4	1	< 4	3
Ni	22	29	12	7	15	40	23	12	34	11
Pb	6.2	5.8	8.9	7.1	3.1	10.3	1.4	2.2	2.4	2.4
W	3	2	3	3	22	9	< 1.3	1	22	26
Zn	14	40	13	31	7	12	81	52	3	< 5

Msilt= Metasiltstone Gran = Granite Po = Porphyritic Rhy = Rhyolite Msed=Metasedimentary rock
Mineral abbreviations after Whitney and Evans (2010)

SAMPLE	P511D01	P511G01	P017C01	P526B01	C0459A	C0460A	C0463J	C0467A	C0467D	C0467F
Rock type	Msilt	Msilt	Msilt	Msilt	Msed	Msed	Po	Msed	Msed	Msed
Alteration	Ab2/K-Fe3/Ca-Fe±K1/K-Fe4	Ab2/Ca-Fe±K1/K-Fe4	Ab2/K-Fe3	Ab2/Fe-Mg-K1	Ca-Fe (HT)	Ca-Fe (HT)	Ca-Fe (HT)	Ca-Fe (HT)	Ca-Fe (HT)	Ca-Fe (HT)/K-Fe (HT-LT)
Lab	INRS	INRS	INRS	INRS	INRS	INRS	INRS	INRS	INRS	INRS
Zone	NW Frank's	NW Frank's	Frank's West	Lou Lk.	NICO	NICO	NICO	NICO	NICO	NICO
SiO_2 (wt. %)	60.450	56.43	65.35	61.98	37.96	36.30	42.98	42.33	41.83	30.80
TiO_2	0.711	0.68	0.06	0.44	0.33	0.30	0.36	0.32	0.35	0.30
Al_2O_3	15.46	8.36	18.33	16.58	6.53	6.31	7.29	5.83	6.58	5.20
Fe_2O_3(t)	5.19	10.78	3.84	3.23	36.31	36.04	28.63	28.06	33.80	41.54
MgO	1.55	7.19	0.19	1.71	3.83	5.81	5.81	6.70	3.62	13.84
MnO	0.03	0.15	0.00	0.07	0.36	0.36	0.20	0.21	0.21	0.07
CaO	1.95	8.02	0.17	3.44	11.71	10.85	8.17	8.93	9.45	2.66
Na_2O	7.64	1.98	9.71	7.15	0.80	0.46	0.24	0.52	0.76	0.05
K_2O	1.42	3.40	1.14	2.53	1.72	2.86	5.03	2.39	1.96	4.35
P_2O_5	0.15	0.08	0.00	0.09	0.06	0.07	0.07	0.06	< 0.07	0.06
LOI	1.13	1.22	0.41	0.92	-0.30	0.63	0.93	0.03	-0.18	0.44
S	0.22	0.06	0.02	0.02	0.18	0.23	0.24	0.28	0.25	0.05
Total	96.24	98.47	99.33	98.29	100.03	100.39	100.03	98.23	99.38	99.48
Ba (ppm)	32	58	30	509	29	77	86	45	51	33
Be	N.A.	N.A.	N.A.	N.A.	N.A.	N.A.	N.A.	N.A.	N.A.	N.A.
Cr	158	101	14	54	32	30	31	49	76	37
Cs	1.1	0.8	0.3	0.2	0.4	23.3	< 30	17.6	9.2	19.6
Ga	N.A.	N.A.	N.A.	N.A.	N.A.	N.A.	N.A.	N.A.	N.A.	N.A.
Ge	N.A.	N.A.	N.A.	N.A.	N.A.	N.A.	N.A.	N.A.	N.A.	N.A.
Hf	5.2	6.2	13.8	4.4	3.6	3.1	2.8	4.1	4.1	3.5
In	< 0.3	0.4	< 0.3	< 0.3	N.A.	N.A.	44.3	N.A.	N.A.	N.A.
Li	N.A.	N.A.	N.A.	N.A.	N.A.	N.A.	N.A.	N.A.	N.A.	N.A.
Nb	27.4	41.7	2.3	13.2	7.0	6.3	7.1	7.5	9.5	6.4
Rb	71	157	22	83	24	315	857	291	120	451
Re	N.A.	N.A.	N.A.	N.A.	N.A.	N.A.	N.A.	N.A.	N.A.	N.A.
Sb	N.A.	N.A.	N.A.	N.A.	N.A.	N.A.	N.A.	N.A.	N.A.	N.A.
Sc	18.9	23.7	1.5	10.9	6.7	6.3	9.5	6.3	7.7	5.7
Se	N.A.	N.A.	N.A.	N.A.	N.A.	N.A.	N.A.	N.A.	N.A.	N.A.
Sn	36	16.6	1.9	14.8	21.3	13.6	0.6	16.8	24.0	6.6
Sr	12	16	14	188	11	14	16	8	7	5
Ta	1.47	1.30	0.19	1.29	0.68	0.52	0.90	0.57	0.65	0.50
Te	N.A.	N.A.	N.A.	N.A.	N.A.	N.A.	N.A.	N.A.	N.A.	N.A.
Th	32.4	52.0	10.5	20.0	10.42	7.6	7.3	8.3	8.1	8.5
Tl	N.A.	N.A.	N.A.	N.A.	N.A.	N.A.	N.A.	N.A.	N.A.	N.A.
U	13.2	50.7	3.9	6.1	5.9	87.1	23.2	11.0	3.2	2.5
V	88.8	273.4	23.0	51.8	36.8	41.6	45.4	35.7	40.3	36.6
Zr	191	241	517	161	106	101	86	163	158	135
Ag	0.3	0.4	1	0.23	< 2	< 2	< 2	< 2	< 2	< 2
As	45	27	82	< 20	443	479	14	9655	336	537
Bi	2.4	1.5	< 0.6	< 0.6	3983	268	6	3587	1636	17
Co	16	27	30	10	77	94	14	7832	96	11
Cu	2084	16	253	97	456	314	390	600	204	1
Mo	1	5	2	< 0.6	0.8	8	0.7	65	3	0.8
Ni	32	42	41	22	10	24	23	81	8	9
Pb	3.1	18.7	1.8	8.2	11	3	3	5	2	0.8
W	360	3	1030	2	0.8	25	0.7	2948	4821	1
Zn	23	29	40	75	23	25	35	20	16	14

Msilt= Metasiltstone Gran = Granite Po = Porphyritic Rhy = Rhyolite Msed=Metasedimentary rock
Mineral abbreviations after Whitney and Evans (2010)

SAMPLE	C0478A	C0480G1	C0480O2	C0480V2A
Rock type	Msed	Msed	Msed	Msed
Alteration	K/Ca-Fe (HT)/K-Fe (LT)	Ca-Fe (HT)	Ca-Fe (HT)	Ca-Fe (HT)
Lab	INRS	INRS	INRS	INRS
Zone	NICO	NICO	NICO	NICO
SiO_2 (wt. %)	48.59	44.41	43.00	33.05
TiO_2	0.42	0.27	0.38	0.28
Al_2O_3	8.66	5.89	7.09	5.71
Fe_2O_3(t)	19.72	29.82	32.29	48.78
MgO	7.34	4.54	3.35	3.13
MnO	0.16	0.19	0.17	0.13
CaO	6.87	10.74	9.52	5.18
Na_2O	0.47	0.92	0.88	0.64
K_2O	5.69	1.62	1.65	2.56
P_2O_5	0.07	0.06	0.06	0.05
LOI	1.59	0.20	0.14	-0.76
S	0.02	0.24	0.19	0.05
Total	99.69	98.94	99.45	98.79
Ba (ppm)	454	43	44	96
Be	N.A.	N.A.	N.A.	N.A.
Cr	43	28	82	61
Cs	20.2	1.4	0.4	29.7
Ga	N.A.	N.A.	N.A.	N.A.
Ge	N.A.	N.A.	N.A.	N.A.
Hf	3.1	2.7	2.8	2.4
In	N.A.	N.A.	N.A.	N.A.
Li	N.A.	N.A.	N.A.	N.A.
Nb	10.1	6.0	11.8	5.1
Rb	460	41	23	32
Re	N.A.	N.A.	N.A.	N.A.
Sb	N.A.	N.A.	N.A.	N.A.
Sc	9.9	7.9	11.2	6.5
Se	N.A.	N.A.	N.A.	N.A.
Sn	15.1	21.7	35.2	19.5
Sr	26	7	11	7
Ta	0.78	0.40	0.76	0.50
Te	N.A.	N.A.	N.A.	N.A.
Th	8.2	6.9	11.1	6.1
Tl	N.A.	N.A.	N.A.	N.A.
U	2.3	11.6	8.6	9.1
V	57.1	53.3	49.8	48.4
Zr	109	103	106	80
Ag	< 1	< 2	< 3	< 2
As	7	4	193	36
Bi	3	49	1729	29
Co	13	23	205	59
Cu	6	97	357	22
Mo	21	0.6	4	7
Ni	25	18	23	22
Pb	0.9	2	5	1
W	< 75	0.6	5044	16
Zn	24	23	26	17

Msilt= Metasiltstone Gran = Granite Po = Porphyritic Rhy = Rhyolite Msed=Metasedimentary rock
Mineral abbreviations after Whitney and Evans (2010)

Sample	C1665B02	C1665B04	C1665D03	C1666-M612910	C1705-M612913	C1705-M612914	C1690-N249998	P012E01	P012E03	P012E04
La	65.1	122	74.5	63.3	151	16.5	50.7	52.8	33.9	24.8
Ce	149	278	163	161	360	43.2	109	230	117	80
Pr	N.A.	N.A.	N.A.	N.A.	N.A.	N.A.	N.A.	N.A.	N.A.	N.A.
Nd	N.A.	N.A.	N.A.	N.A.	N.A.	N.A.	N.A.	N.A.	N.A.	N.A.
Sm	N.A.	N.A.	N.A.	N.A.	N.A.	N.A.	N.A.	N.A.	N.A.	N.A.
Eu	N.A.	N.A.	N.A.	N.A.	N.A.	N.A.	N.A.	N.A.	N.A.	N.A.
Gd	N.A.	N.A.	N.A.	N.A.	N.A.	N.A.	N.A.	N.A.	N.A.	N.A.
Tb	N.A.	N.A.	N.A.	N.A.	N.A.	N.A.	N.A.	N.A.	N.A.	N.A.
Dy	N.A.	N.A.	N.A.	N.A.	N.A.	N.A.	N.A.	N.A.	N.A.	N.A.
Ho	N.A.	N.A.	N.A.	N.A.	N.A.	N.A.	N.A.	N.A.	N.A.	N.A.
Er	N.A.	N.A.	N.A.	N.A.	N.A.	N.A.	N.A.	N.A.	N.A.	N.A.
Tm	N.A.	N.A.	N.A.	N.A.	N.A.	N.A.	N.A.	N.A.	N.A.	N.A.
Yb	N.A.	N.A.	N.A.	N.A.	N.A.	N.A.	N.A.	N.A.	N.A.	N.A.
Lu	N.A.	N.A.	N.A.	N.A.	N.A.	N.A.	N.A.	N.A.	N.A.	N.A.
Y	130	225	79.8	159	180	55.6	91.5	152	123	67.3

SAMPLE	P526D03	P526D04	P011F02	C1142B02	C1242G01	C1242C10	C1661B02	P519B01	C0445B1	C0478F
La	93	78.2	27.1	14.4	12.4	22.0	38.0	40.7	36.0	32.3
Ce	340	159	66.7	35.6	26.0	42.2	66.8	88.7	64.6	62.3
Pr	N.A.	N.A.	N.A.	4.5	3.0	4.7	7.1	9.3	6.4	6.9
Nd	N.A.	N.A.	N.A.	17.9	10.7	16.8	23.6	33.2	20.3	24.5
Sm	N.A.	N.A.	N.A.	4.0	1.9	2.9	4.2	6.0	3.0	4.5
Eu	N.A.	N.A.	N.A.	0.54	0.27	0.44	0.55	0.77	0.39	0.44
Gd	N.A.	N.A.	N.A.	4.3	1.5	2.4	4.0	5.2	2.4	3.4
Tb	N.A.	N.A.	N.A.	0.72	0.20	0.40	0.51	0.68	0.44	0.52
Dy	N.A.	N.A.	N.A.	5.0	1.2	2.3	3.0	4.1	2.7	3.0
Ho	N.A.	N.A.	N.A.	0.97	0.25	0.54	0.56	0.85	0.56	0.58
Er	N.A.	N.A.	N.A.	3.1	0.8	1.8	1.6	2.6	1.7	1.9
Tm	N.A.	N.A.	N.A.	0.45	0.14	0.31	0.25	0.40	0.28	0.31
Yb	N.A.	N.A.	N.A.	2.8	1.0	2.2	1.7	2.7	1.9	2.2
Lu	N.A.	N.A.	N.A.	0.35	0.18	0.38	0.28	0.42	0.34	0.41
Y	159	20.6	36.6	30.0	6.3	15.1	16.2	24.2	16.7	19.3

SAMPLE	C1141C03	C1143A02	C1622F03	P524A01	P010A01	C1243-M612925	C1615G02	M612927	C1643A02	C1702-M612906
La	37.3	75.5	34.0	50.7	35.8	20.0	15.1	38.6	5.7	2.9
Ce	73.5	146	70.8	101	71.7	43.6	34.6	79.1	14.3	6.5
Pr	8.5	15.7	7.0	10.6	7.9	4.9	3.4	8.2	1.4	0.8
Nd	33.0	56.1	24.6	38.0	28.2	19.6	11.6	29.4	5.8	3.1
Sm	6.7	9.5	4.7	6.8	5.5	4.1	1.7	4.6	1.7	0.9
Eu	1.18	1.19	0.77	1.20	0.90	0.70	0.22	0.57	0.43	0.16
Gd	6.2	6.4	4.5	6.0	4.9	3.9	1.3	3.3	2.9	1.1
Tb	0.91	0.76	0.62	0.76	0.66	0.66	0.13	0.33	0.70	0.27
Dy	6.0	4.4	3.9	4.6	3.8	4.0	0.7	1.6	5.6	2.0
Ho	1.08	0.71	0.82	0.95	0.78	0.87	0.14	0.32	1.20	0.53
Er	3.4	2.3	2.3	2.7	2.3	2.8	0.5	1.0	3.9	1.9
Tm	0.49	0.32	0.36	0.39	0.35	0.39	0.08	0.15	0.60	0.28
Yb	3.2	2.2	2.4	2.7	2.4	2.7	0.7	1.2	4.1	2.2
Lu	0.44	0.32	0.37	0.41	0.36	0.38	0.12	0.20	0.55	0.32
Y	36.0	24.0	23.0	28.2	23.9	24.9	4.9	9.9	32.0	16.3

SAMPLE	P511D01	P511G01	P017C01	P526B01	C0459A	C0460A	C0463J	C0467A	C0467D	C0467F
La	94.0	55.5	0.7	52.8	38.5	7.5	2.7	10.4	21.8	0.5
Ce	198	188	1.5	109	76.9	17.8	5.1	21.5	43.2	2.3
Pr	22.3	26.8	0.2	11.7	9.1	2.5	0.7	2.6	5.2	0.5
Nd	85.4	112	0.8	41.4	34.5	11.4	3.3	10.4	19.6	3.0
Sm	19.0	27.3	0.3	7.6	6.4	3.5	1.1	2.2	3.8	1.1
Eu	2.35	1.36	0.02	1.16	2.12	1.58	0.66	0.50	0.82	0.10
Gd	19.6	25.3	0.6	6.6	5.4	4.9	1.8	2.7	3.7	1.3
Tb	3.29	4.00	0.15	0.86	0.78	0.90	0.36	0.51	0.63	0.22
Dy	21.5	24.7	1.3	5.1	4.5	5.7	2.6	3.5	4.1	1.4
Ho	4.40	4.94	0.36	0.99	0.90	1.17	0.56	0.79	0.90	0.29
Er	12.7	14.4	1.3	2.9	2.7	3.4	1.7	2.5	2.8	0.9
Tm	1.77	2.01	0.23	0.42	0.40	0.46	0.26	0.40	0.42	0.14
Yb	10.3	11.8	1.7	2.9	2.9	3.1	1.8	3.0	2.9	1.0
Lu	1.26	1.51	0.26	0.43	0.47	0.51	0.29	0.59	0.51	0.17
Y	130	140	10.8	29.3	28.0	36.0	17.4	25.0	28.0	9.8

SAMPLE	C0478A	C0480G1	C0480O2	C0480V2A
La	25.5	38.4	161	40.0
Ce	46.7	67.8	289	70.1
Pr	5.7	8.1	34.1	8.2
Nd	21.8	30.89	130	31.3
Sm	4.5	6.0	23.5	6.3
Eu	1.44	1.20	4.35	1.18
Gd	4.0	5.6	18.6	5.5
Tb	0.59	0.89	2.32	0.75
Dy	3.3	5.1	11.0	4.0
Ho	0.67	1.00	1.95	0.76
Er	2.1	3.0	5.4	2.2
Tm	0.32	0.44	0.75	0.32
Yb	2.2	3.1	5.1	2.4
Lu	0.36	0.60	0.94	0.44
Y	20.6	30.7	58.2	22.7

ANNEXE - 7 : ÉCHANTILLONS UTILISÉS ET ANALYSES REPRÉSENTATIVES POUR LE CHAPITRE 7 : ALTÉRATIONS ET MINÉRALISATIONS DU SYSTÈME DE FAB

Les minéraux sont abbrégés suivant Whitney et Evans (2010) sauf Qtz pour quartz.

Sample	Precursor	Alteration	Alteration type	Main Hydrothermal minerals	Lab
09CQA-1158A03	Dacite porphyritic intrusion	HT K-Fe	Replacement, pervasive	Kfs-Mag	INRS-ETE, ACME/2-AF
09CQA-1158C03	Dacite porphyritic intrusion	Ca-Fe-K	Replacement, pervasive	Amp-Mag-Kfs	INRS-ETE, ACME/2-AF
09CQA-1158D03	Dacite porphyritic intrusion	HT Ca-Fe	Replacement, pervasive	Amp-Mag-Py	INRS-ETE, ACME/2-AF
09CQA-1159A03	Dacite porphyritic intrusion	HT K-Fe	Replacement, pervasive	Bt-Mag-Kfs-Chl-Py-Ccp	INRS-ETE, ACME/2-AF
09CQA-1160B02	Dacite porphyritic intrusion	HT K-Fe	Replacement, pervasive/Weak Brecciation	Bt-Mag-Kfs-Py-Ccp-Chl	INRS-ETE, ACME/2-AF
09CQA-1161A03	Granitic	Weakly altered	N/A	N/A	INRS-ETE, ACME/2-AF
10CQA-0185B02	Dacite porphyritic intrusion	Ca-Fe-K	Replacement, Pervasive	Amp-Mag-Ttn-Bt-Py	ALS/ME-MS61u, ME-MS81u, F-ELE81a, Becquerel/CL-NAA06
10CQA-0187A02	Dacite porphyritic intrusion	HT K-Fe	Replacement, pervasive/Weak Brecciation	Kfs-Mag	ALS/ME-MS61u, ME-MS81u, F-ELE81a, Becquerel/CL-NAA06
10CQA-0191B01	Dacite porphyritic intrusion	Ca-Fe-K	Replacement, Selective/Breccia filling	Amp-Mag-Kfs	ALS/ME-MS61u, ME-MS81u, F-ELE81a, Becquerel/CL-NAA06
10CQA-0192C01	Dacite porphyritic intrusion	HT K-Fe	Breccia filling/Replacement, selective	Bt-Kfs-Mag-Amp-Py-Ccp	ALS/ME-MS61u, ME-MS81u, F-ELE81a, Becquerel/CL-NAA06
10CQA-0192G02	Dacite porphyritic intrusion	HT Ca-Fe	Vein/Pervasive replacement	Amp-Mag-Ap	ALS/ME-MS61u, ME-MS81u, F-ELE81a, Becquerel/CL-NAA06
10CQA-0192I02	Porphyritic monzonite	Weakly altered	N/A	N/A	ALS/ME-MS61u, ME-MS81u, F-ELE81a, Becquerel/CL-NAA06
10CQA-0193A02	Porphyritic monzonite	Weakly altered	N/A	N/A	ALS/ME-MS61u, ME-MS81u, F-ELE81a, Becquerel/CL-NAA06
10CQA-0197B02	Dacite porphyritic intrusion	HT Ca-Fe	Replacement, pervasive/Weak Brecciation	Amp-Mag	ALS/ME-MS61u, ME-MS81u, F-ELE81a, Becquerel/CL-NAA06
10CQA-0553F05	Dacite porphyritic intrusion	HT Ca-Fe	Replacement, selective in deformation zone	Amp-Mag-Ap/Kfs	ALS/ME-MS61u, ME-MS81u, F-ELE81a, Becquerel/CL-NAA06
10CQA-0557D2	Dacite porphyritic intrusion	HT Ca-Fe	Replacement, pervasive/Weak Brecciation	Amp-Mag-Ttn	ALS/ME-MS61u, ME-MS81u, F-ELE81a, Becquerel/CL-NAA06
10CQA-0559C01	Dacite porphyritic intrusion	HT Ca-Fe	Pervasive replacement/Vein	Amp-Mag-Ap/Mag	ALS/ME-MS61u, ME-MS81u, F-ELE81a, Becquerel/CL-NAA06
10CQA-0562B02	Dacite porphyritic intrusion	HT K-Fe/HT Ca-Fe	Replacement, Pervasive	Amp-Mag/Bt-Mag-Kfs-Ccp-Py	ALS/ME-MS61u, ME-MS81u, F-ELE81a, Becquerel/CL-NAA06
10CQA-0562C02	Dacite porphyritic intrusion	HT K-Fe/HT Ca-Fe	Replacement, Pervasive	Amp-Mag/Bt-Mag-Kfs	ALS/ME-MS61u, ME-MS81u, F-ELE81a, Becquerel/CL-NAA06
10CQA-0562C05	Dacite porphyritic intrusion	HT K-Fe/HT Ca-Fe	Replacement, Pervasive	Amp-Mag/Bt-Mag-Kfs	ALS/ME-MS61u, ME-MS81u, F-ELE81a, Becquerel/CL-NAA06
10CQA-0566A02	Dacite porphyritic intrusion	Ca-Fe-K	Replacement, pervasive/Weak Brecciation	Amp-Kfs-Mag	ALS/ME-MS61u, ME-MS81u, F-ELE81a, Becquerel/CL-NAA06

Sample	Precursor	Alteration	Alteration type	Main Hydrothermal minerals	Lab
10CQA-0566C02	Dacite porphyritic intrusion	HT K-Fe	Replacement, pervasive/Weak Brecciation	Kfs-Mag-Bt-Ccp-Py	ALS/ME-MS61u, ME-MS81u, F-ELE81a, Becquerel/CL-NAA06
10CQA-0572B02	Dacite porphyritic intrusion	Weakly altered/K	Replacement, Pervasive	Kfs	ALS/ME-MS61u, ME-MS81u, F-ELE81a, Becquerel/CL-NAA06
10CQA-0572D02	Dacite porphyritic intrusion	HT K-Fe			ALS/ME-MS61u, ME-MS81u, F-ELE81a, Becquerel/CL-NAA06
10CQA-0576A01	Dacite porphyritic intrusion	K	Replacement, Pervasive	Kfs	ALS/ME-MS61u, ME-MS81u, F-ELE81a, Becquerel/CL-NAA06
10CQA-0578A02	Granitic	Weakly altered	N/A	N/A	INRS-ETE
10CQA-0579B02	Dacite porphyritic intrusion	HT Ca-Fe	Replacement, Pervasive	Amp-Mag	ALS/ME-MS61u, ME-MS81u, F-ELE81a, Becquerel/CL-NAA06
10CQA-0579E02	Dacite porphyritic intrusion	Ca-HT K-Fe	Replacement, Pervasive	Amp-Mag/Bt-Mag-Kfs	ALS/ME-MS61u, ME-MS81u, F-ELE81a, Becquerel/CL-NAA06
10CQA-0582A02	Dacite porphyritic intrusion	HT Ca-Fe	Replacement, Pervasive	Amp-Mag	ALS/ME-MS61u, ME-MS81u, F-ELE81a, Becquerel/CL-NAA06
10CQA-1249A02	Dacite porphyritic intrusion	Weakly altered/K	Replacement, pervasive	Kfs	INRS-ETE, ALS/F-ELE81a
10CQA-1250A02	Dacite porphyritic intrusion	Weakly altered/K	Replacement, pervasive	Kfs	INRS-ETE, ALS/F-ELE81a
10CQA-1252A02	Dacite porphyritic intrusion	Weakly altered/K	Replacement, pervasive	Kfs	INRS-ETE, ALS/F-ELE81a
10CQA-1254A03	Dacite porphyritic intrusion	Weakly altered/K	Replacement, pervasive	Kfs	INRS-ETE, ALS/F-ELE81a
10CQA-1256A03	Porphyritic monzonite	K	Replacement, pervasive	Kfs	INRS-ETE, ALS/F-ELE81a
CQA-06-0384A	Porphyritic monzonite	Weakly altered	N/A	N/A	INRS-ETE, CGC/Dionex
CQA-06-0388A	Dacite porphyritic intrusion	HT Ca-Fe	Replacement, Pervasive	Amp-Mag	INRS-ETE, CGC/Dionex
CQA-06-0390B	Dacite porphyritic intrusion	K	Replacement, Pervasive	Kfs	INRS-ETE, CGC/Dionex
CQA-06-0391D	Dacite porphyritic intrusion	K	Replacement, Pervasive	Kfs	INRS-ETE, CGC/Dionex
CQA-06-0391F	Dacite porphyritic intrusion	HT Ca-Fe			INRS-ETE, CGC/Dionex
CQA-06-0392B	Hydrothermal breccia	HT K-Fe	Replacement, Pervasive/Weak brecciation	Kfs-Mag-Bt-Py-Ccp-Chl	INRS-ETE, CGC/Dionex
CQA-06-0434A	Dacite porphyritic intrusion	HT K-Fe	Replacement, Pervasive/ Weak brecciation	Kfs-Bt-Mag	INRS-ETE, CGC/Dionex
CQA-06-0434C	Dacite porphyritic intrusion	HT K-Fe	Replacement, Pervasive/ Weak brecciation	Kfs-Bt-Mag	INRS-ETE, CGC/Dionex
CQA-06-0435A	Dacite porphyritic intrusion	Ca-Fe-K	Replacement, pervasive/Vein	Amp-Mag-Ap	INRS-ETE, CGC/Dionex
CQA-06-0435C	Dacite porphyritic intrusion	HT Ca-Fe/HT K-Fe	Replacement, Pervasive/Vein	Amp-Mag-Ap/Bt	INRS-ETE, CGC/Dionex
CQA-06-0435D	Dacite porphyritic intrusion	HT Ca-Fe	Replacement, Pervasive	Amp-Mag-Ap	INRS-ETE, CGC/Dionex
CQA-06-0435F	Dacite porphyritic intrusion	HT Ca-Fe	Replacement, Pervasive	Amp-Mag-Ap	INRS-ETE, CGC/Dionex

Sample	Precursor	Alteration	Alteration type	Main Hydrothermal minerals	Lab
10CQA-1257A02	Porphyritic monzonite	Weakly altered	Replacement, pervasive	Kfs	INRS-ETE, ALS/F-ELE81a
10CQA-1258A2	One Fp porphyry	Na	Replacement, pervasive	Ab	INRS-ETE, ALS/F-ELE81a
11PUA 031F01	One Fp porphyry	HT Ca-Fe/K	Replacement, pervasive	Amp-Mag/Kfs	INRS-ETE
11PUA 033B01	Porphyritic monzonite	LT Ca-Fe	Replacement, Local	Ep	INRS-ETE
11PUA 062B02	Porphyritic monzodiorite	HT K-Fe/HT Ca-Fe	Vein	Amp-Kfs	INRS-ETE
11PUA 072A02	Dacite porphyritic intrusion	HT Ca-Fe	Replacement, pervasive	Amp-Mag-Ttn	INRS-ETE
11PUA 084E03	Granitic	Weakly altered	N/A	N/A	INRS-ETE
11PUA 085A02	Dacite porphyritic intrusion	HT Ca-Fe/K	Replacement, Pervasive/Vein	Amp	INRS-ETE
11PUA 086B01	Dacite porphyritic intrusion	HT Ca-Fe	Vein	Amp-Mag-Ap	INRS-ETE
11PUA 086B02	Dacite porphyritic intrusion	HT Ca-Fe	Vein	Amp-Mag-Ap	INRS-ETE
11PUA 1000B03	Dacite porphyritic intrusion	HT K-Fe	Replacement, Pervasive	Amp-Mag	INRS-ETE
11PUA 1000C01	Dacite porphyritic intrusion	HT Ca-Fe	Replacement, Pervasive/Vein	Amp-Mag	INRS-ETE
11PUA 1000E01	Dacite porphyritic intrusion	Na	Replacement, Pervasive	Ab	INRS-ETE
11PUA 1000G01	Dacite porphyritic intrusion	HT K-Fe	Replacement, Pervasive/Vein	Kfs-Bt-Mag-Chl-Ccp-Py	INRS-ETE
11PUA 1028B01	Granitic	Weakly altered	N/A	N/A	INRS-ETE
11PUA 560A02	Undivided porphyry	Weakly altered	N/A	N/A	INRS-ETE
11PUA 566B02	Undivided porphyry	K	Replacement, Pervasive	Kfs	INRS-ETE
11PUA 601A02	Dacite porphyritic intrusion	LT Ca-Fe	Replacement, Selective	Ep-Kfs	INRS-ETE
11PUA 607A02	Porphyritic monzonite	Weakly altered	N/A	N/A	INRS-ETE
CQA-05-0248C	Dacite porphyritic intrusion	HT K-Fe	Replacement, Pervasive	Bt-Mag-Kfs	INRS-ETE, CGC/Dionex
CQA-05-0249C	Dacite porphyritic intrusion	Na-Ca-Fe	Replacement, Pervasive	Ab-Amp	INRS-ETE, CGC/Dionex

Analyses représentatives INRS

SampleID	09CQA-1158A03	09CQA-1158C03	09CQA-1158D03	09CQA-1159A03	09CQA-1160B02	09CQA-1161A03	10CQA-0185A02	10CQA-0191B01	10CQA-0192C01	10CQA-0192G02	10CQA-0192I02
SiO_2 (wt. %)	65.5	55.4	49.6	54.6	56.0	60.6	61.9	62.0	62.3	54.4	70.3
TiO_2	0.48	0.42	0.47	0.79	0.72	0.62	0.243	0.624	0.436	0.44	0.24
Al_2O_3	16.1	14	2.88	12.2	14.9	18.9	18.7	14.5	14.3	5.81	14.7
Na_2O	2.70	1.84	0.45	1.44	2.19	3.19	3.99	1.39	1.46	1.35	3.24
K_2O	7.92	4.80	0.24	7.64	7.43	5.44	9.51	8.79	9.76	0.81	5.49
Fe_2O_3(t)	5.92	10.41	17.59	15.53	12.54	5.21	3.19	5.86	7.28	12.12	2.15
CaO	1.27	2.90	10.54	1.12	1.77	2.92	0.15	3.37	2.04	10.32	1.62
MgO	1.30	8.05	15.59	3.61	3.81	1.70	0.91	2.71	1.76	14.51	0.73
MnO	0.02	0.12	0.15	0.03	0.03	0.07	0.04	0.09	0.07	0.25	0.05
P_2O_5	0.12	<0.08	0.19	0.15	0.12	0.18	0.05	<0.006	0.22	<0.006	0.05
LOI	0.80	3.00	1.90	1.60	1.60	1.90	0.77	1.14	0.92	1.81	0.82
S	<0.01	<0.01	0.01	0.13	0.22	<0.01	<0.006	0.02	0.02	0.02	<0.004
F (ppm)	1450	7300	12500	2970	4470	955		870	1000	9850	
Cl								980	850	330	
Sc	5.0	5.9	20.7	20.8	17.6	10.1	4.6	16.7	4.1	98.1	4.7
V	72	105	246	134	159	58	17	79	75	155	16
Cr	94	55	36	121	204	96	10	33	17	57	17
Co	10	<8	23	37	32	<8	<5	9	46	48	<5
Ni	27	38	73	52	102	<20	<9	9	18	60	<8
Cu	24	12	5	95	201	112	4	192	840	46	16
Pb	25.4	19.1	7.5	11.5	8.6	16.4	<0.06	23.7	38.0	10.0	20.7
Zn	23.0	132	73.0	18.0	26.0	46.0	22.5	59.3	54.0	142	45.1
As	<40	<40	<40	<30	<40	<40	<10	<30	<30	<30	<30
Ag	0.2	<0.2	<0.2	0.3	<0.2	<0.2	<0.4	<0.4	<0.4	<0.4	<0.4
Cd	<8	14	29	30	18	<8	3	8	11	22	3
Sn	8	<7	13	18	20	<7	7	16	18	29	6
W	7	4	2	4	3	167	7	2	3	8	6
Bi	<0.7	<0.7	<0.6	<0.5	<0.6	<0.7	<1.2	<1.3	<1.3	<1.4	<1.3
Rb	299	251	2.4	210	319	209	367	302	319	29.3	241
Cs	0.95	2.58	0.19	2.02	2.63	0.84	0.50	1.67	1.72	<0.3	1.20
Sr	125	101	4.0	57	94	341	39.1	132.9	97.7	51	205
Ba	1119	624	2.1	1027	1057	1368	1092	1191	1149	74	715
Zr	283	264	49	142	183	348	208	286	305	172	229
Hf	7.48	6.68	1.50	3.68	4.99	8.35	5.74	7.89	8.45	4.60	6.99
Nb	20.0	4.25	8.91	12.5	14.0	14.3	16.9	21.9	18.7	19.2	16.8
Ta	2.12	0.21	0.72	0.93	1.31	1.23	1.61	2.30	1.80	0.79	1.78
La	50.6	43.8	12.9	165	32.3	49.9	60.1	70.0	64.8	23.0	72.1
Ce	99.5	48.2	36.3	217	74.0	97.2	119	153	131	68.3	136
Pr	10.8	3.37	4.65	17.9	9.06	10.8	12.0	18.1	15.8	9.60	15.6
Nd	39.3	10.0	18.7	52.5	34.9	40.2	40.4	59.3	52.1	34.3	49.4
Sm	6.85	1.26	3.48	7.37	6.80	6.81	6.30	9.60	8.60	6.80	8.00
Eu	0.96	0.25	0.46	1.22	1.29	1.50	0.91	1.35	1.27	1.02	1.14
Gd	5.58	1.03	3.15	5.05	5.7	5.17	5.76	7.97	7.04	5.78	6.26
Tb	0.78	0.10	0.42	0.84	0.81	0.68	0.73	1.13	0.95	0.89	0.83
Dy	5.03	0.92	2.90	4.85	5.18	4.32	4.36	6.41	5.35	5.26	4.85
Ho	0.93	0.08	0.53	0.95	1.02	0.79	0.86	1.36	1.13	1.17	1.00
Er	3.00	0.60	1.77	2.82	3.09	2.47	2.47	3.65	3.07	3.09	2.72
Tm	0.43	0.10	0.26	0.43	0.46	0.37	0.38	0.56	0.46	0.49	0.42
Yb	2.81	0.70	1.89	3.01	3.01	2.32	2.58	3.70	3.21	3.39	2.87
Lu	0.37	0.09	0.32	0.46	0.44	0.31	0.40	0.58	0.50	0.61	0.42
Y	16.9	<0.3	6.9	29.0	21.0	12.0	25.0	39.0	33.0	35.0	30.0
Th	39.3	57.1	49.3	15.1	23.5	24.2	31.0	41.0	46.0	172.0	36.0
U	49.9	31.3	9.97	10.7	12.1	4.87	4.52	7.84	10.5	23.7	6.47
Sb	<70	<70	<60	<50	<60	<70	<12	15	<13	<14	<13
Te	<2	<2	<2	<1	<2	<2	<2.4	<2.5	<2.7	<3	<2.5

SampleID	10CQA-0193A02	10CQA-0197B02	10CQA-0559C01	10CQA-0576A01	10CQA-0578A02	10CQA-0579B02	10CQA-0582A02	10CQA-1249A02	10CQA-1250A02	10CQA-1252A02	10CQA-1254A03
SiO_2 (wt. %)	73.0	54.2	48.9	73.6	75.0	58.5	61.7	62.5	67.5	67.0	66.3
TiO_2	0.213	0.1984	0.244	0.21	0.11	0.76	0.81	0.75	0.44	0.50	0.48
Al_2O_3	14.2	0.531	2.56	14	12.9	14.4	15.5	15.3	15.4	16	16.1
Na_2O	3.07	0.11	0.74	2.89	2.79	3.45	2.33	2.10	2.47	2.32	2.93
K_2O	5.50	0.07	0.60	6.07	6.27	2.90	4.59	9.41	6.65	6.04	5.90
Fe_2O_3(t)	1.84	19.28	9.62	1.94	1.38	7.97	7.44	3.71	3.04	3.82	3.03
CaO	1.84	11.34	14.95	0.89	0.32	5.68	5.48	3.55	2.49	3.34	2.94
MgO	0.45	13.83	16.80	0.51	0.26	4.91	3.93	2.44	0.82	0.95	0.79
MnO	0.03	0.27	0.11	0.03	0.02	0.07	0.12	0.08	0.04	0.09	0.07
P_2O_5	0.04	0.14	4.03	0.04	0.01	0.14	0.15	<0.01	0.07	0.10	0.09
LOI	0.55	0.63	1.81	0.93	0.62	1.17	1.25	0.75	0.93	1.20	1.96
S	0.01	0.03	0.05	<0.004	<0.004	0.02	0.02	0.01	0.01	0.01	0.01
F (ppm)		3700	15000	260		3040	1190	610	940	650	1180
Cl		260	350	71		240	170				
Sc	4.2	163	7.0	4.2	2.4	20.1	19.5	22.6	5.9	6.8	6.6
V	12	294	144	13	2	139	130	55	29	32	29
Cr	22	77	<6	19	9	180	113	35	38	22	18
Co	<5	49	38	<5	<5	26	23	11	<5	<5	8
Ni	<8	52	91	<8	<8	41	173	10	23	<9	10
Cu	6	26	11	<3	14	5	30	51	3	12	27
Pb	24.5	2.9	0.3	28.3	12.7	5.4	29.9	21.0	20.7	26.9	47.6
Zn	30.9	112	26.8	40.9	<10	11.4	110	35.7	27.2	46.4	55.5
As	<30	<30	68	<30	<30	<30	<30	<10	<10	<10	<10
Ag	<0.3	<0.4	<0.3	<0.3	<0.4	<0.4	<0.4	<0.3	<0.4	<0.4	<0.4
Cd	3	30	16	3	<3	13	13	6	4	65	3
Sn	6	21	11	4	3	15	4	13	6	7	9
W	4	52	2	3	2	4	8	2	10	5	16
Bi	<1.1	<1.3	<1	<1.1	<1.3	<1.4	<1.4	<1.1	<1.2	<1.2	<1.2
Rb	218	0.9	40.8	314	371	143	223	262	302	348	285
Cs	1.60	<0.26	1.90	6.6	3.4	1.8	4.9	2.4	3.7	1.8	3.3
Sr	193.1	2.14	13.0	167	54.5	191	278	125.7	181.6	198	204
Ba	532	4.04	21	564	156.6	384	675	1113	936	1006	899
Zr	190	47	34	163	148	229	228	273	307	313	316
Hf	5.81	1.80	1.15	5.02	5.15	5.88	6.00	7.29	8.19	8.04	8.26
Nb	14.8	6.27	3.24	14.2	20.1	14.9	14.2	23.5	19.4	21.6	19.8
Ta	1.44	0.87	<0.05	1.44	1.71	1.11	1.19	1.37	1.5	2.00	1.33
La	65.0	9.00	173	68.1	41.0	36.0	47.0	65.9	54.4	61.0	61.7
Ce	124	27.4	319	131	87.0	73.2	97.0	159	107	123	120
Pr	14.1	4.00	28.2	13.5	8.80	8.40	10.8	18.7	11.6	12.6	12.9
Nd	44.3	15.4	88.5	44.4	28.6	31.4	39.0	66.6	40.2	43.8	44.8
Sm	7.10	3.90	11.5	7.00	4.80	6.30	7.10	11.9	7.00	7.60	7.70
Eu	0.90	0.53	1.49	0.79	0.43	1.29	1.24	1.40	0.99	1.10	1.13
Gd	5.53	3.71	11.1	5.71	3.79	5.87	6.31	10.6	6.23	7.18	6.81
Tb	0.79	0.66	1.31	0.79	0.54	0.91	0.95	1.5	0.91	0.98	0.98
Dy	4.40	4.10	7.31	4.50	3.30	5.33	5.41	8.44	5.28	5.67	5.51
Ho	0.95	0.94	1.55	0.92	0.71	1.09	1.08	1.67	1.05	1.17	1.08
Er	2.52	2.63	4.26	2.66	2.23	3.11	3.06	4.77	3.09	3.29	3.20
Tm	0.39	0.44	0.61	0.40	0.38	0.46	0.45	0.73	0.47	0.49	0.49
Yb	2.69	3.53	3.85	2.67	2.65	2.98	2.94	4.38	2.96	3.24	3.05
Lu	0.40	0.79	0.67	0.41	0.41	0.45	0.44	0.67	0.46	0.49	0.48
Y	28.0	29.0	51.6	27.0	21.0	32.0	32.0	50.0	31.0	34.0	33.0
Th	33.0	47.0	48.0	37.0	46.0	23.0	26.0	70.1	42.0	38.0	40.0
U	4.55	7.32	6.35	8.67	7.76	8.84	7.39	10.1	11.5	11.5	10.9
Sb	<11	<13	<10	<11	<13	<14	<14	<11	<12	<12	<12
Te	<2.3	<2.6	<2	<2.1	<2.5	<3	<3	<2.3	<2.5	<2.4	<2.4

SampleID	10CQA-1256A03	10CQA-1257A02	10CQA-1258A01	11PUA03 1F01	11PUA03 3B01	11PUA06 2B02	11PUA07 2A02	11PUA08 4E03	11PUA08 5A02	11PUA08 6B01	11PUA08 6B02
SiO_2 (wt. %)	61.9	71.7	65.6	63.4	63.8	39.7	59.3	71.8	64.1	52.3	39.5
TiO_2	0.26	0.27	0.71	0.54	0.48	0.89	0.73	0.22	0.48	0.25	0.31
Al_2O_3	18	12.9	16.6	15.5	14.9	20.1	14.5	13.6	15.1	3.1	1.3
Na_2O	0.11	2.86	7.29	2.90	2.40	0.69	2.35	3.10	2.31	1.07	0.37
K_2O	12.16	5.23	2.88	5.16	8.47	5.08	3.80	5.65	8.36	0.55	0.25
Fe_2O_3(t)	2.29	2.88	0.34	4.40	4.87	18.80	7.64	1.81	3.59	12.49	11.19
CaO	0.09	0.96	0.84	2.90	1.12	3.05	5.81	1.11	1.44	10.97	20.40
MgO	2.20	0.56	0.23	2.04	0.48	4.44	4.98	0.59	1.01	16.92	10.86
MnO	0.04	0.07	0.01	0.03	0.02	0.38	0.12	0.03	0.02	0.11	0.09
P_2O_5	0.05	0.07	<0.01	0.14	0.06	0.21	0.16	0.04	0.08	0.13	10.75
LOI	1.91	0.92	0.39								
S	<0.006	<0.006	<0.006	0.04	0.01	0.05	0.04	0.02	0.02	0.11	0.16
F (ppm)	360	1350	170								
Cl											
Sc	4.8	5.0	3.2	9.0	3.0	13.0	21.0	4.0	6.0	17.0	13.0
V	17	9	9	58	89	110	135	12	45	181	228
Cr	14	12	44	53	28	56	200	13	20	8	8
Co	16	<5	<5	15	8	33	28	3	8	62	50
Ni	<9	<9	10	23	12	32	49	<4	17	109	62
Cu	45	8	10	7	11	<7	<7	9	18	11	46
Pb	3.8	21.9	2.1	16.3	19.6	8.8	9.2	18.1	18.3	1.3	6.2
Zn	28.9	49.5	8.0	21.0	25.0	278	46.0	18.0	25.0	48.0	37.0
As	<10	<10	<10	<20	<20	<20	<20	<20	<20	<20	147
Ag	<0.4	<0.3	<0.3	0.5	0.5	0.5	0.4	0.4	0.5	<0.17	<0.15
Cd	4	4	1	2	2	8	3	<0.9	2	6	6
Sn	6	7	4	6	10	38	2	4	8	12	11
W	<1.3	5	1	4	10	10	3	9	3	<0.6	3
Bi	<1.3	<1.1	<1.1	<0.6	<0.5	<0.6	<0.5	<0.5	<0.6	<0.6	<0.5
Rb	463	281	99	265	316	393	213	310	322	26.1	14.2
Cs	1.8	3.9	<0.23	3.0	2.4	2.9	4.2	5.4	2.8	2.2	0.64
Sr	42.4	79.7	95.2	303	134	201	231	122	143	7.00	30.0
Ba	972	451	379	1115	1138	695	661	377	1192	12	11
Zr	221	202	314	340	303	326	213	206	313	88	33
Hf	6.2	5.96	7.86	8.34	8.19	9.40	5.73	6.01	8.25	2.22	0.859
Nb	16.1	13.3	18.9	15.8	21.0	24.1	14.0	18.9	20.8	7.29	11.2
Ta	1.01	0.99	2.00	1.3	2.2	2.4	1.35	2.00	2.00	0.23	0.51
La	74.5	50.3	35.0	54.5	34.7	82.1	47.6	58.9	46.6	26.3	437.0
Ce	140	98.0	90.0	107	84.0	163	96.0	118	101	51.7	850
Pr	14.5	10.6	10.3	11.1	9.70	16.6	10.1	12.2	11.0	5.87	74.5
Nd	49.6	37.1	35.3	38.7	35.3	58.0	36.7	41.0	39.4	21.1	239
Sm	8.10	6.60	5.90	6.79	7.02	9.80	6.92	7.24	7.48	4.07	32.80
Eu	1.09	0.82	0.87	1.30	1.06	0.98	1.07	0.69	1.10	0.61	3.47
Gd	6.10	5.91	5.46	5.81	6.17	8.75	6.31	6.24	6.47	4.06	30.9
Tb	0.70	0.88	0.69	0.72	0.88	1.13	0.85	0.82	0.88	0.58	3.16
Dy	3.50	5.28	4.18	4.22	5.28	6.71	5.00	4.96	5.25	3.57	17.4
Ho	0.66	1.12	0.84	0.86	1.08	1.37	1.02	1.04	1.07	0.75	3.59
Er	2.05	3.48	2.37	2.52	3.17	3.98	2.96	3.18	3.19	2.21	10.30
Tm	0.34	0.56	0.36	0.38	0.47	0.58	0.43	0.49	0.47	0.32	1.39
Yb	2.31	3.76	2.34	2.50	3.07	3.84	2.85	3.23	3.13	2.21	8.64
Lu	0.38	0.60	0.32	0.38	0.43	0.57	0.42	0.48	0.45	0.41	1.42
Y	20.0	34.0	24.0	26.4	32.7	41.5	31.0	32.7	33.6	26.4	126
Th	37.0	37.0	12.8	26.0	43.3	50.2	26.0	46.1	40.4	49.5	74.3
U	7.34	4.89	2.60	6.80	11.2	12.0	6.84	7.90	11.2	9.90	21.8
Sb	<13	<11	<11	7	<5	<6	5	<5	<6	<6	<5
Te	<2.6	<2.3	<2.3	<1.2	<1.1	<1.3	<1.1	<1	<1.1	<1.1	<1

SampleID	11PUA1000B03	11PUA1000C01	11PUA1000E01	11PUA1000G01	11PUA1028B01	11PUA560A02	11PUA566B02	11PUA601A02	11PUA607A02	CQA-05-0248C	CQA-05-0249C
SiO_2 (wt. %)	54.4	58.6	64.6	48.9	70.4	72.7	75.9	67.3	66.8	67.0	61.3
TiO_2	0.75	0.75	1.12	0.65	0.31	0.20	0.07	0.49	0.47	0.47	0.02
Al_2O_3	14.2	16.4	19	12.9	15.5	13.9	12.1	15.8	15.8	13.7	21.9
Na_2O	2.13	3.77	7.82	1.98	2.84	3.17	2.33	2.62	2.80	1.75	6.70
K_2O	7.43	3.74	3.27	5.05	5.86	5.67	6.23	5.78	5.97	7.93	3.86
Fe_2O_3(t)	16.30	9.03	1.50	21.00	2.22	1.73	1.21	3.27	3.04	7.33	3.17
CaO	1.79	4.08	1.89	2.25	1.87	1.31	0.35	2.92	2.82	0.93	3.33
MgO	3.15	4.34	0.44	3.25	0.52	0.29	0.11	0.89	0.78	1.90	0.50
MnO	0.02	0.03	0.01	0.03	0.04	0.02	0.03	0.09	0.07	0.03	0.03
P_2O_5	0.17	0.17	<0.002	0.21	0.06	0.04		0.09	0.08	0.10	<0.034
LOI										0.90	1.30
S	0.02	0.03	0.02	1.11	0.01	0.01	0.00	0.03	0.03	<0.0067	<0.0067
F (ppm)										1617	354
Cl										129	277
Sc	15.0	23.0	2.0	16.0	5.0	4.0	1.0	7.0	6.0	13.4	<0.34
V	187	135	66	163	21	13	<2	30	27	95	59
Cr	93	141	46	79	26	14	11	19	19	191	60
Co	32	23	3	221	4	2	<2	5	6	<13.3	<13.5
Ni	34	39	<4	475	6	<4	<4	6	7	<33.3	<33.7
Cu	43	35	19	1750	<7	<7	<7	<7	43	7	32
Pb	4.9	4.3	5.4	15.9	28.4	29.8	27.2	55.5	47.4	<30	<20
Zn	22.0	25.0	9.0	30.0	19.0	27.0	28.0	112	73.0	18.6	8.2
As	<20	<20	<20	<20	<20	<20	<20	<20	26	<79.9	<80.9
Ag	0.4	0.26	0.5	0.4	0.4	0.3	0.21	0.5	0.5		
Cd	6	4	2	11	1	<0.9	<0.9	1	1	<6.7	<6.7
Sn	18	7	37	17	2	2	12	5	5		
W	4	3	2	3	6	6	8	13	14		
Bi	<0.6	<0.6	<0.6	0.6	<0.6	<0.6	<0.6	<0.6	<0.6		
Rb	352	244	190	223	305	307	405	344	321	237	185
Cs	4.6	3.9	0.7	1.3	11.3	6.4	6.7	4.6	10	1.4	1.4
Sr	103	192	119	117	192	156	52.0	199	212	98.6	271
Ba	893	458	263	659	697	479	32	825	864	1401	361
Zr	217	186	323	194	250	186	121	315	328	251	392
Hf	5.62	4.78	8.78	4.9	7.23	5.65	4.96	8.24	8.61	7.00	10.0
Nb	14.4	12.6	35.8	20.5	19.9	16.7	27.3	20.5	21.0	13.0	0.5
Ta	1.27	1.11	2.5	1.07	2.10	1.77	3.15	2.10	2.00	1.30	0.03
La	51.0	56.6	15.0	39.1	70.2	69.9	47.3	62.5	62.6	53.1	4.0
Ce	110	92.0	48.4	92.0	139	136	99.0	127	128	91.7	10
Pr	11.9	9.00	7.08	10.4	14.1	13.9	11.5	13.3	13.3	9.80	1.10
Nd	43.5	32.1	33.2	37.8	47.7	46.2	40.8	45.8	45.6	31.5	4.00
Sm	8.22	6.59	11.30	6.96	8.05	7.44	8.71	8.11	7.98	6.00	0.60
Eu	1.39	1.13	2.40	1.26	1.04	0.79	0.32	1.14	1.16	0.80	0.18
Gd	7.46	6.60	11.9	6.29	7.10	6.46	7.88	7.02	7.10	4.00	0.50
Tb	0.97	0.96	2.1	0.83	0.95	0.79	1.11	0.91	0.91	0.7	0.07
Dy	5.60	6.09	12.6	5.02	5.85	4.65	6.58	5.53	5.43	4.00	0.60
Ho	1.12	1.22	2.44	1.02	1.21	0.91	1.32	1.10	1.08	0.90	0.12
Er	3.40	3.55	6.89	3.10	3.71	2.81	4.09	3.31	3.24	2.50	0.40
Tm	0.50	0.52	0.97	0.47	0.57	0.41	0.63	0.48	0.48	0.40	0.07
Yb	3.36	3.27	5.77	3.08	3.73	2.79	4.31	3.19	3.21	2.60	0.60
Lu	0.51	0.46	0.74	0.48	0.54	0.42	0.63	0.47	0.47	0.40	0.12
Y	34.8	37.3	71.3	31.2	37.8	29.4	43.3	34.5	34.2	25.0	4.00
Th	16.1	19.0	21.0	17.0	47.7	40.3	56.6	43.2	43.5	25.0	1.7
U	9.50	6.52	10.3	25.9	9.90	9.50	14.5	10.9	11.8	9.00	5.00
Sb	<6	<6	<6	<5	<6	<6	<6	7	8		
Te	<1.3	<1.2	<1.3	<1	<1.1	<1.2	<1.1	<1.3	<1.2		

SampleID	CQA-06-0384A	CQA-06-0388A1	CQA-06-0390B	CQA-06-0391D	CQA-06-0391F	CQA-06-0392B	CQA-06-0434A	CQA-06-0434C	CQA-06-0435A	CQA-06-0435C	CQA-06-0435D
SiO_2 (wt. %)	67.4	57.7	68.6	69.3	60.3	62.6	59.7	60.0	51.7	26.3	34.7
TiO_2	0.31	0.70	0.16	0.16	0.60	0.52	0.41	0.40	0.41	0.70	0.28
Al_2O_3	15.4	14.8	14.2	14.1	12.8	13.7	13.2	13.4	10.2	4.4	1.6
Na_2O	3.07	2.75	2.61	1.92	1.59	0.12	0.80	0.93	1.24	0.14	0.47
K_2O	5.27	2.90	7.21	7.34	1.55	6.87	7.99	8.78	6.26	3.54	0.74
Fe_2O_3(t)	2.80	7.30	2.50	2.40	9.20	7.00	13.90	11.20	17.10	46.80	28.30
CaO	2.91	6.16	1.08	1.29	8.52	1.43	0.49	0.51	5.20	4.10	15.20
MgO	0.84	4.29	0.30	0.35	3.32	4.07	2.05	1.55	6.80	11.18	11.29
MnO	0.10	0.14	0.10	0.08	0.58	0.19	0.08	0.05	0.06	0.06	0.06
P_2O_5	0.07	0.13	<0.034	<0.034	0.11	0.10	0.22	0.16	0.39	1.21	6.53
LOI	0.70	1.30	0.80	0.70	0.90	2.60	1.40	1.30	0.80	0.50	0.40
S	<0.0066	<0.0072	0.03	0.05	<0.0069	<0.007	0.02	0.10	<0.0071	<0.0072	0.01
F (ppm)	680	691	366	352	585	597	517	933	4825	15300	13536
Cl	434	312	121	113	802	148	213	256	507	568	283
Sc	5.5	20.5	2.2	2.2	17.6	7.0	4.3	8.0	22.2	3.2	11.8
V	25	139	<13.8	<13.8	157	96	166	119	285	1112	580
Cr	157	242	122	165	302	118	128	90	71	24	31
Co	<13.1	25	<13.8	<13.8	19	14	<14.1	16	24	48	33
Ni	<32.8	51	<34.5	<34.4	<34.5	<34.9	74	37	45	130	78
Cu	37	70	29	21	23	49	122	2070	44	18	21
Pb	44.2	29.4	44.2	61.7	30.8	<30	<30	32.7	<30	<30	<30
Zn	83.0	99.0	63.0	40.0	215	136	41.0	38.0	28.0	38.0	14.0
As	<78.8	<86.6	<82.7	<82.6	<82.8	<83.7	<84.5	<81.7	<85.2	<86.5	<81.5
Ag	<3	<3	<3	<3	<3	<3	<3	<3	<3	<3	<3
Cd	<6.6	<7.2	<6.9	<6.9	<6.9	<7	<7	<6.8	<7.1	22	13
Sn	5	3	3	4	5	34	19	15	18	10	11
W											
Bi	<2	<2	<2	<2	1.4	<2	<2	1.3	<2	<2	<2
Rb	213	98.1	296	340	63.9	245	289	268	176	305	45.7
Cs	3.6	4.5	2.6	5.5	1.8	1.6	1.9	2.3	1.2	7.4	1.2
Sr	347	221	180	240	190	109	54.0	85.0	70.0	9.0	21.0
Ba	1066	466	921	874	187	676	1322	1214	696	68	11
Zr	224	159	226	258	144	297	236	236	194	66	28
Hf	6.17	4.32	6.25	6.53	3.97	8.00	6.64	5.7	5.13	1.67	0.33
Nb	14.3	10.6	13.9	14.6	9.9	22.9	12.6	15.6	7.3	7.1	3.1
Ta	1.17	0.99	1.24	1.32	0.89	1.94	1.39	1.47	0.33	0.27	0.17
La	48.9	39.1	48.9	54.7	52.4	66.1	28.2	27.7	27.8	36.1	227
Ce	109	88.2	108	113	95.5	139	71	66	61.6	67.5	419
Pr	10.0	9.10	9.60	10.7	9.20	14.2	7.40	7.60	7.70	6.50	41.2
Nd	36.2	34.1	32.9	36.3	34.8	51.4	27.0	27.9	28.5	22.9	135
Sm	6.40	6.40	5.40	5.60	6.40	9.30	4.50	5.10	4.90	3.40	17.70
Eu	1.20	1.08	0.80	0.79	1.61	1.47	0.66	0.71	0.76	0.39	2.08
Gd	4.90	5.80	4.00	4.30	6.10	7.30	3.90	4.50	4.70	3.50	17.3
Tb	0.73	0.86	0.63	0.66	0.89	1.09	0.61	0.66	0.63	0.45	2.02
Dy	3.8	4.93	3.4	3.58	5.00	5.69	3.16	3.72	3.74	2.47	10.9
Ho	0.83	1.02	0.72	0.75	1.03	1.19	0.65	0.80	0.80	0.49	2.10
Er	2.27	2.82	2.08	2.20	2.85	3.27	1.99	2.39	2.37	1.57	6.31
Tm	0.33	0.41	0.34	0.33	0.41	0.49	0.31	0.35	0.34	0.22	0.85
Yb	2.19	2.44	2.14	2.24	2.55	3.08	1.97	2.25	2.24	1.38	5.39
Lu	0.35	0.37	0.35	0.36	0.38	0.48	0.33	0.35	0.41	0.25	1.01
Y	22.2	27.0	20.2	21.2	28.1	31.7	18.3	21.2	21.8	15.8	74.2
Th	21.1	17.3	24.1	27.1	15.49	34.3	35.3	27.7	54.6	71.4	24.1
U	5.74	6.02	6.63	7.16	5.66	9.05	88.9	69.6	12.3	6.38	8.19
Sb	<30	<40	<40	<40	<40	<40	<40	<40	<40	<40	<40
Te	<3	<3	<3	<3	<3	<3	<3	<3	<3	<3	<3

Analyses représentatives ALS

Sample	10CQA-0187A02	10CQA-0553F05	10CQA-0557D02	10CQA-0562B02	10CQA-0562C02	10CQA-0562C05	10CQA-0566A02	10CQA-0566C02	10CQA-0572B02	10CQA-0572D02	10CQA-0579E02
Ti (wt. %)	0.28	0.27	0.81	0.41	0.40	0.38	0.32	0.25	0.30	0.27	0.34
Al	7.97	6.17	3.77	6.84	7.28	6.57	7.45	6.38	7.88	7.45	6.04
Fe	9.80	11.60	8.39	4.87	6.23	13.05	2.24	14.05	2.71	5.44	13.40
Mn	0.017	0.062	0.164	0.034	0.025	0.027	0.047	0.022	0.022	0.020	0.036
Mg	0.32	2.96	5.31	2.54	2.75	3.49	1.82	0.88	0.54	0.87	3.98
Na	0.67	2.37	0.53	2.20	1.62	1.32	2.59	0.92	2.03	1.37	0.20
K	6.58	1.98	0.33	2.88	5.22	4.84	5.35	5.68	5.34	6.50	3.92
Ca	0.69	3.89	7.06	3.80	2.55	1.33	3.03	0.55	1.36	0.72	3.31
P	0.108	0.501	0.029	0.061	0.06	0.114	0.014	0.123	0.039	0.122	>1
S	<0.01	0.01	<0.01	0.01	0.01	0.01	<0.01	1.97	0.02	0.02	0.01
F (ppm)	430	3010	2620	2690	3240	6910	700	1850	1220	1850	5170
Cl	340	290	650	330	370	390	500	160	480	380	
V	73	426	131	123	120	225	54	128	34	129	207
Cr	13	29	44	145	109	145	16	9	16	10	54
Co	6.9	49.8	30.7	23.3	19.1	26.2	9.4	126	9.4	9	26.9
Ni	13.1	44.3	22.3	38.4	32.3	56.1	8.4	338	7.2	25	69.8
Cu	7.1	10.3	16.4	209	21.8	9.6	23.7	655	49.6	37.1	34.3
Pb	135	59.4	17.5	5.8	5.3	258	12.8	88.6	18.7	69.9	670
Zn	21	41	63	15	14	24	23	15	25	23	35
As	9	41	7.1	3.1	4.4	5.8	2.7	50	5.9	7	61
Se	2	2	4	2	2	2	2	15	2	2	4
Te	<0.05	<0.05	<0.05	<0.05	<0.05	<0.05	0.05	0.29	0.05	<0.05	0.06
Ag	0.25	0.16	0.38	0.11	0.07	0.14	0.10	0.33	0.06	0.15	0.19
Cd	<0.02	0.03	<0.02	<0.02	<0.02	<0.02	0.04	<0.02	0.03	0.02	<0.02
In	0.012	0.098	0.728	0.078	0.064	0.029	0.126	0.027	0.023	0.014	0.09
Sn	13.3	13.5	42.9	14.5	15.9	9.3	11.0	9.3	6.8	9.6	8.7
Mo	1.35	0.50	0.58	4.13	43.7	2.92	0.96	2.36	2.03	1.50	1.86
Re	0.002	<0.002	0.002	0.004	0.021	0.002	<0.002	0.003	<0.002	<0.002	0.003
W	24.5	2.3	6.3	2.8	1.8	2.6	3	2.7	4.8	3.3	2.1
Bi	0.23	1.24	0.77	0.16	0.17	0.06	0.47	1.17	0.40	0.65	0.78
Rb	180	71.4	24.4	97.6	294	345	156	175	281	204	171
Cs	3.35	0.76	1.55	1.88	4.77	7.46	1.32	2.04	1.77	2.09	1.48
Sr	152	122	151	168	124	65.1	105	89.6	161	111	50.7
Ba	1790	310	30	470	710	580	870	1040	950	1060	600
Zr	282	188	88.2	184	152	159	230	225	258	236	141
Hf	8.5	5.6	3.0	5.6	4.6	4.8	7.0	6.8	7.9	6.9	4.3
Nb	17.4	14.5	67.1	14.4	11.0	11.2	23.3	10.5	20.9	17.8	10.0
Ta	1.82	1.06	2.20	1.25	0.94	0.80	1.09	1.35	1.93	1.64	0.76
La	19.3	47.5	108	58.5	51.7	16.7	41.1	20.1	54.5	37.7	308
Ce	38.8	112	295	120	111	51.7	116	49.9	108	83.7	>500
Y	52.5	39.3	113	28.8	32.0	28.0	39.7	21.1	31.8	29.7	131
Th	42.6	56.2	329	20.3	19.0	27.1	38.8	37	42.2	42.6	95.7
U	460	198	45.3	10.8	10.2	770	7.7	315	11.3	227	3010
Tl	1.6	0.3	0.1	0.4	0.7	0.7	0.5	0.6	0.6	0.8	0.5
Sb	1.0	1.1	7.8	1.3	1.1	0.8	1.6	0.8	1.2	1.0	2.5
Be	0.89	7.70	8.50	1.88	2.11	1.56	4.43	0.91	3.05	1.85	1.54
Li	10.2	26.5	31.9	12.8	24.9	40.2	8.6	11.4	7.4	11.4	34.8
Ga	16.8	19.1	20.8	20.2	20.0	28.3	20.5	24.9	20.7	21.9	28.4
Ge	0.22	0.32	0.40	0.25	0.26	0.28	0.24	0.34	0.24	0.21	0.59